Springer Proceedings in Physics 189

Jeyasingh Ebenezar *Editor*

Recent Trends in Materials Science and Applications

Nanomaterials, Crystal Growth, Thin films, Quantum Dots, & Spectroscopy (Proceedings ICRTMSA 2016)

Springer

Springer Proceedings in Physics

Volume 189

The series Springer Proceedings in Physics, founded in 1984, is devoted to timely reports of state-of-the-art developments in physics and related sciences. Typically based on material presented at conferences, workshops and similar scientific meetings, volumes published in this series will constitute a comprehensive up-to-date source of reference on a field or subfield of relevance in contemporary physics. Proposals must include the following:

- name, place and date of the scientific meeting
- a link to the committees (local organization, international advisors etc.)
- scientific description of the meeting
- list of invited/plenary speakers
- an estimate of the planned proceedings book parameters (number of pages/articles, requested number of bulk copies, submission deadline).

More information about this series at http://www.springer.com/series/361

Jeyasingh Ebenezar
Editor

Recent Trends in Materials Science and Applications

Nanomaterials, Crystal Growth, Thin films, Quantum Dots, & Spectroscopy (Proceedings ICRTMSA 2016)

Springer

Editor
Jeyasingh Ebenezar
Department of Physics
Jamal Mohamed College (Autonomous)
Tiruchirappalli, Tamil Nadu
India

ISSN 0930-8989 ISSN 1867-4941 (electronic)
Springer Proceedings in Physics
ISBN 978-3-319-44889-3 ISBN 978-3-319-44890-9 (eBook)
DOI 10.1007/978-3-319-44890-9

Library of Congress Control Number: 2016954591

Printed on acid-free paper

This Springer imprint is published by Springer Nature
The registered company is Springer International Publishing AG
The registered company address is: Gewerbestrasse 11, 6330 Cham, Switzerland

Foreword 1

I am delighted to know that the Department of Physics, Jamal Mohamed College, Tiruchirappalli, had organized an International Conference on Recent Trends in Materials Science and Applications (ICRTMSA 2016) on 29th February 2016. Any conference has its aim, dissemination of knowledge, sharing of ideas, and exposure to latest trends and techniques. Judging by the overwhelming response at the conference and by the large number of papers containing the results of original research carried out by researchers and scientists, I have no doubt that this conference ICRTMSA 2016 has fulfilled its stated objectives in ample measure. The organizers have taken considerable efforts right from organizing the conference to compiling the papers presented in a nice form as a "**Springer Proceedings in Physics**." This once again reflects the high quality of research that was delivered in the conference.

This proceedings is divided into six self-sufficient parts providing relevant information on most recent topics such as nanomaterials, quantum dots, thin film, crystal growth, and spectroscopy. It combines detailed discussions on fundamentals, preparation, characterization of novel materials, and theoretical description of such complex topics as quantum dots, with good exposition of the results obtained and their excellent interpretation and identification of the plausible applications. My appreciations are due to the editor for his excellent work.

I hope that this proceedings will contribute immensely to the body of knowledge in materials science and will be a valuable reference not only to an uninitiated novice, but also to seasoned researchers in these fields.

Dr. R.V. Mangalaraja
President
Chilean Metallurgy and Materials Society
Professor and Director
Department of Materials Engineering
University of Concepcion
Concepcion, Chile

Foreword 2

The International Conference on Recent Trends in Materials Science and Applications (ICRTMSA 2016), organized on 29th February 2016, was an initiative taken by the Department of Physics, Jamal Mohamed College, Tiruchirappalli, South India, to bring together active researchers from various disciplines of materials science and enable them to showcase their state-of-the-art research results, interact with the peers in new cross-disciplinary fields, and enhance their knowledge.

I understand that more than 120 research articles were received from various parts of the world, which demonstrates the international reach of the conference. I am also given to understand that after a strict review process, characteristic of all Springer editions, 52 articles have been selected and brought out in fine print as "**Springer Proceedings in Physics**."

The book attempts to present important selected topics in materials science such as nanomaterials, quantum dots, thin film, crystal growth, and spectroscopy in such a way that it will serve as an introductory text for the undergraduate and post-graduate students in materials science, nanoscience, and technology, as well as can be used as a book of reference by the researchers in this field. Kudos to the editor and the publishers for their nice compilation.

I am sure that this book will meet the needs of updating of knowledge by students aspiring to pursue a meaningful research career in materials science.

Prof. Ajayan Vinu, FRSC, FFMAS
Professor of Nanomaterials
Future Industries Institute
Division of Information Technology
Engineering and the Environment
University of South Australia
Adelaide, Australia

Preface

In recent years, materials science has emerged as one of the most important and exciting areas of research in the fields of science, engineering, and technology. This is mainly because of the fact that materials science has led to the recognition of the fundamental similarities underlying the structures, phenomena, and properties of a wide variety of interesting and technologically important materials. The identification and development of novel materials every decade has paved the way, in a very much large measure, for the advancement of knowledge in science.

The three fundamental constituents of materials science and engineering are perhaps crystal growth, thin film fabrications, and development of nanomaterials. Development of devices for technologically important applications such as sensors, detectors, and integrated circuits for data acquisition and analysis calls for the growth of crystals of suitable size and perfection. Similarly, continued technological advances in the fields of optoelectronic, photonic, gas sensors, solar cells, etc., which have spawned many emergent cutting edge technologies were made possible with the development of thin films made from newer materials. Further, the development of various novel nanostructured materials with highly remarkable properties appears to have taken the developments in science and technology to every conceivable sphere of human endeavor.

Taking cognizance of these variegated importances of research in materials science, the Department of Physics, Jamal Mohamed College, Tiruchirappalli, South India, an autonomous A-grade college, recognized as a college with potential for excellence by the National Accreditation and Assessment Council, constituted by the University Grants Commission (UGC) of the Government of India, organized an International Conference on Recent Trends in Materials Science and Applications (ICRTMSA 2016) during 29th February 2016. This proceeding is a compendium of the materials presented in the plenary sessions, invited lectures, and papers presented at this conference. It provides an overview of materials science, starting from the experimental and theoretical methods of preparation, processing etc., for the identification of the structural changes, properties, and applications. It contains a total of 58 chapters organized into six parts (Part I–VI including "Invited and Plenary Talk").

Part I comprises of six chapters consisting of lectures delivered by the invited speakers on topics such as cavitation technology, biological applications of core shell nanoparticles, quantum dots and device fabrication, spectroscopic and quantum computation techniques, electrodepostion method for nanostructured thin film preparation, and the prospects and constraints of emerging nanotechnology.

Part II focuses on the significant advances in nanoscience and nanotechnology and covers topics including synthesis and annealing effects, and spectral, thermal, microstructural, magnetic, electrochemical, and dielectric properties of nanomaterials for wide range of applications including gas sensing, photocathode for solar cells, optical limiting, antibacterial, photocatalytic, super-capacitor electrode, optoelectronic, storage device, and window layer applications.

Part III is devoted to the studies of the electronic and optical properties related to the quantum dots, the artificial atoms. Stress is on Group II–VI and III–V ternary and quaternary semiconducting materials, as they are considered to be promising candidates due to their potential applications in short wavelength laser diodes, amplifiers, and switches. The size-dependent dots exhibit some exotic electronic and optical properties which can be applied for fabricating novel optoelectronic devices such as optical and electro-optic modulators, inter-band lasers, optical switches, optical amplifiers, and inter-subband long wavelength detectors. The experimental synthesis of the cadmium sulfide (CdS) quantum dots and their related optical properties is also discussed.

Part IV deals with the experimental understanding of surface and thin film materials, their deposition, processing and fabrication techniques, spectroscopic, surface, resistivity, AC impedance, conductivity and magnetic studies, sensing and optical properties that are used to produce optoelectronic, photonic, gas sensor, and solar cells, Li-ion battery and magneto-optic memory devices. It focuses specially on the solvent effect on the preparation and properties of thin films, preparation of nanostructured thin films for sensing application, studies on phase transformation behavior, and organic and potential material preparation for solar cell applications.

Part V discusses the synthesis and crystal growth of technologically important single crystals for nonlinear optical and electro-optic applications. In particular, it covers the synthesis, growth, spectral, thermal, mechanical, dielectric, and optical properties of organic, inorganic, and semi-organic single crystals grown by slow evaporation, top-seeded solution growth, and vertical Bridgman growth techniques, studies of the dielectric properties of organic single crystals and fluorinated anti-ferroelectric liquid crystal and ion irradiation studies on semi-organic single crystals. Also the X-ray crystallography studies of many biological compounds such as of E-methyl-2-(1,3-dimethyl-2,6-diphenylpiperidin-4-ylidene) hydrazinecarboxylate, 4-ethoxyanilinium hydrogen succinate, and 4-methoxyanilinium chloride 4-methoxy aniline crystallized by slow evaporation method are focussed. Their structures are solved and refined using full-matrix least squares technique by SHELX program package and their applications are presented.

Finally, Part VI elaborates on spectroscopy, an important tool in the field of pharmaceutical sciences. It emphasizes the structural design, highest occupied molecular orbital and lowest unoccupied molecular orbital (HOMO-LUMO),

thermodynamical parameters, etc., of some pharmaceutically and biologically active drugs using quantum computational chemistry methods and computer modeling techniques. The same chapter also discusses the theoretical and experimental evaluation of ultrasonic velocity in liquid mixtures and studies the effect of the variations in the ultrasonic velocity on the behavior of polymer systems, such as intra- and intermolecular association, dipolar interactions, complex formation, and structural changes which in turn are helpful in the production and use of polymers in pharmaceuticals and industry.

As this proceedings contains results of experimental and theoretical research, it will serve as an essential reading for a wider audience which includes students, teachers, professionals, researchers, and industrialists involved in all branches of materials science and engineering, particularly for those who are preparing for an entry into or are already associated with materials science, and nanoscience and technology.

Constructive suggestions for the betterment of the proceedings will be much appreciated and gratefully acknowledged.

Tiruchirappalli, India Jeyasingh Ebenezar

Acknowledgements

This issue of the Springer Proceedings in Physics is a compilation of the papers presented in the plenary sessions, invited lectures, and paper/poster sessions held at the "International Conference on Recent Trends in Materials Science and Applications (ICRTMSA 2016) on 29th February 2016." The articles were selected after a stringent process of refereeing by a review committee comprising national and international experts and an in-house refereeing process by the Springer Editorial Team.

Judging by the participation of a large group of scientists and researchers and the papers received, the conference is a grand success. On this occasion, I register my heartfelt thanks to the members of National Advisory Committee and Conference Organizing Committee, colleagues in the department, and well wishers for their valuable suggestions, guidance, and support. I would also like to register my gratitude to our magnanimous management of the college for granting permission and providing all the necessary support for organizing the conference.

I would like to thank all the invited speakers, each one of them an eminent person in his respective field, for having taken time out of their busy schedules for not only delivering the lecture, but also providing us an excellent handout of their talks in time. My thanks are also due to all the participants and young researchers who took part actively in the presentations and all the discussions that followed.

I would like to thank wholeheartedly all the reviewers who have conscientiously opted to review papers and have carried out an excellent job within a short span of time in spite of their pressing engagements.

I would also like to thank the Springer Publishers for having accepted our proposal and bringing out this proceedings in fine print.

Finally I would like to acknowledge the partial financial support from UGC received in the form of autonomous grant for the conduct of the conference.

Jeyasingh Ebenezar
Tiruchirappalli, India

Contents

Contributors

Abdosllam M. Abobaker Department of Communications Engineering, College of Electronic Technology, Bani Walid, Libya

S. Agilan Department of Physics, Coimbatore Institute of Technology, Coimbatore, Tamilnadu, India

Arockiasamy Ajaypraveenkumar Department of Physics, Noorul Islam Centre for Higher Education, Kumaracoil, Kanyakumari District, Tamilnadu, India; Nano Computational Laboratory, Department of Nano Technology, Noorul Islam Centre for Higher Education, Kumaracoil, Kanyakumari District, Tamilnadu, India

Z.C. Alex Department of Sensor and Biomedical Technology, School of Electronics Engineering, VIT University, Vellore, India

A. Anancia Grace Catalysis and Nanomaterials Research Laboratory, Department of Chemistry, Loyola College, Chennai, India

Mohd Anis Crystal Growth Laboratory, Department of Physics, Milliya Arts, Science and Management Science College, Beed, Maharashtra, India

B. Anitha PG and Research Department of Physics, Bishop Heber College (Autonomous), Tiruchirappalli, India

C. Annie Josphine Department of Physics, PSGR Krishnammal College for Women, Coimbatore, Tamilnadu, India

M. Arivanandhan Centre for Nanoscience and Technology, Anna University, Chennai, Tamil Nadu, India

D. Arivukarasan PG and Research Department of Physics, Bishop Heber College (Autonomous), Tiruchirappalli, India

V.M. Arivunithi Department of Physics, Pachaiyappa's College, Chennai, India

V. Arjunan Department of Chemistry, Arignar Anna Government Arts and Science College, Karaikal, India

G. Johnsy Arputhavalli Department of Physics, Karunya University, Coimbatore, Tamilnadu, India

B. Arul Prakasam Department of Chemistry, Annamalai University, Chidambaram, India

M.S. Aruna Gandhi School of Advanced Sciences, VIT University, Vellore, Tamil Nadu, India; School of Engineering, Presidency University, Bengaluru, Karnataka, India

Mohamad I. Attia Pharmaceutical Chemistry Department, College of Pharmacy, King Saud University, Riyadh, Kingdom of Saudi Arabia

D. Bakkiyaraj Research & Development Centre, Bharathiar University, Coimbatore, India

P. Bala Sundari Department of Physics, Dr.N.G.P. Institute of Technology, Coimbatore, Tamil Nadu, India

L. Balakrishnan Department of Physics, School of Advanced Sciences, VIT University, Vellore, India

N. Balamurugan GTAT Corporation, Shanghai, China

J. Balavijayalakshmi Department of Physics, PSGR Krishnammal College for Women, Coimbatore, Tamilnadu, India

H. Belmabrouk Laboratoire d'Electronique et Microélectronique, Faculté des Sciences de Monastir, Université de Monastir, Monastir, Tunisia

Ray J. Butcher Inorganic and Structural Chemistry, Howard University, Washington, USA

J. Chandrasekaran Department of Physics, Sri Ramakrishna Mission Vidhyalaya College of Arts and Science, Coimbatore, India

K. Chandrasekharan Laser and Nonlinear Optics Lab Department of Physics, National Institute of Technology Calicut, Calicut, Kerala, India

Roman Dabrowski Institute of Chemistry, Military University of Technology, Warsaw, Poland

Isha Das Department of ECE, AMET University, Chennai, India

D. David Kirubakaran PG and Research Department of Physics, Bishop Heber College (Autonomous), Tiruchirappalli, India

Suganthi Devadason Department of Physics, Hindustan University, Chennai, India

L. Devi Research and Development Centre, Bharathiar University, Coimbatore, India

Kartick Ch. Dey Department of Physics, Acharya Prafulla Chandra Roy Government College, Siliguri, WB, India

A. Dhanalakshmi Research and Development Center, Bharathiar University, Coimbatore, Tamil Nadu, India

M.C. Divyasree Laser and Nonlinear Optics Lab Department of Physics, National Institute of Technology Calicut, Calicut, Kerala, India

C.A. Duque Grupo de Materia Condensada-UdeA, Instituto de Física, Facultad de Ciencias Exactas y Naturales, Universidad de Antioquia UdeA, Medellín, Colombia

J. Ebenezar Department of Physics, Jamal Mohamed College (Autonomous), Tiruchirappalli, India

R. Ganapathi Raman Department of Physics, Noorul Islam Centre for Higher Education, Kumaracoil, Kanyakumari District, Tamilnadu, India; Nano Computational Laboratory, Department of Nano Technology, Noorul Islam Centre for Higher Education, Kumaracoil, Kanyakumari District, Tamilnadu, India

R. Ganesamoorthy Department of Chemistry, School of Advanced Sciences, VIT University, Vellore, India

A. Gayathri Department of Mathematics, SCSVMV University, Kanchipuram, India

D. Geetha Department of Physics, Annamalai University, Chidambaram, Tamil Nadu, India

S. Girivel Department of Physics, SCSVMV University, Kanchipuram, India

M.A. Gracia-Pinilla Facultad de Ciencias Físico-Matemáticas, Universidad Autónoma de Nuevo León, San Nicolás de los Garza, Nuevo León, Mexico; Centro de Investigación en Innovación y Desarrollo en Ingeniería y Tecnología, Universidad Autónoma de Nuevo León, PIIT, Apodaca, Nuevo León, Mexico

E. Gunasundari Department of Physics, School of Advanced Sciences, VIT University, Vellore, India

S. Gurulakshmi SAS, VIT University, Vellore, India; Guru Nanak College, Chennai, India

Abdulrahman Syedahamed Haja Hameed Department of Physics, Jamal Mohamed College, Tiruchirappalli, Tamil Nadu, India

S.S. Hussaini Crystal Growth Laboratory, Department of Physics, Milliya Arts, Science and Management Science College, Beed, Maharashtra, India

R. Jagan Department of Chemistry, Indian Institute of Technology Madras, Chennai, India

Joazaizulfazli Jamalis Department of Chemistry, Universiti Teknologi Malaysia, Skudai, Malaysia

B. Janarthanan Department of Physics, Karpagam University, Coimbatore, India

RO.MU. Jauhar MRDL, PG and Research Department of Physics, Pachaiyappa's College, Chennai, India

P. Jayaprakash PG and Research Department of Physics, Arignar Anna Government Arts College, Cheyyar, Tamil Nadu, India

J. Jayarubi Department of Physics, Government Arts College, Melur, Madurai, India

R. Jeba Beula Department of Physics, Karunya University, Coimbatore, India

A. Jennifer Christy PG and Research Department of Physics, Bishop Heber College (Autonomous), Tiruchirappalli, India

S.K. Jesudoss Catalysis and Nanomaterials Research Laboratory, Department of Chemistry, Loyola College, Chennai, India

A. Jeya Rajendran Advanced Materials Research Lab, Department of Chemistry, Loyola College, Chennai, Tamil Nadu, India

L. John Kennedy Materials Division, School of Advanced Sciences, Vellore Institute of Technology (VIT) University, Chennai, India

A. John Peter PG and Research Department of Physics, Government Arts College, Melur, Madurai, India

Roy Johnson Centre for Ceramic Processing, ARCI, Hyderabad, Tamilnadu, India

Linu M. Johny Department of Physics, Loyola College, Chennai, India

J. Judith Vijaya Catalysis and Nanomaterials Research Laboratory, Department of Chemistry, Loyola College, Chennai, India

A. Juliat Josephine PG and Research Department of Physics, Holy Cross College (Autonomous), Tiruchirappalli, India

Ramesh B. Kamble Department of Physics, Indian Institute of Science, Bangalore, Karnataka, India

A.S. Kamzin Ioffe Physical-Technical Institute, Russian Academy of Sciences, St. Petersburg, Russia

B. Karthikeyan Department of Physics, National Institute of Technology, Tiruchirappalli, India

Chandrasekaran Karthikeyan Department of Physics, Jamal Mohamed College, Tiruchirappalli, Tamil Nadu, India

S. Karthikeyan Madras Christian College, Chennai, India

K. Kasthuri Department of Physics, SCSVMV University, Kanchipuram, India

P. Kathirgamanathan Organic Electronics, Wolfson Centre, Brunel University, Uxbridge, UK

R. Kathirvel PG and Research Department of Chemistry, Jamal Mohamed College (Autonomous), Tiruchirappalli, Tamil Nadu, India

V. Kavitha Department of Physics, Periyar University, Salem, Tamil Nadu, India

M. Lydia Caroline PG and Research Department of Physics, Arignar Anna Government Arts College, Cheyyar, Tamil Nadu, India

S. Madeswaran SAS, VIT University, Vellore, India

J. Madhavan Department of Physics, Loyola College, Chennai, India

V. Mahesh Kumar Department of Physics, Karunya University, Coimbatore, India

Pradip Kumar Mandal University of North Bengal, Siliguri, WB, India

D. Mangalaraj Department of Nanoscience and Technology, Bharathiar University, Coimbatore, India

Ramalinga Viswanathan Mangalaraja Advanced Ceramics and Nanotechnology Laboratory, Department of Materials Engineering, University of Concepcion, Concepcion, Chile

A. Manimegalai School of Electronics Engineering, VIT University, Vellore, India

Héctor D. Mansilla Department of Organic Chemistry, Faculty of Chemical Sciences, University of Concepcion, Concepcion, Chile

M.K. Marchewka Institute of Low Temperature and Structure Research, Polish Academy of Sciences, Warsaw, Poland

Jobin Job Mathen Department of Physics, Loyola College, Chennai, India

S.R. Meher Department of Physics, School of Advanced Sciences, VIT University, Vellore, India

G. Melwin School of Advanced Sciences, VIT University, Vellore, Tamil Nadu, India

F. Michael Raj Advanced Materials Research Lab, Department of Chemistry, Loyola College, Chennai, Tamil Nadu, India

S. Mohamed Rabeek PG and Research Department of Chemistry, Jamal Mohamed College (Autonomous), Tiruchirappalli, Tamil Nadu, India

S. Mohan School of Sciences and Humanities, Vel Tech University, Chennai, India

T. Mohandas Department of Physics, Shri Angalamman College of Engineering and Technology, Trichy, India

S. Monisha N.M.S.S. Vellaichamy Nadar College, Madurai, India

A. Moses Ezhil Raj Department of Physics, Scott Christian College (Autonomous), Nagercoil, India

S. Muniyappan Department of Physics, Pachaiyappa's College, Chennai, India

P. Murugakoothan Department of Physics, Pachaiyappa's College, Chennai, India; MRDL, PG and Research Department of Physics, Pachaiyappa's College, Chennai, India

M. Nageshwari PG and Research Department of Physics, Arignar Anna Government Arts College, Cheyyar, Tamil Nadu, India

K. Nakkeeran Department of Engineering, School of Engineering, Fraser Noble Building, King's College, University of Aberdeen, Aberdeen, UK

S. Narasimman Department of Sensor and Biomedical Technology, School of Electronics Engineering, VIT University, Vellore, India

Rajesh Narayana Perumal Department of Physics, Centre for Crystal Growth, SSN College of Engineering, Kalavakkam, India

B. Natarajan Post Graduate and Research Department of Physics, Raja Doraisingam Government Arts College, Sivagangai, Tamil Nadu, India

Shanmugam Nethaji Department of Biochemistry, Marudupandiyar College, Thanjavur, Tamil Nadu, India

N.S. Nirmala Jothi Department of Physics, Loyola College, Chennai, India

D. Nithya Devi Department of Nanoscience and Technology, Bharathiar University, Coimbatore, India

Shizuyasu Ochiai Department of Electrical Engineering, Aichi Institute of Technology, Toyota, Japan

R. Padmanaban Department of Physics, SCSVMV University, Kanchipuram, India

Thangaraj Pandiyarajan Advanced Ceramics and Nanotechnology Laboratory, Department of Materials Engineering, University of Concepcion, Concepcion, Chile

M. Peer Mohamed PG and Research Department of Physics, Arignar Anna Government Arts College, Cheyyar, Tamil Nadu, India; Department of Physics, C. Abdul Hakeem College, Melvisharam, Tamil Nadu, India

G. Peramaiyan Institute of Physics, Academia Sinica, Nankang, Taipei, Taiwan

S. Periandy Department of Physics, Kanchi Mamunivar Centre for Post Graduate Studies, Puducherry, India

Jiban Podder Department of Chemical and Biological Engineering, University of Saskatchewan, Saskatoon, Canada

Surekha Podili Department of Physics, Annamalai University, Chidambaram, Tamil Nadu, India

S. Poongodi Department of Nanoscience and Technology, Bharathiar University, Coimbatore, India

P. Prabakaran Department of Physics, Loyola College, Chennai, India

M. Prakash PG and Research Department of Physics, Urumu Dhanalakshmi College, Thiruchirappalli, Tamil Nadu, India

S. Prathap Department of Physics, Arul Anandar College, Madurai, India

A. Ragu Department of Physics, Urumu Dhanalakshmi College, Tiruchirappalli, Tamilnadu, India

S. Raja Crystal Growth and Thin Film Laboratory, Department of Physics, Bharathidasan University, Tiruchirappalli, Tamil Nadu, India

Neethipathi Rajabairavi Department of Biotechnology, Selvam Arts and Science College, Namakkal, Tamil Nadu, India

Chellappan Soundar Raju Department of Botany, Vivekananda College, Madurai, Tamil Nadu, India; Department of Botany, Jamal Mohamed College, Tiruchirappalli, Tamil Nadu, India

V. Ramadas Post Graduate and Research Department of Zoology, Raja Doraisingam Government Arts College, Sivagangai, Tamil Nadu, India

K. Ramamurthi Crystal Growth and Thin Film Laboratory, Department of Physics and Nanotechnology, Faculty of Engineering and Technology, SRM University, Kattankulathur, Tamil Nadu, India

M. Ramar Academy of Scientific and Innovative Research (AcSIR), CSIR-National Physical Laboratory Campus, New Delhi, India; CSIR-Network of Institutes for Solar Energy, CSIR—National Physical Laboratory, New Delhi, India; Department of Basic Sciences, College of Fisheries Engineering, Tamil Nadu Fisheries University, Nagapattinam, Tamil Nadu, India

P. Ramesh Babu Department of Physics, School of Advanced Sciences, VIT University, Vellore, India

R. Ramesh Babu Crystal Growth and Thin Film Laboratory, Department of Physics, Bharathidasan University, Tiruchirappalli, Tamil Nadu, India

P.S. Ramesh Department of Physics (DDE Wings), Annamalai University, Chidambaram, India

S. Ramya Department of Physics, Dr.N.G.P. Institute of Technology, Coimbatore, Tamil Nadu, India

E. Ranjith Kumar Department of Physics, Dr. NGP Institute of Technology, Coimbatore, India

Brijesh Rathi Department of Chemistry, Sri Venkateswara College, University of Delhi, New Delhi, India

C. Ravi Dhas PG and Research Department of Physics, Bishop Heber College (Autonomous), Tiruchirappalli, India

S.S. Rawat Academy of Scientific and Innovative Research (AcSIR), CSIR-National Physical Laboratory Campus, New Delhi, India; CSIR-Network of Institutes for Solar Energy, CSIR—National Physical Laboratory, New Delhi, India

N. Renuka Engineering Technology and Science, Abu Dhabi Men's College, Higher Colleges of Technology, Abu Dhabi, UAE; Crystal Growth and Thin Film Laboratory, Department of Physics, Bharathidasan University, Tiruchirappalli, Tamil Nadu, India

R. Roop Kumar Birla Institute of Technology and Science, Dubai Campus, Dubai International Academic City, Dubai, United Arab Emirates

T. Roshini Department of Computer Engineering, Rochester Institute of Technology, Rochester, USA

Elizabeth Rufus Department of Sensor and Biomedical Technology, School of Electronics Engineering, VIT University, Vellore, India

Suresh Sagadevan Department of Physics, AMET University, Chennai, India

P. Sagayaraj Department of Physics, Loyola College, Chennai, India

P. Sakthivel Department of Chemistry, School of Advanced Sciences, VIT University, Vellore, India; Department of Physics, Urumu Dhanalakshmi College, Tirchy, India

K. Saminathan Department of Physics, University V.O.C College of Engineering, Anna University, Thoothukudi, Tamil Nadu, India

P. Sangeetha PG and Research Department of Physics, Arignar Anna Government Arts College, Cheyyar, Tamil Nadu, India

C. Sanjeeviraja Department of Physics, Alagappa Chettiar College of Engineering and Technology, Karaikudi, India

K. Saravanan Department of Ophthalmology, West Virginia University Eye Institute, Morgantown, WV, USA

G. Sathiyan Department of Chemistry, School of Advanced Sciences, VIT University, Vellore, India

M. Sathyanarayanan PG and Research Department of Chemistry, Jamal Mohamed College (Autonomous), Tiruchirappalli, Tamil Nadu, India

S. Sebastian PG and Research Department of Physics, St. Joseph's College of Arts and Science (Autonomous), Cuddalore, Tamilnadu, India

M. Seeni Mubarak PG and Research Department of Chemistry, Jamal Mohamed College (Autonomous), Tiruchirappalli, Tamil Nadu, India

P. Selvakumar Crystal Growth and Thin Film Laboratory, Department of Physics, Bharathidasan University, Tiruchirappalli, Tamil Nadu, India

S. Selvasekarapandian Materials Research Centre, Coimbatore, India

P. Senthil Raj PRIST University, Vallam, Thanjavur, India

K. Senthilarasan Department of Physics, Urumu Dhanalakshmi College, Tiruchirappalli, Tamilnadu, India

K. Senthilnathan Department of Physics, School of Advanced Sciences, VIT University, Vellore, Tamil Nadu, India

Appakan Shajahan Department of Botany, Jamal Mohamed College, Tiruchirappalli, Tamil Nadu, India

S. Sharmila Department of Physics, Karpagam University, Coimbatore, India

N.N. Shejwal Intelligent Materials Research Lab, Department of Physics, Dr. Babasaheb Ambedkar Marathwada University, Aurangabad, Maharashtra, India

M.D. Shirsat Intelligent Materials Research Lab, Department of Physics, Dr. Babasaheb Ambedkar Marathwada University, Aurangabad, Maharashtra, India

N.K. Siji Narendran Laser and Nonlinear Optics Lab Department of Physics, National Institute of Technology Calicut, Calicut, Kerala, India

M. Silambarasan Department of Physics, Annamalai University, Chidambaram, India

S. Siva Bala Solanki Department of Physics, Centre for Crystal Growth, SSN College of Engineering, Kalavakkam, India

R. Sivacoumar Department of Sensor and Biomedical Technology, School of Electronics Engineering, VIT University, Vellore, India

K. Sivakumar Department of Physics, Anna University, Chennai, India

Manickam Sivakumar Faculty of Engineering, Department of Chemical and Environmental Engineering, University of Nottingham Malaysia Campus, Kuala Lumpur, Selangor, Malaysia

S. Sivasanker National Centre for Catalysis Research, Indian Institute of Technology Madras, Chennai, India

T. Solaiyammal Department of Physics, Pachaiyappa's College, Chennai, India

R. Srivastava CSIR-Network of Institutes for Solar Energy, CSIR—National Physical Laboratory, New Delhi, India

S. Sudha PG and Research Department of Physics, Arignar Anna Government Arts College, Cheyyar, Tamil Nadu, India

T. Sudha Department of Physics, PSGR Krishnammal College for Women, Coimbatore, India

P. Sudhagar School of Chemistry and Chemical Engineering, Queens University, Belfast, North Ireland, UK

K. Sudhakar Department of Physics, Pachaiyappa's College, Chennai, India

C.K. Suman CSIR-Network of Institutes for Solar Energy, CSIR—National Physical Laboratory, New Delhi, India

R. Thangamuthu Electrochemical Materials Science Division, CSIR-Central Electrochemical Research Institute, Karaikudi, India

K. Thangavel Department of Electronics, SNR Sons College, Coimbatore, India

Kanika Thukral CSIR-National Physical Laboratory, New Delhi, India

C. Udhayakumar Department of Chemistry, Annamalai University, Chidambaram, India

P. Uma Mageshwari Department of Physics, Government Arts College, Melur, Madurai, India

A. Usharani Department of Physics, SCSVMV University, Kanchipuram, India

M. Vadivel Crystal Growth and Thin Film Laboratory, Department of Physics, Bharathidasan University, Tiruchirappalli, Tamil Nadu, India

Kandhan Varutharaju Department of Botany, Jamal Mohamed College, Tiruchirappalli, Tamil Nadu, India

Roy Vellaichamy Department of Physics and Materials Science, City University of Hong Kong, Kowloon, Hong Kong

P. Velusamy Crystal Growth and Thin Film Laboratory, Department of Physics, Bharathidasan University, Tiruchirappalli, Tamil Nadu, India

R. Venkatesh PG and Research Department of Physics, Bishop Heber College (Autonomous), Tiruchirappalli, India

K. Venkatramanan Department of Physics, SCSVMV University, Kanchipuram, India

M. Victor Antony Raj Department of Physics, Loyola College, Chennai, India

N. Vijayan CSIR-National Physical Laboratory, New Delhi, India

S. Xavier Department of Physics, St. Joseph's College of Arts and Science (Autonomous), Cuddalore, Tamil Nadu, India; Bharathiyar University, Coimbatore, Tamil Nadu, India

Part I
Invited and Plenary Talks

Cavitation Technology—Potential Way of Generating Nanomaterials and Nanoemulsions for Wider Technological Applications

Manickam Sivakumar

Abstract Development of nanomaterials is continuously on the rise owing to their variety of technological applications and thus gets increased attention not only in the academic research but also on an industrial scale. Nanomaterials behave in a different way compared to their counterpart and showing markedly different properties which may be physical, chemical, biological, electronic, etc. Common techniques that are employed in the development of nanomaterials are high energy ball milling, hydrothermal synthesis, co-precipitation, microemulsion, sol-gel processing, etc. Due to the inherent disadvantages existing with these conventional techniques newer processing methods are always have great consideration. In this connection, cavitation induced by ultrasound exhibits many advantages. Not only the nanomaterials are obtained using this technique, even the nanoformulations such as nanoemulsions could be generated using this technology.

1 Introduction

With a continuous demand of nanomaterials that have been employed in a wide spectrum of technological products, it is the need of the hour to look for novel techniques by which they could be manufactured in a facile way. On this line, cavitation brought about by passing ultrasonic waves in a liquid could be a potential way to assist the generation of nanomaterials. Cavitation is the generation, growth and violent collapse of vaporous bubbles. The end of cavitation process leads to intense conditions of temperatures and pressures, shockwaves and microjets which support the generation of nanomaterials. The major benefits of this technique in the generation of nanomaterials are: milder reaction conditions (low temperature and pressure), utilization of simple precursors, extreme reaction rates, smaller particle size with narrow distribution, high stability of the generated nanomaterials and

M. Sivakumar (✉)
Faculty of Engineering, Department of Chemical and Environmental Engineering, University of Nottingham Malaysia Campus, Kuala Lumpur 43500, Selangor, Malaysia
e-mail: Sivakumar.Manickam@nottingham.edu.my

J. Ebenezar (ed.), *Recent Trends in Materials Science and Applications*, Springer Proceedings in Physics 189, DOI 10.1007/978-3-319-44890-9_1

higher energy efficiency. Following are some of the nanomaterials and nanoemulsions that have been developed using this technique.

2 Nano Oxides and Ferrites

The successful preparation of nanosized ferrites with precise stoichiometry is a synthetic challenge as the rigorous conditions employed in the conventional methods only lead to bulk materials with poor homogeneity, high porosity and poor control of particle size. Whereas ultrasonic cavitation successfully generated these magnetic nanostructured ferrites in a simple way [1, 2]. Besides, this approach was utilized to generate metal oxides such as zinc oxide and metal ferrites such as zinc ferrite and manganese zinc ferrites [3–6]. In the first stage, at room temperature the aqueous phase containing the precursors was dispersed into the vegetable oil phase to obtain the preemulsified droplets. Following this, in the second stage ultrasound mediated hydrolysis and oxidation generated the resultant oxides and ferrites. The size of as-prepared zinc ferrite nanoparticles was 4 nm, whereas the heat treated showed the size of 12 nm (Fig. 1a–d). In case of manganese zinc ferrite, the as-prepared showed the size of 20 nm, whereas the heat treated resulted in the size of 33 nm. Similarly, the generated ZnO displayed the size in the range of 200–250 nm.

3 Nanoporous Catalysts

Ultrasound was also successful to induce a large number of pores in the *in situ* generated catalysts such as CuO-ZrO_2 [7]. More importantly with a change in ultrasound intensity from 20 to 70 %, the number of pores generated also increased with the average size of pores was in the range of 4–6 nm. In situ generation of Pt along with its deposition on TiO_2 was induced by ultrasound [8–10]. Where, smaller particles with the size of 2 nm were deposited uniformly on the surface of

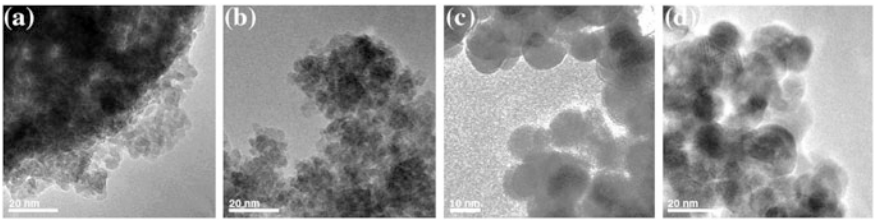

Fig. 1 Transmission electron micrograph of as-prepared (**a**, **b**) and heat treated (**c**, **d**) zinc ferrite nanocrystals (adapted from [3])

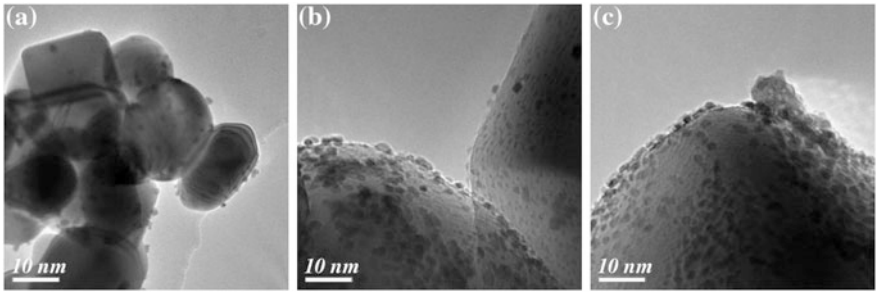

Fig. 2 Transmission electron micrographs of Pt on TiO_2 (**a–c**) (adapted from [9, 11])

TiO_2 (Fig. 2a–c). Independent of the loading of Pt, the size of Pt particles remained the same. It was also noted that the ultrasonically deposited Pt on TiO_2 showed higher catalytic activity for the conversion of CO [11].

4 Nanoemulsions

A range of nanoemulsions incorporated with the active components have been generated using ultrasonic cavitation. These nanoemulsions are successfully used in food, pharma, agriculture and in cosmetic applications. In drug delivery, nanoemulsions seem to be an appealing alternative to administer poorly water soluble drugs. Two-stage emulsification approach was proposed in the generation of nanoemulsions. In the first stage, ultrasound induced acoustic field generates interfacial waves which cause an instability at the interface of oil-aqueous system and erupts the oil phase into the aqueous phase to form larger primary droplets. The above formed larger droplets are then continuously broken into smaller droplets due to the local intense turbulence induced by ultrasound [12]. Overall the droplet break-up depends on the shear generated from ultrasound and the coalescence of droplets varies on the rate at which the surfactant adsorbs on the surface of the newly formed droplets [13].

Nanoemulsion incorporated with aspirin was generated using the above approach. It was observed that the conventional magnetic stirring for 7 h led to an average droplet size of 1160 nm with the PDI of 0.971. But, ultrasound application within a minute resulted in generating the droplets of 232 nm with the PDI of 0.309. Also, higher stability was noted with ultrasonically generated nanoemulsions.

To determine the energy efficiency, using aspirin nanoemulsion as a model system, ultrasound was also compared with high pressure microfluidiser system (for

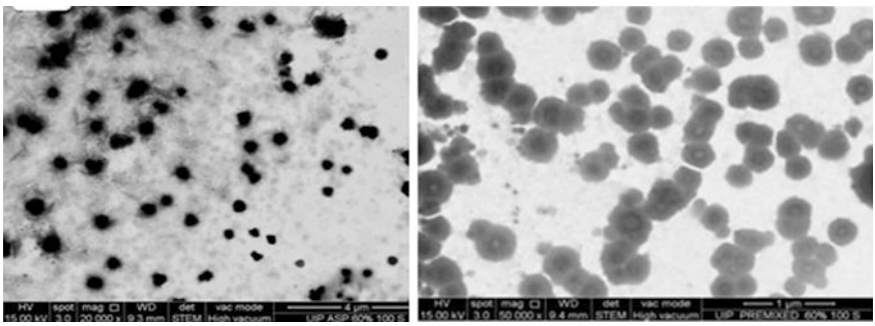

Fig. 3 SEM micrographs of aspirin nanoemulsion generated using ultrasound (adapted from [14])

a variety of parameters) which is a commonly employed in the industries. It has been observed that to achieve a similar droplet size of 160 nm (Fig. 3), ultrasound was 18 times more energy efficient than microfluidiser [14]. Similarly Curcumin nanoemulsion was generated using ultrasonic bath and utilizing a simple strategy [15].

From these investigations, it could be noted that the key factor for efficient ultrasonic emulsification is supplying an optimum ultrasonic energy density which is critical as the excess energy input beyond the optimum only increased the droplet size. Also, premixing is essential before subjected to ultrasound as it controls the PDI or size distribution of the resultant droplets. Besides, the conventional emulsion (O/W or W/O), multiple nanoemulsions also referred as double emulsion or emulsions of emulsions were also generated using ultrasound [16]. Besides their generation, their activities were also compared with the normal emulsions [17]. In addition to employing ultrasound, the hydrodynamic mode was also been successfully utilized in the generation of normal nanoemulsions encapsulated with curcumin [18].

5 Conclusion

It could be clearly noted that cavitation through ultrasound is influential and capable technique to produce a range of nanomaterials and nanoemulsions incorporated with various active components. But it has to be noted that optimization using different operating parameters should be followed carefully to obtain the unique advantages of smaller particle size with narrow distribution. Overall cavitation is a simple and energy efficient route which avoids many of the necessities required in the conventional techniques that continuously attracting the attention of researchers and hence this technique has a great future.

References

1. Sivakumar, M., Gedanken, A., Zhong, W., Jiang, H.Y., Du, Y.W., Bhattacharya, D., Brukental, I., Yeshurun, Y., Felner, A.: Chem. Mater. **16**, 3623–3632 (2004)
2. Sivakumar, M., Gedanken, A., Zhong, W., Du, Y.W., Felner, A.: J. Mater. Chem. **14**(4), 764–769 (2004)
3. Sivakumar, M., Takami, T., Ikuta, H., Bhattacharya, D., Yasui, K., Towata, A., Tuziuti, T., Iida, Y.: J. Phys. Chem. B **110**(31), 15234–15243 (2006)
4. Sivakumar, M., Yasui, K., Towata, A., Tuziuti, T., Iida, Y.: Curr. Appl. Phys. **6**(3), 591 (2006)
5. Sivakumar, M., Towata, A., Yasui, K., Tuziuti, T., Kozuka, T., Iida, Y., Maiorov, M.M., Blums, E., Sivakumar, N., Ashok, M.: Ultrason. Sonochem. **19**(3), 652–658 (2012)
6. Sivakumar, M., Towata, A., Yasui, K., Tuziuti, T., Iida, Y.: Chem. Lett. **35**(1), 60 (2006)
7. Sivakumar, M., Gedanken, A.: New J. Chem. **30**(1), 102–107 (2006)
8. Sivakumar, M., Iida, Y., Yasui, K., Tuziuti, T.: 9th European Society of Sonochemistry (ESS-9), Badajoz, Spain, 25–30 April (2004)
9. Sivakumar, M., Yasui, K., Tuziuti, T., Towata, A., Iida, Y.: Ultrason. Sonochem. **17**, 621–627 (2010)
10. Sivakumar, M., Towata, A., Yasui, K., Tuziuti, T., Tsujimoto, M., Zhong, Z., Chen, L., Iida, Y.: 10th European Society of Sonochemistry (ESS-10), Hamburg, Germany, 4–8 June (2006)
11. Sivakumar, M., Towata, A., Yasui, K., Tuziuti, T., Kozuka, T., Tsujimoto, M., Zhong, Z., Iida, Y.: Ultrason. Sonochem. **17**, 213–218 (2010)
12. Sivakumar, M., Tang, S.Y., Tan, K.W.: Green chemistry for environmental remediation. In: Sanghi R., Singh V. (eds.) vol. 7, pp. 155–208, Scrivener, Wiley (2012)
13. Sivakumar, M., Tang, S.Y., Tan, K.W.: Ultrason. Sonochem. **21**(6), 2069–2083 (2014)
14. Tang, S.Y., Parthasarathy, S., Sivakumar, M.: Ultrason. Sonochem. **20**(1), 485–497 (2013)
15. Tan, K.W., Tang, S.Y., Thomas, R., Neela, V., Sivakumar, M.: Pure Appl. Chem. (IUPAC J.) **88**(1–2), 43–60 (2016)
16. Tang, S.Y., Sivakumar, M., Billa, N.: Colloids Surf. B **102**, 653–658 (2013)
17. Tang, S.Y., Sivakumar, M., Ng, A.M.-H., Shridharan, P.: Int. J. Pharm. **430**, 299–306 (2012)
18. Parthasarathy, S., Tang, S.Y., Sivakumar, M.: Ind. Eng. Chem. Res. **52**(34), 11829–11837 (2013)

Ag/TiO_2 (Metal/Metal Oxide) Core Shell Nanoparticles for Biological Applications

D. Mangalaraj and D. Nithya Devi

Abstract This paper deals with the preparation of silver/titanium dioxide core shell nanoparticles using sobar method and the characterization of the prepared particles. The advantage of this method over the other available chemical methods is explained. Attempts have been made to employ the prepared particles to specific biological applications.

1 Introduction

Core/shell nanoparticles are gradually attracting more and more attention, since these nanoparticles have emerged at the frontier between materials chemistry and many other fields, such as electronics, biomedical, pharmaceuticals, optics and catalysis. Core shell nanoparticles are highly functional materials with modified properties. Sometimes properties arising from either core or shell materials can be quite different. The properties can be modified by changing either the constituting materials or the core to shell ratio. Because of the shell material coating, the properties of the core particle such as reactivity decrease or thermal stability can be modified, so that the overall particle stability and dispersibility of the core particle increases. The purpose of coating on the core particle are many fold, such as the surface modification, ability to increase the functionality, stability and dispersibility, control release of core, reduction in consumption of precious material. The majority of the core shell nanoparticles are used in biomedical field for bioimaging, controlled drug release, targeted drug delivery, cell labeling and tissue engineering application [1].

D. Mangalaraj (✉) · D. Nithya Devi
Department of Nanoscience and Technology, Bharathiar University,
Coimbatore 641046, India
e-mail: dmraj800@yahoo.com

J. Ebenezar (ed.), *Recent Trends in Materials Science and Applications*,
Springer Proceedings in Physics 189, DOI 10.1007/978-3-319-44890-9_2

2 Why Titanium Dioxide (TiO_2) and Silver (Ag) Nanoparticles?

Metal nanoparticles, with a high specific surface area and a high fraction of surface atoms, have been studied extensively due to their unique physico-chemical characteristics including catalytic activity, optical properties, electronic properties, antimicrobial activity and magnetic properties. Among metal nanoparticles, silver nanoparticles have been known to have inhibitory and bactericidal effects. The high surface area and high fraction of surface atoms of Ag nanoparticles lead to high antimicrobial activity as compared with bulk silver metal. Hence silver nanoparticles have been chosen to be our core material which can acts as an antimicrobial as well as an anticancer agent. Inspite of using silver nanoparticles, we need an additional layer to prevent silver from oxidizing and similarly to reduce the usage of silver concentration. Hence we preferred metal—oxide layer to effectively overcome the detrimental effects of silver nanoparticles. Among various semiconductors, TiO_2 nanoparticles are investigated widely due to their significant properties such as photosensitivity, non-toxicity, easy availability, strong oxidizing power, and long-term stability. The photocatalytic properties of TiO_2 have led to extensive research into its potential uses as a disinfectant, antibiotic, biological sensor, tumor cell–killing agent, and gene targeting device. Bulk forms of TiO_2 are generally biologically and chemically inert. The size, shape, and aggregation of titanium dioxide nanoparticles are the important factors in the anticancer activity and In vivo toxicological analysis.

3 Characteristic Features of Silver and TiO_2 Nanoparticles in Drug Delivery

Silver nanoparticles usually involve some form of moisture layer that the silver ions are transported through, to create long term protective barrier against bacterial and fungal properties. Silver nanoparticles display a synergistic effect and also a cytotoxic effect on cell viability which have a chief role in antitumor effect. They aid in gathering and transporting drug into the cancer cells and they also obstruct the metabolism of cancer proliferation [2–6]. TiO_2 is a biocompatible material which in nanosized form causes some inflammation effects and confirms the idea that nanomaterials have different properties compared with bulk materials. Some evidence shows that the nano-TiO_2 causes H_2O_2 and hydroxyl free radical formations which results to cell toxicity in mammals. The surface of TiO_2 nanoparticles is highly reactive because of surface defects and such TiO_2 nanoparticles readily bind ligands including dopamine, ascorbic acid and alizarin. The endocytosis of nanoparticles depends on the size, shape and charge of the nanoparticles as well as the cell type being treated. The unique characteristic feature such as small

size and quantum size effect could make silver and TiO_2 nanoparticles suitable for many applications [7–13].

4 Chemical Preparation Technique—Stober Method

Many methods allow preparing particles from solution or from vapour phase. One of the most popular methods is called Stober method. The method is based on the hydrolysis and poly condensation of alkyl compounds in basic (ammonia) alcoholic solutions, therefore on the sol-gel method reactions. The particles size strongly depends on the water and ammonia concentration, but also on the nature of the alcohol used as a solvent. When using alcohols of higher molecular weight, the reaction is slowed down and both median particle size and the spread of the size distribution increased simultaneously. By using the Stober method, it is possible to achieve excellent control of particle size, narrow size distribution and smooth spherical morphology. This method is the extension of sol gel method, where the particles undergo hydrolysis and condensation process. Sol gel processes are mainly classified into three different approaches (i) gelation of solutions of a colloidal powder, (ii) hydrolysis and poly condensation of metal alkoxides or metal salt precursors followed by hyper critical drying of the gels (iii) hydrolysis and poly condensation of metal alkoxides precursor followed by aging and drying under ambient atmosphere [14]. Figure 1 shows the schematic illustration of the Stober synthesis of nanomaterials.

5 Stober Chemistry

Chemistry involved in the sol-gel process is very important for the proper fabrication of desired material. Initial conditions such as pH, temperature, etc., control the extended sol-gel chemistry. The hydrolysis and poly condensation of alkoxides proceed according to the following mechanism,

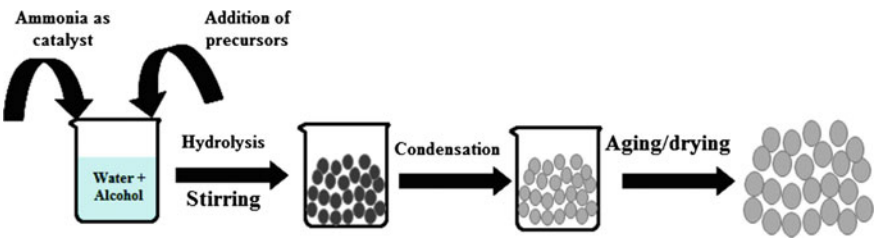

Fig. 1 Schematic illustration of Stober method

Hydrolysis: $M(OR)n + nH_2O \rightarrow M(OH)n + nROH$

Condensation: $M(OH)n + M(OH)n \rightarrow (OH)n - 1\,M{-}O{-}M{-}(OH)n - 1 + H_2O$

6 Preparation of Bio-surfactants Induced Ag–TiO_2 Core Shell Nanoparticles

(a) Preparation of Ag nanoparticles

Silver NPs were prepared by the reduction of silver nitrate with Hydrazine monohydrate at RT, according to the method described previously by Lendel and Leopold. Briefly 11.6 mg of $N_2H_4{\cdot}H_2O$ was dissolved in 100 ml of distilled water and was mixed with 0.1 M of NaOH. Then 36 ml of the above solution, was added with 10 mM of $AgNO_3$ (4 ml) under gentle stirring at RT. A rapid colour change was observed and finally a clear blackish-yellow Ag NPs was obtained [15].

(b) Preparation of Ag NPs @ biosurfactants

A typical procedure for the synthesis of biosurfactants induced Ag NPs preparation is gives as follows: the prepared Ag NPs were slowly added to 2-propanol (H_2O/2-propanol, ratio maintained at 4:20). Under gentle stirring, ammonia (6 ml, 25 %) and biosurfactants (80 µl) were added to the above mixture. The mixture was

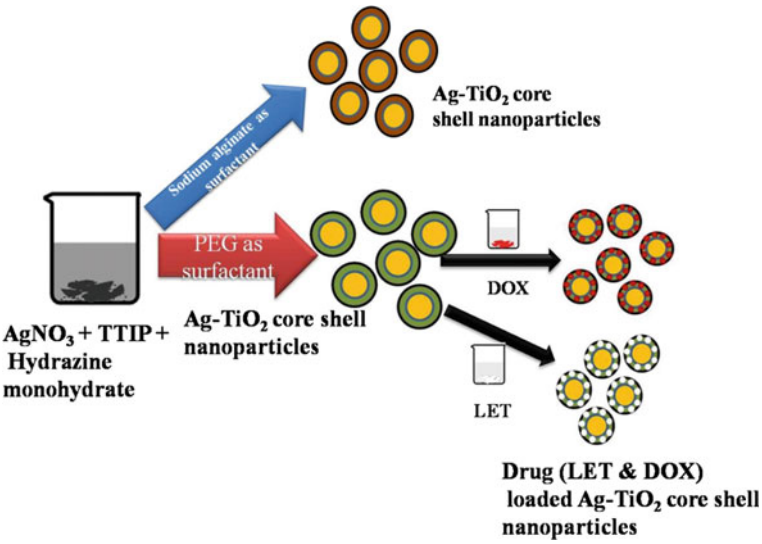

Fig. 2 Schematic diagram of biosurfactants (PEG and sodium alginate) induced Ag–TiO_2 core shell nanoparticles

sonicated for about 15 min to get homogeneous dispersion. Figure 2 shows the schematic diagram of synthesis of pure and drug loaded Ag–TiO_2 core shell nanoparticles.

(c) **Preparation of Ag NPs @ biosurfactants @ TiO_2**

Aqueous solution of Tween 80 of 0.1 M was dissolved in pre-mixed dispersion of above prepared mixture (core particles). With the above mixed core particles, different concentrations of titanium precursor (0.8, 1.6 and 2.4 ml) dissolved in 2 ml of ethanol was added. The mixture was sonicated for at least 30 min in an ultrasound bath to get homogeneous dispersion. After sonication, the mixture was stirred for 2 h at room temperature. The colour of the solution changed to grey from blackish yellow which confirmed the coating of titanium dioxide over silver nanoparticles. The product was washed with ethanol and water and calcined at 400 °C for 2 h [15].

(d) **Anti-cancer drug loading**

90–80 mg of Ag–TiO_2 core shell nanoparticles was dissolved in 8 ml of DMSO and 10–20 mg of anticancer drugs (DOX and LET) separately dissolved in 2 ml of DMSO with equivalent molar ratio of TEA. These solutions were mixed and magnetically stirred for 1 h [16]. This solution was poured into 20 ml of distilled water for 10 min to form anticancer drug incorporated nanoparticles. DMSO and free drug was removed by dialysis. The resulting solution was used for analysis or lyophilized.

7 Characterization Techniques

The X-ray diffraction (XRD) recording were carried out at room temperature using a PANalytical X'Pert-Pro diffractometer with Cu Kα radiation ($\lambda = 1.5406$ Å) over a scanning interval (2Θ) from 20° to 80°. The average crystallite sizes were estimated using the Scherrer formula from the X-ray line broadening. The infra-red spectrum of the samples was obtained by using a Fourier trans-form infrared (FTIR) spectrometer (Bruker Tensor, Germany). The sample was prepared in a KBr pellet for the investigation within the range of 4000–400 cm^{-1}. The morphology of the Ag–TiO_2 and anticancer drug loaded core shell nanostructures was observed by field emission scanning electron microscopy (FESEM) (FEI Quanta-250 FEG) and Transmission electron microscope (TEM, Hitachi H600) operating at 80 kV. UV-vis spectral analysis was done by using JoscoV-650 spectrophotometer. The chemical composition of the surface layer was determined by X-ray photoelectron spectroscopy (XPS, AXIS165) spectrometer. The stability and charge of the nanoparticles were determined by Zeta potential analyzer. The entrapment efficiency, drug loading and drug releasing profile were calculated using JoscoV-650 UV-vis spectrophotometer.

8 Silver Releasing Tests

A mass of 0.1 g of the product was soaked in 25 ml of Phosphate buffer solution (PBS) in polypropylene bottle at 37 °C and rotated at 300 rpm, for periods of intervals ranging from 1 to 7 days. The liquid was collected on the 1st, 3rd, 6th and 7th days and replaced with fresh Phosphate buffer solution (PBS). At selected intervals, the concentrations of silver ions released from the product into the Phosphate buffer solution (PBS) were measured using UV-vis spectroscopy. The experiments were performed in triplicate to obtain the average value. The samples were analysed and the average and standard deviation with error value were calculated. Statistical analysis was performed by using Microsoft Excel [17].

9 In-Vitro Studies

(a) **Antibacterial assay**

The strains of Staphylococcus aureus bacteria were grown in Luria-Bertania (LB) medium containing 10 g/L tryptone, 5 g/L yeast extract, and 5 g/L NaCl. The bacteria were inoculated in the LB medium in a self regulating thermostat for 8 h at 37 °C. One millilitre original bacterial inoculum was added into 9 ml 0.9 % normal saline and they were diluted into LB broth for 8 h at 37 °C. Once the standard culture was prepared, two methods were used to study the antibacterial activity such as (i) optical density tests and (ii) colony count method [18].

(b) **Optical density tests**

To examine the bacterial growth rate and to determine the growth curve in the presence of the prepared Ag–TiO_2 core shell nanoparticles, *S. aureus* were grown in 50 ml LB medium as in single agar plate colony supplemented with 0, 20, 40, 60, 80 and 100 µg of Ag–TiO_2 core shell nanoparticles. Growth rates and bacterial concentrations were determined by measuring optical density at 600 nm each 2 h for 24 h at 37 °C (OD of 0.1 corresponds to a concentration of 105 cells) [19].

(c) **Colony-counting method**

The minimal inhibitory concentrations were measured by plate count method. Viable cell counts were determined by tenfold serial dilution of 1 mL broth culture in phosphate buffer solution (PBS), followed by inoculation of 0.1 mL aliquots on nutrient agar, by incubation of the plates at 37 °C for 24 h prior to colony plate counting. After the incubation, the number of colonies grown on the agar was counted.

(d) **Estimation of protein leakage from bacterial cell membranes**

Protein leakage from bacterial cells was detected using Lowry's method using bovine serum albumin (BSA) as standard. The concentration of Ag–TiO_2 core shell

nanoparticles was adjusted to 100 µg/ml, and the concentration of bacterial cells was 10^5 CFU/ml [20]. Each culture was incubated in a shaking incubator at 37 °C for 6 h and 1 ml of culture sample was obtained from each culture. The sample was centrifuged at 4 °C for 30 min at 300 rpm and the supernatant was frozen at −20 °C until assay. The protein content of the supernatant was estimated [21].

(e) **In vitro haemolysis analysis of Ag/TiO_2 of core shell nanoparticles**

Haemolysis assay was performed using fresh blood of sheep. The erythrocytes were collected by centrifugation at 1500 rpm for 15 min and then washed three times with phosphate buffered saline (PBS) buffer at pH 7.4. The stock dispersion was prepared by mixing 3 ml of centrifuged erythrocytes into 11 ml of PBS. The prepared PEG and sodium alginate induced core shell nanoparticle dispersion were prepared in PBS buffer with above mentioned concentration (100 µg/ml). One hundred microlitre of stock dispersion was added to 1 ml of nanoparticle dispersions. The solutions were mixed and incubated for 4 h at 37 °C in an incubator shaker. The percentage of haemolysis was measured by UV-vis analysis of the supernatant at 394 nm absorbance after centrifugation at 13,000 rpm for 15 min. One millilitre of PBS was used as negative control with 0 % haemolysis and 1 ml of DD H_2O was used as the positive control with 100 % haemolysis. All haemolysis data points were represented as the percentage of the complete haemolysis.

(f) **Measurement of drug encapsulation efficiency**

Drug entrapment efficiency was determined by centrifuging aqueous dispersion of LET and DOX loaded Ag–TiO_2 core shell nanoparticles at 25,000 rpm for 15 min and measuring the amount of LET and DOX in the supernatant with the help of UV-vis spectrophotometer, absorbance at 240 nm (LET) and 480 nm (DOX). The amount of LET and DOX were subtracted from initial amount of anticancer drug taken to calculate drug entrapment efficiency of nanoparticles [22].

(g) **Drug release study**

The releasing experiments were carried out in vitro as follows: 2 mg of incorporated nanoparticles were distributed into 10 ml phosphate buffer solution (PBS, 0.1 M, pH 7.4) and this solution was introduced into dialysis membrane tubes. The dialysis membrane was then placed in a 250 ml bottle with 90 ml of PBS solution. This bottle was continuously stirred for 6 h at 37 °C. At specific time intervals (every one hour), 3 ml media was withdrawn to determine drug release by absorbance measurement at wavelength of 240 nm (LET) and 480 nm (DOX); another 3 ml of PBS solution was added to the dialyzed solution to compensate the withdrawn volume [23]. The concentration of released drugs from the nanoparticles into PBS solution was evaluated by UV-vis spectroscopy. Cumulative percentage released at different time points were fitted into different release models: Zero order kinetics, First order kinetics, Higuchi and Korsmeyer-peppas plot. The Correlation coefficient close to unity was taken as order of release.

10 Conclusion

Biosurfactants induced Ag–TiO_2 core shell nanoparticles were prepared by Stober method (extended sol gel method) with titanium (IV)-iso propoxide and silver nitrate as starting precursors. The silver nitrate was chemically reduced to silver nanoparticles with hydrazine monohydrate as reducing agent. The prepared core shell nanoparticles were confirmed by various characterization studies such as FESEM, TEM, XPS and XRD. These analyses showed the formation of core shell structure with Ag in metallic state and TiO_2 in pure anatase phase. Further the influence of prepared core shell nanoparticles on the bacterial properties has been analyzed and the results showed PEG induced core shell nanoparticles had higher activity.

With this core shell nanoparticles, the anticancer drugs has been loaded and its cumulative % release results indicates the zero order kinetics with super case II model, which make the drug to release in a controlled and relaxing manner from the carrier into the targeted site. The interaction between these metal and metal oxide makes it suitable for various fields such as photocatalysis, water purification and mainly focuses its needs in biological field due to its higher efficacy.

References

1. Chaudhuri, R.G., Paira, S.: Chem. Rev. **112**, 2373–2433 (2012)
2. Wu, K.C.W., Yamachi, Y., Hong, C.Y., Yang, Y.H., Liang, Y.H., Funastu, T., Tsunoda, M.: Chem. Commun. **47**, 5232–5234 (2011)
3. Shi, H., Magaye, R., Castranova, V., Zhao, J.: Part. Fibre Toxicol. **10**, 15 (2013)
4. Coronado, D.R., Gattorno, G.R., Espinosa-Pesqueira, M.E., Cab, C., De Cossa, R., Oskam, G.: Nanotechnology **19**, 145605 (2008)
5. Bonetta, S., Bonetta, S., Motta, F., Strini, A., Carraro, E.: AMB Express **3**, 59 (2013)
6. Thevenot, P., Cho, J., Wavhal, D., Timmons, R.B., Tang, L.: Nanomed. Nanotechnol. Biol. Med. **4**, 226–236 (2008)
7. Reidy, B., Haese, A., Luch, A., Dawson, K.A., Lynch, I.: Material **6**, 2295–2350 (2013)
8. Asharani, P.V., Mun, Gl, Hande, M.P., Valiyavettil, S.: ACS Nano **3**, 279–290 (2009)
9. Tvan, Q.H., Ngugen, V.Q., Le, A.T.: Adv. Nat. Sci. Nanosci. Nanotechnol **4**, 033001 (2013)
10. Das, S.K., Bhunia, M.K., Bhaumik, A.: Dalton Trans. **39**, 4382–4390 (2010)
11. Li, S., Guoliang, Ye, Chen, G.: J. Phys. Chem. C **113**, 4031–4037 (2009)
12. Zhang, H.J., Wen, D.Z.: Surf. Coat. Technol. **201**, 5720–5723 (2007)
13. Su, W., Wang, S., Wang, X., Fu, X., Weng, J.: Surf. Coat. Technol. **205**, 465–469 (2010)
14. Farooqui, M.D.A., Chauhan, P.S., Krishanmoorthy, P., Shaik, J.: J. Nanomater. Biostruct. **5**, 43–49 (2010)
15. Yunqing, W., Lingxin, C., Ping, L.: Chem.Eur. J. **18**, 5935–5943 (2012)
16. Jeong, Y.-I.L., Chung, K.-C., Choi, K.C.: Arch. Pharm. Res. **34**, 159–167 (2011)
17. Nithyadevi, D., Sureshkumar, P., Mangalaraj, D., Ponpandian, N., Viswanathan, C., Meena, P.: Appl. Surf. Sci. **327**, 504–516 (2015)
18. Kim, J., Sungeun, K., Kim, J., Jongchan, L., Yoon, J.: Korean Soc. Environ. Eng. **27**, 771–776 (2005)
19. Wang, J.X., Wen, L.X., Wang, Z.H., Chen, J.F.: Mater. Chem. Phys. **96**, 90–97 (2006)

20. Bradford, M.M.: Anal. Biochem. **72**, 248–254 (1976)
21. Guerlava, P., Izac, V., Tholozan, J.L.: Curr. Microbiol. **36**, 131–135 (1998)
22. Jeong, Y.-I.L., Choi, K.C., Song, C.E.: Arch. Pharm. Res. **29**, 712–719 (2006)
23. Noveen, K., Aravind, G., Sumit, S., Prashanthi, P.: Int. J. Pharm. Pharm. Sci. **5**, 615–621 (2013)

Quantum Dots and Their Potential Applications to Device Fabrication

A. John Peter

Abstract Size dependent low dimensional semiconductors can be assembled with the optimum quantum efficiency with the desirable properties for fabricating novel optical nano-devices. As a result, the enhancement of electronic and optical properties is observed when the geometrical dimensions are reduced. Optical transitions occurring between confined quantum states or bound to continuum states either in the valence band or in the conduction band or between them are specific of quantum semiconductor structures. The operating wavelength of interband optical devices is dependent on the band gap of a semiconductor on contrary the intraband optical devices exhibit the possibilities of wavelength controlling by design because it involves the transition energy between the levels either in the conduction band or in the valence band. In addition, the quantum confinement of the carriers enhances the interaction between energy levels leading to optical transitions with a narrow bandwidth. The applications of external perturbations and the geometrical confinement induce significant modifications in the electronic and optical properties of a quantum dot. Thus, the reduced dimensionality systems exhibit the novel properties with the superior performance in nano-optical devices including optical amplifiers, high-speed electro-optical modulators, inter-subband long wavelength photo-detectors, diodes, lasers and long wavelength fibre optical communication networks.

1 Introduction

A semiconductor system which has the dimension lower than three dimensions is known as low dimensional semiconductor system. Low-dimensional systems have revolutionized semiconductor physics and had a tremendous impact on technology [1]. If the geometrical dimensions of a semiconductor material are reduced in one,

A. John Peter (✉)
PG and Research Department of Physics, Government Arts College,
Melur, Madurai 625106, India
e-mail: a.john.peter@gmail.com

J. Ebenezar (ed.), *Recent Trends in Materials Science and Applications*,
Springer Proceedings in Physics 189, DOI 10.1007/978-3-319-44890-9_3

two or three directions of space below the de-Broglie wavelength of a charge carrier or simply reducing to only a few nano-meters the resulting structures are then called nanostructures. A structure is called quantum well, quantum wire and quantum dot structure, if it is one, two or three dimensions are reduced to nano metre size, respectively. Low dimensional semiconducting materials show unique differences in electronic properties with respect to bulk materials. Heterostructures of different epitaxially grown crystalline materials allow selective carrier confinement and further control over both the emissive and electronic properties.

Reduced dimensional semiconducting materials are realized owing to the recent invention of growth techniques like Molecular Beam Epitaxy, Metal organic Chemical Vapour Deposition, Liquid Phase epitaxy and Electron Lithography. The quantum confinement of the charge carriers leads to the formation of discrete energy levels in any low dimensional semiconductors systems. In fact, the quantum mechanical effects dominate when the dimensions are reduced. The quantized energies and the motion of the charged particle cause a widening band gap if the size of the material is smaller than the exciton Bohr radius [2].

The confinement of electrons and holes in these nano structures modifies the electronic as well as the optical and vibrational properties of the material. A semiconductor quantum well in which narrow band gap semiconductor material is sandwiched between different wide band gap materials by means of hetero-junctions, causes the electron confinement in two dimensions. This two dimensional confinement results in new optical properties that are different from bulk material, such as optical absorption and gain spectra peculiar to the step like density of states, strong exciton resonance observable at room temperature, large optical nonlinearity and quantum confined stark effect due to an electric field induced energy shift of the resonance. These properties lead to the way to a variety of new optical devices; e.g., quantum well lasers, high speed optical modulators, optical switches, optical bi-stable devices such as self-generated electro-optic effect devices etc., [3, 4].

2 Theory and Model

Within the framework of effective mass approximation, the Hamiltonian of a hydrogenic impurity is taken in this problem. It is characterized with its radius R and height L along z-direction. The Hamiltonian is given by

$$H(\rho, \varphi, z) = -\frac{\hbar^2}{2m_e^*}\nabla^2 - \frac{e^2}{\varepsilon r} + V(z) \tag{1}$$

where e is the absolute value of electron charge, r is the distance between the carrier and the impurity ion, m_e^* is the effective mass of inner dot material, ε is the static dielectric constant and e is the electron charge. $V(z)$ is the confinement potential.

With the inclusion of impurity, the trial wave function can be chosen as,

$$\Psi(\bar{r}_e) = f(\rho)\, h(z)\, e^{-im\phi_j} e^{-\alpha\rho^2} e^{-\beta z^2} \quad m = 0, \pm 1, \pm 2, \ldots \tag{2}$$

where m is the electron (hole) z-component angular momentum quantum number. The radial wave function $f(\rho)$ and the corresponding confinement energy equation of the electron can be obtained by using the m-order Bessel function J_m and the modified Bessel function K_m. The z-axis wave function $h(z)$ can be found using linear combinations of analytical functions $\sin(\xi)$ and $\cos(\xi)$ (inside the dot), or $\exp(\xi)$ (outside the dot). In (2), f_e is the ground state solution of the Schrödinger equation for the electron. α and β are variational parameters responsible for the in-plane correlation and the correlation of the relative motion in the z-direction respectively.

The Schrödinger equation is solved variationally by finding $\langle H \rangle_{\min}$ and the binding energy of the hydrogenic donor in the quantum dot is given by the difference between the energy with and without Coulomb term. The calculation of the electronic structure of the quantum dot systems for a fixed alloy content is computed first by calculating its lowest binding energy and subsequently the donor binding energy by adding the Coulomb term. The expectation values of the Hamiltonian (1) calculated using a trial function with two variational parameters are minimized to obtain the ground-state energies of the electron.

The donor binding energy of the system is obtained as

$$E_b = E_e - \langle H \rangle_{\min} \tag{3}$$

where E_e is the free electron self-energy in the same quantum dot.

Investigation of some optical properties of any low dimensional semiconductor system is required for any electronic transition systems. The dipole transition transitions are allowed using the selection rules $\Delta l = \pm 1$ where l is the angular momentum quantum number. Any transition rate from the ground state to the final state, the intersubband in the influence of electromagnetic spectrum, is described by Fermi's Golden rule as

$$f = \frac{2m_0(E_f - E_i)}{\hbar^2} \left| \langle \psi_j | r | \psi_i \rangle \right|^2 \tag{4}$$

where m_0 is the electron mass in vacuum and $E_f - E_i$ is the transition energy from i state to f state. ψ and E are the wave functions and energies of the confinement levels for the initial (i) and final (f) states. The investigation on the optical transitions with the help of oscillator strength gives an additional information on the fine structure and the selection rules of the optical absorption coefficients. The charge carriers in a doped semiconductor are considered to be important for observation of intersubband optical absorption. Discrete energy levels are formed in any low dimensional semiconductor systems, subsequently the quantum confinement takes place in these systems and the optical transitions can be achievable between these energy levels. Eventually, this effect will alter the intersubband optical absorption

spectra drastically. The strength of the intersubband energy optical transition is associated with the Fermi's Golden rule.

By using the density matrix approach, within a two-level system approach, the intersubband optical transition energies and the related optical absorption coefficient are computed in saturation limit. The dependence of the nonlinear spectral processes in the presence of geometrical confinement is brought out the various photon energy. The interband optical transition energy is computed taking into account the exciton in the Hamiltonian.

3 Results and Discussion

Numerical computations are performed to obtain the donor impurity binding energy and thereby the intersubband optical transition energies taking into account the system $Ga_{0.9}In_{0.1}N/GaN$ semiconductor quantum dot. The units of length and energy used throughout are the effective Bohr radius $R^* = \hbar^2\varepsilon/m*e^2$ and the effective Rydberg $R_y^* = m*e^4/2\varepsilon^2\hbar^2$ where ε is the dielectric constant and m* is the effective mass of electron in the conduction band minimum of the inner material. The donor binding energy is found to enhance when the dot radius is reduced due to the geometrical confinement. Figure 1 shows the variation of intersubband optical transition energies of the donor electron as a function of dot radius for $Ga_{0.9}In_{0.1}N/GaN$ quantum dot. These energies are obtained between the ground state and the first excited state for electron in the conduction band in the $Ga_{0.9}In_{0.1}N/GaN$. The largest intersubband transitions are observed for the $Ga_{0.9}In_{0.1}N/GaN$ quantum dot because it has higher binding energies [5]. Further, it is found that these energies tend to increase when the dot radius is decreased. It is because the quantum size effect dominates in this region. And hence, one can

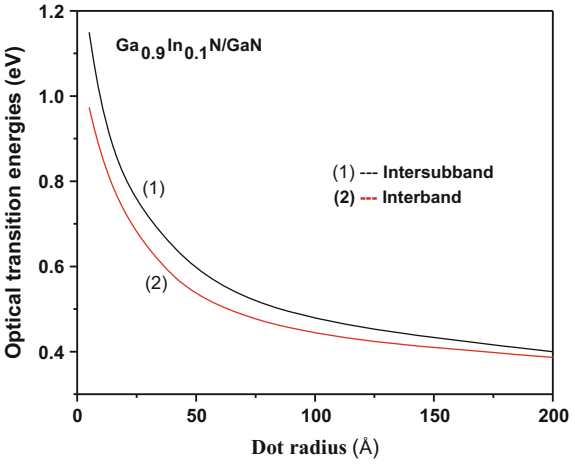

Fig. 1 Variation of optical transition energies due to the intersubband and interband as a function of dot radius in a GaInN/GaN cylindrical quantum dot

conclude that optical transition energies are determined by the geometrical confinement effect. Moreover, the preferred absorption wavelengths for suitable potential applications can be obtained by the proper selection of materials, the composition, dimension and the external perturbations.

4 Conclusion

In conclusion, the donor binding energy of a hydrogenic impurity and the intersubband and intraband optical transition energies in the GaInN/GaN quantum dot have been carried out by varying the size of the quantum dot. The optical transition energies of electron and the exciton due to intersubband and interband transition as a function of dot radius have been investigated and the corresponding oscillator strength have been investigated. The short wavelength laser diodes and intersubband optical devices operating in the near-infrared spectral range based on group III nitride materials are very powerful. The results will be helpful for finding out the suitable wavelength for the efficient optical devices. We hope that the present obtained results would stimulate more research works on realizing high efficiency nitride opto-electronic devices such as light emitters in the telecommunication bands and the single photon sources.

References

1. Davies, J.H.: The Physics of Low-dimensional Semiconductors: An Introduction. Cambridge University Press, Cambridge (1998)
2. Peter, A.J.: Phys. Lett. A **374**, 2170 (2010)
3. Saravanan, S., et al.: J. Lumin. **169**, 86 (2016)
4. Weng, G.E., et al.: Nano-Micro Lett. **3**(3), 200 (2011)
5. Jaya Bala, K., et al.: Adv. Nano Res. 3(1), 13 (2015)

Exploring the Behaviors of Organic and Bio-active Compounds by Spectroscopic and Quantum Computational Techniques

S. Xavier

Abstract The research exploration will involve in investigating the molecular structure, the reactivity centers, bonding and anti-bonding nature, nonlinear optical, electronic and thermodynamic nature of the molecule. The research is made on two levels: First level is done upon using the spectroscopic techniques—FTIR, FT-Raman, UV and NMR characterizing techniques; secondly the same data is analyzed through theoretical methods using *ab initio* and DFT theories which involve basic principle of solving the Schrodinger equation for many body systems. Finally the two levels are compared and discussed. The bio-active property of the molecule is analyzed and the target molecule is found well fit with the breast cancer protein using molecular docking techniques. Higher the basis sets and methods are used closer will be the result to the experimental data. This makes analysis of the any organic, inorganic, and pharmaceutical, bio-samples more economic, feasible and less time consuming. The results of two organic 1-phenyl-2-nitropropene and 1-phenyl-1-propanol are selected, analyzed and discussed.

1 Introduction

Contributing scientific data to the pharmacist and industrialists is the objective of this research study. Complete information about the physical and chemical properties of the molecules play a vital role in manufacture of the drug or any material to the scientific society. Recent research on molecular level helps one to build up the system with less error. Basing on the objective of the study two organic molecules which are biologically active have been selected and went down through the spectroscopic analysis.

First molecule is 1-phenyl-2-nitropropene. It is the organic compound containing nitro and propene group attached to the benzene ring. Since the compound possess the nitro group it has various biological activities. It is used as the cognitive

S. Xavier (✉)
St. Joseph's College of Arts and Science (Autonomous), Cuddalore, Tamil Nadu, India
e-mail: puduvaixavier@gmail.com

J. Ebenezar (ed.), *Recent Trends in Materials Science and Applications*,
Springer Proceedings in Physics 189, DOI 10.1007/978-3-319-44890-9_4

enhancer, which triggers the inactive central nerve system [1]. The derivatives of the compound is also used as pro-apoptotic anticancer agents [2, 3] (Fig. 1).

The second molecule is 1-phenyl-1-propanol. It is the aromatic hydrocarbon substituted with propanol functional group. It is used as intermediate for preparation of fluoxetine anti-depressant drug, a major drug for pediatric depression. It is also used for obsessive disorder both for adult and pediatric for diseases like bulimia nervosa, panic disorder and premenstrual dysphonic disorder [4] (Fig. 2).

The above said two molecules have been analyzed in two categories: one is experimental and another is using computational techniques. In the experimental techniques FT-IR, FT-Raman, UV-Vis and NMR spectroscopic techniques have been used for the structural information. The data is correlated, compared and

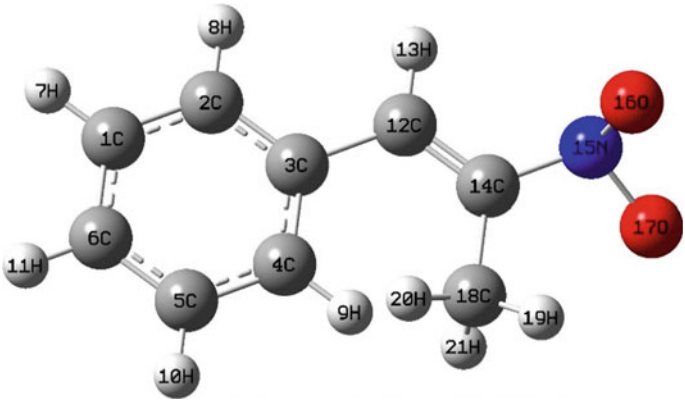

Fig. 1 Molecular structure of 1-phenyl-2-nitropropene

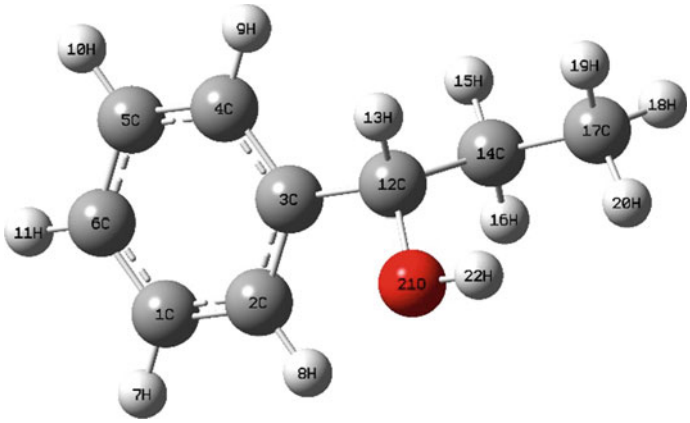

Fig. 2 Molecular structure of 1-phenyl-1-propanol

discussed with data obtained from the quantum computational methods. For the computational works Gaussian 09W software have used, in which all the ab initio methods and basis sets are inbuilt to do the calculations.

2 Conformational Analysis

The conformational analysis have been carried out for both molecule. To know the most stable conformer of the compound, in 1-phenyl-2-nitropropene the dihedral angle C3–C18–C14–N15 has been selected and keeping all other angles are rigid the molecule is rotated for 360° in steps of 10° for 36 steps. While going through the graph drawn between scan coordinate and energy, the conformer at 80° with 0.1636 a.u is considered to be stable conformer. Similarly for the 1-phenyl-1-propanol the dihedral used was O21–C14–C12–C17 and stable conformer is obtained at 300° with energy 0.059 hartree (Fig. 3a, b).

3 The Geometry of the Molecules

The geometry of the molecules have been calculated and compared with the literature values. The bond length first molecule at 13C–14C is found to little deviated, and N–O usually will have 1.21 Å but in the molecule it is lengthened as 1.48 Å. In the same way bond angle is deviated by 0.5° to the value of the literature. In the second molecule the bond length is not changed much but due to the addition of the propanol group the structure of the hexagonal ring is slightly deviated. The same values are obtained from the computational study using B3LYP/6-311++G (d,p).

4 Vibrational Modes of the Molecules

While studying the vibrational modes of the molecules. FT-IR and FT-Raman spectra have recorded. The fundamental modes of the vibrations are identified in both the spectra. In the vibrational study of the molecule, the phenyl CH out-of-plane vibrations are found influenced by the N–O and CC vibrations, whereas the CH of propene are not in any way influenced by the other groups. In the case of the CC vibrations, they are not influenced by the other groups of N–O and CH vibrations. Similarly CN wavenumber nearer to 1500 cm^{-1} indicates C=N

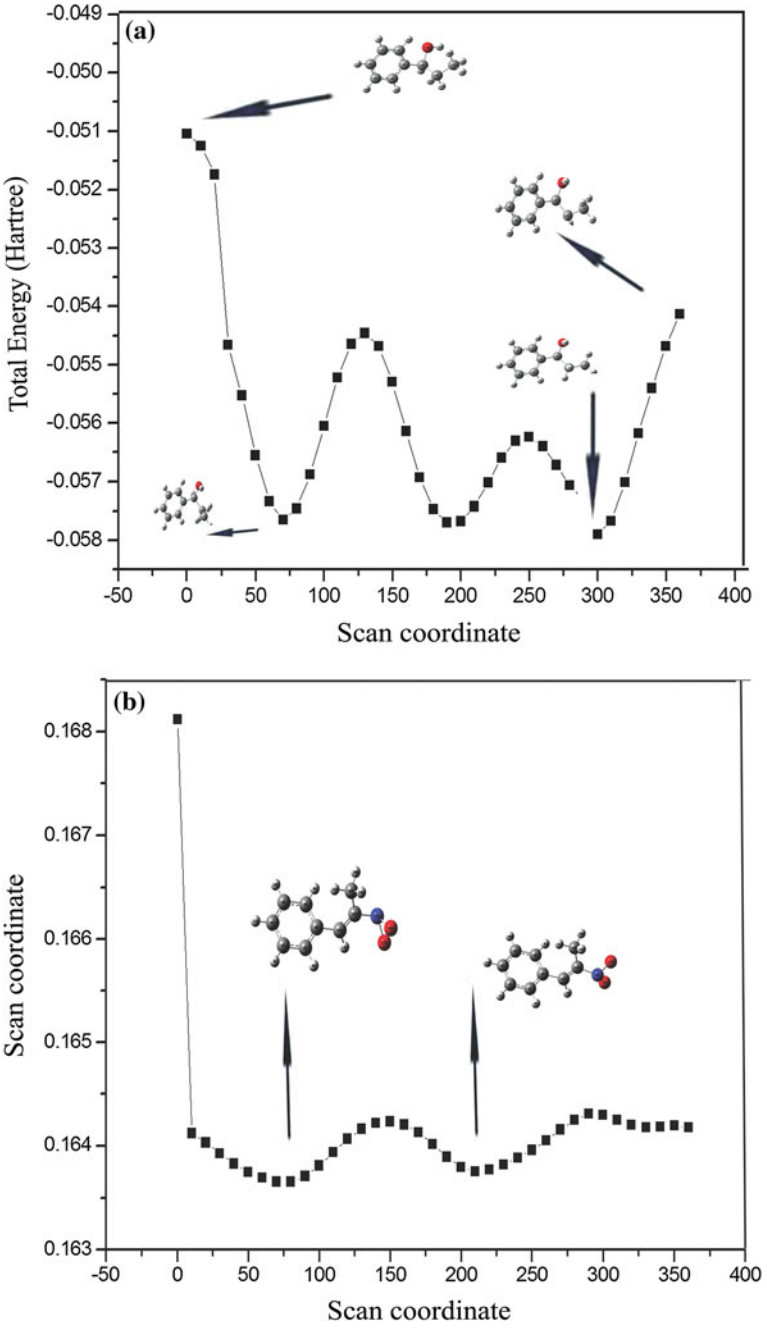

Fig. 3 Potential energy surface (PES) diagram of **a** 1-phenyl-1-propanol, and **b** 1-phenyl-2-nitropropene

while wavenumber nearer 1300 cm^{-1} indicates the presence of C–N, which may be due to the conjugation of electrons between the two adjacent NO bonds with this CN bonds.

The second compound consist of 22 atoms and 60 fundamental vibrations are possible. In the case of the OH vibrations, the in-plane and out-of-plane vibrations pushed above the range because of many CH vibrations in the molecule. In the same way the CH stretching vibrations of aliphatic ring in the compound pushed away from the usual limit, and four vibrations of CH out-of-plane suppressed below the expected range. Conversely the CC bonds are not affected by the presence of OH and CH bonds (Figs. 4a, b and 5a, b).

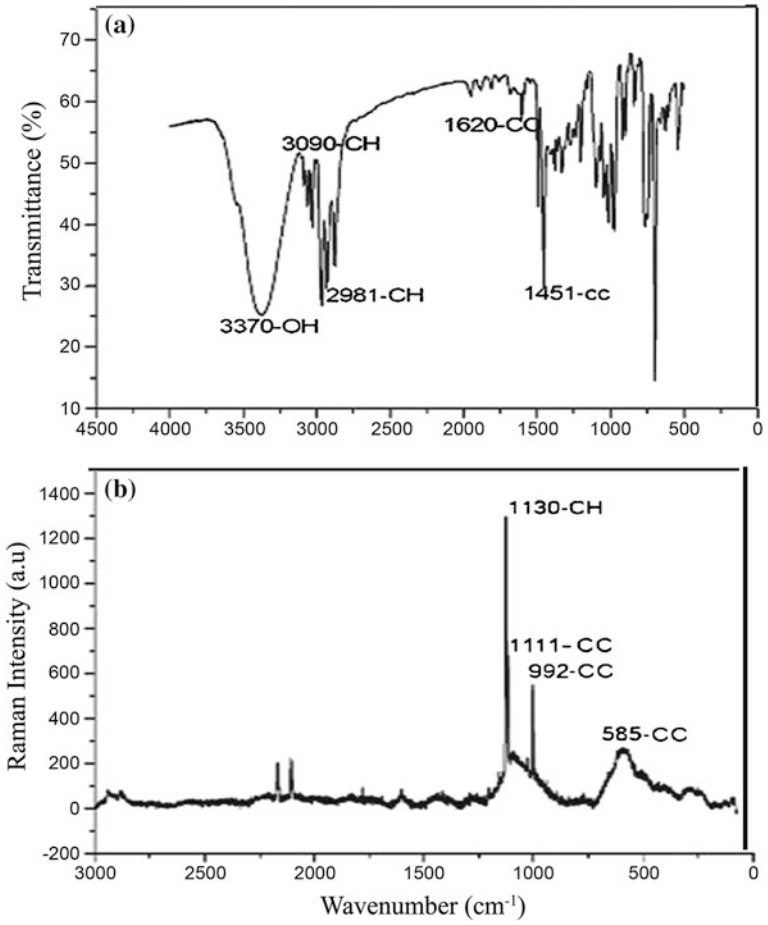

Fig. 4 **a** FT-IR, and **b** FT-Raman spectra of 1-phenyl-2-nitropropene

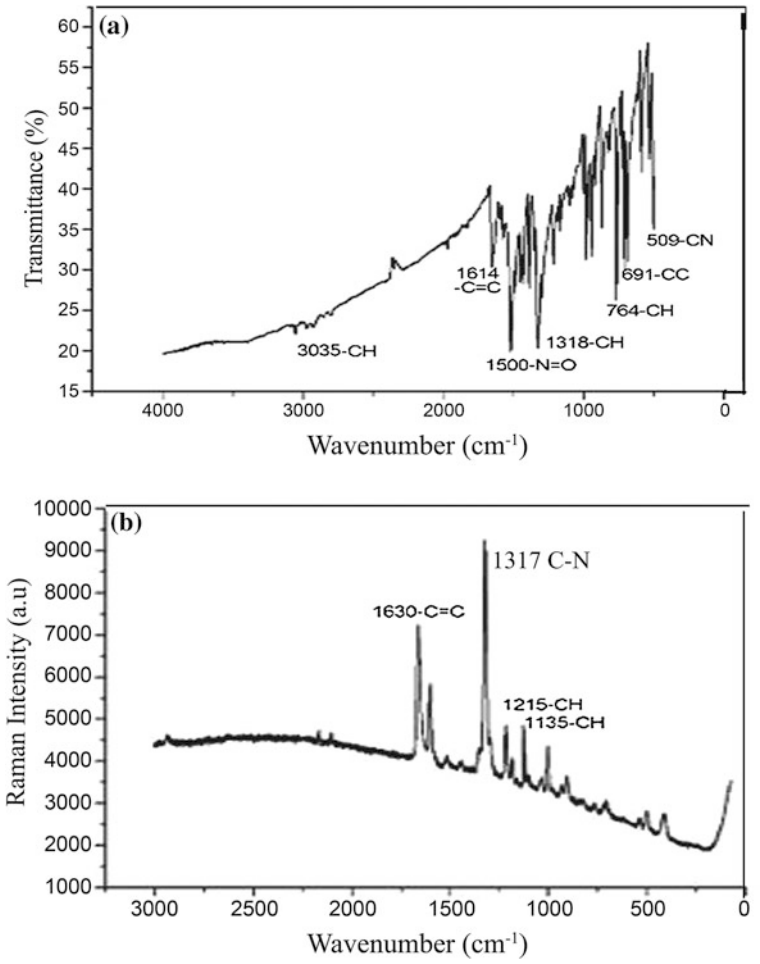

Fig. 5 **a** FT-IR, and **b** FT-Raman spectra of 1-phenyl-1-propanol

5 Natural Bond Orbital (NBO), UV-Vis, HOMO-LUMO Analysis

For the 1-phenyl-2-nitropropene the intra and inter charge distribution between acceptor and donor or LUMO to HOMO was analyzed in the natural bonding orbitals. There were several transition observed. Among them transitions which retains the highest stabilization energy in the bond formation or chromophore are considered to be responsible for the electronic transition with the corresponding molecular transitions. In this case three transition with highest stabilization energy are observed (Fig. 6a, b).

The most probable transition is n–π* transition from O16 to N15–O17 (159.57 kcal/mol), and the next probable transitions are C12–C14 to N15–O17

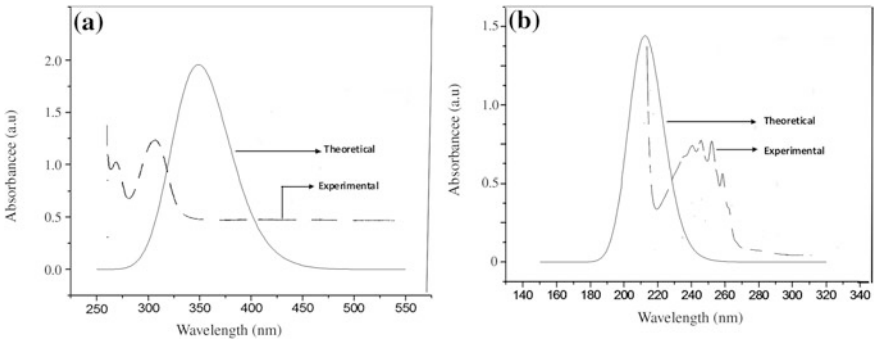

Fig. 6 UV-Vis spectra of **a** 1-phenyl-2-nitropropene, and **b** 1-phenyl-1-propanol

(π–π*, 21.04 kcal/mol), which takes place within the substitution group and C1–C2 to C5–C6 (π–π*, 20.60 kcal/mol), inside the benzene ring.

Here the surprising result observed in the UV spectral analysis is that in gas phase the oscillator strength or absorption coefficient is considerably high only for the second transition C12–C14 to N15–O17 (π–π*, 21.04 kcal/mol), whereas that of the first and third transitions are negligibly small, hence only one peak is present in the UV-Vis spectrum corresponding to this transition. But in ethanol phase where the experimental spectrum is also recorded, the oscillator strength and the absorption coefficients are high only for first and third transitions. i.e. for O16 to N15–O17 (n–π*, 159.57 kcal/mol) and C1–C2 to C5–C6 (π–π*,20.60 kcal/mol) transitions, hence two peaks have appeared correspondingly. The second transition which present in gas phase does not present in ethanol phase. The experimental wavelength and the computational wavelength shows much deviation particularly peaks with low oscillators strength, hence proper correction factors may be introduced in the computational methods which are employed to calculate.

For the 1-phenyl-1-propanol the natural bonding orbitals three transition with highest stabilization energies observed are correlated with three transition observed in the UV-Vis spectrum. According to NBO prediction, these transitions are C2–C3 to C1–C6 (π–π*, 21.05 kcal/mol), C1–C6 to C4–C5 (π–π*, 20.66 kcal/mol), and C4–C5 to C2–C3 (π–π*, 20.48 kcal/mol). The experimental UV-Vis spectrum shows three peaks at wavelengths 247, 216 and 210 nm respectively and they are assigned to π–π* transitions with strong oscillator strengths.

6 NMR Spectral Analysis

In the NMR analysis, the 14C, 12C are found to be with high chemical shift because they are very near to the electron withdrawing nitro group. Whereas 18C is much shielded by the methyl hydrogen. In the case of hydrogen atoms in the benzene it is

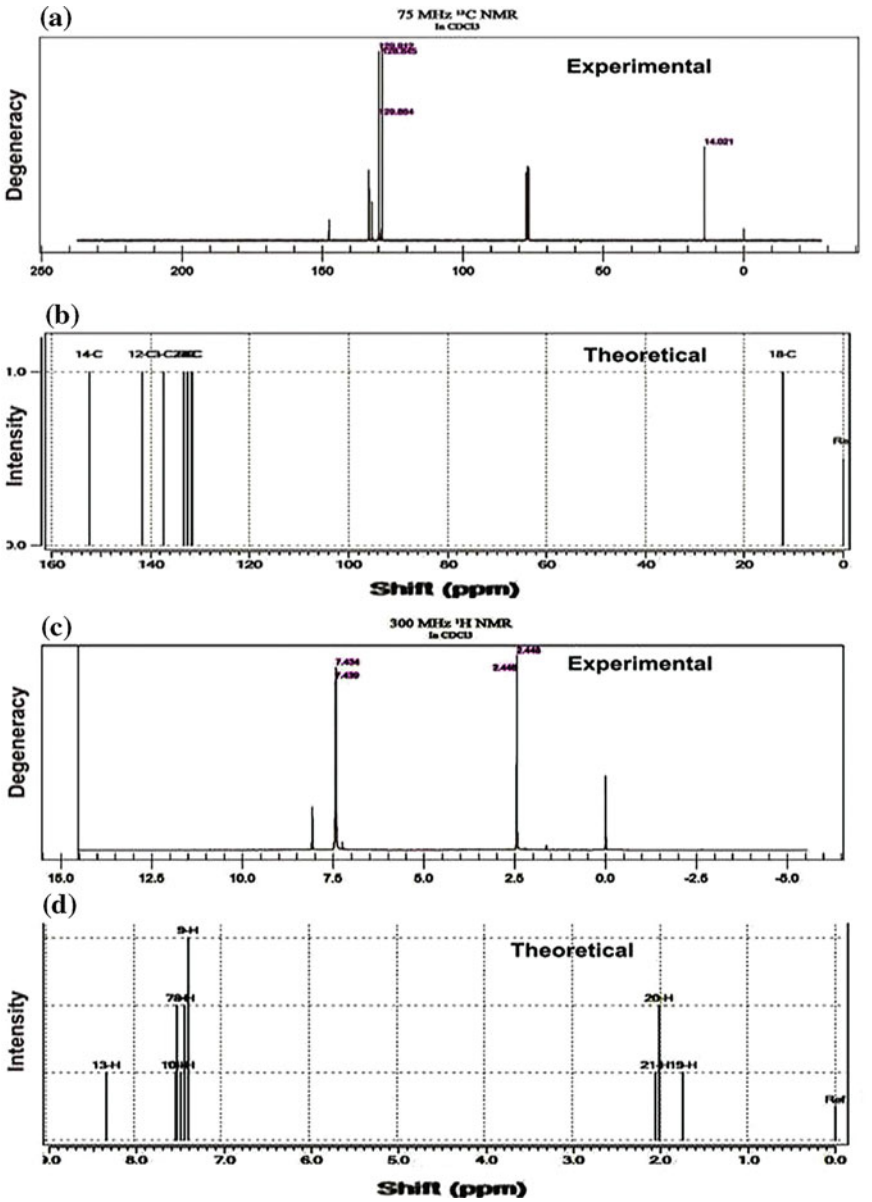

Fig. 7 NMR spectra ^{1}H (**a**–**b**), and ^{13}C (**c**–**d**) for 1-phenyl-2-nitropropene

between 8 and 7 ppm but the in the methyl group it is much low around 1.5 ppm. In the second molecule the trend similarly observed, the 12C carbon which is attached to the OH group is found to be with low chemical shift along with methyl group carbon. Other trends are as in the previous molecule (Figs. 7a–d and 8a–d).

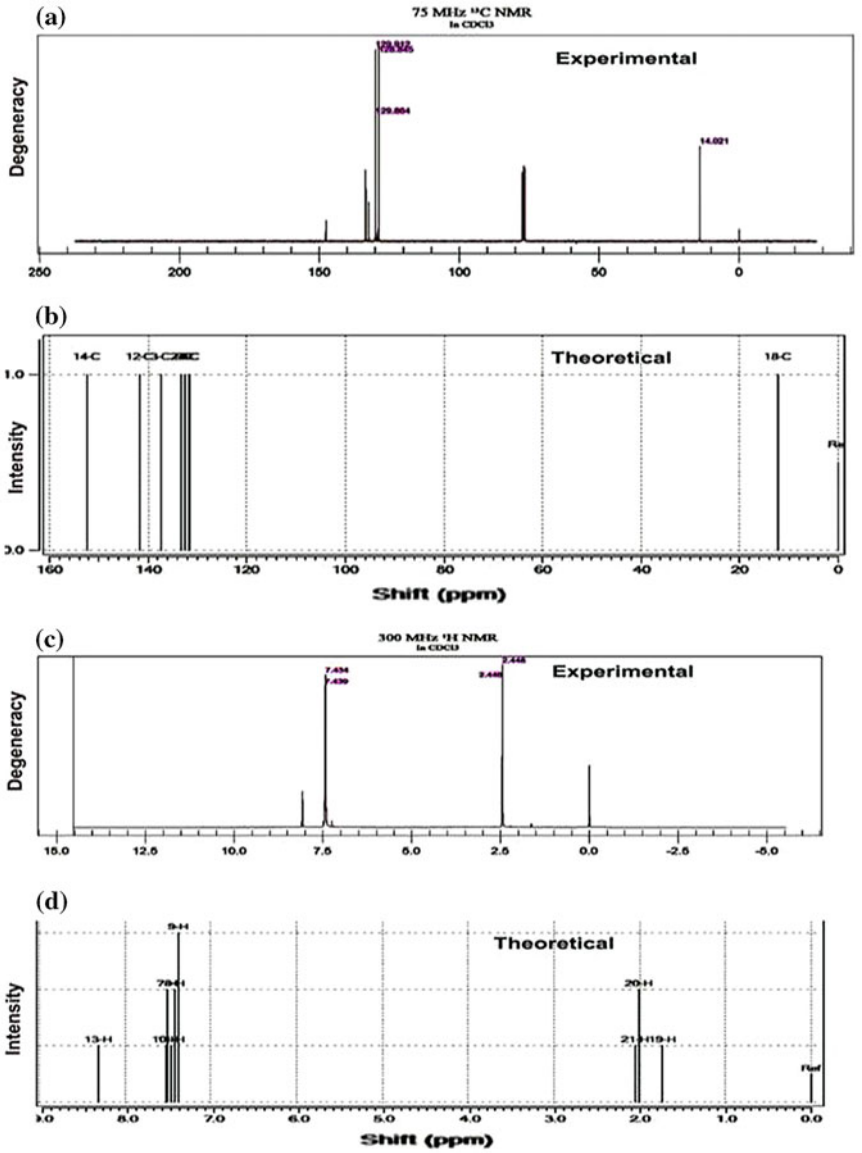

Fig. 8 NMR spectra ^{1}H (**a**–**b**), and ^{13}C (**c**–**d**) for 1-phenyl-1-propanol

7 Mulliken and Molecular Electrostatic Potential (MEP) Analysis

In the Mullikan analysis the 3C in the first molecule which is ipso carbon atom through the whole functional group is attached is found much positive than other carbon atoms. And the nitro group which are also found negative as expected. All

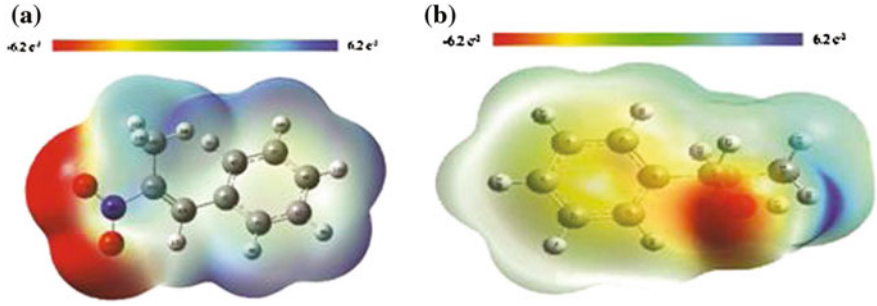

Fig. 9 Molecular electrostatic map of **a** 1-phenyl-2-nitropropne, and **b** 1-phenyl-1propanol

the hydrogen atoms appear positively charged. The same trend is seen globally through the MEP map. In the case of the second molecule the 3C is found be more positive and C14 and C17 are found to be negative along with the oxygen atoms. The MEP map clearly shows different negative and positive zones with the red and blue region (Fig. 9a, b).

8 Molecular Docking Study

PASS [5] is an online tool which predicts different types of activities based on the structure of a compound. PASS analysis of 1-pheny-2-nitropropene (1P2NP) predicts amongst other activities, Antineoplastic (breast cancer) activity with Pa (probability to be active) value of 0.792. The docking analysis is used to identify the possibility of protein ligand binding site. The structure of the target receptor is Breast Cancer (5HI2), Brain cancer (PDBID: 1QH4) and Lung cancer (PDBID: 2ITO) were obtained from RCSB protein data Bank (http://www.rcsb.org/pdb). Docking study can be done to find the best orientation of ligand with protein. Autodock.2 docking [6, 7] software tool is used for docking study. The protein structure were prepared with the help of Autodock Tools graphical user interface. Polar hydrogen was added to the protein and atomic charges were calculated by Kollman method. The water molecule and co-crystalline liquid were removed. The 1P2NP molecule were prepared for docking by minimizing the energy by B3LYP/6-311++G(d,p) method. The active site to the energies was defined to add residues of active side with the use of grid size 90 Å × 90 Å × 90 Å using Autogrid [8, 9]. The Lamarckian Genetic Algorithm is implemented in Autodock were employed for docking [8]. AutoDock Binding Energy (Kcal/mol) and inhibition constants (μM) were computed and Tabulated in Table 1.

In the protein the lowest free energy at −6.71 kcal/mol and most docked inhibitor interaction with ligand within 5HI2 binding site are shown in Figs. 10 and 11. They exhibit two N=O…H hydrogen bonding. The computation suggest confirm

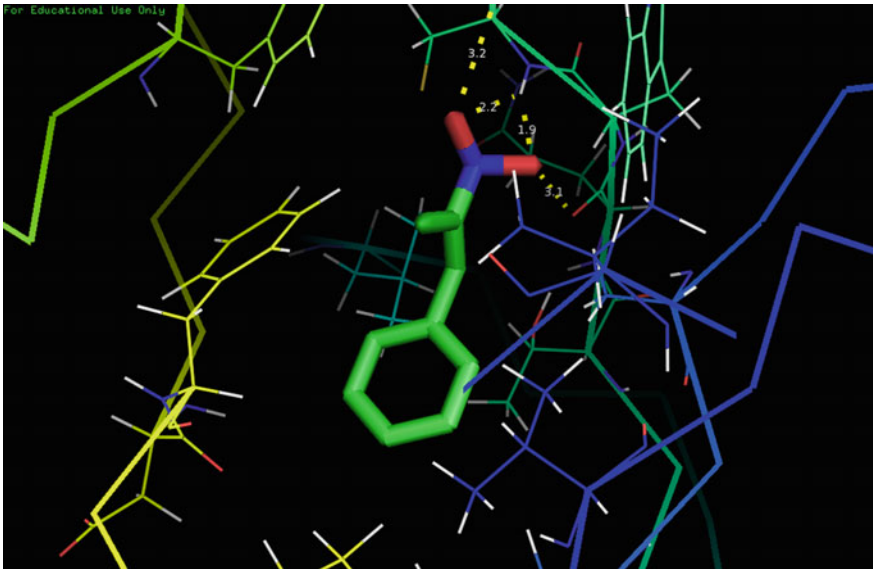

Fig. 10 Schematic representation of 1P2NP docking with 5HI2 breast cancer using stick model

Table 1 PASS prediction for the activity spectrum of the title compound, Pa represents probability to be active and Pi represents probability to be inactive

Pa	Pi	Activity
0.841	0.004	Bisphosphoglycerate phosphatase inhibitor
0.840	0.020	Ubiquinol-cytochrome-c reductase inhibitor
0.825	0.009	Feruloyl esterase inhibitor
0.832	0.025	Aspulvinone dimethylallyltransferase inhibitor
0.808	0.006	Fusarinine-C ornithinesterase inhibitor
0.792	0.004	Antineoplastic (breast cancer)
0.802	0.020	Acrocylindropepsin inhibitor
0.802	0.020	Chymosin inhibitor
0.802	0.020	Saccharopepsin inhibitor
0.782	0.007	Phosphatidylcholine-retinol O-acyltransferase inhibitor
0.783	0.012	Glutamyl endopeptidase II inhibitor
0.782	0.011	Dehydro-L-gulonate decarboxylase inhibitor
0.771	0.013	GST A substrate

Table 2 Summary of hydrogen bonding of 1P2NP molecule with cancer protein targets

Protein (PDB ID)	Bonded residues	No. of hydrogen bond	Bond distance
5HI2	Protein: A: CYS 532/O	4	3.2
	Protein: A: CYS 532/HN		1.9
	Protein: A: CYS 532/HN		2.2
	Protein: A: GLN 530/O		3.1

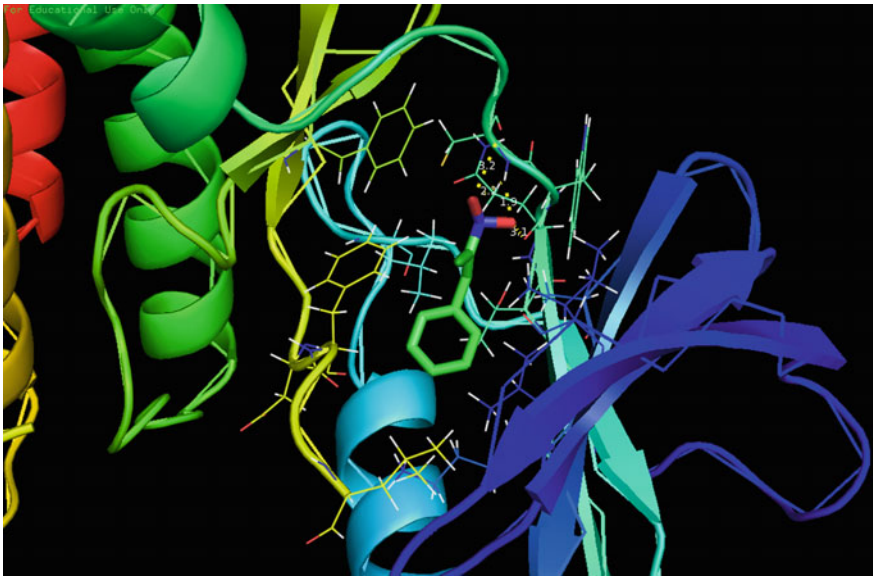

Fig. 11 Schematic representation of 1P2NP compound docking with 5HI2 breast cancer using ribbon model

the N=O moiety is engaged in hydrogen bond with amino acid residues as shown in Table 2. By conclusion IP2NP molecule exhibit inhibiting activity against breast cancer. Biological need to be carried to validate the computational assumptions.

9 Conclusion

All these studies are carried out with hybrid functional B3LYP with the basis set 6-311++G (d,p). The results are found closer to the experimental and literature values. The vibrational modes of the computational have been scaled to rationalize the experimental values. Among all the studies the NMR theoretical seems to be so closer to the experimental values. From the molecular docking study it is concluded that the target molecule exhibit the inhibitor activity in the breast cancer protein. Still the conclusions have to be authenticated with the experimental studies.

Acknowledgements We acknowledge gratefully for providing the **Quantum Computational Research Lab** in the PG and Research Department of Physics, St. Joseph's college of Arts and Science (Autonomous), Cuddalore for all the computational works.

References

1. Heal, D.J., Smith, S.L., Gosden, J., Nutt, D.J.: Amphetamine, past and present–a pharmacological and clinical perspective. J .Psychopharmacol. **27**(6):479–96 (2013)
2. Kaap, S., Quentin, I., Tamiru, D., Shaheen, M., Eger, K., Steinfelder, H.J.: Structure activity analysis of the pro-apoptotic, antitumor effect of nitrostyrene adducts and related compounds, Biochem. Pharmacol. 65, 603 (2003)
3. Xavier, S., Periandy, S.: Spectroscopic (FT-IR, FT-Raman, UV and NMR) investigation on 1-phenyl-2-nitropropene by quantum computational calculations, Spectrochim. Acta Part A Mol. Biomol. Spectrosc. **149**, 216–230 (2015)
4. Xavier, S., Periandy, S., Ramalingam, S.: NBO, conformational, NLO, HOMO-LUMO, NMR and electronic spectral study on 1-phenyl-1-propanol by quantum computational methods, Spectrochimica. Acta Part A: Mol. Biomol. Spectrosc. **137**, 306–320 (2015)
5. Lagunin, A., Stepanchikova, A., Filimonov, D., Poroikov, V.: PASS: prediction of activity spectra for biologically active substances. Bioinformatics, **16**, 747 (2000)
6. Morris, G.M., Huey, R., Lindstrom, W.: AutoDock4 and AutoDockTools4: Automated docking with selective receptor flexibility, J. Comput. Chem. **30**, 2785–2791 (2009)
7. Morris, G.M., Huey, R., Olson, A.J.: Using AutoDock for ligand-receptor docking, Curr. Protoc. Bioinf. **23**, 13514–13524 (2008)
8. Garrett, M.M., David, S.G., Robert, S.H., Ruth, H., William, E.H., Richard, K.B., Arthur, J.O.: Automated docking using a Lamarckian genetic algorithm and an empirical binding free energy function, J. Comput. Chem. **19**, 1639–1662 (1998)
9. Ruth, H., Garrett, M.M., Arthur, J.O., David, S.G.: Software news and update- A semiempirical free energy force field with charge-based desolvation, J. Comput. Chem. 28, 1145–1152 (2007)

Understanding, Prospects and Constraints of Emerging Nanotechnology

Manickam Sivakumar

Abstract Much effort is currently being devoted in Nanotechnology owing to its diverse range of technological applications. Nanotechnology deals with the design, characterization, production and application of structures, devices and systems by controlling their size and shape at nanometre scale. It focuses on manipulating the most basic components of all matter (atoms and molecules) with great precision and exploiting the novel properties or phenomena observed at that length scale as compared to their bulk-scale counterparts. Thus size effects become predominant at the nano scale. Most of the observed effects at this nano scale could be explained by surface and quantum confinement phenomena. It is an emerging interdisciplinary technology and promises significant advances in various technological applications. Nanotechnology is the new industrial revolution as it has the potential to revolutionise various sectors of the society. Still the potential of this technology has not been fully exploited as many questions still remain to be answered. Notwithstanding these advantages, it is a challenge to the government and industries as yet there are no specific regulations for assessing the toxicity or environmental impact of nanoparticles.

1 Introduction

Nanoscience which typically deals with the manipulation or controlling of materials at an atomic or molecular scale (1–100 nm) to create novel structures, devices and systems as the properties differ significantly in fundamental and valuable ways from those at larger scale (bulk matter). Whereas, nanotechnology concerns with the design, characterisation, production and application of structures, devices, and systems (Fig. 1) by controlling the size and shape at nanometre scale [1]. Alternatively it refers to many different technologies which are extremely small in

M. Sivakumar (✉)
Faculty of Engineering, Department of Chemical and Environmental Engineering,
University of Nottingham Malaysia Campus, Kuala Lumpur 43500, Selangor, Malaysia
e-mail: Sivakumar.Manickam@nottinghm.edu.my

J. Ebenezar (ed.), *Recent Trends in Materials Science and Applications*,
Springer Proceedings in Physics 189, DOI 10.1007/978-3-319-44890-9_5

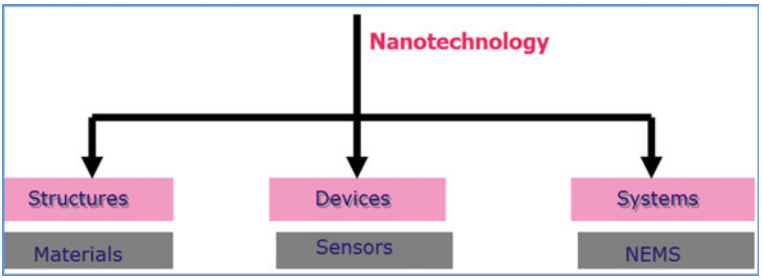

Fig. 1 Nanotechnology applied to structures, devices and systems

scale. In most of the instances, the focus of nanoscience and nanotechnology is on the manipulation of the most basic components of all matter i.e. atoms and molecules with great precision in the nanoscale range of 1–100 nm and then exploiting the novel properties or phenomena at that scale. By this it fills the gap between single atoms/molecules and microstructures.

It is an inherently interdisciplinary science encompassing physics, chemistry, biology, engineering, material science, computer science etc. This century belongs to interface science more precisely between molecular sciences and technology where the role of nanotechnology will be dominating and to prove this already a diverse range of nanomaterials and devices are on the technology road map of various high-tech industries. It is changing the nature of almost every human-made objects and influencing the economy in a greater way. In a more simple term nanotechnology could be described as "making things out of atoms". Although it is a small science but has a huge potential and the wide range of applications is the one force which drive the excitement surrounding the nano.

Although nanoparticles are generally considered an invention of modern science, they actually have a long history as they were used by artisans as far back as the 9th century in Mesopotamia to generate the glittering effect on the surface of pots [2]. The inspiration for molecular nanotechnology is Richard Feynman who gave a lecture on "There is plenty of room at the bottom" during a meeting at American Physical Society in 1959. He indicated that the problems in chemistry and biology can be greatly helped if our ability to see what we are doing and do thing on an atomic level is ultimately developed. Added to this, he precisely mentioned that those developments cannot be avoided [3].

2 Classification of Nanomaterials Based on Dimensions

Nanomaterial has at least one of its dimensions in the nanometric regime. Figure 2 shows the classification of nanomaterials based on dimensions in the nanometre range, number of directions where the electron confinement occurs and on the number of free directions for the electrons to move.

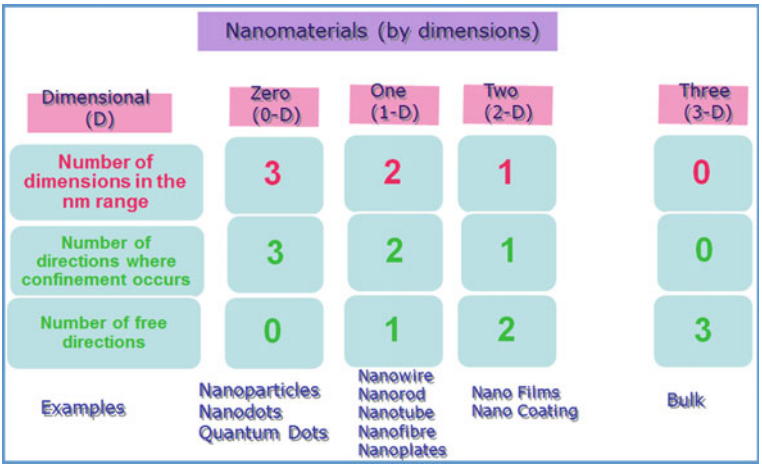

Fig. 2 Classification of nanomaterials by dimensions

3 Observation/Imaging of Nanomaterials

Since the naked eye can see only to about 20 μm it is not possible to observe the nanomaterials with naked eye. Even the light microscopes have the capability to see only up to about 1 μm as the wavelength (600 nm) of light is larger compared to the size of nanomaterial (less than 100 nm). Due to this, light can't bounce-off from the surface of nanomaterial to give an image. Thus, electron microscopes (EMs) are used as the wavelength (0.008 nm at 20 kV) of electrons is smaller and can easily bounce-off from the surface to create images with higher resolution. In 1980s a new way to see the nanoscale materials was developed using scanning probe microscopes such as atomic force microscopy (AFM) and scanning tunnelling microscopy (STM). In AFM, a tiny tip moves up and down in response to the electromagnetic forces between the atoms of the surface and the tip and the motion is recorded to create an image of the atomic surface. Whereas, in STM the flow of electrical current occurs between the tip and the surface and the strength of the current is used to create an image of the atomic surface. Using these techniques not only we are able to see the really smaller atoms but we can move them too.

4 Size-Dependent Properties of Nanomaterials

By looking at the above, is nanoscience just seeing and moving really small things? Definitely no. At the nanoscale when the particle size becomes smaller and smaller, the properties of the materials change at that smaller nano scale in an interesting way. Because, the properties or behaviour of the materials are size-dependent. Due

to this, gold in the nanoscale will not be as gold as in the micron scale. Depending on the size, they maybe red, blue, yellow, and other colours owing to the difference in the reflection and absorption of light with its thickness. Due to the small size, electrons are not free to move about as in bulk gold and this restricted movement makes the nanoparticles to react differently with light.

The size is very important as in the everyday scale Newton's law (F = ma) works perfectly but at the atomic or molecular level quantum mechanics is needed to describe the phenomena and properties. Nanomaterials are in a borderline (atomic or molecular and micro/macro) where either or both the approaches may be appropriate. The physical (hardness, melting point, diffusion rate), chemical (reactivity, catalysis), optical (colour, transparency) and electrical (conductivity) properties of the materials are size-dependent. Table 1 gives the characteristics of size-dependent gold building blocks.

Alternatively we can expect strange things at the nanoscale. Table 2 shows how the materials when reduced to nanoscale can show different properties compared to what they exhibit on macroscale enabling unique applications.

Nanomaterials are designed in a variety of shapes such as particles, tubes, wires, films, flakes, shells, etc. but all have one or more nanometre-sized dimension. For example, in case of CNTs, the diameter is in the nanoscale but the length can be several 100 nm or even longer. Whereas the nanoplates and nanofilms show the thickness in the nanoscale but the other two dimensions can be much larger. In nanotechnology, the size is manipulated without affecting the composition as the size is independent degree of freedom. The tightly controlled size and size

Table 1 Characteristics of size-dependent gold building blocks

	Size	Metal/non-metal	Colour
Atoms	10^{-10} m	–	Colourless
Clusters	<1 nm	Metal	Orange
Nanoparticles	3–30 nm	Metal (transparent)	Red
Particles	30–500 nm	Metal (turbid)	Crimson to blue
Bulk (film)	μm	Metal	Yellow

Table 2 Properties of metals: nano versus bulk

	Bulk	Nano
Cu	Opaque	Transparent
Al	Stable	Combustible
Au	Solid (room temperature); chemically inert	Liquid (room temperature); potent chemical catalyst
Pt	Inert	Catalyst
Si	Insulator; grey	Conductor; red
Au	Yellow	Red
Hg	Metal	Non-metal
Cd	Melting point of 1700 °C	Melting point of 800 °C

distribution are very important to obtain unique size-dependent properties. It is preferred that nanomaterials must be composed of monodispersed or nearly monodispersed nanoparticles.

5 Key Factors that Impact the Properties of Nanoscale Materials

The key factors to understand the nanoscale-related properties are dominance of electromagnetic forces, importance of quantum mechanical models, higher surface area to volume ratio and random (Brownian) motion. It is very important to understand these four factors when researching new materials and properties. Increased surface area (surface phenomena) and quantum confinement effect (quantum phenomena) are the principal factors responsible for much of the fascination existing with nanotechnology.

5.1 Surface Effect or Phenomena

For the same volume, nanomaterials have larger surface area and thus more surface is available for interaction. With a reduction in the size of particles, greater proportion of atoms will be found at the surface compared to inside or higher the percentage of atoms with smaller particle size. Whereas, when the particle is larger a smaller fraction of atoms (or molecules) are on the surface. In this case, atoms on the surface have fewer neighbours than those on the interior. It is to be noted that only atoms on the surface interact with another material and take part in a chemical reaction. Table 3 gives the relation between the particle size and surface molecules (%).

5.1.1 Impacts of Smaller Particle Size

Surface Area

The first and the most important consequence of a small particle size is huge surface area. With larger surface area, surface effects dominate. Larger surface energy

Table 3 Relation between the particle size and surface molecules (%)

Particle size (nm)	Surface molecules (%)
1	100
10	27.1
100	2.97
1000	0.3
10,000	0.03

makes nanomaterials thermodynamically unstable or metastable. Due to which the interaction of nanoparticles is induced leading to agglomeration or coagulation.

Conductivity

As particle size decreases, the band gap widens or the distance between conduction and valence band increases which lead to a decrease in thermal conductivity.

5.2 Quantum Phenomena

In the bulk materials, the electronic energy levels are continuous. Whereas, in nanocrystals they are not continuous but discrete which is due to the confinement of electronic wave function to the physical dimension of the particles. Quantum confinement (QC) is achieved by reducing the volume of the solid to the extent that the energy levels inside become discrete. This leads to creating small droplets of isolated electrons, the number of which will be few and countable. By this the charge and energy of sufficiently small volume of materials are quantised just like atom. This results into making fake atoms. In a particle, the freely moving electrons (excited or conduction) which may be in hundreds or thousands are confined inside a volume. Whereas, the vast majority of the electrons are tightly bound within inner orbitals which are not confined. Novel electronic devices are developed using this QC effect [4].

Two fabrication approaches could be followed to constrain the dimensions of a given volume. First, the bottom-up approach which builds low-volume structures atom by atom. In the second top-down approach, materials are removed from one or more of the three dimensions (L/W/H) of a larger solid. The above two approaches produce a structure small enough for quantum behaviour to manifest. Although three dimensions are available to confine electron, the QC indicates confining at least one of the dimensions to less than 100 nm. With the continuous confining of more of the dimensions leads to progressive discretisation which is a new way to understand the real atoms and the behaviour of electrons. In QC, different quantum structures are obtained depending on the constrainment. For example, constraining the electrons inside a region of minimal width leads to quantum well; further constraining the depth of electrons domain leads to quantum wire; with the minimisation of all the three dimensions results into quantum dot [4].

Thus, quantum wells and wires have at least one dimension for the electrons to move freely (partial confinement), but quantum dot exhibits total confinement. The above quantum structures are ideal candidates for high-density data storage. Metal particles of 1–10 nm and semiconductors up to 100 nm can behave like QDs. Due to this, the applications necessitating QC employ semiconductors as the dimensions can be more easily achieved. Overall, QC of electrons provides one of the most

powerful means to control the electrical, optical, magnetic, and thermoelastic properties of solid state functional materials [4].

6 Nanomanufacturing

There are a range of techniques applied in the nanomanufacturing which are classified under bottom-up and top-down approaches that include ball milling, sol-gel, wet chemical precipitation, epitaxy etc.

The desired objectives to be looked in the nanomanufacturing are:

1. The synthetic methods should be reproducible
2. The methods should produce monodispersed nanoparticles
3. The produced nanoparticles should be free from surface defects
4. The methods should be easy, cheap, scalable and environmentally friendly

Many different approaches have been applied to the fabrication of nano-entity, such as co-precipitation, microemulsion, supercritical sol-gel processing, hydrothermal synthesis, or high energy ball milling. Directed to the problems of these conventional methods, new synthetic methods have received increased attention in recent years. Its impact is more pronounced in the area of pharmaceuticals as increasing number of newly developed drugs are sparingly soluble in water and are often also insoluble in organic solvents, and thus the formulation of these drugs is a major obstacle to their clinical application. Because of their extremely low solubility, these drugs usually also possess poor bioavailability. Common ways of solving this problem include the use of solubilizers, cyclodextrins, and mixtures of solvents. But these methods have various shortcomings. An alternative to overcome these obstacles is the nanoformulation of these drugs. Nanotechnology is projected to influence with great promise for the future of cosmetics, diagnostics, drug therapies and biotechnologies. It has the potential to meet the needs of growing population, challenges of climate change and other ecological disturbances.

7 Applications

The following Table 4 shows the nanoparticles in our daily life.

Besides very common applications, in the petroleum engineering it is highly useful in the oil exploration. Conventional sensors to detect the oil are not reliable and inaccurate under harsh conditions. Whereas, owing to the small size nanosensors have the capability to probe the properties of oil that are deep in the reservoirs. They are extremely sensitive in measuring temperature, pressure, and underground stress. Besides, they are able to work under harsh conditions (extreme

Table 4 Nanoparticles in our daily life

Carbon black (nanoscale carbon)	Used for writing and painting added to rubber to make tires with more wear resistance
Nanophosphors	CRTs display colours
Nanoscale alumina and silica	To polish or smoothen silicon wafers
Iron oxide nano magnetic particles	Hard disks in the computers
Nano zinc oxide and titania	To block the UV light (useful in sunscreens and cosmetics)
Nano platinum	Catalytic converters (nano size is important for the critical operation)
Nanoscale thin films	Silicon chips (computers, digital cameras, photonic devices)
Nanoscale silica	Dental tooth fillers

high temperature and pressure). They also work safely even in the presence of electromagnetic fields. More importantly they are accurate and reliable [5]. The exhaust gases from the car contain CO and NO which are poisonous and harmful. To overcome the release of these gases, nano catalysts such as Pt is exploited in the catalytic converter, the usage of which converts the harmful CO and NO into harmless CO_2 and N_2 [6].

8 Challenges

The challenges existing with nanotechnology are (a) to develop instruments to assess exposure to engineered nanomaterials in the air and water (b) to develop and validate methods to evaluate the toxicity of engineered nanomaterials (c) to develop models to predict the potential impact of engineered nanomaterials on the environment and human health (d) to develop reverse systems to evaluate the impact on the environment and the health impact of engineered nanomaterials over their entire life-span which speaks to the life-cycle issue (e) to develop the tools to properly assess the risk to human health and to the environment. The Food and Drug Administration (FDA) attempts to ensure materials that are safe and effective. Whereas, Environmental Protection Agency (EPA) ensures that there is no demonstrable harm to an environment or to people in that environment. Even the regulatory agencies need to have adequate resources to monitor nano molecules properly [7].

Health, safety and environmental (HSE) effects of nanomaterials are very important and have not been looked seriously and it is the area of focus in the recent days. The health hazards of nanomaterials are not well defined. There is no long-term data on human exposure as well as on environmental damage. New technologies that show great promise have a history of being rushed to market without adequate HSE testing. Nanoparticles have been proven to bioaccumulate,

ending up in humans. NASA studies show that mice that are exposed to airborne nanotubes develop tumour like pulmonary growth after 90 days of exposure [8].

9 Risk Assessment and Management

Many assumptions about risk assessment and risk management that work in the macro world but some issues may be unique to nanomaterials owing to their small size. It is predicted that the surface area of a nanoparticle is really a key parameter in determining how much of the material produces a toxic effect. The charge of a particle affects how much can be absorbed across the cell membrane.

The risk assessment in nanotechnology has four components: (a) identification of hazard, where the adverse effects of nanomaterials are qualitatively evaluated (b) assessing the exposure, where the types (routes and media) magnitude or levels of exposure are evaluated (c) evaluation of dose response, where the relationship between dose and incidence of an adverse effect is looked into (d) characterisation of risk, where the probable incidence of adverse health effects under various conditions of exposure is quantitatively estimated [9].

Following are some of the ethical issues related to nanotechnology: (a) research ethics and the use of implanting nano-devices in humans (for example, implanting artificial devices) (b) increasing of uneven military power (c) increasing of economical gap between developed and developing countries (d) increasing possibilities of misused personal information i.e. revealing a medical information to insurance companies.

10 Conclusion

Nanotechnology is an example of the medici effect at work and people from diverse fields working together more intensively to solve the important problems in our society. It is changing practically every part of our lives and it is a field for people who want to solve technological challenges facing societies across the world. It is a combination of education, science, engineering, business, policy and many more. Nanotechnology promises significant advances in electronics, materials, biotechnology, alternative energy sources and other applications. Nanocrystals, nanotubes, nanowires and nanofibers are considered to be the next generation materials. There are few key challenges facing society globally; water, energy, health, sustainable development, environment, knowledge and economy and nanotechnology is believed to solve some of these.

References

1. Dowling, A.P.: Mater. Today, 7 **12**, 30–35 (2004)
2. Dutta, R.K., Sharma, P.K., Kobayashi, H., Pandey, A.C.: Adv. Polym. Sci. **247**, 233–276 (2012)
3. Feynmann, R.P. Available at http://nano.xerox.com/nanotech/feynman.html.
4. Rogers, B., Adams, J., Pennathur, S.: Nanotechnology: Understanding small systems, 3rd edn. CRC Press, USA (2007)
5. Barron, A.R., Tour, J.M., Busnaina, A.A., Jung, Y.J., Somu, S., Kanj, M.Y., Potter, D., Resasco, D., Ullo, J.: Oilfield Rev. **22**(3), 38–49 (2010)
6. Knecht, M.R.: TR Walsh. From surface analysis to applications, Springer, Bio-inspired nanotechnology (2014)
7. Maynard, A.D., Aitken, R.J., Butz, T., Colvin, V., Donaldson, K., Oberdörster, G., Philbert, M. A., Ryan, J., Seaton, A., Stone, V., Tinkle, S.S., Tran, L., Walker, N.J., Warheit, D.B.: Nature **444**(7117), 267–269 (2006)
8. Lam, C.W., James, J.T., McCluskey, R., Hunter, R.L.: Toxicol. Sci. **77**(1), 126–134 (2004)
9. Suzuki, T.: Nanotechnology Commercialisation, CRC Press, USA (2016)

Electrodeposition—A Simple and Effective Method for the Preparation of Metal Oxide Nanostructured Thin Films

D. Mangalaraj and S. Poongodi

Abstract In the present study, we have explained the preparation of tungsten trioxide thin films having different nanostructures such as, nanoparticles, nanosphere like chain, nanosheets, porous nanowalls, porous nanosphere, nanospindles, nanoplatelets with hierarchical flower like structure, nanoflakes and hierarchical flower like structure using facile electrodeposition method at room temperature. By varying the pH value of the electrolyte by using an organic acid like oxalic acid, we could obtain various nanostructured WO_3 thin films. The prepared thin films have been characterised using differnt analytical techniques and the results are presented.

1 Introduction

Thin film technology is one of the versatile technologies that have grown worldwide into major research areas in the recent years. The need for synthesis of new materials for industrial applications has resulted in a tremendous increase of innovative thin film processing technologies [1]. Today, thin film coatings serve as the key elements in many applications such as, microelectronics, catalysis, corrosion protection, chemical sensors, biosensors, displays, etc. [2–5]. Thin film studies have paved the way for the development of new areas of research in solid state physics and chemistry which are mainly based on phenomena associated with unique characteristics of the thickness, geometry and structure of the film [6]. Thin film materials exhibit properties, which are different from that of bulk materials due to their physical dimension, geometry and microstructure [7]. These properties are affected by their high surface-to-volume ratio and influence many phenomena such as gas adsorption, diffusion, and catalytic activity [8, 9]. Any material can easily be integrated into various types of devices by changing it into the thin film form.

D. Mangalaraj (✉) · S. Poongodi
Department of Nanoscience and Technology,
Bharathiar University, Coimbatore 641046, India
e-mail: dmraj800@yahoo.com

J. Ebenezar (ed.), *Recent Trends in Materials Science and Applications*,
Springer Proceedings in Physics 189, DOI 10.1007/978-3-319-44890-9_6

Flow chart

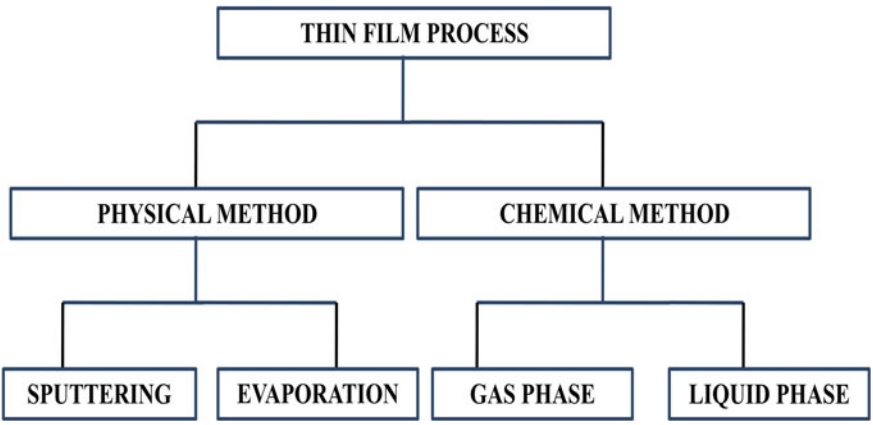

2 Physical Deposition Process

In physical deposition techniques, formation of the film is accomplished by direct transportation of atoms from source to the substrate through gas phase [9]. The physical routes are of two different forms viz., sputtering and evaporation. Basically, commercial physical deposition systems require a low-pressure environment and are classified as Physical vapor deposition (PVD) techniques. The various methods such as evaporation, thermal evaporation, electron beam evaporation, sputtering and reactive PVD are included in the family of physical vapour deposition systems. In these methods, the material to be deposited is placed in such a way that particles of the material which escape from the surface are allowed to arrive on a substrate to form a solid layer. In this method, the whole system is kept in a vacuum deposition chamber. The thin film deposition by physical means is commonly regarded as directional rather than conformal as the particles tend to follow a straight path.

Generally, these conventional physical routes (such as sputtering and evaporation) render better control over stoichiometry and produce uniform, compact and good quality thin films. They are safe (without emission of toxic gas) and provide a high deposition rate at room temperature. However these techniques require highly sophisticated instruments which are very expensive and therefore expanding to large scale becomes a major problem. On the other hand, because of their desirable cheapness and possibility of scaling up to industrial level, the chemical techniques for thin film deposition have become an essential alternative during the past few decades. In the case of chemical techniques, the thin film deposition is conformal

rather than directional. Among the various chemical methods, the most significant methods for synthesizing thin films are electrodeposition, chemical vapour deposition, cathode electrolytic deposition, anodic oxidation, chemical bath deposition, dip coating, hydrothermal and sol-gel method etc.

In the present work, as a demonstration, we have employed electrodeposition techniques for the synthesis of pure tungsten trioxide (WO_3) nanostructured thin films. A large number of conducting and semiconducting thin films can be prepared with desired properties by these methods. Moreover, thin films having large surface area with desired thickness can be synthesized with cost-effective equipment at low temperatures.

3 Electrodeposition Method

One of the standard methods of electroplating is the electrodeposition method. In the electrodeposition method, two metal electrodes are dipped into an electrolyte solution and the desired metal is deposited on the cathode (working electrode) on applying the external field across the electrodes. Depending on the electrical parameters such as electrode potential and current density, the thin film thickness can be controlled in a precise manner. Electrodeposition method has been used for the preparation of thin and thick films of metals, magnetic materials, super capacitive materials and chalcogenides [10, 11].

The use of electrodeposition for growth of semiconducting materials is comparatively new, being first introduced in the late 1970s [12]. For synthesizing the semiconductor materials via electrodeposition method, an electrolyte containing the appropriate ions and three electrodes such as working electrode, counter electrode and reference electrode are required, which are shown in Fig. 1. When a small dc power typically in the range of milliwatt is applied across the anode and the cathode, the positive ions are attracted towards the cathode, discharged and chemically react to form the required material.

In the present study, the WO_3 nanostructured thin films have been prepared using a SP-50 electrochemical work station (Fig. 2) supplied by Bio-Logic science and instruments (France).

4 Principles of Electrodeposition

Figure 3 shows the schematic diagram of a simple electroplating cell. The DC source, which is usually a rectifier or a motor generator, supplies current in one direction through the external portion of the circuit, when a potential difference is applied across the system. The current flow is the flow of electrons in the external circuit. The mechanism of electrical transfer in the solution is by means of

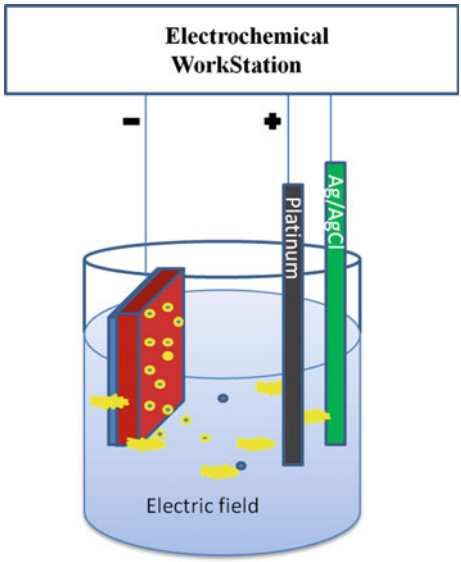

Fig. 1 Schematic diagram showing the main parts of a simple electrolytic cell

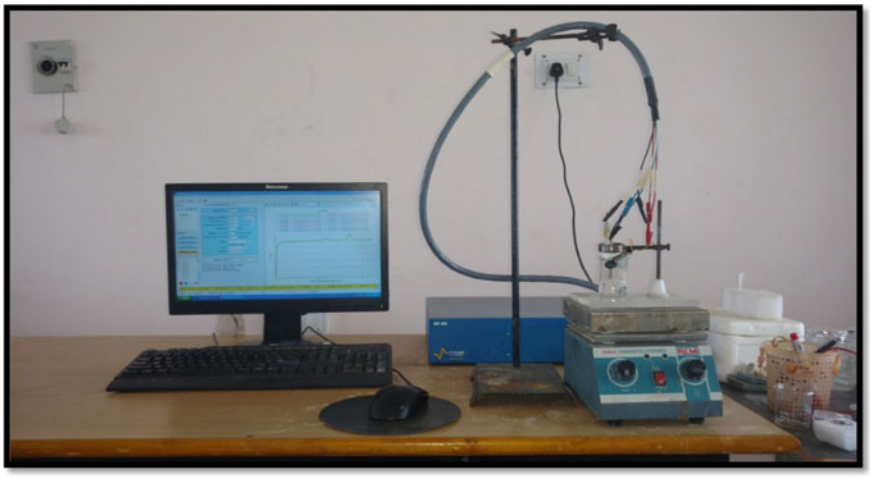

Fig. 2 SP-50 bio-logic science electrochemical work station

electrically charged "particles" called ions. Positive ions (cations) travel towards the negative electrode (cathode) and negative ions (anions) travel toward the positive electrode (anode) when the potential is applied, thus completing the electrical circuit. The electrolyte usually contains other components which influence the process [13].

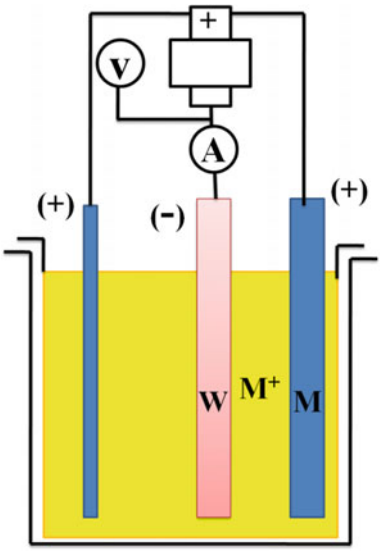

Fig. 3 Schematic of a simplified plating cell

(i) **Working electrode (WE)**

In the present work, FTO coated glass substrate with geometric dimension of about 3×1.5 cm^2 is used as the working electrode. Generally, FTO substrate is employed for synthesizing the electrochromic WO_3 film electrode for smart windows applications due to the fact that it can be bent and tempered without affecting the conductivity of the FTO coating.

(ii) **Counter electrode (CE)**

An electrode which is used to close the current circuit in the electrochemical cell is termed as counter electrode (also known as auxiliary electrode). Generally, counter electrode is made of an inert material (e.g. Pt, Au, graphite, glassy carbon). Also it does not take part in the electrochemical reaction owing to the fact that as the current is flowing between the WE and the CE, the total surface area of the CE (source/sink of electrons) must be higher than the area of the WE so that it will not be a limiting factor in the kinetics of the electrochemical process under investigation. In this work, Platinum wire (0.5 mm thick and 200 nm long) is employed as the counter electrode.

(iii) **Reference electrode**

The reference electrode is an electrode which has a stable and well-known electrode potential and serves as an experimental reference point in the electrochemical cell for potential control and measurement. The high stability of the reference electrode potential is usually reached by employing a redox system with constant (buffered or saturated) concentrations of each participant of the redox reaction. Moreover, the current flow through the reference electrode is kept close to zero (ideally, zero)

which is achieved by using the CE to close the current circuit in the cell together with a very high input impedance on the electrometer (>100 GΩ). In the present work, we have used the reference electrode consisting of a silver wire (1 mm, length—10 cm) coated with AgCl and dipped into a 1 M KCl solution. The compartment is a Teflon tube (ID = 2.5 mm, OD = 4 mm) with a "thirsty glass" plug (length 3 mm) and a tight Teflon stopper on the top.

5 Synthesis of WO_3 Nanostructured Thin Films

5.1 Preparation of the Electrolyte Precursor

All the chemicals used in this work were of analytical reagent grade and purchased from Himedia Co. Ltd., India and used without any further purification. In a typical synthesis, the precursor solution was prepared by dissolving 1.25 g of tungsten (W) powder in 40 ml of hydrogen peroxide (H_2O_2) (30 %) under constant stirring in a cold bath (0–10 °C) for 24 h. The excess hydrogen peroxide was decomposed by refluxing the solution at 80 °C for 6 h by the addition of glacial acetic acid under stirring, after filtering the clear solution. The resultant peroxo tungstic acid was then diluted to 50 mM with water and isopropanol in 50:50 ratios. The addition of iso-propanol improves the stability of the precursor solution by preventing the precipitation of peroxo complex for an extended period of time (3 days) [14]. The resulting electrolyte had a pH of 4.5. Different concentrations of oxalic acid were then added to adjust the pH values from 4 to 0.3. Here, the addition of oxalic acid to the precursor was done to slow down the condensation reaction as well as inhibit the growth of the hydrated tungsten trioxide particles. Also, the addition of the chelating agent into the precursor sol did not lead to the formation of precipitate or gel [15].

5.2 Preparation of WO_3 Thin Films

By using electrolytes with different pH (4, 3.5, 3, 2.51, 2, 1.51, 0.9, 0.5, 0.3) values, various nanostructured WO_3 thin films such as

- Nanoparticles
- Nanospheres
- Nanosquare plates
- Porous nanowalls
- Porous nanoballs
- Nanospindles
- Nanoplatelets with hierarchical flower structure

- Nanoflakes and
- 3D hierarchical structures

were deposited under potentiostatic conditions using a three electrode electrochemical station with a platinum wire as the counter electrode, Ag/AgCl as the reference electrode and FTO coated glass with WO_3 seed layer as the working electrode (3×1.5 cm^{-2}). The electrodeposition was carried out potentiostatically at −0.45 V against the reference electrode at room temperature without stirring for 30 min. The resulting films were rinsed immediately with distilled water and dried in air. The electrodeposited films were then annealed in a muffle furnace at 450 °C for 2 h in air after which structural characterization and electrochromic studies were carried out.

6 Results and Discussion

6.1 Structural Analysis

WO_3 nanostructure thin films have been prepared by the electrodeposition technique with the electrolyte consisting of peroxo-tungstic acid with pH values ranging from 4 to 0.3 in the presence of an organic acid such as oxalic acid. The crystalline phase purity and structure of the electrodeposited WO_3 thin film as functions of the pH value were determined by X-ray diffraction (XRD). The XRD patterns of the WO_3 thin films are shown in Fig. 4. The major diffraction peaks can be indexed to (002), (020), (200), (120), (202), (130), (222), (303), (134) and (−234) crystal Planes. All the diffraction peaks are assignable to the monoclinic phase of WO_3

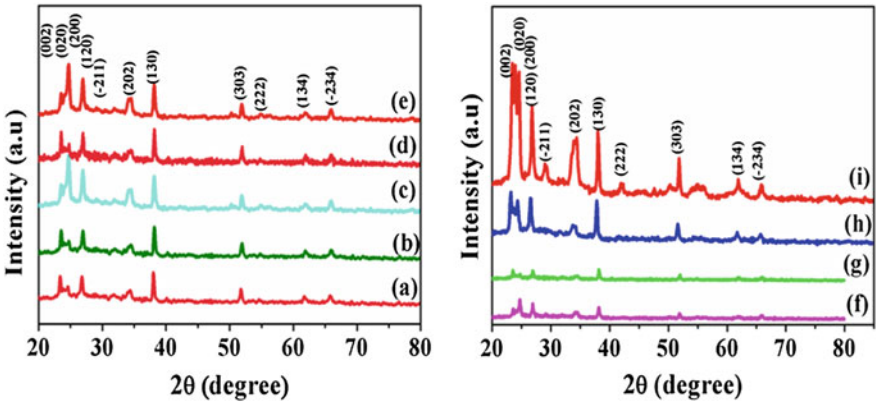

Fig. 4 XRD patterns of electrodeposited WO_3 thin films: **a** pH = 4, **b** pH = 3.51, **c** pH = 3.0, **d** pH = 2.51, **e** pH = 2.0, **f** pH = 1.51, **g** pH = 0.9, **h** pH = 0.5 **i** pH = 0.3

structure (JCPDS NO. 89-4476) and no hydrated WO_3 is found, indicating the purity of the WO_3 obtained.

In addition, the intensities of the diffraction peaks are obviously different from each other, revealing different preferred growth directions due to the different pH values. The improved crystallinity will enhance the electrochromic performance of the WO_3 thin films by reducing the charge transfer resistance during the double injection/ejection of ions and electrons into the WO_3 film. Thus, the WO_3 film electrodeposited at pH = 0.3 exhibits enhanced electrochromic performance compared to the film electrodeposited at pH = 3.51. These results indicate that addition of organic acid into the electrolyte plays a crucial role in controlling the crystallinity of the WO_3 thin films.

6.2 *Morphological Analysis*

Figure 5 shows the FESEM images of the electrodeposited, annealed (450 °C) WO_3 thin films obtained at different pH values (4–0.3) by the addition of organic acid. The figure reveals that the annealing process not only manifests in the enhancement of orientation and surface grain size but also results in well resolved and highly textured morphology [16]. The observation of triplet peaks along (002), (020) and (200) orientations in the XRD pattern (Fig. 4) gives evidence of the formation of WO_3 films with textured nature. The surface morphology of these films exhibits considerable variations depending on the pH value of the electrolyte. Figure 5a, b shows the FESEM images of the electrodeposited WO_3 thin film when the pH is fixed at 4. The entire film has flat and compact small agglomerated nanoparticles like morphology at this stage. When the pH is changed to 3.51 by adding organic acid, the WO_3 film is composed of chain like nanospheres as in Fig. 5c, d. The entire film consists of uniformly dispersed nanosheets like structures for the pH value of about 3 as shown in Fig. 5e, f. Further, when the pH is decreased to 2.51, the entire film is composed of nanoporous walls like structures (Fig. 5g, h). As shown in Fig. 5i, j, by adding an organic acid like oxalic acid to decrease the pH further, the formation of porous nanosphere can be achieved (pH = 2).

Figure 6a, b shows the FESEM images of the electrodeposited WO_3 thin film when the pH is fixed at 1.51. The entire film has flat and compact small nanospindles like morphology at this stage with thickness ranging from 50 to 90 nm. When the pH is adjusted to 0.9, the WO_3 film is composed of nanoplatelets with an increased thickness of about 40–50 nm as in Fig. 6c, d. Figure 6e, f shows that homogenously distributed, well aligned nanoflakes array have grown in an almost perpendicular direction over the entire film when the pH is adjusted to 0.5. The thickness of these nanoflakes ranges from 10 to 20 nm with a height of about 1 μm. Finally, when the pH is decreased to 0.3, the entire film turns out to be composed of homogenously distributed, well aligned hierarchical flower like WO_3 nano arrays with diameters of 1 μm over a large area. Further observations of high magnification images divulge

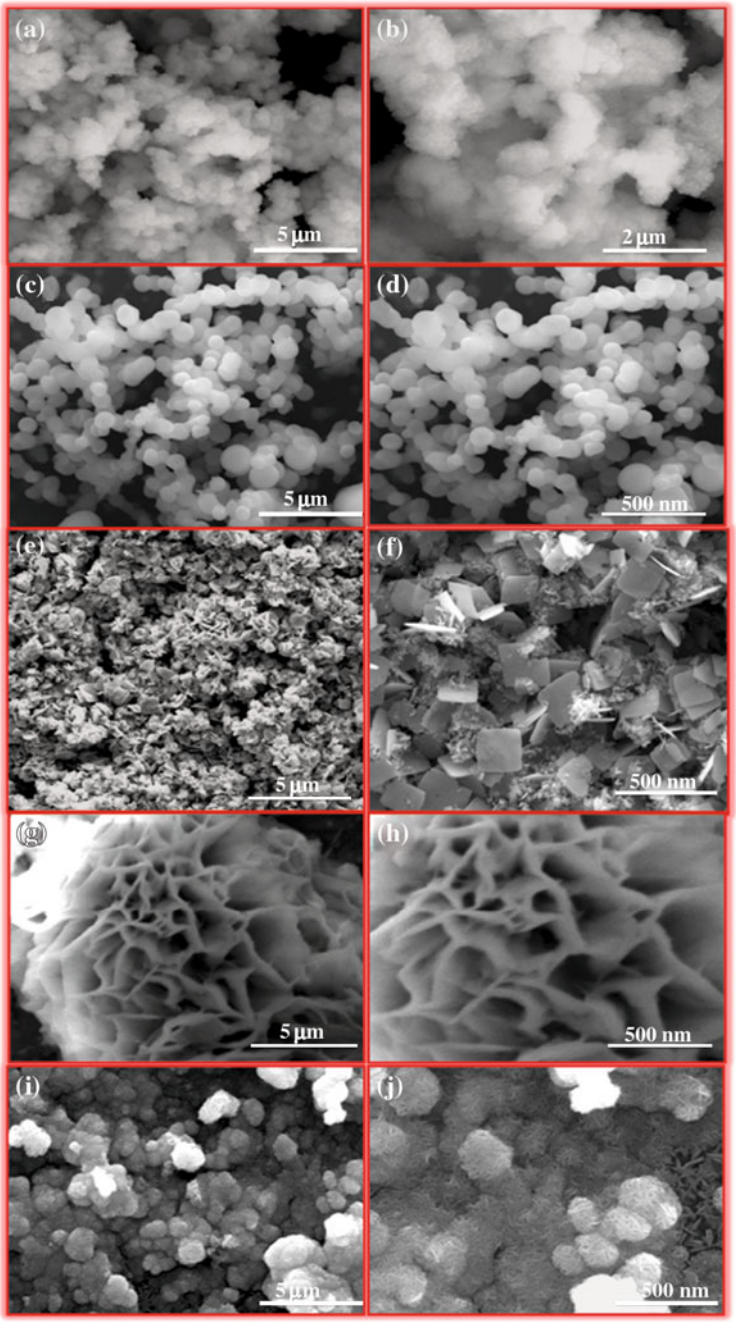

Fig. 5 FESEM images of electrodeposited WO_3 nanostructured thin films: **a** and **b** pH = 4, **c** and **d** pH = 3.51, **e** and **f** pH = 3.0, **g** and **h** pH = 2.51, **i** and **j** pH = 2.0

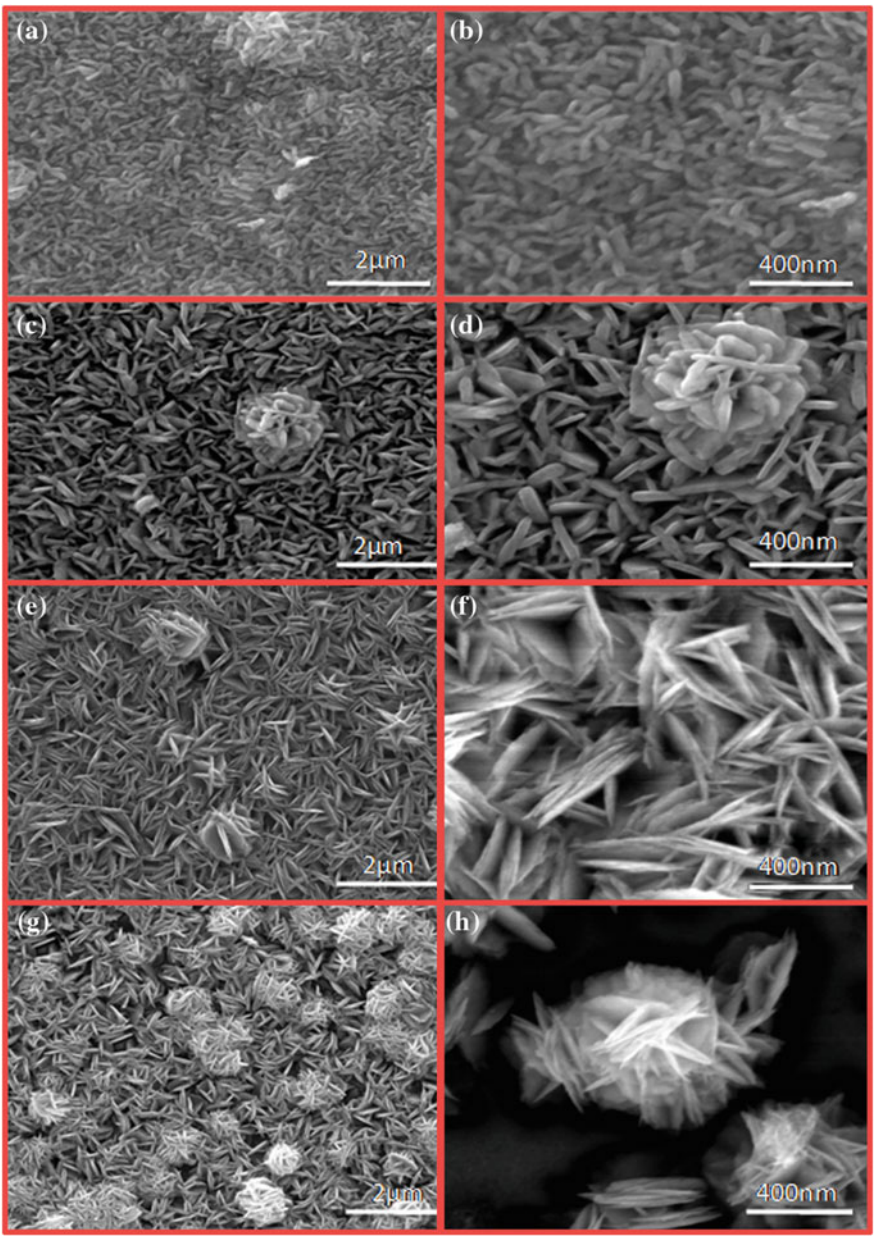

Fig. 6 FESEM images of electrodeposited WO_3 nanostructured thin films: **a** and **b** pH = 1.51, **c** and **d** pH = 0.9, **e** and **f** pH = 0.5, **g** and **h** pH = 0.3

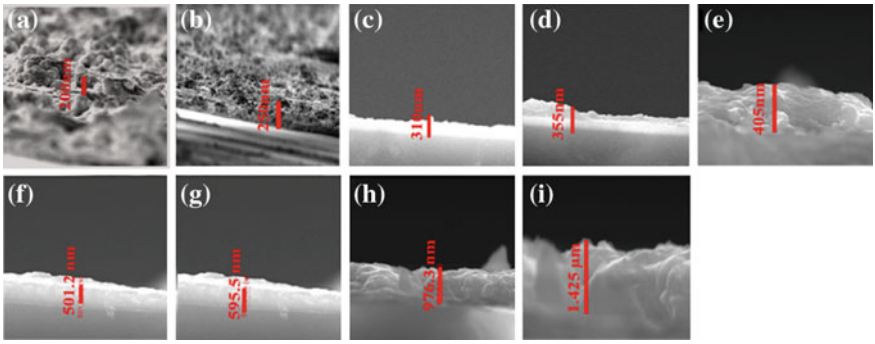

Fig. 7 Cross section images of electrodeposited WO_3 nanostructured thin films at various pH values: **a** pH = 4, **b** pH = 3.51, **c** pH = 3.0, **d** pH = 2.51, **e** pH = 2, **f** pH = 1.51, **g** pH = 0.9, **h** pH = 0.5, **i** pH = 0.3

that the hierarchical flower like morphology is comprised of self-assembled nanoflakes with thickness ranging from about 10–20 nm (Fig. 6g, h).

Their corresponding cross section images are shown in (Fig. 7a–i). From these results, we can conclude that decreasing the pH of the electrolyte by means of increasing the concentration of oxalic acid leads to different nanostructures.

7 Conclusion

In the present study, various WO_3 nanostructured thin films—nanoparticles, nanosphere like chain, nanosheets, porous nanowalls, porous nanosphere, nanospindles, nanoplatelets with hierarchical flower like structure, nanoflakes and hierarchical flower like structure have been successfully fabricated by facile electrodeposition method at room temperature. By varying the pH value of the electrolyte by using an organic acid like oxalic acid, we could obtain various nanostructured WO_3 thin films. X-ray diffraction and Raman spectra confirmed that the prepared nanostructured thin films are pure WO_3 with monoclinic phases. From all the observations, we can conclude that the oxalic acid in the electrolyte plays an important role in determining the surface morphology.

References

1. West, A.R.: Solid State Chemistry. Wiley, Singapore (2003)
2. Elshabini, A., Barlow, F.: Thin Film Technology Handbook. McGraw-Hill, New York (1998)
3. Anderson, J., Boudart, M.: Catalysis: Science and Technology, 1. Springer, Berlin (1981)
4. Talbot, D., Talbot, J.: Corrosion Science and Technology. CRC Press, Boca Raton (1998)

5. Madou, M., Morison, S.: Chemical Sensing with Solid State Devices. Academic Press Inc, Boston (1989)
6. Chopra, K.L.: Thin Film Phenomena. McGraw Hill, New York (1969)
7. Nitzsche, K.: Schichtmeßtechnik, 1. Vogel Buchverlag, Würzburg (1996)
8. Ohring, M.: The Material Science of Thin Films. Academic Press, Inc., San Diego (1992)
9. Chopra, K.L., Das, S.R. Thin Film Solar Cells. Plenum Press, New York (1983)
10. Machado, G., Guerra, D.N., Leinen, D., Ramos-Barrado, J.R., Marotti, R.E., Dalchiele, E.A.: Thin Solid Films **490**, 243 (2005)
11. Chang, S.T., Leu, I.C., Hon, M.H.: Electrochem. Solid State Lett. **5**(8), C71–C74 (2002)
12. Dharmadasa, I.M., Haigh, J.: J. Electrochem. Soc. **153**(1), G47–G52 (2006)
13. Lou, H.H., Yinlun H.: Encyclopedia of Chemical Processing (2006)
14. Ou, J., Balendhran, S., Field, M.R., McCulloch, D.G., Zoolfakar, A.S., Rani, R.A., Zhuiykov, S., O'Mullaneb, A.P., Zadeh, K.K.: Nanoscale **4**, 5980 (2012)
15. Sun, M.U., Ning, X.U., Cao, Y.W., Yao, J.N., Wang, E.G.: J. Mater. Sci. Lett. **19**, 1407 (2000)
16. Antonik, M.D., Schneider, J.E., Wittman, E.L., Snow, K., Vetelino, J.F., Lad, R.J.: Thin Solid Films **256**, 247 (1995)

Part II
Nanomaterials

Spectroscopic Investigation on rGO:ZnO Composites Nanostructures

Thangaraj Pandiyarajan, Ramalinga Viswanathan Mangalaraja, B. Karthikeyan, Héctor D. Mansilla and M.A. Gracia-Pinilla

Abstract This report presents the preparation and spectroscopic properties of rGO:ZnO composite nanostructures. The reduced graphene oxide (rGO) and rGO:ZnO composite structures were prepared through modified Hummer's and solution precipitation techniques, respectively. The decoration of star like ZnO nanostructures on rGO surface was identified through transmission electron microscopy (TEM) analysis. Raman spectral measurements revealed the co-existence of vibrational modes of ZnO and rGO which confirmed the formation of composites nanostructures. The absorption spectra of ZnO hybrid and rGO nanostructures exhibited bands at 370 and 261 nm which were attributed to the free excitonic absorption of ZnO and rGO absorption band, respectively.

T. Pandiyarajan (✉) · R.V. Mangalaraja (✉)
Advanced Ceramics and Nanotechnology Laboratory, Department of Materials Engineering, University of Concepcion, Concepcion, Chile
e-mail: rtpandiyarajan@gmail.com

R.V. Mangalaraja
e-mail: mangal@udec.cl

B. Karthikeyan
Department of Physics, National Institute of Technology, Tiruchirappalli 620 015, India

H.D. Mansilla
Department of Organic Chemistry, Faculty of Chemical Sciences, University of Concepcion, Concepcion, Chile

M.A. Gracia-Pinilla
Facultad de Ciencias Físico-Matemáticas, Universidad Autónoma de Nuevo León, Av. Universidad, Cd. Universitaria, San Nicolás de los Garza, Nuevo León, Mexico

M.A. Gracia-Pinilla
Centro de Investigación en Innovación y Desarrollo en Ingeniería y Tecnología, Universidad Autónoma de Nuevo León, PIIT, 66600 Apodaca, Nuevo León, Mexico

J. Ebenezar (ed.), *Recent Trends in Materials Science and Applications*, Springer Proceedings in Physics 189, DOI 10.1007/978-3-319-44890-9_7

1 Introduction

Over the decades, hybridization of carbon (carbon fibers, CNT and graphene) materials with nano semiconductors offers powerful tools to alter its host properties [1–4]. Naturally, ZnO is a II–VI wide band gap semiconductor with band gap of 3.37 eV and high exciton binding energy (60 meV) at room temperature [5] makes the materials utilized in various fields like optics, sensor and catalysis [6]. Similarly, graphene is a two-dimensional (2D) carbon-based honeycomb lattice material with hexagonal atomic structure and is being used in energy storage, photocatalysis and various electronic applications [7]. The hybridization of graphene sheet with ZnO nanostructures exhibits novel physical and chemical properties over their parent materials and been utilized in different technological fields such as optoelectronics, sensors, energy and environmental industries. For instance, Haldorai et al. [8] have developed high performance supercapacitors by use of rGO:ZnO composites. Kavitha et al. [9] have prepared rGO:ZnO hybrid nanostructures through hydrothermal and solution precipitation techniques and their results revealed the hybrid nanostructures exhibit enhanced optical limiting properties and been used in optoelectronic industries. Palanisamy et al. [10] have developed amperometric sensor for hydrogen peroxide (H_2O_2) using reduced graphene oxide (rGO)/zinc oxide (ZnO) composites which are prepared through electrochemical route with good operational and storage stability. Similarly, Chen and his group [11] have prepared rGO:ZnO composites via hydrothermal route and their results showed that the prepared composites exhibit exceptional photocatalytic activities against methyl orange (MO).

In this work, Hummer's and solution precipitation techniques were applied for the synthesis of reduced graphene oxide and reduced graphene oxide:ZnO hybrid nanostructures respectively, to investigate their spectroscopic properties.

2 Materials and Methods

2.1 Synthesis of Reduced Graphene Oxide (rGO)

All chemicals used in the experiment were of high purity reagents purchased from Sigma-Aldrich without further purification. The graphene oxide and reduced graphene oxide were prepared using modified Hummer's and hydrazine reduction route, respectively [9]. The preparation of graphitic oxide was as follows: Initially, 4 g of graphite powder were mixed with 70 mL of H_2SO_4 and stirred for 2 h. 6 g of $KMnO_4$ were added to the above solution and the temperature of the mixtures was kept at less than 20 °C. The temperature of the above mixture was then raised to 35 °C and stirred for 30 min. The resulting solution was diluted by adding 180 mL of distilled water under continuous stirring and a dark brown colour suspension was obtained. The final reaction was terminated by the addition of 300 mL of distilled

water and 30 % of H_2O_2 solution. Further, the above solution was continuously stirred for 2 h, and the mixture was washed thoroughly with 5 % of HCl in an aqueous solution. The obtained precipitates were filtered and dried at 40 °C under vacuum for 24 h. The 0.5 g of as-prepared graphitic oxide was re-dispersed in 500 mL of distilled water and sonicated for 2 h continuously lead to exfoliation of graphitic oxide into graphene oxide (GO). Later, the prepared graphene oxide was reduced by adding 0.5 ml of hydrazine hydrate (N_2H_4) into the exfoliated GO solution (0.5 g in 500 mL) under vigorous stirring. The mixture was heated to 90 °C and kept it for 24 h under constant stirring. The final solution became black in colour and the reduced graphene sheets were washed thoroughly with distilled water several times to remove the residuals. Finally, the obtained reduced graphene oxide (rGO) sheets were dried in a hot air oven at 80 °C for 5 h.

2.2 Synthesis of ZnO

The pure ZnO nanostructures were prepared by adding dropwise 200 ml of 0.1 M NaOH dissolved in double distilled water into 200 ml of 0.05 M zinc acetate dihydrate $Zn(CH_3COO)\cdot 2H_2O$ dissolved in double distilled water. These mixtures were stirred for 4 h at 60 °C. The white coloured dispersion formed was kept at room temperature for 12 h to get the precipitates. Then the precipitates were washed with distilled water and ethanol to remove the unreacted products. Final products were collected and dried in a hot air oven at 100 °C for 3 h to get pure ZnO powders.

2.3 Synthesis of rGO:ZnO Composites

To prepare hybrid nanostructures, 100 ml of 0.05 M zinc acetate dihydrate and 0.05 g of polyvinyl pyrrolidone (PVP) dissolved in double distilled water were mixed and stirred for 30 min to form zinc acetate-PVP complex. Then, 70 mg of rGO was added to the above mixture and sonicated for 1 h to make the homogeneous mixing. 100 ml of 0.1 M NaOH dissolved in 100 ml double distilled water was added dropwise into the above mixture and was stirred for 4 h at 60 °C. The white with light black coloured dispersion formed was kept at room temperature for 12 h to get the precipitates. The resultant precipitates were washed with distilled water and ethanol to remove the unreacted products. The obtained product was dried in a hot air oven at 100 °C for 3 h. The samples were named as ZnO and rGO: ZnO for zinc oxide and rGO and zinc oxide composite, respectively.

2.4 Characterization

The prepared materials were characterized by using powder X-ray diffraction (XRD) technique (Bruker, D4 Endeavor) with diffraction angle (2θ) in the range of 20°–80° to identify the crystalline nature. The morphology and decoration of ZnO on rGO surface were characterized via transmission electron microscope (TEM, JEOL Model JSM–6390LV). Raman spectroscopy analysis was done using Thermo Scientific DXR Raman Microscope with 532 nm laser as exciting light source with 5 mW power. The optical properties of the materials were analysed through absorption spectroscopy by using Shimadzu UV-Vis 2550 spectrometer.

3 Results and Discussion

3.1 Structural Characterization

Figure 1 represents the XRD pattern of rGO:ZnO hybrid nanostructures.

The rGO:ZnO hybrid structures exhibit hexagonal wurtzite phase of ZnO (JCPDS No:01-089-1397). The diffraction peaks are located at 2θ = 31.2°, 33.9°, 35.7°, 46.9°, 56.1°, 62.3°, 65.9°, 67.5°, 68.4°, 72.56° and 76.86° which correspond to (100), (002), (101), (102), (110), (103), (200), (112), (201), (004) and (202) planes of the wurtzite structure, respectively. The diffraction peak of rGO was not observed in the rGO:ZnO composite due to the lower concentration of rGO and the destroyed regular stacks of rGO in the hybrid structures [12].

The morphologies of prepared ZnO nanostructures and decoration of ZnO on the reduced graphene sheets were identified by using TEM analysis and are shown in Fig. 2. TEM images clearly demonstrate the triangular shaped morphology of

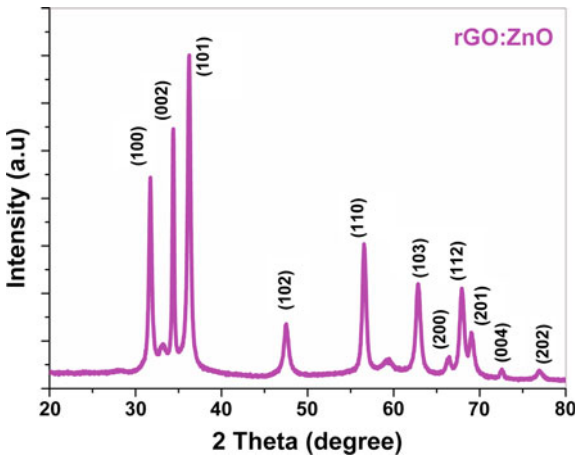

Fig. 1 XRD spectrum of rGO:ZnO composite nanostructures

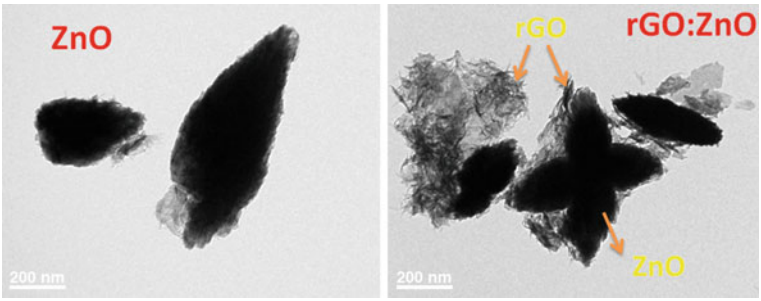

Fig. 2 TEM images of ZnO and rGO:ZnO composites nanostructures

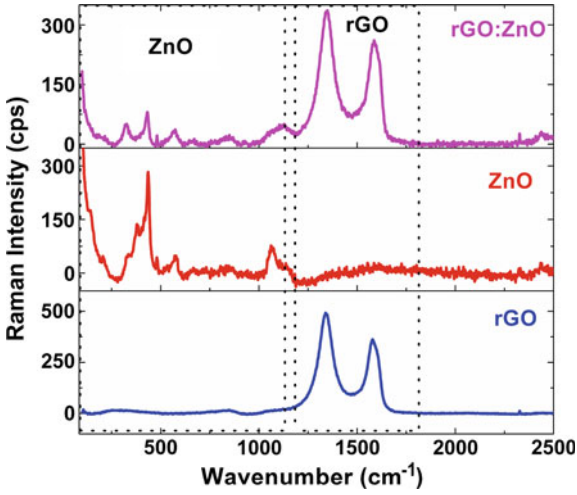

Fig. 3 Raman spectra of rGO, ZnO and rGO:ZnO composites nanostructures

prepared ZnO and the star like morphology of rGO:ZnO composite. Furthermore, the decoration of ZnO nanostructures on the reduced graphene oxide surface was identified.

The formation of composite nanostructures was identified through Raman spectroscopy and is depicted in Fig. 3. According to the selection rule, the wurtzite structure of ZnO exhibits six optically active phonons [13] namely $E_{2L} + E_{2H} + A_{1T} + A_{1L} + E_{1T} + E_{1L}$,where, A_1 and E_1 modes are polar optical mode and E_2 mode is non-polar optical mode. E_2 phonon mode has two wavenumbers namely E_2^{low} and E_2^{high} modes which are associated with the vibration of zinc sub lattices and oxygen motions, respectively, belongs to the characteristics peaks of ZnO structures. The peak located at 431 cm^{-1} is assigned to E_2^{high} mode and the multiphonon Raman mode is appeared at 325 cm^{-1}, due to the vibration of $E_2^{high} - E_2^{low}$. Also, the bands at 481, 574 and 1129 cm^{-1} are ascribed to the $2LA$, $A_1(LO)$ and $2LO$ phonon modes, respectively [14]. The Raman peaks at 1338 and 1577 cm^{-1} are ascribed to D and G bands of reduced graphene oxide, respectively [15]. The appearance of

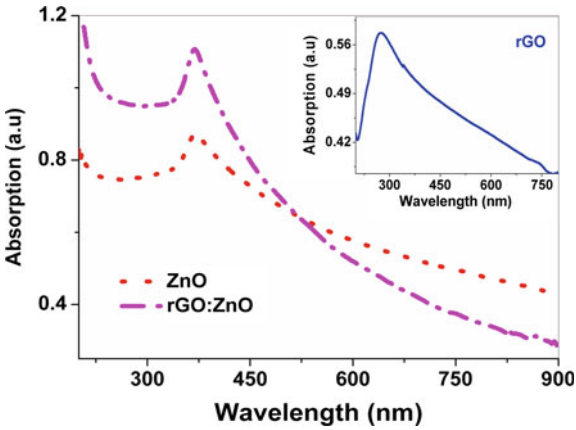

Fig. 4 Absorption spectra of ZnO and rGO:ZnO composites nanostructures. *Inset figure* represents the absorption spectrum of rGO

peaks from reduced graphene oxide and ZnO confirms the formation of composite structures.

3.2 Absorption Spectra

The absorption spectra of ZnO, rGO and rGO:ZnO composites nanostructures are shown in Fig. 4. The rGO nanostructures show a band at 272 nm that confirmed the formation of high quality reduced graphene oxide. ZnO nanostructures exhibit a band at 370 nm which attributed to the free Excitonic absorption of ZnO [16]. Similarly, rGO:ZnO composite nanostructures show the excitonic absorption band of ZnO and there is no rGO absorption band as similar kind results have been reported by Liu and his group [16].

4 Conclusion

The rGO and rGO:ZnO composite nanostructures were successfully synthesized via Hummer's and solution precipitation methods, respectively. The powder diffraction measurements showed that the prepared materials are highly crystalline with wurtzite structure of ZnO. The triangular shaped ZnO and decoration of star like ZnO on the rGO surface were observed through TEM. Furthermore, the formation of composite nanostructures was identified through Raman spectral measurements by observing co-existence of rGO and ZnO Raman modes.

Acknowledgements The authors gratefully acknowledge the FONDECYT-CONICYT Project No: 3140178 Government of Chile, Santiago, for the financial assistance.

References

1. Ji, T.H., Sun, M., Han, P.: A review of the preparation and applications of graphene/semiconductor composites. Carbon **70**, 319–322 (2014)
2. Yang, M.Q., Zhang, N., Pagliaro, M., Xu, Y.J.: Artificial photosynthesis over graphene-semiconductor composites. Are we getting better? Chem. Soc. Rev. **43**, 8240–8254 (2014)
3. Lv, T., Pan, L., Liu, X., Sun, Z.: Enhanced photocatalytic degradation of methylene blue by ZnO–reduced graphene oxide–carbon nanotube composites synthesized via microwave-assisted reaction. Catal. Sci. Technol. **2**, 2297–2301 (2012)
4. Han, C., Yang, M.Q., Weng, B., Xu, Y.J.: Improving the photocatalytic activity and anti-photocorrosion of semiconductor ZnO by coupling with versatile carbon. Phys. Chem. Chem. Phys. **16**, 16891–16903 (2014)
5. Pandiyarajan, T., Karthikeyan, B.: Birth of room temperature Magnons and Raman line enhancement in ZnO nanostructures containing Cobalt oxide. J. Raman Spectrosc. **44**, 1534–15393 (2013)
6. Djurišić, A.B., Chen, X., Leung, Y.H., Ng, A.M.C.: ZnO nanostructures: growth, properties and applications, J. Mater. Chem. **22**, 6526–6535 (2012)
7. Zhu, Y., Murali, S., Cai, W., Li, X., Suk, J.W., Potts, J.R., Ruoff, R.S.: Graphene and graphene oxide: synthesis, properties, and applications. Adv. Mater. **22**, 3906–3924 (2010)
8. Haldorai, Y., Voit, W., Shim, J.J.: Nano ZnO@reduced graphene oxide composite for high performance supercapacitor: green synthesis in supercritical fluid. Electrochim. Acta **120**, 65–72 (2014)
9. Kavitha, M.K., John, H., Gopinath, P., Philip, R.: Synthesis of reduced graphene oxide–ZnO hybrid with enhanced optical limiting properties. J. Mater. Chem. C **1**, 3669–3676 (2013)
10. Palanisamy, S., Chen, S.M., Sarawathi, R.: A novel nonenzymatic hydrogen peroxide sensor based on reduced graphene oxide/ZnO composite modified electrode. Sens. Actuators B: Chem. **166–167**, 372–377 (2012)
11. Chen, T.T., Chang, I.C., Yang, M.H., Chiu, H.T., Lee, C.Y.: The exceptional photo-catalytic activity of ZnO/RGO composite via metal and oxygen vacancies. Appl. Catal. B **142–143**, 442–449 (2013)
12. Rabieh, S., Nassimi, K., Bagheri, M.: Synthesis of hierarchical ZnO–reduced graphene oxide nanocomposites with enhanced adsorption–photocatalytic performance. Mater. Lett. **162**, 28–31 (2016)
13. Pandiyarajan, T., Baesso, M.L., Karthikeyan, B.: Enhanced ultraviolet-blue emission and Raman modes in ZnO:Cr_2O_3 composite nanoparticles. Eur. Phys. J. D **68**, 28(1–9) (2014)
14. Šćepanović, M., Grujić-Brojčin, M., Vojisavljević, K., Bernik, S., Srećković, T.: Raman study of structural disorder in ZnO nanopowders. J. Raman Spectrosc. **41**, 914–921 (2010)
15. Mohanty, N., Nagaraja, A., Armesto, J., Berry, V.: High-throughput ultrafast synthesis of solution—dispersed graphene via a facile hydride chemistry. Small **6**, 226–231 (2010)
16. Liu, X., Pan, L., Zhao, Q., Lv, T., Zhu, G., Chen, T., Lu, T., Sun, Z., Sun, C.: UV-assisted photocatalytic synthesis of ZnO–reduced graphene oxide composites with enhanced photocatalytic activity in reduction of Cr(VI). Chem. Eng. J. **183**, 238–243 (2012)

Supercontinuum Generation in a Silicon Nanowire Embedded Photonic Crystal Fiber for Optical Coherence Tomography Applications

E. Gunasundari, K. Senthilnathan, P. Ramesh Babu, J. Ebenezar and K. Nakkeeran

Abstract In this paper, we design a silicon nanowire embedded photonic crystal fiber (SN-PCF) using fully vectorial finite element method. Further, we analyze the various optical properties, namely, waveguide dispersion and nonlinearity by varying the core diameter from 400 to 500 nm for a wide range of wavelengths from 0.8 to 1.7 μm. The proposed structure exhibits a low second (-0.4909 ps^2/m) and third order (0.6595 10^{-3} ps^3/m) dispersions with very high nonlinearity (1358 $W^{-1}m^{-1}$) for 480 nm core diameter at 0.8 μm wavelength. Besides, we investigate the evolution of supercontinuum at 0.8, 1.3 and 1.55 μm wavelengths for an incredibly low input pulse energy of 2.5 pJ. The numerical results corroborate that the proposed SN-PCF provides a wider supercontinuum bandwidth of 1250 nm at 0.8 μm, 1100 nm at 1.3 μm and 800 nm at 1.55 μm wavelengths. We demonstrate longitudinal resolution of 0.16 μm at 0.8 μm wavelength for ophthalmology and dermatology, 0.41 μm at 1.3 μm wavelength for dental imaging and 0.8 μm at 1.55 μm wavelength also for dental imaging. To our knowledge, these are the highest resolution ever achieved in biological tissue at 0.8, 1.3 and 1.55 μm wavelengths.

E. Gunasundari · K. Senthilnathan · P. Ramesh Babu (✉)
Department of Physics, School of Advanced Sciences, VIT University, Vellore 632 014, India
e-mail: prameshbabu@vit.ac.in

J. Ebenezar
Department of Physics, Jamal Mohamed College (Autonomous), Tiruchirappalli 620 020, India

K. Nakkeeran
Department of Engineering, Fraser Noble Building, King's College, University of Aberdeen, Aberdeen AB24 3UE, UK

J. Ebenezar (ed.), *Recent Trends in Materials Science and Applications*, Springer Proceedings in Physics 189, DOI 10.1007/978-3-319-44890-9_8

1 Introduction

Optical coherence tomography (OCT) is a new technology for noninvasive cross-sectional imaging of tissue structure in biological system by directing a focused beam of light at the tissue to be imaged [1]. This technique is used for both transparent and non-transparent biological tissues and its performance depends on longitudinal (axial) and transverse (lateral) resolution, dynamic range, measurement speed and center wavelength of light source. Nowadays, OCT is used for not only opthalmology but also for dermatology, dental as well as for the early detection of cancer in digestive organs. Previously, typical sources for OCT applications were superluminescent diodes (SLDs) and sources based on an amplified spontaneous emission (ASE) from doped fibers or semiconductors [2]. All of these sources have a limited spectral bandwidth and a restricted wavelength range. Therefore, SLDs having 10–15 μm longitudinal resolutions that are used for most of the standard OCT applications are being replaced with PCF based supercontinuum (SC) light sources [2, 3].

The wavelength range of the OCT light source is spread from 0.8 to 1.6 μm wavelength. This wavelength region is of particular interest for OCT because it penetrates deeply into biological tissue and permits spectrally resolved imaging of water absorption bands [4]. In the spectral region, loss is minimum due to absorption and scattering. Ultrahigh-resolution OCT imaging in the spectral region from 0.8 to 1.6 μm requires extremely broad bandwidths because longitudinal resolution depends on the coherence length. The coherence length is inversely proportional to the spectral width and proportional to square of the center wavelength of the light source. This can be achieved by SC using PCFs. The opthalmology and dermatology OCT imaging are mainly operated at near 0.8 μm center wavelength [1, 5]. The dentistry OCT imaging is done at 1.3 μm wavelength [6]. Currently, the broadband light source can be employed to take the OCT image of human tooth samples at 1.5–1.6 μm [7].

Recently, the research focus is on SC as it happens to be one of the proven techniques for the generation of high intense ultrafast broadband light source. It arises from the nonlinear interaction and propagation of ultrashort pulse in the nonlinear material. The SC light source is used in various fields such as ranging, imaging, remote sensing and computation. Most commonly used microstructured fibers to produce SC are photonic crystal fibers (PCFs), birefringent PCF, tapered fibers, hollow fibers, single and multiple sub-wavelength size core fibers and different material doped silica fibers [8–16]. The PCFs turn out to be a very good platform to produce high power light source in OCT system. Because PCFs can produce wider SC spectrum due to their design flexibility which result in enhanced nonlinear effects by reducing the core area and by appropriately tailoring the dispersion characteristics. In a typical PCF based SC source, the effective mode area of the PCF is roughly $\sim 1\ \mu m^2$ with several meter of PCF [17]. Further, by reducing

the core down to nm size and tapering the micro-structured core, the effective optical nonlinearity can be increased [18]. Although these previous studies have demonstrated efficient generation of SC in on-chip integration, those sources demand a large propagation length for generating high spectral broadening.

A promising alternative solution is provided by silicon waveguide sources [19], which have the advantage of employing an emerging silicon-on-insulator (SOI) integrated-photonics platform. Silicon has excellent transmission properties compared to silica and does not require high power density to bring in nonlinearity owing to its huge nonlinear coefficient [20]. Till date, many reports for SCG in silicon nanowire are available [18–21]. Recently, the possibility of SCG of 500 nm bandwidth at telecommunication wavelength has been demonstrated with various input peak powers for various SOI waveguide lengths. Such a dielectric silicon waveguide with a nanocore diameter could provide a remarkably strong field confinement, enhanced light-matter interactions and strong tunable dispersions when embedded into PCF [22]. The resulting silicon photonic device known as silicon nanowire embedded photonic crystal fiber (SN-PCF) has been proposed very recently [23]. These small core structures are ideal devices for nonlinear processes such as pulse compression and SC generation within short fiber lengths [24–26].

In this work, we report a broadband SC in highly nonlinear SN-PCF at center wavelengths of 0.8, 1.3 and 1.55 μm using low power (25 W) femtosecond pulses which can be used in ultrahigh-resolution OCT system for ophthalmology, dermatology and dental imaging. Section 2 presents the design analysis of the proposed structure through a full vector finite element method. In Sect. 3, we explore the various optical properties including group velocity dispersion (GVD), third order dispersions (TOD), effective mode area and effective nonlinearity by varying the core diameter from 420 to 480 nm. We investigate the nonlinear pulse propagation in the anomalous dispersion regime and analyze the evolution of SC for 25 W input peak power of 2 mm length of SN-PCF for 480 nm core diameter in Sect. 4. Finally, we summarize the findings in Sect. 5.

2 Design of the Proposed SN-PCF

The schematic cross section of the proposed SN-PCF is as shown in Fig. 1. It is composed of circular air holes in the cladding arranged in a triangular pattern and a circular nanosize core. Here, the air-hole diameter is 1120 nm and increasing the core diameter from 420 to 480 nm for analyzing the optical properties.

We have already explored all the optical properties for the various core diameters ranging from 1000 to 300 nm [23]. In this work, we choose to vary the core diameter from 420 to 480 nm for analyzing the optical properties for a wavelength range from 0.8 to 1.7 μm for generating SC. The justification for this range of study is because of tight mode confinement within the core and nearly zero dispersion with high nonlinearity. Figure 2a, b illustrates the mode field distribution at 0.8 μm

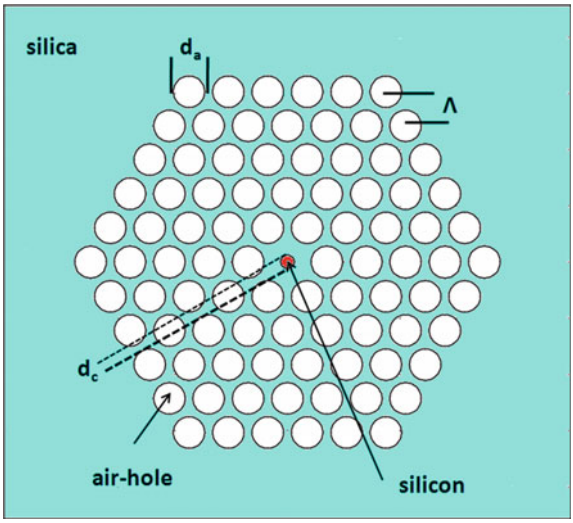

Fig. 1 Geometrical structure of the proposed SN-PCF with 480 nm core diameter

wavelength for 480 nm core diameter. In order to determine the dispersion of SN-PCF, it is necessary to compute the effective refractive index of the fundamental mode and the same is done by finite element method. In Fig. 3, we plot the effective index as a function of wavelength for various core diameters.

3 Optical Properties of SN-PCF

In this section, we explore the various linear and nonlinear properties. In Sect. 3.1, we study the impact of dispersions of fundamental mode for different core diameters. Finally, in Sect. 3.2, we compute the effective nonlinearity by calculating the effective mode area.

3.1 Waveguide Dispersion

The group velocity dispersion (GVD) and third order dispersion (TOD) of the mode are determined, respectively, from the second and third derivative of the n_{eff} as a function of wavelength. We use the following equations for determining the GVD and TOD,

$$\beta_2 = \frac{\lambda^3}{2\pi c^2}\frac{d^2 n_{eff}}{d\lambda^2} \tag{1}$$

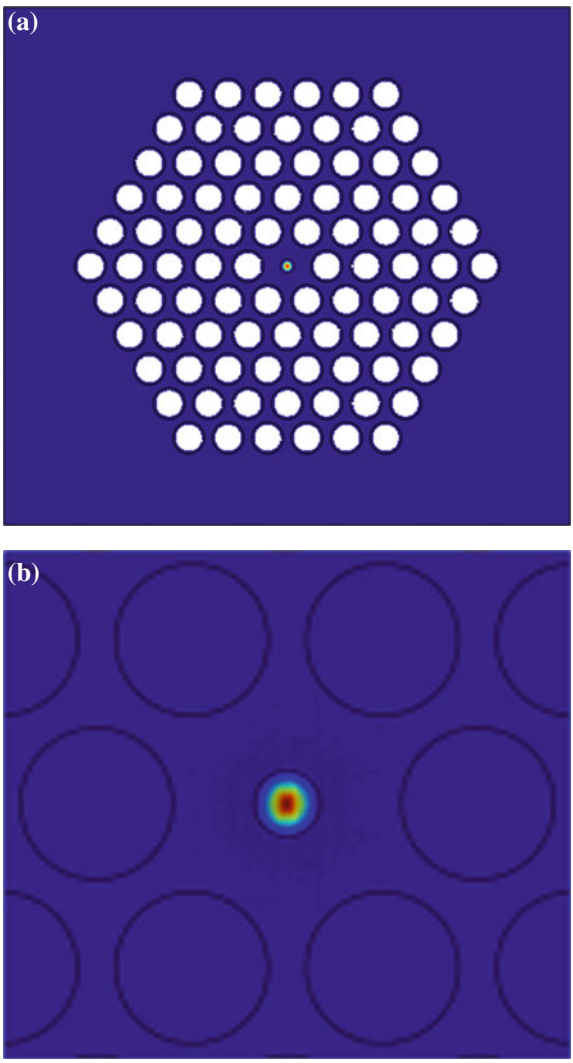

Fig. 2 Mode field distribution in **a** 2D view and **b** contour view of the proposed SN-PCF at 0.8 μm wavelength at 480 nm core diameter

and

$$\beta_3 = -\frac{\lambda^4}{4\pi^2 c^3}\left[\lambda\frac{d^3 n_{eff}}{d\lambda^3} - 3\frac{d^2 n_{eff}}{d\lambda^2}\right], \tag{2}$$

where λ is the wavelength, n_{eff} is the refractive index of the fundamental mode and c is the velocity of light in vacuum. In this work, we ignore the effect of material dispersion on account of the fact that its magnitude is very much lesser than that due to waveguide dispersion.

The variations of GVD and TOD with respect to wavelength for various core diameters are as shown in Figs. 4 and 5. As is seen in Fig. 4, when the core

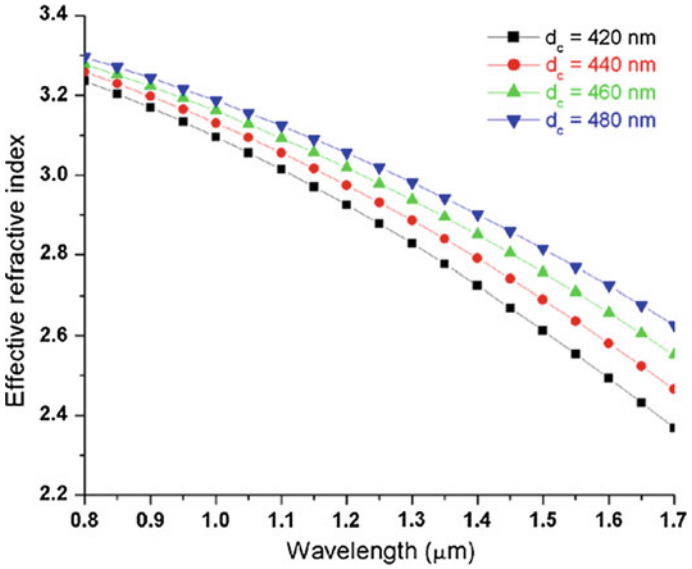

Fig. 3 Variations of effective refractive index for various core diameters of SN-PCF

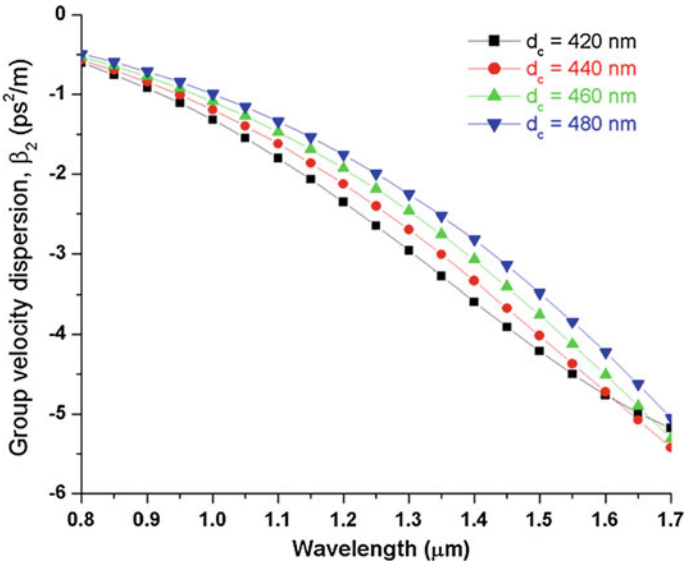

Fig. 4 Variations of group velocity dispersion of the proposed SN-PCF for different core diameters

diameter is reduced from 480 to 440 nm, the GVD decreases upon increasing the wavelength due to the increase in field distribution towards the core-cladding boundary. However, at 420 nm core diameter, the GVD decreases up to 1.65 μm

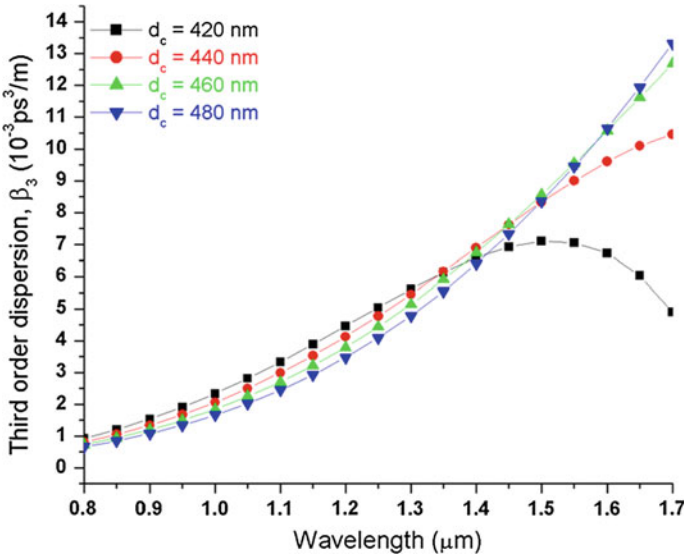

Fig. 5 Variations of third order dispersion of the proposed SN-PCF for different core diameters

wavelength beyond which, this dispersion switches to normal regime. From the Fig. 4 it is clear that the 480 nm core diameter exhibits a less anomalous GVD (-0.4909 ps^2/m) at 0.8 μm wavelength. Further, we report a less TOD (0.6595×10^{-3} ps^3/m) at 0.8 μm wavelength for 480 nm core diameter and this is evident from Fig. 5.

3.2 *Effective Nonlinearity*

Due to the small core diameter and high nonlinear index coefficient of silicon (4×10^{-18} m^2/W), the SN-PCF exhibits tight mode confinement compared to conventional PCF. But a significant fraction of the optical mode propagates in air as the evanescent field. Hence, an accurate estimation of the nonlinear coefficient γ^V is needed for small core diameter. This is carried out based on vectorially-based nonlinear Schrödinger equation (VNSE) [27]:

$$\gamma^V = k_0 \left(\frac{\epsilon_0}{\mu_0}\right) \frac{\int n_0^2(x,y) n_2(x,y) |e_m|^4 dA}{|\int (e_m \times h_m^*).\hat{z} dA|^2} \tag{3}$$

where k_0, ε_0, μ_0 and n_0 are the free-space wavenumber ($2\pi/\lambda$), free-space dielectric constant, free-space permeability and refractive index of silicon, respectively. Here n_2 is the nonlinear index coefficient of silicon whose value is two orders greater than that of silica.

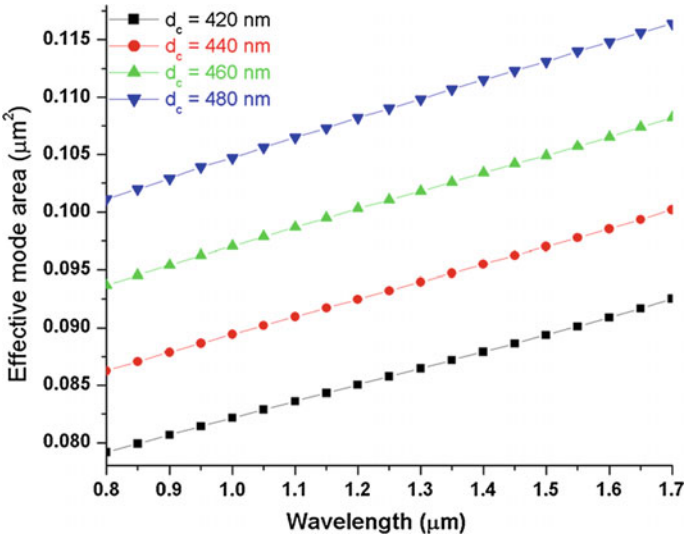

Fig. 6 Variations of effective mode area as a function of wavelength for different core diameters

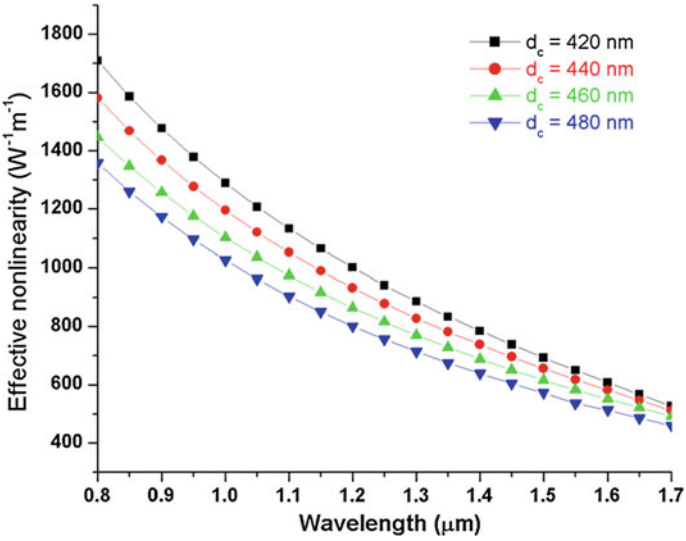

Fig. 7 Variations of effective nonlinearity for different core diameters of the proposed SN-PCFs

It is known that the mode confinement determined by the effective mode area becomes much pronounced upon reducing the core diameter of the proposed fiber. Figure 6 depicts the variation of effective mode area with respect to wavelength for various core diameters. The results show a slowly increasing mode area with the increase in wavelength. The proposed structure possesses a minimum effective mode area for lower wavelengths at 420 nm core diameter.

Next, we proceed to compute the effective nonlinearity by using (3). Figure 7 describes the variation of effective nonlinearity as a function of wavelength for various core diameters. As it is evident from Fig. 7, the effective nonlinearity decreases as the wavelength increases. This is due to the fact that the mode area becomes larger at higher wavelengths. For lower wavelengths, the small core diameters exhibit strong nonlinearity due to the tight mode confinement.

4 Simulation of Supercontinuum Generation

The SC generation in the SN-PCF is demonstrated by the generalized higher order nonlinear Schrödinger equation (NLS) with the effects of two-photon absorption and free-carrier absorption as follows [20].

$$\frac{\partial A}{\partial z} = -\frac{1}{2}(\alpha + \alpha^f)A - \frac{i}{2}\beta_2\frac{\partial^2 A}{\partial T^2} + \frac{\beta_3}{6}\frac{\partial^3 A}{\partial T^3} + i\gamma^V\left[1 + \frac{\omega}{\omega_0}\right]A\int_{-\infty}^{\infty}\left[R(T-\tau)|A|^2\right]d\tau \tag{4}$$

Here, A(z, T), α, α^f, β_2, β_3, γ^V and R(T − τ) represent the field envelope, linear loss, free-carrier contribution, GVD, TOD, effective nonlinearity and Raman response function, respectively. In this simulation, we ignore the effects of free carrier absorption, two photon absorption and loss owing to their insignificant role in the interaction. The nonlinear response function $R(t)$ is defined by [20],

$$R(t) = (1 - f_R)\delta(t) + f_R h_R(t). \tag{5}$$

The above expression includes both instantaneous electronic and delayed Raman contributions, with $f_R = 0.043$ representing the Raman contribution to the nonlinear response. The delayed Raman response $h_R(t)$ of silicon is expressed as:

$$h_R(t) = \Omega_R^2\tau_1\exp\left(\frac{-T}{\tau_2}\right)\sin\left(\frac{T}{\tau_1}\right), \tag{6}$$

where the parameters τ_1 (= 10 fs) and τ_2 (= 3 ps) correspond to the Raman shift and the bandwidth of the Raman gain spectrum, respectively and Ω_R is related to τ_1.

The pulse propagation in SN-PCF is studied by solving the hitherto mentioned NLS type equation using symmetrized split-step Fourier method [28]. We analyze the pulse evolution of SC by considering the hyperbolic secant profile as the input pulse and the same is given by [29]:

$$A(0,t) = N\sqrt{P_0}\,\mathrm{sec}\,h\left[\frac{t}{T_0}\right], \tag{7}$$

where P_0 is the peak power of the input pulse and T_0 is the input soliton duration defined as $T_{FWHM}/1.763$. T_{FWHM} is the input pulse duration at full width at half maximum (FWHM). The soliton order, N is defined as,

$$N^2 = \frac{L_D}{L_{NL}} = \frac{\gamma P_0 T_0^2}{|\beta_2|}, \tag{8}$$

where L_D $(= \frac{T_0^2}{|\beta_2|})$ and L_{NL} $(= \frac{1}{T_0^2})$ are the dispersion length and nonlinear length, respectively.

Table 1 Optical parameters of SN-PCF at 0.8, 1.3 and 1.55 μm wavelengths for 480 nm core diameter

Parameters	$\lambda_c = 0.8$ μm	$\lambda_c = 1.3$ μm	$\lambda_c = 1.55$ μm
$\beta_2\,(\mathrm{ps}^2/\mathrm{m})$	−0.4909	−2.2499	−3.8404
$\beta_3\,(10^{-3}\,\mathrm{ps}^3/\mathrm{m})$	0.6595	4.7787	9.4495
$\gamma\,(\mathrm{W}^{-1}\,m^{-1})$	1358	714	536

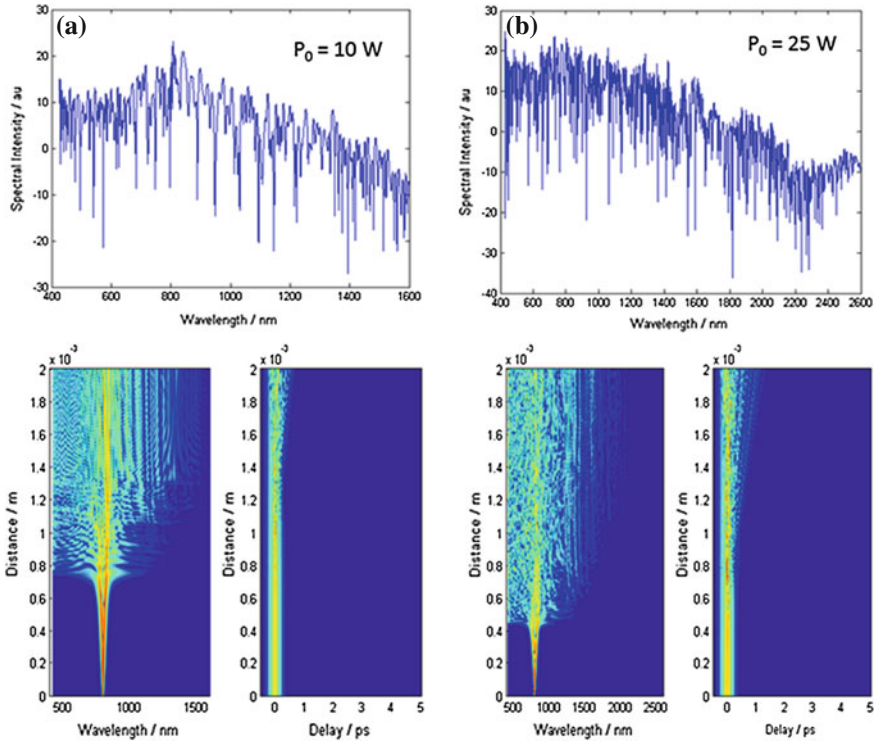

Fig. 8 Spectral, temporal evolution and intensity spectrum of the proposed SN-PCF at 0.8 μm wavelength of incident peak powers of **a** 10 W and **b** 25 W

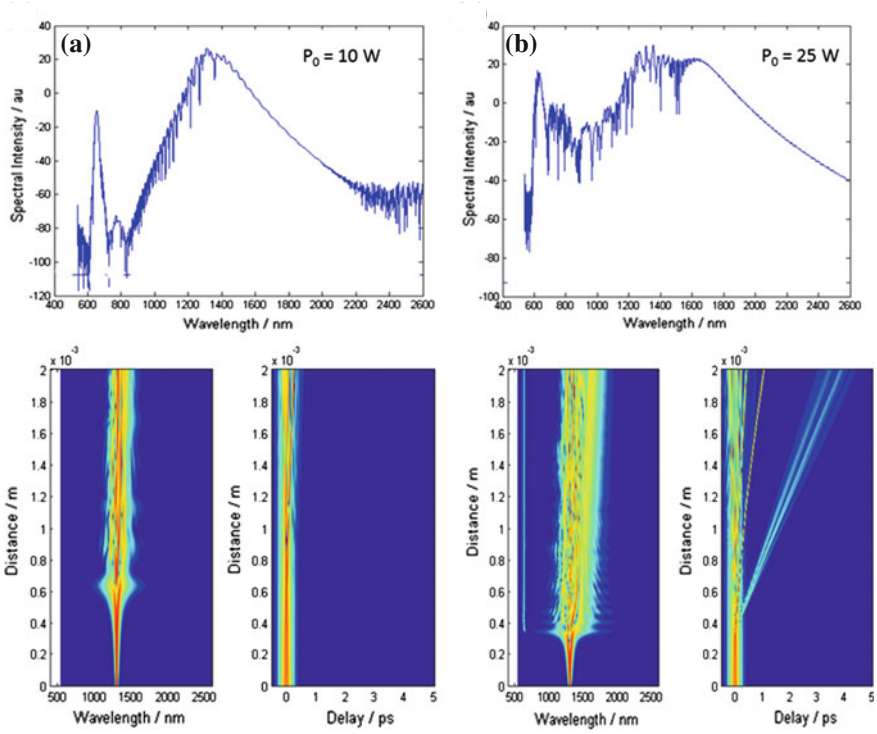

Fig. 9 Spectral, temporal evolution and intensity spectrum of the proposed SN-PCF at 1.3 μm wavelength of incident peak powers of **a** 10 W and **b** 25 W

We consider the propagation of a secant hyperbolic input pulse of peak power 25 W with 100 fs pulse width through the SN-PCF. We point out that, in the simulation, we consider the maximum value of core diameter (480 nm) since the proposed SN-PCF meets the requirements (less GVD with small TOD and high nonlinearity) of SC generation at 0.8, 1.3 and 1.55 μm wavelengths as tabulated in Table 1.

Figures 8a, b, 9a, b and 10a, b illustrate the intensity spectra of the proposed SN-PCF for various input peak powers at center wavelengths of 0.8, 1.3 and 1.55 μm, respectively. In this case, we consider the SN-PCF of length, 2 mm. From these figures, it is seen that the intensity spectra gradually get broadened and

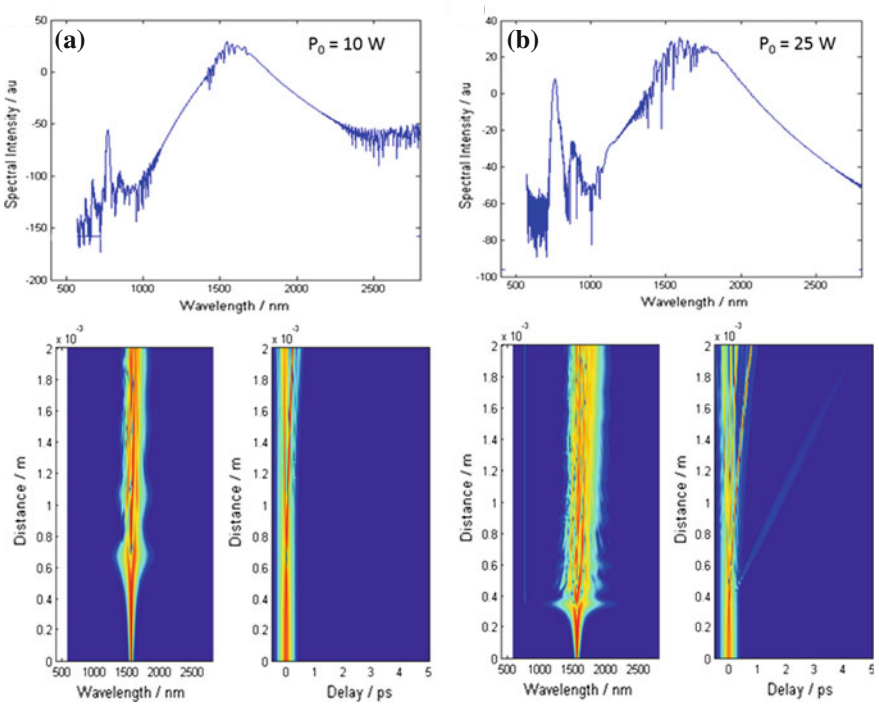

Fig. 10 Spectral, temporal evolution and intensity spectrum of the proposed SN-PCF at 1.55 μm wavelength of incident peak powers of **a** 10 W and **b** 25 W

flattened upon increasing the input power, P_0 due to soliton fission and larger contribution of nonlinear effects such as self-phase modulation and Raman effect. Therefore, it is clearly seen that the SC spectral width depends on the incident power of the pulse. Figures 11a, b, 12a, b, and 13a, b represent the intensity spectra for various lengths of the proposed SN-PCFs at the center wavelengths of 0.8, 1.3 and 1.55 μm, respectively with a peak power of 25 W. From these figures, we find that the same behaviour is noticed with the variation in length of the fiber. Hence, SC spectral width is dependent on the fiber length also.

The spectral evolution and intensity spectra of the proposed SN-PCF for 480 nm core diameter with the input peak power of 25 W with 100 fs pulse width at the wavelengths of 0.8, 1.3 and 1.55 μm, respectively are as shown in Figs. 14a–c, 15a–c and 16a–c. The calculated SC bandwidths are 1250, 1100 and 800 nm at the

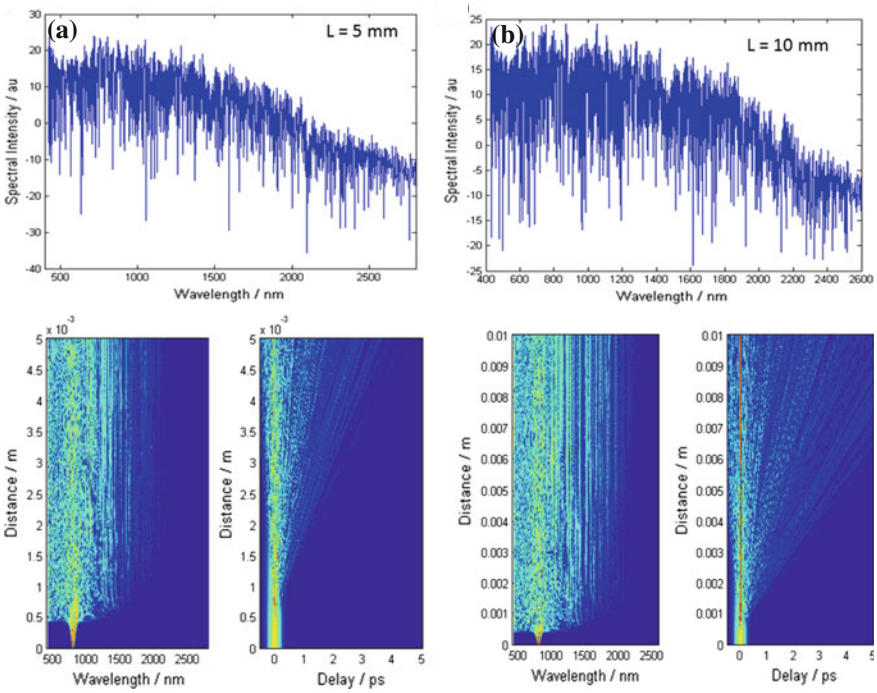

Fig. 11 Spectral, temporal evolution and spectral intensity at 0.8 μm wavelength of two different lengths of SN-PCFs **a** 5 mm and **b** 10 mm

center wavelengths of 0.8, 1.3 and 1.55 μm, respectively. From these results, it is evident that high quality SC spectrum is readily generated with relatively a short piece of fiber and a less input power due to the soliton fission and Raman effect. One of the important parameters in estimating the axial resolution of the OCT source is coherence length, l_c, which is given as, [3]:

$$l_c = \frac{2\ln 2}{\pi}\frac{\lambda_c^2}{\Delta\lambda}. \tag{9}$$

Further, the axial resolution, l_r, is related to coherence length, l_c as,

$$l_r = \frac{l_c}{n_{tissue}}. \tag{10}$$

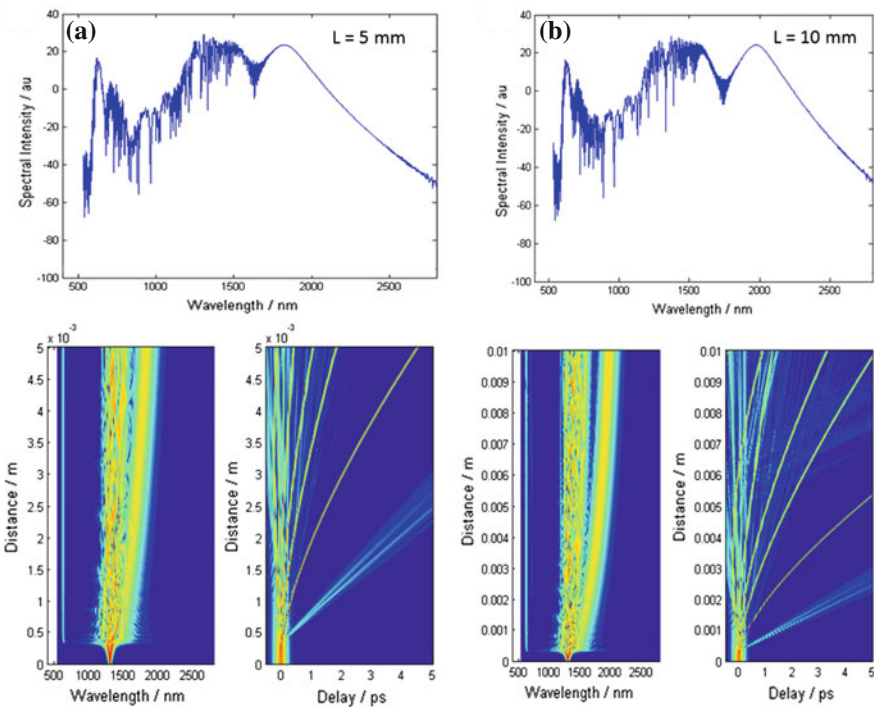

Fig. 12 Spectral, temporal evolution and spectral intensity at 1.3 μm wavelength of two different lengths of SN-PCFs **a** 5 mm and **b** 10 mm

Here, n_{tissue} is the refractive index of the biomedical tissues. The calculated l_c and l_r values at 0.8, 1.3 and 1.55 μm wavelengths are tabulated in Table 2. The calculated l_r values are 0.16, 0.41 and 0.8 μm when typical n_{tissue} values are 1.44, 1.65 and 1.65, respectively, their corresponding centre wavelength being 0.8, 1.3 and 1.55 μm, respectively [5]. These calculated l_r values are better than that of [3] as well as SLDs with OCT imaging axial resolution of approximately 10–15 μm. From Table 2, it is seen that the wider bandwidth and greater longitudinal resolution are obtained at 0.8 μm due to the small second and third order dispersions and high nonlinearity.

The proposed SN-PCF fiber can be used as a nanofiber-based light source to generate SC in three different central wavelengths for ophthalmology, dermatology and dentistry OCT imaging applications.

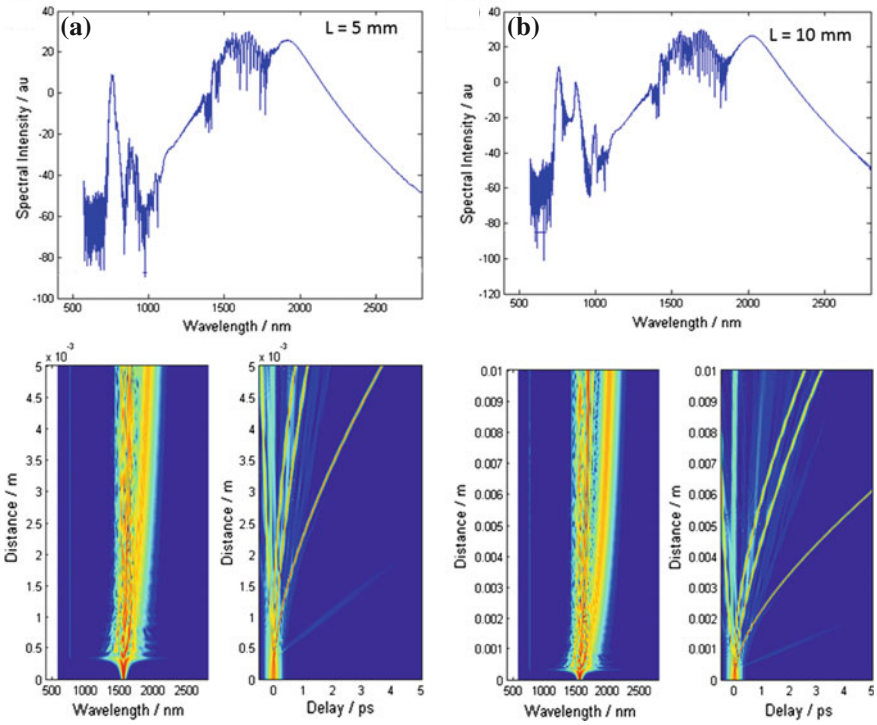

Fig. 13 Spectral, temporal evolution and spectral intensity at 1.55 μm wavelength of two different lengths of SN-PCFs **a** 5 mm and **b** 10 mm

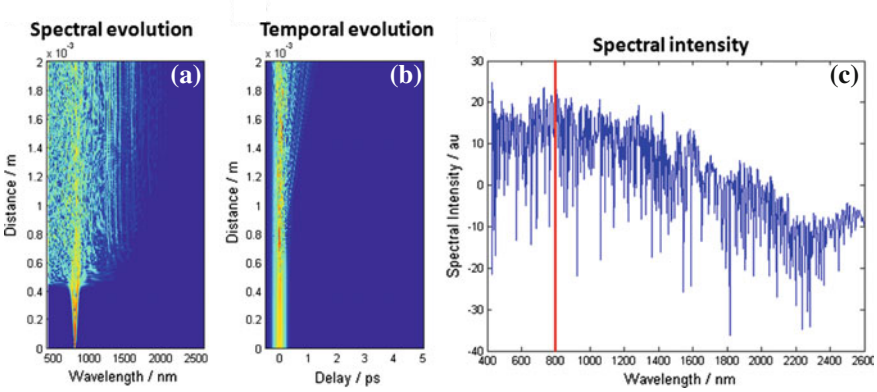

Fig. 14 **a** Spectral evolution **b** temporal evolution and **c** intensity spectrum of SC at 0.8 μm wavelength of the proposed SN-PCF using 25 W input power

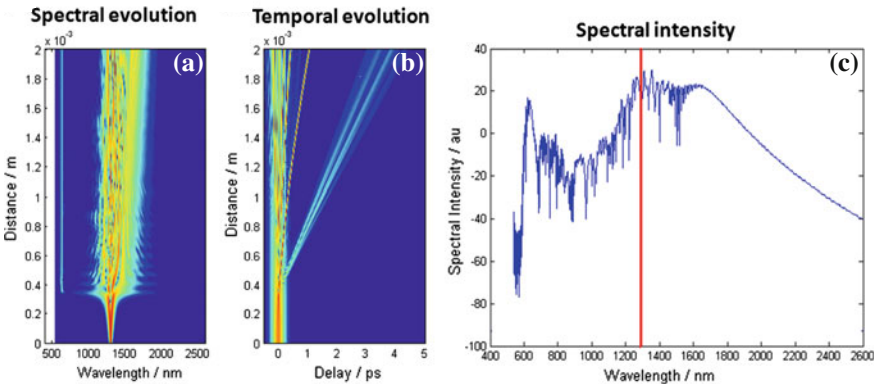

Fig. 15 **a** Spectral evolution **b** temporal evolution and **c** intensity spectrum of SC at 1.3 μm wavelength of the proposed SN-PCF using 25 W input power

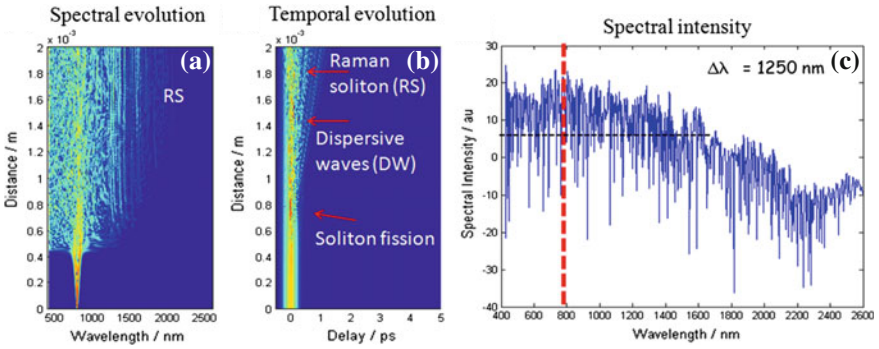

Fig. 16 **a** Spectral evolution **b** temporal evolution and **c** intensity spectrum of SC at 1.55 μm wavelength of the proposed SN-PCF using 25 W input power

Table 2 Calculated OCT related parameters of the 2 mm length of SN-PCF for 25 W incident peak power

Parameters	$\lambda_c = 0.8$ μm	$\lambda_c = 1.3$ μm	$\lambda_c = 1.5$ μm
$\Delta\lambda$(nm)	1250	1100	800
l_c (μm)	0.23	0.68	1.33
l_r (μm)	0.16	0.41	0.8

5 Conclusion

The proposed SN-PCF exhibits a high nonlinearity, a less small group velocity dispersion and a less third order dispersion which form the desirable requirements for realizing a broadband supercontinuum source. By solving higher order NLS type equation using split-step Fourier method, we have observed a broad bandwidth of 1250 nm at 0.8 μm wavelength when the peak power is 25 W in a short piece of

SN-PCF of 2 mm. This broad bandwidth of the light source permits high resolution for bright OCT imaging in the wavelength ranges from 0.8 to 1.6 μm. The longitudinal resolutions have been computed to be 0.16, 0.41 and 0.8 μm at center wavelengths of 0.8, 1.3 and 1.55 μm, respectively. Thus, we envisage that the proposed SN-PCF capable of generating wider bandwidth supercontinuum might turn out to be an appropriate candidate for being deployed as a ultrahigh-resolution OCT system in various fields of medicine such as ophthalmology, dermatology, dental imaging, etc.

Acknowledgements KSN wishes to thank CSIR [No: 03(1264)/12/EMR-11] and DST [No: SR/FTP/PS-66/2009], Government of India, for the financial support through the project.

References

1. Bouna, B., Tearney, G.J., Boppart, S.A., Hee, M.R., Brezinski, M.E., Fujimoto, J.G.: High-resolution optical coherence tomographic imaging using a mode-locked Ti-Al_2O_3 laser source. Opt. Lett. **20**(13), 1486–1488 (1995)
2. Drexler, W., Morgner, U., Kartner, F.X., Pitris, C., Boppart, S.A., Li, X.D., Ippen, E.P., Fujimoto, J.G.: In vivo ultrahigh-resolution optical coherence tomography. Opt. Lett. **24**(17), 1221–1223 (1999)
3. Namihira, Y., Hossain, M.A., Koga, T., Islam, M.A., Razzak, S.M.A., Kaijage, S.F., Hirako, Y., Higa, H.: Design of highly nonlinear dispersion flattened hexagonal photonic crystal fibers for dental optical coherence tomography applications. Opt. Rev. **19**(2), 78–81 (2012)
4. Stephen Boppart, A.: Optical coherence tomography: technology and applications for neuroimaging. Psychophysiology. **40**(4): 529–541 (2003) (Blackwell Publishing Inc. Printed in the USA)
5. Ohmi, M., Yamazaki, R., Kunizawa, N., Takahashi, M., Haruna, M.: In vivo observation of micro-tissue structures by high-resolution optical coherence tomography with a femtosecond laser. Jpn. Soc. Med. Biol. Eng. **42**(4), 204–210 (2004)
6. Herz, P.R., Chen, Y., Aguirre, A.D., Fujimoto, J.G., Mashimo, H., Schmitt, J., Koski, A., Goodnow, J., Peterson, C.: Ultrahigh resolution optical biopsy with endoscopic optical coherence tomography. Opt. Exp. **12**(15), 3532–3542 (2004)
7. Lee, J.H., Jung, E.J., Kim, C.S.: Incoherent, CW supercontinuum source based on erbium fiber ASE for optical coherence tomography imaging. In: Proceedings of Optoelectronics and Communication Conference FD3, pp. 13–17 (2009)
8. Zhu, Z.M., Brown, T.G.: Experimental studies of polarization properties of supercontinua generated in a birefringent photonic crystal fiber. Opt. Exp. **12**(5), 791–796 (2004)
9. Haverkamp, N., Telle, H.R.: Complex intensity modulation transfer function for supercontinuum generation in microstructure fibers. Opt. Exp. **12**(4), 582–587 (2004)
10. Zhu, Z.M., Brown, T.G.: Polarization properties of supercontinuum spectra generated in birefringent photonic crystal fibers. Opt. Soc. Am. B **21**(2), 249–257 (2004)
11. Wadsworth, W.J., Joly, N., Knight, J.C., Birks, T.A., Biancalana, F., St, P., Russell, J.: Supercontinuum and four-wave mixing with Q-switched pulses in endlessly single-mode photonic crystal fibres. Opt. Exp. **12**(2), 299–309 (2004)
12. Hori, T.J., Takayanagi, J., Nishizawa, N., Goto, T.: Flatly broadened, wideband and low noise supercontinuum generation in highly nonlinear hybrid fiber. Opt. Exp. **12**(2), 317–324 (2004)
13. Husakou, A.V., Herrmann, J.: Supercontinuum generation in photonic crystal fiber made from highly nonlinear glasses. Appl. Phys. B **77**(2–3), 227–234 (2003)

14. Town, G.E., Funaba, T., Ryan, T., Lyytikainen, K.: Optical supercontinuum generation from nanosecond pump pulses in an irregularly microstructured air-silica optical fiber. Appl. Phys. B **77**(2–3), 235–238 (2003)
15. Hilligsoe, K.M., Paulsen, H.N., Thogersen, J., Keiding, S.R., Larsen, J.J.: Initial steps of supercontinuum generation in photonic crystal fibers. J. Opt. Soc. Am. B **20**(9), 1887–1893 (2003)
16. Saitoh, K., Koshiba, M.: Highly nonlinear dispersion-flattened photonic crystal fibers for supercontinuum generation in a telecommunication window. Opt. Exp. **12**(10), 2027–2032 (2004)
17. Husakou, A.V., Herrmann, J.: Supercontinuum generation of higher-order solitons by fission in photonic crystal fibers. Phys. Rev. Lett. **87**(20), 203901–203904 (2001)
18. Foster, M., Gaeta, A.L., Cao, Q., Trebino, R.: Soliton-effect compression of supercontinuum to few-cycle durations in photonic nanowires. Opt. Exp. **13**(18), 6848–6855 (2005)
19. Boyraz, O., Koonath, P., Raghunathan, V., Jalali, B.: All optical switching and continuum generation in silicon waveguides. Opt. Exp. **12**(17), 4094–4102 (2004)
20. Yin, L., Lin, Q., Agrawal, G.P.: Soliton fission and supercontinuum generation in silicon waveguides. Opt. Lett. **32**(4), 391–393 (2007)
21. Driscoll, J.B., Liu, X., Yasseri, S., Hsieh, I., Dadap, J.I., Osgood Jr., R.M.: Large longitudinal electric fields (Ez) in silicon nanowire waveguides. Opt. Exp. **17**(4), 2797–2804 (2009)
22. Biancalana, F., Tran, V., Stark, S., Schmidt, M.A., St, P., Russell, J.: Emergence of geometrical optical nonlinearities in photonic crystal fiber nanowires. Phys. Rev. Lett. **105**(9), 093904–093907 (2010)
23. Gunasundari, E., Senthilnathan, K., Sivabalan, S., Abdosllam Abobaker, M., Nakkeeran, K., Ramesh Babu, P.: Waveguiding properties of a silicon nanowire embedded photonic crystal fiber. Opt. Mater. **36**(5), 958–964 (2014)
24. Tong, L., Lou, J., Mazur, E.: Single-mode guiding properties of subwavelength-diameter silica and silicon wire waveguides. Opt. Exp. **12**(6), 1025–1035 (2004)
25. Salem, A.B., Cherif, R., Zghal, M.: Low-energy single-optical-cycle soliton self-compression in air-silica nanowires. J. Nanophoton. **5**(1): 059506(1-6) (2011)
26. Salem, A.B., Cherif, R., Zghal, M.: Soliton-self compression in highly nonlinear chalcogenide photonic nanowires with ultralow pulse energy. Opt. Exp. **19**(21), 19955–19966 (2011)
27. Afshar, S.V., Monro, T.M.: A full vectorial model for pulse propagation in emerging waveguides with subwavelength structures part I: Kerr nonlinearity. Opt. Exp. **17**(4), 2298–2318 (2009)
28. Dudley, J.M., Taylor, J.R.: Supercontinuum Generation in Optical Fibers. Cambridge University Press, Cambridge (2010)
29. Agrawal, G.P.: Nonlinear Fiber Optics. Academic Press, New York, USA (2007)

Synthesis and Characterization of $CuInSe_2$ Nanoparticles by Hydrothermal Method

Suresh Sagadevan, Jiban Podder and Isha Das

Abstract $CuInSe_2$ semiconductor nanoparticles were synthesized by the hydrothermal method. X-ray diffraction (XRD), scanning electron microscopy (SEM), transmission electron microscopy (TEM), FT-Raman, UV-spectroscopy and photoluminescence (PL) spectrum analyses had been done to study of the synthesized samples crystallinity, morphological and optical properties. The chalcopyrite (tetragonal) structure was confirmed by XRD pattern of $CuInSe_2$. The Raman spectrum of the $CuInSe_2$ showed the dominant A_1 modes at 176 cm^{-1}. The synthesized samples were composed of cubes which is shown by SEM and TEM analyses with the size of nanometers. The optical property of the synthesized nanoparticles was studied from the photoluminescence spectrum. At different frequencies for different temperatures the dielectric properties of $CuInSe_2$ nanoparticles were studied. $CuInSe_2$ nanoparticles dielectric constant and the dielectric loss decreased with increase in frequency.

1 Introduction

The fast depletion of the fossil fuels has been causing great concern and has prompted the material scientists to take interest in the development of new energy resources. Their efforts are showing the way to find and exploit renewable energy sources that include photovoltaic electric generators. Among such energy sources, Copper indium selenide ($CuInSe_2$) I–III–VI_2 semiconductor materials are drawing much attention because of its great optical absorption coefficient, noble photo

S. Sagadevan (✉)
Department of Physics, AMET University, Chennai, India
e-mail: sureshsagadevan@gmail.com

J. Podder
Department of Chemical and Biological Engineering,
University of Saskatchewan, Saskatoon SK S7N 5A9, Canada

I. Das
Department of ECE, AMET University, Chennai, India

J. Ebenezar (ed.), *Recent Trends in Materials Science and Applications*,
Springer Proceedings in Physics 189, DOI 10.1007/978-3-319-44890-9_9

stability and promising application in heterojunctions photovoltaic and optoelectronic devices [1]. Their good optical absorption coefficient, low band gap ($\sim$1.05 eV), good radiation stability, large exciton Bohr radius of 10.6 nm [2–5] are additional plus points. The last two decades have witnessed remarkable improvement in the rapid growth of synthesis and assembly of semiconductor nano-crystals. The band gap energy of nano-crystals is the dynamic feature that stimulates its use, as it can be tuned by its size, shape and composition. The stoichiometric composition, morphology, and impurities influence the electronic properties of the semiconductor nano-particles that depend on the method and condition of preparation. For solar energy conversion, at room temperature the band gap of $CuInSe_2$ around 1.04 eV is very close to the optimum. For this argumentation, $CuInX_2$ (X = S, Se and Te) are deliberated to be attractive for solar cell applications [6, 7]. Various techniques have been stated on the preparation of $CuInSe_2$ nanoparticles like microwave synthesis, microwave irradiation, sol-gel, wet chemical, solvothermal and hydrothermal methods [8–14]. In this paper, the study had been done on structural, morphological and optical properties and ternary $CuInSe_2$ nanoparticles were synthesized using hydrothermal technique. For the applications purpose in optoelectronic devices above prepared materials could be utilized. For the first time, the present research work reveals, that the $CuInSe_2$ nanoparticles dielectric properties like the dielectric constant, the dielectric loss and AC conductivity could be determined.

2 Experimental Details

The analytical grade chemicals were used for the experiment. Therefore following materials that are copper (II) chloride, indium (In), and selenium (Se) were used without any purification and used as source materials. Deionized water was used as solvent. In a typical procedure 1:1:2 mol ratio of $CuCl_2$, In, and Se were added to 50 mL of deionized water and the solution was stirred for 1 h. Thereafter, the resulting solution was shifted to a 100 mL autoclave stainless steel and the same was sealed and maintained at 150 °C for 2 h in a resistive heating box furnace. Later, it was kept at room temperature to cool down. It had black color precipitate that confirmed the material formation and the fine powder of $CuInSe_2$ nanoparticles were filtered off. To remove the residual impurities, the powder was washed with distilled water and ethanol three to four times approximately. It was then dried at 45 °C for 1 h. The XRD pattern of the $CuInSe_2$ nanoparticles was noted by using a powder X-ray diffractometer (Schimadzu model: XRD 6000 using CuKα (λ = 0.154 nm) radiation, with a diffraction angle between 20° and 80°. Raman spectrum was obtained using a Bruker RFS 27: stand-alone model Raman spectrometer. Scanning Electron Microscopy (SEM) studies were carried out on JEOL,

JSM-67001. Image of Transmission Electron Microscope (TEM) was taken using an H-800 TEM (Hitachi, Japan) with an accelerating voltage of 100 kV. In the range of 300–900 nm UV-Vis absorption spectrum was recorded for the $CuInSe_2$ nanoparticles using a Varian Cary 5E spectrophotometer. Using an excitation wavelength of 244 nm photoluminescence spectrum was recorded. The dielectric properties of the $CuInSe_2$ nanoparticles were analyzed over the frequency range 50 Hz–5 MHz using a HIOKI 3532-50 LCR HITESTER.

3 Results and Discussion

3.1 X-ray Diffraction (XRD) Analysis

Analysis for the phase structure and purity of the $CuInSe_2$ nanoparticles were done by X-ray diffraction (XRD). As shown in Fig. 1 pure single phase of $CuInSe_2$ with chalcopyrite tetragonal structure could be indexed for all the diffraction peaks in the XRD pattern. In addition the high purity of $CuInSe_2$ sample was observed with no peaks of other impurities. For both sphalerite and chalcopyrite the major peaks were common.

3.2 Morphological (SEM and TEM) Analysis

The synthesized $CuInSe_2$ nanoparticles are shown by the SEM images as given in Fig. 2. From the SEM images, it is clearly noticed that the samples have nanocubes-like-morphology. The typical TEM image of $CuInSe_2$ nanoparticles is shown in Fig. 3. It brings to light that the nanocubes are monodispersed uniformly.

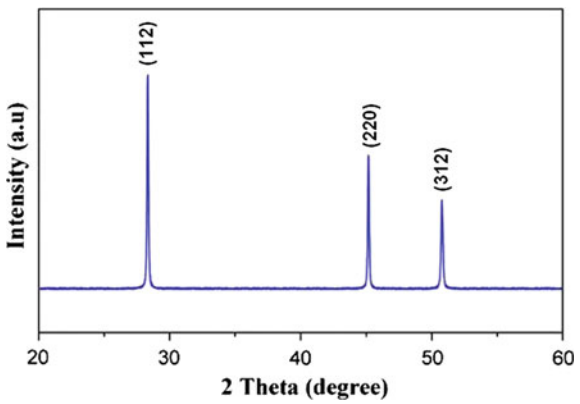

Fig. 1 XRD pattern of $CuInSe_2$

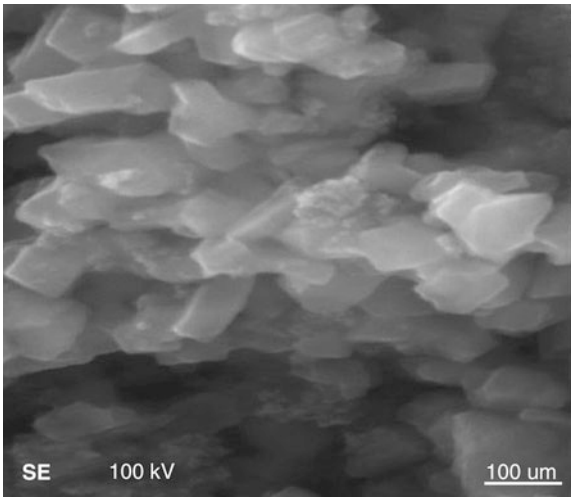

Fig. 2 SEM image of $CuInSe_2$

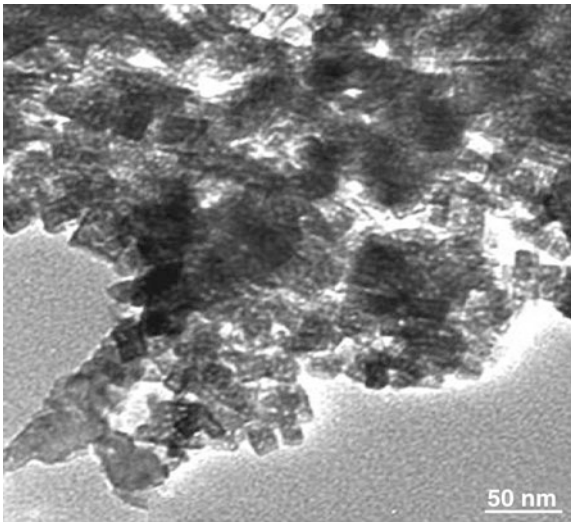

Fig. 3 TEM image of $CuInSe_2$

3.3 FT-Raman Spectrum Analysis

Raman spectrum of $CuInSe_2$ is exhibited in Fig. 4. The spectrum exhibits the vibration bands in the range of 100–400 cm^{-1}. Raman spectrum gives important information relevant to secondary phases, lattice strains and chemical composition. The Raman spectrum exhibits A_1 mode of $CuInSe_2$ at approximately 175 cm^{-1}, usually noticed in the I–III–VI_2 chalcopyrite compounds. The surface morphology and the phase composition in $CuInSe_2$ are the characteristics on which the intensity of Raman peaks strongly depends. The most intense band is A_1 band in the spectra

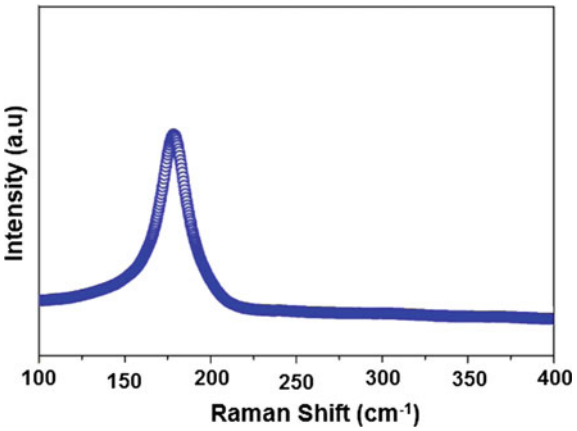

Fig. 4 Raman spectrum of $CuInSe_2$

of chalcopyrite type compounds [15]. Currently, the dominant peaks at 176 cm^{-1} are associated with A_1 modes of chalcopyrite $CuInSe_2$ [16].

3.4 Optical Properties

Figure 5 shows the UV–Vis absorption spectrum of the $CuInSe_2$ nanoparticles. An absorption peak centered at approximately 460 nm which is shown in result. By using the direct band gap method the band gap of the $CuInSe_2$ nanoparticles is calculated. For $CuInSe_2$ thin film the value was reported 1.04 eV which is consistent with the $CuInSe_2$ nanoparticles value and that was found to be 1.05 eV. Although in the present method the sample used for UV–Vis absorption measurement was the one with the smallest size, it was still too large to observe the

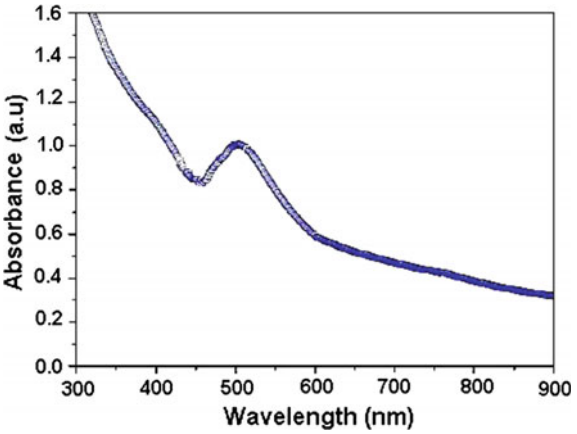

Fig. 5 The absorption spectrum of $CuInSe_2$ nanoparticles

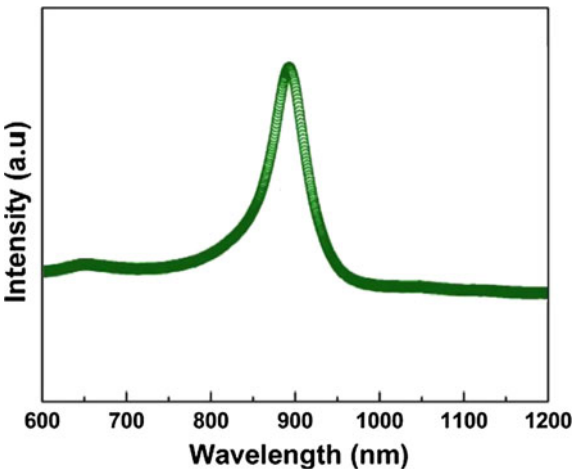

Fig. 6 PL spectrum of $CuInSe_2$

blue-shift due to quantum confinement effect. Figure 6 shows the PL spectrum of as synthesized $CuInSe_2$. The spectrum was recorded at room temperature with an excitation wavelength of 244 nm. Corresponding to energy gap of 1.14 eV the emission peak at 1081 nm, which is due to defect. The corresponding energy gap of 1.42 eV, is larger than the reported value of 1.04 eV for bulk α–CIS when the broad emission peak of $CuInSe_2$ sample centered at 870 nm [17].This emission peak is blue, shifted from the optical absorption peak. This emission is related to the intermediate optical band gap states that appear in defective $CuInSe_2$ and, therefore, emissions related with these exciton have wavelengths smaller than the optical band gap of $CuInSe_2$ [18]. This defect emission is sharp at 870 nm. This with variation of intensity of power of the excitation wavelength does not shift.

3.5 Dielectric Properties

At the different frequencies and temperatures the pellets of $CuInSe_2$ nanoparticles in disk form were examined for the dielectric constant and the dielectric loss. In Fig. 7 the variations of dielectric constant with frequency and temperature for $CuInSe_2$ nanoparticles are shown. At low frequencies the dielectric constant of $CuInSe_2$ nanoparticles is high and it decreases rapidly at all temperatures with the applied frequency. The value of the dielectric constant is very high due to the presence of all the four polarizations, namely, space charge, orientation, electronic, and ionic at low frequencies and due to the loss of these significant polarizations at higher frequencies, its value is low [19]. It is also observed from the plot that with an increase in the temperature, the dielectric constant increases and this is attributed to the presence of space charge polarization near the grain boundary interfaces, on which the purity and exactness of the sample rely [20]. Hence compare to the

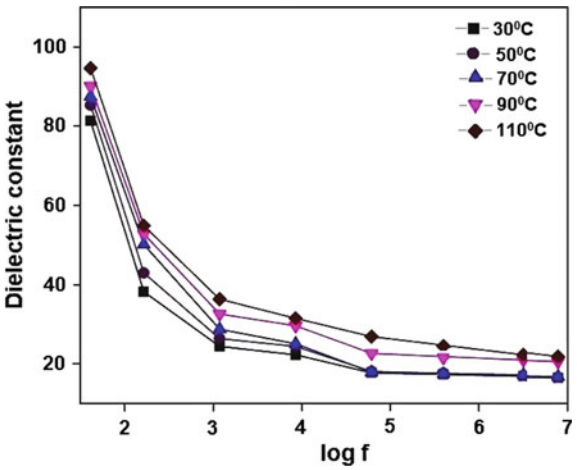

Fig. 7 Dielectric constant with log frequency

conventional materials the dielectric constant of nanostructured materials requires to be larger. As a result of the grain boundary interfaces structure the space charge polarization increases and outcomes into the large dielectric constant of nanocrystalline materials at adequately high temperature. The sharp increase in the dielectric constant at low frequencies and at lower temperatures causing dielectric loss at sufficiently high temperature. When the temperature increases, decrease in dielectric constant results due to the space charge and the ion jump polarization decrease. With reference to frequency and temperature the variations of the dielectric loss of $CuInSe_2$ nanoparticles are shown in Fig. 8. It has been observed that with the increases in frequency the dielectric loss decreases. At higher frequencies the loss angle is nearly the same value for all temperatures. The dielectric losses in dielectric materials occur due to absorption current. A part of the electric

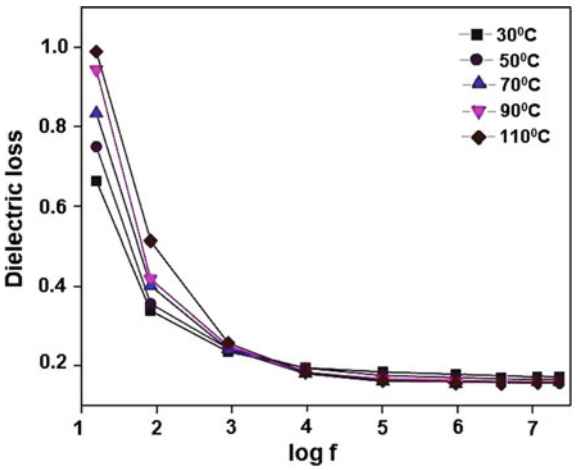

Fig. 8 Variation of dielectric loss with log frequency

energy required in polar dielectrics for the orientation of the molecules along the direction of the applied electric field to overcome the forces of internal friction [21]. One more part of the electric energy is being utilized by various kind of molecular transfer from one position to another that also involves energy and for the rotation of dipolar molecules [22].

3.6 AC Conductivity Studies

The ac conductivity of the $CuInSe_2$ nanoparticles can be computed by the following relation:

$$\sigma_{ac} = 2\pi\varepsilon_0\varepsilon_r f \tan\delta \quad (1)$$

where ε_0 is the permittivity in free space, ε_r is the dielectric constant, f is the frequency and tan δ is the loss factor. When in the metal ions electrons jumping from low valence state to high valence state the electrical conduction in $CuInSe_2$ nanoparticles appears. The frequency reliance behaviour for the ac conductivity in the various temperatures is shown in Fig. 9. With the increase in frequency the ac conductivity increases for all temperatures. When there is an increase in the frequency of the applied ac field it is observed that ac conductivity gradually increases because of the electron hopping frequency. Conductivity increases with higher frequencies when there is reduction in space charge polarization.

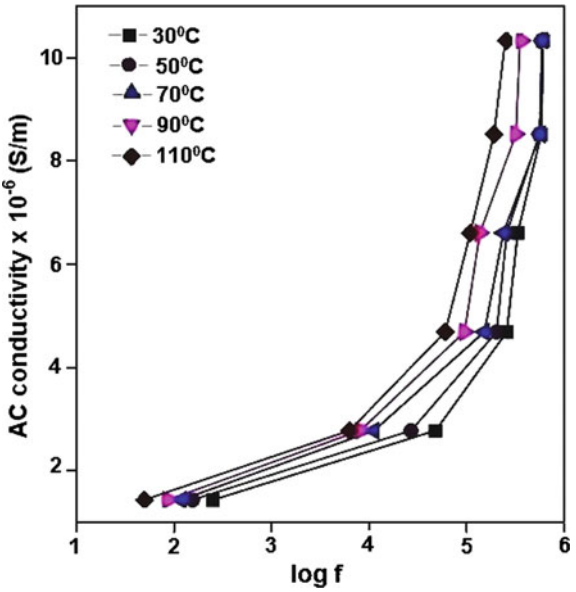

Fig. 9 Variation of AC conductivity with log frequency

4 Conclusion

$CuInSe_2$ nanoparticles were synthesized by using hydrothermal method. The synthesized $CuInSe_2$ confirmed chalcopyrite (tetragonal) structure using XRD. The synthesized samples were composed of cubes which were ascertained by SEM and TEM analyses and the size in nanometers. The dominant Raman scattering vibration was connected to the A_1 mode. The emission wavelength and the corresponding energy gap of synthesized sample was obtained from PL spectrum. $CuInSe_2$ nanoparticles were analyzed by using variations of the dielectric constant like dielectric loss with frequency and temperature. The physical and electrical properties of the above synthesized $CuInSe_2$ nanoparticles could be an acceptable substitute for the fabrication of more appropriate solar cell devices. The AC electrical conductivity study showed that the conduction is depended both on frequency and temperature.

References

1. Guillemoles, J.F., Kronik, L., Cahen, D., Rau, U., Jasenek, A., Schock, H.W.: Stability issues of Cu (In, Ga) Se_2-based solar cells. J. Phys. Chem B. **104**, 4849 (2000)
2. Guillen, C., Herrero, : Improvement of the optical properties of electrodeposited $CuInSe_2$ thin films by thermal and chemical treatments. J. Sol. Energy Mater. Sol. Cells. **43**, 47–57 (1996)
3. Nadenau, V., Braunger, D., Hariskos, D., Kaiser, M., Koble, C., Oberacker, A., Ruckh, M., Ruhle, U., Schaffler, R., Schmid, D., Walter, T., Zweigart, S., Schock, H.W.: Solar cells based on $CuInSe_2$ and related compounds: material and device properties and processing. Progr. Photovolt.: Res. Appl. **3**, 363–382 (1995)
4. Niki, S., Fons, P.J., Yamada, A., Kurafuji, T., Chichibu, S., Nakanishi, H., Bi, W.G., Tu, C. W.: High quality $CuInSe_2$ films grown on pseudo-lattice-matched substrates by molecular beam epitaxy. Appl. **69**, 647 (1996)
5. Zhang, L., Liang, J., Peng, S., Shi, Yunhui, C.: Solvothermal synthesis and optical characterization of chalcopyrite $CuInSe_2$ microspheres. Mater. Chem. Phys. **106**, 296–300 (2007)
6. Grisaru, H., Oleg, P., Gedanken, A.: Microwave-assisted polyol synthesis of $CuInTe_2$ and $CuInSe_2$ nanoparticles. Inorg. Chem. **42**, 7148–7155 (2003)
7. Wei, G., Forrest, S.R.: Intermediate-band solar cells employing quantum dots embedded in an energy fence barrier. Nano Lett. **7**, 218–222 (2007)
8. Shim, J.B., Kim, C.G., Jeon, D.J., Chung, T.M., An, K.S., Lee, S.S., Lim, J.S., Jeong, S.J., Park, B.K. and Lee, Y.K.: Hydrothermal synthesis of $CuInSe_2$ nanoparticles in acetic acid. J. Phys. Chem. Solids. **74**, 867–871 (2013)
9. Lu, W.L., Fu, Y.S., Tseng, B.H.: Preparation and characterization of $CuInSe_2$ nanoparticles. J. Phys. Chem. Solids **69**, 637–640 (2008)
10. Wu, C.H., Chen, F.S., Lin, S.H., Lu, C.H.: Preparation and characterization of $CuInSe_2$ particles via the hydrothermal route for thin-film solar cells. J. Alloys. Compd. **509**, 5783–5788 (2011)
11. Lin, Pei-Ying, Yaw-Shyan, Fu: Fabrication of $CuInSe_2$ light absorption materials from binary precursors via wet chemical process. Mater. Lett. **75**, 65–67 (2012)

12. Lu, Chung-Hsin, Chung-Han, Lee, Chung-Hsien, Wu: Microemulsion-mediated solvothermal Synthesis of copper indium diselenide powders. Sol. Energy Mater. Sol. Cells **94**, 1622–1626 (2010)
13. Yang, Yi-Han, Yit-Tsong, Chen: Solvothermal preparation and spectroscopic characterization of copper indium diselenide nanorods. J. Phys. Chem. B **110**, 17370–17374 (2006)
14. Kim, Ki-Hyun, Young-Gab, Chun, Byung-Ok, Park, Kyung- Hoon, Yoon: Synthesis of $CuInSe_2$ and $CuInGaSe_2$ nanoparticles by solvothermal route. Mater. Sci. Forum **449–452**, 273–276 (2004)
15. Zaretskaya, E.P., Gremenok, V.F., Riede, V., Schmitz, W., Bente, K., Zalesski, V.B., Ermakov, O.V.: Raman spectroscopy of $CuInSe_2$ thin films prepared by selenization. J. Phys. Chem. Solids **64**, 1989 (2003)
16. Chen, H., Yu, S.M., Shin, D.W., Yoo, J.B.: Solvothermal synthesis and characterization of chalcopyrite $CuInSe_2$ nanoparticles. Nanoscale Res. Lett. **5**, 217–223 (2010)
17. Guo, Q., Kim, S.J., Kar, M., Shafarman, W.N., Birkmire, R.W., Stach, E.A., Agrawal, R., Hillhouse, H.W.: Development of $CuInSe_2$ nanocrystal and nanoring inks for low-cost solar cells. Nano Lett. **8**, 2982 (2008)
18. Liborio, L.M., Bailey, C.L., Mallia, G., Tomić, S. and Harrison, N.M.: Chemistry of defect induced photoluminescence in chalcopyrites: the case of $CuAlS_2$. J. Appl. Phys. **109**, 023519 (2011)
19. Suresh, S., Arunseshan, C.: Dielectric properties of cadmium selenide (CdSe) nanoparticles synthesized by solvothermal method. Appl. Nanosci. **4**, 179–184 (2014)
20. Suresh, S.: Studies on the dielectric properties of CdS nanoparticles. Appl Nanosci. **4**, 325–329 (2014)
21. Sagadevan, S.: Synthesis and electrical properties of TiO_2 nanoparticles using a wet chemical technique. Am. J. Nanosci. Nanotech. **1**(1), 27–30 (2013)
22. Suresh, S.: Synthesis, structural and dielectric properties of zinc sulfide nanoparticles. Int. J. Phys. Sci. **8**, 1121–1127 (2013)

Fabrication of Tin Oxide Nano-fibers by Electro Spinning Generator

K. Thangavel, T. Roshini and E. Ranjith Kumar

Abstract High quality Tin oxide fibers were fabricated on well cleaned glass substrates by simple electrospinning generator. The surface morphology, crystalline structure, composition, thermal stability and optical properties of the prepared fibers (with annealed temperatures 400, 500 and 600 °C) were studied using through FESEM, HRTEM, XRD, EDAX, TGA, PL and UV-Vis characterization techniques. The fibers are continuous almost straight, defect free, nanoscale diameter (10–300 nm) and cover the entire length of the collector. They exhibit pure tetragonal rutile structure with lattice parameters 4.8133 (Å) (a) and 3.2900 (Å) (c). The chemical composition of fibers confirms the SnO_2 crystallization starts around 220 °C and the complete removal of PVA at 500 °C. The absorption edge of SnO_2 nano-fibers is nearly 3.5 eV. The nano-fibers of SnO_2 can be used as excellent UV emitter, touch screens (TCO), and it will be excellent material for nanodevices fabrication.

1 Introduction

Recent years, the development and usage of touch screen in all electronic devices is default option and more user-friendly in nature. The screen should be transparent to light and conduct electric current. Many sensors, solar cells etc., are using Indium Tin Oxide (ITO), Transparent Conducting Oxide (TCO). In this way SnO_2 is one of the excellent conducting oxides, due to this high degree of transparency in the visible region, low operating temperature, high thermal stability, robust physical

K. Thangavel
Department of Electronics, SNR Sons College, Coimbatore 641006, India

T. Roshini
Department of Computer Engineering, Rochester Institute of Technology, Rochester 14623-5604, USA

E. Ranjith Kumar (✉)
Department of Physics, Dr.N.G.P. Institute of Technology, Coimbatore 641048, India
e-mail: ranjueaswar@gmail.com

J. Ebenezar (ed.), *Recent Trends in Materials Science and Applications*,
Springer Proceedings in Physics 189, DOI 10.1007/978-3-319-44890-9_10

and chemical interaction with adsorbed species. SnO_2 is an n type semiconductor with a wide direct band gap (3.6 eV) at room temperature [1, 2].

Most of the thin film researchers find numerous problems in fabrication of metal oxide on glass plates using non vacuum techniques. Physical Vapor Deposition (PVD) method includes many stages such as evaporation, transportation, and condensation of materials in the vacuum environment [3]. Non vacuum technique especially electrospin coating technique [4] can avoid the difficulties and achieves many features such as self-assembly, defect free, nanometer size diameter, well interconnecting of fibers etc., [5]. Thus the research on fabrication of SnO_2 by electrospinning technique and characterization is the targeted task for us and introduce a new breakthrough in transparent conducting oxide among the semiconductor researchers.

2 Experimental Details

The cost effective microcontroller aided electro-spin coating unit is shown in Fig. 1. The 3 g purity tested (99 % Sigma Aldrich) PVA, and 6 g Tin (II) chloride (99.99 % Sigma Aldrich) were dissolved with 40 ml triple distilled water in two separate beakers, and then the solutions were mixed in three different ratios 1:1, 1:2 and 1:3 in three separate beakers using magnetic stirrer for three hours at room temperature. The mixtures were stored for one day aging period at room temperature to attain high viscous state for this sol-gel technique [6, 7]. The prepared precursor solution was filled without any air bubbles in the syringe. Well cleaned glass plates were placed in the collector setup which is 15 cm from the tip of the needle. The precursor solution loaded syringe was fitted in the syringe holder setup and aligned to be in the same horizontal axis with shaft of the stepper motor. The variable electro-static high voltage of (0–30 kV) was applied across the syringe needle and metal collector terminal. The high voltage applied between the needle and metal holder was used to extract high surface tension across needle tip and

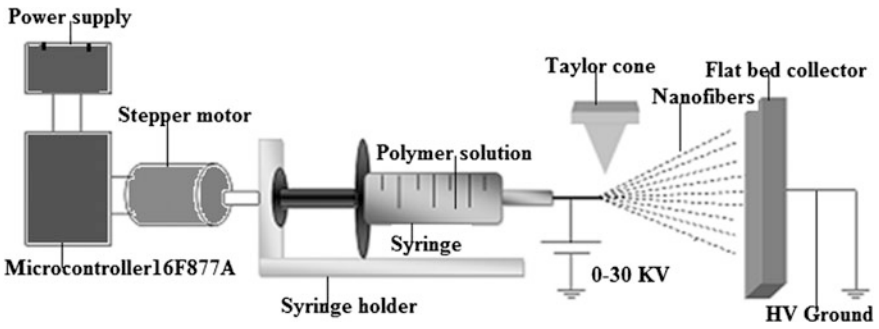

Fig. 1 Electro-spin coating set up

collector. Due to the forward movement of piston and applied high voltage, the Taylor cone was formed (without decomposition of PVA and Tin (II) chloride) and made as nano-fibers. The composite nano-fibers of PVA and Tin (II) chloride were spawned on the cleaned glass substrate (mounted on collector holder). The nano-fibers deposited glass substrates were collected labeled and preserved in desiccators then and there. The pure SnO_2 nano-fibers were obtained by calcining the deposited glass substrates at 400, 500 and 600 °C in a muffle furnace for 1 h to remove the organic polymer components in the samples and to crystallize SnO_2 [8].

3 Results and Discussion

3.1 Structural Properties

Figure 2 shows the powder XRD patterns of tin oxide nano-fibers. The peaks at 2θ values 26.59°, 33.94°, 38.01°, 44.24°, 51.85°, 54.79°, 57.82°, 62.06°, 64.64°, 66.11°, 71.48°, and 78.92° correspond to the lattice planes of (1 1 0), (1 0 1), (2 0 0), (1 1 1), (2 1 1), (2 2 0), (0 0 2), (3 1 0), (1 1 2), (2 0 2), (3 2 1) respectively [9, 10]. All the peaks in the XRD graphs are well matched with the JCPDS data number 41-1445 with tetragonal rutile structure of SnO_2, as shown in Fig. 2. The lattice parameters 'a' and 'c' of the SnO_2 nano-fibers are determined from the peaks of the XRD patterns using the formula for a tetragonal system (1). The calculated values of 'a' and 'c' of SnO_2 nano-fibers are 4.8133 Å (a), and 3.2900 Å (c). These values are in close agreement with the standard values mentioned in matched JCPDS card 41-1445, [i.e. 4.738 Å (a) 3.1872 Å (c)]. The values of the different crystal parameters are listed in Table 1.

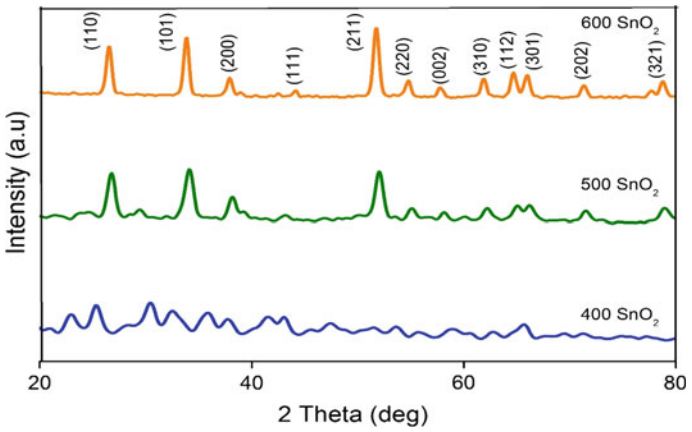

Fig. 2 XRD patterns of the SnO_2 nano-fibers with different calcination temperatures (400, 500, and 600 °C)

Table 1 Crystal size, lattice parameter, strain, and dislocation density of SnO_2 thin films prepared at 400, 500 and 600 °C

Annealed Temperature (°C)	Miller indices			Crystal size (nm)	Lattice constant (D)		Strain ($\times 10^{-7}$ lines^{-2} m^4)	Dis-location density (δ) ($\times 10^{-7}$ lines^{-2} m^2)
	h	k	l		a (Å)	c (Å)		
400	1	1	0	13.65			2.300	4.600
	1	0	1	11.59	4.75	3.16	4.300	6.000
	2	0	0	13.44			7.700	4.300
500	1	0	1	14.78			2.100	2.100
	1	0	0	12,86	4.81	3.20	3.200	5.000
	0	0	2	15.21			4.200	2.300
600	1	0	1	21.72			2.000	5.300
	1	0	0	14.08	4.88	3.21	2.400	7.400
	0	0	2	20.72			2.500	5.300

$$\frac{1}{d^2} = \frac{h^2 + k^2}{a^2} + \frac{l^2}{c^2} \tag{1}$$

Scherrer formula was used to calculate the average crystallite size [11].

$$D = \frac{0.9\lambda}{\beta \cos\theta} \tag{2}$$

The strain (ε) was calculated from the slope of β cosθ versus sinθ plot by using the relation [12].

$$\beta = \frac{\lambda}{D\cos\theta} - \varepsilon \tan\theta \tag{3}$$

The dislocation density (δ) was determined from the relation.

$$\delta = \frac{1}{D^2} \tag{4}$$

3.2 SEM, TEM and EDX Analysis

The external morphology and size of the prepared nano-fibers have been examined by FESEM and HRTEM. Figure 3a, b denote FESEM images of PVA and Tin (II) chloride composite nano-fibers and (c, d) illustrates SnO_2 nano-fibers. Figure 4

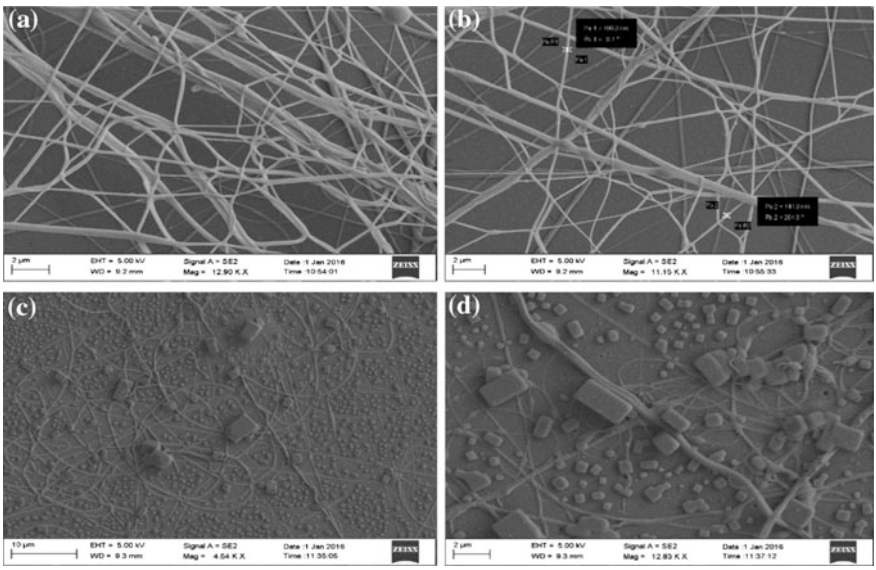

Fig. 3 FESEM images of (**a** and **b**) PVA and Tin (II) chloride nano-fibers, (**c** and **d**) SnO_2 nano-fibers deposited on glass substrates

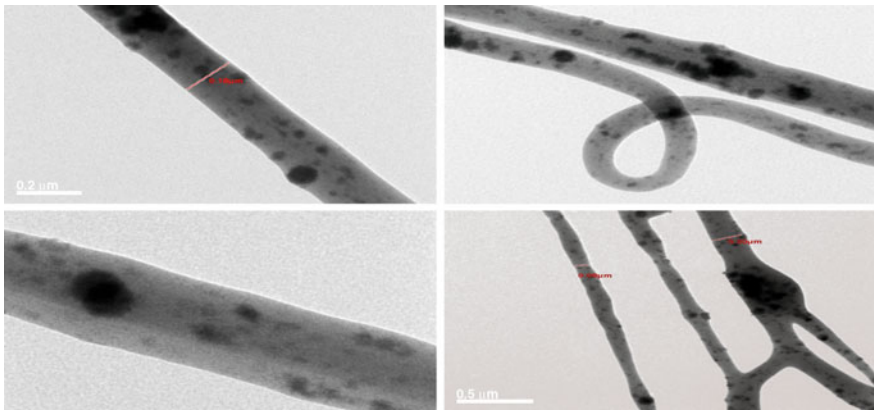

Fig. 4 TEM images of PVA embedded with SnO_2 particles

shows TEM images of nano-fibers of PVA and Tin (II) chloride prepared at 400 °C. It is clearly showed that the SnO_2 with PVA nano-fibers are distinct with slight variation of diameter (±5 nm) from the Fig. 3a, b, upon annealing the SnO_2 nano-fibers are formed with uniform size and unique characteristics. The chemical composition of the fabricated nano-fibers was explored by EDAX analysis. Figure 5a, b portrays the classic EDAX spectra of the nano-fibers. The EDAX

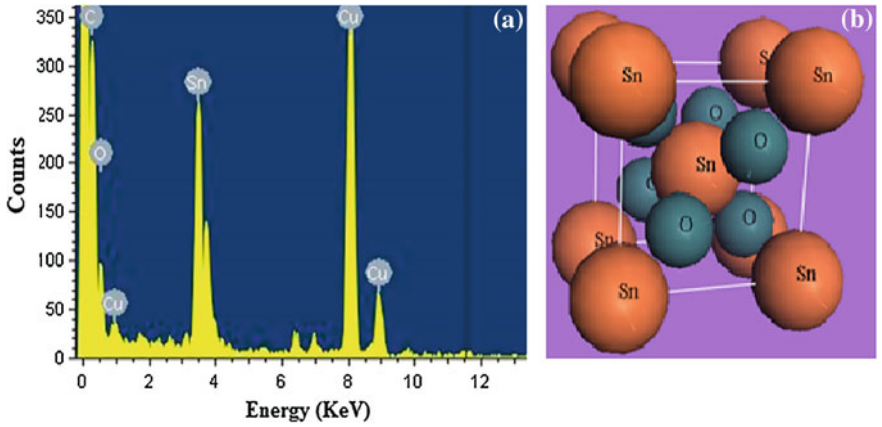

Fig. 5 **a** EDAX Spectrum and **b** Tetragonal rutile structure of SnO_2 nano-fibers

Table 2 UV-Vis Optical properties of SnO_2 nano-fibers

Annealed temperature (°C)	Band gap (E_g eV)
400	3.51
500	3.49
600	3.46

investigation of nano-fibers displays that the Sn and O elements only. The molecular formula of the fiber is identified as SnO_2 (Table 2).

3.3 Thermal Analysis

Thermal stability of the nano-fibers has been studied by TGA from 27 to 800 °C. The complete thermal behavior of the nano-fibers with time and temperatures showed in Fig. 6. It indicates different main weight losses taking place in the thermogravimetric (TG) characteristics curve. Due to the loss of the residual water molecules in the precursor composite fibers, 7 % of weight loss is occurred in the range 30–175 °C [13–15]. Due to the decomposition of the chloride group the first endothermic peak around 115 °C appeared in Differential Scanning Calorimeter (DSC) curve [16]. The range between 200 to 400 °C, 27 % of weight loss appeared due to loss of the volatile components. The breaking of carbon–carbon (–C–C–) bonds of the main structure of PVA and tin chloride, leads the other two weight losses around 23 % in the range of 400–600 °C. From the DSC curve, we identified the exothermic peaks around 175, 190, 431 and 525 °C due to chloride side chain vaporization [17]. The decomposition of the PVA becomes constant beyond 500 °C. Thermal analysis results indicate that there is no weight loss occurs after 500 °C.

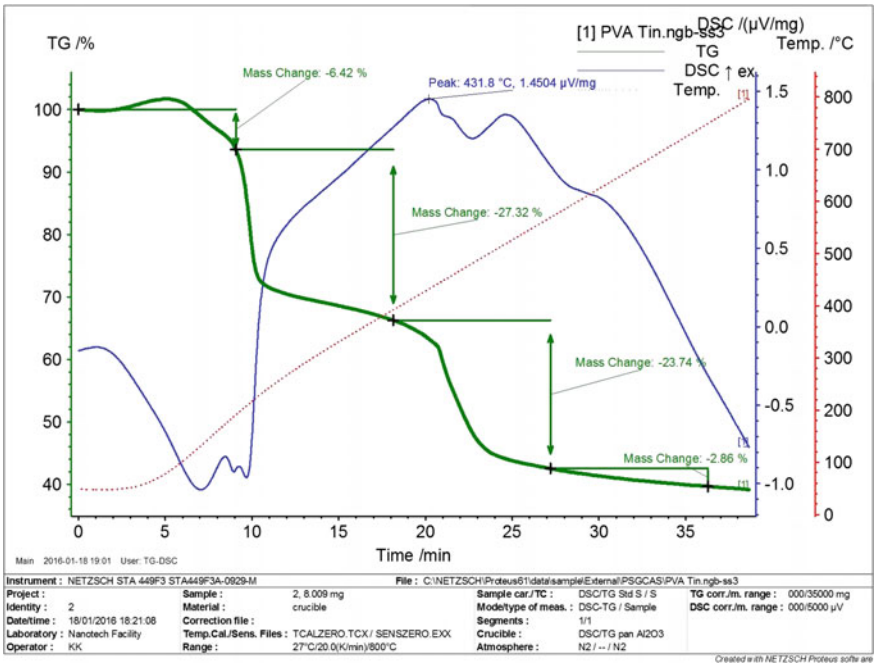

Fig. 6 TGA-DSC thermal decomposition of electrospun PVA/SnO_2 composite nano-fibers with mass change graph

3.4 *Photoluminescence (PL) Analysis*

The data presented are PL spectra of all the fibers which were taken by using spectrometer and they are as show in Fig. 7a–d. It is observed that the strong UV-Visible emission band for the corresponding UV excitation of 290 nm. The Violet PL emission at 590 nm and the corresponding average energy is 3.5 eV which is lower when compared to the pure SnO_2 (3.6 eV). It is attributes to the direct electronic transition between donor levels to valence band [18]. In particular SnO_2 semiconductor nanosystems the oxygen vacancy is one of the active luminescent center thus greatly influences in the PL emission. The occurrence of PL band is associates to luminescent centers and dangling in the SnO_2 nano-fibers [19].

3.5 *Optical Studies*

The optical properties of all the fibers were studied by using spectrometer from 190 to 2500 nm. The absorbance spectra of all fibers are as shown in Fig. 8a–d. Range from 200 to 800 nm. The spectra results expose that the absorption edge of SnO_2

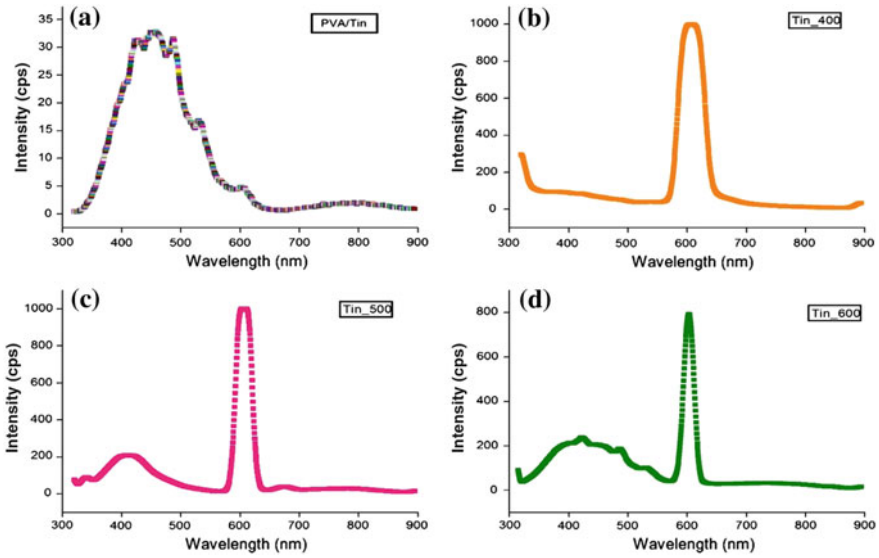

Fig. 7 PL spectra of **a** PVA/Tin (II) chloride and **b–d** Tin oxide (SnO_2) nano-fibers

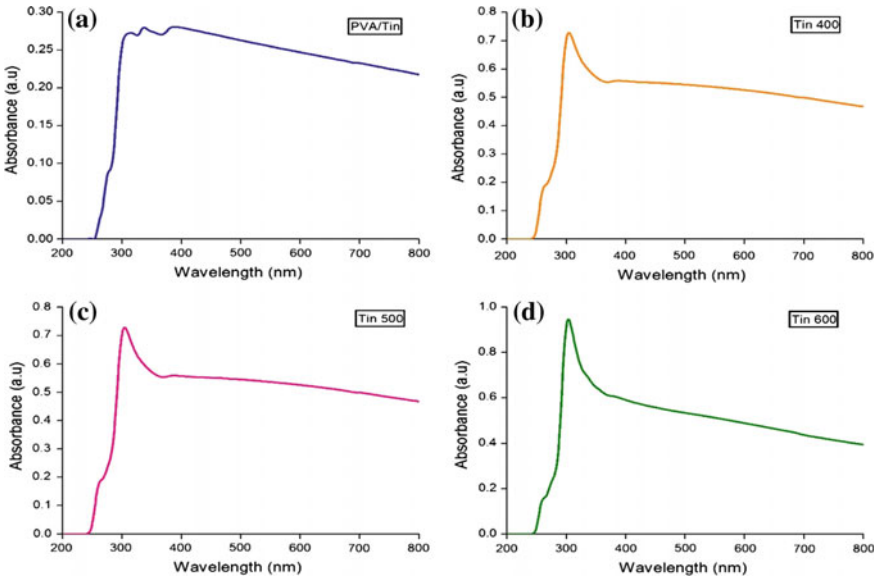

Fig. 8 Absorbance spectra of **a** PVA/Tin (II) chloride and **b–d** Tin oxide (SnO_2) nano-fibers

nano-fibers varied from 3.46 to 3.51 eV. The absorption edge is maximum for the fibers annealed at 400 °C and minimum at 600 °C. These results clearly show that band gap energy is closely associated with annealing temperatures at 290 nm excitation, SnO_2 nanoparticles exhibit emission at 600 nm [20].

4 Conclusion

In summary, high quality SnO_2 nano-fibers were fabricated by using indigenously prepared simple electrospinning unit. The fibers are continuous, almost straight, defect free, and cover the entire length of the glass substrate. The diameter of the SnO_2 fiber is in the order of few tens of nanometer with large draw ratio. The crystallization nature of the SnO_2 is tetragonal rutile structure and the measured lattice parameter of the fibers are close to the JCPD data (41-1445). The crystal size increases while surface area decreases with increase in annealing temperature. The optical band gap energy of SnO_2 is about 3.5 eV. Instead of high technological vacuum deposition method, this novel technique of preparing such very high quality SnO_2 nanofiber thin films will be a breakthrough in preparing many window layers, photo electrodes, counter electrodes, touch screen sensors, UV emitting films, and in many micro and nano electronic devices.

References

1. Batzill, M., Diebold, U.: Pro. Surf. Sci. **79**, 47–154 (2005)
2. Eun-Kyung Kim, S., Oliver, M.: Meta. Mat. Int. **16** 441–446 (2010)
3. Glocker, D.A., Shah, S.I. (eds.): Handbook of thin film process technology. Institute of Physics Publishing, Bristol and Philadelphia (1998)
4. Thangavel, K., Balamurugan, A., Venkatachalam, T., Ranjith kumar, E.: Superlattices Microstruct. **90**, 45–52 (2016)
5. Pillai C.K.S., Sharma, C.P.: Trends Biomater. Artif. Organs **22** (3), 179–201 (2009)
6. Mai, L., Lin, X., Chunhua Han, X.X., Luo, Y., Zhao, S., Zhao, Y.: Nano Lett. **10**, 4750–4755 (2010)
7. Barth, S., Hernandez-Ramirez, F., Holmes, J.D., Romano-Rodriguez, A.; Prog. Mat Sci. **55**, 563–627 (2010)
8. Bhagwat, M., Shah, P., Ramaswamy, V.: Mat. Lett. **57**, 1604–1611 (2003)
9. Chen, Wei, Ghosh, Debraj, Chen, Shaowei: J. Mater. Sci. **43**, 5291–5299 (2008)
10. Chen, D., Gao, L.: Che. Phy. Lett. **398**, 201–206 (2004)
11. Kumar, N.S., Bangera, K.V., Shivakumar G.K.: Appl. Nanosci. **4**, 209–216 (2014)
12. Ayeshamariam, A., Vidhya, V.S., Sivakumar, T., Mahendran, R., Perumalsamy, R., Sethupathy, N., Jayachandran, M.: Open J. Metal **3**, 1–7 (2013)
13. Liao, Y., Fukuda, T., Kamata, N., Tokunaga, M.: Nanosci. Res. Lett. **9**(1), 267 (2014)
14. Thompson, C.J., Chase, G.G., Yarin, A.L., Reneker, D.H.: Polymer **48**, 6913e6922 (2007)
15. Maria, S., Peresin, Y.H., Arja-Helena, V., Rojas, O.J., Pawlak, J.J, Seppa, J.V.: Bio Macromol. **11**(9), 2471e2477 (2010)
16. Zhang, G., Liu, M.: J. Mat. Sci. **34**, 3213–3219 (1999)

17. Chandraiaha, M., Sahooa, B., Pandaa, P.K.: Trans. Indian Ceram. Soc. **73**, 263–269 (2014)
18. Gu, F., Wang, S.F., Lu, M.K., Qi, Y.X., Zhou, G.J., Xu, D., Yuan, D.R.: J. Crystal Growth **255**, 357–360 (2003)
19. Pillai, S.K, Sikhwivhilua, L.M., Hillie, T.K.: Mat. Chem. Phys. **120**, 619–624 (2010)
20. Wang, Y., Ramos, I., Santiago-Aviles, J.J.: Optical bandgap and photo conductance of electrospun tin oxide nano-fibers. J. Appl. Phys. **102**, 093517 (2007)

Hierarchical ZSM-5 Zeolite Nanosurfaces with High Porosity—Structural, Morphological and Textural Investigations

S.K. Jesudoss, J. Judith Vijaya, A. Anancia Grace, L. John Kennedy, S. Sivasanker and P. Kathirgamanathan

Abstract The present paper describes the successful synthesis of hierarchical ZSM-5 zeolite nanosurfaces with high porosity from the rice straw ash (RSA) by means of the hydrothermal method at varying time intervals in the presence of small amount of tetrapropylammonium bromide as a single template. The synthesized samples were characterized by X-ray diffraction (XRD), Fourier transform infrared spectroscopy (FT-IR), high resolution scanning electron microscopy (HR-SEM), and nitrogen adsorption–desorption analysis (BET). The XRD pattern confirms the formation of pure ZSM-5 zeolite crystalline phase without any impurity phases. The IR spectrum shows a vibration band at 548 cm^{-1}, which is assigned to the double 5-rings of MFI-type zeolites. The surface area results reveal the formation of additional mesoporosity without destroying the intensive microporosity in a hierarchical ZSM-5 zeolite, which is due to the addition of TPABr during the synthesis. The characterization results conclude that the long time process of hierarchical ZSM-5 zeolite nanosurfaces with high porosity have produced high crystallinity.

S.K. Jesudoss · J. Judith Vijaya (✉) · A. Anancia Grace
Catalysis and Nanomaterials Research Laboratory, Department of Chemistry, Loyola College, Chennai 600 034, India
e-mail: jjvijaya78@gmail.com

L. John Kennedy
Materials Division, School of Advanced Sciences, Vellore Institute of Technology (VIT) University, Chennai Campus, Chennai 600 127, India

S. Sivasanker
National Centre for Catalysis Research, Indian Institute of Technology Madras, Chennai 600 036, India

P. Kathirgamanathan
Organic Electronics, Wolfson Centre, Brunel University, Kingston Lane, Uxbridge UB 8 3PH, Uxbridge, UK

J. Ebenezar (ed.), *Recent Trends in Materials Science and Applications*, Springer Proceedings in Physics 189, DOI 10.1007/978-3-319-44890-9_11

1 Introduction

Zeolites are crystalline and porous hydrated aluminosilicates having a three-dimensionally linked framework structures and tetrahedrally built from corner sharing TO_4 (T = Si or Al) units [1]. Generally, it is prepared by the hydrothermal method of the gel containing silica, alumina, cation, template and water. The application of zeolites includes catalysts, adsorbents, and ion exchangers for their excellent thermal stability, better catalytic activity and unique crystal structure [2, 3]. Every year, there are a significant number of reports published on new zeolite framework types, and more than 170 zeolite framework structures are known.

ZSM-5 (MFI type) is a prominent high silica and pentasil family of zeolite with pore diameters in the range of 0.54–0.56 nm [4]. It was first synthesized by Argauer and Landolt in 1972 [5]. Hierarchical ZSM-5 (HZSM-5) zeolite contains both micropores and mesopores in the zeolite surface [6]. The synthesis of HZSM-5 zeolite is very cheap, environmentally friendly and easy process. To achieve the economical synthesis of HZSM-5 zeolite, a small amount of TPABr template could be used to create ZSM-5 crystallization and to determine the crystal growth of the zeolite surfaces with additional high porosity. It has been observed that the template helps to modify the surface morphology and crystallite size by increasing the surface area and deter the precipitation of extra framework in the HZSM-5 zeolite synthesis [7].

In India, paddy cultivation is one of the major crop productions and a large quantity of straw is left out in the farmland. In rice straw, 23 % of residue produced in the excess amount left in the soil as uncollected or to a large extent open-field burnt. Rice husk is a solid waste product from the rice processing industry, which is suitable for recycling process [8]. In the same way, the use of rice straw residue is a major breakthrough instead of using rice plants. Mostly, rice straw is used as a fodder, to a smaller extent in paper factories, and as building materials in the construction of the house or other applications [9]. During over firing of rice straw at or above 700 °C, the amorphous silica will transform to crystalline silica [10]. The burnt rice straw will form RSA with the quantity that varies from 70 to 85 % of SiO_2 composition depending upon the burning conditions, furnace nature, rice variety, straw moisture content, climate and the geographical area [11]. The presence of silica ash creates many ecological problems related to pollution and waste dispose. Furthermore, at a higher temperature, the final silicosis products can cause health problems to living beings. These silicosis products might contain crystalline silica, for example, quartz and cristobalite [12]. Therefore, the applications of the above mentioned agricultural waste are used to produce beneficial advanced materials, which are attractive since we are facing global environmental problems. A high quality and value added product silica were obtained from the burning of low-cost raw material rice straw, which is ecological. In the rice crop, agricultural waste, RSA is a potentially attractive source for the large-scale industrial production of aluminosilicates like ZSM-5 zeolites. An attempt on the synthesis of HZSM-5

zeolite from the extracted silica of RSA with high purity of ash produced by the uncontrolled burnt off the rice straw as a biological source of silicate.

In the present work, a new strategy has been designed for the synthesis of hierarchical ZSM-5 zeolite porous nanosurfaces with high porosity from RSA using a small amount of single TPABr template with the superior performance of crystallinity, surface morphology, surface area and porosity. Physicochemical characterization of the synthesized HZSM-5 zeolite samples has been characterized using XRD, FT-IR, HR-SEM and N_2 adsorption-desorption measurements.

2 Experimental Section

2.1 Materials

Rice straw (RS) was collected from the local area in the vilupuram (Tamilnadu, India). This collected rice straw was thoroughly washed and precleaned with water and dried at 90 °C for 24 h. The cleaned rice straw has been burnt to remove the unwanted compounds or impurities in the waste material to form RSA. This has been achieved by burning in a muffle furnace at 900 °C for 6 h with heating and cooling rate at 4 °C min^{-1}. Later, Dey et al. method [1] was followed for the extraction of silica from RSA. It is used as a silica source for the synthesis of hierarchical ZSM-5 zeolite and usually involves the formation of aluminosilicate gel, which is determined by the reaction of soluble silicate and aluminate anions [13]. The following chemicals were used in the preparation of hierarchical ZSM-5 zeolite. Aluminium metal foil (SD Fine-Chem Ltd., 99 %), sodium hydroxide pellets (AR, 98 %), TPABr (Sigma-Aldrich, 98 %), ammonium nitrate (SD Fine-Chem Ltd., 98 %) and deionized water (DI) of analytical grade were used without further purification.

2.2 Preparation of Hierarchical ZSM-5 Zeolite (HZSM-5)

In a typical synthesis procedure of HZSM-5 zeolite, a stoichiometric amount of silicate mixture of RSA is dispersed into the required amount of aluminate mixture of Al metal foil and NaOH solution. A small quantity of tetrapropylammonium bromide (TPABr) and mixed with distilled water. This solution is slowly added to the silicate-aluminate gel solution and the whole mixture is kept under stirring at room temperature for 18 h. The obtained dispersion gel mixture is then transferred into a stainless steel autoclave with Teflon liner and heated in an oven at 160 °C for 3–5 days. After the reaction, the product is filtered, washed with ethanol and dried at 70 °C overnight. The Na-ZSM-5 product is then calcined at 500 °C for 5 h in a muffle furnace to remove the templates. Then, the calcined Na-ZSM-5 zeolite

catalyst is converted to its ammonium form by ion exchange with 1 M ammonium nitrate (NH_4NO_3) solution for three times at 80 °C for 2 h followed by filtering, washing and drying at 70 °C for 4 h and calcinated again at 500 °C for 5 h. The final product of HZSM-5 zeolite sample was obtained, and this sample was used for further analytical studies.

2.3 Analytical Techniques

The crystallinity of HZSM-5 zeolite was identified by Powder X-ray diffraction (XRD). The samples diffraction patterns were recorded on a Rigaku Miniflex II diffractometer with CuKα as the radiation source at a wavelength of 0.154 nm with the 2θ angle ranging from 5° to 60° with a 0.02 step size. The characteristic vibration bands of the HZSM-5 zeolite catalysts are confirmed by Fourier transform infrared spectra (FTIR, Perkin–Elmer) in the range of 4000–400 cm^{-1} at room temperature using the KBr pellet techniques. The morphology of the synthesized samples was analyzed by High-resolution scanning electron microscopy (HR-SEM, Hitachi S-4800) measurements. N_2 adsorption–desorption isotherms were obtained with a commercial instrument (Micromeritics ASAP 2020) at liquid N_2 temperature in order to find out the surface area and pore volume of the synthesized samples. The samples were degassed at 200 °C for 6 h, prior to adsorption measurements.

3 Results and Discussion

3.1 XRD Studies

The powder XRD patterns of the as-synthesized HZSM-5 sample prepared by the hydrothermal method from RSA with the single organic template in three different time intervals ranging from 3 to 5 days is shown in Fig. 1a–c. The presence of characteristic diffraction peaks at 2θ = 7.98°, 8.82°, 14.82°, 23.14°, 23.96° and 24.44° are associated with (011), (020), (031), (051), (303) and (313) planes, respectively with the d-spacing values of 1.11, 1.00, 0.59, 0.39, 0.37 and 0.36 nm, respectively. These patterns were completely indexed to the ZSM-5 type framework topology and correspond to the JCPDS card no: 42-0024. The XRD result clearly indicates that there are no other diffraction peaks of the impurity phase observed and the specific MFI topology was maintained in the synthesized HZSM-5 samples. The sharp peaks obtained in XRD pattern confirms the formation of highly good crystallinity materials of HZSM-5 zeolite phases, with no evidence of impurity crystalline phases. The peak intensity of the HZSM-5 (3 days) zeolite was slightly lower than that of the HZSM-5 (4 and 5 days) zeolite, which is due to the pore walls of the macropores that were not completely converted into MFI type

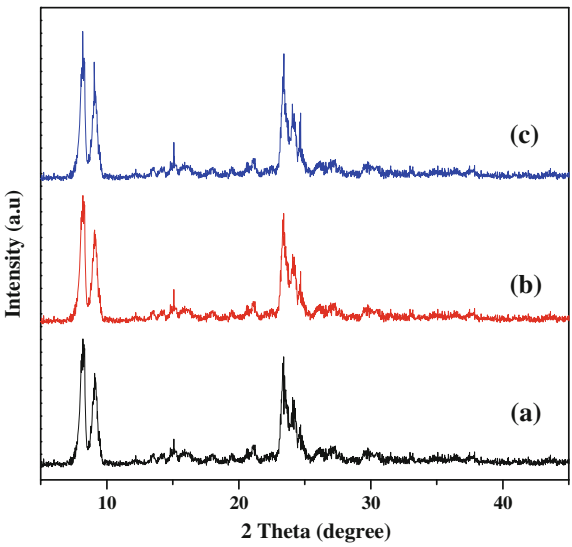

Fig. 1 XRD patterns of HZSM-5 zeolite prepared at **a** 3 days **b** 4 days and **c** 5 days

framework. Our XRD results were compared with other known established experimental reports for the confirmation of the HZSM-5 zeolite crystallinity [14]. The average crystallite size was calculated by using the Debye-Scherrer formula [15],

$$L = \frac{0.89\lambda}{\beta \cos\theta}$$

where, L is the average crystallite size, λ, X-ray wavelength (0.154 Å), θ, Bragg diffraction angle and β, the full-width at half maximum (FWHM) of the obtained peaks. Fitting the measured peaks with two Gaussian curves in order to find the true peak position and width corresponding to monochromatic CuKα radiation obtained by the peak position and the FWHM.

3.2 IR Spectrum Analysis

The formation of HZSM-5 zeolite nanosurfaces obtained at 160 °C for different time periods (3–5 days) was also characterized by FT-IR studies. The vibrational frequencies of silanol groups were analyzed by FT-IR spectrum. As shown in Fig. 2a–c, the characteristic absorption bands of HZSM-5 zeolite were found at around 466, 548, 789, 1091, 1220, 1600, 3436 and 3642 cm^{-1} respectively. The bending vibration of TO_4 (T = Si, Al) in HZSM-5 zeolite was observed at 466 cm^{-1}. It is mainly noted that the framework vibration bands at 548 cm^{-1} showed the five-membered rings in MFI type zeolites [16], which can be used to

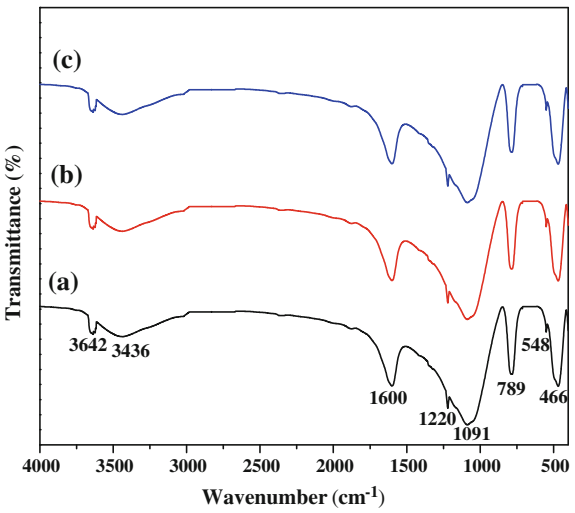

Fig. 2 FT-IR spectra of HZSM-5 zeolite prepared at **a** 3 days **b** 4 days and **c** 5 days

determine the crystallinity of HZSM-5 materials [17]. The Si–O–T linkage was evidenced from the absorption bands at 1220 cm^{-1} (external asymmetric stretching), 1091 cm^{-1} (internal asymmetric stretching) and 789 cm^{-1} (external symmetric stretching) corresponds to the siliceous materials. The characteristic band at 3642 cm^{-1} is due to the isolated silanol groups (Si–O–H) and the band at 3436 cm^{-1} corresponds to Al–OH framework (Brønsted acid sites) in MFI type framework. The bending vibration of water molecules observed at 1600 cm^{-1} is due to the absorption of moisture by the samples during the compaction of the KBr powder. HZSM-5 zeolite is always absorbing moisture, because of their hydrophilic properties, when they exposed to the atmosphere [18, 19]. Thus, both the XRD and FT-IR studies confirmed the synthesized HZSM-5 zeolite has MFI type topology.

3.3 HR-SEM Measurements

Figure 3a shows the SEM images of the HZSM-5 sample prepared at 5 days. The formation of well crystalline MFI type of zeolites, with a relatively uniform porous-like nanosurfaces with a high porosity of about 300–500 nm is observed. Additionally, some individual particles which appear in the images are due to agglomeration with sizes ranging from 15 to 20 nm. The surface morphology of H-ZSM-5 nanosurfaces was slightly rough and might be attributed to the primary HZSM-5 nanosurfaces with high porosity. The SEM image in Fig. 3b clearly shows that these HZSM-5 micro-holes have a porous nanosurface. The morphology of porous nanosurfaces is composed of numerous small nanoparticles primarily HZSM-5 nanosurfaces, as implicit by the XRD results.

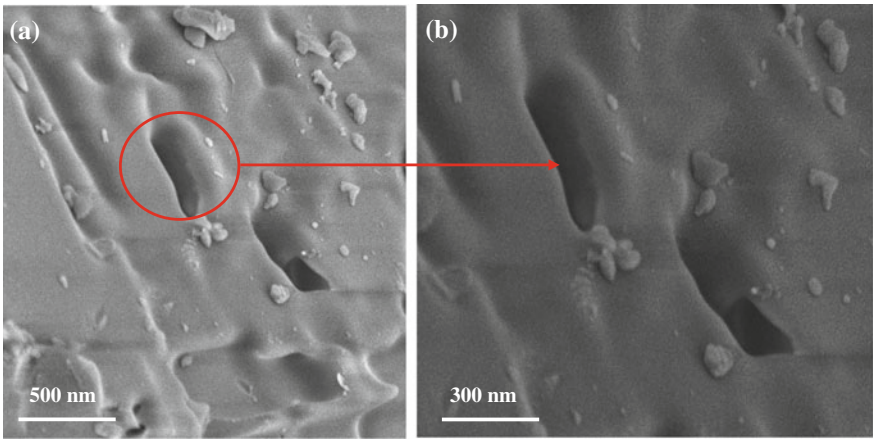

Fig. 3 **a**, **b** HR-SEM images of HZSM-5 zeolite prepared at 5 days for different magnifications

3.4 N_2 Adsorption–Desorption (BET) Analysis

The nitrogen adsorption and desorption isotherms of the prepared HZSM-5 samples (3–5 days) are shown in Fig. 4a–c. All the samples demonstrate a type IV isotherm that contains a vertical uptake under $P/P_0 = 0.02$, at a low-pressure range is due to the presence of micropores, and a hysteresis loop from $P/P_0 = 0.45$ to $P/P_0 = 1$ is due to the presence of both micropores and mesopores. The HZSM-5 (5 days) zeolite hysteresis loop is slightly broader than the HZSM-5 (4 and 3 days) zeolites, which corroborate the creation of extra mesoporosity in the HZSM-5 (5 days) zeolite. The extra mesoporosity in HZSM-5 (5 days) sample was created without

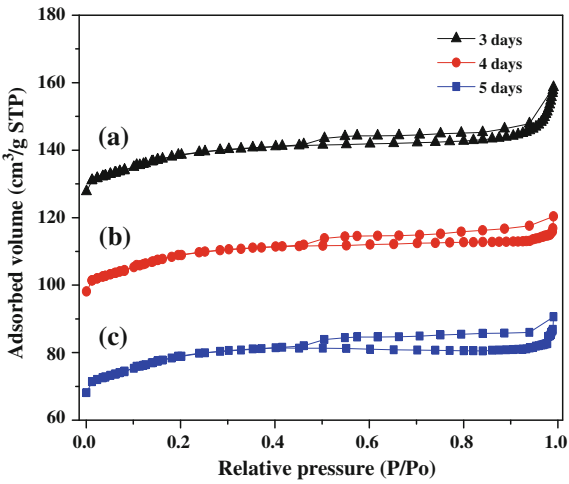

Fig. 4 N_2 adsorption-desorption isotherms of HZSM-5 zeolite prepared at **a** 3 days **b** 4 days and **c** 5 days

Table 1 Textural properties of HZSM-5 zeolites

Synthesis time (days)	S_{BET} (m^2/g)	S_{micro} (m^2/g)[a]	S_{meso} (m^2/g)	V_{total} (cm^3/g)	V_{micro} (cm^3/g)	V_{meso} (cm^3/g)[b]
5	102.53	69.86	32.67	0.0622	0.0288	0.0334
4	76.99	47.84	29.15	0.0576	0.0276	0.0300
3	56.38	31.27	25.11	0.0522	0.0254	0.0268

[a]Measured by *t*-plot method. [b]$V_{meso} = V_{total} - V_{micro}$

destroying the microporosity, due to the small amount of TPABr template added during the synthesis and it should lead to the most rapidly diffusion of reactant molecules and superior performance of catalytic activity [20, 21]. The textural properties of the samples data calculated from the isotherms are presented in Table 1. As the synthesized reaction time increases, the zeolites surface area also increases. The increasing conversion of RSA into HZSM-5 zeolite with respect to time intervals increases the microporosity. The total surface area and total pore volume of the samples are 102.53 m^2/g and 0.0622 cm^3/g (5 days), 76.99 m^2/g and 0.0576 cm^3/g (4 days) and 56.38 m^2/g and 0.0522 cm^3/g (3 days) respectively. Thus, these HZSM-5 porous nanosurfaces with high porosity could play a vital role for the better catalytic performance [22, 23].

4 Conclusion

In summary, the synthesis of hierarchical ZSM-5 zeolite nanosurfaces with high porosity has been developed by a hydrothermal method using the RSA as the silica source. The additional mesoporosity was created in the surface by the addition of TPABr template during the synthesis. The synthesized samples were investigated by using XRD, FT-IR, HR-SEM and N_2 adsorption-desorption measurements. The HZSM-5 (5 days) sample shows a better crystallinity, higher surface area, increasing total pore volume and modify the surface morphology than the HZSM-5 (3 and 4 days) samples, which is confirmed by different analytical techniques. The surface morphology of the ZSM-5 zeolite particles has led to the formation of porous like nanosurfaces with high porosity. This synthesized product is an economic, ecological and industrially applicable advanced material in the current area of research.

Acknowledgements The authors duly acknowledge the financial support rendered by Loyola college, Tamil Nadu, India through Loyola College-Times of India (LC-TOI) Major Research Project scheme vide (Project Code: 2LCTOI14CHM003, dated 25.11.2014) to the first author.

References

1. Dey, K.P., Ghosh, S., Naskar, M.K.: Organic template-free synthesis of ZSM-5 zeolite particles using rice husk ash as silica source. Ceram. Int. **39**, 2153–2157 (2013)
2. Jiang, J., Duanmu, C., Yang, Y., Gu, X., Chen, J.: Synthesis and characterization of high siliceous ZSM-5 zeolite from acid-treated palygorskite. Powder Technol. **251**, 9–14 (2014)
3. Motsi, T., Rowson, N.A., Simmons, M.J.H.: Kinetic studies of the removal of heavy metals from acid mine drainage by natural zeolite. Int. J. Miner. Process. **101**, 42–49 (2011)
4. Egeblad, K., Christensen, C.H., Kustova, M., Christensen, C.H.: Templating mesoporous zeolites. Chem. Mater. **20**, 946–960 (2008)
5. Argauer, R.J., Landolt G.R.: US Patent 3 702 886 A. (1972)
6. Narayanan, S., Vijaya, J.J., Sivasanker, S., Yang, S., Kennedy, L.J.: Hierarchical ZSM-5 catalyst synthesized by a Triton X-100 assisted hydrothermal method. Chinese J. Catal. **35**, 1892–1899 (2014)
7. Pan, F., Lu, X., Wang, Y., Chen, S., Wang, T., Yan, Y.: Synthesis and crystallization kinetics of ZSM-5 without organic template from coal-series kaolinite. Micropor. Mesopor. Mater. **184**, 134–140 (2014)
8. Azizi, S., Yousefpour, M.: Synthesis of zeolites NaA and analcime using rice husk ash as silica source without using organic template. J. Mater. Sci. **45**, 5692–5697 (2010)
9. Gadde, B., Menke, C., Wassmann, R.: Rice straw as a renewable energy source in India, Thailand, and the Philippines: overall potential and limitations for energy contribution and greenhouse gas mitigation. Biomass Bioenerg. **33**, 1532–1546 (2009)
10. Hamdan, H., Muhid, M.N.M., Endud, S., Listiorini, E., Ramli, Z.: ^{29}Si MAS NMR, XRD and FESEM studies of rice husk silica for the synthesis of zeolites. J. Non-Cryst. Solids **211**, 126–131 (1997)
11. Azizi, S.N., Yousefpour, M.: Spectroscopic studies of different kind of rice husk samples grown in North of Iran and the extracted silica by using XRD, XRF, IR, AA and NMR techniques. Eurasian J. Anal. Chem. **3**, 298–306 (2008)
12. Yusof, A.M., Nizam, N.A., Rashid, N.A.A.: Hydrothermal conversion of rice husk ash to faujasite-types and NaA-type of zeolites. J. Porous Mater. **17**, 39–47 (2010)
13. Barrer, R.M.: The hydrothermal chemistry of zeolites. Academic Press, London (1982)
14. Wang, L., Yin, C., Shan, Z., Liu, S., Du, Y., Xiao, F.S.: Bread-template synthesis of hierarchical mesoporous ZSM-5 zeolite with hydrothermally stable mesoporosity. Colloids Surf. A **340**, 126–130 (2009)
15. Becheri, A., Dürr, M., Nostro, P.L., Baglioni, P.: Synthesis and characterization of zinc oxide nanoparticles: Application to textiles as UV-absorbers. J. Nanopart. Res. **10**, 679–689 (2008)
16. Guo, Y.P., Wang, H.J., Guo, Y.J., Guo, L.H., Chu, L.F., Guo, C.X.: Fabrication and characterization of hierarchical ZSM-5 zeolites by using organosilanes as additives. Chem. Eng. J. **166**, 391–400 (2011)
17. Narayanan, S., Vijaya, J.J., Sivasanker, S., Yang, S., Kennedy, L.J.: Hierarchical ZSM-5 catalyst synthesized by a Triton X-100 assisted hydrothermal method. Chinese J. Catal. **35**, 1892–1899 (2014)
18. Chester, A.W., Derouane, E.G.: Zeolite Characterization and Catalysis: A Tutorial. Springer, (2009)
19. Vijaya, J.J., Kennedy, L.J., Sekaran, G., Nagaraja, K.S.: Synthesis, characterization and humidity sensing properties of Cu–Sr–Al mixed metal oxide composites. Mater. Res. Bull. **43**, 473–482 (2008)
20. Schmidt, F., Lohe, M.R., Buchner, B., Giordanino, F., Bonino, F., Kaskel, S.: Improved catalytic performance of hierarchical ZSM-5 synthesized by desilication with surfactants. Micropor. Mesopor. Mater. **165**, 148–157 (2013)
21. Sang, Y., Liu, H., He, S., Li, H., Jiao, Q., Wu, Q., Sun, K.: Catalytic performance of hierarchical H-ZSM-5/MCM-41 for methanol dehydration to dimethyl ether. J. Energy Chem. **22**, 769–777 (2013)

22. Wang, Y.Y., Gin, G.Q., Guo, X.Y.: Growth of ZSM-5 coating on biomorphic porous silicon carbide derived from durra. Micropor. Mesopor. Mater. **118**, 302–306 (2009)
23. Fernandez, C., Stan, I., Gilson, J.P., Thomas, K., Vicente, A., Bonilla, A., Ramirez, J.P.: Hierarchical ZSM-5 zeolites in shape-selective xylene isomerization: Role of mesoporosity and acid site speciation. Chem. Eur. J. **16**, 6224–6233 (2010)

A Comparative Study on Designing Efficient Pulse Compressors and Pulse Stretchers Using Tapered Photonic Crystal Fibers

A. Manimegalai, K. Senthilnathan, K. Nakkeeran and P. Ramesh Babu

Abstract We design various tapered photonic crystal fibers (PCFs), namely, hexagonal tapered PCF (H-TPCF), octagonal tapered PCF (O-TPCF) and decagonal tapered PCF (D-TPCF) for generating self-similar ultrashort pulses (USPs) and stretched pulses. Here, we report on pulse compression as well as pulse stretching using the above mentioned PCFs wherein both dispersion and nonlinear profiles vary exponentially. Of these PCFs, we use dispersion decreasing PCFs for pulse compression process and dispersion increasing PCFs for pulse stretching process. From the detailed analysis, we find that H-TPCFs could generate high quality USPs with more compression percentage whereas D-TPCFs could produce high quality stretched pulses with more stretching percentage.

1 Introduction

Optical pulse compressor plays a vital role for generating USPs that find many applications in various areas such as optical sampling systems, infrared time resolved spectroscopy, ultra fast physical processes, ultrahigh-bit-rate optical communication systems, etc. [1–3]. Over a decade, nonlinear pulse compression is highly preferred than the linear pulse compression due to several reasons [1, 4]. Although three nonlinear pulse compression techniques, namely, adiabatic pulse compression, higher order soliton pulse compression and self-similar techniques have been developed, self-similar technique is being widely chosen because it offers efficient pulse compression [1, 5, 6]. Self-similar analysis has been used to study the

A. Manimegalai
School of Electronics Engineering, VIT University, Vellore 632014, India

K. Senthilnathan (✉) · P. Ramesh Babu
Department of Physics, School of Advanced Sciences, VIT University, Vellore 632014, India
e-mail: senthee@gmail.com

K. Nakkeeran
School of Engineering, University of Aberdeen, Aberdeen AB24 3UE, UK

J. Ebenezar (ed.), *Recent Trends in Materials Science and Applications*, Springer Proceedings in Physics 189, DOI 10.1007/978-3-319-44890-9_12

linearly chirped pulses in conventional optical fibers [7]. Besides, the generation of USPs and train of USPs using self-similar analysis has been numerically investigated in tapered PCFs with the exponentially decreasing dispersion and increasing nonlinear profiles [8, 9]. Recently, the pulse stretcher has been proposed using photonic quasi-crystal fibers (PQFs) [10]. Very recently, we have reported the various types of tapered PCFs for generating USPs with exponentially varying dispersion and nonlinear profiles [11]. In this work, we compare the generation of USPs and stretched pulses at 1550 nm in exponentially varying dispersion and nonlinearity profiles of hexagonal, octagonal and decagonal tapered PCFs.

This chapter is planned as follows. In Sect. 2, we introduce the theoretical model that explains the pulse propagation in the tapered PCFs. In Sect. 3, we compare the structural design and explore the optical properties of hexagonal, octagonal and decagonal tapered PCFs. In Sect. 4, we compare the generation of USPs in above mentioned PCFs and in Sect. 5, the generation of stretched pulses is compared. We conclude the research findings in Sect. 6.

2 Theoretical Model: Self-similar Pulse Compressor

For generating the USPs using tapered PCFs, we use the following modified nonlinear Schrödinger equation (NLS) equation which governs the light pulse propagation in a tapered PCF and it is written as [12]

$$\frac{\partial U}{\partial z} - i\frac{\beta_2(z)}{2}\frac{\partial^2 U}{\partial t^2} + i\gamma(z)|U|^2 U + U\frac{g(z)}{2} = 0, \tag{1}$$

where U is the slowly varying envelope of the wave, z is the longitudinal coordinate, and t is the time in the moving reference frame. The parameters $\beta_2(z)$ and $\gamma(z)$ are the second order dispersion coefficient and Kerr nonlinearity, respectively. Here, $g(z)$ is the distributed gain/loss. We assume that the self-similar solution of above equation is,

$$\begin{aligned} U(z,t) = &\sqrt{\frac{|\beta_{20}|e^{(-\sigma z)}}{\gamma_0 e^{\rho z}}}\frac{1}{T_0 e^{-\sigma z}}\operatorname{sec} h\left[\frac{t-T_c}{T_0 e^{-\sigma z}}\right] \\ &\times \exp\left[i\alpha_{10} + i\frac{\beta_{20}}{2\sigma T_0^2}\times(1-e^{\sigma z}) + i\frac{\sigma e^{\sigma z}}{2\beta_{20}}(t-T_c)^2\right] \end{aligned} \tag{2}$$

Here, T_c, β_{20}, γ_0, α_{10}, σ and ρ are the center of the pulse, the initial dispersion, initial nonlinearity, the integration constant, the dispersion rate and the nonlinear rate respectively [7]. The above solution is valid if and only if the following conditions are satisfied.

$$\beta_2(z) = \beta_{20} \exp(-\sigma z) \tag{3}$$

$$\gamma(z) = \gamma_0 \exp(\rho z) \tag{4}$$

3 Designing Tapered Photonic Crystal Fibers

In this section, we describe the design of various tapered PCFs using the above mentioned self-similar condition for generating chirped solitary pulses. It has been demonstrated that the dispersion and nonlinear profiles could be engineered through the tapering process which is usually carried out by simultaneously stretching and heating the fiber [13, 14]. In general, the tapering is done by reducing the pitch and diameter [11]. Fiber tapering provides a convenient way to reduce the mode-field diameter of fibers and thereby allowing for a better pulse compression. We, thus, emphasize that the tapered PCFs are very much suitable for effective pulse compression when compared to conventional PCFs. In this work, we design various tapered PCFs wherein dispersion and nonlinear profiles vary exponentially in line with the self-similar analysis. By exploiting these optical properties, we demonstrate the effective pulse compression and pulse stretching schemes. The proposed geometric hexagonal and octagonal tapered structures consist of five rings of air holes whereas the decagonal structure possesses four rings of air holes. The tapered PCFs can be designed by simultaneous reduction of their geometrical parameters namely, air-hole diameter d, and pitch Λ. While tapering the PCF, we decrease the value of the pitch as per the self-similar condition [8].

$$\Lambda(z) = \Lambda(z_0) \exp(-\sigma z) \tag{5}$$

The geometrical structures of the proposed H-TPCF and O-TPCF and D-TPCFs are shown in Fig. 1.

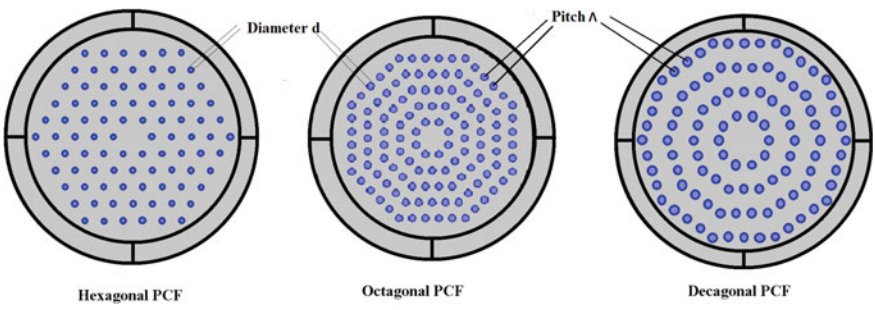

Fig. 1 Geometric structures H-TPCF, O-TPCF and D-TPCF

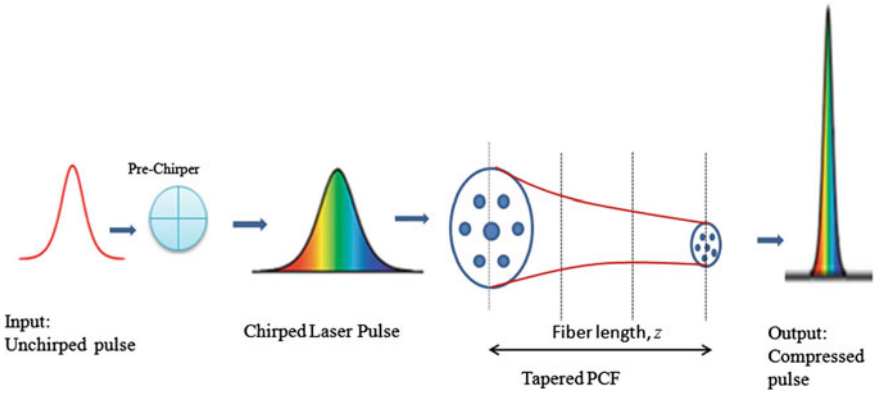

Fig. 2 Proposed H-TPCF pulse compressor

4 A Comparative Study of Self-similar Pulse Compression in Hexagonal, Octagonal and Decagonal Tapered PCFS

The four possible self-similar conditions lead to the design of exponentially varying dispersion and nonlinearity tapered PCFs. It is well known that the dispersion decreasing profiles are suitable for efficient pulse compression for generating USPs. The proposed H-TPCF pulse compressor is shown Fig. 2. It consists of a pre-chirper which provides the desired linear chirping to the unchirped pulse. Then, the chirped pulse undergoes compression when it traverses in a tapered PCF.

4.1 Design and Optical Properties

Based on self similar conditions, we have designed H-TPCF, O-TPCF and D-TPCF [15] for two cases: (i) Group velocity dispersion (GVD) decreases and nonlinearity increases (ii) Both GVD and nonlinearity decrease.

4.1.1 GVD Decreases and Nonlinearity Increases

By varying the design parameters such as the pitch, Λ, and air hole diameter, *d,* one can easily design the tapered PCFs. Figure 3a–c shows the variation of design parameters, namely, relative air hole diameter and pitch with respect to propagation distance, z for H-TPCF, O-TPCF and D-TPCF. The variations of GVD and nonlinearity against propagation distance are illustrated in Fig. 4a–c. For H-TPCF, we vary the relative air hole diameter, d/Λ, from 0.2796 to 0.2910 and the pitch from 4 to 3.5 μm. We calculate the initial GVD as -95.97 ps^2/km for the PCF parameters

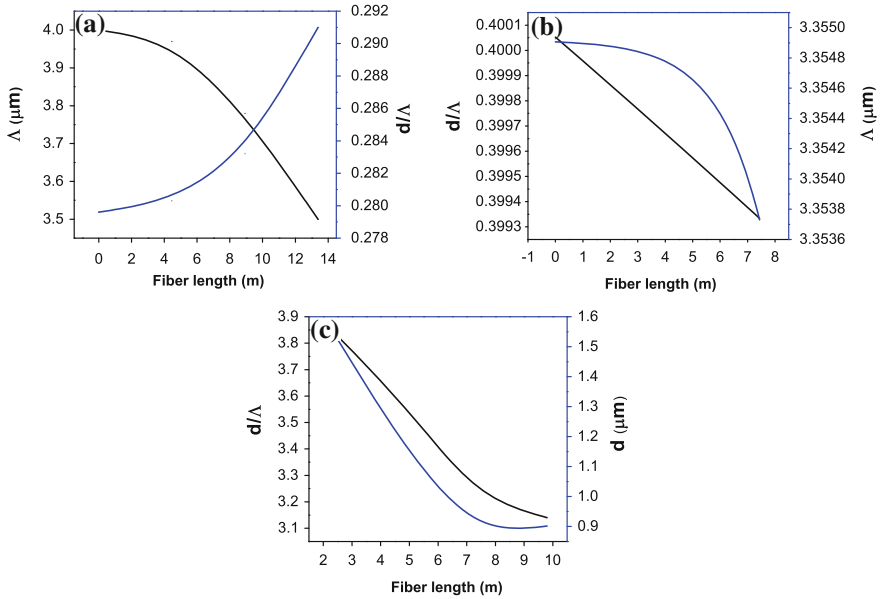

Fig. 3 **a** Variation of d/Λ and Λ along z of H-TPCF. **b** Variation of d/Λ and Λ along z of O-TPCF. **c** Variation of d/Λ and d along z of D-TPCF

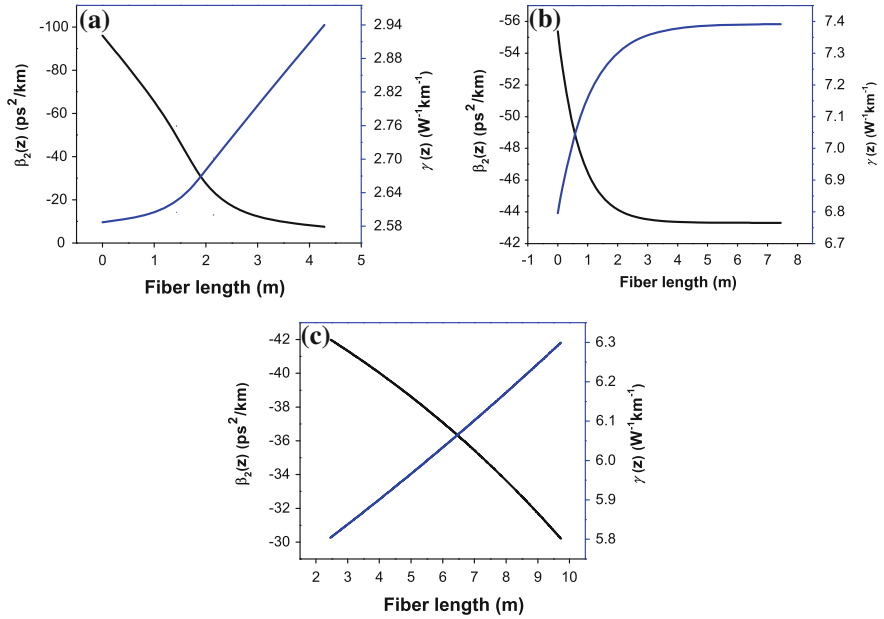

Fig. 4 Variation of GVD, $\beta_2(z)$, and nonlinearity, $\gamma(z)$, as a function of propagation distance, z **a** H-TPCF **b** O-TPCF and **c** D-TPCF

of $d/\Lambda = 0.2796$ and $\Lambda = 4$ μm. The cumulative dispersion β_2 at the end of the PCF is found to be −7.52 ps^2/km. We next calculate the effective nonlinearity by using effective mode area, A_{eff}. The initial and final value of A_{eff} are found to be 40.72 and 35.83 μm^2, respectively. The initial nonlinearity is 2.587 W^{-1} km^{-1}. By considering the value of A_{eff}, the effective nonlinearity of the tapered fiber is estimated by using the relation, $\gamma = \frac{2\pi n_2}{\lambda A_{eff}}$ where n_2 is nonlinear index (2.6×10^{-20} m^2/W). The decrease in effective area leads to significant increase in intensity of the pulses. For O-TPCF, the relative air hole diameter, d/Λ, is varied from 0.4 to 0.399352 and the Λ from 3.35490 to 3.35373 μm. We compute the initial GVD as −55.37 ps^2/km and the cumulative dispersion at the end of the PCF is determined to be −43.21 ps^2/km. The nonlinearity in this tapered PCF increases from 6.79 to 7.34 W^{-1} km^{-1}. The decagonal tapered PCF is designed by decreasing the relative air hole diameter from 0.4 to 0.28707 and the pitch from 3.832 to 3.14 μm. The initial and final GVD are −42 and −27.7106 ps^2/km, respectively. The nonlinearity in this tapered PCF increases from 5.82 to 5.20 W^{-1} km^{-1}.

4.1.2 Both GVD and Nonlinearity Decrease

Now we design the H-TPCF, O-TPCF and D-TPCF to get both decreasing dispersion and nonlinearity profiles. In H-TPCF, we decrease the diameter of air hole and keep the pitch as a constant. Here, the relative air hole diameter is varied exponentially from 0.2530 to 0.2346, the diameter of the air holes is varied from 0.62 to 0.575 μm and the pitch is fixed as 2.45 μm. Figures 5a–c and 6a–c depict the variations of design parameters and calculated optical properties against the propagation distance, z. In O-TPCF, we reduce the diameter of air hole without varying the pitch. We choose a H-TPCF of length 7.44 m as in the previous case. The relative air hole diameter is kept at 0.4 μm and the diameter of the air holes is varied from 1.342 to 2.8 μm and the pitch is kept at 3.35 μm. For this case, D-TPCF is designed by decreasing the relative air hole diameter from 0.363 to 0.2768 and the diameter of the air holes is varied from 1.22 to 0.93 μm and the pitch is kept at 3.36 μm.

4.2 A Comparison on Self-similar Pulse Compression

Figure 7 depicts the comparison of compressed USPs obtained from H-TPCF, O-TPCF AND D-PCF for dispersion decreasing and nonlinearity increasing profiles. On the other hand, Fig. 8 represents the comparison of compressed USPs for both dispersion and nonlinearity decreasing profiles. In Table 1, we compare the important physical parameters for quantifying the compression process, namely,

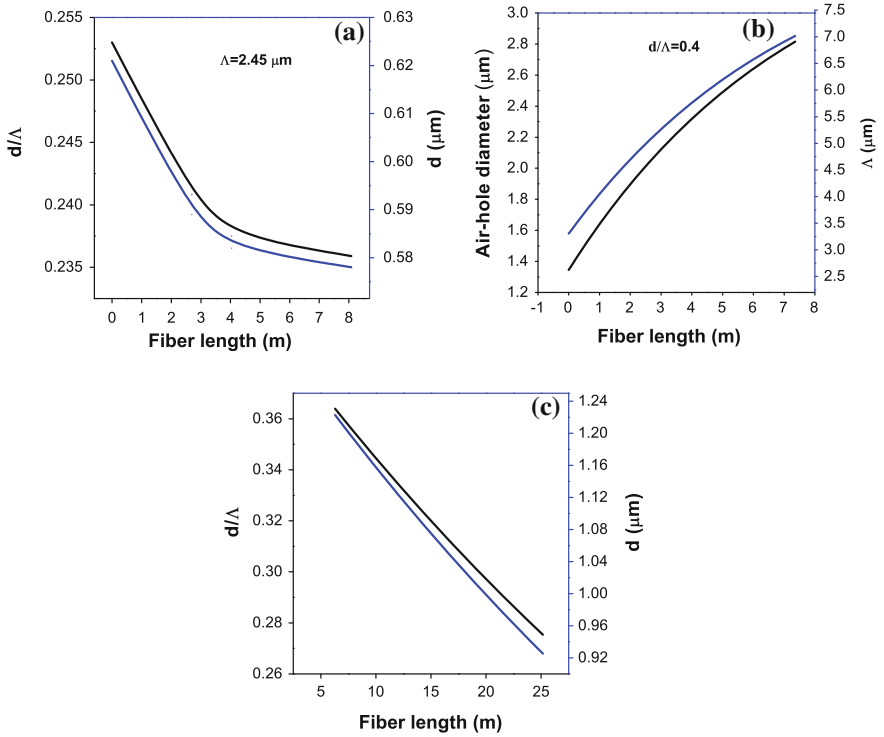

Fig. 5 **a** Variation of d/Λ and d along z of H-TPCF. **b** Variation of d and Λ along z of O-TPCF. **c** Variation of d/Λ and d along z of D-TPCF

compression factor and the percentage of compression. It is known that the pulse compression factor is the ratio of input to output pulse width. The compression percentage for dispersion decreasing and nonlinear increasing profiles of H-TPCF is 78 % which is almost 2 times greater than that of dispersion and nonlinear decreasing profiles of H-TPCF. At this juncture, it is mandatory to examine whether the resulting compressed pulse is free from pedestal. Here, we quantify the quality of the compressed pulses based on the amount of pedestal energy generated. The amount of pedestal energy is defined as the ratio between the total energy of the transmitted pulse and the energy of a hyperbolic secant pulse which has the same width and peak with that of the transmitted pulse [13]. That is, the pedestal energy $(\%) = (E_{total} - E_{sech})/E_{total} \times 100(\%)$ where, E_{total} and E_{sech} are energies of the pulse at initial and final fiber length. In general, the pedestal cannot be seen in the linear scale and hence we provide the compression scheme in the logarithmic scale as shown in Figs. 9 and 10. From these figures, it is very clear that the compressed pulses possess less pedestals in H-TPCF (0.36 %) than that of O-TPCF (7.1710 %)

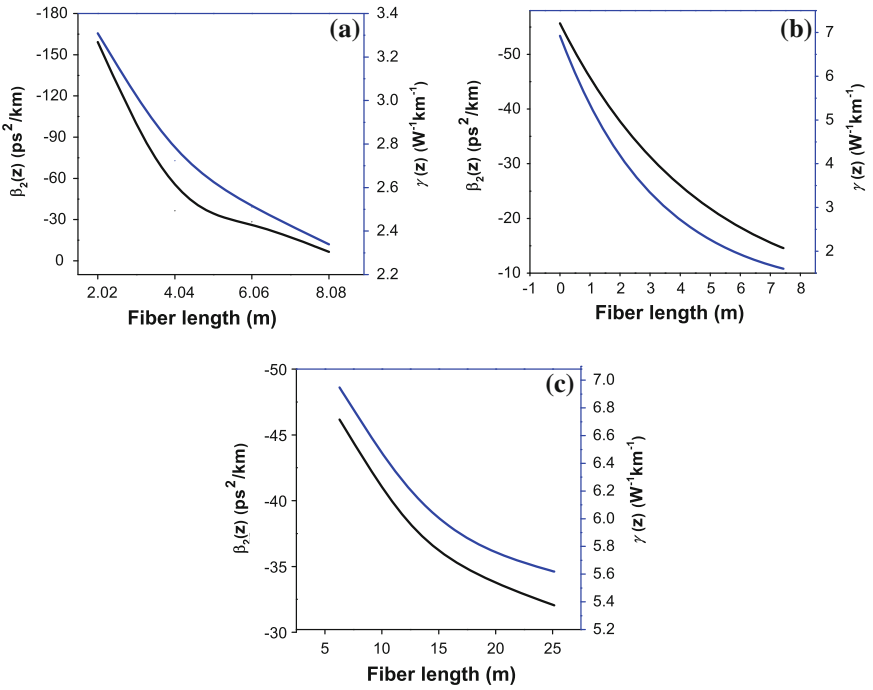

Fig. 6 Variation of GVD, $\beta_2(z)$, and nonlinearity, $\gamma(z)$, as a function of propagation distance, z **a** H-TPCF **b** O-TPCF and **c** D-TPCF

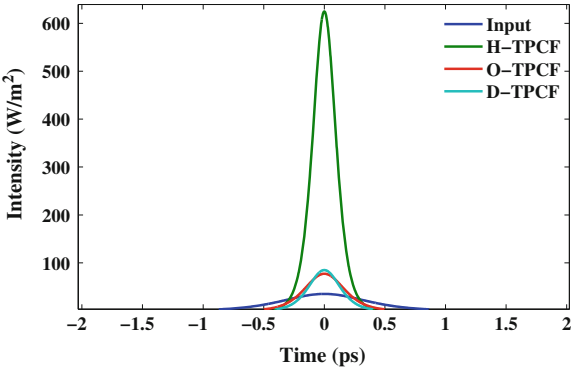

Fig. 7 Chirped input and compressed output pulses of H-TPCF, O-TPCF and D-TPCF

and D-TPCF (9.3385 %). Thus, based on the detailed analysis, we infer that one can achieve the compressed pulses without any significant amount of pedestals using dispersion decreasing and nonlinear increasing profiles of H-TPCF.

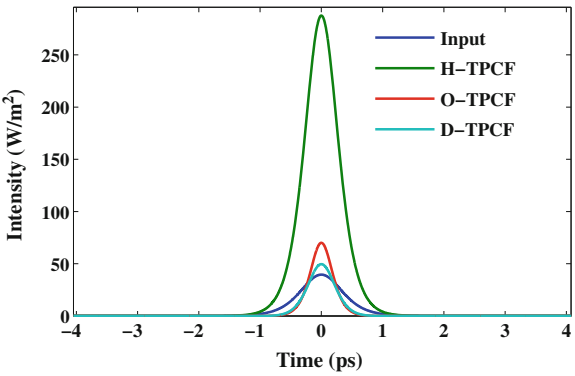

Fig. 8 Chirped input and compressed output pulses of H-TPCF, O-TPCF and D-TPCF

Table 1 Compression factor of self similar H-TPCF, O-TPCF and D-TPCF

Tapered PCF	Cases	Initial width (ps)	Final width (ps)	Compression factor	Compression %
Hexagonal	Case 1	0.8	0.178	4.5	78.3883
	Case 2	0.8	0.3636	2.2	52
Octagonal	Case 1	0.8	0.3800	2.1	52.4742
	Case 2	0.8	0.41025	2	48.90
Decagonal	Case 1	0.8	0.30021	2.7	62.4742
	Case 2	0.8	0.4622	1.7	42.2165

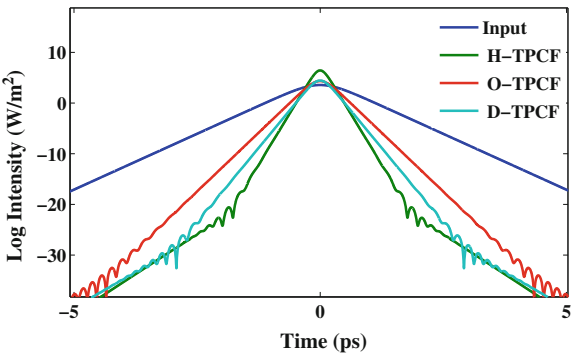

Fig. 9 Logarithmic scale of input and compressed pulses

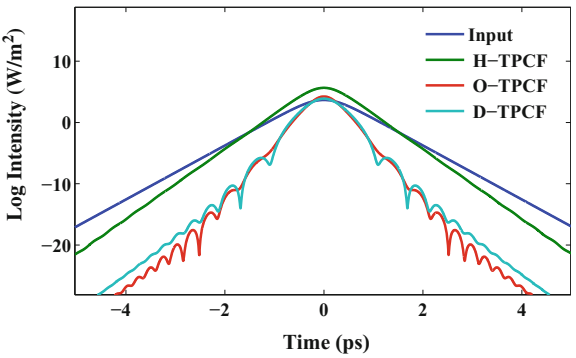

Fig. 10 Logarithmic scale of input and compressed pulses

5 A Comparative Study of Self-similar Pulse Stretching in Hexagonal, Octagonal and Decagonal Tapered PCFS

It is known that while the dispersion decreasing profile facilitates the compression of the laser pulses, the dispersion increasing profile supports the pulse broadening. Thus, in this section, we focus on the dispersion increasing profiles to design the pulse stretchers.

5.1 Design and Optical Properties

It has been shown that the chirped solitary wave does exist even for the following two cases: (i) Increasing GVD and decreasing nonlinearity (ii) Both GVD and nonlinearity increase. Based on the above self-similar conditions, one can design the various tapered PCFs (H-TPCF, O-TPCF and D-TPCF) for pulse stretching.

5.1.1 GVD Increases and Nonlinearity Decreases

For obtaining GVD increasing profile, we keep either pitch or the air hole diameter as a constant. The increasing GVD and decreasing nonlinearity profile of H-TPCF is designed by arbitrarily varying diameter of air hole and as well the pitch. Here, the relative air hole diameter is varied exponentially from 0.3 to 0.2804, the diameter of the air hole d is varied from 1.141 to 0.953 μm and the pitch is varied exponentially from 3.804 to 4 μm. Figure 11a–c shows the variation of design parameters, namely, relative air hole diameter and pitch with respect to propagation

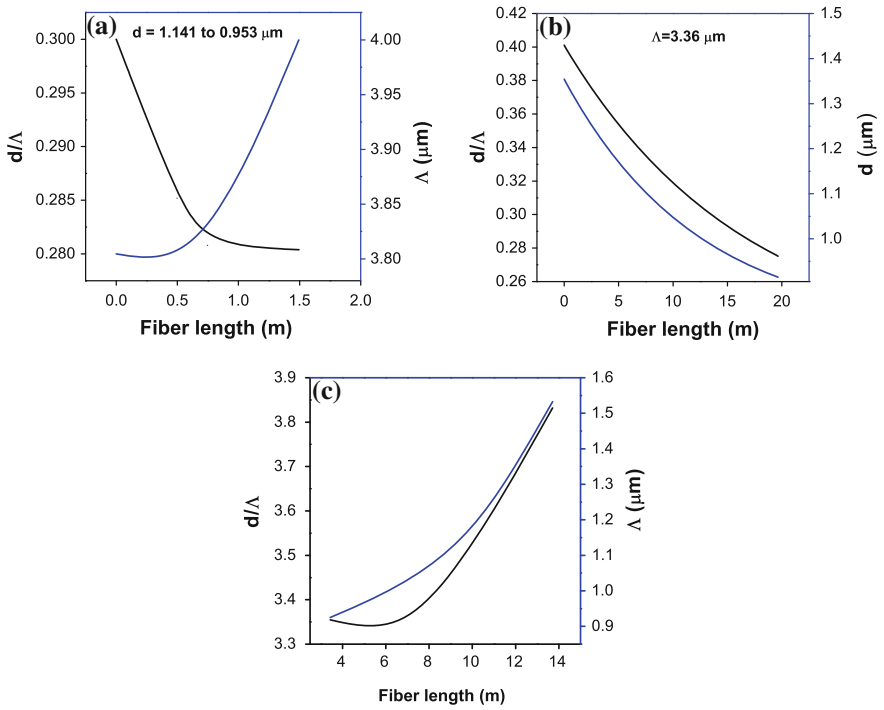

Fig. 11 **a** Variation of d/Λ and Λ along z of H-TPCF. **b** Variation of d/Λ and d along z of O-TPCF. **c** Variation of d/Λ and Λ along z of D-TPCF

distance. This tapered PCF is designed for a length of L(=4 L_D) where L_D = 373.413 m. We calculate the initial GVD as =−0.8616 ps^2/km and the cumulative dispersion β_2 at the end of the PCF is found to be to −15.8639 ps^2/km. The initial nonlinearity is 2.714 W^{-1} km^{-1}. In O-TPCF, the relative air hole diameter is varied from 0.39994 to 0.275 and the pitch is fixed as 3.3549 μm and the diameter of the air hole d is varied from 1.342 to 0.9637 μm. Here, the GVD increases from −20.9631 to −55.3713 ps^2/km. The nonlinearity in this tapered PCF decreases from 6.794 to 5.112636 W^{-1} km^{-1}. The D-TPCF is designed by decreasing the relative air hole diameter from 0.4 to 0.28707. The initial and final GVD are −42 and −27.7106 ps^2/km. The nonlinearity in this tapered PCF decreases from 6.7 to 5.4 W^{-1} km^{-1}. The variations of GVD and nonlinearity against distance are illustrated in Fig. 12a–c for various tapered PCFs.

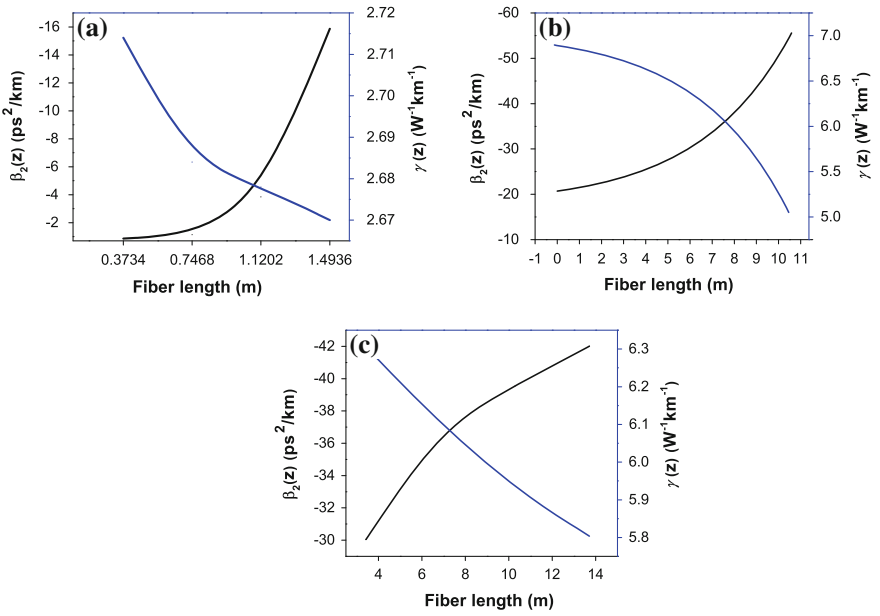

Fig. 12 Variation of GVD, $\beta_2(z)$, and nonlinearity, $\gamma(z)$, as a function of propagation distance, z **a** H-TPCF **b** O-TPCF and **c** D-TPCF

5.1.2 Both GVD and Nonlinearity Increase

Now we design the hexagonal, octagonal and decagonal tapered PCFs to get both increasing dispersion and nonlinear profiles. In H-TPCF, we decrease the diameter of the air hole and keep the pitch as a constant. Here, the relative air hole diameter is varied exponentially from 0.2530 to 0.2346, the diameter of the air holes is varied from 0.62 to 0.575 μm and the pitch is fixed as 2.45 μm. Figures 13a–c and 14a–c depict the variations of design parameters and calculated optical properties against the propagation distance. In O-TPCF, we reduce the diameter of air hole without varying the pitch. We choose a PCF of length 7.44 m as in the previous case. The relative air hole diameter is kept at 0.4 and the diameter of the air holes is varied from 1.342 to 2.8 μm and the pitch is kept at 3.35 μm. For this case, D-TPCF is designed by decreasing the relative air hole diameter from 0.363 to 0.2768 and the diameter of the air holes is varied from 1.22 to 0.93 μm. Further, the pitch is kept at 3.36 μm.

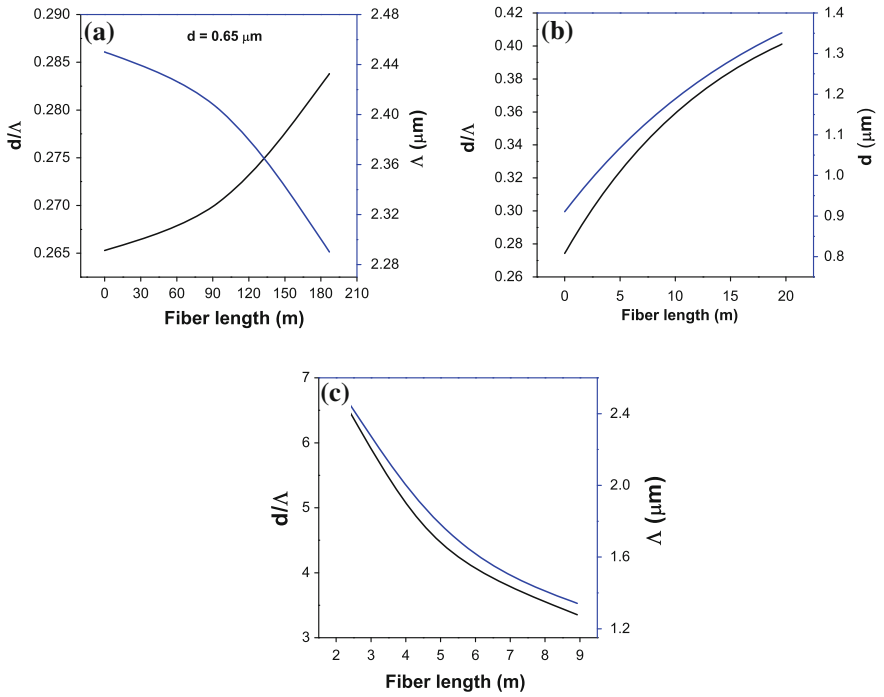

Fig. 13 **a** Variation of d/Λ and Λ along z of H-TPCF. **b** Variation of d/Λ and d along z of O-TPCF. **c** Variation of d/Λ and Λ along z of D-TPCF

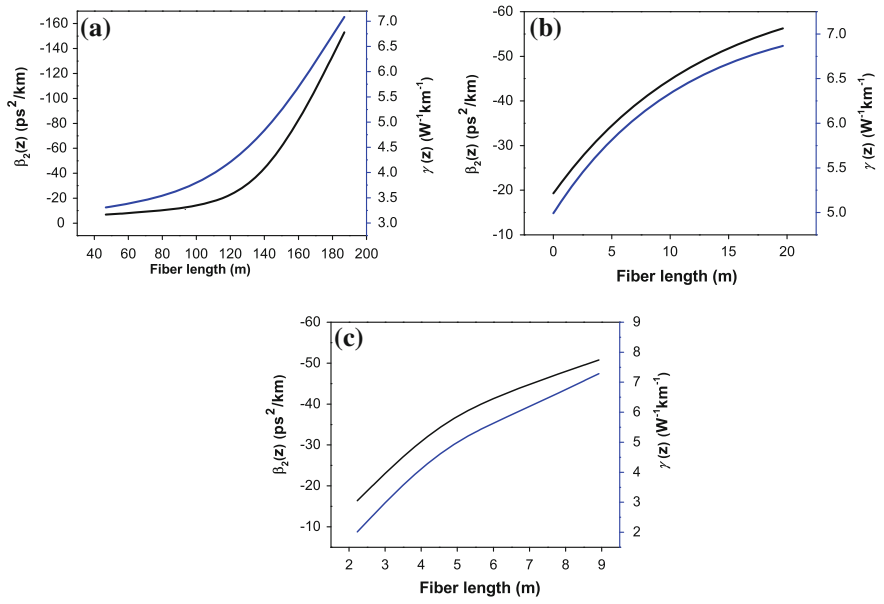

Fig. 14 Variation of GVD, $\beta_2(z)$, and nonlinearity, $\gamma(z)$, as a function of propagation distance, z **a** H-TPCF **b** O-TPCF and **c** D-TPCF

5.2 A Comparison on Self-similar Pulse Stretching

Figure 15 depicts the comparison of stretched pulses obtained from H-TPCF, O-TPCF and D-TPCF for dispersion increasing and nonlinearity decreasing profiles. On the other hand, the comparison of stretched pulses is represented in Fig. 16 for both dispersion and nonlinearity increasing profiles. In Table 2, we compare

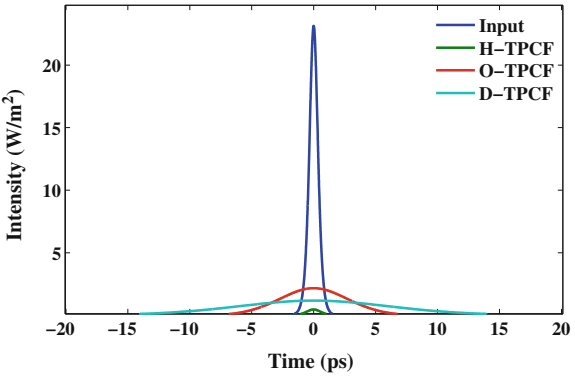

Fig. 15 Chirped input and stretched output pulses of H-TPCF, O-TPCF AND D-TPCF

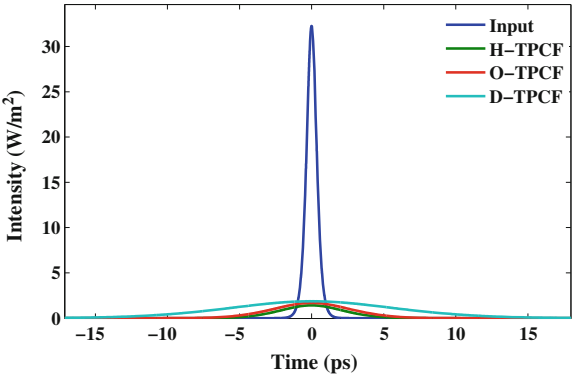

Fig. 16 Chirped input and stretched output pulses of H-TPCF, O-TPCF AND D-TPCF

Table 2 Self similar tapered PCFs-stretching factor

Tapered PCF	Cases	Initial width (ps)	Final width (ps)	Stretching factor	Stretching %
Hexagonal	Case 1	0.8	1.403	0.57	76
	Case 2	0.8	1.4953	0.535	87
Octagonal	Case 2	0.8	5.3428	0.4197	85.0266
	Case 3	0.8	5.200	0.1538	84.7620
Decagonal	Case 1	0.8	12.458	0.0642	93.5786
	Case 2	0.8	11.5571	0.0692	93.0774

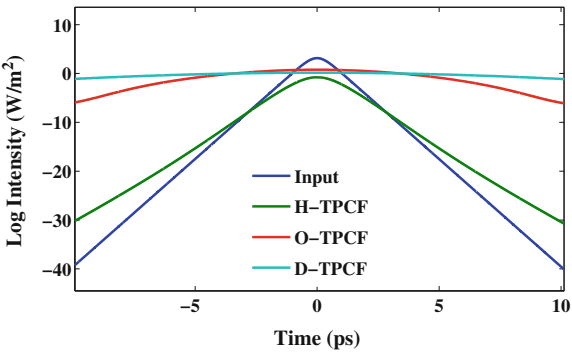

Fig. 17 Logarithmic scale of chirped input and output stretched pulses of H-TPCF, O-TPCF and D-TPCF

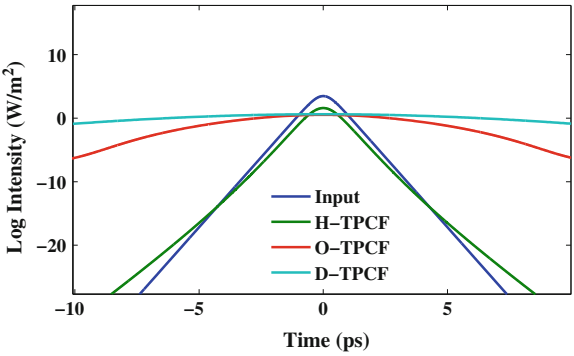

Fig. 18 Logarithmic scale of chirped input and output stretched pulses of H-TPCF, O-TPCF and D-TPCF

stretching factor as well in stretching percentage for the above mentioned tapered PCFs. Pulse stretching factor is the ratio of input to output pulse width. The stretching percentage for dispersion increasing and nonlinearity decreasing profiles of D-TPCF is 93.5786 % which is greater than that of dispersion and nonlinearity increasing profiles of O-TPCF. Figures 17 and 18 represent the stretched pulses in terms of logarithmic scale for H-TPCF, O-TPCF and D-TPCF. The pedestal energy is lesser in D-TPCF (8.5350 %) than that of O-TPCF (17.8443 %) and H-TPCF (77.5415 %). Thus, we find that the D-TPCF of dispersion increasing and nonlinearity decreasing profiles provides high stretching ratio when compared to other types of tapered PCFs.

6 Conclusion

In this work, based on the self-similar condition for the generation of chirped solitary pulses, we have designed the exponentially varying dispersion and nonlinear profiles of various tapered PCFs, namely, H-TPCF, O-TPCF and D-TPCF.

Then, we have successfully generated the self-similar ultrashort pulses and stretched pulses by exploiting the optical properties of the above mentioned tapered PCFs. Thus, we have explored the pulse compression studies for the exponentially decreasing dispersion and nonlinear increasing/decreasing profiles of various tapered PCFs. Based on the numerical results, we infer that we have been able to generate USPs with the maximum compression factor and minimum pedestal energy for the dispersion decreasing profiles of H-TPCF. In addition, we have also carried out the pulse stretching for the exponentially increasing dispersion and nonlinear decreasing/increasing profiles. It has been found that stretched pulses with maximum stretching percentage with minimum pedestal energy could be generated with the dispersion increasing and nonlinear increasing profiles of D-TPCF.

References

1. Agrawal, G.P.: Application of Nonlinear Fiber Optics, 2nd edn. Academic Press, New York (2001)
2. Holzwarth, R., Udem, T., Hansch, T.W., Knight, J.C., Wadsworth, W.J., Russell, P.S.J.: Optical frequency synthesizer for precision spectroscopy. Phys. Rev. Lett. **85**(11), 2264–2267 (2000)
3. Valdmanis, J., Mourou, G.: Sub-picosecond electrooptic sampling: principles and applications. IEEE J. Quantum Electron. **22**(1), 69–78 (1986)
4. Fu, L., Fuerbach, A., Littler, I.C.M., Eggleton, B.J.: Efficient optical pulse compression using chalcogenide single-mode fibers. Appl. Phys. Lett. **88**(8), 081116 (2006)
5. Mollenauer, L.F., Stolen, R.H., Gordon, J.P.: Experimental observation of picosecond pulse narrowing and solitons in optical fibers. Phys. Rev. Lett. **45**(13), 1095–1098 (1980)
6. Chan, K.C., Liu, H.F.: Short pulse generation by higher order soliton-effect compression: effects of optical fiber characteristics. IEEE J. Quantum Electron. **31**(12), 2226–2235 (1995)
7. Kruglov, V.I., Peacock, A.C., Harvey, J.D.: Exact self-similar solutions of the generalized nonlinear Schrödinger equation with distributed coefficients. Phys. Rev. Lett. **90**(11), 113902 (2003)
8. Raja, R.V.J., Senthilnathan, K., Porsezian, K., Nakkeeran, K.: Efficient pulse compression using tapered photonic crystal fiber at 850 nm. IEEE J. Quantum Electron. **46**(12), 1795–1802 (2010)
9. Olupitan, S., Senthilnathan, K., Ramesh Babu, P., Aphale, S.S., Nakkeeran, K.: Generation of a train of ultrashort pulses at near infrared regime in a tapered PCF using raised-cosine pulses. IEEE Photonics J. **4**(5), 1420–1437 (2012)
10. Sivbalan, S., Raina, J.P.: High normal dispersion and Large mode area phonic quasi-crystal fiber stretcher. IEEE Photonics Tech. Lett. **23**(16), 1139–1141 (2011)
11. Manimegalai, A., Senthilnathan, K., Nakkeeran, K., Ramesh Babu, P.: Tapering photonic crystal fibers for generating self-similar pulses at 1550 nm. Opt. Eng. **55**, 067108-07 (2016)
12. Moores, J.D.: Nonlinear compression of chirped solitary waves with and without phase modulation. Opt. Lett. **21**(8), 555557 (1996)
13. Knight, J.C., Birks, T.A., Russell, P.S.J., Martin, D.M.: All silica single mode optical fiber with photonic crystal cladding. Opt. Lett. **21**, 1459–1547 (1996)
14. Tse, M.L.V., Horak, P., Poletti, F., Richardson, D.J.: Designing tapered holey fibers for soliton compression. IEEE J. Quantum Electron. **44**, 192–198 (2008)
15. Comsol Multiphysics 3.4. (2008) [Online]. Available www.comsol.com

Structural, Dielectric and Gas Sensing Properties of Mn-Ni Ferrite Nanoparticles

P. Bala Sundari, E. Ranjith Kumar, S. Ramya and A.S. Kamzin

Abstract $Mn_{0.4}Ni_{0.6}Fe_2O_4$ nanoparticles synthesized by evaporation and auto-combustion methods were studied. The structural properties of prepared and annealed samples were analyzed by X-ray diffraction (XRD). The annealing temperature played a major role in the structural and phase composition, which indicates that the annealed sample contains some secondary phase. The microstructure and particle size of the annealed samples were analyzed by TEM. The dielectric properties were measured using impedance analyzer in the frequency range 1–5 MHz. The effect of particle size with the impact of annealing temperature on the dielectric properties is also analyzed. The prepared nanoparticles were subjected to the gas sensor measurement for different aspects. Liquefied petroleum gas sensing investigations of the prepared samples demonstrate that the sample prepared by auto combustion method possesses an improved response than the sample prepared by evaporation method.

1 Introduction

Metal-oxide nanoparticles have been subject of much interest because of their structural, electronic and magnetic properties. LPG sensor has become the recent topic of research in view of industrial applications, because of its inflammable nature, which presents many hazards to human being as well as environment. By the prominent goodness of magnetic and semiconducting properties, the ferrites have been widely used in the electronics industry. In the present research, we have been interested in carrying out our investigations with different materials that

P. Bala Sundari · E. Ranjith Kumar (✉) · S. Ramya
Department of Physics, Dr.N.G.P. Institute of Technology,
Coimbatore 641048, Tamil Nadu, India
e-mail: ranjueaswar@gmail.com

A.S. Kamzin
Ioffe Physical-Technical Institute, Russian Academy of Sciences,
St. Petersburg 194021, Russia

J. Ebenezar (ed.), *Recent Trends in Materials Science and Applications*,
Springer Proceedings in Physics 189, DOI 10.1007/978-3-319-44890-9_13

possess better responses that our previous work. The gas sensing properties of the ferrites are dependent on its chemical composition and nanostructural characteristics, which can be controlled in the synthesis and fabrication processes. For the gas sensing studies, there is a need for developing synthesis and production processes that are quite simple and yield controlled particle sizes. Spinel ferrite nanoparticles have been prepared by various methods such as sol-gel auto combustion method [1], evaporation method [2], microwave-induced combustion method [3], co-precipitation [4], sol-gel [5], and reverse micelle reaction process [6]. In this paper, auto combustion and simple evaporation methods were adapted to synthesis Mn-$NiFe_2O_4$ nanoparticles and their structural and dielectric properties are also analyzed [7–9]. Details of the obtained data and their results of the prepared and heated samples are presented below.

2 Experimental Method

2.1 Evaporation Method

In this simple evaporation method, manganese nitrate with 99.7 % purity, nickel nitrate with 99.8 % purity ferric nitrate with 99.8 % purity and freshly extracted egg white were used to prepare Mn-Ni ferrite nanoparticles with stoichiometry ratio [10]. Subsequently, 0.4 M of manganese nitrate, 0.6 M of nickel nitrate and 2 M of ferric nitrate were dissolved in deionized distilled water and added slowly to the egg white solution with vigorous stirring at 80 °C to obtain a well-dissolved solution. A dried precursor was obtained from the solution after heating the solution at 100 °C. The final precursor was annealed at different temperature.

2.2 Auto Combustion Method

An auto combustion method also used to prepare manganese nickel ferrite nanoparticles. The same chemicals were used to prepare Mn-Ni ferrite nanoparticles, but instead egg white here we used Urea for combustion process [10]. Subsequently, 0.4 M of manganese nitrate, 0.6 M of nickel nitrate, 2 M of ferric nitrate and urea were dissolved and mixed in deionized water. Then the mixed solution was heated at 160 °C to dehydrate until self-ignition took place. Being ignited in air at room temperature, the dried gel burnt in a self propagating combustion, giving rise to the evolution of a large amount of gases and producing a dry and loose ferrite powder. The obtained sample was annealed at 600 and 900 °C for 5 h.

2.3 Equipment Used for Characterization

The structural properties of the samples were recorded by using Rigaku X-ray diffraction unit. Technai G20-stwin model High resolution transmission electron microscopy (HRTEM) has been used to calculate particles size of the samples. Digital LCR meter is used to measure the dielectric constant and loss of the samples in the frequency range from 100 kHz to 5 MHz. The gas sensing behavior of the samples is also studied. The sensor response set-up is shown in Fig. 1. The detailed procedure of the gas sensing measurement is already reported in our previous report [11].

3 Results and Discussion

3.1 Structural Analysis

Figures 2a and 3a depicts the XRD pattern of $MnNiFe_2O_4$ synthesized under two different preparation methods. The spacing between different peaks is indicating that the prepared samples of Mn-Ni ferrites have no secondary impurity phase. Due to the decomposition after annealing at 600 °C few impurity peaks are presented, which are due to the α-Fe_2O_3 phase [12, 13]. These secondary peaks are slowly dissolved at higher annealing temperature. The lattice parameter (a) and crystalline size (t) are calculated by using formulas which are reported in our recent report [14]. The variations in these crystal parameters for different samples are listed in Table 1. Particle size and microstructure of the sample annealed at 900 °C samples of Mn-$NiFe_2O_4$ nanoparticles synthesized by two different methods (Evaporation and Auto combustion) were recorded transmission electron microscope (TEM) are shown in Figs. 2b and 3b. It clearly indicates that the annealed samples are almost spherical in shape. The size of the particles calculated by TEM is well matched with

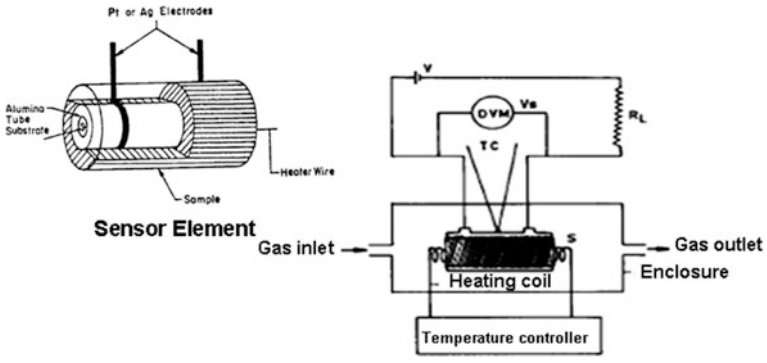

Fig. 1 Gas sensor measurement set-up

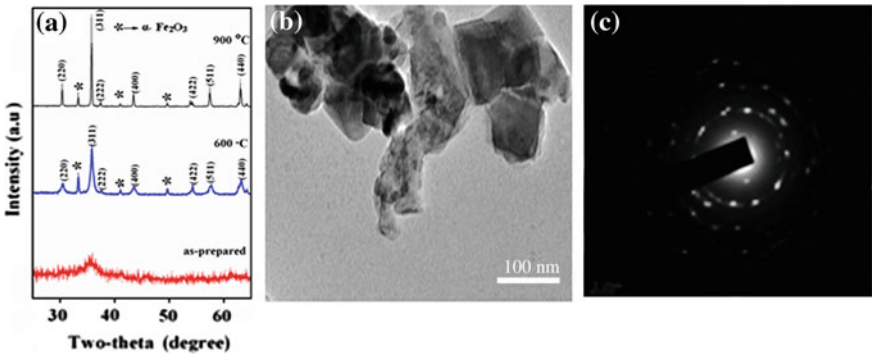

Fig. 2 The **a** XRD, **b** TEM and **c** SAED patterns for $MnNiFe_2O_4$ nanoparticles prepared by evaporation method

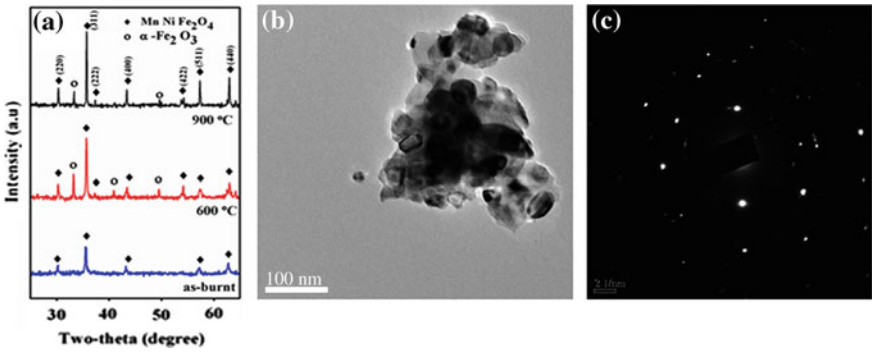

Fig. 3 The **a** XRD, **b** TEM and **c** SAED patterns for $MnNiFe_2O_4$ nanoparticles prepared by auto combustion method

the XRD measurement (see Table 1). The SAED pattern of annealed (900 °C) Mn-$NiFe_2O_4$ nanoparticles was shown in the Figs. 2c and 3c. The polycrystalline nature of the samples was clearly identified by the bright spots.

3.2 Dielectric Properties

Figures 4a, b and 5a, b shows variations in dielectric parameters of $MnNiFe_2O_4$ nanoparticles synthesized by evaporation and auto combustion methods were studied in the frequency range of 100 kHz–5 MHz by Digital LCR meter. The obtained results clearly show the nature of the dielectric materials. The dielectric properties slowly varied at lower frequency region and stay behind at higher order frequencies. The results show that the dielectric properties of the samples are more

Table 1 Crystal parameters of Mn substituted $NiFe_2O_4$ nanoparticles

Parameters	Evaporation method			Auto combustion method		
	As prepared	600 °C	900 °C	As-burnt	600 °C	900 °C
Particle size (t) nm	–	48	98	25	55	62
Lattice constant (a) Å	–	8.46	8.44	8.44	8.45	8.47

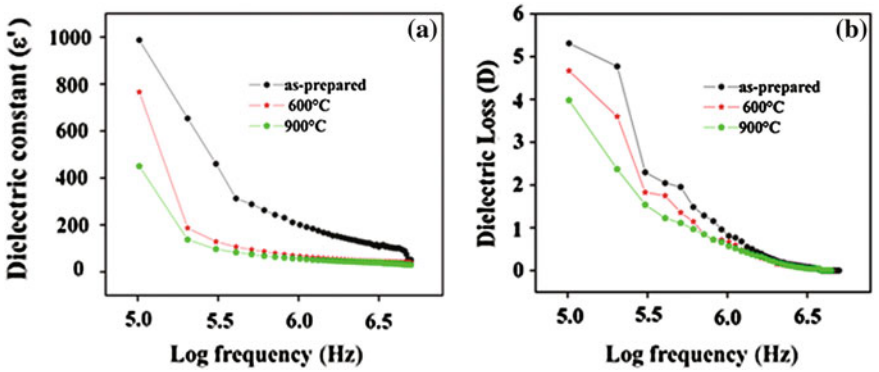

Fig. 4 Variation of **a** dielectric constant and **b** dielectric loss with respect to log frequency of $MnNiFe_2O_4$ nanoparticles prepared by evaporation method

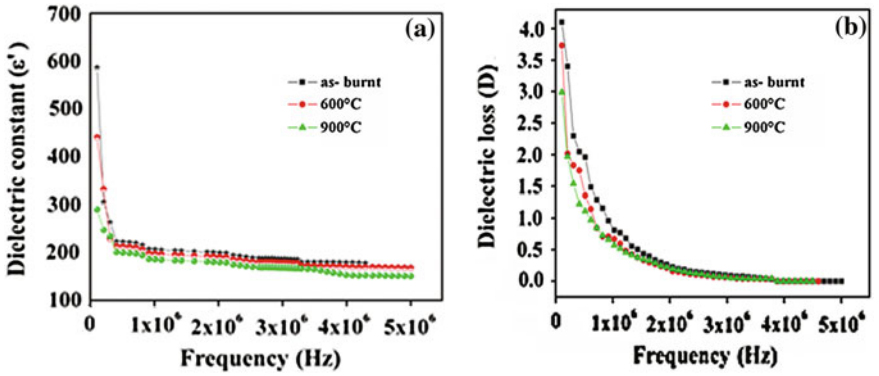

Fig. 5 Variation of **a** dielectric constant and **b** dielectric loss with respect to log frequency of $MnNiFe_2O_4$ nanoparticles prepared by auto combustion method

influenced by particle size with impact of annealing temperature [13]. The space charge polarization is an important factor to decide the dielectric properties. The nanocrystalline material gets accumulated at the grain boundaries resulting in the formation of dipole moment. This dipole moment will easily respond to the AC

electric field, at low frequencies. At higher frequencies the dielectric constant reaches a constant value due to electronic polarization. The dielectric loss slowly decreased by increasing the frequency as well as annealing temperature due to the variation of particles size. The variation of dielectric constant and loss under these conditions clearly indicates the common performance of ferrite samples. In dielectric materials, absorption current is an important parameter for dielectric losses occurrence. Amount of electric energy is required to arrange the molecules along the applied field direction in polar dielectrics. The remaining part of electric energy is used to transfer a molecule from one point to another point and also to rotate of dipolar molecules. Defects, inhomogeneity, space charge formation etc. are some of the factors to produce absorption current [15, 16].

3.3 Gas Sensors Properties

The gas sensing response of the synthesized samples of $MnNiFe_2O_4$ nanoparticles by auto-combustion and evaporation methods is shown in Fig. 6 [17]. Sensing

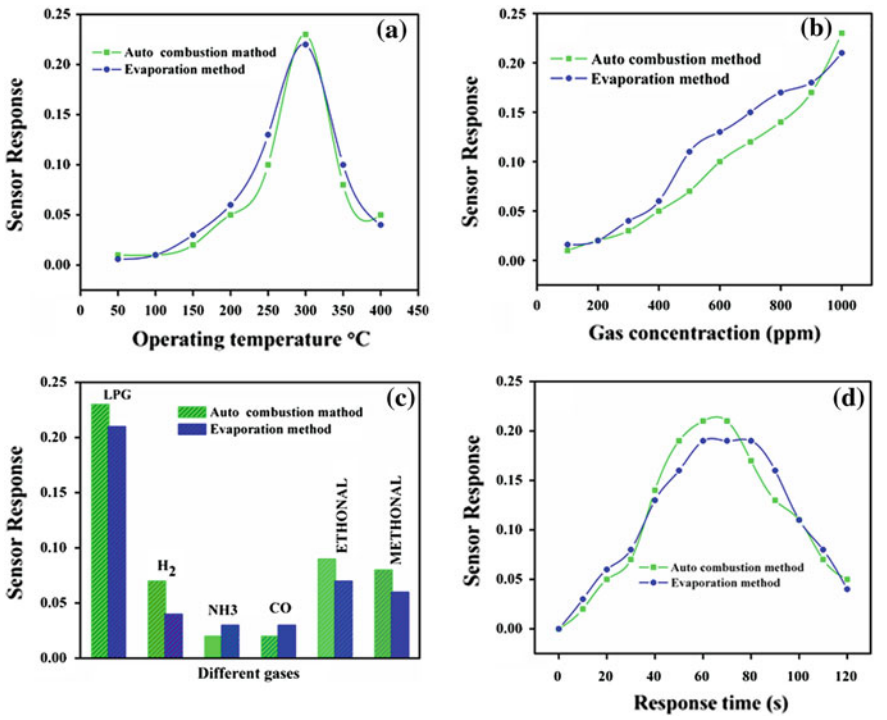

Fig. 6 Gas sensing response of $MnNiFe_2O_4$ nanoparticles: **a** Effect of operating temperature on gas sensing response at 1000 ppm LPG gas, **b** Effect of different concentration of LPG gas on sensing response, **c** Sensor Response to 1000 ppm of different gases at 300 °C and **d** Sensor response as a function of response-recovery time to 1000 ppm LPG gas at 300 °C

response of these samples with respect to operating temperature towards 1000 ppm of LPG gas is shown in Fig. 6a. The sensing ability of $MnNiFe_2O_4$ reaches a maximum value at 300 °C. The sensing behavior of the sample synthesized by auto combustion method is better than the evaporation method which is clearly identified by the response curves shown in Fig. 6a. The operating temperature should be optimized to produce high sensitive $MnNiFe_2O_4$ sensor element to the target gas.

The sensing ability for different gas concentrations of LPG at 300 °C for these samples prepared by two methods is shown in Fig. 6b. As mentioned behavior on sensing response in previous section is observed that it increases with increase in gas concentration and reaches a maximum at 1000 ppm. This similar behavior is identified for both samples, but the sensing response (S) of auto combustion method sample is 0.23, which is higher than evaporation method sample. Figure 6c shows the sensing behavior for different gases to 1000 ppm gas at 300 °C. The selectivity is an important parameter to identify the best performance of $MnNiFe_2O_4$ sensor by the presence of few testing gases. $MnNiFe_2O_4$ sensor shows significant sensing performance to LPG than the other test gases. According to the experimental results, $MnNiFe_2O_4$ sensor can highly detect LPG in occurrence of other gases. Figure 6c clearly identified that the auto combustion method influence more in the sensing response for LPG.

Similarly, the sensing response of $MnNiFe_2O_4$ of remaining as mentioned gases such as NH_3, CO, ethanol and methanol shows 0.07 and 0.04 for H_2, 0.03 and 0.02 for NH_3 gas, 0.03 and 0.02 for CO gas, 0.08 and 0.06 for ethanol and 0.07 and 0.05 for methanol gas. The sensor shows the highest response to LPG as 0.23 and 0.21 for auto-combustion method and evaporation method respectively. Response and recovery times are the important parameters of gas sensors, which are defined as the time taken to reach 90 % of the final signal. The $MnNiFe_2O_4$ sensor exhibited short response and recovery time, of 20 (S) respectively at 300 °C for 1000 ppm LPG for auto combustion method sample and 30 (S) for evaporation method sample as shown in Fig. 6d. Thus this material is also revealed that the auto combustion method sample is well supported for quick response than the sample prepared by evaporation method.

4 Conclusion

$MnNiFe_2O_4$ nanoparticles were synthesized by two different chemical methods. The XRD pattern confirms that the prepared samples have normal spinel structure. The influence of annealing on size variation in the samples was identified from the XRD. The size of the particle calculated from the TEM analysis had shown uniformity with XRD and the SAED pattern shows that the prepared samples are polycrystalline in nature. The role of annealing on dielectric behavior of

$MnNiFe_2O_4$ nanoparticles reveals that the prepared samples are behaving as a normal ferrite material. The sensor based studies shows that the $MnNiFe_2O_4$ nanoparticles synthesized by auto combustion method has good sensor response and selectively detects LPG.

References

1. Raut, A.V., Barkule, R.S., Shengule, D.R., Jadhav, K.M.: Synthesis, structural investigation and magnetic properties of Zn^{2+} substituted cobalt ferrite nanoparticles prepared by the sol–gel auto-combustion technique. J. Magn. Magn. Mater. **358–359**, 87–92 (2014)
2. RanjithKumar, E., Jayaprakash, R., SanjayKumar.: The role of annealing temperature and bio template (egg white) on the structural, morphological and magnetic properties of manganese substituted MFe_2O_4 (M=Zn, Cu, Ni, Co) nanoparticles. J. Magn. Magn. Mater. **351,** 70–75 (2014)
3. Elshahawy, A.M., Mahmoud, M.H., Makhlouf, Salah A., Hamdeh, H.H.: Role of Cu^{2+} substitution on the structural and magnetic properties of Ni-ferrite nanoparticles synthesized by the microwave-combustion method. Ceram. Int. **41**, 11264–11271 (2015)
4. Kumar, A., Yadav, N., Rana, D.S., Kumar, P., Arora, M., Pant, R.P.: Structural and magnetic studies of the nickel doped $CoFe_2O_4$ ferrite nanoparticles synthesized by the chemical co-precipitation method. J. Magn. Magn. Mater. **394**, 379–384 (2015)
5. Singh, S., Yadav, B.C., Prakash, R., Bajaj, B.: Synthesis of nanorods and mixed shaped copper ferrite and their applications as liquefied petroleum gas sensor. Appl. Surf. Sci **257**, 10763–10770 (2011)
6. Penchal Reddy, M., Madhuri, W., Ramamanoher Reddy, N., Siva Kumar, K.V., Murthy, V.R. K., Ramakrishna Reddy, R.: Influence of copper substitution on magnetic and electrical properties of MgCuZn ferrite prepared by microwave sintering method. Mater. Sci. Eng. C **30**, 1094–1099 (2010)
7. Ranjith Kumar, E., Jayaprakash, R., Patel, R.: Structural and morphological studies of manganese substituted $CoFe_2O_4$ and NiFe2O4 nanoparticles. Super. Microstruct. **62**, 277–284 (2013)
8. Ranjith Kumar, E., Jayaprakash, R., Chandarasekaran, J.: Effect of fuel ratio and the impact of annealing temperature on particle size, magnetic and dielectric properties of manganese substituted $CuFe_2O_4$ nanoparticles. Super. Microstruct. **64**, 343–353 (2013)
9. Ranjith Kumar, E., Jayaprakash, R., Prakash, T.: The effect of annealing on phase evolution, microstructure and magnetic properties of Mn substituted $CoFe_2O_4$ nanoparticles. J. Magn. Magn. Mater. **358–359**, 123–127 (2014)
10. Ranjith Kumar, E., Jayaprakash, R.: Effect of annealing temperature on structural and magnetic properties of manganese substituted $NiFe_2O_4$ nanoparticles. Mater Sci Semi. Proc. **17**, 173–177 (2014)
11. Ranjith Kumar, E., Jayaprakash, R., Sarala Devi, G., Siva Prasada Reddy, P.: Magnetic, dielectric and sensing properties of manganese substituted copper ferrite nanoparticles. J. Magn. Magn. Mater, **351**, 70–75 (2014)
12. Hu, P., Yang, H., Pan, D., Wang, H., Tian, J., Zhang, S., Wang, X., Volinsky, A.A.: Heat treatment effects on microstructure and magnetic properties of Mn–Zn ferrite powders. J. Magn. Magn. Mater. **322**, 173–177 (2010)
13. Ranjith Kumar, E., Jayaprakash, R., Seehra, M.S., Prakash, T., Kumar, S.: Effect of α-Fe_2O_3 phase on structural, magnetic and dielectric properties of Mn-Zn ferrite nanoparticles. J. Phys. Chem. Solids **74**, 943–949 (2013)

14. Ranjith Kumar, E., Arunkumar, T., Prakash, T.: Heat treatment effects on Structural and dielectric properties of Mn substituted $CuFe_2O_4$ and $ZnFe_2O_4$ nanoparticles prepared by auto-combustion method. Super Microstruct. **85**, 530–535 (2015)
15. Koops, C.G.: On the Dispersion of Resistivity and Dielectric Constant of Some Semiconductors at Audiofrequencies. Phys. Rev. **83**, 121 (1951)
16. Jose, M., Sumithra, V., Rajan, S., Kumar, P.: Dielectric properties of nanocrystalline ZnS. Acad. Rev. **XVII**(No. 1 & 2 SB), 93–100 (2010). ISSN: 0973-7464
17. Ranjith Kumar, E., Siva Prasada Reddy, P., Sarala Devi, G., Sathiyaraj, S.: Structural and Gas Sensing properties of Mn Substituted $ZnFe_2O_4$ Nanoparticles by Auto combustion and evaporation method. J. Magn. Magn. Mater. **398**, 281–288 (2014)

Synthesis and Characterization of Cobalt Ferrite ($CoFe_2O_4$) Nanoparticles Prepared by Hydrothermal Method

Suresh Sagadevan, Jiban Podder and Isha Das

Abstract Hydrothermal method was employed for the synthesis of Cobalt ferrite ($CoFe_2O_4$) nanoparticles. The crystallinity, morphological and optical properties of the $CoFe_2O_4$ nanoparticles were studied by using X-ray diffraction (XRD), Scanning Electron Microscopy (SEM), Transmission Electron Microscopy (TEM), FT-IR, and dielectric analyses. The grain size and crystal structure of the $CoFe_2O_4$ was confirmed by XRD. SEM and TEM analyses showed that the synthesized samples had particles of the size of nanometers. The $CoFe_2O_4$ nanoparticles dielectric properties were analyzed at different frequencies and temperatures such as the dielectric constant, the dielectric loss, and AC conductivity.

1 Introduction

Nowadays metal-oxide nanoparticles gaining attention as study subject because of their significant properties such as optical, magnetic and electronic, which over and over again differ from those of the bulk. Ferrite nanoparticles have appealed a lot of interest of the research community because of their wide area of applications such as magnetic recording, catalysis and biotechnology [1–3]. Among ferrites, Cobalt ferrite is specifically interesting owing to its magnetic properties like moderate saturation magnetization, strong anisotropy, high coercivity at room temperature

S. Sagadevan (✉)
Department of Physics, AMET University, Chennai, India
e-mail: sureshsagadevan@gmail.com

J. Podder
Department of Chemical and Biological Engineering,
University of Saskatchewan, Saskatoon, SK S7N 5A9, Canada

I. Das
Department of ECE, AMET University, Chennai, India

J. Ebenezar (ed.), *Recent Trends in Materials Science and Applications*,
Springer Proceedings in Physics 189, DOI 10.1007/978-3-319-44890-9_14

and it possesses photo-magnetic material [4]. Its properties depend on the techniques involved in the synthesis. The composition and the size of magnetic nanoparticles influence the biological application [5]. When compared to bulk material, the size reductions of magnetic material outcomes in novel properties like super-paramagnetism due to small volume [6]. Cobalt ferrites nanoparticles are being the subject of interest for research because of their encouraging and effective applications in biomedical industries. In this process cobalt ferrites nanoparticles crystallize into inverse spinel structure, in which divalent Co^{2+} ions are positioned octahedrally. At the same time one half of the Fe^{3+} ions are placed at the tetrahedral sites with the other half being placed at the octahedral sites. Hence, different experimental methods such as co-precipitation method, sol–gel techniques, microwave sintering method, hydrothermal method, spray-spin-heating-coating method and sonochemical method have been used in the ferrite nanoparticles synthesis [7–12]. In the present study, hydrothermal method was employed to prepare the Cobalt ferrite ($CoFe_2O_4$) nanoparticles. The structural, spectral, optical, and electrical properties of the Cobalt ferrite ($CoFe_2O_4$) nanoparticles were determined accurately using XRD, FT-IR spectroscopy, SEM, TEM, and Dielectric measurements.

2 Experimental Synthesis

Typical synthetic procedures required analytical grade, in which 2.5 g cobalt nitrate was dissolved in 50 ml of ethylene glycol ($C_2H_6O_2$) at 50 °C and ferric nitrate 0.6 g was dissolved in 50 ml of water. Both solutions were mixed together and further 10 ml of Ethylene Glycolic acid (EG) was added drop by drop to the above solution with continuous stirring. To make stable sol, the solution was vigorously stirred using a magnetic stirrer at the same temperature for 40 min. The prepared EG mixed solution was transferred to Teflon coated autoclave and heat treated in the furnace at 300 °C for 5 h. After the hydrothermal reaction time the autoclave was cooled at room temperature. Finally a dark powder was obtained. The XRD patterns of the Cobalt ferrite ($CoFe_2O_4$) nanoparticles were observed by using a powder X-ray diffractometer (Schimadzu model: XRD 6000) using CuK_α radiation, with a diffraction angle between 20° and 70°. Scanning Electron Microscopy (SEM) studies were carried out on JEOL, JSM- 67001. Image of Transmission Electron Microscope (TEM) was taken using H-800 TEM (Hitachi, Japan) with an accelerating voltage of 100 kV. The FTIR spectrum of the $CoFe_2O_4$ nanoparticles was taken using an FTIR model Bruker IFS 66 W Spectrometer. The dielectric properties of the $CoFe_2O_4$ were analyzed over the frequency range 50 Hz–5 MHz using a HIOKI 3532-50 LCR HITESTER.

3 Results and Discussion

3.1 Structural Characterization

The XRD patterns of the $CoFe_2O_4$ powders are shown in Fig. 1. All the diffraction peaks were indexed to the cubic structure of cobalt ferrite without other crystalline impurity peaks. All peaks obtained by XRD analysis were assigned by comparison with data obtained from the Joint Committee on powder Diffraction Standards (JCPDS).The Scherrer formula was used to calculate average grain size (D), given as

$$D = \frac{0.9\lambda}{\beta \cos\theta} \tag{1}$$

where λ is the X-ray wavelength (CuK_α radiation and equals to 0.154 nm), θ represents the Bragg diffraction angle, and β is the FWHM (Full Width Half Maxima) of the XRD peak which appears at the diffraction angle θ. The average grain size was calculated from X-ray line broadening using Scherrer equation and it was found to be about 14 nm.

3.2 FT-IR Analysis

The FT-IR spectrum is a very useful technique to deduce structural investigation of chemical compounds. In order to examine the spinel phase formation of cobalt

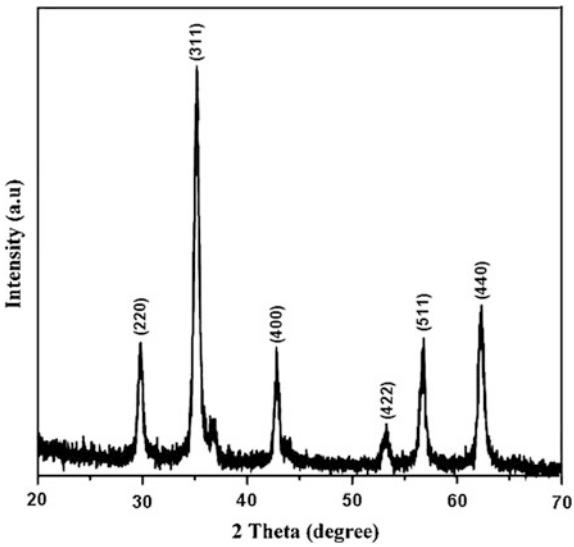

Fig. 1 XRD pattern of $CoFe_2O_4$

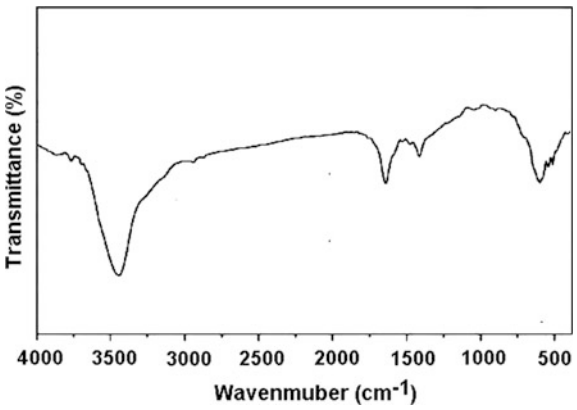

Fig. 2 FTIR spectrum of $CoFe_2O_4$

ferrite nanoparticles infrared spectroscopy was used. In ferrites, as a result of vibrations of the oxygen ions with the cations present in the octahedral and tetrahedral sites in the unit cell, the IR spectral absorption bands are produced. Figure 2 depicts the FTIR spectrum of cobalt ferrite nanoparticles. The FT-IR spectrum of the $CoFe_2O_4$ nanoparticles shows broad bands at 3426 cm^{-1} which are assigned to the stretching vibrations of both absorbed and free water on the surface of nanoparticles. The C-H stretching bands observed at 2928 and 2867 cm^{-1} confirm the presence of $CoFe_2O_4$ nanoparticles. The bands at 1624 and 1398 cm^{-1} are assigned to C=O stretching vibration. Two strong bands are observed around 585 and 450 cm^{-1} for $CoFe_2O_4$ nanoparticles.

3.3 Morphological Characterization

The structural morphology of nanoparticles was investigated by means of SEM. Figure 3 shows the SEM images of $CoFe_2O_4$ nanoparticles. The image of ferrite nanoparticles brings to light the microscopic structure and morphology which are in agreement with the XRD results. The image of ferrite particles indicates considerable degree of agglomeration that is due to its magnetic nature and the weak surface interaction of primary particles which are held together by the Van der Waals forces. The surface morphology of ferrite particles is extremely porous in nature which can be seen. Morphology and particle size were investigated with the help of TEM and resulting image is shown in Fig. 4. Most of the particles appear spherical in shape; however, some particles seem elongated which are shown in the TEM image. The average particle size is measured to be ≈22 nm.

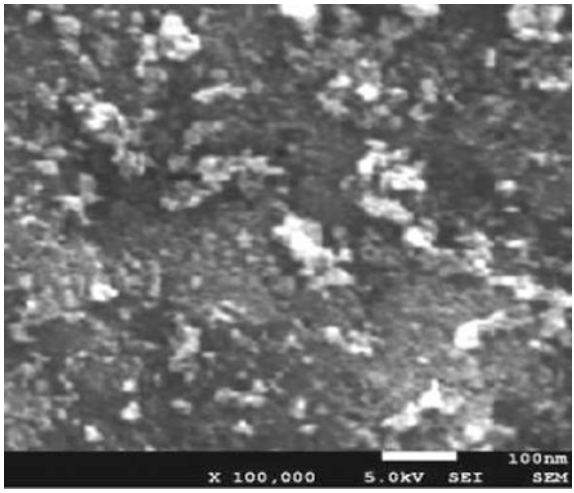

Fig. 3 SEM image of $CoFe_2O_4$ nanoparticles

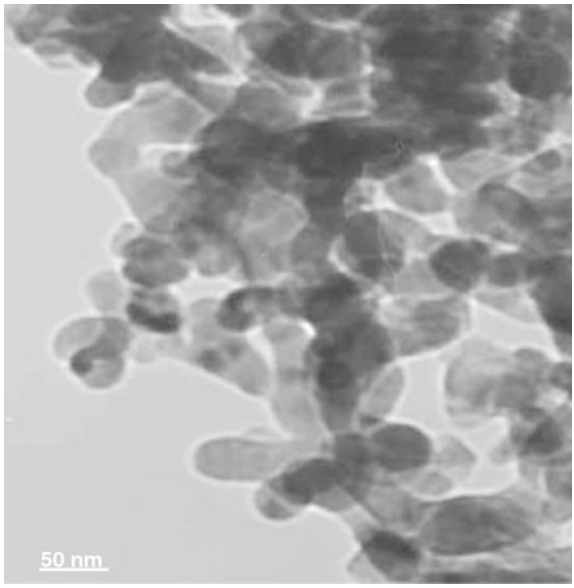

Fig. 4 TEM image of $CoFe_2O_4$ nanoparticles

3.4 Dielectric Properties

The variations observed in the dielectric constant with frequency and temperatures for the $CoFe_2O_4$ nanoparticles are shown in Fig. 5. At low frequencies the dielectric

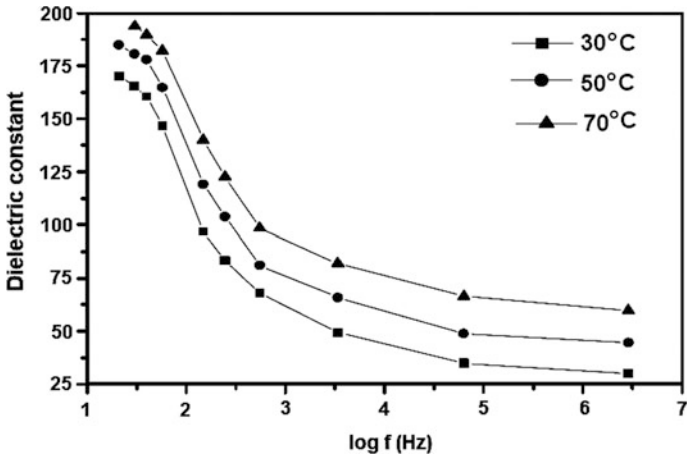

Fig. 5 Variation of dielectric constant with log frequency

constant of $CoFe_2O_4$ nanoparticles is high and it decreases rapidly at all temperatures with the applied frequency. It is also observed from the plot that with an increase in the temperature, the dielectric constant increases and this is attributed to the presence of space charge polarization near the grain boundary interfaces, on which the purity and exactness of the sample rely [13]. Hence the dielectric constant of nanostructured materials needs to be larger than that of the conventional materials. Due to the grain boundary interfaces structures, the space charge polarization increases and results into the large dielectric constant of nanocrystalline materials at sufficiently high temperature. Figure 6 shows the variations of the dielectric loss of $CoFe_2O_4$ nanoparticles with frequency and temperature. At all temperatures and at

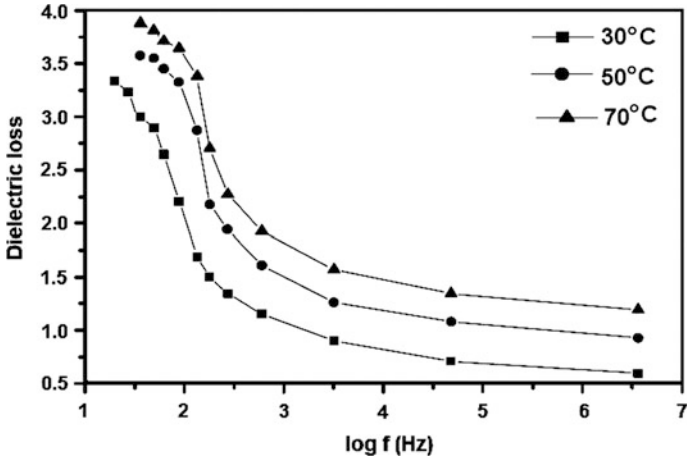

Fig. 6 Variation of dielectric loss with log frequency

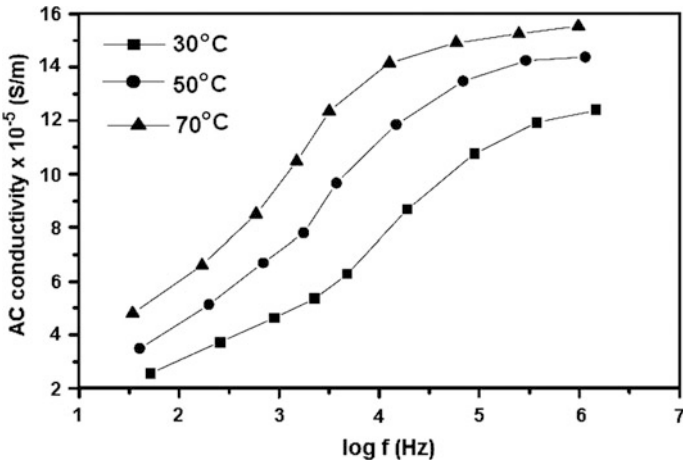

Fig. 7 AC conductivity plot for $CoFe_2O_4$ nanoparticles

higher frequencies the loss angle remains nearly same, where the dielectric loss decreases when the frequency increases. Due to absorption current in dielectric materials dielectric losses occur [14]. A part of the electric energy required in polar dielectrics for the orientation of the molecules along the direction of the applied electric field to overcome the forces of internal friction [15]. One more part of the electric energy is being utilized by various kind of molecular transfer from one position to another that also involves energy and for the rotation of dipolar molecules.

3.5 AC Conductivity Studies

The electrons jumping from the low valence state to high valence state as a result of movement of ions exist which leads to electrical conduction in $CoFe_2O_4$ nanoparticles. The frequency dependence behaviour of the ac conductivity within the temperature interval 30, 50 and 70 °C is shown in Fig. 7. The ac conductivity has shown increase with the increase in frequency for all temperatures. The increase in frequency enhances the electron jumping frequency and hence it is observed that ac conductivity gradually gets increased with the increase in the frequency of the applied ac field. The increased conductivity at higher frequencies may occur because of the reduction in space charge polarization [16].

4 Conclusion

By using hydrothermal method $CoFe_2O_4$ nanoparticles were synthesized successfully. The cubic structure was confirmed from the XRD pattern. The synthesized samples were ascertained by SEM and TEM analyses and the sizes calculated were

in nanometers. The variations of the $CoFe_2O_4$ nanoparticles dielectric constant, the dielectric loss, and AC conductivity were analyzed with variation in frequency and temperature. The dielectric analysis reports that with increase in frequency both the dielectric loss and the dielectric constant decreased. With increase in the temperature and the frequency the AC electrical conductivity initiates to increase.

References

1. Suda, M., Nakagawa, M., Iyoda, T., Einaga, Y.: Reversible photo switching of ferromagnetic FePt nanoparticles at room temperature. J. Am. Chem. Soc. **129**, 5538 (2007)
2. Wang, B., Li, B., Zhao, B., Li, C.Y.: Amphiphilic Janus gold nanoparticles via combining "Solid-State Grafting-to" and "Grafting-from" methods. J. Am. Chem. Soc. **130**, 11594–11595 (2008)
3. Shinkai, M.: Functional magnetic particles for medical application. J. Biosci. Bioeng. **94**, 606 (2002)
4. Giri, A.K., Pellerin, K., Pongsaksawad, W., Sorescu, M., Majetich, S.: Effect of light on the magnetic properties of cobalt ferrite nanoparticles. IEEE Trans. Magn. **36**, 3029–3031 (2000)
5. Corot, C., Robert, P., Ideé, J.M., Port, M.: Recent advances in iron oxide nanocrystal technology for medical imaging. Adv. Drug Deliv. Rev. **58**, 1471 (2006)
6. Bueno, A.R., Gregori, M.L., Nóbrega, M.C.S.: Ultrafast dynamics of 1 μm ZnO epitaxial films by time-resolved measurements. Mater. Chem. Phys. **105**, 229–233 (2007)
7. Sajjia, M., Oubaha, M., Hasanuzzaman, M.: Developments of cobalt ferrite nanoparticles prepared by the sol-gel process. Ceram. Int. **40**, 1147–1154 (2014)
8. Kurian, M., Nair, D.S.: on the efficiency of cobalt zinc ferrite nanoparticles for catalytic wet peroxide oxidation of 4-chlorophenol. J. Environ. Chem. Eng. **2**, 63–69 (2014)
9. Sorescu, M., Diamandescu, L., Peelamedu, R.: Structural and magnetic properties of NiZn ferrites prepared by microwave sintering. J. Magn. Magn. Mater. **279**, 195–201 (2004)
10. Jovanović, S., Spreitzer, M., Otoničar, M.: pH control of magnetic properties in precipitation-hydrothermal-derived $CoFe_2O_4$. J. Alloys Compd **589**, 271–277 (2014)
11. Liu, M., Obi, O., Lou, J.: Strong magnetoelectric coupling in ferrite/ ferroelectric multiferroic heterostructures derived by low temperature spin-spray deposition. J. Phys. D Appl. Phys. **42**, 045007 (2009)
12. Abbas, M., Rao, B.P., Islam, M.N.: Size-controlled high magnetization $CoFe_2O_4$ nanospheres and nanocubes using rapid one-pot sonochemical technique. Ceram. Int. **40**, 3269–3276 (2014)
13. Sures, S., Arunseshan, C.: Dielectric properties of cadmium selenide (CdSe) nanoparticles synthesized by solvothermal method. Appl. Nanosci. **4**, 179–184 (2014)
14. Suresh, S.: Synthesis, structural and dielectric properties of zinc sulfide nanoparticles. Int. J. Phys. Sci. **8**, 1121–1127 (2013)
15. Suresh, S.: Studies on the dielectric properties of CdS nanoparticles. Appl. Nanosci. **4**, 325–329 (2014)
16. Sagadevan, S., Podder, J., Das, I.: Hydrothermal synthesis of zirconium oxide nanoparticles and its characterization. J. Mater. Sci. Mater. Electron. **27**, 5622–5627 (2016)

Generation of Few-Cycle Laser Pulses Using A Photonic Quasi-crystal Fiber

M.S. Aruna Gandhi, G. Melwin, P. Ramesh Babu, Abdosllam M. Abobaker, K. Nakkeeran and K. Senthilnathan

Abstract We explore the optical properties of a proposed solid-core photonic quasi-crystal fiber (SC-PQF) of 10-fold for the wavelengths from 300 to 1100 nm. The proposed SC-PQF exhibits a admissible low dispersion of −8.6481 ps^2/km, a third order dispersion of 0.00415 ps^3/km and a large nonlinearity of 1684 W^{-1} km^{-1} at 450 nm, which turn out to be the desired optical properties for generating the few-cycle laser pulses. By exploiting these optical properties, we numerically demonstrate the generation of few-cycle laser pulses at 450 nm wavelength by means of higher-order soliton effect compression.

1 Introduction

In recent years, there has been a considerable interest for generating laser pulses comprising a less number of field oscillations called few-cycle laser pulses at different wavelengths. Few-cycle pulses in the femtosecond range are highly useful in the development of femtosecond laser technology. It should be emphasized that these few-cycle pulses help probe the dynamics of electrons in the matter. It is anticipated that the attosecond laser technology shall led to attoelectronics [1]. Thus, the high-intensity few-cycle laser pulses are at the forefront of the recent research in the ultrafast laser physics.

M.S. Aruna Gandhi · G. Melwin · P. Ramesh Babu · K. Senthilnathan (✉)
School of Advanced Sciences, VIT University, Vellore 632 014, Tamil Nadu, India
e-mail: senthee@gmail.com

M.S. Aruna Gandhi
School of Engineering, Presidency University, Bengaluru 560 089, Karnataka, India

A.M. Abobaker
Department of Communications Engineering, College of Electronic Technology, Bani Walid, Libya

K. Nakkeeran
School of Engineering, Fraser Noble Building, University of Aberdeen, Aberdeen AB24 3UE, UK

J. Ebenezar (ed.), *Recent Trends in Materials Science and Applications*,
Springer Proceedings in Physics 189, DOI 10.1007/978-3-319-44890-9_15

In general, fiber-based pulse compression techniques are smartly used for generating the few-cycle laser pulses. In recent years, the generation of few and single cycle pulses in highly nonlinear photonic crystal fibers (PCFs) has been numerically studied using soliton effect pulse compression [2–4]. More recently, the higher order soliton pulse compression technique has been deployed in a waveguide [5–7]. It is demonstrated that the optical properties of PCFs could be engineered by varying the structural parameters such as pitch and diameter of the air-holes. Nonetheless, it is highly difficult to study the optical properties in PCFs for a wide range of wavelengths [8]. The recent invention of a special fiber known as photonic quasi-crystal fiber (PQF) which has the ability to surpass the limitations of the PCFs. For the first time, Kim et al. [9] have proposed the idea of PQF which exhibits the unique optical properties. It is reported that PQF provides interesting optical characteristics such as a scalable dispersion, a low confinement loss, a large nonlinearity and a maximum cut off ratio that can help sustain single mode condition [10].

2 Geometric Design of SC-PQF

Figure 1 depicts the 2D geometrical structure of the 10-fold SC-PQF. The perfectly matched layer is designed for calculating the confinement loss. The 10-fold SC-PQF design has the basis of penrose quasi-crystal structure [11]. Here, the diameter of the air hole, d, is chosen as 0.9 μm and pitch, Λ, the distance between the two air holes as 1.5 μm. The perfectly matched layer is designed for calculating the confinement loss. We calculate the effective refractive index (n_{eff}) for computing the waveguiding properties for the wavelengths from 300 to 1100 nm.

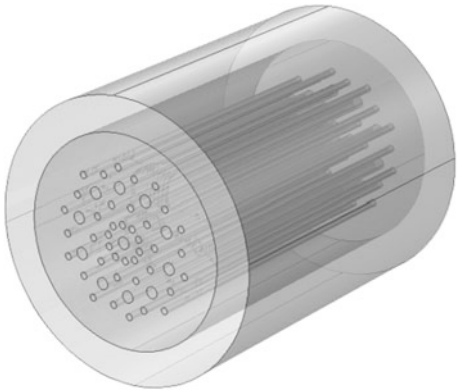

Fig. 1 Geometrical structure of the proposed SC-PQF

3 Optical Properties of SC-PQF

Here, we aim at achieving desired optical properties, namely, single mode condition, confinement loss, second order dispersion, third order dispersion and nonlinearity. Hence, we first calculate the effective refractive index (n_{eff}) for the proposed SC-PQF.

3.1 Dispersion

Having computed the effective index, we next compute the second derivative of the real part of effective refractive index of the fundamental mode for calculating dispersion. Figure 2 illustrates the variation of group velocity dispersion (GVD) over a range of wavelengths from 300 to 1100 nm. We find that the proposed fiber exhibits both anomalous and normal GVD. In Fig. 2, one can observe anomalous GVD from 300 to 930 nm and normal GVD from 940 to 1100 nm. We have been able to achieve a less GVD of −8.6481 ps^2/km at 940 nm wavelength for the proposed SC-PQF. This optical property turns out to be one of crucial requirements for generating few-cycle pulses.

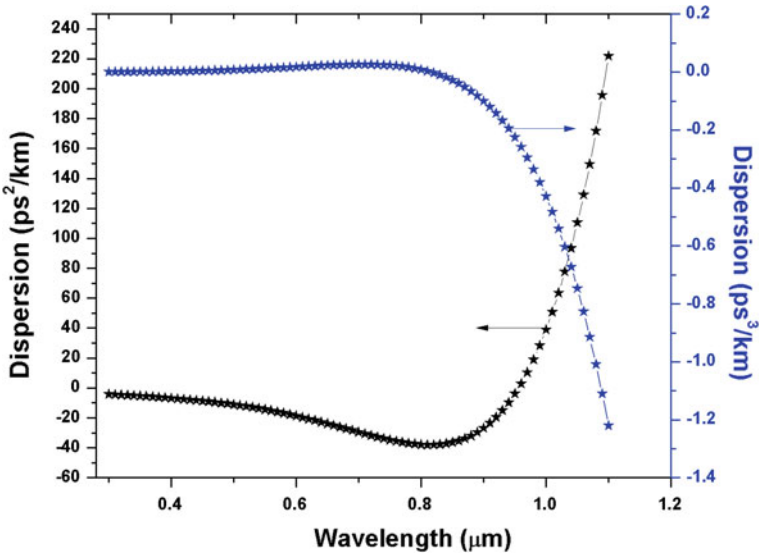

Fig. 2 GVD and TOD as a function of wavelength

3.2 *Effective Area and Nonlinearity*

In this section, we intend computing the nonlinearity by calculating effective area. Hence, we compute the effective mode field area by calculating the effective refractive index of fundamental mode. We obtain a large nonlinearity of 1684 W^{-1} km^{-1} with effective mode field area of 2.65226 μm^2 at 450 nm wavelength. Figure 3 illustrates the variation of nonlinearity with respect to wavelength. It is observed that the effective area of the fundamental mode increases as and when the wavelength is increased. On the other hand, the nonlinearity shows the opposite trend with wavelength. It is because the mode confinement becomes tight at lower wavelengths and vice versa.

4 Pulse Compression Using SC-PQF

By exploiting the above discussed optical properties, in this section, we delineate the generation of few-cycle pulses at various wavelengths using higher-order soliton pulse compression technique. It is well demonstrated that the fundamental optical soliton is a light pulse which is generated when the chirp produced by the anomalous dispersion gets dynamically balanced by the chirp introduced by the self-phase modulation. The temporal shape of this fundamental soliton does not change during the course of propagation. However, the temporal shape of the higher-order soliton does change, i.e., it undergoes periodic compression and broadening of its temporal width during the propagation [12]. Thus, the compression can easily be achieved by finding an optimum length of the fiber.

Here, the split-step Fourier method is employed for solving the HNLSE numerically. The HNLSE is given by [13],

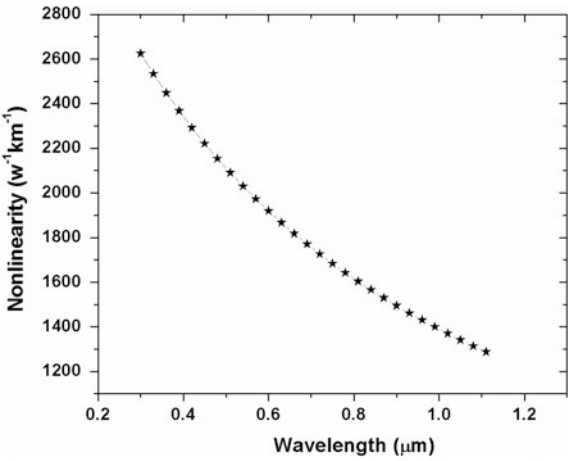

Fig. 3 Nonlinearity as a function of wavelength

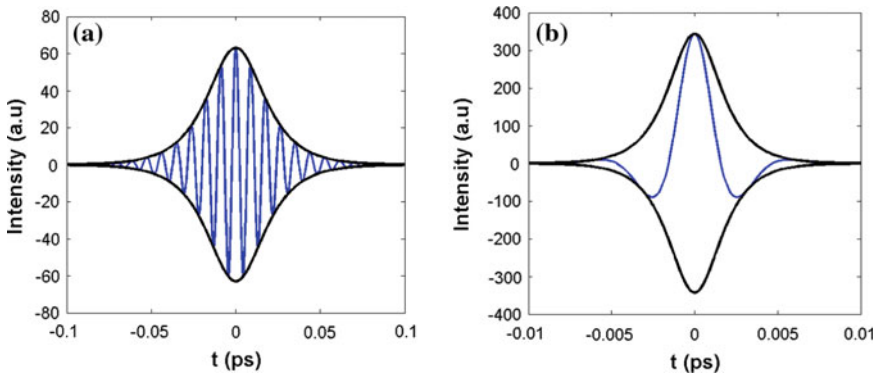

Fig. 4 **a** Input and **b** output pulses encompassing field oscillations at 450 nm wavelength

$$\frac{\partial A}{\partial z} + \frac{i\beta_2}{2}\frac{\partial^2 A}{\partial T^2} - \frac{i\beta_3}{6}\frac{\partial^3 A}{\partial T^3} = i\gamma\left[|A|^2 A + \frac{i}{\omega_0}\frac{\partial}{\partial T}\left(|A^2|A\right) - T_R A\frac{\partial |A|^2}{\partial T}\right],$$

where A is the slowly varying amplitude of the pulse envelope, z is the distance, T is the time, β_2 and β_3 are second-order and third-order dispersions, respectively, γ is the nonlinear coefficient and T_R is the response time due to Raman effect. We consider the following chirp-free hyperbolic secant pulse as an input,

$$A(0, T) = \sqrt{P_0}\,\mathrm{sec}\,h\left(\frac{T}{T_0}\right),$$

where P_0 and T_0 are the peak power and the input soliton duration, respectively. An hyperbolic secant pulse $A(0, T)$ is propagated into the fiber with $\beta_2 = -8.6481$ ps^2/km, $\gamma = 1684$ W^{-1} km^{-1}. The width of input pulse is 15 fs. Figure 4a, b depicts the compression of an input pulse of width 15 fs at 450 nm wavelength using a SC-PQF. The joint action of retarded optical nonlinearity and dispersion can also suppress oscillations on the temporal envelope of high-intensity femtosecond light pulses in the proposed SC-PQF.

Figure 4a explains the number of oscillations of the input pulse of 5.34 cycles. Figure 4b represents the output pulse which consists of 1.4 cycles with less than 4 fs at 450 nm.

5 Conclusion

The waveguiding properties of a SC-PQF with a solid-core have been investigated. It has been found that the proposed SC-PQF exhibits the desired optical properties over a wide range of wavelengths from 300 to 1100 nm. Further, we have achieved a low dispersion ($\beta_2 = -8.6481$ ps^2/m) and an enhanced nonlinearity ($\gamma = 1684$ W^{-1} m^{-1}) at 450 nm wavelength. The soliton effect compression of the femtosecond pulses in the proposed SC-PQF at 450 nm wavelength has also been numerically studied. The crux of the work lies in a 15 fs pulse having been compressed to 4 fs encompassing 1.4 cycles of pulse generation. We are of the opinion that the reported fiber could be used for the generation of supercontinuum.

Acknowledgements KSN wishes to thank CSIR [No: 03(1264)/12/EMR-11] for the financial support through the project.

References

1. Kärtner, F.X.: Few-Cycle Laser Pulse Generation and its Applications. Springer Science & Business Media, Berlin (2004)
2. Foster, M., Gaeta, A., Cao, Q., Trebino, R.: Soliton-effect compression of supercontinuum to few-cycle durations in photonic nanowires. Opt. Express **13**(18), 6848–6855 (2005)
3. Voronin, A.A., Zheltikov, A.M.: Solitons evolving toward few- and single-cycle pulses in photonic-crystal fibers. Laser Phys. **18**(12), 1416–1419 (2008)
4. Amorim, A.A., Tognetti, M.V., Oliveira, P., Silva, J.L., Bernardo, L.M., Kärtner, F.X., Crespo, H.M.: Sub-two-cycle pulses by soliton self-compression in highly nonlinear photonic crystal fibers. Opt. Lett. **34**(24), 3851–3853 (2009)
5. Chan, K., Cao, W.: Improved soliton-effect pulse compression by combined action of negative third-order dispersion and Raman self-scattering in optical fibers. J. Opt. Soc. Am. B **15**(9), 2371–2375 (1998)
6. Chen, M.Y., Subbaraman, H., Chen, Ray T.: One stage pulse compression at 1554 nm through highly anomalous dispersive photonic crystal fiber. Opt. Express **19**(22), 21809–21817 (2011)
7. Li, Q., Kutz, J.N., Wai, P.K.A.: Cascaded higher-order soliton for non-adiabatic pulse compression. J. Opt. Soc. Am. B, **27**(11), 2180–2189 (2010)
8. Cerqueira Jr., S.A.: Recent progress and novel applications of photonic crystal fibers. Rep. Prog. Phys. **73**(2), 024401 (2010)
9. Kim, S., Kee, C.-S., Lee, J.: Novel optical properties of six-fold symmetric photonic quasicrystal fibers. Opt. Express **15**(20), 13221–13226 (2007)
10. Zhao, H., Zaccaria, R.P., Verma, P., Song, J., Sun, H.B.: Validity of the V parameter for photonic quasi-crystal fibers. Opt. Lett. **35**(7), 1064–1066 (2010)
11. Freedman, B., Bartal, G., Segev, M., Lifshitz, R., Christodoulides, D.N., Fleischer, J.W.: Wave and defect dynamics in nonlinear photonic quasicrystals. Nature **440**(7088), 1166–1169 (2006)
12. Vasantha Jayakantha, R., Senthilnathan, K., Porsezian, K., Nakkeeran, K.: Efficient pulse compression using tapered photonic crystal fiber at 850 nm. IEEE J. Quantum Electron. **46** (12), 1795–1803 (2010)
13. Agrawal, G.P.: Nonlinear Fiber Optics. Academic Press, USA (2013)

Synthesis, Structural, Optical and Dielectric Properties of Cadmium Sulfide Nanoparticles as Photocathode for a Solar Cell

F. Michael Raj and A. Jeya Rajendran

Abstract Cadmium sulfide nanoparticles were prepared by chemical co-precipitation method using cadmium acetate, sodium sulfide and tetrabutylammonium bromide (TBAB) as a capping agent. The synthesized nanoparticles were characterized by using UV-Vis spectroscopic analysis, X-ray diffraction analysis (XRD), Field emission scanning electron microscopic analysis (FESEM), Energy dispersive X-ray analysis (EDAX) and BET surface area nitrogen adsorption-desorption analysis. The band gap of capped CdS was calculated by using UV-Vis absorption spectrum as 3.23 eV. The X-ray diffraction pattern revealed that the synthesized cadmium sulfide nanoparticles were polycrystalline nature with wurtzite hexagonal structure and crystallite size was calculated as 7.2 nm by using Debye Scherer method. The surface area, pore volume and pore size were found to be 93.15 m^2/g, 1.64 $\times$ 10^{-2} cm^3/g and 6.2 Å by BET nitrogen adsorption-desorption analysis. The dielectric constant, dielectric loss and AC conductivities were studied over a range of frequency (50 Hz–5 MHz) and temperature (40–200 °C). Solar cell was fabricated using cadmium sulfide as photocathode, titanium dioxide as photoanode, potassium iodide/iodine as an electrolyte solution, ruthenium dye as a sensitizer and power conversion efficiency was found to be 2.7 %.

1 Introduction

Semiconductor binary chalcogenide materials such as CdS and PbS have attracted considerable attention due to their unique optical and spectroscopic properties from that of the bulk materials [1]. CdS nanoparticles are the most widely studied binary chalcogenide among II–VI semiconductor materials due to its wide bandgap of 2.42 eV. The advantage of CdS as a semiconductor with discrete energy levels,

F. Michael Raj · A. Jeya Rajendran (✉)
Advanced Materials Research Lab, Department of Chemistry, Loyola College, Chennai 600034, Tamil Nadu, India
e-mail: jeyarajendran@yahoo.com

J. Ebenezar (ed.), *Recent Trends in Materials Science and Applications*,
Springer Proceedings in Physics 189, DOI 10.1007/978-3-319-44890-9_16

tunable bandgap, size dependant optical properties, good chemical stability and could be prepared easily [1]. Generally, the nanoparticles exhibit variation in their properties in comparison to the bulk material due to two factors namely the increase in surface to volume ratio and change in electronic structure of the material by the quantum confinement effect [2, 3]. The semiconductor nanoparticles have been synthesized through various methods including hydrothermal, micro-emulsion, sol-gel, sonochemical, microwave irradiation, co-precipitation and solvothermal methods [4–11] and so on. However, these methods normally consist of two or more steps and vigorous conditions, such as high pressure or high temperature are required to attain nanoparticles [12]. Furthermore, co-precipitation method has some advantages like inexpensive, minimum time requirement and instruments, convenient operation to produce high yield of product formation at low temperature condition. The role of surfactant is very crucial in co-precipitation method to overcome the agglomeration of nanoparticles to improve the surface area and favourable behaviours in catalytic applications.

In this paper, we report the synthesis of CdS nanoparticles by chemical co-precipitation method using tetrabutylammonium bromide as a capping agent, an effective route for preparation of CdS nanoparticles. The structural, optical, dielectric properties and J-V characteristics of the fabricated solar cell were studied to determine the power conversion efficiency.

2 Experimental

2.1 Synthesis of CdS Nanoparticles

All the chemicals used in the experiment were analytical grade and used without further purification. Millipore double distilled water was used throughout the experiment. The CdS nanoparticles were synthesized by chemical co-precipitation method using cadmium acetate dihydrate and sodium sulfide as the starting materials. 50 mL of 0.1 M cadmium acetate solution was taken in 250 mL round bottom flask and stirred for 30 min using magnetic stirrer. After 20 min, 50 mL of 0.05 M tetrabutylammonium bromide (TBAB) dissolved in water was added and continued stirring for 30 min to get homogeneous solution and then 50 mL 0.1 M solution of sodium sulfide was added dropwise to the solution of cadmium acetate under continuous stirring until the formation of yellow precipitate and stirring was continued for 3 h to complete the reaction. The pH was maintained between 9 and 10 by adding ammonia solution. The chemical reaction is,

$$\mathbf{Cd(CH_3COO)_2 + Na_2S \rightarrow CdS + 2CH_3COONa}$$

The solution was allowed to settle down for 2 h, and the particles were precipitated. The solid yellow product was washed by using ethanol. The reaction product was repeatedly washed with ethanol to remove the unreacted surfactant

impurities from the CdS nanoparticles and centrifuged for 20 min for three times with ethanol at high rpm level. The product was dried at 150 °C for 3 h under reduced pressure. The dried samples were ground using mortar and pestle to make fine powder for uniform crystallite size.

2.2 Characterization

The optical absorption spectrum was recorded by using **Jasco V-700** UV-Vis spectrophotometer in the range of 200–800 nm. XRD spectrum was recorded by **Philips X'pert** X-ray diffractometer using CuK_{α} radiation (λ = 0.154 nm) at 40 kV and 30 mA from 20° to 70°. The composition of elements in nanomaterials was determined by energy dispersive X-ray spectrometer (EDZ, **HITACHI S2400**). The nanostructures of the samples were characterized by **FEI Quanta 200** Environmental SEM with EDAX analyser. The BET nitrogen adsorption-desorption analysis was carried out by **Quantachrome NOVAWIN** instruments. Dielectric properties were studied by using **HIOKI 3532-50 LCR Hi TESTER** model LCR meter as the function of frequency, 50 Hz–5 MHz and the temperature, 40–200 °C. J-V characteristics were measured by using **YOKOGAWA GS610** Source Measure Unit.

2.3 Fabrication of Solar Cell

2.3.1 Preparation of Photoanodes

To prepare TiO_2 photoanode, the Fluorine doped Tin Oxide (FTO) coated glass substrates were cleaned and dried with acetone. The commercially available TiO_2 powder (1 g) was made into paste with acetone in water using mortar and pestle. The paste was applied on the FTO coated glass substrate by doctor blade method [13] and heated at 250 °C for 3 h to remove the organic substances.

2.3.2 Preparation of Photocathode

CdS nanoparticles were synthesized by using cadmium acetate and sodium sulfide using chemical co-precipitation method. The CdS powder was made into paste with acetone in water using mortar and pestle. The paste was applied on cleaned and dried FTO coated glass substrate by doctor blade method and heated in an oven for 3 h.

2.3.3 Fabrication of DSSC

The prepared TiO_2 coated photoanode (0.25 cm^2) was immersed in commercially available ruthenium dye for 10 min and then washed with acetone to remove excess dye on the surface and dried at 250 °C in an oven for 3 h. Then, the sensitized TiO_2 photoanodes and CdS photocathodes were assembled and internal space was filled with an potassium iodide/iodine redox electrolyte. The cell current was measured by using YOKOGAWA GS 610 Source measure unit and values were recorded.

3 Results and Discussion

3.1 X-ray Diffraction Analysis

The X-ray diffraction pattern of as-synthesized CdS nanoparticles in the diffraction angle of range 20°–70° was showed in Fig. 1. The peaks observed in the XRD pattern match well with those of the CdS reported in the JCPDS file No. 041-1049 which confirms the hexagonal wurtzite structure [14]. The average crystallite size was calculated using the Scherer formula as 7.2 nm.

$$T = \frac{0.89\lambda}{\beta \cos\theta} \tag{1}$$

where T = crystallite size, λ is the wavelength of X-ray (1.5404 Å), β is the full width half maximum in radian and θ is the Bragg's diffraction angle obtained from 2θ value corresponds to the maximum intensity peak in XRD pattern. The strain and crystallite size of the sample were calculated from Williamson Hall equation [14],

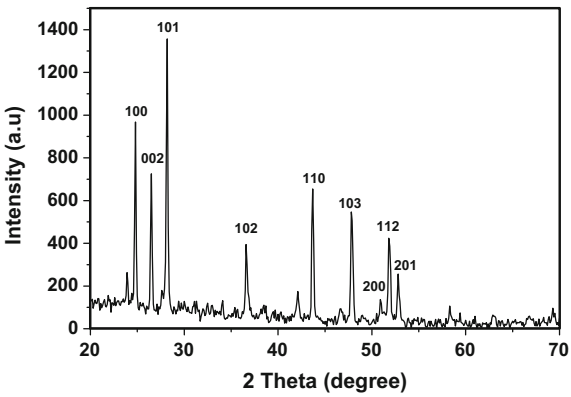

Fig. 1 XRD pattern of TBAB capped CdS nanoparticles

$$\beta \cos\theta = K\lambda/T + 2\varepsilon \sin\theta \quad (2)$$

where K—Debye Scherer's constant (0.89), T—average crystallite size, ε—lattice strain. In this method while plotting the graph of 4 sinθ against β cosθ gives a straight linear plot, the crystallite size and the strain (ε) were calculated from the intercept and the slope respectively. The calculated average crystallite size and the strain of TBAB capped CdS were found to be 7.2 nm and 4.53×10^{-3} respectively.

3.2 BET (Brunauer-Emmett-Teller) Surface Area and BJH (Barrett-Joyner-Halenda)

Poresize analysis

The BET nitrogen adsorption-desorption isotherms of the CdS nanospheres (Fig. 2) correspond to a type V isotherm in the Brunauer classification [13] by the hysteresis loop which confirms the characteristic mesoporous nature of as-synthesized CdS nanospheres. The nitrogen gas was used as adsorbate for the analysis time of 120 min. The observed BET surface area of the as-synthesized CdS nanospheres was determined as 93.15 m^2/g. The calculated BJH pore size and pore volume are 6.2 Å and 1.64×10^{-2} cm^3/g at 273 K. Due to the high surface area of the CdS nanosphere, more adsorption sites for absorbing the dye for better efficiency in dye sensitized solar cell.

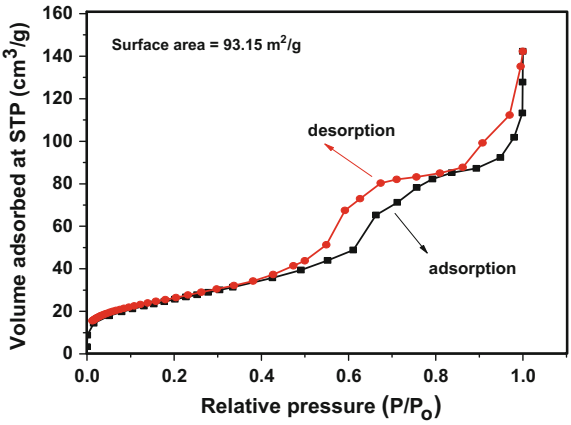

Fig. 2 Nitrogen adsorption–desorption isotherm of TBAB capped CdS nanoparticles

3.3 *Field Emission Scanning Electron Microscopic Analysis and EDAX*

The surface morphology and shape of CdS nanoparticles were studied by FESEM analysis. Figure 3 which shows polycrystalline nature and the synthesized particles exhibited spherical granule like structure [13]. The EDAX spectrum in Fig. 4 confirms the presence of Cd and S peaks in CdS nanoparticles with no other impurity elements. The average atomic percentage ratio of Cd:S was 51.5:48.5.

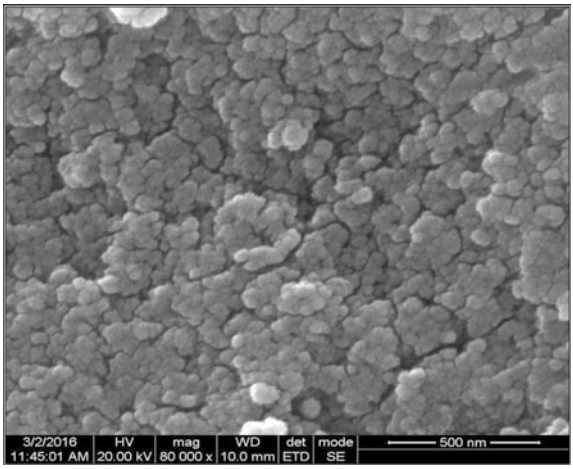

Fig. 3 FESEM image of as synthesized TBAB capped CdS nanoparticles

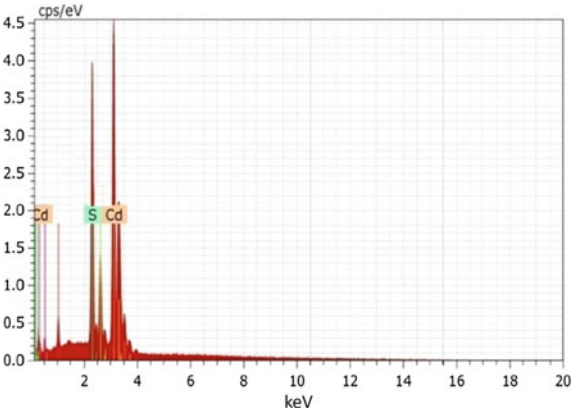

Fig. 4 EDAX spectrum of as synthesized CdS nanoparticles

3.4 UV-Vis Analysis

Figure 5 shows the UV-Vis spectrum of pure CdS nanoparticles and TBAB capped CdS nanoparticles with the absorption edges of 528 and 484 nm respectively. The bandgap value for capped CdS was calculated by Tauc's plot method as 3.23 eV and the optical size was calculated from the Brus equation [7] which relates the bandgap energy and optical size of CdS nanoparticles as 5.8 nm.

3.5 Dielectric Studies

Dielectric studies were recorded as the function of frequency 50 Hz–5 MHz and the temperature ranges from 40 to 200 °C for the CdS nanoparticles which was taken in the form of pellet, with diameter 12.7 mm and thickness 0.76 mm and it was kept in between the parallel plate capacitors. The dielectric constant was calculated by the formula,

$$\varepsilon_r = \mathbf{Cd}/\mathbf{A}\varepsilon_o \tag{3}$$

where d-thickness of the sample, A is the area of the sample, ε_o is the permittivity of free space (8.85×10^{-12} C^2 N^{-1} m^{-2}) and C is the capacitance. The dielectric constant (ε_r) is the factor by which the effective field is decreased by the polarization of the dielectric. The dielectric constant was high (Fig. 6) at low frequencies and decreased when the frequency was raised and remains constant at high frequencies. Figure 7 shows the variation of dielectric constant with respect to temperature which reveals that the dielectric constant is high at low temperature at all frequencies. The variation of dielectric loss (tan δ) with respect to frequency at

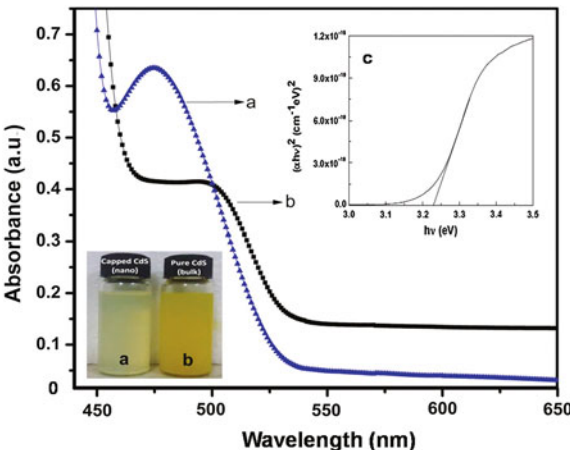

Fig. 5 UV-Vis spectrum of as synthesized **a** TBAB capped and **b** bulk CdS nanoparticles **c** Tauc's plot for TBAB capped CdS

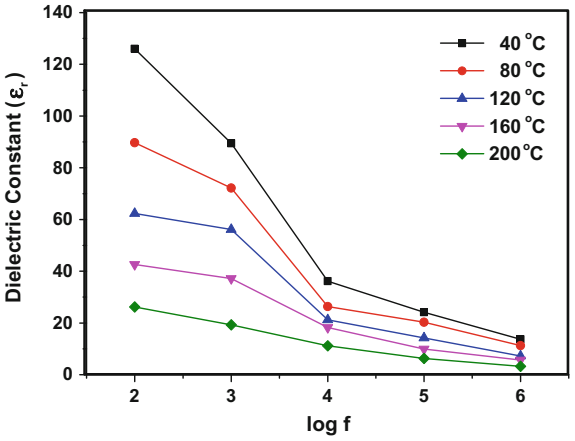

Fig. 6 Dielectric constant of CdS versus frequency at different temperatures

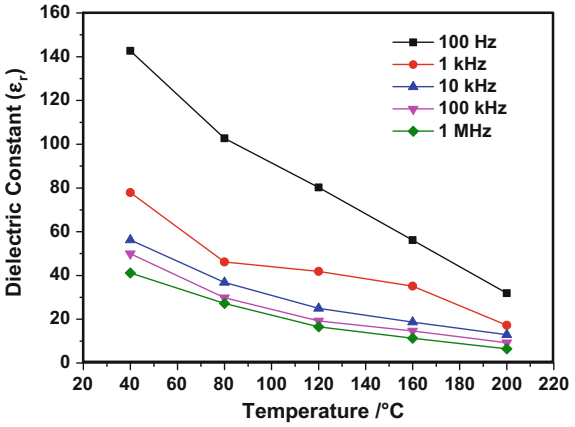

Fig. 7 Dielectric constant of CdS versus temperature at different frequencies

different temperature is given in Fig. 8 which is found to decrease and attain the constant value on raising frequency. The dielectric loss is high (Fig. 9) at low temperature and decreases slowly at higher temperature due to space charge polarization. At low frequencies, the dipoles can easily be aligned with the changing field and at high frequencies, the low dielectric loss may be related to the purity of the nanoparticles, having negligible defects with good optical quality which could be useful in the fabrication of electro-optic devices [14].

The variation of AC conductivity of the capped CdS nanoparticles versus frequency at different temperature is given in Fig. 10. The AC conductivity (σ_{ac}) of CdS nanoparticles was calculated using,

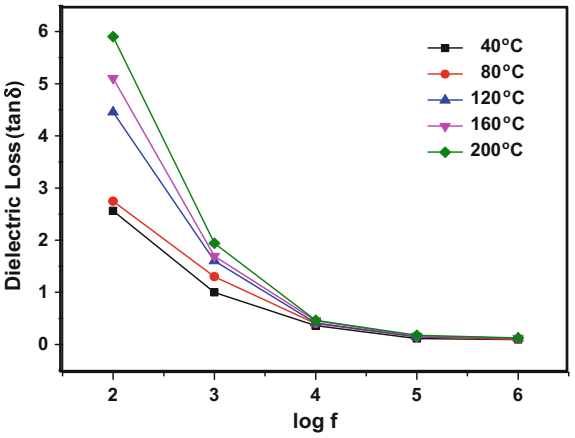

Fig. 8 Dielectric loss of CdS versus frequency at different temperatures

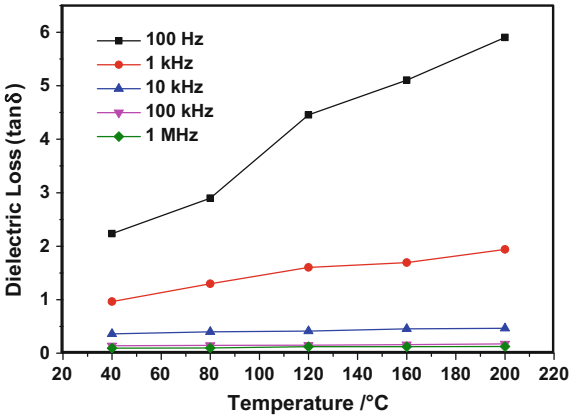

Fig. 9 Dielectric loss of CdS versus temperature at different frequencies

$$\sigma_{ac} = 2\pi f \tan\delta\, \varepsilon_o\, \varepsilon_r \tag{4}$$

where, f-frequency of applied field, tanδ is a dielectric loss, ε_r is the relative permittivity of the sample and ε_o is permittivity of free space (8.854×10^{-12} $C^2\ N^{-1}\ m^{-2}$). The electrical properties of semiconductor nanomaterials has paid considerable attention towards the conduction mechanism [14].

The variation of AC conductivity with the temperature (Fig. 11) at different frequencies of CdS nanoparticles, in which AC conductivity value remains constant up to the temperature of 100 °C and then decreases for higher frequencies. The increase in AC conductivity with the temperature is due to the mobility of charge carriers and is responsible for hopping mechanism of conduction which are responsible for the electronic polarization of CdS [15].

The band gap energy was also calculated by the equation [16–18],

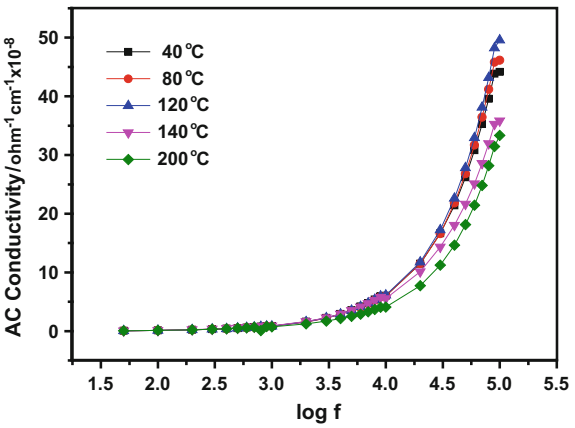

Fig. 10 Variation of AC conductivity versus frequency at different temperatures

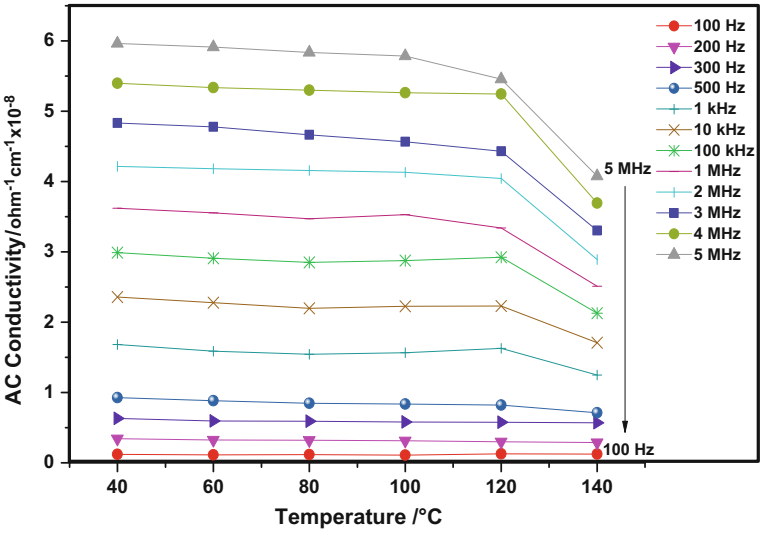

Fig. 11 AC conductivity of CdS versus temperature at different frequencies

$$E_g = 6K_BT/(1 - S) \tag{5}$$

$$S = 1 - \left(6K_BT/E_g\right) \tag{6}$$

where K_B—Boltzmann constant (1.38×10^{-23} m^2 kg s^{-2} K^{-1}), S—exponential factor, E_g—energy band gap, T—temperature. The calculated value of band gap energy is 3.1 eV for capped CdS nanoparticles which is comparable as calculated from UV-Vis spectral data.

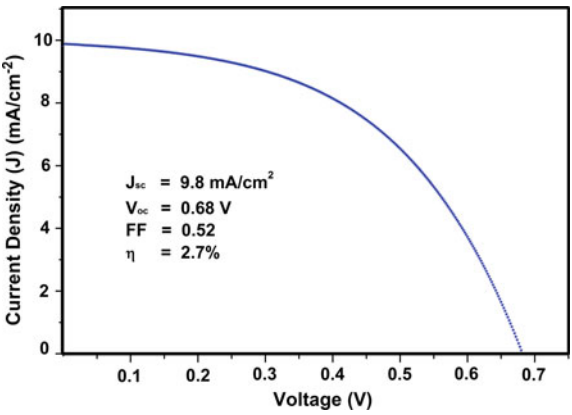

Fig. 12 J-V curve of CdS nanoparticles

3.6 J-V Characteristics Studies

The photocurrent density versus voltage (J-V), characteristics of fabricated solar cell device was shown in Fig. 12. The solar cell was fabricated by coating titanium dioxide as photoanode and cadmium sulfide material as photocathode on FTO glass with 0.25 cm^2 in area by doctoral blade method. Ruthenium N719 red dye was used as a sensitizer and potassium iodide/iodine as redox electrolyte solution. The short current density (J_{sc}), open circuit voltage (V_{oc}), fill factor (FF), power conversion efficiency (PCE) were found to be 9.8 mA/cm^2, 0.68 V, 0.52, 2.7 % respectively for CdS nanoparticles. The conversion efficiency was high compared to other binary semiconductor nanoparticles like ZnS, ZnSe and is also yet to be improved either by replacing suitable photoanode materials or by synthesizing different morphological structures of CdS.

4 Conclusion

Cadmium sulfide nanoparticles as hexagonal phase with crystallite size of 7.2 nm were synthesized by low cost, easiest, high yield chemical co-precipitation method. The optical bandgap of the CdS nanoparticles was obtained from UV-Vis spectrum as 3.23 eV semiconducting material. Morphology of CdS is found to be spherical in shape by FESEM analysis and element composition was confirmed by EDAX which reveals the presence of Cd and S in the nanoparticles. The specific surface area of the synthesized material is calculated by BET nitrogen adsorption-desorption analysis as 93.15 m^2/g. The high surface area is effective to absorb more amount of dye on the surface of CdS in DSSC to enhance more efficiency. Dielectric properties like dielectric constant, dielectric loss and AC conductivities were studied. The conversion efficiency of fabricated dye sensitized solar cell was found to be 2.7 %.

Acknowledgements The authors gratefully acknowledge the financial support provided by UGC (India) for the project [**F.No. 41-1005/2012 (SR)**].

References

1. Kandasamy, K., Singh, H.B., Kulshreshtha, S.K.: Synthesis and characterization of CdS and CdSe nanoparticles prepared from novel intramolecularly stabilized single-source precursors. J. Chem. Sci. **121**, 293–296 (2009)
2. Ikhmayies, S.J.: Characterization of nanocrystalline CdS thin films prepared by thermal evaporation. J. Mater. Chem. **3**, 28–33 (2013)
3. Thilagavathi, T., Geetha, D.: Nano ZnO structures synthesized in presence of anionic and cationic surfactant under hydrothermal process. Appl. Nanosci. **4**, 127–132 (2012)
4. Prabhu, R.R., Abdul Khaddar, M.: Characterization of chemically synthesized CdS nanoparticles. Pramana J. Phys. **65**, 801–807 (2005)
5. Khiew, P.S., Haung, N.H., Radiman, S., Ahmad, M.S.: Synthesis and characterization of conducting polyaniline-coated cadmium sulphide nanocomposites in reverse microemulsion. Mater. Lett. **58**, 516–521 (2004)
6. Elango, M., Nataraj, D., Thamilselvan, M.: Synthesis and characterization of nickel doped cadmium sulphide. Mater. Res. Bull. **47**, 1533–1538 (2012)
7. Rao, B.S., Kumar, B.R., Reddy, V.R., Rao, T.S.: Preparation and characterization of CdS nanoparticles by chemical co-precipitation technique. Chalcogenide Lett. **8**, 177–185 (2011)
8. Meera, J., Sumithra, V., Seethu, R., Prajeshkumar, J.M.: Dielectric properties of Nanocrystalline ZnS. Acad. Rev. **1**, 93–100 (2010)
9. Choubey, S.K., Tiwary, K.P.: Microwave assisted synthesis of CdS nanoparticles for structural and optical characterization. IJIRSET **3**, 10670–10674 (2014)
10. Elango, M., Gopalakrishnan, K., Vairam, S., Thamilselvan, M.: Structural, optical and magnetic studies on non-aqueous synthesized CdS:Mn nanomaterials. J. Alloy. Compd. **538**, 48–55 (2012)
11. Arellano, I.H.J., Mangadlao, J., Ramiro, I.B., Suazo, K.F.: 3-component low temperature solvothermal synthesis of colloidal cadmium sulfide quantum dot. Mater. Lett. **64**, 785–788 (2010)
12. Lu, H.Y., Chu, S.Y., Tan, S.S.: The characteristics of low-temperature- synthesized ZnS and ZnO nanoparticles. J. Cryst. Growth. **269**, 385–391 (2004)
13. Chou, C.S., Yang, R.Y., Weng, M.H., Yeh, C.H.: Study of the applicability of TiO_2/Dye composite particles for a Dye sensitized Solar Cell. Adv. Powder. Technol. **19**, 541–558 (2007)
14. Onwudiwe, D.C., Strydom, C.A., Oluwafemi, O.S.: Effect of some nitrogen donar ligands on the optical and structural properties of CdS nanoparticles. New J. Chem. **37**, 834–842 (2013)
15. Pathak, C.S., Mandal, M.K., Agarwala, V.: Synthesis and characterization of Zinc sulphide Nanoparticles Prepared by Mechanochemical Route. Superlattices Microstruct. **58**, 135–143 (2013)
16. Khan, Z.R., Zulfequar, M., Khan, M.S.: Chemical synthesis of CdS nanoparticles and their optical and dielectric studies. J. Mater. Sci **46**, 5412–5416 (2011)
17. Jeya Rajendran, A., Prabhu, M., Eswara Moorthi, K., Celine Rose, I.R., Santhanaraj, D., Sugandhi, K., Radhika, S.: Dielectric and conductivity studies of stereo-selectively synthesized d- and l- nor- ephedrine. J. Therm. Anal. Calorim. **119**, 369–379 (2015)
18. Onwudiwe, D.C., Arfin, T., Strydom, C.A.: Synthesis, Characterization and dielectric properties of N-butyl aniline capped CdS nanoparticles. Electrochim. Acta **116**, 217–223 (2014)

Third Order Nonlinear Optical Studies of ZnS Nanostructures Synthesized by Laser Ablation Technique

M.C. Divyasree, N.K. Siji Narendran and K. Chandrasekharan

Abstract We report the nonlinear optical (NLO) studies of ZnS nanostructures (NS) in polyvinyl pyrrolidone/dimethyl formamide (PVP/DMF) synthesized by laser ablation technique. We used a frequency doubled Q-switched Nd:YAG laser operating at 532 nm with a repetition rate of 10 Hz, 7 ns pulse width for ablation. The obtained nanoparticles showed a maximum absorption peak at 270.5 nm and were further chararacterized by Transmission Electron Microscope (TEM), X ray diffractometer (XRD), and Scanning Electron Microscope (SEM) from which the formation of NS was confirmed. The third order nonlinear optical susceptibility ($\chi^{(3)}$) of nanocomposite was measured using the single beam Z-scan technique. The mechanism behind the nonlinear absorption was confirmed to be two photon absorption (2PA) as the open aperture Z-scan curves of ZnS NS were fitted well to the theoretical model for 2PA. Also, the unvarying values of the nonlinear absorption coefficient (β_{eff}) with different on-axis input intensities endorse 2PA as the principal absorption mechanism. The $\chi^{(3)}$ value measured was 4.7×10^{-12} esu which ensures its potential usefulness in photonic applications exploiting optical limiting property.

1 Introduction

Investigation of NLO properties of semiconductor nanoparticles is an enhanced research area as it contributes much in optoelectronic applications [1]. In which II–IV compound semiconductors, especially ZnS shows good optical nonlinearity which is applicable in electro-luminescent devices and optical limiters [2]. When semiconductor nanoparticles embedded in a solid polymer matrix, it becomes more stable and processable. These organic-inorganic composites show attractive optical properties like fluorescence, electroluminescence and optical nonlinearity [3].

M.C. Divyasree · N.K. Siji Narendran · K. Chandrasekharan (✉)
Laser and Nonlinear Optics Lab Department of Physics, National Institute of Technology Calicut, Calicut 673601, Kerala, India
e-mail: csk@nitc.ac.in

J. Ebenezar (ed.), *Recent Trends in Materials Science and Applications*,
Springer Proceedings in Physics 189, DOI 10.1007/978-3-319-44890-9_17

ZnS NS were synthesized in situ in PVP/DMF solution and they formed stable composites. This physical method of laser ablation can be considered as a clean tool for the preparation of NS, as the possibility of contamination is very less.

In this paper, we adopted laser ablation technique for the preparation of ZnS NS and its linear characterizations were done by UV-Vis spectrophotometer and fluorometer. Formation of ZnS NS was analysed by XRD, SEM and TEM. Due to its good solubility, chemical stability and less poisonous nature, PVP was selected as the polymer medium for laser ablation [4]. NLO characterizations were done by Q-switched Nd: YAG Laser at a wavelength of 532 nm. The nonlinear refractive index coefficient (n_2), β_{eff} and $\chi^{(3)}$ were calculated.

2 Experimental

2.1 *Preparation and Characterisation of ZnS Nanostructures*

ZnS NS were synthesized by ablating a ZnS pellet in 1 wt% PVP/DMF solution using Nd:YAG Q-switched laser (Quanta-Ray INDI-40) having wavelength 532 nm with pulse width 7 ns and repetition rate of 10 Hz [5]. A lens of focal length 25 cm was used to focus the beam having an energy of 50 mJ per pulse. The pellet was ablated for 30 min. A pale white coloured colloidal solution of ZnS-PVP composite was obtained. The structural characterization of the sample was carried out by XRD (RIGAKU-MINIFLEX 600) using CuK_α radiation. The solution exhibited an absorption peak at 270.5 nm and was measured using UV-Vis spectrophotometer (SHIMADZU-UV 2450). The photoluminescence (PL) measurement of ZnS/PVP was performed by PERKIN ELMER LS 45 at an excitation wavelength of 270 nm. After removing the PVP/DMF by centrifugation the ZnS NS were further characterized by TEM (JEOL, JEM-2100) and SEM (HITACHI SU6600). The EDX spectra showed the improved Zn:S stoichiometry [6].

2.2 *Z-Scan Technique*

The NLO studies of the ZnS NS were done by the well-known Z-scan method introduced by Sheik-Bahae et al. [7]. It relies on the fact that the intensity of a focused laser beam, which passes through a sample, varies along the axis of a lens. The light intensities transmitted through the sample were measured as a function of the sample position with respect to the focal plane either through a small aperture (closed-aperture(CA) Z-scan) or without an aperture (open-aperture(OA) Z-scan), in order to resolve n_2 and β. The schematic diagram of the experimental set up of z scan analysis is given in Fig. 5. A Nd: YAG Q-switched laser, with the pulse width

of 7 ns, was used as the light source. A lens of 150 mm focal length was used to focus the laser beam onto the tested sample, which was moved along the optical axis (z-direction) through the focus by a stepper motor driven translational stage. The laser beam waist (ω_0) measured was 17.56 μm at the focus. Both the transmitted and reference beam energies were recorded by an energy ratio meter. The sample used for the nonlinear measurement has a thickness of 1 mm, which is much smaller than the diffraction length z_0 ($z_0 = \pi\omega_0^2/\lambda$) of the beam which allows the thin sample approximation in this experiment.

3 Results and Discussion

Figure 1 shows the XRD diagram of the sample ensuring the structure of ZnS NS as hexagonal Wurtzite -8H ZnS (JCPDS card no: 39-1363) [8]. The sharp diffraction peaks are obtained at 28.47, 47.43 and 56.31 with corresponding planes (008), (110) and (118) respectively. The average size of the ZnS NS is calculated with the help of Debye-Scherrer formula, $D = 0.9\lambda/\beta \cos\theta$, where λ is the wavelength of X-ray radiation (1.5418 Å), β is the full width at half maximum (FWHM) in radians of the highest intense peak corresponding to (008) plane, θ is the angle of diffraction [9]. The size of the NS is calculated as 58.4 nm.

Figure 2 shows the UV-Vis absorption and PL spectra of the ZnS NS. The absorption peak is obtained at 270.5 nm. A blue shift in the absorption peak with respect to bulk ZnS is observed. The band gap is estimated to be 4.59 eV from the absorption spectra [10]. Since the wavelength of laser source used for the Z-scan measurement was 532 nm, the possible absorption mechanism could have a major contribution from 2PA. PL spectrum of ZnS NS gives a strong emission peak centered at 355.5 nm for an excitation wavelength of 270 nm. The well-defined peak of PL spectrum indicates the good optical quality of ZnS NS [11].

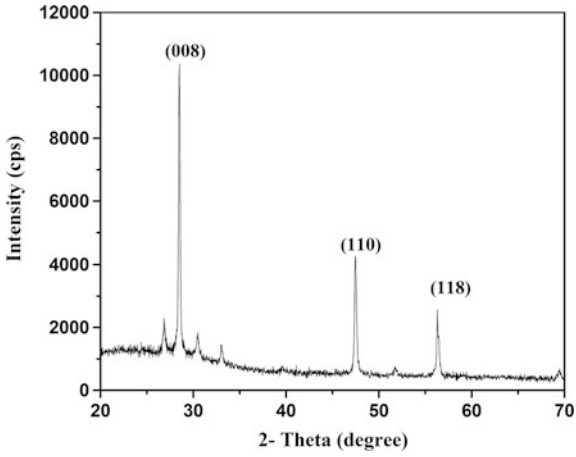

Fig. 1 X-ray diffraction pattern of ZnS NS

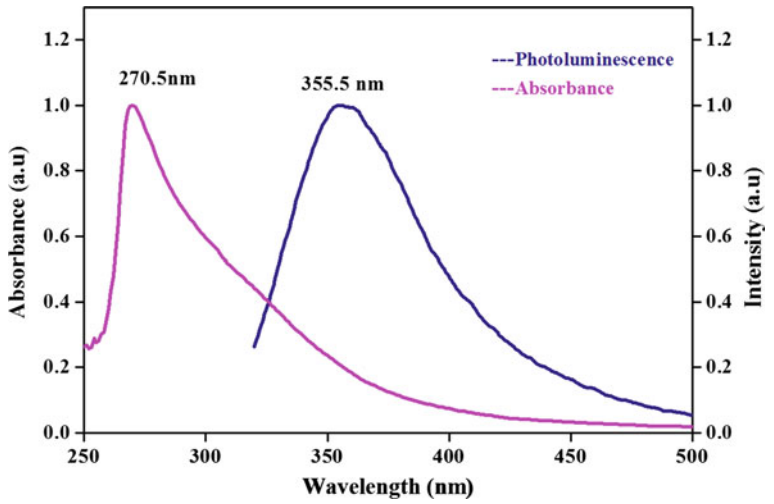

Fig. 2 Absorption and Photoluminescence spectra of ZnS/PVP

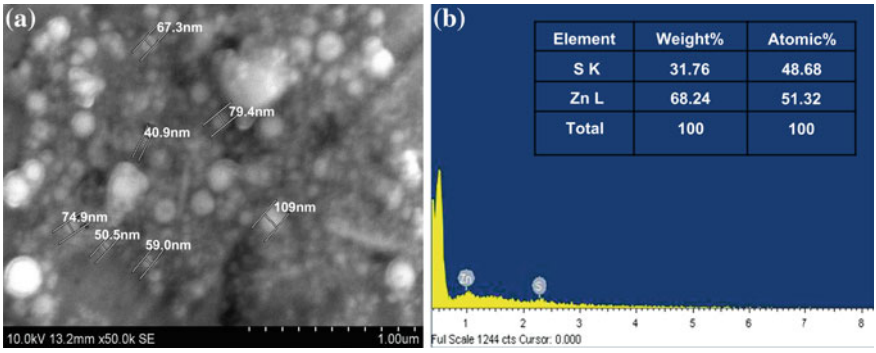

Fig. 3 **a** SEM image and **b** EDX spectrum of ZnS NS

Figure 3a, b represents the SEM image and EDX spectrum of the given sample which assures the formation of ZnS NS and the spherical morphology of the structure thus formed. The elemental concentration of the sample is given in the inset of EDX spectrum.

Figure 4 gives the TEM micrograph of the prepared NS. Some of the nanoparticles got agglomerated and hence form larger particles. The average size of the NS is found to be 28 nm and are in spherical shape. The difference in size obtained from the two characterizations may be due to the agglomeration of the nanoparticles [12].

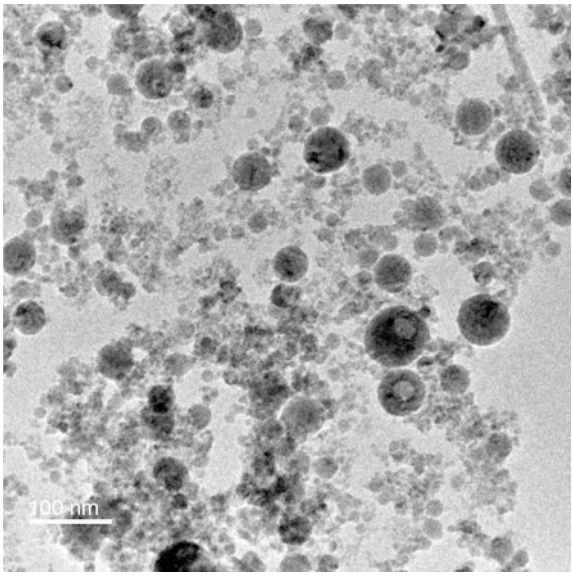

Fig. 4 TEM image of ZnS NS

Figure 6a, b shows the normalized Z-scan Open Aperture (OA) and Closed Aperture (CA) signatures of the sample at 50 μJ respectively. From the OA curve, it is clear that the transmission is symmetric about the focus (z = 0) where it has the minimum transmittance. Here the symbols correspond to experimental data which is exactly fitted with the theoretical model (solid line) for the saturable absorption associated with 2PA. From the linear absorption spectra, it is clear that sample has a maximum absorption peak at 270.5 nm which is around half the excitation wavelength used for Z-scan, and that shows the possibility of 2PA be the major nonlinear absorption mechanism. This is further confirmed by conducting open aperture Z-scan for the sample at different energies to find the variation of β_{eff} with on-axis input intensities (Fig. 7a). And from Fig. 7b it is clear that β_{eff} remains constant on increasing on-axis intensity, which also ensures 2PA as the absorption mechanism [13].

Figure 6a comprises the OA Z-scan curve, indicating the presence of nonlinear absorption. The nonlinear absorption coefficient is obtained to be 1.5×10^{-10} m W^{-1} by fitting the experimental data with the following corresponding equation for OA Z-scan.

$$T(z) = \frac{1}{\sqrt{\pi} q_0(z)} \int_{-\infty}^{\infty} \ln\left[1 + q_0(z) e^{-\tau^2}\right] d\tau$$

where $k = 2\pi/\lambda$ is the wave vector, I_0 is the on-axis irradiance of the laser beam at focus ($z = 0$), $q_0(z) = \beta_{eff} I_0 Leff/(1 + z^2/z_0^2)$, β_{eff} is the nonlinear absorption coefficient [14].

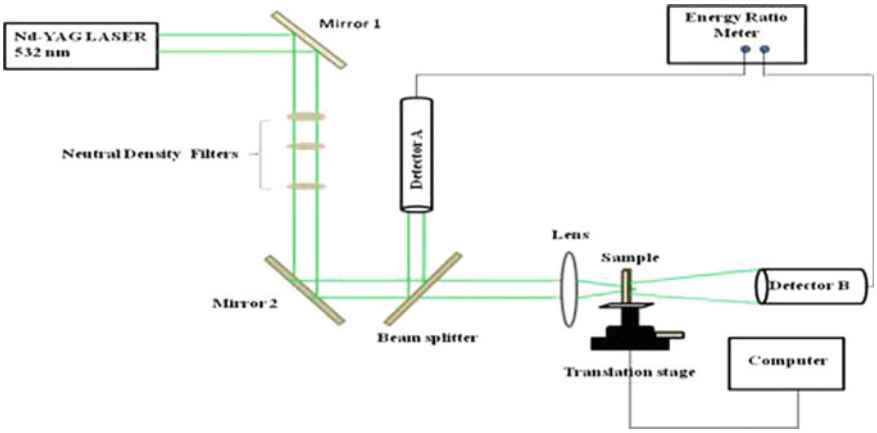

Fig. 5 Schematic diagram of the Z-scan experimental setup

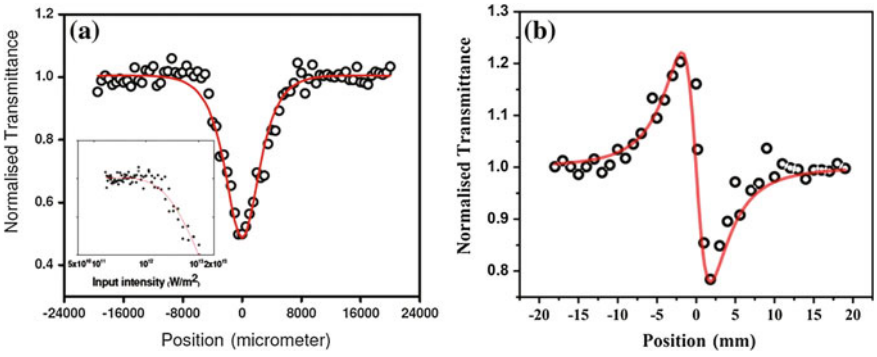

Fig. 6 **a** OA Z-scan of the ZnS NS, optical limiting graph is given in the *inset* **b** CA Z-scan divided by the OA Z-scan (C/O) of the ZnS NS

Figure 6b shows the pure nonlinear refraction curve for the sample at 50 μJ which is obtained by removing the nonlinear absorption component by division method. The curve exhibits a peak-valley configuration, indicating a negative nonlinear refractive index coefficient n_2, which characterizes the self-defocusing property of the sample. The nonlinear refractive index n_2 is calculated to be 4.1×10^{-11} m^2 W^{-1}, by fitting the following equation for the closed by open aperture [15].

$$T = 1 - \frac{4\Delta\phi_0\left(\frac{z}{z_0}\right)}{(1+(z/z_0)^2)(9+(z/z_0)^2)}$$

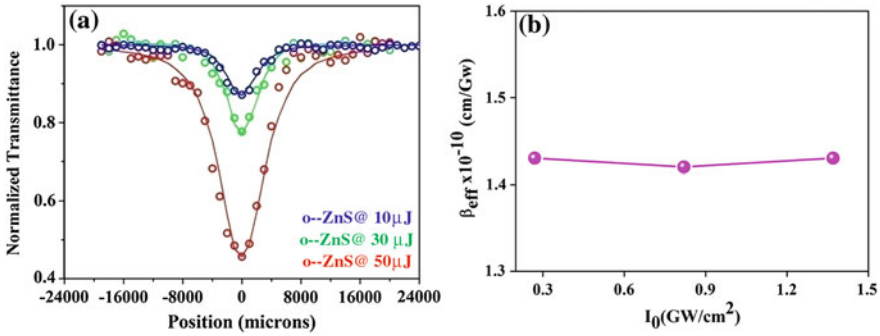

Fig. 7 **a** Normalized OA signatures of ZnS NS at different energies **b** β_{eff} versus on-axis intensity I_0

where T is the normalized transmittance for the pure refractive nonlinearity, $\Delta\phi_0$ is the on-axis nonlinear phase shift at the focus. The nonlinear refraction coefficient n_2 was calculated using the relation n_2 (esu) = [$cn_0/40\pi$] γ (m^2 W^{-1}). Where, $\gamma = \Delta\Phi_0\lambda/2\pi I_0 L_{eff}$, c is the velocity of the effective light in ms^{-1} and n_0 is the linear refractive index (n_0 = 1.4). Also L_{eff} = [1 − exp (−αL)]/α where, L is the sample length, α is the linear absorption coefficient (α = 3.6), z is the position of the sample. We obtained the saturation intensity I_{sat} to be 1.2×10^{12} W m^{-2}. The real and imaginary parts of the nonlinear susceptibility were calculated using the relations $\mathrm{Re}(\chi^{(3)}) = 2n_0^2\varepsilon_0 c\gamma$ and $\mathrm{Im}(\chi^{(3)}) = n_0^2\varepsilon_0 c\lambda\beta/2\pi$ [7]. The corresponding values were obtained as 4.2×10^{-13} esu and 4.72×10^{-12} esu. The magnitude of the nonlinear susceptibility was 4.74×10^{-12} esu, as the pure PVP/DMF solution showed very poor nonlinear optical properties on Z-scan analysis. The nonlinear refractive and absorptive coefficients show the good optical limiting properties of ZnS/PVP NS which can be applied in passive optical limiters, using for the protection of human eyes and optical sensors from laser beams [16] (Fig. 7).

4 Conclusion

ZnS NS in PVP/DMF solution were synthesized by laser ablation technique using a 532 nm Q-switched Nd:YAG laser. The absorption peak of the ZnS/PVP composite is blue shifted compared to bulk ZnS. The formation of ZnS NS was affirmed with XRD, SEM and TEM images. The PL spectrum indicates the optical quality of the sample. The values of nonlinear refractive index coefficient n_2, nonlinear absorption coefficient β_{eff}, and third order susceptibility $\chi^{(3)}$ were calculated using the Z-scan technique. The peak-valley signature obtained from CA Z-scan set up indicates the

negative nonlinear refractive index coefficient of the sample in effect its self-defocusing property. The ZnS NS in PVP/DMF shows good optical limiting property and can be applied in nonlinear optical devices.

Acknowledgements Authors are thankful to the Ministry of Human Resource and Development, India for providing necessary funds for the research work in time.

References

1. Dehghani, Z., Nazerdeylami, S., Saievar-Iranizad, E., Majles Ara, M.H.: Synthesis and investigation of nonlinear optical properties of semiconductor ZnS nanoparticles. J. Phys. Chem. Solids. **72**, 1008–1010 (2011)
2. Jun, G., Guanghui, S.: One-pot fast synthesis of spherical ZnS/Au nanocomposites and their optical properties. J. Mater. Sci. **48**, 636–643 (2013)
3. Fang, X., Zhai, T., Gautam, U.K.: ZnS nanostructures: from synthesis to applications. Prog. Mater Sci. **56**, 175–287 (2011)
4. Cunxiu, W., Liusan, G., Yanil, M.: Optical nonlinearity of ZnS-polyvinyl pyrrolidone nanocomposite suspension. J. Phys. D Appl. Phys. **42**, 45403 (2009)
5. Sudheesh, P., Siji Narendran, N.K., Chandrasekharan, K.: Third order nonlinear optical responses in derivatives of phenyl hydrazone by Z scan and optical limiting studies—influence of noble metal nanoparticles. Opt. Mater. **36**, 304–309 (2013)
6. Johannes, Z.M., Peter, A.A.: Preparation and characterization of ZnS, CdS and HgS/Poly (methylmethacrylate)Nanocomposites. Polym. J. **6**, 2332–2344 (2014)
7. Sheik-Bahae, M., Said, A.A., Wei, T.H., Hagan, D.J., Van Stryland, E.W.: Sensitive measurement of optical nonlinearities using a single beam. IEEE J. Quant Electron. **26**, 760–769 (1990)
8. Feijiu, W., Jie, L., Zhengjun, W., Ai-Jing, L., Hui, L., Xibin, Y.: Interfacial heterostructure phenomena of highly luminescent ZnS/ZnO quantum dots. J. Electrochem. Soc. **158**, 30–34 (2011)
9. Vijai Anand, K., Vinitha, G., Jayavel, V.: Enhanced third-order nonlinear optical properties of high purity ZnS nanoparticles. J. Nonlinear Optic. Phys. Mat. **24**, 1550016–1550027 (2015)
10. Lei, G., Su, C., Li, C.: Controllable synthesis of ZnS/PMMA nanocomposite hybrids generated from functionalized ZnS quantum dots nanocrystals. Colloid Polym. Sci. **285**, 1593–1600 (2007)
11. Dinsmore, A.D., Hsu, D.S., Gray, H.F., Qadri, S.B., Tian, Y., Ratna, B.R.: Mn-doped ZnS nanoparticles as efficient low-voltage cathodoluminescent phosphors. Appl. Phys. Lett. **75**, 802–804 (1999)
12. Sharma, M., Tripati, S.K.: Preparation and nonlinear characterization of zinc selenide nanoparticles embedded in polymer matrix. J. Phys. Chem. Solids **73**, 1075–1081 (2012)
13. Khatei, J., Suchand Sandeep, C.S., Reji, P., Koteswara Rao, K.S.R.: Near resonant two photon absorption in luminescent CdTe quatum dots. Appl. Phys. Lett. **100**, 81901 (2012)
14. Siji Narendranan, N.K., Rahul, S., Pranitha, S., Arunkumar, C., Chandrasekharan, K.: Ultrafast and short pulse optical nonlinearities of meso-tetrakis-(2,3,5,6-tetrafluoro-*N*,*N*,*N*-trimethyl-4-aniliniumyl) porphyrin and its metal complexes. Opt. Mater. **49**, 59–66 (2015)
15. Siji Narendran, N.K., Rahul, S., Arunkumar, C., Chandrasekharan, K.: Third-order nonlinear optical investigations of meso-tetrakis (2, 3, 5, 6-tetrafluoro-*N*,*N*-dimethyl-4-anilinyl) porphyrin and its metal complexes. Spectrochim. Acta Mol. Biomol. Spectros. **136**, 838–844 (2015)
16. Shirk, J.S.: Protecting the war fighter's vision in a laser-rich, battlefield environment. Opt Photon. News. **11**, 19–23 (2000)

Structural, Dielectric and Magnetic Properties of La Substituted $CoFe_2O_4$ Nanoparticles

M. Vadivel, R. Ramesh Babu, P. Selvakumar, M. Arivanandhan and K. Ramamurthi

Abstract We report the effect of lanthanum (La^{3+}) substitution on the physical properties of cobalt ferrite ($CoFe_2O_4$) magnetic nanoparticles by co-precipitation method. X-ray diffraction analysis reveals the formation of single phase cubic inverse spinel structure of $CoFe_2O_4$ and $CoFe_{1.9}La_{0.1}O_4$, and $CoFe_{2-x}La_xO_4$ ($0.2 < x < 0.5$) with a mixed impurity phase, $LaFeO_3$. Fourier transform infrared spectral analysis confirms the presence of Fe-O symmetrical stretching vibration at tetrahedral site. SEM studies reveal that the surface microstructure of $CoFe_2O_4$ nanoparticles was effectively modified by La^{3+} ion substitution. Energy dispersive spectral analysis confirms the presence of elements in the synthesized nanoparticles. Transmission electron microscopy studies reveal that the particle size increases with increasing La^{3+} ion concentrations. Dielectric properties reveal that the value of dielectric constant (ε') and dielectric loss (ε'') are gradually increases with increasing La^{3+} ion concentration as well as temperature. Magnetic measurement reveals that the saturation magnetization decreases from 61.45 to 25.13 emu/g with increasing La^{3+} ion concentrations.

M. Vadivel · R. Ramesh Babu (✉) · P. Selvakumar
Crystal Growth and Thin Film Laboratory, Department of Physics, Bharathidasan University, Tiruchirappalli 620024, Tamil Nadu, India
e-mail: rampap2k@yahoo.co.in

M. Arivanandhan
Centre for Nanoscience and Technology, Anna University, Chennai 600025, Tamil Nadu, India

K. Ramamurthi
Crystal Growth and Thin Film Laboratory, Department of Physics and Nanotechnology, Faculty of Engineering and Technology, SRM University, Kattankulathur 603203, Tamil Nadu, India

J. Ebenezar (ed.), *Recent Trends in Materials Science and Applications*, Springer Proceedings in Physics 189, DOI 10.1007/978-3-319-44890-9_18

1 Introduction

Over the past few years, greater attention has been focused on the synthesis and characterization of spinel ferrite magnetic nanomaterials due to their remarkable applications in high density information storage and microwave devices, etc. [1]. Cobalt ferrite ($CoFe_2O_4$) is one member of the ferrite family with remarkable material qualities such as moderate saturation magnetization (80 emu/g), high coercivity (5400 Oe) at room temperature, high electrical resistivity and high Curie temperature [2, 3]. Several synthetic techniques including co-precipitation [2, 4], oil-in-water [3], citrate-precursor [5, 6], micro-emulsion [7] have been adopted to prepare $CoFe_2O_4$ and substituted $CoFe_2O_4$ magnetic nanoparticles. Among these methods, co-precipitation has been widely used for the preparation of $CoFe_2O_4$ magnetic nanoparticles because of its simple experimental arrangement, low cost and relatively high production rate.

It is well known that the substitution of transition metal and rare earth metal cations in spinel $CoFe_2O_4$ system plays an important role to tailor the physico-chemical properties of material. In particular, the substitution of rare earth metal cation in $CoFe_2O_4$ system produces a remarkable change in its magnetic behavior due to the variation in magnetic moment from 0 (La^{3+}) to 10.5 μ_B (Dy^{3+}) [5]. Hence, several researchers have been investigated the importance of rare earth cation substitution in $CoFe_2O_4$ system for various significant and prospective applications [8–14]. Among the rare earth cations, lanthanum (La^{3+}) is one of the potential candidates in tuning the structural, dielectric and magnetic properties of a material because of its larger ionic radius (0.103 nm) [5]. Kumar et al. [2] and ur Rahman et al. [14] reported that the change in dielectric behaviour for different concentrations of La^{3+} substitution in $CoFe_2O_4$ nanoparticles by chemical co-precipitation method. But, no research article has been focused on the change in dielectric properties for various temperatures in La^{3+} substituted $CoFe_2O_4$ nanoparticles by co-precipitation method. Keeping all these things in mind, in the present communication, La^{3+} substituted $CoFe_2O_4$ magnetic nanoparticles were prepared for various La^{3+} ion concentrations ($CoFe_{2-x}La_xO_4$; $0 < x < 0.5$, step 0.1) by co-precipitation method and their physical and chemical properties are investigated.

2 Experimental Details

2.1 Synthesis of $CoFe_{2-X}La_xO_4$ Nanoparticles

Iron (III) chloride hexahydrate ($FeCl_3 \cdot 6H_2O$, Merck, 99 %), cobalt (II) chloride hexahydrate ($CoCl_2 \cdot 6H_2O$, Merck, 98 %), lanthanum (III) chloride heptahydrate ($LaCl_3 \cdot 7H_2O$, Sigma Aldrich, 99.99 %) and sodium hydroxide (NaOH, Merck, 97 %) were purchased and used as received. NaOH and double distilled water

was used as precipitation agent and solvent, respectively for the preparation of $CoFe_{2-x}La_xO_4$ nanoparticles.

The experimental details for the preparation of pure $CoFe_2O_4$ nanoparticles by co-precipitation method were discussed elsewhere [15]. For the preparation of La^{3+} substituted $CoFe_2O_4$ nanoparticles ($CoFe_{2-x}La_xO_4$), 0.4 M iron (III) chloride hexahydrate, 0.2 M cobalt (II) chloride hexahydrate and 0.2 M lanthanum (III) chloride heptahydrate ($0 < x < 0.5$, step 0.1) were dissolved in double distilled water and the chloride mixture solutions were stirred vigorously at room temperature for 30 min. After that, 3 M NaOH pellets were dissolved in double distilled water and it was added dropwise into the prepared chloride solution. Due to the dropwise addition of NaOH, the precipitation was occurred immediately and then the net solution mixture was stirred at 80 °C for 3 h. After completion of the reaction process, the black color precipitated particles were collected and washed thoroughly using double distilled water with ethanol. Then the synthesized nanoparticles were dried at 50 °C in oven for 24 h and then annealed at 600 °C for further characterization studies.

2.2 Characterization

The crystalline phase and functional groups of the synthesized nanoparticles were confirmed by X-ray diffraction (XRD) (Rigaku Ultima III X-ray diffractometer) and Fourier transform infrared (FTIR) spectroscopy (JASCO 460 plus) analyses, respectively. Surface morphology and chemical composition were studied by scanning electron microscopy (SEM) (JEOL JSM-6390) and energy dispersive spectral analyses, respectively. Size of the nanoparticles was analyzed by JEOL JEM-2100F transmission electron microscopy (TEM) study with an accelerating voltage of 200 kV. Vibrating sample magnetometer (VSM) analysis was carried out by Lakeshore-7404 with a maximum magnetic field of ±15 kOe. The dielectric constant (ε') and dielectric loss (ε'') were recorded using HIOKI 3532-50 LCR HiTESTER as a function of frequency (100 Hz–1 MHz) and temperature (room temperature—100 °C). In order to record the dielectric behaviour, 1 mm thickness and 13 mm diameter pellets were used and the value of dielectric constant ε' and dielectric loss ε'' can be calculated using the relation $\varepsilon' = Cd/(\varepsilon_0 A)$ and $\varepsilon'' = \varepsilon' D$, respectively, where A, C and d is the area, capacitance and thickness of the pellet, respectively and ε_0 is the dielectric permittivity of free space and D is the dissipation factor.

3 Results and Discussion

3.1 X-ray Diffraction Analysis

The X-ray diffraction patterns of $CoFe_{2-x}La_xO_4$ ($0 < x < 0.5$, step 0.1) nanoparticles is shown in Fig. 1. As can be seen from Fig. 1, the presence of all the diffracted peaks of $CoFe_2O_4$ and $CoFe_{1.9}La_{0.1}O_4$ nanoparticles confirms the formation of the cubic inverse spinel structure. $CoFe_{1.8}La_{0.2}O_4$, $CoFe_{1.7}La_{0.3}O_4$, $CoFe_{1.6}La_{0.4}O_4$ and $CoFe_{1.5}La_{0.5}O_4$ are formed with a mixed impurity phase of $LaFeO_3$ which may due to the large difference in ionic radius between Fe^{3+} (0.064 nm) and La^{3+} (0.103 nm) ions [10]. The weight percentage of $CoFe_2O_4$ and $LaFeO_3$ phases was calculated using the following relation [16]

$$W_A = \left(\frac{I_A}{I_A + I_B}\right) \times 100$$

$$W_B = \left(\frac{I_B}{I_A + I_B}\right) \times 100$$

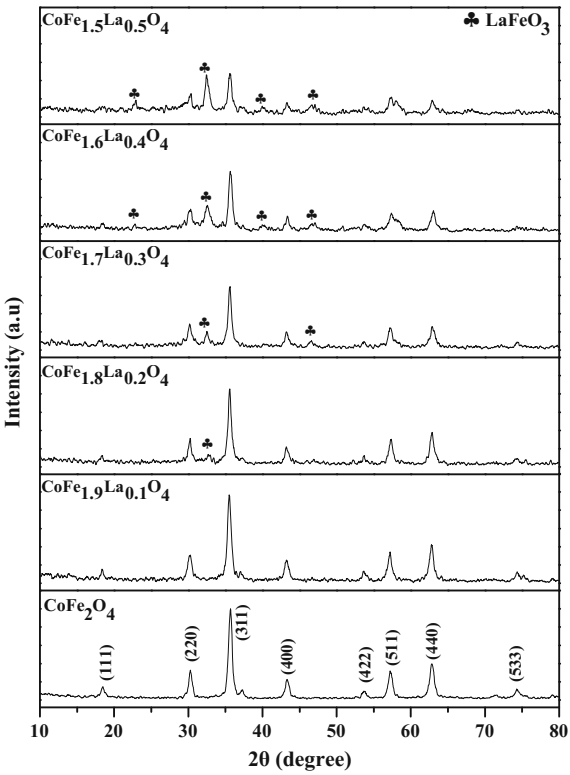

Fig. 1 XRD pattern of $CoFe_{2-x}La_xO_4$ ($0 < x < 0.5$, step 0.1) nanoparticles

where, W_A and W_B are the weight percentages of $CoFe_2O_4$ and $LaFeO_3$ phases, respectively. I_A and I_B are the sum integrated intensity of $CoFe_2O_4$ and $LaFeO_3$ phases, respectively. The calculated weight percentages of $CoFe_2O_4$ and $LaFeO_3$ phases are determined to be 92.40 and 7.60, 87.64 and 12.36, 81.00 and 19.00 and 80.00 and 20.00 for 0.2, 0.3, 0.4 and 0.5 concentrations, respectively. Rahman et al. [17] reported the formation of $GdFeO_3$ as secondary phase in Gd substituted $CoFe_2O_4$ nanoparticles with increasing Gd^{3+} ion concentrations. Further, in the present work, the observed slight variation in the diffracted peak position with increasing La^{3+} ion concentrations indicates that the strain induced in $CoFe_2O_4$ lattice because of its higher ionic radius. The diffracted peak intensity also decreases with increasing La^{3+} ion concentration which indicates that the crystallinity of the prepared nanoparticles decreases by the substitution of La^{3+} ion.

From XRD results, the average crystallite size, lattice constant, unit cell volume, X-ray density, measured density, porosity, hopping length at tetrahedral site and hopping length at octahedral site were calculated and the values are presented in Table 1. From fullwidth at halfmaximum value, the average crystallite size is calculated for (311) diffracted peak using Debye-Scherrer's formula $t = k\lambda/(\beta \cos\theta)$, where k is a constant, λ is the wavelength of X-rays used, θ is the diffraction angle and β is the fullwidth at halfmaximum of the appropriate diffraction peak. The obtained result implies that the crystallite size increases by increasing La^{3+} ion concentrations. The lattice constant a was calculated from (311) peak using the relation $a = d\sqrt{h^2 + k^2 + l^2}$, where d is the interplanar distance and (hkl) are the Miller indices. The obtained results indicate that the lattice constant increases with increasing La^{3+} ion concentrations which may be caused by the lattice distortion when substituted the higher ionic radius materials. Kumar et al. [4] and Peng et al. [10] reported the similar behaviour in La^{3+} and Gd^{3+} substituted $CoFe_2O_4$ nanoparticles by co-precipitation and hydrothermal method, respectively. Moreover, density of the samples (d_x) was calculated using the relation $d_x = 8M/NV$, where, 8 is the number of molecules per unit cell and N, M and V is the Avogadro's number, molecular weight and volume of the unit cell, respectively. The obtained results reveal that the X-ray density linearly increases with increasing La^{3+} ion concentrations. Using the Archimedes principle, the measured density was calculated and the obtained results show that the measured density increases with increasing La^{3+} ion concentrations. Porosity was calculated using the values of X-ray density and measured density which show an increasing trend with increasing La^{3+} ion concentrations. Hopping length for tetrahedral (L_A) and octahedral (L_B) sites was calculated using the following relation, $L_A = a\sqrt{3/4}$ and $L_B = a\sqrt{2/4}$ and the calculated values are given in Table 1 and it is concluded that the hopping length of L_A and L_B varies directly with lattice constant.

Table 1 Parameters calculated from XRD studies for $CoFe_{2-x}La_xO_4$ nanoparticles

Composition	Crystallite size t_{311} (nm)	Lattice constant a (Å)	Unit cell volume V_{cell} (Å^3)	X-ray density d_x (g cm^{-3})	Measured density d_m (g cm^{-3})	Porosity p (%)	Hopping length at tetrahedral site L_A (nm)	Hopping length at octahedral site L_B (nm)
$CoFe_2O_4$	15	8.3811	588.7	5.294	3.874	27	3.629	2.963
$CoFe_{1.9}La_{0.1}O_4$	15	8.3847	589.4	5.475	4.090	25	3.630	2.964
$CoFe_{1.8}La_{0.2}O_4$	17	8.3903	590.6	5.650	4.169	26	3.632	2.966
$CoFe_{1.7}La_{0.3}O_4$	18	8.3953	591.7	5.827	4.282	27	3.635	2.968
$CoFe_{1.6}La_{0.4}O_4$	15	8.4059	593.9	5.990	4.336	28	3.639	2.971
$CoFe_{1.5}La_{0.5}O_4$	18	8.4162	596.1	6.154	4.526	26	3.644	2.975

3.2 FT-IR Spectral Analysis

FTIR spectra of the prepared nanoparticles annealed at 600 °C with x = 0.0, 0.1, 0.2, 0.3, 0.4 and 0.5 compositions are shown in Fig. 2. In general, two main metal oxygen bands are observed in all spinel structures below 1000 cm^{-1} which represents the presence of tetrahedral and octahedral vibrations [9]. In the present work, a strong and sharp absorption peak observed at 587 cm^{-1} confirms the formation of Fe-O symmetrical stretching vibration at tetrahedral site.

The vibrational peaks observed at 3423 and 1624 cm^{-1} suggests the presence of O-H bending and H-O-H stretching vibrations, respectively. Furthermore, the vibrational frequency observed at tetrahedral site has slightly shifted towards higher frequency region (from 587 to 602 cm^{-1}) with increasing the La^{3+} ion concentrations which is due to the change in cation-oxygen bond length between the tetrahedral and octahedral site.

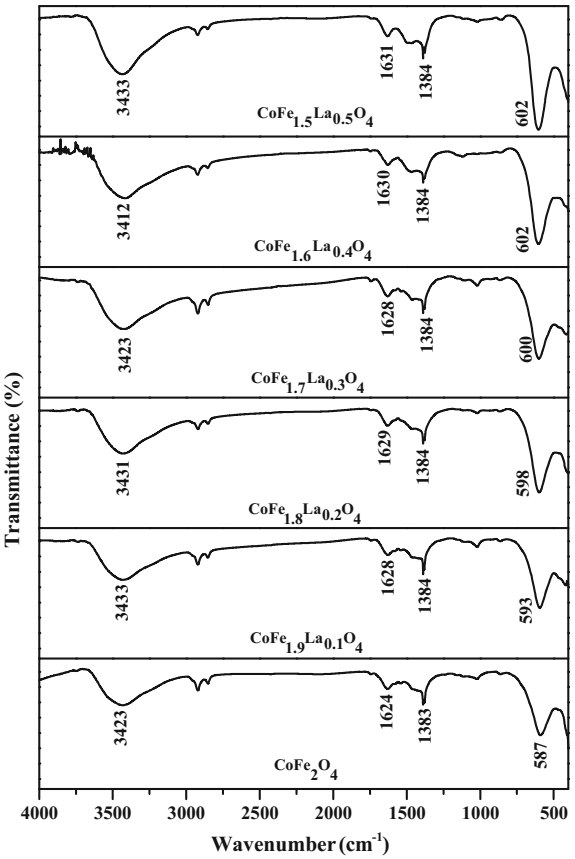

Fig. 2 FTIR spectra of $CoFe_{2-x}La_xO_4$ (x = 0.0, 0.1, 0.2, 0.3, 0.4 and 0.5) nanoparticles

3.3 SEM and EDS Spectral Analyses

SEM and EDS images of $CoFe_{2-x}La_xO_4$ with selected compositions (x = 0.0, 0.2 and 0.5) are shown in Figs. 3a–f. From SEM micrographs (Fig. 3a), it can be clearly observed that the microstructure of the prepared $CoFe_2O_4$ nanoparticles show a flake like structure with small agglomeration and the particles seems to be irregular in shape on the surface. But, by the introduction of La^{3+} ion in $CoFe_2O_4$ crystal lattice, the size of the particles modified significantly and the particles observed on the surface show regular in shape (Figs. 3b, c).

From EDS measurement, it is confirmed that no impurity detected in the synthesized nanoparticles and the observed weight and atomic percentage of Co, Fe, O and La elements are shown in table format in the inset of EDS spectra (Figs. 3d–f).

3.4 TEM Measurements

Figure 4 displays the TEM images of $CoFe_2O_4$, $CoFe_{1.9}La_{0.1}O_4$, $CoFe_{1.7}La_{0.3}O_4$ and $CoFe_{1.5}La_{0.5}O_4$ nanoparticles and their corresponding histogram images are shown in the inset of Fig. 4.

From TEM image of pure $CoFe_2O_4$ nanoparticles (Fig. 4a), it is observed that the presence of particles on the surface consists of regular grains with some agglomeration. The presence of agglomeration is due to high temperature annealing (600 °C) and interaction between the magnetic nanoparticles [15]. It is also interesting to note

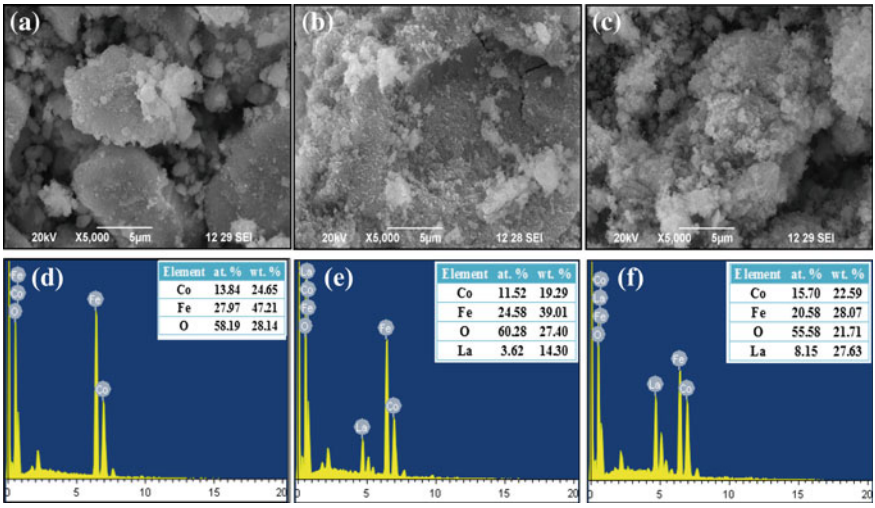

Fig. 3 SEM and EDS images of $CoFe_{2-x}La_xO_4$ nanoparticles with x = 0.0 (**a**, **d**), x = 0.2 (**b**, **e**), and x = 0.5 (**c**, **f**), respectively

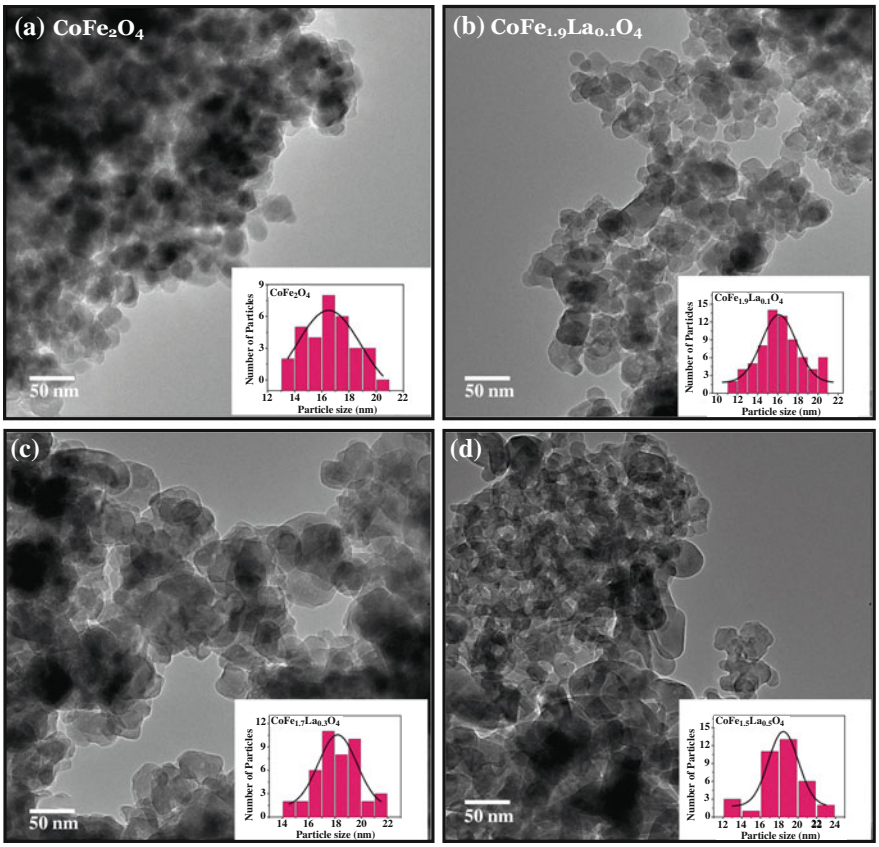

Fig. 4 TEM images of $CoFe_{2-x}La_xO_4$ (**a** x = 0.0, **b** 0.1, **c** 0.3 and **d** 0.5) nanoparticles

that the substitution of La^{3+} ion induces a considerable change in its microstructure and it has greatly influenced the size of the synthesized nanoparticles (Fig. 4b–d). From TEM measurements, the average particle size was calculated for the particles that are separated from each other and the calculated values of $CoFe_2O_4$, $CoFe_{1.9}La_{0.1}O_4$, $CoFe_{1.7}La_{0.3}O_4$ and $CoFe_{1.5}La_{0.5}O_4$ nanoparticles are found to be 16.4, 16.0, 18.2 and 18.4 nm, respectively. The increase in particle size with increasing La^{3+} ion concentrations designates the ionic difference between La^{3+} and Fe^{3+} ions. The particle size obtained from TEM results is well agreed with the crystallite size calculated from XRD investigation.

3.5 Dielectric Properties

Figure 5a illustrates the frequency dependence dielectric constant (ε′) for various La^{3+} ion concentrations which reveals that the dielectric constant is very high at lower frequency region whereas it gradually decreases with increasing frequency and reaches a minimum value at higher frequency region [1]. Such kind of variation can be explained using Maxwell-Wagner and Koop's phenomenological theory [14, 17]. They have explained that the dielectric materials consist of well conducting grains and are separated by poorly conducting grain boundaries. The higher value of dielectric constant at lower frequency region due to high resistive grain boundaries whereas the decrease in dielectric constant at higher frequency is attributed to the low resistive grains. Moreover, the large value of dielectric constant at lower frequency region may be the presence of four types of polarizations such as space charge, electronic, ionic and dipolar polarizations [1, 14].

Moreover, from the figure, it can be clearly observed that the dielectric constant found to increase with increasing La^{3+} ion concentrations which can be explained by the following reasons. The incorporation of La^{3+} ion in Fe^{3+} site of $CoFe_2O_4$ nanoparticles induces the lattice distortion and increased bond length at octahedral B site because of its larger ionic radius when compared with that of Fe^{3+} ions. The variation in lattice expansion is also observed in XRD analysis. The formation of $LaFeO_3$ mixed phase (x = 0.2–0.5) at the grain boundaries may enhances the space charge polarization and hence the enhanced dielectric constant [18–20]. Figure 5b explains the variation of dielectric loss (ε″) for various La^{3+} ion concentrations. The obtained results exhibit the similar behaviour as in the case of dielectric constant.

The change in dielectric constant with frequency for various temperatures is shown in Fig. 6a–f. The observed results reveal that the dielectric constant initially increases very slowly for lower temperatures whereas increases rapidly at higher temperatures. The change in behaviour can be explained as follows: at low

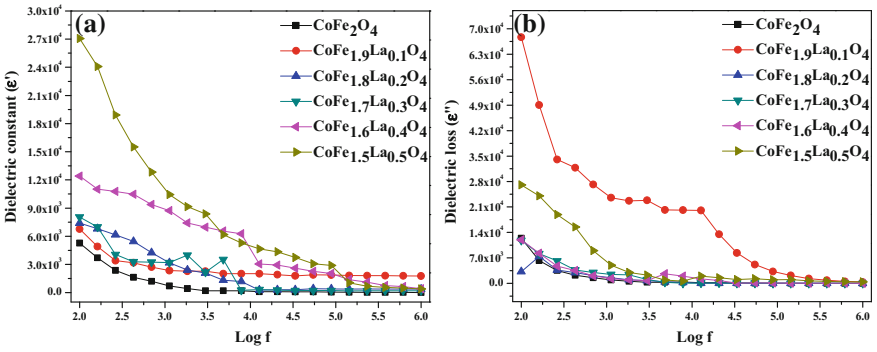

Fig. 5 **a** Variation of dielectric constant (ε′) as a function of frequency in $CoFe_{2-x}La_xO_4$. **b** Variation of dielectric loss (ε″) as a function of frequency in $CoFe_{2-x}La_xO_4$

temperatures, dipole cannot orient themselves with respect to the direction of the applied electric field and hence it has low dielectric constant value whereas at higher temperatures the bound charge carriers gets liberated and thus enhances the dielectric constant [1, 15, 19]. Inset of Fig. 6a–f show the variation of dielectric constant for various temperatures at 100 Hz which reveals that the dielectric constant gradually increases with increasing temperature.

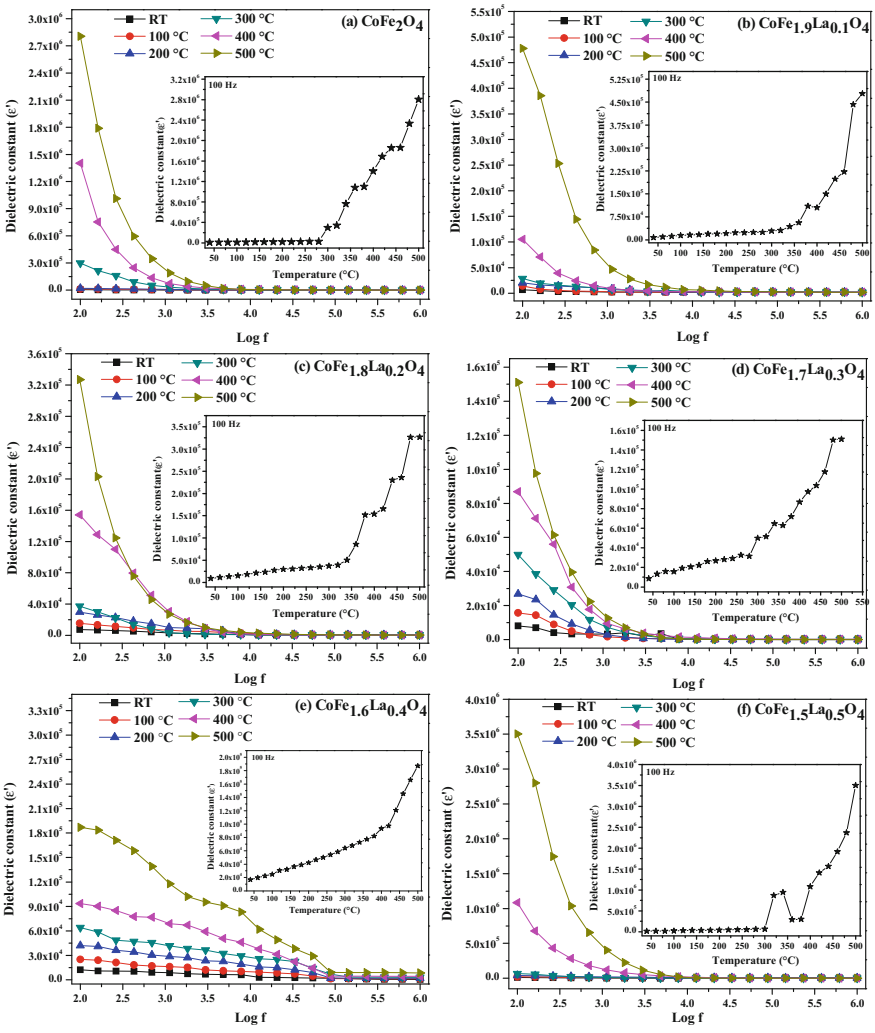

Fig. 6 **(a)–(f)** Frequency dependent dielectric constant at different temperatures for the prepared $CoFe_{2-x}La_xO_4$ ($0 < x < 0.5$, step 0.1) nanoparticles. *Inset* Dielectric constant as a function of temperatures at 100 Hz

The dielectric loss of $CoFe_{2-x}La_xO_4$ nanoparticles is also exhibits the similar profile as observed in the dielectric constant and the obtained results are shown in Fig. 7a–f. Inset of Fig. 7a–f shows the variation of dielectric loss as a function of temperature at 100 Hz which is also exhibit the similar trend as observed in the dielectric constant.

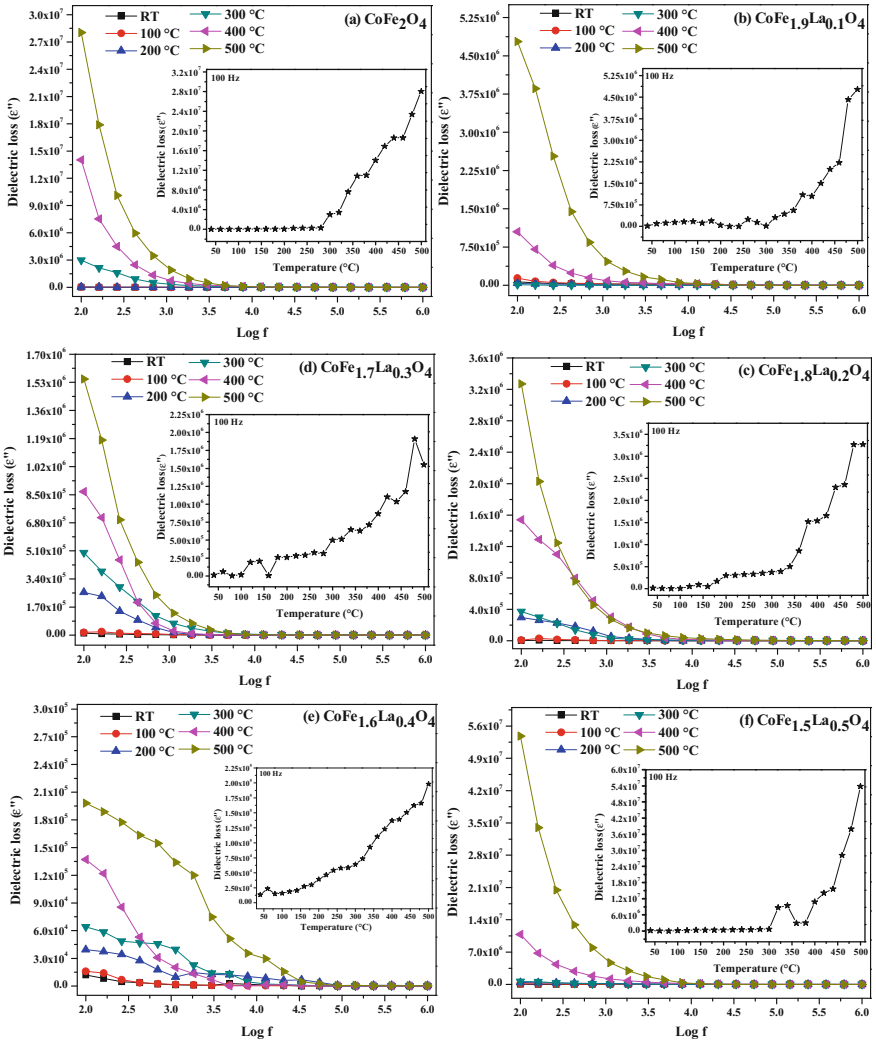

Fig. 7 **(a)–(f)** Frequency dependent dielectric loss at different temperatures for the prepared $CoFe_{2-x}La_xO_4$ ($0 < x < 0.5$, step 0.1) nanoparticles. *Inset* Dielectric loss as a function of temperatures at 100 Hz

3.6 VSM Measurements

Figure 8 displays the room temperature hysteresis loop of $CoFe_{2-x}La_xO_4$ ($0 < x < 0.5$, step 0.1) nanoparticles. From the results one can obtain the information about the saturation magnetization (M_s), coercivity (H_c) and remanent magnetization (M_r) value of the samples and the values are shown in Table 2.

Table 2 clearly points out that the M_s value gradually decreases with increasing La^{3+} ion concentrations. Generally, the decrease in M_s with increasing dopant concentration can be explained by the following aspects. In spinel ferrite system, M_s is strongly depends upon the super-exchange interactions between the tetrahedral (A) and octahedral (B) site cations. But, in the present work, the substitution of non magnetic La^{3+} ion in Fe^{3+} site reduces the magnetic interaction between the tetrahedral and octahedral sites and thus weakening the super-exchange interaction with increasing La^{3+} ion concentrations. On the other hand, the decrease in M_s with increasing La^{3+} ion concentrations is due to the zero magnetic moment of La^{3+} (0 μB) ion when compared with Fe^{3+} (5 μB) ion [2–6]. Moreover, coercivity, remanence magnetization and magneton number decreases up to $x = 0.4$, and thereafter increases for $x = 0.5$ concentration. The variation in H_c with increasing La^{3+} ion concentrations can be explained by the value of magnetocrystalline anisotropy of the materials and it can be calculated using the relation $K = M_s H_c / 0.98$ [9] and the values are given in Table 2. The magneton number was calculated using the relation, $n_B = M_w \times M_s / 5585$ [9], where, M_w and M_s represents the molecular weight and saturation magnetization of the corresponding materials, respectively, which reveal that the n_B decreases with increasing La^{3+} ion concentrations which may be attributed to the reduction in super-exchange interaction between the tetrahedral (A) and octahedral (B) sites.

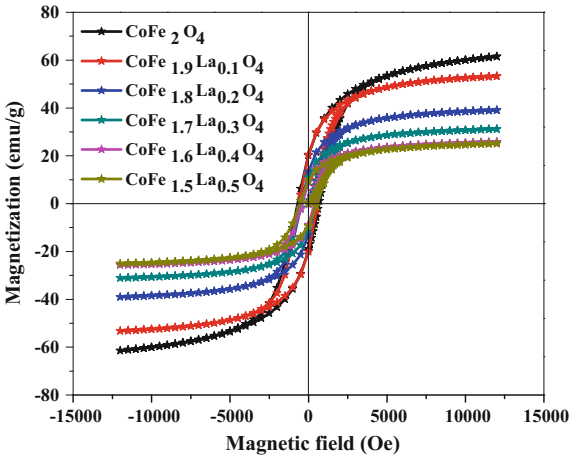

Fig. 8 Magnetic hysteresis loops of $CoFe_{2-x}La_xO_4$ nanoparticles at room temperature

Table 2 Observed and calculated magnetic values of $CoFe_{2-x}La_xO_4$ nanoparticles

Composition	Saturation magnetization M_s (emu/g)	Coercivity H_c (Oe)	Remanent magnetization M_r (emu/g)	Remanence ratio M_r/M_s	Magneton number n_B	Magnetocrystalline anisotropy constant $K \times 10^4$ (erg/g)
$CoFe_2O_4$	61.45	681.04	20.02	0.326	2.581	4.359
$CoFe_{1.9}La_{0.1}O_4$	53.26	585.10	20.24	0.380	2.317	3.246
$CoFe_{1.8}La_{0.2}O_4$	39.04	436.60	13.13	0.336	1.756	1.776
$CoFe_{1.7}La_{0.3}O_4$	31.11	428.02	10.87	0.349	1.446	1.387
$CoFe_{1.6}La_{0.4}O_4$	25.72	395.13	8.88	0.345	1.233	1.059
$CoFe_{1.5}La_{0.5}O_4$	25.13	558.64	9.49	0.378	1.242	1.462

4 Conclusion

In summary, $CoFe_{2-x}La_xO_4$ magnetic nanoparticles were successfully synthesized by chemical co-precipitation method for various La^{3+} ion concentrations. XRD analysis indicates that the lattice constant gradually increases with increasing La^{3+} ion concentrations. FTIR spectral analysis confirms the Fe-O symmetrical stretching vibration of $CoFe_{2-x}La_xO_4$ nanoparticles. Size of the particles was considerably influenced by La^{3+} ion substitution. Dielectric constant significantly enhanced by the substitution of La^{3+} ion. Saturation magnetization gradually decreases with increasing La^{3+} ion concentration which is due to the zero magnetic moment of La^{3+} ion and thus weakening the super-exchange interaction between tetrahedral (A) and octahedral (B) sites.

Acknowledgements One of the authors M. Vadivel is thankful to UGC-BSR, Government of India for the award of 'Research Fellowship in Science for Meritorious Students-2013 [File No. F.7-197/2007(BSR)]'. The authors are thankful to School of Physics, Bharathidasan University, Tiruchirappalli for extending FTIR facility.

References

1. Nongjai, R., Khan, S., Asokan, K., Ahmed, H., Khan, I.: J. Appl. Phys. **112**, 084321 (2012)
2. Kumar, P., Sharma, S.K., Knobel, M., Singh, M.: J. Alloys Compd. **508**, 115 (2010)
3. Kahn, M.L., Zhang, Z.J.: Appl. Phys. Lett. **78**, 3651 (2001)
4. Kumar, P., Sharma, S.K., Knobel, M., Chand, J., Singh, M.: J. Electroceram. **27**, 51 (2011)
5. Kumar, L., Kar, M.: Ceram. Int. **38**, 4771 (2012)
6. Kumar, L., Kumar, P., Kar, M.: Phys. B **448**, 38 (2014)
7. Burianova, S., Vejpravova, J.P., Holec, P., Plocek, J., Niznansky, D.: J. Appl. Phys. **110**, 073902 (2011)
8. Naik, S.R., Salker, A.V.: J. Mater. Chem. **22**, 2740 (2012)
9. Kambale, R.C., Song, K.M., Koo, Y.S., Hur, N.: J. Appl. Phys. **110**, 053910 (2011)
10. Peng, J., Hojamberdiev, M., Xu, Y., Cao, B., Wang, J., Wu, H.: J. Magn. Magn. Mater. **323**, 133 (2011)
11. Guo, L., Shen, X., Song, F., Lina, L., Zhu, Y.: Mater. Chem. Phys. **129**, 943 (2011)
12. Pant, R.P., Arora, M., Kaur, B., Kumar, V., Kumar, A.: J. Magn. Magn. Mater. **322**, 3688 (2010)
13. Kumar, P., Chand, J., Singh, M.: Integr. Ferroelectr. **134**, 53 (2012)
14. ur Rahman, A., Rafiq, M.A., Karim, S., Maaz, K., Siddique, M., Hasan, M.M.: Physica B **406**, 4393 (2011)
15. Vadivel, M., Ramesh Babu, R., Sethuraman, K., Ramamurthi, K., Arivanandhan, M., J. Magn. Magn. Mater. **362**, 122 (2014)
16. Low, I.M., Albetran, H., De La Prida, V., Manurung, P., Ionescu, M., Effect of Chromium doping on the crystallization and phase stability in anodized TiO_2 nanotubes. In: Kriven, W. M., Gyekenyesi, A.L., Westin, G., Wang, J (eds.), pp. 152. Wiley, New Jersey (2013)
17. Rahman, MdT, Vargas, M., Ramana, C.V.: J. Alloys Compd. **617**, 547 (2014)
18. Bharathi, K.K., Markandeyulu, G.: J. Appl. Phys. **103**, 07E309 (2008)
19. Kolekar, Y.D., Sanchez, L.J., Ramana, C.V.: J. Appl. Phys. **115**, 144106 (2014)
20. Ramana, C.V., Kolekar, Y.D., Bharathi, K.K., Sinha, B., Ghosh, K.: J. Appl. Phys. **114**, 183907 (2013)

Synthesis and Characterization of Nano Hydroxyapatite with Guar Gum Composites

K. Senthilarasan, P. Sakthivel and A. Ragu

Abstract Hydroxyapatite with Guar Gum (HAp/GG) composites was synthesized by wet chemical method. Di ammonium hydrogen phosphate, calcium hydroxide and guar gum were used as starting materials. The powder sample was characterized by the Fourier Transform infra-red (FTIR), Transmission electron microscope (TEM), Thermal gravimetric analysis, X-ray diffraction, antibacterial activity and anti-inflammatory test. With respect to the result achieved from the above analysis, it was found that nano hydorxyapatite with guar gum composite can successfully be produced through the wet chemical precipitation method. TEM technique demonstrated that the powder were nano sized and had a rod-like morphology. FTIR reveals the functional groups. XRD pattern illustrate the crystallite size and lattice parameter values. Antibacterial activity exhibits the activity in *Escherichia coli* and *Staphylococcus aureus* bacteria.

1 Introduction

Hydroxyapatite (HAp) are particularly attractive materials for bone and tooth implants since they closely resembles human tooth and bone mineral and have proved to be biologically compatible with these tissues [1]. HAp ceramics show no toxicity, inflammatory response, pyrogenic response or fibrous tissue formation between implant and bone, also, these materials have the ability to bond directly to the host bone [2]. Hydroxyapatite, on the other hand, has high bioactivity, with many medical applications in the form of porous, dense, granules and as coating [3]. The development of modern medical science has improved biomaterials role in replacing damaged tissue, organs and improving their functions. Hydroxyapatite one of the apatite minerals with a chemical formula of $Ca_{10}(PO_4)_6OH_2$ is a major inorganic constituent about 60–70 % of the inorganic portion of the bone matrix

K. Senthilarasan · P. Sakthivel (✉) · A. Ragu
Department of Physics, Urumu Dhanalakshmi College,
Kattur, Tiruchirappalli 620019, Tamilnadu, India
e-mail: sakthiphy13@gmail.com

J. Ebenezar (ed.), *Recent Trends in Materials Science and Applications*,
Springer Proceedings in Physics 189, DOI 10.1007/978-3-319-44890-9_19

and possesses the high ability of ion-exchange against various cations which make that HAp has high biocompatibility and bio activity properties [4]. In recent years, the development and utilization of polysaccharide isolated from natural sources have attracted increasing attention in biochemistry and pharmacology, due to their sustainability, ground endosperm of the seed of the guar plant, *Cyamopsis tetragonaloba* (L) Taub. (Syn. *Cyamopsis psoralodies*) [5]. Guar gum is high molecular weight carbohydrate polymer, has the characteristic of being rigid and non-ionic. It consists of (1,4)-β-D-manno-pyranosyl units with α-D-galacto-Pyranosyl units attached by 1,6 linkage [6]. It is used to paper industry, food industry. Ceramic industry and pharmaceutical industry, cosmetic industry [7].

2 Experimental Details

2.1 Materials

The raw materials required to start the processing of the composite were: calcium hydroxide $Ca(OH)_2$ and Ammonium dihydrogen phosphate $(NH_4)_2{\cdot}PO_4$ were obtained from Merk(India). Guar gum was purchased from Loba(India). Ethanol and double distilled water were used as the solvent.

2.2 Synthesis of Nano HAp

Nano HAp was synthesized by following a modified wet chemical method. At room temperature, 5.56 g of calcium hydroxide was dissolved in a ethanol-water mixed solution and stirred for 4 h. A solution of 6.7 g Ammonium dihydrogen phosphate was dissolved in a 100 ml volume of water and then added to the $Ca(OH)_2$ solution over a period of 24 h. The liquid products were then subjected to Microwave exposure for various timings under trial and error method. The products were grained by mortar vessel to se get fine products nano composite.

2.3 Synthesis of nHAp with Guar Gum

Guar gum was dissolved in double distilled water and purified by filtering the sample several times. Then added suitable amount nHAp/GG periodically by keeping it a mechanical stirrer. The products were dried using by Microwave oven and Final products were obtained.

3 Characterization

3.1 FTIR

The Fourier transform infrared (FTIR) spectra were recorded on a Perkin Elmer spectrometer, in the range of 400–4000 cm^{-1}.

3.2 XRD

X-ray diffraction studies of the powder product were carried out for phase identification using XRD Rigaku with monochromatic CuKα radiation (λ = 0.15405 nm). The sample were scanned in the Bragg angle, 2θ range from 10° to 90°.

3.3 TEM

Transmission Electron Microscope (TEM) experiments were performed on a Tecnai T20 electron microscope with an acceleration voltage of 200 kV.

3.4 Thermal Analysis

Thermogravimetric analysis (TGA) and Differential thermal analysis (DTA) studied were performed on a Perkin-Elmer instrument from 30 to 800 °C at a heating rate of 25 °C/min.

3.5 Anti Microbial Activity

This test was carried out according to disc diffusion method [8, 9] using plant extracts. *Escherichia coli* and *Staphylococcus aureus* specie of bacteria were spread on nutrient agar plates for bacteria. Using sterile forceps, the sterile filter papers containing the crude extracts (50, 100, 150 µl) were laid down on the surface of inoculated agar plate. The plates were incubated at 37 °C for 24 h for the bacteria and at room temperature (30 ± 1) for 24–28 h. All experiments were carried out in triplicate and the reported data represents average values ± SD.

3.6 *Anti-inflammatory Activity*

Anti-inflammatory activity was studied by protein denaturation method [10]. The reaction mixture (5 ml) consisting of 2 ml of different concentration of samples (100, 200, 300, 400 and 500 µg/ml) and 2.8 mL of phosphate buffered saline was mixed with 0.2 mL of egg albumin and incubated at (37 ± 1) °C for 15 min. Each experiment was done in triplicate and the average was taken. The percentage of inhibition of protein denaturation was calculated by using the following formula.

$$\% \text{ of inhibition} = A_C - A_t / A_C \times 100$$

where, At = absorbance of test sample, Ac = absorbance of control

4 Result and Discussion

FTIR

FTIR spectra of nHAp/GG are presented in Fig. 1 and show the absorbance bands that confirm the chemical structural characteristics of nHAp/Guar gum. There is a broad envelope between 3800 and 2600 cm^{-1} due to the O–H stretch of water and nHAp/GG [11]. The peak at 1636 cm^{-1} is assigned to bending mode of water. The stretching and bending modes of PO_4^{3-} appeared at 602 and 565 cm^{-1} as intense

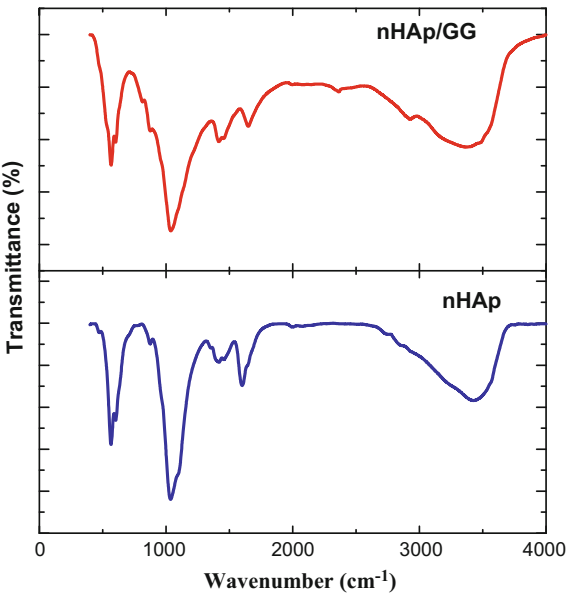

Fig. 1 FTIR spectrum for nHAp and nHAp/GG composites

Table 1 Some important functional group in nHAp, GG, nHAp/GG

nHAp	Guar gum	nHAp/GG	Assignment
602	–	602	PO_4^{3-} bending mode
1035	1020	1035	PO_4^{3-} stretching mode
1600	1648	1642	Bending mode of H_2O
–	2923	2924	Polymer peak
3425	3414	3356	OH stretching

sharp peak [12]. The bands in the range 1084–953 cm^{-1} highlight the presence of PO_4^{3-} ions in the lattice. The CO_3^{2-} ion peaks were at 1417, 896–827 cm^{-1} The result indicates the interaction between Guar gum and nHAp (Table 1).

X-ray Diffraction

The XRD pattern of nano HAp/GG composites was taken. The reflection planes corresponding to the XRD spectrum peaks of nano HAp/GG composites are shown in Fig. 2. Crystallite sizes of hydroxyapatite were analyzed by using powder XRD spectra. In the XRD pattern diffraction peaks were identified as the hexagonal phase of nHAp/GG powder (JCPDS card no: 09-0432). The observed sharp peaks in the XRD pattern confirmed that the samples are having the crystalline nature of

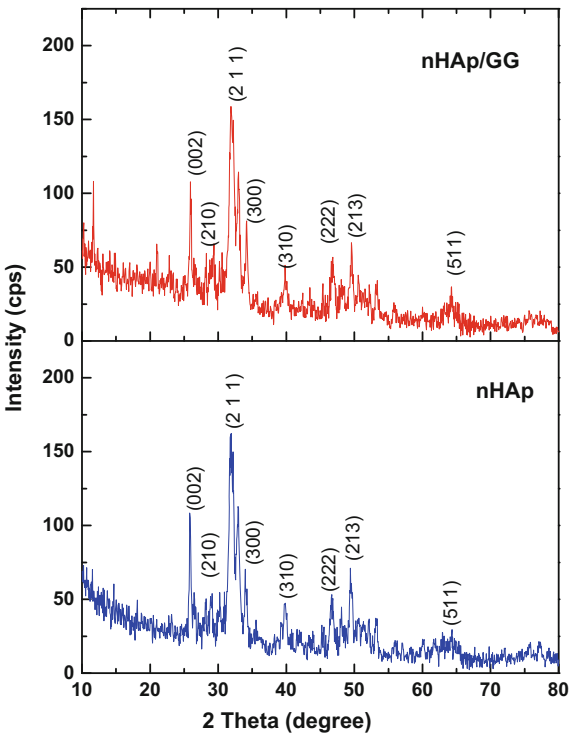

Fig. 2 XRD spectrum for nHAp and nHAp/GG composites

nHAp/GG. It was determined using the Scherrer formula. The broadened diffraction peaks were observed at 2θ = 25.8°, 29°, 31.7° and 34.0° respectively. These phases were assigned to the Miller's Indices reflection planes (002), (210), (211) and (300) corresponding to the various diffraction planes.

The average crystallite size of the prepared nHAp/GG was calculated from the Scherrer relation

$$D = \frac{0.9\lambda}{\beta \cos\theta}$$

The surface area (S) estimated using the following empirical formula

$$S = \frac{6 \times 10^3}{D\rho}$$

where λ is the wavelength of the X-ray used (λ = 0.15406 nm), θ is the diffraction angle in degrees, β is the full width at half maximum. D is the crystallite size and ρ is the density of the nHAp.

The lattice constant of a-axis and c-axis of the nHAp/GG were calculated using the equation belonging to hexagonal system

$$\frac{1}{d^2} = \frac{4}{3}\left(\frac{h^2 + hk + k^2}{a^2}\right) + \frac{l^2}{c^2}$$

where, d is the distance between two adjacent planes h, k and l are the Miller indices a and c are lattice constants of the unit cell.

The volume of unit cell was calculated using the following equation [13]

$$V = \frac{\sqrt{3}}{2}a^2 c$$

TEM

TEM was used to examine the presence of nHAp/GG crystallites. TEM micrograph of the sample is shown in Fig. 3. The microstructure of nHAp/GG particles, were in rod-like morphology. The rod containing some fine holes in their infrastructure. These holes are fundamentally some structural defects that can be related to the kind of synthesis of them. Since, synthesis of nHAp/GG was carried out in alkaline environment; there were some high corrosive hydroxyl groups in the synthesis reactor which may cause the defects in the structure. In addition, the selected area electron diffraction (SAED) of the precipitates showed diffraction rings of patterns, which implied that the precipitates were crystalline in nature. This is agreeable with XRD results.

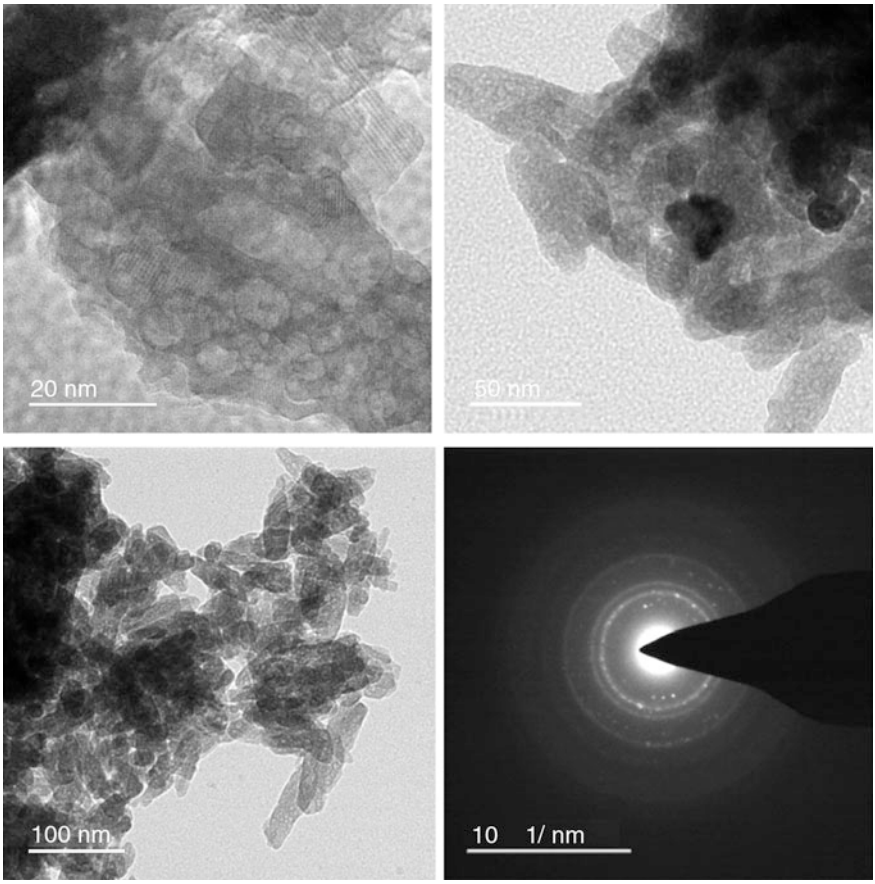

Fig. 3 TEM image of various magnification and SAED image for nHAp/GG composites

TGA

The thermogram of the synthesized material shows three distinct stages of decomposition (Fig. 4). There is a minute weight loss (6.12 %) around 180 °C. It is assigned to weakly entrapped water in the material. The second stage weight loss occurs between 180 and 300 °C. It is assigned to the dehydration of calcium hydroxide [14]. It is followed by major weight loss between 300 and 800 °C. It is due to decomposition of calcium hydroxide, carbonate to water and carbon dioxide [15]. In the DTA curve, a sharp exothermic peak is located at 400 °C. The broadened peaks shows the composites are agglomerated towards semi crystalline nature and phase stability. There is no clear endothermic peak in DTA curves, owing to their thermosetting-like amorphous nature of blend components.

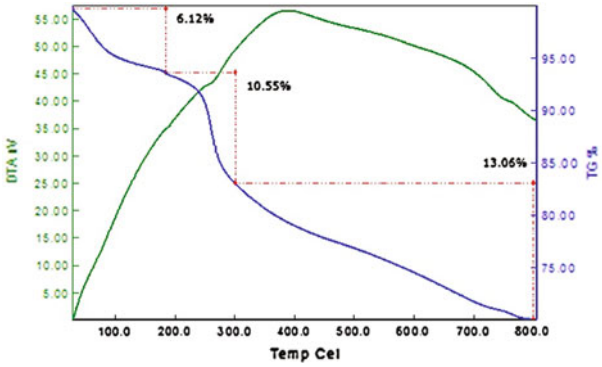

Fig. 4 Thermal behavior of nHAp/GG composites

Antimicrobial activity

Escherichia coli and *Staphylococcus aureus*, which were already known to be multi-resistant to antibiotics, were subjected for antimicrobial studies and found to be resistant to nHAp/GG composite also, tested nHAp/GG Composite. The main inhibition zone of nHAp/GG was 1.19 ± 0.08 mm for 50 µl, 2.78 ± 0.19 mm for 100 µl, 4.92 ± 0.34 mm for 150 µl for *E. coli*. The main inhibition zone of nHAp/GG was 1.42 ± 0.07 mm for 50 µl, 1.63 ± 0.11 mm for 100 µl, 3.54 ± 0.69 mm for 150 µl for *S. aureus*. The results showed that the antimicrobial activity was directly proportional to the concentration of nHAp/GG composite. The higher doses of 150 µl of nHAp/GG possess moderate activity of chloramphenicol, which is used as a standard drug (Fig. 5; Table 2).

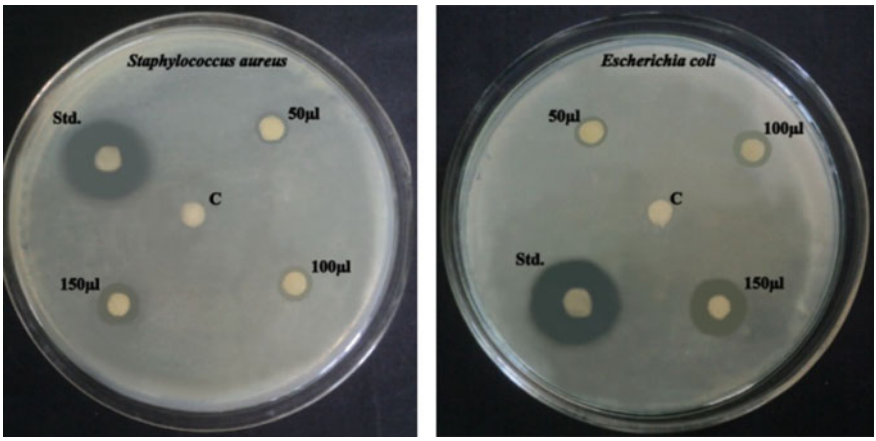

Fig. 5 Antibacterial activity of nHAp/GG composites

Table 2 Antibacterial activity of nHAp/GG composites

Microorganisms	50 µl	100 µl	150 µl	Chloramphenicol bacteria (SD)
E.Coli (mm)	1.19 ± 0.08	2.78 ± 0.19	4.92 ± 0.34	10.58 ± 0.74
S. aureus (mm)	1.42 ± 0.07	1.63 ± 0.11	3.54 ± 0.24	9.86 ± 0.69

Table 3 Anti-inflammatory test for nHAp/GG composites

Concentrations (µg/ml)	% of inhibition	
	nHAp/GG composite	Diclofenac sodium (DF)
100	18.52 ± 1.29	28.56 ± 1.99
200	36.71 ± 2.56	44.54 ± 3.11
300	47.68 ± 3.33	57.65 ± 4.03
400	69.23 ± 4.84	71.65 ± 5.01
500	87.09 ± 6.09	91.48 ± 6.41
EC_{50}	290.24	242.54

Anti-inflammatory activity

The results showed that the anti-inflammatory activity was directly proportional to the concentration of nHAp/GG composites (Table 3).

5 Conclusion

Hydroxyapatite/Guar gum was synthesized by the wet chemical method. The hydroxyapatite powder was characterized at macroscopic level by XRD, FTIR, TGA/DTA and in vitro tests. FTIR investigations also showed all typical absorption characteristics of nHAp/GG. The XRD analysis showed that the prepared nHAp/GG sample was in nano crystalline nature. The TEM images confirm that the composites show rod-like morphology. The thermal behavior of hydroxyapatite was studied by TGA/DTA. Antibacterial activity results show that nHAp/GG is active against gram-negative bacteria. Anti-inflammatory nature of the compound is observed at the highly concentration of the sample. The physical and chemical performance of synthesized composite materials meet at some extent the requirements of bone tissue engineering material. In vivo study will confirm the its compatibility with the bone tissue engineering materials. The nano sized HAp/GG powder produced can be highly useful as a bone replacement material.

Acknowledgements The authors thank the management of Urumu Dhanalakshmi College, Tiruchirappalli for providing research facilities in the campus.

References

1. Willmann, G.: Interceram **42**, 206 (1993)
2. Willmann, G.: British Ceram. Trans. **95**, 212 (1996)
3. Levernia, C., Schoenung, J.M.: Ceram **70**, 95 (1991)
4. Verma, G., Barick, K.C., Manoj, N., Sahu, A.K. and Hassan, P.A.: Rod-like micelle templated synthesis of porous hydroxyapatite. Ceram. Int. **39**, 8995–9002 (2013)
5. kawamura, Y.: Guar gum (CTA), p. 1(4) (2008)
6. Siva Prasad, S., et al.: Indian J. Adv. Chem. Sci. **1**, 28–32 (2012)
7. Chudzikowski, R.J.: J. Soc. Cosmet. Chem. **22**, 43–60 (1971)
8. Awoyinka, O., Balogun, I.O., Ogunnowo, A.A.: Phytochemical screening and in vitro bioactivity of cnidosocolus aconitifolius (Enphorbiaceae). J. Med. Plant Res. **1**(3), 63–65 (2007)
9. NCCLS National committee for clinical laboratory standards: Performance Standards for antimicrobial discsusceptibility tests. NCCLS publications, PA, 2–5 (1993)
10. Padmanabhan, P., Jangle, S.N.: Evaluaation of in-vitro anti inflammatory activity of herbal preparation, a combination of four herbal plants. Int. J. App. Basic Med. Sci. **2**(1), 109–116 (2012)
11. Kuriakose, T.A., et al.: J. Cryst. Growth **263**, 517–523 (2004)
12. Anee, T.K., et al.: Mater. Chem. Phys. **80**, 725–730 (2003)
13. Ragab, H.S., et al.: IOSR J. Pharm. Biol. Sci. **9**(1) ver.VI, 77–85 (2014)
14. Anee, T.K., Ashok, M., Palanisamy, M., Kalkura, S.N.: Mater. Chem. Phys. **80**, 725 (2003)
15. Liu, D.M., Yang, Q., Troczynski, T., Tseng, W.J.: Biomaterials **23**, 1679 (2002)

Effect of Cobalt Incorporation on Structural, Morphological, Optical and Antibacterial Properties of Rod Shaped ZnO Nanoparticles

A. Dhanalakshmi, B. Natarajan and V. Ramadas

Abstract The prepared Cobalt-doped Zinc oxide nanoparticle (ZnO:Co) was analyzed for Cobalt incorporation of rod shaped ZnO Nanoparticles (NPs) using Antibacterial study. Scanning electron microscope (SEM) and X-ray diffraction (XRD) were analyzed the structural property of the prepared samples. The crystalline size values were decreased due to Cobalt incorporated with Zinc oxide. Scanning electron microscope confirmed that the particles be in rod shape. Energy gap of the particles were strong-minded from optical property of UV absorption spectrum, it further confirmed for the reason of increases band gap in the addition of Cobalt. The emission property and the exchange of Cobalt ions with the Zinc oxide were confirmed by photoluminescence spectrum. The antibacterial efficiency of ZnO and ZnO:Co (Cobalt doped ZnO) samples were determined using disc diffusion technique and showed better antibacterial activity against the animal pathogenic bacteria *Pseudomonas aeruginosa* than other species used in this study, when higher value of doping level (10 %) and with longer duration of incubation period.

1 Introduction

In current researchers taken the numerous investigations on transition metals (TMs) doped ZnO semiconductor, because of its enormous binding energy (60 meV) of excitation and 3.37 eV of direct energy band gap even at room

A. Dhanalakshmi
Research and Development Center, Bharathiar University,
Coimbatore 641 046, Tamil Nadu, India

B. Natarajan (✉)
Post Graduate and Research Department of Physics, Raja Doraisingam
Government Arts College, Sivagangai 630 561, Tamil Nadu, India
e-mail: b_natraj_b@rediffmail.com

V. Ramadas
Post Graduate and Research Department of Zoology, Raja Doraisingam
Government Arts College, Sivagangai 630 561, Tamil Nadu, India

J. Ebenezar (ed.), *Recent Trends in Materials Science and Applications*,
Springer Proceedings in Physics 189, DOI 10.1007/978-3-319-44890-9_20

temperature. The high intense of research efforts to taken TMs like ZnO:Co have been concerned variety of application for example transparent electronics, spintronics and optoelectronics and its individual property [1–4]. Besides, TMs doped ZnO nanoparticles receive part in an extensive collection of biological applications like biomedical and food industries. Expectably (1–100 nm) NPs performed which permit interacting strongly by cell membranes. Compared to pure ZnO, Cobalt doped ZnO (ZnO:Co) NP showed a significant impact against pathogenic organisms. Antimicrobial agent as mainly helpful and control the bacterial infection. The reason of low toxicity, ZnO is an environmentally affable substance for high chemical steadiness and used as an active ingredient for applications in dermatological field [5–9]. Many researchers reports TMs doped ZnO NPs for the chemical and physical property of ZnO synthesized by the number of methods [10–14]. Sol-gel, thermal hydrolysis, hydrothermal, thermal plasma, co-precipitation method prepared the nano size and shaped morphology ZnO and ZnO:Co NPs [15–20]. From these methods, co-precipitation is the best, also vast quantity of yield and low cost. In this research article investigate the rod shaped ZnO and ZnO:Co NPs have been synthesized through co-precipitation method and the prepared ZnO:Co NPs highly efficient for the Antibacterial Properties.

2 Materials and Methods

2.1 Preparation Technique of ZnO and ZnO:Co NPs

The ZnO:Co NPs were synthesized using co-precipitation method. 0.2 M solution of Zinc acetate dihydrate (Zn $(CH_3COO)_2{\cdot}2H_2O$) and 10 at.% of Cobalt chloride hexahydrate ($CoCl_2{\cdot}6H_2O$) were used as the doping precursors respectively. For adjusting the pH using NaOH solution and it maintained at 8.5 ± 0.3. The temperature maintained at 85 °C, and it was stirred continuously by using magnetic stirrer for about 2 h. Finally, the solution kept cool at room temperature and held in reserve without interruption for 1 h to obtain the required precipitate. After washing the precipitate with ethanol and water frequently and it dried in hot air oven at 200 °C for 1 h.

XRD analysis recorded via (Bruker D8) highly developed (X-ray) Diffractometer using Cukα_1 (1.5406 Å) as a source. The SEM micrographs of the experimental samples have been obtained using Scanning Electron Microscope (INPECT-F Model). The absorbance of ZnO was located at room temperature using Spectrophotometer (Shimadzu UV-Vis 1800). Further, Photoluminescence study of ZnO and ZnO:Co NPs were recorded through Spectrofluorometer (Perkin Elmer LS55).

2.2 Assessment of Antibacterial Study

Antibacterial effect of ZnO and ZnO:Co NPs have been taken by Disc Diffusion Method, the zone of inhibitions on growth of cultures of pathogenic bacteria species like in the order of *Escherichia coli* (*E. coli*), *Klebsiella pneumonia* (*K. pneumonia*), *Pseudomonas aeruginosa* (*P. aeruginosa*), *Staphylococcus aureus* (*S. aureus*), *Salmonella typhimurium* (*S. typhimurium*) *and Streptococcus agalactiae* (*S. agalactiae*). At once culture of each organism was adjusted to an OD of 0.1 and swabbed onto Mueller Hilton agar plates. Each plate was incubation maintained at 37 °C for 24 and 48 h. The inhibition zone of diameter was given in the scale of mm and its photographs were recorded.

3 Results and Discussion

3.1 Structural Investigation of ZnO and ZnO:Co NPs Through XRD Analysis

The investigation of structural analysis for prepared samples using XRD study. Figure 1 represented the XRD patterns of pure ZnO and Co doped ZnO nanoparticles. The XRD spectra depicted the hexagonal wurtzite structure, no other impurity were added for the addition of Co concentrations. From XRD result resemblances that the (101) peak is only 100 % intensity compare than that of other. But in the case of ZnO:Co NPs all the peaks intensity were reduced compared to the ZnO NPs and also the diffraction peaks positions of ZnO:Co slightly shifted. The main reasons of these change suggesting that Co^{2+} ions occupy the Zinc sites. The lattice parameters of a, c and (c/a) values were reported in Table 1. The similar XRD results were suggested by the earlier researchers for ZnO [21] and ZnO:Co NPs [22, 23].

Average crystalline sizes value (D) for the prepared samples were estimated using Debye–Scherrer's formula [24]

$$D = 0.9\frac{\lambda}{\beta \cos\theta} \tag{1}$$

where λ is wavelength (CuK_{α}) used this present study, β *is* FWHM value and θ is the Bragg's angle. The average crystalline size of ZnO found as 46 nm and for ZnO:Co is thus 32 nm.

The lattice constants (a and c) have estimated by using the formula

$$\frac{1}{d^2} = \frac{4}{3}\left[\frac{h^2 + hk + l^2}{a^2}\right] + \frac{l^2}{c^2} \tag{2}$$

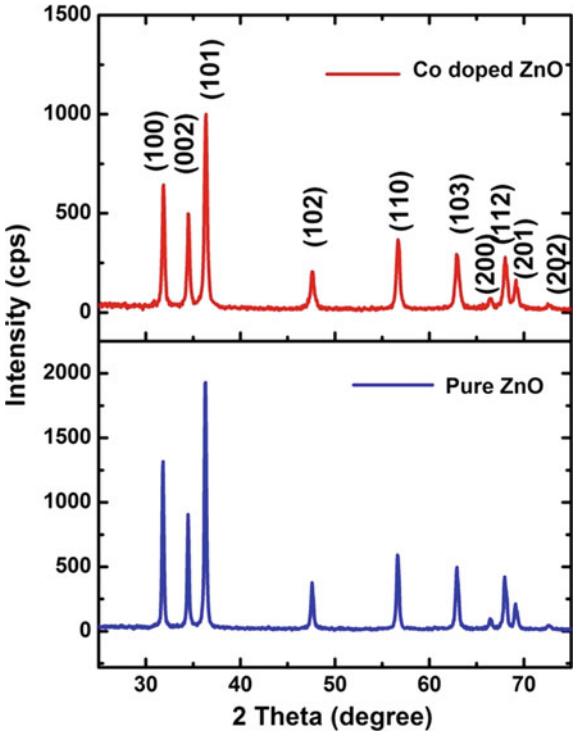

Fig. 1 XRD pattern of synthesized pure ZnO and Co doped ZnO nanoparticles

Table 1 Structural characterization parameters of ZnO and ZnO:Co NPs from the XRD spectra such as, lattice parameters, ratio of lattice parameters, crystallite size (*D*), the unit cell volume (*v*) and APF value in (%)

Samples	Lattice parameters			(*D*) nm	(*v*) Å^3	APF (%)
	a	*c*	*c/a*			
ZnO	3.247	5.205	1.603	46	47.52	75.39
ZnO:Co	3.243	5.190	1.600	32	47.27	75.49

Standard values a = 3.248 Å and c = 5.206 Å (JCPDS card no. 36-1451)

The calculated (a and c) are closer to the standard values in JCPDS card number 36-1451 for ZnO and ZnO:Co NPs. These results showed that, the lattice constants are not much affected by the replace of Co ions into the O sites.

The unit cell volume (v) was calculated by given relation [25],

$$v = \frac{\sqrt{3}}{2} a^2 c \tag{3}$$

The Atomic packing fraction (APF) values were calculated using formula

$$APF = \frac{2\pi a}{3c\sqrt{3}} \tag{4}$$

where (a and c) are called the lattice parameters. APF values are also given in Table 1.

From this result reported that the APF increases with addition of Co interact to the ZnO. For the bulk hexagonal ZnO materials, the APF is about 74 %. But in the present case of ZnO and ZnO:Co, APF value is nearly 75 % with hexagonal nature. Thus APF in both samples are a little larger than that of bulk materials.

3.2 Morphological Analysis of ZnO and ZnO:Co NPs by SEM

The surface morphological study of the ZnO and ZnO:Co NPs were recorded using Scanning electron microscope (SEM). The images of samples have micro and nano level structure and well defined grains with hexagonal cross section structures which are analogous to the construction reported by Udayakumar et al. [26]. SEM studies further confirmed that the particle size in nm with network of hexagonal rod like structure. SEM morphology of Fig. 2a, b for the ZnO NPs its revealed that long rod-shaped in 3 µm and very fine particle in 500 nm with different in sizes respectively. Figure 2c, d exhibited ZnO:Co NPs having network of rod in 10 µm and small rod shape particle agglomerated in 500 nm respectively. The similar rod shaped morphology was reported by the earlier researchers for ZnO and ZnO:Co NPs [27].

3.3 Optical Property of ZnO and ZnO:Co NPs by UV/Vis Spectroscopy

In Fig. 3, the absorption peak exhibited for ZnO at 363 nm and ZnO: Co peak at 350 nm. The interaction duo to the Co with ZnO the blue shift was occur, this means that the blue shift attributed the peak shifted in lower wavelength region and this make an increasing band gap energy for the addition of Co ions dopant with ZnO [28]. The absorption edge steadily shifts to lower wavelength with decreasing size of the NPs. Therefore, the optical property of ZnO and ZnO:Co NPs were very well correlated to the structural property of XRD and SEM. The energy band gap value (Eg) is given as the absorption coefficient of $>10^4$ cm^{-1} and in the semi-conducting resources, The Eg values of experimental samples were calculated using Tauc relation [29].

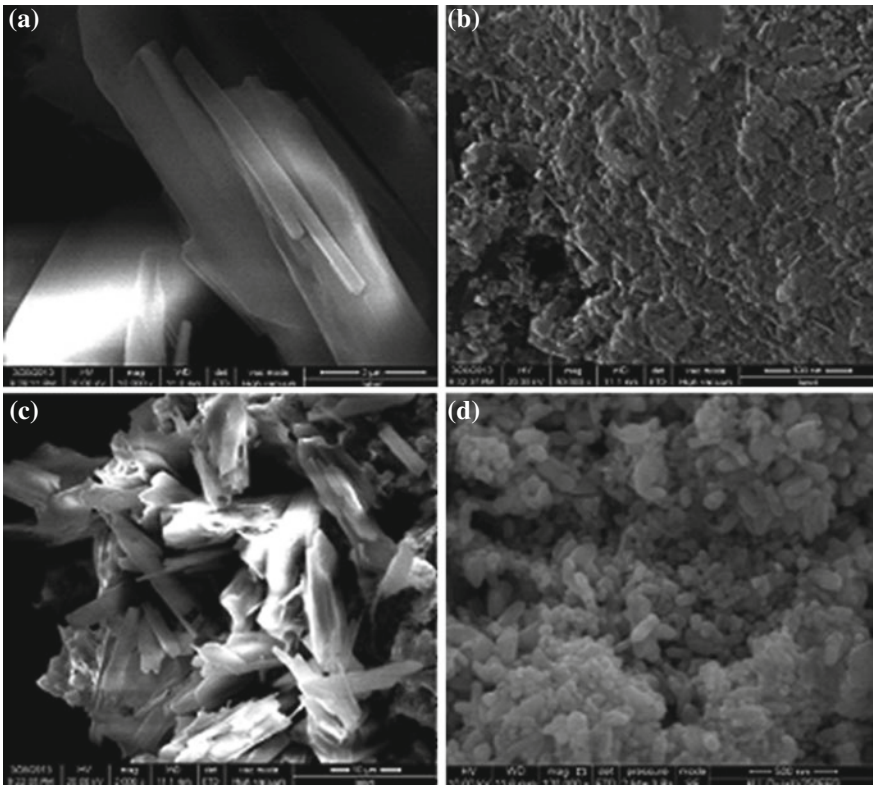

Fig. 2 SEM images at different magnifications for Pure ZnO **a** 3 μm and **b** 500 nm and Co doped ZnO, **c** 10 μm and **d** 500 nm

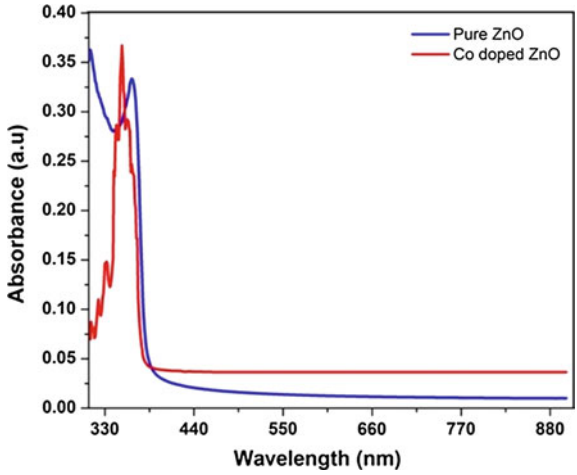

Fig. 3 Optical absorption spectrum for ZnO, Co doped ZnO nanoparticles

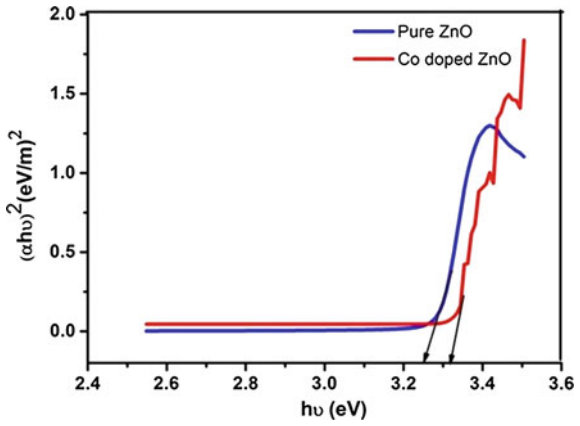

Fig. 4 The plot of $(\alpha h\nu)^2$ versus hν for ZnO and Co doped ZnO nanoparticles

$$\alpha h\upsilon = A\left(h\upsilon - E_g\right)^m \tag{5}$$

Here, where α is absorption coefficient well-known by α value is 2.303 log (T/d), thickness (d), transmission (T) and hν is the energy of photon. Figure 4 showed the plots of hν versus $(\alpha h\nu)^2$ for prepared samples. The plots indicated that the materials were in direct band gap nature. The E_g value has been calculated by using intercept of the extrapolation to zero with energy of photon axis i.e. $(\alpha h\nu)^2 - 0$. The Eg values were calculated for ZnO 3.25 eV and for ZnO:Co 3.32 eV which indicates increases energy gap due to higher Co concentration of 10 % as shown in Fig. 4. This leads to the effective band gap and close to its bulk value (3.3 eV). Thus, there will be blue shifted in the absorption spectra with decreasing crystallite size as observed in the present study. This increased band gap in the blue shift region could be attributed due to change in the energy band gap on orbital's hybridization and it was sensible to leads that, the energy band gap values increased for the addition of Co interactions [30].

3.4 Photoluminescence Study for ZnO and ZnO:Co NPs

The Photoluminescence analysis is a powerful tool to understand the nature of the defects of synthesized NPs. The PL spectra of the samples obtained within the range of 300–700 nm even at 37 °C and for the excitation of wavelength (325 nm) was depicted in Fig. 5. The results of ZnO indicated four important emission peaks such as UV emission located at ∼360 and strong 384–394, blue band at ∼458

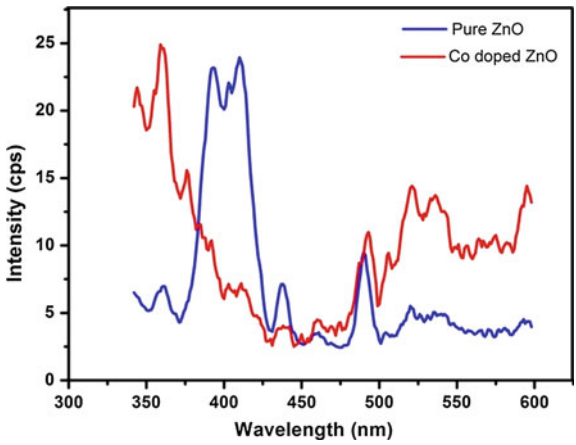

Fig. 5 PL Spectra of ZnO and Co doped ZnO nanoparticles

nm, bluish green band at ~490 nm, and a pale green band at ~530 nm. The strong and broad UV emission correlated to the Near-Band Edge (NBE) emission which corresponds to the exciton recombination of ZnO NPs suggested by previous researchers [31]. The possibilities of pale blue and pale bluish green emissions were owing to the surface defects in the NPs. In the case of ZnO:Co NPs, UV emission (~360 nm) peak intensity increased, the main emission of UV (384–394 nm) was completely reduced in the addition of Co. The reason of decreasing intensity with the high concentration (10 at.%) of Co^{2+} appropriate defect states below the conduction band, in addition a little amount of the excited electrons stay (keep relax to the defect states) in the conduction band [32]. The facts could be generally due interactions between bands and localized electrons of Co^{2+} ions substituting Zn sites [33–35]. The blue (455 nm), bluish green (490 nm) and green band (530 nm) emission peaks intensity were increased in the interaction of Co^{2+} ions which attributed in Zn lattice site.

3.5 Antibacterial Efficiency of ZnO and ZnO:Co NPs

The antibacterial study of ZnO and ZnO:Co NPs on pathogenic bacteria species with two different incubation periods was adopted using disc diffusion method. The bacterial strains like, *E. coli*, *K. pneumonia*, *P. aeruginosa and S. aureus*, *S.phimurium* and *S. agalactiae* were employed in the antibacterial test. Figure 6 indi-

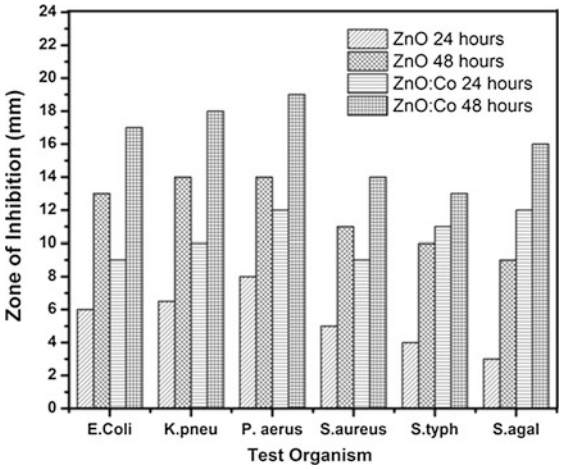

Fig. 6 *Bar graph* for Inhibition zones caused by ZnO and Co doped ZnO nanoparticles against six different pathogenic bacteria

cated that the inhibition zones for ZnO and ZnO:Co NPs in 24 and 48 h. From the result shows that well defined zones were formed due to ZnO and ZnO:Co extremely affected the bacterial growth.

The inhibition zone of ZnO and ZnO:Co were increased with increasing incubation periods (48 h). In this study ZnO NPs have been associated to numerous mechanisms including Reactive Oxygen Species (ROS) on the surface of the prepared NPs [36], and the nano-sized particles can easily damage the bacterial cell membranes [37]. But in the case of ZnO:Co NPs, increase the option of Co incorporation and Zn ions keen on the ZnO lattices. The reduction of crystallite size as estimated from the XRD data (Table 1) and the grain size reduction in ZnO:Co NPs confirmed from SEM images. Figure 6 which provided more contact area for micro-organisms. So the further reduced crystalline size in the addition of Co concentration of (10 %) which is the reason of enhanced of antibacterial efficiency than that of the ZnO NPs. The higher incubation period from 24 to 48 h was resulted is increase in the diameters of inhibition zones for ZnO and ZnO:Co NPs as shown in Fig. 7. From this results concluded that ZnO:Co NPs have showed the maximum antibacterial activity on the *Pseudomonas aeroginosa* and *Klebsiella pneumonia* followed by *Escherichia coli*, *Staphylococcus auereus*, *Salmonella typhimurium and Streptococcus agalactiae*.

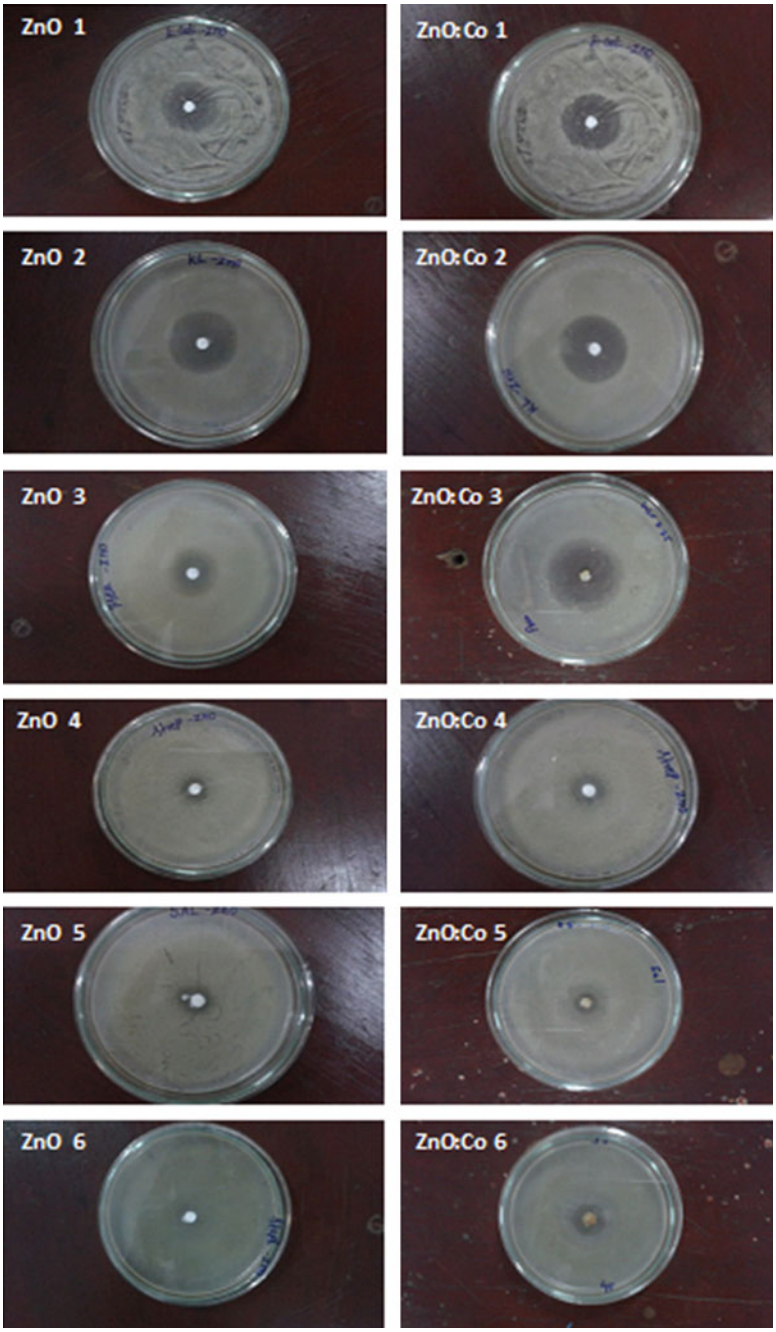

Fig. 7 Inhibition zones of ZnO and Co doped ZnO Nanoparticles against six different pathogenic bacteria at 48 h

4 Conclusion

The synthesized nanoparticles with hexagonal crystal structure were characterized. The crystalline size of 46 and 32 nm for ZnO and ZnO:Co NPs confirmed by XRD. SEM images resemblance that the rod-like shape. UV–Vis study exposed that the optical band energy gap of NPs have 3.25 and 3.32 eV. Four main emission bands which indicated their further elevated structural and optical quality confirmed from PL spectra. Such luminescent, by biocompatible capping can have biological, pharmaceuticals and medical applications. Antibacterial property of ZnO and ZnO:Co showed better antibacterial activity against the animal pathogenic bacteria *Pseudomonas aeruginosa* than other pathogenic bacteria species when higher value of doping level (10 %) and with longer duration of incubation period. The highest antibacterial efficiency at higher doping level was the interstitial incorporation of Co and Zn, the resultant increase of carrier concentration and the decreased crystallite size values as evidenced by the PL, UV-Vis and XRD results.

References

1. Yang, H.M., Nie, S.: Sol–gel synthesis, structural, optical and magnetic properties of Co-doped ZnO nanoparticles. Mater. Chem. Phys. **114**, 279–282 (2009)
2. Yang, M., Guo, Z.X., Qiu, K.H., Long, J.P., Yin, G.F., Guan, D.G., Liu, S.T., Zhou, S.J.: Synthesis of Co-doped ZnO nanoparticles by sol-gel method and its characterization. Appl. Surf. Sci. **4201**, 256–263 (2010)
3. Nirmala, M., Smitha, P., Anukaliani, A.: Optical and electrical properties of undoped and (Mn, Co) co-doped ZnO nanoparticles synthesized by DC thermal plasma method. Superlattices Microstruct. **50**, 563–571 (2011)
4. Konenkamp, R., Word, R.C., Schlegel, C.: Nanorod, nanotube and nanomaterials research progress. Appl. Phys. Let. **85**, 6004 (2004)
5. Ravichandran, K., Snega, S., Jabena Begum, N., Swaminathan, K., Sakthivel, B., Rene Christena, L., Chandramohan, G., Ochiai, Shizuyasu: Enhancement in the antibacterial efficiency of ZnO nanopowders by tuning the shape of the nanograins through fluorine doping. Superlattices Microstruct. **69**, 17–28 (2014)
6. Zhang, L., Ding, Y., Povey, M., York, D.: ZnO nanofluids—A potential antibacterial agent. Prog. Nat. Sci. **18**(8), 939–944 (2008)
7. Tam, K.H., Djurisic, A.B., Chan, C.M.N., Xi, Y.Y., Tse, C.W., Leung, Y.H., Au, D.W.T.: Antibacterial activity of ZnO nanorods prepared by a hydrothermal method. Thin Solid Films **516**(18), 6167–6174 (2008)
8. Irimpan, Litty, Nampoori, V.P.N., Radhakrishnan, P.: Spectral and nonlinear optical characteristics of nanocomposites of ZnO–Ag. Chem. Phys. Lett. **445**, 265–269 (2008)
9. Jones, N., Ray, B., Ranjit, K.T., Manna, A.C.: Antibacterial activity of ZnO nanoparticle suspensions on a broad spectrum of microorganisms. Fem. Microbial. Lett. **279**(1), 71–76 (2008)
10. Kairyte, Kristina, Kadys, Arunas, Luksiene, Zivile: Antibacterial and antifungal activity of photoactivated ZnO nanoparticles in suspension. J. Photochem. Photobiol., B **128**, 78–84 (2013)

11. Wang, X.C., Mi, W.B., Dong, S., Chen, X.M., Yang, B.H.: Structural, optical and thermal studies of cobalt doped zinc oxide. J. Alloys compd. **478**, 507 (2009)
12. Yuan, D., Wang, G.S., Xiang, Y., Chen, Y., Gao, X.Q., Lin, G.: Controllable synthesis of spindle-like zinc oxide nanostructures. J. Alloys Compd. **478**, 489–492 (2009)
13. Driessen, M.D., Miller, T.M., Grassian, V.H.: Photocatalytic oxidation of trichloroethylene on zinc oxide: characterization of surface-bound and gas-phase products and intermediates with FT-IR spectroscopy. J. Mol. Catal. A. **131**, 149 (1998)
14. Sedky, M., Abu-Abdeen., Abdalaziz, A., Almulhem.: Nonlinear I-V characteristics in doped ZnO based-cramic varistor. Physica B. **388**, 266 (2007)
15. Zheng, Y., Chen, C., Zhan, Y., Lin, X., Zheng, Q., Wei, K., Zhu, J.: Handbook of zinc oxide and related materials. J. Phys. Chem. C **112**, 10773 (2008)
16. Shailaja raj, M., Roselin, P.: The antibacterial activity of ZnO nanoparticles against propionibacterium acnes. Int. J. Pharma. Bio. Sci. **3**(1), 267–276 (2012)
17. Zhang, Y., Shi, E.W., Chen, Z.Z.: Preparation process of Zn doped CuO nanocrystals and characterization. Mater. Sci. Semicond. Process. **13**, 132–136 (2010)
18. Georgekutty, R., Seery, M.K., Pillai, S.C.: A highly efficient Ag-ZnO photocatalyst: synthesis, properties, and mechanism. J. Phys. Chem. C **112**, 13563–13570 (2008)
19. Chitra, K., Annadurai, G.: Antimicrobial activity of wet chemically engineered spherical shaped ZnO nanoparticles on food borne pathogen. Int. Food Res. J. **20**(1), 59–64 (2013)
20. Nirmala, M., Anukaliani, A.: Characterization of undoped and Co doped ZnO by precipitation method. Phys. B **406**, 911–915 (2011)
21. Saleh, R., Prakoso, S.P., Fishli, A.: The influence of Fe doping on ZnO thin films. J. Phys. Condens. Matter. **18**(Article ID 269692), 9 pages (2011)
22. White, M.A., Ochsenbein, S.T., Gamelin, D.R.: Colloidal nanocrystals of ZnO. Chem. Mater. **20**(22), 7107–7116 (2008)
23. Yu, Y., Ji, G.B., Cao, J.M., Liu, J.S., Zheng, M.B.: The effect of cobalt incorporation into zinc oxide nanoparticles. J. Alloy. Compd. **471**(1–2), 268–271 (2009)
24. Anandhi, R., Mohan, R., Swaminathan, K., Ravichandran, K.: Influence of aging time of the starting solution on the physical properties of fluorine doped zinc oxide films deposited by a simplified spray pyrolysis technique. Superlattices Microstruct. **51**(5), 680–689 (2012)
25. Goswami, A.: Thin film fund, new age international (P) limited Publications, New Delhi (2005)
26. Udayakumar, S., Renuka, V., Kavitha, K.: Structural, optical and thermal studies of cobalt doped hexagonal ZnO by simple chemical precipitation method. J. Chem. Pharm. Res. **4**(2), 1271–1280 (2012)
27. Jung, D.: Syntheses and characterizations of transition metal-doped ZnO. Solid State Sci. **12** (4), 466–470 (2010)
28. Virendra, P., Charlnene, D., Deepti, Y., Shaikh, A.J., Nadanathangam, V.: Spectroscopic characterization mof zinc oxide nanorods synthesized by solid state reaction. Spectrochimica Acta Part A **65**, 173–178 (2006)
29. Suwanboon, S., Amornpitoksuk, A., Haidoux, A., Tedenac, J.C.: Preparation and characterization of ZnO and Mg-ZnO nanoparticles. J. Alloys Compd. **462**, 335 (2008)
30. Cozzoli, P.D., Curri, M.L., Agostiano, A., Leo, G., Lomascolo, M.: ZnO nanocrystals by a non-hydrolytic route: synthesis and characterization. J. Phys. Chem. B. **107**, 4756 (2003)
31. Guo, Y., Cao, X., Lan, X., Zhao, C., Xue, X., Song, Y.: Mn doped ZnO nanonails and their magnetic properties. J. Phys. Chem. C **112**, 8832 (2008)
32. Wang, A.H., Zhang, B.L., Wang, X.C., Yao, N., Gao, N.F., Ma, Y.K., Zhang, L., Ma, H.Z.: Structural, optical and thermal studies of Co doped ZnO nanopowders. J. Phys. D Appl. Phys. **41**, 215–308 (2008)
33. Pal, Bappaditya, Giri, P.K.: Defect mediated magnetic interaction and high Tc ferromagnetism in Co doped ZnO nanoparticles. ASP. J. Nanosci. Nanotechnol. **11**, 1–8 (2011)
34. Lee, Y.R., Ramdas, A.K., Agarwal, R.L.: Structural, optical and thermal studies of Co doped ZnO nanoparticles. Phys. Rev. B. **38**, 10600 (1988)

35. Park, W.I., Yi, C.G., Jang, H.M.: Fabrication and electrical characteristics of high-performance ZnO nanoparticles. Appl. Phys. Lett. **79**(13), 2022–2024 (2001)
36. Vasanthi, M., Ravichandran, K., Begum, N.J., Muruganantham, G., Snega, S., Panneerselvam, A., Kavitha, P.: Influence of Sn doping level on antibacterial activity and certain physical properties of ZnO films deposited using a simplified spray pyrolysis technique. Superlattices Microstruct. **55**, 180–190 (2013)
37. Padmavathy, N., Vijayaraghavan, R.: Enhanced bioactivity of ZnO nanoparticles—an antibacterial study. Sci Technol. Adv Mater. **9**, 035004, 7 (2009)

Spinel $NiCo_2O_4$ Nanostructures: Synthesis, Morphological, Optical and Electrochemical Properties

M. Silambarasan, P.S. Ramesh and D. Geetha

Abstract The three different ratios of $NiCo_2O_4$ nanostructures have been synthesized using nickel nitrate hexa hydrate, cobalt nitrate hexa hydrate and potassium hydroxide via co-precipitation method and their morphological, optical and electrochemical properties is proposed. Room temperature (RT) photoluminescence investigation reveals near band emission (NBE) in all samples. Then the synthesized $NiCo_2O_4$ nanostructures were utilized to modify the glassy carbon electrode (GCE) for electrochemical characterization. The cyclic voltammetry test of the 1:1, 1:2 and 1:5 $NiCo_2O_4$ modified glassy carbon electrodes ($NiCo_2O_4$/GCE) shows without any redox peaks on both anodic and cathodic sweeps, which indicates the ideal capacitive behavior and the corresponding specific capacitance are 753, 788 and 574 Fg^{-1} respectively at 5 mV s^{-1}. The cost effective $NiCo_2O_4$ nanostructures are suitable for the applications in optoelectronic and energy storage devices.

1 Introduction

Nanostructured materials have attracted significant attention in past few decades and been expected to play a vital role in the future technological advance in electronics, optoelectronics, and memory devices [1–3]. Conductive transition metal oxide (TMO) nanostructures in particular offer fundamental opportunities for investigating the effect of size and dimensionality on their collective electronic,

M. Silambarasan · D. Geetha
Department of Physics, Annamalai University,
Annamalai Nagar, Chidambaram 608002, India

P.S. Ramesh (✉)
Department of Physics (DDE Wings), Annamalai University,
Annamalai Nagar, Chidambaram 608002, India
e-mail: psrddephyau@gmail.com

J. Ebenezar (ed.), *Recent Trends in Materials Science and Applications*,
Springer Proceedings in Physics 189, DOI 10.1007/978-3-319-44890-9_21

optical, magnetic, and catalytic properties [4–6]. A NiO and Co_3O_4 nano-sized material are most intriguing inorganic p-type semiconducting materials and has direct optical band gaps at 3.6–4.0 eV [7] and 2.13–3.95 eV [8]. Nickel and cobalt oxide nano-powders have an extensive applications in different fields of industry including anode materials for rechargeable Li-ion batteries (LIB), solid state sensors, gas sensors, heterogeneous catalysts, electro chromic (EC) devices, magnetic materials and energy storage devices [9–11]. Mixed metal oxides (MMO) with spinel structure are of intense interests in both fundamental science and technological applications. Among the mixed metal oxides, spinel-type AB_2O_4, where element A and B denote divalent, trivalent and quadrivalent metallic cations, respectively, are most intriguing materials with improved reactivity than the corresponding mono metal oxides. In particular, the cobalt based spinel metal oxides MCo_2O_4 (M = Ni, Cu, Zn, Mg, Mn, Cd, etc.) are technologically interesting materials and explored in the emerging field [12].

The spinel nickel cobaltite ($NiCo_2O_4$) is one of the essential spinel metal oxides in the family of cobaltite materials, which has been broadly investigated because it is cheeper and natural abundance [13–16]. In the spinel compound of nickel cobaltite as mixed metal oxides, where nickel atoms are occupying the octahedral sites and cobalt atoms are distributed over both octahedral and tetrahedral sites [17]. There are various routes have been developed to synthesis $NiCo_2O_4$ nanostructures. Such as sol-gel, hydro-thermal, chemical bath deposition and electro chemical deposition method [16, 18–20] and so forth. However, to the best of our knowledge, there is no reports on these materials to check the optical property. In this work, it was aimed to synthesize and planed to investigate their morphological, optical and electrochemical properties.

2 Experimental Method

2.1 Synthesis of Nickel Cobaltite

All chemicals used in this work were analytical grade without purification. 1 mm of Nickel nitrate hexa hydrate ($Ni(NO_3)_2{\cdot}6H_2O$) and 1 mmol of cobalt nitrate hexa hydrate ($Co(NO_3)_2{\cdot}6H_2O$) were suspended in de-ionized water. Quantitative aqueous KOH is added drop wise to the above solution under constant electromagnetic stirring until the precipitate was obtained, the obtained precipitate washed by distilled water and anhydrous ethanol for several times to remove unexpected ions. Then dried at 80 °C for 3 h under vacuum, finally the powder was treated in a crucible at 400 °C for 4 h. For comparison purposes, other $NiCo_2O_4$ products (1:2 and 1:5) was also synthesized under the similar approach using as same as KOH precipitant.

2.2 Materials and Electrochemical Characterization

All the characteristics were investigated after calcination process. Crystallographic phase of the samples was carried out by Powder X-ray diffraction (XRD) using Bruker, D2-PHASER system with CuKα (λ = 1.54056 nm) radiation at a scan rate of 1°/min in the 2θ range of 10° to 80°. The functional group of nanostructures was characterized by Fourier transform infrared spectrometer over a wave-number range of 400–4000 cm^{-1} using a Perkin Elmer spectrometer. Phase compositions of the products were recorded at 514.3 nm using a Laser Raman Spectrophotometer under ambient condition. The morphology of the prepared products was observed through a (SUPRA 55) field emission scanning electron microscope (FE-SEM). The elemental composition of the products was accomplished using Energy dispersive X-ray Spectroscopy, in attached with FE-SEM. The morphologies were analyzed by a TEM CM-200 transmission electron microscope (TEM). The opical band gap of the nanomaterials was determined by UV-Vis spectroscopy (Shimadzu UV 1700). The PL emission spectra were recorded by spectro-flurometer (Jobin–Yvon, FLUOROLOG–FL3-11) using 325 He-Cd lasers.

2.3 Electrode Preparation

The electrochemical characterization of the $NiCo_2O_4$ were carried out on an CHI 660 °C electrochemical workstation by cyclic voltammetry (CV) conducted using three electrode design. A bare glassy carbon electrode (GCE) was cleaned and washed with double-distilled water. The nickel cobaltite (1.55 mg ml^{-1}) were dispersed in an ethanol solution to get slurry. The resultant slurry sonicated for 10 min. Then 10 ml of slurry was placed onto glassy carbon electrode surface using a micropipette, and then dried at 70 °C for 1 h under vacuum to evaporate the solvent. The nickel cobaltite modified GCE as the working electrode, a saturated calomel electrode (SCE) as the reference electrode and a Platinum foil act as the counter electrode, respectively. The electrochemical test are conducted in 2 M potassium hydroxide electrolyte solution at room temperature.

3 Result and Discussion

3.1 XRD Characterization

The purity and crystallinity of the nanostructures was examined by powder X-ray diffraction (XRD) and corresponding spectra of $NiCo_2O_4$ samples (1:1, 1:2, 1:5) are shown in Fig. 1a–c. The peak positions appearing at around 18.98°, 31.27°, 36.91°, 44.17°, 59.35°, 64.82° and 77.05° can be indexed as (111), (220), (311), (400), (511),

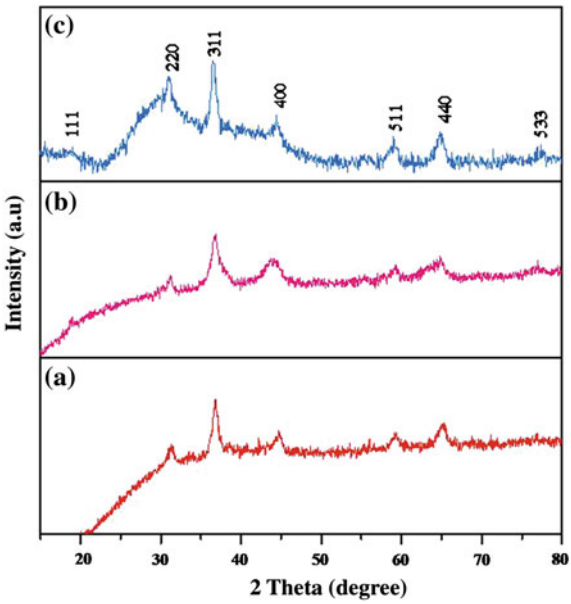

Fig. 1 XRD pattern of $NiCo_2O_4$ samples **a** 1:1, **b** 1:2, and **c** 1:5

(440) and (533) crystal planes of $NiCo_2O_4$, respectively in all samples. All diffraction peaks can be perfectly indexed to cubic spinel structure of $NiCo_2O_4$ (JCPDS; 73-1702). From the XRD spectra (Fig. 1c), addition of cobalt sources slightly increase the intensity at (311) plane. The crystalline size of the $NiCo_2O_4$ (1:1) nanostructure was around 6 nm using the Scherrer equation for $2\theta = 36.91^{\circ}$. Based on the Debye-scherrer equation, the crystalline size is approximately 6 and 10 nm for 1:2 and 1:5 $NiCo_2O_4$ nanostructures respectively. No additional peaks of other phases such as NiO and Co_3O_4 can be detected, indicating high purity of the as-prepared $NiCo_2O_4$ nanostructures. The chemical reaction of the $NiCo_2O_4$ is given below

$$\begin{aligned} &Ni(NO_3)_2{\cdot}6H_2O + Co(NO_3)_2{\cdot}6H_2O \\ &\quad + 6KOH \xrightarrow[80\,^{\circ}C]{\nabla} Ni(OH)_2 + 2Co(OH)_2 + 6KNO_3 \end{aligned} \tag{1}$$

$$Ni(OH)_2 + 2Co(OH)_2 + 1/2O_2 \xrightarrow[400^{\circ}C]{\nabla} NiCo_2O_4 + 3H_2O \uparrow \tag{2}$$

3.2 *Functional Group Analysis*

The chemical constituents of the three $NiCo_2O_4$ nanostructures were investigated by the FTIR spectra is shown in Fig. 2a–c. The vibration bands are observed at 3403, 3370, 1628, 1616, 1383 and 1374 cm^{-1} are assigned to the O–H stretching, relating to adsorbed water in the three samples [21]. The pair of metal oxide bands

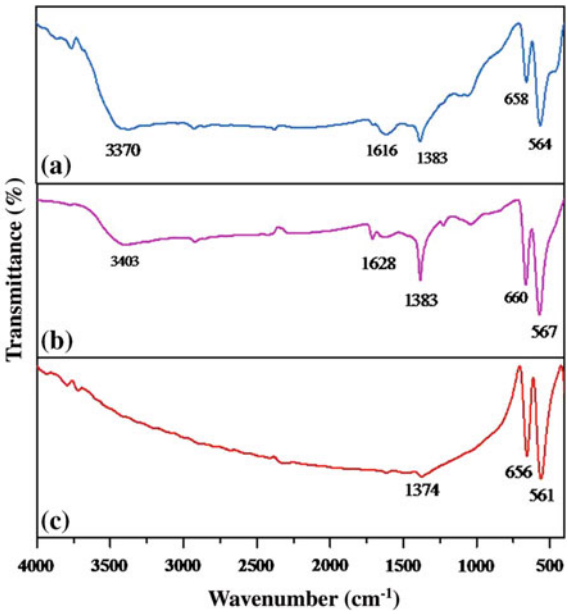

Fig. 2 FTIR spectra of $NiCo_2O_4$ **a** 1:1, **b** 1:2, and **c** 1:5 using KOH as precipitant

located at below 1000 cm^{-1} for three $NiCo_2O_4$ nanostructures, the bands are characteristic of metal–oxygen bonds in a spinel type crystal structure, which is due to the difference in bond length between the metal cations and oxygen anions occupying on tetrahedral and octahedral sites [22]. These observations is further confirmed the spinel type of $NiCo_2O_4$ nanostructures.

3.3 Raman Analysis

Phase composition of the as-prepared $NiCo_2O_4$ (1:1, 1:2, 1:5) was further investigated by Raman spectroscopies are shown in Fig. 3a–c In all samples, there are four peaks located at approximately 194, 480, 523 and 684 cm^{-1} can be found, which corresponds to the F_{2g}, E_g, F_{2g} and A_{1g} vibrational modes of $NiCo_2O_4$ nanostructures respectively, they are mainly associated with Ni–O and Co–O vibrations of the spinel $NiCo_2O_4$. These results are well matched with the previous reports [23].

3.4 Morphological Analysis

The FESEM and TEM images of the as-prepared nickel cobaltites (1:1, 1:2, 1:5) nanostructures are shown in Figs. 4, 5 and 6. The FESEM micrographs of 1:1

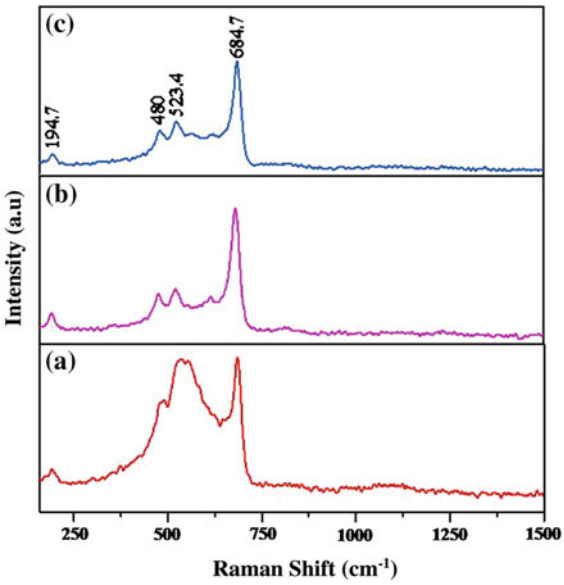

Fig. 3 Raman spectra of $NiCo_2O_4$ **a** 1:1, **b** 1:2, and **c** 1:5

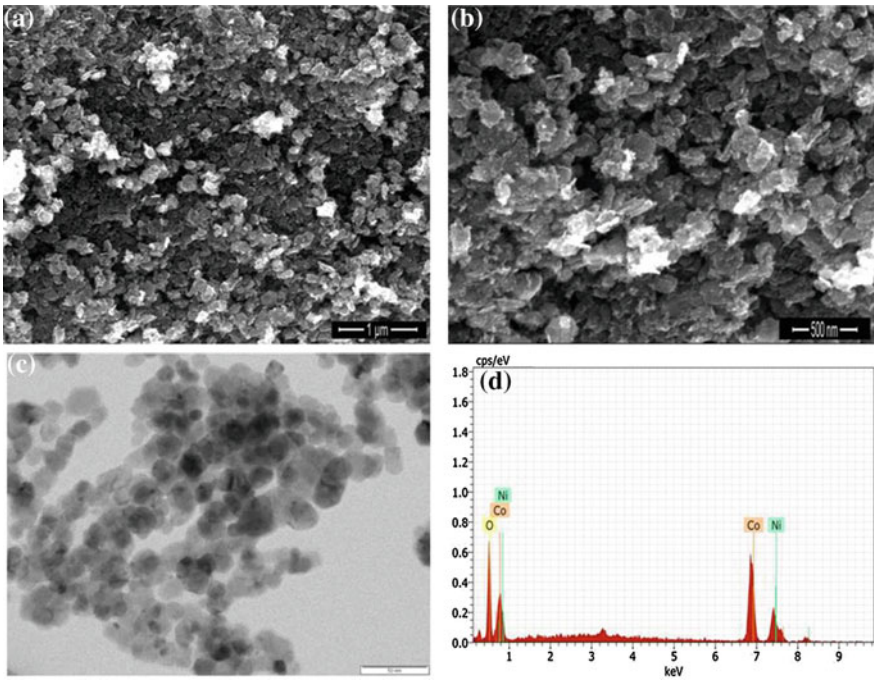

Fig. 4 **a**, **b** FESEM, **c** TEM, and **d** EDX images of $NiCo_2O_4$ (1:1) nanostructures

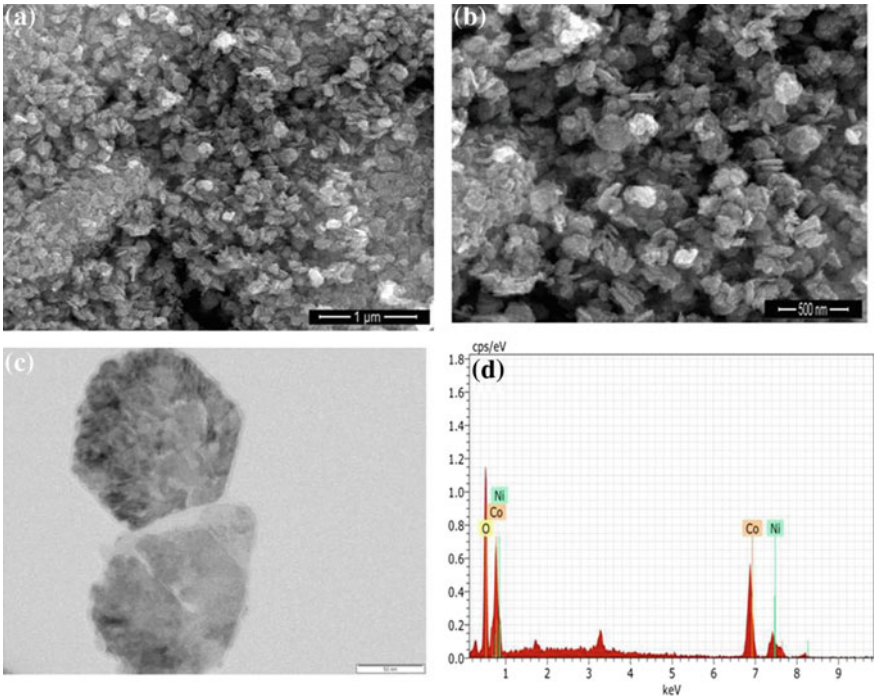

Fig. 5 **a**, **b** FESEM, **c** TEM and **d** EDX images of $NiCo_2O_4$ (1:2) nanostructures

$NiCo_2O_4$ (Fig. 4a, b) shows agglomerated irregular plates like structures. The corresponding microstructure is revealed by TEM image (Fig. 4c) with particle size is about around 10 nm. Figure 5a, b clearly demonstrate agglomerated hexagonal plate like structure observed in 1:2 $NiCo_2O_4$. The corresponding TEM image (Fig. 5c) confirms hexagonal plate like structure with the particle size is around 20 nm. In Fig. 6a–c, the FESEM and TEM images of 1:5 $NiCo_2O_4$ nanoparticles aggregated together to form inhomogeneous nanoclusters can be observed, and it indicates that the size of the nanoparticles is below 20 nm. Furthermore, the energy-dispersive X-ray (EDX) was performed to examine the elemental composition of the $NiCo_2O_4$ nanostructures is shown in Figs. 4d, 5d and 6d. The EDX pattern of three products are indicate the presence of Ni, Co and O peaks only. Table 1, shows the weight percentages of three ratios of $NiCo_2O_4$ nanostructures. From this table, the weight percentages show good agreement with the experimental concentration used for preparing $NiCo_2O_4$ nanostructures.

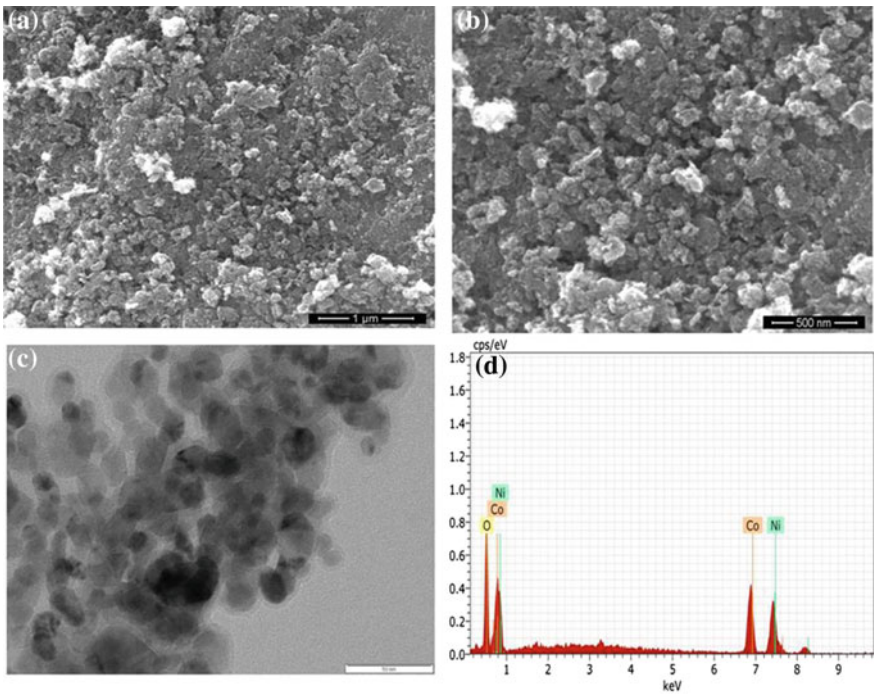

Fig. 6 **a**, **b** FESEM, **c** TEM and **d** EDX images of $NiCo_2O_4$ (1:5) nanostructures

Table 1 The quantitative analysis of the compositional elements present for $NiCo_2O_4$ using EDS spectra

Samples	Weight percentage of the elements		
	Ni	Co	O
1:1	29.14	29.26	41.60
1:2	13.59	34.77	51.64
1:5	19.95	43.45	36.60

3.5 Optical Properties

UV-Visible absorption spectra was systematically carried out in order to study the optical absorbance properties of the synthesized 1:1, 1:2, 1:5 $NiCo_2O_4$ is shown in Fig. 7. The absorption peaks centered at 278, 277, 278 nm. The fundamental absorption corresponds to excitation of an electron from the valence band to conduction band can be used to quantify the nature and value of the optical energy band gap. With increasing cobalt concentration the absorption peak slightly shifts towards higher wavelength side. Based on the optical absorption spectra, the band gap energy value was calculated by Tauc equation:

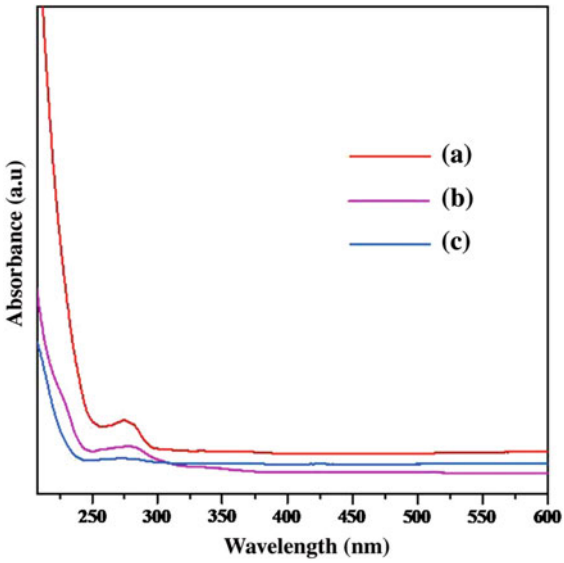

Fig. 7 UV-Vis absorbance spectra of $NiCo_2O_4$ **a** 1:1, **b** 1:2, and **c** 1:5

$$(\alpha hv)^n = B(hv - E_g) \tag{3}$$

Here, hv is the photon energy, α is absorbance, B is a constant relative to the material and n indicates either 2 for direct transition or 1/2 for an indirect transition [24]. Figure 8a–c shows the $(\alpha hv)^2$ versus hν curves of the 1:1, 1:2, 1:5 $NiCo_2O_4$ nanostructures. The calculated band gap values of the three $NiCo_2O_4$ nanostructures are around 3.4, 3.6 and 4.9 eV respectively. Band gap of all $NiCo_2O_4$ are mainly due to the comprehensive influence of morphology and crystalline size of nanostructure, which were controlled by the condition of synthesis.

Photoluminescence (PL) is a useful tool for investigating the optical properties of nanostructures. Figure 9 shows the room photoluminescence spectra of as-synthesized $NiCo_2O_4$ samples. It can be seen that the spectra of three samples consist of broad near-band edge (NBE) emission centered at around 320 nm. The NBE is due to the radiative recombination of the electrons through an exciton-exciton collision process [25]. Figure 9 shows the NBE emission intensity of $NiCo_2O_4$ was decreased when increasing cobalt concentration. A large variation in emission intensity suggesting that the enhancement may be depends on the surface properties of nickel cobaltite. The optical property indicates the $NiCo_2O_4$ may have promising applications in the field of short wavelength optoelectronic and photonic devices.

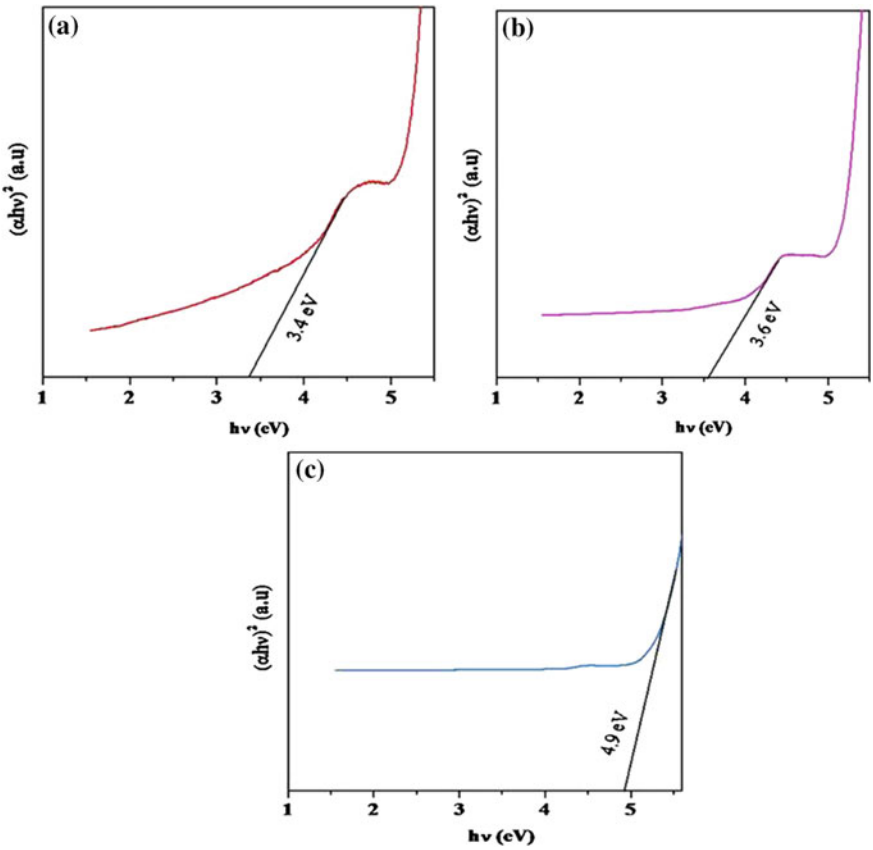

Fig. 8 Plot of the $(\alpha h\nu)^2$ versus photon energy ($h\nu$) for $NiCo_2O_4$ **a** 1:1, **b** 1:2, and **c** 1:5

3.6 Electrochemical Studies on $NiCo_2O_4$ Modified GCE

Figure 10 demonstrates the electrochemical performance of three different $NiCo_2O_4$ modified GCE. Cyclic voltammetry (CV) is employed to explore the electrochemical properties and quantify the specific capacitance of the $NiCo_2O_4$/GCE electrodes between the potential window of 0.02–0.5 V in 2 M KOH electrolyte using a three-electrode configuration. Different scan rate of voltammetric performance of the three samples depicts in Fig. 10a–c at mass loading 1.55 mg cm^{-2}. The all samples shows highly reversible and rectangular shaped curves, which exhibit ideal capacitive nature; those were nearly perfect mirror images. It is observed that CV curves obtained without peak, which reveals that the electrode charge is stored and released at a pseudoconstant rate over the complete voltammetric cycle [26]. Furthermore, the shape of the CV curve increases with increasing

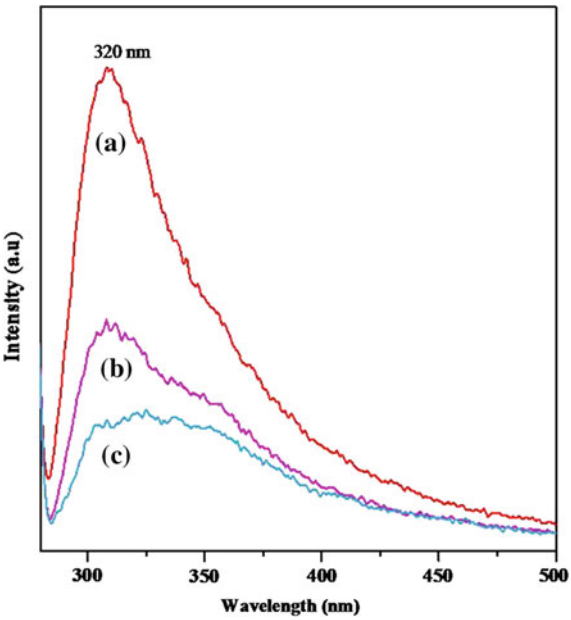

Fig. 9 Room temperature PL spectra of $NiCo_2O_4$ **a** 1:1, **b** 1:2, and **c** 1:5

sweep rate from 5 to 50 mV/s, which suggests its good electrochemical reversibility. The specific capacitance of the $NiCo_2O_4$/GCE electrodes was quantified via the cyclic voltammetric current value, scan rate and weight of the $NiCo_2O_4$ materials according to the following formula:

$$Cs(\mathrm{Fg}^{-1}) = Q/(\Delta V \cdot m) \tag{4}$$

where *Cs* represents the specific capacitance, *Q* the anodic and cathodeic charges on each scanning, *m* is the mass of the electro active material (mg) and ΔV is the applied voltage window of the voltammetric curve (mV s^{-1}).

The specific capacitances of three different ratios of $NiCo_2O_4$/GCE electrodes derived from the cyclic voltammetry are also compared, as shown in Table 2. The 1:2 $NiCo_2O_4$/GCE electrode delivered a high specific capacitance of 788 Fg^{-1} at scan rate of 5 mV s^{-1} which is higher than the 1:1 and 1:5 ratio of $NiCo_2O_4$/GCE. This highest capacitance could be attributed to the hexagonal nanoplates and high specific surface area of 1:2 $NiCo_2O_4$/GCE electrode which may facilitated fast ion transfer by enhancing electrochemical responses. The low specific capacitance obtained in the 1:5 ratio of $NiCo_2O_4$/GCE electrode, which may be attributed to the presence of large aggregated nanoparticles. The specific capacitance decreases with increasing scan rate. This is basic issue for all electrochemical supercapacitors. At low sweep rate, greatest usage of the electroactive surface of $NiCo_2O_4$ can be in excellent contact with the movement of electrolyte ions, whereas with the increase the sweep rate, the movement of electrolyte ions is limited because of their slow diffusion.

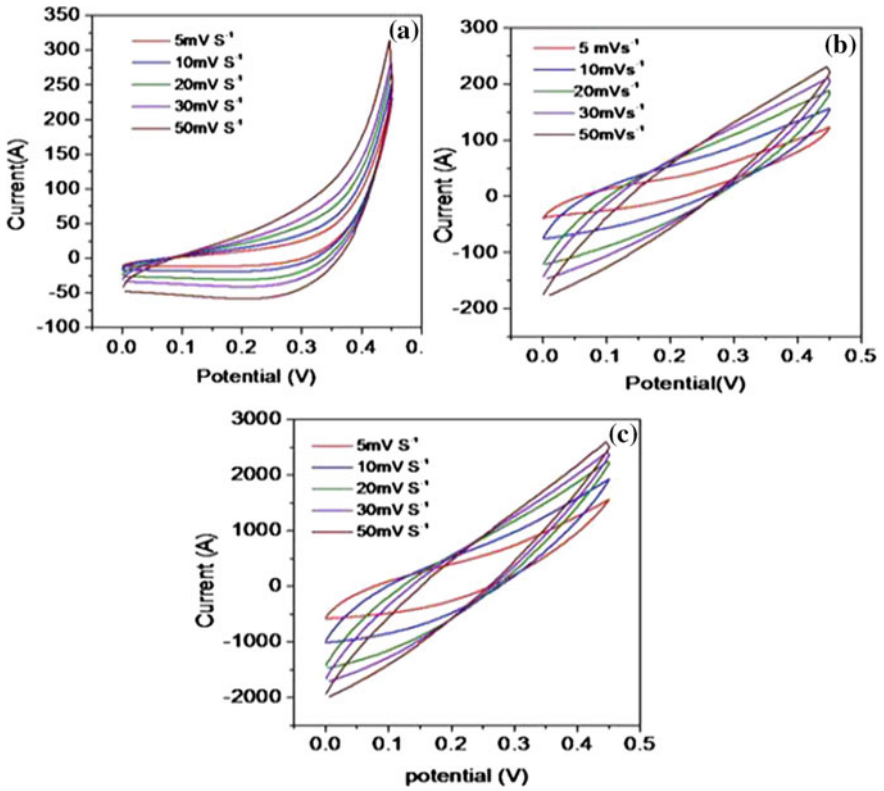

Fig. 10 CV curves of the three $NiCo_2O_4$/GCE electrodes performed at various scan rates: **a** 1:1, **b** 1:2, and **c** 1:5

Table 2 Specific capacitance of $NiCo_2O_4$ at different scan rates

Products	Sweep rate (mV/s)				
	5	10	20	30	50
	Specific capacitance (F/g)				
1:1	753	455	189	161	83
1:2	788	475	227	156	96
1:5	574	431	194	140	55

4 Conclusion

In conclusion, we have effectively synthesized three spinel $NiCo_2O_4$ nanostructures using KOH as precipitant by co-precipitation method. The XRD, FTIR, Raman, and EDX analyses suggesting the pure $NiCo_2O_4$ nanomaterials. Room temperature photoluminescence tests reveal NBE emission in all $NiCo_2O_4$ nanostructures. The electrochemical test of nickel cobaltite modified GCE has delivered highest specific

capacitance depending on the morphological properties. The hexagonal plate like Nickel cobaltite (1:2) electrode delivered highest specific capacitance 788 Fg^{-1} than 1:1 and 1:5 ratios of $NiCo_2O_4$ nanostructures. The low cost, available resources and environmental friendliness of $NiCo_2O_4$ nanostructures required promising candidate for practical applications.

References

1. Cui, Y., Lieber, C.M.: Science **291**, 851–853 (2001)
2. Alivisatos, A.P.: Science **271**, 933 (1996)
3. Sun, S., Murray, C.B., Weller, D., Folks, L., Moser, A.: Science **287**, 1989–1992 (2000)
4. Cox, P.A.: Transition metal oxides: an introduction to their electronic structure and properties. Clarendon Press, Oxford (1992)
5. Tejuca, L.G., Fierro, J.L.F, Tascon, J.M., vol. 36. New York, Academic, (1989)
6. Fernandez-Garcia, M., Martinez-Arias, A., Hanson, J.C., Rodriguez, J.A.: Chem. Rev. **104**, 4063–4104 (2004)
7. Chen, H.L., Lu, Y.M., Hwang, W.S.: Surf. Coat. Technol. **198**, 138–142 (2005)
8. Xu, R., Zeng, H.C.: Langmuir **20**, 9780–9790 (2004)
9. Seung Ho Choi and Yun Chan Kang: ACS Appl. Mater. Interfaces **6**, 2312–2316 (2014)
10. Li, W.Y., Xu, L.N. and Chen, J.: Adv. Funct. Mat. **15**(5), 851–857 (2005)
11. Ahmad, Tokeer, Ramanujachary, Kandalam V., Lofland, Samuel E., Ganguli, Ashok K.: Solid State Sci. **8**(5), 425–430 (2006)
12. Eranna, G.: CRC Press, Boca Raton (2012)
13. Jiang, H., Ma, J., Li, C.Z.: Chem. Commun. **48**, 4465–4467 (2012)
14. Cui, B., Lin, H., Li, J.B., Li, X., Yang, J., Tao, J.: Adv. Funct. Mater. **18**, 1440–1447 (2008)
15. Carriazo, D., Patino, J., Gutiérrez, M.C., Ferrer, M.L., Monte, F.D.: RSC Adv. **3**, 13690–13695 (2013)
16. Wei, T.Y., Chen, C.H., Chien, H.C., Lu, S.Y., Hu, C.C.: Adv. Mater. **22**, 347–351 (2010)
17. Kim, J.G., Pugmire, D.L., Battaglia, D., Langell, M.A.: Appl. Surf. Sci. **165**, 70–84 (2000)
18. Boldrin, P., Hebb, A.K., Chaudhry, A.A., Otley, L., Thiebaut, B., Bishop, P., Darr, J.A.: Ind. Eng. Chem. Res. **46**, 4830–4838 (2007)
19. Salunkhe, R.R., Jang, K., Yu, H., Yu, S., Ganesh, T., Han, S.H., Ahn, H.: J Alloys Compd. **509**, 6677–6682 (2011)
20. Wanga, T., Guoa, Y., Zhaoa, B., Yua, S., Yang, H.P., Lua, D., Fua, X.Z., Sun, R., Wong, C. P.: J. Power Sources **286**, 371–379 (2015)
21. Yan, D., Zhang, H., Chen, L., Zhu, G., Li, S., Xu, H., Yu, A.: Appl. Mater. Interfaces **6**, 15632–15637 (2014)
22. Srivastava, M., Uddin, M.E., Singh, J., Kim, N.H., Lee, J.H.: J Alloys Compd. **590**, 266–276 (2014)
23. Liu, Z.Q., Xiao, K., Xu, Q.Z., Li, N., Su, Y.Z., Wanga, H.J., Chen, S.: RSC Adv **3**, 4372–4380 (2013)
24. Pankove, J.I.: Optical processes in semiconductors. Prentice-Hall, Englewood Cliffs (1971)
25. Rattanaa, T., Suwanboon, S., Amornpitoksuk, P., Haidou, A., Limsuwan, P. J. Alloys Compd. **480**, 603–607 (2009)
26. Jiang, J.H., Kucernak, A.: Electrochim. Acta **47**, 2381–2386 (2002)

Impact of Annealing on Structural and Magnetic Properties of Manganese Co-Doped Magnesium-Cobalt Ferrite Nanoparticles

J. Balavijayalakshmi and C. Annie Josphine

Abstract Manganese co-doped magnesium-cobalt ferrite nanoparticles ($Mg_{0.4}Co_{0.4}Mn_{0.2}Fe_2O_4$) are synthesized by co-precipitation method and are annealed at 130, 600 and 900 °C. The synthesized nanoparticles are characterized using X-ray diffraction (XRD) analysis, FT-IR spectral analysis, Scanning Electron Microscopy (SEM) analysis, Transmission Electron Microscopy (TEM) analysis and Vibrating Sample Magnetometer (VSM) analysis. The crystallite size is found to be 17 and 19.6 nm for the samples annealed at 600 and 900 °C respectively. The crystallite size and lattice constant increases as the samples are annealed at higher temperatures. FT-IR analysis confirms the characteristic absorption bands at 590 and 546 cm^{-1} for tetrahedral sites and 416 cm^{-1} for octahedral sites. SEM analysis shows uniformly distributed spherical shaped nanoparticles. The microstructure and particle size are analyzed by TEM analysis. The saturation magnetization, remanent magnetization and coercivity increases due to the inclusion of manganese and as the annealing temperature increases. These samples can be used for gas sensing applications.

1 Introduction

Nano structured magnetic materials have wide areas of applications in water purification, high density data storage, ferro fluids, bio-molecule separation, colour imaging, medical diagnosis, drug delivery and so forth [1, 2]. Among the ferro spinels, Magnesium ferrite belongs to a class of compounds having the general formula $MgFe_2O_4$ crystallizing with the spinel structure. It is a typical spinel in

J. Balavijayalakshmi (✉) · C. Annie Josphine
Department of Physics, PSGR Krishnammal College for Women, Coimbatore, Tamilnadu, India
e-mail: balavijayalakshmiroopa@gmail.com

J. Ebenezar (ed.), *Recent Trends in Materials Science and Applications*, Springer Proceedings in Physics 189, DOI 10.1007/978-3-319-44890-9_22

which the cation distribution in the crystal lattice site is very much sensitive to heat treatment due to high diffusibility of Mg^{2+} ions [3]. The physical and chemical properties of ferrites are dependent upon factors such as annealing temperature, annealing time, rate of heating and rate of cooling, etc. [4]. In case of cobalt ferrite, the incorporation of cobalt ions results in an increase in coercivity, which is due to the coupling of the spins of cobalt and iron ions [5, 6]. Also, manganese ferrite is considered versatile and of higher significance owing to its high saturation magnetization and low power loss at high frequencies. Many literatures are available reporting the structural, magnetic and dielectric properties of mixed ferrites [7–10]. But no such literatures are available in Mg-Co mixed ferrites doped with manganese. Hence in the present work, an attempt has been made to synthesize manganese co-doped magnesium-cobalt ferrite nanoparticles ($Mg_{0.4}Co_{0.4}Mn_{0.2}Fe_2O_4$) by co-precipitation method and to investigate its structural and magnetic properties. The impacts of annealing on structural and magnetic properties are also studied. These materials can be tested for gas sensing applications.

2 Materials and Methods

The high purity analytical grade magnesium chloride, cobaltous chloride, manganese chloride and sodium hydroxide were used. Manganese doped magnesium-cobalt mixed ferrite ($Mg_{0.4}Co_{0.4}Mn_{0.2}Fe_2O_4$) nanoparticles were prepared by taking 0.4 M of magnesium chloride [$MgCl_2{\cdot}6H_2O$], 0.4 M of cobaltous chloride [$CoCl_2{\cdot}6H_2O$], 0.2 M manganese(II)chloride [$MnCl_2{\cdot}4H_2O$] and 2 M of anhydrous ferric chloride [$FeCl_3$] dissolved in de-ionised water. The neutralization was carried out with sodium hydroxide solution and pH was maintained at 8. The precipitate was thoroughly washed with distilled water and dried. The synthesized nanoparticles were annealed at 130, 600 and 900 °C and were subjected to X-ray diffraction technique to calculate the average nano-crystalline size using Debye—Scherrer formula. The FT-IR spectra of the sample were recorded and the characteristic absorption bands were observed. The morphological analysis of the sample was studied using Scanning Electron Microscope (SEM). The microstructure and particle size are analyzed by TEM analysis. The magnetic measurements were made using Vibrating sample magnetometer (VSM).

3 Resuts and Discussion

3.1 XRD Analysis

XRD structural analysis of manganese co-doped magnesium-cobalt ferrite nanoparticles ($Mg_{0.4}Co_{0.4}Mn_{0.2}Fe_2O_4$) annealed at 130, 600 and 900 °C are shown

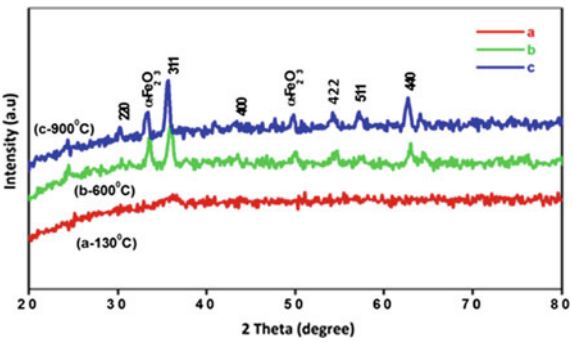

Fig. 1 XRD spectra $Mg_{0.4}Co_{0.4}Mn_{0.2}Fe_2O_4$ nanoparticles annealed at (*a*) 130 °C (*b*) 600 °C (*c*) 900 °C

in Fig. 1. The peaks are indexed with reference to the JCDPS card nos. 89-3084 for $MgFe_2O_4$, 22-1086 for $CoFe_2O_4$ and 74-2403 for $MnFe_2O_4$ and are found to be (220), (311), (400), (511) and (440). The well defined (311) peak appears to be more intense. The diffractograms showed the characteristic reflections of the cubic spinel phase. An impurity peak of hematite (α-Fe_2O_3) is observed in the sample annealed at 600 and 900 °C. The formation of α-Fe_2O_3 may be due to the loss of one or more of divalent cations during the washing and drying stages [11, 12]. Earlier reported results also shown the presence of α-Fe_2O_3 phase in the formation of Mn-Zn ferrite nanoparticles [13].

The diffraction pattern shows the amorphous nature of the sample annealed at 130 °C. As the annealing temperature increased to 600 and 900 °C, the peaks become sharper and narrower, indicating the crystalline nature of the sample. The average crystallite size (D) is calculated using the Debye Scherrer formula $D = 0.9\lambda/\beta\cos\theta$ where D is the crystallite size, λ is the wavelength of the X-ray radiation, θ is the diffraction angle, β is the full width half maximum [14]. The average crystallite size from X-ray technique is found to be 17 nm for the sample annealed at 600 °C and 19.6 nm for the sample annealed at 900 °C. It is found that the crystallite size increases as the annealing temperature increases [13]. This increase in crystallite size may be attributed due to the fusion of two or more smaller particles due to annealing at higher temperatures [15, 16]. The annealing process also reduces the defects and internal strains due to coalescence of crystallites; this in turn results in an increase in the average size of the nanoparticles.

The lattice constant is calculated using the relation

$$a = d_{hkl}\left(h^2 + k^2 + l^2\right)^{1/2}$$

where d is the interplanar distance of each plane and (hkl) are Miller indices. The lattice constant is estimated as 8.289 and 8.360 Å for the samples sintered at 600 and 900 °C respectively. The increase in lattice constant due to annealing could be explained by the surface disorder of nanoparticles. In ferrite nanoparticles, the

surface disorder is due to chemical bond frustration and oxygen vacancies at different sub-lattices on the surface [15]. During the annealing process, the surface unit cells get completed after getting atmospheric oxygen and reduce the surface disorder, thereby increasing the lattice constant.

3.2 FT-IR Analysis

Figure 2 shows the FT-IR spectra of manganese co-doped magnesium-cobalt ferrite ($Mg_{0.4}Co_{0.4}Mn_{0.2}Fe_2O_4$) nanoparticles annealed at 130, 600 and 900 °C. The FT-IR spectra are recorded in the wave number range of 4000–400 cm^{-1}. The absorption band around 1650 cm^{-1} may be due to the H-O-H bending vibrations of free or absorbed water. The bands around 2375 and 1530 cm^{-1} are due to traces of adsorbed or atmospheric CO_2 [17]. These bands disappeared as the samples are annealed at 900 °C. The two main broad metal-oxygen bands are seen in the infrared spectra of all spinels, especially ferrites. Waldron et al. [18] have reported that the higher absorption band around 600 cm^{-1}corresponds to the intrinsic vibrations of tetrahedral complexes and the lower absorption band around 400 $cm^{-1}$is attributed to the vibrations of octahedral complexes. In the present study, the higher absorption band (ν_1) observed in the range 590 and 546 cm^{-1}, is caused by the stretching vibrations of the tetrahedral metal-oxygen bond and the lowest band (ν_2) observed in the range 416 cm^{-1}, is caused by the metal-oxygen vibrations in the octahedral sites [18]. The absorption band shifts to higher

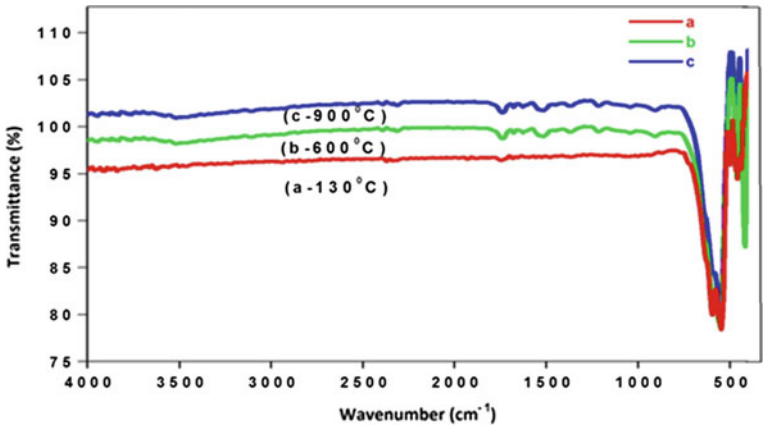

Fig. 2 FT-IR spectra of $Mg_{0.4}Co_{0.4}Mn_{0.2}Fe_2O_4$ nanoparticles annealed at (*a*) 130 °C (*b*) 600 °C (*c*) 900 °C

wavenumber as the samples are annealed at higher temperatures. The shift ensures that there is a variation in the cationic distribution.

3.3 SEM Analysis

Scanning electron micrographs of manganese co-doped magnesium-cobalt ferrite nanoparticles ($Mg_{0.4}Co_{0.4}Mn_{0.2}Fe_2O_4$) annealed at 130, 600 and 900 °C of uniform magnifications are shown in Fig. 3a–c. SEM micrographs show spherical shaped

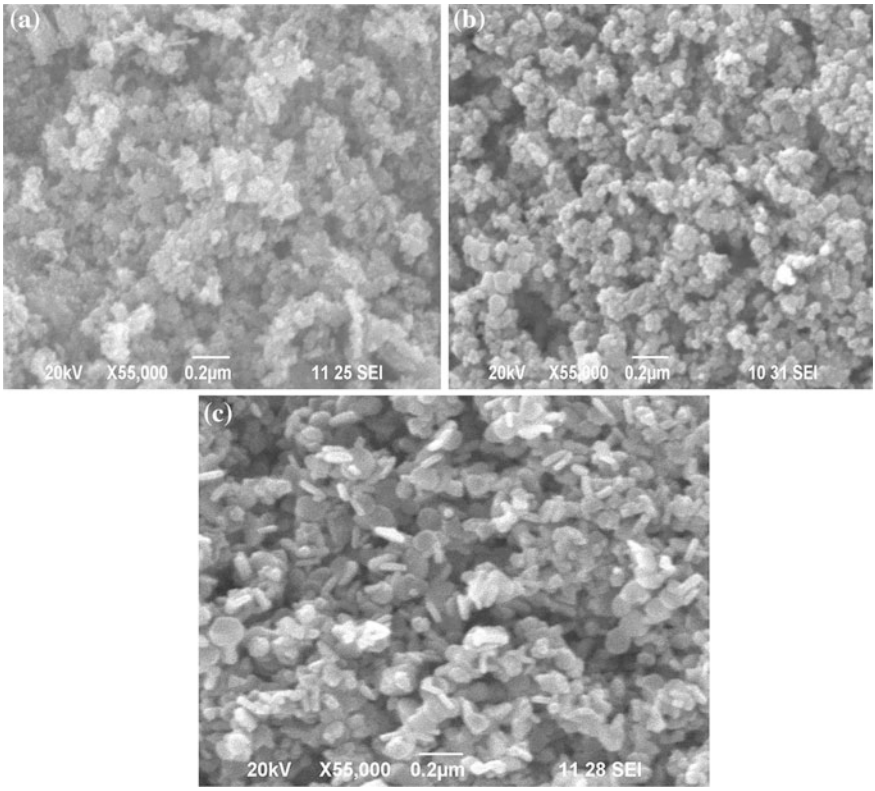

Fig. 3 **a–c** SEM Micrographs of $Mg_{0.4}Co_{0.4}Mn_{0.2}Fe_2O_4$ nanoparticles annealed at **a** 130 °C **b** 600 °C **c** 900 °C

particles distributed uniformly for the samples annealed at 130 and 600 °C. But for the samples annealed at 900 °C, the spherical shaped particles have been elongated and in few places rod like shape have also been observed. The increase in particle size of the samples could also be evidenced with the effect of annealing.

3.4 EDX Spectral Analysis

Figure 4 shows the EDX spectrum of manganese co-doped magnesium-cobalt ferrite nanoparticles $Mg_{0.4}Co_{0.4}Mn_{0.2}Fe_2O_4$ annealed at 600 °C. The chemical composition of the sample is confirmed from the EDAX analysis. It confirms the presence of the stoichiometric amount of Mg, Co, Mn, Fe and O without impurities.

3.5 TEM Analysis

Figure 5a–d shows the TEM micrographs of manganese co-doped magnesium-cobalt ferrite nanoparticles $Mg_{0.4}Co_{0.4}Mn_{0.2}Fe_2O_4$ annealed at 600 °C. TEM micrographs show the spherical shaped nanoparticles and the particle size is found to be around 40 nm.

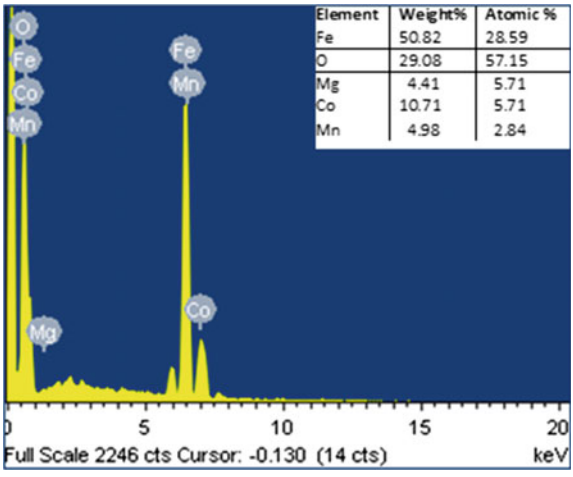

Fig. 4 EDX spectrum of $Mg_{0.4}Co_{0.4}Mn_{0.2}Fe_2O_4$ nanoparticles annealed at 600 °C

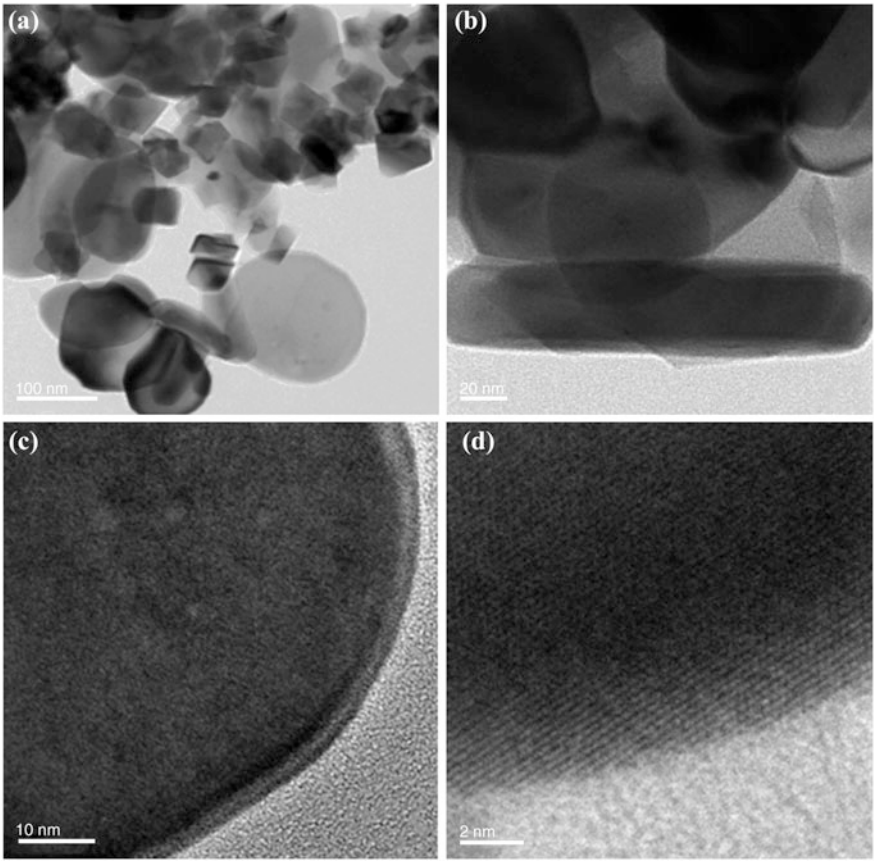

Fig. 5 **a–d** TEM images of $Mg_{0.4}Co_{0.4}Mn_{0.2}Fe_2O_4$ nanoparticles annealed at 600 °C

3.6 SAED Analysis

Figure 6 shows the SAED patterns of manganese co-doped magnesium-cobalt ferrite nanoparticles $Mg_{0.4}Co_{0.4}Mn_{0.2}Fe_2O_4$ annealed at 600 °C. The SAED pattern of high resolution TEM image confirms the crystalline nature of the sample with equal lattice arrangement.

3.7 VSM Analysis

VSM measurements of manganese co-doped magnesium-cobalt ferrite ($Mg_{0.4}Co_{0.4}Mn_{0.2}Fe_2O_4$) nanoparticles annealed at 130, 600 and 900 °C are shown in Fig. 7a–c.

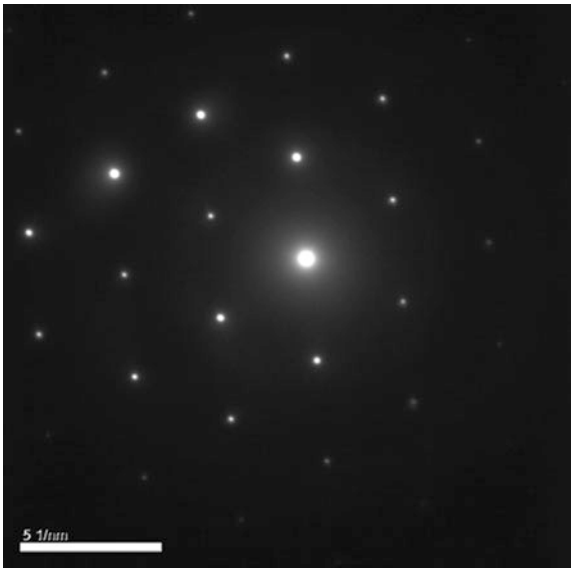

Fig. 6 SAED pattern of $Mg_{0.4}Co_{0.4}Mn_{0.2}Fe_2O_4$ nanoparticles annealed at 600 °C

The saturation magnetization (M_s), remanent magnetization (M_r), coercivity (H_c) and squareness ratio are listed in Table 1. From the table it is found that the saturation magnetization, remanent magnetization and coercivity increases due to inclusion of the manganese as dopant when compared with magnesium-cobalt ferrite system [19]. The replacement of non-magnetic Mg^{2+} ions by magnetic Mn^{2+} and Co^{2+} ions enhances the magnetic properties. Gagan kumar et al. have also reported that the magnetic properties have been enhanced due to the presence of Co^{2+} ions in magnesium-manganese ferrite nanoparticles processed via solution combustion technique [20]. Further the formation of α-Fe_2O_3 clusters, as evidenced from XRD analysis may also be responsible for increasing the ferromagnetic effect. It is further confirmed from the hysteresis loop that all the samples show ferromagnetic nature.

It is observed that as the annealing temperature increases the saturation magnetization (M_s), remanent magnetization (M_r), coercivity (H_c) increases. This increase in magnetic properties are due to the particle coarsening at higher temperatures, which in turn increases the crystallite size as could also be evidenced from XRD analysis [21]. The squareness ratio (R) is the ratio of remanent magnetization to saturation magnetization (i.e.) M_r/M_s is calculated to find the existence of intergrain exchanges [22]. It is observed from the Table 1 that the magnetostatic interactions takes place as the value of R is less than 0.5 [23].

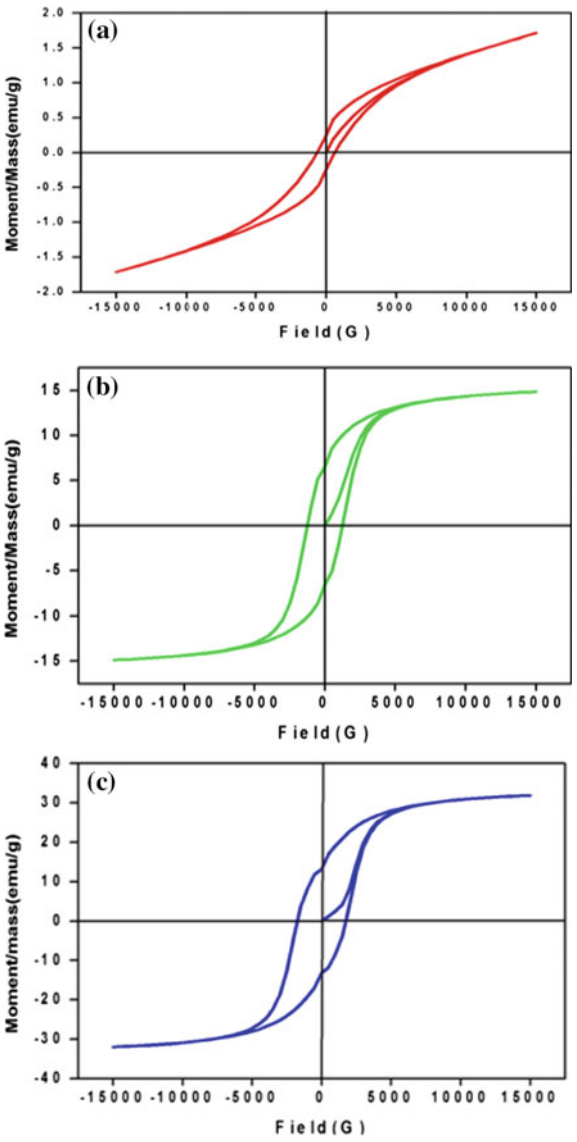

Fig. 7 **a**–**c** VSM measurements of $Mg_{0.4}Co_{0.4}Mn_{0.2}Fe_2O_4$ nanoparticles annealed at **a**130 °C **b** 600 °C **c** 900 °C

Table 1 The saturation magnetization (M_s), remanent magnetization (M_r), coercivity (H_c) and squareness ratio values of $Mg_{0.4}Co_{0.4}Mn_{0.2}Fe_2O_4$ nanoparticles

Annealing temperature (°C)	Saturation magnetization (M_s) (emu/g)	Remanent magnetization (M_r) (emu/g)	Coercivity (G)	Squareness ratio (R) = M_r/M_s
130	1.7151	0.24401	628.90	0.1422
600	14.862	6.5366	1242.2	0.4398
900	31.952	13.231	1739.3	0.4140

4 Conclusion

Manganese co-doped magnesium-cobalt ferrite nanoparticles ($Mg_{0.4}Co_{0.4}Mn_{0.2}Fe_2O_4$) are synthesized by co-precipitation method and are annealed at 130, 600 and 900 °C. The crystallite size is calculated from XRD analysis using Debye-Scherrer equation and is found to be 17 and 19.6 nm for the samples annealed at 600 and 900 °C respectively. The crystallite size increases as the samples are annealed at higher temperatures. FT-IR analysis confirms the characteristic absorption bands at 590 and 546 cm^{-1} for tetrahedral sites and 416 cm^{-1} for octahedral sites. The bands shift to higher wavenumber due to annealing effect. SEM analysis shows uniformly distributed spherical shaped nanoparticles. The particle size is found to be around 40 nm using TEM images. The SAED pattern confirms the crystalline nature of the sample. The saturation magnetization, remanent magnetization and coercivity increases due to the inclusion of manganese and as the annealing temperature increases. The annealing has significant effect on the structural and magnetic properties due to the variation in the cationic distribution. These samples can be tested for gas sensing applications.

References

1. Shimada, T., Tachibana, T., Nakagawa, T., Yamamoto, T.A.: Site occupation study of $ZnFe_2O_4$ and $NiFe_2O_4$ by far-infrared reflectivity. J. Alloys Compd. **379**, 122–126 (2004)
2. Smith, J., Wijn, H.P.J.: Ferrites. Philips Technical Library. Wiley, NewYork (1959)
3. Pradeep, A., Priyadharsini, P., Chandrasekaran, G.: Sol-gel route of nano particles of $MgFe_2O_4$ and XRD, FTIR and VSM study. J. Magn. Mag. Mater. **320**, 2779 (2008)
4. Landolt-Borstein.: Magnetic Oxides and Related Compounds. 3/4b, Springer, Berlin (1970)
5. Spaldin, N.: Magnetic Materials: Fundamentals and Device Applications. Cambridge University Press, Cambridge (2003)
6. Pillai, V., Shah, D.O.: Synthesis of high-coercivity cobalt ferrite particles using water-in-oil microemulsions. J. Magn. Magn. Mater. **163**, 243–248 (1996)
7. Zakaria, A.K.M., Asgar, M.A., Eriksson, S.G., Ahmed, F.U., Yunus, S.M., Azad, A.K.: Physica B **385–386**, 106–109 (2006)
8. Sláma, J., Dosoudil, R., Šáková, M. U., Šák, E.U., Grusková, A., Jančárik, V.: J. Magn. Magn. Mater. **304**, e758–e761 (2006)
9. Zhou, B., Zhang, Y.W., Liao, C.S., Yan, C.H., Chen, L.Y., Wang, S.Y.: Rare-earth-mediated magnetism and magneto-optical Kerr effects in nanocrystalline $CoFeMn_{0.9}RE_{0.1}O_4$ thin films. J. Magn. Magn. Mater. **280**, 327–333 (2004)
10. Gama, L., Hernandez, E.P., Cornejo, D.R., Costa, A.A., Rezende, S.M., Kiminami, R.H.G.A., Costa, A.C.F.M.: Magnetic and structural properties of nanosize Ni–Zn–Cr ferrite particles synthesized by combustion reaction. J. Magn. Magn. Mater. **317**, 29–33 (2007)
11. Mangalaraja, R.V., Ananthakmar, S., Manohar, P., Gnanama, F.D., Awano, M.: Material Science and Engineering A **367**(1–2), 301–305 (2004)
12. Suwalka, O.P., Sharma, R.K., Sebastian, V., Lakshmi, N., Venugopalan, K.: A study of nano NiCoZn-ferrite prepared by co-precipitation. J. Magn. Magn. Mater. **313**(1), 198–203 (2007)
13. Kumar, Ranjith: Jayaprakash, E., Seehra, R., Prakash, M.S., Sanjay Kumar, T.: Effect of α-Fe_2O_3 phase on structural, magnetic and dielectric properties of Mn–Zn ferrite nanoparticles. J. Phys. Chem. Solids **74**, 943–949 (2013)

14. Cullity, B.D.: Elements of X-ray diffraction, Addison-Wesely (1959)
15. Nadeem, K., Rahman, S., Mumtaz, M.: Prog. Nat. Sci. Mater. Int. **25**, 111–116 (2015)
16. Balavijayalakshmi, J., Suriyanarayanan, N., Jayaprakash, R.: Effects of sintering on structural and magnetic properties of Cu substituted cobalt-nickel mixed ferrite nano particles. J. Magn. Magn. Mater. **362**, 135–140 (2014)
17. Wu, K.H., Ting, T.H., Li, M.C., Ho, W.D.: Sol–gel auto-combustion synthesis of SiO_2-doped NiZn ferrite by using various fuels. J. Magn. Magn. Mater. **298**, 25–32 (2006)
18. Waldron, R.D.: Infrared spectra of ferrites. Phys. Rev. **99**, 1727 (1955)
19. Balavijayalakshmi, J., Sudha, T., Karthika, K.: Investigation on structural and magnetic properties of cobalt doped magnesium ferrite nanoparticles. Int. J. ChemTech Res. **7**(3), 1279–1283 (2015)
20. Kumar, Gagan, Rani, Ritu, Singh, Vijayender, Sharma, Sucheta, Batoo, Khalid M., Singh, M.: Magnetic study of nano-crystalline cobalt substituted Mg-Mn ferrites processed via solution combustion technique. Adv. Mat. Lett. **4**(9), 682–687 (2013)
21. Köseoğlu, Y., Alan, F., Tan, M., Yilgin, R., Öztürk, M.: Low temperature hydrothermal synthesis and characterization of Mn doped cobalt ferrite nanoparticles. Ceram. Int. **38**, 3625–3634 (2012)
22. Wang, Z.L., Liu, Y., Zhang, Z.: Handbook of Nanophase and Nanostructured Materials, Materials Systems and Applications I, vol. III. Kluwer Academic, Plenum Publishers, USA (2003)
23. Stoner, E.C., Wohlfarth, E.P.: A mechanism of magnetic hysteresis in heterogeneous alloys. Philosophical Transactions of Royal Society of London, Series A, Mathematical and Physical Sciences, **240**(826), 599–642 (1948)

Biosynthesis of Novel Zinc Oxide Nanoparticles (ZnO NPs) Using Endophytic Bacteria *Sphingobacterium thalpophilum*

Neethipathi Rajabairavi, Chellappan Soundar Raju, Chandrasekaran Karthikeyan, Kandhan Varutharaju, Shanmugam Nethaji, Abdulrahman Syedahamed Haja Hameed and Appakan Shajahan

Abstract In the present work, we describe the synthesis of zinc oxide nanoparticles (ZnO NPs) using culture supernatant of endophytic bacterial isolate *Sphingobacterium thalpophilum* and their antibacterial efficiency against bacterial pathogens. In the process of reduction aqueous zinc nitrate being extra-cellular which lead to the development of an easy bioprocess for synthesis of ZnO NPs. The ZnO NPs were characterized by X-ray Powder Diffraction (XRD), Field emission scanning electron microscopy (FESEM) and Energy dispersive X-ray analysis (EDAX). Ultraviolet-Visible (UV-Vis) Spectrometer and Fourier transfer infrared rays (FTIR) analysis. Antibacterial efficiency of ZnO NPs are tested with two bacterial pathogens *Pseudomonas aeruginosa* and *Enterobacter aerogens* using the disc diffusion method to determine their ability as potential antimicrobial agents. This ZnO NPs showed improved antibacterial activity on both tested strains. This was confirmed by zone of inhibition measurements.

N. Rajabairavi (✉)
Department of Biotechnology, Selvam Arts and Science College, Namakkal 637003, Tamil Nadu, India
e-mail: mailtobairavi@gmail.com

C.S. Raju
Department of Botany, Vivekananda College, Tiruvedakam West, 625234 Madurai, Tamil Nadu, India

C. Karthikeyan · A.S.H. Hameed
Department of Physics, Jamal Mohamed College, Tiruchirappalli 620 020, Tamil Nadu, India

C.S. Raju · K. Varutharaju · A. Shajahan
Department of Botany, Jamal Mohamed College, Tiruchirappalli 620020, Tamil Nadu, India

S. Nethaji
Department of Biochemistry, Marudupandiyar College, Thanjavur 613 403, Tamil Nadu, India

J. Ebenezar (ed.), *Recent Trends in Materials Science and Applications*, Springer Proceedings in Physics 189, DOI 10.1007/978-3-319-44890-9_23

1 Introduction

Zinc oxide (ZnO) could have many applications; such as optical, piezoelectric, magnetic, and gas sensing, ceramics, rubber processing, wastewater treatment, food package and antimicrobial agent [1–3]. Zinc oxide nanoparticles (ZnO NPs) are as a generally recognized as safe (GRAS) material, nontoxic and biocompatible [4]. Several reports stated that metal oxides induce cell death and cytotoxicity [5, 6]. The size, shape, surface area, surface reactivity, its charge, chemical composition and media interactions are the unique physicochemical properties of nanoparticles. Inorganic nanoparticles structures exhibit significantly novel and improved physical, chemical, and biological properties [1]. These nanoparticles have a vast anti-potential against pathogenic microorganisms, increase with decreasing particle size [7]. Conventional methods of nanotechnology are the organic compounds as a reducing agent, lower time consumption and rapid production of nanoparticles [8]. The presence of toxic chemicals on the surface led to adverse effects [1].

The development of reliable processes for the synthesis of metal nanomaterial has its great importance in the field of nanotechnology. Biological synthesis of nanoparticles is a cost effective and eco-friendly technology [9, 10]. There are several reports in the literature on the cell-associated biosynthesis of nanoparticles using several microorganisms [8, 11]. Cell mass or their leached cell components of microorganisms reduce the size of the metal ions. Our attempt is to isolate endophytic bacteria *Sphingobacterium thalpophilum* from sterilized plant parts of *Withania somnifera.* This is subjected to extra-cellular biosynthesis of ZnO NPs. This study is the first report describing the culture supernatant of *S. thalpophilum* for biosynthesis of ZnO NPs and their antibacterial efficiency against pathogenic bacteria.

2 Materials and Methods

2.1 Bacterial Strains and Culture Conditions

The fresh bacterial strain *S. thalpophilum* (from our collection; Genbank accession: KM019199.1) was maintained on nutrient agar medium at 37 °C for 24 h. Further, the culture was subcultured into nutrient broth medium at continuous orbital shaking in on 150 rpm (LM-570RD, Yihder, Thiwan), 37 °C for 24 h. The supernatant was collected after centrifugation at 5000 rpm for 5 min in overnight bacterial culture and it is used for synthesis of ZnO NPs.

2.2 Biosynthesis of Zinc Oxide Nanoparticles

The 100 ml of cell free supernatant and 100 ml of Zinc nitrate solution (1 mM) was taken in 500 ml beaker. The beaker containing mixture solution was placed on

magnetic stirrer at room temperature for 24 h and it was dried at 120 °C. This dried sample was annealed at 700 °C for 5 h because the energy from the heat can enhance the vibration and diffusion of the lattice atoms for crystallization.

2.3 Characterization Techniques

The ZnO NPs were characterized by X-ray diffractometer (model: X'Pert Pro Pan alytical). The diffraction patterns were recorded in the range of 20^{o} to 80^{o} for the ZnO samples where the monochromatic wavelength of 1.54 Å was used. The synthesized nanoparticles retained the wurtzite hexagonal structure, which was confirmed by X-ray diffraction studies (XRD). The size and morphology of ZnO NPs were analyzed by Field emission scanning electron microscope (FESEM; model: Supra 55) with EDAX (model: Ultra 55). The excitation spectra of these samples were measured by Ultraviolet visible spectrophotometer (UV-Vis; model: Lamda 35) operated at a resolution of 1 nm. A Fourier transfer infrared rays (Nicolet FT-IR Avatar 360, America) was employed to monitor the isocyanate concentration.

2.4 Antibacterial Studies

An agar disc diffusion method for antibacterial tests was carried out using nutrient agar plate. The inoculums were prepared with nutrient broth cultures of test bacteria *Pseudomonas aeruginosa* and *Enterobacter aerogens*. The bacterial suspension was loaded on a sterile cotton swab that was rotated several times and pressed firmly against the inside wall of the tube to remove excess inoculum from the swab. The dried surface of a nutrient agar plate was inoculated by streaking the swab over the entire sterile agar surface. The discs with the synthesized of ZnO NPs (0.3 g, 11 mm diameter) were placed on the top of the inoculated plates and incubated at 37 °C for 24 h. The antibacterial activity was evaluated by measuring the zone of growth inhibition surrounding the discs. The larger diameter zone of inhibition was the greater antimicrobial activity [7].

3 Results and Discussion

3.1 Biosynthesis of Zinc Oxide Nanoparticles

The formation of ZnO NPs by the culture supernatants of *S. thalpophilum* was investigated. The appearance of a brown color in the reaction vessels suggested the

Fig. 1 Solutions of ZnO before (*left*) and after (*right*) exposure to the culture supernatant of *S. thalpophilum*

formation of nanoparticles. In the present study before reaction, ZnO solution was colorless but its color was changed into brown after reacted with *S. thalpophilum* culture supernatant (Fig. 1). This result indicates the synthesis of nanoparticles.

3.2 X-ray Diffraction Analysis

The X-ray diffraction peaks of ZnO NPs synthesized using *S. thalpophilum* supernatant (Fig. 2). The XRD peaks are located at angles (2θ) of 31.761, 34.424 and 36.26242 corresponding to (100), (002) and (101) planes of the ZnO NPs. Similarly, other peaks found at angles (2θ) of 47.541, 56.61, 62.85 and 67.97 are corresponding to (102), (110), (103) and (112) planes of ZnO NPs. The standard diffraction peaks show the hexagonal wurtzite structure of ZnO NPs with the p63mc space group. This is also confirmed by the JCPDS data (Card no: 36-1451).

The lattice constants 'a' and 'c' of wurtzite structure can be calculated by using the relation [12] and the formula as follows,

$$\frac{1}{d^2} = \frac{4}{3}\left(\frac{h^2 + hk + k^2}{a^2}\right) + \frac{l^2}{c^2}$$

With the first order approximation (n = 1) for the (100) plane, the lattice constant 'a' is obtained through the relation $a = \frac{\lambda}{\sqrt{3}\sin\theta}$ and lattice constant 'c' is derived for the plane (002) by the relation $c = \frac{\lambda}{\sin\theta}$. For ZnO NPs, values of the lattice parameters 'a' and 'c' are estimated **3.2506** and **5.2063 Å** respectively.

The average crystal size of the samples is calculated after appropriate background correction from X-ray line broadening of the diffraction peaks of (101) plane using Debye Scherrer's formula [13],

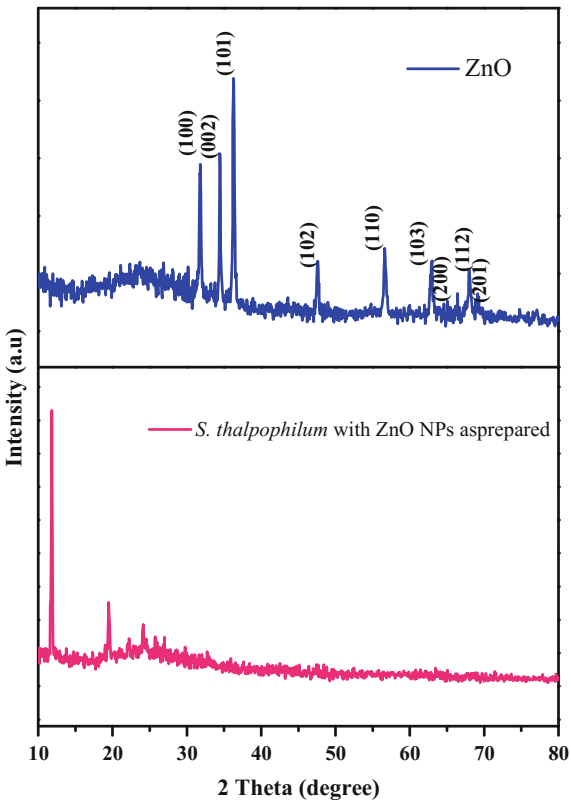

Fig. 2 X-ray powder diffraction patterns of ZnO NPs

$$\text{Average crystal size D} = \frac{k\lambda}{\beta_{D\cos\theta}}$$

Where D-is the size in nanometers, λ is the wavelength of the radiation (1.5406 Å for CuKα), k is a constant (0.94), β_D-is the peak width at half-maximum in radian along (101) plane and is Bragg's diffraction angle. The ZnO NPs average particle size is 37 nm respectively.

3.3 Field Emission Scanning Electron Microscope

The FESEM images of the ZnO NPs synthesized using *S. thalpophilum* supernatant. From the figures, we can find that the ZnO NPs form a triangle chips-like structure with uniform grain boundary formed (Fig. 3a, b). The chips average sizes of 112 nm are found respectively.

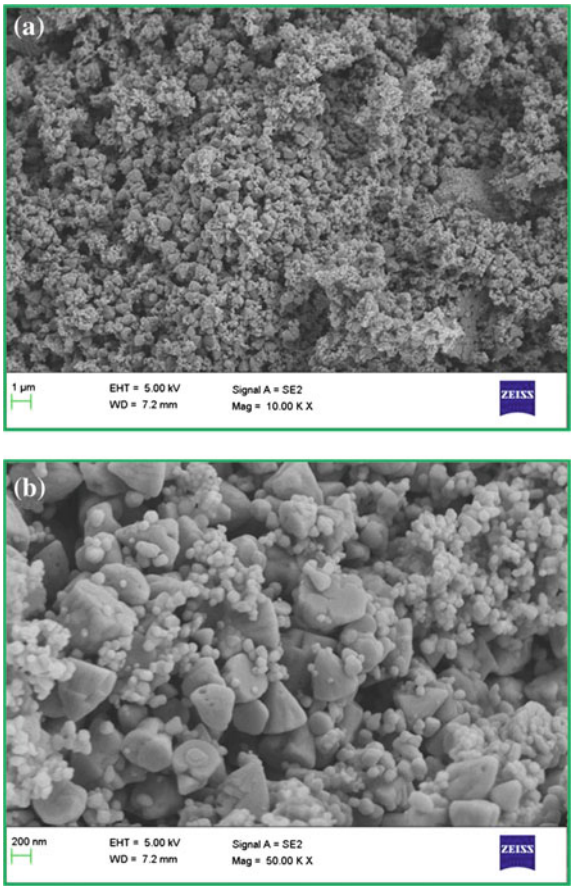

Fig. 3 FESEM images of ZnO NPs. **a** 10 KX image shows triangle chips-like structure with uniform grains of ZnO NPs X. **b** 50 KX image

3.4 Energy Dispersive X-ray Analysis

The compositional analysis of the ZnO synthesized using *S. thalpophilum* supernatant is carried out using EDAX. From the EDAX analysis, ZnO NPs atomic percentage of Zn and O are found to be 48.76 and 51.24 % respectively (Fig. 4a).

3.5 Ultraviolet Visible Spectrophotometer

The adsorption of ZnO NPs was determinate 379 nm by UV-Vis spectrophotometer (Fig. 4b). It has been found that the key factors which play important role in protein

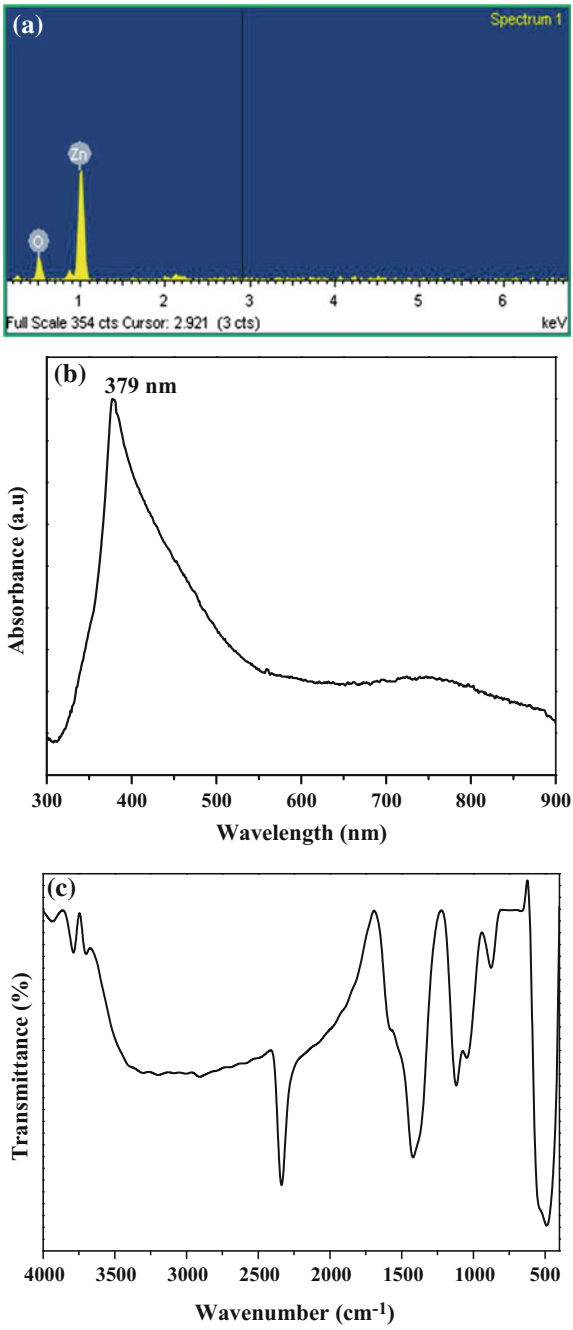

Fig. 4 Characterization of ZnO NPs. **a** EDAX spectrum, **b** UV-spectrum and **c** FT-IR spectrum of synthesized ZnO NPs using *S. thalpophilum* culture supernatant

adsorption on various materials are the electrostatic interaction, hydrophobic interaction and specific chemical interaction between protein and nanoparticles surface.

3.6 Fourier Transform Infrared Spectroscopy

The standard peaks of ZnO NPs around 488.34 cm^{-1} (Fig. 4c). This peak was attributed to the ZnO stretching frequency of Zn–O bonds. It further confirms the formation of ZnO NPs synthesized by using *S. thalpophilum* culture supernatant.

3.7 Antimicrobial Studies

Antibacterial activity of ZnO NPs was compared with water control and ZnO NPs with *S. thalpophilum* culture (Fig. 5a, b). ZnO NPs synthesized by endophytic bacteria *S. thalpophilum* tested against pathogenic bacteria is showed in the zone of inhibition of 14.3 mm with *P. aeruginosa* and 11.1 mm with *E. aerogens* with minimum concentration of ZnO NPs (Fig. 6). None of the effects were observed from ZnO NPs with *S. thalpophilum* culture and water control. The inhibition of bacterial growth by ZnO NPs could be attributed to damage of the bacterial cell membrane and extrusion of the cytoplasmic contents thereby resulting in the death of the bacterium. This depends on the nature of surface of different microbes. Sharma et al. [14] was also reported that the antimicrobial activity dependent on the concentration of the ZnO NPs and impact of the types of surfactant used. The result was concordant with Zhang et al. [15]. Similarly, reports of Sunkar and Valli Nachiyar

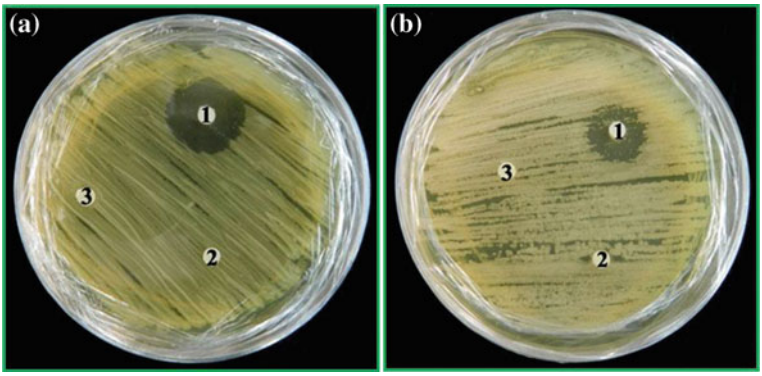

Fig. 5 Antibacterial efficiency of ZnO NPs against **a** *P. aeruginosa* and **b** *E. aerogens* (*Note* **1**—ZnO NPs; **2**—ZnO NPs with *S. thalpophilum* culture; **3**—water control)

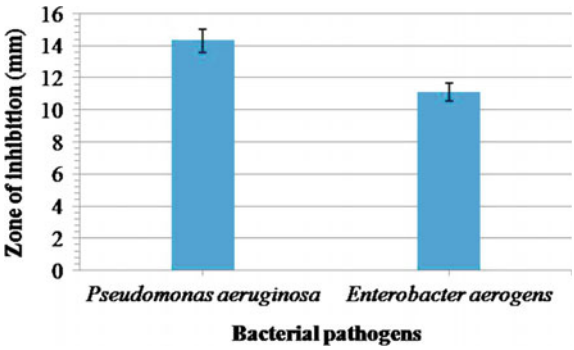

Fig. 6 Zone inhibition of ZnO NPs on bacterial pathogens

[16] regarding antibacterial activity of nanoparticles, produced by endophytic bacterium, *Bacillus cereus* isolated from *Garcinia xanthochymus* showed zone of inhibition at higher level.

4 Conclusion

In this study we demonstrated the extra-cellular synthesis of ZnO NPs by endophytic bacterial isolate *S. thalpophilum* for antimicrobial agent. The ZnO NPs were characterized by XRD studies, UV-Vis spectrometer, FTIR analysis, FESEM and EDAX. The antimicrobial activity of the zinc oxide nanoparticles has been examined on two common bacterial pathogens *P. aeruginosa* and *E. aerogens*. The ZnO NPs exhibits the better bactericidal activity which eradicated both bacterial species. Inorganic metal oxides may serve as effective disinfectants, due to their relatively non-toxic profile, chemical stability and efficient antibacterial activity. Zinc oxide is one of the metal oxide which has the significant bacterial growth inhibition efficiency, by catalysing the development of reactive oxygen species (ROS) from water and oxygen, which disrupt the integrity of the bacterial membrane [17]. ROS contain the most reactive hydroxyl radical (OH), the less toxic superoxide anion radical (O_2^-) and hydrogen peroxide with a weaker oxidizer (H_2O_2). This can damage DNA, cell membranes etc., leading to cell death. Generally, nanoparticles with better photocatalytic activity have a larger specific surface area and a smaller crystal size which increase oxygen vacancies, resulting in more ROS [18, 19].

References

1. Gunalan, S., Sivaraj, R., Rajendran, V.: Green synthesized ZnO nanoparticles against bacterial and fungal pathogens. Prog. Nat. Sci. Mat. Internat. **22**, 693–700 (2012)
2. Wang, A., Lu, J., Xu, M., Xing, B.: Sorption of pyrene by regular and nanoscaled metal oxide particles: influence of adsorbed organic matter. Environ. Sci. Tech. **42**, 7267–7272 (2008)

3. Espitia, P.J.P., Soares, N.F.F., Coimbra, J.S.R., de Andrade, N.J., Cruz, R.S., Medeiros, E.A.A.: Zinc oxide nanoparticles: synthesis, antimicrobial activity and food packaging applications. Food Biopro. Technol. **5**, 1447–1464 (2012)
4. Raghupathi, K.R., Koodali, R.T., Manna, A.C.: Size-dependent bacterial growth inhibition and mechanism of antibacterial activity of zinc oxide nanoparticles. Langmuir **27**, 4020–4028 (2011)
5. Magrez, S., Kasas, V., Salicio, N., Pasquier, J., Seo, W., Celio, M., Catsicas, S., Schwaller, B., Forro, L.: Cellular toxicity of carbon-based nanomaterials. Nano Lett. **6**, 1121–1125 (2006)
6. Long, T.C., Saleh, N., Tilton, R.D., Lowry, G.V., Veronesi, B.: Titanium, Dioxide (P25) produces reactive oxygen species in immortalized microglia (Bv2): implications for nanoparticle neurotoxicity. Environ. Sci. Tech. **40**, 4346–4352 (2006)
7. Suyana, P., Nishanth Kumar, S., Dileep Kumar, B.S., Nair, B.N., Pillai, S.C., Peer Mohamed, A., Warriera, K.G.K., Hareesh, U.S.: Antifungal properties of nanosized ZnS particles synthesised by sonochemical precipitation. RSC Adv. **4**, 8439–8445 (2014)
8. Shivaji, S., Madhu, S., Singh, S.: Extracellular synthesis of antibacterial silver nanoparticles using psychrophilic Bacteria. Proc. Bioch. **46**, 1800–1807 (2011)
9. He, S., Guo, Z., Zhang, Y., Zhang, S., Wang, J., Gu, N.: Biosynthesis of gold nanoparticles using the bacteria *Rhodopseudomonas capsulate*. Mat. Lett. **61**, 3984–3987 (2007)
10. Husseiny, M.I., Abd El-Aziz, M., Badr, Y., Mahmoud, M.A.: Biosynthesis of gold nanoparticles using *Pseudomonas aeruginosa*. Spect. Acta Part A. **67**, 1003–1006 (2007)
11. Shahverdi, A.R., Minaeian, S., Shahverdi, H.R., Jamalifar, H., Nohi, A.-A.: Rapid synthesis of silver nanoparticles using culture supernatants of *Enterobacteria*: a novel biological approach. Proc. Bioch. **42**, 919–923 (2007)
12. Suryanarayana, C., Norton, M.G.: X-ray Diffraction: A Practica Approach. Plenum Press, New York (1998)
13. Chauhan, R., Kumar, A., Chaudharya, R.P.: Synthesis and characterization of copper dopped ZnO nanoparticles. J. Chem. Pharm. Res. **2**, 178–183 (2010)
14. Sharma, D., Rajput, J., Kaith, B.S., Kaur, M., Sharma, S.: Synthesis of ZnO nanoparticles and study of their antibacterial and antifungal properties. Thin Solid Fil. **519**, 1224–1229 (2010)
15. Zhang, L., Jiang, Y., Ding, Y., Povey, M., York, D.: Investigation into the antibacterial behavior of suspensions of ZnO nanoparticles (ZnO nanofluides). J. Nanopart. Res. **9**, 479–489 (2007)
16. Sunkar, S., Valli Nachiyar, C.: Biogenesis of antibacterial silver nanoparticles using the endophytic bacterium *Bacillus cereus* isolated from *Garcinia xanthochymus*. Asian Spac. J Trop. Biomed. **2**, 953–959 (2012)
17. Gordon, T., Perlstein, B., Houbara, O., Felner, I., Banin, E., Margel, S.: Synthesis and characterization of zinc/iron oxide composite nanoparticles and their antibacterial properties. Col. Surf. A. Physicochem. Eng. Aspec. **374**, 1–8 (2011)
18. Becker, J., Raghupathi, K.R., Pierre, J.S., Zhao, D., Koodali, R.T.: Tuning of the crystallite and particle size of ZnO nanocrystallite materials in solvothermal synthesis and their photocatalytic activity for dye degradation. J. Phys. Chem. C **115**, 13844–13850 (2011)
19. Haja Hameed, A.S., Karthikeyan, C., Sasikumar, S., Senthil Kumar, V., Kumaresan, S., Ravi, G.: Impact of alkaline metal ions Mg^{2+}, Ca^{2+}, Sr^{2+} and Ba^{2+} on the structural, optical, thermal and antibacterial properties of ZnO nanoparticles prepared by the coprecipitation method. J. Mater. Chem. B. **1**, 5950–5962 (2013)

Hollow $ZnSnO_3$ Crystallites: Structural, Electrical and Optical Properties

P. Prabakaran, M. Victor Antony Raj, Jobin Job Mathen, S. Prathap and J. Madhavan

Abstract Zinc stannate ($ZnSnO_3$) hollow cubic crystallites were successfully synthesized by hydrothermal reaction at 120 °C. X-ray diffraction (XRD) and Scanning Electron Microscopy (SEM) studies were employed to characterize the structure and morphology of the as-synthesized $ZnSnO_3$ crystallites and it is found that $ZnSnO_3$ exhibits almost uniform cubic structure. The FT-IR analysis confirmed the functional groups. Dielectric constant and dielectric loss were found to decrease with increase in frequency. UV and Photoluminescence spectra analysis were also performed.

1 Introduction

Zinc stannate ($ZnSnO_3$), has drawn considerable attention due to its potential applications in gas sensors [1–4]. Besides structure, the controlled synthesis of various shapes of $ZnSnO_3$ crystals allows researchers to tailor its physical and chemical properties for the practical applications of functional materials with good sensor response and selectivity. Several methods including low-temperature ion exchange [2], co-precipitation [5], low-temperature solution-phase synthesis and hydrothermal methods [6–8] have been used to fabricate various morphologies of $ZnSnO_3$ crystals [1, 2, 5, 6, 9].

The current investigation is focused on the synthesis of zinc stannate via hydrothermal technique. The characterization, such as XRD, FTIR, SEM, UV, PL and dielectric studies were carried out to reveal the structural, morphological, optical and electrical properties of $ZnSnO_3$.

P. Prabakaran · M. Victor Antony Raj · J.J. Mathen · J. Madhavan (✉)
Department of Physics, Loyola College, Chennai 600034, India
e-mail: jmadhavang@yahoo.com

S. Prathap
Department of Physics, Arul Anandar College, Karmathur, Madurai 625514, India

J. Ebenezar (ed.), *Recent Trends in Materials Science and Applications*,
Springer Proceedings in Physics 189, DOI 10.1007/978-3-319-44890-9_24

2 Experimental Studies

The hydrothermal method was carried out for the preparation of $ZnSnO_3$ cubic crystallites [10]. All chemicals were of analytical grade. In a typical procedure, the solution of zinc acetate ($Zn(CH_3COO)_2{\cdot}2H_2O$) (0.8 M) and stannic chloride hydrated ($SnCl_4{\cdot}5H_2O$) (0.8 M) was prepared in double distilled water and stirred continuously for 4 h at room temperature. Then, hexamethylenetetramine ($(CH_2)_6N_4$) (0.015 M) was added as capping agent and a suitable amount of NaOH was added drop-wise to the reaction mixture with continuous stirring until the final solution pH value of about 10 was achieved. The reaction mixture was decanted into a Teflon-lined stainless steel autoclave of 150 ml in volume and maintained at 120 °C for 15 h and cooled to room temperature naturally. After the hydrothermal process, the precipitate was washed out with distilled water in an ultrasonic bath and the product was separated with a centrifuge. The obtained $ZnSnO_3$ was utilized for further characterization.

3 Results and Discussion

3.1 X-ray Diffraction Studies

The powder XRD analysis was carried out using Rich Seifert diffractometer with CuK_α (λ = 1.5418 Å) radiation. The intensity values are recorded between the ranges 10–80°. The XRD pattern of the as-synthesized product is depicted in Fig. 1. The diffraction peaks can be indexed to the standard $ZnSnO_3$ with the perovskite structure (JCPDS no: 11-0274), confirming that the as-synthesized product has a typical face centered cubic (FCC) crystal structure.

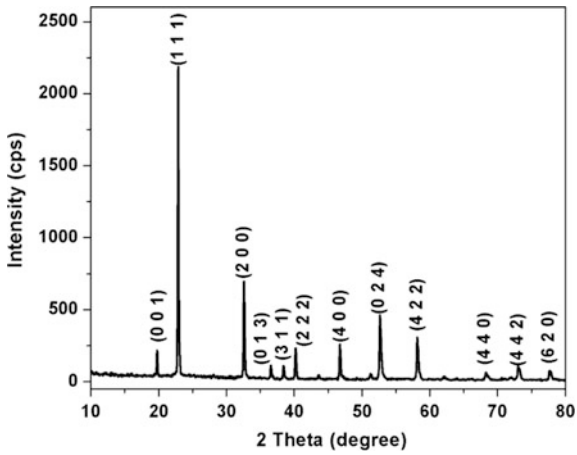

Fig. 1 XRD pattern of as-synthesized $ZnSnO_3$

No diffraction peaks due to impurities or other crystalline byproducts, such as ZnO or SnO_2 were detected. Crystallite size was calculated using Scherer formula:

$$D = \frac{K\lambda}{\beta \cos\theta}$$

where β is the full width at half maximum (FWHM) of the peak, λ is X-ray wavelength of CuKα radiation, θ is the diffraction angle and K = 0.94, a dimensionless constant. The average crystallite size was found to be 36 nm.

3.2 SEM Analysis

The scanning electron microscope (SEM) uses a focused beam of high-energy electrons to generate a variety of signals at the surface of solid specimens. The signals that derive from electron-sample interactions reveal information about the sample including external morphology, chemical composition, crystalline structure and orientation of materials making up the sample.

The morphology of the sample was obtained using SEM analysis. The SEM micrograph of $ZnSnO_3$ nanoparticles prepared via hydrothermal method is shown in Fig. 2. This image indicates that the $ZnSnO_3$ products usually exhibit a geometrically cubic-shape.

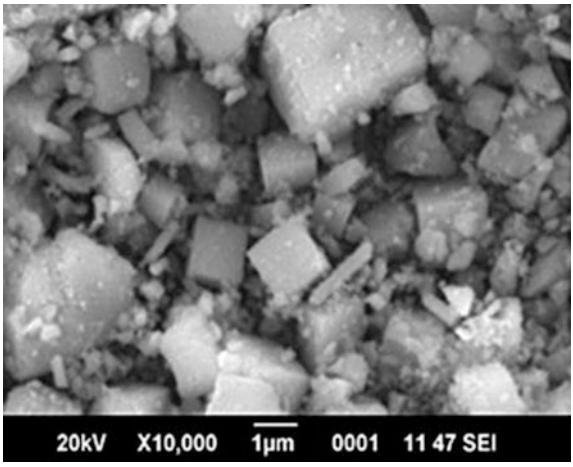

Fig. 2 SEM image of $ZnSnO_3$ cubic crystallites

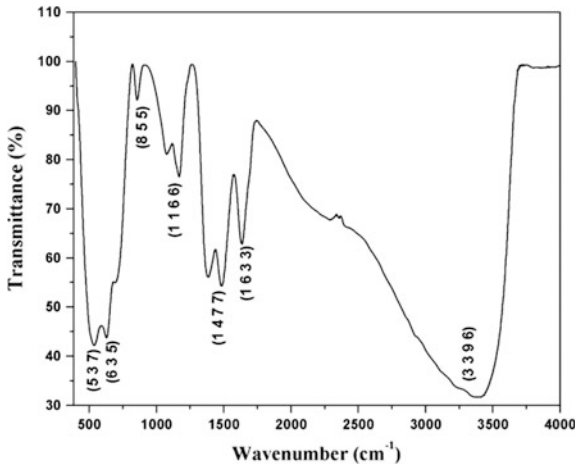

Fig. 3 FT-IR spectrum of $ZnSnO_3$

3.3 Fourier Transform Infrared Spectroscopy

FT-IR studies were performed using Perkin Elmer Spectrum FT-IR Spectrophotometer. FT-IR spectrum was recorded for $ZnSnO_3$ in range 400–4000 cm^{-1} and is shown in Fig. 3. A broad absorption peak occurs at 3396 cm^{-1} is assigned to O–H stretching vibration and the small pinnacle at wavenumber 1633 cm^{-1} is ascribed to the O–H bend vibration [11, 12]. The peak observed at 1166 cm^{-1} is due to the Sn–O bending. A broad absorption peak occurs at 537–635 cm^{-1} for $ZnSnO_3$ is due to symmetric stretching vibration of ZnO and SnO_2 groups and this band could be assigned to the Sn–O–Zn bonding of the $ZnSnO_3$ [13]. Huang et al. [14] previously reported that two peaks observed at 3221 and 3417 cm^{-1} were related to the presence of large amount of –OH in the precursor and the absorbance of water. The present study emphasized that the prepared hollow $ZnSnO_3$ is water free. These observed peaks are attributed to the formation of $ZnSnO_3$.

3.4 UV Spectral Analysis

The spectroscopic properties of any given sample can be understood by analyzing its UV-Vis spectrum. Figure 4 shows the absorption spectrum of $ZnSnO_3$ nanoparticles synthesized by hydrothermal method. The absorption edge is found to be centered at 380 nm, beyond which the sample is completely transparent [15].

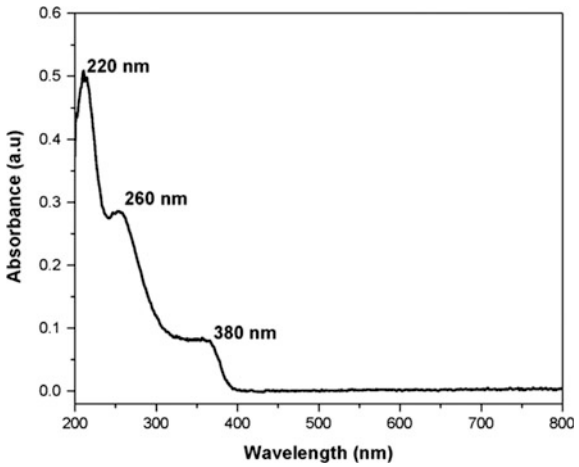

Fig. 4 Absorbance spectrum of $ZnSnO_3$

3.5 Photoluminescence Study

Although zinc stannate semiconductors have wide band gaps, they possess the radiative defect states in a broad visible region. Figure 5 shows the PL spectrum of $ZnSnO_3$ nanoparticles. The sample exhibited emission peaks both in the UV as well as in the visible region. The spectrum pronounced the excitonic emission is near at band edge and defect-related emission at 383 and 614 nm, respectively corresponding to the cubic $ZnSnO_3$ nanoparticles [16].

The defect-related green emission peak at 579 nm is attributed to the oxygen vacancies and/or Zn interstitials [17]. The oxygen vacancies act as luminescent

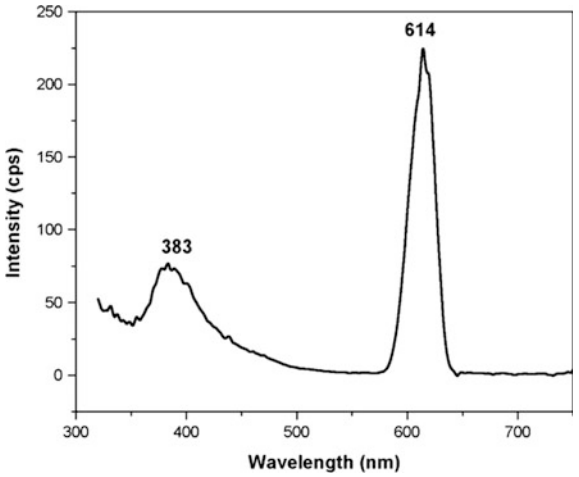

Fig. 5 PL spectrum of $ZnSnO_3$

centers and can form defect levels located highly in the band gap region, trapping electrons from the valence band, contributing to the luminescence.

3.6 Dielectric Studies

The dielectric studies were carried out using HIOKI 3532-50 HITESTER LCR impedance analyzer. The measurements were made at frequencies ranging from 50 Hz to 5 MHz at temperatures 100, 200, 300 and 400 °C. It is well known that polarizability is proportional to dielectric parameters. The polarized molecules or atoms can align in accordance with the applied electric field and cause

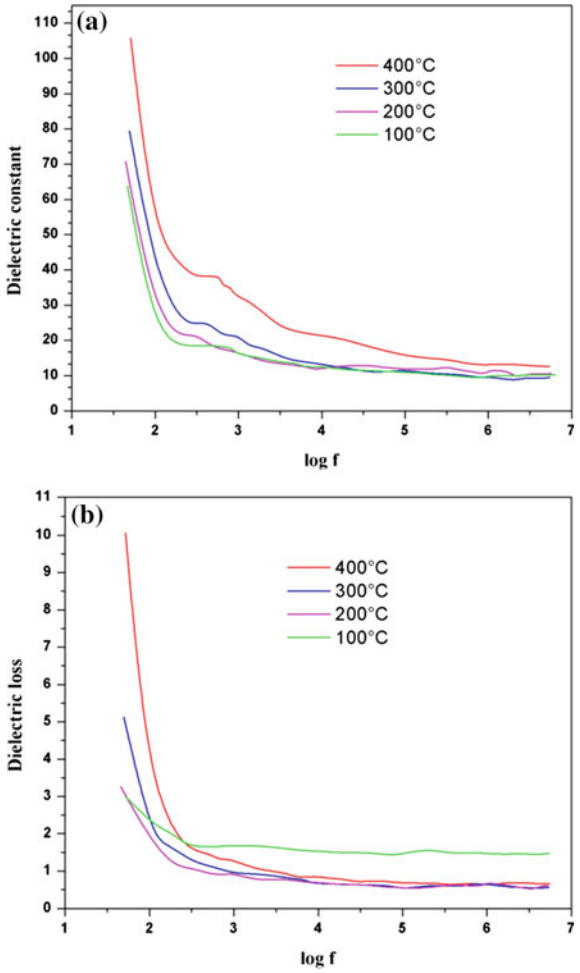

Fig. 6 **a** Variation of dielectric constant with log f. **b** Variation of dielectric loss with log f

electromagnetic energy to be transferred into materials. Figure 6a portrays the frequency dependence of dielectric constant and is found to be higher at low frequency and it drops down at 1 kHz and possesses a constant behavior. The higher value at lower frequencies is due to the space charge polarization. Moving to the higher frequency, the dipoles find difficult to orient at the same pace as the alternating field, so the contribution to the relative permittivity goes on in a continuously decreasing manner. The plateau level beyond 1 kHz can be attributed to the orientational polarization effects due to relaxing dipoles. The frequency dependence of the dielectric loss of $ZnSnO_3$ is shown in Fig. 6b. The higher value of dielectric loss at the lower frequency and its decrease in trend with increase in frequency are due to the free charge motion within the material.

4 Conclusion

In summary, we have prepared hollow $ZnSnO_3$ using a facile hydrothermal method and characterized by XRD, SEM, FTIR, UV-Vis, PL and Dielectric measurements. The structure and morphology of the synthesized particles exhibit a cubic geometry. Optical and electrical properties of $ZnSnO_3$ nanoparticles were investigated.

References

1. Shen, Y.S., Zhang, T.S.: Preparation, structure and gas sensing properties of ultramicro $ZnSnO_3$ powder. Sens. Actuators, B **12**, 5–9 (1993)
2. Chen, Y.J., Xue, X.Y., Li, Q.H., Wang, C., Wang, Y.G., Wang, T.H.: Linear ethanol sensing of SnO_2 nanorods with extremely high sensitivity. Appl. Phys. Lett. **88**, 083105 (2006)
3. Zhang, T.S., Shen, Y.S., Zhang, R.F.: Ilmenite structure-type beta CdSnO used as on ethonal sensing material. Mater. Lett. **23**, 69–71 (1995)
4. Wu, X.H., Wang, Y.D., Li, Y.F., Zhang, Z.L.: Study on $ZnSnO_3$ sensitive material based on combustible gases. Mater. Chem. Phys. **77**, 588–593 (2002)
5. Kovacheva, D., Petrov, K.: Preparation of crystalline $ZnSnO_3$ from Li_2SnO_3 by low-temperature ion exchange. Solid State Ionics **109**, 327–332 (1998)
6. Zeng, Y., Zhang, T., Fan, H.T., Lu, G.Y., Kang, M.H.: Growth and selective acetone detection based on ZnO nanorod arrays. Sen. Actuators B **143**, 449–453 (2009)
7. Zeng, Y., Zhang, T., Fan, H.T., Fu, W.Y., Lu, G.Y, Sui, Y.M., Yang, H.B.: One-pot synthesis and gas-sensing properties of hierarchical $ZnSnO_3$ nanocages. J. Phys. Chem. C. **113**, 1900–1905 (2009)
8. Xu, J.Q., Jia, X.H., Lou, X.D., Shen, J.N.: One-step hydrothermal synthesis and gas sensing property of $ZnSnO_3$ microparticles. Solid State Electron. **50**, 504–508 (2006)
9. Geng, B.Y., Fang, C.H., Zhan, F.M., Yu, N.: Synthesis of polyhedral $ZnSnO_3$ microcrystals with gas-sensing properties. Small **4**, 1337–1343 (2008)
10. Zeng, Y.I., Zhang, K., Wang, X., Sui, Y., Zou, B., Zheng, W., Zou, G.: Rapid and selective H_2S detection of hierarchical $ZnSnO_3$ nanocages. Sens. Actuators B **159**, 245–250 (2011)
11. Fu, X.L., Wang, X.X., Ding, Z.X., Leung, D.Y.C., Zhang, Z.Z., Long, J.L., Zhang, W.X., Li, Z.H., Fu, X.Z.: Hydroxide $ZnSn(OH)_6$: a promising new photocatalyst for benzene degradation. Appl. Catal. B. Environ. **91**, 67–72 (2009)

12. Wu, M.M., Li, X.L., Shen, G.P., Li, J., X, R.R., Proserpio, D.M.: Hydrothermal synthesis and structural characterization of a novel hydroxo stannate: $Sr_2Sn(OH)_8$. J. Solid State Chem. **151**, 56–60 (2000)
13. Nehru, L.C., Sanjeeviraja, C.: Microwave-assisted solution combustion synthesis of nanostructured Zn_2SnO_4. Nanosci. Nanotechnol. **3**(1), 10–13 (2013)
14. Huang, J., Xiaojuan, X., Cuiping, G., Wang, W., Geng, B., Sun, Y., Liu, J.: Size-controlled synthesis of porous $ZnSnO_3$ cubes and their gas-sensing and photocatalysis properties. Sens. Actuators B **171–172**, 572–579 (2012)
15. Borhade, A.V., Baste, Y.R.: Study of photocatalytic asset of the $ZnSnO_3$ synthesized by green chemistry. Arab. J. Chem. **25**, 134–139 (2012)
16. Dong, S., Sun, J., Li, Y., Yu, C., Li, Y., Sun, J.: $ZnSnO_3$ hollow nanospheres/reduced graphene oxide nanocomposites as high-performance photocatalysts for degradation of metronidazole. Appl. Catal. B **144**, 386–390 (2014)
17. Liu, C., Roder, R., Zhang, L., Ren, Z., Chen, H., Zhang, Z., Ronning, C., Gao, P.X.: Highly efficient visible-light driven photocatalysts: a case of zinc stannate based nanocrystal assemblies. J. Mater. Chem. A **2**, 4157–4159 (2014)

Study of PVA/CA/NH_4SCN/Ethylene Carbonate/Al_2O_3 Polymer Nano-Composite Electrolyte System

S. Gurulakshmi, S. Madeswaran, S. Karthikeyan, S. Selvasekarapandian and S. Monisha

Abstract Poly (vinyl alcohol)—Cellulose acetate (PVA/CA) blend polymer doped with Ammonium thiocyanate salt in the presence of Ethylene Carbonate (EC) as a plasticizer were prepared by simple solution casting technique. PVA/CA blend ratio was first optimized for highest conductivity value (3.63×10^{-6} S/cm). The ionic conductivity of PVA/CA blend was further enhanced by adding 0.5 mol wt% NH_4SCN and 0.3 mol wt% EC. The value of the ionic conductivity at room temperature was increased to 7.7×10^{-4} S/cm. AC impedance spectroscopy studies were used to calculate ionic conductivity values. Fourier Transform—Infrared Spectroscopy measurements revealed the existence of blending and salt complexation with host polymer. Activation energy and relaxation time were observed for the prepared plasticized membranes using Arrhenius plot and loss tangent spectra. The ionic conductivity at room temperature was further increased to the value of 2.1×10^{-3} S/cm by the addition of nano-alumina particles.

S. Gurulakshmi (✉) · S. Madeswaran
SAS, VIT University, Vellore, India
e-mail: ssgurulaxmi@gmail.com

S. Gurulakshmi
Guru Nanak College, Chennai, India

S. Karthikeyan
Madras Christian College, Chennai, India

S. Selvasekarapandian
Materials Research Centre, Coimbatore, India

S. Monisha
N.M.S.S. Vellaichamy Nadar College, Madurai, India

J. Ebenezar (ed.), *Recent Trends in Materials Science and Applications*,
Springer Proceedings in Physics 189, DOI 10.1007/978-3-319-44890-9_25

1 Introduction

Among all the clean energy devices the Proton Exchange Membrane Fuel Cell (PEMFC) attracts more attention. Polymer electrolyte membrane is the most important component of the PEMFC because of its role of proton conduction between electrodes. It stops the electrons from entering into the electrolyte. Polymer electrolyte acts as a good insulator at the same time it has high ionic conductivity. Currently, a perfluorinated polymer called Nafion (Dupont) is used as a PEM material. However, it has some drawbacks such as high fuel crossover, complex to be synthesized and is very expensive.

The common polymers used in PEM materials are made of polyimides, polysulfone, polybenzimidazole, polyetheretherketone (PEEK) [1, 2], Polyethylene oxide (PEO), Polyvinylidene fluoride, poly (acrylonitrile), poly (vinyl chloride) and poly (vinylidene fluoride-co-hexafluoropropylene) [3, 4]. Many approaches are available to increase the conductivity such as cross-linking two polymers, adding plasticizers to polymer electrolytes, adding inorganic inert fillers and blending of two polymers [4–10]. Polymer blends are physical mixtures of structurally different polymers that interact through secondary forces and that are miscible at the molecular level. The most common interactions present in the blend are hydrogen bonding, ionic and dipole interaction. It is reported by many researchers that polymer blending has improved the conductivity and structural stability of an electrolyte [4]. Also, the incorporation of plasticizer and inorganic fillers into polymer electrolytes has contributed the enhancement of ion pair dissociation into free ions which lead to high ionic conductivity [4].

The main objective of the work is to improve the ionic conductivity above 10^{-3} S/cm at ambient temperature for practical applications [11]. This paper focuses on developing composite polymer electrolyte blend in the presence of a plasticizer and nano-particle as filler. The Poly (vinyl alcohol) (PVA) and Cellulose Acetate (CA) are selected for the polymer blending. Among the polymers, PVA has excellent physical properties such as electrochemical stability, good film forming capability, non-toxicity, and biocompatibility. CA is one of the most commercially available cellulose derivatives which are used in several applications such as textiles, dialysis, reverse osmosis and gas separation [12]. However, PVA does not have fixed charges and swells easily in water which makes the conductivity and mechanical strength into an undesirable level. Hence, PVA needs to be modified to improve the proton conductivity and its mechanical strength. In literature, PVA/CA blend has been reported for ultra purification and reverse osmosis process [2, 11] but no report has been found on PVA blend with Cellulose Acetate as a polymer electrolyte membrane. It was reported that the addition of nanosized ceramic fillers such as TiO_2, Al_2O_3, SiO_2 significantly improve the mechanical strength and ionic conductivity [13, 14]. The dispersion of nanofillers in the polymer matrix reduces the crystallinity. It alters the flexibility of the chain structure and movement of free ions within the polymer electrolyte and hence improves the ionic conductivity [14].

In the present study, PVA was first blended with Cellulose Acetate with different molar ratios and the maximum conductivity of 3.63×10^{-6} S/cm was obtained for 97 mol wt% of PVA/3 % mol wt% of CA blend polymer. By fixing this ratio for blend polymer, Conductivity value was increased to a value of 2.55×10^{-4} S/cm with the addition of 0.5 mol wt% of ammonium thiocyanate. Then Ethylene Carbonate (EC) was introduced as a plasticizer. Its mol wt% was optimized and the conductivity was improved to 7.7×10^{-4} S/cm for 0.3 mol wt% of Ethylene Carbonate. Finally, Conductivity was improved to a value of 2.1×10^{-3} S/cm for 0.4 mol wt% of Alumina nano-size fillers.

The amorphous nature of plasticized polymer blend—salt complex was analyzed by the X-ray Diffraction (XRD) and the incorporation of Ammonium salt and plasticizer with the polymer blend was confirmed by FT-IR studies. Electrical studies of all prepared membranes were characterized by AC Impedance spectroscopic studies.

2 Experimental Technique

2.1 Sample Preparation

Polyvinyl alcohol (PVA, M_w = 125,000, 88 % hydrolyzed, AR Grade, MERCK made) and Cellulose Acetate (CA, Loba made) have been used as a host polymers in the present work. Ammonium thiocynate (Sigma-Aldrich) was doped, as ammonium provides protons for ionic conduction. Ethylene Carbonate (Merk) was used as a plasticizer. Nano-Alumina (size < 50 nm, Sigma-Aldrich made) was used as inorganic filler. DiMethyl Sulfoxide (DMSO) was used as a solvent. Films with different ratio of (1) PVA/CA, (2) PVA/CA/NH_4SCN, (3) PVA/CA/NH_4SCN/EC and PVA/CA/NH_4SCN/EC/Al_2O_3 were prepared by solution casting technique. Each mixture was stirred at 45 °C to achieve complete dissolution. The resulting homogeneous solution was poured onto the clean polypropylene Petri dishes and dried in a hot air oven. After drying, the films were peeled off from the Petri dishes and kept in desiccators until use.

2.2 Sample Characterization

X-ray diffraction pattern of the polymer electrolytes has been obtained using Philips X-ray Diffractometer with CuK_α radiation. Fourier Transform Infrared Spectroscopy studies were carried out for all the prepared samples using SHIMADZU—8000 spectrophotometers in the range 400–4000 cm^{-1}. Electrical conductivity measurement has been carried out on the polymer electrolytes using a computer controlled HIOKI 3532 LCR meter in the frequency range 42 Hz–1 MHz. The compositions of

Table 1 Compositions of PVA/CA

Code	Composition
PC973	97 mol wt% of PVA with 3 mol wt% of CA
PCN5	0.5 mol wt% of NH_4SCN with PC973
PCNE3	0.3 mol wt% of Ethylene Carbonate with PCN5

PVA/CA, Salt, plasticizer and fillers optimized for higher conductivity were represented by the codes as mentioned in Table 1.

3 Results and Discussion

3.1 X-ray Diffraction Analysis

Figure 1 shows the X-ray Diffraction patterns of the PVA, CA, PVA-CA blend, PVA/CA/NH_4SCN and PVA/CA/NH_4SCN/EC membranes. A broad peak with high intensity at 19.7° and small peaks with low intensity at 23° and 42° appeared in the PVA pattern; exhibit a semi-crystalline nature of PVA [15]. Next curve CA has a weak peak around 10° and the curve PC973 shows the blending of 97 mol wt% of PVA with 3 mol wt% of CA. By adding CA to PVA the characteristic peak intensity of PVA greatly decreases whereas that of CA slightly increases. This is because CA and PVA chains are blended at the molecular level in the continuous phase, leading to the disordered packing of PVA chains [16]. From PCN5 curve, there is a broad peak and has no separate peaks for NH_4SCN salt, which confirms the complete dissolution of salt into the polymer matrix [17]. The PCNE3 curve shows the plasticizing effect of the polymer complex membrane. The addition of Ethylene Carbonate increases the broadness of peak and decrease the intensity which results in

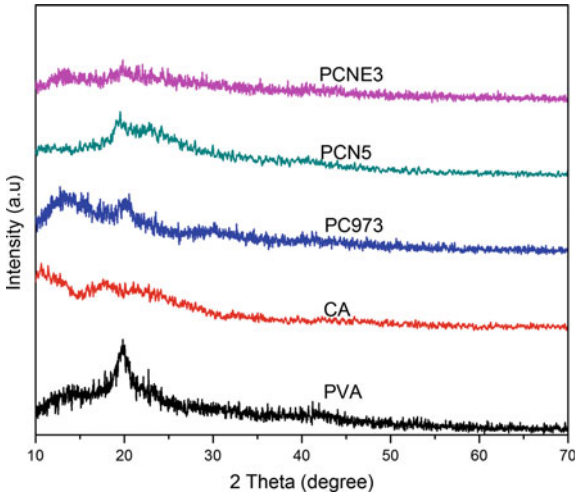

Fig. 1 X-ray diffraction patterns of the PVA, CA, PC973, PCN5 and PCNE3 membranes

the increase in the amorphous nature. Due to this, the overall ionic conductivity of the electrolyte is expected to be improved. This interpretation is based on the Hodge et al. criterion [18]. According to him, the ionic conduction in the polymer electrolyte occurred mostly in the amorphous region and the change in the intensity and broad nature of peaks in the polymer electrolytes gives the amorphous nature of the polymer electrolytes.

3.2 FTIR Analysis

FTIR is used to identify the existence of blending reactions and the molecular interactions in PVA-CA membranes. Figure 2 shows the FTIR spectrum of the CA, PVA, 97 mol wt% PVA/3 mol wt% CA, PVA/CA/0.5 mol wt% NH_4SCN and PVA/CA/NH_4SCN/0.3 mol wt% EC and their assignments have been listed in Table 2. In the pure PVA, the absorption peaks at around 3287 and 2925 cm^{-1} are assigned to OH stretching and symmetric stretching of C–H respectively [19]. The characteristic absorption of C–O groups also visible at 1716 cm^{-1}.

Upon blending PVA with CA, the OH stretching peak (3287 cm^{-1}) of PVA decreases and shifts to higher wave number (3468 cm^{-1}) indicating the occurrence of blending reaction between hydroxyl groups of PVA and CA. It agrees with the result of Coates [20] and Awadhia and Agarwal [21]. In the spectrum of PC973 blend membrane, peaks observed at 3468, 2925, 1734, 1431, 1368, 1028 cm^{-1} have been attributed to the OH-stretching, symmetric stretching of CH, C=O stretching, CH bending, CH symmetrical mode of CA, C–O–C stretching peak of CA.

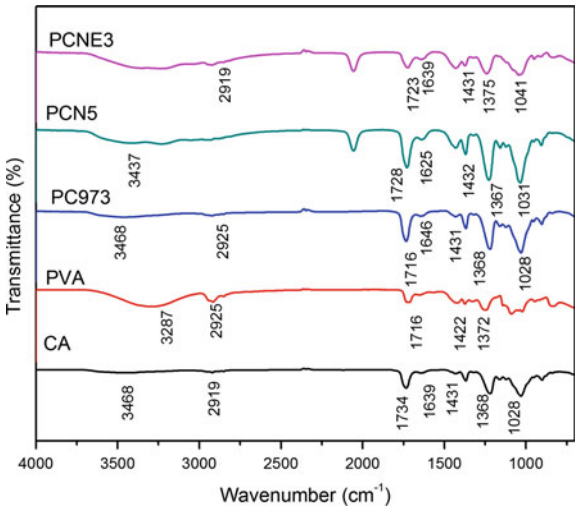

Fig. 2 FTIR spectrum of the CA, PVA, PC973, PCN5 and PCNE3

Table 2 FTIR spectrum of the CA, PVA, 97 mol wt% PVA/3 mol wt% CA, PVA/CA/0.5 mol wt% NH_4SCN and PVA/CA/NH_4SCN/0.3 mol wt % EC and their assignments

Vibration peaks (cm^{-1})					
PVA	CA	PC973	PCN5	PCNE3	Assignments
3287.35	3468	3468.45	3437.99	–	O–H stretching
2925.9	2919.3	2925.9	–	2919.3	Symmetric C–H stretching of PVA
1716.17	1734.43	1716.17	1728.28	1723.5	C=O stretching
–	1639.9	1646.52	1625.81	1639.92	
1422	1431.7	1431.7	1432.7	1431.7	CH bending
1372	1368.65	1368.65	1367.47	1375.98	CH symmetrical bending
–	1028.46	1028.46	1031.32	1041.65	C–O–C stretching peak of CA

The PC973 blend peaks shifted when the NH_4SCN salt is added to the polymer blend. The peak at 3468 cm^{-1} corresponding to OH stretching gets shifted to 3437 cm^{-1} for the salt addition and the carbonyl group C=O of the PC973 peak gets shifted into 1728 cm^{-1} for 0.5 mol wt% of NH_4SCN. These confirm the complex formation of salt and polymer. It supports the interaction between the salt and PVA/CA blend not only arises from OH group but also from C–O group of PVA [22]. The doublet C=O stretching in Ethylene Carbonate is observed at 1723 and 1639 cm^{-1}. This indicates the interaction between the salt and Ethylene Carbonate.

3.3 AC Impedance Analysis/Conductivity Studies

Using complex impedance spectroscopy the electrical properties of the prepared samples have been studied. Figure 3 shows the complex impedance plot for 0–5 mol wt% NH_4SCN doped polymer electrolytes at 303 K. The AC impedance spectra for 0 % NH_4SCN salt show a semicircle in the higher frequency region and a low frequency region spike. The high-frequency semi circle is due to the parallel combination of bulk resistance (due to the migration of protons) and bulk capacitance (due to immobile polymer chain) and a low frequency spike is due to the charge accumulation at the electrode—electrolyte interface [23]. Since the blocking electrodes have been used in the impedance analysis, the electrode/electrolyte interface could be treated as a capacitance. For an ideal capacitance, it should show a vertical spike in the impedance plot. But the spike inclined at an angle (θ) less than 90° has been found instead of the vertical spike which may be attributed to the non homogeneity or roughness of the electrode/electrolyte interface [23]. While adding the salt and plasticizer into the polymer blend, the impedance spectra show only a linear spike. Which means the sample with salt and plasticizers are very capacitive in nature. The disappearance of the high-frequency semicircular portion in the polymer complex impedance plot indicates that the majority of the current carriers in the electrolyte medium are ions [24, 25].

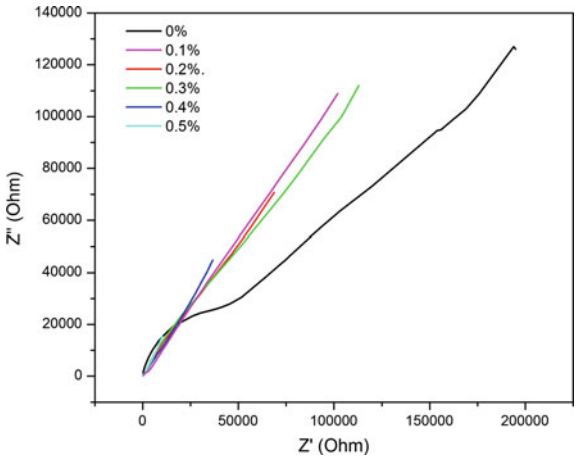

Fig. 3 Cole–Cole plot for different molecular weight % [0, 0.1, 0.2, 0.3, 0.4 and 0.5 %] of NH_4SCN

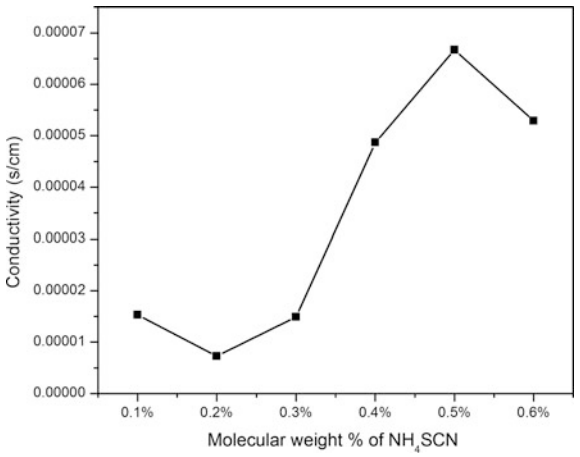

Fig. 4 Conductivity versus different molecular weight % of NH_4SCN

The bulk resistance was calculated from intersecting of the high frequency semicircle or the low-frequency spike on the X axis. The ionic conductivity (σ) values are calculated by using the following equation:

$$\sigma = l/R_b A \tag{1}$$

where l and A are thickness and area of the electrolyte film and R_b is the bulk resistance of the electrolyte film.

At room temperature the ionic conductivity of PVA/CA blend polymer is 3.63×10^{-6} S/Cm. The ionic conductivity is observed to increase gradually up to 2.55×10^{-4} S/Cm for 0.5 % of NH_4SCN doped electrolyte (Fig. 4). The increase in conductivity with the increase in salt content in the polymer electrolyte can be attributed to the dissociation of more ions. At concentration above 0.5 % NH_4SCN

the conductivity decreases, this may be due to the distance between the dissociated ions become too close that they are able to recombine and formed neutral ion pairs [26].

The conductivity of the polymer electrolyte can be enhanced by adding plasticizers. Plasticizers like Ethylene Carbonate (EC) have low viscosity and the incorporation of EC can decrease the local viscosity around the charge transporting ions and in turn increases the ionic mobility. EC also have a high dielectric constant and it can weaken the columbic force between cation and anion of the salt and result in salt dissociation [19]. Figure 5 shows the addition of EC increases the conductivity up to 7.7×10^{-4} S/Cm for the concentration of 0.3 mol wt%. Further addition of EC decreases the ionic conductivity that may be due to the re association of ions which reduces the density of charge carriers [27].

Figure 6 shows the conductivity value increases with the addition of nano-alumina and the maximum conductivity value 2.1×10^{-3} S/cm is found for

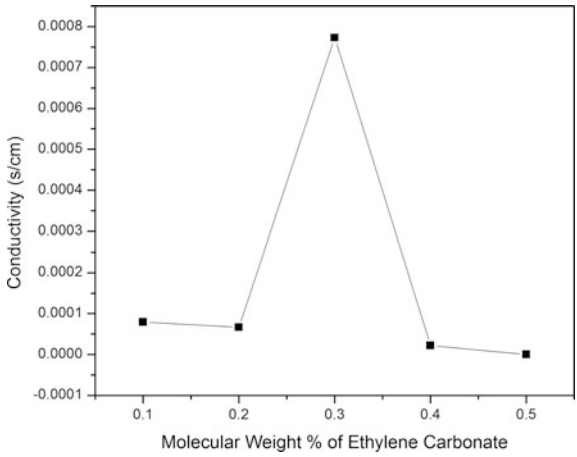

Fig. 5 Conductivity versus different molecular weight % of Ethylene Carbonate

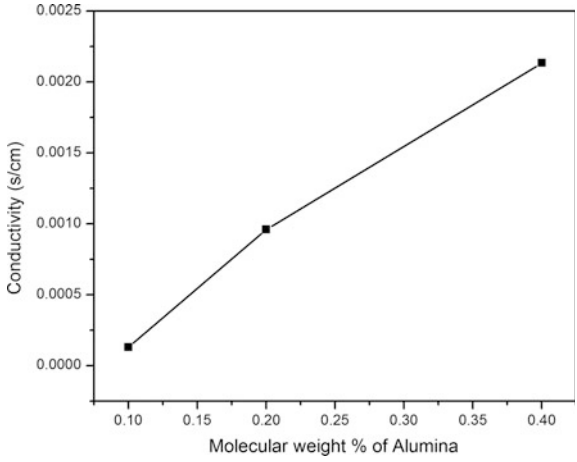

Fig. 6 Conductivity versus different molecular weight % of Alumina

0.4 mol wt% concentration of Alumina nano particles. Here Alumina acts as a filler and increases amorphous phase of the polymer composite, which enhances the ionic conduction through polymer chain.

3.4 Temperature Dependence of Ionic Conductivity

The temperature dependent conductivity has been shown in the Fig. 7. This shows that the conductivity value varies linearly as temperature increases and it can be studied with the help of Arrhenius equation given by

$$\sigma = (\sigma_o/T)\exp(-E_a/KT) \quad (2)$$

where σ_o is the pre-exponential factor and E_a is the activation energy (combination of energy for defect formation and the energy for migration of ion) of the polymer electrolytes. The experimental data has been fitted using least square analysis; a straight line fit has been obtained for 0.1–0.5 mol wt% of NH_4SCN doped polymer electrolytes. The conductivity and activation energy values of all prepared polymer electrolyte have been tabulated in Table 3.

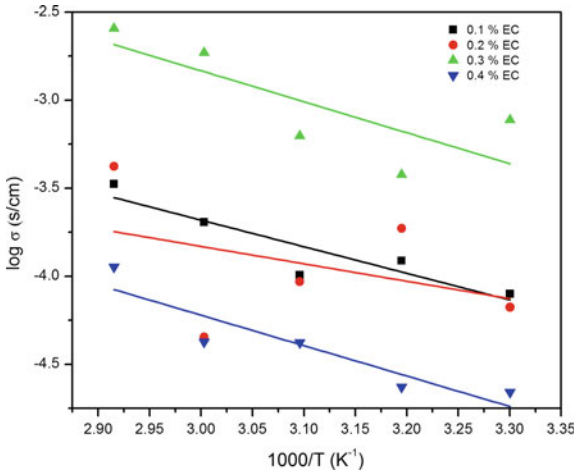

Fig. 7 Arrhenius plot for 0.1–0.4 molecular weight % of EC

Table 3 Conductivity and activation energy values of all prepared polymer electrolyte

Mol wt% of EC	Conductivity (S/cm)	Activation energy (ev)
0.1	0.793E−04	0.29983
0.2	0.667E−04	0.34903
0.3	7.73E−04	0.19636
0.4	0.219E−04	0.34246

The temperature versus conductivity plots (Arrhenius plot) for various EC concentrations were studied and their activation energy and conductivity values are listed in Table 2. The activation energy can be determined by the slope or intercept of a compensated Arrhenius plot. The activation energy is calculated for the entire prepared polymer electrolyte by linear fit of Arrhenius plot. It has been found that the highest conductivity polymer electrolyte (0.3 mol wt% EC system) has the lowest activation energy (0.196 eV). This indicates that addition of plasticizer promotes faster mobility of conducting ions due to enhanced segmental motion of the polymer chain and due to the free volume [28].

3.5 *Loss Tangent Spectra Analysis*

The dielectric loss tangent (tan δ) can be defined by the equation:

$$\tan \delta = \varepsilon''/\varepsilon' \tag{3}$$

The variation of tan δ with frequency for all the prepared PVA/CA/NH_4SCN with different ratio of Ethylene Carbonate membranes at room temperature was represented in Fig. 8. It has been observed that tan δ increases with increase in frequency and reaches a maximum value and decreases for further increase of frequency as per the Debye equation. The relaxation parameters were calculated for all the plasticized polymer electrolytes at room temperature and were listed in Table 4. It was noted that the highest conductive polymer electrolyte (PCNE3) has a lower relaxation time of 1.224×10^{-6} s.

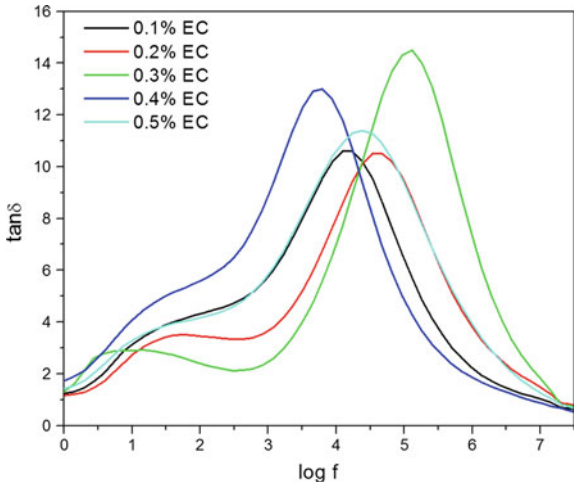

Fig. 8 Loss tangent spectra for different molecular weight % of EC

Table 4 Relaxation time for the plasticized polymer electrolytes at room temperature

Mol wt% EC	Log f	f	ω	Relaxation time (s)
0.1	4.092	12359.5	77617.5	12.88E−6
0.2	4.633	42953.6	269748.9	3.707E−6
0.3	5.114	130017	816506.5	1.224E−6
0.4	3.673	4709.77	29577.38	33.8E−6
0.5	4.374	23659.2	148579.8	6.730E−6

4 Conclusion

PVA/CA blend polymer electrolyte with different weight percentage of Ammonium Thiocyanate and Ethylene Carbonate with Alumina nanoparticles were prepared by solution casting technique using DMSO as a solvent. The amorphous nature of the PVA/CA blend was confirmed by the XRD analysis. The complex formation between polymer and salt was confirmed by FTIR analysis. The ionic conductivity value for all the prepared polymer electrolytes has been evaluated using AC impedance spectroscopic analysis at different temperatures. The membrane shows the maximum ionic conductivity of 7.7×10^{-4} S/cm at 303 K with the polymer composition of 97 % PVA/3 % CA/0.5 % NH_4SCN/0.3 % EC from the Cole-Cole plot. The temperature dependence of ionic conductivity of all electrolytes reflects the Arrhenius behavior as ionic conductivity increased with temperature. The increase in conductivity may be due to the increase in amorphous nature of the polymer membrane as confirmed by XRD. It was observed that the highest conducting polymer electrolyte has the lowest activation energy (0.199 eV) and lowest relaxation time (1.224×10^{-6} s) from Arrhenius plot and loss tangent spectra respectively. The addition of nano alumina facilitates the ion transportation in the amorphous solid polymer electrolyte and increases the ionic conductivity to 2.1×10^{-3} s/cm.

References

1. Ramly, N.N.B., Bin Ali, A.M.M.: The preparation and characterization of Sulfonated Poly (Ether Ether Ketone) and Cellulose Acetate (SPEEK-CA) membrane in Proton Exchange Membrane Fuel Cells (PEMFCs) by UV-Crosslink Technique. In: IEEE Colloquium on Humanities and Engineering Research (Dec 2012)
2. Nithya, H.S., Selvasekarapandian, S., Cristopher Selvin, P., Kumar, D.A., Hema, M.: Structural and ionic conductivity studies on P(ECH-EO):γ-BL:$LiClO_4$ plasticized polymer electrolyte. Ionics **17**, 587–593 (2011)
3. Rajeswari, N., Selvasekarapandian, S., Karthikeyan, S., Sanjeeviraja, C., Iwai, Y., Kawamura, J.: Structural, vibrational, thermal, and electrical properties of PVA/PVP biodegradable polymer blend electrolyte with CH_3COONH_4. Ionics **19**, 1105–1113 (2013)
4. Ali, R.M., Harun, N.I., Ali, A.M.M., Yahya, A.Z.A.: Effect of ZnS dispersoid in structural and electrical properties of plasticized CA-NH_4I. Physics Procedia **25**, 293–298 (2012)

5. Kang, J., Li, W., Wang, X., Lin, Y., Xiao, X., Fang, S.: Polymer electrolytes from PEO and novel quaternary ammonium iodides for dye-sensitized solar cells. Electochim. Acta. **48**, 2487–2491 (2012)
6. Buraidah, M.H., Teo, L.P., Majid, S.R., Arof, A.K.: Ionic conductivity by correlated barrier hopping in NH_4I doped Chitosan solid electrolyte. Phys. B **404**, 1373–1379 (2009)
7. Singh, P.K., Pratap, R., Chandra, A.: Nanocrystalline ZnS dispersed in polymer electrolyte (PEO:NH_4I) preparation and electrical conductivity measurements. Prog. Cryst. Growth. Charac. Mater. 175–182 (2002)
8. Dey, A., Karan, S., De, S.K.: Effect of nanofillers on thermal and transport properties of potassium iodide-polyethylene oxide solid polymer electrolyte. Solid State Comm. **149**, 1282–1287 (2009)
9. Ahmed, A., Rahman, M.Y.A., Suait, M.S.: Preparation and characterization of PVC-$LiC1O_4$ based composite polymer electrolyte. Phys. B **403**, 4128–4131 (2008)
10. Prathan, D.K., Choudhary, R.N.P., Samataray, B.K., Karan, N.K., Katiyar, R.S.: Effect of plasticizer on structural and electrical properties of polymer nanocomposite electrolytes. Int. Jorn. Electochem. Sci. **2**, 861–871 (2005)
11. Neburchilov, V., Martin, J., Wang, H., Zhang, J.: A review of polymer electrolyte membranes for direct methanol fuel cell. J. Power Sources **169**, 221–238 (2007)
12. Cao, Y., Wu, J., Meng, T., Zhang, J., He, J., Li, H.Q.: Acetone soluble cellulose acetates prepared by one-step homogeneous acetylation of corn husk cellulose in an Ionic liquid 1-allyl-3-methylimidazolium chloride. Carbohydrate Polymer. **69**, 665–672 (2007)
13. Huang, X., Ma, X., Wang, R., Zhang, L., Deng, Z.: Combined effect of surface-charged latex nanoparticle AHPS and Al_2O_3 nano-fillers on electrochemical performance of the anionic gel polymer electrolytes PVA/P (MA-*co*-AHPS). Solid State Ionics **267**, 54–60 (2014)
14. Masoud, E.M., Bellihi, A.A., Bayoumy, W.A., Mousa, M.A.: Organic-inorganic composite polymer electrolyte based on PEO-$LiCl_4$ nano-alumina filler for lithium polymer batteries: dielectric and transport properties. J. Alloy. Compd. **575**, 223–228 (2013)
15. Cullity, B.D.: Elements of X-ray Diffraction. Addison-Wesley Publishing Company, Inc. (1956)
16. Zhou, K., Zhang, Q.G., Han, G.L., Zhu, A.M., Liu, Q.L.: Pervaporation of water–ethanol and methanol–MTBE mixtures using poly (vinyl alcohol)/cellulose acetate blended membranes. J. Membr. Sci. **448**, 93–101 (2013)
17. Rajendran, S., Sivakumar, M., Subadevi, R.: Li-ion conduction of plasticized PVA solid polymer electrolytes complexed with various lithium salts. Solid State Ionics **167**, 335–339 (2004)
18. Hodge, R.M., Edward, G.H., Simon, G.P.: Water absorption and states of water in semicrystalline poly (vinyl alcohol) films. Polymer **37**, 1371 (1996)
19. Zhong, S., Cui, X., Gao, Y., Liu, W., Dou, S.: Fabrication and properties of poly(vinyl alcohol) based polymer electrolyte membrane for DMFC application. Int. J. Hydrogen Energy 1–8 (2014)
20. Coates, J.: Interpretation of IR Spectra; A Practical Approach: Encyclopedia of Analytical Chemistry, pp. 10815–10837. Wiley, Chichester (2000)
21. Awadhia, A., Agarwal, S.L.: Structural, thermal and electrical characterization of PVA: DMSO:NH_4SCN gel electrolytes. Solid State Ionics **178**, 951–958 (2007)
22. Bhuvaneswari, R., Karthikeyan, S., Selvasekarapandian, S., Vinoth Pandi, D., Vijaya, N., Arun, A., Sanjeeviraja, C.: Preparation and characterization of PVA complexed with amino acid, proline. Ionics **21**, 387–399 (2015)
23. Hema, M., Selvasekerapandian, S., Sakunthala, A., Arunkumar, D., Nithya, H.: Structural, vibrational and electrical characterization of PVA—NH_4Br polymer electrolyte system. Phys. B **403**, 2740–2747 (2008)
24. Jannasch, P.: Recent developments in high-temperature proton conducting polymer electrolyte membranes. Curr. Opin. Colloid Interface Sci. **8**, 96–102 (2003)

25. Rajendiran, S., Kesavan, K., Nithya, R., Ulaganathan, M.: Transport, structural and thermal studies on nanocomposite polymer blend electrolytes for Li-ion battery applications. Curr. Appl. Phys. **12**, 789–793 (2012)
26. Xu, W., Liu, C., Xue, X., Su, Y., Lv, Y., Xing, W., Lu, T.: New Proton exchange membranes based on poly(vinyl alcohol) for DMFCs. Solid State Ionics **171**, 121–127 (2004)
27. Shukur, M.F., Ithnin, R., Illias, H.A., Kadir, M.F.Z.: Proton Conducting Polymer electrolytes based on plasticized Chitosan-PEO blend and application in electrochemical devices. Opt. Mater. **35**, 1834–1841 (2013)
28. Miyamoto, T., Shibayama, K.: Free-volume model for ionic conductivity in polymers. J. Appl. Phys. **44**, 5372 (1973)

Preparation and Characterization of Porous Hollow Sphere of Ni Doped CuS Nanostructures for Electrochemical Supercapacitor Electrode Material

Surekha Podili, D. Geetha and P.S. Ramesh

Abstract Porous metal sulfide nanostructures are promising materials for developing high performance electrochemical devices. Herein, Porous hollow nano structures of Ni doped CuS were successfully synthesized by hydrothermal method with surfactant (CTAB) as stabilizer and ethylene glycol as solvent. Prepared samples were systematically characterized by X-ray diffraction, UV-Vis spectrometry, Fourier transform infrared spectroscopy (FTIR), SEM/EDS, Thermal analysis (TG/DTA) and Atomic force microscopy (AFM). The size of Ni doped CuS morphologies was about 5–10 nm corresponding to the Ni doping concentrations of 0.05, 0.1–0.6 mM respectively. The characterization revealed the presence of CuS (Covellite). The supercapacitor performance of this nanostructure was characterized by cyclic voltammetry in 2 M KOH as electrolyte. The porous hollow nano Ni doped CuS exhibit higher specific capacitance (400 Fg^{-1} at 5 mV/s), which was higher than that of common CuS nano structures (287 Fg^{-1} at 5 mV/s). The enhanced performance is mainly due to the pore in the Ni doped CuS nanostructures.

1 Introduction

High-performance electrical energy storage devices are importantly required today for supplying electricity to mobile, information-rich and energy-conscious society. Herein, energy storage device contains supercapacitors or ultra-capacitor in receipt of significant attention as energy storage devices, many metal oxide nanomaterials are examined for their electrochemical nature [1]. Due to its high cost, poor conductivity of those metal oxides has limiting the commercial applications.

S. Podili · D. Geetha (✉)
Department of Physics, Annamalai University, Annamalai Nagar, Chidambaram 608002, Tamil Nadu, India
e-mail: geeramphyau@gmail.com

P.S. Ramesh
Department of Physics (DDE Wings), Annamalai University, Annamalai Nagar, Chidambaram 608002, Tamil Nadu, India

J. Ebenezar (ed.), *Recent Trends in Materials Science and Applications*, Springer Proceedings in Physics 189, DOI 10.1007/978-3-319-44890-9_26

Hence, there is permanently a demand in the expansion of materials for supercapacitor applications [2]. In the present scenario metal chalcogenide nanostructures are used in energy storage applications [3]. Among these CuS was attractive because of its abundant, being nontoxic, cheap and most stable under ambient environment nature.

The Copper sulfide (CuS) has attracted great attention, because of not only its tremendous optical, electrical properties but for their utility in various operational setting such as semiconductor layer allow for enhancement of solar-to-electric energy, in portal remote sensing and radar, but also due to its different applications such as solar cells, nano medicine nano switches, a major focus of optical filters and catalysts. Some time before, different morphologies of copper sulfides have been fabricated [4–7]. The properties and characterization of Copper sufide is marginally altered due to doping with supplementary nano materials. Transition metals are at all times used as dopant in semiconductors, consecutively to revise the properties.

Here, this work revealed the controlled synthesis of Ni doped CuS nano material by hydrothermal method assisted with surfactant (CTAB). The morphology and structures of Ni doped CuS nano crystals are taken for the present study. The Ni doped CuS with special properties can be expected that ensure selective growth of covellite and to extend for assembling new electronic and nano devices.

2 Experimental

2.1 Materials

Copper nitrate trihydrate ($Cu(NO_3)\cdot 3H_2O$), Thiourea (Tu, $Sc(NH_2)_2$), Ethylene Glycol (EG), cetyl trimethyl amoniame bromide (CTAB) and Nickel nitrate hexa hydrate ($Ni(NO_3)_2\cdot 6H_2O$) are analytical grade and were used without any further purification.

2.2 Preparation

A mixture of 1 mM copper nitrate trihydrate and 2 mM thiourea with 0.1 mM CTAB was added to 40 ml ethylene glycol. Then this chemical solution was strongly stirred for 45 min and the temperature was maintained at 130 °C for 10 h and kept back in oven. The Ni concentration was speckled by altering the quantity of nikel nitrate hexahydrate (0.1, 0.3, 0.5 and 0.6 mM). Ni doped CuS nanocrystals were obtained in the form of black powder. As a result the prepared powder sample was more than a few times washed with acetone, ethanol and de ionized water and dried in hot air oven at 60 °C for 6 h.

2.3 Characterization Methods

The XRD patterns of selected sample products were recorded using X'PERT-PRO diffractometer with Cu Kα radiation λ = 1.54060 Å, the 2θ range from 10° to 80°. The optical UV-Vis absorption spectra of samples in de-ionized water were recorded using SHIMADZU-UV 1650 PC spectrometer. The FTIR spectra were recorded by using (NICOLET-AVATAR 330) ranging from 650 to 4000 cm^{-1}. SEM/EDS analysis was carried out on a Scanning Electron Microscope (JEOL-JSM—5610 LV) with INCA EDS. Atomic force microscope (AFM) image of sample was performed AGILENT—NP410A series 5500 instrument in contact mode. Silicon nitrate cantilevers are required to obtain all images. Thermal analysis (TG/DTA) was carried out by thermal Analyzer NETZSCH—STA 449F3 JUPITER, Temperature range from 0 to 800 °C at the heating rate 20°/min.

2.4 Electrochemical Performance Investigation

Electrochemical characterizations were carried out in 2 M KOH aqueous electrolyte using a three electrode configuration system. The CuS was employed as the working electrode, a platinum (pt) wire counter electrode, and an Ag/AgCl reference electrode. Cyclic voltammetry measurements were performed with in a potential window of −1.5 to 2.0 V versus Ag/AgCl at a scan rate from 10 to 30 mVs^{-1} on the CHI6060 electrochemical workstation.

3 Results and Discussion

3.1 Structural Analysis (XRD)

Figure 1a–e shows the XRD patterns of Ni doped CuS samples at 130 °C. Figure 1a shows the XRD pattern of (0.1 mM) CTAB assisted CuS; where in all present peaks can able to be perfectly indexed as the hexagonal phase of CuS and well matched with the (JCPDS No. 06—0464). All the diffraction peaks can be readily indexed to the hexagonal covellite CuS crystal structure. As shown in Fig. 1b–e, the intensity of the diffraction peaks decreased with increasing Ni concentration from 0.1 to 0.6 mM. The lattice parameters are calculated from the XRD line position. The lattice parameter values are refined through Rietveld refinement method, after doping with Ni the values of a and c are somewhat changed, due to the distance of copper sulfide (2.28–2.33 Å) and nickel sulfide (2.17 Å) [8]. The unit cell volume is also distorted as a result of the change of lattice parameters a and c. The changes of a, c that verifies

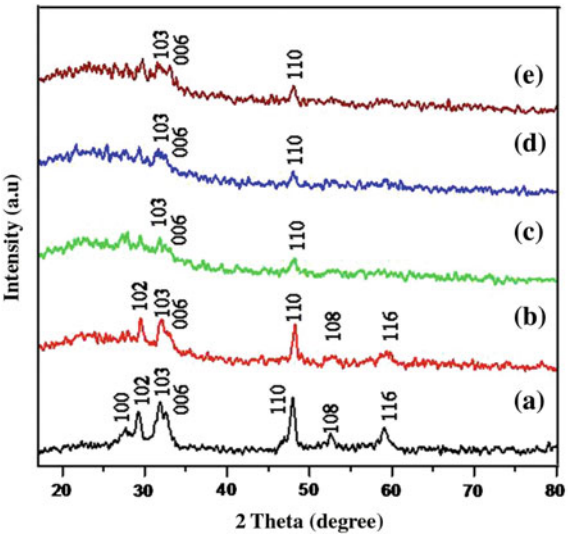

Fig. 1 XRD patterns of (0.1 mM) CTAB assisted CuS doped with Ni: *a* 0.0, *b* 0.1 mM, *c* 0.3 mM, *d* 0.5 mM and *e* 0.6 mM

the cell volume of Ni doped with CuS nanocrystals. A few XRD peaks of CuS: Ni is obviously broader compared with pure CuS, because of the lattice distortion.

No other crystalline phase, such as Cu_2S, $Cu_{1.8}S$ and $Cu_{1.96}S$ was observed, indicating the high purity of the product. The diffraction peak corresponding to 110, 103, 006 planes were chosen for calculating the crystalline size of CuNiS phase as these peak positions are finely isolated and by means of high intensity. It is obvious that, by mixing the Ni with different ratios of CuS followed by calcinations at 150 °C led to enhance the crystalline size of NiCuS phases. From half width of XRD peaks, the average crystalline size is estimated as <10 nm by the scherrer formula, which agrees well with values from the AFM observation. The average grain size was found to be 9, 7, 5, 8 and 8 nm for CTAB assisted CuS, CuS/ Ni (0.1), CuS/Ni (0.3), CuS/Ni (0.5) and CuS/Ni (0.6) respectively. The diffraction peaks are broadened because of their very small size.

It is important to mention that the synergistic effect leads to the survival of Cu^+ and Ni^{3+} in the host sulfide collectively with Cu^{2+} and Ni^{3+}. The presence of dual in the sulfide mixture valances must change their textural, morphological and catalytic properties.

3.2 Optical Absorption Analysis (UV-Vis)

The optical properties of the prepared nanostructures have been studied and shown in Fig. 2a–d. Copper sulfide as bulk material shows both an indirect optical band gap between nearly 1.5 and 1.27 eV and direct band gap between around 2.4 and 2.36 eV [9]. UV Spectra of Ni doped CuS were not identical to CTAB assisted

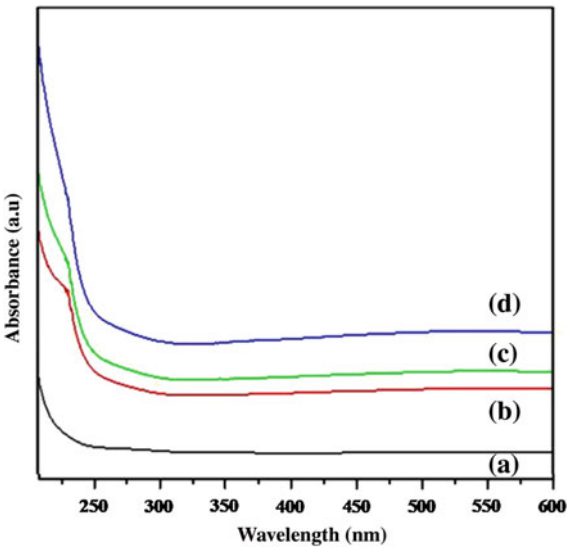

Fig. 2 UV-Visible absorption spectra of (0.1 mM) CTAB assisted CuS doped with Ni: *a* 0.1 mM, *b* 0.3 mM, *c* 0.5 mM and *d* 0.6 mM

CuS. Ni doped CuS nano suspensions shows that absorption is observed in the UV region and a broad range of absorption in the visible region due to overlap of absorption bands of different energies from moderately poly disperse sized nanoparticles.

The absorption peak are observed in Fig. 2a–d, and also smallest shift are observed when increasing doping concentration. The dominate characteristic of Ni doped CuS is typically the surface plasmon resonance (SPR) it can be expressed by classical Mie theory. The resonance position and the peak width based on many features and gain insight into more than a few physical properties of Ni doped CuS nanocomposites.

When Ni was doped on CuS the particle size below <10 nm it shows absorption peak is maximum wavelength. For Ni doped Cus small spherical nano clusters, the resonance which is positioned around 250–280 nm in vacuum. However, minute changes in the electronic properties of the adjacent medium of the cluster direct to shifts of the peak, and increases width while decreasing cluster size because of the electrons are oscillating at the cluster surface [10]. A broader SPR peak indicted a broader size distribution. There was no significant difference between hydrodynamic diameters of <10 nm. AFM image (9 nm) showed the smaller size and distribution.

3.3 Spectral Analysis (FTIR)

The chemistry of the sample was investigated by the Fourier transform Infra red (FTIR) spectrum as recorded and shown in the Fig. 3a–e. The majority of intensive bands were established then the intervals 1016–1116 cm^{-1}, 1395–1740 cm^{-1} and

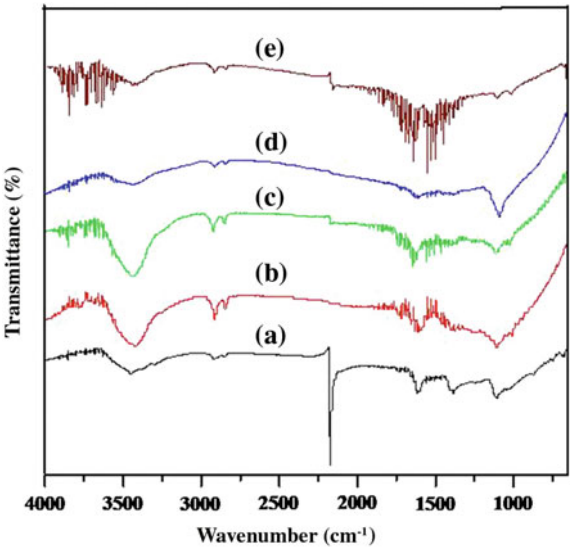

Fig. 3 FTIR Transmission spectra of (0.1 mM) CTAB assisted CuS doped with Ni: *a* 0.0, *b* 0.1 mM, *c* 0.3 mM, *d* 0.5 mM and *e* 0.6 mM

2852–2959 cm^{-1}. According to the literature data, the characteristic infrared bands at 614 and 1064 cm^{-1} were observed for sulfur. These data reveals that the FT-IR spectrum of copper sulfide good agreement with FT-IR spectrum of the corresponding reported literature [11].

The FT-IR investigation of these results is agreement with the results reported by Breck and he established that the nickel (metal oxide) cations are by entering in the CuS nano structure some of the shifts are going on during the process of exchanged ions, then peaks are placed right side of unique band at 1000 cm^{-1}. The above shift of the C=O and N–H vibration implied that the mixed materials in the system may form an amide bond and these bonds bring together with the CuS nanocrystals.

3.4 Surface Morphological Analysis

(i) SEM/EDS studies

Figure 4a–e shows the SEM morphology of CTAB stabilized CuS, doped with various concentration of Nickel. It reveals that the initially formed nanoparticles have rough surface of spherical nanoparticles in CTAB assisted CuS. On the influence of dopent in lower concentration (0.1 mM Ni), the surface changes into rough surface. Further the increase in the concentration of Ni into 0.3, 0.5 and 0.6 mM forms the porous spherical nano particles. At the 0.5 mM Ni concentration more number of aggregated porous particles is created. The size of the Ni doped nanoparticles ranges from 5 to 21 nm.

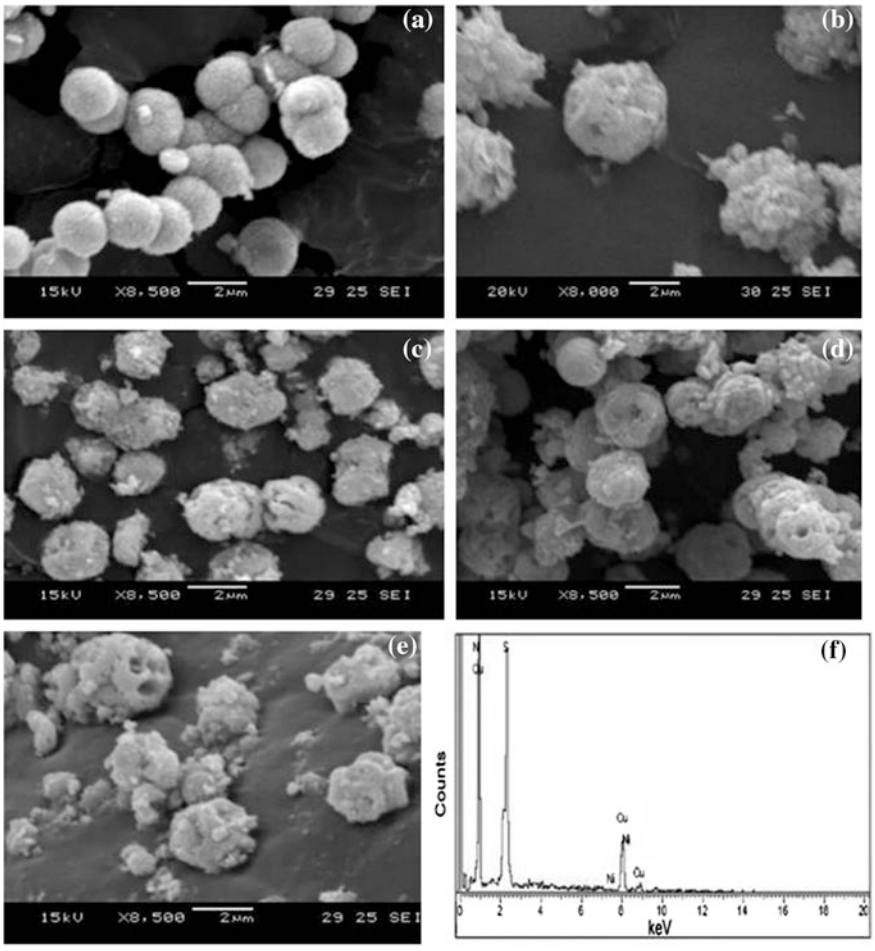

Fig. 4 The SEM images of (0.1 mM) CTAB assisted CuS doped with Ni: **a** 0.0, **b** 0.1 mM, **c** 0.3 mM, **d** 0.5 mM, **e** 0.6 mM and **f** EDS Spectrum

The observed nanocrystallite sizes are in good accordance with those estimated from the XRD pattern. The purity and composition of the products are represented in the EDS spectrum (Fig. 4f).

EDS analysis has been employed to semi-quantitatively investigate the chemical composition of NiCuS nanocomposites (Fig. 4f). Accordingly the molar ratios of Ni, Cu and S obtained from EDS are basically in good agreement with the chemical stoichiometry of NiCuS. The difference is probably due to the different Ni concentration on CuS [12].

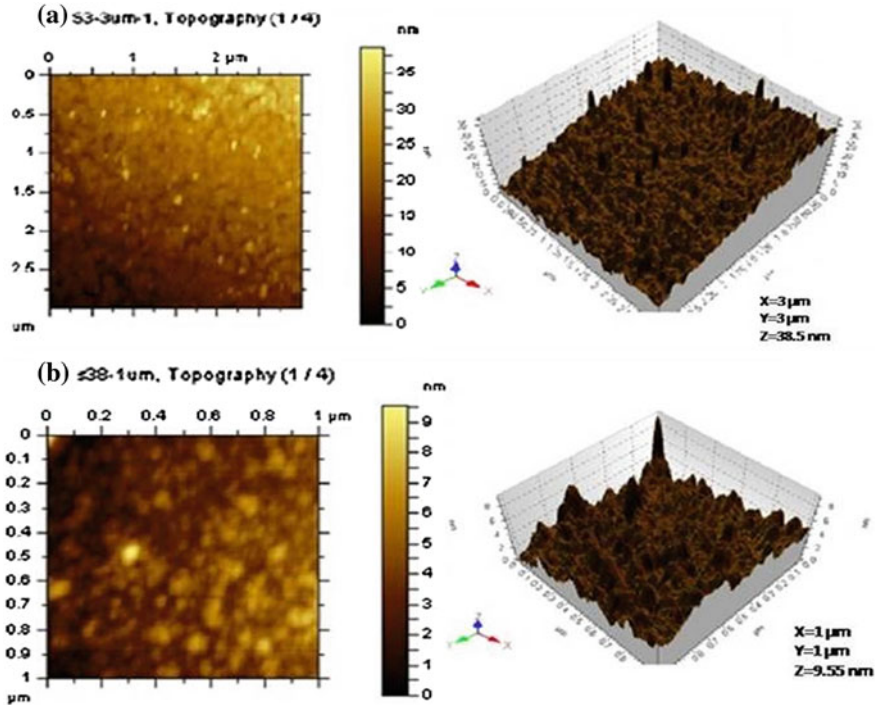

Fig. 5 AFM images of (0.1 mM) CTAB assisted CuS doped with Ni: **a** 0.1 mM and **b** 0.5 mM

(ii) **AFM Studies**

Atomic force microscopy (AFM) has been implemented a structural characterization and provides surface roughness of the sample. Figure 5 (a&b) shows two dimensional (2D) AFM images of 1.0 µm × 1.0 µm as–prepared sample Cu:S (1:2) with Ni (0.1 mM). Figure shows that the powder consists of highly co-ordinated nano sized spherical particles which are well arranged [13]. The particle size of nano material with the addition of Ni is (0.5 mM) on CuS was 9 nm.

3.5 Thermal Analysis (TG/DTA)

Thermal behavior of the CuS, CuS–Ni (0.1) samples was studied in temperature range of 0–800 °C and 0–600 °C with temperature rise of 20 °C min^{-1} under inert nitrogen atmosphere. TG/DTA thermo grams are shown in Fig. 6a–b. From DTA curves, water is lost at 150 °C in pure CuS product, it will agree with the existence of different water sites in the structures because of Mg, Ca, Na and K cations are present [14]. According to DTA curves the weight loss extents of CuS is 17.1 %

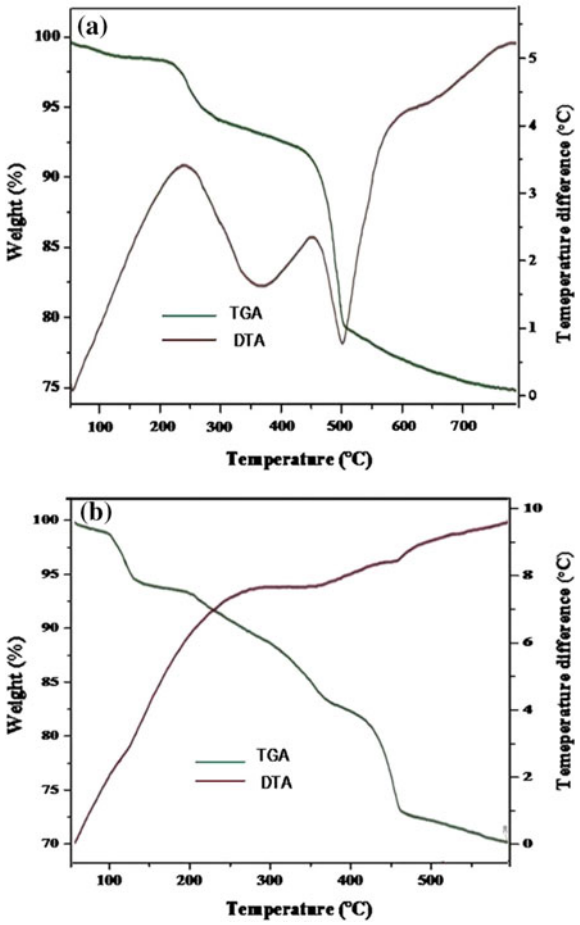

Fig. 6 TG/DTA curves of (0.1 mM) CTAB assisted CuS doped with Ni: **a** 0.0 and **b** 0.1 mM

and the weight loss extents of CuS: Ni (0.1) is 14.70 % are obtained. Generally the CuS undergoes endothermic changes from 150 to 490 °C, due to desorption of water in Cu. From the TG curve maximum weight loss extends at 72.4 and 76.3 °C respectively.

3.6 Cyclic Voltammetry Studies

Electrochemical behaviors of pure CuS and Ni doped CuS nanostructure were investigated by cyclic voltammetry (CV) in a potential range of −1.5 to 2.0 V at a scan rate of 5, 10 and 30 mV/s in 2 M KOH electrolyte solution are shown in Fig. 7. Figure 7a, b show ideal rectangular shapes, it indicates clear faraday pseudocapacitance behavior. At a low sweep rate of 5 mV s^{-1}, cathodic peaks are

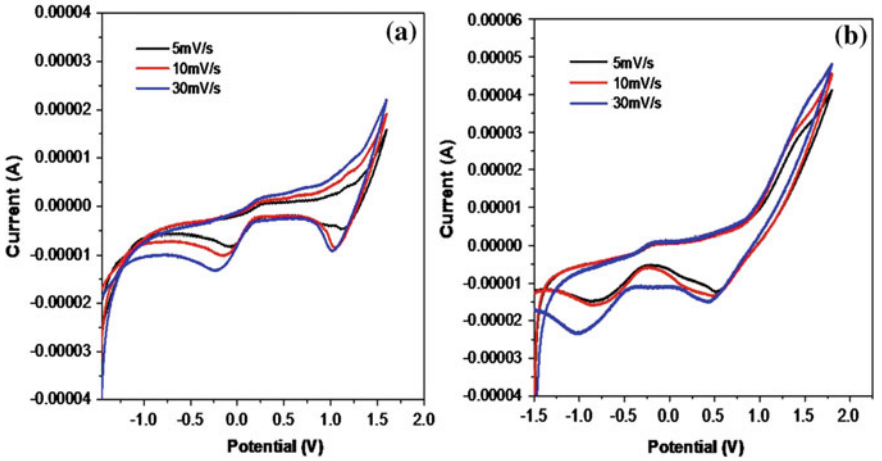

Fig. 7 CV curves of **a** (0.1 mM) CTAB assisted CuS, and **b** (0.1 mM) CTAB assisted CuS doped with Ni 0.5 mM

Table 1 Specific capacitance of the CTAB assisted with Ni doped CuS and CTAB assisted CuS electrode at different scan rates

Sample	Scan rate (mV/s)		
	5	10	30
	Specific capacitance (F/g)		
CTAB/Ni/CuS	400	310	203
CTAB/CuS	287	191	91

visible. When in increase scan rate, the position of cathodic peak shifts negatively due to the resistance of the electrode. The result exhibit that the pure CuS and Ni doped CuS electrode has the reversible redox processes and good rate ability in a KOH electrolyte.

The specific capacitance of the electrodes can be calculated via the cyclic voltammetric curve according to the following formula

$$Cs\left(\mathrm{Fg}^{-1}\right) = Q/(\Delta V \cdot m)$$

where Cs is represent the specific capacitance specific capacitance based on the mass of electrode materials, Q is the anodic and cathodic charges on each scanning, m is the mass of the active material (g) in the electrodes and ΔV is the applied voltage window of the voltammetric curve (mVs^{-1}). The specific capacitances of two different electrodes derived from the cyclic voltammetry are also compared, as shown in Table 1. Based on the above equation, the specific capacitance of the CTAB assisted with Ni doped CuS electrode is quantified to be 400 Fg^{-1} at 5 mV s^{-1} scan rate which is higher than that of CTAB assisted CuS 287 Fg^{-1}.

The charge storage mechanism of Ni–CuS composite generally governed by electrochemical redox reactions related to M-S/M-S–OH (M represents to Cu or Ni ions) [15]. The specific capacitance (C_s) of active electrode materials severely

decreased with increasing scan rate. This behavior due to the argument that a high scan rate prevents the accessibility of ions entering into all the pores of electro-active materials, and thus the transport of electrolyte ions are limited and only the outer active surface can be potentially utilized for the energy storage storage [16].

4 Conclusion

Nano Ni doped CuS porous nano structure was prepared by hydrothermal route. Capping of CTAB facilitated the formation of uniform nanoparticles. The experimental results showed that morphology of Ni doped CuS. In addition, the transition metals are doped with copper sulfide then the CuS nano structure is affected. Hence, CuS concentration ratio may be kept as (1:2) and then the metal transition ion (Ni) were doped in four different concentrations viz., 0.1, 0.3, 0.5 and 0.6 mM. A possible insitu reduction–sulfidation mechanism could be dependable for the formation of nano structures. Even though a good deal still remains to gain knowledge of detailed mechanism, the current path may give a general strategy to control the growth of inorganic nanomaterials. Such a simple and low cost synthetic technique can be extensive to controlled synthesis of copper sufide and other metals doped copper sulfide nano structures. Electrochemical property such as CV confirmed the supercapacitive behavior of Ni doped CuS electrodes. A maximum specific capacitance of this material was about 400 Fg^{-1} which suggest a potential application of nanomaterials in supercapacitor application. The present results indicate that the NiCuS composite could be promising and inexpensive electrode materials for electrochemical capacitors.

Acknowledgements The authors appreciatively thanks to the financial support afford by University grants commission (UGC), India, (No. F.No- 43-533/2014 (SR).

References

1. Krishnamoorthy, K., Kim, S.-J.: Preparation of CuO nanostructures coating on copper as supercapacitor materials. Mater. Res. Bull. **48**, 3136 (2013)
2. Boukhalfa, S., Evanoff, K., Yushin, G.: Atomic layer deposition of vanadium oxide on carbon nanotubes for high-power supercapacitor. Energy Environ. Sci. **5**, 6872 (2012)
3. Gao, M.-R., Xu, Y.-F., Jiang, J., Yu, S.H.: Nanostructured metal chalcogenides: synthesis, modification, and applications in energy conversion and storage devices. Chem. Soc. Rev. **42**, 2986 (2013)
4. Du, X.S., Yu, Z.Z., Dasari, A., Ma, J., Meng, Y.Z., Mai, Y.W.: Facile synthesis and assembly of Cu_2S nanodisks to corncoblike nanostructures. Chem. Mater. **18**, 5156–5158 (2006)
5. Feng, X.P., Li, Y.X., Liu, H.B., Li, Y.L., Cui, S., Wang, N., Jiang, L., Liu, X.F.: Yuan, controlled growth and field emission properties of CuS nanowalls. J. Nanotechnol. **18**, 145706 (2007)

6. Xu, J., Cui, X.J., Zhang, J.H., Liang, H.W., Wang, H.Y., Li, J.F.: Preparation of CuS nano particle embedded in poly vinyl alcohol nano fibre via electro spinning. Bull. Mater. Sci. **31**, 189–192 (2008)
7. Zhang, H.T., Wu, G., Chen, X.H.: Controlled synthesis and optical properties of covellite (CuS) nanoflakes. Mater. Chem. **98**, 298 (2006)
8. Suja, R., Geetha, D., Ramesh, P.S.: Preparation and characterization of CuS nanomaterials by solvothermal method. Int. J. Sci. Eng. Res. **4**(3), 1–3 (2013)
9. Yang, C., Fan, H., Xi, Y., Chen, J., Li, Z.: Effects of depositing temperatures on structure and optical properties of TiO_2 film deposited by ion beam assisted electron beam evaporation. Appl. Surf. Sci. **254**, 2685–2689 (2008)
10. Farrag, M., Thamer, M., Tschurl, M., Burgi, T., Hei, Zu: Preparation and spectroscopic properties of monolayer-protected silver nanoclusters. J. Phys. Chem. C **116**(14), 8034–8043 (2012)
11. Nezamzadeh-Ejhieh, A., Moazzeni, N.: Sunlight photodecolorization of a mixture of methyl orange and bromocresol green by CuS incorporated in a clinoptilolite zeolite as a heterogeneous catalyst. J. Indust. Eng. Chem. **19**(5), 1433–1442 (2013)
12. Kalanur, S.S., Chae,S.Y., Joo, S.S.: Transparent Cu1.8S and CuS thin films on FTO as efficient counter electrode for quantum dot solar cells. Electrachimica Acta **103**, 91 (2013)
13. Wei, H., Yi, L., Zhao, N., Tang, A., Gao, M., Tang, Z.: Synthesis and shape-tailoring of copper sulfide/indium sulfide-based nanocrystals. J. Am. Chem. Soc. **130**, 13152–13161 (2008)
14. Pabalan, R.T., Bertetti, F.P.: Cation-exchange properties of natural zeolites. Rev. Mineral. Geochem. **45**, 453–518 (2001)
15. Li, X., Xiong, S., Li, J., Bai, J., Qian, Y.: Mesoporous NiO ultrathin nanowire networks topotactically transformed from α-Ni $(OH)_2$ hierarchical microspheres and their superior electrochemical capacitance. J. Mater. Chem. **22**, 14276 (2012)
16. Zhong, J.H., Wang, A.L., Li, G.R., Wang, J.W., Ou, Y.N., Tong, Y.X.: $Co_3O_4/Ni(OH)_2$ composite mesoporous nanosheet networks as a promising electrode for supercapacitor applications. J. Mater. Chem. **22**, 5656 (2012)

Effect of Cobalt Substitution on Structural and Magnetic Properties of Magnesium Ferrite Nanoparticles

J. Balavijayalakshmi and T. Sudha

Abstract Cobalt substituted magnesium ferrite ($Mg_{(1-x)}Co_xFe_2O_4$, where x = 0.2, 0.4, 0.6 and 0.8) nanoparticles are prepared by co-precipitation method and samples are annealed at 600 °C. The synthesized nanoparticles are characterized using FT-IR spectral analysis, X-ray diffraction (XRD) analysis, Scanning Electron Microscopy (SEM) analysis, Transmission Electron Microscopy (TEM) analysis and Vibrating Sample Magnetometer (VSM) analysis. The FT-IR spectra show main absorption bands are shifted to higher values as the concentration of cobalt increases. The average nano-crystallite sizes are found to be in the range 7–9 nm. The SEM micrographs show uniformly distributed granular like structure. TEM indicate the presence of rectangular shaped nanoparticles. The magnetic properties of these samples are studied using Vibrating Sample Magnetometer (VSM). As the magnetic properties are enhanced due to the cobalt substitution the synthesized samples can be used as a gas sensor.

1 Introduction

Nano-structured materials are now being studied intensively due to their novel physicochemical properties. Applications of gas sensors have been growing at a consistent pace in the recent years. The mixed-metal oxide gas sensors offer advantages over other gas sensors devices due to their simple implementation, low cost and good reliability for real time control systems. To search for new good gas-sensing materials and the new properties of conventional materials has become an active research field. Among different ferrites, magnesium ferrite enjoys a special attention because of its vast applications in high density recording media, heterogeneous catalysis, adsorption, sensors and magnetic technologies. The technological importance of cobalt ferrite has motivated several studies on the synthesis as well as the physical properties of this material. The substitution of cobalt ions in

J. Balavijayalakshmi (✉) · T. Sudha
Department of Physics, PSGR Krishnammal College for Women, Coimbatore, India
e-mail: balavijayalakshmiroopa@gmail.com

J. Ebenezar (ed.), *Recent Trends in Materials Science and Applications*,
Springer Proceedings in Physics 189, DOI 10.1007/978-3-319-44890-9_27

magnesium ferrite may increase the coercivity, which might be due to the coupling of the spins of cobalt and iron ions [1, 2]. Various methods such as ceramic method [3], co-precipitation method [4], sol–gel method [5, 6], hydrothermal method [7], citrate method [8] and combustion method [9] are used for preparation of spinel ferrites. Hence an attempt is made to synthesize cobalt substituted magnesium ferrite nanoparticles ($Mg_{(1-x)}Co_xFe_2O_4$, where x = 0.2, 0.4, 0.6 and 0.8) by co-precipitation method.

2 Materials and Methods

Cobalt substituted magnesium ferrite ($Mg_{(1-x)}Co_xFe_2O_4$, where x = 0.2, 0.4, 0.6 and 0.8) nanoparticles are prepared by taking stoichiometric amounts of magnesium chloride [$MgCl_2.6H_2O$], cobaltous chloride [$CoCl_2{\cdot}6H_2O$] and anhydrous ferric chloride [$FeCl_3$] dissolved in distilled water. The neutralization is carried out with sodium hydroxide solution and pH is maintained at 8. The precipitate is thoroughly washed with distilled water, dried and annealed at 600 °C. These samples are subjected to X-ray diffraction, FT-IR spectral analysis, SEM, EDX, TEM, SAED and VSM measurements and the results are discussed below.

3 Results and Discussion

3.1 FT-IR Spectral Analysis

The infrared absorption spectrum is recorded at room temperature by using SHIMADZU IR-Affinity-1 in the range of 4000–400 cm^{-1} using KBr pellet method. The spectrum transmittance (%) against wave number is used for interpretation of the results. The FT-IR spectra of the cobalt substituted magnesium ferrite nanoparticles ($Mg_{(1-x)}Co_xFe_2O_4$, where x = 0.2, 0.4, 0.6 and 0.8) annealed at 600 °C is shown in Fig. 1a–d.

The two main broad metal–oxygen bands are observed in the infrared spectrum of all spinels, especially ferrites. The higher absorption band observed in the range 570 cm^{-1}, is caused by the stretching vibrations of the tetrahedral metal–oxygen bond. They are found to be shifted to higher values as the concentration of cobalt increases. The lowest band observed in the range 439 cm^{-1}, is caused by the metal–oxygen vibrations in the octahedral sites [10, 11]. They are found to be shifted to lower values as the cobalt concentration increases. The absorption band appeared broad for tetrahedral sites and this may be due to the migration of cations from octahedral sites to tetrahedral sites. The absorption peaks at 1435, 1627 and 3520 cm^{-1} are due to traces of adsorbed or atmospheric CO_2 [12].

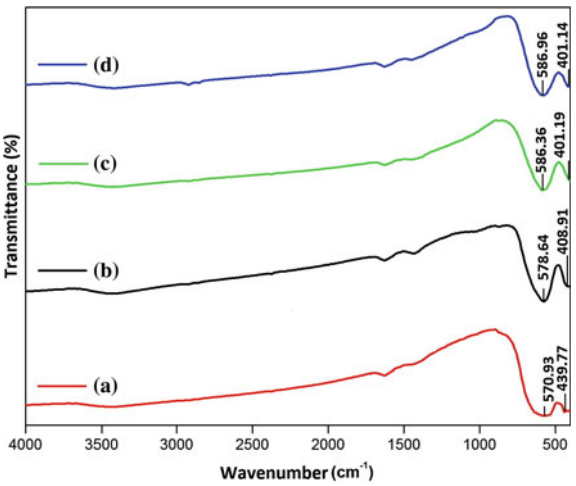

Fig. 1 FT-IR Spectra of Cobalt substituted Magnesium Ferrite nanoparticles ($Mg_{(1-x)}Co_xFe_2O_4$) **a** x = 0.2, **b** x = 0.4, **c** x = 0.6, **d** x = 0.8 annealed at 600 °C

3.2 Structural Analysis

X-ray diffraction patterns of cobalt substituted magnesium ferrite nanoparticles ($Mg_{(1-x)}Co_xFe_2O_4$, where x = 0.2, 0.4, 0.6 and 0.8) annealed at 600°C is shown in Fig. 2a–d. The data are collected in a 2θ range from 10° to 80° at a step size of 0.02 using Shimadzu 6000 X-ray diffractometer equipped with Cu-kα radiation of a wavelength of λ = 1.5406 Å. All the main peaks are indexed with reference to the standard JCPDS card nos. 89-3084 and 22-1086 for magnesium ferrite and cobalt ferrite respectively and are found to be (220), (311), (400), (511) and (440) [13]. The well-defined (311) peak appears to be more intense. All the diffractograms showed the characteristic reflections of the cubic spinel phase. It is observed from the Fig. 2 that the relative intensity increases and the full width at half maximum decrease as the samples are annealed at 600 °C. The average crystallite size (D) is calculated using the Scherrer formula [14] and the average crystallite size is found to be around 7–9 nm. The lattice parameter is calculated for the most prominent plane (311) of the samples and is found to be 8.3939 Å.

3.3 SEM Analysis

The surface morphology of cobalt substituted magnesium ferrite nanoparticles ($Mg_{(1-x)}Co_xFe_2O_4$, where x = 0.2, 0.4, 0.6 and 0.8) annealed at 600 °C are shown in Fig. 3a–d. From the scanning electron micrographs, it is clear that the method of synthesis of cobalt substituted magnesium ferrite has resulted in uniformly distributed granular like ferrite nanoparticles and multigrain agglomerates with well defined crystallite nature as the concentration of cobalt increases.

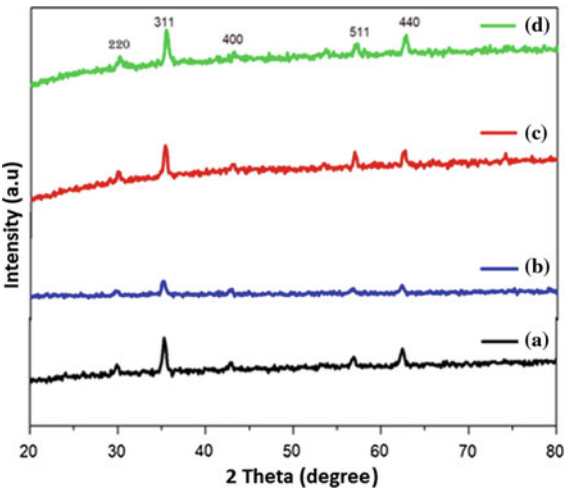

Fig. 2 XRD pattern of Cobalt substituted Magnesium Ferrite nanoparticles ($Mg_{(1-x)}Co_xFe_2O_4$) **a** x = 0.2, **b** x = 0.4, **c** x = 0.6, **d** x = 0.8 annealed at 600 °C

3.4 EDAX Analysis

Figure 4 shows the EDAX spectrum of cobalt substituted magnesium ferrite nanoparticles $Mg_{0.4}Co_{0.6}Fe_2O_4$ annealed at 600 °C. The chemical composition of the sample is confirmed from the EDAX analysis. The EDAX spectrum confirms the presence of the stoichiometric amount of Mg, Co, Fe and O without impurities. The weight percentage and atomic percentage ratio of all the elements has been given in the inset of Fig. 4.

3.5 TEM Analysis

Figure 5a–d shows the HR-TEM micrographs of $Mg_{0.6}Co_{0.4}Fe_2O_4$ nanoparticles annealed at 600 °C. TEM micrographs show the rectangular shaped particles and the particle size is found to be around 10 nm, which is in good agreement with XRD results.

3.6 SAED Analysis

Figure 6 shows the SAED pattern of $Mg_{0.6}Co_{0.4}Fe_2O_4$ nanoparticles annealed at 600 °C. The SAED pattern confirms the crystalline nature of the samples. Each ring corresponds to the lattice planes obtained from the XRD analysis.

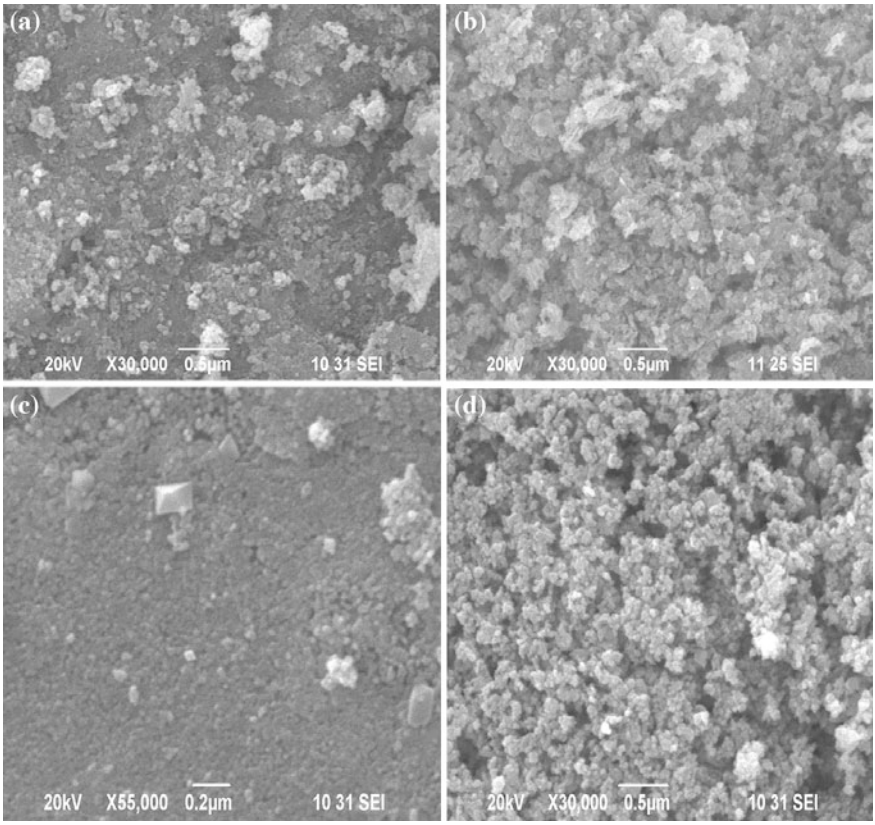

Fig. 3 SEM micrograph of Cobalt substituted Magnesium Ferrite nanoparticles ($Mg_{(1-x)}Co_xFe_2O_4$) **a** x = 0.2, **b** x = 0.4, **c** x = 0.6, **d** x = 0.8 annealed at 600 °C

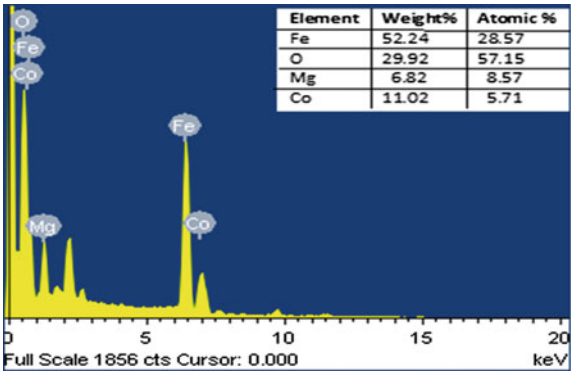

Fig. 4 EDAX spectrum of $Mg_{0.6}Co_{0.4}Fe_2O_4$ nanoparticles annealed at 600 °C

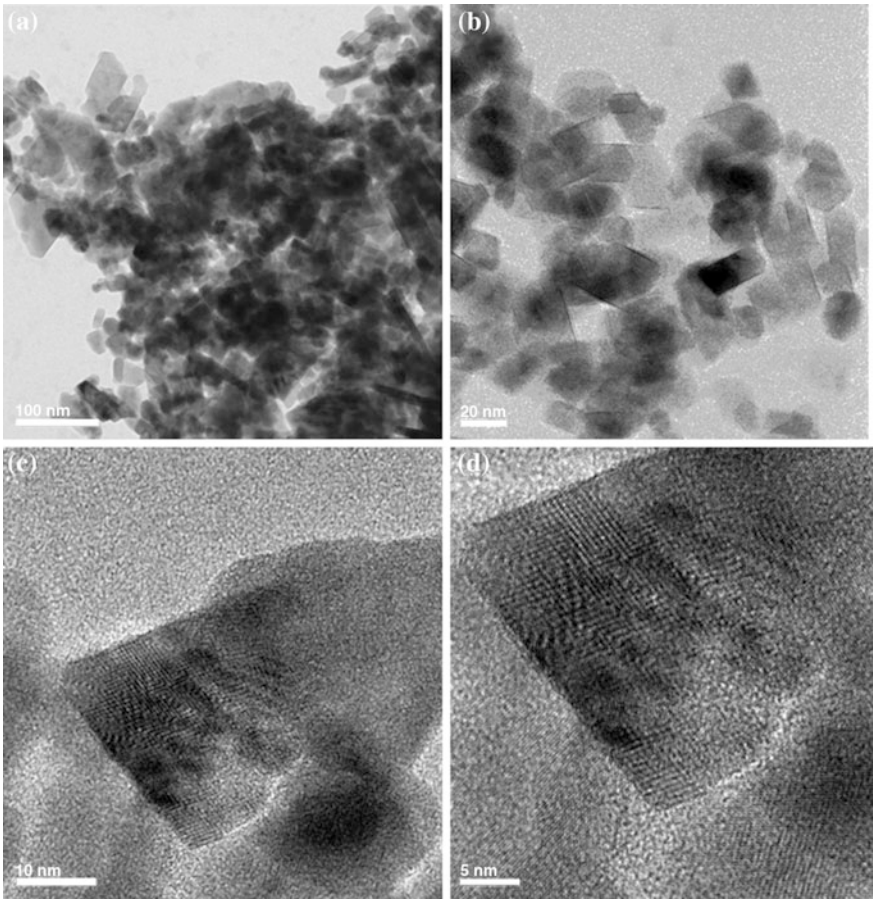

Fig. 5 **a–d** HR-TEM micrographs of $Mg_{0.6}Co_{0.4}Fe_2O_4$ nanoparticles annealed at 600 °C

3.7 VSM Measurements

The magnetic measurements of cobalt substituted magnesium ferrite nanoparticles ($Mg_{(1-x)}Co_xFe_2O_4$, where x = 0.2, 0.4, 0.6 and 0.8) annealed at 600 °C is shown in Fig. 7a–d. The saturation magnetization (M_s), remanent magnetization (M_r), coercivity (H_c) and squareness ratio values of cobalt substituted magnesium ferrite nanoparticles $Mg_{(1-x)}Co_xFe_2O_4$ (x = 0.2, 0.4, 0.6, 0.8) annealed at 600 °C is listed in Table 1.

It is observed that the saturation magnetization (M_s), remanent magnetization (M_r) and coercivity (H_c) increases as the concentration of cobalt substitution increases. The increase in the value of saturation magnetization, remanent magnetization and coercivity may be attributed due to the fact that the occupancy of cations between tetrahedral and octahedral sites varies with the substitution of cobalt ions in

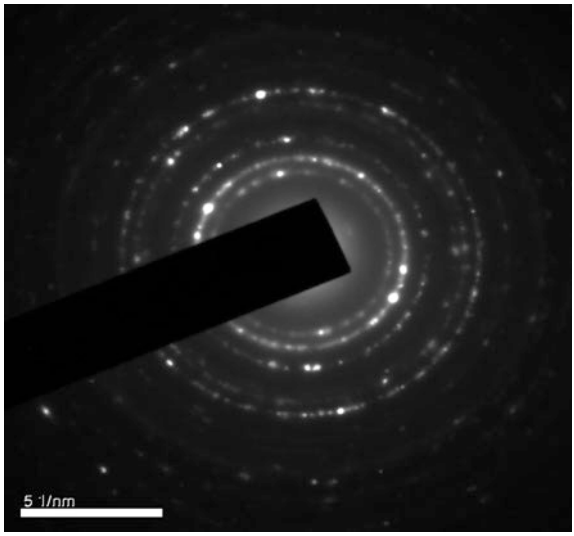

Fig. 6 SAED pattern of $Mg_{0.6}Co_{0.4}Fe_2O_4$ nanoparticles annealed at 600 °C

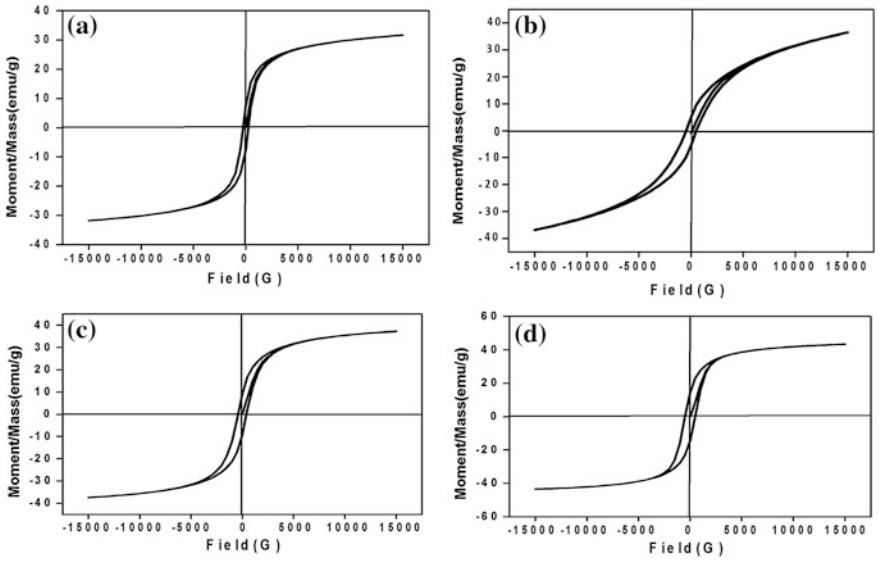

Fig. 7 VSM measurements for Cobalt substituted Magnesium Ferrite nanoparticles ($Mg_{(1-x)}Co_xFe_2O_4$) **a** x = 0.2, **b** x = 0.4, **c** x = 0.6, **d** x = 0.8 annealed at 600 °C

Table 1 The saturation magnetization (M_s), remanent magnetization (M_r), coercivity (H_c) and squareness ratio values of $Mg_{(1-x)}Co_xFe_2O_4$ (x = 0.2, 0.4, 0.6,0.8) nanoparticles

Composition	Saturation magnetization (Ms) (emu/g)	Remanent magnetization (Mr) (emu/g)	Coercivity (G)	Squareness ratio (R) = Mr/Ms
$Mg_{0.8}Co_{0.2}Fe_2O_4$	31.75	7.60	254.2	0.2394
$Mg_{0.6}Co_{0.4}Fe_2O_4$	34.35	8.23	327.2	0.2397
$Mg_{0.4}Co_{0.6}Fe_2O_4$	37.35	9.07	404.5	0.2427
$Mg_{0.2}Co_{0.8}Fe_2O_4$	43.44	14.36	495.5	0.3305

magnesium ferrite nanoparticles. Co^{2+} ions have the tendency to occupy both tetrahedral A-sites and octahedral B-sites, thereby influencing both Mg^{2+} ions and Fe^{3+} ions to occupy tetrahedral and octahedral position in a inverse spinel [15]. These cobalt substitution ions in the tetrahedral sites cause Fe^{3+} ions to migrate to octahedral sites. This increases the concentration of Fe^{3+} ions in octahedral sites and so increases the magnetization in the octahedral sublattice, which in turn enhances the magnetization of the nanoparticles. Smit and Wijn [16] and Kulkarni and Joshi [17] have reported M_S value for bulk particle of $MgFe_2O_4$ as 27 emu/g. The difference in the value of M_S can be explained may be due to the change in the concentration of cation distribution. From the hysteresis loops, the squareness ratio of the sample is derived to determine the intergrain exchanges exist [18] and it is evidenced from Table 1 that there exist magnetostatic interactions [19].

4 Conclusion

Cobalt substituted magnesium ferrite nanoparticles ($Mg_{(1-x)}Co_xFe_2O_4$, where x = 0.2, 0.4, 0.6 and 0.8) annealed at 600 °C are prepared by the co-precipitation method. The FT-IR spectra show main absorption bands around 570 and 439 cm^{-1} corresponding to the vibration modes of the tetrahedral and octahedral sites respectively. They are found to be shifted to higher values as the concentration of cobalt increases. XRD pattern reveals that the synthesized ferrites consist of nanocrystalline particles with size in the range from 7 to 9 nm. The SEM micrographs show uniformly distributed granular like structure. The EDAX spectrum confirms the presence of the stoichiometric amount of Mg, Co, Fe and O without impurities. TEM micrographs show rectangular shaped particles and the particle size is found to be around 10 nm, which is in good agreement with XRD results. The SAED pattern confirms the crystalline nature of the samples. Each ring corresponds to the lattice planes obtained from the XRD analysis. The saturation magnetization (M_s), remanent magnetization (M_r) and coercivity (H_c) increase as the concentration of cobalt substitution increases. As the magnetic properties are enhanced due to the cobalt substitution the synthesized samples can be used as a gas sensor.

References

1. Spaldin, N.: Magnetic Materials: Fundamentals and Device Applications. Cambridge University Press, NY (2003)
2. Pillai, V., Shah, D.O.: Synthesis of high-coercivity cobalt ferrite particles using water-in-oil microemulsions. J. Magn. Magn. Mater. **163**, 243–248 (1996)
3. Johnson, D.W., Ghate, B.B., Wang, B.Y.: Scientific approach to processing of ferrites, Advances in Ceramics, pp. 15–27. American Ceramic Society, Columbus (1985)
4. Bujoreanu, V.M., Fournes, L., Wattiaux, A., Etourneau, J., Segal, E.: Cations distribution and magnetic properties of manganese ferrite powder prepared by coprecipitation from MnO_2 and $FeSO_4{\cdot}7H_2O$. Int. J. Inorg. Mater. **3**, 525–529 (2001)
5. Suder, S., Srivastava, B.K., Krisnamurty, A.: Model for infrared and Raman studies of molecular crystals. Ind. J Pure Appl. Phys. **42**, 366–367 (2004)
6. Lee, Jae-Gwang, Park, Jae Yun, oh, Young-Jei, Kim, Chul Sung: Magnetic properties of $CoFe_2O_4$ thin films prepared by a sol-gel method. J. Appl. Phys. **84**(5), 2801–2804 (1998)
7. Pannaparayil, T., Komarneni, S.: Synthesis and characterization of ultrafine cobalt ferrites. IEEE Trans. MAG. **25**, 4233–4235 (1989)
8. Lal, M., Sharma, D.K., Singh, M.: Effect of processing and polarizer on the electrical properties of Mn-Zn ferrites. Ind. J Pure Appl. Phys. **43**, 291–294 (2005)
9. Ravindranathan, P., Patil, K.C.: Novel solid solution precursor method for the preparation of ultrafine Ni-Zn ferrites. Ceram. Bull. **66**, 688 (1987)
10. Waldron, R.D.: Infrared spectra of ferrites. Phys. Rev. **99**, 1727–1735 (1955)
11. Porta, P., Stone, F.S., Turner, R.G.: The distribution of nickel ions among octahedral and tetrahedral sites in $NiAl_2O_4$ $MgAl_2O_4$ solid solutions. J. Solid State Chem. **11**, 135 (1974)
12. Puviarasan, N., Arjunan, V., Mohan, S.: FT-IR and FT-Raman studies on 3-aminophthalhydrazide and N-aminophthalimide. J Chem. **26**, 323–333 (2002)
13. Pradeep, A., Priyadharsini, P., Chandrasekaran, G.: Sol-gel route of synthesis of nanoparticles of $MgFe_2O_4$ and XRD, FTIR and VSM study. J. Magn. Magn. Mater. **320**, 2774–2779 (2008)
14. Cullity B.D.: Elements of X-ray Diffraction. Addison-Wesely. New York (1959)
15. Chandra, K., Singhal, S., Goyal, S.: Magnetic and Mössbauer spectral studies of nano crystalline cobalt substituted magnesium ferrites ($MgxCo_{1-x}Fe_2O_4$). Hyperfine Interact. **183**, 75–80 (2008)
16. Smit, J., Wijn, H.P.J.: Ferrites. Cleaver-Hume Press, London (1959)
17. Kulkarni, R.G., Joshi, H.H.: Comparison of magnetic properties of $MgFe_2O_4$ prepared by wet-chemical and ceramic methods. J. Solid State Chem. **64**, 141–147 (1986)
18. Wang, Z.L., Liu, Y., Zhang, Z.: Handbook of Nanophase and Nanostructured Materials, Materials Systems and Applications I, vol. III. Kluwer Academic, Plenum Publishers, USA (2003)
19. Stoner, E.C., Wohlfarth, E.P.: A mechanism of magnetic hysteresis in heterogeneous alloys. Philosophical Transactions of Royal Society of London, Series A, Mathematical and Physical Sciences, **240**(826), 599–642 (1948)

Structural and Optical Studies of Ni/S Co Doped TiO_2 Nanorods via Sol-Gel Route

V. Kavitha, P.S. Ramesh and D. Geetha

Abstract Nano crystalline TiO_2 particles doped with various concentrations of Ni/S were successfully synthesized via sol-gel route using titanium tetra isopropoxide while titanium precursor, Ni $(NO_3)_2.6H_2O$ (nickel source) and CS $(NH_2)_2$ (sulfur source). The prepared particles were characterized by standard analytical techniques such as X-ray diffraction (XRD), Fourier transform infrared spectroscopy (FT-IR), UV-Vis absorption spectroscopy, scanning electron microscopy/energy dispersive spectroscopy (SEM/EDS), and transmission electron microscopy (TEM). The photocatalytic activity of Ni/S-TiO_2 is estimated through photocatalytic degradation of Rhodamine B solution under UV irradiation. The XRD data exhibit that the average crystallite size decreases with increase in Ni/S proportions in TiO_2 and the crystal structure of TiO_2 does not change upon the loading of Ni/S. The particles shape changes from spherical to rod and hence rod-like particles are dominant and lightly stuck together. The spectra of pure TiO_2 and doped TiO_2 explains emission peak is a blue shift and seen that maximum peak is around 410 nm. This maximum peak shift mainly aspect to increased electron density at oxygen site. In PL spectra emissions observed for all the doped samples are attributed to the oxygen vacancies and Ti vacancies introduced after Ni/S doping. Compared with pure TiO_2 nanoparticles, Ni/S doped TiO_2 photocatalyst exhibited high photocatalytic activity under ultraviolet (UV) irradiation in the degradation of Rhodamine B aqueous solution. The maximum 97 % of degradation efficiency of Rhodamine B was observed at 3:1 Ni/S-TiO_2 within 120 min. The photocatalytic efficiency of Rhodamine B of Ni/S doped TiO_2 nanoparticle was higher than that of pure TiO_2.

V. Kavitha
Department of Physics, Periyar University, 636011 Salem, Tamil Nadu, India

P.S. Ramesh (✉)
Department of Physics, Wing DDE, Annamalai University, 608002 Chidambaram, Tamil Nadu, India
e-mail: psrddephyau@gmail.com

D. Geetha
Department of Physics, Annamalai University, 608002 Chidambaram, Tamil Nadu, India

J. Ebenezar (ed.), *Recent Trends in Materials Science and Applications*,
Springer Proceedings in Physics 189, DOI 10.1007/978-3-319-44890-9_28

1 Introduction

In recent years, the titanium dioxide (TiO_2) nanostructures have fascinated significant interest because of their unique properties and many potential applications in various fields such as catalysis [1, 2], photo-catalysis [3, 4], sensors [5, 6], solar cells [7, 8], energy storage [9], and gene therapy [10]. It has been established that the physical and chemical properties of TiO_2 nanostructure and great potential applications based on their particle size, crystalline structure and morphology [11].

In the present scenario, photocatalysis has attracting intensive interest owing to its promising applications particularly in environmental remediation and clean energy production. TiO_2 powder is most attractive semiconductors for a photocatalyst and broadly applied in diverse fields, such as decomposition of organic contaminants, water and gas streams treatment, and water photo splitting into H_2 and O_2 [12–14]. Generally, the photocatalytic activity of the TiO_2 depends on more than a few factors such as crystal size, phase and surface area and also depends upon additional factors one is separation efficiency of electron-hole pair, recombination rate of photogenerated electron and hole pairs [15–17].

Doping with metal and non-metal ions is a popular method which facilitates UV light activity of TiO_2. Many investigations have been conducted to extend optical absorption of TiO_2 based materials to the visible light region and to improve photocatalytic activity by nonmetal doping using N [18], C [19, 20], S [21] or multi elemental doped materials [22, 23]. The doping of different transitional metal ions into TiO_2 could shift its optical absorption edge from UV to visible light range, but a prominent change in TiO_2 band gap was not observed [24]. However, transition metal ion-doped TiO_2 suffers from some serious disadvantages, such as thermal instability and low quantum efficiency of the photoinduced charge carriers (electron—hole pairs) [25]. In order to further develop the photocatalytic activity, co-doped titania with double non-metal [26–28], metal–non-metal [29–31] and metal–metal ion [32] has attracted more attention. Most of these explorations have been demonstrated under UV light, because titanium dioxide exhibit relatively high photocatalytic activity and chemical stability under UV light.

In particular, TiO_2 photocatalysts co-doped with S and another metal had attracted many attentions in recent years. For example, prepared Ag and S doped TiO_2 photocatalysts by a photo induced deposition method with high photocatalytic activity for the degradation of Congo red both under UV light, solar light irradiation [33]. The Cu and S co-doped TiO_2 photocatalysts by a sol-gel method with degradation of methyl orange [34].

The aim of the present work is to prepare TiO_2 particles co-doped with Nickel and Sulfur (Ni/S-TiO_2) via sol-gel route, to develop the photocatalytic performance using Rhodamine B. In comparison with other synthesis methods, sol-gel process has notable advantages such as high purity and low temperature, etc.

2 Experimental

2.1 Materials

All of the chemical reagents of analytical grade and were used as without any further purification. Titanium (IV) isopropoxide, ($C_{12}H_{28}O_4Ti$, purity 97 % Sigma Aldrich) was used as starting to prepare crystalline TiO_2 nanoparticles. Ni $(NO_3)_2{\cdot}6H_2O$, CS $(NH_2)_2$ and nitric acid were dopant precursor obtained from Hi-media. Rhodamine B was purchased from sigma-Aldrich. De-ionized water is used for to prepare TiO_2 nanoparticles.

2.2 Synthesis

TiO_2 nanoparticles were synthesized via sol-gel route, involving hydrolysis and condensation of Titanium tetra isopropoxide (TTIP). The 5 ml of TTIP was dissolved in 20 ml of isopropanol. This chemical solution drop wise added into the de-ionized water maintained at pH (2–4) using HNO_3. The solution was well stirred for 30 min, to get clear solution. The dopant precursors Ni $(NO_3)_2.6H_2O$ and CS $(NH_2)_2$ are dissolved in de-ionized water and added into the above solution. The solution of both Ni/S and Ti were stirred for 8 h until a transparent gel is formed. After a period, the gel was dried at 100 °C and washed with ethanol several times, grinded into fine sample powder and then calcined at 500 °C for 4 h. This route was adopted as an optimized method for the preparation of TiO_2 nanoparticles.

2.3 Characterization

The X-ray diffraction patterns of the synthesized samples were recorded on a XPERT-PRO X-ray diffractometer with Cu-Kα radiation (λ = 0.15418 nm) and the 2θ range from 20° to 70°. UV-Visible spectra were recorded using UV-1650 shimadzu spectrophotometer. The photoluminescence (PL) spectra of the sample were characterized on a VARIAN photoluminescence. Fourier transform infrared (FT-IR) spectroscopy test was recorded with AVATAR 330 FT-IR spectrometer in the ranging from 4000 to 400 cm^{-1}. SEM image was taken using JEOL, Model JSM 6390. SEM/EDS analysis was carried out on a Scanning Electron Microscope (JEOL-JSM—5610 LV with INCA with EDS. Transmission electron microscope (TEM) analysis were carried out using a JEOL JEM—2011.

2.4 Photocatalytic Activity

The photocatalytic activity of pure TiO_2 nanoparticles and doping samples were investigated by measuring the photodegradation of Rhodamine B in aqueous solution under UV light irradiation. After the visible light irradiation, the color solution changes from initial pink-red to colorless, revealing that the chromophoric structure of the Rhodamine B is destroyed with the photoreaction time.

3 Results and Discussion

3.1 X-ray Diffraction Studies

Figure 1 shows XRD diffraction patterns of (Ni/S) co-doped TiO_2 nanoparticles synthesized via sol-gel route. The diffraction pattern of TiO_2 is good agreement with JCPDS card No 21-1272 for TiO_2. The peak positions obtained at 25.61, 37.61, 38.58, 48.21, 53.98, 55.06, 62.74, 68.88, and 70.28 are typical patterns of anatase, corresponding crystal planes are (101), (004), (112),(200), (105), (211), (204), (116), and (220) respectively. It can also be seen from Fig. 1 Ni/S-TiO_2 are present in anatase phase, while the adding of Ni does not influence the crystallization performance of TiO_2. In addition, the reflection peak of Ni in Ni/S-TiO_2 is

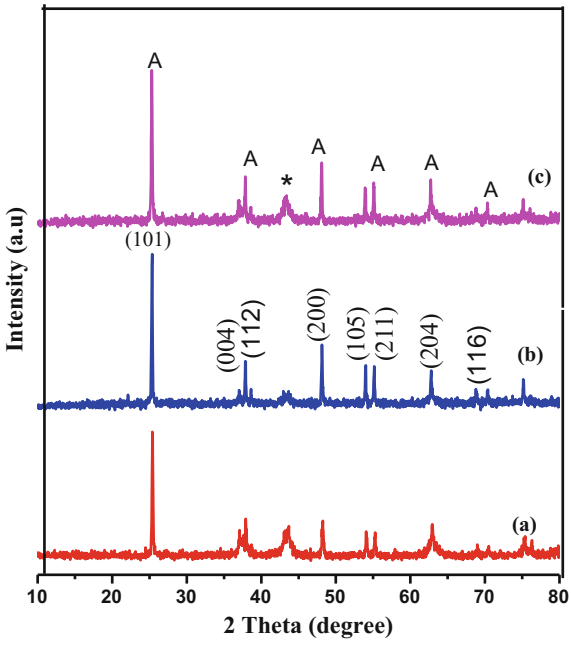

Fig. 1 X-ray diffraction of Ni/S co-doped TiO_2 **a** (1:1) Ni/S **b** (2:1) Ni/S, **c** (3:1) Ni/S *A* and *asterisk* indicates anatase and Ni

presents at 2θ = 44.01°, which is indicated with an asterisk and it well accords with JCPDS No: 04-0850 for Ni with face centered cubic (FCC) crystalline structure. The reflection peak corresponds to the Ni (111) crystal plane, revealing that Ni has been successfully loaded on TiO_2 [35]. The average particle size was estimated using the Scherrer's equation:

$$D = 0.89\lambda/\beta \cos\theta$$

where λ is the wavelength of the Cu Kα radiation, β is the full width at half maximum (FWHM) of the diffraction peak and θ is the Bragg angle. The average crystallite size was found to be 40 nm, 37 nm, and 36 nm for Ni/S-TiO_2 (1:1), Ni/S-TiO_2 (2:1) and Ni/S-TiO_2 (3:1), respectively.

3.2 *Functional Group Analysis (FT-IR)*

The infrared spectroscopy of pure TiO_2 and Ni/S-doped TiO_2 is represented in Fig. 2. The absorption band at 1626.3 cm^{-1} is attributed to the stretching vibration of O–H groups in absorption water [36]. The strong peaks corresponding to 1131 cm^{-1} are the characteristic frequencies of SO_4^{2-} with bidentate bond [37, 38]. Therefore, the most possible doping process is the SO_4^{2-} incorporated into the network of Ti–O–Ti. The presence of sulfate might be responsible for the formation of anatase nucleus and preventing the growth of crystalline size. Some weak bands

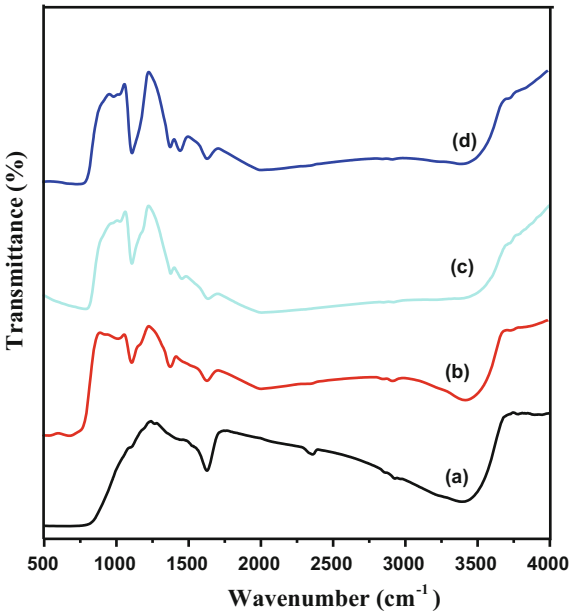

Fig. 2 FT-IR spectra of **a** Pure TiO_2 **b** (1:1) Ni/S **c** (2:1) Ni/S **d** (3:1) Ni/S

between 3400 and at 1630 cm^{-1} are seen, which decreased due to the existence of Ni/S over TiO_2 surface [39, 40]. These bands are attributed to the stretching vibration modes of the O–H groups and the bending modes of the absorbed water molecules, respectively. Further, the broad intense band seen below 900 cm^{-1} is due to Ti–O–Ti vibrations. This shifts to the lower wave numbers and is sharpening which can be attributed to increase in the size of TiO_2 particles after nickel reduction. These results imply additional transmittance bands in Ni/S-doped TiO_2, in comparison to pure TiO_2 powders [39].

3.3 Surface Morphological Analysis

3.3.1 Scanning Electron Microscopy (SEM/EDS)

SEM is one of the powerful tools to analyze surface morphology of the sample and it provides information regarding the growth mechanism, size and shape of the nanoparticles. The surface morphology of the TiO_2 nanoparticles is shown in Fig. 3a–c. The shape of the particles changes from spherical to rod and hence rod-like nanoparticles are dominant and lightly stuck together, with particle size around
35–45 nm.

Energy dispersive X-ray spectrometer (EDS) is an efficient analytical technique used for the elemental composition analysis of a product. The EDS of the TiO_2 nanomaterials are shown in Fig. 4. The EDS result demonstrates the phase of titanium (Ti), Nickel (Ni) and oxygen (O) and sulfur (S) are present in the sample.

3.3.2 Transmission Electron Microscopy (TEM)

Figure 5 presents TEM micrographs of Ni/S-doped (3:1) TiO_2 photocatalysts obtained by the sol-gel method. It can be seen that there were many rod like nanoparticles. It showed good agreement with the result of SEM.

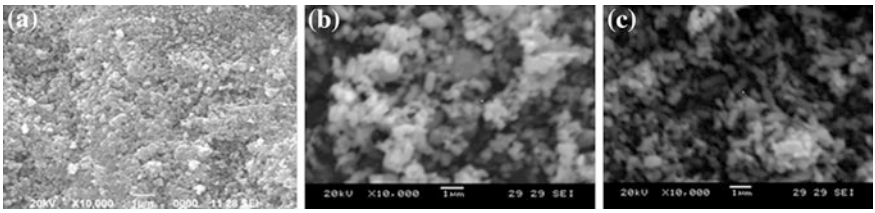

Fig. 3 SEM image of **a** (1:1) Ni/S **b** (2:1) Ni/S **c** (3:1) Ni/S

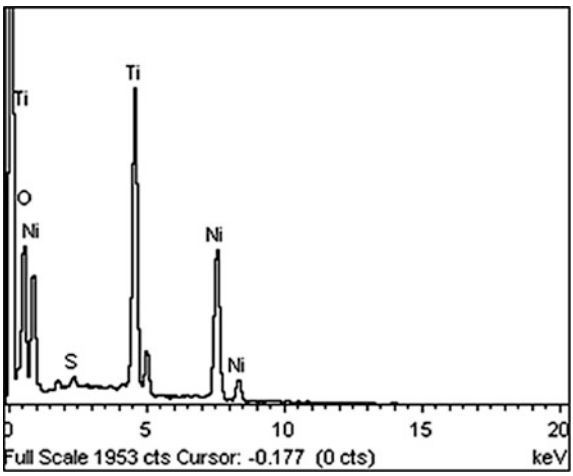

Fig. 4 EDS spectrum of (3:1) Ni/S doped TiO_2

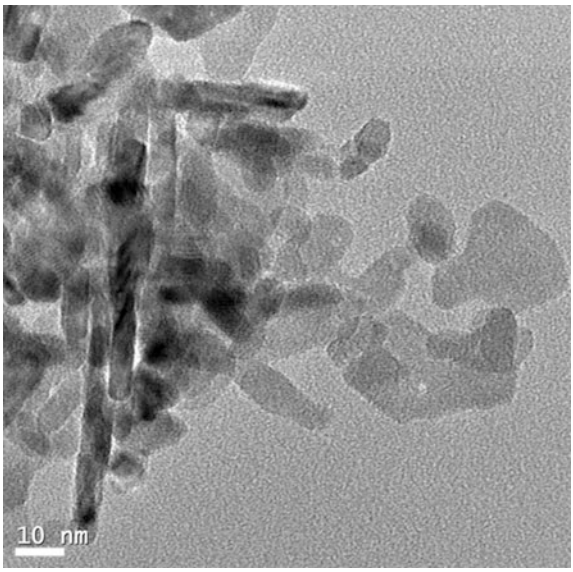

Fig. 5 TEM micrograph of (3:1) Ni/S-TiO_2

3.4 Optical Absorption Analysis (UV-Vis Spectroscopy)

The UV-Vis absorbance spectra of pure TiO_2 and Ni/S doped TiO_2 samples are shown in Fig. 6. The absorption of Ni/S-TiO_2 was located at 300 nm in the UV region. Upon increasing the Ni/S content, the intensity of absorption peak rapidly increased. The longer wavelength absorption can be assigned to the formation of impurity levels within the band gap energy of titanium dioxide. The absorption

wavelength is greater than 400 nm it will affect the formation of electron-hole pairs and separation in a photocatalytic application in the visible region [41, 42].

The band gap energy (eV) of the nanomaterials was quantified using Tauc equation. The E_{bg} estimated from the intercept of tangents to the plots is 3.82 eV for TiO_2, 3.2, 3.1, 2.8 eV for Ni/S doped TiO_2.

3.5 Photoluminescence Studies (PL)

The photoluminescence spectra of all prepared powder samples exhibit broad peaks in the wavelength ranging from 350 to 530 nm with the excited wavelength of 290 nm in Fig. 7. The spectra of Ni/S-TiO_2 and TiO_2 are similar and demonstrate the peak approximately 410 nm. When compared with the band gap energy of TiO_2 (3.2 eV), the broad asymmetric peak seen around 410 nm demonstrates that the emission does not arise. Previous works have proposed that the photoluminescence signals obtained from TiO_2 are generally originating from the surface states resulting from the defects present on the surface of TiO_2 sample [43, 44]. A comparison of the photoluminescence spectra of pure TiO_2 and doped TiO_2 samples with the reported ones shows that the PL signals are largely arising from the levels induced by the defects present in them. The PL spectra of pure TiO_2 and doped TiO_2 show emission peak is blue shift and peak maximum is around 410 nm.

3.6 Photocatalytic Evaluation

Irradiation of UV rays on an aqueous solution of Rhodamine B in the synthesized samples leads to decrease in absorption intensity. The degradation of the

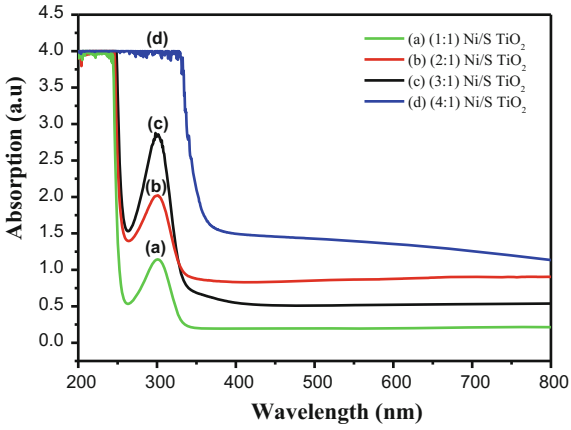

Fig. 6 UV-Visible spectra of **a** (1:1) Ni/S **b** (2:2) Ni/S **c** (3:3) Ni/S **d** Pure TiO_2

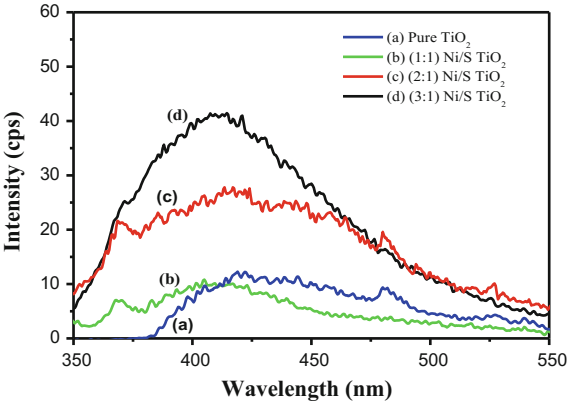

Fig. 7 PL spectra of **a** pure TiO_2 **b** (1:1) Ni/S **c** (2:2) Ni/S **d** (3:3) Ni/S

Rhodamine B under UV light irradiation was determined using a UV-Vis spectrophotometer. The result obtained during the illumination of the Ni/S doped TiO_2 photocatalysts with UV light are revealed in Figs. 8, 9. The photocatalytic response of TiO_2 and Ni/S-TiO_2 was evaluated by monitoring the photo degradation of Rhodamine B in aqueous solution. Typically 25 mg (2.5×10^{-4}) of Rhodamine B dye was added to 250 ml of distilled water used as stocked solution. Prior to the experiment, a suspension was prepared by adding 50 mg of catalyst to 50 ml of Rhodamine B solution. The mixed solution was irradiated using mercury vapor lamp (λ_{max} = 365 nm) under stirring. Further samples were taken out every 30 min and the photocatalyst was separated from the mixture solution and then the UV–Vis absorption of the clarified solution was investigated with a UV–Vis spectrometer. The absorbance of Rhodamine B solution was determined at a wavelength of 465 nm, which corresponds to the maximum absorption wavelength of Rhodamine B.

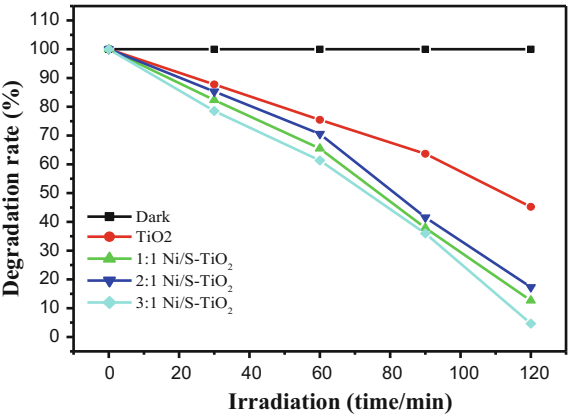

Fig. 8 Typical plot for comparison of change in concentration versus irradiation time in presence of pure TiO_2 and various % of Ni/S doped TiO_2

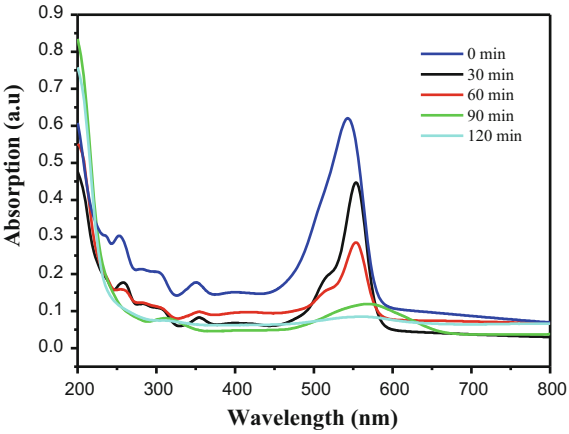

Fig. 9 UV-Visible absorption spectra of Rhodamine B photo degradation under UV light using (3:1) Ni/S doped TiO_2

Figure 8 shows the change in concentration as a function of irradiation time for the dye derivative in the absence and presence of pure and different percentage of Ni/S-doped TiO_2. It is evident that under UV irradiation, no observable loss of Rhodamine B takes place if the reaction was performed in the absence of photocatalysts which exhibits that Rhodamine B is stable under UV irradiation. They reveal that the photocatalytic activities and photodegradation rates increase with increase of Ni/S-TiO_2 nanoparticles. In addition, the Ni/S-doped TiO_2 nanoparticles are more photoactive than the pure TiO_2. It has been found that irradiation of aqueous suspension of Rhodamine B in the presence of prepared photocatalyst illustrates favorable result and leads to decrease in absorption intensity.

The UV-Visible absorption spectra of Rhodamine B degradation are shown in Fig. 9. It decreases in the absorption band of Rhodamine B in the visible state during the irradiation of 120 min. It is found that the maximum absorbance at 553 nm gradually decreases with passage of time and disappears almost completely after 120 min, which indicates the Rhodamine B dye in the presence of synthesized 3:1 Ni/S-doped TiO_2 under UV-light irradiation.

4 Conclusion

The Ni doped titania nanorods were synthesized by sol-gel method and calcinated at 500 °C. The synthesized materials were systematically characterized by XRD, SEM, TEM, UV-Vis, PL and photoconductivity measurements. The Ni/S-doped TiO_2 nanorods are anatase in phase with no other additional impurity phase in the samples. The XRD result indicates that the average crystallite size decreases with increase in Ni concentrations in TiO_2 which is consistent with the morphology observed by SEM and TEM images. The shape of the particles changes from spherical to rod and hence rod-like particles are dominant and lightly stuck together,

with particle size around 35–45 nm. The spectra of pure TiO_2 and Ni/S doped TiO_2 show a blue shift of the emission peak and the peak maximum is seen around 410 nm. The observed trap depth value is greater in the samples than the previously published results on TiO_2 nanoparticles. The present work suggest that semiconducting oxide materials can have promising potential applications in optoelectronic devices such as solar cells, photoconductors in replacement of expansive materials by fine controlling of the compositions and morphology in the oxide materials.

References

1. Yang, G., Yan, Z., Xiao, T., Yang, B.: Low-temperature synthesis of alkalis doped TiO_2 photocatalysts and their photocatalytic performance for degradation of methyl orange. J. Alloys Comp. **580**, 15–22 (2013)
2. De la Cruz, N., Dantas, R.F., Gimenez, J., Esplugas, S.: Photolysis and TiO_2 photocatalysis of the pharmaceutical propranolol: Solar and artificial light. Appl. Catal. B: Environ. **130–131**, 249–256 (2013)
3. Fittipaldi, M., Gatteschi, D., Fornasiero, P.: The power of EPR techniques in revealing active sites in heterogeneous photocatalysis: the case of anion doped TiO_2. Catal. Today **206**, 2–11 (2013)
4. Kamegawa, T., Sonoda, J., Sugimura, K., Mori, K., Yamashita, H.: Degradation of isobutanol diluted in water over visible light sensitive vanadium doped TiO_2 photocatalyst. J. Alloys Comp. **486**, 685–688 (2009)
5. Moon, H.G., Jang, H.W., Kim, J.S., Park, H.H., Yoon, S.J.: A route to high sensitivity and rapid response Nb_2O_5-based gas sensors: TiO_2 doping, surface embossing, and voltage optimization. Sens. Actuat. B **153**, 37–43 (2011)
6. Lee, J., Kim, D.H., Hong, S.H., Jho, J.Y.: A hydrogen gas sensor employing vertically aligned TiO_2 nanotube arrays prepared by template-assisted method Sens. Actuat. B **160**, 1494–1498 (2011)
7. Gratzel, M.: Photoelectrochemical cells. Nature **414**, 338–344 (2001)
8. Shalan, A.E., Rashad, M.M., Yu, Y., Lira-Cantu, M., Abdel-Mottaleb, M.S.A.: Controlling the microstructure and properties of titania nanopowders for high efficiency dye sensitized solar cells Electrochim. Acta **89**, 469–478 (2013)
9. Kim, J.H., Zhu, K., Kim, J.Y., Frank, A.J.: Tailoring oriented TiO_2 nanotube morphology for improved Li storage kinetics Electrochim. Acta **88**, 123–128 (2013)
10. Dhandapani, P., Maruthamuthu, S., Rajagopal, G.: Bio-mediated synthesis of TiO_2 nanoparticles and its photocatalytic effect on aquatic biofilm. J. Photochem. Photobiol. B: Biol. **110**, 43–49 (2012)
11. Song, K., Han, X., Shao, G.: Electronic properties of rutile TiO_2 doped with 4*d* transition metals: First-principles study. J. Alloys Comp. **551**, 118–124 (2013)
12. Fujishima, A., Zhang, X.T.: Titanium dioxide photocatalysis: present situationand future approaches. C. R. Chim. **9**, 750–760 (2006)
13. Hoffmann, M.R., Martin, S.T., Choi, W., Detlef, W.B.: Environmental applications of semiconductor photocatalysis. Chem. Rev. **95**, 69–96 (1995)
14. Zaleska. A.: Doped-TiO_2. A review, Recent Patents Eng. **2**, 157–164 (2008)
15. Kavan, L., Gratzel, M., Gilbert, S.E., Klemenz, C., Scheel, H.J.: Electrochemical and photoelectrochemical investigation of single crystal anatase. J. Am. Chem. Soc. **118**, 6716–6723 (1996)
16. Li, W., Zeng, T.: Preparation of TiO_2 anatase nanocrystals by $TiCl_4$ hydrolysis with additive H_2SO_4. PLoS ONE **6**, e21082 (2011)

17. Mir, N., Salavati-Niasari, M.: Photovoltaic properties of corresponding dye sensitized solar cells: effect of active sites of growth controller on TiO_2 nanostructures. Sol. Energy **86**, 3397–3404 (2012)
18. Yu, J.C., Ho, W.K., Yu, J.G., Yip, H.Y., Wong, P.K., Zhao, J.C.: Efficient visible-light induced photocatalytic disinfection on sulfur-doped nanocrystalline titania. Environ. Sci. Technol. **39**, 1175–1179 (2005)
19. Ho, W.K., Yu, J.C., Lee, S.C.: Synthesis of hierarchical nanoporous F-doped TiO_2 spheres with visible light photocatalytic activity. Chem. Commun. **10**, 1115–1117 (2006)
20. Sun, H.Q., Wang, S., Ang, H.M., Tadé, M.O., Li, Q.: Halogen element modified titanium dioxide for visible light photocatalysis. Chem. Eng. J. **162**, 437–447 (2010)
21. Liu, G., Chen, Z.G., Dong, C.L., Zhao, Y.N., Li, F., Lu, G.Q., Cheng, H.M.: Visible light photocatalyst: iodine-doped mesoporous titania with a bicrystalline framework. J. Phys. Chem. B **110**, 20823–20828 (2006)
22. Hong, X.T., Wang, Z.P., Cai, W.M., Lu, F., Zhang, J., Yang, Y.Z., Ma, N., Liu, Y.J.: Visiblelight- activated nanoparticle photocatalyst of iodine-doped titanium dioxide. Chem. Mater. **17**, 1548–1552 (2005)
23. Usseglio, S., Damin, A., Scarano, D., Bordiga, S., Zecchina, A., Lamberti, C.: (I2)n encapsulation inside TiO_2: a way to tune photoactivity in the visible region. J. Am. Chem. Soc. **129**, 2822–2828 (2007)
24. Wu, J.C.S., Chen, C.H.: A visible-light response vanadium-doped titania nanocatalyst by sol–gel method. J. Photochem. Photobiol. A: Chem. **163**, 509–515 (2004)
25. Choi, W., Termin, A., Hoffmann, M.R.: The role of metal ion dopants in quantum-sized TiO_2: correlation between photoreactivity and charge carrier recombination dynamics. J. Phys. Chem. B **98**(51), 13669–13679 (1994)
26. Ohno, T., Tsubota, T., Nakamura, Y., Sayama, K.: Preparation of S, C cation-codoped $SrTiO_3$ and its photocatalytic activity under visible light. Appl. Catal. A: Gen. **288**, 74–79 (2005)
27. Lin, L., Zheng, R.Y., Xie, J.L., Zhu, Y.X., Xie, Y.C.: Synthesis and characterization of phosphor and nitrogen co-doped titania. Appl. Catal. B: Environ. **76**, 196–202 (2007)
28. Li, X., Xiong, R., Wei, G.: S-N Co-doped TiO_2 photocatalysts with visible-light activity prepared by sol-gel method. Catal. Lett. **125**, 104–109 (2008)
29. Hamal, D.B., Klabunde, K.J.: Synthesis, characterization, and visible light activity of new nanoparticle photocatalysts based on silver, carbon, and sulfur-doped TiO_2. J. Colloid Interf. Sci. **311**, 514–522 (2007)
30. Obata, K., Irie, H.K.: Enhanced photocatalytic activities of Ta, N co-doped TiO_2 thin films under visible light Chem. Phys. **339**, 124–132 (2007)
31. Pingxiao, W., Jianwen, T., Zhi, D.: Preparation and photocatalysis of TiO_2 nanoparticles doped with nitrogen and cadmium. Mater. Chem. Phys. **103**, 264–269 (2007)
32. Zhang, D.R., Kim, Y.H., Kang, Y.S.: Preparation and photocatalysis of TiO_2 nanoparticles doped with nitrogen and cadmium. J. Curr. Appl. Phys. **6**, 801–804 (2006)
33. Gomathi Devi, L., Kavitha, B., Nagaraj.: Bulk and surface modification of TiO_2 with sulphur and silver: Synergetic effects of dual surface modification in the enhancement of photocatalytic activity. Mater. Sci. Semicond. Process. 40832–8392 (2015)
34. Hamadanian, M., Reisi-Vanani, A., Majedi, A.: A.: Synthesis, characterization and effect of calcination temperature on phase transformation and photocatalytic activity of Cu, S-codoped TiO_2 nanoparticles. Appl. Surf. Sci. **256**, 1837–1844 (2010)
35. Liu, Yanhua, Wang, Zilong, Fan, Weibo, Geng, Zhongrong, Fengn, Libang: Enhancement of the photocatalytic performance of Ni-loaded TiO_2 photocatalyst under sunlight. Ceram. Int. **40**, 3887–3893 (2014)
36. Xu, G.Q., Zheng, Z.X., Wu, Y.C.: Feng. N. Effect of silica on the microstructure and photocatalytic properties of titania. Ceram. Int. **35**, 1–5 (2009)
37. Sivakumar, S., Pillai, P.K., Mukundan, P., Warrier, K.G.K.: Sol–gel synthesis of nanosized anatase from titanyl sulfate. Mater. Lett. **57**, 330–335 (2002)

38. Parida, K.M., Sahu, N., Biswal, N.R., Naik, B., Pradhan, A.C.: Preparation, characterization, and photocatalytic activity of sulfate-modified titania for degradation of methyl orange under visible light. J. Colloid Interface Sci. **318**, 231–237 (2008)
39. Ibram Ganesh, A.K., Gupta, P.P., Kumar, P.S.C., Sekhar, K., Radha, G., Sundararajan, G.: Preparation and characterization of Ni-Doped TiO_2 materials for photocurrent and photocatalytic applications. Sci. World J. 1–16 (2012)
40. Begum, N.S., Ahmed, H.M.F., Gunashekar, K.R.: Effects of Ni doping on photocatalytic activity of TiO_2 thin films prepared by liquid phase deposition technique. Bull. Mater. Sci. **31**, 747–751 (2008)
41. Zeng, P., Zhang, X., Zhang, X., Chai, B., Peng, T.: Efficient photocatalytic hydrogen production over Ni@C/TiO_2 nanocomposite under visible light irradiation. Chem. Phys. Lett. **503**, 262–265 (2011)
42. Dai, K., Peng, T.Y., Ke, D.N., Wei, B.Q.: Photocatalytic hydrogen generation using a nanocomposite of multi-walled carbon nanotubes and TiO_2 nanoparticles under visible light irradiation. Nanotechnology **20**, 125603 (2009)
43. Sasikala, R., Sudarsan, V., Sudakar, C., Naik, R., Panicker, L., Bharadwaj, S.R.: Modification of the photocatalytic properties of self doped TiO_2 nanoparticles for hydrogen generation using sunlight type radiation. Int. J. Hydrogen Energy **34**, 6105–6113 (2009)
44. Madhukumar, P., Badrinarayan, S., Sastry, M.: Nanocrystalline TiO_2 studied by optical, FTIR and X-ray photoelectron spectroscopy: correlation to presence of surface states. Thin Solid Films **358**, 122–130 (2000)

Facile Synthesis, Formation Mechanism and Optical Properties of ZnO Nanostructures

Linu M. Johny, N.S. Nirmala Jothi and P. Sagayaraj

Abstract ZnO is a very promising material because of its wide range of applications in electronics, photonics, optics and as energy storage materials. Zinc oxide nanorods were synthesized using a simple hydrothermal method at lower temperature and nano spheres by solvothermal method. The formation process of ZnO nanorods and nanospheres is discussed. The X-ray diffraction pattern indicates that the nanorods and nanospheres have hexagonal wurtzite structure. The high resolution transmission electron microscopy (HRTEM) images reveal that the synthesized ZnO nanorods grow along ⟨001⟩ direction. The optical properties were studied by UV visible absorption and photoluminescence spectroscopy.

1 Introduction

Nanomaterials of transparent conducting oxides with unique morphologies are currently of great interest to researchers because of wide possibilities in different technological applications. ZnO is a wide band gap (3.37 eV) transition metal oxide n-type semiconductor with large exciton binding energy (60 meV) and has wide range of applications because of its optical, electrical, magnetic, piezoelectric properties [1–3]. It is used in fabricating devices like gas sensors, solar cells and lithium ion batteries [4–6] etc. ZnO nanostructures with different morphologies like nanorods, nanotubes, nanowires, nanosheets, nanobelts, nanoflowers, hierarchial nanostructures [7–12] have been synthesized by various physical methods and wet chemical methods. The synthesis of 1D ZnO have been reported by different physical methods like chemical vapour deposition (CVD), pulsed laser deposition (PLD), MOVCD, template assisted growth [13, 14] and also by wet chemical methods like hydrothermal/solvothermal method, sol-gel method [7, 15, 16]. The

L.M. Johny · N.S. Nirmala Jothi (✉) · P. Sagayaraj
Department of Physics, Loyola College, Chennai, India
e-mail: jmjnirmala@yahoo.co.in

J. Ebenezar (ed.), *Recent Trends in Materials Science and Applications*,
Springer Proceedings in Physics 189, DOI 10.1007/978-3-319-44890-9_29

synthesis by wet chemical method is comparatively easy at relatively low temperature. 1D nanostructures with dissimilar surfaces will differ in their geometric and electronic structures and therefore show different functional properties. Therefore, for fabricating devices, it is necessary to control the crystal morphology, size and shape of the faces of metal oxide crystal. Thus one dimensional nanostructures can be used to fabricate various nano devices like UV detectors, nano lasers, solar cells, gas sensors and as anode materials for lithium ion batteries [4–6, 17–19]. Here we report the synthesis and characterization of ZnO nanorods by hydrothermal method at low temperature and nanospheres with hexagonal faces by a simple solvothermal method. The crystalline nature of the sample was characterized using XRD, the morphology of the sample was examined using HRTEM, the band gap was determined by UV-Vis absorption and reflectance spectra, optical properties were studied using room temperature photoluminescence.

2 Experimental

2.1 Synthesis of ZnO Nanorods

All chemicals used were of analytical grade and were used without any further purification. 100 ml of 0.1 M ammonia solution and 50 ml of 0.1 M zinc acetate dihydrate solution was prepared. Ammonia solution was taken in a burette and slowly added drop wise into 50 ml zinc acetate solution under mild stirring. A white gelatinous precipitate is formed. It was then stirred for about an hour. The precipitate was thoroughly washed with water several times. The washed precipitate was ultrasonically dispersed in 80 ml of deionized water. It was then transferred to a Teflon lined stainless steel autoclave and kept in a furnace at 100 °C for 12 h. The precipitate was then washed, filtered and dried in vacuum at 80 °C for further characterization.

2.2 Synthesis of ZnO Nanospheres

All chemicals used were of analytical grade and were used without any further purification.1 mmol of zinc acetete dehydrate was dissolved in 160 ml of 1-propanol. It was magnetically stirred for an hour and transferred into a 200 ml Teflon lined autoclave and heated at 160 °C for 24 h. A white precipitate formed was washed with water and ethanol several times and dried at 80 °C for 12 h. It was then calcined at 500 °C for 2 h.

3 Formation and Growth Mechanism

3.1 ZnO Nanorods

ZnO is a polar crystal with Zn rich positive plane $\langle 001 \rangle$ and an oxygen rich negative plane $\langle 00\bar{1} \rangle$. Since we have not used any templates or surfactants for the growth of ZnO nanorods, the concentration of Zn^{2+} to OH^- ions in the solution plays a major role in the morphology of the crystal structure. The ratio of NH_4OH: $Zn(CH_3COO)_2.2H_2O$ is 2:1, the OH^- ions are not just a source of hydroxyl ions, but will also act as a capping agent . Due to the high concentration of OH^- ions, they will be adsorbed on the $\langle 001 \rangle$ plane of ZnO. Thus OH^- ions will allow the growth of crystal along $\langle 001 \rangle$ direction [20]. The overall reaction for the growth of ZnO rods may be summarized as follows

Reaction of $Zn(CH_3COO)_2 \cdot H_2O$ with NH_4OH

$$NH_3H_2O \leftrightarrow NH_4^+ + OH^-$$

$$Zn^{2+} + 2OH^- \rightarrow Zn(OH)_2$$

Hydrothermal treatment of $Zn(OH)_2$

$$Zn(OH)_2 + 2OH^- \leftrightarrow [Zn(OH)_4]^{2-}$$

$$[Zn(OH)_4]^{2-} \leftrightarrow Zn^{2+} + 4OH^-$$

$$Zn^{2+} + 2OH^- \leftrightarrow ZnO + H_2O$$

It is concluded that the concentration of OH^- ions in the solution and $[Zn(OH)_4]^{2-}$ radical plays an important role during hydrothermal process for the formation of ZnO rods.

3.2 ZnO Nanospheres

The formation of ZnO nanospheres is facilitated by the hydrolysis of caboxylate (zinc acetate) and by the condensation reaction in the alcohol medium. The hydroxyl group that binds to the Zn species is released by esterification. Susequently a Zn–O–Zn bond is generated by the condensation of Zn hydroxyl species with elimination of water.

Reaction of $Zn(CH_3COO)_2 \cdot 2H_2O$ with C_3H_7O

$$2C_3H_7OH + Zn(CH_3COO)_2 \rightarrow 2CH_3COOC_3H_7 + Zn(OH)_2$$

$$Zn(OH)_2 \rightarrow ZnO + H_2O$$

4 Characterization

XRD studies to analyze the crystalline nature was made using X PAN analytical X'pert PRO diffractometer with Cu-Kα λ = 1.54060 Å. The optical absorption spectra of ZnO nanoparticles were characterized by UV-Vis spectrophotometer Shimadzu UV-3600. The High Resolution Transmission Electron Microscopy (HRTEM) and selected area diffraction pattern (SAED) were obtained on a Jeol/JEM 2100 operated at a voltage of 200 kV. Room temperature PL was recorded on a Cary Eclip spectrophotometer with an excitation wavelength of 255 nm.

5 Results and Discussion

5.1 XRD Analysis

The XRD pattern of the zinc oxide nanorods is given in Fig. 1a and that of nanospheres is given in Fig. 1b. The peaks present in the spectrum confirms the polycrystalline nature of the nanostructures, corresponding to that of hexagonal ZnO with lattice constants a = 3.249 Å and c = 5.206 Å. The peak positions matched well with the standard data for ZnO (JCPDS card no. 36-1451). No other crystalline by products are found in the pattern, indicating that the as prepared ZnO has a pure wurtzite nature. The average crystallite size D was calculated using Scherrer equation $D = 0.9\lambda/\beta\cos\theta$. The average crystallite size is about 26 nm and that of nanospheres is 18 nm.

5.2 Williamson-Hall Analysis

In X-ray diffraction, the peak broadening is caused mainly by particle size and lattice strain. Average particle size is usually measured using X-ray profile analysis. It is also seen that crystal imperfections, like lattice dislocations lead to lattice strain and is a measure of lattice constants. To estimate the crystallite size and lattice

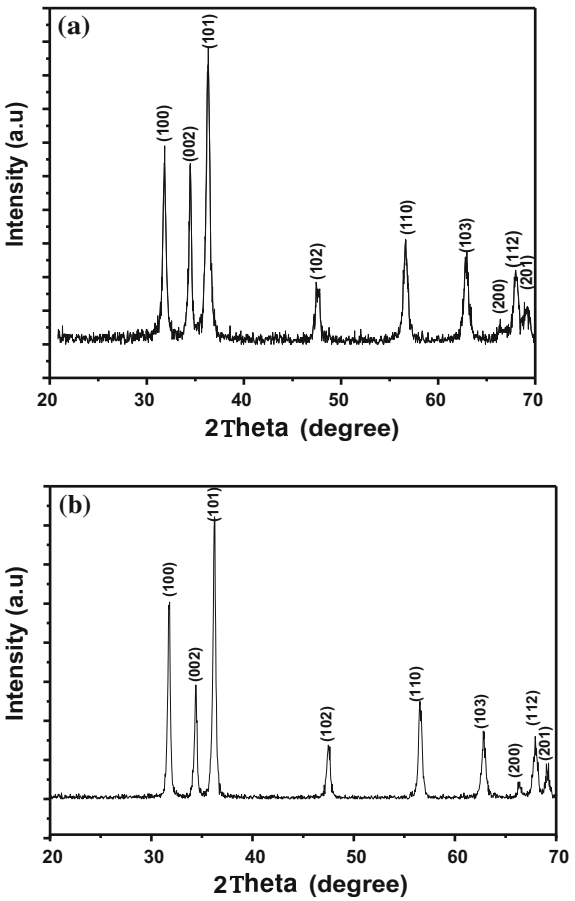

Fig. 1 XRD spectra of ZnO **a** nanorods, and **b** nanospheres

strain the W-H analysis of XRD data was used. In nanocrystalline ZnO the strain induced by crystal imperfections and distortion is calculated by using the formula:

$$\varepsilon = \frac{\beta_{hkl}}{\tan\theta} \tag{1}$$

where ε is the strain, β_{hkl} is the FWHM of the diffraction peak and θ is the Bragg angle. Though the particle size and strain result in peak broadening, they are independent of each other and therefore the peak can be written as sum of particle size and strain as follows:

$$\beta_{hkl} = \frac{k\lambda}{D\cos\theta} + 4\varepsilon\tan\theta \tag{2}$$

From the above two equations, we get

$$\beta_{hkl} \cos\theta = \frac{k\lambda}{D} + 4\varepsilon \sin\theta \tag{3}$$

Equations (2) and (3) are known as W-H equations. A W-H plot for the nanostructures is obtained with 4sinθ along the x-axis and β cosθ along the y-axis as shown in Fig. 2a, b. The crystallite size of ZnO nanospheres from the plot is around 20 nm which is in good agreement with that calculated using Scherrer formula, but for ZnO nanorods it is found to be 45 nm. The particle size for nanorods does not match with that calculated using Scherrer formula because of the morphology and oriented growth of the crystal in a particular direction. As crystallite size measures the size of the coherent diffracting domains, the crystallite size may not be generally the same as the particle size due to the formation of

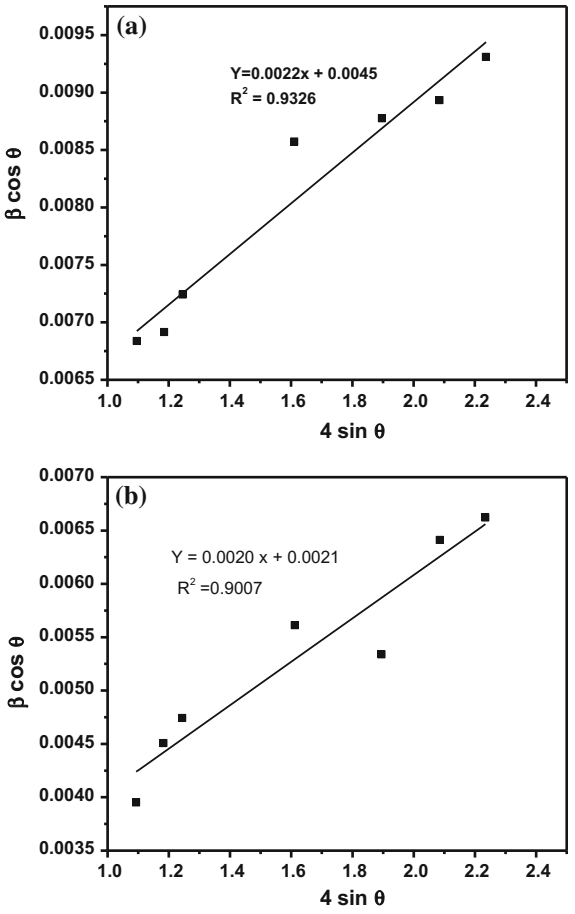

Fig. 2 Willamson Hall plot for ZnO **a** nanorods, and **b** nanospheres

polycrystalline aggregates. The micro strain due to the lattice deformation for ZnO nanorods is found to be 0.22 % and that for ZnO nanospheres is 0.20 %.

5.3 *High Resolution Transmission Electron Microscopy (HRTEM)*

Figure 3a, b gives the HRTEM micrographs of synthesized ZnO nanorods. The samples show almost uniform nanorods with around 25 nm diameter and 150 nm length with an aspect ratio of 6 without much agglomeration. As we can see small bright spots making up the rings, each spot arising from Bragg reflection of an individual crystallite, it is concluded that the ZnO samples have polynanocrystalline

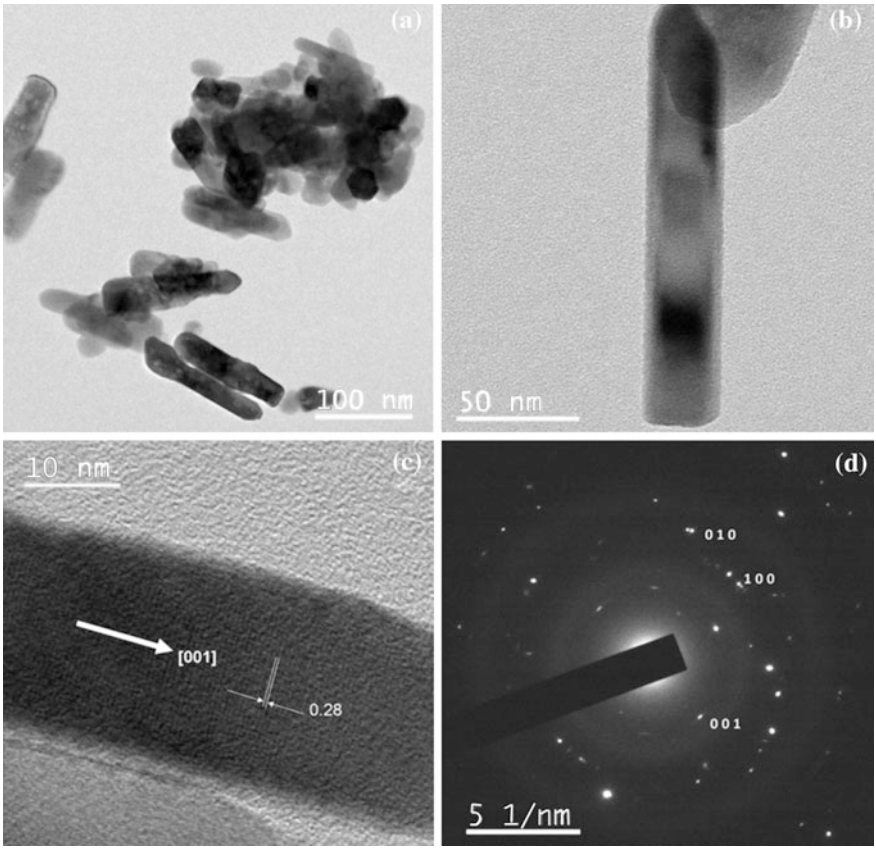

Fig. 3 HRTEM images of ZnO **a** nanorods, **b** single nanorod, **c** Lattice resolved image of single nanorod, and **d** SAED pattern

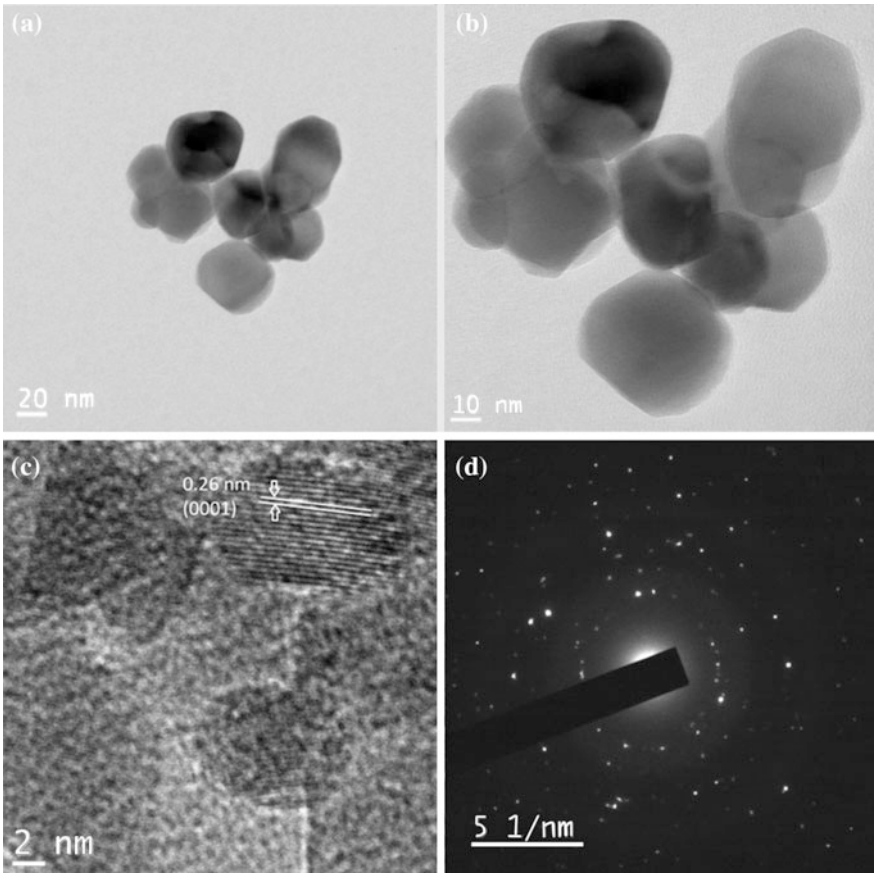

Fig. 4 HRTEM images of ZnO **a** nanospheres, **b** nanospheres with hexagonal faces, **c** Lattice resolved image of single nanosphere, and **d** SAED pattern

nature. Figure 3c shows the image of a single nanorod grown along the ⟨001⟩ direction. The fringe width of 0.28 nm corresponds to the ⟨010⟩ plane of ZnO.

Figure 4a, b gives the HRTEM micrographs of synthesized ZnO nanospheres. The samples show almost uniform spheres with around 20 nm diameter without much agglomeration. The hexagonal faces of the spheres can be clearly seen in TEM images. Figure 4c shows the hexagonal face of a single nanosphere. As we can see small bright spots making up the rings, each spot arising from Bragg reflection of an individual crystallite, it is concluded that the ZnO nanostructures have polynanocrystalline nature (Figs. 3d, 4d).

5.4 UV-Vis Spectroscopy

UV-Vis spectroscopy was used to characterize the optical absorptions of ZnO nanoparticles. Figure 5a, b shows the absorption peak of UV spectra of nanorods and nanospheres are at 312 and 340 nm respectively. To determine the optical band gap of the synthesized ZnO the reflectance spectra was carried out. The diffuse reflectance (DR) spectrum for ZnO nanorods, and nanospheres with their corresponding Tauc's plot is shown in Figs. 6a, b and 7a, b. To determine the exact band gap value of ZnO, the reflectance values were converted to absorbance by applying Kubelka-Munk function [21]. The band gap can be determined by the following formula.

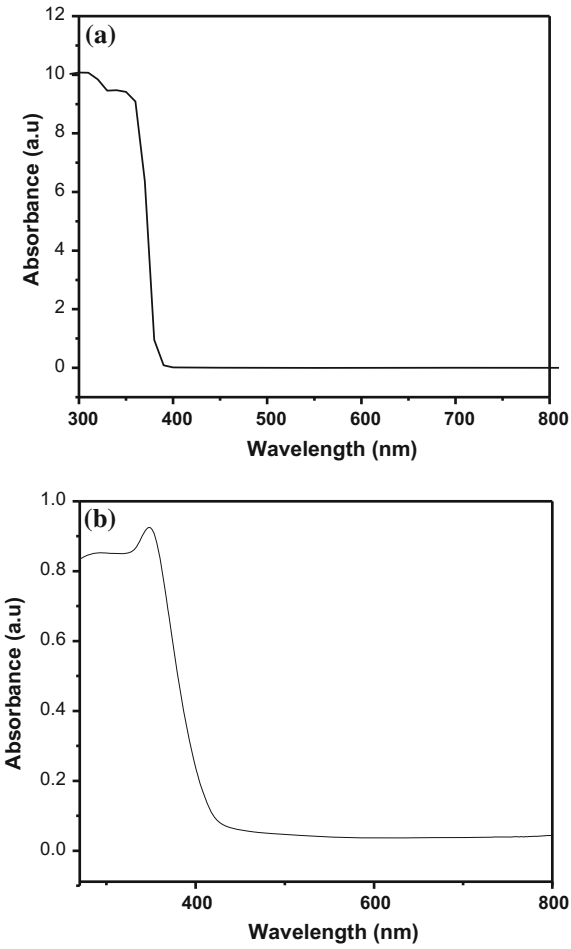

Fig. 5 UV-Vis absorption spectrum of ZnO **a** nanorods, and **b** nanospheres

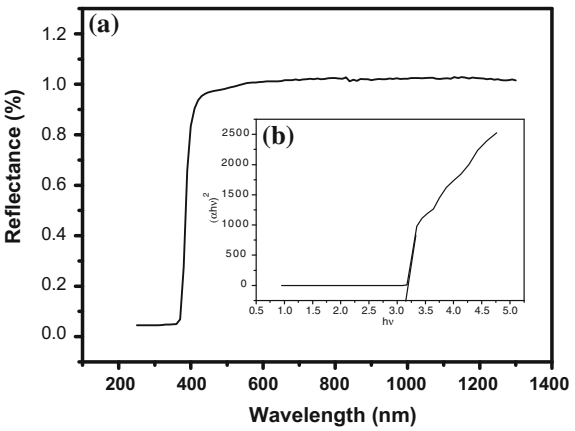

Fig. 6 **a** DR spectrum, **b** Tauc's plot for ZnO nanorods

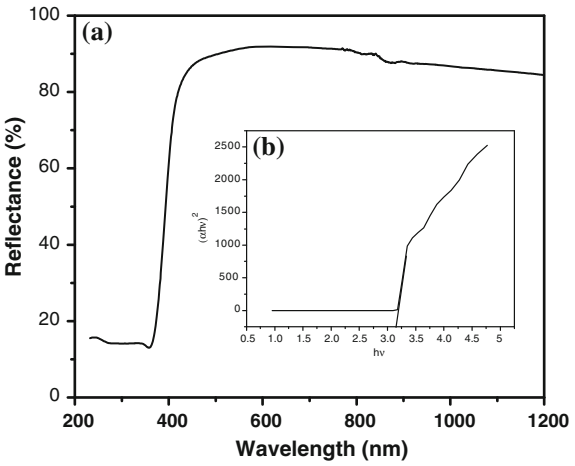

Fig. 7 **a** DR spectrum, **b** Tauc's plot for ZnO nanospheres

$$a = \frac{K(hv - E_g)^{n-2}}{hv}$$

where α is the absorption coefficient, K is a constant, Eg is the band gap, and n = 1 for direct transition. The relationship between the absorption co-efficient α and the photon energy hν for direct allowed transition is given as $(ahv)^2 = B(hv - E_g)$ where hν is the photon energy E_g is the apparent optical band gap. The direct band gap of $(\alpha h\nu)^2$ against hν plot is extrapolated to intersect the energy axis at α = 0. The band gap is found to be 3.34 eV for nano rods and 3.39 eV for nano spheres respectively.

5.5 Photoluminescence Studies

Figure 8a shows the photoluminescence spectra of ZnO nanorods. The emission spectra was obtained at an excitation wavelength of 255 nm using a Xe flash lamp. The spectra shows emission only in the blue region with a strong emission peak centered at 428 nm and two peaks at 405 and 448 nm respectively and the well known green luminescence of ZnO at 510 + 50 nm is quenched. Photoluminescence (PL) is an effective tool to study the optical properties and also about the defect levels in semiconductor materials. The origin of luminescence centers are investigated as it finds application in the field of optoelectronics. Luminescence of ZnO in different regions of the visible spectrum (UV-Blue, Green, Yellow) can be due to intrinsic or extrinsic point defects. The deep level emission in ZnO has been attributed to different intrinsic defects in the crystal of ZnO such as oxygen vacancies (V_O), oxygen interstitial (O_i), zinc vacancies (V_{Zn}), zinc interstitial (Z_{ni}) and oxygen anti-site (O_{Zn}) and zinc anti-site (Zn_O) [22]. Previous PL studies on ZnO nano structures show that the optical properties of ZnO change with crystal morphology even in the absence of dopants [23]. It has been reported that the optical properties ZnO rods are enhanced with increase in their aspect ratio. Zeng et al. [24] reported that blue emission of ZnO nano particles originate from transitions involving Zn interstitial defect states. It is also reported that low temperature annealing provides enough ionization energy and increases the concentration of charge in Zn interstitials, strengthening blue emissions. Monticone et al. [25] also have reported that for ZnO prepared at high OH^- ion concentration the emission in the green region is strongly suppressed. It can therefore be concluded that the strong blue emissions are due to the transition from the Zn interstitial defect states because of the morphology and as the sample is synthesized at low temperatures.

Figure 8b shows the PL spectra of ZnO nanospheres. The emission spectra was obtained at an excitation wavelength of 340 nm using a Xe flash lamp. The spectra shows emission only in the UV region at 388 nm and blue region with a strong emission peak centered at 415 nm and two shoulders are at 401 and 423 nm respectively and the well known green luminescence of ZnO at 510 + 50 nm is quenched. Two minor peaks are seen at 473 and 481 nm respectively. The peak at 388 nm is considered as the characteristic band edge emission of ZnO or the excitonic recombination [23, 25]. Blue emission in ZnO is due to the transition from the Zn interstitial defect states Z_{ni} slightly below the conduction band to the valence band. Blue emissions can also be due to the extended Z_{ni} states which are slightly below the simple Z_{ni} state to the valence band [23]. The many peaks in the blue region can be attributed to emissions from the extended Z_{ni} to the valence band. Zeng et al. have also done an interesting observation that for blue emissions the excitation wavelength is not in accordance with the band gap, it takes either a slightly higher or lower value. Here the excitation given for ZnO nanorods is

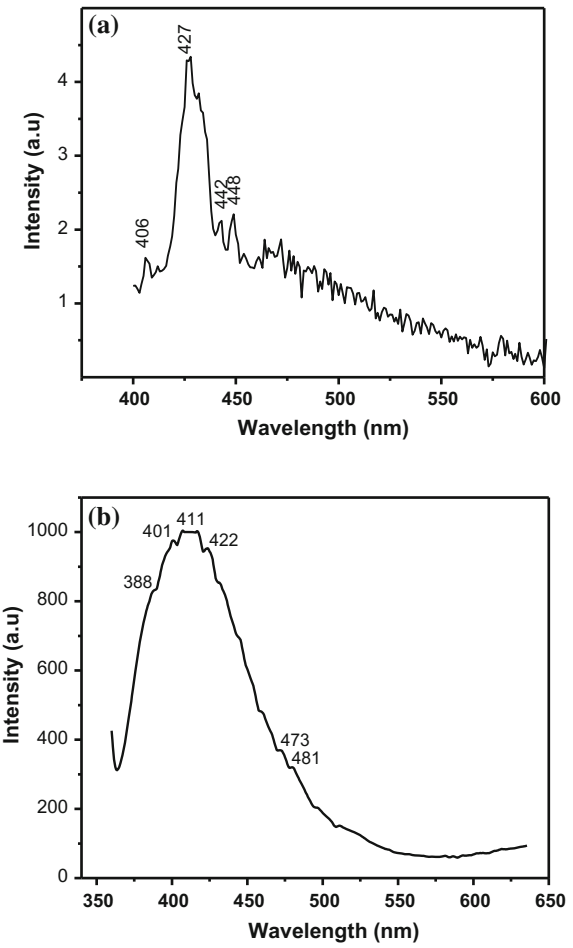

Fig. 8 PL spectrum of ZnO **a** nanorods, and **b** nanospheres

slightly below the band gap and for ZnO nanospheres it is near band gap value. Therefore it can be concluded that the blue emissions from the nano ZnO spheres is due to the transitions from the several extended sub states related to the Z_{ni} defect states below the conduction band edge.

6 Conclusion

ZnO nanorods are synthesized by a hydrothermal technique at low temperature and ZnO nanospheres are synthesized by solvothermal method. The structural, morphological and optical properties were analyzed. XRD showed that the synthesized ZnO nanorods and nano spheres have hexagonal wurtzite structures. UV-Vis

spectroscopy confirmed the band gap of ZnO nanorods to be 3.34 eV and nanospheres to be 3.39 eV. The PL spectra of ZnO rods was found to be dominated by a strong and sharp emission in the blue region and the exciton emission in the UV region and well known emission in the green region was suppressed. The PL spectra of ZnO nanospheres found to be dominated by a strong and sharp emission in the blue region and the exciton emission in the UV region but the well known emission in the green region was suppressed. 1D ZnO nanostructures are considered ideal as it finds applications in devices like gas sensors, Li ion batteries etc. The blue luminescence of ZnO nanorods and nanospheres would have potential in visible light emission and biological fluorescence labeling application. It can also be used to fabricate UV detectors and solar cells.

References

1. Grundmann, M., Wenckstern, H.V., Pickenhain, R., Nobis, Th, Rahm, A., Lorenz, M.: Electrical properties of ZnO thin films and optical properties of ZnO-based nanostructures. Superlattices Microstruct. **38**, 317–328 (2005)
2. Xu, Q., Zhou, S., Schmidt, H.: Magnetic properties of ZnO nanopowders. J. Alloys Compd. **487**, 665–667 (2009)
3. Hsu, C.L., Chen, K.C.: Improving piezoelectric nanogenerator comprises ZnO nanowires by bending the flexible PET substrate at low vibration frequency. J. Phys. Chem. C **116**(16), 9351–9355 (2012)
4. Wang, X., Li, W., Liu, J., Wang, F., Kong, J., Qiu, S., Cuizhu, H., Lua, L.: Synthesis of nestlike ZnO hierarchically porous structures and analysis of their gas sensing properties. ACS Appl. Mater. Interfaces **4**, 817–825 (2012)
5. Barpuzary, D., Banik, A., Panda, A.N., Qureshi, M.: Mimicking heteroleptic dyes for an efficient 1D-ZnO based dye-sensitized solar cell using the homoleptic ruthenium(II) dipyridophenazine complex as a photosensitizer. J. Phys. Chem. C **119**(8), 3892–3902 (2015)
6. Shen, X., Mu, D., Chen, S., Wu, B., Wu, F.: Enhanced electrochemical performance of ZnO-loaded/porous carbon composite as anode materials for lithium ion batteries. Appl. Mater. Interfaces **5**, 3118–3125 (2013)
7. Liu, B., Zeng, H.C.: Hydrothermal synthesis of ZnO nanorods in the diameter regime of 50 nm. J. Am. Chem. Soc. **125**(15), 4430–4431 (2003)
8. Xu, C., Shin, P., Cao, L., Gao, D.: Preferential growth of long ZnO nanowire array and its application in dye-sensitized solar cells. J. Phys. Chem. C **114**(1), 125–129 (2010)
9. Wang, C., Mao, B., Kang, Z., Tian, C.: Solution synthesis of ZnO nanotubes via a template-free hydrothermal route. Solid State Commun. **141**(11), 620–623 (2007)
10. Wang, X.D., Song, V.Z., Wang, L.: Nanowire and nanobelt arrays of zinc oxide from synthesis to properties and the novel devices. J. Mater. Chem. **17**(8), 711–720 (2007)
11. Su,Y., Li, J., Luo, Z., Lua, B., Li, P.: Microstructure, growth process and enhanced photocatalytic activity of flower-like ZnO particles RSC Adv. (2016)
12. Zhang, Y., Xu, J., Xiang, Q., Li, H., Pan, Q., Xu, P.: Brush-like hierarchical ZnO nanostructures: synthesis, photoluminescence and gas sensor properties. J. Phys. Chem. C **113**, 3430–3435 (2009)
13. Lu, L., Chen, J., Li L., Wang, W.: Direct synthesis of vertically aligned ZnO nanowires on FTO substrates using a CVD method and the improvement of photovoltaic performance . Nanoscale Res Lett. **7**(1), 293 (2012)

14. Wang, X., Ding, Y., Yuan, D., Hong, J., Liu, Y., Wong, C.P., Hu, C., Wang. Z.L.: Reshaping the tips of ZnO nanowires by pulsed laser irradiation. Nano Res. **5**(6) (2012)
15. Vassieres, L., Keis, K., Lindquist, S.E.: Purpose built anisotropic metal oxide materials: 3D highly oriented arrays of ZnO. J. Phys. Chem. B **105**(17), 3350–3352 (2001)
16. Hung, C.H., Whang, W.T.: A novel low-temperature growth and characterization of single crystal ZnO nanorods. Mater. Chem. Phys. **82**(3), 705–710 (2003)
17. Yu, H.C., Bo, T.C., Chih, K.C., Ying, Y., Chun, T.Y., Heng, L., Tzy, R.L., Chien, C.L., Hao, C.K., Shing, C.W., Tien, C.L.: Ultrastrong mode confinement in ZnO surface plasmon nanolasers. ACS Nano **9**(4), 3978–3983
18. Alenezi, M.R., Alshammari, A.S., Alzanki, T.H., Jarowski, P., Henley, S.J., Ravi, S., Silva, P.: ZnO nanodisk based UV detectors with printed electrodes. Langmuir **30**(13), 3913–3921 (2014)
19. Li, F., Gong, F., Xiao, Y., Zhang, A., Zhao, J., Fang, S., Jia, D.: ZnO twin-spheres exposed in (001) facets: stepwise self-assembly growth and anisotropic blue emission. Acsnano **7**(12), 10482–10491 (2013)
20. Alenezi, M.R., Henley, S.J., Emerson, N.G., Ravi, S., Silva, P.: From 1D and 2D ZnO nanostructures to 3D hierarchical structures with enhanced gas sensing properties
21. Baraneedharan, P., Siva, C., Nehru, K., Sivakumar, M.: Investigations on structural, optical and electrochemical properties of blue luminescence SnO_2 nanoparticles. J. Mater. Sci.: Mater. Electron. **25**, 255–261 (2014)
22. Naveed ul, H.A.: Linköping studies in science and technology. Dissertation No. 1378 luminescence properties of ZnO nanostructures and their implementation as white light emitting diodes (LEDs) by ISBN: 978-91-7393-139-7
23. Zeng, H., Duan, G., Li, Y., Yang, S., Xu, X., Cai, W.: Blue luminescence of ZnO nanoparticles based on non-equilibrium processes: defect origins and emission controls. Adv. Funct. Mater. **20**, 561–572 (2010)
24. Cao, B., Teng, X., Heo, S.H., Li, Y., Cho, S.O., Li, G., Cai, W.: Different ZnO nanostructures fabricated by a seed-layer assisted electrochemical route and their photoluminescence and field emission properties. J. Phys. Chem. C **111**(6), 2470–2476 (2007)
25. Monticone, S., Tufeu, R., Kanaev, A.V.: Complex nature of the UV and visible fluorescence of colloidal ZnO nanoparticles. J. Phys. Chem. B **102**, 2854–2862 (1998)

Part III
Quantum Dots

Electromagnetically Induced Transparency in a Group III–V Nano-well for Terahertz Applications

J. Jayarubi, A. John Peter and H. Belmabrouk

Abstract In the present work, employing effective mass approximation, the potential energy band profile for the conduction band and valence bands is studied in a $Ga_{1-x}Al_xN/GaN/Ga_{1-x}Al_xN$ (x = 0.2) and the free electron distribution is found. The self-consistent method is employed to obtain the energy eigenvalue and wavefunctions of charge carriers. The confined energies with the geometrical confinement are computed. The electron and hole potentials are computed from the Poisson equation. The effects of dielectric mismatch between the inner and the outer materials are inserted in the potential terms. The internal polarizations which are the addition of spontaneous and piezo electric polarization are included in the Hamiltonian. The transmission probability which is the ratio between the transmitted flux and incident flux is computed for a fixed quantum well. J-V characteristics are computed using the transfer matrix method. The current density with the applied voltage is computed for fixed Al concentration in the barrier material.

1 Introduction

The phenomenon of electromagnetically induced transparency for the terahertz emission is given quite an attention in the theoretical and experimental aspects for the past few years. Electromagnetically induced transparency can be applied in the information technology, optical communications, quantum computing, quantum information processing and storage of data. In general, two level system is employed as the basic unit for storing information. Solid state devices need selfassembled quantum dots which carry a large number of qubits. Quantum interference related to the intersubband optical transition in superlattices has been

J. Jayarubi · A. John Peter (✉)
Department of Physics, Government Arts College, Melur, Madurai 625106, India
e-mail: a.john.peter@gmail.com

H. Belmabrouk
Laboratoire d'Electronique et Microélectronique, Faculté des Sciences de Monastir, Université de Monastir, 5019 Monastir, Tunisia

J. Ebenezar (ed.), *Recent Trends in Materials Science and Applications*,
Springer Proceedings in Physics 189, DOI 10.1007/978-3-319-44890-9_30

attracted much for the past few years. Electromagnetically induced transparency has many applications in the quantum information technology, optical communications, quantum computing and quantum information processing. Quantum interference related to the intersubband optical transition in superlattices has been attracted much for the past few years and eventually, the optically thick medium becomes transparent [1]. Polaritons are generated when the light is illuminated with the matter. The charged particles are induced with the incoming photon producing polaritons which are the coupling between the host long wavelength optical phonons and the photons. The charges with the background dielectric medium forming oscillating electric diploes produce polarization. The nonlinear optical properties are considered to be important when it suffers larger amplitude. The studied quantum heterostructures, will have a lot of potential applications in heterojunction lasers, optical fibers, photonics and photodetectors [2]. Thus, the electromagnetically induced transparency in metamaterials promises important applications in optical networks and terahertz communications. Nitride based UV and visible LEDs and LDs with the higher quantum efficiencies have been carried out earlier [3, 4].

The present paper is devoted to investigating the current density as a function of voltage in a group III-nitride wide gap semiconductor quantum well. The problem involves employing single band effective mass approximation. The potential energy band profile for the conduction band and valence bands is carried out in the $Ga_{1-x}Al_xN/GaN/Ga_{1-x}Al_xN$ (x = 0.2) heterostructure. The free electron distribution is obtained. The self-consistent method is used to get the respective energy eigenvalue and wavefunctions of charge carriers. The confined energies in the quantum well are obtained with the consideration of spatial confinement. The electron and hole potentials are computed using Poisson equation. The effects of dielectric mismatch between the inner and the outer materials are inserted in the potential terms. The Hamiltonian includes the spontaneous and piezoelectric polarizations which are applied at the heterostructure of the interface between inner and outer materials. The transmission probability which is the ratio between the transmitted flux and incident flux is found. The current density, J-V characteristics are calculated using the transfer matrix method. The second section is devoted to the theoretical aspect of our computations and the third section brings out the obtained results of the present model. The main conclusion is given in the last section.

2 Theoretical Model and Calculation

The transmission of electrons with the initial wave vector $\vec{k} = (\vec{k}_{||}, k_z)$ through a $Ga_{1-x}Al_xN/GaN/Ga_{1-x}Al_xN$ quantum well is considered. Here $k_{||}$ is the wave vector in the plane of the interfaces between the inner and outer materials. k_z is the wave vector which is considered to be normal to the barrier showing the transmission

direction. The Hamiltonian describing the electron motion in each layer of the heterostructure, in a Ga_{1-x} $Al_xN/GaN/Ga_{1-x}Al_xN$ quantum well, is given by

$$\widehat{H}\psi(z) = -\frac{\hbar^2}{2}\frac{d}{dz}\left[\frac{1}{m_e^*(z)}\frac{d\psi_n(z)}{dz}\right] + V(z)\psi_n(z) \tag{1}$$

where $m_e^*(z)$ is the effective mass of the electron of the system, $\psi_n(z)$ is its envelope function. $V(z)$ is the confined potential as given

$$V(z) = \begin{cases} 0 & |z| < L_w \\ eF_wL_w + eF_b(z - L_w) + V_0 & |z| \geq L_w \end{cases} \tag{2}$$

where e is the absolute value of the electron charge. The barrier height, V_0, is given as

$$V_0 = Q_c\Delta E_g \tag{3}$$

where Q_c is the conduction band offset parameter and the ΔE_g is the band gap difference between inner and outer barrier materials. The distribution between the conduction band and valence band is taken as 70:30. The $F_w(F_b)$ are the internal electric fields given by [5]

$$F_{well} = \frac{P_{SP(GaAlN)} - P_{SP(GaN)} - P_{PE(GaN)}}{\varepsilon_0\left(\varepsilon_w + \varepsilon_B\frac{L_W}{2L_B}\right)} \tag{4}$$

$$F_{well} = \frac{P_{SP(GaN)} + P_{PE(GaN)} - P_{SP(GaAlN)}}{\varepsilon_0\left(\varepsilon_B + 2\varepsilon_W\frac{L_W}{L_B}\right)} \tag{5}$$

where ε_0 is the free space dielectric constant. Here, $\varepsilon_W(\varepsilon_B)$ are the relative dielectric constants of the quantum well and the barrier materials, $P_{SP(GaN)}$ and $P_{PZ(GaAlN)}$ are the spontaneous polarizations and piezoelectric polarizations of the inner quantum well material respectively and $P_{SP(GaAlN)}$ is the spontaneous polarization of the barrier material. Generally, the polarity of the crystal and the strains of the semiconductor heter-nanostructure decides the all the strain elements. Since the wurtzite crystal structure of GaN and AlN lack inversion symmetry, which has been taken in this problem, the heterostructure consists of both spontaneous polarization (P_{SP}) and the piezo-electric polarization (P_{PZ}) due to strain caused by the lattice mismatch between GaN and AlN semiconducting materials.

The relations for polarization are obtained by [6]

$$P_{SP(Ga_{1-x}Al_xN)} = -0.090 - 0.034(1 - x) + 0.021x(1 - x) \tag{6}$$

and

$$P_{PE} = 2\frac{a_{AlGaN} - a_{GaN}}{a_{GaN}}\left(e_{31} - e_{33}\frac{C_{13}}{C_{33}}\right) \tag{7}$$

where e_{ij} are the piezoelectric constants and a_{AlGaN} a_{GaN} are the lattice constants of $Ga_{1-x}Al_xN$ and GaN semiconductors.

$$\psi_j(z_j) = A_j e^{ikz} + B_j e^{-ikz} \tag{8}$$

where A_j and B_j are the transmitted and reflected amplitude, j is the each interface of the heterostructure and $k = \sqrt{\frac{2m_e^*(E-V_0)}{\hbar^2}}$ is the wave vector. The normalization constants A and B are obtained by matching the wave functions and its derivatives at the interface. And hence, the envelope function coefficients can be obtained by the transfer matrix relations as

$$\begin{pmatrix} a_{j+1} \\ b_{j+1} \end{pmatrix} = M_j \begin{pmatrix} a_j \\ b_j \end{pmatrix}. \tag{9}$$

where the matrix elements, M_j, can be written as

$$M_j = \frac{1}{\Theta_j}\begin{pmatrix} \Lambda_{j+}^{-} & \Lambda_{j+}^{+} \\ \Lambda_{j-}^{-} & \Lambda_{j-}^{+} \end{pmatrix} with \quad \Theta_j = \Theta_j^{+} - \Theta_j^{-} \tag{10}$$

where $\Theta_j^{\pm} = \left\{\frac{d}{dz}\ln\left[\psi_j^{\pm}(z)\right]\right\}_{z=z_j} - \frac{2m_j^*(E)k_{\|}\left[\beta_{j+1}(E)-\beta_j(E)\right]}{\hbar^2}$

where $\beta_j(E) = \frac{P_j^2}{2}\left(\frac{1}{E-E_{cj}+E_g} - \frac{1}{E-E_{cj}+E_g+\Delta}\right)$ with P being the Kane energy of the system, E_{cj} is the conduction band edge, E_g is the band gap of GaN,

$$\Lambda_{j+}^{\pm} = \left(\frac{m_j^*(E)}{m_{j+1}^*(E)}\left\{\frac{d}{dz}\ln\left[\phi_{j+1}^{\mp}(z)\right]\right\}_{z=z_j} - \Omega_j^{-}\right)\frac{\phi_{j+1}^{\mp}(z)}{\phi_j^{+}(z)}$$

and

$$\Lambda_{j-}^{\pm} = \left(\frac{m_j^*(E)}{m_{j+1}^*(E)}\left\{\frac{d}{dz}\ln\left[\phi_{j+1}^{\mp}(z)\right]\right\}_{z=z_j} - \Omega_j^{+}\right)\frac{\phi_{j+1}^{\mp}(z)}{\phi_j^{-}(z)} \tag{11}$$

Thus, the total transfer matrix, after computing each interface in the heterostructure of the $Ga_{0.8}$ $Al_{0.2}N/GaN/Ga_{0.8}$ $Al_{0.2}N$ quantum well, can be written as

$$M = \prod_{j=1}^{3} M^j \tag{12}$$

The tunneling probability which is the ratio between the transmitted flux and the incident flux is given by

$$T(E_z, k_{||}) = \frac{m_1^*(E_z, k_{||})k_3(E_z, k_{||})}{m_3^*(E_z, k_{||})k_1(E_z, k_{||})}\left|\frac{a_3}{a_1}\right|^2 \tag{13}$$

And the current density is expressed as the applied voltage and it is given by [1]

$$J(V) = em_e^* k_B T/2\pi^2\hbar^3 \int_0^\infty T(E_z, k_{||}) Ln\left(\frac{1+e^{(E_F-E)/k_BT}}{1+e^{(E_F-E-eV)/k_BT}}\right) dE \tag{14}$$

where V is the applied voltage and other parameters are universal constants.

3 Results and Discussion

Numerical computations on the confined energies and the transmission probability $T(E_z, k_{||})$ are performed in a strained hetero-structures of a $Ga_{0.8}$ $Al_{0.2}N$/GaN/$Ga_{0.8}$ $Al_{0.2}N$ quantum well, with fixed $k_{||} = 2 \times 10^8 m^{-1}$.

In Fig. 1, we show that J-V characteristics in a strained hetero-structures in a $Ga_{0.8}$ $Al_{0.2}N$/GaN/$Ga_{0.8}$ $Al_{0.2}N$ quantum well for a constant well width, 30 Å. The current densities are found to be between 10×10^2 A/cm^2 and 7×10^2 A/cm^2. The peak of current density (513 A/cm^2) is observed at 1.95 V. It is observed that

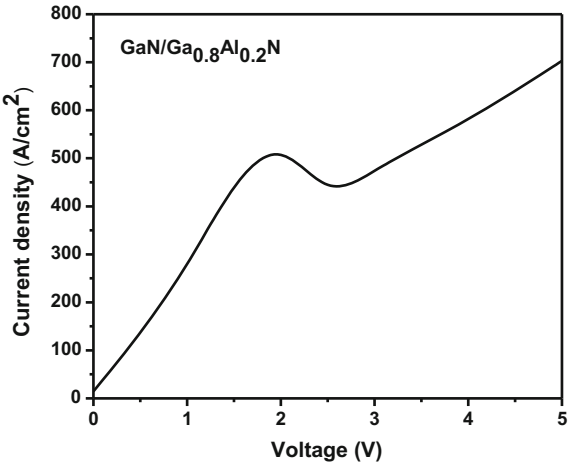

Fig. 1 J-V characteristics as a function of applied voltage in a strained hetero-structures in a $Ga_{0.8}$ $Al_{0.2}N$/GaN/$Ga_{0.8}$ $Al_{0.2}N$ quantum well

the current density increases with the application of voltage and a hump are observed at 2 V. The current density immediately decreases with the increase in the voltage and starts increasing it. It is clear from the observation that the geometrical confinement effects affect the J-V characteristics [7].

4 Conclusion

Within the single band employing effective mass approximation, the conduction band potential has been studied in a nitride based wide band gap semiconducting quantum well. The energy eigenvalues and wavefunctions of charge carriers have been obtained using self-consistent formulism. The self-energies have been found taking into account the geometrical confinement effect. The electron and hole potentials have been obtained from the Poisson equation. The effects of dielectric mismatch between the inner and the outer materials have been included in the potential terms. The internal polarizations which are the combinations of spontaneous and piezoelectric polarizations have been included in the Hamiltonian. The transmission probability has been found for a fixed quantum well. J-V characteristics have been computed using the transfer matrix method. The current density with the applied voltage has been carried out for fixed Al concentration in the barrier material. The electromagnetically induced transparency can be applied to varieties of currently active fields like nonlinear optics, quantum optics and information storing devices. The transparency in optically thick medium, allowing four-wave mixing, creating changes in the refractive index properties are some major applications of electromagnetically induced transparency. The outcomes will be helpful for the optical devices utilizing the J-V characteristics also it is the propagation of the electromagnetic radiation in the polaritonic band gap in any semiconductor and it can be applied to terahertz emission in the optical communication. We believe that the results will be helpful for high current density characteristics for high-efficiency solid-state light emitting devices employing nitride based wide band gap semiconducting materials in future.

References

1. Rached, A., Bhouri, A., Sakr, S., Lazzari, J.-L., Belmabrouk, H.: Superlatt. Microstruct. **91**, 37 (2016)
2. Sher, A.: Lasers Without Inversion and Electromagnetically Induced Transparency. SPIE Press, Bellingham (1999)
3. Zhang, J., et al.: Appl. Phys. Lett. **77**, 2668 (2000)
4. Guo, X., Li, Y.-L., Schubert, E.F.: Appl. Phys. Lett. **79**, 1936 (2001)
5. Galczak, J., Sarzala, R.P., Nakwaski, W.: Opto. Electr. Rev. **2**(4), 369 (2004)
6. Ambacher, O., et al.: J. Phys. Cond. Matter. **14**, 3399 (2001)
7. Zhao, H., Liu, G., Zhang, J., Arif, R.A., Tansu, N.: J. Display Tech. **9**(4), 212 (2013)

Optical Transition Energies in a Group III–V–N Nano-dot

P. Uma Mageshwari, A. John Peter and C.A. Duque

Abstract Group III–V–N materials especially GaInNAs semiconductors are significantly attracted much attention due to its potential applications in lasers and solar cells. GaInAs is lattice matched with GaAs and Ge substrate by altering the host composition for obtaining band gap of the material. In the present paper, the electronic properties are brought out in a $Ga_{1-x}In_xN_yAs_{1-y}$/GaAs quantum dot taking into account the strain effects which are involved in the heterostructure at the interface between the materials. Binding energies are obtained for the ground state and first excited states taking into consideration of quantum confinement effect. Optical transition energies are found for the two level system in the nitride nano-dot. These properties are more influenced in the strong confinement region whereas the effect shows the less impact when the dot size becomes larger. The incorporation of impurities (nitrogen) in the GaInNAs semiconducting material will drastically change its electronic properties considerably.

1 Introduction

Quantum dots having different compounds are found to have interesting properties which can be applied for the improvements in fabricating solid state lasers and single photon emitters. Single quantum dot is considered to be an artificial atom, it has discrete energies which result the enhanced opto-electronic properties. Quaternary semiconducting materials are given quite attention for manufacturing semiconductor lasers in fibre communication for optical telecommunication networks since the loss is minimized if the emission wavelength range lies between 1.33 and 1.55 μm [1]. The band gap of $Ga_xIn_{1-x}N_{1-y}As_{1-y}$ is altered due to the

P. Uma Mageshwari · A. John Peter (✉)
Department of Physics, Government Arts College, Melur, Madurai 625 106, India
e-mail: a.john.peter@gmail.com

C.A. Duque
Grupo de Materia Condensada-UdeA, Instituto de Física, Facultad de Ciencias Exactas y Naturales, Universidad de Antioquia UdeA, Calle 70 no. 52-21, Medellín, Colombia

J. Ebenezar (ed.), *Recent Trends in Materials Science and Applications*,
Springer Proceedings in Physics 189, DOI 10.1007/978-3-319-44890-9_31

addition of small amount of nitrogen content and this property ensures the desired properties of fabricating novel materials which are the base for band gap engineering capabilities for III–V compound devices. Optical devices have the minimum telecommunication fibre losses and dispersion and the controllable geometrical confinement effects are desirable to have the maximum efficiency. The second section explains briefly the theoretical aspect of the computations and the third section gives the obtained results of the present model. The main conclusion is narrated in the last section.

2 Theoretical Formulism

The present system is taken as cylindrical quantum dot. The $Ga_{1-x}In_xN_yAs_{1-y}$ is taken as the outer material and GaAs material is taken as outer material of the dot. Within the framework of single band effective mass approximation, the Hamiltonian of the exciton in a GaInNAs/GaAs quantum dot with the inclusion of strain effect is obtained as

$$H_{exc} = \sum_j \left[-\frac{\hbar^2}{2} \frac{\partial}{\partial z_j} \frac{1}{m_j(z_j)} \frac{\partial}{\partial z_j} + V_j(\rho_j, z_j) \right] - \frac{\hbar^2}{2\mu} \frac{1}{\rho} \frac{\partial}{\partial \rho} \rho \frac{\partial}{\partial \rho} - \frac{e^2}{\varepsilon |r_e - r_h|} \tag{1}$$

where $j = e$ and h refers an electron and a hole respectively, μ is the reduced mass, ε is the dielectric constant for the material inside the quantum dot and $V_j(\rho_j, z_j)$ is the strain induced confinement potential of the particle j. The strain effects are included with the barrier confinement potential in the calculations. The lattice constant of the inner material of the dot, $Ga_{1-x}In_xN_yAs_{1-y}$ structure is decided by the general relation known as Vegard's law and it is given as

$$\begin{aligned} a(x,y) = {} & (1-x)(1-y)\, a(\mathrm{GaAs}) + x(1-y)\, a(\mathrm{InAs}) \\ & + y(1-x)\, a(\mathrm{GaN}) + xy\, a(\mathrm{InN}). \end{aligned} \tag{2}$$

The strained band gap between the heavy hole and the electron is expressed by [2]

$$E_{e-hh}(x,y) = E_g(x,y) + \delta E_c(x,y) - \delta E_{hh}(x,y). \tag{3}$$

The electron effective mass in the present system is taken as

$$m_j^* = \begin{cases} m_I^* & -L/2 \le z_j \le L/2 \\ m_{II}^* & |z_j| > L/2 \end{cases} \tag{4}$$

where m_I^* and m_{II}^* refer the effective masses of the inside and outside the quantum dot.

For the variational calculations, the trial wave function is chosen as

$$\psi_{exc}(\bar{r}_e;\bar{r}_h) = Nf(\rho_e)h(z_e)f(\rho_h)h(z_h)\exp(-\alpha\rho_{eh}^2 - \beta z_{eh}^2) \tag{5}$$

where N is the normalization constant, the wave functions $f(\rho_j)$ denotes the motion of the charge carrier in the in-plane direction and $h(z_j)$ refers the motion of the electron (hole) in z-direction. They are the solutions of lowest binding energy of Schrödinger equation for the charge carriers. The above trial wave function is employed with the two variational parameters α and β, the former variational parameter is related to in-plane correlation and the latter is for the relative motion in the z-direction. Thus, it is well known that these two variational parameters are the accountable of anisotropy of cylindrical nature of the quantum dots. And hence, it is hoped that this type of Gaussian wave function is more appropriate in the strong confinement region. A two parameter variational Gaussian wave function is used to calculate the energy eigen values considering the correlation of the electron-hole relative motion. The ground state energies with the geometrical confinement effect is obtained by finding out the expectation value of the energy of the Hamiltonian, (1), as

$$\langle E_{exc}\rangle = \min_{\alpha,\beta} \frac{\langle \psi_{r_e}|H_{exc}|\psi_{r_e}\rangle}{\langle \psi_{r_e}|\psi_{r_e}\rangle} \tag{6}$$

The exciton binding energy in a $Ga_{1-x}In_xN_yAs_{1-y}$/GaAs quantum dot, is given by

$$E_b = E_e + E_h - E_{exc} \tag{7}$$

and the interband emission energy associated with the exciton in the present problem is expressed as

$$E_{ph} = E_e + E_h + E_g - E_{exc} \tag{8}$$

where E_e and E_h are the confinement energies of electron and hole respectively. E_g is the band gap energy of GaInNAs material.

3 Results and Discussion

The electronic property is obtained in a $Ga_{1-x}In_xN_yAs_{1-y}$/GaAs quantum dot numerically. The variational method is employed to obtain the binding energy of the exciton and the interband emission energy related to the electron-hole pair. The effects of strain contribution from the spontaneous polarization and the piezoelectric polarization, the geometrical confinement are inserted in the Hamiltonian in order to obtain the above properties. The units of length and energy used throughout are the

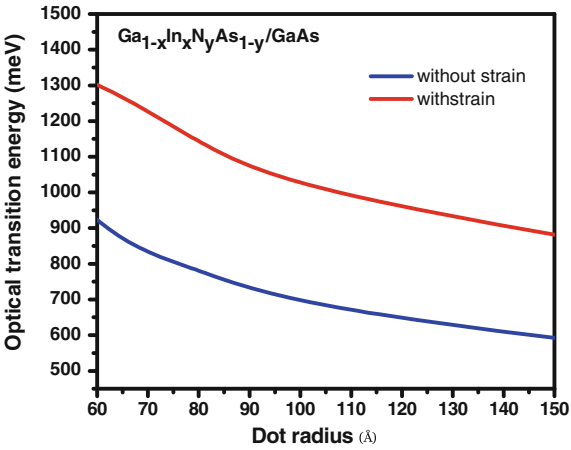

Fig. 1 Variation of optical transition energy with the dot radius with and without the inclusion of strain effect in a $Ga_xIn_{1-x}N_{1-y}As_{1-y}$ quantum dot

effective Bohr radius $R* = \hbar^2\varepsilon/m*e^2$ and the effective Rydberg $R_y^* = m*e^4/2\varepsilon^2\hbar^2$ where ε is the dielectric constant and m* is the effective mass of electron in the conduction band minimum of the inner material.

Figure 1 Variation of optical transition energy with the dot radius with and without the inclusion of strain effect in a $Ga_xIn_{1-x}N_{1-y}As_{1-y}$ quantum dot. It is observed that the optical transition energy reduces monotonically as the dot radius is increased in both the cases of with and without the inclusion of strain effects. The enhancement of interband emission energies with the reduction of dot size is due to the quantum confinement of electron-hole with respect to z-plane [3]. It is obviously shown that the effects of exciton has influence on the interband emission energy. This illustration clearly conveys the quantum size effect. The interband emission energy becomes less for all the dot size with the inclusion of strain effects in the Hamiltonian in the present calculations. The difference of optical transition energy, 380 meV, is observed at 60 Å quantum dot whereas 345 meV is observed for 90 Å. The increase of 35 meV optical transition energy is obtained for the increase of 30 Å. It is also observed that the desired wavelength, 1.50 μm is observed for the dot size 80 Å for the N alloy content, 0.0554. Our results are in good agreement with the earlier investigation [4].

4 Conclusion

The exciton binding energies and thereby optical transition energies have been obtained in a $Ga_{1-x}In_xN_yAs_{1-y}/GaAs$ quantum dot taking into account the spatial confinement effect. The effects of stain involving at the interface between the materials in the heterostructure have been found. The results show that the obtained electronic properties show enhanced properties in the strong confinement region

whereas these properties are considered to be effect in the weak confinement region. Further, the incorporation of nitrogen in the $Ga_{1-x}In_xN_yAs_{1-y}$ material will subtaincially alters its electronic properties. The obtained result will be useful for fabricating optical devices in the mid-infrared optical fiber system.

References

1. Kapon, K.: Semiconductor Lasers I & II. Academic Press, New York (1999)
2. Sangeetha, R., et al.: Canadian. J Phys. **92**, 1 (2014)
3. Li, X.D., Chen, T.P., Liu, P., Liu, Y., Leong, K.C.: Opt. Express **21**, 14131 (2013)
4. Aissat, A., et al.: 1st WSEAS International Conference on Computational Chemistry, Cairo, Egypt, p. 115 (2007)

Synthesis, Structural, Optical, Morphological and Elemental Characterization of CTAB Capped CdS Quantum Dots by Facile Chemical Precipitation Technique

S. Muniyappan, V.M. Arivunithi, T. Solaiyammal, K. Sudhakar, R. Roop Kumar and P. Murugakoothan

Abstract In the present work, we report synthesis of CTAB capped cadmium sulphide quantum dots (CdS QDs) employing facile chemical precipitation technique in non aqueous medium at room temperature. Cadmium nitrate tetra hydrate and sodium sulphide flakes and cetyltrimethyl ammonium bromide (CTAB) was used as a precursors and capping agent respectively. The Powder X-Ray Diffraction (PXRD) confirms the hexagonal wurtzite structure and Field Emission Scanning Electron Microscopy (FESEM) shows the nanocrystalline nature. FESEM images showed a distribution of spherical particles with the diameter of 5.6–7.8 nm with the mean diameter of 7.1 nm. The change in band gap with size-quantization was investigated by reflectance UV spectroscopy. The functional groups were analyzed by the Fourier Transform Infrared Spectroscopy (FTIR) and elemental composition of the synthesized sample was determined by the EDX analysis.

1 Introduction

Nanomaterials have drawn interests and attention due to their special characteristics that differ from that of the bulk properties of solids and molecules. Since novel properties of nanomaterials depends on their size, structure and shape may provide a new direction for synthesis methods in nanoscience [1]. Nanocrystals of quantum dots (QDs) with dimensions smaller than the bulk excitonic Bohr radius exhibit unique size quantization effects and strongly size dependent electrical, optical,

S. Muniyappan · V.M. Arivunithi · T. Solaiyammal · K. Sudhakar · P. Murugakoothan (✉)
Department of Physics, Pachaiyappa's College, Chennai, India
e-mail: murugakoothan03@yahoo.co.in

R. Roop Kumar
Birla Institute of Technology and Science, Dubai Campus,
Dubai International Academic City, Dubai, United Arab Emirates

J. Ebenezar (ed.), *Recent Trends in Materials Science and Applications*,
Springer Proceedings in Physics 189, DOI 10.1007/978-3-319-44890-9_32

magnetical and electrochemical properties [2]. The fabrication of quantum dots (QDs) having sizes less than 6 nm is currently of interest because of their unique optical and electronic properties [3]. Quantum dots of group II–VI semiconductors have attracted special attention, because they are easy to synthesize in the size range required for quantum confinement [4]. Quantum confinement effect modifies the electronic density of states of the nanocrystals when the sizes of the nanoparticles are comparable to that of the excitonic Bohr radius of those materials. When the particle radius lies below the excitonic Bohr radius, the band gap energy is widened, leading to a blue shift in the band gap, emission spectra etc. In the case of semiconductor nanoparticles, radiative or nonradiative excitonic recombination at the surface states becomes dominant in its optical properties with a decrease of particle size. Hence, the decay of an exciton at the surface states will affect the qualities of the material for optoelectronic devices. These size-dependent optical properties have many potential applications in the areas of solar energy conversion, LEDs, chemical or biological sensors, and photocatalysis. Wide band gap II–VI semiconductors are expected to be the novel materials for the optoelectronic devices [5]. Nanocrystalline CdS, CdTe, CdSe and ZnSe have been synthesized by a variety of methods including precipitation, sputtering, electrochemical deposition and inverse micelles. A reduction in the particle size strongly influences the crystallinity, melting point and structural stability [4].

Among above semiconductors, cadmium sulphide (CdS) is the most promising material for absorbing visible radiation because of its primary band gap of 2.42 eV [6]. Generally, in the case of direct band gap semiconductors, electron can shift from the lowest-energy state in the conduction band to the highest-energy state in the valence band by emitting photon without change in the crystal momentum but it is not so in indirect band gap semiconductors. In this respect, direct band gap semiconductors are highly meant for optoelectronic device applications. CdS also belong to the category of direct band gap II–VI semiconductor in which it can be used for optoelectronic device applications [7].

In this scenario, CdS is an important semiconductor material, owing to its unique electronic, optical properties and thus its wide range of potential applications, such as in bio-imaging, photocatalysis and so on [8]. Within this vision, synthesis and structural characterization of CdS quantum dots was selected to be the topic of study of the present research work.

2 Experimental

2.1 Synthesis

CdS quantum dots were prepared through facile chemical precipitation technique using non-aqueous medium. Typically, 3.72 g cadmium nitrate ($Cd(NO_3)_2{\cdot}4H_2O$) {Merck, 99 %} and 0.7 g of cetyltrimethyl ammonium bromide (CTAB) {Himedia,

99 %} were dissolved in 30 ml methanol while stirring at ambient temperature (~27 °C). In another container, 0.9 g of sodium sulphide (Na_2S) {Himedia, 99 %} was dissolved in 30 ml of methanol; then, it was added to the former solution under stirring. Once the reaction took place, the precipitate was directly centrifuged and subsequently washed several times (5–10 times) with double-distilled water and ethanol, and left in a dark environment for complete dryness. After that, the dried sample was annealed at 200 °C for 2 h. Finally, the annealed sample was subjected to various characterizations.

2.2 Characterization Studies

The Powder X-Ray Diffraction (PXRD) profile was analyzed using ISO DEBYEFLEX 2000 diffractometer employing Cu Kα (λ = 1.5406 Å) radiation. The UV-vis-NIR reflectance spectrum was recorded in the wavelength range from 190 to 900 nm in the diffuse reflectance spectrum (DRS) mode using LABINDIA Model UV 3092 spectrophotometer. The Shimadzu FT-IR instrument with a 1.0 cm^{-1} resolution was used to identify the functional groups present in the samples. Field emission scanning electron microscopy (FESEM) along with Energy Dispersive X-ray spectroscopy (EDX) were used to investigate the morphology and composition of prepared products using ZEISS ultra™ 55 note field emission scanning electron microscope.

3 Results and Discussion

3.1 Powder XRD Analysis

The Powder X-ray diffraction pattern of synthesized CdS sample after calcination at 200 °C is shown in Fig. 1. The nanocrystalline hexagonal wurtzite structure of cadmium sulphide is confirmed by the presence of (101) plane peak appeared at 2θ = 28.1° [Ref. ICCD Card no. 41-1049]. The broadened characteristic diffraction peak indicates the smaller size of the CdS nanoparticles. The crystalline size was obtained using Scherrer's formula as follows [9],

$$D = 0.94\,\lambda/\beta\,\cos(\theta) \tag{1}$$

where D is the particle diameter, 0.94 is the shape factor (in case of spherical particles), β is the full-width-at-half-maximum (FWHM) of the diffraction peak, λ is the wavelength (1.5406 Å) of the X-ray radiation and θ is the angle of diffraction. The crystallite size of CdS quantum dots was determined by Scherrer's relation and is found to be approximately 2.8 nm.

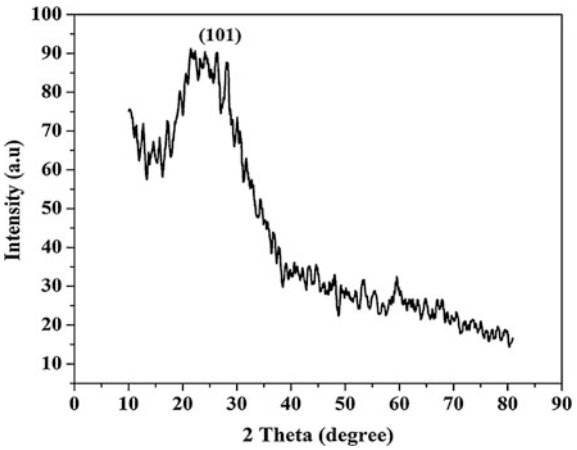

Fig. 1 Powder XRD spectrum of CTAB capped CdS quantum dots

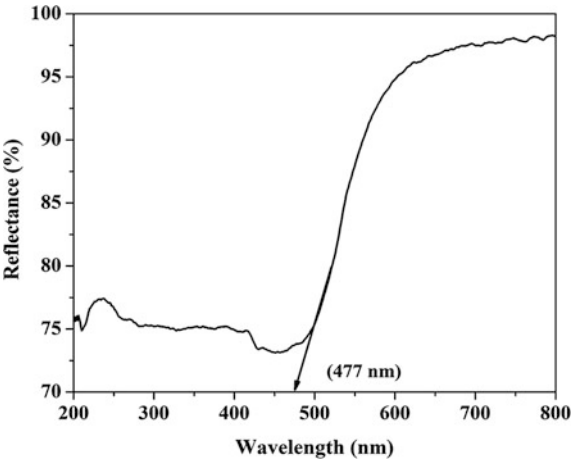

Fig. 2 UV-vis-NIR reflectance spectrum of CTAB capped CdS quantum dots

3.2 UV-Reflectance Studies

UV-vis-NIR reflectance spectrum of CTAB capped CdS quantum dots is shown in Fig. 2. The size dependent optical properties of nanoparticles provide a very convenient and useful way to monitor their formation. The peaks at higher energy than the absorption edge of bulk CdS indicate quantum confinement effects in nanoparticles [10]. The band gap energy can be calculated by the relation, $E_g = 1239.8/\lambda$ eV (λ in nm) [11]. The absorption edge for the synthesized CdS quantum dots is found at 477 nm corresponds to a band gap of 2.59 eV, which is blue shifted from the bulk band gap of CdS 2.42 eV (515 nm) [12]. It is clearly seen from the spectrum that the absorption edge shifts towards lower wavelength leads to blue shift in the absorption edge of the synthesized CdS quantum dots.

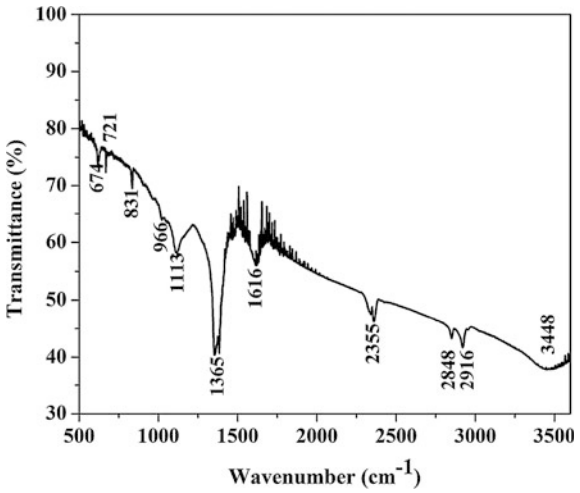

Fig. 3 FTIR spectrum of CTAB capped CdS quantum dots

In contrast to the bulk CdS, nanoparticle shows conventional blue shift in the absorption edge which indicates that the synthesized material is in the nanoscale regime.

3.3 FTIR Spectral Analysis

The Fourier transform infrared (FTIR) spectrum of CTAB capped CdS quantum dots is shown in Fig. 3. The peaks emerged at 721 and 674 cm^{-1} have been assigned to CdS stretching bands. The broad absorption peak of the sample at 3448 cm^{-1} corresponds to hydroxyl (–OH) group, which indicate the existence of water adsorbed on the surface of nanocrystals [1]. The vibration at 966 cm^{-1} corresponds to the head group of trimethylammonium cation. The vibration at 2916 and 2848 cm^{-1} are due to the alkyl tail group [13]. Due to the interaction of a CTAB molecule with the CdS nanoparticles, the head group vibration shifts from 966 to 831 cm^{-1} [13]. The observations confirm the interaction of CTAB molecule with the CdS nanoparticles.

3.4 FESEM Analysis

Figure 4 gives the FESEM images of CTAB capped CdS quantum dots via facile chemical precipitation technique annealed at 200 °C. The images clearly show that the particles were almost dot like structure with better uniformity in size. In addition to that, the dots appear quite spherical in shape and conducive symmetry is

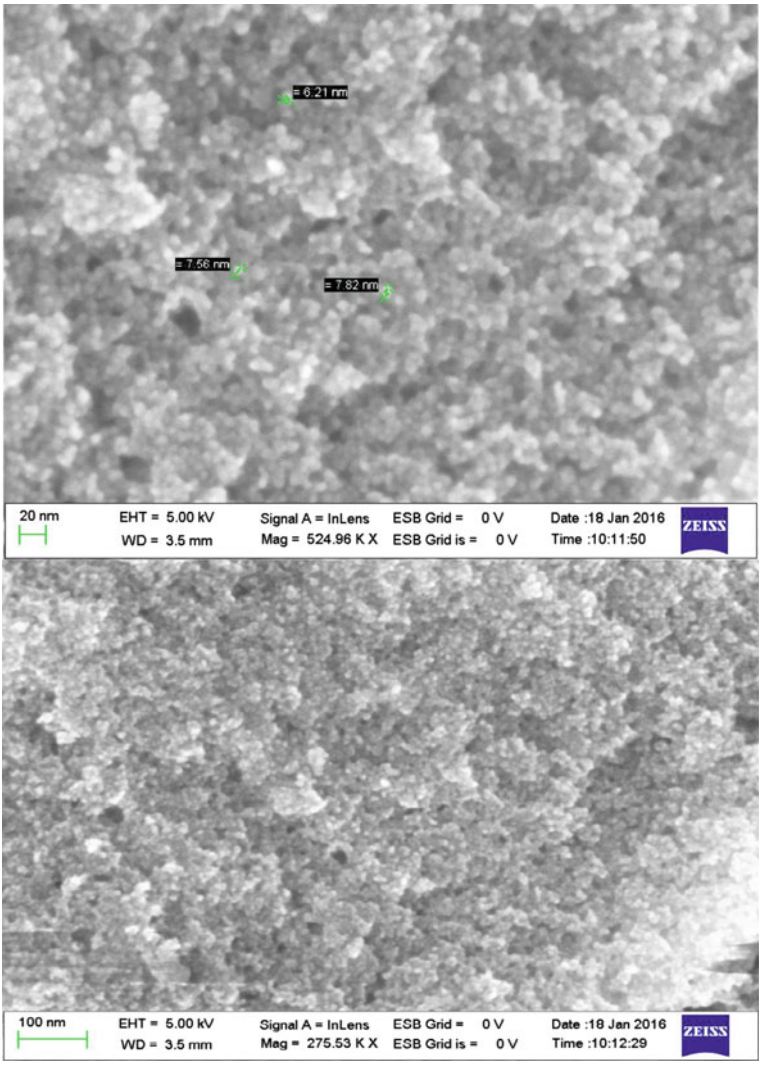

Fig. 4 FESEM images of the CTAB capped CdS quantum dots

maintained. The particle sizes are in the range of 6.2–7.8 nm with mean particle diameter of 7.1 nm. The nanoparticles were clearly well observed and no significant aggregation of bulk particles is formed, indicating effective capping of CTAB on the CdS nanoparticle surfaces. It is important to remember that the Scherrer's formula estimates the size of single-crystalline domains (having periodic lattice) but not the actual particle size of the same [14]. Hence regarding this work, it is expected that the particle size estimated from FESEM is appreciable rather than the XRD values.

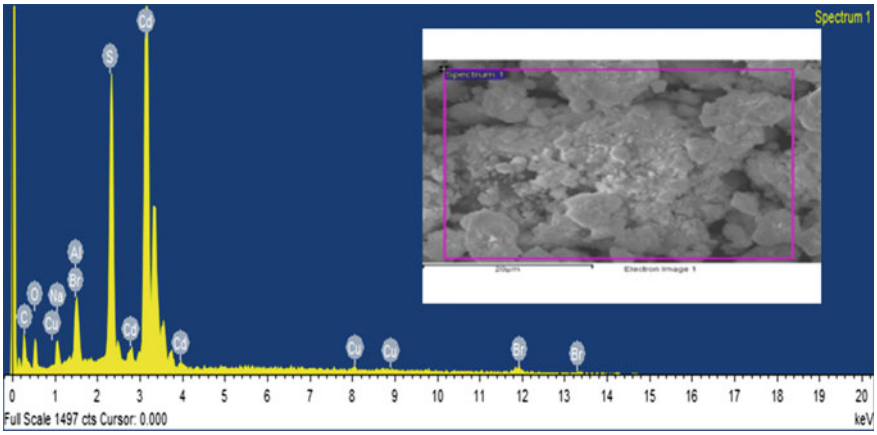

Fig. 5 EDX spectrum CTAB capped CdS quantum dots

3.5 EDX Analysis

The energy dispersive X-ray (EDX) spectrum of CTAB capped CdS quantum dots is given in Fig. 5. The spectrum has prominent peaks of Cd and S. From the peaks, it is confirmed that the quantum dots synthesized by facile chemical precipitation technique belongs to CdS having some impurities. The weight contributions are 54.862 and 12.64 % for cadmium and sulphur respectively. Both the elements together contribute 67.26 % of the total weight. The remaining percentage is attributed to the presence of capping agent.

4 Conclusion

In conclusion, CdS quantum dots were successfully synthesized by facile chemical precipitation technique. Powder XRD results reveals that CdS quantum dots have hexagonal wurtzite structure and crystallite size was found to be approximately 2.8 nm using Scherrer's equation. UV reflectance spectrum exhibits the blue shift of the synthesized nanoparticles and the band gap is found to be 2.59 eV. FTIR spectrum confirmed qualitatively the functional groups of CTAB capped CdS quantum dots. FESEM images clearly shows that the spherical like morphology of the material and the particle size is found to be approximately with the mean diameter of 7.1 nm. EDX spectrum tells about the elemental composition of the synthesized CdS quantum dots. Finally, this work opens up an easy way to synthesize the quantum dots and they can be promising agents for optoelectronic device applications.

References

1. Kotkata, M.F., Masoud, A.E., Mohamed, M.B., Mahmoud, E.A.: Synthesis and structural characterization of CdS nanoparticles. Physica E **41**, 1457–1465 (2009)
2. Myung, N., Ding, Z., Bard, A.J.: Electrogenerated chemiluminescence of CdSe nanocrystals. Nano Lett. **11**, 1315–1319 (2002)
3. Lin, Y.-W., Tseng, W.-L., Chang, H.-T.: Using a layer-by-layer assembly technique to fabricate multicolored-light-emitting films of CdSe, CdS and CdTe quantum dots. Adv. Mater. **18**, 1381–1386 (2006)
4. Banerjee, R., Jayakrishnan, R., Ayyub, P.: Effect of the size-induced structural transformation on the band gap in CdS nanoparticles. J. Phys.: Condens. Matter **12**, 10647–10654 (2000)
5. Rahdar, A.: Effect of 2-mercaptoethanol as capping agent on ZnS nanoparticles: structural and optical characterization. J. Nanostruct. Chem. **3**, 10 (2013)
6. Tyagi, C., Sharma, A., Kurchania, R.: Synthesis of Cds quantum dots using wet chemical co-precipitation method. J. Non-Oxide Glasses **6**, 23–26 (2014)
7. Pattabi, M., Amma, S.: B.: Synthesis and stability studies of thiophenol capped CdS nanoparticles. Sol. Energy Mater. Sol. Cells **90**, 2377–2383 (2006)
8. Sun, S.Q., Li, T.: Synthesis and characterization of CdS nanoparticles and nanorods via solvo-hydrothermal route. Cryst. Growth Des. **7**, 11 (2007)
9. Ananth, S., Vivek, P., Saravana Kumar, G., Murugakoothan, P.: Performance of Caesalpinia sappan heartwood extract as photo sensitizer for dye sensitized solar cells. Spectrochim. Acta Part A Mol. Biomol. Spectrosc. **137**, 345–350 (2015)
10. Saravanan, L., Pandurangan, A., Jayavel, R.: Synthesis of cobalt-doped cadmium sulphide nanocrystals and their optical and magnetic properties. J. Nanopart. Res. **13**, 1621–1628 (2011)
11. Ananth, S., Vivek, P., Arumanayagam, T., Murugakoothan, P.: Natural dye extract of lawsonia inermis seed as photo sensitizer for titanium dioxide based dye sensitized solar cells. Spectrochim. Acta Part A Mol. Biomol. Spectrosc. **128**, 420–426 (2014)
12. Aboulaich, A., Billaud, D., Abyan, M., Balan, L., Gaumet, J.-J., Medjadhi, G., Ghanbaja, J., Schneider, R.: One-pot noninjection route to CdS quantum dots via hydrothermal synthesis. ACS Appl. Mater. Interfaces **4**, 2561–2569 (2012)
13. Nisha, K.D., Navaneethan, M., Hayakawa, Y., Ponnusamy, S., Muthamizhchelvan, C.: Structural and morphological evolution of CdS nanosheets-based superstructures by surfactant assisted solvothermal method. Mater. Chem. Phys. **136**, 1038–1043 (2012)
14. Kalasad, M.N., Rabinal, M.K., Mulimani, B.G.: Ambient synthesis and characterization of high-quality cdse quantum dots by an aqueous route. Langmuir **25**(21), 12729–12735 (2009)

Part IV
Thin Film

Structural, Optical and Ethanol Gas Sensing Performance of Aluminium Doped Zinc Oxide (AZO) Thin Films by Nebulizer Spray Technique

C. Ravi Dhas, R. Venkatesh, A. Jennifer Christy, D. Arivukarasan, B. Anitha, D. David Kirubakaran, A. Juliat Josephine, P. Sudhagar, A. Moses Ezhil Raj and C. Sanjeeviraja

Abstract Aluminium doped zinc oxide (AZO) nano—structured films were deposited by nebulizer spray technique. The role of aluminium dopant concentration over the structural, optical and electrical properties was examined by different analytical techniques. The structural results from X-ray diffraction showed that preferential orientation of films obtained along the (002) direction. The surface morphology of the films showed a hexagonal facet with the nano—structured film. The parameters such as resistivity and activation energy were determined from electrical studies. The sensitivity of the films towards ethanol gas was investigated at room temperature.

C. Ravi Dhas (✉) · R. Venkatesh · A. Jennifer Christy · D. Arivukarasan
B. Anitha · D. David Kirubakaran
PG and Research Department of Physics, Bishop Heber College (Autonomous), Tiruchirappalli 620017, India
e-mail: ravidhasc@gmail.com

A. Juliat Josephine
Department of Physics, Holy Cross College, (Autonomous), Tiruchirappalli 620002, India

P. Sudhagar
School of Chemistry and Chemical Engineering, Queens University, Belfast, North Ireland BT9 5AG, UK

A. Moses Ezhil Raj
Department of Physics, Scott Christian College (Autonomous), Nagercoil 629001, India

C. Sanjeeviraja
Department of Physics, Alagappa Chettiar College of Engineering and Technology, Karaikudi 630003, India

J. Ebenezar (ed.), *Recent Trends in Materials Science and Applications*, Springer Proceedings in Physics 189, DOI 10.1007/978-3-319-44890-9_33

1 Introduction

Zinc Oxide thin film has dragged attention of most researchers owing to its attractive optical and electrical properties, being an abundant low cost material with high chemical and mechanical stability, when compared with existing transparent conductive oxide materials such as ITO and FTO [1]. The multifunctional Zinc Oxide material finds application in variety of fields such as chemi-resistive gas sensors [2], optoelectronic devices and solar cells [3], and Thin film transistors [4]. The preparation techniques are primarily adopted by DC & RF sputtering, sol-gel and spray pyrolysis [5–7]. In spray pyrolysis technique the properties of the films purely depends on parameters such as substrate temperature, molarity of the precursor solution, annealing treatment in vacuum or inert gas ambient, addition of dopants, spray rate, type and carrier gas flow and nozzle geometry of the spray system [8]. Device quality ZnO thin films can be achieved by simple and economical spray pyrolysis route. The *n*-type conductivity in ZnO is well—known to be originating from non-stochiometry and native crystal defects such as zinc interstitials and oxygen vacancies [9]. Enhancing the number of carriers in ZnO crystals can be achieved by an appropriate doping process [10]. Here in this work we have used Jet nebulizer spray rather than conventional spray pyrolysis technique because it offers fine atomic species to be evolved from the outlet of the nozzle which in turn provides nanostructure and high quality thin films.

The objective of the present work is to prepare AZO films by Jet Nebulizer spray technique. The doping concentration of aluminium was varied in the starting solution, to study the crystal structure, morphology, elemental composition, optical and photoluminescence behaviour of prepared AZO films. Ethanol sensing behaviour of the films was analysed for two different ppm levels of ethanol at room temperature.

2 Experimental

Aluminium doped zinc oxide thin films have been deposited on glass substrates by using Jet nebulizer spray technique under ambient conditions. A nebulizer is small machinery having the ability to change the precursor solution into mist. The specially designed jet nebulizer controls the size of the droplets and the rate of flow of solution, depending upon the geometry of the nebulizer and the carrier gas pressure. This is normally used in the medical field for treating asthma patients. An attempt has been made to modify this jet nebulizer as a spray gun for preparing thin films.

The modified jet nebulizer gun to prepare thin films is shown in Fig. 1. This consists of the following parts: a micro-pinhole air nozzle, specially prepared liquid sucking cone with a small hole and the outlet hole with proper diameter. These parts can be easily modified as far as the film preparation is concerned. Normally sprayed solution is kept at the bottom portion of the nebulizer. The carrier gas with constant

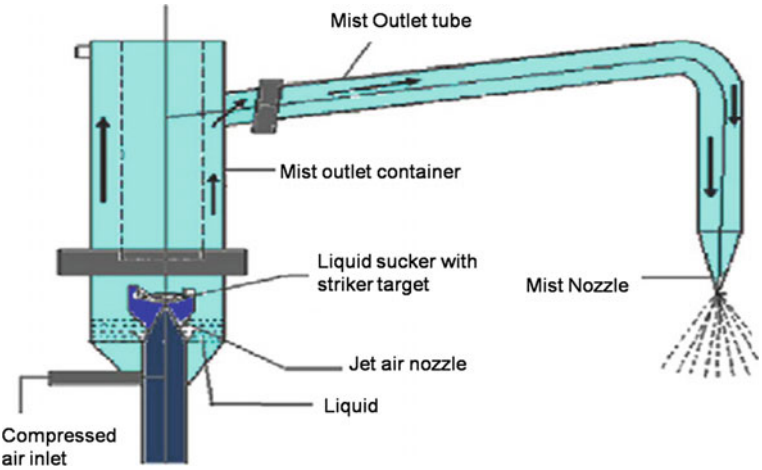

Fig. 1 Schematic diagram of Jet Nebulizer spray technique

pressure of 1.1 kg/cm^2 was connected to the bottom portion of the nebulizer. The solution was agitated between the walls of the pinhole and split up into very tiny droplets. These tiny droplets again and again make an impact with each other and there will be a reduction in the size of the droplets and it will form mist. These mists have moved with high speed throughout the outlet horizontal glass tube ending up with spray nozzle.

The solutions were prepared from the starting material Zinc chloride ($ZnCl_2$) at 0.1 M and a dopant source Aluminium Chloride ($AlCl_3$) by varying Al/Zn ratio (2, 4, 6, 8 and 10 at.%). To prepare the precursor solution, the required amount of salt is dissolved in double distilled water by continuous stirring in magnetic stirrer for 15 min. Before deposition, substrates were cleaned thoroughly in chromic acid and ultrasonicated in distilled water for 15 min. The deposition parameters such as substrate temperature, pressure and time of deposition were optimized as constant and only aluminium dopant concentration was varied to obtain pin hole free and adherent films of Al:ZnO. The solution was sprayed through the glass nozzle over the preheated amorphous glass substrate. The list of deposition parameters are presented in the Table 1.

The prepared AZO thin films were characterized by X-ray diffractometer (X'PERT PRO PANanalytical) using the Cu Kα wavelength of 1.54060 Å. The

Table 1 Parameters for AZO thin film deposition by spray pyrolysis

Spray parameters	Optimum value
Solvent	Double distilled water
Substrate	Glass
Carrier gas	Compressed air
Substrate temperature	300 °C
Pressure	1.1 kg/cm^2

surface morphology and chemical state of the films was examined by a Scanning Electron Microscopy (VEGA3 TESCAN) attached with Energy Dispersive Analysis (Bruker) was carried out for each sample. The optical studies of the films were recorded by UV-Vis-NIR double beam spectrophotometer (Perkin Elmer LAMBDA—35). The photoluminescence (Varian Cary Eclipse fluorescence Spectrometer) emission spectra was analysed with a fluorescence spectrophotometer. The electrical resistivity measurements of the films were made by using Keithley 2400 Source meter (SMU) in four probe method.

3 Results and Discussion

3.1 X-Ray Diffraction Studies

The crystalline nature of pure and Al doped ZnO films analysed by X-ray diffraction are shown in Fig. 2. The obtained peaks are indexed by standard JCPDS card No (01-080-0075) and the films are in hexagonal wurtzite structure [11]. It is worthwhile to mention that doping concentration play a crucial role in determination of orientation in the obtained films, associated with the nucleation process. The films was found to be preferentially oriented along (002) plane with the c—axis orientation and also other planes such as (100), (101), (102), (110) and (103) were observed. No other characteristic peaks related Zn or Al were observed, which revealed the existence of a single phase ZnO. Similar results of AZO films were reported by [12]. The ideal information is to be noted that the ZnO thin films show mainly the (002) as the preferential plane when zinc chloride or zinc acetate is used as precursor in starting solution [13] and also caused by the minimization of internal stress and surface energy [14]. The intensity of (002) peak decreased and the crystallinity of films and emergence of (100) and (101) plane were observed while increasing the aluminium concentration, which may be the reason for the intrinsic stress formation created by the difference in ionic radius between zinc and aluminium (r_{Zn}^{2+} = 0.074 nm and r_{Al}^{3+} = 0.054 nm) and also segregation of Al^{3+} ions in grain boundaries took place [15].

The lattice parameters ‘a’ and ‘c’ are calculated using the formula (1) [16].

$$\frac{1}{d_{hkl}^2} = \frac{4}{3\,a^2(h^2 + hk + k^2)} + \frac{l^2}{c^2} \tag{1}$$

where d_{hkl} is interplanar spacing between planes of given Miller indices ‘h’, ‘k’ and l. The calculated lattice parameters are listed in Table 2, which indicate that they are very well supported by standard values of bulk ZnO.

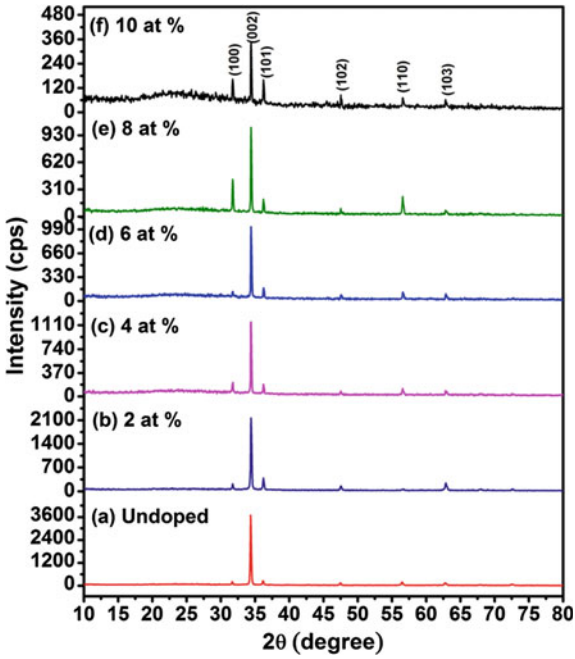

Fig. 2 XRD Pattern of AZO films

Table 2 The lattice constants, crystallite size, activation energy and energy band gap of AZO films

Sample	Lattice Constants (Å)		Crystallite Size (D) (nm)	Activation Energy (eV)	Energy band gap (eV)
	a	c			
0 at.% AZO	3.2583	5.2129	25.6684	0.6592	3.4
2 at.% AZO	3.2485	5.2091	22.8595	0.6307	3.2
4 at.% AZO	3.2526	5.2075	34.4357	0.5924	3.1
6 at.% AZO	3.2509	5.2047	40.6365	0.5897	2.9
8 at.% AZO	3.2519	5.2063	36.6844	0.4988	2.8
10 at.% AZO	3.2506	5.2075	49.2831	0.3909	2.7

The mean crystallite size of the sample is estimated by using Scherrer formula [17]:

$$D = \frac{K\lambda}{\beta \cos\theta} \tag{2}$$

where β is the full width at half maximum (FWHM) of the peak, K is shape factor which is equal to 0.9, λ is the wavelength of X-ray used (1.5406 Å for Cu Kα) and θ is the Bragg's angle [9, 18]. The crystallite size of the sample is tabulated in Table 2.

The crystallite size of the sample decreases with the increase in aluminium concentration whereas for 2 at.% of AZO thin film the value of crystallite size is found to be 22 nm and at 4 at.% of AZO thin film it is around 34 nm. This discrepancy arises due to the increase in the thickness of films which has already been reported by Sahay and Nath [15].

3.2 Scanning Electron Microscope

The surface morphology of AZO thin films as visualized by the SEM is given in Fig. 3 which shows that the films grown as nanorods on the surface with hexagonal facets. From Fig. 3 it was observed that the surface morphology of the films was strongly influenced by the concentration of aluminium. As the dopant concentration increased, the films appeared to be in-homogeneity, with the appearance of small heaps and voids. The grains were found to be irregular in shape and size while the top planes of the nanorods remained hexagonal. The layer leads to porous and rough surfaces upon increasing the aluminium content results in more scattering of light due to the lack of grain boundaries. The variation in grain size with the

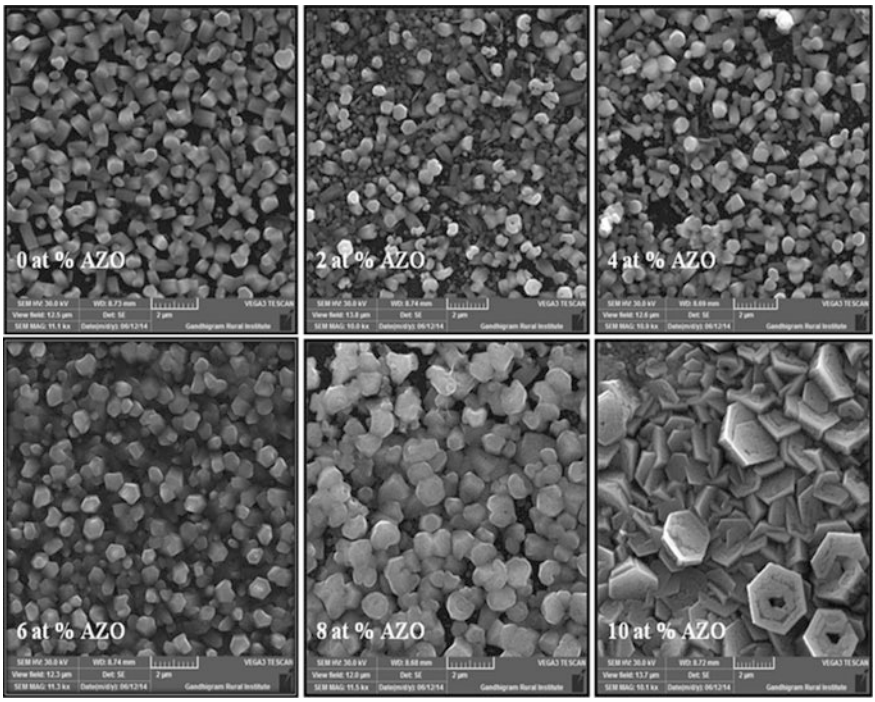

Fig. 3 SEM micrographs of AZO films

increased aluminium concentration can be attributed to the difference in ionic radius of zinc and aluminium [19], which could be correlated to the decrease of XRD peak intensity and less crystallinity in the films. While increasing the aluminium concentration, the porosity of the films also increased leading to the formation of crystallites with the hexagonal facets. At higher Al dopant concentrations, it tended to segregate the grain boundaries, hindering the development of longer grains [20].

3.3 Energy Dispersive X-Ray Analysis

The film composition was examined by energy dispersive X-ray analysis (EDS), which confirmed the expected elements such as Zn, O, Al being present. In addition to this, the presence of carbon which originates from carbon mesh is listed in Table 3. Figure 4 shows the EDAX result for undoped ZnO and 10 at.% Aluminium doped ZnO thin films.

Table 3 Elemental composition of AZO thin films derived from EDS

Sample	Zn	O	Al	Si	C	Ca
Undoped ZnO	41.91	58.09	–	–	–	–
10 at.% AZO	41.48	43.40	1.57	–	13.55	–

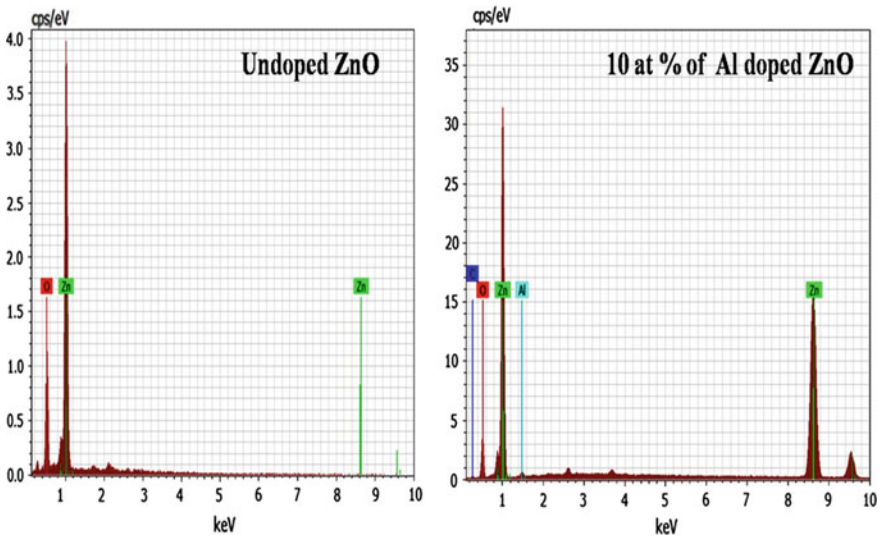

Fig. 4 EDAX analysis of AZO thin films

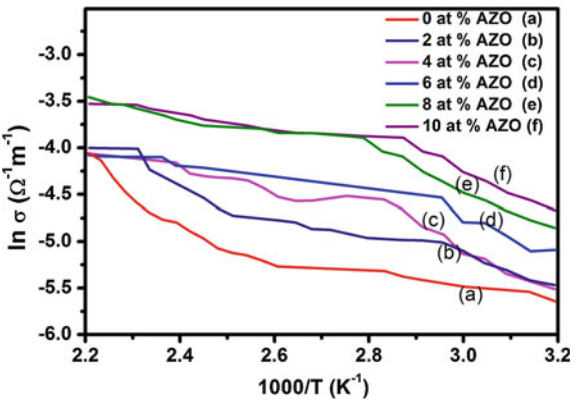

Fig. 5 Arrehenius plot of AZO thin films

3.4 Electrical Studies

Figure 5 shows the Arrhenius plot of the AZO thin film with temperature. It is apparent from Fig. 5 that the conductivity enhancement in AZO films observed due to the incorporation of aluminium from 2 to 10 at.%.

The increase in conductivity with aluminium dopant concentration may be attributed to the replacement of Zn^{2+} by Al^{3+} ions which introduce more number of electrical carriers in the doped films. The plot also suggested that the samples behaved in the semiconducting nature. Since thermal excitation is the source of the increment in electrical conductivity, the variation in conductivity can be analysed by the following relation [21],

$$\sigma = \sigma_0 \exp\left(\frac{-\Delta E}{kT}\right) \tag{3}$$

where σ_0 is constant, k is the Boltzmann constant, T is the temperature of the sample and ΔE is the activation energy.

The thermal activation energy was calculated from the slope derived from the plots of ln σ versus 1000/T(K) in Fig. 5. From Table 2 it has been noted that the decrease in thermal activation energy with the increase of aluminium concentration. The decrease in the activation energy with the increasing aluminium concentration might be due to an increase in the carrier concentration [22].

3.5 Optical Studies

The optical transmittance measurements of undoped zinc oxide and AZO films were made in the wavelength range of 350–1100 nm is shown in Fig. 6. In this present work all the films were prepared under low substrate temperature (300 °C).

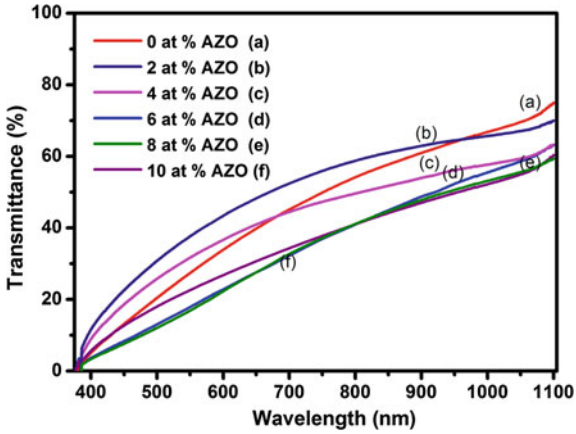

Fig. 6 Transmittance spectra of AZO thin films

The films seemed to be powdery and whitish in appearance, at the higher aluminium concentrations [23]. As the aluminium concentration increases the transmittance decreases from 70 to 55 % could be due to the scattering of photons by crystal defects caused by the incorporation of Al.

The reduction observed in the optical transmission of heavily doped films might also results from absorption of photons by free carriers [24]. The optical band gap of AZO thin films was calculated from the absorbance spectra using Tauc plot. The band gap of the AZO thin film estimated using the following relation [25],

$$\alpha h\nu = A\,(h\nu - E_g)^n \tag{4}$$

where 'hν' is the energy of incident photon, 'A' is a constant, 'α' is the absorption co-efficient, 'E_g' is the optical band gap, 'n' depends on the transition involved, the values n = 1/2, 3/2, 2, 3 corresponds to direct allowed transition, direct forbidden, indirect allowed transition, indirect forbidden respectively. Plotting $(\alpha h\nu)^2$ against photon energy hν, the band gap value can be determined by extrapolating the straight line portion at α = 0 and is shown in Fig. 7. The optical band gap values were found to be 3.4, 3.2, 3.1, 2.9, 2.8, and 2.7 eV for AZO thin films and it is listed in Table 2. It was clear that the optical band gaps were reduced as the Al concentration increased, which could be due to the band shrinkage effect because of the increasing carrier concentration [26]. These values were in good agreement with the literature [21, 27].

3.6 Photoluminescence

At excitation wavelength of 325 nm, the PL emission spectrum at room temperature for all the films measured in the wavelength range from 320 to 650 nm and the results are shown in Fig. 8. ZnO comprises a near band edge (NBE) emission in UV

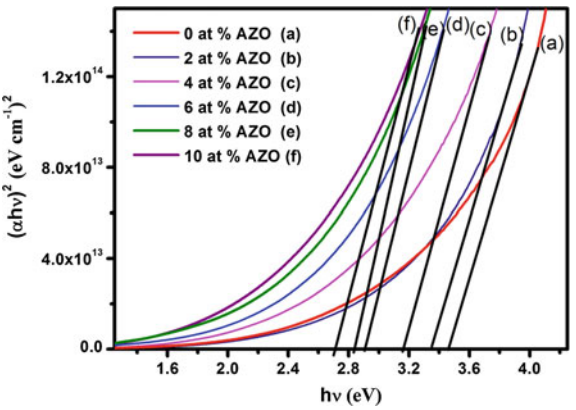

Fig. 7 Tauc plot of AZO thin films

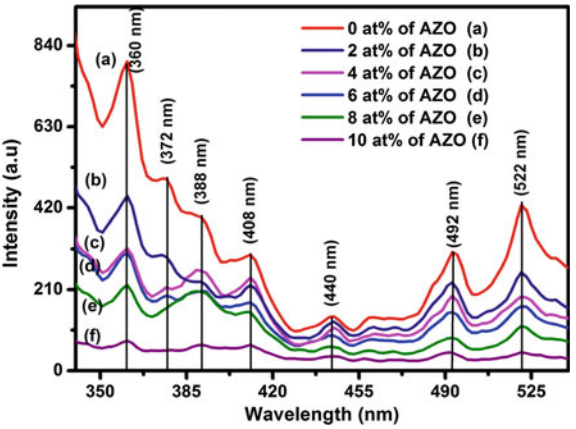

Fig. 8 Photoluminescence spectra of AZO thin films

region and a broad deep level emission in visible region. The NBE emission recorded in UV region due to the recombination of free excitons of ZnO. The deep—level emission consists of violet, blue and green bands related to native crystal defects of ZnO [28, 29].

The emission at ultra violet (UV) region was observed at 360, 372 and 388 nm. The Intensity of UV emission peak is dominant and confirms that the grown films possess a very good crystallinity [29, 30]. The violet peak appeared at 408 and 419 nm can be attributed to the Zn vacancies and the radiative centres causes interface traps between the grain boundaries [31, 32]. The peak corresponding to 440 nm belongs to blue emission occurs because of exciton recombination between localized electrons of Zn interstitials and the holes in the valence band [33]. The electron transition from the the ionized oxygen vacancies to the valence band may be the reason for the blue green emission peak obtained at 492 nm [34]. The most common emission in ZnO was the presence of green emission at 522 nm. Borseth et al. [35] observed that deep level green emission was attributed to both vacancies

of zinc and oxygen. The increase in intensity of deep level emission with addition of aluminium induces the probability of forming oxygen vacancies.

3.7 Ethanol Gas Sensing Response

Figure 9 shows the gas sensing setup used for ethanol sensing. The sensor made of ZnO and AZO films placed inside the vacuum chamber of known volume (57,000 cm^3). Ohmic contacts were made on the sensor films and were connected with a Keithley 2400 Source meter for necessary measurements. Initially, the sensitivity measurements were performed at the room temperature in air ambient and taken as reference. The ethanol liquid was placed in a beaker above the heater inside the chamber which was evacuated to a base pressure of 10^{-3} m bar using a rotary pump. The resistance of the sensor is measured with respect to time in ethanol vapour-air ambient. When the resistance value reaches the saturation stage, the gas completely removed from the chamber by opening the outlet valve.

Figures 10 and 11 show the transient response curve of the AZO films to the ethanol gas of 100 and 200 ppm. All the sensors showed decrease in resistance upon an exposure to the ethanol vapour and an increase in resistance when the ethanol vapour was removed. The response and recovery time of the AZO film sensor in few minutes compared to undoped ZnO film and the obtained value of sensitivity was low for 100 ppm ethanol when compared to 200 ppm ethanol. The sensitivity of the sensor S (%), calculated using the following formula,

$$S\,(\%) = \frac{R_{gas} - R_{air}}{R_{air}} \times 100. \tag{5}$$

From Figs. 10 and 11, it is clear that the film prepared at 10 at.% of AZO shows the highest sensitivity compared to the other dopant concentration of AZO films.

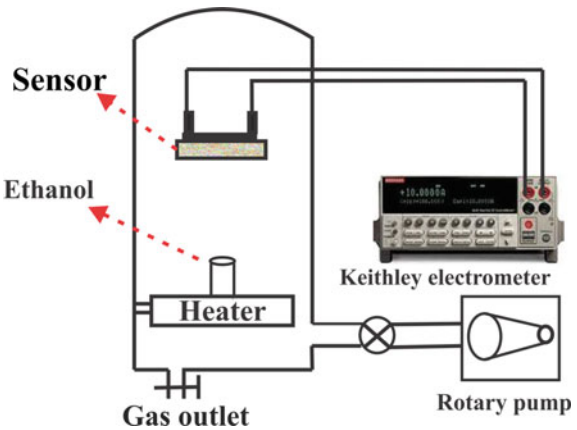

Fig. 9 Schematic diagram of Gas Sensing Apparatus

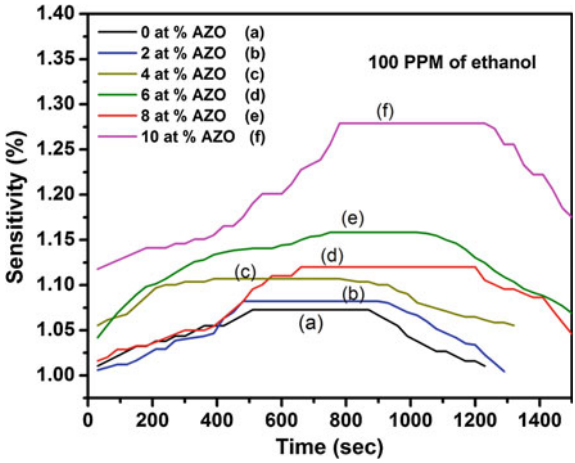

Fig. 10 Ethanol Sensing of AZO films (100 ppm)

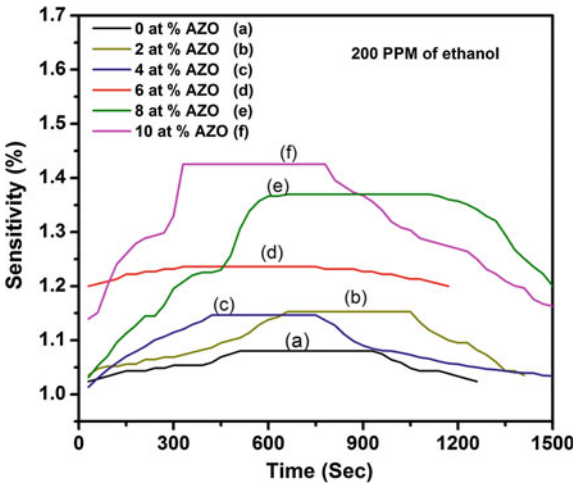

Fig. 11 Ethanol Sensing of AZO films (200 ppm)

This is extremely due to the porous shaped morphology and the reduced crystallization observed from XRD causes more number of grain boundaries for adsorption ethanol gas in AZO nanostructured films. The following chemical equations explain the reaction process of adsorbed ethanol over AZO films (6)–(8) [36].

$$C_2H_5OH\,(gas) \rightarrow C_2H_5OH\,(ads) \tag{6}$$

$$C_2H_5OH\,(ads) + O^- + \Delta H_2 \rightarrow e^- + CH_3CHO\,(gas) + H_2O + \Delta H \tag{7}$$

$$C_2H_5OH\,(ads) + O^{2-}(ads) \rightarrow 2e^- + CH_3CHO\,(gas) + H_2O + \Delta H \tag{8}$$

The free carriers released due to the interaction of ethanol vapour and pre-adsorbed O^- alters the resistance of the sensor film. When the ethanol vapour is closed to recover the sensor to the original state, the adsorption of oxygen molecules cover the surface of AZO film and the electrons trapped during the process will bring the resistance of the sensor to its initial value. The response curves (Figs. 10 and 11) of AZO films indicates that recovery time of sensor towards the initial value is minimum when ethanol has completely removed from the testing chamber.

The surface–volume ratio of AZO film at 10 at.% is higher than that of the other dopant concentration of AZO films. The crystallization of the AZO films is relatively poor as the concentration of aluminium dopant increased, supported by XRD and PL results indicating that many defects such as oxygen vacancies formed in the nano-sized ZnO [37, 38]. So, more active centres were available to adsorb ethanol molecules [39], which resulted in an increase in the sensitivity of AZO nano structured films. The reason behind the high sensitivity of 10 at.% aluminium doped zinc oxide films is due to the replacement of Al^{3+} in Zn^{2+} sites modifies the work function and carrier concentration on the surface which corroborates with optical and electrical results. This phenomenon causes a rapid change in resistance (high sensitivity) even for lesser number of gas molecules reacted with sensor. Therefore AZO films can enhance the gas sensing properties, and the film prepared at 10 at.% of AZO was the best film among the other prepared films.

4 Conclusion

Simple nebulizer Spray pyrolysis technique was adopted for the preparation of Al doped Zinc oxide thin film. The XRD patterns of the films exhibit the preferential orientation along (002) plane with hexagonal structure. The surface morphology of the films found to be varied with increasing dopant concentration. The reduced activation energy and energy band gap with increase in aluminium concentration in ZnO thin films may be the reason for the increase in the carrier concentration. The intensity of the NBE emission of photoluminescence spectra decreases with increase in aluminium concentration indicates defect levels created due to the incorporation of dopant. The sensing response of all the deposited films towards ethanol was investigated at room temperature. The film prepared at 10 at.% of AZO is the best film for gas sensing application.

Acknowledgements This work was financially supported by the University Grants Commission, New Delhi, India [F.no.42-903/2013(SR)] under Major Research Project Scheme (MRP) and Rajiv Gandhi National Fellowship (F1-17.1/2011-12/RGNF-SC-TAM-4843). The authors would like to record their sincere thanks to the commission.

References

1. Mousavi, S.H., Haratizadeh, H., Minaee, H.: The effect of morphology and doping on photoluminescence of ZnO nanostructures. Opt. Commun. **284**, 3558–3561 (2011)
2. Roy, S., Basu, S.: Improved zinc oxide film for gas sensor applications. Bull. Mater. Sci. **25**, 513–515 (2002)
3. Repins, I., Contreras, M.A., Egaas, B., DeHart, C., Scharf, J., Perkins, C.L., To, B., Noufi, R.: 19.9 %-efficient ZnO/CdS/CuInGaSe2 solar cell with 81.2 % fill factor. Prog. Photovoltaics Res. Appl. **16**, 235–239 (2008)
4. Nayak, P.K., Yang, J., Kim, J., Chung, S., Jeong, J., Lee, C., Hong, Y.: Spin-coated Ga-doped ZnO transparent conducting thin films for organic light-emitting diodes. J. Phys. D Appl. Phys. **42**, 035102 (2009)
5. Xiu, X., Pang, Z., Lv, M., Dai, Y., Ye, L., Han, S.: Transparent conducting molybdenum-doped zinc oxide films deposited by RF magnetron sputtering. Appl. Surf. Sci. **253**, 3345–3348 (2007)
6. Shi, J., Ma, H., Ma, G., Ma, H., Shen, J.: Structure and ultrafast carrier dynamics in *n*-type transparent Mo:ZnO nanocrystalline thin films. Appl. Phys. A **92**, 357–360 (2008)
7. Gençyılmaz, O., Atay, F., Akyüz, İ.: Ellipsometric investigation of optical parameters and characterization of spray pyrolysis-derived ZnO films. Metall. Mater. Trans. A **46**, 4247–4254 (2015)
8. Lucio-López, M.A., Luna-Arias, M.A., Maldonado, A., de la L. Olvera, M., Acosta, D.R.: Preparation of conducting and transparent indium-doped ZnO thin films by chemical spray. Sol. Energy Mater. Sol. Cells **90**, 733–741 (2006)
9. Sukkar, M., Tuller, H.: Defect equilibria in ZnO varistor materials. In: Additives and Interfaces in Electronic Ceramics. Proceedings of the Special Conference held at Cincinnati 4–5 May 1982. Advances in Ceramics, p. 71 (1982)
10. Jeong, S.H., Park, B.N., Lee, S.B., Boo, J.H.: Structural and optical properties of silver-doped zinc oxide sputtered films. Surf. Coat. Technol. **193**, 340–344 (2005)
11. Caglar, M., Ilican, S., Caglar, Y., Yakuphanoglu, F.: The effects of Al doping on the optical constants of ZnO thin films prepared by spray pyrolysis method. J. Mater. Sci. Mater. Electron. **19**, 704–708 (2008)
12. Islam, M.N., Ghosh, T.B., Chopra, K.L., Acharya, H.N.: XPS and X-ray diffraction studies of aluminum-doped zinc oxide transparent conducting films. Thin Solid Films **280**, 20–25 (1996)
13. Manouni, A.E., Manjón, F.J., Mollar, M., Marí, B., Gómez, R., López, M.C., Ramos-Barrado, J.R.: Effect of aluminium doping on zinc oxide thin films grown by spray pyrolysis. Superlattices Microstruct. **39**, 185–192 (2006)
14. Bao, D., Gu, H., Kuang, A.: Sol-gel-derived c-axis oriented ZnO thin films. Thin Solid Films **312**, 37–39 (1998)
15. Sahay, P.P., Nath, R.K.: Al-doped zinc oxide thin films for liquid petroleum gas (LPG) sensors. Sens. Actuators B Chem. **133**, 222–227 (2008)
16. Fang, G., Li, D., Yao, B.-L.: Fabrication and characterization of transparent conductive ZnO: Al thin films prepared by direct current magnetron sputtering with highly conductive ZnO (ZnAl2O4) ceramic target. J. Cryst. Growth **247**, 393–400 (2003)
17. Allah, F.K., Abé, S.Y., Núñez, C.M., Khelil, A., Cattin, L., Morsli, M., Bernède, J.C., Bougrine, A., del Valle, M.A., Díaz, F.R.: Characterisation of porous doped ZnO thin films deposited by spray pyrolysis technique. Appl. Surf. Sci. **253**, 9241–9247 (2007)
18. Lokhande, B.J., Patil, P.S., Uplane, M.D.: Deposition of highly oriented ZnO films by spray pyrolysis and their structural, optical and electrical characterization. Mater. Lett. **57**, 573–579 (2002)
19. Zhou, H.-M., Yi, D.-Q., Yu, Z.-M., Xiao, L.-R., Li, J.: Preparation of aluminum doped zinc oxide films and the study of their microstructure, electrical and optical properties. Thin Solid Films **515**, 6909–6914 (2007)
20. Gómez-Pozos, H., Maldonado, A., Olvera, M.D.l.L.: Effect of the [Al/Zn] ratio in the starting solution and deposition temperature on the physical properties of sprayed ZnO:Al thin films. Mater. Lett. **61**, 1460–1464 (2007)

21. Ilican, S., Caglar, Y., Caglar, M., Yakuphanoglu, F.: Electrical conductivity, optical and structural properties of indium-doped ZnO nanofiber thin film deposited by spray pyrolysis method. Phys. E **35**, 131–138 (2006)
22. Tewari, S., Bhattacharjee, A.: Structural, electrical and optical studies on spray-deposited aluminium-doped ZnO thin films. Pramana **76**, 153–163 (2011)
23. Aktaruzzaman, A.F., Sharma, G.L., Malhotra, L.K.: Electrical, optical and annealing characteristics of ZnO: Al films prepared by spray pyrolysis. Thin Solid Films **198**, 67–74 (1991)
24. Joseph, B., Manoj, P.K., Vaidyan, V.K.: Studies on the structural, electrical and optical properties of Al-doped ZnO thin films prepared by chemical spray deposition. Ceram. Int. **32**, 487–493 (2006)
25. Tarasov, K., Raccurt, O.: A wet chemical preparation of transparent conducting thin films of Al-doped ZnO nanoparticles. J. Nanopart. Res. **13**, 6717–6724 (2011)
26. Ravichandran, K., Anbazhagan, A., Dineshbabu, N., Ravidhas, C.: Influence of Mo doping on transparent conducting properties of ZnO films prepared by a simplified spray technique. J. Mater. Sci. Mater. Electron. **26**, 7649–7654 (2015)
27. Shukla, R.K., Srivastava, A., Srivastava, A., Dubey, K.C.: Growth of transparent conducting nanocrystalline Al doped ZnO thin films by pulsed laser deposition. J. Cryst. Growth **294**, 427–431 (2006)
28. Cui, L., Zhang, H.-Y., Wang, G.-G., Yang, F.-X., Kuang, X.-P., Sun, R., Han, J.-C.: Effect of annealing temperature and annealing atmosphere on the structure and optical properties of ZnO thin films on sapphire (0001) substrates by magnetron sputtering. Appl. Surf. Sci. **258**, 2479–2485 (2012)
29. Willander, M., Nur, O., Sadaf, J.R., Qadir, M.I., Zaman, S., Zainelabdin, A., Bano, N., Hussain, I.: Luminescence from zinc oxide nanostructures and polymers and their hybrid devices. Materials **3**, 2643–2667 (2010)
30. Sha, Z.D., Wang, J., Chen, Z.C., Chen, A.J., Zhou, Z.Y., Wu, X.M., Zhuge, L.J.: Initial study on the structure and optical properties of ZnO film on Si(1011) substrate with a SiC buffer layer. Phys. E **33**, 263–267 (2006)
31. Jeong, S.-H., Kim, B.-S., Lee, B.-T.: Photoluminescence dependence of ZnO films grown on Si(100) by radio-frequency magnetron sputtering on the growth ambient. Appl. Phys. Lett. **82**, 2625–2627 (2003)
32. Jin, B.J., Im, S., Lee, S.Y.: Violet and UV luminescence emitted from ZnO thin films grown on sapphire by pulsed laser deposition. Thin Solid Films **366**, 107–110 (2000)
33. Kumar, B., Gong, H., Chow, S.Y., Tripathy, S., Hua, Y.: Photoluminescence and multiphonon resonant Raman scattering in low-temperature grown ZnO nanostructures. Appl. Phys. Lett. **89**, 071922 (2006)
34. Yadav, R.S., Mishra, P., Pandey, A.C.: Growth mechanism and optical property of ZnO nanoparticles synthesized by sonochemical method. Ultrason. Sonochem. **15**, 863–868 (2008)
35. Børseth, T.M., Svensson, B.G., Kuznetsov, A.Y., Klason, P., Zhao, Q.X., Willander, M.: Identification of oxygen and zinc vacancy optical signals in ZnO. Appl. Phys. Lett. **89**, 262112 (2006)
36. Li, L.M., Du, Z.F., Wang, T.H.: Enhanced sensing properties of defect-controlled ZnO nanotetrapods arising from aluminum doping. Sens. Actuators B Chem. **147**, 165–169 (2010)
37. Nagase, T., Ooie, T., Makita, Y., Nakatsuka, M., Shinozaki, K., Mizutani, N.: A novel method for the preparation of green photoluminescent undoped zinc oxide film involving excimer laser irradiation of a sol-gel-derived precursor. Jpn. J. Appl. Phys. **39**, L713 (2000)
38. Vanheusden, K., Warren, W.L., Seager, C.H., Tallant, D.R., Voigt, J.A., Gnade, B.E.: Mechanisms behind green photoluminescence in ZnO phosphor powders. J. Appl. Phys. **79**, 7983–7990 (1996)
39. Gurlo, A., Ivanovskaya, M., Bârsan, N., Schweizer-Berberich, M., Weimar, U., Göpel, W., Diéguez, A.: Grain size control in nanocrystalline In2O3 semiconductor gas sensors. Sens. Actuators B Chem. **44**, 327–333 (1997)

The Effect of Solvent on the Structural, Morphological, Optical and Electrical Properties of Spray Pyrolysed Boron Doped CdO Thin Films

P. Velusamy, R. Ramesh Babu, K. Ramamurthi and N. Balamurugan

Abstract In this communication, the influence of solvent (water and mixed solvent) on the structural, surface microstructural, dc-electrical and optical properties of spray deposited cadmium oxide (CdO) thin films doped with different weight percentages (wt%) of boron (B) on microscopic glass substrates at 300 °C is reported. The X-ray diffraction (XRD) analysis suggests that the samples are polycrystalline in nature and the crystallinity is enhanced by B doping concentrations. The average crystallite size of (200) plane is ranging 29–90 and 40–138 nm for water, and mixed solvent of water and methanol (1:1), respectively. Oxidation state of B doped CdO thin film was confirmed by X-ray photoelectron spectroscopy (XPS) analysis. The surface microstructures of B doped CdO thin films are effectively modified by solvent and the average particle size varies between 301 and 466 nm for water solvent and 221 and 705 nm for mixed solvent used B doped CdO films. The direct optical band gap energy values varies between 2.11 and 2.35 eV for water and 2.43 and 2.54 eV for mixed solvent used B doped CdO thin films. High average transmittance (80 %) and high mobility of 64.42 $cm^2/V{\cdot}s$ were obtained for 1.0 wt% B doped CdO thin film deposited using mixed solvent. The mixed solvent used 1.0 wt% B doped CdO thin film has high figure of merit ($16.2 \times 10^{-3}\ \Omega^{-1}$). The variations in electrical resistivity, carrier concentration, mobility and optical transmittance with respect to spray solvents have been discussed.

P. Velusamy · R. Ramesh Babu (✉)
Crystal Growth and Thin Film Laboratory, Department of Physics,
Bharathidasan University, Tiruchirappalli 620024, Tamil Nadu, India
e-mail: rampap2k@yahoo.co.in

K. Ramamurthi
Crystal Growth and Thin Film Laboratory, Department of Physics and Nanotechnology,
Faculty of Engineering and Technology, SRM University,
Kattankulathur 603203, Tamil Nadu, India

N. Balamurugan
GTAT Corporation, 3202-3203 Park Place,
1601West Nanjing Road, Shanghai 20004, China

J. Ebenezar (ed.), *Recent Trends in Materials Science and Applications*,
Springer Proceedings in Physics 189, DOI 10.1007/978-3-319-44890-9_34

1 Introduction

In the recent years, the studies on transparent conducting oxide (TCOs) semiconductor thin films (CdO, ZnO, SnO_2, In_2O_3) have received considerable attention, mainly due to their proven and potential applications in solar cells and optoelectronic devices. TCOs are also essential for developing electro-optic devices, owing their unique combination of low resistivity and high UV-Vis-NIR transmittance [1, 2]. Among the available TCOs, CdO thin films can be used as transparent contacts and windows layers instead of tin oxide (SnO_2) and cadmium sulfide (CdS) in the SnO_2/*n*-CdS/*p*-CdTe heterostructure solar cells [3, 4]. CdO possess a relatively simple cubic crystal structure (FCC) with Fm-3m space group and high optical transmittance and conductivity as high as ranging from 10^2 to 10^4 S/cm, due the presence of either oxygen vacancies (V_o) or interstitial cadmium (Cd_i). Hence, CdO are useful in the applications such as photodiodes, phototransistors, photovoltaics, transparent electrodes, liquid crystal displays, IR detectors and anti-reflecting coatings [5, 6]. However, CdO is not much popular due to their small optical band gap (2.2 eV) [7]. Generally, the optoelectronic properties of TCOs are controlled through doping with selected metal ions like Al, In, Ga, Sm and Ce [8–12]. It was observed that when the radius of dopant ions is slightly smaller than that of Cd^{2+} then the optoelectronic properties are improved [11].

CdO and doped CdO thin films were prepared by various techniques such as sol-gel, thermal evaporation, vacuum evaporation, RF sputtering, DC magnetron sputtering, metal oxide chemical vapour deposition, pulsed laser deposition and spray pyrolysis techniques [12]. Among these spray pyrolysis technique is well suited for the preparation of doped TCO thin films because of its simple and inexpensive experimental arrangement, ease of adding different doping materials, reproducibility, high growth rate and mass production capability for uniform large area coating [9]. There are reports available on doped CdO thin films deposited using different solvents. Bhosale et al. reported the overall solvent effect on the structural, electrical and work functions of spray deposited ITO/SiO_2/n-Si hetrojunction solar cells [13]. Golobostanfard et al. reported that the surface morphology of sprayed TiO_2 films was strongly affected by species of solvents [14]. Tomakin [15] demonstrated that the methanol solvent yielded high-quality and dense Al-doped ZnO thin films. From the reports, it is observed that the solvent plays an important role in tuning the morphology of the deposited films. To the best of our knowledge, there is no detailed report on water and mixed solvent of water and methanol (1:1), as a spraying solvent, used boron doped CdO thin films by spray deposition. In this work, the effect of water and mixed solvent on the structural, microstructural, optical and electrical properties of B doped CdO thin films is studied and the obtained results are compared and discussed in detail.

2 Experimental Details

Thin films of undoped and B doped CdO were deposited onto preheated microscopic glass substrates at 300 °C using a simple chemical spray pyrolysis technique. Prior to deposition, the substrate was cleaned in soap solution, hot chromic acid solution, rinsed with double distilled water, ultrasonic treated and dried in air in order to achieve a better adherence between film and substrate. The appropriate quantity of cadmium acetate dihydrate [$(CH_3\ COO)_2{\cdot}Cd{\cdot}2H_2O$] was used to prepare 0.1 M precursor solution by dissolving in deionized water and mixed solvent (deionized water and methanol, 1:1 ratio) separately. The B doping was achieved by adding boric acid (H_3BO_3) with different concentrations (0.0, 1.0, 3.0 and 5.0 wt%) to the precursor solution, which formed the final spray solution. Except the B doping concentration, other deposition parameters and preparative conditions were kept constant during all the experiments. They are as follows: substrate temperature —300 °C, nozzle-substrate distance—30 cm, spray angle—45°, compressed air flow rate—45 kg/cm^2, spray time—3 s, and spray interval—57 s. The final spray solution was sprayed onto the preheated microscopic glass substrates. The high resistive chromel–alumel thermocouple was used to maintain the substrate temperature through a digital temperature controller (INDFUR PID) with ±5 °C accuracy. The fine droplets of the precursor solution when sprayed onto the substrates held at relevant growth temperature undergo a thermal decomposition to form CdO thin films with uniform yellow-color. On process completion, the deposited films were allowed to naturally cool down to room temperature. For each concentration the several sets of thin films were deposited.

The structural characterization of the spray deposited undoped and B doped CdO thin films were performed using Philips X-ray diffractometer with CuK_α wavelength (1.5406 Å). All the films were characterized in Bragg-Brentano geometry with θ and 2θ coupled. The scan length for the diffraction angle (2θ) is ranging from 10° to 90° irrespective of the variation in B doping concentration. Thickness of CdO and B doped CdO thin films measured using reflectometry method by Filmetrics (Model: F20-XT) is around 350 nm. The oxidation state of elements was confirmed by X-ray photoelectron spectroscopy (XPS). Scanning electron microscopy (Hitachi S-3000H) was employed to investigate the surface microstructures of B doped CdO thin films. The optical transmittance was studied using Perkin Elmer make (Model: Lambda-35) spectrophotometer in the wavelength ranging from 300 to 900 nm. The electrical parameters such as resistivity, carrier mobility, type and concentration of charge carriers were estimated by Hall effect set up (Model: Ecopia—HMS 3000) at room temperature. The Van der Pauw technique was used to measure the electrical parameters. A specially designed Hall probe on printed circuit board was used to fix the samples with dimensions of 1 cm × 1 cm.

3 Results and Discussion

3.1 X-Ray Diffraction Analysis

XRD spectra of B doped CdO thin films deposited using water and mixed solvent are comparatively shown in Fig. 1a, b. They reveal that the CdO thin films are polycrystalline in nature with cubic structure (FCC) and Fm-3m space group. XRD spectra shows four characteristic peaks which are assigned to (111), (200), (220), and (311) planes. A relatively strong intensity peak was obtained at 2θ of 38.34° for undoped CdO thin film, which indicates a preferential (200) growth orientation. The intensity of the peak (200) is higher for the film prepared using mixed solvent and it indicates a better crystallite formation, because cadmium acetate dissolves much more in mixed solvent when compared to water solvent. Therefore, the thin films prepared using mixed solvent have a good crystallinity. All the diffraction peaks were indexed by matching with the standard data from international center for diffraction data (ICDD), reference code: 00-005-0640 [6]. The phase corresponding to the cadmium monoxide, boric acid or any other Cd-B-O combination of cadmium and Boron compound was not detected in the XRD patterns. The structural parameters such as texture coefficient and crystallite size were calculated and given in Table 1. The calculated '*a*' values of CdO are in good agreement with the

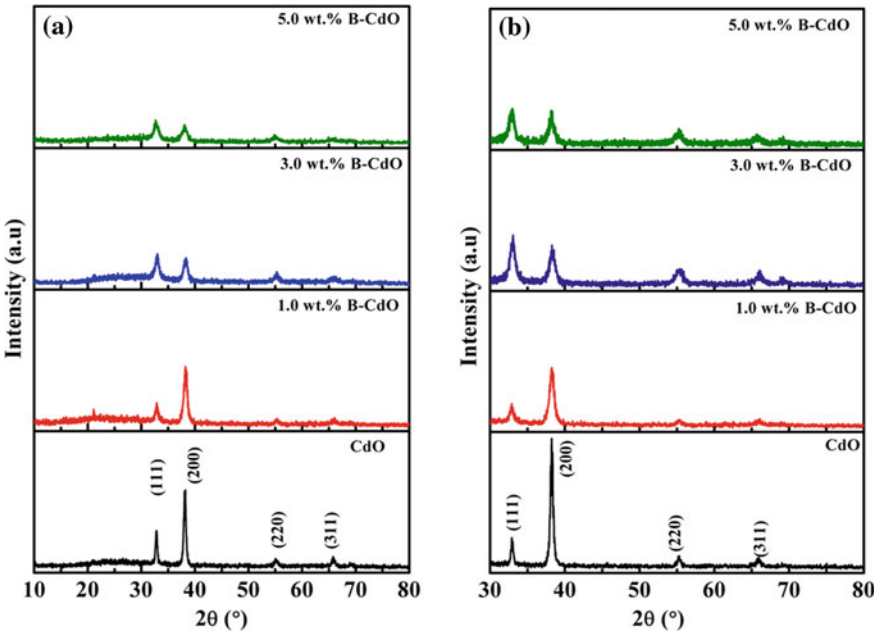

Fig. 1 XRD pattern of undoped and B doped CdO thin films deposited using **a** water solvent and **b** mixed solvent

Table 1 Lattice constant, FWHM, Crystallite size, Texture coefficient and Peak intensity of B doped CdO thin films

B-doping (wt%)	(a) (Å)		FWHM (°)		Crystallite size (D) (nm)		Texture coefficient				Peak intensity (cps)	
	W*	(W + M)**	W*	(W + M)**	W*	(W + M)**	W*		(W + M)**		W*	(W + M)**
							(111)	(200)	(111)	(200)		
CdO	4.7303	4.6960	0.118	0.094	90	138	0.36	1.63	0.31	1.68	652	1088
1.0 %	4.6986	4.7034	0.259	0.165	29	51	0.33	1.66	0.54	1.45	512	501
3.0 %	4.7104	4.7032	0.211	0.188	40	45	1.41	0.58	1.11	0.88	240	350
5.0 %	4.7011	4.6989	0.141	0.212	60	40	1.23	0.76	1.50	0.49	166	308

W*-water solvent, (W + M)**-mixed solvent

reported value of 0.4695 nm [11]. For the higher B doping concentration (3.0 wt%), the growth orientation of CdO is shifted from plane (200) to (111) for both the solvents. This shift is presumably dedicated to the incorporation of B dopant in CdO lattice and thereby altering the nucleation and growth processes of the deposited films.

The crystallite size (D) of B doped CdO films were calculated from (200) plane using Scherrer's formula [12]

$$D = \frac{0.9\,\lambda}{\beta\cos\theta} \tag{1}$$

where 'β' is the full width at half maximum (FWHM) of the peak and 'λ' is the X-ray wavelength (1.5406 Å). The lattice constant and crystallite size values of CdO and B doped CdO films deposited using water and mixed solvent were calculated and are given in Table 1. It is found that the average crystallite size varies between 29 and 90 nm for water and 40 and 138 nm for mixed solvent with respect of B doping concentration. This is probably indicating that solvent is contributing for the change in crystallinity of B doped CdO thin films. The preferred growth orientation of CdO films was investigated through texture coefficient (TC) as defined in [11] as:

$$TC = \frac{\left[\frac{I_m(hkl)}{I_o(hkl)}\right]}{\left[\frac{1}{N}\sum\frac{I_m(hkl)}{I_o(hkl)}\right]} \tag{2}$$

where I_m (hkl) is the measured relative intensity of reflections from a given (hkl) plane, I_0 (hkl) is the relative intensity of the reflections from the same plane as indicated in a standard sample of randomly oriented polycrystalline CdO powder [6].'N' denotes the total number of reflections, which are 4 in the present case. The highest value of texture coefficient obtained for mixed solvent used CdO thin film is 1.68 for (200) plane. It clearly indicates that the (200) plane is the preferred growth orientation for spray deposited CdO thin film (Table 1).

3.2 XPS Analysis

XPS analysis was carried out for 1.0 wt% B doped CdO thin films in order to figure out the oxidation states of B, Cd, and O elements. The XPS spectra obtained using MgK_α radiation at 1.2536 keV is shown in Fig. 2. The binding energy corresponding to the peaks Cd $3d_{5/2}$, Cd $3d_{3/2}$, O 1s, and B 1s, obtained from XPS analysis is 406, 413, 530, and 192 eV, respectively. These values are in good agreement with the reported values [11]. The binding energy (406 and 413 eV) of Cd 3d indicates the Cd^{2+} states. The binding energy corresponding to the peak O 1s is 530 eV confirms the O^{2-} oxidation state. A less intense binding energy peak at 192 eV may be attributed to the B 1s with B^{3+} oxidation state.

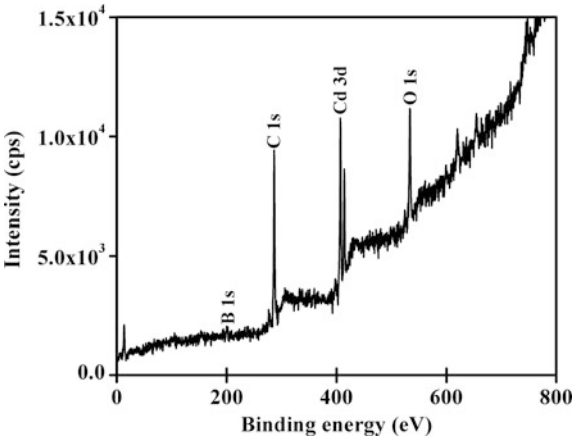

Fig. 2 Typical XPS spectrum of 1.0 wt% B doped CdO thin films deposited using mixed solvent

3.3 SEM Analysis

Figure 3a–d, a1–d1 show the surface microstructure of water and mixed solvent used B doped CdO thin films, respectively. From the figure it is observed that the surface microstructures of CdO thin films show uniform and homogeneous distribution of particles for both the solvents (3a, a1). In addition, the surface microstructure of CdO films shows an increase in particle size for 1.0 wt% B doping concentration; thereafter particle size decreases with increasing doping concentration for both the solvents. The surface microstructure of 1.0 wt% B doped CdO thin film deposited using water solvent (Fig. 3b) consist of randomly distributed spherical shaped particle with some agglomeration and pinholes. Figure 3c, d seem to have spherical and some elongated spherical shape particles with patches. The film doped with 1.0 wt% of B (Fig. 3b1) prepared using mixed solvent consists of relatively large sized with spherical shaped particles with pinholes. Figure 3c1, d1 seem to be homogenous, compact, pinhole free and spherical shape particles uniformly distributed throughout the surface of the substrate.

The average particle size of water and mixed solvent used undoped and B doped CdO thin films were measured from the corresponding SEM microstructures using histogram images (Fig. 4a–d, a1–d1). The average particle size (d) varies between 301 and 466 nm for water solvent and 221 and 705 nm for mixed solvent used B doped CdO thin films (Table 2).

SEM analysis reveals that mixed solvent used B doped CdO thin film has higher particle size and uniform distribution of spherical shape particles when compared to water solvent used B doped CdO thin film. It seems to be the solvents play an important role in thin film coating processes and also effectively modifies the surface morphology of B doped CdO thin films.

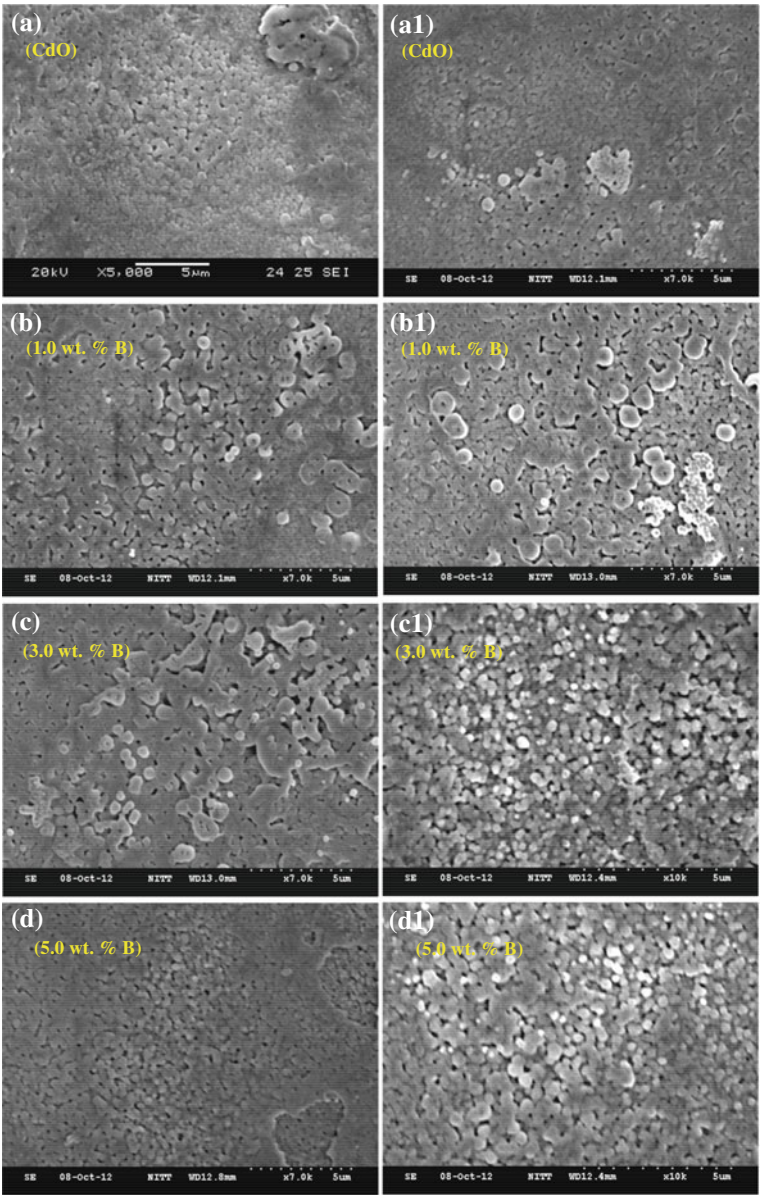

Fig. 3 Surface microstructure of undoped and B doped CdO thin films deposited using **a–d** water solvent and **a1–d1** mixed solvent

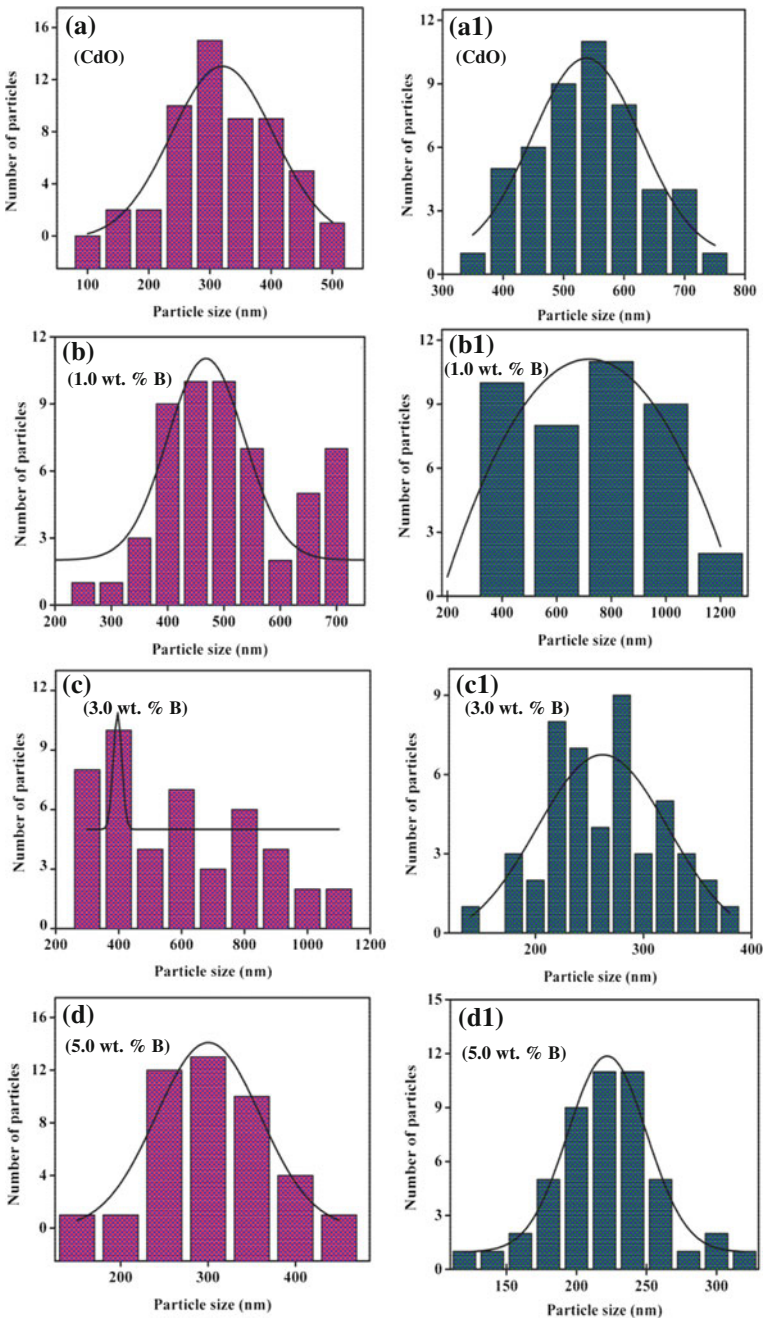

Fig. 4 Histogram image of undoped and B doped CdO thin films deposited using **a–d** water solvent and **a1–d1** mixed solvent

Table 2 Particle size (SEM), Average transmittance and Optical band gap of B doped CdO films deposited using water and mixed solvent

B-doping (wt%)	Particle size (d) (nm)		Average transmittance (500–900 nm) (%)		Optical band gap (eV)	
	W*	(W + M)**	W*	(W + M)**	W*	(W + M)**
CdO	322	539	39	75	2.27	2.43
1.0 %	466	705	24	80	2.29	2.46
3.0 %	396	261	28	78	2.35	2.51
5.0 %	301	221	35	74	2.11	2.54

W*-water solvent, (W + M)**-mixed solvent

3.4 UV-Visible-NIR Spectral Analysis

Figure 5a, b show the optical transmittance spectra of undoped and B doped CdO thin films deposited using different solvents. All the deposited films show good optical transmittance in the visible and near—infrared region with slight difference in percentage of optical transparency.

The B doped CdO thin films deposited using mixed solvent shows high transmittance ranging between 75 and 80 % in the 500–900 nm wavelength region where as water solvent used films, the transmittance ranging between 24 and 39 %. The average transmittance (AT) of B doped CdO thin films vary randomly with respect of B doping concentration (Table 2). 1.0 wt% of B doped CdO thin film deposited using mixed solvent has high AT (80 %). Figure 5a, b clearly evidence that the absorption edge is shifted to high energy side following the increasing carrier concentration due to the Moss–Burstein (M–B) effect [16]. The absorption edge of B doped CdO films obtained with mixed solvent exhibit is an obvious blue

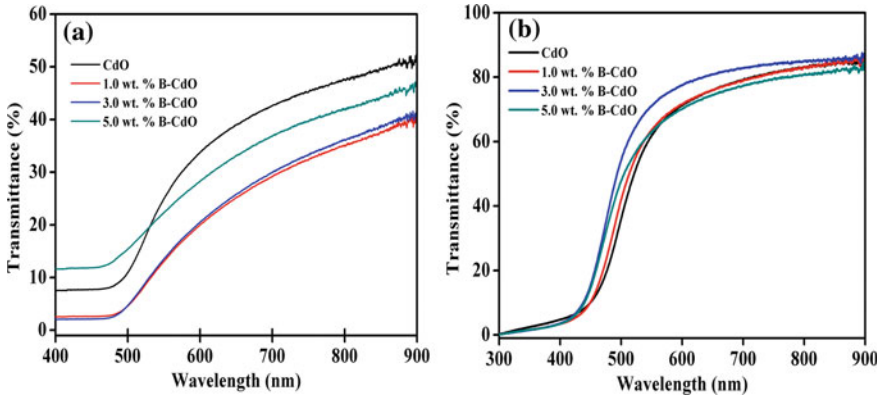

Fig. 5 Optical transmittance spectra of **a** water solvent **b** mixed solvent used undoped and B doped CdO films

shift, which shows that the optical band gap of the films are broadened with mixed solvent. The optical energy band gap of B doped CdO thin films were calculated from the transmittance data. The absorption coefficient (α) is given by [9]

$$(\alpha) = \frac{1}{t}\ln\left(\frac{1}{T}\right) \tag{3}$$

where, T is transmittance and t is film thickness. The thickness of the films is ~350 nm. The relation between the absorption coefficient and the incident photon energy ($h\nu$) is given by the equation [10]

$$(\alpha h\nu)^2 = A(E_g - h\nu) \tag{4}$$

where 'A' is a constant and 'E_g' is the optical band gap. The direct optical band gap was estimated by extrapolating the linear portion of $(\alpha h\nu)^2$ *Vs* $h\nu$ plot to x axis (Fig. 6a, b). The intercept on the x axis (at y = 0) gives the direct optical band gap. It is noticed that the band gap is gradually increased following the increase in B dopant concentration up to 3.0 wt% for mixed solvent and 1.0 wt% for water solvent (Table 2). The band gap values varies between 2.43 and 2.54 eV for mixed solvent, 2.11 and 2.35 eV for water solvent used B doped CdO film (Table 2). This variation may responsible for specific and non- specific interaction between solvent and solute molecules [14]. The observed lower band gap (water solvent) value could be originated from the native point defects such as oxygen vacancies and cadmium interstitials.

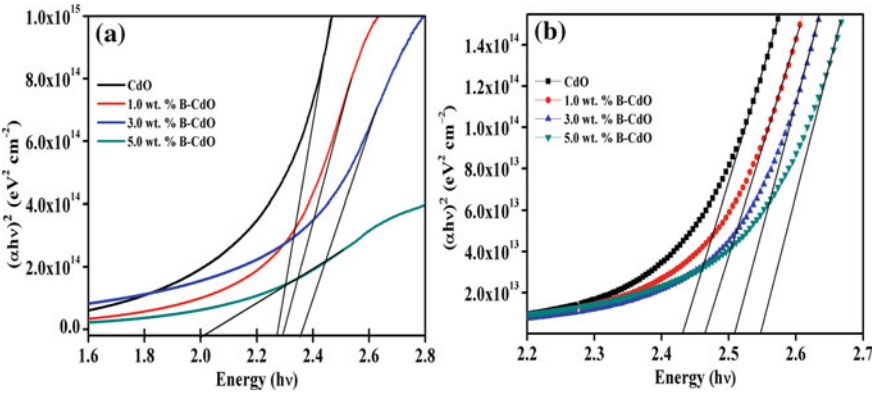

Fig. 6 Plots of hν versus $(\alpha h\nu)^2$ of undoped and B doped CdO films deposited using **a** water solvent and **b** mixed solvent

3.5 *Electrical Measurement*

The room temperature electrical properties of spray deposited undoped and B doped CdO thin films were measured by Hall measurements (Van der Pauw configuration). The variation in electrical properties such as carrier concentration (n_e), carrier mobility (μ_e), resistivity (ρ) and conductivity (σ) of undoped and B doped CdO thin films deposited using water and mixed solvent are comparatively shown in Fig. 7a–d and the measured values are given in Table 3. The negative sign of Hall coefficient confirms the *n*-type conductivity of deposited CdO thin films. From Fig. 7a, B doped CdO thin films deposited using water solvent has high carrier concentration when compared to mixed solvent. From Fig. 7b–d, mixed solvent used B doped CdO thin films show high mobility, high conductivity and low resistivity than that of water solvent used B doped CdO thin films. The carrier mobility (μ_e) of CdO thin films initially increases then decreases with increasing B doping concentration (Fig. 7b), this may be due to ionized scattering centers in CdO film.

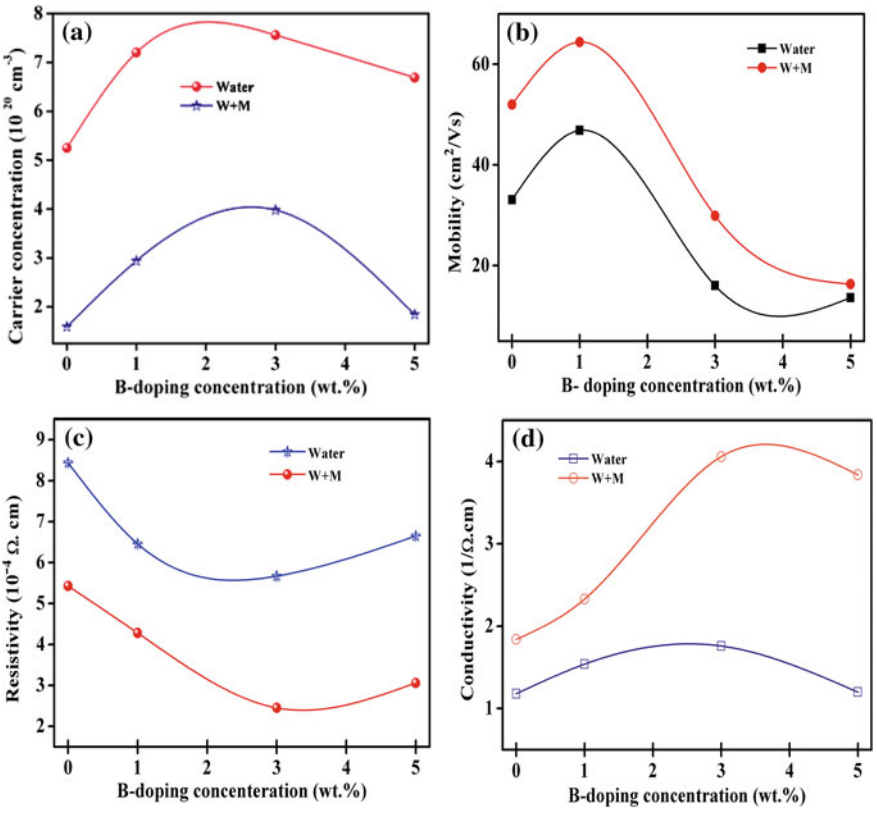

Fig. 7 Electrical properties of water and mixed solvent used undoped and B doped CdO thin films **a** carrier concentration, **b** mobility, **c** resistivity and **d** conductivity with respect to B concentration

Table 3 Comparison of electrical properties of undoped and B doped CdO thin films

B-doping (wt%)	Carrier concentration (10^{20}/cm^3)		Carrier mobility (cm^2/Vs)		Resistivity (10^{-4} Ω. cm)		Conductivity (10^3/Ω. cm)		FOM (Ω^{-1})	
	W*	(W + M)**	W*	(W + M)**	W*	(W + M)**	W*	(W + M)**	W*	(W + M)**
CdO	5.25	1.59	33.10	52.01	8.44	5.43	1.18	1.84	8.24×10^{-6}	5.19×10^{-3}
1.0 %	7.20	2.94	46.86	64.42	6.46	4.28	1.54	2.33	8.23×10^{-8}	16.2×10^{-3}
3.0 %	7.56	3.98	16.03	29.91	5.67	2.45	1.76	4.06	5.11×10^{-7}	5.17×10^{-3}
5.0 %	6.69	1.84	13.64	16.33	6.65	3.06	1.20	3.84	3.13×10^{-6}	1.68×10^{-3}

W*-water solvent, (W + M)**-mixed solvent

A low ρ (2.45×10^{-4} Ω cm) and high σ (4.06×10^{3} Ω^{-1} cm^{-1}) were obtained for 3.0 wt% B doped CdO film deposited using mixed solvent (Fig. 7c, d). Since the ionic radius of B^{3+} (0.027 nm) is smaller than that of Cd^{2+} (0.097 nm), ionic substitution is most likely happen in the present study [17]. The increasing n_e may originate from this mechanism; the substitution of B^{3+} for Cd^{2+} ions in CdO structure will result in liberating one more conduction electrons in the conduction band that may be reason for increasing n_e [18].

3.6 Opto-Electronic Properties—Figure of Merit

The figure of merit (ϕ_{TC}) plays an important role in optoelectronic device applications. In order to analyse the effect on the combination of optoelectronic performance such as figure of merit for B doped CdO thin films deposited using water and mixed solvent, the ϕ_{TC} values were calculated. The calculations were made using the formula proposed [12] for transparent conducting oxide thin films

$$\phi = \frac{T^{10}}{R_{Sh}} \tag{5}$$

where T is transmittance at a particular wavelength and R_{sh} is sheet resistance of B doped CdO thin films. Figure of merit values calculated for B doped CdO films deposited using water and mixed solvent are given in Table 3. It can be noticed that the 1.0 wt% of B doped CdO thin film deposited using mixed solvent has high figure of merit (16.2×10^{-3} Ω^{-1}). Thus the results show that the film deposited using mixed solvent has high optical transmittance, high electrical conductivity, low resistivity and high figure of merit when compared to the films deposited using water solvent.

4 Conclusion

A detailed investigation of solvent effect on the structural, microstructural, optical and electrical properties of undoped and B doped CdO thin films, deposited by cost effective spray pyrolysis technique on glass substrates was presented. It has been concluded that the solvent strongly affect the structural, optical and electrical properties of B doped CdO films. XRD study reveals that the films are polycrystalline with cubic structure and highly orientated along the (200) direction. The lattice parameter values are unaffected by variation of solvent. The growth orientation is shifted from (200) to (111) plane for B doped CdO films deposited using water and mixed solvent. The B doped CdO films deposited using mixed solvent has good crystallinity. The SEM image reveals that surface morphology of B doped

CdO thin film was effectively modified by mixed solvent. A low resistivity (2.45×10^{-4} Ω cm) with good carrier concentration (3.98×10^{20} cm^{-3}) and high optical transmittance (80 %) were obtained for 3.wt% B doped CdO thin films deposited using mixed solvent and high carrier mobility (64.42 cm^2/Vs) was obtained for 1.0 wt% B doped CdO thin film deposited using mixed solvent. The study concludes that B doped CdO films prepared using mixed solvent has uniform surface with better crystallanality, high electrical conductivity and optical transparency which could be useful for various applications.

References

1. Chopra, K.L., Major, S., Pandy, D.K.: Thin Solid Films **102**, 1 (1983)
2. Mathew, X.: J. Phys. D Appl. Phys. **33**, 1565 (2000)
3. Ferro, R., Rodriguez, J.A.: Sol. Energy Mater. Sol. Cells **64**, 363 (2000)
4. Champness, C.H., Chan, C.H.: Sol. Energy Mater. Sol. Cells **37**, 72 (1995)
5. Bhosale, C.H., Kambale, A.V., Kokate, A.V., Rajpure, K.Y.: Mater. Sci. Eng. B **122**, 67–71 (2004)
6. Powder Diffraction File, International Centre for Diffraction Data (ICDD), Reference Code: 00-005-0640
7. Chopra, K.L., Ranjan Das, S.: Thin Film Solar Cells. Plenum Press, New York (1993)
8. Khan, M.K.R., et al.: Curr. Appl. Phys. **10**, 790–796 (2010)
9. Zheng, B.J., Lian, J.S., Zhao, L., Jiang, Q.: Vacuum **85**, 861–865 (2011)
10. Moholkara, A.V., Agawanec, G.L., Sima, K.U., Kwona, Y., Rajpurec, K.Y., Kima, J.H.: Appl. Surf. Sci. **257**, 93–101 (2010)
11. Velusamy, P., Ramesh Babu, R., Ramamurthi, K., Viegas, J., Elangovan, E.: J. Mater Sci. Mater Electron **26**, 4152–4164 (2015)
12. Velusamy, P., Ramesh Babu, R., Ramamurthi, K., Dahlem, M. S., Elangovan E.: RSC Adv. **5**, 102741 (2015)
13. Bhosale, C.H., Kambale, A.V., Kokate, A.V., Rajpure, K.Y.: Mater. Sci. Eng. **122B**, 67–71 (2005)
14. Golobostanfard, M.R., Abdizadeh, H.: Ceram. Int. **38**, 5843–5851 (2012)
15. Tomakin, M.: Superlattices Microstruct. **51**(3), 372–380 (2012)
16. Elangovan, E., Ramamurthi, K.: J. Optoelectron. Adv. Mater. **5**, 45 (2003)
17. Dakhel, A.A.: Sol. Energy **82**, 513–519 (2008)
18. Dakhel, A.A.: J. Mater. Sci. **46**, 6925–6931 (2011)

AC Impedance Spectroscopy Studies of PtPc Doped Alq_3 Thin Film

M. Ramar, S.S. Rawat, R. Srivastava and C.K. Suman

Abstract The Platinum phthalocyanine (PtPc) was doped in Tris (8-hydroxyquinolinato) aluminum (Alq_3) for tailoring the electrical and optical properties. The electrical properties of the optimally doped Alq_3 thin film based on different device application were studied extensively by AC impedance spectroscopy. The absorption peak of the thin film was observed at 381 nm and 598 nm that correspond to the absorption of Alq_3 and PtPc, respectively. The photo-luminescence intensity (PL) peak of thin film excited with wavelength 380 nm was found at 510 nm. The electron mobility calculated from trap-free space-charge limited region (SCLC) of current-voltage characteristics is 0.3×10^{-7} $cm^2\ V^{-1}s^{-1}$. The frequency dependent impedance spectra show single relaxation process. The Cole-Cole plots indicates that the PtPc doped Alq_3 thin film can be represented by a single parallel resistance R_P and capacitance C_P network with a series resistance R_S. The values of R_P decreases with increase of applied bias. The variation of AC conductivity (σ_{ac}) with frequency shows two different region viz frequency dependent and frequency independent.

M. Ramar · S.S. Rawat
Academy of Scientific and Innovative Research (AcSIR), CSIR-National Physical Laboratory Campus, Dr. K. S. Krishnan Marg, New Delhi 110012, India

M. Ramar · S.S. Rawat · R. Srivastava · C.K. Suman (✉)
CSIR-Network of Institutes for Solar Energy, CSIR—National Physical Laboratory, Dr. K. S. Krishnan Marg, New Delhi 110012, India
e-mail: sumanck@nplindia.org

M. Ramar
Department of Basic Sciences, College of Fisheries Engineering, Tamil Nadu Fisheries University, Nagapattinam 611001, Tamil Nadu, India

J. Ebenezar (ed.), *Recent Trends in Materials Science and Applications*,
Springer Proceedings in Physics 189, DOI 10.1007/978-3-319-44890-9_35

1 Introduction

The organic semiconductor (OS) thin films are widely used in organic electronic and optoelectronic devices such as high efficiency organic light emitting diodes (OLEDs), organic solar cells (OSCs) and organic field-effect transistor (OFETs) [1–3]. The doping of organic semiconductors was first studied in the year 1960 [4]. It has been observed that doping is most efficient at low concentrations where the doping molecules are well separated from each other. Doping of organic semiconductor can tailor the electrical and optical properties of the intrinsic OS. Doping enables the control of energetic barriers to carrier transfer from OS to electrode (organic/metal) and from OS to OS (organic/organic) interface, leading to possibility of ohmic contacts and low operating voltages for organic semiconductor devices [5]. The dopants themselves, acting as charge scattering centers (insulator) or charge trapping sites [6], hamper charge transport, especially at high concentration. Tris (8-hydroxyquinolinato) aluminum (Alq_3) was used as on electron transport and emissive layer in OLED [7] and still remains mostly used materials. Hence tailoring the electro-optical properties of Alq_3 is highly required.

In this paper we have discussed about the AC Impedance spectroscopy studies in the broad frequency range 100 Hz–1 MHz of PtPc doped Alq_3 thin films. The optical properties has been studied and discussed by absorption and photo luminance.

2 Experimental Section

The electron only devices (EOD) were fabricated on glass substrates in the structure of Aluminium/Doped organic semiconductor/Aluminium. The thickness of active layer Platinum phthalocyanine (PtPc) doped Tris (8-hydroxyquinolinato) aluminum (Alq_3) was kept 100 nm. Both sides aluminium electrode thickness were kept constant $\sim$100 nm. The optimized doping concentration of PtPc was 6 % by weight.

Current density-voltage (*J–V*) characteristics of EOD were measured with a programmable Keithley 2400 power source. Impedance spectroscopy (IS) measurement was performed using Impedance/Gain-Phase Analyzer (Solartron, model SI 1260) System.

3 Result and Discussion

The optical properties of the thin film were studied from absorption and photoluminescence (PL) spectroscopy. Figure 1 shows the absorption and PL spectrum in the wavelength range of 200–1000 nm. The maximum absorption was observed at

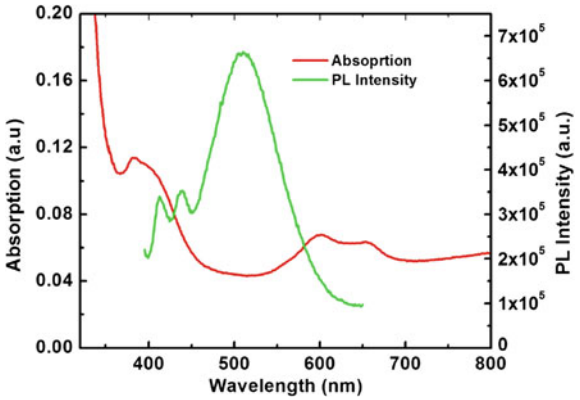

Fig. 1 Absorption and photoluminescence (PL) intensity spectra of PtPc doped Alq_3 thin film

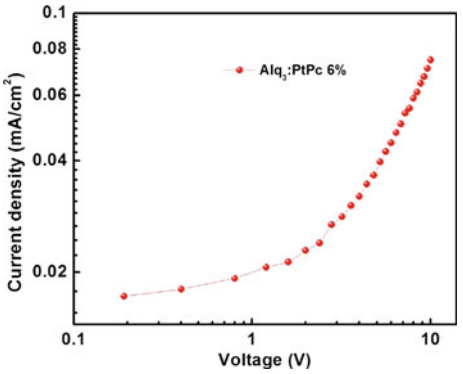

Fig. 2 Log—log plot of current density—voltage (J–V) characteristics of electron-only device

a wavelength of 381 and 598 nm which corresponds to Alq_3 and PtPc, respectively. The photo-luminescence intensity (PL) peak was observed at 510 nm, when excited by a wavelength of 380 nm. The absorption and PL both show the broad spectrum in the vicinity of the mentioned peak value.

The *J–V* characteristics of the electron only device are shown in Fig. 2. In this figure; two regions are clearly shown. At low voltage region the slope of double logarithmic *J–V* plot is ~ 1, corresponding to an Ohmic conduction mechanism and the high voltage region slope value is ~ 2, which is a sign of space-charge-limited current (SCLC) with exponential trap distributions.

This indeed indicates the significant Ohmic injection of electrons in the fabricated electron only device. To calculate the electron mobility in the trap-free SCLC region, we use the Mott-Gurney equation for trap-free SCLC [8].

$$J = \frac{9}{8}\mu\varepsilon\varepsilon_0\frac{v^2}{d^3} \tag{1}$$

where ε is the dielectric constant,ε_0 is the permittivity of free space, μ is the carrier mobility, v is the applied voltage, d is the active layer thickness and J is the current density. At high applied bias voltage, current density was found to follow Eq. (1), which could be ascribed as the field and charge carrier density dependence of the mobility. The results show that the electron mobility in the PtPc doped Alq_3 is $\sim 0.3 \times 10^{-7}$ cm^2 V^{-1} s^{-1}. The electron mobility of PtPc doped Alq_3 device is of two order increase compare to Alq_3 (mobility $\sim 0.9 \times 10^{-9}$ cm^2 V^{-1} s^{-1}) device.

Figures 3 and 4 show the frequency dependence of the real (Re Z) and imaginary (Im Z) parts of impedance at different bias voltages. The complex impedance $Z(f)$, can be represented as a function of frequency as,

$$Z(f) = Z'(f) + Z''(f) \tag{2}$$

where Z' and Z'' are the real and imaginary parts of impedance. It is observed that the magnitude of Re Z start to decreases with frequency between 150 and 1300 Hz. The magnitude of Re Z decreases with applied bias voltage changes but for all

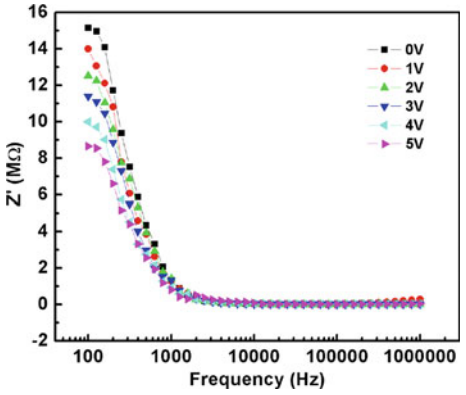

Fig. 3 The frequency dependence of the real part of impedance at different bias voltages

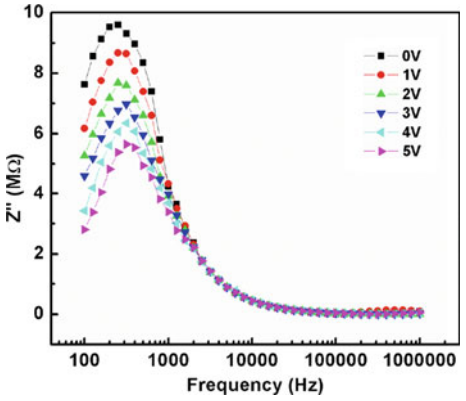

Fig. 4 The frequency dependence of the imaginary part of impedance at different bias voltages

voltage the value of Re Z merges in the above 1700 Hz. The curves also display single relaxation process and indicate an increase in ac conductivity with frequency. The ImZ reaches a maximum peak value of $Im(Z)_{max}$ for all bias voltage at different frequency. The value of $Im(Z)_{max}$ shifts to different frequency with applied bias voltage. The frequency corresponding to Im $(Z)_{max}$ called relaxation frequency shifts to lower values with increase of applied bias voltage. This is an indication of increasing loss in the materials with increase of applied bias voltage.

The Cole-Cole plots of the ReZ and ImZ at frequency range of 100 Hz–1 MHz for different dc bias voltages for the electron only device are shown in Fig. 5. The plot shows a single semicircle at bias voltages 0–5 V and the size of the semicircle decreases simultaneously as the dc bias voltage increases. Therefore, the PtPc doped Alq_3 device can be modeled as an RC equivalent electrical circuit of which a contact series resistance R_S with a single parallel resistance (R_P) and the capacitance (C_P) network. The impedance of the RC equivalent electrical circuit can be giving by [9]

$$Z = \mathrm{Re}Z + i\mathrm{Im}Z$$

$$Z = \left[R_S + \frac{R_P}{1+\omega^2 R_P^2 C_P^2}\right] - i\left[\frac{\omega R_P^2 C_P}{1+\omega^2 R_P^2 C_P^2}\right] \tag{3}$$

By eliminating the angular frequency, the semicircle of the Cole-Cole plot can be written as

$$\left[\mathrm{Re}Z - \left(R_S + \frac{R_P}{2}\right)\right]^2 + (-\mathrm{Im}Z)^2 = \left(\frac{R_P}{2}\right)^2 \tag{4}$$

This relation defines a circle centered at (R_S + R_P/2, 0) with radius of R_P/2. The minimum ReZ value represents R_S and it is almost same at different applied bias voltage. The R_S can be considered as originating from the electrode contact. The maximum ReZ value corresponds to the summation of R_S and R_P to the capacitance. The capacitance C_P increases with increase of applied bias voltage, but the R_P decreases as the applied bias voltage increases are shown in Fig. 6.

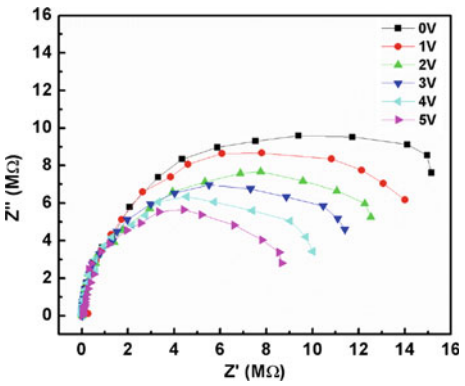

Fig. 5 Cole-Cole plots at various bias voltages

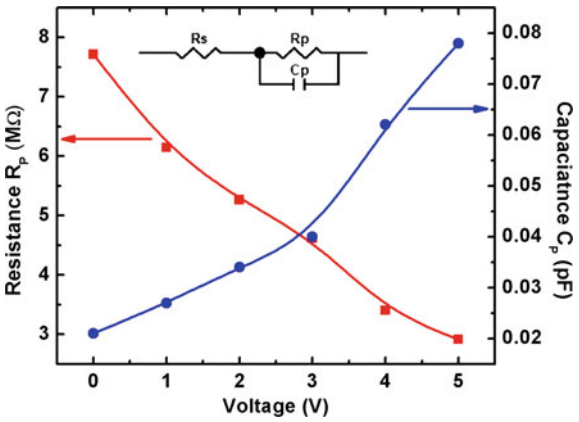

Fig. 6 The variation of parallel resistance R_P and capacitance C_P with bias voltages (*Inserted figure* shows that the RC equivalent circuit)

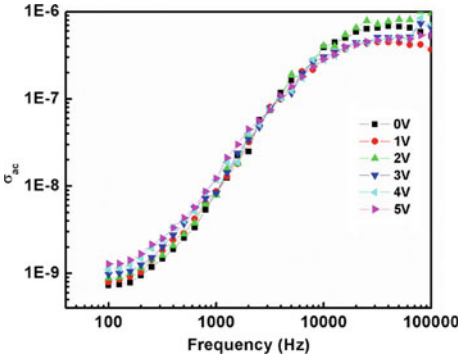

Fig. 7 The frequency dependent conductivity at different bias voltages

The decrease of R_P with bias voltage is then due to a large number of injected electrons increase as the bias voltage increases. This also indicates that the effective conductivity of the organic material will increase with the bias voltage.

The ac electrical conductivity was obtained by the relation [10]

$$\sigma_{ac} = \frac{l}{AZ'} \tag{5}$$

where l is the thickness of sample, A is the area and Z' is the impedance. Figure 7 shows the variation of ac conductivity with frequency at different bias voltages. It is clear that the ac conductivity increases with increasing frequency. For all the voltages, there are two different regions in the ac conductivity, the frequency independent and dependent region. The onset (switch from frequency-independent to frequency-dependent region) shifts towards higher side with applied bias voltages. The frequency dependent region display a power law dependence as predicted for conducting materials by [11].

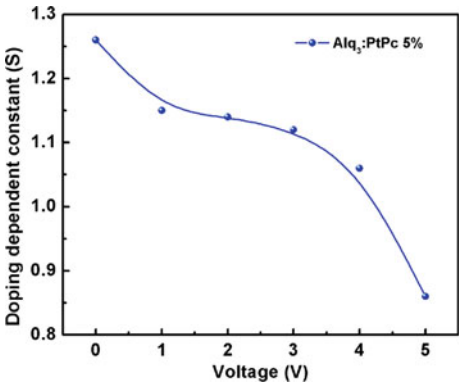

Fig. 8 The voltage dependent S for Al/Alq_3: PtPc/Al device

$$\sigma_{ac} = \sigma_{dc} + A\omega^s \tag{6}$$

where σ_{ac} is the frequency-independent conductivity, ω. is the angular frequency of the applied AC electric field in the frequency sensitive region, A and S ($0 \leq S \leq 1$) were material and doping dependent constants. It is found that the value of S decreases with applied bias voltage increases as shown in Fig. 8. The trend of exponent value S can be explained by correlated barrier hopping (CBH) model.

4 Conclusion

The absorption peaks are found for both Alq_3 and PtPc indicating homogeneous distribution of both molecules in the thin film. The electron mobility of doped Alq_3 is 0.3×10^{-7} cm^2 V^{-1} s^{-1} which is two times higher than the pristine Alq_3. The electron only device of doped Alq_3 can be modeled as an equivalent parallel RC network as observed by Cole-Cole plot. The R_P and C_P are highly dependent on voltage. The ac conductivity is found to obey universal power law. The exponent 's' can be well explained by CBH model.

Acknowledgements The authors gratefully recognize the financial support from the Council of Scientific and Industrial Research (CSIR), New Delhi, India.

References

1. Cao, Y., Yu, G., Zhang, C., Menon, R., Heeger, A.J.: Synth. Met. **87**, 171 (1997)
2. Zhang, F., Johansson, M., Andersson, M.R., Ummelen, J.C., Inganas, O.: Adv. Mater. **14**, 662 (2002)
3. Ramar, M., Tyagi, P., Suman, C.K., Srivastava, R.: RSC Adv. **4**, 51256 (2014)

4. Pope, M., Swenberg, C.E.: Electronic Process in Organic Crystals and Polymers. Oxford University Press, Oxford (1999)
5. Zhou, X., Pfeiffer, M., Blochwitz, J., Werner, A., Nollau, A., Fritz, T., Leo, K.: Appl. Phys. Lett. **78**, 410 (2001)
6. Matsushima, T., Adachi, C.: Thin Solid Films **517**, 874 (2008)
7. Tang, C.W., Vanslyke, S.A.: Appl. Phy. Lett. **51**, 913 (1987)
8. Mott, N.F., Gurney, R.W.: Electronic Processes in Ionic Crystals, 2nd edn. Oxford University, Oxford (1948)
9. Macdonald, J.R.: Impedance Spectroscopy. Wiley, New York (1987)
10. Suman, C.K., Prasad, K., Choudhary, R.N.P.: Adv. Appl. Ceram. **104**, 294 (2005)
11. Jonscher, K.: Nature **267**, 673 (1977)

Microstructure and Phase Transformation Behaviour of Co–Ni–Al Alloy by Spark Plasma Sintering

G. Johnsy Arputhavalli, S. Agilan and Roy Johnson

Abstract The CoNiAl alloys are prepared by using the spark plasma sintering (SPS) technique. The present study investigates the crystalline structure, Phase analyses, Physical and mechanical properties of the stoichiometric $Co_{38}Ni_{35}Al_{27}$ alloys. The significant control over the magnetic and structural transformation temperature and high ductility of CoNiAl makes it a potential high-temperature Ferromagnetic shape memory alloy (FSMA). The test specimens were prepared at SPS temperature of 1000 °C at a sintering pressure of 50 MPa. The microstructural identification and the phase analyses of the mechanically alloyed powders and the SPS sintered specimens were investigated using optical microscopy, scanning electron microscopy and X-ray diffraction. The room temperature XRD results revealed that the sintered samples have body centred cubic β phase. A comparison of the room temperature XRD results for alloy powders and that of the sintered alloys has been studied. From the SEM images, we observe that the sintered alloys have martensitic twin variants. Also in the optical microscope, we observe the martensitic variants in the β phase structure. From the thermal studies, we analysed the phase transformation behaviour of the sample from β' martensite to β martensite at 120°.

G.J. Arputhavalli (✉)
Department of Physics, Karunya University, Coimbatore, Tamilnadu, India
e-mail: johnsyjane@karunya.edu

S. Agilan
Department of Physics, Coimbatore Institute of Technology, Coimbatore, Tamilnadu, India

R. Johnson
Centre for Ceramic Processing, ARCI, Hyderabad, Tamilnadu, India

J. Ebenezar (ed.), *Recent Trends in Materials Science and Applications*,
Springer Proceedings in Physics 189, DOI 10.1007/978-3-319-44890-9_36

1 Introduction

The study of ferromagnetic shape memory alloys (FSMAs) is of great interest because of its high-speed actuation system. The development of sensor and actuator based application requires high-speed actuation mechanism. The application of magnetic field creates large strain in FSMA which leads to high-speed actuation system [1]. Among several ferromagnetic alloys, like Ni–Mn–Ga [2, 3], Ni–Mn–Al [4], Fe–Pd [5, 6], Fe–Pd–Cu [7], etc., Co–Ni–Al alloys are promising FSMAs because of their higher ductility and a large range of control over the magnetic and structural transformation temperatures [8–11]. Though we find many potentials like large magnetic field induced strain in Ni–Mn–Ga, their brittleness is a significant drawback in these kinds of alloys. In this regard, efforts have been made in searching for other kinds of FSMA alloys; particularly Cobalt based alloy systems, such as Co–Ni–Ga [12] and Co–Ni–Al [13]. The present study is concerned with the Co–Ni–Al system.

The method of preparing alloy and its chemical compositions strongly influences the MT temperature, phase structure and crystal structure. The $\beta + \gamma$ two-phase alloy has good ductility compared to single β phase alloy, which has a great advantage for practical application [13]. By considering the above factors, we obtain the $\beta + \gamma$ two-phase alloy having the stoichiometric composition as $Co_{38}Ni_{35}Al_{27}$ through spark plasma sintering technique. In the literature, we find arc melting method and Bridgman method for the preparation of CoNiAl alloy [14, 15]. Among several method of preparing the alloy, Powder metallurgy (PM) technique is believed as a selected method for the improvement in ductility. Particularly SPS is a new method to compact the alloy powders with less sintering temperature and high sintering rate, which produce a dense, less porous and fine grained alloy in less time interval. These factors make uniqueness and advantageous over other conventional sintering techniques [16–18], So far, only a few investigations have been reported for Ni–Mn–Ga, Cu–Ni–Al, Ti–Ni alloys fabricated by the SPS method. We obtain highly dense alloy through SPS sintering method and the sample exhibited a hardness of 373 VHN. The crystalline structure $\beta + \gamma$ phase attributes the good ductility nature. Hence, in the present investigation, we discuss the crystalline structure and Phase constitution of SPS sintered $Co_{38}Ni_{35}Al_{27}$ alloy. To the best of our knowledge, this may be the first investigation on SPS sintered Co–Ni–Al alloy system.

2 Experimental Details

Co–Ni–Al polycrystalline pellets of 20 mm diameter were produced using spark plasma sintering method under ambient atmosphere. High purity raw materials in the form of few micron size powder were purchased from sigma Aldrich

(Co-99.9 %), (Ni-99.99 %) and (Al-99.9 %). These powders were taken under proper stoichiometric proportion and mechanically grounded for two hours. These stoichiometric $Co_{38}Ni_{35}Al_{27}$ alloy powders were sintered to 20 mm disks by SPS with Dr. Sinter 1050, Sumitomo Coal Mining Co Ltd, Kanagawa, Japan. A schematic picture of the die, punches, and spacers is shown in Fig. 1. The SPS system was evacuated to 5 Pa and uniaxial pressure of 50 MPa was applied with a heating rate of 150 °C/min to peak temperatures of 1000 °C with a dwell time of 5 min. The sintered samples were furnace cooled to room temperature and the SPS pellets were grounded to remove the carbon contamination. The analysis of the crystal structures and phases of the alloy powder and the SPS sample were carried out with X-ray Diffractometer using Cu–Kα radiation at room temperature (Shimadzu XRD-6000 instrument). The Surface morphology and compositional analysis were analyzed by using Joel scanning electron microscope with an attached energy dispersive spectrometer (EDS). The surface morphology was also analyzed by Optical Microscope. The thermal studies of the SPS alloy were analysed using the thermal analyzer (STA 449 F3, Netzsch, Germany) provided with the platinum heating element and *S*-type thermocouple used for DSC analysis. The bulk density of the sintered samples was measured by adopting the ASTM C373 procedure using

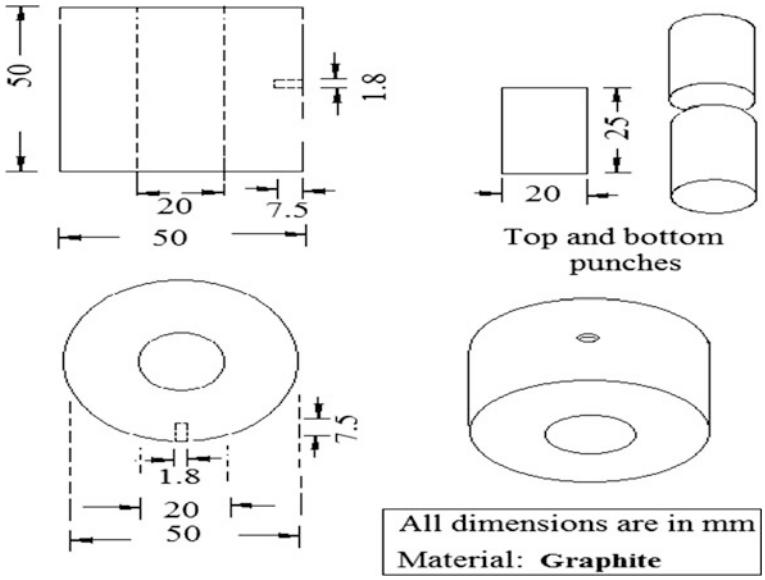

Fig. 1 Schematic drawing to the scale and the dimensions of the die, punches, and spacers that were used to process $Co_{38}Ni_{35}Al_{27}$ alloy

an analytical balance with density measuring kit (LA 120S, Sartorius AG Germany). The hardness values of the cut samples were determined by Vickers hardness testing (Leco, St. Joseph, MI) ASTM C-1327.

3 Result and Discussion

3.1 Structural Studies

The XRD pattern of metal mix powder and the SPS Alloy indicates in Fig. 2, shows a favourable orientation along (110) plane. The other high-intensity planes for the powder alloy that are observed in the spectra are also the typical peaks of Co–Ni–Al alloy. Similar observations are also made by Liu et al. in cubic β structure [19]. The ordered β phase structure confirms the austenite phase with the lattice parameter a = 11.39 Å. The crystalline planes of the Co–Ni–Al alloy and the JCPDS data (file no-654244) are compared [20]. The data shows that the cubic β phase peak of SPS alloy is shifted towards the lower angle side by 0.2°, which may be due to the existence of internal stress in the SPS alloy.

The powdered alloy XRD pattern shows the absolute polycrystalline growth of cubic β structure at (110), (200), (002), (211) and (311) planes and γ structure at (111), (200), (220) and (202) planes. Two XRD reflections for the SPS alloy observed at 44.5° and 82.3° are corresponding to (110) and (211) respectively, which indicates that the alloy is in a martensite phase with the cubic structure a = 11.39Å. The e/a ratio of the cubic structure $Co_{38}Ni_{35}Al_{27}$ was found to be 7.73.

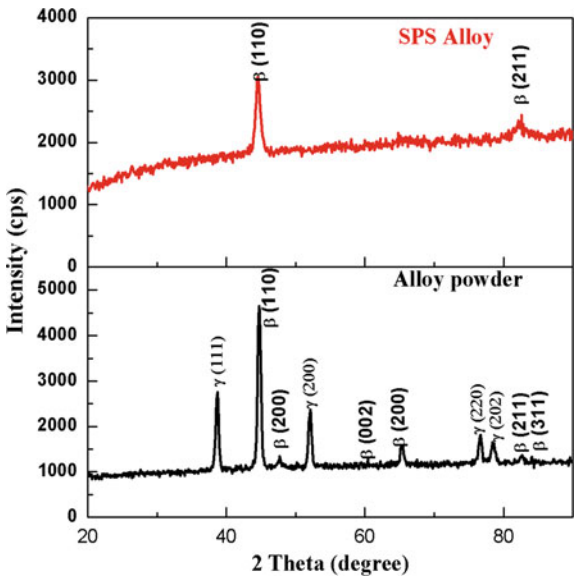

Fig. 2 X-ray diffraction pattern of $Co_{38}Ni_{35}Al_{27}$ alloy powder and $Co_{38}Ni_{35}Al_{27}$ SPS alloy at room temperature. The Co rich sample indicates the highly ordered β phase cubic structure and few γ structures

3.2 *Microstructural and Compositional Analysis*

Figure 3 shows the microstructure of the SPS alloy. The SEM and the optical image shows that the sintered specimens have no evident of pores and with nearly fully dense compacted alloy, which was consistent with the results of the measured density. The Fig. 3a, b shows the microstructural images of SPS alloy which has both β phase and γ phase structure. It also shows the grain and grain boundary corresponding to β phase and γ phase (white patches) respectively. The γ phase is known to improve the ductility of the brittle β phase [18]. From Fig. 3c we infer that when the rate of sintering process was high, the diffusion rate was also high. Also, it is clear that the sintering temperature has a minor impact on the density and hardness of the alloy, which indicates that the milled powders sintered at 1000 °C can produce a fully dense compact. Further increasing the sintering temperature does not improve the densification further; however, the microstructure and phase constitutions vary with sintering temperature [21]. In Fig. 3d, during cooling the

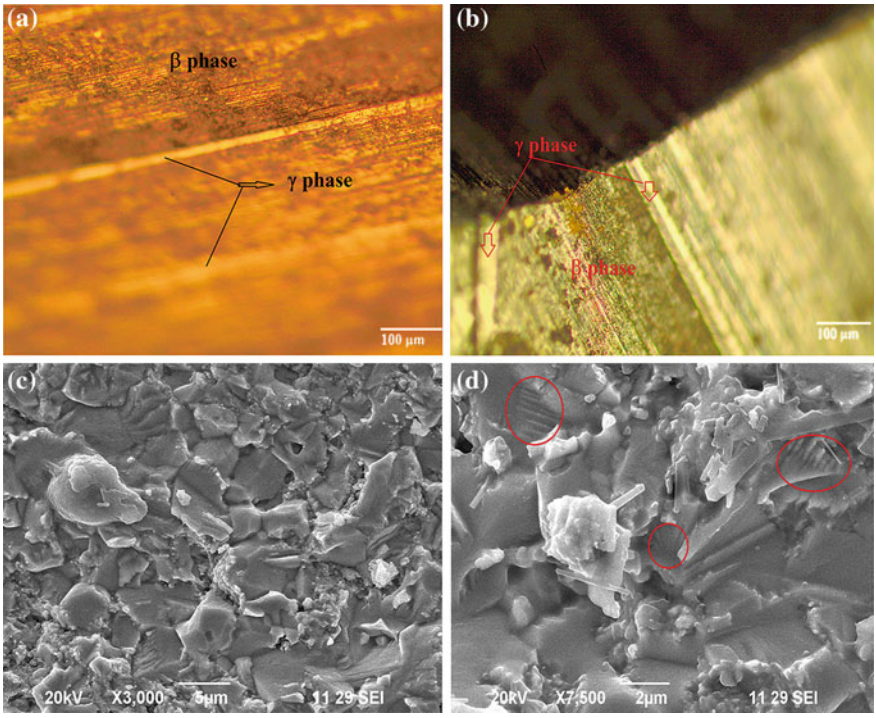

Fig. 3 SEM and optical micrograph of $Co_{38}Ni_{35}Al_{27}$ SPS alloy shows the existence of martensitic plate in the austenite matrix

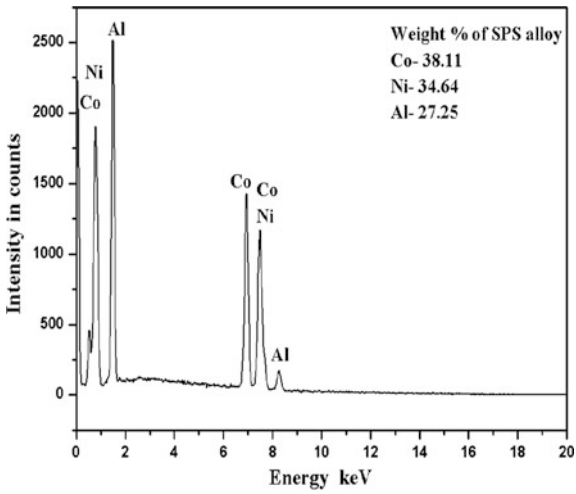

Fig. 4 EDS spectrum of $Co_{38}Ni_{35}Al_{27}$ SPS alloy

sample, we observe that the lamellar microstructure in the SEM shows that they are partially martensitic in the austenitic matrix. The same kind of microstructure was also observed by [22, 23]. The starting ratios of powder metal taken for alloying are Co-38 %, Ni-35 % and Al-27 %. From the Fig. 4, it is clear that the weight percentage of the SPS alloy is same as that of the powdered metal taken for alloying. This shows that the milling process undergone for several hours has yielded the desired result.

3.3 Thermal Studies

TG and DSC curves recorded for powder mix sample and SPS samples are shown in Figs. 5 and 6. In (Fig. 5) the powder mix sample exhibited an exothermic peak at around 635 °C, which indicates that the exothermic corresponds to the reaction between the cobalt, nickel and aluminium to form an alloy. In (Fig. 6) the SPS sample exhibited two endothermic peaks during heating, which may correspond to β′ martensite to β martensite at around 120°, this is followed by a small exothermic peak at 360°, which may be due to continuous ordering of β martensite, after that no peak has been observed. The SPS sample shows very high thermal stability with almost nil TG response. Further, no endothermic or exothermic DSC peaks were observed indicating the absence of any thermal events. It can also be inferred from the comparative evaluation of the (Figs. 5 and 6) that the formation of the eutectic under SPS conditions leads to alloying.

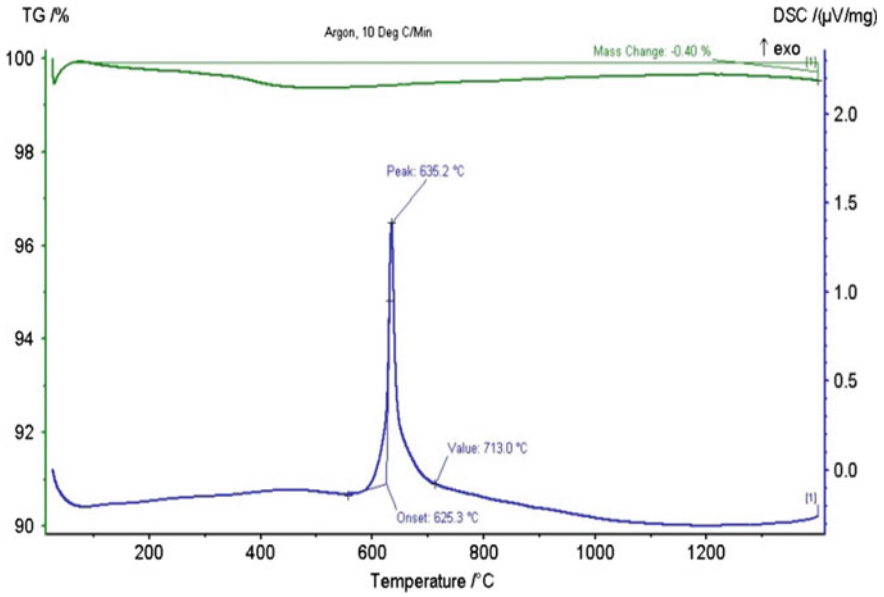

Fig. 5 TG and DSC *curves* recorded for powder $Co_{38}Ni_{35}Al_{27}$ metal mix

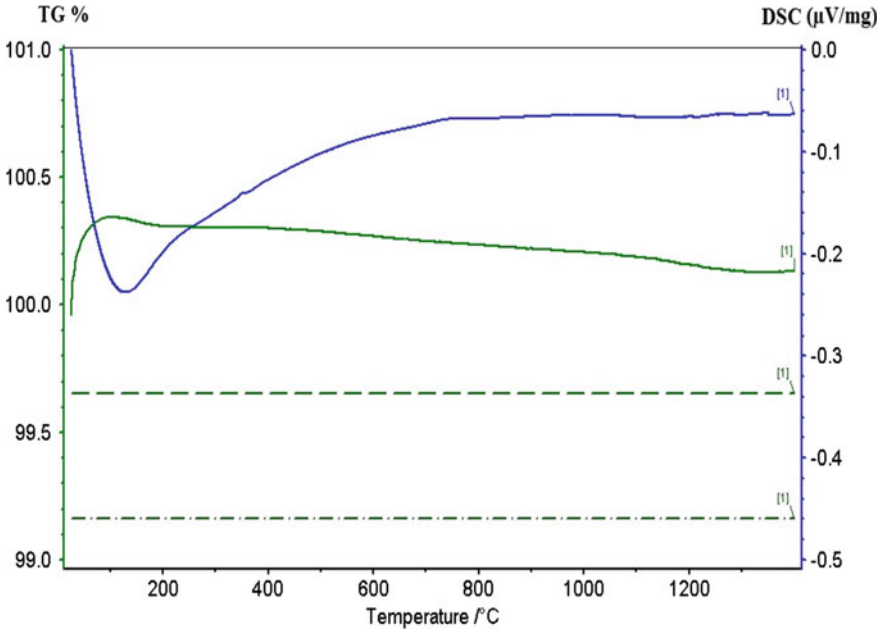

Fig. 6 TG and DSC *curves* recorded for SPS pellets

3.4 Density and Hardness Measurements

Bulk densities of the sintered samples were measured by using the analytical balance with density measuring kit. The bulk density was found by the relation,

$$\text{Bulk Density} = \text{D}/(\text{W} - \text{S})$$

The Spark Plasma Sintered CoNiAl has resulted in the sintered density of 5.88 g/cc. We observed rapid densification process have taken place with the mechanical pressure of 50 MPa in combination with the rapid heating rates of 150 ° C/min and the pulsed direct current electric field. Application of 50 MPa pressure has not only broke the agglomerates but also eliminates the pores from compacts coupled with enhanced diffusion. Rapid sintering rate surpasses the low-temperature regimes and reaches the elevated temperature regime where densifying mechanisms (grain boundary and volume diffusion) are predominant. Further, the direct current pulses generate spark discharges and plasma between the powder particles which clean the surfaces from adsorbed chemical species for enhanced grain-boundary diffusion and also results in Joule heating.

The cut sample was mounted using acrylate based resin moulds and grinding and polishing machine (Struers, Tegraforce-5, Germany) is used for grinding and polishing of the sample. Hardness values are measured as an average of five indents. The sample exhibited a hardness of 373 VHN that can be attributed to the density of 5.88 g/cc in combination with the finer grain sizes. From this, we infer that because of the finer grain size, a large fraction of the atoms resides in the grain boundaries.

4 Conclusion

Co-Ni-Al polycrystalline pellets have been prepared by spark plasma sintering technique after grinding the powder for two hours. The alloy sintered at 1000 °C was found to be completely dense compact, and the increased sintering temperature does not affect the hardness of the sample. From the XRD pattern of the SPS alloy, we observe that the alloy is in highly oriented martensite phase with cubic structure. The microstructure of alloy is composed of lamellar and $\beta + \gamma$ phase structure, which prove the ductile nature of the alloy. The SEM shows that they are partially martensitic in the austenitic matrix. The phase transformation from β' martensite to β martensite was observed in the DSC studies and the formation of eutectic behaviour is observed for SPS conditions.

References

1. Matsunaga, Y., Tagawa, T., Wada, T., Taya, M.: Design of ferromagnetic shape memory alloy composites based on TiNi for robust and fast actuators, smart structures and materials 2002. Act. Mater Behav. Mech. **172**, Proc. SPIE 4699 (2002)
2. Pushpanathan, K., Sathya, S., Ravichandran, S.: Structural and magnetic transformation in ferromagnetic Ni–Mn–Ga alloy. Proc. Indian Natl. Sci. Acad. **79**(3), 373–378 (2013)
3. Jesintha Rani, R., Senthur Pandi, R., Seenithurai, S., Vinodh Kumar, S., Muthuraman, M., Mahendran, M.: Structural, thermal and magnetic characterization of Ni–Mn–Ga ferromagnetic shape memory alloys. Am. J. Condens. Matter Phys. **1**(1), 1–7 (2011)
4. Famodu, O.O., Hattrick-Simpers, J., Aronova, M., Chang, K.-S., Murakami, M., Wuttig, M., Okazaki, T., Furuya, Y., Knauss, L.A., Bendersky, L.A., Biancaniello, F.S., Takeuchi1, I.: Combinatorial investigation of ferromagnetic shape-memory alloys in the Ni–Mn–Al ternary system using a composition spread technique. Mater. Trans. **45**(2), 173–177 (2004)
5. Pérez-Landazábal, J.I., Lambri, O.A., Bonifacich, F.G., Sánchez-Alarcos, V., Recarte, V., Tarditti, F.: Influence of defects on the irreversible phase transition in FePd ferromagnetic shape memory alloys. Acta Materialia. **86**, 110–117(2015)
6. Cui, J., Shield, T.W., James, R.D.: Phase transformation and magnetic anisotropy of an iron–palladium ferromagnetic shape-memory alloy. Acta Mater. **52**, 35–47 (2004)
7. Hamann, S., Gruner, M.E., Irsen, S., Buschbeck, J., Bechtold, C., Kock, I., Mayr, S.G., Savan, A., Thienhaus, S., Quandt, E., Fähler, S., Entel, P., Ludwig, A.: The ferromagnetic shape memory system Fe–Pd–Cu. Acta Mater. **58**, 5949–5961 (2010)
8. Hamilton, R.F., Sehitoglu, H., Efstathiou, C., Maier, H.J., Chumlyakov, Y.: Pseudoelasticity in Co–Ni–Al single and polycrystals. Acta Mater. **54**, 587–599 (2006)
9. Morito, H., Oikawa, K., Fujita, A., Fukamichi, K., Kainuma, R., Ishida, K.: Large magnetic-field-induced strain in Co–Ni–Al single-variant ferromagnetic shape memory alloy. Scripta Mater. **63**, 379–382 (2010)
10. Lu, J.B., Shi, H., Sedlakova-Ignacova, S., Espinoza, R., Kopeček, J., Sittner, P., Bartova, B., Schryvers, D.: Microstructure and precipitates in annealed $Co_{38}Ni_{33}Al_{29}$ ferromagnetic shape memory alloy. J. Alloy. Compd. **572**, 5–10 (2013)
11. Bartova, B., Wiese, N., Schryvers, D., Chapman, J.N., Ignacova, S.: Microstructure of precipitates and magnetic domain structure in an annealed $Co_{38}Ni_{33}Al_{29}$ shape memory alloy. Acta Mater. **56**, 4470–4476 (2008)
12. Dogan, E., Karaman, I., Chumlyakov, Y.I., Luo, Z.P.: Microstructure and martensitic transformation characteristics of CoNiGa high temperature shape memory alloys. Acta Materialia. **59**, 1168–1183 (2011)
13. Oikawa, K., Ota, T., Gejima, F., Ohmori, T., Kainuma, R., Ishida, K.: Phase equilibria and phase transformations in new B2-type ferromagnetic shape memory alloys of Co–Ni–Ga and Co–Ni–Al systems. Mater. Trans. **42**(11), 2472–2475 (2001)
14. Hamilton, R.F., Sehitoglu, H., Efstathiou, C., Maier, H.J., Chumlyakov, Y.: Pseudo elasticity in Co–Ni–Al single and polycrystals. Acta Mater. **54**, 587–599 (2006)
15. Lu, J.B., Shi, H., Sedlakova-Ignacova, S., Espinoza, R., Kopeček, J., Sittner, P., Bartova, B., Schryvers, D.: Microstructure and precipitates in annealed $Co_{38}Ni_{33}Al_{29}$ ferromagnetic shape memory alloy. J. Alloy. Compd. **572**, 5–10 (2013)
16. Munir, Z., Anselmi-tamburini, U., Ohyanagi, M.: The effect of electric field and pressure on the synthesis and consolidation of materials: a review of the spark plasma sintering method. J. Mater. Sci. **41**, 763–777 (2006)
17. Eugene, A.O., Sastry, K., Ludo, F.: Consolidation enhancement in spark-plasma sintering: Impact of high heating rates. J. Appl. Phys. **102**, 114913 (2007)
18. Ishida, K., Kainuma, R., Ueno, N., Nishizawa, T.: Ductility enhancement in NiAl (B2) base alloys by microstructural control. Metall. Trans. A **22A**, 441 (1991)
19. Liu, Z.H., Wang, H.Y., Yu, S.Y., Dai, X.F., Chen, J.L., Wu, G.H., Liu, Y.: Phase equilibrium of ferromagnetic shape memory alloy $Co_{39}Ni_{33}Al_{28}$. Scripta Mater. **54**, 1299–1304 (2006)

20. Lu, X.S., Li, F.H.: Acta Phys. Sinica: WulimXuebao. **29**, 182 (1980)
21. Li-hua, C., Yu-yong, C., Lai-qi, Z., Jun-pin, L.: Effect of spark plasma sintering temperature on microstructure and mechanical properties of melt-spun TiAl alloys. Trans. Nonferrous Met. Soc. China **22**, 528–533 (2012)
22. Scheerbaum, N., Kraus, R., Liu, J., Skrotzki, W., Schultz, L., Gutfleisch, O.: Reproducibility of martensitic transformation and phase constitution in Ni–Co–Al. Intermetallics **20**, 55–62 (2012)
23. Efstathiou, C., Sehitoglu, H., Wagoner Johnson, A.J., Hamilton, R.F., Maier, H.J., Chumlyakov, Y.: Large reduction in critical stress in Co–Ni–Al upon repeated transformation. Scripta Materialia. **51**, 979–985 (2004)

Synthesis and Characterization of Bay Substituted Perylene Diimide Small Molecule for Organic Solar Cell Application

R. Ganesamoorthy, G. Sathiyan, R. Thangamuthu and P. Sakthivel

Abstract We report the synthesis of *N*,*N*′-Bis(hexyl)-1,7-di(thiophenyl)perylene-3,4:9,10-tetracarboxylic acid diimide (T-PDI-H) based small molecule by Suzuki coupling method for organic photovoltaic (OPV) application. The synthesized small molecule was confirmed by FT-IR and NMR techniques. The T-PDI-H showed broad and strong absorption in the UV-Visible region. From UV-Visible spectra we observed a low optical band gap (E_g^{opt}) of 1.96 eV for T-PDI-H. From the cyclic voltammetry, the calculated HOMO, LUMO and electrochemical band gap (E_g^{ele}) for the small molecule was −5.77, −3.44 and 2.33 eV respectively. Thermogravimetric analysis was employed to elucidate the thermal stability of T-PDI-H small molecule, it showed good thermal stability up to 400 °C. The preferred property for the high power conversion efficiency (PCE) OPV device, molecule must possess broad and strong absorption in the UV-Vis region, low band gap, and high thermal and environmental stability. T-PDI-H small molecule might satisfy the above standards with the chance to give maximum power conversion efficiency (PCE).

1 Introduction

Bay substituted, conjugated perylene diimide based polymers and small molecules were versatile building block for OPV's as well as hybrid photovoltaics [1, 2]. Importance of PDI's in the OPV to convert the enormous light energy into electricity mainly relied on its solubility, conductivity, band gap and solar spectrum matched absorption in the UV-Vis to near IR region [3]. The OPV's were low cost, very cheap, light weight, elastic, easily producible and cost effective solution

R. Ganesamoorthy · G. Sathiyan · P. Sakthivel (✉)
Department of Chemistry, School of Advanced Sciences, VIT University, Vellore 632014, India
e-mail: sakthivel.p@vit.ac.in

R. Thangamuthu
Electrochemical Materials Science Division, CSIR-Central Electrochemical Research Institute, Karaikudi 630006, India

J. Ebenezar (ed.), *Recent Trends in Materials Science and Applications*, Springer Proceedings in Physics 189, DOI 10.1007/978-3-319-44890-9_37

processing than compared with the classical inorganic silicon based solar cells [4]. The drawbacks of OPV were low PCE (1.5–2.5 %) for commercial devices and very short life time [5].

The fundamental part of the OPV was the active layer coating. The active layer coating was sandwiched between the cathode and anode. Active layer was fabricated with an electron donating small molecule or high molecular weight conjugated polymer as the donor and high electron affinity small molecule, polymer or fullerene derivatives as an acceptor in a blend or a bilayer form [6]. If the active layer was a blend means it was called as a bulk heterojunction solar cell (BHJ). Photo induced electron transfer from the electron rich donor to electron deficient acceptor was the reason behind the conversion of white sun light into electricity which hanged on the ionization potential of the donor and electron affinity of the acceptor [6]. First PDI small molecule dye with regioisomers was introduced in 1986 as an acceptor in bilayer OPV by Tang [7]. Polymers and small molecules of PDI based dyes were reported as an acceptor in OPV's [8, 9]. The drawbacks of perylene polymers were reproducibility, solubility and pureness [10]. On the other hand in the case of small molecules it was contrary and bulk preparation in short span of time was possible [11]. Various modification was introduced on the perylene core to boost the PCE of the perylene based OPV's. Imide group functionalization was the one which resulted in the increase of solubility properties but it didn't not show any significant change in the electrochemical and optical properties [6]. Second one was the bay substitution, especially with an electron donating molecule, resulted the improvement of energy levels with the improvement of optical and electrochemical properties [9, 10]. In PDI's bay position was substituted with highly steric bulky group would hinder the π-π non-covalent interactions which in turn decrease the aggregation and increase the charge transport properties [6].

Highly electron deficient and charge transporting PDI based small molecules and polymers were most widely used as electron acceptors [12–14]. Chen et al. [15] first introduced the new D-A-D type perylene diimide dye which containing the oligothiophene in the bay position in 2005. After six years back Perrin et al. analysed the effect of substituents at the bay position of the perylene core [16]. They concluded that electron withdrawing group in the bay position would increases the electron accepting *n*-character and in the presence of highly electron donating group would enhance the p-character. In 2011 Choi et al. [17] synthesised a bay annulated D-A-D type small molecule which showed very good hole mobility and he used it as a donor in BHJ-OPV and reported 1.42 % of PCE. In 2012 Balaji et al. [18] reported another D-A-D type PDI dye which had the electron donating pentathiophene at the bay position. They found the important property of the perylene core that was the conversion of *n*-type character to *p*-type character after the thermal annealing process. In 2014 Dinçalp et al. [19] reported a benzimidazole substituted PDI and studied the role of bulky group in the bay position of the small molecule and they used it as donor and achieved 0.01 % PCE. From the above results it was clear more steric and high electron donating moiety in the bay position of the perylene core would yield a very good donor small molecule for OPV applications.

In this paper, we reported the synthesis and the characterization of bay substituted D-A-D type perylene based small molecule donor in which we examined the role of thiophene moiety in the absorption, optical, electrochemical band gap, thermal stability, highest occupied molecular orbital (HOMO) and lowest unoccupied molecular orbital (LUMO) energy level.

2 Experimental

2.1 Chemicals

High purity analytical grade (A.R) chemicals were purchased and used as received from the reputed chemical suppliers. Bromine, dichloromethane (DCM), tetrahydrofuran (THF), hydrochloric acid (37 % HCl), Conc. H_2SO_4, anhydrous potassium carbonate and anhydrous magnesium sulphate were purchased from SD fine chemicals. 2-isopropoxy-4,4′,5,5′-tetramethyl-1,3,2-dioxaborolane, perylene-3,4,9,10-tetracarboxylic dianhydride (PTCDA) and $Pd(PPh_3)_4$ were purchased from Sigma Aldrich, Mumbai, India. *N*-methylpyrolidinone (NMP), *N*-butyl lithium (2.5 M in hexane), acetic acid and *N*-hexylamine were supplied by Alfa Aesar. Conventional methods were used to purify the solvents prior to the usage.

2.2 Synthesis of 4,4,5,5-Tetramethyl-2-(Thiophen-2-Yl)-1,3,2-Dioxaborolane (TBPE)

The synthetic procedure for the preparation of TBPE was followed from the previous report by Jeon et al. [20]. 40 mL (100 mmol) of n-Butyllithium (2.5 M solution in hexane), was added dropwise into a solution of thiophene 8.41 mL, (50 mmol) in 100 mL of tetrahydrofuran at −78 °C under an inert nitrogen atmosphere. The resulting reaction mixture was stirred at −78 °C for 1 h, and then 2-isopropoxy-4,4,5,5-tetramethyl-1,3,2-dioxaborolane 20.39 mL, (100 mmol) was injected into the flask, and the new solution was warmed to room temperature and stirred for another 12 h. After cooling to room temperature reaction mixture was poured into the ice water and extracted with DCM. The extract was washed with brine and dried over anhydrous sodium sulphate. After evaporation of the solvent, the residue was purified by column chromatography using hexane as an eluent to afford the product as light green crystals. M. F: $C_{10}H_{15}BO_2S$. Yield: 25 %, m.p-65–70 °C, ^{1}H-NMR [400 MHz, $CDCl_3$, δ = 7.26, s]: 7.65–7.62 (dd, thiophene, 2H), 7.20–7.16, (t, thiophene H, 1H). ^{13}C-NMR [400 MHz, $CDCl_3$, δ = 77.16, 3 peaks]: 137.1, 132.3, 128.1, (thiophene carbon) 84.0, (carbon attached with boron), 24.7 (methyl carbon).

2.3 Synthesis of 1,7-Dibromo-Perylene-3,4,9,10-Tetracarboxylic Dianhydride (Br-PTCDA)

Brominataion of PTCDA was followed from the previous report [8]. 19.7 g, (50 mmol) of PTCDA was taken in a 250 mL three neck round bottom (RB) flask to this 200 mL of Conc. H_2SO_4 was added and the mixture was further stirred for 1 h. Catalytic amount of Iodine 252 mg, was added to the solution and stirred at room temperature under nitrogen atmosphere for another 3 h. After that 5.2 mL, (100 mmol) of bromine was added drop wise to a period of 8 h. Finally the reaction mixture was stirred at 85 °C for 8 h. After cooled to room temperature the reaction mixture was poured into the crushed ice and washed with plenty of water to neutralise the acid and filtered off. It was dark red in colour. It was a mixture of 1, 7- and 1, 6-dibromo isomers. M. F: $C_{24}H_8Br_2O_6$, yield: 84 %. The insoluble Br-PTCDA compound can't be isolated [19]. FT-IR (KBr, cm^{-1}): 3157 (aromatic ν_{C-H}), 1768, 1745 ($\nu_{C=O}$), 1504 (aromatic $\nu_{C=C}$), 1296, 1282, 1238, 1130, 1053, 1507, 1406, 1301 (ν_{C-O}) and 860, 733 (ν_{C-Br}).

2.4 Synthesis of N,N'-Bis(Hexyl)-1, 7-Dibromoperylene-3,4,9,10-Tetracarboxylic Diimide (Br-PDI-H)

The Br-PDI-H was prepared from the reported literature [21]. 10.5 g (19.5 mmol) of Br-PTCDA in NMP (150 mL) was taken in a 250 mL RB flask and the resulted reaction mixture was sonicated for 0.5 h to disperse the reactant. To the above mixture *N*-hexylamine 7 mL (53 mmol) and acetic acid 50 mL were added drop wise successively. The mixture was stirred for 48 h at 85 °C under N_2 atm. After cooled to room temperature the reaction mixture was poured into the crushed ice and neutralised with dil. HCl. The precipitate was filtered off. The crude product was purified by column chromatography using hexane and DCM 80:20 as an eluent. A dark red fine powder was obtained in 35.70 % yield. M. F: $C_{36}H_{32}Br_2N_2O_4$, m.p.185 °C, FT-IR (KBr, cm^{-1}): 2914, 2903, 2848 (aromatic ν_{C-H}), 1695 ($\nu_{C=O}$), 1651 (aromatic $\nu_{C=C}$), 1591 (ν_{C-O}), 1433 (ν_{C-N}), 1392, 1238, 1198, 1153, 808, 746, 663. ^{1}H-NMR [400 MHz, $CDCl_3$, δ = 7.26, s]: 0.95 (t, 6H), 1.32–1.48 (m, 12H), 1.72–1.77 (m, 4H), 4.12–4.20 (t, 4H), 8.60 (d, 2H), 8.9 (s, 2H), 9.40 (d, 2H). ^{13}C-NMR [400 MHz, $CDCl_3$, δ = 77.16, 3 peaks]: 162.7, 162.2 (C=O), 137.9, 132.8, 132.6, 129.8, 129.1, 128.4, 126.9, 123.2, 122.7, 120.7 (aromatic carbon), 40.7, 29.9, 29.2, 27.7, 22.4, 13.9 (hexyl amine carbon).

2.5 N,N'-Bis(Hexyl)-1,7-Di(Thiophenyl)Perylene-3,4:9,10-Tetracarboxylic Acid Diimide (T-PDI-H)

Preparation of T-PDI-H was followed by previous report [15]. 0.358 g (0.5 mmol) of Br-PDI-H was kept in 3 neck R. B flask and 20 mL of dry THF was added. The solution was first sonicated and purged with N_2 for half an hour. $Pd(PPh_3)_4$ Catalyst 144 mg was added to the reaction mixture. The temperature was raised to 50 °C and 3 mL of 2 M solution of K_2CO_3 was added. To the above reaction mixture thophene-5-boronic acid pinacol ester 0.210 g, (1 mmol) was added and refluxed for overnight under N_2 atm. After it had been cooled to room temperature, 3 mL of 2 N HCl was added and the mixture was extracted with CH_2Cl_2 and dried over anhydrous Na_2SO_4. The residue was purified by column chromatography using hexane and DCM 95:5 as eluent to give the product (T-PDI-H) as a pink colour solid in 27 % yield (195 mg). M. F: $C_{44}H_{38}N_2O_4S_2$. m.p: 277 °C. FT-IR (KBr, cm^{-1}): 2954, 2920 and 2850 (aromatic $\nu_{C\text{-}H}$), 1693 ($\nu_{C=O}$), 1651 ($\nu_{C=C}$), 1585 (ν_{C-O}), 1328 (ν_{C-N}), 1431, 1398, 1328, 1246, 810, 706 (ν_{C-S}). ^{1}H-NMR [400 MHz, $CDCl_3$, δ = 7.26 ppm, s]: 8.56 (s, 1H, perylene H), 8.22–8.20 (d, 1H, perylene H), 7.96–7.94 (d, 1H, perylene H), 7.48–7.47 (d, 1H, thiophene H), 7.29–7.26 (d, 1H, thiophene H), 7.18–7.17 (d, 1H, thiophene H), 4.19–4.15 (t, 2H), 1.74–1.71 (t, 2H), 1.41–1.43 (m, 2H), 1.30–1.21 (m, 2H), 0.82 (t, 3H). ^{13}C-NMR [400 MHz, $CDCl_3$, δ = 77.16, 3 peaks]: 162.0, 161.8 (C=O), 142.4, 134.3, 133.1, 133.0, 131.9, 131.7, 128.6, 128.4, 128.3, 127.9, 126.6, 127.2, 126.4, 121.0, 120.9 (aromatic carbon), 39.7, 30.5, 28.6, 27.0, 25.7, 21.5, 13.0 (hexyl amine carbon).

3 Characterization

Fourier transform-infrared (FT-IR) spectra were measured by the KBr disc method using Shimadzu IR Affinity-1S spectrophotometer. FT-IR spectra were recorded in the transmittance mode over the range of 500–4000 cm^{-1}. UV-Vis spectra was recorded with the Hitachi U-2910 spectrophotometer. UV-Vis experiment was carried out for the spin casted small molecule thin films (2400 rpm) with the same instrument. Fluorescence spectra were measured by using Hitachi F-7000 fluorescence spectrophotometer. ^{1}H and ^{13}C NMR spectra were recorded on Bruker 400 MHz spectrometer using $CDCl_3$ as the solvent. The electrochemical behaviour of the small molecule was studied by using CH Instrument. Cyclic voltammogram was recorded in three electrode cells with glassy carbon working electrode, a standard calomel electrode as reference electrode and Pt as a counter electrode. 0.1 M tetrabutylammonium hexafluorophosphate (Bu_4NPF_6)/DCM as the supporting electrolyte at a scan rate of 25 mV/s. Thermogravimetric analysis (TGA) was conducted under the inert nitrogen atmosphere with a SDT Q600 instrument in CECRI Karikudi. The sample was heated at a heating rate of 20 °C min^{-1} in the temperature range from 35 to 800 °C.

4 Result and Discussion

D-A-D type small molecule donor T-PDI-H dye was synthesized by using Suzuki coupling method. The synthetic route and chemical structures for the small molecular dye was given in the Scheme 1. T-PDI-H small molecule preparation was initiated with the bromination of PTCDA in Conc. sulfuric acid at 80 °C using catalytic amount of the I_2 granules. Due to poor solubility isolation of isomers in the brominated crude was difficult. Hence, the crude brominated product was directly used for imidization. In the imidization process anhydride was treated with hexylamine in NMP and acetic acid solvent under inert nitrogen atmosphere. Finally suzuki coupling was carried out between the Br-PTCDA and TBPE to synthesis the small molecular dye. The new dye was highly soluble in organic solvents, such as dichloromethane and chloroform.

4.1 FTIR Analysis

FT-IR spectroscopy was a vital tool to confirm the functional group in the new small molecular dye T-PDI-H. FT-IR transmittance spectrum for the small molecule dye was given in the Fig. 1. Aromatic C–H stretching frequencies were appeared in between the range 2954-2850 cm^{-1}. C=O in plane asymmetric stretching was appeared in the 1693 cm^{-1}. C=O out-of-plane symmetric stretching was appeared at 1651 cm^{-1} [22]. C=C stretching frequencies appeared at 1585 cm^{-1}. C–N stretching frequencies were appeared at 1322 cm^{-1}. C–O stretching was appeared at 1238 cm^{-1} and the C–S stretching frequencies were appeared at 800 cm^{-1}. The drastic change in the C=O functional group stretching confirms the formation of

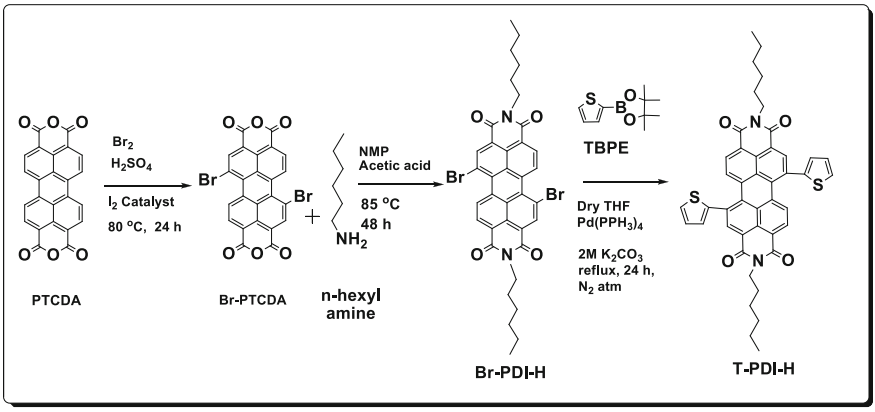

Scheme 1 Synthesis of *N*,*N*′-Bis(hexyl)-1,7-di(thiophenyl)perylenePerylene-3,4:9,10-tetracarboxylicacid diimide (T-PDI-H) small molecular dye

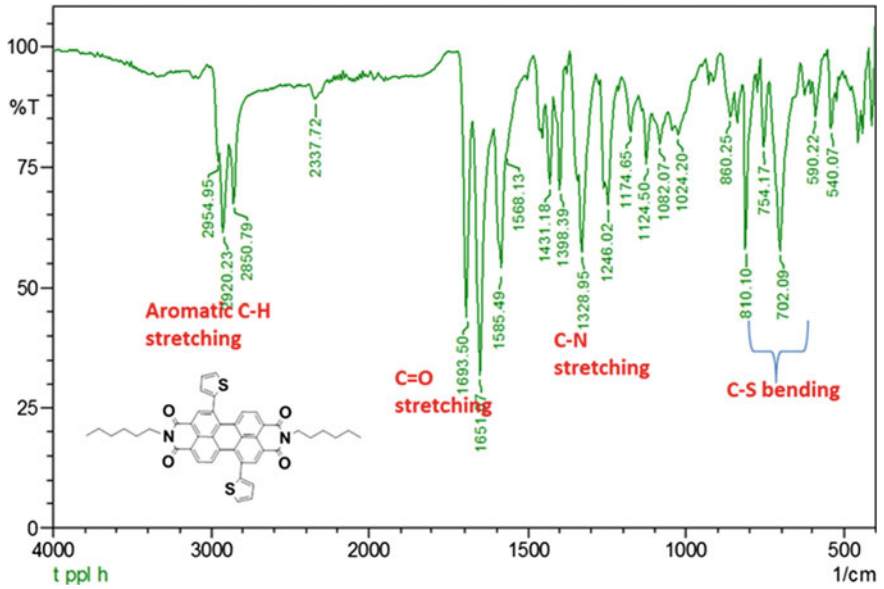

Fig. 1 FT-IR spectrum of T-PDI-H

imide and C–C coupling bond in the perylene dianhydride core. For Br-PTCDA, C=O stretching was appeared in the 1768 cm^{-1}. Similarly aromatic C–H stretching frequencies were also showed drastic shift from 3061 to 2854 cm^{-1} [23]. From the above results we confirmed the incorporation of thiophene moiety into the perylene core.

4.2 NMR Analysis

^{1}H-NMR and ^{13}C-NMR spectra were performed in $CDCl_3$ solution at room temperature. ^{1}H-NMR and ^{13}C-NMR for Br-PDI-H was given in the following Figs. 2 and 3 respectively. ^{1}H-NMR and ^{13}C-NMR for T-PDI-H small molecule was given in the Figs. 4 and 5 respectively. All the results confirmed the product formation. The appearance of peryelene protons in slight upper field than compared with parent perylenediimide as one singlet and two doublets in the range between 8.5 and 7.9 ppm confirms the electron rich thiophene group was inducted into the perylene core structure. The thiophene protons showed pair of doublet signals and a triplet peak bearing the same intensity observed in the range of 7.5–7.1 ppm. Similar trend was observed for some of the reported perylene based small molecule [15]. In the ^{13}C-NMR spectrum of D-A-D type small molecule C=O peak appears at 162 ppm. Coupling carbons appeared adjacent to the carbonyl carbon. Aliphatic protons are appeared in the up field region.

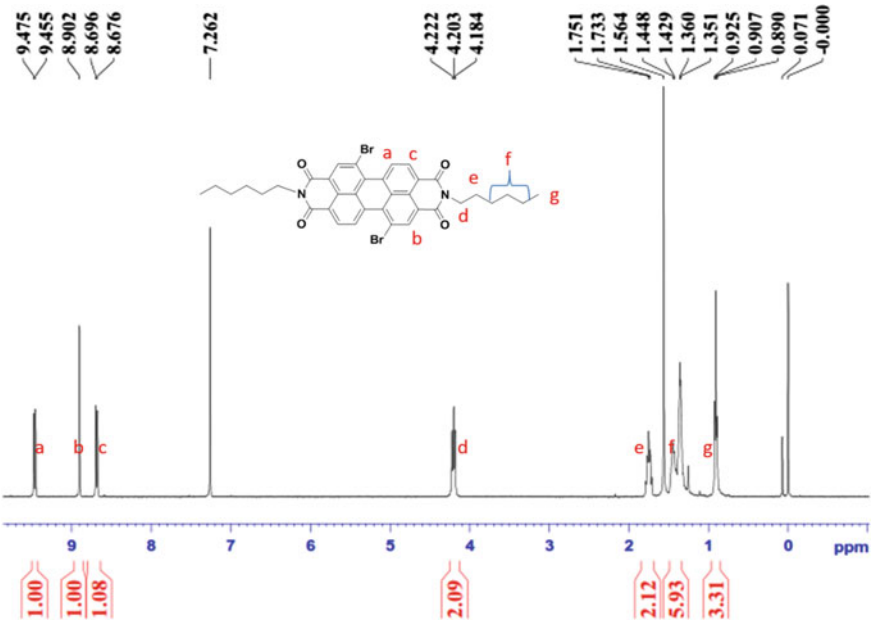

Fig. 2 [1]H-NMR spectrum of Br-PDI-H

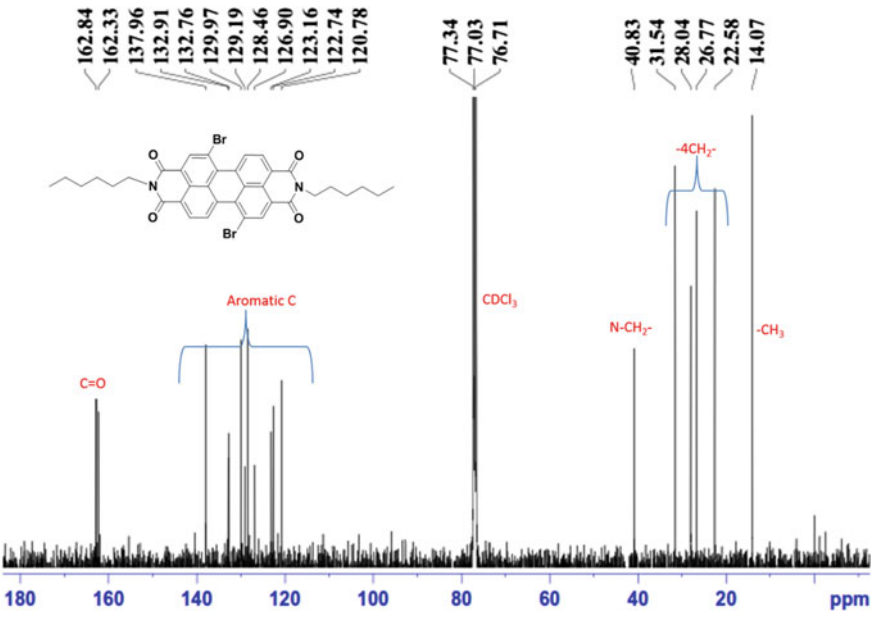

Fig. 3 [13]C-NMR spectrum of Br-PDI-H

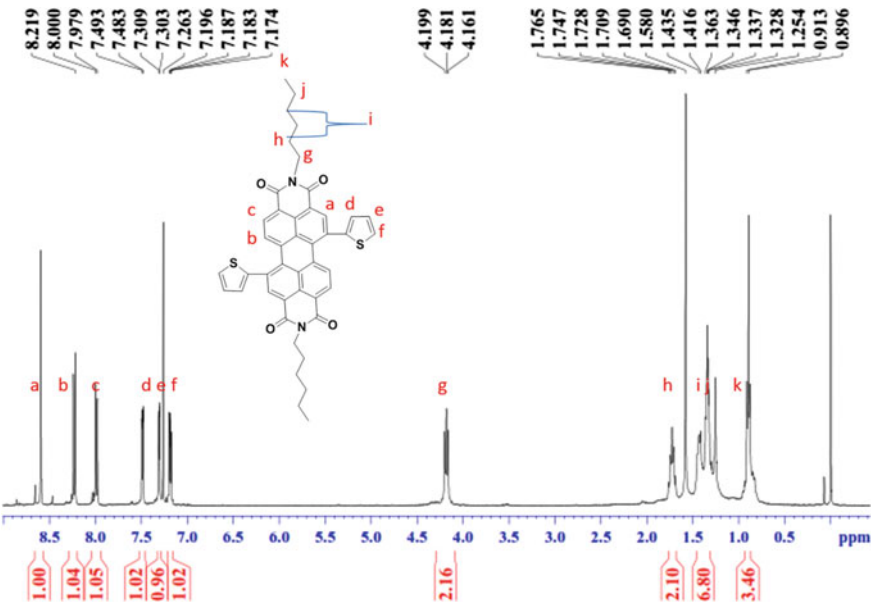

Fig. 4 [1]H-NMR spectrum of T-PDI-H

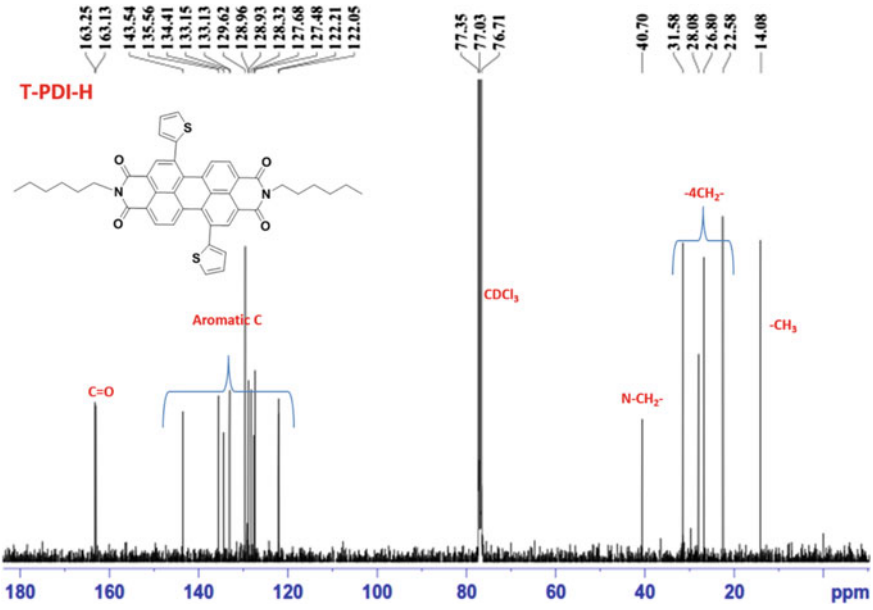

Fig. 5 [13]C-NMR spectrum of T-PDI-H

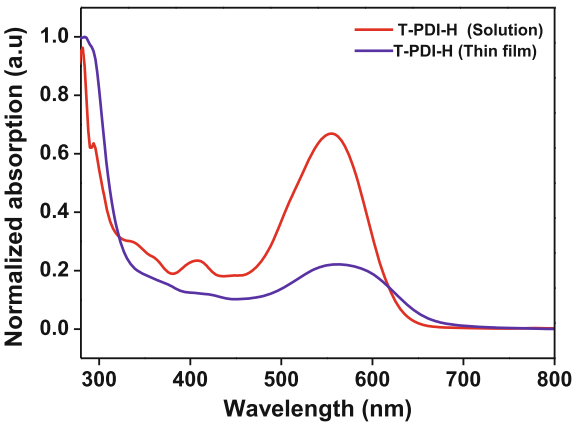

Fig. 6 UV-Visible spectra of T-PDI-H in 4×10^{-7} M Chloroform solution (*squares*) and thin film (*circles*)

Table 1 UV-Vis data for T-PDI-H in $CHCl_3$ solution and thin film

Dye molecule	Absorption		Ɛ in ($M^{-1}.cm^{-1}$) (thin film)*
	Solution (nm)	Film (nm)	
T-PDI-H	283, 338, 410, 557	285, 345, 417, 569	3.50×10^6 (3.20×10^6) 1.3×10^6 (1.0×10^6) 1.1×10^6, (0.9×10^6)

Ɛ−Molar absorption coefficient. *Molar absorption coefficient for thin film is mentioned in brackets

4.3 UV-Vis Analysis

Absorption spectra of T-PDI-H small molecule in solution and thin film were measured by using chloroform solvent (4.0×10^{-7} M). Absorption spectra and predicted data for the small molecule were given in Fig. 6 and Table 1 respectively. The T-PD-H was showed four absorption bands first band at 283, 285 nm, second band at 338, 345 nm, third band at 410, 417 nm and fourth band at 557, 569 nm for solution and thin film respectively. The intense absorption band was appeared at 283 and 338 nm was due to the thiophene groups [24]. The bathochromic shift of absorption spectra of the T-PDI-H relative to thiophene was due to extended conjugation with the perylene core. Second absorption band at 410 nm was assigned to the electronic S_0–S_2 transition which confirms the donor thiophene substituents in the bay position [25]. Appearance of third band at 557 nm was attributed to the S_o–S_1 transition of conjugated thiophene moiety [26]. In the thin film absorption spectra of T-PDI-H showed slight red shift (10 nm) than the fourth band. This variation in the fourth band was attributed to the rigid packing of the T-PDI-H in solid state resulted an increased π–π* intermolecular interactions. The broadening and red-shift of the bands was resulted in reduced band gap. The optical

band gap of the synthesized T-PDI-H was calculated by the following equation [11]. Onset absorption edge for this small molecule was 632 nm.

$$E_g^{opt} = (1240/\text{Onset absorption edge})\,\text{eV} = 1.96\,\text{eV}.$$

4.4 Photoluminescence Analysis (PL)

PL spectrum for T-PDI-H was measured in chloroform (4.0×10^{-7} M) at the 283 nm excitation wavelength and compared with absorption spectrum of T-PDI-H, corresponding spectra was given in Fig. 7. In the small molecule there was no visible fluorescence emission observed it confirms the possibility of intramolecular charge transfer (ICT) induced fluorescence quenching in the solution and thin film state. The emission spectrum of the T-PDI-H was observed at 666 nm for the excitation wavelength of 283 nm. The emission spectrum showed extremely weak fluorescence than the parent PDI due to the effective ICT at the given excitation wavelength between the electron rich thiophene-donor and electron deficient perylene-acceptor [27].

4.5 Cyclic Voltammetry Analysis

Cyclic voltammetry analysis for the T-PDI-H small molecule was performed in DCM with 0.1 M Bu_4NPF_6 as a supporting electrolyte at a scan rate of 25 mV/S. in an electrochemical workstation which contains glassy carbon as a working electrode, Pt as a counter electrode and an Ag/AgCl as a reference electrode. The oxidation and reduction cyclic voltammograms of the T-PDI-H small molecule was shown in Fig. 8. The electrochemical redox waves were often broad and irreversible and the onset potentials were generally used to estimate the electrochemical band gap. The onset oxidation and reduction potential could be used to estimate the HOMO and LUMO energy level respectively. The CV data was given in the

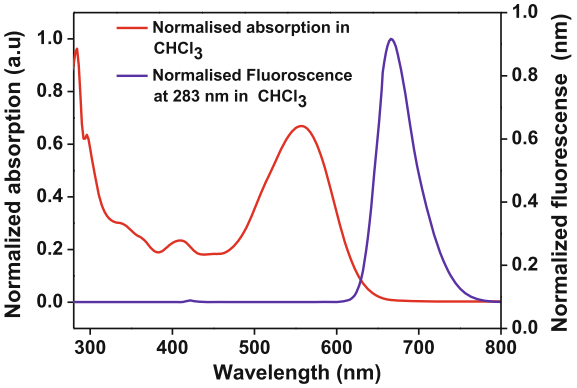

Fig. 7 Comparison of fluorescence spectrum (*circle*) at 283 nm with UV visible spectrum (*squares*) for T-PDI-H in 4×10^{-7} M Chloroform solution

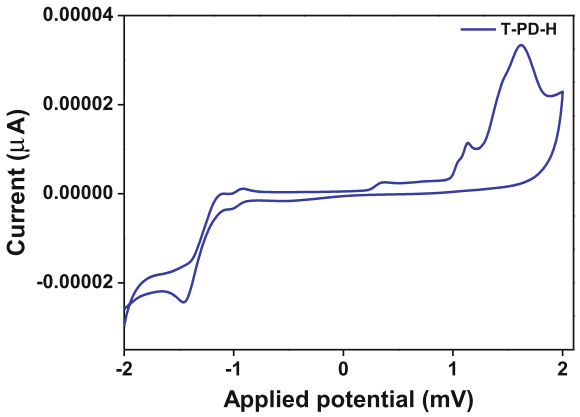

Fig. 8 CV graph for T-PDI-H

Table 2 Optical and electrochemical properties of T-PDI-H

Derivative name	λ_{abs} $CHCl_3$ (nm)[a]	E^{ox}_{onset} eV	E^{red}_{onset} eV	HOMO (eV)[b]	LUMO (eV)[c]	E_g^{ele} (eV)[d]	Absorption onset (nm)	E_g^{opt} (eV)[e]
T-PDI-H	283, 338, 410, 557	1.16	−1.17	−5.77	−3.44	2.33	632	1.96

[a]Absorption peaks in chloroform
[b]HOMO = –(4.8 – $E_{1/2}$, Fc, Fc^+ + E^{ox}_{onset})
[c]LUMO = –(4.8 – E1/2, Fc, Fc^+ + E^{red}_{onset})
[d]Redox potential for T-PDI-H was measured in DCM with 0.1 M Bu_4NPF_6 with a scan rate of 25 mVs-1 (vs. Fc/Fc^+)
[e]E_g^{opt} = 1240/absorption edge

Table 2. From the CV calculated HOMO, LUMO and E_g^{ele} for the small molecule was −5.77, −3.44 and 2.33 eV respectively. It implies that the incorporation of electron donating substituents does not alter the position of the LUMO level but altered the HOMO level significantly. Calculated electrochemical band gap was 2.33 eV. The decrease in electrochemical bandgap was due to the introduction of electron donating groups at the bay region of the PDI.

4.6 Thermal Analysis

Thermogravimetric analysis of the small molecule T-PDI-H was measured in nitrogen atmosphere at a heating rate of 20 °C/min from 30 to 800 °C. The TGA graph was given in the Fig. 9. For the small molecule 5 % weight loss was appeared at 277 °C and 10 % weight loss was appeared at 359 °C. The degradation temperature of the small molecule T-PDI-H was appeared at 426 °C with weight loss of 30 % might be endorsed for the high thermal stability of small molecule. The high thermal stability of the small molecule was due to the rigid perylene core groups which is almost similar to the reported perylene based polymer [12]. The

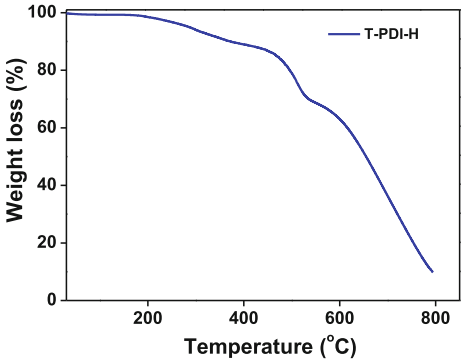

Fig. 9 TGA analysis graph for T-PDI-H

25 % weight loss at temperature less than 430 °C was ascribed to the degradation of the two thiophene group in the small molecule which is well matched with the calculated 24 % weight loss by losing the two thiophene. Onset thermal decomposition temperature (T_{ID}) for the small molecule was found at 427 °C.

4.7 Band Gap Diagram

Energy level diagram was constructed and compared for the small molecule with the standard P_3HT donor and $PC_{61}BM$ acceptor corresponding diagram was given in the Fig. 10. It was clear that the energy levels of the T-PDI-H was almost closer to the standard P_3HT polymer. Hence the new T-PDI-H small molecule with the low electrochemical and optical band gap would be a very good donor material for the OPV application.

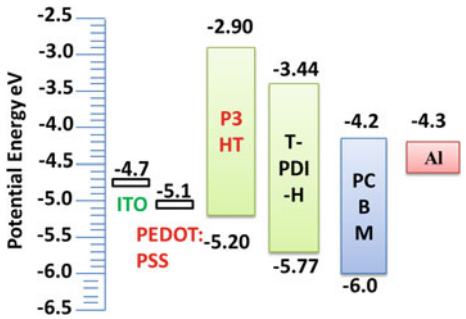

Fig. 10 Energy Level comparison diagram for T-PDI-H with P3HT

5 Conclusion

In summary a new bay substituted D-A-D type perylene based *N,N′*-Bis(hexyl)-1,7-di(thiophenyl)perylene-3,4:9,10-tetracarboxylic acid diimide (T-PDI-H) small molecular dye was synthesized by Suzuki coupling method, molecule structure was confirmed by FT-IR, ^{1}H-NMR and ^{13}C-NMR studies. The absorption value for this small molecule extended up to 650 nm and it resulted in reduced band gap value i.e., E_g^{opt} 1.96 eV with high molar absorption coefficient. Electron donating thiophene moiety not only increases the absorption in UV-Vis spectra but also declined the fluorescence property than compared with parent PDI dye due to the extended conjugation of the thiophene and intramolecular charge transfer process. From the CV, calculated HOMO, LUMO and E_g^{ele} for the small molecule were −5.77, −3.44 and 2.33 eV respectively. The contrary band gap was resulted due to the faultiness in absorption onset calculations. The new D-A-D type small molecule was stable up to 277 °C. Energy level of the new small molecule was compared with the P_3HT and $PC_{61}BM$ acceptor. From the above results we concluded that the new T-PDI-H small molecule will be a suitable candidate as a donor for the OPV application.

Acknowledgements This project has been supported by the Ministry of Department of Science and Technology (DST), India, under the Science and Engineering Research Board (SERB) NO. SB/FT/CS-185/2011. We thank the VIT management for the lab and instrument facility and VIT-SIF lab, SAS, Chemistry Division for NMR and GC-MS Analysis.

References

1. Zho, Y., Yan, Q., Zheng, Y.Q., Wang, J.Y., Zhao, D., Pei, J.: New polymer acceptors for organic solar cells: the effect of regio-regularity and device configuration. J. Mater. Chem. A. **1**, 6609–6613 (2013)
2. Das, J., Siram, R.B.K., Cahen, D., Rybtchinski, B., Hodes, G.: Thiophene-modified perylenediimide as hole transporting material in hybrid lead bromide perovskite solar cells. J. Mater. Chem. A. **3**, 20305–20312 (2015)
3. Kotowski, D., Luzzati, S., Scavia, G., Cavazzini, M., Bossi, A., Catellani, M., Kozma, E.: The effect of perylene diimides chemical structure on the photovoltaic performance of P3HT/perylene diimides solar cells. Dyes Pigm. **120**, 57–64 (2015)
4. Sakthivel, P., Gunasekar, K., Woo, H.Y., Kranthiraja, K., Saravanan, C., Gunasekar, K., Kim, H., Shin, W.S., Jeong, J.E., Woo, H.Y., Jin, S.H.: Carbazole linked phenylquinoline-based fullerene derivatives as acceptors for bulk heterojunction polymer solar cells: effect of interfacial contacts on device performance. J. Mater. Chem. A. **2**, 6916–6921 (2014)
5. Scharber, M.C., Sariciftci, N.S.: Efficiency of bulk-heterojunction organic solar cells. Prog. Polm. Sci. **38**, 1929–1940 (2013)
6. Sathiyan, G., Sivakumar, E.K.T., Ganesamoorthy, R., Thangamuthu, R., Sakthivel, P.: Review of carbazole based conjugated molecules for highly efficient organic solar cell application. Tetrahedron Lett. **57**, 243–252 (2016)
7. Tang, C.W.: Two layer organic photovoltaic cell. Appl. Phys. Lett. **48**, 183–185 (1986)
8. Huang, J., Fu, H., Wu, Y., Chen, S., Shen, F., Zhao, X., Liu, Y., Yao, J.: Size effects of oligothiophene on the dynamics of electron transfer in π-conjugated oligothiophene-perylene bisimide dyads. J. Phys. Chem. C **112**, 2689–2696 (2008)

9. Zhan, X., Tan, Z., Domercq, B., An, Z., Zhang, X., Barlow, S., Li, Y., Zhu, D., Kippelen, B., Marder, S.R.: A high-mobility electron-transport polymer with broad absorption and its use in field-effect transistors and all-polymer solar cells. J. Am. Chem. Soc. **129**, 7246–7247 (2007)
10. Zhou, E., Tajima, K., Yang, C., Hashimoto, K.: Band gap and molecular energy level control of perylene diimide-based donor–acceptor copolymers for all polymer solar cells. J. Mater. Chem. **20**, 2362–2368 (2010)
11. Kozma, E., Kotowski, D., Catellani, M., Luzzati, S., Famulari, A., Bertini, F.: Synthesis and characterization of new electron acceptor perylene diimide molecules for photovoltaic applications. Dyes Pigm. **99**, 329–338 (2013)
12. Lin, Y., Li, Y., Zhan, X.: Small molecule semiconductors for high-efficiency organic photovoltaics. Chem. Soc. Rev. **41**, 4245–4272 (2012)
13. Lu, Z., Zhang, X., Zhan, C., Jiang, B., Zhang, X., Chen, L., Yao, J.: Impact of molecular solvophobicity vs. solvophilicity on device performances of dimeric perylene diimide based solution-processed non-fullerene organic solar cells. Phys. Chem. Chem. Phys. **15**, 11375–11385 (2013)
14. Chen, W., Yang, X., Long, G., Wan, X., Chen, Y., Zhang, Q.: A perylene diimide (PDI)-based small molecule with tetrahedral configuration as a non-fullerene acceptor for organic solar cells. J. Mater. Chem. C. **3**, 4698–470 (2015)
15. Chen, S., Liu, Y., Qiu, W., Sun, X., Ma, Y., Zhu, D.: Oligothiophene-functionalized perylene bisimide system: synthesis, characterization, and electrochemical polymerization properties. Chem. Mater. **17**, 2208–2215 (2005)
16. Perrin, L., Hudhomme, P.: Synthesis, electrochemical and optical absorption properties of new perylene-3,4:9,10-bis(dicarboximide) and perylene-3,4:9,10-bis(benzimidazole) derivatives. Eur. J. Org. Chem. **2011**, 5427–5440 (2011)
17. Segura, J.L., Herrera, H., Bauerle, P.: Oligothiophene-functionalized naphthalimides and perylene imides: design, synthesis and applications. J. Mater. Chem. **22**, 8717–8733 (2012)
18. Choi, H., Paek, S., Song, J., Kim, C., Cho, N., Ko, J.: Synthesis of annulated thiophene perylene bisimide analogues: their applications to bulk heterojunction organic solar cells. Chem. Commun. **47**, 5509–5551 (2011)
19. Dinçalp, H., Çimen, O., Ameri, T., Brabec, C.J., Içli, S.: Synthesis, characterization and optoelectronic properties of a new perylene diimide–benzimidazole type solar light harvesting dye. Spectrochim. Acta, Part A **128**, 197–206 (2014)
20. Jeon, S.K., Thirupathaiah, B., Kim, C., Lim, K.T., Lee, J.Y., Seo, S.Y.: Novel carbazole derivative as a host material for blue phosphorescent organic light-emitting diodes. Dyes Pigm. **114**, 146–150 (2015)
21. Bagui, M., Dutta, T., Zhong, H., Li, S., Chakraborty, S., Keightley, A., Peng, Z.: Synthesis and optical properties of perylene diimide derivatives with triphenylene-based dendrons linked at the bay positions through a conjugated ethynyl linkage. Tetrahedron **68**, 2806–2818 (2012)
22. Liang, Z., Cormier, R.A., Nardes, A.M., Gregg, B.A.: Developing perylene diimide based acceptor polymers for organic photovoltaics. Synt. Met. **161**, 1014–1021 (2011)
23. Mansour, A.F., El-Shaarawy, M.G., El-Bashir, S.M., El-Mansy, M.K., Hammam, M.: Developing perylene diimide based acceptor polymers for organic photovoltaics. Polym. Int. **51**, 393–397 (2002)
24. Pei, J., Wang, J.L., Cao, X.Y., Zhou, X.H., Zhang, W.B.: Star-shaped polycyclic aromatics based on oligothiophene-functionalized truxene: synthesis, properties, and facile emissive wavelength tuning. J. Am. Chem. Soc. **125**, 9944–9945 (2003)
25. Muto, T., Temma, T., Kimura, M., Hanabusa, K., Shirai, H.: Elongation of the π-system of phthalocyanines by introduction of thienyl substituents at the peripheral β positions. Synth. Charact. J. Org. Chem. **66**, 6109–6115 (2001)
26. Gvishi, R., Reisfeld, R., Burshtein, Z.: Excited-state absorption in red perylimide dye in solution. Chem. Phys. Lett. **213**, 338–344 (1993)
27. Shin, W.S., Jeong, S.H., Kim, M.K., Jin, S.H., Kim, M.R., Lee, J.K., Lee, J.W., Gal, Y.S.: Effects of functional groups at perylene diimide derivatives on organic photovoltaic device application. J. Mater. Chem. **16**, 384–390 (2006)

XRD, FT-IR, SEM and Electrical Studies of $Li_4Mn_{4.5}V_{0.5}O_{12}$

S. Sharmila, B. Janarthanan and J. Chandrasekaran

Abstract In the present work, molten salt method has been used to synthesize cathode material ($Li_4Mn_{4.5}V_{0.5}O_{12}$) and the structural, morphological and electrical properties have been analyzed. XRD pattern revealed the formation of cubic spinel structure without any impurity or secondary phase. The presence of functional groups was revealed from FT-IR spectrum. SEM analysis elucidates the formation of sub-micron sized polyhedral shaped particles without any agglomeration. dc conductivity of the sample was studied with the help of complex impedance spectroscopy in a wide range of temperature. Maximum conductivity of 2.09×10^{-5} S cm^{-1} has been obtained at 380 °C.

1 Introduction

A rechargeable Li-ion battery plays a vital role in electronic equipment such as mobile phones, laptops, camcorders, etc. [1]. Commercially, Li-ion batteries use graphite as an anode and $LiCoO_2$ as a cathode due to long cycle life, low working potential, and high energy density. The limiting factor behind this cathode material is high cost and toxicity, which opens a new challenge to the researchers to identify an eco-friendly material with good electrical performance. A number of research works has been carried out on different electrode materials such as Ni oxides, Mn oxides, vanadate and phosphates as cathodes [2]. Among these cathodes, Mn based oxides receives great interest due to its main advantages such as low cost and

S. Sharmila (✉) · B. Janarthanan
Department of Physics, Karpagam University, Coimbatore, India
e-mail: sharm_4@yahoo.co.in

J. Chandrasekaran
Department of Physics, Sri Ramakrishna Mission Vidhyalaya
College of Arts and Science, Coimbatore, India

J. Ebenezar (ed.), *Recent Trends in Materials Science and Applications*,
Springer Proceedings in Physics 189, DOI 10.1007/978-3-319-44890-9_38

eco-friendly nature, which may be available in different forms i.e.$LiMnO_2$, $LiMn_2O_3$, Li_2MnO_4, $Li_4Mn_5O_{12}$ (or Li $[Mn_{1.67}Li_{0.33}]$ O_4) and $Li_2Mn_4O_9$. $LiMnO_2$, $LiMn_2O_3$ and Li_2MnO_4 lose its potential during cycling due to the occurrence of Jahn-Teller distortion [3, 4].

Thackeray et al. [5] have inferred that the suitability of $Li_4Mn_5O_{12}$ as a cathode material due to the absence of Jahn-Teller distortion. Similarly, Hao et al. [6], Jiang et al. [7], Julien et al. [8], Zhang et al. [9], Li et al. [10], Tian et al. [11], Choi et al. [12], Zhao et al. [13], Kim et al. [14], etc. synthesized $Li_4Mn_5O_{12}$ in different methods and obtain good electrical and electrochemical performance.

In the present work, an effort has been taken to prepare V doped $Li_4Mn_5O_{12}$ to enhance its electrical property. Similar kind of effort had already made by Sharmila et al. [15] and Nithya et al. [16] for the anode ($Li_4Ti_5O_{12}$) material and succeeded. $Li_4Mn_{4.5}V_{0.5}O_{12}$ was prepared by a simple molten salt method with no organic additives and also absence of agglomeration has provided an additional advantage of the method.

2 Experimental Method

2.1 Synthesis

The Stoichiometric amount of $LiOH{\cdot}H_2O$, MnO_2 and V_2O_5 were mixed together and grained well for 30 min. LiCl and KCl were added in the molar ratio 60:40 and grained well. The obtained homogenous mixture was heated in a muffle furnace at 800 °C for 10 h. The resultant powder was washed thoroughly with distilled water for several times and finally with ethanol to remove the residual salts.

2.2 Characterization

XRD have been recorded on X'Pert PRO diffractometer equipped with CuKα radiation (λ = 0.1540 nm) in the range of 2θ = 10° to 80° with a step size of 0.0500° to identify the structure of the material. FT-IR spectrum has been recorded on Shimadzu/Nicolet in the range 400–4000 cm^{-1} to identify the functional groups and Scanning electron microscopy has been utilized to study the surface morphology of the material (JEOL-JSM-6390, Japan). Electrical properties of the sample have been studied by impedance measurement in a wide range of temperature (120–380 °C) using computer controlled HIOKI 3532 LCR HITESTER in the frequency range of 50 Hz to 10 kHz.

3 Results and Discussion

XRD pattern of $Li_4Mn_{4.5}V_{0.5}O_{12}$ sample was shown in Fig. 1. The presence of sharp and well defined peaks indicating the highly crystalline nature of the material. The obtained peaks are in good agreement with standard JCPDS card no.46-0810 and indicating the formation of fd-3 m space group. No impurity peaks were detected, which elucidates the eutectic mixture of molten salt. The dopant V^{5+} entered into the lattice structure without any changes in its structural characteristics. Lattice constant 'a' and cell volume of $Li_4Mn_{4.5}V_{0.5}O_{12}$ (8.2098Å and 553.35 $Å^3$) was found to be higher than $Li_4Mn_5O_{12}$ (8.161 Å and 543.66 $Å^3$—JCPDS card value) The atomic density of Mn^{4+} is larger than V^{5+} results in decreasing the lattice density of $Li_4Mn_{4.5}V_{0.5}O_{12}$. The grain size was calculated as 40.28 nm using Debye-Scherer formula.

Fourier-transform Infrared spectrum (FT-IR) of $Li_4Mn_{4.5}V_{0.5}O_{12}$ was shown in Fig. 2. The band around 615 cm^{-1} attributed to Mn-O vibrations in MnO_6 octahedron [17]. The weak to moderate band around 980 cm^{-1} and 1065 cm^{-1} are ascribed to γOH…O and δOH [18]. The peak at 3465 cm^{-1} assigned to stretching band of OH^- [15].

The surface morphology of the sample was studied with the help of SEM analysis and shown in Fig. 3. It exhibited the particles with uniform morphology in sub-micron sized and polyhedral shape. Due to the addition of molten salts, the reaction occurs at a high temperature in a liquid medium and preventing agglomeration [19]. The sizes (by length) of the particles were measured in the range of

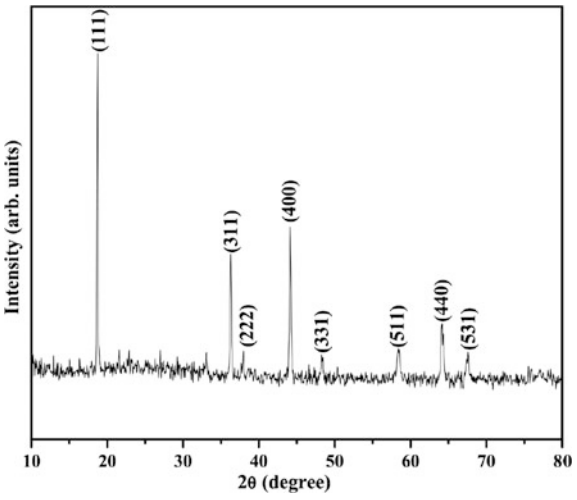

Fig. 1 XRD pattern of $Li_4Mn_{4.5}V_{0.5}O_{12}$

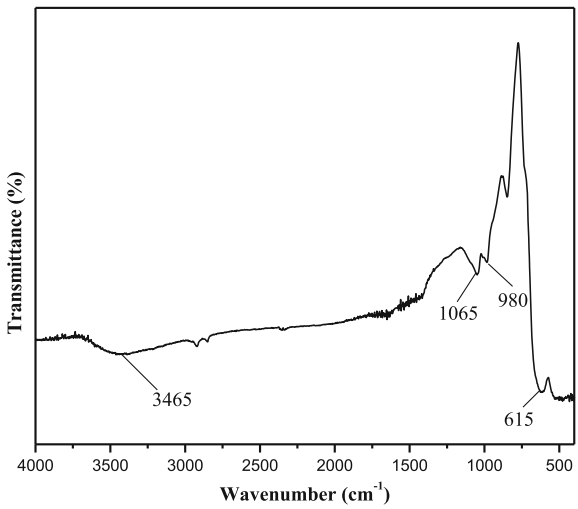

Fig. 2 FT-IR spectrum of $Li_4Mn_{4.5}V_{0.5}O_{12}$

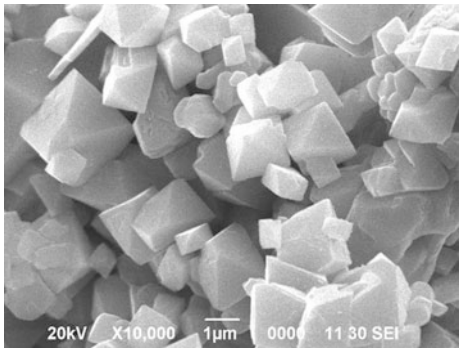

Fig. 3 SEM image of $Li_4Mn_{4.5}V_{0.5}O_{12}$

$\sim$0.5–2 μm. In addition, the SEM image indicating the absence of coarse particles, which also confirmed that the dopant entered into the lattice structure.

The electrical behavior of the material has been studied using complex impedance spectroscopy over a wide range of frequency and temperature. It gives clear information about the nature of the material. The parallel combination of the single R-C circuit explains the complex impedance of the electrode. Figure 4a–c shows the Nyquist plot of $Li_4Mn_{4.5}V_{0.5}O_{12}$ over different temperatures (120–380 °C). At all the temperatures, it exhibits the formation of single semi-circle elucidates the parallel combination of bulk resistance R_b and bulk capacitance C_b, also revealed that the conduction process occurs only through the bulk of the material and not by

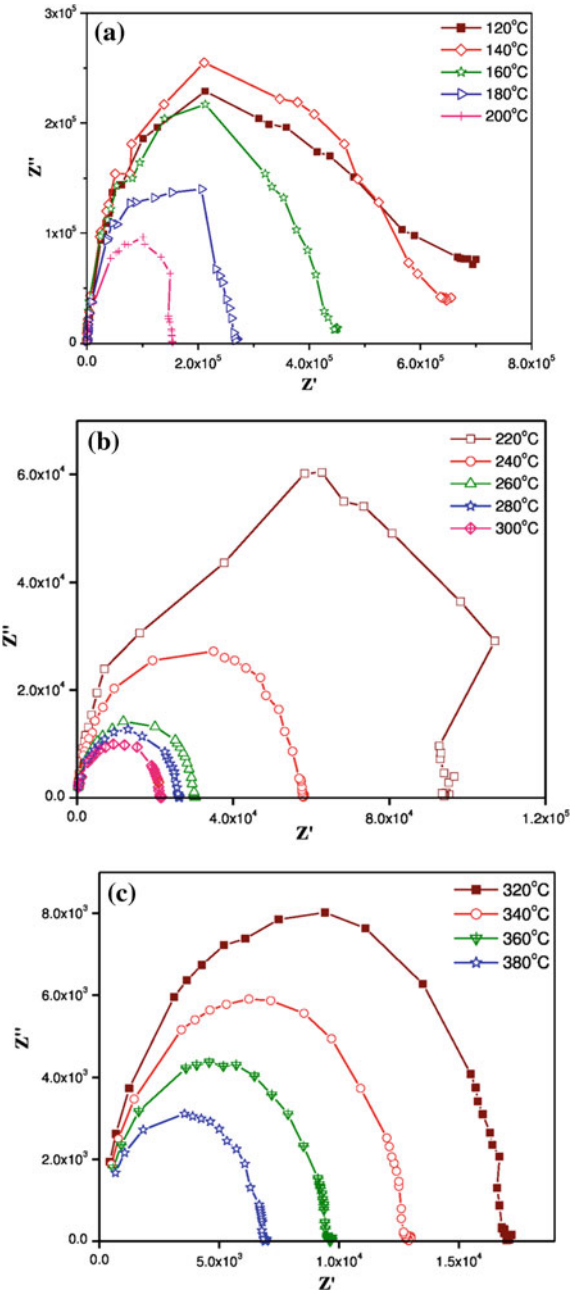

Fig. 4 **a–c** Nyquist plot of $Li_4Mn_{4.5}V_{0.5}O_{12}$ at different temperature

grain boundary. Bulk resistance can be obtained by the interception of the semicircle on X-axis, whose values were found to decrease with increase in temperature. Bulk capacitance can be calculated using the relation $2\pi\gamma_{max}R_bC_b = 1$, which is in the order of pF, also indicating that the conduction occurs through the bulk of the material [20]. With the rise in temperature, the resistance value starts to decrease relating the negative temperature coefficient of resistance (NTCR) property, revealed the material as semiconducting. The ionic conductivity was calculated using the formula $\sigma = (l/R_bA)$ S cm^{-1}, where 'l' is the thickness of the sample and 'A' is the area of the sample, which was found to increase with an increase in temperature.

Figure 5a–c shows the variation of real part of the impedance (Z′) with frequency at different temperatures. At low frequency region, Z′ found to be high, which decreases gradually and merge together at high frequency for all the temperatures. By increasing the temperature the magnitude of Z′ decreases which may be due to increasing in ac conductivity of the material. The merging of a curve at high frequency indicates the release of space charge [21].

Variation of Z″ with frequency at different temperatures was shown in Fig. 6a–c. The curve indicates that Z″ attain maximum value at a certain frequency, which is different for different temperatures and decrease towards high frequency side. Due to the presence of immobile electrons the broadening of peak occurs, indicating the temperature dependent relaxation process [22]. By increasing the temperature, the peak shift towards the high frequency region elucidates the existence of space charges [23].

Conductance spectra of $Li_4Mn_{4.5}V_{0.5}O_{12}$ at different temperatures were shown in Fig. 7a–c. The curve exhibits two regions (i) At low frequency region frequency independent plateau and (ii) At high frequency a dispersive region [24]. The curve at low frequency region corresponds to dc conductivity. The conductivity was found to increase with an increase in temperature according to Jonscher's universal power law $\sigma(w) = \sigma_{dc} + A\omega_p^n$, where 'n' represents frequency exponent, 'ω' is the hopping frequency and σ_{dc} representing dc conductivity of the material. Mobility and charge carrier concentration can be obtained from the graph with the help of non-linear curve fitting method and the values were given in Table 1. Maximum conductivity obtained at 380 °C. The obtained parameters are closer to the calculated values of the cole-cole plot. It also satisfies the Arrhenius relation: $\sigma_{dc} = \sigma_0 \exp(Ea/KT)$, where σ_0 is the pre-exponential factor and E_a is the activation energy.

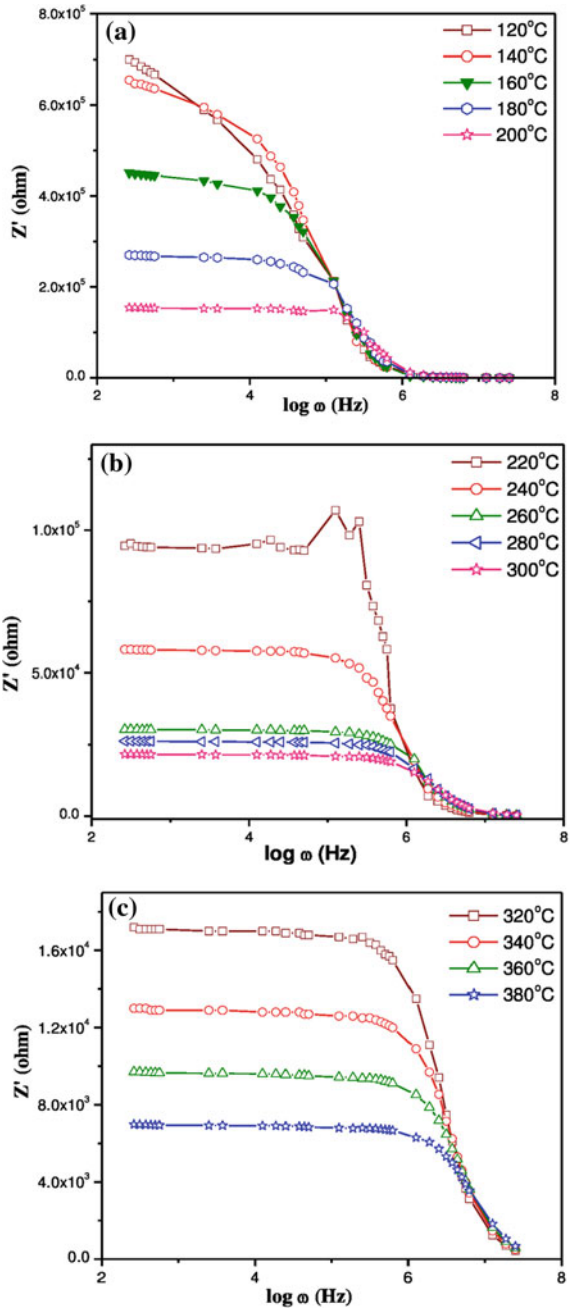

Fig. 5 **a–c** Variation of Z' versus frequency at different temperature

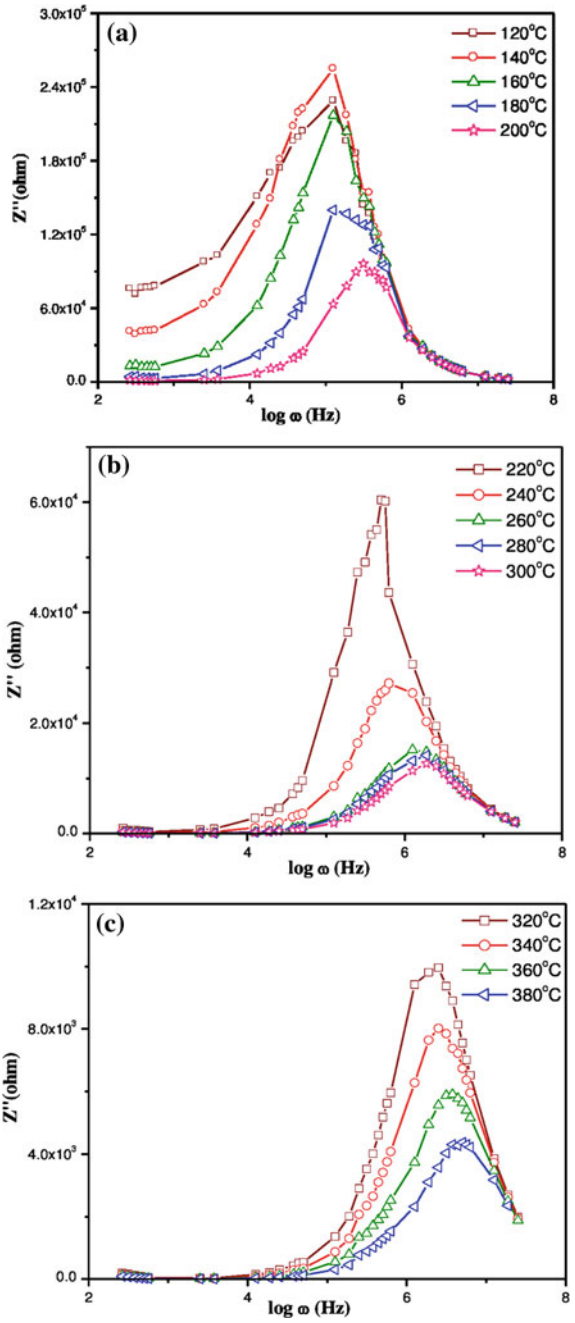

Fig. 6 **a–c** Variation of Z'' versus frequency at different temperature

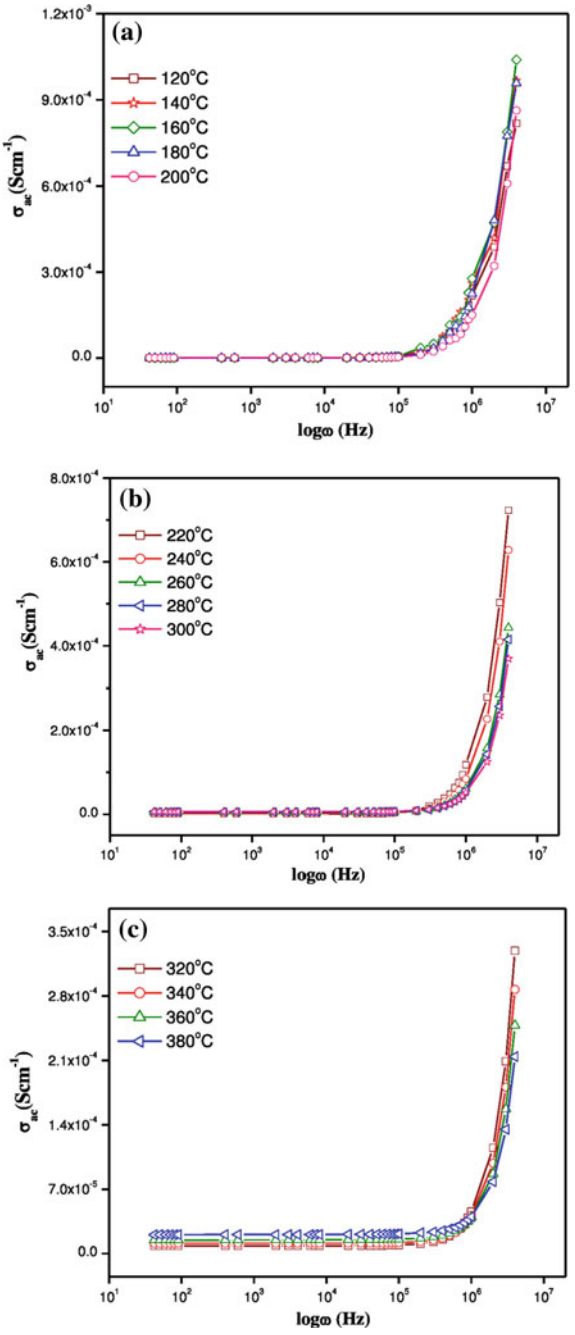

Fig. 7 **a–c** Conductance spectra of $Li_4Mn_{4.5}V_{0.5}O_{12}$ at different temperatures

Table 1 Electrical parameters of $Li_4Mn_{4.5}V_{0.5}O_{12}$

Temp. (°C)	R_b (Ω)	C_b (pF)	Conductivity (S cm^{-1})		ω_p x 10^4 Hz	N × 10^{-9} (S $cm^{-1\ kHz-1}$)	μ x 10^{21} cm^2 V^{-1} s
			Cole-cole	σ_{dc}			
120	6.919×10^5	1.15	2.298×10^{-7}	2.32×10^{-7}	0.1812	50.31	2.88
140	6.479×10^5	1.22	2.455×10^{-7}	2.423×10^{-7}	0.192	51.95	2.91
160	4.48×10^5	1.77	3.55×10^{-7}	3.623×10^{-7}	0.284	55.23	4.09
180	2.67×10^5	2.98	5.957×10^{-7}	5.602×10^{-7}	0.571	44.44	7.88
200	1.537×10^5	2.07	1.034×10^{-6}	1.023×10^{-6}	2.621	18.46	34.63
220	9.49×10^4	2.09	1.676×10^{-6}	1.623×10^{-6}	4.845	16.51	61.42
240	5.74×10^4	2.77	2.77×10^{-6}	2.623×10^{-6}	10.265	13.10	125.06
260	3.04×10^4	1.74	5.232×10^{-6}	5.22×10^{-6}	23.079	12.06	270.63
280	2.585×10^4	2.05	6.153×10^{-6}	6.223×10^{-6}	28.74	11.97	324.84
300	2.153×10^4	1.84	7.387×10^{-6}	7.323×10^{-6}	34.62	12.12	377.62
320	1.705×10^4	2.33	9.329×10^{-6}	9.235×10^{-6}	43.43	12.60	457.75
340	1.284×10^4	2.066	1.238×10^{-5}	1.20×10^{-5}	63.36	12.09	646.14
360	9.621×10^3	2.06	1.653×10^{-5}	1.48×10^{-5}	78.29	11.96	773.02
380	6.88×10^3	2.31	2.311×10^{-5}	2.09×10^{-5}	111.507	12.23	1067.28

4 Conclusion

$Li_4Mn_{4.5}V_{0.5}O_{12}$was successfully synthesized via simple molten salt method at 800 °C. The structural parameters are determined from X-ray diffraction which confirmed the phase purity and cubic spinel structure of $Li_4Mn_{4.5}V_{0.5}O_{12}$. Different types of functional groups and the type of vibrations were verified by FTIR spectrum. SEM results indicate that the prepared $Li_4Mn_{4.5}V_{0.5}O_{12}$ had uniform morphology and the particle size was in the range of μm without agglomeration. Well defined semicircle arc are obtained from the cole-cole plot and also the conductivity was found to increase with an increase in temperature from 2.32×10^{-7} S cm^{-1}at 120 °C to 2.09×10^{-5} S cm^{-1} at 380 °C. With these results we concluded that the $Li_4Mn_{4.5}V_{0.5}O_{12}$ may serve as a good cathode material for rechargeable Li-ion battery.

Acknowledgements The authors acknowledge Department of Physics, Bharathiar University for extending electrical studies.

References

1. Park, O.K., Cho, Y., Lee, S., Yoo, H.-C., Song, H.-K., Cho, J.: Who will drive electric vehicles, olivine or spinel?. Ener. Env. Sci. **4**, 1621-1633 (2011)
2. Fu, L.J., Liu, H., Li, C., Wu, Y.P., Rahm, E., Holze, R., Wu, H.Q.: Electrode materials for lithium secondary batteries prepared by sol–gel methods. Prog. Mater Sci. **50**, 881–928 (2005)
3. Xiong, L., Xu, Y., Tao, T., Song, J., Goodenough, J.B.: Excellent stability of spinel $LiMn_2O_4$-based composites for lithium ion batteries. J. Mater. Chem. **22**, 24563–24568 (2012)
4. Gummow, R.J., de Kock, A., Thackeray, M.M.: Improved capacity retention in rechargeable 4 V lithium/lithium-manganese oxide (spinel) cells. Solid State Ionics **69**, 59–67 (1994)
5. Thackeray, M.M., de Kock, A., Rossouw, M.H., Liles, D., Bittihn, R., Hoge, D.: Spinel electrodes from the Li-Mn-O system for rechargeable lithium battery applications. J. Electrochem. Soc. **139**, 363–366 (1992)
6. Hao, Y.J., Lai, Q.Y., Xu, X.Y., Wang, L.: Electrochemical performance of symmetric supercapacitor based on $Li_4Mn_5O_{12}$ electrode in Li_2SO_4 electrolyte. Mater. Chem. Phys. **126**, 432-436 (2011)
7. Jiang, Y.P., Xie, J., Cao, G.S., Zhao, X.B.: Electrochemical performance of $Li_4Mn_5O_{12}$ nano-crystallites prepared by spray-drying-assisted solid state reactions. Electrochim. Acta **56**, 412–417 (2010)
8. Julien, C.M., Zaghi, K.: Electrochemistry and local structure of nano-sized $Li_{4/3}Me_{5/3}O_4$ (Me=Mn, Ti) spinels. Electrochim. Acta **50**, 411–416 (2004)
9. Zhang, Y.C., Wang, H., Xu, H.Y., Wang, B., Yan, H., Ahniyaz, A., Yoshimur, M.: Low-temperature hydrothermal synthesis of spinel-type lithium manganese oxide nanocrystallites. Solid State Ionics. **158**, 113–117 (2003)
10. Li, Y., Makita, Y., Lin, Z., Lin, S., Nagaoka, N., Yang, X.: Synthesis and characterization of lithium manganese oxides with core-shell $Li_4Mn_5O_{12}$@Li_2MnO_3 structure as lithium battery electrode materials. Solid State Ionics **196**, 34–40 (2011)
11. Tian, Y., Chen, D., Jiao, X., Duan, Y.: Facile preparation and electrochemical properties of cubic-phase $Li_4Mn_5O_{12}$ nanowires. Chem. Commun. **20**, 2072–2074 (2007)

12. Choi, W., Manthiram, A.: Influence of fluorine substitution on the electrochemical performance of 3 V spinel $Li_4Mn_5O_{12-\eta}F_\eta$ cathodes. Solid State Ionics **178**, 1541–1545 (2007)
13. Zhao, Y., Lai, Q., Zeng, H., Hao, Y., Lin, Z.: $Li_4Mn_5O_{12}$ prepared using L-lysine as additive and its electrochemical performance. Ionics **19**, 1483–1487 (2013)
14. Kim, J., Manthiram, A.: (1998) Low temperature synthesis and electrode properties of $Li_4Mn_5O_{12}$. J. Electrochem. Soc. **145**, L53–L55 (1998)
15. Sharmila, S., Senthilkumar, B., Nithya, V.D., Vediappan, K., Lee, W., Kalai Selvan, R.: Electrical and electrochemical properties of molten salt-synthesized $Li_4Ti_{5-x}Sn_xO_{12}$ (x = 0.0, 0.05 and 0.1) as anodes for Li-ion batteries. J. Phys. Chem. Solids **74**, 1515–1521 (2013)
16. Nithya, V.D., Kalai Selvan, R., Vediappan, K., Sharmila, S., Lee, C.W.: Molten salt synthesis and characterization of $Li_4Ti_{5-x}Mn_xO_{12}$ (x = 0.0, 0.05 and 0.1) as anodes for Li-ion batteries. Appl. Surf. Sci. **261**, 515–519 (2012)
17. Julien, C.M., Massot, M.: Lattice vibrations of materials for lithium rechargeable batteries I. Lithium manganese oxide spinel. Mater. Sci. Eng. B. **97**, 217–230 (2003)
18. Noel, P.G.R.: A Guide to the complete Interpretation of Infrared Spectra of Organic Structures. Wiley, New York
19. Nithya, V.D., Sharmila, S., Vediappan, K., Lee, C.W., Vasylechko, L., Kalai Selvan, R.: Electrical and electrochemical properties of molten-salt synthesized 0.05 mol Zr- and Si-doped $Li_4Ti_5O_{12}$ microcrystals. J. App. Electrochem. **44**, 647–654 (2014)
20. Sharmila, S., Janarthanan, B., Chandrasekaran, J.: Preparation and characterization of pure and Ti^{4+}doped $Li_4Mn_5O_{12}$ spinels as cathodes for Li-ion batteries. Inter. J Sci. Eng. Res. **6**, 1763–1768 (2015)
21. Mohanty, N.K., Satpathy, S.K., Banarji, B., Nayak, P., Choudhary, R.N.P.: Complex impedance properties of $LiSr_2Nb_5O_{15}$ ceramic. J. Adv. Ceram. **1**, 221–226 (2012)
22. Shukla, A., Choudhary, R.N.P., Thakur, A.K.: Effect of Mn^{4+} substitution on thermal, structural, dielectric and impedance properties of lead titanate. J. Mater. Sci. Mater. Electron. **20**, 745–755 (2009)
23. Shukla, A., Choudhary, R.N.P., Thakur, A.K.: Thermal, structural and complex impedance analysis of Mn^{4+} modified $BaTiO_3$ electroceramic. J. Phy. Chem. Solids **70**, 1401–1407 (2009)
24. Senthilkumar, B., Kalai Selvan, R., Vinothbabu, P., Perelshtein, I., Gedanken, A.: Structural, magnetic, electrical and electrochemical properties of $NiFe_2O_4$ synthesized by the molten salt technique. Mat. Chem. Phy. **130**, 282–285 (2011)

Fabrication of ZnO Thin Film Based VOC Sensor

S. Narasimman, L. Balakrishnan, S.R. Meher, R. Sivacoumar, Elizabeth Rufus and Z.C. Alex

Abstract ZnO thin films devised by RF magnetron sputtering were studied for monitoring volatile organic compounds (VOCs) such as acetone, ammonia and ethanol gases in the concentration range of 50–250 ppm under room temperature. The fabricated films were inspected by X-ray diffractometer (XRD), UV-Vis spectrometer, energy dispersive X-ray spectrometer (EDS) and scanning electron microscope (SEM). The XRD results stipulate that the films having wurtzite structure with (0 0 2) preferential orientation and the grain size of the film were calculated as 12.39 nm using Scherrer's formula. The UV-Vis spectrum showed that the film having 95 % of the transparency in the visible region. The band gap of the film was calculated from Tauc's plot and was found to be around 3.2 eV. The EDS spectrum affirms the occupancy of Zn and O elements in the ZnO film. The microscopic structure of the film was examined by SEM and the average grain size was estimated as $\sim$13 nm which is having acceptable harmony with XRD results. The sensor response was appraised by change in electrical resistance of the film under the atmospheric medium of VOC gases at room temperature. The sensor gives a better response ($\sim$5.2) towards acetone compared with other vapours.

1 Introduction

The extensive use of new products in our daily life has been reported an elevated concentration of indoor pollutants, particularly volatile organic compounds (VOC) that defiles indoor air quality and also creates the impacts on human health [1]. The huge amount of VOCs may cause human nervous system, kidney failure

S. Narasimman · R. Sivacoumar · E. Rufus · Z.C. Alex
Department of Sensor and Biomedical Technology, School of Electronics Engineering, VIT University, Vellore 632014, India

L. Balakrishnan (✉) · S.R. Meher
Department of Physics, School of Advanced Sciences, VIT University, Vellore 632014, India
e-mail: bslv85@gmail.com

J. Ebenezar (ed.), *Recent Trends in Materials Science and Applications*, Springer Proceedings in Physics 189, DOI 10.1007/978-3-319-44890-9_39

and also abnormal heartbeat [2]. Consequently, most of the researchers focused on VOCs observation and its growth [3–5]. Metal oxide semiconductors (MOS) are one of the most accustomed materials and employed for gas sensing applications [6]. Among those, ZnO is innocuous material with several considerable properties encompasses *n*-type semiconductivity, large band gap energy of 3.4 eV and high exciton binding energy of 60 meV. In league with these properties, ZnO can be considered as a unique candidate for fabricating many devices differs from sensors to UV laser diodes and transparent displays [7]. ZnO based gas sensors were fabricated intensively owing to its ease of materialize, long term chemical stability and also well established preparation methods, such as RF sputtering [8], sol-gel [9] and metal oxidation [10].

Among the various methods, RF magnetron sputtering contains limited deposition steps with highly controlled facility to develop superior quality films. The conventional gas sensing mechanism in metal oxide sensor function involves a resistance variation of the film in the atmospheric medium of the gas. Initially, the atmospheric oxygen is adsorbed on the MOS film surface at room temperature. Once the target gas was released, it may react with adsorbed oxygen species thereby electrons will be extracted from the conduction band of the MOS film surface. This may results the resistance value increases [11].

Though many of them worked in ZnO based gas sensors, still some difficulty have been arisen to improve the sensitivity. The current work audits the sensitivity of fabricated ZnO thin film sensor in the direction of VOC such as acetone, ammonia and ethanol vapours.

2 Experimental Details

Anterior to the thin film deposition, the substrate (glass) was ultrasonically cleaned and annealed at 400 °C for 2 h to remove contaminates. ZnO film was grown on glass substrates by sputtering Zn metal target in oxygen ambience at an operating frequency of 13.56 MHz. The Zn metal target employed for the deposition of films having 99.9 % purity level. The target and substrate were fixed inside the chamber. Then the chamber was voided to the stay pressure of 2×10^{-5} mbar. The deposition process starts with pre-sputtering (about 20 min) to remove the contaminants from the target surface and to make the uniform plasma. Then the inert argon gas was sent at the pressure rate of 0.001 mbar and subsequently reactive oxygen gas was introduced at the pressure rate of 0.002 mbar. The deposition process was continued for 30 min under argon and oxygen atmospheric pressure. The substrate temperature was kept at 450 °C, applied RF power is 80 W and distance between the target-substrate is 6 cm respectively throughout the film growth.

3 Results and Discussion

3.1 Structural Analysis

The crystalline structure of the grown film was carried out by XRD. Figure 1 manifests the XRD form of ZnO thin film grown on glass substrate. The diffraction form (Fig. 1) reported that the deposited ZnO on glass substrate has c-axis preferential orientation, and giving a broad peak at the angle equals to 34.019° which matches with (002) plane of wurtzite structure with reference to JCPDS Card No (36-1451). The mean crystallite size of the ZnO film was calculated as ~12.39 nm using Scherrer's formula,

$$D = \frac{C\lambda}{\beta \cos\theta} \tag{1}$$

where, D is crystallite size, β is line broadening in radians, C is the shape factor usually taken to be 0.89, θ is Bragg diffraction angle and λ is wavelength of radiation (λ = 1.54 Å). The formation of film with small crystallites will be very much suitable for gas sensor application.

3.2 UV-Visible Analysis

Figure 2a, b indicates the optical absorbance and transmittance spectra of ZnO film in the UV-Visible region. It discloses sharp absorption edge around 365 nm. Further, the ZnO thin film shows maximum transmittance of 95 %. The optical band gap with direct transition can be calculated from the following Tauc's relation,

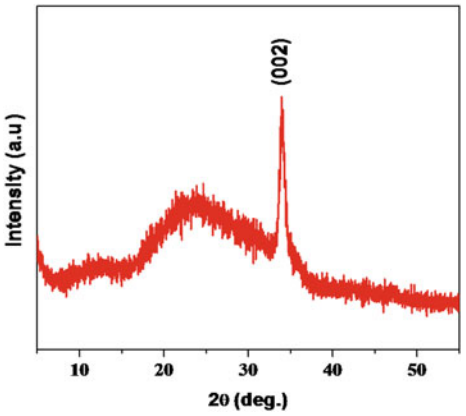

Fig. 1 XRD form of ZnO thin film

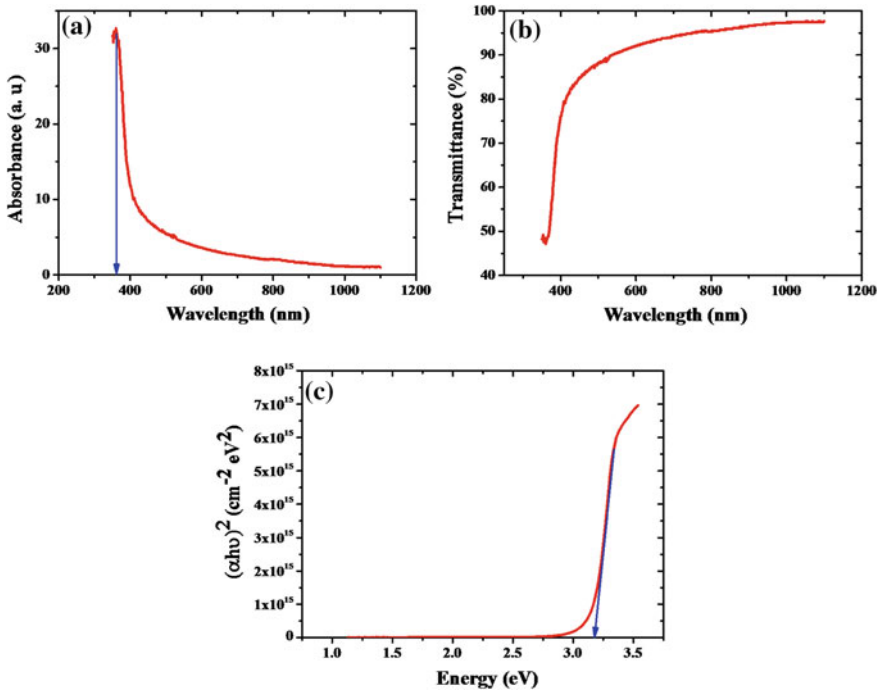

Fig. 2 **a** Absorption spectrum, **b** Transmission spectrum and **c** Tauc's plot of ZnO film

$$\alpha(h\nu) = C(h\nu - E_g)^{1/2} \tag{2}$$

where, α is absorption coefficient, $h\upsilon$ is photon energy, C is constant and E_g is energy gap [12]. The optical band gap is found to be around 3.2 eV from the linear extrapolation between $h\upsilon$ versus $(\alpha h\nu)^2$ and is shown in Fig. 2c.

3.3 *Elemental and Morphology Analysis*

Elemental studies of the ZnO film was done by energy dispersive X-ray spectroscope (EDS). Figure 3 shows the EDS spectrum of ZnO thin film and it affirms that Zn and O elements present in the ZnO film. The observed atomic percentages of the elements are also shown inset of the Fig. 3. The surface of the ZnO film was inspected by scanning electron microscope (SEM). Figure 4 selectively exhibits the surface SEM images of ZnO film with better magnification. It confirms that the grown film is homogeneous and continuous. The mean grain size is found to be $\sim$13 nm which retains a good coordination with XRD results. The formation of

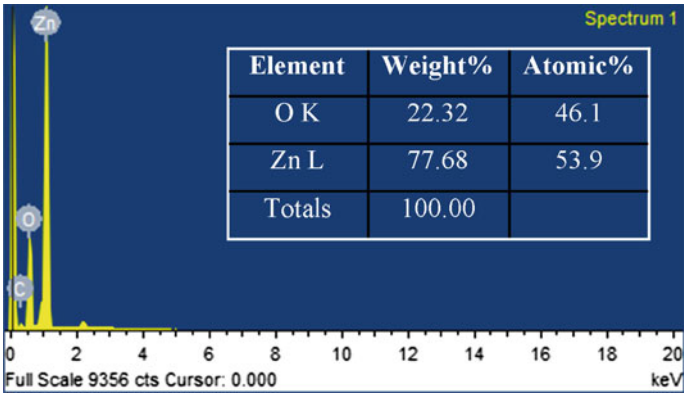

Fig. 3 EDS spectrum of ZnO film

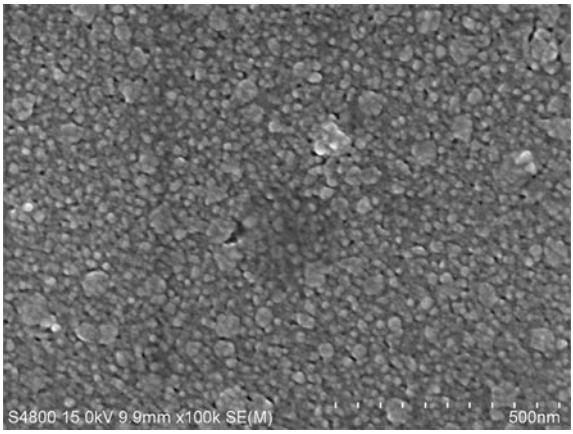

Fig. 4 SEM image of RF magnetron sputtered ZnO thin film

smaller grain film plays a major role in varying the thickness of the depletion layer through more oxygen adsorption on the grain boundaries in the surface.

3.4 VOC Sensing Analysis

Figure 5a–c showed the response curve of ZnO thin film gas sensor as a function of VOC vapor concentration (acetone, ammonia and ethanol). The measurements were taken at room temperature. In the current study, the sensitivity (S) was determined using below equation,

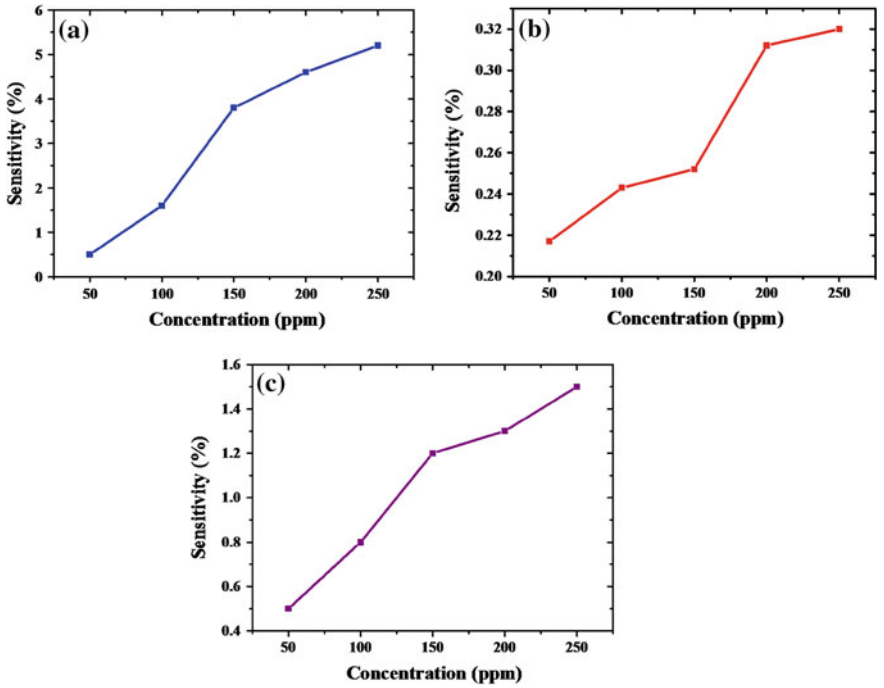

Fig. 5 Sensitivity response of the grown ZnO thin film for **a** acetone, **b** ammonia and **c** ethanol

$$S = \frac{\left|R_{gas} - R_{air}\right|}{R_{air}} \tag{3}$$

where, R_{gas} is the film resistance in the medium of target gas and R_{air} is the film resistance in air. As shown in the sensitivity plot, the responses of the film increase upon exposing VOC vapours. The response is almost linear up to 200 ppm and become saturated above 200 ppm. A schematic representation of VOC sensing mechanism is shown in the Fig. 6. In VOC sensing mechanism, the oxygen is adsorbed over the ZnO surface as per the following reactions,

$$O_2(g) \leftrightarrow O_2(\text{adsorb}) \tag{4}$$

$$O_2(\text{adsorb}) + e^- \leftrightarrow O_2^-(\text{RT}) \tag{5}$$

The adsorption is followed by the withdrawl of electrons from the conduction band of the *n*-type semiconductor and resulted as the formation of depletion region thereby reducing the resistance of ZnO film. This adsorbed oxygen reacts with the target gas and yields,

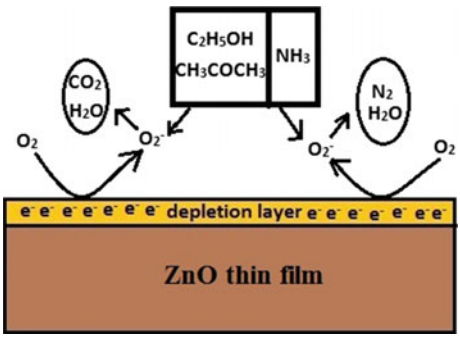

Fig. 6 Schematic representation of VOC sensing mechanism

$$C_2H_5OH + 6O_2^- \rightarrow 2CO_2 + 3H_2O + 12e^- \quad (6)$$

$$CH_3COCH_3 + 4O_2^- \rightarrow 3CO_2 + 3H_2O + 8e^- \quad (7)$$

$$4NH_3 + 3O_2^- \rightarrow 6H_2O + 2N_2 + 3e^- \quad (8)$$

The above reactions deliver the withdrawn electrons back to the conduction band. These electrons reduce the depletion region thickness and also decrease the resistance of the ZnO film. It is observed that for all the gas vapours, the sensitivity increases with increase in gas concentration. The ZnO thin film gas sensor gives better sensitivity towards acetone ($\sim$5.2) compared with other gases at room temperature. The more sensitivity towards acetone than other gases is due to enhanced catalytic reaction.

4 Conclusion

ZnO thin film was fabricated on the glass substrate by RF magnetron sputtering. The XRD analysis reported that the film grown on glass substrate having better crystallinity with wurtzite structure. The EDS spectrum affirms the occupancy of Zn and O elements in the film. The SEM analysis reveals that the film having uniformly distributed nanostructure grains of average size $\sim$13 nm. It is observed that the ZnO thin film is more sensitive to acetone vapour compared with other vapours.

Acknowledgements The authors convey their sincere gratitude to Department of Science and Technology (DST), New Delhi, India for providing the financial support through FIST (Fund for Improvement of S&T Infrastructure in Higher Education Institution) project [SR/FST/ETI-015/2011].

References

1. Franciosoa, L., Forleo, A., Taurinoa, A.M., Siciliano, P., Lorenzelli, L., Guamier, V.: Linear temperature micro hotplate gas sensor array for automotive cabin air quality monitoring. Sens. Actuators, B **134**, 660–665 (2008)
2. Michael, L.B., Denise, W.: Henshel Diane: An investigation of the relationship between air emissions of volatile organic compounds and the incidence of cancer in Indiana counties. Environ. Res. **100**, 242–254 (2006)
3. Baptise, S.J., Franck, B., Michel, F., Helene, N.M.: A selective gas detection micro-device for monitoring the volatile organic compounds pollution. Sens. Actuators, B **119**, 227–233 (2006)
4. Yen, L.C., Ming, C.C., Hsiang, W.Y., Hua, M.R.: A self-heating gas sensor with integrated NiO thin film for formaldehyde detection. Sens. Actuators, B **122**, 503–510 (2007)
5. Rella, R., Spadavecchia, J., Manena, M.G., Capone, S., Taurino, A., Martino, M.: Acetone and ethanol solid-state gas sensor based TiO_2 nanoparticles thin film deposited by matrix assisted pulsed laser evaporation. Sens. Actuators, B **127**, 426–431 (2007)
6. Huang, J., Wan, Q.: Gas sensors based on semiconducting metal oxide one-dimensional nanostructures. Sensors **12**, 9903–9924 (2009)
7. Ozgur, U., Alivov, Y., I., Liu, C., Teke, A., Reshchikov, M.A., Dogan, S., Avurutin, V., Cho, S., Morkoc, H.: A comprehensive review of ZnO materials and devices. J. Appl. Phys. **98**, 041301 (2005)
8. Supab, C., Niyom, H., Pongri, M., Nikom, M.: Zinc oxide nanobelts by RF sputtering for ethanol sensor. Physica E **39**, 53–56 (2007)
9. Paraguay, D.F., Miki-Yoshida, M., Morales, J., Solis, J.: Influence of Al, In, Cu, Fe and Sn dopants on the response of thin film ZnO gas sensor to ethanol vapor. Thin Solid Films **373**, 137–140 (2000)
10. Jen, H.T., Liang, H.C.: Fabrication of gas sensing devices with ZnO nanostructure by low-temperature oxidation of Zinc particles. Sens. Actuators B **131**, 572–576 (2008)
11. Al-Hardan, N.H., Abdulla, M.J., Abdul Aziz, A.: A sensing mechanism of hydrogen gas sensor based on RF sputtered ZnO thin films. Int. J. Hydrogen Energy **35**, 4428–4434 (2010)
12. Kripal, R., Gupta, A.K., Srivastava, R.K., Mishra, S.K.: Photoconductivity and photoluminescence of ZnO nanoparticles synthesized via co-precipitation method, Spectrochimi. Acta Part A **79**, 1605–1612 (2011)

Effect of Titanium Coating on the Structural and Optical Properties of TiO_2 Thin Films for Improved Performance in Dye-Sensitized Solar Cells

R. Jeba Beula, Suganthi Devadason and V. Mahesh Kumar

Abstract In favor of enhancing the performance of TiO_2 photoanode-based dye sensitized solar cells (DSSCs), a thin layer of titanium was coated on Indium doped tin oxide (ITO) conductive glass substrate prior to the coating of TiO_2 by using sol-gel spin coating technique. Titanium coating was obtained by DC sputtering method using titanium target and its effect on the structure, morphology of TiO_2 and the photovoltaic properties of the subsequent DSSCs were studied. Porous morphology was observed in the TiO_2 film with titanium coating. The photoelectric conversion efficiency of DSSC based on TiO_2 with titanium coating is larger than that without titanium coating. An efficiency of 3 % was obtained for titanium coated TiO_2 electrode. The improvement of the solar cell may be due to the increase in dye adsorption of TiO_2 thin film with titanium coating. In this work, the novelty lies in the role of titanium which is for the first time coated beneath the TiO_2 film resulting in the improved structure and morphology of the photo anode and thereby an enhanced DSSC efficiency.

1 Introduction

The DSSC with thick and porous nanocrystalline electrode is the most affordable photo-electrochemical system for better adsorption of dye molecules owing to their wide surface area. Exclusive studies on the properties and various applications of metal oxide semiconductors namely TiO_2, SnO_2, and ZnO are well documented in the literature. TiO_2, however has been widely explored for solar cell fabrication [1, 2]. TiO_2 with a bandgap of 3.2 eV is found to exhibit enhanced electrical and optical properties for the three well known crystalline structures (rutile, anastase and brookite) [3, 4]. An irradiated DSSC injects electrons and holes from the dye

R. Jeba Beula (✉) · V. Mahesh Kumar
Department of Physics, Karunya University, Coimbatore, India
e-mail: beular@karunya.edu

S. Devadason
Department of Physics, Hindustan University, Chennai, India

J. Ebenezar (ed.), *Recent Trends in Materials Science and Applications*,
Springer Proceedings in Physics 189, DOI 10.1007/978-3-319-44890-9_40

molecule into TiO_2 band gap and electrolyte respectively [5, 6]. Increase in electron injection and optical absorption are the key factors for the improved efficiency of the solar cells which however requires more porosity in the TiO_2 film [7–9].

Many techniques have been employed to prepare high-quality TiO_2 films, including pulsed laser deposition (PLD), magnetron sputtering, atomic layer deposition and sol-gel method [10–12]. The sol-gel method seems best choice among others since it does not involve high temperature requirement shunning unwanted crystallite structure creation that is not appropriate for absorbing solar energy [13, 14]. On the other hand, sol-gel processes suffer from a serious problem wherein increase of thickness of the deposited film (>1 μm) creates crack formation due to capillary stress and shrinkage during heat treatment [15]. It is necessary to deposit thick film without any cracks for better efficiency of solar cell. Some groups [16, 17] reported that a compact TiO_2 blocking layer made up of Titanium tetraisopropoxide between ITO substrate and TiO_2 nanoparticles can increase the photovoltaic efficiency. Therefore, In this paper we reported the uncomplicated methodology guiding to the deposition of well-adhered and thick TiO_2 electrodes by sputtering titanium layer between substrate and TiO_2 nanocrystalline particles. The influence of titanium layer on the structural and morphological properties of TiO_2 thin film and photovoltaic properties of resulting DSSC are also discussed.

2 Experimental Methods

2.1 Preparation of TiO_2 Sol

The precursor solution was prepared by mixing titanium (IV) butoxide (2.5 ml), triton x -100 (0.65 ml) and 10 ml of ethanol. In which, triton x-100 was used as a stabilizer to avoid precipitation in solution. After stirring this solution for half an hour, a mixture of 1 ml HNO_3, 10 ml ethanol, 10 ml distilled water and few drops of Poly ethylene glycol(PEG) was added drop by drop and magnetic stirring was sustained for 4 h. In addition to that the sol was aged for 2 h.

2.2 Deposition of TiO_2 Thin Film

Intium tin oxide (ITO) substrates were washed by means of aqua regia, acetone, ethanol and double distilled water successively for 15 min each in ultrasonic bath prior to coating. Titanium was coated on one of the ITO substrate by DC sputtering method (D.C Sputtering vacu Tech, Model-12A4D) using titanium target. The base pressure of the deposition chamber was kept at 6×10^{-5} torr during the process of coating Ti on the substrate. Then, bare ITO and Titanium coated ITO substrates were spin coated (HOLMARC/ HO-TH-05) by the prepared sol with the rotation

speed of 3000 rpm for 30 s followed by drying in air for 1 min. The process was repeated for 3–4 times so as to attain the desired thickness of the TiO_2 film. Then, the film was dried at 100 °C for half an hour and finally annealed at 450 °C for 1 h. TiO_2 films coated on bare ITO substrate is named as S1 and the film coated on Ti-coated ITO substrate as S2. Thickness of the film S1 and S2 are ~ 2 μm.

2.3 Fabrication of Solar Cell Devices

To complete dye adsorption, the TiO_2 photoanodes were dipped in a natural dye prepared by blackberry at room temperature for 24 h. The solar cells were fabricated by assembling the blackberry sensitized TiO_2 films as the working electrode and Ti-coated glass substrate as the counter electrode. Then the prepared polymer electrolyte using Polyethylene Glycol (PEG) in acitonitrile, glacial acetic acid (0.6 ml), 1-methyl-3-propylimidazolium Iodide (0.3 M), KI (0.1 M) and I_2 (0.05 M) was introduced into the gap between the TiO_2 working electrode and titanium counter electrode of the solar cell which was clamped firmly together using binder clips.

2.4 Working Principle of DSSC

Initially, in the mechanism of DSSC, the blackberry sensitizer absorbs the incident photon and gets injected into the conduction band of TiO_2 photoanode resulting in the oxidation of photosensitizer. These injected electrons gets diffused in the direction of back contact of ITO substrate and at last reaching the titanium counter electrode. The oxidized sensitizer accepts electrons from the polymer electrolyte containing redox (I_3^-/I^-) mediator [18].

2.5 Characterization Techniques

The structural and morphological characterization were carried out for prepared TiO_2 thin films by X-ray diffractometer with Cu Kα radiation of wavelength 1.5418 Å (Shimadzu XRD 6000) and Scanning Electron Microscope (Joel JSM6390) respectively . Optical characterization was carried out by UV-Visible spectrometer (JASCO UV Vis NIR, V-670) between 200 to 800 nm . Photovoltaic characteristics of the DSSCs were analyzed by electrochemical analyzer (CHI 6008). The photovoltaic performance parameters of DSSCs were measured using a 100 W Xenon light illumination with the light intensity of 35 mW/cm^2. The chosen area of dye adsorbed TiO_2 working electrodes was 0.25 cm^2. Electrochemical impedance

spectroscopy (EIS) was also performed by the same electrochemical analyzer in the frequency range of 40 Hz to 60 MHz under illumination.

3 Results and Discussion

3.1 Structural Studies

The crystal phase and crystallite size of the TiO_2 films was explored using X-ray diffractometer. Figure 1 illustrates the XRD pattern of S1 which shows amorphous phase of TiO_2 thin film. Again, Fig. 2 shows the diffraction pattern of S2 where the diffraction peaks located at 25.4°, 37.8°, 48.2° and 54° match to the (101), (004), (200) and (105) planes of the anatase phase (JCPDS No. 21-1272), indicating a formation of TiO_2 nanocrystalline nature. There was no peaks corresponds to Ti layer in the spectrum which clearly indicates that the Ti layer is fully oxidized during annealing at 450 °C. Thus Ti layer helps in the formation of nanostructured TiO_2 films of crystalline anatase structure without any impurities. The process of annealing is an important factor for the formation of the crystal phase and an annealing temperature of 450 °C favors the formation of anatase phase [19]. When comparing with the TiO_2 film consisted of rutile and brookite phase, TiO_2 film with anatase phase has the outstanding performance for DSSCs as reported [20]. The average crystallite size calculated by Scherrer formula using the (1 0 1) plane is found to be 10.8 nm for the film S2.

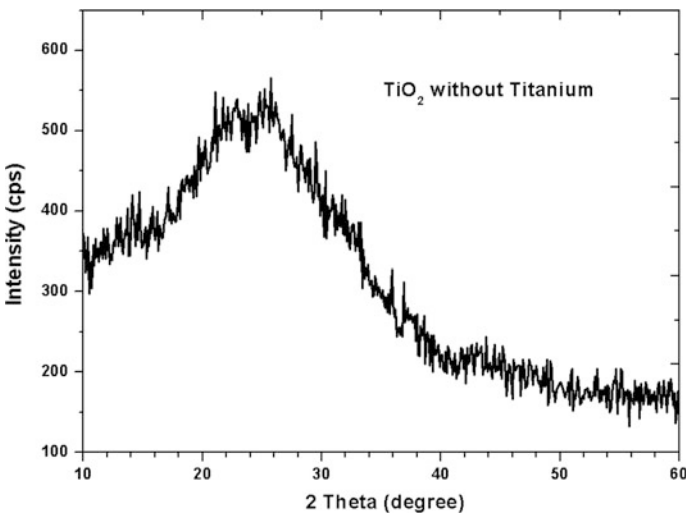

Fig. 1 XRD pattern of TiO_2 thin film without titanium layer

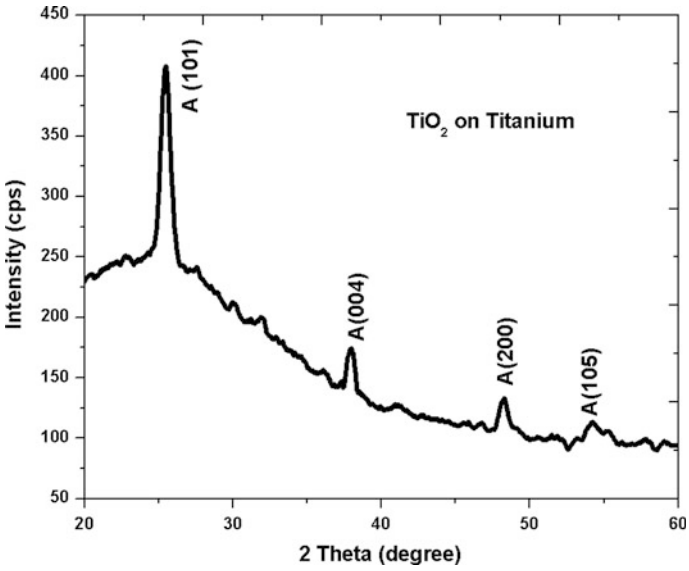

Fig. 2 XRD pattern of TiO_2 thin film with titanium layer

3.2 Morphological Studies

Figure 3a, b shows the surface morphology of the prepared TiO_2 thin films on bare ITO substrate in different magnifications. It can be observed that huge micro cracks appear in the TiO_2 film S1 which may be due to the higher thickness of the film forming cracks on annealing due to lattice mismatch between film and substrate, the same was reported by Ineta et al. [21]. Cracks formation may be due to the poor necking between TiO_2 particles as a result of shrinkage during the heat treatment which will lead to the poor performance of a cell. Therefore, it is necessary to develop the chemical connection between the TiO_2 nanoparticles and also to create the pores on the surface for a better performance of a solar cell.

To improve chemical connectivity between TiO_2 particles and its adherence to substrate, we sputtered Titanium on ITO substrate prior to the spin coating of TiO_2 sol. As thick Ti layer crack often or even peel of from the substrate a thin layer of Ti was coated on ITO substrate. By adding just one Ti layer on ITO substrate before the coating with TiO_2 solution, the morphology had largely changed. As shown in Fig. 3c, d, we successfully fabricated the TiO_2 film with pores on the surface without the formation of crack for the same thickness of the film as S1. The thin TiO_2 layer which was formed from titanium during annealing process binds the TiO_2 nanoparticles making its stronger or connects the TiO_2 nanoparticles with ITO substrate thereby supporting the collected electrons to travel much faster towards the substrate [22].

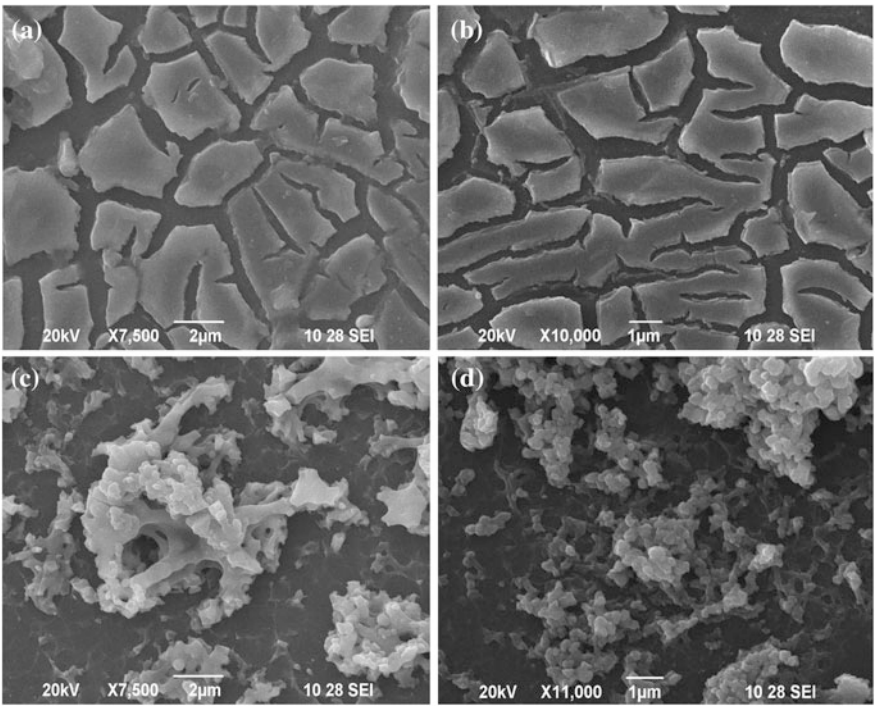

Fig. 3 SEM images of TiO_2 films without titanium layer (**a**) and (**b**) with titanium layer (**c**) and (**d**) in different magnifications

3.3 Optical Studies

Figure 4a, b represents the respective UV-Visible absorption spectra of TiO_2 films before and after sensitization with blackberry dye respectively. Before sensitization the spectral lines for both TiO_2 films show a single absorption band at about 300 nm representing the intrinsic transition between the valence band and conduction band [23]. From Fig. 4b it is obvious that, there was no change in the spectral line of S1 after the loading of dye. But the spectrum of S2 film shows increased absorbance at about 300 nm and a small absorbance at around 450 nm, indicating the increased dye loading amount which can drastically increase effective light absorption [24]. The dye molecule does not completely gets absorbed at the inner surface of porous TiO_2 film when the particle size in TiO_2 film with Ti-layer is comparable with the interparticle distance in the porous TiO_2. However, in our study due to large particle size the dye molecule penetration is much feasible into the porous TiO_2 layer in turn favoring more dye adsorption.

Figure 5a, b shows the graph for determining the direct band gap energy values of prepared samples using $\alpha = A(h\nu - E_g)^2$ equation, where α is the absorption coefficient as a function of frequency, $h\nu$ is the energy of incident photon with

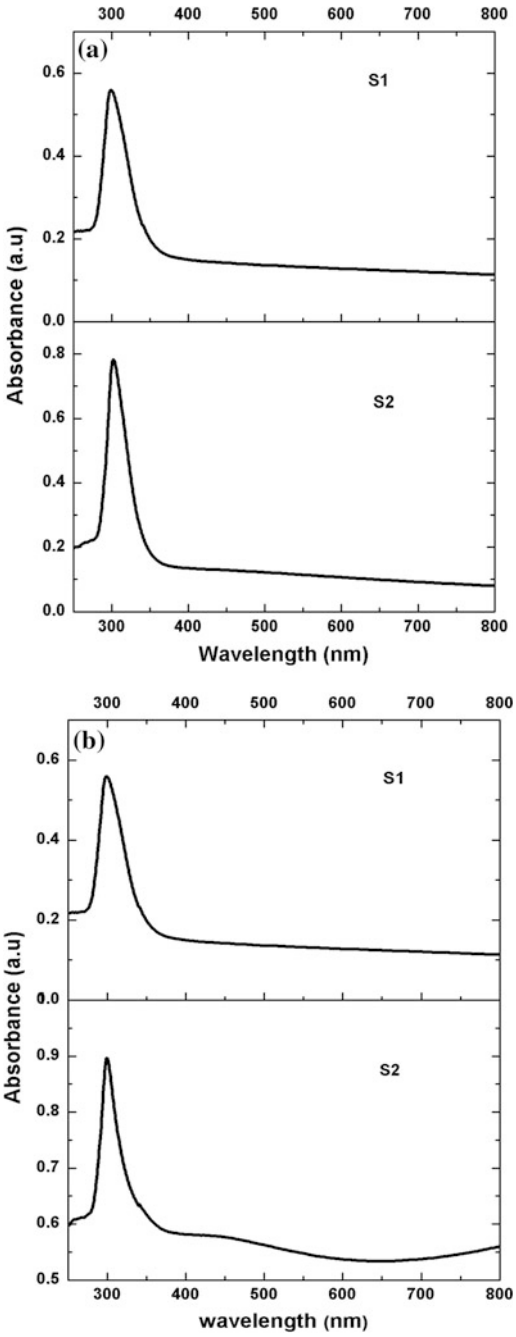

Fig. 4 Absorbance spectra of prepared TiO_2 films S1 (without titanium) and S2 (with titanium coating) (**a**) before and (**b**) after dye immersion

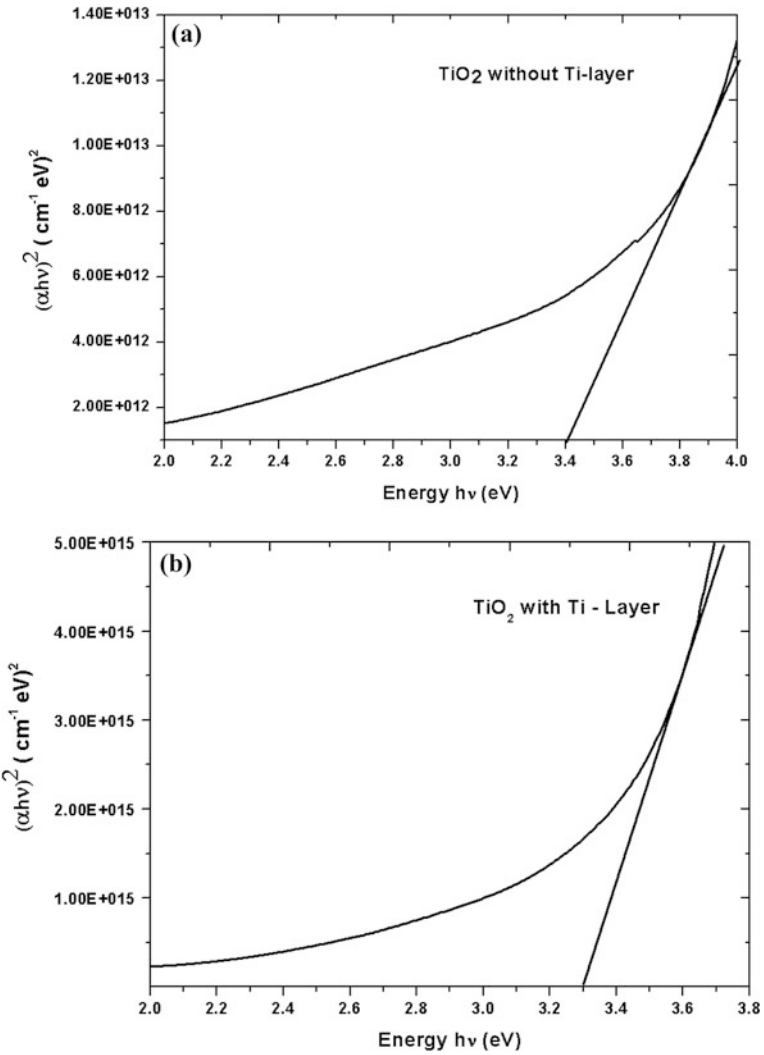

Fig. 5 Determination of direct band gap of prepared TiO_2 thin films

frequency ν, E_g is the optical band gap energy and A is the frequency independent constant for a direct transition. By extrapolating the linear part of the curve to zero, a direct band gap of 3.4 and 3.29 eV were obtained for TiO_2 thin films without (Fig. 5a) and with (Fig. 5b) titanium coating, respectively. Therefore, titanium coating improves the crystalline arrangement of TiO_2 film in the anatase nature and band gap value is red shifted to 3.29 eV which makes it suitable for photovoltaic application.

3.4 Photovoltaic Characteristics

Figure 6 shows the photovoltaic characteristics of fabricated DSSCs. From the J–V curve, the parameters of short circuit current density (J_{sc}) in mA/cm^2, open circuit voltage (V_{oc}) in volts, fill factor (FF) and energy conversion efficiency (η) in % were obtained for DSSC corresponds to S1 electrode are 0.07 mA/cm^2, 0.92 V, 0.15, and 1.2 % respectively. While the photovoltaic parameters of the DSSC that were obtained from S2 electrode are J_{sc} = 0.175 mA/cm^2, V_{oc} = 0.86 V, FF = 0.143 and the overall energy conversion efficiency is 3 %. When using bare ITO substrate the corresponding DSSC had low photovoltaic conversion efficiency due to the lattice mismatch between substrate and TiO_2 nanoparticles. However when using titanium coated ITO substrate due to the enhanced necking between TiO_2 particles and between TiO_2 film and substrate resulted in more adsorption of dye and hence provided a good path for the electrons to transfer more efficiently. From the data that were obtained, the overall efficiency of DSSC is highly associated with the thin coating of TiO_2 (formed from Ti-layer) due to its tendency to occupy the surface of ITO substrate [25]. In addition, the titanium coating also restricts the charges to recombine at the electrolyte and ITO substrate.

From the dark J–V curve (Fig. 7) it is clear that Ti coating also limits the contact between the redox electrolyte and substrate thereby reducing the dark current.

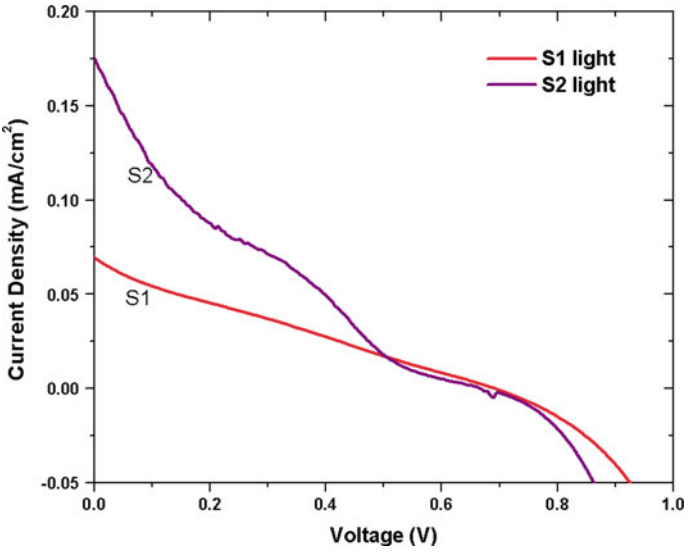

Fig. 6 J–V characteristics of DSSCs assembled with TiO_2 nanoparticles on bare ITO substrate (*S1*) and TiO_2 nanoparticles on titanium coated ITO substrate (*S2*)

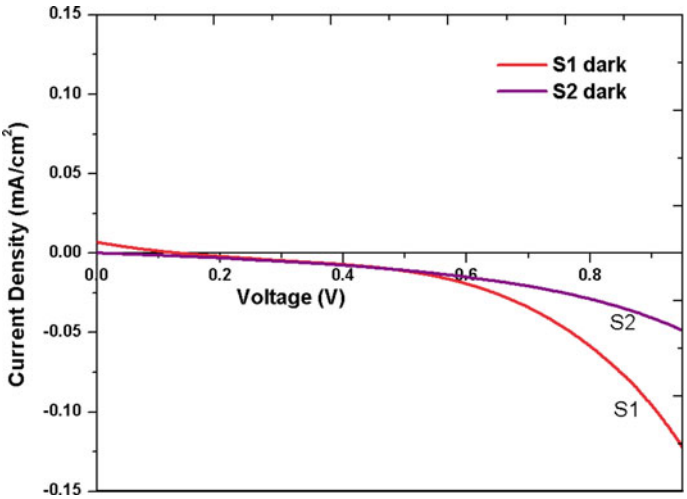

Fig. 7 Dark J–V characteristics of DSSCs assembled with TiO_2 nanoparticles on bare ITO substrate (*S1*) and TiO_2 nanoparticles on titanium coated ITO substrate (*S2*)

Eventhough this study shows the improvement in the cell performance further work is still needed in order to obtain higher efficiency [26].

3.5 Electrochemical Impedance Analysis

Figure 8a, b represents the Nyquist and Bode plots of electrochemical impedance spectra from which one can understand the internal working of solar cell. In Fig. 8a, the half arc obtained at the highest frequency region of Niquist plot describes the electron transport from excited sensitizer dye to the TiO_2 or reverse effect from the injected photo-electrons in TiO_2 to the polymer electrolyte. A slight reduction of bulk resistance was observed in Niquist plot owing to the introduction of Ti layer in the preparation process. The linear behavior in the Niquist plot in the low frequency region narrates the Warburg diffusion of the redox mediator inside the polymer-electrolyte and also reveals the sluggish ionic diffusion in the polymer electrolyte. From this it can be clearly seen that the charge transport in the electrolyte is predominantly from ionic diffusion transmission [27]. A comparable frequency shift from higher region to lower region is noted for DSSC corresponds to S2 electrode than S1 electrode as clearly seen from Fig. 8b. Overall this analysis reveals the reduction of charge recombination between TiO_2 and polymer electrolyte.

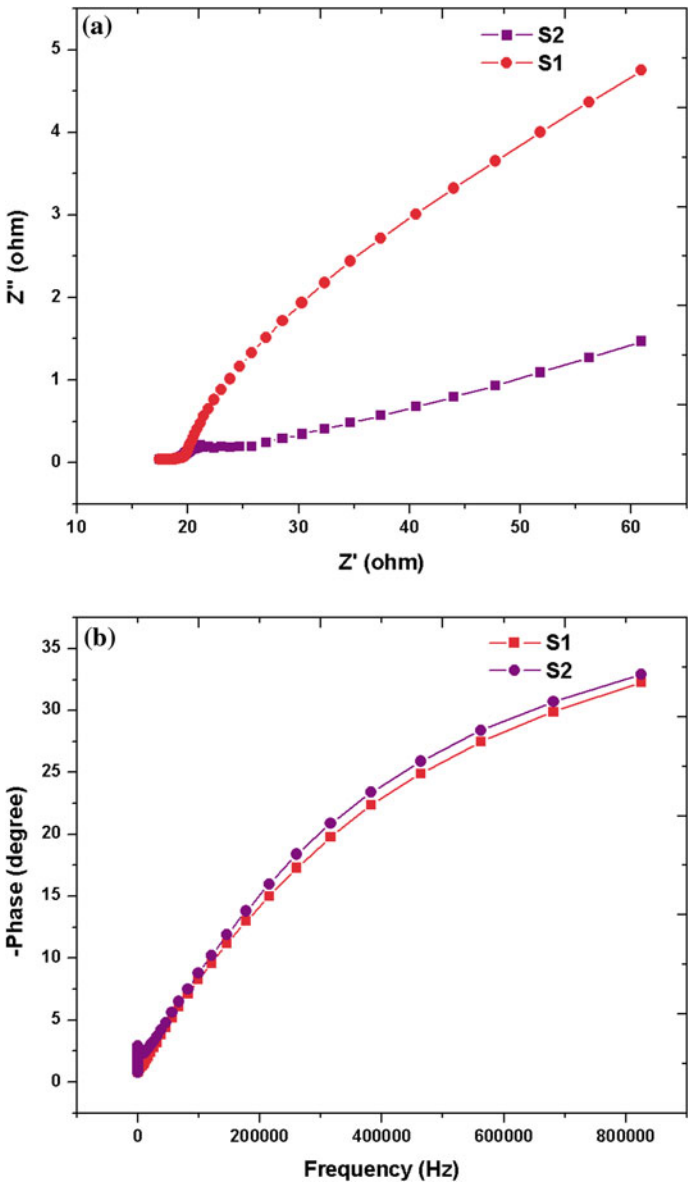

Fig. 8 EIS spectra of fabricated DSSCs **a** Nyquist plot, **b** Bode plot under light

4 Conclusion

This study presents a preparation of TiO_2 nanocrystalline films on pure and Titanium coated ITO glass substrates by sol-gel spin coating method. A profound effect on the structural, morphological, optical characteristics and on the conversion efficiency is obtained for titanium coated TiO_2 films. An efficiency of around 3 % is obtained for DSSC corresponding to TiO_2 film with titanium coating as the working electrode. More dye adsorption and the reduction of carrier recombination at the ITO and polymer electrolyte interface are the main causes for the improved performance of a solar cell. In addition, we verified that titanium coating could stabilize the structure of TiO_2 nanoparticles in anatase phase thereby enhancing the performance of the related DSSC.

References

1. Bandara, H.M.N., Rajapakse, R.M.G., Murakami, K., Kumara, G.R.R.A., Anuratha Sepalage, G.: Dye-sensitized solar cell based on optically transparent TiO_2 nanocrystalline electrode prepared by atomized spray pyrolysis technique. Electrochim. Acta **56**, 9159–9161 (2011)
2. Girtan, M., Stanculescu, A., Leontie, L., Habelhames, F., Antohe, S.: On titanium oxide spray deposited thin films for solar cells applications. Proc. Rom. Acad. Ser. A **13**, 335–342 (2012)
3. Hou, Y.Q., Zhuang, D.M., Zhang, G., Zhao, M., Wu, M.S.: Influence of annealing temperature on the propertiesof titanium oxide thin film. Appl. Surf. Sci. **218**, 97–105 (2003)
4. Castillo, N., Olguin, D., Conde-Gallardo, A., Jimenez-Sandoval, S.: Structural and morphological properties of TiO_2 thin films prepared by spray pyrolysis. Rev. Mex. Fis. **50**, 382–387 (2004)
5. Hagfeldt, A., Grätzel, M.: Molecular photovoltaics. Acc. Chem. Res. **33**, 269–277 (2000)
6. Zhang, Q., Cao, G.: Nanostructured photoelectrodes for dye-sensitized solar cells. Nano Today **6**, 91–109 (2011)
7. Asagoe, K., Suzuki, Y., Ngamsinlapasathian, S., Yoshikawa, S.: TiO_2-anatase nanowire dispersed composite electrode for dye-sensitized solar cells. J. Phys: Conf. Ser. **61**, 1112–1116 (2007)
8. Baxter, J.B., Aydil, E.S.: Nanowire-based dye-sensitized solar cells. Appl. Phys. Lett. **86**, 053114 (2005)
9. Pavasupree, S., Ngamsinlapasathian, S., Nakajima, M., Suzuki, Y., Yoshikawa, S.: Synthesis, characterization, photocatalytic activity and dye-sensitized solar cell performance of nanorods/nanoparticles TiO_2 with mesoporous structure. J. Photochem. Photobiol., A **184**, 163–169 (2006)
10. Yu, J.G., Zhao, X.J., Zhao, Q.N.: Photocatalytic activity of nanometer TiO_2 thin films prepared by the sol-gel method. Mater. Chem. Phys. **69**, 25–29 (2001)
11. Liu, J., Yang, D., Shi, F., Cai, Y.: Sol-gel deposited TiO_2 film on NiTi surgical alloy for biocompatibility improvement. Thin Solid Films **429**, 225–230 (2003)
12. Mechiakh, R., Meriche, F., Kremer, R., Bensaha, R., Boudine, B., Boudrioua, A.: TiO_2 thin films prepared by sol-gel method for waveguiding applications: correlation between the structural and optical properties. Opt. Mater. **30**, 645–651 (2007)
13. Nair, A.S., Jose, R., Shengyuan, Y., Ramakrishna, S.: A simple recipe for an efficient TiO_2 nanofiber-based dye-sensitized solar cell. J. Colloid Interface Sci. **353**, 39–45 (2011)
14. Greiner, A., Wendorff, J.H.: Electrospinning: a fascinating method for the preparation of ultrathin fibers. Angew. Chem. Int. Ed. **46**, 5670–5703 (2007)

15. Mohammadi, M.R., Cordero-Cabrera, M.C., Ghorbani, M., Fray, D.J.: Synthesis of high surface area nanocrystalline anatase-TiO_2 powders derived from particulate sol-gel route by tailoring processing parameters. J. Sol-Gel. Sci. Technol. **40**, 15–23 (2006)
16. Liu, B., Aydil, E.S.: Growth of oriented single-crystalline rutile TiO_2 nanorods on transparent conducting substrates for dye-sensitized solar cells. J. Am. Chem. Soc. **131**, 3985–3990 (2009)
17. Wang, J.Y., Zhang, T.J., Wang, D.F., Pan, R.K., Wang, Q.Q., Xia, H.M.: Improved morphology and photovoltaic performance in TiO2 nanorod arrays based dye sensitized solar cells by using a seed layer. J. Alloys Compd. **551**, 82–87 (2013)
18. Nwanya, A.C., Ezema, F.I., Ejikeme, P.M.: Dyed sensitized solar cells: a technically and economically alternative concept to p-n junction photovoltaic devices. Int. J. Phys. Sci. **6**, 5190–5201 (2011)
19. Zhao, J., Wan, P., Xiang, J., Tong, T., Dong, L., Gao, Z., Shen, X., Tong, H.: Synthesis of highly ordered macro-mesoporous anatase TiO_2 film with high photocatalytic activity. Microporous Mesoporous Mater. **138**, 200–206 (2011)
20. Tsuge, Y., Inokuchi, K., Onozuka, K., Shingo, O., Sugi, S., Yoshikawa, M., Shiratori, S.: Fabrication of porous TiO_2 films using a spongy replica prepared by layer-by-layer self-assembly method: Application to dye-sensitized solar cells. Thin Solid Films **499**, 396–401 (2006)
21. Ineta, L., Gunars, B., Andrejs, L., Gundars, M., Martins, V.: Preparation and characterization of nanostructured Fe-TiO_2 thin films produced by electrophoretic deposition. Mater. Sci. Eng. **49**, 012060 (2013)
22. Maiyalagan, T., Viswanathan, B., Varadaraju, U.V.: Fabrication and characterization of uniform TiO_2 nanotube arrays by sol-gel template method. Bull. Matter. Sci. **29**, 705–708 (2006)
23. Zhu, G., Xu, T., Lv, T., Pan, L., Zhao, Q., Sun, Z.: Graphene-incorporated nanocrystalline TiO_2 films for CdS quantum dot-sensitized solar cells. J. Electroanal. Chem. **650**, 248–251 (2011)
24. Jin-Kook Lee, J.K., Jeong, B., Jang, S., Kim, Y.-G., Jang, Y.-W., Lee, S., Kim, M.: Preparations of TiO_2 pastes and its application to light-scattering layer for dye-sensitized solar cells. J. Ind. Eng. Chem. **15**, 724–729 (2009)
25. Liao, M.Y., Fang, L., Xu, C.L., Wu, F., Huang, Q.L., Saleem, M.: Effect of seed layer on the growth of rutile TiO_2 nanorod arrays and their performance in dye-sensitized solar cells. Mater. Sci. Semicond. Process. **24**, 1–8 (2014)
26. Mathew, S., Yella, A., Gao, P., Humphry-Baker, R., Curchod, B.F.E., Ashari-Astani, N., Tavernelli, I., Rothlisberger, U., Nazeeruddin, MdK, Grätzel, M.: Dye-sensitized solar cells with 13 % efficiency achieved through the molecular engineering of porphyrin sensitizers. Nat. Chem. **6**, 242–247 (2014)
27. Kern, R., Sastrawan, R., Ferber, J., Stangl, R., Luther, J.: Modeling and interpretation of electrical impedance spectra of dye solar cells operated under open-circuit conditions. Electrochim. Acta **47**, 4213–4225 (2002)

$CuInS_2$ Layer Deposition Through Nebulizer Spray Technique for Solar Cell Fabrication

C. Ravi Dhas, A. Jennifer Christy, R. Venkatesh, B. Anitha, A. Juliat Josephine, D. David Kirubakaran, D. Arivukarasan, P. Sudhagar, A. Moses Ezhil Raj and C. Sanjeeviraja

Abstract $CuInS_2$ (CIS) thin films were fabricated by jet nebulizer spray technique at various substrate temperatures such as 250, 300, 350 and 400 °C. The XRD revealed the formation of chalcopyrite crystalline phase with (1 1 2) preferential orientation. The film prepared at 300 °C has better crystallinity with minimum dislocation density and strain. The microstructure of the prepared CIS thin films was investigated by means of scanning electron microscope (SEM). The elemental quantification and stoichiometric ratio of the CIS films were confirmed by EDS. The conductivity of CIS thin films was carried out by four probe method and it showed that all the films were in semiconducting nature. The optical band gap was found using Tauc plot and it was varied from 1.3 to 1.45 eV. A peak around 298 cm^{-1} was observed in Raman spectra attributed to the mixture of both CH- and CA-ordering.

C. Ravi Dhas (✉) · A. Jennifer Christy · R. Venkatesh · B. Anitha
D. David Kirubakaran · D. Arivukarasan
PG and Research Department of Physics, Bishop Heber College (Autonomous), Tiruchirappalli 620017, India
e-mail: ravidhasc@gmail.com

A. Juliat Josephine
PG and Research Department of Physics, Holy Cross College (Autonomous), Tiruchirappalli 620002, India

P. Sudhagar
School of Chemistry and Chemical Engineering, Queens University, Belfast BT9 5AG, Northern Ireland, UK

A. Moses Ezhil Raj
Department of Physics, Scott Christian College (Autonomous), Nagercoil 629001, India

C. Sanjeeviraja
Department of Physics, Alagappa Chettiar College of Engineering and Technology, Karaikudi 630003, India

J. Ebenezar (ed.), *Recent Trends in Materials Science and Applications*, Springer Proceedings in Physics 189, DOI 10.1007/978-3-319-44890-9_41

1 Introduction

Chalcopyrite semiconductors have a vast potential as absorber layer thin film for solar cell application [1]. $CuInS_2$ (CIS) is one of the I–III–VI_2 type semiconductors and the most attractive material for solar cell due to its band gap [2]. 13 % efficiency has been reported for CIS solar cell in the laboratory [3]. Among chalcopyrite family, the sulphur compounds such as $CuInS_2$, $CuGaS_2$ and $CuInGaS_2$ are paid more attention to in-order not to use selenium toxic precursor materials [4, 5]. Fabrication of $CuInS_2$, $CuInGaS_2$ thin films via two-stage evaporation and/or co-sputtering followed by the reactive annealing using hydrogen sulphur (H_2S) gas have been reported, enormously [5, 6]. In addition to this, H_2S gas is highly toxic and extra care is to be taken in the laboratory [1]. Considering these aspects, vacuum deposition method can be overcome by depositing thin films by chemical methods. Chemical bath, wet chemical method and electrochemical method, etc. have been used to deposit both absorber and window layer of thin film solar cells [7, 8]. Chemical Spray pyrolysis is an attractive and widely used method because uniform crystallinity can be obtained at low cost for large area films [9]. Many authors have reported using Chemical Spray pyrolysis method [9, 10] but also reported that it is difficult to obtain single phase CIS thin films [11–13]. Efficient photovoltaic solar cell could be manufactured by optimizing the surface composition and the control of film bulk [14].

In this work, we have demonstrated that the CIS thin films have been fabricated by nebulizer spray for the first time to our knowledge. The structural, morphological, electrical, optical and Raman studies were analysed for different substrate temperatures.

2 Materials and Methods

2.1 Materials

Copper Chloride ($CuCl_2$), Indium Chloride ($InCl_3$) and Thiourea $SC(NH_2)_2$ were purchased from Alfa Aesar, analytical grade with the purity of 99 %.

2.2 Experimental

The experimental technique follows the jet nebulizer spray apparatus setup which has been reported earlier [15]. Aqueous precursor solutions were prepared using Copper Chloride ($CuCl_2$), Indium Chloride ($InCl_3$) and Thiourea $SC(NH_2)_2$ as copper, indium and sulphur source, respectively with the molar ratio of 1:1:4 and dissolved in a 50 ml of distilled water. This solution was vigorously stirred at room temperature.

The prepared solution was taken in the nebulizer container and sprayed on clean glass substrate at different substrate temperatures like 250, 300, 350 and 400 °C. The generated aerosols were transported by a carrier gas with constant pressure of 0.8 kg/cm^2 on the preheated glass substrate, with the spray rate of 0.75 ml/min. The deposition time for the whole process was about 40 min. During the deposition, the transported aerosols underwent decomposition reaction on the substrate surface to produce CIS thin films.

2.3 Characterization

The phase identification, morphological and elemental composition of CIS were characterized by X-ray Diffraction with a PANanalytical X'PERT PRO diffractometer using the CuK_α rays at the wavelength of 1.54 Å, Scanning Electron Microscopy (VEGA3 TESCAN), Energy Dispersive Spectra (Bruker). Electrical and Hall measurements were carried out by four probe methods with the Keithley 2400 source meter. A JASCO UV-Vis NIR-V-670 Spectrophotometer was used to analyse the optical characterization. A Horiba-Jobin, LabRAMHR was employed to record the Raman spectra.

3 Results and Discussion

3.1 Determination of Film Thickness

The thickness of the deposited CIS thin films was measured by using gravimetric method. The well-cleaned glass plate was weighed in a high precision digital balance. After the deposition, the coated glass plate was weighed. The difference in weight gives the mass of the deposited material (M). The standard formula for the thickness is given by [16],

$$T = \frac{M}{A * d}\ (\mathrm{m}) \tag{1}$$

where A is the area of the substrate and D is the density of the material. The calculated value of the film thickness is found to be around 1.1 μm.

3.2 Structural Properties

XRD patterns of CIS thin films deposited at different substrate temperatures are shown in Fig. 1. According to the JCPDS card no. 65–1572 (I-42d space group), all

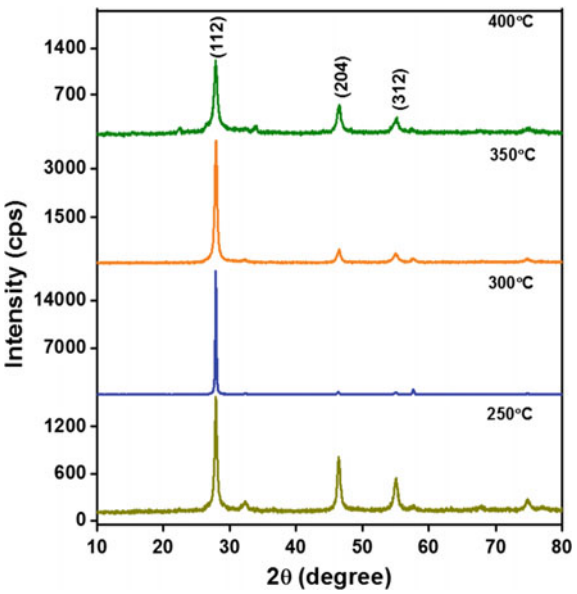

Fig. 1 X-ray diffraction of CIS thin films at different substrate temperatures

the deposited films are in tetragonal structure with the preferential orientation along (1 1 2) plane at 2θ = 27.9°. The preferential orientation of (1 1 2) plane grows because it has the lowest surface energy [17]. The weak peaks at 2θ = 46.4°, 54.9° correspond to (2 0 4) and (3 1 2) planes respectively present at 250 °C whereas these peak get suppressed and (1 1 2) plane enhanced at 300 °C. The improvement in the crystallinity is due to the diffusion of atoms absorbed on the surface and the atoms migrate towards its sufficient energy. Further increasing the substrate temperature to 350 °C, the intensity of the (1 1 2) plane decreases whereas (2 0 4) and (3 1 2) planes begin to emerge. This may be attributed to the phase transition from chalcopyrite to sphalerite, happening unconditionally during film deposition by spray pyrolysis at 350 °C which has been observed by other authors [18, 19]. Thus the properties of film are strongly dependent on the substrate temperature.

The crystallite size was estimated using Debye Scherrer's equation [20],

$$D = \frac{K\lambda}{\beta \cos\theta}(\text{nm}) \tag{2}$$

where 'D' is the average crystallite size (Å), 'K' is the shape factor taken as 0.9, 'λ' is the wave length of X-ray (Kα = 1.5406 Å), 'β' is Full Width Half Maximum (degree), 'θ' is diffraction angle. From Fig. 2 and Table 1, it is obvious that the maximum crystallite size is obtained at 300 °C and hence it is expected to increase the photovoltaic efficiency [21]. According to Ostwald ripening, combining small particles to a large one leads to increase in crystallite size and hence results in the potential energy difference between small and large particles and can cause solid

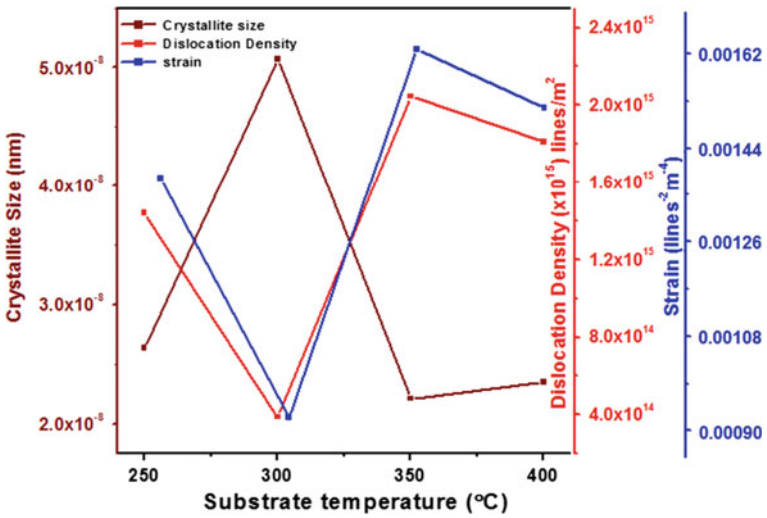

Fig. 2 Substrate temperature versus crystallite size, dislocation density and strain of CIS thin films

Table 1 Crystallite size, dislocation density and strain of CIS thin films

Substrate temperature (°C)	Crystallite Size (D) (nm)	Dislocation density × 10^{15} (lines/m^2)	Strain (lines^{-2} m^{-4})
250	26.34	1.4413	0.00138
300	50.72	0.3887	0.00093
350	22.11	2.0456	0.00163
400	23.50	1.8107	0.00152

state diffusion [22]. Decrease in crystallite size at higher temperature is due to coalescence of particles [23].

The dislocation density (δ) and strain (ε) of CIS thin films [15] were calculated (Table 1) from the relation (3) and (4),

$$\delta = \frac{1}{D^2}(\text{lin/m}^2) \tag{3}$$

$$\varepsilon = \frac{\beta \cos\theta}{4}(\text{lin}^{-2}\,\text{m}^{-4}) \tag{4}$$

Figure 2 shows the variation of substrate temperature with the dislocation density and strain. The presence of low value in dislocation density and strain at 300 °C may be due to the transition of interstitial atoms from its grain boundary to the crystallites [24]. Jain and Verma reported that large crystallite contains less strain [25].

3.3 Surface Properties

The surface morphology of CIS thin films deposited at different substrate temperature is shown in Fig. 3. The substrate temperature plays a vital role in the development of film growth. At 250 °C, the grains are non-uniformly distributed due to the late arrival of droplets on the substrate surface [26]. Smooth and dense formation of grains is clearly observed at 300 °C due to the shrinkage and compaction of droplets arriving at the substrate. Similar results were observed by [27]. The appearance of nanorod like structure obtained at 300 °C might be due to the better nucleation of crystalline facet which possesses lower surface energy, as in our case it is (1 1 2) plane, witnessed from XRD results [17]. The increase in substrate temperature leads to the growth of the crystallites and reduces the separation of grain boundaries. For higher substrate temperatures like 350 and 400 °C, morphology of the films turned into needle shape and spherical grains were observed. Substrate temperature plays a crucial role in tuning the morphology of the $CuInS_2$ films. In nebulizer spray technique, thermal decomposition ability of the precursor, solvent evaporation rate and radius of cone evolved from spray nozzle are the determining factors for the morphology of the films.

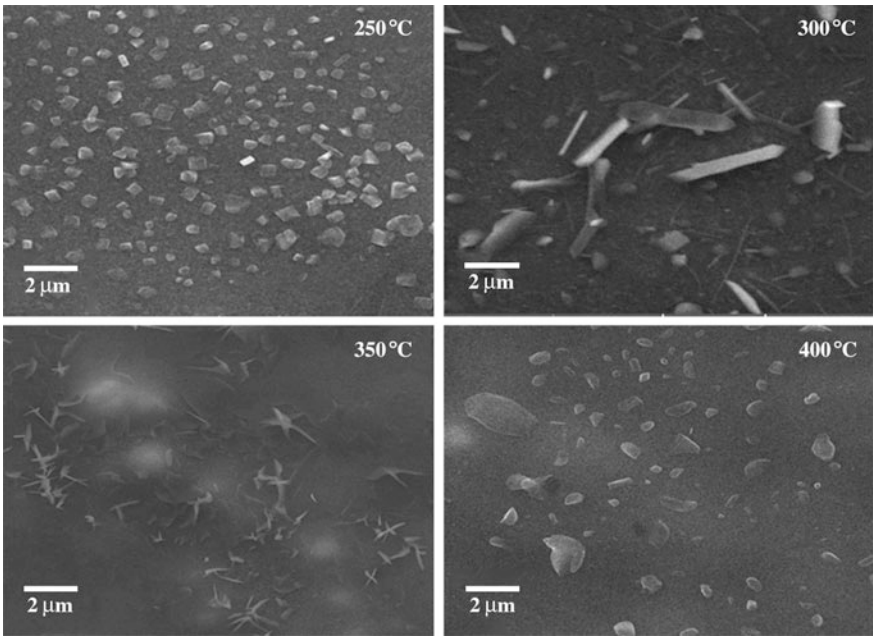

Fig. 3 SEM images of CIS thin film at different substrate temperatures

3.4 Energy Dispersive X-ray Analysis (EDS)

Figure 4 shows the EDS spectra of CIS thin films deposited at different substrate temperatures. The elemental composition of CIS thin films determined by EDS analysis is shown in Table 2. Though the elemental composition analysis reveals better stoichiometry for all the deposited films, Cu/In ratio is a highly sensitive parameter in $CuInS_2$. If Cu/In = 1 and hence it will be most preferable for solar cell

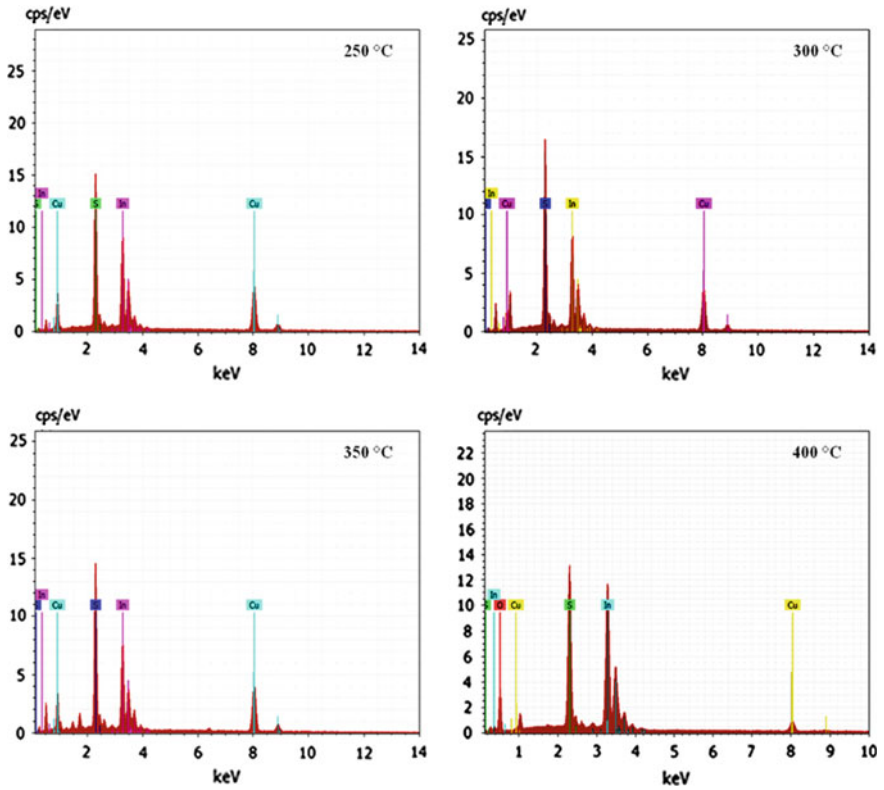

Fig. 4 Energy dispersive X-ray analysis of CIS thin films at different substrate temperatures

Table 2 Elemental composition of CIS thin films

Substrate temperature (°C)	Composition ratio (at.%)				Nature of the film
	Copper	Indium	Sulphur	Cu/In ratio	
250	27.16	24.43	48.41	1.11	Cu-rich
300	25.90	24.37	49.73	1.06	Stoichiometry
350	23.62	28.44	47.94	0.83	In-rich
400	21.54	26.69	51.77	0.80	In-rich

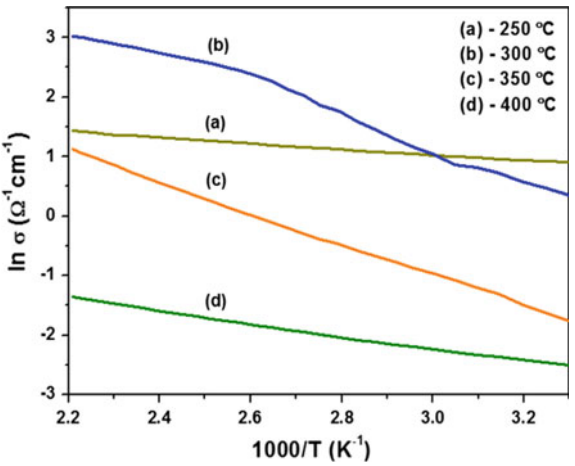

Fig. 5 Conductivity versus temperature of CIS thin films at different substrate temperatures

application. Even a small variation in this ratio will affect the optical and electrical properties of CIS thin films [28]. The calculated Cu/In ratio is equal to 1 for CIS film prepared at 300 °C, and hence this will be optimum condition in the present work.

3.5 Electrical Properties

The temperature (T) dependence of the conductivity (σ) was measured to identify the transport mechanisms in the deposited films. Figure 5 depicts the plots of ln σ versus 1000/T of the deposited CIS films in the temperature range of 302–452 K. The conductivity of the CIS thin film increases with the increase in temperature, indicating the semiconducting nature. The activation energy, which determines the potential barrier height, can be calculated from this Arrhenius plots, and it is found to be 0.25, 0.24, 0.48 and 0.26 eV. The difference in the activation energy also depends on the change in grain size, as indicated in XRD. It is the fact that larger crystallite size has smaller number of grain boundaries which reduces the scattering phenomenon and reduction in thermal activation energy [29].

The electrical resistivity and carrier concentration of the CIS thin films are calculated using the van der Pauw technique at room temperature by the Hall effect measurement system and it is represented in Fig. 6. The CIS film prepared at 250 °C exhibited lower resistivity and higher carrier concentration, which might be attributed to the presence of a Cu-rich phase on the films surface [30] as given in Table 2. As the substrate temperature is increased to 300 °C, the resistivity of the film increases, and the carrier concentration is reduced. The CIS thin films deposited at 300 °C exhibits better semiconducting nature compared to 250 °C which is suitable for fabricating solar cell devices. The plausible reason for high

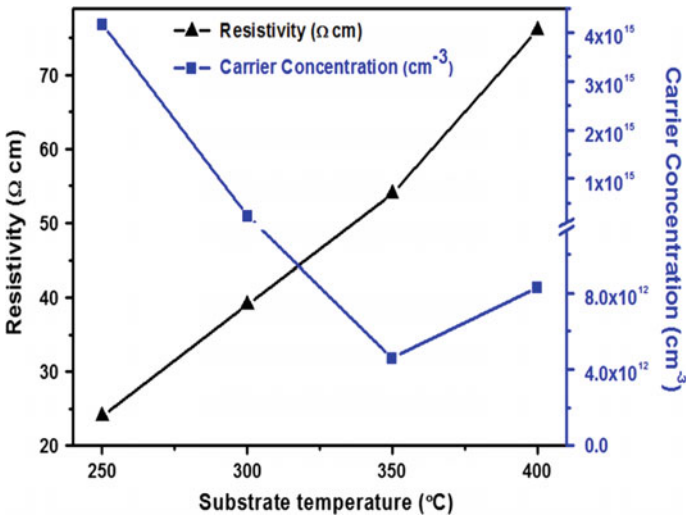

Fig. 6 Substrate temperature versus resistivity, carrier concentration of CIS thin films

resistivity of CIS film prepared at 350 °C owing to the indium (In) rich nature, results in compensation for the indium atoms as a replacement to copper vacancies (V_{cu}) and acts as donor which drastically reduces the concentration of the carriers and it is supported by the literature [31]. The little amount of oxygen present at 400 °C as observed from EDS Fig. 4, leads to increase in resistivity (Table 3).

3.6 Optical Properties

Figure 7 shows the optical absorbance of the CIS thin films deposited at different substrate temperatures in the wavelength range 300–1900 nm. It is observed that the high absorbance occurs at 300 °C which is well suited for the absorber layer of solar cell and further increase in substrate temperature causes decrease in absor-

Table 3 Electrical measurements of CIS thin films

Substrate temperature (°C)	Activation energy (eV)	Resistivity (Ω cm)	Carrier concentration (cm^{-3})
250	0.25	24	4.17×10^{15}
300	0.24	39	2.33×10^{14}
350	0.48	54	4.59×10^{12}
400	0.26	76	8.27×10^{12}

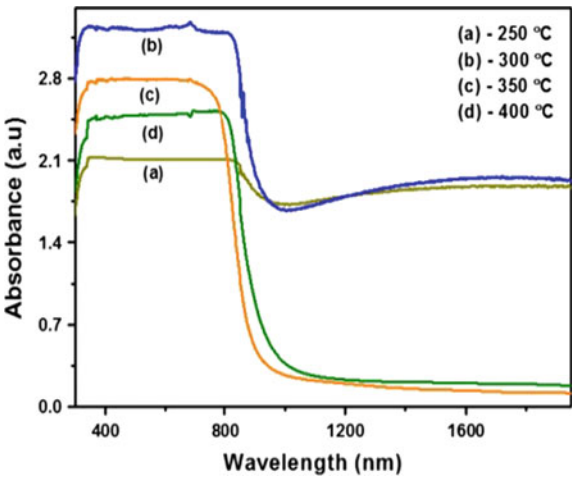

Fig. 7 Absorption co-efficient versus wavelength of CIS thin films at different substrate temperatures

bance. High absorbance occurred in the visible region and decreased in the infra-red region for all the films deposited at different substrate temperatures [32].

The optical bang gap of the CIS thin film can be obtained using the Tauc relation [15],

$$\alpha h\nu = A\left(h\nu - E_g\right)^n \tag{5}$$

where α, hν, E_g and n are absorption co-efficient, incident photon energy, band gap and n = ½ to 2. Since CIS is a direct band gap semiconducting material, the value of n can be taken as ½ [33].

By extrapolating tangents to x-axis, the band gap energy values of the deposited films are obtained and are shown in Fig. 8. The optical band gap values of the deposited CIS thin films are found to be 1.19, 1.13, 1.35 and 1.28 eV with the increasing substrate temperature. Optical band gap variation occurs due to the change in crystallite size and chemical composition of CIS films as evident from XRD and EDS.

3.7 Raman Spectra

Normally, Raman spectra are used to identify the surface phases present in the film. CIS thin film is usually found with two different structures such as CH- and CA-ordering which correspond to chalcopyrite and CuAu structures respectively and can be easily visualised using Raman spectroscopy. Figure 9 shows the Raman spectra of thin films prepared at different substrate temperatures. Similarly, A1 modes for CH- and CA-ordering are reported to be observed as the biggest peaks, which appear at 294 and 305 cm^{-1}, respectively [34, 35]. The broad peaks at

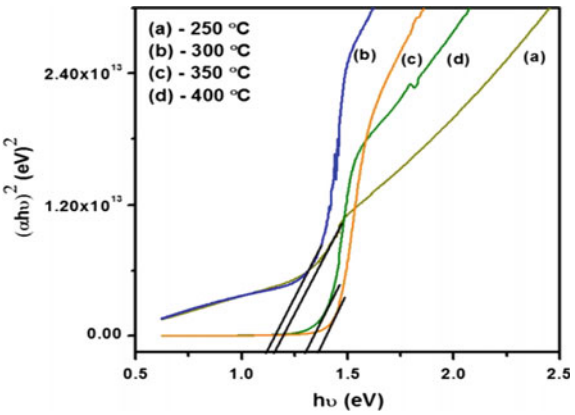

Fig. 8 Optical band gap determination of CIS thin films at different substrate temperatures

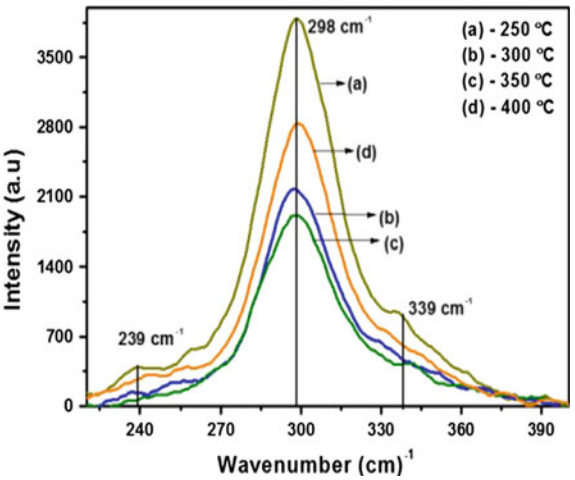

Fig. 9 Raman Spectra of CIS thin films at different substrate temperatures

298 cm^{-1} show that CIS thin films are formed with the mixture of both CH- and CA-ordering. A small peak near 239 and 339 cm^{-1} represents CH-ordering [36]. No other peaks corresponding to β-In_2S_3, $CuIn_5S_8$ and Cu_xS were detected [37]. The FWHM of A1 mode is low for the film deposited at 300 °C compared to other film which is an indication of better crystallinity as evidenced from XRD results.

4 Conclusion

CIS thin films were deposited at different substrate temperature by nebulizer spray technique. XRD results indicated that all the films are in tetragonal structure with preferential orientation (1 1 2) plane and maximum crystallite size with low

dislocation density and strain is observed at 300 °C. Nano-rod structure morphology was obtained for the film deposited at 300 °C. Better stoichiometric nature of CIS thin films was confirmed by EDS analysis. High electrical conductivity and optical absorbance have been observed. The broad Raman peaks at 298 cm^{-1} show that CIS thin films are formed with the mixture of both CH- and CA-ordering. With low cost, large scale area of solar cell can be fabricated easily by nebulizer spray technique with the optimized condition of 300 °C.

Acknowledgements This work was financially supported by the University Grants Commission, New Delhi, India [F.no. 42-903/2013(SR)] under Major Research Project Scheme (MRP). The authors would like to record their sincere thanks to the Commission.

References

1. Aydin, E., Sankir, M., Sankir, N.D.: Conventional and rapid thermal annealing of spray pyrolyzed copper indium gallium sulfide thin films. J. Alloys Compd. **615**, 461–468 (2014)
2. Muhammad, N.M., Sundharam, S., Dang, H.-W., Lee, A., Ryu, B.-H., Choi, K.-H.: CIS layer deposition through electrospray process for solar cell fabrication. Curr. Appl. Phys. **11**, S68–S75 (2011)
3. Klaer, J., Bruns, J., Henninger, R., Siemer, K., Klenk, R., Ellmer, K.: Efficient thin-film solar cells prepared by a sequential process. Semicond. Sci. Technol. **13**, 1456 (1998)
4. Guillen, C., Herrero, J.: $CuInS_2$ and $CuGaS_2$ thin films grown by modulated flux deposition with various Cu contents. Phys. Status Solidi. (A) **203**, 2438–2443 (2006)
5. Liu, X., Liu, Z., Meng, F., Chichibu, S.F., Sugiyama, M.: Preparation of $CuInS_2$ thin films by sulfurization using ditertiarybutylsulfide. Thin Solid Films **558**, 400–404 (2014)
6. Kaigawa, R., Neisser, A., Klenk, R., Lux-Steiner, M.-C.: Improved performance of thin film solar cells based on Cu (In, Ga) S_2. Thin Solid Films **415**, 266–271 (2002)
7. Coughlan, C., Singh, A., Ryan, K.M.: Systematic study into the synthesis and shape development in colloidal $CuIn_xGa_{1-x}S_2$ nanocrystals. Chem. Mater. **25**, 653–661 (2013)
8. Pan, G.-T., Lai, M.-H., Juang, R.-C., Chung, T.-W., Yang, T.C.-K.: The preparation and characterization of Ga-doped $CuInS_2$ films with chemical bath deposition. Sol. Energy Mater. Sol. Cells **94**, 1790–1796 (2010)
9. Bates, C.W., Nelson, K.F., Raza, S.A., Mooney, J.B., Recktenwald, J.M., Macintosh, L., Lamoreaux, R.: Spray pyrolysis and heat treatment of $CuInSe_2$ for photovoltaic applications. Thin Solid Films **88**, 279–283 (1982)
10. Shirakata, S., Murakami, T., Kariya, T., Isomura, S.: Preparation of $CuInSe_2$ thin films by chemical spray pyrolysis. Jpn. J. Appl. Phys. **35**, 191 (1996)
11. Krunks, M., Kijatkina, O., Rebane, H., Oja, I., Mikli, V., Mere, A.: Composition of $CuInS_2$ thin films prepared by spray pyrolysis. Thin Solid Films **403**, 71–75 (2002)
12. Oja, I., Nanu, M., Katerski, A., Krunks, M., Mere, A., Raudoja, J., Goossens, A.: Crystal quality studies of $CuInS_2$ films prepared by spray pyrolysis. Thin Solid Films **480**, 82–86 (2005)
13. Zouaghi, M., Nasrallah, T.B., Marsillac, S., Bernede, J., Belgacem, S.: Physico-chemical characterization of spray-deposited $CuInS_2$ thin films. Thin Solid Films **382**, 39–46 (2001)
14. Katerski, A., Mere, A., Kazlauskiene, V., Miskinis, J., Saar, A., Matisen, L., Kikas, A., Krunks, M.: Surface analysis of spray deposited copper indium disulfide films. Thin Solid Films **516**, 7110–7115 (2008)
15. Ravidhas, C., Anitha, B., Raj, A.M.E., Ravichandran, K., Girisun, T.S., Mahalakshmi, K., Saravanakumar, K., Sanjeeviraja, C.: Effect of nitrogen doped titanium dioxide (N-TiO_2) thin

films by jet nebulizer spray technique suitable for photoconductive study. J. Mater. Sci.: Mater. Electron. **26**, 3573–3582 (2015)
16. Sartale, S., Lokhande, C.: Preparation and characterization of nickel sulphide thin films using successive ionic layer adsorption and reaction (SILAR) method. Mater. Chem. Phys. **72**, 101–104 (2001)
17. Morinaga, Y., Sakuragi, K., Fujimura, N., Ito, T.: Effect of Ce doping on the growth of ZnO thin films. J. Cryst. Growth **174**, 691–695 (1997)
18. Guillen, C., Herrero, J., Gutiérrez, M., Briones, F.: Structure, morphology and optical properties of $CuInS_2$ thin films prepared by modulated flux deposition. Thin Solid Films **480**, 19–23 (2005)
19. Bandyopadhyaya, S., Chaudhuri, S., Pal, A.: Synthesis of $CuInS_2$ films by sulphurization of Cu/In stacked elemental layers. Sol. Energy Mater. Sol. Cells **60**, 323–339 (2000)
20. Ravidhas, C., Josephine, A.J., Sudhagar, P., Devadoss, A., Terashima, C., Nakata, K., Fujishima, A., Raj, A.M.E., Sanjeeviraja, C.: Facile synthesis of nanostructured monoclinic bismuth vanadate by a co-precipitation method: structural, optical and photocatalytic properties. Mater. Sci. Semicond. Process. **30**, 343–351 (2015)
21. Sahal, M., Marí, B., Mollar, M.: $CuInS_2$ thin films obtained by spray pyrolysis for photovoltaic applications. Thin Solid Films **517**, 2202–2204 (2009)
22. Kumar, P., Jain, N., Agrawal, R.: Effect of substrate temperature on optical properties of Bi_2S_3 chalcogenide thin films. Chalcogenide Lett. **7**, 89–94 (2010)
23. Ravidhas, C., Anitha, B., Arivukarasan, D., Venkatesh, R., Christy, A.J., Jothivenkatachalam, K., Nithya, A., Moses Ezhil Raj, A., Ravichandran, K., Sanjeeviraja, C.: Tunable morphology with selective faceted growth of visible light active TiO_2 thin films by facile hydrothermal method: structural, optical and photocatalytic properties. J. Mater. Sci. Mater. Electron. **27**, 5020–5032 (2016)
24. Senthilarasu, S., Sathyamoorthy, R., Lalitha, S., Subbarayan, A., Natarajan, K.: Thermally evaporated ZnPc thin films—band gap dependence on thickness. Sol. Energy Mater. Sol. Cells **82**, 179–186 (2004)
25. Jain, V.K., Verma, A.: Physics of Semiconductor Devices: 17th International Workshop on the Physics of Semiconductor Devices 2013. Springer Science & Business Media, Berlin (2013)
26. Suresh, R., Ponnuswamy, V., Mariappan, R.: Consequence of source material on the surface properties of nebulizer spray coated cerium oxide thin films. Vacuum **109**, 94–101 (2014)
27. Mahendran, C., Suriyanarayanan, N.: Effect of temperature on structural, optical and photoluminescence properties of polycrystalline $CuInS_2$ thin films prepared by spray pyrolysis. Phys. B **405**, 2009–2013 (2010)
28. Kavcar, N., Carter, M., Hill, R.: Characterization of $CuInSe_2$ thin films produced by thermal annealing of stacked elemental layers. Sol. Energy Mater. Sol. Cells **27**, 13 (1992)
29. Mishra, P., Dave, V., Chandra, R., Prasad, J., Choudhary, A.: Effect of processing parameter on structural, optical and electrical properties of photovoltaic chalcogenide nanostructured RF magnetron sputtered thin absorbing films. Mater. Sci. Semicond. Process. **25**, 307–319 (2014)
30. Zhang, L., Liu, F.-F., Li, F.-Y., He, Q., Li, B.-Z., Li, C.-J.: Structural, optical and electrical properties of low-temperature deposition Cu (In_xGa_{1-x}) Se_2 thin films. Sol. Energy Mater. Sol. Cells **356–361**, 99 (2012)
31. Akl, A.A., Afify, H.: Growth and microstructure, optical and electrical properties of sprayed $CuInSe_2$ polycrystalline films. Mater. Res. Bull. **43**, 1539 (2008)
32. Han, A., Zhang, Y., Song, W., Li, B., Liu, W., Sun, Y.: Structure, morphology and properties of thinned Cu (In, Ga) Se_2 films and solar cells. Semicond. Sci. Technol. **27**, 035022 (2012)
33. Lalitha, S., Sathyamoorthy, R., Senthilarasu, S., Subbarayan, A., Natarajan, K.: Characterization of CdTe thin film—dependence of structural and optical properties on temperature and thickness. Sol. Energy Mater. Sol. Cells **82**, 187–199 (2004)
34. Rudigier, E., Barcones Campo, B., Luck, I., Jawhari, T., Pérez Rodríguez, A., Scheer, R.: Quasi real-time Raman studies on the growth of Cu–In–S thin films. J. Appl. Phys. **95**, 5153–5158 (2004)

35. Alvarez-Garcıa, J., Pérez-Rodrıguez, A., Barcones, B., Romano-Rodrıguez, A., Morante, J., Janotti, A., Wei, S.-H., Scheer, R.: Polymorphism in $CuInS_2$ epilayers: origin of additional Raman modes. Appl. Phys. Lett. **80**, 562–564 (2002)
36. Lee, D.-Y., Kim, J.: Deposition of $CuInS_2$ films by electrostatic field assisted ultrasonic spray pyrolysis. Sol. Energy Mater. Sol. Cells **95**, 245–249 (2011)
37. Nakamura, S., Ando, S.: Preparation of $CuInS_2$ thin films by metal–organic decomposition. J. Phys. Chem. Solids **66**, 1944–1946 (2005)

Part V
Crystal Growth

Synthesis, Growth and Characterization of Potassium Niobate ($KNbO_3$) Single Crystal by Top Seeded Solution Growth Method

S. Raja, R. Ramesh Babu, K. Ramamurthi and N. Balamurugan

Abstract Potassium niobate ($KNbO_3$), a lead free perovskite single crystal, was grown by top seeded solution growth method using K_2O as self flux. The synthesized powder and grown crystal of $KNbO_3$ were studied by various characterization techniques. The thermal stability of $KNbO_3$ was determined by Thermo Gravimetric and Differential Thermogram (TG-DTG) analyses. X-ray diffraction (XRD), Fourier transform infrared spectroscopy (FTIR) and Raman spectral studies reveal the formation of single phase orthorhombic structure of $KNbO_3$ with space group *C*m2m. In addition, Rietveld refinement analysis of XRD of $KNbO_3$ confirms that there is no impurity or secondary phase formation in the grown crystal. Energy dispersive X-ray (EDS) analysis confirms the elemental composition and the presence of K, Nb and O. Chemical etching studies on the grown crystal reveal the layer by layer growth behavior.

1 Introduction

In recent years, perovskite alkaline niobates have received much attention due to their remarkable properties namely piezoelectric, ferroelectric, nonlinear optical, electro-optical and photorefractive properties [1]. Perovskite is one of the most studied structures in inorganic compound, which has general chemical formula of

S. Raja · R. Ramesh Babu (✉)
Crystal Growth and Thin Film Laboratory, Department of Physics, Bharathidasan University, Tiruchirappalli 620024, Tamil Nadu, India
e-mail: rampap2k@yahoo.co.in

K. Ramamurthi
Crystal Growth and Thin Film Laboratory, Department of Physics and Nanotechnology, Faculty of Engineering and Technology, SRM University, Kattankulathur 603203, Tamil Nadu, India

N. Balamurugan
GTAT Corporation, 3202-3203 Park Place, 1601 West Nanjing Road, Shanghai 20004, China

J. Ebenezar (ed.), *Recent Trends in Materials Science and Applications*, Springer Proceedings in Physics 189, DOI 10.1007/978-3-319-44890-9_42

ABX_3, where, A is a bigger cation (Na^{1+}, K^{1+}, Ca^{2+}, Sr^{2+}, Ba^{2+}), B is a smaller cation (Ti^{4+}, Nb^{5+}, Mn^{4+}, Zr^{4+}), and X is an anion (O^{2-}, F^{1-}, Cl^{1-}) [2]. Among the many alkaline niobates, potassium niobate ($KNbO_3$) is one of well known ferroelectric oxides with low toxicity, higher chemical stability and environmental compatibility (lead free). It is characterized by several phase transitions (cubic to tetragonal at 435 °C, tetragonal to orthorhombic at 216 °C and orthorhombic to rhombohedral at −10 °C) [3]. In addition, $KNbO_3$ exhibits several outstanding properties like high nonlinear optical, electro-optical coefficients and high refractive indices which makes it a promising candidate for piezoelectric, photorefractive, electro-optic, acousto-optic and non-linear optics, optical waveguides, optical parametric oscillation, frequency doublers, sensing, imaging applications, cryptography, signal processing circuits, photocatalytic, photovoltaic and holographic memory storage devices [4–13]. In the past several decades, there is a considerable effort has been devoted for the growth of high quality $KNbO_3$ single crystal. Although several methods such as Bridgman, Czochralski, Kyropoulos and top-seeded solution growth were used to grow $KNbO_3$ crystal, it is still difficult to obtain a good quality single crystal in large dimensions. This is because of its incongruently melting and stoichiometric deviation at high temperature which leads to formation of color, impurity inclusion and crystal cracking. Hence the adequate reproducibility of growth of $KNbO_3$ is still seems to be a major problem. Among the growth methods, Top Seeded Solution Growth (TSSG) technique offers some advantages in growing perovskite oxide single crystals of good quality, high compositional homogeneity, and controlled morphology [14]. The main advantage of TSSG method is that the crystals grow at temperature well below the melting temperature of the material particularly for melt incongruent materials. Therefore, in the present study, we have made an attempt to grow $KNbO_3$ crystals using TSSG technique and studied its thermal, structural and morphological properties.

2 Experiment

In order to synthesis $KNbO_3$ powder, the commercially available high purity potassium carbonate (K_2CO_3, 99.99 %, Alfa Aesar) and niobium (V) oxide (Nb_2O_5, 99.99 %, Alfa Aesar) were used as precursor materials. 52.5(K_2CO_3):47.5 (Nb_2O_5) molar ratio of powder mixture was crushed and grinded well with addition of a few drop of ethanol using agate mortar and pestle, respectively to obtain homogenization. Then the homogeneous powder was taken in a platinum (Pt) crucible and heat-treated with a heating rate of 50 °C/h in air atmosphere and remained at 950 °C for 24 h to deplete CO_2 and to produce a $KNbO_3$ powder. Then the temperature of the system reduced to room temperature at a cooling rate of 50 °C. The synthesized $KNbO_3$ powder is then heated to above the melting point (∼1050 °C) of $KNbO_3$ and kept there for 24 h to ensure that the molten solution

became stable. A platinum wire was used as seed to pull out the crystal from the molten solution at the rate of 0.2 mm/h, and then the obtained $KNbO_3$ seed crystal was attached to the alumina rod then it was lowered into the melt with rotation at the angular velocity of 10 rpm. In order to find the possible growth temperature, the number of trial and error method has been followed, the seed crystal was dipped into the melt and the temperature of system was slowly increased until the bottom of seed crystal melted off. Then the temperature of system was lowered approximately 5 °C and the seed again inserted to the melt. Then the temperature was programmed downwards at the rate of 0.7 °C/h for crystal growth. After the growth, the crystal was pulled from the melt at the rate of 0.5 mm/h and cooled down to 615 °C at the rate of 5 °C/h, and down to 415 °C at the rate of 3 °C/h, then further down to room temperature at the rate of 2 °C/h to avoid the crystal cracking during the cooling.

2.1 Characterization

Thermal stability of the sample was studied by TG-DTG analyses using HITACHI STA 7300 thermal analyzer. The crystal structure and phase purity of $KNbO_3$ were analyzed by powder X-ray diffraction (X'pert Pro PAN analytical) study using CuK_α radiation ($\lambda = 0.154$ nm) over a 2θ scan range of 10°–80°. Laser Raman spectrophotometer (Renishaw invia reflux) with Argon ion (Ar^+) laser source of wavelength 514.5 nm was employed to record the Raman spectra of $KNbO_3$ in the range of 100 and 2000 cm^{-1} at room temperature to confirm structural compositions. The frequencies of molecular vibrations of $KNbO_3$ were confirmed by a JASCO 460 plus FTIR spectrophotometer. The elemental composition of $KNbO_3$ was confirmed by Hitachi-S-3500W energy dispersive X-ray spectrometer (EDS). The growth feature of $KNbO_3$ crystal was investigated by chemical etching studies using polarized optical microscope (Polovision-IT).

3 Result and Discussion

3.1 Structural Properties

Figure 1 shows the TG-DTG curves of $KNbO_3$. An endothermic peak observed in DTG curve at 1055 °C represents the melting point of $KNbO_3$ crystal. The minimum percentage of weight loss reveals the grown $KNbO_3$ crystal has a good thermal stability. Figure 2a and b depicts the XRD pattern of synthesized $KNbO_3$ powder and grown $KNbO_3$ crystal. The results indicate that $KNbO_3$ crystals mainly consist of (001), (110), (111), (220), (221), (202), (222), (132), and (420) reflection planes, which are good agreement with the standard JCPDS data (card no.:

32-0822). XRD studies revealed that the $KNbO_3$ crystallizes in orthorhombic structure with space group *C*m2m. The lattice constant was calculated using the relation, $\frac{1}{d_{hkl}} = \frac{h^2}{a^2} + \frac{k^2}{b^2} + \frac{l^2}{c^2}$. Moreover, the structural parameters and crystal perfection were analysed by Rietveld refinement using GSAS program. XRD diffraction data in 2θ range 20°–80° was used for the refinement. The XRD profiles of samples after Rietveld refinement are shown in Fig. 2c, where solid black line represents the observed values and red line represents the calculated values and green line indicates the difference in the peak position. From the Rietveld refinement analysis, the formation of single phase $KNbO_3$ with *C*m2m space group was confirmed. The calculated lattice constant is listed in Table 1.

3.2 FTIR Studies

FTIR spectrum of $KNbO_3$ is shown in Fig. 3. The presence of absorption band in the lower wavenumber region at 648 cm^{-1} reveals the occurrence of Nb–O bond formation, which is believed to be the vibrational mode of corner shared NbO_6 octahedron site of orthorhombic $KNbO_3$. The absorption bands at 3434 cm^{-1}, represent O–H asymmetric stretching vibrations which are due to the moisture content of KBr pellet. The absorption band at 1629 cm^{-1} can be assigned to bending mode of OH–H adsorbed on the surface of the samples [10].

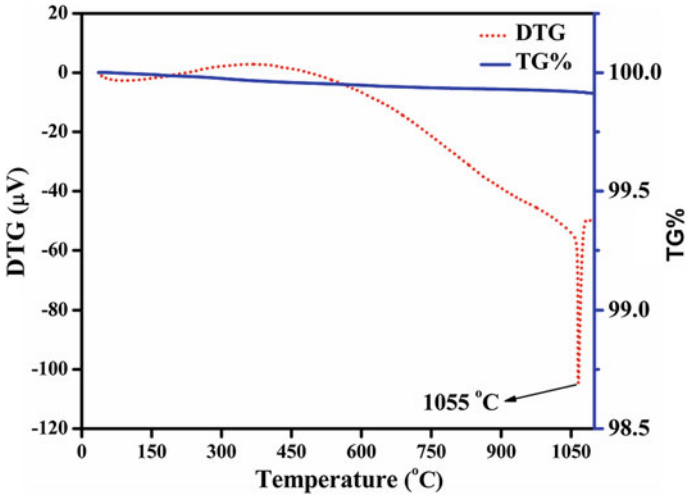

Fig. 1 TG-DTG of $KNbO_3$

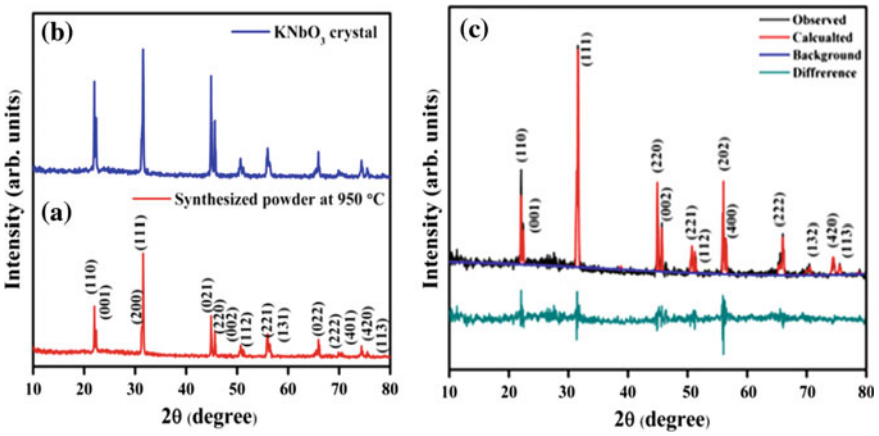

Fig. 2 Powder X-ray diffraction pattern of $KNbO_3$ **a** synthesized powder **b** grown crystal and **c** after Rietveld refinement

Table 1 Structural parameters of $KNbO_3$ crystal

Structural parameters	Refined parameters	JCPDS (32-0822)
Lattice constant (Å)	a = 5.698 b = 5.721 c = 3.971	a = 5.695 b = 5.721 c = 3.973
Volume ($Å^3$)	129.44	129.48
Space group	*C*m2m	*C*m2m

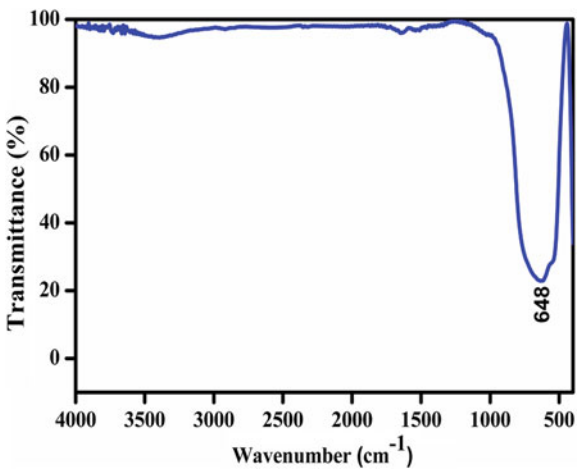

Fig. 3 FTIR spectrum of $KNbO_3$ crystal

3.3 Raman Analysis

Figure 4 shows the Raman spectrum of $KNbO_3$ crystal. The obtained spectrum clearly presents the transverse and longitudinal phonon modes $B_1(TO_2)$, $B_1(TO_1)$, $B_1(TO_3)$, $A_1(TO_3)$, $A_1(LO_3)$ at 185, 280, 535, 602 and 836 cm^{-1}, respectively. These values were consistent with previous ones reported by Golovina et al. for $KNbO_3$ material [10]. All the modes of vibrations of $KNbO_3$ are assigned to the internal mode of NbO_6 octahedron. The peak observed at 590 cm^{-1} represents non-degenerate symmetric Nb–O stretching vibrations and a peak observed at 527 cm^{-1} is assigned to the doubly degenerate symmetric O–Nb–O stretching vibrations. Further a peak at 273 cm^{-1} is due to the triply degenerate symmetric O–Nb–O bending vibration mode of the NbO_6 octahedra of $KNbO_3$ compound. The result confirms the formation of $KNbO_3$ with orthorhombic structure.

3.4 Elemental Analysis

In the present study energy dispersive X-ray analysis was employed to estimate the elemental composition of $KNbO_3$ single crystal. Figure 5 shows the EDS spectrum of $KNbO_3$ crystal. EDS reveals the presence of potassium (K), niobium (Nb) and oxygen (O) elements, without any trace element (impurity ions) or contamination [15]. The ratio of the elements in atomic (at.%) and weight (wt%) are given in the inset of Fig. 5.

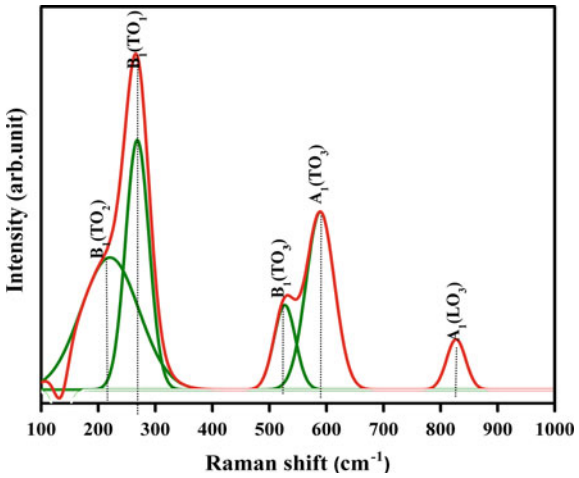

Fig. 4 Raman spectrum of $KNbO_3$ crystal

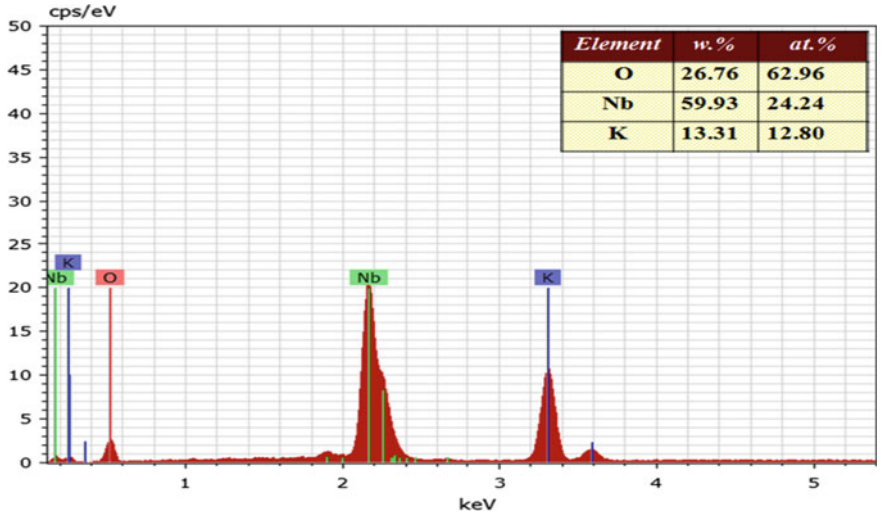

Fig. 5 EDS spectrum of $KNbO_3$ crystal

3.5 *Etching Studies*

Chemical etching is an essential technique for the identification of crystal defects, which is able to develop some of the features such as growth hillocks, etch spirals, rectangular etch pits, grain boundaries etc. on the crystal surface. In order to analyze the growth features, the grown $KNbO_3$ crystal was subjected to chemical etching studies. Approximately 5 mm × 5 mm × 1 mm size samples were used for chemical etching study. $KNbO_3$ crystals etched with mixed etchant (HCl + HNO_3) for 15 and 30 s and then immediately etched crystal faces washed with deionized water, then dried in air and placed for observations under optical microscope. The obtained images are shown in Fig. 6. The smooth surface of as grown crystal is shown in Fig. 6a. Further Fig. 6b reveals the layer by layer growth mechanism of grown crystal etched with mixed etchant of HCl and HNO_3 for 15 and 30 s. Some

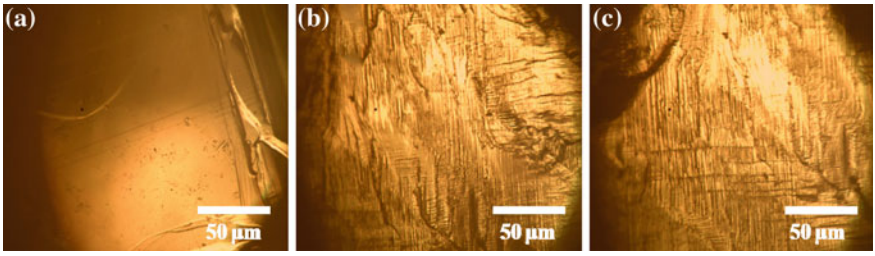

Fig. 6 Surface of **a** as grown $KNbO_3$ crystal, $KNbO_3$ crystal etched with HCl + HNO_3 etchant for **b** 15 s and **c** 30 s

irregularly spaced inclined striations oriented in the crystal were also observed (Fig. 6c).

4 Conclusion

Single crystal of $KNbO_3$ was grown by top seeded solution growth technique using K_2O as a self flux. The grown crystal was characterized by various techniques. Thermal studies reveal that the grown $KNbO_3$ crystal has good thermal stability. XRD and Rietveld refinement results reveal that the prepared $KNbO_3$ crystal has single phase orthorhombic structure. The FTIR and Raman spectra posses a finger print of symmetric O–Nb–O stretching vibration and O–Nb–O bending vibration modes of NbO_6 octahedra of $KNbO_3$. The elemental composition of as grown crystal confirms the presence of K, Nb and O elements. Chemical etching studies reveal the layer by layer growth mechanism of $KNbO_3$ crystal with irregularly spaced inclined striations.

Acknowledgements The authors would like to gratefully acknowledge the Department of Science and Technology (DST), Government of India, for financial support (DST Ref No.: SR/LOP/0027/SERC/2010(G) dated 12.09.2011).

References

1. Xing, W., Looser, H., Wüest, H., Arend, H.: J. Cryst Growth **78**(3), 431–437 (1986)
2. Feng, L.M., Jiang, L.Q., Zhu, M., Liu, H.B., Zhou, X., Li, C.H.: J. Phys. Chem. Solids **69**, 967–974 (2008)
3. De Zhong, S.: Prog. Cryst. Growth Charact. **20**(1), 161–174 (1990)
4. Nakamura, K., Tokiwa, T., Kawamura, Y.: J. Appl. Phys. **91**, 11 (2002)
5. Ryf, R., Montemezzani, G., Gunter, P.: J. Opt. A: Pure Appl. Opt. **3**, 16–19 (2001)
6. Pliska, T., Fluck, D., Gunter, P.: J. Opt. Soc. Am. 152 (1998)
7. Zaitsev, B.D., Kuznetsova, I.E., Joshi, S.G.: J. Appl. Phys. **90**, 7 (2001)
8. Wang, Y., Chen, Z., Ye, Z., Huang, J.Y.: J. Cryst. Growth. 34142–34145 (2012)
9. Ladj, R., Magouroux, T., Eissa, M., Dubled, M., Mugnier, Y., Dantec, R.L., Galez, C., Valour, J.P., Fessi, H., Elaissari, A.: Colloid Surf. A: Phys. Chem. Eng. Aspects **439**, 131–137 (2013)
10. Yan, L., Zhang, J., Zhou, X., Wu, X., Lan, J., Wang, Y., Liu, G., Yu, J., Zhi, L.: Int. J. Hydrogen Energy **38**, 3554–3561 (2013)
11. Grinberg, I., West, D.V., Torres, M., Gou, G., Stein, D.M., Wu, L., Chen, G., Gallo, E.M., Akbashev, A.R., Davies, P.K., Spanier, J.E., Rappe, A.M.: Nature **503**, 509–512 (2013)
12. Montemezzani, G., Gunter, P.: J. Opt. Soc. Am. **7**, 12 (1990)
13. Buse, K.: J. Opt. Soc. Am. **10**, 7 (1993)
14. Yanovsky, V.K., Voronkova, V.I.: J. Cryst. Growth **52**, 654–659 (1981)
15. Wenshan, W., Qun, Z., Zhaohua, G.: J. Cryst. Growth **83**(1), 62–68 (1987)

Influence of Bias on Dielectric Properties of Mesophases of a Laterally Fluorinated Antiferroelectric Liquid Crystal

Kartick Ch. Dey, Pradip Kumar Mandal and Roman Dabrowski

Abstract A laterally fluorinated antiferroelectric liquid crystal exhibiting SmA*, SmC* and SmC_A* phases was investigated using bias dependent dielectric spectroscopy. The critical field (Ec) for suppression of GM in SmC* phase was observed to increase with decrease of temperature. After suppression of Goldstone mode, domain mode (DM) arises at higher fields, the critical frequency (f_{DM}) of which is $\sim 10^4$ Hz and was recognized as surface domain mode. f_{DM} follows Arrhenius law. The activation energy (E_a) was found to be 19.8 kJ/mol. DM was also suppressed at high bias field. The weak low frequency P_L mode was not observed in SmC_A* phase instead a strong hereditary mode (HM) was observed in the low frequency region which also suppressed under dc bias field. The critical field for suppression of this mode was same at all temperatures. Variation of both ε''_{HM} and f_{SM} within bias field 0.3 V/μm signifies that molecular dynamics of the mode is different from that of GM. The dielectric strength of soft mode (ε''_{SM}) converges and critical frequency (f_{SM}) diverges at T_c following the Curie-Weiss law.

1 Introduction

Since the first observation of tri-stable switching in chiral smectic by Chandani et al. [1, 2] several groups [3–10] devoted their efforts to study the antiferroelectric materials due to their promising option for future displays as because these materials exhibit microsecond response time, hemispherical viewing angle, no-ghost

K.Ch. Dey (✉)
Department of Physics, Achrya Prafulla Chandra Roy Govt. College, Siliguri 734010, WB, India
e-mail: kartickdey136@gmail.com

P.K. Mandal
University of North Bengal, Siliguri 734013, WB, India

R. Dabrowski
Institute of Chemistry, Military University of Technology, Warsaw 00208, Poland

J. Ebenezar (ed.), *Recent Trends in Materials Science and Applications*, Springer Proceedings in Physics 189, DOI 10.1007/978-3-319-44890-9_43

effect, intrinsic analogue grey-scale, in plane switching [11]. Therefore the prospects of such materials are very high in a number of applications with such outstanding properties [12, 13]. The molecules that exhibit antiferroelectric phase must possess at least three ring esters such as terphenylates, phenyl biphenylates or biphenyl benzoates with a partially fluorinated achiral chain at one end and a chiral centre connected at other end of the core by a polar linkage group [14, 15]. The lateral fluoro- substituted derivatives of such material exhibits additional transverse dipole moment which enhances the steric hindrance and electro–optic properties [16]. Present antiferroelectric compound has been studied using frequency dependent dielectric spectroscopy in combination with bias, which is one of the powerful techniques to explore the molecular dynamics of liquid crystalline system. In this report we represent the bias dependent dielectric behaviour of a laterally fluorinated antiferroelectric liquid crystal (S)-(+)-4′-(1-methylheptylcarbonyl) biphenyl-4-yl 4-[6-(4,4,4,3,3,2,2-heptafluorobutoxy)hex-1-oxy]-3-fluoro benzoate synthesized by Zurowska et al. [17] in Military University of Technology. Liquid Crystals with biphenyl benzoates core and partially fluorinated alkoxyalkoxy terminal chain show high tilt ($\sim 45^{o}$) and unusual optical property which produce perfect dark state and enhanced contrast. These kinds of materials are also promising for solving the problem of low pitch and low melting point of liquid crystals with perfluoroalkanoyl unit [17].

2 Experimental

The structure, phase sequence and transition temperatures of the compound under investigation as obtained from optical polarizing microscopy (OPM) are shown in Fig. 1. The dielectric permittivity measurements were performed using HIOKI 3532–50 impedance analyzer (50 Hz–5 MHz). The sample was taken in isotropic phase within an Indium-Tin oxide (ITO) coated homogeneous (HG) EHC cell of 10 μm thickness and low resistivity ($\sim 20\Omega$). The filled cell then cooled down slowly @ 0.2 °C/min from isotropic phase using Mettler FP82 hot stage and FP90 processor in order to have surface stabilized bookshelf arrangement of molecules. For better alignment of the molecules an ac field of low frequency and moderate strength was applied for half an hour. For bias application Aplab made LD 6402 regulated power supply (0–64 V, 0–2A) was used. There is an automatic data

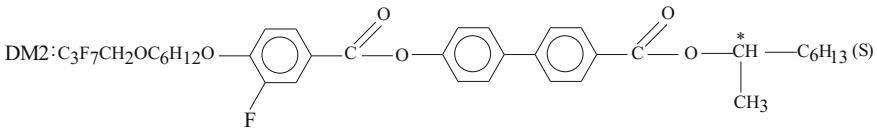

Cr (25) 57.3 SmC_A^* (74.2) 80.5 SmC^* (107.8) 108 SmA* (112.2) 112.2 Iso

Fig. 1 Molecular structure representation and transition temperatures of the antiferroelectric liquid crystal compound

acquisition system in our laboratory using RS232 interfacing with a PC. The dielectric spectra were taken at fixed temperature with increasing dc bias field from 0 to 4.0 V/μm. Such bias dependent data were taken at 107, 91, 75 °C in SmC* phase and at 63, 50, 42 °C in SmC_A* phase. Soft mode (SM) relaxation was pronounced in SmA* phase but in SmC* phase usually it is super imposed over stronger Goldstone mode. So for the study of temperature dependence of dielectric strength and critical frequency of soft mode in the vicinity of SmA*–SmC*, suppression of GM is necessary under application of bias. Therefore a fixed bias of 3.0 V/μm was applied to the sample and dielectric spectra measured during cooling at a regular interval of temperature starting from SmA* to SmC_A* phase.

The frequency response curves were fitted to the following modified Cole-Cole equation in order to extract the absorption peak height (ε″) and relaxation frequency (f_c) of different modes [18].

$$\varepsilon^* = \varepsilon_\infty + \sum_k \frac{\Delta\varepsilon_k}{1 + (i\omega\tau_k)^{1-\alpha_k}} - i\frac{\sigma}{\omega \in_0}$$

where $\Delta\varepsilon_k = \varepsilon_0 - \varepsilon_\infty$ is dielectric increment (ε_0 and ε_∞ are the real part of permittivity at low and high frequency limit), α_k is asymmetry parameter signifying deviation from Debye type behavior of k-th mode relaxation process, τ_k is relaxation time, σ is the conductivity of the cell that arises due to charge impurities which contributes mainly in low frequency region and $\in_0$ (=8.85 pF/m) is the permittivity of free space.

3 Results and Discussion

3.1 SmC Phase*

Bias dependent dielectric spectra were taken at 107, 91 and 75 °C in SmC* phase. The dielectric absorption strength of Goldstone mode (ε''_{GM}) at critical frequency was strongly decreased with increasing bias field at all temperatures and was suppressed completely at a certain bias. The bias field required to suppress GM, called critical field (Ec) was observed to increase with decrease of temperature (Fig. 2a). At 107 °C, ε''_{GM} was suppressed at 0.3 V/μm, at 91 °C, ε''_{GM} was suppressed at 0.4 V/μm and at 75 °C it was suppressed at 0.5 V/μm. The similar temperature dependence of E_c was observed by Marzec et al. [19]. The critical frequency of GM is observed to remain almost constant at 2 kHz at 107 °C, 1.9 kHz at 91 °C and 1.4 kHz at 75 °C (Fig. 2b) before its suppression.

After the suppression of GM a relatively weak mode arises, the critical frequency of which increases gradually with bias and finally becomes almost constant (except at 75 °C) and the strength of the mode decreases slowly with bias. Beresnev et al. [20] discovered that ferroelectric liquid crystals with high spontaneous polarization

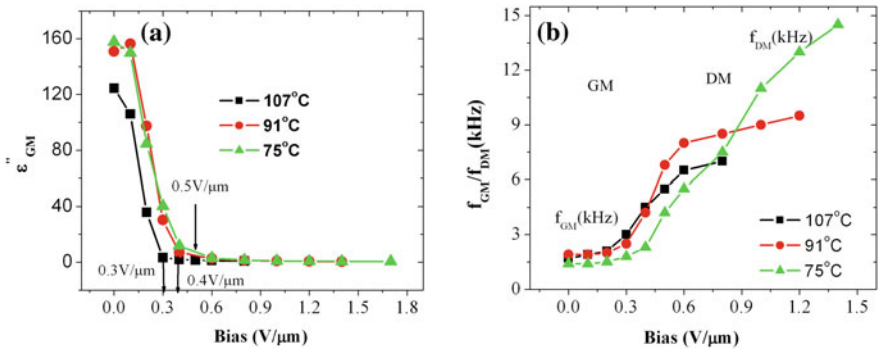

Fig. 2 Bias dependence of **a** absorption strength (ε''_{GM}) and **b** critical frequencies (f_{GM} and f_{DM}) at three temperatures

can form solid ferroelectric like domain after suppression of GM. Relaxation mode arising out of such domain is termed as domain mode. Haase et al. [21] gave the same argument regarding the arising of domain mode. He observed two types of domain mode—(a) Bulk Domain mode (DB) and (b) Surface Domain mode (DS). The DB mode is weaker and lies in the lower frequency ranges ($\sim 10^3$ Hz) and is suppressed at lower field and the stronger DS mode lies comparatively in higher ranges of frequencies ($\sim 10^4$ Hz) and suppressed at higher bias. The domain mode observed in our compound is stronger and its critical frequency (f_{DM}) also falls in $\sim 10^4$ Hz range, hence it is recognized as surface domain mode (Fig. 2b). The maximum values of f_{DM} (7 kHz at 107 °C, 9.5 kHz at 91 °C and 14.5 kHz at 75 °C) increases with decrease of temperature. The values of $\ln(f_{DM})$ plotted against 1/T (T is in absolute scale) and observed to fit well linearly, signifying that f_{DM} follows Arrhenius law (Fig. 3). The activation energy (E_a) determined from the gradient of linearly fitted line was E_a = 19.8 kJ/mol. Marzec et al. [19] obtained E_a = 32 kJ/mole and [21] obtained E_a = 18 kJ/mol.

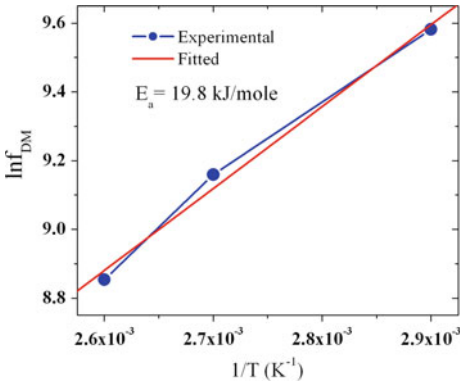

Fig. 3 Arrhenius plot for the domain mode

3.2 *SmC$_A$* Phase*

In the antiferroelectric phase two well separated relaxation processes are observed in kHz and hundred kHz ranges. Though there is controversy about the origin of these modes, the idea that low frequency mode (P_L) arises due to the phase fluctuation [3] of antiferroelectric polarization and the high frequency mode (P_H) arises due to the anti-phase fluctuation of the polarization of adjacent layers [4, 22, 23] are satisfactory.

In case of our compound a high frequency mode (P_H) was observed to appear just at the transition SmC*–SmC$_A$* (T_{AF}). In low frequency region a sharp mode (fc—few hundred Hz) was observed, which seems to be continuation of Goldstone mode pertaining to SmC* phase and observed over a large temperature range well inside SmC$_A$* phase. This mode which is not characteristic of the phase is termed as hereditary mode [4]. The reason for appearance of this mode is co-existence of the SmC$_A$* and SmC* phase when cooled down slowly from isotropic phase. As the hereditary mode is very strong, the weak P_L mode was annihilated and was not observed. At all temperatures (63, 50 and 42 °C) under gradual increase of bias, the absorption strength of the hereditary mode (ε''_{HM}) decreases sharply from 7.44 at 0.0 V/μm to 1.38 at 0.3 V/μm and then slowly to 0.3 at 1.0 V/μm and finally suppressed (Fig. 4a). Similarly at all temperatures critical frequency of HM (f_{HM}) initially decreases from 425 Hz at 0.0 V/μm to 325 Hz at 0.3 V/μm then increases gradually to 550 Hz at 0.8 V/μm. Then for bias field 1.0 V/μm bias the f_{HM} remains constant to 550 Hz in 63 °C but in 50 and 42 °C decreases to 400 and 350 Hz respectively (Fig. 4b). The behaviour of decrease of f_{HM} with bias up to 0.3 V/μm is different from that of f_{GM}. Hence the molecular dynamics is also different for the mode. The critical frequency and absorption strength of mode in high frequency range in SmC$_A$* increases slightly initially with bias and then remain unaffected in all temperatures (Fig. 5a, b).

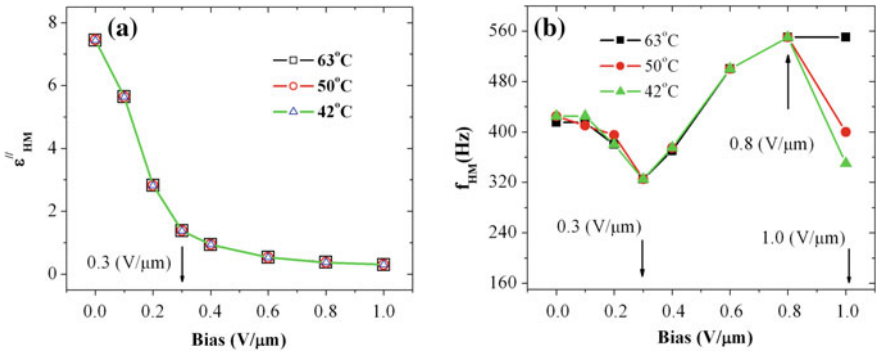

Fig. 4 Bias dependence of **a** absorption peak height (ε''_{HM}) and **b** critical frequency (f_{HM}) of hereditary mode at different temperatures

3.3 *In the Vicinity of SmA*–SmC* Transition*

On approaching SmA*–SmC* transition, the molecules undergo tilt fluctuation. Therefore the binding forces and corresponding elastic constant of the molecules get soft against this fluctuation. Therefore the dielectric permittivity (ε''_{SM}) converses and the critical frequency (f_{SM}) diverges in the vicinity of T_c following Curie-Weiss law [24]. The relaxation mode which satisfies above criteria is usually known as soft mode (SM). The mode is very weak due to small amplitude of tilt fluctuation and is highly temperature dependent. It is not usually affected by dc bias as its origin is not related to polarization. Its critical frequency lies in the ranges of few hundred kHz. To explore the temperature dependence of this mode near T_c a dc bias field of 3.0 V/μm was applied in combination with measuring ac field to suppress the GM. The f_{SM} of the compound decreases sharply from 210 kHz at 112.7 °C to 110 kHz at 108.5 °C (T_c) during cooling and on further cooling it increases sharply to 210 kHz at 105 °C (Fig. 6a) and finally it decreases gradually to 128 kHz at 44 °C. Corresponding absorption strength (ε''_{SM}) increases sharply from 3.07 at 112.7 °C to 5.23 at 108.5 °C (T_c) (Fig. 6b) and decreases sharply to 3.92 at 105 °C and then increases gradually to 4.62 at 44 °C. So the f_{SM} varies with temperature under bias in accordance with Landau theory near T_c. The SM in this compound continues till 40 °C under bias even after the transition from SmC* to SmC_A* (74.2 °C) because the antiferroelectric conformation was incomplete as we have discussed earlier section. After attaining complete antiferroelectric conformation after 42 °C the P_H mode was observed but P_L should have been suppressed at such a high bias field. The f_{PH} was observed to increase slowly from 340 kHz at 37 °C to 386 kHz at 25 °C (Fig. 6a) but ε''_{PH} remains constant at 1.6 from 37 °C to 25 °C under fixed bias field of 3.0 V/μm (Fig. 6b).

The ε''_{SM} and f_{SM} remain almost constant at different values over the range of bias at different temperatures. The dielectric properties of SM under gradual increase of

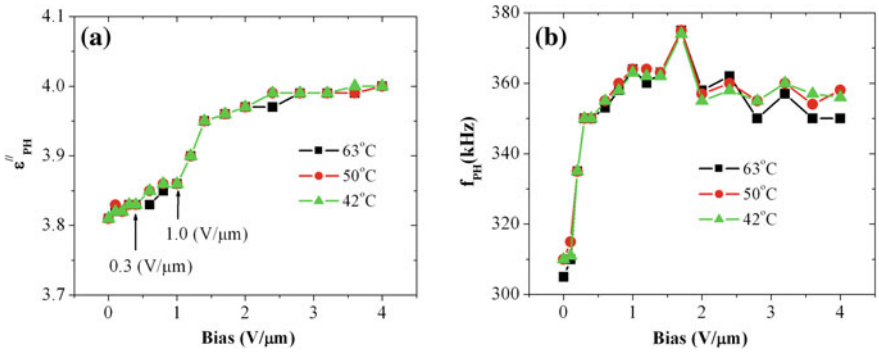

Fig. 5 Bias dependence of **a** absorption peak height (ε''_{PH}) and **b** critical frequency (f_{PH}) of high frequency mode at different temperatures

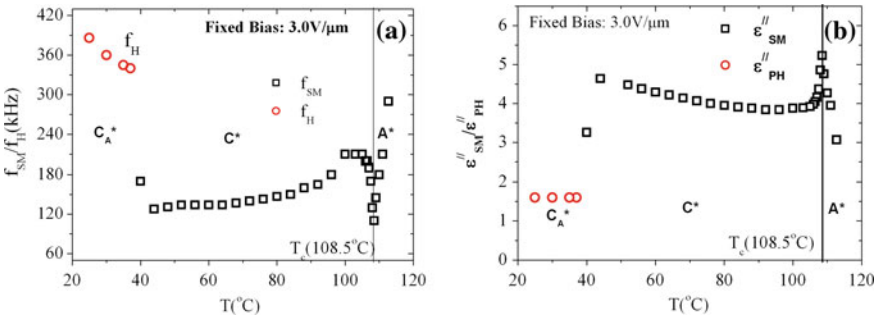

Fig. 6 Temperature dependence of **a** critical frequency **b** absorption peak height of soft mode and P_H mode under fixed bias of 3.0 V/μm

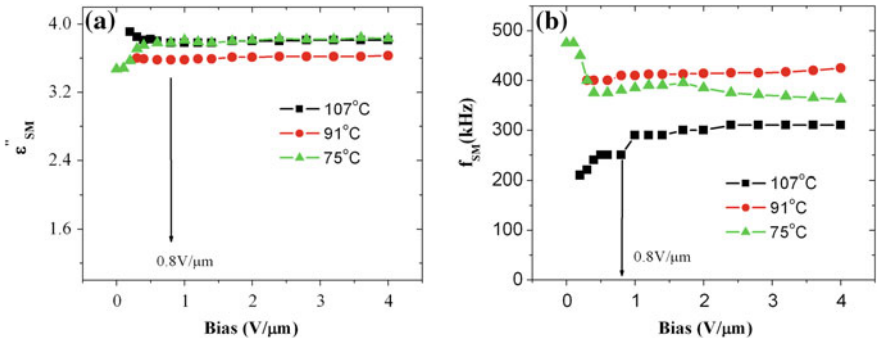

Fig. 7 Bias dependence of **a** absorption peak height (ε''_{SM}) and **b** critical frequency (f_{SM}) of soft mode at different temperatures

bias at temperatures 107, 91 and 75 °C are well commensurate with that under fixed bias. The value of ε''_{SM} near T_c at 107 °C is high (∼3.8), then away from T_c at 91 °C it decreases to ∼3.6 and then gradually increases to 3.8 upto 75 °C (Fig. 7a) (also correlate the Fig. 6b). Similarly the f_{SM} value at 107 °C, near T_c is low (∼310 kHz), but increases to 414 kHz away from T_c at 91 °C then decreases to 385 kHz upto 75 °C (Fig. 7b) (also correlate Fig. 6a).

4 Conclusion

After suppression of GM in SmC* phase domain mode was observed which was recognized as surface domain mode as its critical frequency $\sim 10^4$ Hz. f_{DM} follows Arrhenius law. The activation energy (E_a) was determined 19.8 kJ/mol. The surface domain mode was also suppressed at high bias field.

Hereditary mode was observed in SmC_A* phase due to incomplete antiferroelectric conformation which resemblances with GM of SmC*. It was also suppressed under bias. The critical field for suppression of this mode was same in all three temperatures (63, 50 and 42 °C) in SmC_A* phase. The bias variation of both ε''_{SM} and f_{HM} within bias field 0.3 V/μm signifies that molecular dynamics of the mode is different from that of GM.

The soft mode becomes pronounced under bias and the ε''_{SM} and f_{SM} follows Curie–Weiss law near T_c. The soft mode was observed to extend over a large temperature range below T_c. The P_H appeared after 40 °C under bias of 3.0 V/μm.

References

1. Chandani, A.D.L., Hagiwara, T., Suzuki, Y., Ouchi, Y., Takezoe, H., Fukuda, A.: Tristable switching in surface stabilized ferroelectric liquid crystals with a large spontaneous polarization. Jpn. J. Appl. Phys. **27**(2), L729–L732 (1988)
2. Chandani, A.D.L., Ouchi, Y., Takezoe, H., Fukuda, A., Terashima, K., Furukawa, K., Kishi, A.: Novel phases exhibiting tristable switching. Jpn. J. Appl. Phys. **28**(7), L1261–L1261 (1989)
3. Panarin, Yu.P., Kalinovskaya, O., Vij, J.K.: The relaxation processes in helical antiferroelectric liquid crystals. Ferroelectrics **213**, 101–108 (1998)
4. Buivydas, M., Gouda, F., Andersson, G., Lagerwall, S.T., Stebler, B.: Collective and non-collective excitations in antiferroelectric and ferrielectric liquid crystals studied by dielectric relaxation spectroscopy and electro-optic measurements. Liq. Cryst. **23**(5), 723 (1997)
5. Moritake, H., Uchiama, Y., Myojin, K., Ozaki, M., Yoshino, K.: Dielectric properties in antiferroelectric liquid crystals and their DC bias effects. Ferroelectrics **147**, 53 (1993)
6. Hiller, S., Pikin, S.A., Hasse, W., Goodby, J.W., Nishiama, I.: Relaxation processes in the antiferroelectric phase as studied by dielectric spectroscopy. Jpn. J. Appl. Phys. **33(2)(8B)**, L1170-L1264 (1994)
7. Ghosh, S., Nayek, P., Roy, S.K., Majumder, T.P., Dabrowski, R.: Dielectric relaxation spectroscopy and electrooptical studies of a new, partially fluorinated orthoconic antiferroelectric liquid crystal material exhibiting V-shaped switching. Liq. Cryst. **37**(4), 369–375 (2010)
8. Perkowski, P., Skrzypek, K., Piecek, W., Dziaduszek, J., Raszewski, Z., Czupryński, K.: Dielectric behavior of antiferroelectric phase induced in a binary mixture. Ferroelectrics **395**, 27–34 (2010)
9. Pandey, G., Dhar, R., Agarwal, V.K., Dabrowski, R.: Dielectric spectroscopy of ferro- and antiferroelectric phases of (S)-(+)-4′- (1-methylheptyloxycarbonyl)biphenyl-4-yl 4-(6-heptan oyloxyhex-1-oxy) benzoate. Ferroelectrics **343**, 139–149 (2006)
10. D'have, K., Dahlgren, A., Rudquist, P., Lagerwall, J.P.F., Andersson, G., Matvszczuk, M., Lagerwall, S.T., Dabrowski, R., Drzewinski, W.: Antiferroelectric liquid crystals with 45° tilt —a new class of promising electro-optic materials. Ferroelectrics **244**, 115–128 (2000)
11. Oton, J.M., Quintana, X., Castillo, P.L., Lara, A., Urruchi, V., Bennis, N.: Opto-electron Rev. **12**(3), 263–269 (2004)
12. Kula, P., Herman, J., Perkowski, P., Mrukiewicz, M., Jaroszewicz, L.R.: On the influence of the chiral side linking bridge type upon the synclinic vs. anticlinic balance in the case of 2′,3′-difluoroterphenyl derivatives. Liq. Cryst. **40**(2), 256–266 (2013)
13. Weglowska, D., Dabrowski, R.: Highly tilted ferroelectric liquid crystals with biphenylyl benzoate rigid core. Liq. Cryst. **41**(8), 1116–1129 (2014)

14. Zurowska, M., Dabrowski, R., Dziaduszek, J.: Influence of alkoxy chain length and fluorosubstitution on mesogenic and spectral properties of high tilted antiferroelectric esters. J. Mat. Chem. **21**(7), 2144–2153 (2011)
15. Sokol, E., Drzewinski, W., Dziaduszek, J.: The synthesis and properties of novel partially fluorinated ethers with high tilted anticlinic phase. Ferroelectrics **343**, 41–48 (2006)
16. Pirkl, S., Glogarova, M.: Ferroelectric liquid crystals with high spontanious polarization, 17th chapter, ferroelectrics—physical effects. In: Lallart, M. (ed.) InTech Janeza Trdine 9, 51000 Rijeka, Croatia (2011)
17. Zurowska, M., Dabrowski, R., Dziaduszek, J., Czuprynski, K., Skrzypek, K., Filipowicz, M.: Synthesis and mesomorphic properties of chiral esters comprising partially fluorinated alkoxyalkoxy terminal chains and a 1-methylheptyl chiral moiety. Mol. Cryst. Liq. Cryst. **495**, 145–157 (2008)
18. Botcher, C.J.F., Bordewijk, P.: Theory of Electric Polarization. Elsevier, Amsterdam (1978)
19. Marzec, M., Dabrowski, R., Fafara, A., Haase, W., Hiller, S., Wrobel, S.: Goldstone mode and domain mode relaxation in ferroelectric phases of 4′-[(S, S)-2,3-epoxyhexyloxy] phenyl 4-(decyloxy)benzoate (EHPDB). Ferroelectrics **180**, 127–135 (1996)
20. Beresnev, L.A., Loseva, M.V., Chernova, N.I., Kononov, S.G., Adomenas, P.V., Pozhidayev, E.P.: Pis'ma Zh. Eksp. Teor. Fiz. **51**, 457 (1990)
21. Haase, W., Hiller, S., Pfeiffer, M., Beresnev, L.A.: The domain mode in ferroelectric liquid crystals; electrooptical and dielectric investigations. Ferroelectrics **140**, 37–44 (1993)
22. Dey, K.C., Mandal, P.K., Dabrowski, R.: Effect of lateral fluorination in antiferroelectric and ferroelectric mesophases: synchrotron X-ray diffraction, dielectric spectroscopy and electro-optic study. J. Phys. and Chem. Solids **88**, 14–23 (2016)
23. Haldar, S., Dey, K.C., Sinha, D., Mandal, P.K., Haase, W., Kula, P.: X-ray diffraction and dielectric spectroscopy studies on a partially fluorinated ferroelectric liquid crystal from the family of terphenyl esters. Liq. Cryst. **39**(10), 1196–1203 (2012)
24. Gouda, F., Skarp, K., Lagerwall, S.T.: Dielectric studies of the soft mode and goldstone mode in ferroelectric liquid crystals. Ferroelectrics **113**, 165–206 (1991)

On the Determination of Load Dependent Parameters and Dielectric Tensor Analysis of an Organic Diphenylacetic Acid Single Crystal

RO.MU. Jauhar, G. Peramaiyan and P. Murugakoothan

Abstract An organic diphenylacetic acid (DPA) single crystal was synthesized and grown by the slow evaporation technique. Formation of the crystalline compound was confirmed by single crystal X-ray diffraction study. The title compound crystallizes in the monoclinic crystal system. The load dependent parameters of the grown crystal were studied by Vicker's microhardness technique. The four independent tensor coefficients of dielectric permittivity were found to be $\varepsilon_{11} = 29.92$, $\varepsilon_{22} = 28.74$, $\varepsilon_{33} = 27.38$ and $\varepsilon_{13} = 0.81$ from the dielectric measurement.

1 Introduction

Organic compounds have gained much interest from materials scientists for their large optical nonlinearity and potential applications in optical communication, photorefractivity due to their large π-electron delocalization and they often possess interesting ferroelectric, superconducting properties etc. [1]. The molecule of diphenylacetic acid assists the formation of enantiomerically enhanced products from chiral precursors without the intervention of chiral chemical reagents or catalysts by its ability to promote absolute asymmetric synthesis. Diphenylacetic acid readily cocrystallizes with acridines originating chiral crystals. It is the propeller like arrangement of the phenyl rings that causes a chiral conformation in the diphenylacetic acid molecule in an otherwise achiral molecule [2, 3]. In the present work we report the synthesis, growth, load dependent parameters and dielectric tensor analysis of diphenylacetic acid crystal grown from slow evaporation solution growth method.

RO.MU. Jauhar · P. Murugakoothan (✉)
MRDL, PG and Research Department of Physics, Pachaiyappa's College, Chennai 600030, India
e-mail: murugakoothan03@yahoo.co.in

G. Peramaiyan
Institute of Physics, Academia Sinica, Nankang, Taipei 11529, Taiwan

J. Ebenezar (ed.), *Recent Trends in Materials Science and Applications*,
Springer Proceedings in Physics 189, DOI 10.1007/978-3-319-44890-9_44

2 Experimental

2.1 Material Synthesis and Crystal Growth

Single crystal of diphenylacetic acid was grown by dissolving diphenylacetic acid (Hi media) in ethanolic medium. The solution was stirred continuously for 6 h and filtered using Whatman filter paper. The structural formula of diphenylacetic acid is shown in Fig. 1.

Solvent selection is one of the important criteria to optimize the conditions for growing good quality single crystals. The solubility of DPA was estimated gravimetrically in ethanol solvent for five different temperatures, such as 25, 30, 35, 40 and 45 °C using a constant temperature water bath with temperature accuracy of ±0.01 °C. The solutions prepared at the respective temperatures were dried off and weighed. A graph is then plotted between temperature and concentration of the solute and is shown in Fig. 2. From the graph it is observed that the solubility of

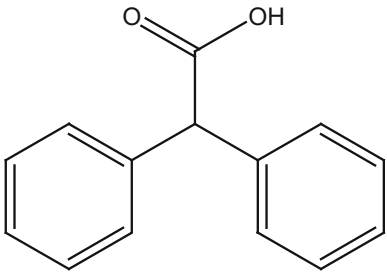

Diphenylacetic acid

Fig. 1 Structural formula of diphenylacetic acid

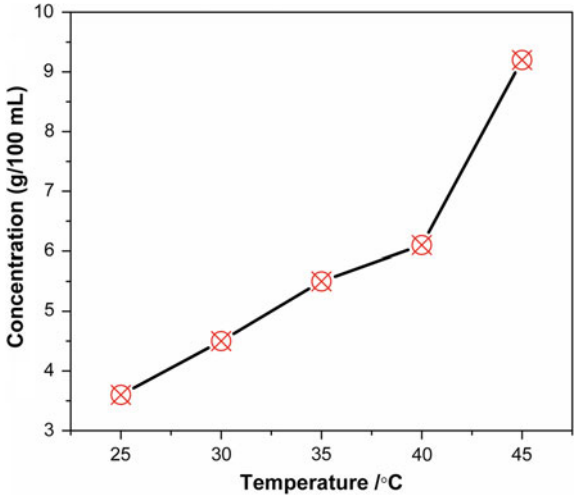

Fig. 2 Solubility curve of DPA

DPA increases with increase in temperature, revealing the positive solubility gradient of the titular material. The solubility of DPA is found to be 9.2 g in 100 mL of ethanol at 45 °C. The photograph of the as grown crystal is shown in Fig. 3.

3 Results and Discussion

3.1 Single Crystal XRD (SXRD)

The SXRD study revealed that the DPA crystal belongs to monoclinic crystal system with space group $P2_1/c$. The estimated lattice parameters are, a = 12.238(6) Å, b = 7.216(4) Å, c = 17.421(8) Å, β = 133.31(3), V = 1119.6(5) $Å^3$ and Z = 4 [4]. The morphology of DPA crystal is shown in Fig. 4, which reveal six well developed crystallographic planes (1 0 0), (1 0 −1), (−1 0 0), (−1 0 1), (0 1 0) and (0 −1 0).

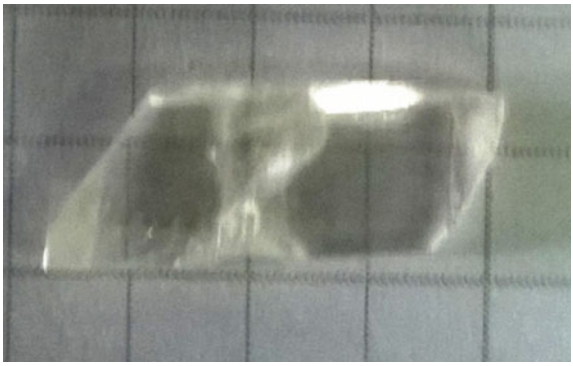

Fig. 3 As grown DPA crystal

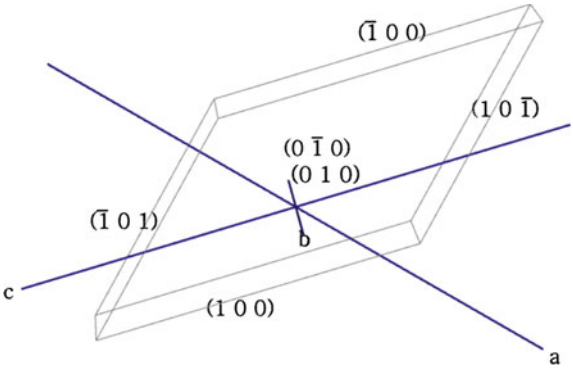

Fig. 4 Morphology of DPA crystal

3.2 *Microhardness Studies*

Vicker's micro hardness study was carried out for DPA crystal for various loads ranging from 5 to 80 g using Leitz–Wetzlar Vicker's micro hardness tester. The variation of microhardness (H_v) with load (P) is shown in Fig. 5. Vickers' micro hardness number was calculated using relations [5],

$$H_v = 1.8544(P/d^2)\,kg/mm^2 \tag{1}$$

where 'P' and 'd' are the applied load and the mean diagonal length of the indenter impression respectively. From the figure, it is observed that the hardness number increases with an increase of applied load. This behavior is known as the reverse indentation size effect (RISE) [5]. The relation between load and the size of indentation can be found using Meyer's law,

$$P = K_1 d^n \tag{2}$$

where K_1 is a constant and 'n' is the Meyer's index. The slope of log P versus log d is shown in Fig. 6. From the figure the work hardening coefficient (n) is found to be 2.41. Using (1) and (2) it is found that,

$$H_V = 1.8544\,k_1 d^{n-2} \tag{3}$$

or

$$H_V = 1.8544\,k_1^{(1+2/n)}\,P^{(1-2/n)} \tag{4}$$

or

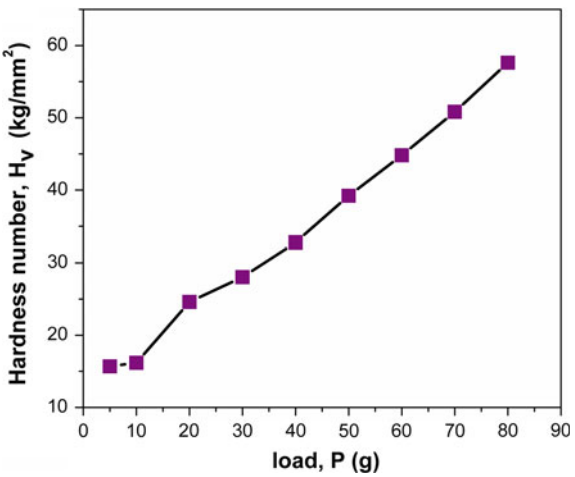

Fig. 5 Plot of load P versus hardness number, H_v of DPA crystal

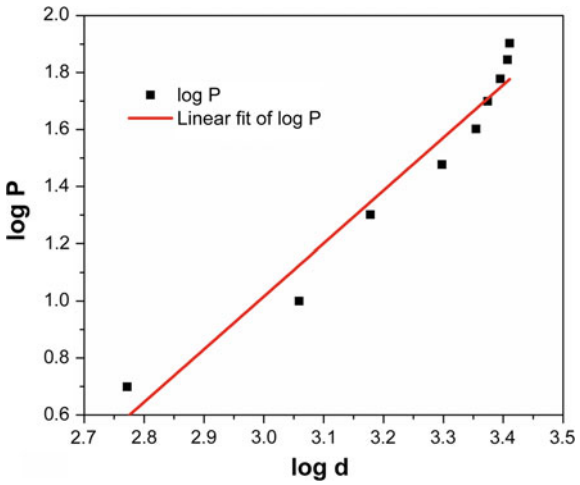

Fig. 6 Plot of log d versus log P

$$H_V = b\,P^{(n-2)/n} \tag{5}$$

where $b = 1.8544\ k_1^{(1+2/n)}$ is a constant. It shows that H_v increases with increase in P, if $n > 2$ and it decreases with increase of load, if $n < 2$. This agrees well with the experimental data and hence confirms the reverse indentation size effect. It is reported that "n" lies between 1 and 1.6 for hard materials and for softer ones it is above 1.6 [6–9]. Thus DPA crystal belongs to the soft-material category. The elastic stiffness constant (C_{11}) for different loads were calculated using Wooster's empirical formula $C_{11} = H^{7/4}$. According to [10], radial-median and Palmqvist are the two types of crack systems formed in a material as a result of indentation. For $C/a \leq 2.5$, the cracks developed are of Palmqvist type, where C is the crack length and a is half the diagonal length of the indentation mark [11]. For the title crystal DPA, the obtained crack is of Palmqvist type. The fracture resistance indicates the toughness of the material.

The fracture toughness (K_c) is given by,

$$K_c = P/\left(\beta C^{3/2}\right) \tag{6}$$

where C is the crack measured from the centre of indentation mark to the crack tip and geometrical constant β for the Vicker's indenter. The brittleness index for different loads were calculated using the relation,

$$B_i = H_v/K_c \tag{7}$$

The yield strength (σ_y) of the material can be calculated, for $n > 2$, using the relation,

$$\sigma_{y=}(H_v/2.9)[1-(n-2)]\{12.5(n-2)/(1-n-2)\}^{n-2} \quad (8)$$

The above equation may be further reduced to $\sigma_y = H_v/3$ if $n \leq 2$. The load dependent parameters like H_v, n, fracture toughness (K_c), brittleness index (B_i) and yield strength (σ_y) are presented in Table 1.

3.3 *Dielectric Studies*

The relative dielectric permittivity of DPA crystal was determined as a function of frequency ranging from 50 Hz to 5 MHz at 40 °C using a HIOKI 3532-50 LCR HITESTER instrument. As the dielectric permittivity is a second rank tensor, the monoclinic system has four independent components ε_{11}, ε_{22}, ε_{33} and ε_{13} corresponding to X, Y and Z directions [12, 13]. The crystal was cut along the

Table 1 The elastic stiffness constant, fracture toughness and brittle index for different loads of DPA crystal

P (g)	H_V (kg/mm^2)	$C_{11} \times 10^9$ (Pa)	σ_y (kg/mm^2)
5	15.6825	0.05832	7.73
10	16.1887	0.05833	7.98
20	24.6169	1.369	12.14
30	28.0304	3.376	13.83
40	32.7928	10.195	16.18
50	39.1990	35.552	19.33
60	44.8097	90.686	22.11
70	50.8296	219.157	24.71
80	57.6225	527.332	28.43

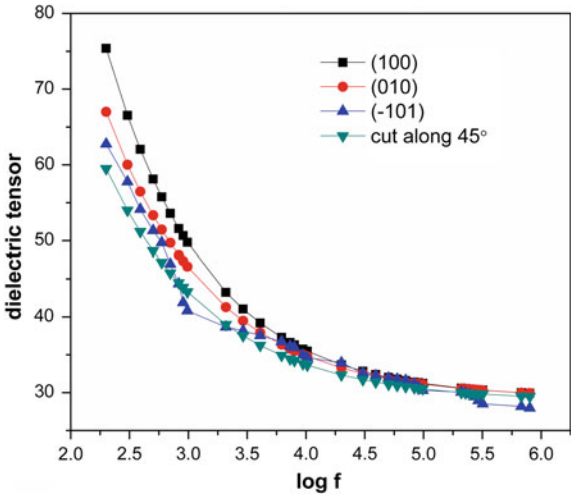

Fig. 7 Plot of log f versus dielectric tensor for DPA crystal

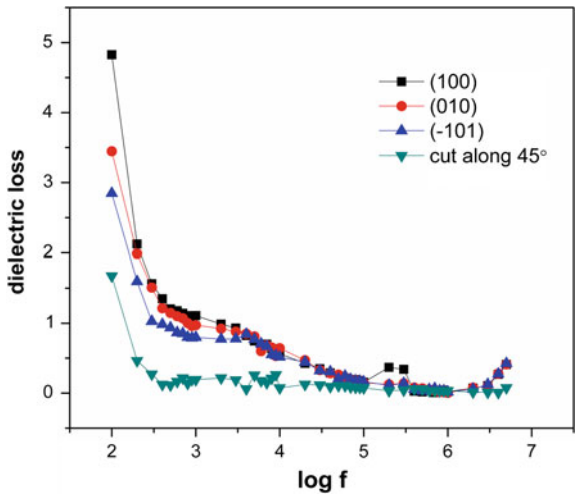

Fig. 8 Plot of log f versus dielectric loss

(1 0 0), (0 1 0), (−1 0 1) and the fourth plane was cut along 45° between X and Z directions with the thickness of 1.76 mm. The fourth component, ε_{13} can be obtained from the following relation:

$$\varepsilon'_{33} = \varepsilon_{11}\sin^2\theta + 2\varepsilon_{13}\sin\theta\cos\theta + \varepsilon_{33}\cos^2\theta \tag{9}$$

The variation of dielectric permittivity along the four crystallographic planes with frequencies is shown in Fig. 7. The calculated relative permittivity values are in the ranges 75.31–29.92, 66.99–28.74, 62.74–27.38, 59.49–29.46. It is observed that the relative permittivity decreases with increase in frequency and is observed to be high at lower frequency region. The dielectric permittivity ε_{13} is found to be 0.81. The positive value depicts that the polarization occurs in the positive direction of the Z-axis. The dielectric loss is also studied as a function of frequency which is shown in Fig. 8.

4 Conclusion

Single crystals of diphenylacetic acid were grown adopting slow evaporation solution growth technique. Single crystal XRD revealed that the title material crystallizes in the monoclinic crystal system. From the microhardness studies it is observed that the material belongs to the soft material category and the crack developed was of palmqvist type. Dielectric tensor analysis revealed the anisotropic nature of the grown material.

References

1. Prasad, P.N., Williams, D.J.: Introduction to Nonlinear Optical Effects in Molecules and Polymers. Wiley, New York (1990)
2. Koshima, H., Ding, K., Chisaka, Y.: Matsuura, generation of chirality in a two-component molecular crystal of acridine and diphenylacetic acid and Its absolute asymmetric photodecarboxylating condensation. T.J.: Am. Chem. Soc. **118**, 12059 (1996)
3. Koshima, H.: Solid state bimolecular photoreaction in a simple polycrystalline mixture of acridine and carbazole. Mol. Cryst. Liq. Cryst. **440**, 207 (2005)
4. Silva, M.R., Cardoso, C., Beja, A.M., Paixao, J.A., Domingos, S.R.: Propeller-like conformation of diphenylacetic acid. J. Chem. Crystallogr. **38**, 403–406 (2008)
5. Güder, H.S., Sahin, E., Sahin, O., Göçmez, H., Duran, C., Ali Çetinkara, H.: Vickers and knoop indentation microhardness study of β-SiAlON ceramic. Acta Phys. Pol. A. **120**, 1026–1033 (2011)
6. Vijayan, N., Bhagavannarayana, G., Ramesh Babu, R., Gopalakrishnan, R., Maurya, K.K., Ramasamy, P.: A comparative study on solution- and bridgman-grown single crystals of benzimidazole by high-resolution X-ray diffractometry, fourier transform infrared, microhardness, laser damage threshold, and second-harmonic generation measurements. Cryst. Growth Des. **41**, 784–789 (2006)
7. Onitsch, E.M.: Systematic metallographic and mineralogic structures. Mikroskopia **2**, 131–151 (1947)
8. Hanneman, M.: Metall. Manchu. **23**, 135 (1941)
9. Ruban Kumar, A., Kalainathan, S.: Microhardness studies on calcium hydrogen phosphate (brushite) crystals. Mater. Res. Bull. **45**, 1664–1667 (2010)
10. Ponton, C.B., Rawlings, R.D.: Vickers indentation fracture toughness test Part 1 Review of literature and formulation of standardised indentation toughness equations. Mater. Sci. Technol. **5**, 865–872 (1989)
11. Banwari, L., Bamzai, K.K., Kotru, P.N., Wanklyn, B.M.: Microhardness, fracture mechanism and dielectric behaviour of flux-grown GdFeO3 single crystals. Mater. Chem. Phys. **85**, 353 (2004)
12. Sornamurthy, B.M., Peramaiyan, G., Pandi, P., Das, S., Bhagavannarayana, G., Manivannan, V., Mohan Kumar, R.: Studies on the growth, thermal and optical properties of 4-aminopyridinium p-aminobenzoate dihydrate single crystals. J. Cryst. Growth **397**, 1–5 (2014)
13. Yu, F., Zhang, S., Zhao, X., Yuan, D., Wang, C.-M., Shrout, T.R.: Characterization of neodymium calcium oxyborate piezoelectric crystal with monoclinic phase. Cryst. Growth. Des. **4**, 1871–1877 (2010)

Studies on the Structural, Thermal, Fluorescence and Linear–Non-linear Optical Properties of Glycine Sodium Acetate Single Crystal for Electro-Optic Device Applications

N.N. Shejwal, S.S. Hussaini, Ramesh B. Kamble, Mohd Anis and M.D. Shirsat

Abstract In the present communication, glycine sodium acetate (GSA) single crystal is grown by the slow evaporation method at room temperature. The cell parameters are confirmed by powder X-ray diffraction technique. This research paper focuses on structural, thermal, second harmonic generation, photoluminescence, linear and non-linear optical properties of glycine sodium acetate single crystals. The Kurtz-Perry powder technique confirmed the second harmonic generation efficiency of the grown crystal is 1.7 times more than that of the standard potassium dihydrogen phosphate (KDP) crystal. The high optical transparency (88 %) of the grown crystal is determined by employing UV-visible studies. The optical band gap of grown crystal is found to be 5.12 eV. The transmittance data is used to evaluate the potential optical constants viz. optical conductivity, refractive index, extinction coefficient and complex dielectric constant. The different functional groups are identified using Fourier transform infrared (FT-IR) spectral analysis. The thermal stability of the grown crystal is found to be 176 °C by means of thermo gravimetric analysis. The presence of sodium element is also confirmed by atomic absorption spectroscopy technique. The photoluminescence study of grown crystal is investigated in the range of 300–900 nm and confirms the near infrared emission in the electromagnetic spectrum.

N.N. Shejwal · M.D. Shirsat (✉)
Intelligent Materials Research Lab, Department of Physics, Dr. Babasaheb Ambedkar Marathwada University, Aurangabad 431004, Maharashtra, India
e-mail: mdshirsat@gmail.com

S.S. Hussaini · M. Anis
Crystal Growth Laboratory, Department of Physics, Milliya Arts, Science and Management Science College, Beed 431122, Maharashtra, India

R.B. Kamble
Department of Physics, Indian Institute of Science, Bangalore 560012, Karnataka, India

J. Ebenezar (ed.), *Recent Trends in Materials Science and Applications*,
Springer Proceedings in Physics 189, DOI 10.1007/978-3-319-44890-9_45

1 Introduction

The advances in nonlinear optical materials are resulted in distinguished progress in optical modulation which leads to the diversified applications such as fiber optical communication system, holography, optoelectronic devices and laser industries [1]. In the current year, the investigation on amino acid designed nonlinear optical (NLO) materials is stimulated as a forefront candidate for photonic devices due to a new and unique zwitterionic nature and charge transfer ability through acceptor-donor groups. The coordination through amino acceptor-donor groups with semi organic metal complexes mainly offer excellent second harmonic generation (SHG) coefficient, enriched transparency, wide optical band gap and higher thermal stability [2, 3]. A variety of amino acids mixed organometallic complexes have already been reported in earlier literature [4–6]. The gamma glycine single crystal in presence of sodium acetate was reported by [7]. The L-Arginine acetate single crystal was grown and studied by [8]. The L-Threonine zinc acetate single crystal studies have been reported as a promising NLO material by [9]. Glycine is a simple colorless organic compound commonly found in proteins, containing zwitterionic structure which is responsible for its optical activity. It exhibits large second order susceptibility, good transmission in UV as well as visible region and good thermal stability is required for NLO applications [10]. The physicochemical properties of organometallic compound are enhanced due to the addition of amino acids and also alter the cento symmetry. The literature survey reveals that the linear and nonlinear optical performance of glycine sodium acetate materials is not reported. Hence, the present communication is focuses on the growth and characterization of glycine sodium acetate single crystal through different techniques in order to know its applicability in photonic devices.

2 Experimental

2.1 Material Synthesis and Crystal Growth

Stoichiometric amounts of Glycine and sodium acetate taken in 1:1 and ratio was dissolved in deionized water for the synthesis of glycine sodium acetate (GSA). The homogenous solution is obtained by constant stirring of 6 h using magnetic stirrer. The clear transparent solution of glycine sodium acetate was filtered well by using Whatman filter paper in large sized beaker which was covered with transparent film to avoid the external impurities. The solution was allowed to crystallize by slow evaporation process at room temperature. In the period of 15 days, good quality transparent crystals with optimum dimensions were obtained. The grown glycine sodium acetate crystals are shown in Fig. 1a.

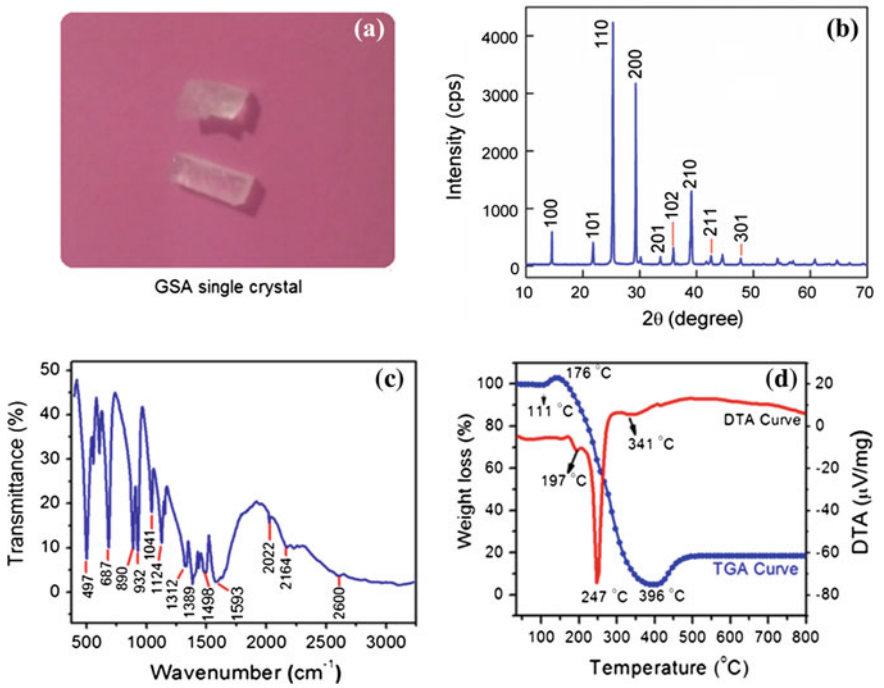

Fig. 1 **a** Single crystal image, **b** powder XRD pattern, **c** FT-IR spectra, and **d** TG/DTA curves of GSA crystal

2.2 Analysis Techniques

The grown crystal is subjected to various characterizations techniques in order to investigate its suitability in the field of NLO applications. The powder X-ray diffraction is carried out to confirm the crystal structure and cell dimension with the help of XPERT-PRO diffractometer system using Bruker AXS D8 advance Cu wavelength (1.5406 Å). The presence of sodium metal in the grown crystals was confirmed by atomic absorption spectrometer. The functional group is confirmed by using PERKIN ELMER RX1 Fourier transform infrared spectrometer. The thermal analysis studies are carried out by using Perkin Elmer Diamond thermal analyzer instruments. The Cary Eclipse Win FLR EL07073870 Instrument was employed to record the photoluminescence emission spectrum of grown crystal. The optical parameters are identified with the help of Shimadzu UV-2450 spectrophotometer. The Kurtz and Perry powder technique has been employed to test the non-linear optical nature of grown crystal.

3 Results and Discussions

3.1 Powder X-ray Diffraction Studies

The powder X-ray diffraction technique is employed to determine the crystal structure. The sharp X-ray diffraction pattern of glycine sodium acetate (GSA) crystal shows the well-defined peak at a specific position (2θ) with intensity variation. It indicates the purity of glycine sodium acetate (GSA) crystal as shown in Fig. 1b. The calculated lattice parameter of GSA crystal are, a = 7.17 Å, b = 7.17 Å, and c = 5.58 Å, whereas the angles are $\alpha = 90°$, $\beta = 90°$ and $\gamma = 120°$ and volume (V) = 286.86 $Å^3$ which agreed with the reported literature [7, 11].

3.2 FT-IR Studies

The infrared spectroscopy is an effective and most popular technique used for identifying molecules and the chemical functional group of the sample. Fourier transform infrared radiation spectrum is a plot of transmission of IR radiation as a function of wavelength is shown in Fig. 1c. The NH_3^+ asymmetric stretching vibrations are observed at peak 2602 cm^{-1}. The peak at 1593 cm^{-1} corresponds to strong asymmetric COO^- stretching vibration. The peak observed at 687 cm^{-1} is attributed to COO^- bending vibrations. In the mid energy region of the spectrum, the peak at 1312 cm^{-1} corresponds to CH_2 twisting vibrations in GSA crystal. The absorption peak at 1398 cm^{-1} is attributed to symmetric stretching vibrations of COO^-. The peak found at 1041 cm^{-1} is due to the CCN asymmetric stretching vibration. The absorptions due to the carboxyl group of free glycine are observed at around 497 cm^{-1}. The large shifting in frequencies of carboxyl group and NH^{3+} and functional group analysis confirmed that, the glycine molecule would be coordinated with sodium ion through its carboxyl and amine group due to zwitterions nature [7, 12].

3.3 Thermal Studies

The thermo gravimetric and differential thermal analyses (TG-DTA) of GSA crystal were carried out between the temperatures of 30–400 °C in the nitrogen atmosphere to determine the thermal stability of the grown crystal. The TG/DTA curves of glycine sodium acetate crystal are illustrated in Fig. 1d. From the DTA curve, the melting point is confirmed by a sharp endothermic peak appeared at 247 °C followed by second minor endothermic transition takes place at 341 °C. The thermo gravimetric analysis does not show any kind of phase transition till the melting of glycine sodium acetate crystal. The absence of phase transition improves the temperature range for the applicability of the crystal for photonic applications. The absence of weight loss

around 100 °C confirmed that the water molecules are absent in the crystalline structure of grown crystal. The TGA curve shows that grown crystals exhibit a sharp single weight loss starts at 176 °C which ends at 396 °C. There is no weight loss observed in TGA curve below 176 °C temperature. Differential thermal analysis (DTA) reveals a minor endothermic peak around 197 °C of sample which may be due to conversion of γ-glycine into α-glycine [11]. The decomposition process continues at higher temperature accompanied by weight loss of material.

3.4 Atomic Absorption Studies

The quantitative determination of metal element in the grown crystal is confirmed by using atomic absorption spectroscopy (AAS) technique which is a spectro analytical procedure employing the absorption of optical radiation by free atom in the gaseous state. The sodium (Na) element is found to be 9.3 ppm in the grown crystal. The presence of single sodium metal confirmed the purity of the grown crystal. The coordination of glycine with sodium element in the mixture leads to the formation of resultant non-centrosymmetric structure.

3.5 Photoluminescence

The photoluminescence studies furnished the quality information regarding the electronic states of the material, influence of intrinsic impurities on the material emission spectra etc. The glycine sodium acetate crystal is photo excited with the energy wavelength of 260 nm and the emission spectrum is recorded in the range of 300–900 nm as shown in Fig. 2. The stable single peak is observed in the range from 787 to 812 nm at room temperature. The single peak maxima at 799 nm, indicates that GSA crystal has infrared emission. The GSA materials with near infrared emission might be of suitable for NIR optical imaging and sensing determination of biological targets [13, 14].

3.6 UV Spectral Studies

The significant optical parameters such as transmission, optical dielectric constant, optical band gap, extinction coefficient of the grown crystals has been investigated by using Shimadzu UV-2450 spectrophotometer in the range of 200–900 nm. The transmission studies assist to examine the behaviour of electron in two different energy states due to the absorption of UV and visible light. The recorded

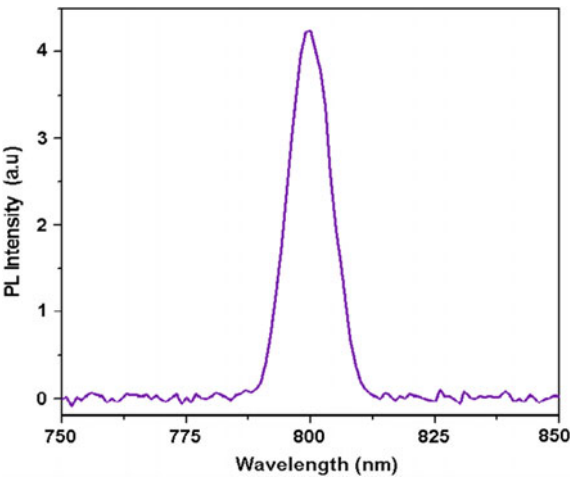

Fig. 2 Photoluminescence (PL) curve of GSA

transmission spectrum of GSA crystal is depicted in Fig. 3a. The glycine sodium acetate crystal exhibits high transmittance (88 %) with lower cut off wavelength at 240 nm. The enriched transparency window and lower cut off wavelength of GSA crystal indicates its suitability for SHG device applications [15]. The very low absorption in the visible region clearly indicates that the grown crystal can be used for photonics and optoelectronic applications. The optical absorption coefficient (α) is determined using the equation $\alpha = 2.303 \log (1/T)/t$. The optical band gap ($E_g$) was determined from the relation [15] given as follows,

$$(\alpha h\nu)^2 = A\left(h\nu - E_g\right) \tag{1}$$

where, A is a constant, E_g is the optical band gap and $h\nu$ is the incident photon energy. The optical band gap of GSA crystal is determined using the Tauc's graph depicted in Fig. 3b. The optical band gap of GSA is found to be 5.12 eV. The crystal with wide optical band gap reveals its suitability for the design and fabrication of UV tunable lasers and optoelectronic devices [16]. The extinction coefficient is evaluated using the relation,

$$K = \lambda\alpha/2\pi \tag{2}$$

The variation of extinction coefficient (K) as shown in Fig. 3c within the material medium indicates that the loss of optical energy is due to the absorption and scattering of light within the material medium. The high transmittance, low absorption and reflectance of GSA crystal urge its applicability for antireflection coating in the solar thermal devices [17]. The variation of optical conductivity (σ_{op}) with photon energy is shown in Fig. 3d. The GSA exhibits lowered extinction coefficient and higher optical conductivity which make it excellent material for high speed information processing and computing devices [17]. The complex dielectric

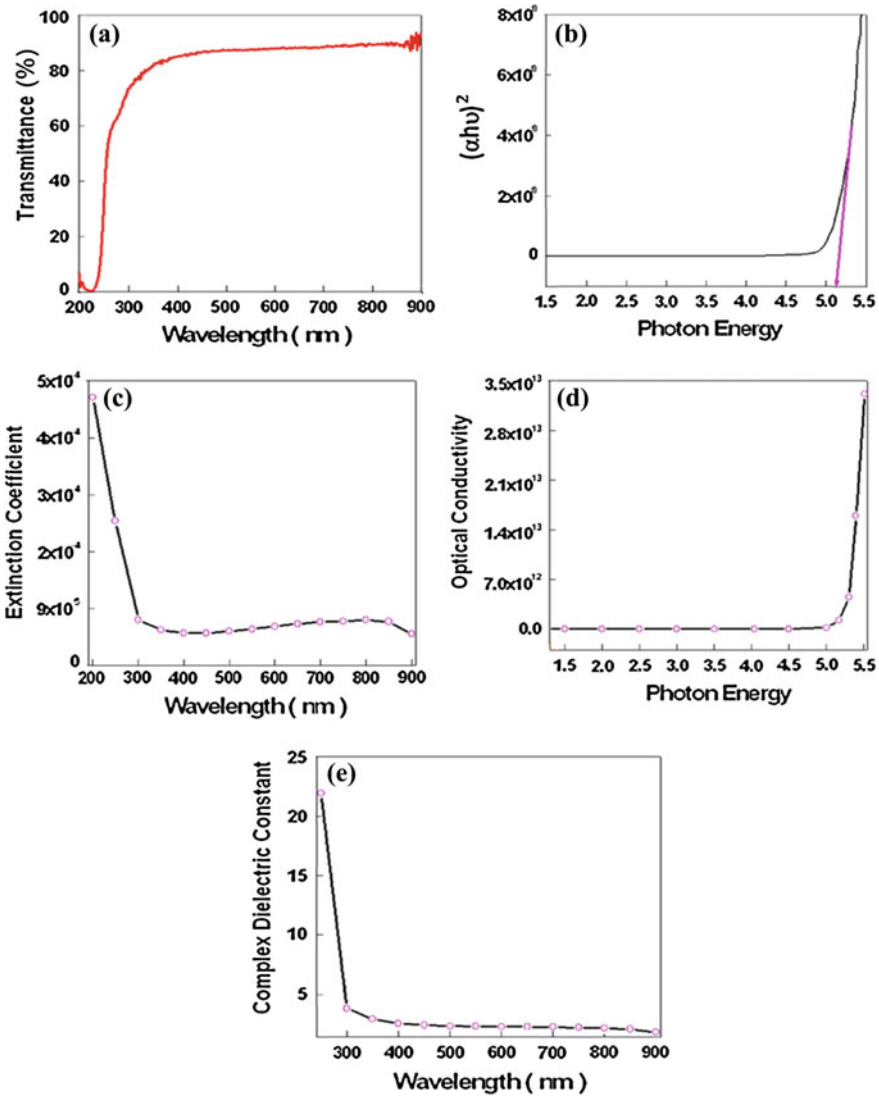

Fig. 3 **a** UV transmittance, **b** optical band gap, **c** extinction coefficient, **d** optical conductivity, **e** complex dielectric constant for GSA single crystal

constant ($\varepsilon = \varepsilon_r + \varepsilon_i$) characterizes the optical properties of the grown crystals is shown in Fig. 3e. The lower value of dielectric constant with wide band gap of GSA crystal suggests the suitability of optoelectronic devices. The GSA crystal with promising optical properties emphasizes it's prominence for distinct electro-optic applications.

3.7 Non-linear Optical Studies

The second harmonic generation (SHG) conversion efficiency of glycine sodium acetate is measured by Kurtz-Perry powder technique. The crystal was grounded into a fine powder and densely packed into capillary tube. An actively Q switched Nd: YAG laser emitting a fundamental wavelength of 1064 nm with energy 3.5 mJ/pulse of width 8 ns was incident on the capillary tube. The green optical emission (532 nm) was detected by photomultiplier tube detector and output voltage was recorded on cathode ray oscilloscope as 18 mV. The SHG output signal of standard KDP material was found to be 11 mV. In the present analysis, the SHG conversion efficiency of glycine sodium acetate is found to be 1.7 times more than that of KDP. The coordination of sodium with hydrogen bond in asymmetric nature may be the reason for NLO efficiency enhancement. The higher SHG efficiency of glycine sodium acetate crystal is most desirable for designing of NLO devices.

4 Conclusion

The optically good quality single crystal of glycine sodium acetate (GSA) was grown by slow evaporation technique at room temperature. The crystalline nature was determined by powder X-ray diffraction technique. The Kurtz-Perry powder technique confirmed the SHG efficiency of the grown crystal to be 1.7 times more than that of standard KDP. The high optical transparency (88 %) of the grown crystal with lower cutoff wavelength of 240 nm was determined employing UV-visible studies. The optical band gap of grown crystal was found to be 5.12 eV. The transmittance data is used to evaluate the potential optical constants viz. reflectance, refractive index, extinction coefficient and complex dielectric constant. The different functional groups were identified by using Fourier transform infrared (FT-IR) spectral analysis. The thermal stability of the grown crystal was found to be 176 °C. The presence of sodium element is also confirmed by atomic absorption spectroscopy technique. The photoluminescence study of grown crystal is investigated in the range of 300–900 nm and confirmed the infra-red emission in the electromagnetic spectrum. The high optical transparency, lower extinction coefficient, cut-off wavelength, and wide optical band gap make GSA crystal, very suitable for fabrication of NLO devices.

Acknowledgements The authors are thankful to University Grants Commission, New Delhi for financial assistance. Authors are also thankful to Prof. P.K. Das, Indian Institute of Science, Bangalore for SHG analysis and National chemical laboratory, Pune for rendering the characterization facilities.

References

1. Ushasree, P.M., Jayaval, R., Subramanian, C., Ramasamy, P.: Growth of zinc thiourea sulfate (ZTS) single crystals: a potential semiorganic NLO material. J. Cryst. Growth **197**, 216–220 (1999)
2. Ramajothi, J., Dhanuskodi, S., Nagarajan, K.: Crystal growth, thermal, optical and micro hardness studies of tris (thiourea) zinc sulphate—a semiorganic NLO material. Cryst. Res. Technol. **39**(5), 414–420 (2004)
3. Jeyakumari, A.P., Ramajothi, J., Dhanuskodi, S.: Structural and micro hardness studies of a NLO material–bis thiourea cadmium chloride. J. Cryst. Growth **269**, 558–564 (2004)
4. Angeli Mary, P.A., Dhanuskodi, S.: Growth and characterization of a new nonlinear optical crystal: bis thiourea zinc chloride. Cryst. Res. Technol. **36**, 1231–1237 (2001)
5. Shirsat, M.D., Hussaini, S.S., Dhumane, N.R., Dongre, V.G.: Influence of lithium ions on the NLO properties of KDP single crystals. Cryst. Res. Technol. **43**(7), 756–761 (2008)
6. Hussaini, S.S., Dhumane, N.R., Dongre, V.G., Shirsat, M.D.: Effect of glycine on the optical properties of zinc thiourea chloride (ZTC) single crystal. Optoelectron. Adv. Mater. **2**(2), 108–112 (2008)
7. Baraniraj, T., Philominathan, P.: Growth and characterization of gamma glycine single crystals grown from alpha glycine in the presence of sodium acetate. J. Miner. Mat. Charact. Engg. **10**(4), 351–356 (2011)
8. Gnanasekaran, P., Madhavan, J.: L-arginine acetate single crystals for NLO applications. Indian J. Sci. Technol. **1**, 7–10 (2008)
9. Puhal Raj, A., Ramachandra Raja, C.: Synthesis, growth, structural, spectroscopic, thermal and optical properties of NLO single crystal: L-threonine zinc acetate. Photonics Optoelectron. **2**(3), 56–64 (2013)
10. Dhumane, N.R., Hussaini, S.S., Dongre, V.G., Shirsat, M.D.: Growth and characterisation of glycine doped zinc (tris) thiourea sulfate (ZTS) crystal for opto-electronics applications. Front. Micro. Optoelectron. **19**, 113–118 (2008)
11. Ashok Kumar, R., Ezhil Vizhi, R., Sivakumar, N., Vijayan, N., Rajan Babu, D.: Crystal growth, optical and thermal studies of nonlinear optical γ-glycine single crystal grown from lithium nitrate. Optik. **123**, 409–413 (2012)
12. Suresh, S., Ramanand, A., Jayaraman, D., Mani, P.: Studies on growth and characterization of Triglycine acetate (TGAc) NLO single crystals. Optoelectron. Adv. Mat. Rapid Commun. **4** (11), 1766–1770 (2010)
13. Arunkumar, A., Ramasamy, P., Vishnu, K., Jayaraj, M.K.: Growth, structural, thermal, optical, and electrical properties of potassium succinate-succinic acid crystal. J. Mater. Sci. **49**, 3598–3607 (2014)
14. Amiot, C.L., Xu, S., Liang, S., Pan, L., Zhao, J.X.: Near-infrared fluorescent materials for sensing of biological targets. Sensors **8**, 3082–3105(2008)
15. Dhas, S.A.M.B., Natarajan, S.: Growth and characterization of a new organic NLO material: glycine nitrate. Opt. Commun. **278**, 434–438 (2007)
16. Anis, M., Muley, G.G., Rabbani, G., Shirsat, M.D., Hussaini, S.S.: Optical, photoconductivity, dielectric and thermal studies of L-arginine doped zinc thiourea chloride crystal for photonics applications. Adv. Perform. Mat. **30**(3), 129 (2015)
17. Anis, M., Muley, G.G., Shirsat, M.D., Hussaini, S.S.: Influence of formic acid on electrical, linear and nonlinear optical properties of potassium dihydrogen phosphate (KDP) crystals. Phys. B **449**, 61–66 (2014)

Growth of Organic Single Crystal by Transparent Vertical Bridgman Technique and Its Characterization

S. Siva Bala Solanki, Rajesh Narayana Perumal and Shizuyasu Ochiai

Abstract Organic single crystal of benzyl carbamate was grown by transparent vertical Bridgman technique. The grown crystal was subjected to single-crystal XRD, optical transmittance analysis, second harmonic generation analysis, laser damage threshold and photoconductivity analysis. The grown crystal cell parameters were confirmed by single-crystal X-ray diffraction analysis. From the UV–Vis–NIR transmittance spectrum analysis the cut off wavelength was found to be 275 nm. The second harmonic generation property of the powdered benzyl carbamate was confirmed by the emission of green light. The powder density value of benzyl carbamate crystal was found to be 0.955 GW/cm^2. Benzyl carbamate showed positive photoconductivity nature and the calculated photosensitivity value was 2.84.

1 Introduction

Benzyl carbamate is derived from the parent compound of benzyl chloroformate [1]. Therefore Benzyl carbamate belongs to benzyl chloroformate family. The benzyl chloroformate melts at −20 °C and the benzyl chloroformate family compounds such as ethyl chloroformate, phenyl chloroformate, methyl chloroformate, benzyl alcohol, benzyl acetate, benzyl salicylate and benzyl benzoate, has melting points at −81, −38, −61, −15, −51, 19 and 18 °C respectively [2]. Even though, benzyl carbamate has high melting point around 93 °C, it is non-hygroscopic, noncentrosymmetric, having a space group of $Pca2_1$ and molecular formula as $C_8H_9NO_2$ [3, 4]. Therefore it finds a key application in second- and third-order non-linear optics that include harmonic generation, optical switches, photonic

S. Siva Bala Solanki · R. Narayana Perumal (✉)
Department of Physics, Centre for Crystal Growth, SSN College of Engineering, Kalavakkam 603110, India
e-mail: rajeshnp@ssn.edu.in

S. Ochiai
Department of Electrical Engineering, Aichi Institute of Technology, Toyota 470-0392, Japan

J. Ebenezar (ed.), *Recent Trends in Materials Science and Applications*,
Springer Proceedings in Physics 189, DOI 10.1007/978-3-319-44890-9_46

devices, electro-optical modulators, memory, and other interconnects [5, 6]. The advantage of using vertical Bridgman technique compared to Czochralski method and solution growth method is that it has the feasibility to grow large size organic single crystals [7]. The aim of the present work is to grow a bulk single crystal of benzyl carbamate using vertical Bridgman technique. In this paper, we report the growth of organic single crystals and characterization by single crystal XRD. This study was used to confirm the cell parameters and optical transmittance study was used to find the transmission of light in the crystal and cut-off wavelength. Second harmonic generation analyses confirm the NLO properties of the material. Laser damage threshold analysis was used to analyse the power density. A photoconductivity study discusses the photoconductivity and photosensitivity of the grown benzyl carbamate crystal.

2 Melt Growth

In vertical Bridgman technique the ampoule design is one of the important factors for growing organic single crystals [8]. The ampoule was designed having a dimension of 24 cm × 1.5 cm, in which the cone length was 4.4 cm. The cone angle of the ampoule was 10°07″. Before loading the material into ampoule, deionized water and acetone are used to clean it and later was annealed at 200 °C for 12 h. The designed single wall ampoule with cone angle is shown in Fig. 1a [4].

The benzyl carbamate (99 % pure) purchased from Sigma-Aldrich was loaded into the ampoule and then sealed off at 10^{-4} millibar. The sealed ampoule was located into the furnace. The furnace temperature was raised up to the melting point of the material. The translation rate was optimized to 0.2 mm/h for improving the quality of the crystal. When the melt reaches homogeneity, the ampoule was lowered from hot zone to cold zone. Initially a small single crystal (3 mm) appeared at the bottom of the ampoule. This crystal reached a size of 90 mm in length and 15 mm in diameter within days. Once the entire melt was solidified, a high-quality crystal was harvested. The standard diamond wheel cutter was used to remove the grown crystal from ampoule. The photograph of as-grown crystal with cut and the polished portion of grown benzyl carbamate crystal are shown in Fig. 1b, c respectively [4].

3 Results and Discussions

3.1 Single Crystal X-ray Diffraction Analysis

Enraf Nonius CAD4 single crystal X-ray diffractometer was used to analyses the cell parameter of grown benzyl carbamate crystal at room temperature (26 °C). The

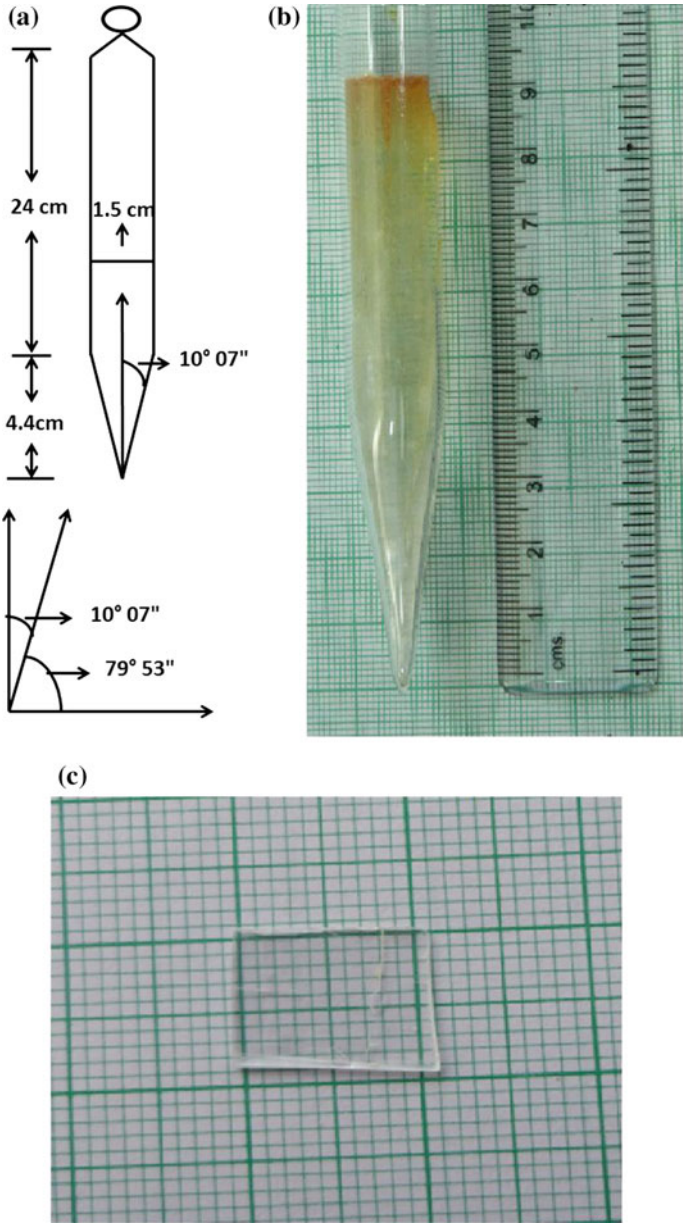

Fig. 1 **a** Schematic diagram of single wall ampoule with cone angle, **b** photograph of the as-grown crystal and **c** cut and the polished portion of the benzyl carbamate single crystal

obtained lattice parameters were, a = 10.08 (±0.07) Å, b = 5.42 (±0.04) Å, c = 29.61 (±0.2) Å and α = β = γ = 90°. These values were found to be in good agreement with the earlier reported values [3, 4].

3.2 Optical Studies

Single crystals are mainly used for optical applications. The optical transmittance range and cut-off wavelength are fundamental criteria to tailor the material for appropriate application. Therefore lower the cut-off wavelength, higher will be the transmission and this transparent nature in the visible region is a desirous property for this material for NLO applications. Perkin-Elmer Lambda-35 spectrophotometer has been used to determine the optical transmission of the grown crystal, in the range 200–1100 nm. The slit width of the instrument was 2 mm with a speed of 240 nm/min. The cut and polished 5 × 5 × 1 mm crystal sample was used for transmission studies. The grown benzyl carbamate crystal shows 52.5 % above transmittance in the visible region, and a UV cut-off wavelength was observed to be 275 nm, which was due to n → π* transition in the complex. The anticipated lower cut-off for transmittance analysis must be between 200 and 400 nm for active application [9]. Transmission curve is shown in the Fig. 2. This material can be used for optoelectronic device fabrication and NLO application.

3.3 Second Harmonic Generation Analysis

The well grounded powder sample was placed inside the glass tube at a small distance away from the focused spot of Nd:YAG laser to avoid the damage of the sample. The monochromator was used to filter (remove second harmonic signal) the

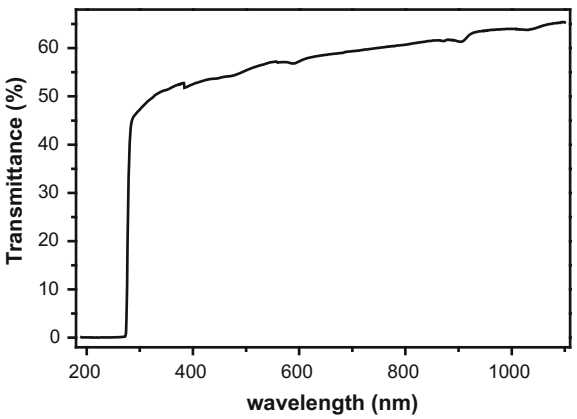

Fig. 2 Optical transmission spectrum of the benzyl carbamate single crystal

fundamental light and this signal was passed through the powder sample. The output wave was focused on the photomultiplier tube which is connected to an oscilloscope at its near end. The second harmonic generation was confirmed by the emission of green light. The fundamental light was focused at different points on the same sample at a uniform distance each having relative output of green light emitted at 532 nm. An energy of 0.68 J was applied on KDP and benzyl carbamate sample, the corresponding output obtained were 8.02 and 6.9 mJ. The SHG efficiency of benzyl carbamate was found to be about 0.86 times that of KDP.

3.4 Laser Damage Threshold

The surface laser damage threshold of benzyl carbamate crystal was determined using a Q-switched Nd:YAG laser with fundamental wavelength of 1064 nm and pulse duration of 10 ns. The power density was calculated using the formula,

$$P_d = E/\tau\pi r^2$$

where P_d is Power density, E is the input energy (mJ), τ is the pulse duration (ns) and r is the radius of the spot (1 mm). A small dot appeared on the sample at 75 mJ and its corresponding powder density was 0.955 GW/cm^2. The optical micrograph image of the pristine surface and damaged surface is shown in Fig. 3a, b. The laser damage thresholds of some NLO crystals are given in Table 1 [10].

3.5 Photoconductivity Study

Photoconductivity studies were carried out for benzyl carbamate crystal using Keithley 6487 picoammeter at room temperature. The sample (5 mm × 5 mm 2 mm) was fixed in the sample holder. Initially the Dark current (I_D) was measured

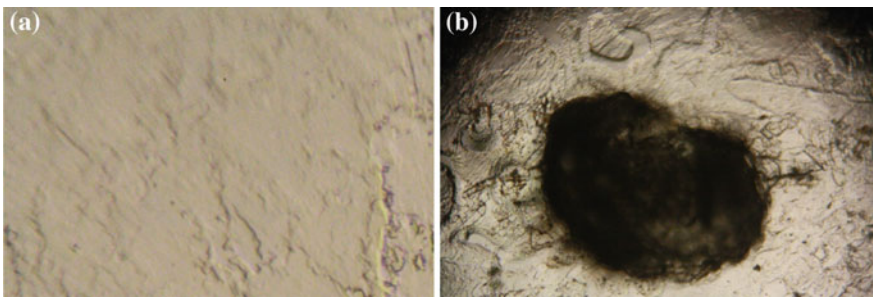

Fig. 3 Optical micrograph of laser induced surface damage of the benzyl carbamate crystal **a** pristine surface **b** damaged surface

Table 1 Laser damage threshold values of some organic, semi-organic and inorganic crystals

Compounds	Laser damage threshold (GW/cm^2)
Potassium dihydrogen phosphate (KDP)	0.2
Urea	1.5
β-Barium borate	5.0
L-Arginine phosphate	10
Benzyl carbamate	0.955

by varying voltage from 0 to 84 V, then halogen lamp (50 w, 12 v) was used for the measurement of photocurrent. The variation of both dark current (I_D) and photocurrent (I_L) with an applied field for benzyl carbamate crystal is shown in Fig. 4. It can be seen that the photocurrent of benzyl carbamate crystal is always greater than the dark current, therefore, benzyl carbamate has positive photoconductivity. This phenomenon can be attributed to the generation of mobile charge carriers caused by the absorption of photons [11]. The photosensitivity of the material was calculated using the expression

$$S = I_{ph}/I_D = (I_L - I_D)/I_D$$

where $I_{ph} = (I_L - I_D)$, I_{ph} being the photoconductivity, I_L being the current under illumination and I_D being the dark current. Photosensitivity value of benzyl carbamate was 2.84 for applied voltage of 84 V.

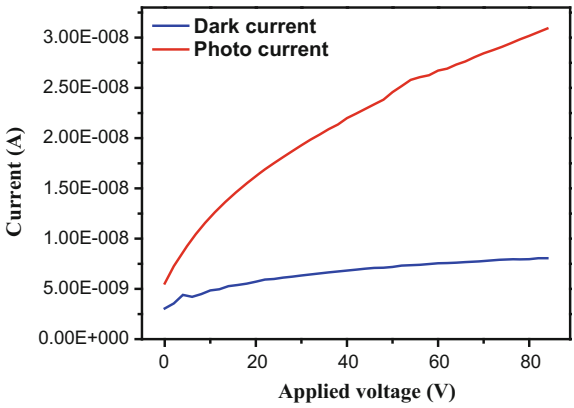

Fig. 4 Photoconductive study of the benzyl carbamate single crystal

4 Conclusion

Vertical Bridgman technique has been used to grow good quality polar and chiral natured benzyl carbamate single crystal. The grown crystal was analysed by various characterization techniques. Single crystal X-ray diffraction study was used to confirm that the crystal belongs to the orthorhombic system with space group $Pca2_1$. In optical transmittance studies, it shows that crystal has the good transmittance in the visible region and in NIR region. The cut-off wavelength was observed to be 275 nm. In SHG studies, the red laser light was converted into green light. The laser damage threshold for this crystal was found to be 0.955 GW/cm^2. Photoconductivity studies showed that the grown crystal exhibits positive photoconductivity. Hence, it can be concluded that the crystal is suitable for device fabrication in optoelectronic industries.

Acknowledgements The authors hereby gratefully acknowledge the financial support by the Department of Science and Technology, New Delhi, India, under the grant of project ref-SR/S2/CMP-117/2012.

References

1. Sánchez-Sancho, F., Romero, J.A., Fernández-Ibáñez, M.: Benzyl carbamate. e-EROS Encycl. Reagents Org. Synth. (2010)
2. Chemspider. http://www.chemspider.com/
3. Mata, I., Molins, E., Amat, M., Llor, N., Checa, B.: C–H…X (X = O, N or π) interactions in benzyl carbamate. Acta Cryst. **C68**, o114–o118 (2012)
4. Siva Bala Solanki, S., Perumal, R.N., Suthan, T., Bhagavannarayana, G.: Growth and characterization of organic single crystal benzyl carbamate. J. Cryst. Growth, **427**, 24–28 (2015)
5. Chemla, D.S., Zyss, J.: Nonlinear Optical Properties of Organic molecules and Crystals. Academic Press, New York (1987)
6. Prasad, P.N., Williams, D.J.: Introduction to Nonlinear Optical Effects in Organic Molecules and Polymers. Wiley, New York (1991)
7. Suthan, T., Rajesh, N.P., Mahadevan, C.K., Sajan, D., Bhagavannarayana, G.: Growth and characterization of organic material 2-hydroxypyridine single crystal by modified vertical Bridgman technique. Mater. Chem. Phys. **130**, 915–920 (2011)
8. Suthan, T., Dhanaraj, P.V., Rajesh, N.P., Mahadevan, C.K., Bhagavannarayana, G.: Growth and characterization of benzil single crystals using nanotranslation by the modified vertical Bridgman technique. CrystEngComm **13**, 4018–4024 (2011)
9. Singh, B.K., Sinha, N., Singh, N., Kumar, K., Gupta, M.K., Binay Kumar.: Structural, dielectric, optical and ferroelectric property of urea succinic acid crystals grown in aqueous solution containing maleic acid. J. Phys. Chem. Solids, **71**, 1774–1779 (2010)
10. Vijayan, N., Bhagavannarayana, G., Ramesh Babu, R., Gopalakrishnan, R., Maurya, K.K., Ramasamy, P.: A comparative study on solution- and Bridgman-grown single crystals of benzimidazole by high-resolution X-ray diffractometry, fourier transform infrared, microhardness, laser damage threshold, and second-harmonic generation measurements. Cryst. Growth Design **6**, 1542–1546 (2006)
11. Helen, F., Kanchana, G.: Growth, mechanical, dielectric, thermal and optical studies of a nonlinear optical crystal: L-histidinium dipicrate dehydrate. Mater. Chem. Phys. **151**, 5–13 (2015)

Effect of Oxygen Ion Irradiation on the Structural and Optical Properties of L-Arginine Acetate Single Crystals

N. Renuka, R. Ramesh Babu, N. Vijayan, Brijesh Rathi and Kanika Thukral

Abstract In the present work, a potential nonlinear optical single crystal, L-arginine acetate (LAA) was grown by slow evaporation solution growth technique. The grown LAA single crystal was irradiated with oxygen ions at the dose rate of 600 krad and 1 Mrad in order to tune the structural and optical properties. The structural properties of pristine and oxygen ions irradiated LAA single crystals were studied using Powder X-ray diffraction and Fourier Transform Infrared spectroscopy. The results obtained reveal the structural changes that are generated due to irradiation. Optical behavior of prisitine and oxygen ions irradiated crystals was studied by UV-Vis-NIR and photoluminescence spectra recorded at room temperature.

1 Introduction

Ion beams play a significant role in the process of tuning the properties of materials. Based on the radiation behavior, the engineering materials are categorized into two different types. The first one comprises organic solids which are sensitive to the energy deposited in their electronic system and the second one comprises metals

N. Renuka
Engineering Technology and Science, Abu Dhabi Men's College, Higher Colleges of Technology, Abu Dhabi, UAE

N. Renuka · R. Ramesh Babu (✉)
Crystal Growth and Thin Film Laboratory, Department of Physics, Bharathidasan University, Tiruchirappalli 620024, Tamil Nadu, India
e-mail: rampap2k@yahoo.co.in

N. Vijayan · K. Thukral
CSIR-National Physical Laboratory, Dr. K. S. Krishnan Road, New Delhi 110012, India

B. Rathi
Department of Chemistry, Sri Venkateswara College, University of Delhi, New Delhi 110021, India

J. Ebenezar (ed.), *Recent Trends in Materials Science and Applications*, Springer Proceedings in Physics 189, DOI 10.1007/978-3-319-44890-9_47

which are insensitive to the energy deposited in their electronic system. However, exposure to swift heavy ions alters this general behavior [1, 2]. Depending on the mass, kinetic energy and nuclear charge, an ion can produce modifications within a thin surface layer or it can penetrate deeply to produce long and narrow distorted area along its path [3]. When a high energetic ion beam impinges on a material, it causes two different types of changes in the material due to the coulomb interaction between the target atom and the energetic ion beam: (i) inelastic collisions of the energetic ion with the atomic electrons of the material; and (ii) elastic scattering from the nuclei of the atoms of the material, which is extremely responsible for relocating the atoms of matter from their lattice position [4]. The exposure of the heavy ions renders the material return to equilibrium state during which the material undergoes surface and bulk modifications which depends on the mass of the projectile ion, physical properties of the target material, its energy and beam dimension. It is well established that electronic stopping power plays a major role in the defect creation mechanism provided it exceeds a threshold which strongly depends on the nature of the target material [5]. There are reports available on heavy ion irradiation especially on crystalline materials to tune their physical and chemical properties [6–12].

L-Arginine Acetate (LAA) is a potential semi-organic nonlinear optical crystal and its optical, mechanical and thermal properties have already been reported by our group [13]. The main objective of the present work is to enhance or tune the structural and optical properties of LAA single crystals by heavy ion irradiation.

2 Crystal Growth and Sample Preparation

The title compound, L-Arginine Acetate (LAA) was grown by slow evaporation solution growth technique at room temperature by taking the equimolar ratio of L-arginine and acetic acid [13]. The cut and polished crystals ($5 \times 5 \times 1$ mm^3) were subjected to Oxygen ions irradiation with the dose rate of 600 krad (1.16328×10^{10}) and 1 Mrad (1.9388×10^{10}) at IUAC, New Delhi.

3 Result and Discussion

3.1 Powder XRD Analysis

Figure 1 illustrates the powder X-ray diffraction pattern of pristine LAA and sample of oxygen ions irradiated at 600 krad and 1 Mrad. The lattice parameters of LAA were calculated from the XRD data using checkcell software package and are presented in Table 1. An apparent demarcation has been observed between the X-ray diffraction patterns of pristine and irradiated samples in counts and as well as

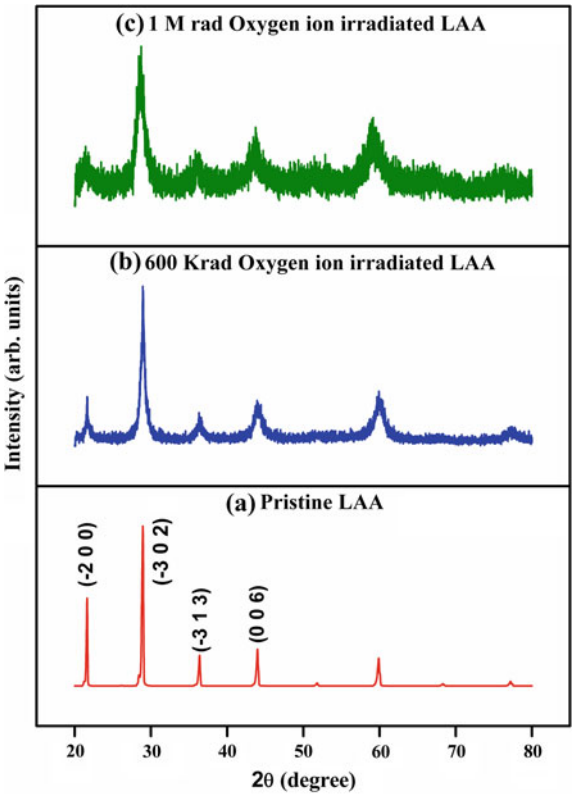

Fig. 1 X-ray diffraction pattern of LAA single crystals **a** pristine and **b** Oxygen ions irradiated at 1 Mrad (*Black*), **c** 600 krad (*Green*)

Table 1 Lattice parameters of pristine and oxygen ions irradiated LAA single crystal

Parameter	*a* (Å)	*b* (Å)	*c* (Å)	α (°)	β (°)	γ (°)	*V*(Å)
Pristine	9.2294	5.1779	13.2858	90	111.4	90	591.122
600 krad oxygen ions irradiated LAA	9.2390	5.1754	13.2681	90	111.24	90	591.318
1 Mrad oxygen ions irradiated LAA	9.2414	5.3464	13.2949	90	111.99	90	609.082
Reported [14]	9.2290	5.1780	13.2710	90	111.4	90	586.0

in the peak shape. However, the lattice parameters and cell volume observed for pristine and sample irradiated at 600 krad are in good agreement with the reported values [14] and no significant changes in lattice parameters values were observed for the sample irradiated at 600 krad whereas the sample irradiated at 1 Mrad shows a slight impact on lattice parameters and cell volume. The difference in lattice parameters of the pristine and irradiated samples may be [15]. It is assumed that densification of the grains affect the cell volume and therefore the lattice

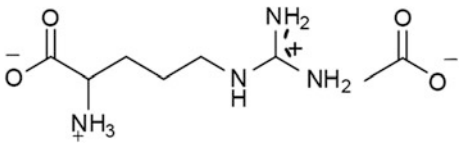

Fig. 2 General chemical formula of L-arginine acetate

parameters. In other words, in pristine sample, the cations and anions are well settled in their positions without any strain or disorder and highly dense, while on exposure to radiation, the cations and anions face a strain due to defects or disorderliness at bonds and bond angles and repulsion between the atoms, thus increasing the volume of the crystal and decreasing the density. The most possible reason may be as oxygen anion present in the crystal structure displaces and creates vacancy defects in the crystal structure, to compensate the vacancy, other nitrogen atoms take place by self-charge compensation. In the present case, as far as L-arginine acetate ($C_6H_{14}N_4O_2CH_3$–COO) structure (Fig. 2) is concerned, the reason for change in lattice parameters may be the oxygen ion shields at *a*, *b* and *c* axis. It is attributed to the change in lattice parameters that the distance between two sites via coulomb interactions and the repulsion caused by the self-compensated defect of oxygen vacancies located in the crystal. It can be observed from the results obtained in the present case that the magnitude of the radiation also plays an important role. The change in bond length between the atoms due to displacement of oxygen anions and results strain in the structure, and thus the change in lattice parameters takes place. It has been concluded from the results that sample irradiated at low fluence does not affect the lattice parameters and cell volume, but high fluence radiation affects its internal stoichiometry and displaces the oxygen anions and results strain and therefore it affects the lattice parameters and cell volume of the crystal as listed in Table 1.

3.2 FTIR Spectral Studies

FTIR spectra of pristine and oxygen ions irradiated samples, recorded between 400 and 4000 cm^{-1}, are shown in Fig. 3a–c. The observed vibrational bands and their assignments are given in Table 2. They are in good agreement with the reported values [14]. The broad envelope between 2300 and 3750 cm^{-1} includes overlapping of stretching modes due to N–H and C–H. The peak at 2961 cm^{-1} is assigned to the aliphatic C–H stretching mode. Multiple fine structures at the lower energy mode of the spectrum indicates strong hydrogen bonding interaction of $–NH_3^+$ group with $–COO^-$ group in the crystal. The C=O stretch of $–COO^-$ is observed at 1691 cm^{-1}. The asymmetric N–H bend of NH_3^+ shows its peak at 1642 cm^{-1}. All the other peaks below 1400 cm^{-1} are due to COO^- and other bending modes. From these observations, it is concluded that the acetic acid proton is not transformed $–COO^-$ group of L–arginine, but to its one of the deprotonated amino group. No change in

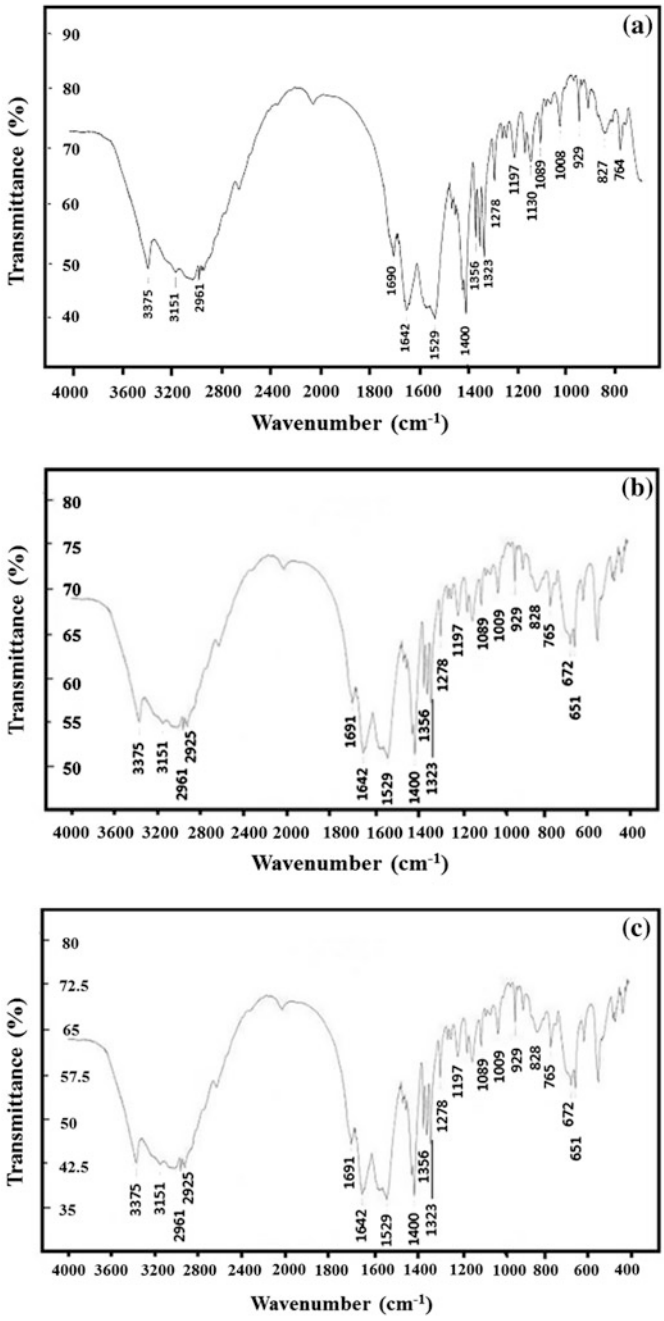

Fig. 3 FTIR spectrum of **a** pristine LAA **b** of 600 krad oxygen ions irradiated LAA, **c** 1 Mrad oxygen ions irradiated LAA

Table 2 Frequency assignments of pristine and irradiated LAA

Frequency (cm^{-1})			Assignments
Pristine	600 krad	1 Mrad	
2961	–	2961	Aliphatic C–H stretching mode
1690	–	1691	C=O stretching of COO^-
1642	1640	1642	Asymmetric NH bend of NH_3^+
1356	1356	1356	CH_3 bending
1323	1323	1323	Twisting of CH_2
1278	1277	1278	C=O stretching of carboxylic group
1197	1197	1197	COO^- vibrations
1130	1130	–	CH_3 symmetric bending
1089	1089	1089	C–CN stretching vibrations
1008	1010	1010	In plane CH_3 rocking
929	929	929	C–CH bending
827	–	828	Rocking of CH_2
764	764	764	Torsion of COO

the chemical nature was observed for low oxygen ion (600 krad) irradiation (Fig. 3.1 b) but for samples irradiated with 1 Mrad of oxygen ion, the absorption intensity of peaks decreased (Fig. 3.1c). It implies that increasing ion irradiation might supply energy to dislodge molecules in the lattice which in turn weakens inter molecular bonding.

3.3 UV-Visible–NIR Spectral Studies

Figure 4 shows the UV-Visible–NIR spectra of oxygen ions irradiated LAA crystals recorded in the wavelength range of 200 to 1200 nm using SHIMADZU (model-1601) UV-Visible-NIR spectrophotometer. The cutoff wavelength of LAA crystals irradiated with the dose rate of 600 krad and 1 Mrad is 207 and 223 nm, respectively. Figure 4 indicates that there is no significant absorption in the entire visible region. The cutoff wavelength of the pristine [14] and irradiated LAA crystals is below 300 nm and therefore the crystals may be useful for the SHG or other applications in the blue and violet region [16]. The decrease in transmittance may be due to the capture of excited electrons by existing ion vacancies and formation of additional defect centers [7]. The change in absorption could be attributed to the creation of some intermediate energy levels due to the structural rearrangements.

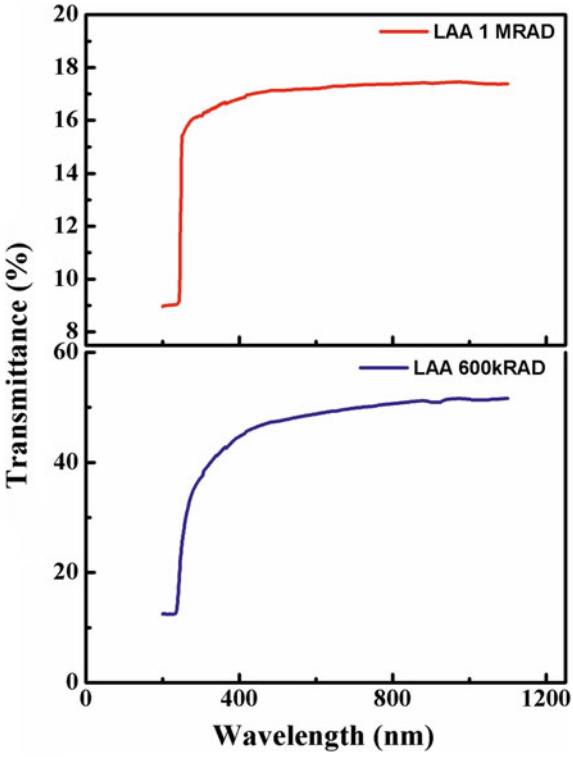

Fig. 4 UV-Visible-NIR Transmittance spectra of oxygen ions irradiated L-arginine acetate single crystals irradiated at the dose rate of 600 krad and 1 Mrad

3.4 Photoluminescence Studies

Photoluminescence (PL) spectroscopy is a contactless, nondestructive method of probing the electronic structure of materials. Figure 5 shows the PL spectra of pristine and oxygen ions irradiated LAA crystals recorded between 200 and 800 nm using a Perkin-Elmer spectrometer (model: LS-55) with the excitation wavelength of 350 nm. The PL emission peak is observed at 526 nm for all samples. The absorption leads to emission in the green region. From the spectra, it can be seen that no shift in the band position of pristine and irradiated samples that clears the existence of states remain unaffected by the irradiation. Further, it is observed that the intensity of the emission peak is high for pristine sample due to dominant radiative transition, whereas it decreases for ion irradiated samples. For higher fluence (1 Mrad), the emission is drastically reduced due to creation of more defects in the sample which may affect the radiative transitions which results in the decrease in intensity with increasing ion concentration [17].

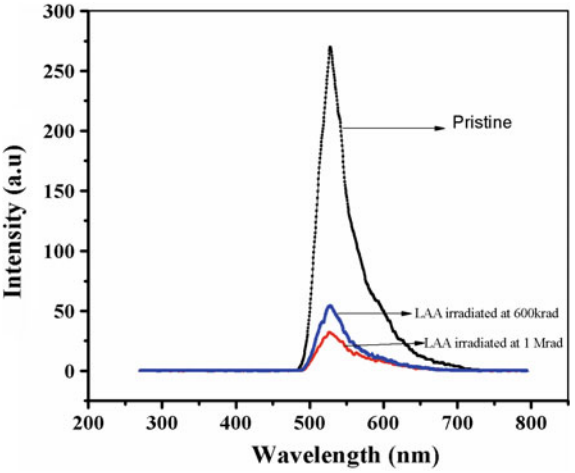

Fig. 5 Photoluminescence spectra of pristine and L-arginine acetate single crystals irradiated at 600 krad and 1 Mrad

4 Conclusion

In the present study, LAA single crystals were irradiated by Oxygen ions and the modifications in the structural and optical properties were studied. The decrease in diffraction intensities and peak broadness reveal the decrease in crystallinity of the irradiated crystal which was confirmed by FTIR studies. The optical transmittance decreases with increasing ion irradiation dose. The decrease in PL intensity with the increase of ion dose is due to radiative transition. Hence, oxygen ions irradiation modifies the structural and optical properties of LAA single crystals.

Acknowledgements Author NR is grateful to Mr. Joe Watkins, Programme Chair, Maths/Physics —Engineering Technology and Science, Abu Dhabi Men's College, Higher Colleges of Technology, UAE for his continuous support and encouragement.

References

1. Harris, L.B., Vella, G.J.: Direct current conduction in ammonium and potassium dihydrogen phosphate. J. Chem. Phys. **58**, 4550–4557 (1973)
2. Narasimha, B., Choudhary, R.N.P., Rao, K.V.: Dielectric properties of LaPO4 ceramics. J. Mater. Sci. **23**, 1416–1418 (1988)
3. Stoneham, A.M.: Energy transfer between electrons and ions in collision cascades in solids. Nucl. Instr. Meth. Phys. Res. B **48**, 389–398 (1990)
4. Kanjilal, D.: Swift heavy ion-induced modification and track formation in materials. Current Sci. **80**, 1560–1566 (2001)
5. Singh, J.P., Singh, R., Ghosh, S., Tripathi, A., Kabiraj, D., Gupta, S., Som, T., Kumar, R., Arora, S.K., Asokan, K., Avasthi, D.K., Kanjilal, D., Mishra, N. C., Mehta, G.K.: Swift heavy ion-based materials science research at NSC. Nucl. Instr. Meth. Phys. Res. B **156**, 206–211 (1999)

6. Kanagasekaran, T., Mythili, P., Kumar, B., Gopalakrishnan, R.: Effect of ion irradiation on the M-Nitroaniline single crystals. Nucl. Instr. Meth. B **268**, 36–41 (2010)
7. Kanagasekaran, T., Mythili, P., Srinivasan, P., Vijayan, N., Bhagavannarayana, G., Kulriya, P.K., Kanjilal, D., Gopalakrishnan, R., Ramasamy, P.: Effects of 50 MeV Si ion irradiation on nonlinear optical benzimidazole single crystals. Cryst. Res. Technol. **42**, 1376–1381 (2007)
8. Krishnakumar, V., Avasthi, D.K., Singh, F., Kulriya, P.K., Nagalakshmi, R.: Study of the damage produced in K[CS(NH2)2]4Br-A non-linear optical single crystal by swift heavy ion irradiation. Nucl. Instr. Meth. B **256**, 675–682 (2007)
9. Kanagasekaran, T., Mythili, P., Srinivasan, P., Vijayan, N., Gopalakrishnan, R., Ramasamy, P.: On the observation of physical, chemical, optical and thermal changes induced by 50 MeV silicon ion in benzimidazole single crystals. Mater. Res. Bull. **43**, 852–863 (2008)
10. Sreeramana Aithal, P., Nagaraja, H.S., Mohan Rao, P., Nampoori, V.P.N., Vallabhan, C.P.G., Avasthi, D.K.: Possibility of waveguide formation on organic nonlinear crystal methyl para-hydroxy benzoate using high energy ion irradiation. Nucl. Instr. Meth. Phys. B **129**, 217–220 (1997)
11. Aithal, P.S., Nagaraja, H.S., Rae, P.M., Nagarajaa, H., Rao, P.M., Avasthi, D., Sarma, A.: Effect of high energy ion irradiation on electrical and optical properties of organic nonlinear optical crystals. Mater. Chem. Phys. **54**, 991–994 (1997)
12. Dong, Y., Xu, J., Zhou, G., Liangbi, S., Xiaodong, H.L.J.: Gamma-ray induced color centers in Yb: YAG crystals grown by Czochralski method. Solid State Commun. **141**, 105–108 (2007)
13. Renuka, N., Vijayan, N., Rathi, B., Ramesh Babu, R., Nagarajan, K., Haranath, D., Bhagavannarayana, G.: Synthesis, growth and optical properties of semi organic nonlinear optical single crystal: l-Arginine acetate. Optik **123**, 189–192 (2012)
14. Muralidharan, R., Mohankumar, R., Jayavel, R., Ramasamy, P.: Growth and characterization of L-arginine acetate single crystals: A new NLO material. J. Cryst. Growth **259**, 321–325 (2003)
15. Fang, T.T., Chen, F.Y.: The defect structure, sintering behavior, and dielectric responses of Cr2O3-doped Sr0.5Ba0.5Nb2O6. J. Appl. Phys. **100**, 014110–014115 (2006)
16. Sethuraman, K., Ramesh Babu, R., Gopalakrishnan, R., Ramasamy, P.: Synthesis, growth, and characterization of a new semiorganic nonlinear optical crystal: l-Alanine Sodium Nitrate (LASN). Cryst. Growth Des. **8**,1863–1869 (2008)
17. Skuratov, V.A., Abu AlAzm, S.M., Altynov, V.A.: Luminescence of aggregate centers in lithium fluoride irradiated with high energy heavy ions. Nucl. Instr. Meth. Phys. B **191**, 758–766 (2002)

Growth and Characterization of Chloro Bis Thiourea Mercury (II) Chloride (CBTMC) Grown by Slow Evaporation Technique for Nonlinear Optical Applications

M. Peer Mohamed, S. Sudha, M. Nageshwari, P. Jayaprakash, P. Sangeetha, M. Prakash and M. Lydia Caroline

Abstract A noncentrosymmetric hard anisotropy crystals of Chloro bis thiourea mercury (II) chloride (CBTMC),[HgCl $[CS(NH_2)_2]_2Cl$], was synthesized using water as solvent and grown by slow solvent evaporation method and its properties are reported for the first time to attest its suitability in nonlinear optical applications. CBTMC single crystals possessing good morphology with size up to $0.6 \times 0.4 \times 0.2\ cm^3$ were collected from the crystallization vessels after 12 days. Crystallography structure diffraction analysis using X-radiation confirms the non-centrosymmetric (polar) space group P_{mmn}, which is the key requirement to exhibit nonlinear optical activity. The crystals are analyzed by powder X-ray diffraction (PXRD) to assess the good crystalline nature. The existence of various functional groups in the synthesized compound were manifested and examined by FTIR spectrum. The thermal analysis disclosed the maximum temperature of operation of 253 °C for CBTMC. The EDAX spectrum emphasized the presence of mercuric chloride in the metal complex. CBTMC crystal was subjected to SEM analysis and it divulged the surface topographies. The UV-Visible spectra revealed the absorption edge down to near UV absorption wavelength at 213 nm, which is a

M. Peer Mohamed · S. Sudha · M. Nageshwari · P. Jayaprakash · P. Sangeetha · M. Lydia Caroline (✉)
PG & Research Department of Physics, Arignar Anna Govt. Arts College, Cheyyar 604407, Tamil Nadu, India
e-mail: lydiacaroline2006@yahoo.co.in

M. Peer Mohamed
Department of Physics, C. Abdul Hakeem College, Melvisharam 632509, Tamil Nadu, India

M. Prakash
PG & Research Department of Physics, Urumu Dhanalakshmi College, Thiruchirappalli 620019, Tamil Nadu, India

J. Ebenezar (ed.), *Recent Trends in Materials Science and Applications*, Springer Proceedings in Physics 189, DOI 10.1007/978-3-319-44890-9_48

deciding property for SHG. From the UV absorption data optical direct band gap is assessed (E_g = 4.62 eV). The powder visible SHG response was judged by Kurtz-Perry method using a fundamental pulsed Nd: YAG laser radiation (λ = 1064 nm) and SHG efficiency was determined to be 0.736 times that of KDP, moreover KDP is phase-matchable.

1 Introduction

The nonlinear optical (NLO) crystals have attracted great interest due to its ability to transmit, process and store information in several fields like photochemistry, optical communication and solid state lasers [1–3]. The thermal and mechanical strength are a prerequisite for NLO crystals in many device applications. Usage of organic crystals in the field of optoelectronics has been hindered due to less transparency, inadequate optical quality and smaller magnitude of laser damage threshold. Inorganic crystals generate supporting mechanical and thermal stability but deficiency in Л-electron delocalization give rise to limited optical nonlinearities. In the event of device fabrication strenuous task is put on organometallic materials owing to their large polarization phenomena, greater resistance to laser damage threshold, less angular sensitivity and good hardness factor for the development in optoelectronic devices [4, 5]. Hence metal thiourea complexes, often named as semiorganics, constitute both crystalline organic and inorganic chromophores of the complex. During last decade, particular interest has been on the synthesis of metal-organic complex of thiourea since they could incorporate the large dipole moments and chemical flexibility of organics with the physical huskiness of inorganics [6, 7]. Among the few simple organic compound thiourea is said to possess high crystallographic symmetry that crystallizes in centrosymmetric (non-polar) rhombic system and as a food ligand [8]. The crystallography structure of thiourea retained the coplanarity of the C, N and S atoms in the molecule [9]. Thiourea evince its resonance structure which was examined systematically by previous workers [10] and exists in more than 700 structures capable of attaining large dipole moment [11] due to its interesting inorganic matrix modifier and also its ability to cover a large network of hydrogen bonds, unifies with complexes of transition metals to exhibit attracting NLO properties. Metals like zinc, cadmium, mercury with d^{10} configuration form stable compounds exhibiting large with SHG response due to breakage of inversion symmetry and transition in the structure of atoms and molecules and their interactions plays a prime goal in modern optical technology [12]. In general, crystals in the category $M[TU]_2[X]_2$, where M = Cd, Co, Hg, Pb, Ti or Zn, TU is thiourea and X is halogen, found to hold 2nd order non-zero NLO response. Complexes arising due to thiourea molecule linked to metal ion chain have been investigated and reported in literature [13–19]. The metal-organic complexes usually show modulation in optical nonlinearities due to large polarization effect with optical anisotropy represents versatile group of NLO crystals [20]. Moreover a large number of active NLO chromophores have been reported on

the development of coordination polymers and group II elements that transcend the use of Zn, Cd, Hg as the templating metal which frequently coordinated with sulphur containing ligand [21]. Combination of the precursors comprising of thiourea and mercury (II) chloride, with stoicheio-metries $HgCl_2$ $(tu)_n$ was elucidated by Aucke and Drago [22]. Also study on mercuric chlorides based materials have been reported in the literature [23–26] due to nonlinear polarization of the molecular materials in the development of optoelectronic devices. The three dimensional structure of Chloro bis thiourea mercury (II) chloride ($HgCl_2(tu)_2$) was solved and refined by Brotherton et al. [27]. In the area of optical and nonlinear optical properties attempts have been taken to grow metal ligand complex Chloro bis thiourea mercury (II) chloride (CBTMC) and discuss its thermal, linear and nonlinear optical properties which are indispensable to make it conceivable as a potential material and to exult in field of nonlinear optical applications.

2 Materials and Methods

2.1 Synthesis and Growth

In accordance to the reaction shown below,

$$\mathbf{HgCl_2 + 2\left[CS(NH_2)_2\right] \rightarrow HgCl\left[CS(NH_2)_2\right]_2Cl}$$

CBTMC was synthesized from the materials mercuric chloride and thiourea in the stoichiometric ratio 1:2 and each reactant dissolved separately in appropriate amounts of water in a glass beaker and stirred magnetically for about 45 min individually. Then these two solutions were mixed to obtain the CBTMC precursor solution and stirred continuously to avoid co-precipitation of different phases.

To get a homogenous clear solution, CBTMC precursor solution was heated to about 50 °C using hot plate unified with magnetic stirring for 6 h. The saturated solution is then filtered and kept undisturbed for slow evaporation to take place. Hard rectangular shaped good morphology single crystals of CBTMC were harvested in span of 12 days is shown in Fig. 1.

2.2 Analyses Techniques

The as-grown single crystals (CBTMC) have been exposed to various studies like single crystal X-ray diffraction, powder X-ray diffraction, Fourier transform infrared (FTIR), UV-Vis absorption studies, thermal analysis, SEM analyses and second harmonic generation test. Single crystal X-ray diffraction technique have been carried out using ENRAF NONIUS CAD4 diffractometer with MoKα (λ = 0.71073 Å) to identify the space group and the cell dimensions. The powder

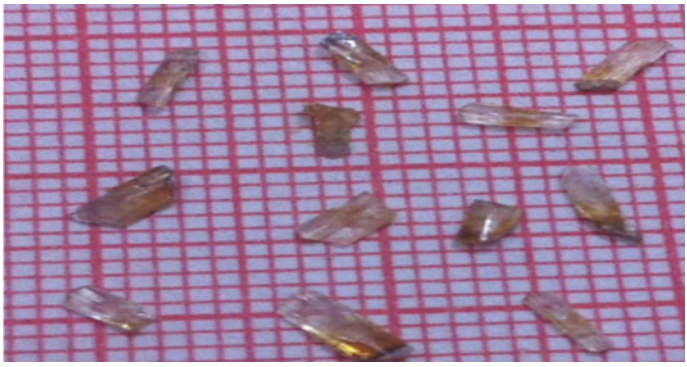

Fig. 1 Photograph of single crystals of CBTMC grown by slow evaporation technique

X-ray diffraction analysis (PXRD) was carried out at room temperature on a Xpert Pro diffractometer equipped with CuKα (λ = 1.54060 Å) radiation scanned over 10–70° at a scan rate of 0.02°/s to analyze the crystallinity. The UV-Vis spectrum was recorded at room temperature in the region 200–800 nm deploying a Shimadzu UV-1061 UV-Vis spectrometer. The ability of thiourea to complex with metal halide was confirmed by IR spectra recorded on a BRUKER 66V Fourier Transform IR (FT-IR) spectrometer in the range 4000–400 cm^{-1} using KBr pressed pellet. The TG/DTA and DSC analyses were performed using SDT Q600 V8.0 Build 95 in the range 27–900 °C with a heating rate of 27 °C min^{-1} in a nitrogen atmosphere. The SEM topographies of CBTMC sample with different magnifications and also EDAX profile was recorded using a computer controlled scanning electron microscope operated at 15 kV (DETECTOR type SUTW-SAPPHIRE analysis system of RESOLUTION 128.97 with HV 30.00 k). The SHG testing efficiency of CBTMC material was demonstrated using Kurtz powder method that utilizes Q-switched High Energy Nd: YAG (quanta ray model lab-170-10) with energy range 1.5–3 mJ with KDP as reference at 1064 nm.

3 Results and Discussion

3.1 Single Crystal X-ray Diffraction

The unit cell dimensions for CBTMC were elucidated by this crystallography structure study, the complex crystallizes, in the acentric space group P_{mmn} of orthorhombic system. The cell dimensions are a = 5.941 ± 0.010 Å, b = 6.459 ± 0.013 Å, c = 12.86 ± 0.02 Å and V = 496 $Å^3$. The unit cell parameters are consistent with the reported crystallographic structure data [27]. The experimental PXRD pattern for CBTMC is depicted in Fig. 2. The diffraction peaks were indexed using the 2θ software using the unit cell parameters acquired in the present. Well

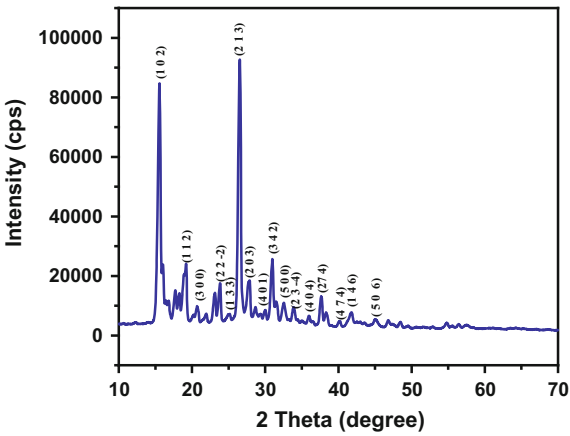

Fig. 2 Powder XRD pattern of CBTMC

outlined Bragg peaks are obtained at a precise 2θ angles showing narrow and intense peak along the Miller planes (102) and (213) planes suggest the crystalline nature of the as-grown crystal.

3.2 FTIR Spectral Analysis

The obtained FTIR profile of CBTMC crystal after being qualitatively analyzed at room temperature is shown in Fig. 3. The wavenumber corresponding to various modes of vibration noticed in this FTIR spectrum are given in the Table 1. Description on IR absorption reports of thiourea is well understood in the literature [28–31]. Comparison of IR spectra of CBTMC with those of IR spectra of thiourea

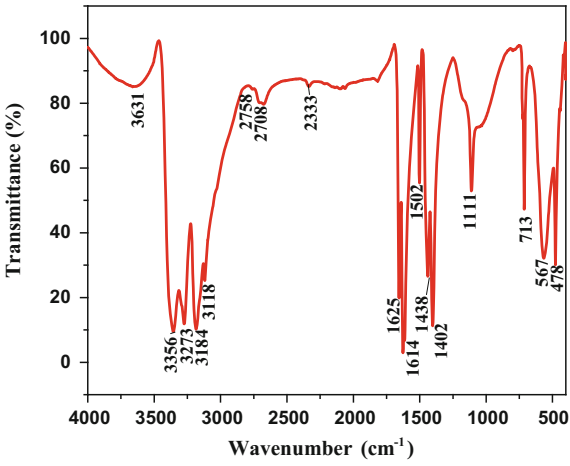

Fig. 3 FTIR spectra of CBTMC

Table 1 Comparison of IR bands of THIOUREA and CBTMC

Thiourea (cm^{-1})	CBTMC (cm^{-1})	Assignments
3376	3356	$-\upsilon_{as}$ (NH_2)
3280	3273	υ_s (NH_2)
3167	3184	δ (NH_2)
1627	1614, 1625	δ (NH_2)
1470	1502	υ_{as} (N–C–N)
–	1438	υ_{as} (C–N)
1417	1402	υ_{as} (C=S)
1089	1055, 1111	ρ (NH_2), υ_s (C–N)
740	713	υ (N–C–N)
494,464	567,478	δ (C–N)

υ stretching, ρ rocking, δ bending, υ_{as} asymmetric stretching, υ_s symmetric stretching

[32, 33], change in the position of peaks was observed. Possibly two prominent ways by which the linkage of mercury with covalent sulphur of thiourea can happen. It can project either through chain linkage of nitrogen or covalent sulfur of thiourea ligand. Majority of metals form complex with sulfur [29]. The characteristics of NH_2 asymmetric and symmetric stretching vibrations are represented by a few bands that appear in the region 3000–3500 cm^{-1}, and also is in accordance with other compounds containing thiourea reported [34]. The peaks observed between 1700 and 2700 cm^{-1} are attributed to overtones and combination vibration bands. We also attribute the wavenumbers corresponding to 1614 and 1625 cm^{-1} to NH_2 deformation. Also the strong IR vibration peak around 1502 cm^{-1} is an indicative of N–C–N stretching vibrations in as-grown CBTMC crystal. The band observed at 1402 cm^{-1} in the complex is attributed to C=S asymmetric stretching vibrations in regard to 1417 cm^{-1} band of thiourea [35]. The peak positioned at 1438 cm^{-1} is an indicative of C–N asymmetric stretching vibration. The increased frequencies for the band due to C–N symmetric and lowering of C–S stretching frequencies show the complex formation of metal ion [22]. The sharp and intense peak around 713 cm^{-1} in the finger print region corresponds to metal complex formation compared to 740 cm^{-1} peak of thiourea. C–N deformation vibration is positioned at 567 and 478 cm^{-1} respectively. By analyzing the shift in the peak positions at low frequencies, where the covalent sulfur-to-metal bond chain locates around 713 cm^{-1} in IR spectra of CBTMC is well established is also confirmed by Brotherton et al. [27].

3.3 Thermal Analysis

Both TG/DTA and DSC profiles of CBTMC are illustrated therein Figs. 4 and 5. The ceramic crucible was heated with the sample and the analysis was carried out in a nitrogen atmosphere at a heating rate of 27 °C min^{-1} in the temperature range 27–

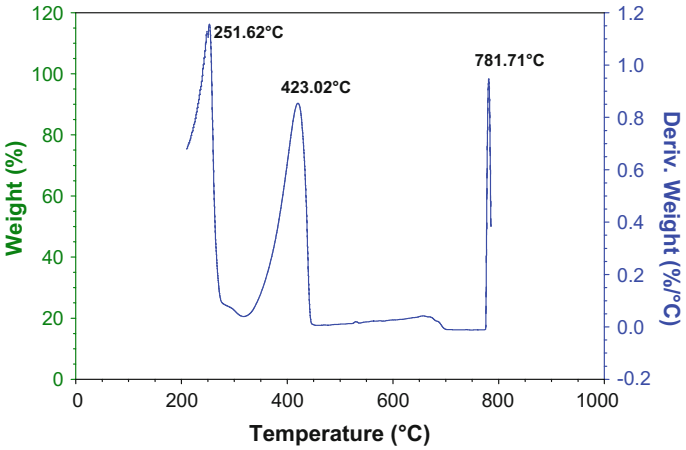

Fig. 4 TGA/DTA curves of CBTMC

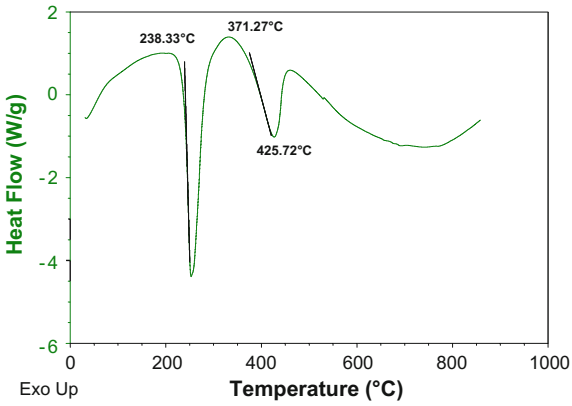

Fig. 5 DSC curve of CBTMC

900 °C. TG-DSC curves of CBTMC crystal reveal no representative weight loss in the measurement temperature up to 200 °C. Absence of weight loss observed below 200 °C concludes that the crystal structure is free of water molecule.

As shown in figure, the TGA response curves show a weight loss of about 29.42 % in the temperature range 240–262 °C. The first exothermic peak at 251.62 °C in the DTA profile may be due to the melting of the sample, which very well matches with a sharp decomposing endothermic peak in DSC trace (253 °C) seen in Fig. 5. Due to the reason that coordination bond energies of the metal (Hg) with surrounding ligands in the complexes are dominant than the organic π-bond system, rise in melting and chemical stability is observed [36]. The second stage of decomposition of about 47.60 % occurs between 387 and 435 °C. Hence almost there is total weight loss of 77.16 % and remaining goes to the formation of

residue (14.44 %), reached after heating above 780 °C. The Cl atoms completely disappeared almost above 750 °C and the residue is almost black, which may be due to some sulfide precipitate and remaining present in the CBTMC. We attribute the thermal stability of CBTMC that could be extended up to temperature of 251 °C in the field of nonlinear optical applications.

3.4 Compositional Analysis

The scanning electron microscopy (SEM) equipped with energy dispersive X-ray analysis (EDAX) was utilized to examine the elements present in CBTMC by choosing one of the as grown-crystal. The EDAX pattern of the CBTMC shown in Fig. 6 depicts all the prominent peaks for the elements composed in the grown crystal. From the SEM elemental mapping we could see the peaks attributed to Cl, S, Hg and O at different energies. X-ray spectroscopy is unable in predicting elements lighter than boron [37]. It is clear that H is not shown in the EDAX mapping.

3.5 SEM Analysis

Image acquisition by SEM analyses was done by tracing the surface of a good quality of the sample using electron dose and analyzed automatically and a software algorithm generated the patterns of the regions. The recorded SEM topography (Fig. 7a–c) at different magnifications confirmed the formation of the pits and insertion on the crystal surface, which may probe changes due to the thermal agitation during the spontaneous nucleation process. SEM images of CBTMC depict the existence of closely packed layers with some differences observed on the

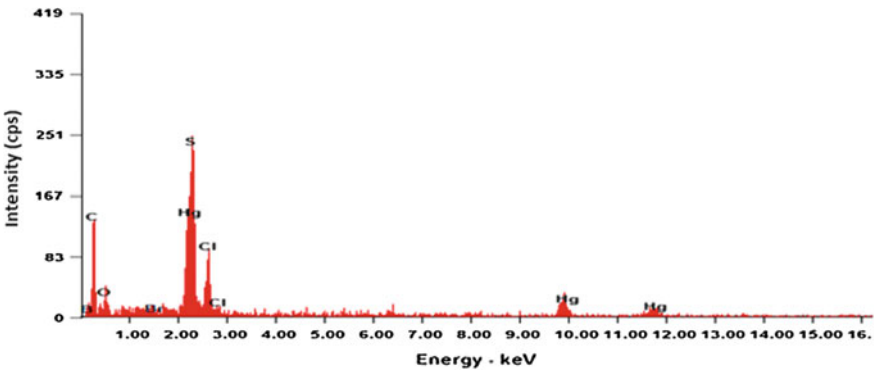

Fig. 6 EDAX spectrum of CBTMC

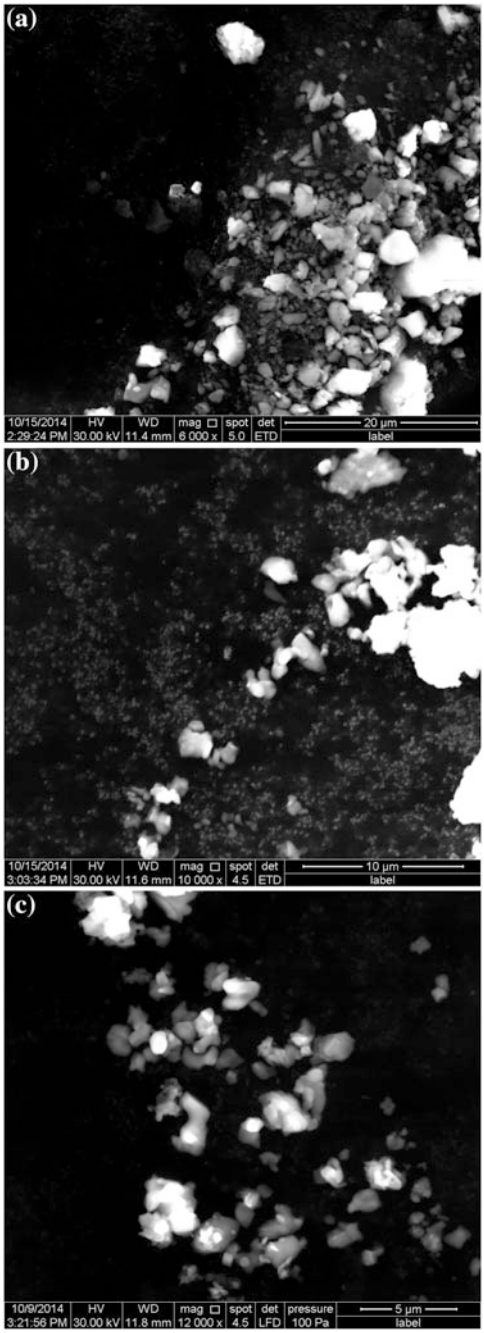

Fig. 7 The SEM images of CBTMC crystal at different resolution **a** 6000×, **b** 10,000×, and **c** 12,000×

surfaces between the various magnification levels. Also SEM topographies of CBTMC reveal square like pits formed during growth process (Fig. 7a, b) and flower like morphology (Fig. 7c) of the specimen observed, which could be due to the inclusion of metal halide in the thiourea also confirmed by EDAX analysis.

3.6 *Linear and Nonlinear Optical Studies*

The UV-Vis spectrum of CBTMC is shown in Fig. 8. The wide spectral transparency window and near UV cut-off wavelength are the most significant NLO parameters essential for the second harmonic laser radiation. The UV cut-off wavelength down to 213 nm is quite near to UV absorption edge is one of the key feature of this crystal to exhibit SHG efficiency [38]. The optical absorption is an effective requirement to understand the band gap of optical materials [39].

Electronic energy gap (E_g) which is the fundamental material parameter requiring control of light harvesting conversion process in laser applications, is worked out from the UV-Vis absorbance data and the optical absorption coefficient (α) near the UV absorption edge is deduced by the equation as below [40],

$$h\upsilon\alpha = A\left(h\upsilon - E_g\right)^{1/2}$$

where E_g denotes Electronic band gap of the crystal and A is a constant. Figure 9 shows the variation of $(\alpha h\gamma)^2$ with $h\gamma$ in the fundamental absorption region. The linear portion of the plot at the absorption edge arrives at a judgement that the crystal has a direct electronic band gap that can help to elucidate the mechanism of optical properties. The direct optical band gap of the crystal can be estimated by the extrapolated line with the photon energy axis (at $\alpha = 0$) of the linear part and found to be 4.62 eV [41]. It is understood that optical response of a crystal mainly originate from the electronic band transitions close to E_g placed between the top of the VB's and bottom of CB's which determines the magnitude of band gap. Also

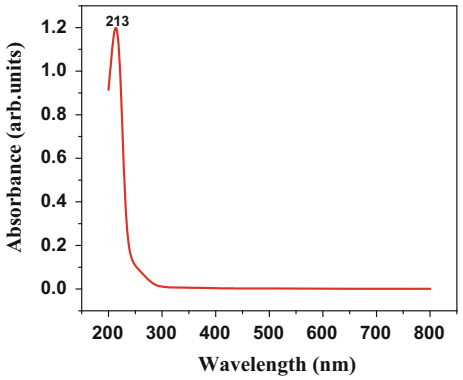

Fig. 8 UV-Vis absorbance spectrum of CBTMC

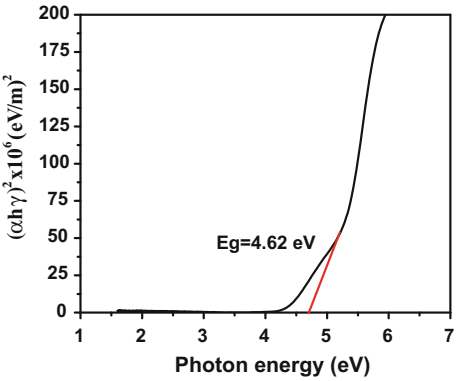

Fig. 9 Energy gap of CBTMC

larger the energy band gap arises due to the less deep UV-absorption edge bring about a wide transmission window in the visible region. Due to the dependence of electronic band on crystalline lattice, inclusion of defect in the lattice tries to decrease the electron band gap width. These defects could shift the centers of VB's and CB's as well as band widths, directing to the overall increase in the band gap. The wide direct energy gap of 4.62 eV calculated by us assures less defect and wide spectral transparency window in the visible region [42, 43] in making CBTMC suitable for photonic and optical applications [44].

To realize the second harmonic generation response of the CBTMC, powder SHG measurement was carried out by Kurtz-Perry method [45]. The measurement was performed with a laser at λ = 1064 nm (10 ns, 10 Hz) for visible SHG with beam energy 0.70 J/pulse. The strong second harmonic green light (λ = 532 nm), a frequency doubled (2ω) optical radiation generated in the visible region observed by naked eyes could also support phase-matchable behavior. The measured SHG efficiency of CBTMC was observed to be 0.736 times than that of KDP.

4 Conclusion

An efficient second harmonic generation thiourea metal-complex (CBTMC) was grown from the solvent of deionized water by solution growth process. Single crystal XRD analysis confirms the noncentrosymmetric acentric space group P_{mmn}, for the organometallic NLO crystal. The FT-IR spectrum confirms co-ordination of mercury (II) chloride with covalent sulfur ligands of thiourea. UV-Vis studies confirm that CBTMC is optically transparent with lower absorption edge at 213 nm. The energy band gap value investigated as a function of wavelength proves the presence of fewer imperfections in the crystal. The thermal studies reveal that the noncentrosymmetric structure is stable up to 253 °C. The SEM photographs exhibit the effectiveness of the metal halides in thiourea. The EDAX spectrum confirms the composition of elements in the metal chromophores. The experimental

verification by powder Kurtz-Perry method proves the existence of NLO response in CBTMC by the generation of green light (λ = 532 nm) due to frequency doubling the output of Nd: YAG 1064 nm laser radiation. Hence the unification of SHG response with good transparency in the visible region with large optical band gap proves CBTMC a promising envisioned candidate for frequency doubling into the UV visible that could open path in nonlinear optical applications.

Acknowledgements The authors (P.M and M.L) thank Sophisticated Analytical Instruments Facility, Indian Institute of Technology (IITM), Chennai, for providing the facilities for single crystal XRD analysis. The authors P.M and M.L are grateful to B.S. Abdur Rahman University, Chennai for SHG measurement.

References

1. Prasad, P.N., Williams, D.J.: Introduction to Nonlinear Optical Effects in Molecules and Polymers, p. 35. John Wiley & Sons Inc., New York (1991)
2. Razzetti, C., Ardoino, M., Zanotti, L., Zha, M., Paorici, C.: Solution growth and characterisation of L-alanine single crystals. Cryst. Res. Technol. **37**, 456–465 (2002)
3. Wong, M.S., Bosshard, C., Pan, F., Gunter, P.: Non-classical donar-acceptor chromophores for second nonlinear optics. Adv. Mater. **8**, 677–680 (1996)
4. Xing, G., Jiang, M., Shao, Z., Xu, D.: Bis(thiourea)cadmium chloride (BTCC) a novel nonlinear optical crystal of organometallic complex. Chin. J. Lasers **14**, 357–364 (1987)
5. Velsko, S.P.: Laser Program Annual Report Lawrence UCRL-JC 105000, vol. 152. Lawrence Livermore National Laboratory, Livermore, California (1990)
6. Newman, P.R., Warren, L.F., Cunningham. P., Chang, T.Y., Cooper, D.E., Burdge, G.L., Polok-Dingels, P., Lowe-Ma, C.K.: Semiorganics, a new class of NLO materials. In: Chiang, C.Y., Chaikan, P.M., Cowan, D. (eds.) Advanced Organic Solid State Materials. Materials Research Society Symposium Proceedings, vol. 173, pp. 557–561 (1990)
7. Venkataraman, V., Dhanraj, G., Wadhawan, V.K., Sherwood, J.N., Bhat, H.L.: Crystal growth and defects characterization of zinc tris (thiourea) sulfate: a novel metal organic nonlinear optical crystal. J. Crystal Growth **154**, 92 (1995)
8. El-Bahy, G.M.S., El-Sayed, B.A., Shabana, A.A.: Vibrational and electronic studies on some metal thiourea complexes. Vib. Spectrosc. **31**, 101–107 (2003)
9. Yamaguchi, A., Penland, R.B., Mizushima, S., Lane, T.J., Curran, C., Quagliano, J.V.: Infrared absorption spectra of inorganic coordination complexes. XIV. Infrared studies of some metal thiourea complexes. J. Am. Chem. Soc. **80**, 527–529 (1958)
10. Marcos, C., Alia, J.M., Adavasio, V., Prieto, M., Granda Garela, S.: Bis thiourea cadmium halides. Acta. Crystallogr. **C54**, 1225–1229 (1998)
11. Hellwege, K.H., Hellwege, A.M., Landolt-Bornstein, B.: Numerical Data and Functional Relationship in Science and Technology, vol. 14, p. 584. Springer, Berlin (1982)
12. Venkataramanan, V., Srinivasan, M.R., Bhat, H.L.: Vibrational spectroscopic study of zinc tris (thiourea) sulfate, a new organometallic nonlinear optical crystal. J. Raman Spectrosc. **25**, 805–811 (1994)
13. Hou, W.B., Xu, D., Yuan, D.R., Liu, M.G.: Investigations on triallylthiourea mercury bromide (ATMP) crystal-growth. Cryst. Res. Technol. **29**, 939–944 (1994)
14. Alia, J.M., Edwards, H.G.M., Stoev, M.D.: A systematic FT-Raman spectroscopic study of twelve bis-thiourea complexes, $A(tu)_2B_2$ (A = Zn, Cd, Hg; B = Cl, Br, I, SCN). Spectrochim. Acta. A **55**, 2423–2435 (1999)

15. Flint, C.D., Goodgame, M.: Infrared spectrum (400–135 cm^{-1}) of some thiourea co-ordination complexes. J. Chem. Soc. (A) 744–747 (1966)
16. Geetha Kumari, R., Ramakrishnan, V., Lydia Caroline, M., Kumar, J., Sarua, A., Kuball, M.: Raman spectral investigation of thiourea complexes. Spectrochim. Acta. A, **73**, 263–267 (2009)
17. Duo-Rong, Y., Nan, Z., Xu-Tang, T., Dong, X., Min-Hua, J., Zong-Shu, S.: Study on crystal growth and properties of a new highly efficient NLO material-organometallic complex tri-allylthiourea mercuric chloride (ATMC). Chin. Sci. Bull. **36**, 1401–1404 (1991)
18. Lydia Caroline, M., Vasudevan, S.: Growth and characterization of bis thiourea cadmium iodide: a semiorganic single crystal. Mater. Chem. Phys. **113**, 67–674 (2009)
19. Mani, G., Kumaresan, S., Lydia Caroline, M., Usha, S.: Synthesis, structural, optical, thermal and dielectric aspects of a semiorganic nonlinear optical crystal by solution growth technique. Optoelectr. Adv. Mater. Rapid Commun. **8**(5–6), 399–405 (2014)
20. Ravindran, B., Madhurambal, G., Mariappan, M., Mojumdar, S.C.: Synthesis and characterization of some crystals of thiourea urea zinc chloride. J. Therm. Anal. Calorim. **104**, 893–899 (2011)
21. Shannon, Ian J.: Zinc, cadmium, mercury. Ann. Rep. Prog. Chem. Sect. A **100**, 141–150 (2004)
22. Aucken, I., Drago, R.S.: Mercury (II) chloride thiourea complexes. In: Rochow, E.G. (ed.) Inorganic Syntheses, vol. 6. John Wiley & Sons Inc, Hoboken, NJ, USA (1960)
23. Marcotrigiano, G.O., Peyronel, G., Battistuzzi, R.: On the thiourea complexes od Mercury(II). Inorg. Chem. Acta. **9**, 5–8 (1974)
24. Shan, Z.-M., Wang, Y.-L., Guo, H.-X., Liu, Q.-A., Zhang, N., Yang, E.-L., Li, L.-Q.: Synthesis, crystal structures, and characterizations of three mercury (II) halides inorganic-organic hybrids with 1,4-diazabicyclo[2.2.2]octane ligand. Inorg. Chem. Acta **366**, 141–146 (2011)
25. Gunasekaran, S., Anand, G., Arun Balaji, R., Dhanalakshmi, R., Kumaresan, S.: Crystal growth and comparison of vibrational and thermal properties of semi-organic nonlinear optical materials. Pramana J. Phys. **75**, 683–690 (2010)
26. Kalaiselvi, D., Jayavel, R.: Synthesis, growth and characterization of L-proline dimercuric chloride single crystals for frequency conversion applications. Appl. Phys. A **107**, 93–100 (2012)
27. Brotherton, P.D., Healy, P.C., Raston, C.L., White, A.H.: Crystal structure of chlorobis (thiourea) mercury (II) chloride. J. Chem. Soc., Dalton. Trans. 334–336(1973)
28. Venkataramanan, V., Bhat, H.L., Srinivasan, M.R., Ayyu, P., Multani, A.M.S.: Vibrational spectroscopic study of the semiorganic nonlinear optical crystal bis (thiourea) cadmium chloride. Raman Spectrosc. **28**, 779–784 (1997)
29. Oussaid, M., Becker, P., Carabatosnedelec, C.: Raman and infra-red spectra bis (thiourea) zinc chloride $Zn[CS(NH_2)_2]_2Cl^{-2}$ single crystal. Phys. Status Solidi B **207**(2), 499–505 (1998)
30. Kuncher, N.R., Mary Trutter, M.: The crystal structure of dichloro bis thiourea zinc. J. Chem. Soc. 3478–3484 (1958)
31. Srinivasan, K., Gunasekaran, S., Krishnan, S.: Spectroscopic investigations and structural confirmation studies on thiourea. Spectrochim. Acta A **75**, 1171–1175 (2010)
32. Ushasree, P.M., Jayavel, R., Subramanian, C., Ramasamy, P.: Growth of zinc thiourea sulfate (ZTS) single crystals: a potential semiorganic material. J. Cryst. Growth **197**, 216–220 (1999)
33. Swaminathan, K., Irving, H.M.N.H.: Infra-red absorption spectra of complexes of thiourea. J. Inorg. Nucl. Chem. **26**, 1291–1294 (1964)
34. Sankar, R., Raghavan, C.M., Jayavel, R.: Bulk growth and characterization of semi-organic nonlinear optical bis thiourea bismuth chloride single crystals. Cryst. Growth Des. **7**, 501–505 (2007)
35. Sabari Girisun, T.C., Dhanuskodi, S., Mangalraj, D., Phillip, J.: Synthesis growth and characterization of bis thiourea zinc bromide for optical limiting applications. Curr. App. Phys. **11**, 838–843 (2011)

36. Ramachandraraja, C., Sundararajan, R.S.: Growth, characterization, vibrational spectroscopic and thermal studies of a new metallorganic nonlinear optical crystal bis thiourea cadmium bromide. Spectrochem. Acta. Part A **71**, 1286–1289 (2008)
37. Piburn, G., Barron, A.R.: Introduction to energy dispersive X-ray spectroscopy, (EDS). http://micron.ucr.edu/public/manuals/EDS-intro.pdf
38. Dmitriev, V.G., Gurzadyan, G.G., Nikoyosyan, D.N.: Hand Book of Nonlinear Optical Crystals, 3rd edn. Springer, Berlin (1999)
39. Yakuphanoglu, F., Arslan, M.: The fundamental absorption edge and optical constants of charge transfer compounds. Opt. Mater. **27**, 29–37 (2004)
40. Ashour, A., El-Kadry, N., Mahmoud, S.A.: On the electrical and optical properties of CdS films thermally by modified source. Thin Solid Films **269**, 117–120 (1995)
41. Tauc, J., Grigorovici, R., Vancu, A.: Optical properties and electronic structure of amorphous germanium. Phys. Status Solidi B **15**, 627–637 (1966)
42. Eya, D.D.O., Ekpunobi, A.J., Okeke, C.E.: Influence of thermal annealing on the optical properties of tin oxide thin films prepared by chemical bath deposition technique. Acad. Open Internet J. **17**, 1311–4360 (2006)
43. Chawla, A.K., Kaur, D., Chandra, R.: Structural and optical characterization of ZnO nano crystalline films deposited by sputtering. Opt. Mater. **29**, 995–998 (2007)
44. Rao, K.V., Smakula, A.: Temperature dependence of dielectric constant of alkali and thallium halide crystals. J. Appl. Phys. **36**, 3953–3954 (1965)
45. Kurtz, S.K., Perry, T.T.: A powder technique for evaluation of nonlinear optical materials. J. Appl. Phys. **39**, 3798–3813 (1968)

Crystal Structure of E-methyl-2-(1,3-Dimethyl-2,6-Diphenylpiperidin-4-Ylidene) Hydrazinecarboxylate Compound

T. Mohandas, P. Sakthivel, C. Udhayakumar, B. Arul Prakasam and Ray J. Butcher

Abstract The title compound crystallizes with three molecules and this compound. The structure was solved by SHELXS and it was refined by SHELXL. This compound adopts triclinic crystal systems with the space group P-1. The two phenyl rings are attached with the centre piperidine ring on each side and the methyl 2-methylene hydrazinecarboxylate system is connected to top of the piperidine ring. In each molecule the piperidine ring exhibits the chair conformations with the corresponding puckering parameters. The final R indices of this structure is 0.061. The bond lengths, torsion angles are calculated and it was tabulated. The molecules are linked by N–H…O interactions and this interactions makes the graph set motif of $R^4_4(8)$. In this structure the C–H…O interactions are also found.

1 Introduction

Bioactive heterocyclic ring systems are used in the past and recent years due to their wide variety of biological properties [1] such as antitumor [2], anti-inflammatory [3], central nervous system [4] anticancer [5] and antimicrobial activity [6]. Piperidone is a promising candidate for the synthesis of various heterocycles and biologically active compounds. 2,6-Diarylpiperidin-4-ones are interesting intermediates [7] in most of the synthesis. Because of the known therapeutic properties of piperidones due to the presence of a keto function that facilitates the introduction

T. Mohandas (✉)
Department of Physics, Shri Angalamman College of Engineering and Technology, Trichy 621105, India

P. Sakthivel
Department of Physics, Urumu Dhanalakshmi College, Tirchy 620019, India
e-mail: sakthiphy13@gmail.com

C. Udhayakumar · B. Arul Prakasam
Department of Chemistry, Annamalai University, Chidambaram, India

R.J. Butcher
Inorganic & Structural Chemistry, Howard University, Washington, USA

J. Ebenezar (ed.), *Recent Trends in Materials Science and Applications*,
Springer Proceedings in Physics 189, DOI 10.1007/978-3-319-44890-9_49

Fig. 1 Molecular structure

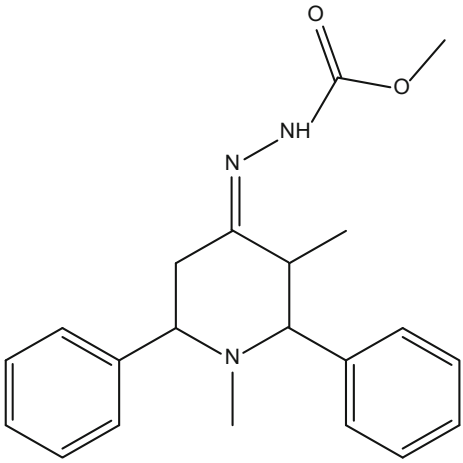

of other new substituents on the piperidine ring, they are widely used in the synthesis of new molecules. Due to this reason the title compound was synthesized and the XRD data was collected using X-ray diffractometer.

2 Materials and Method

1,3-dimethyl-2,6-diphenylpiperidin-4-one (1 m mol) and a few drops of glacial acetic acid were stirred in absolute ethanol for 15 min in ice cold condition. Then, methyl carbazate (1 m mol) was added and stirred for an additional 45 min. After completion of the reaction, addition of water (50 mL), resulted the precipitate which was collected by filtration and washed with a large portion of cold water. The crude product thus collected was recrystallized from ethanol. The title compound was grown by slow evaporation technique. Figure 1 Shows the molecular structure of the title compound.

3 Refinement

The crystal structure was determined by using SHELXL [8–10] and the ORTEP [11], PACKING diagrams are drawn by using PLATON. Figure 2 shows the ORTEP diagram of the title compound and Fig. 3 shows the PACKING diagram of the title compound.

Reflections were merged by SHELXL according to the crystal class for the calculation of statistics and refinement. Reflections Friedel fraction is defined as the number of unique Friedel pairs measured divided by the number that would be possible theoretically, ignoring centric projections and systematic absences.

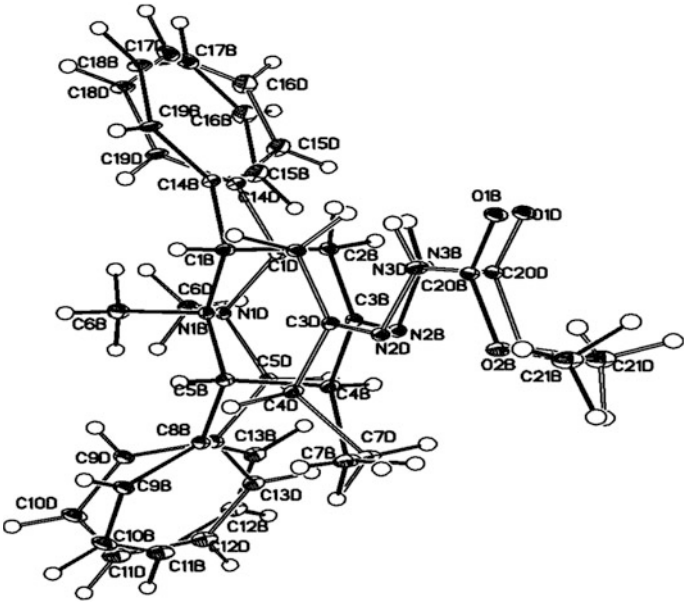

Fig. 2 Ortep diagram of the compound

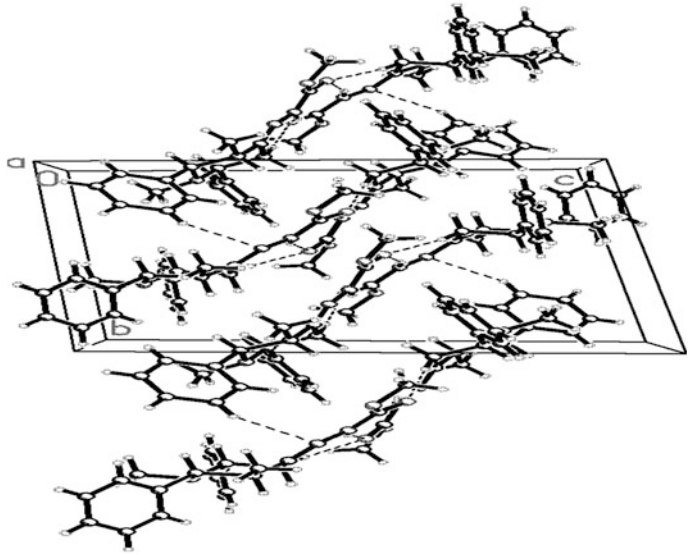

Fig. 3 Packing diagram of the compound

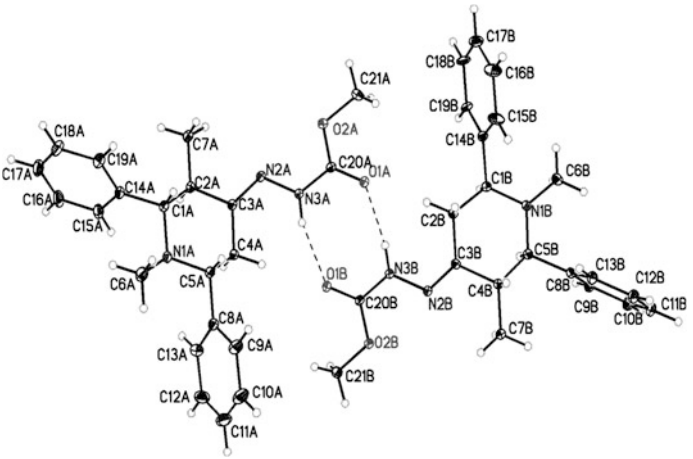

Fig. 4 Graphset diagram of the molecule

The positions of the hydrogen atoms bound to the O and C atoms are identified from the difference electron density maps and their distances are geometrically optimized. $U_{iso}(H) = 1.5$ Ueq(O). The hydrogen atoms bound to the C atoms are treated as riding atoms, with d(C–H) = 0.93 and $U_{iso}(H) = 1.2$ Ueq(C) for aromatic, d(C–H) = 0.97 and $U_{iso}(H) = 1.2$Ueq(C) for methylene and d(C–H) = 0.96 and $U_{iso}(H) = 1.5$ Ueq(C) for methyl groups.

4 Result and Discussion

The title compound, crystallizes with three molecules, A, B and D in the asymmetric unit. This crystal adopts triclinic system with P-1 space group. The complete crystal data are given in Table 1. In each molecule the piperidine ring exists in a chair conformation with the puckering parameters [12] Q = 0.563(3) Å, theta = 176.0(3)° and phi = 93.3(3)° in A, Q = 0.503(7) Å, theta = 175.8(8)° and phi = 110(13)° in B and Q = 0.445(15) Å, theta = 24(2)° and phi = 16(4)° in D. The Dihedral angle between Centre piperidine ring (N1A, C1A-C5A) to the center of the phenyl rings (C8A-C13A) and (C14A-C19A) are 84.48(15)° and 83.91(16)° respectively. The Dihedral angle between Centre piperidine ring (N1B, C1B-C5B) to the center of the phenyl rings (C8B-C13B) and (C14B-C19B) are 85.5(3)° and 83.0(3)° respectively. The dihedral angle between the phenyl rings is 52.37(19)° in molecule A, 56.9(3)° in molecule B and 56.4(5)° in molecule D. A+B inversion dimers linked by N–H…O hydrogen bonds (Table 4) are formed, which both generate $R^4_4(8)$ loops (Fig. 4). The bond distances and bond angles (Tables 2 and 3) in the title compound agree very well with the corresponding values reported in closely related compound [13, 14].

Table 1 Crystal data

Crystal data	
Chemical formula	$C_{21}H_{25}N_3O_2$
Molecular weight	351.4
Crystal system	Triclinic
Space group	P-1
Unit cell dimensions (Å, °)	a = 11.9266 (6), b = 12.1923 (6), c = 15.4573(8)
	α = 78.767(2), β = 81.741(2), γ = 61.406(2)
Volume (Å3)	1932.42(17)
No. of molecules in unit cell (Z)	4
F(000)	751.9
Crystal density	1.21 Mg m^{-3}
Radiation (λ in Å)	MoKα (0.71073)
Temperature	295(2) K
Absorption coefficient (μ mm^{-1})	0.079
Crystal size (mm)	0.28 × 0.21 × 0.15
'θ' range (°)	2.181–26.061
Data collection	
Diffractometer used	Bruker Kappa APEXII diffractometer
Radiation source	Rotating anode graphite monochromator
Scan	ω and φ scan
Absorption correction	Multi-scan
$T_{min,}$ T_{max}	0.994, 0.999
Reflection measured	48,924
Reflection observed	7640
Unique reflections with $I > 2\sigma(I)$	4748
R_{int}	0.033
θ_{max} = 26.1°	θ_{min} = 1.9°
Reflection h, k, l	
$h_{min} \leq h \leq h_{max}$	$-14 \leq h \leq 14$
$k_{min} \leq k \leq k_{max}$	$-15 \leq k \leq 15$
$l_{min} \leq l \leq l_{max}$	$-19 \leq l \leq 19$
Refinement	
Refinement method	F^2
Least square matrix	Full
R[*F*2 > 2σ(*F*2)]	0.061
WR2(for unique reflections)	0.142
Goodness of fit (S)	1.052
No. of parameters refined	515
Final R indices	0.061
Residual electron density	
_ρmax (e Å-3)	0.264
_ρmin (e Å-3)	−0.241

Table 2 Bond length

Atoms	Bond lengths (Å)	Atoms	Bond lengths (Å)
O1B–C20B	1.212(16)	O2B–C20B	1.33(2)
O2B–C21B	1.431(19)	N1B–C1B	1.437(11)
N1B–C5B	1.456(11)	N1B–C6B	1.424(11)
N2B–N3B	1.38(4)	N2B–C3B	1.265(15)
N3B–C20B	1.35(4)	C1B–C2B	1.529(8)
C1B–C14B	1.509(7)	C2B–C3B	1.498(12)
C3B–C4B	1.502(10)	C4B–C5B	1.527(7)
C4B–C7B	1.53(2)	C5B–C8B	1.510(7)
C8B–C9B	1.3904	C8B–C13B	1.3898
C9B–C10B	1.3901	C10B–C11B	1.3906
C11B–C12B	1.3898	C12B–C13B	1.3901
C14B–C15B	1.3899	C14B–C19B	1.3896
C15B–C16B	1.3895	C16B–C17B	1.3907
C17B–C18B	1.3899	C18B–C19B	1.3905

Table 3 Torsional angles

Atoms	Torsion angles (°)
C(3A)-N(2A)-N(3A)-C(20A)	−178.0(2)
C(5A)-N(1A)-C(1A)-C(14A)	178.9(2)
C(6A)-N(1A)-C(1A)-C(14A)	−60.0(3)
C(5A)-N(1A)-C(1A)-C(2A)	55.5(3)
C(6A)-N(1A)-C(1A)-C(2A)	176.6(2)
N(1A)-C(1A)-C(2A)-C(3A)	−51.3(3)
C(14A)-C(1A)-C(2A)-C(3A)	−174.1(2)
N(1A)-C(1A)-C(2A)-C(7A)	−178.2(2)
C(14A)-C(1A)-C(2A)-C(7A)	59.0(3)
N(3A)-N(2A)-C(3A)-C(4A)	3.2(4)
N(3A)-N(2A)-C(3A)-C(2A)	178.7(2)
C(7A)-C(2A)-C(3A)-N(2A)	2.9(4)
C(1A)-C(2A)-C(3A)-N(2A)	−122.8(3)
C(7A)-C(2A)-C(3A)-C(4A)	179.1(2)
C(1A)-C(2A)-C(3A)-C(4A)	53.3(3)
N(2A)-C(3A)-C(4A)-C(5A)	117.8(3)
C(2A)-C(3A)-C(4A)-C(5A)	−57.8(3)
C(6A)-N(1A)-C(5A)-C(8A)	58.9(3)
C(1A)-N(1A)-C(5A)-C(8A)	179.7(2)
C(6A)-N(1A)-C(5A)-C(4A)	−179.2(2)
C(1A)-N(1A)-C(5A)-C(4A)	−58.5(3)

Table 4 Hydrogen bond geometry

D	H	A	D-H	H-A	D-A	D-H..A
N3A	H3AA	O1B	0.86	2.10	2.932	163
N3A	H3AA	O1D	0.86	2.07	2.908	164
C4A	H4AA	O1B	0.97	2.32	3.278	171
C4A	H4AA	O1D	0.97	2.24	3.209	178
N3B	H3BA	O1A	0.86	2.07	2.882	156
C2B	H2BB	O1A	0.97	2.36	3.331	175
C21B	H21D	O2B	0.96	2.57	3.31	134
N3D	H3DA	O1A	0.86	2.04	2.88	164
C2D	H2DA	O1A	0.97	2.49	3.182	128

Symmetry code: 2-x,1-y,1-z

5 Conclusion

Thus, from the reflections of the type hkl, there is no systematic absence. This indicates that the cell is triclinic. The E-statistics analysis of the data reveals centrosymmetric distribution and hence the space group P-1 has been assigned. The piperidine ring exists a chair conformation according to Cremer and Pople. The inversion dimers linked the molecules by N-H…O interaction and makes the graph set motif of $R^4_4(8)$.

References

1. Weintraub, P.M., Sabol, J.S., Kane, J.M., Borcherding, D.R.: Tetrahedron **59**, 2953–2989 (2003)
2. Arutyunyan, G.L., Chachoyan, A.A., Shkulev, V.A., Adamyan, G.G., Agadzhanyan, T.E., Garibdzhanyan, B.T.: Khim. Farm. Zh **29**, 33–35 (1995)
3. Jobin, C., Bradham, C.A., Russo, M.P., Juma, B., Narula, A.S., Brenner, D.A., Sartor, R.B.: J. Immunol. **163**, 3474–3483 (1999)
4. Ganellin, C.R., Spickett, R.G.: J. Med. Chem. **8**, 619–625 (1965)
5. Ileana, B., Dobre, V., Niculescu-Duvaz, I.: J. Prakt. Chem. **327**, 667–674 (1985)
6. Kumar, S., Narain, U., Tripathi, S., Misra, K.: Bioconjugate Chem. **12**, 464–469 (2001)
7. Rani, M., Ramachandran, R., Kabilan, S.: Bioorg. Med. Chem. Lett. **20**, 6637–6643 (2010)
8. Bruker A.X.S.: APEX2, SAINT and SADABS. Bruker AXS Inc., Madison, Wisconsin, USA (2008)
9. Farrugia, L.J.: J. Appl. Cryst. **45**, 849–854 (2012)
10. Sheldrick, G.M.: Acta Cryst. A. **64**, 112–122 (2008)
11. Spek, A.L.: Acta Cryst. D. **65**, 148–155 (2009)
12. Cremer, D., Pople, J.A.: J. Am. Chem. Soc. **97**, 1354–1358 (1975)
13. Park, D.H., Ramkumar, V., Parthiban, P.: Acta Cryst E. **68**, 0524 (2012)
14. Park, D.H., Ramkumar, V., Parthiban, P.: Acta Cryst. E. **68**, 0525 (2012)

Crystal Structure of 4-Ethoxyanilinium Hydrogen Succinate

K. Saminathan, R. Jagan, K. Sivakumar and K. Saravanan

Abstract The compound 4-ethoxyanilinium hydrogen succinate crystallizes in $P2_1/c$ space group with four and half molecules in the asymmetric unit. The molecular arrangement of anions and cations form three dimensional network by N-H…O and O-H…O hydrogen bonds. It is observed the presence of molecular functionalities in the cation can alter the nature of the supramolecular network in the crystalline solid. This helps in the design of the preferred molecular assembly in crystal structures. In the compound presented in the report were prepared by taking suitable proportions of acids and bases and crystallized by slow evaporation method using methanol solvents and their structures were solved by direct methods and refined using full-matrix least squares technique using SHELX 97 program package.

1 Introduction

Carboxylic acids both aliphatic and aromatic establish in crystal engineering in organic frameworks to form fascinating architectures because of its excellent bridging capability with various complementary functional groups ranges from one-, two-, and three- dimensional networks [1]. The basic motifs which carboxylic groups

K. Saminathan (✉)
Department of Physics, University V.O.C College of Engineering, Anna University, Thoothukudi Campus, Thoothukudi 628008, Tamil Nadu, India
e-mail: ksaminathan2002@yahoo.com

R. Jagan
Department of Chemistry, Indian Institute of Technology Madras, Chennai 600036, India

K. Sivakumar
Department of Physics, Anna University, Chennai 600025, India

K. Saravanan
Department of Ophthalmology, West Virginia University Eye Institute, Morgantown, WV, USA

J. Ebenezar (ed.), *Recent Trends in Materials Science and Applications*, Springer Proceedings in Physics 189, DOI 10.1007/978-3-319-44890-9_50

adopt with complementary functional groups are linear dimers (D), catemers of linear chains (C) or rings (R) [2]. The CSD studies reveal that the interaction of dicarboxylic acids with amines (complementary functional groups) forms supramolecular heterosynthons more prevalently than supramolecular homosynthons. Aliphatic dicarboxylic acids prefers to crystallize in the extended trans conformation, there by forming infinite linear or nonlinear tapes or chains due to head to tail hydrogen bonding between adjacent molecules. Succinic acid, compound was widely used as the coformer of Active Pharmaceutical Ingredients (APIs) to form co-crystals with drug molecules [3]. Succinic acid being a versatile acid builds diverse topologies with amines through hydrogen bonding interactions both by means of protonation [4]. Succinic acid when forms adducts with suitable base exhibit various form. From the previously reported records of succinic acid adducts [5] shows the formation different acid-base combinations like, (i) Succinate, (ii) Hydrogen succinate, (iii) Succinic acid co-crystal and (iv) Succinate/succinic acid show interesting supramolecular importance. Para substituted anilines readily form salts and adduct with various acids have been studied and reported [6]. 4-ethoxyaniline is a brownish organic liquid used in the synthesis of phenacetine, dyes and other compounds. It is used to synthesize certain Schiff base related compounds. It is also used in the preparation of complexes, having various biological applications. Anti-inflamatory and antiulcer activity of the Schiff base derived from para-substituted anilines have been reported by researchers [7]. Here we report the crystal structure and hydrogen bonded networks of 4-ethoxyanilinium hydrogen succinate (I).

2 Experimental Methods

Compound (I) was prepared by mixing hot methanolic solution of succinic acid (0.118 g, 1 mM) with hot methanolic solution of 4-ethoxyaniline (0.130 ml, 1 mM) in 1:1 ratio. The mixture was heated and stirred at 40 °C in water bath for about 20 min. The resultant mixture was then allowed to cool to room temperature and left for slow evaporation. The chemical diagram of (I) is shown in Fig. 1.

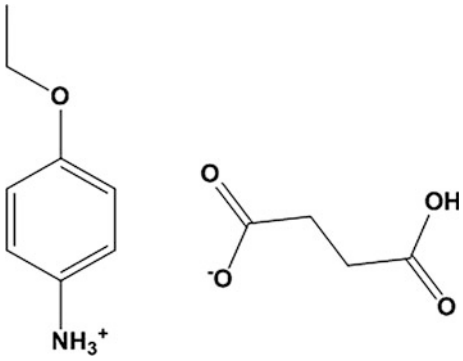

Fig. 1 Chemical diagram of 4-ethoxyanilinium hydrogensuccinate (4EAHS)

2.1 Intensity Data Collection and Refinement

X-ray diffraction data for the crystal (I) were collected using a Bruker AXS Kappa APEX II four circle single crystal CCD diffractometer equipped with graphite-monochromated MoKα (λ = 0.7107 Å) radiation. The crystal of sizes 0.30 × 0.25 × 0.25 mm^3 (I), was cut and mounted on a glass fiber using cyanoacrylate. The unit cell parameters were determined by collecting the diffracted intensities from 36 frames measured in three different crystallographic zones and using the method of difference vectors, data collection was carried out at 293 K using ω-φ scan modes. A total of 37,250 reflections were collected, resulting in 7079 independent reflections with R_{int} = 0.0373 and R_{sigma} = 0.030 respectively. Of the independent reflections, 5741 had I > 2σ (I) were considered as observed. The intensities were corrected for Lorentz and polarization effects followed by multi-scan absorption correction [8]. The molecular structure of was solved by direct methods procedure as implemented in SHELXS-97 [9]. The positions of all the non-hydrogen atoms were included in the full-matrix least squares refinement using SHELXL97 program [9]. Initially isotropic refinements of non-hydrogen atoms were carried out followed by full-matrix least squares refinement with anisotropic thermal parameters for non-hydrogen atoms. The positions of all the hydrogen atoms were identified from difference electron density peaks, and they were constrained to ride on the corresponding non-hydrogen atoms. The hydrogen atom bound to carbon atoms are constrained to a distance of C-H = 0.93−0.97 Å and U_{iso}(H) = 1.2U_{eq}(C) and 1.5U_{eq}(C). The hydrogen atom associated with the carboxyl group was identified from the difference electron density map and was allowed to ride over the parent O atom with best staggered position. The hydrogen atoms bound to the N atom were identified from the difference electron density map

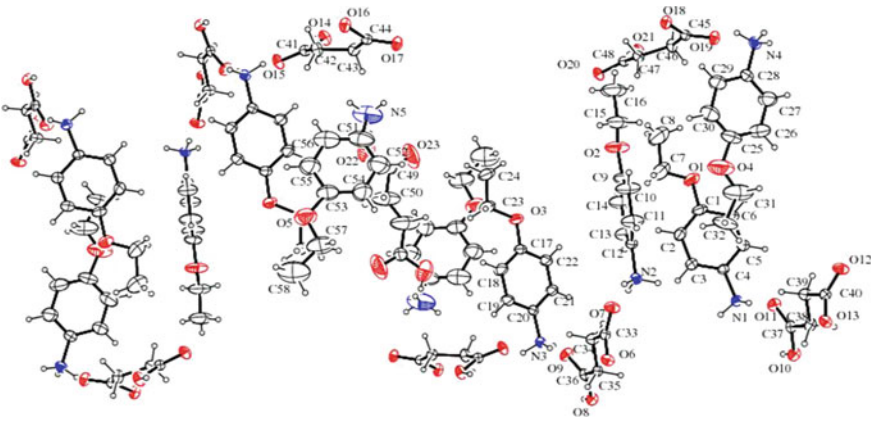

Fig. 2 Displacement ellipsoid plot of (4EAHS) is drawn at 40 % probability level. The ORTEP diagram shows nine sets of anions and cations generated by the symmetry operation −x, −y + 1, −z and −x + 1, −y + 1, −z

and were constrained to a distance of 0.89 Å with $U_{iso}(H) = 1.5U_{eq}(N)$. The final refinement converged to an R-value of R = 0.069 and *w*R = 0.209. The molecular structure of 4EAHS is shown in Fig. 2.

3 Result and Discussion

The asymmetric unit comprises four and half sets of 4-ethoxyanilinium cation and hydrogen succinate anion. The special position anion and cation occupy the crystallographic inversion centre at (0, 1/2, 0) and (1/2, 1/2, 0) of the unit cell. The symmetry operation that generates the equivalent component of cation and anion are −x, −y + 1, −z and −x + 1, −y + 1, −z respectively. The carboxyl and carboxylate of the hydrogen succinate anions are twisted out of plane with each other.

The presence of large number of anions and cations in the asymmetric unit tend to form extensive O-H…O and N-H…O hydrogen bonds which are observed between the ionic molecules is shown in hydrogen bonding Table 4. The O-H…O hydrogen bonds links the hydrogen succinate anions in a *syn-anti* fashion forming a one dimensional chain [−1 0 2] direction. The contribution of the succinate and hydrogen succinate anions of the asymmetric unit form four O-H…O hydrogen bonds along [−1 0 2] direction. The 4-ethoxyanilinium cations intelinks these anionic chain through three N-H…O hydrogen bonds contributed from each cations, resulting in the formation a two dimensional sheet parallel to the (0 1 0) plane. The adjacent (0 1 0) molecular sheets are bridged through weak C-H…O hydrogen bond to build a three dimensional network in the crystalline solid [10]. The packing molecular structure of (I) is show in Fig. 3.

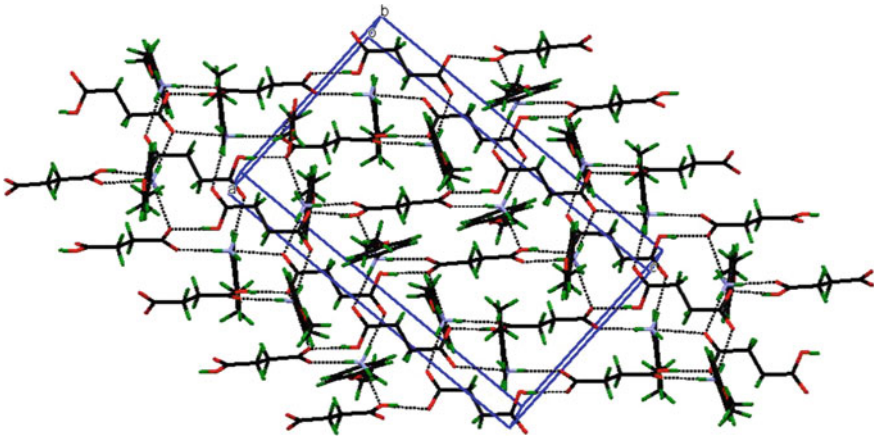

Fig. 3 Part of the crystal structure of (4EAHS) showing the formation of two dimensional hydrogen bonded sheet parallel to the (0 1 0) plane

3.1 Structure Analysis

Table 1 summarizes the crystal data, intensity data collection and refinement details for 4EAHS. The bond lengths are given in Table 2 and the bond angles are given in Table 3 for compounds 4EAHS [11]. The intermolecular hydrogen bonds are listed in Table 4 for the compound.

Table 1 Crystal data and other relevant details for (4EAHS)

Compound code	(4EAHS)
Empirical formula	C_{12} H_{17} NO_5
Formula weight	255.27
Temperature	296(2) K
Wavelength	0.71073 A
Space group	P-1
Crystal system	Triclinic
a(Å)	10.8851(7)
b(Å)	15.1312(9)
c(Å)	18.7769(11)
α(°)	95.774(3)
β(°)	90.389(3)
γ(°)	104.285(3)
Volume (A^3)	2980.2(3)
Molecule/unit cell, z	9
Calculated density (Mg/m^3)	1.280
Absorption coefficient (mm^{-1})	0.100
F(000)	1224
Crystal size	0.35 × 0.20 × 0.20 mm
Theta range for data collection	1.68°–21.82°
Limiting indices	$-11 \leq h \leq 11, -15 \leq k \leq 15, -19 \leq l \leq 19$
Reflections collected/unique	37,250/7079 [R(int) = 0.0373]
Completeness to theta = 21.82	99.10 %
Absorption correction	Semi-empirical from equivalents
Max. and min. transmission	0.9803 and 0.9659
Refinement method	Full-matrix least-squares on F^2
Data/restraints/parameters	7079/97/769
Goodness-of-fit on F^2	1.057
Final R indices [I > 2sigma(I)]	R1 = 0.0685, wR2 = 0.1892
R indices (all data)	R1 = 0.0889, wR2 = 0.2093
Largest diff. peak and hole e A^{-3}	0.526 and −0.534

Table 2 Bond lengths (Å) for non-hydrogen atoms of 4EAHS

Atoms	Distance	Atoms	Distance
C1-C2	1.35(12)	C29-C30	1.37(15)
C1-C6	1.36(11)	C31-O4	1.25(17)
C1-O1	1.37(9)	C31-C3	1.47(16)
C2-C3	1.38(11)	C33-O7	1.23(7)
C3-C4	1.34(10)	C33-O6	1.27(7)
C4-C5	1.35(9)	C33-C34	1.50(8)
C4-N1	1.46(7)	C34-C5	1.49(8)
C5-C6	1.36(10)	C35-C36	1.49(8)
C7-O1	1.34(13)	C36-O	1.23(7)
C7-C	1.55(18)	C36-O8	1.28(7)
C9-C10	1.33(11)	C37-O11	1.22(7)
C9-C14	1.36(12)	C37-O10	1.29(7)
C9-O2	1.37(9)	C37-C38	1.49(8)
C10-C11	1.38(11)	C38-C9	1.50(8)
C11-C12	1.33(10)	C39-C40	1.50(8)
C12-C13	1.34(10)	C40-O12	1.24(7)
C12-N2	1.46(7)	C40-O13	1.26(7)
C13-C14	1.38(11)	C41-O15	1.22(7)
C15-O2	1.38(12)	C41-O14	1.30(7)
C15-C16	1.50(13)	C41-C42	1.49(8)
C17-O3	1.36(8)	C42-C43	1.50(9)
C17-C22	1.36(10)	C43-C44	1.50(8)
C17-C18	1.36(10)	C44-O17	1.23(7)
C18-C19	1.39(10)	C44-O16	1.28(7)
C19-C20	1.35(9)	C45-O19	1.24(7)
C20-C21	1.34(9)	C45-O18	1.27(7)
C20-N3	1.45(7)	C45-C46	1.50(8)
C21-C22	1.36(10)	C46-C47	1.49(9)
C23-O3	1.42(10)	C47-C48	1.49(8)
C23-C24	1.51(12)	C48-O20	1.23(7)
C25-C26	1.29(16)	C48-O21	1.28(7)
C25-C30	1.32(17)	C49-O23	1.18(11)
C25-O4	1.40(13)	C49-O22	1.26(11)
C26-C7	1.43(15)	C49-C50	1.43(14)
C27-C28	1.33(12)	C28-N4	1.45(8)
C28-C29	1.34(12)		

Table 3 Bond angles (°) for non-hydrogen atoms of 4EAHS

Atoms	Angle	Atoms	Angle
C2-C1-C6	118(7)	C27-C28-C29	118(8)
C2-C1-O1	128(8)	C27-C28-N4	121(7)
C6-C1-O1	114(8)	C29-C28-N4	121(7)
C1-C2-C3	122(8)	C28-C29-C30	121(10)
C4-C3-C2	119(7)	C25-C30-C29	121(10)
C3-C-C5	120(6)	O4-C31-C32	119(10)
C3-C4-N1	121(6)	O7-C33-O6	124(5)
C5-C4-N1	119(6)	O7-C33-C34	119(6)
C4-C5-C6	121(7)	O6-C33-C34	117(5)
C5-C6-C1	120(8)	C35-C34-C33	116(5)
O1-C7-C8	107(10)	C36-C35-C34	115(5)
C10-C9-C14	119(7)	O9-C36-O8	124(5)
C10-C9-O2	125(8)	O9-C36-C35	120(5)
C14-C9-O2	116(7)	O8-36-C35	115(5)
C9-C10-C11	120(8)	O11-C37-O10	124(5)
C12-C11-C10	121(7)	O11-C37-C38	123(6)
C11-C12-C13	120(7)	O10-C37-C38	113(5)
C11-C12-N2	120(6)	C37-C38-C39	117(5)
C13-C12-N2	120(6)	C38-C39-C40	113(5)
C12-C13-C14	119(8)	O12-C40-O13	123(5)
C9-C14-C13	121(8)	O12-C40-C39	119(6)
O2-C15-C16	109(10)	O13-C40-C39	117(5)
O3-C17-C22	117(7)	O15-C41-O14	122(5)
O3-C17-C18	125(7)	O15-C41-C42	123(6)
C22-C17-C18	118(6)	O14-C41-C42	115(5)
C17-C18-C19	120(7)	C41-C42-C43	116(5)
C20-C19-C18	120(7)	C42-C43-C44	116(5)
C21-C20-C19	120(6)	O17-C44-O16	123(5)
C21-C20-N3	120(6)	O17-C44-C43	121(5)
C19-C20-N3	120(6)	O16-C44-C43	116(5)
C20-C21-C22	121(7)	O19-C45-O18	123(5)
C21-C22-C17	121(7)	O19-C45-C46	120(5)
O3-C23-C24	108(7)	O18-C45-C46	117(5)
C26-C25-C30	120(10)	C47-C46-C45	116(5)
C26-C25-O4	125(10)	C46-C47-C8	116(5)
C30-C25-O4	115(10)	O20-C48-O21	123(5)
C25-C26-C27	121(10)	O20-C48-C47	122(6)
C28-C27-C26	119(10)	O21-C48-C47	116(5)

Table 4 Hydrogen bonding geometry (Å, º) for 4EAHS

Interaction	D-H	H…A	D…A	D-H…A
C6-H6…O3^{iii}	0.93	2.55	3.39(10)	149
C13-H13…O7	0.93	2.48	3.17(9)	131.7
C18-H18…O22^{i}	0.93	2.58	3.40(11)	148.1
C24-H24B…O23	0.96	2.46	3.40(14)	165.2
C35-H35A…O7^{v}	0.97	2.58	3.53(7)	169.2
N1-H1A…O17^{vi}	0.89	1.96	2.82(7)	163.6
N1-H1C…O11	0.89	1.89	2.78(6)	176
N2-H2A…O7	0.89	1.85	2.73(6)	170.9
N2-H2B…O20^{vi}	0.89	1.91	2.79(7)	173.1
N2-H2C…O8^{v}	0.89	1.96	2.83(6)	163.1
N3-H3A…O9	0.89	1.8	2.68(6)	171.2
N3-H3B…O19^{iii}	0.89	1.94	2.82(7)	170.5
N3-H3C…O13^{v}	0.89	2.01	2.87(6)	162.5
N4-H4A…O12^{vii}	0.89	1.89	2.77(7)	170.1
N4-H4B…O10^{iv}	0.89	2.19	2.97(7)	144.9
N4-H4B…O19	0.89	2.26	2.86(6)	124.4
N4-H4C… O15^{viii}	0.89	1.96	2.84(7)	170.5
O-H8…O16^{ix}	0.82	1.66	2.46(5)	164.9
O10-H10A… O18^{x}	0.82	1.68	2.48(5)	164.6
O14-H14A… O13^{xi}	0.82	1.69	2.50(5)	173.9
O21-H21A… O6^{xii}	0.82	1.65	2.47(5)	172.5

Symmetry code
(i) −x + 1,−y + 1, −z
(ii) x, −y + 1, −z
(iii) −x + 2, −y + 1, −z + 1
(iv) x, y + 1, z
(v) −x + 1, −y, −z + 1
(vi) −x + 1, −y + 1, −z + 1
(vii) −x + 1, −y + 1, −z + 2
(viii) x + 1, y, z + 1
(ix) x + 1, y − 1, z
(x) x, y−1, z
(xi) x, y + 1, z − 1
(xii) x + 1, y + 1, z

4 Conclusion

We have presented our work on the preparation of crystalline 4-Ethoxyanilinium hydrogen succiniate molecular salt and crystal structure determination results. The derived results were helpful in understanding the nature of proton transfer, the direction of specific strong N-H…O and O-H…O hydrogen bonds is observed between the ionic molecules which form two dimensional sheet structure and also the larger number of anions and cations present in the asymmetric unit.

References

1. Desiraju, G.R., Vittal, J.J., Ramanan, A.: Crystal Engineering A Text Book. Word Scientific Publishing Co. Ptc. Ltd., (2011)
2. Begum, N.S., Girija, C.R., Nagendrappa, R.: Cryst. Eng. Comm. **6**, 114 (2004)
3. Basavoju, S., Boström, D., Velaga, S.P.: Cryst. Growth Des. **6**, 2699 (2006)
4. Thakuria, H., Borah, B.M., Pramanik, A., Das, G.: Solid state synthesis and hierarchial supramolecular self-assembly of organic salt cocrystals. J. Chem. Crystallogr. **37**, 807–816 (2007)
5. Samardjiev, I.J., Bordner, J., Coe. J.W.: J. Am. Chem. Soc. **125**, 3268 (2003)
6. Smith, G., Wermuth, U.D., Young, D.J., White, J.M.: Proton transfer versus nontransfer in compounds of the diazo-dye precursor 4-(phenyldiazenyl)aniline (aniline yellow) with strong organic acids: the 5-sulfosalicylate and the dichroic benzenesulfonate salts, and the 1:2 adduct with 3,5-dinitrobenzoic acid. Acta Crystallogr. C. **65**(Pt 10), o543–o548 (2009)
7. Arod, F., Gardon, M., Pattison, P., Chapuis, G.: The α_2-polymorph of salicylideneaniline. Acta Crystallographica C. **61**, o317–o320 (2005)
8. Bruker, A.: SADABS. Bruker AXS Inc., Madison, Wisconsin, USA (2004)
9. Sheldrick, G.M.: A short history of SHELX. Acta Crystallogr. A **64**, 112–122 (2008)
10. Desiraju, G.R.: Supramolecular synthons in crystal engineering—a new organic synthesis. Angew. Chemie. Int. Ed. Engl. **34**, 2311–2327 (1995)
11. Allen, F.H., Kennard, O., Watson, D.G., Brammer, L., Orpen, A.G., Taylor, R.: Tables of bond lengths determined by X-ray and neutron diffraction. Part 1. Bond lengths in organic compounds. J. Chem. Soc., Perkin Trans. **2**, S1–S19 (1987)

Crystal Structure of 4-Methoxyanilinium Chloride 4-Methoxy Aniline

K. Saminathan, R. Jagan, K. Sivakumar and K. Saravanan

Abstract The salt 4-methoxyanilinium chloride methoxyaniline crystallizes in monoclinic space group $P2_1/c$. In the crystal structure the presence of N-H…Cl hydrogen bonds form one dimensional supramolecular ladder built from $R_4^2(8)$ motif along [1 0 0] direction followed by two dimensional sheet parallel to the (1 0 0) plane. The supramolecular architecture is established by N-H…Cl hydrogen bonds. The Cl (halogen) atom acts as hydrogen bond acceptor to all the possible N-H donors of the 4-methoxyanilinium cation and neutral 4-methoxy aniline. In the compounds presented in the report were prepared by taking suitable proportions of acids and bases and crystallized by slow evaporation method using methanol solvents and their structures were solved by direct methods and refined using full-matrix least squares technique using SHELX 97 program package.

1 Introduction

4-methoxyaniline is a colourless crystal and is an important intermediate for the synthesis of dye, medicine and perfume. The formation of acid-base salts of 4-methoxyaniline has been reported earlier [1]. It is also widely used in rubber, textile adhesives, paints, lacquers, photographic industry and also as a protein

K. Saminathan (✉)
Department of Physics, University V.O.C College of Engineering, Anna University, Thoothukudi Campus, Thoothukudi 628008, Tamil Nadu, India
e-mail: ksaminathan2002@yahoo.com

R. Jagan
Department of Chemistry, Indian Institute of Technology Madras, Chennai 600036, India

K. Sivakumar
Department of Physics, Anna University, Chennai 600025, India

K. Saravanan
Department of Ophthalmology, West Virginia University Eye Institute, Morgantown, WV, USA

J. Ebenezar (ed.), *Recent Trends in Materials Science and Applications*,
Springer Proceedings in Physics 189, DOI 10.1007/978-3-319-44890-9_51

modifier. The formation of salt with different acids and their supramolecular structures were also studied [2].

2 Experimental Methods

4MACM was prepared by taking equimolar quantities of hydrochloric acid (0.03 ml, 1 mM) and 4-methoxyaniline (0.115 ml, 1 mM) in methanol solvent. To the methanolic solution of 4-methoxyaniline, hydrochloric acid was added drop wise to form resultant mixture. The resulting solution was then stirred well for 20 min and was left undisturbed for slow evaporation. Good diffraction quality crystals were obtained after few days. The chemical scheme is shown in Fig. 1.

3 Intensity Data Collection and Refinement

X-ray diffraction data for the crystals 4MACM was collected using a Bruker AXS Kappa APEX II four circle single crystal CCD diffractometer equipped with graphite-monochromated MoKα (λ = 0.7107 Å) radiation. The crystal of sizes 0.30 × 0.25 × 0.25 mm^3 (4MACM), was cut and mounted on a glass fiber using cyanoacrylate. The unit cell parameters were determined by collecting the diffracted intensities from 36 frames measured in three different crystallographic zones. The method of difference vectors was done and data collection was carried out at 293 K using ω-φ scan modes. A total of 17,669 reflections were collected, resulting in 4161 independent reflections with R_{int} = 0.033 and R_{sigma} = 0.031 respectively. Of the independent reflections, 2840 had $I > 2\sigma(I)$, which were considered as observed. The intensities were corrected for Lorentz polarization effects followed by multi-scan absorption correction [3].

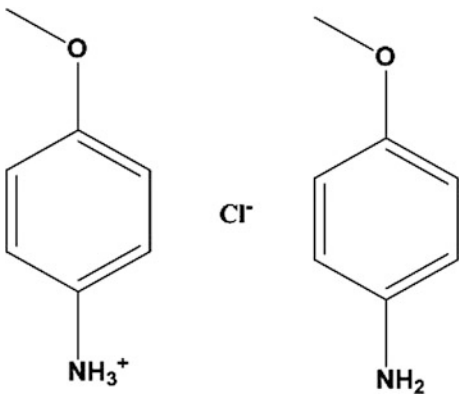

Fig. 1 1.4-methoxyanilinium chloride 4-methoxyaniline (4MACM)

The molecular structure was solved by direct methods procedure as implemented in SHELXS-97. A total of 1062 (E > 1.2) reflections were available for phase refinement procedures. The positions of all the non-hydrogen atoms were included in the full-matrix least squares refinement using SHELXL97 program. Initially isotropic refinements of non-hydrogen atoms were carried out followed by full-matrix least squares refinement with anisotropic thermal parameters for non-hydrogen atoms. The positions of all the hydrogen atoms were identified from difference electron density peaks, and they were constrained to ride on the corresponding non-hydrogen atoms. The hydrogen atom bound to carbon atoms are constrained to a distance of C-H = 0.93–0.97 Å and $U_{iso}(H) = 1.2U_{eq}(C)$ and $1.5U_{eq}(C)$. The hydrogen atom associated with the carboxyl group was identified from the difference electron density map and was allowed to ride over the parent O atom with best staggered position. The hydrogen atoms bound to the N atom were identified from the difference electron density map and were constrained to a distance of 0.89 Å with $U_{iso}(H) = 1.5U_{eq}(N)$. The final refinement converged to an R-value of R = 0.042 and *w*R = 0.140. The molecular structure of 4MACM is shown in Fig. 2.

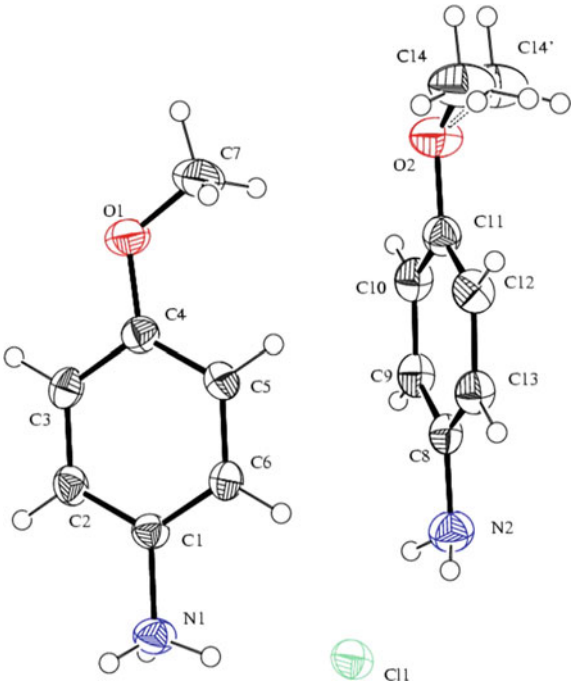

Fig. 2 Displacement ellipsoid plot of 4MACM drawn at 40 % probability level

4 Result and Discussion

The compound 4MACM crystallizes in monoclinic crystal system, space group $P2_1/c$ with 4-methoxyanilinium cation, a chloride anion and a neutral 4-methoxyaniline molecule. In the neutral 4-methoxyaniline molecule the carbon atom of the methoxy group get disordered over two positions with site occupancies of 0.78 and 0.22 for the major and minor components respectively. The C-N distance of the protonated 4-methoxyaniline is C1-N1 = 1.462 Å is longer than the C-N distance of the neutral molecule C8-N2 = 1.398 Å. The elongation is due to the transfer of hydrogen from the hydrochloric acid to the 4-methoxyaniline molecule and other bond length, [4] and bond angle comparable [5].

The supramolecular architecture is established by N-H…Cl hydrogen bonds. The Cl (halogen) atom acts as hydrogen bond acceptor to all the possible N-H donors of the 4-methoxyanilinium cation and neutral 4-methoxy aniline. The nitrogen atom at (x, y, z) from three N-H…Cl hydrogen bond with the chlorine atoms at Cl(−x, −y + 1, −z), Cl1(x, y − 1, z) and Cl1(−x + 1, −y + 1, −z) through the hydrogen atoms H1A, H1B and H1C. These hydrogen bonds form a ladder type super-molecule extending parallel to the [1 0 0] direction as shown in Fig. 3, and is built from fused motif of type $R_4^2(8)$. The $R_4^2(8)$ motifs occupy the crystallographic inversion centers at (0, 1/2, 1/2) and (1/2, 1/2, 1/2) respectively. Parallel [1 0 0]

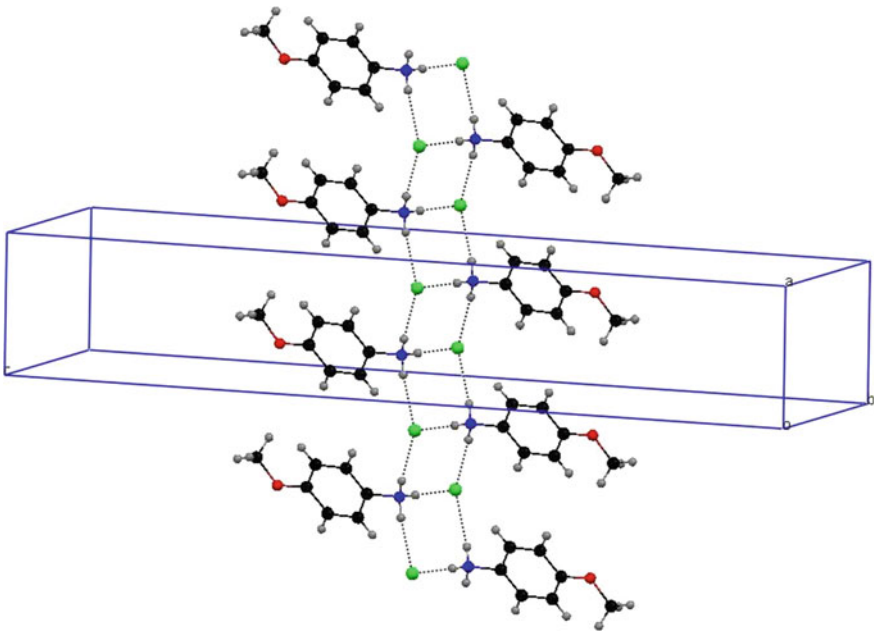

Fig. 3 Part of the crystal structure of 4MACM showing the formation of one dimensional ladder along [1 0 0] direction

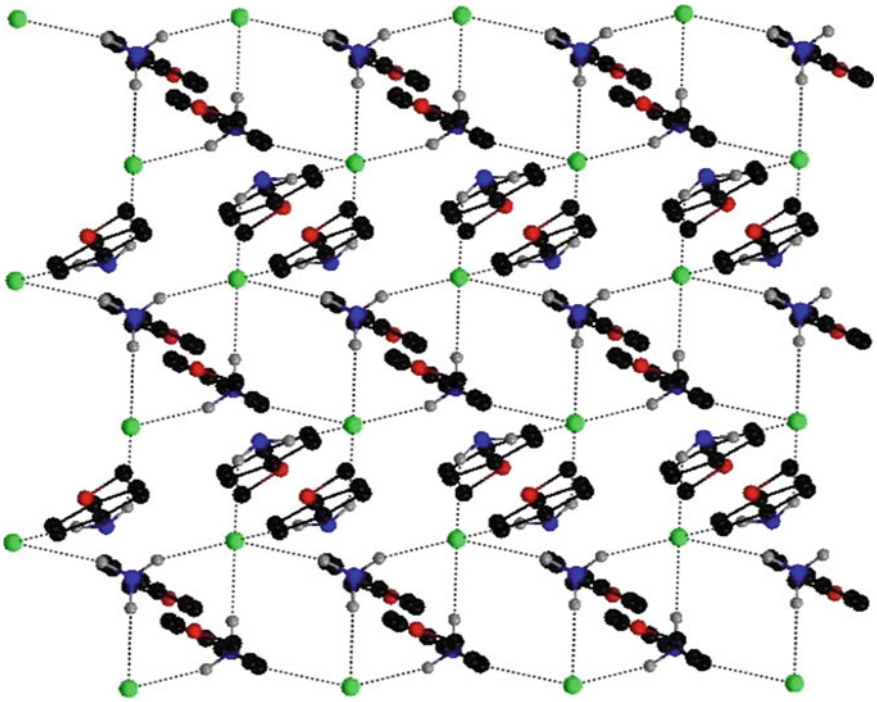

Fig. 4 Part of the crystal structure of 4MACM showing the formation of two dimensional sheet built through N-H…Cl hydrogen bonds parallel to (1 0 0) plane

supramolecular ladders are bridged by neutral 4-methoxyaniline through two N-H…Cl hydrogen bonds N2-H2B…Cl1 and N2-H2A…Cl1^{iii}[symmetry code (iii) −x + 1, −y + 1, −z]. These hydrogen bonds form supramolecular motif of the type $R_8^4(16)$ and $R_4^2(8)$ position on the crystallographic inversion centre at (0, 0, 1/2) and (1/2, 0, 1/2), which construct a two dimensional net extending parallel to the (1 0 0) plane and is shown in Fig. 4 [6, 7].

4.1 Structure Analysis

Table 1 summarizes the crystal data, intensity data collection and refinement details for 4MACM. The bond lengths are given in Table 2 and the bond angles are given in Table 3 for compound 4MACM. The intermolecular hydrogen bonds are listed in Table 4 for the compound.

Table 1 Crystal data and other relevant details for 4MACM

Compound code	4MACM
Empirical formula	C_{14} H_{19} Cl N_2 O_2
Formula weight	282.76
Temperature	296(2) K
Wavelength	0.71073 A
Space group	P21/c
Crystal system	Monoclinic
a(Å)	5.8026(3)
b(Å)	7.0031(4)
c(Å)	35.747(2)
α(°)	90
β(°)	92.181(4)
γ(°)	90
Volume (A^3)	1451.59(14)
Molecule/unit cell, z	4
Calculated density (Mg/m^3)	1.294
Absorption coefficient (mm^{-1})	0.263
F(000)	600
Crystal size	0.35 × 0.30 × 0.25 mm
Theta range for data collection	2.96–29.90°
Limiting indices	$-8 \leq h \leq 8, -9 \leq k \leq 9, -50 \leq l \leq 49$
Reflections collected/unique	17669/4161 [R(int) = 0.0336]
Completeness to theta = 29.90	99.40 %
Absorption correction	Semi-empirical from equivalents
Max. and min. transmission	0.9371 and 0.8635
Refinement method	Full-matrix least-squares on F^2
Data/restraints/parameters	4161/3/187
Goodness-of-fit on F^2	0.985
Final R indices [I > 2 sigma(I)]	R1 = 0.0423, wR2 = 0.1207
R indices (all data)	R1 = 0.0703, wR2 = 0.1403
Largest diff. peak and hole (e A^{-3})	0.218 and −0.194

Table 2 Bond lengths (Å) for non-hydrogen atoms of 4MACM

Atoms	Distance
O1-C4	1.366(2)
O1-C7	1.421(2)
O2-C11	1.380(2)
O2-C14	1.411(3)
O2-C14′	1.414(2)
N1-C1	1.462(2)
N2-C8	1.396(2)
C1-C6	1.374(2)
C1-C2	1.381(2)
C2-C3	1.375(2)
C3-C4	1.386(2)
C4-C5	1.384(2)
C5-C6	1.381(2)
C8-C13	1.385(2)
C8-C9	1.388(2)
C9-C10	1.376(2)
C10-C11	1.382(2)
C11-C12	1.381(2)
C12-C13	1.381(2)

Table 3 Bond angles (°) for non-hydrogen atoms of 4MACM

Atoms	Angle	Atoms	Angle
C4-O1-C7	117.54(13)	C6-C5-C4	119.32(13)
C11-O2-C14	117.4(2)	C1-C6-C5	119.99(13)
C11-O2-C14′	115.1(11)	C13-C8-C9	117.72(14)
C14-O2-C14′	24.3(16)	C13-C8-N2	121.67(14)
C6-C1-C2	121.16(13)	C9-C8-N2	120.54(14)
C6-C1-N1	119.72(13)	C10-C9-C8	121.35(14)
C2-C1-N1	119.11(12)	C9-C10-C11	120.14(15)
C3-C2-C1	118.88(12)	O2-C11-C12	124.56(14)
C2-C3-C	120.51(13)	O2-C11-C10	116.00(14)
O1-C4-C5	124.27(13)	C12-C11-C10	119.44(14)
O1-C4-C3	115.61(12)	C11-C12-C13	119.91(13)
C5-C4-C3	120.12(13)	C12-C13-C8	121.44(14)

Table 4 Hydrogen bonding geometry (Å, °) for 4MACM

Interaction	D-H	H…A	D…A	D-H…A
N1-H1A…Cl1[i]	0.89	2.33	3.1825(12)	161.1
N1-H1B…Cl1[ii]	0.89	2.3	3.1903(15)	178.1
N1-H1C…Cl1[iii]	0.89	2.39	3.2560(13)	164.9
N2-H2A…Cl1[iii]	0.883(9)	2.934(15)	3.6722(17)	142.3(17)
C7-H7B…O2[iv]	0.96	2.62	3.476(2)	148.7
N2-H2B…Cl1	0.877(9)	2.568(12)	3.4010(16)	159.0(19)

Symmetry code
(i) −x, −y + 1, −z
(ii) x, −y − 1, z
(iii) −x + 1, −y + 1, −z
(iv) −x + 1, y − 1/2, −z + 1/2

5 Conclusion

We have presented work on the preparation of crystalline 4-methoxyanilinium chloride 4-methoxy aniline molecular salt and crystal structure determination. In the chloride related the presence of Cl atom is the main hydrogen bond acceptor, in which the supramolecular architecture is dominated by N-H…Cl hydrogen bonds. They tend to form molecular ladder and sheets.

References

1. Tan, T.F., Han, J., Pang, M., Song, H.B., Ma, Y.X., Meng, J.B.: Achiral benzoic acid derivatives as chiral co-crystal building blocks in supramolecular chemistry: adducts with organic amines. Cryst. Growth Des. **6**, 1186–1193 (2006)
2. Fun, H.K., Usmana, A., Chantrapromma, S., Osmana, J., Onga, L.H., Tilleya, D.R., Ishibashic, Y.: Phase transitions in hydrogen-bonded phenol–amine adducts: analysis by ferroelastic theory. Solid State Commun. **127**, 677–682 (2003)
3. Bruker, S.: SADABS. Bruker AXS Inc., Madison, Wisconsin, USA (2004)
4. Allen, F.H., Kennard, O., Watson, D.G., Brammer, L., Orpen, A.G., Taylor, R.: Tables of bond lengths determined by X-ray and neutron diffraction. Part 1. Bond lengths in organic compounds. J. Chem. Soc., Perkin Trans. **2**, S1–S19 (1987)
5. Taylor, R., Kennard, O.: Crystallographic evidence for the existence of C-H…O, C-H…N and C-H…Cl hydrogen bonds. J. Am. Chem. Soc. **104**, 5063–5070 (1982)
6. Desiraju, G.R., Vittal, J.J., Ramanan, A.: Crystal Engineering a Text Book. World Scientific, Singapore (2011)
7. Desiraju, G.R.: Supramolecular synthons in crystal engineering—a new organic synthesis. Angew. Chemie. Int. Ed. Engl. **34**, 2311–2327 (1995)

Part VI
Spectroscopy

Conformational Analysis, Structural and Vibrational Investigations of *trans*–2–Chlorocinnamic Acid and *trans*–4–Chlorocinnamic Acid

L. Devi, V. Arjunan, M.K. Marchewka and S. Mohan

Abstract The various conformers and the exact geometry of the more stable conformer of trans 2-chloro- and trans-4-chlorocinnamic acids have been determined by analysing the potential energy profile of the compounds. The *s–cis* orientation of the carbonyl group (C=O) and the C=C bond appears as the only stable structure in 2CCA and is more stable by 0.6648 kcal mol–1 than the corresponding s–trans conformation. In 4CCA, the *s–cis* conformer is more stable than the s–trans conformer by 0.8939 kcal mol–1. The structure and vibrational characteristic of the compounds have been investigated by using both experimental and quantum chemical methods. The bond distances, bond angles, dihedral angles, the kinetic and thermodynamic stability of the molecule, global and local reactivity parameters, the energy gap between the frontier molecular orbitals, the probable electronic transitions and bonding concepts of the compounds are elaborated in the present investigation. The frontier orbital energy gap of 2CCA and 4CCA are 4.5533 eV and 4.4366 eV, respectively shows that 4CCA is highly reactive than 2CCA molecule. The bond pair donor orbital, $\pi CC \rightarrow \pi^*CC$ interaction from C3–C4 bond pair to C1–C2 and C5–C6 antibonding orbitals have the stabilisation energies 252.31 and 203.28 kcal mol–1, respectively. In the case of 4CCA, $\pi CC \rightarrow \pi^*CC$ interaction from C1–C2 bond pair to C3–C4 and C5–C6 antibonding orbitals gives the strongest stabilisation of 258.75 and 203.58 kcal mol–1. The global and local reactivity descriptors clearly reveals that C9

L. Devi
Research and Development Centre, Bharathiar University,
Coimbatore 641046, India

V. Arjunan (✉)
Department of Chemistry, Arignar Anna Government
Arts & Science College, Karaikal 609605, India
e-mail: varjunftir@yahoo.com

M.K. Marchewka
Institute of Low Temperature and Structure Research, Polish Academy of Sciences,
50-950 Wroclaw 2, 1410 Warsaw, Poland

S. Mohan
School of Sciences and Humanities, Vel Tech University,
Avadi, Chennai 600062, India

J. Ebenezar (ed.), *Recent Trends in Materials Science and Applications*,
Springer Proceedings in Physics 189, DOI 10.1007/978-3-319-44890-9_52

is more favorable for nucleophilic attack while the ring carbon atoms are favorable for both electrophilic and nucleophilic attack.

1 Introduction

In medical and food–related applications cinnamic acid derivatives are considered to be biologically active. They are the potent inhibitory materials against bacteria [1] and fungi [2]. The secondary metabolites of phenylpropanoid biosynthetic origin possess cinnamoyl group. Hydroxyl cinnamates are used as antitumor agents [3, 4]. The *trans*–forms of cinnamic acids have significant activities in the apoptosis of cancer cells [5].

The derivatives of cinnamic acid shows pharmacological properties, including hepatoprotective [6], antioxidant [7], and antidiabetic activities [8]. The conformational behaviour and structural stability of (2E)–3–phenylprop–2–enoic anhydride [9], (2E)–3–(3–chlorophenyl)prop–2–enoic anhydride [10], and 2,3,4,5,6–pentafluoro–trans–cinnamic acid have been investigated [11].

Polymeric materials with cinnamoyl moieties are used in emerging fields such as advanced microelectronics [12], photolithography [13], non–linear optical materials [14], integrated circuit technology [15] and photocurable coatings [16]. The solid state photoreaction of cinnamic acid produce cyclobutane dicarboxylic acid [17] is very much interested. In the structure and function of plant hormones *trans*–3–hydroxycinnamic acid plays a vital role. Crystal structures of α–*trans*– and *p*–methoxycinnamic acids and their relation to thermal mesomorphism have been investigated [18]. In tumor treatment the biological activity is influenced by the chloro– substituent on the cinnamoyl group and act as efficient as the respective parent cinnamic acid without producing the side effects observed by the parent compounds [19–21]. In continuation of the conformational, structural, vibrational, electronic and quantum chemical investigations of *cis*–2–methoxycinnamic acid [22] and *trans*–2–methoxycinnamic acid [23] and considering the industrial and biological significance of *trans*–2–chloro– and *trans*–4–chlorocinnamic acids, the structure, energy, fundamental vibrations, electronic properties and structure–reactivity relations are experimentally and theoretically analysed.

2 Experimental

The compound *trans*–2–chlorocinnamic acid (2CCA) and *trans*–4–chlorocinnamic acid (4CCA) are purchased from Aldrich chemicals, U.S.A. The FTIR and FT–Raman spectra of the compounds are recorded as such without any further purification. The FTIR spectra are recorded in the range 4000–400 cm^{-1} by using KBr pellet and Nujol on a Bruker IFS 66 V spectrometer equipped with a Globar source, Ge/KBr beam splitter and TGS detector. The spectral resolution is 2 cm^{-1}. The FT–Raman spectra of the compounds are recorded in the range 4000–100 cm^{-1} using

the same instrument with FRA106 Raman module equipped with Nd:YAG laser source operating at 1.064 μm with 200 mW powers. A liquid nitrogen cooled–Ge detector is used. The frequencies of all sharp bands are accurate to 2 cm^{-1}.

3 Computational Details

The energies of different conformers of 2CCA and 4CCA and their stability have been determined by analysing the potential energy surfaces. Both the compounds exhibit two stable conformers namely *s–cis* and *s–trans*. The molecular structure of the more stable *s–cis* and *s–trans* conformers of 2CCA and 4CCA are optimised with B3LYP/6–311++G** and B3LYP/cc–pVTZ methods [24–27]. Gaussian–09 [28] program has been used for geometry optimization [29], computation of energies, molecular structure, vibrational frequency, thermodynamic characteristics and reactivity aspects.

The conversion of Raman scattering activities (S_i) into relative Raman intensities (I_i) is explained in explained in the earlier papers [22, 23, 30]. The shape, size, the distribution of charge densities and reactivity sites of the molecules are depicted by the electron density surface mapped with electrostatic potential. The molecular electrostatic potential (MEP) at a point '*r*' in the space around a molecule (in atomic units) and electron density [31, 32] are calculated by B3LYP/cc–pVTZ method. The MEP surface has been simulated by GaussView 5.0.8 visualisation program [33]. The inter- and intra-atomic contributions are revealed by determining the natural atomic orbitals (NAO) energies $\varepsilon_i^{(A)}$ by using Kohn–Sham operator (F) [22, 23].

The global reactivity indices namely chemical potential, electrophilicity, nucleophilicity, hardness, softness and local reactivity descriptors are also calculated. The local reactive sites can be determined by Fukui functions [34, 35] which can be interpreted either as the change of electron density $\rho(r)$ at each point r when the total number of electrons is changed or as the sensitivity of chemical potential (μ) of a system to an external perturbation at a particular point r.

$$f(r) = \left(\frac{\partial \rho(r)}{\partial N}\right)_{v(r)} = \left(\frac{\delta \mu}{\delta v(r)}\right)_N$$

Yang and Parr introduced local softness *s(r)* to predict the reactive sites [35, 36]. The local softness values are used in predicting the electrophilic, nucleophilic and free radical reactive sites, regioselectivity etc.

$$s(r) = \left(\frac{\partial \rho(r)}{\partial \mu}\right)_{v(r)}$$
$$s(r) = f(r)S$$

where, S is the global softness which is inversely related to global hardness (η).

The global and local reactivity parameters are determined with the help of finite difference approximation. The electron populations, ionization potential (I) and electron affinity (A) are obtained from B3LYP/cc–pVTZ method. The is used for predicting The energies of neutral molecules are calculated by restricted B3LYP method. The energies of cations and anions of the compounds are predicted by open shell restricted B3LYP method with the optimised geometry of the neutral molecules.

4 Results and Discussion

4.1 Potential Energy Profile and Molecular Geometry

The more stable conformations of the molecules are predicted with the help of the three planar groups namely (1) the phenyl ring, (2) the olefinic group (C1–C7–C8–C9) and (3) the carboxyl group centered on C(9). The exact orientations of the –CH=CH–COOH group stable in the conformations of 2CCA and 4CCA are determined by B3LYP/6–31G** method. The orientation of the –CH=CH– group has been fixed first and then by rotating this group along C8–C9 bond with the dihedral angle C7–C8–C9–O11 the orientation of the –COOH group has been determined. The geometry corresponding to the minimum in the potential energy surface is more stable than others. The most stable geometry of the compounds among different conformers are predicted by optimising with higher basis set.

The dihedral angle C7–C8–C9–O11 is used to depict the orientation of the acrylic acid group with respect to the phenyl ring. The energy of the conformers is predicted for every 10° rotation of the dihedral angle C7–C8–C9–O11 after fixing to zero initially. The –COOH group has free rotation around C8–C9 bond. The potential energy profiles of 2CCA and 4CCA compounds are presented in Fig. 1a, b.

In cinnamic acid and its esters intramolecular hydrogen bond of the olefinic type C–H···O is the power of enforcing the existence of different types of conformations, rendering synperiplanar (*s–cis*) and antiperiplanar (*s–trans*) arrangements of C=C–C=O part. The carbon atom is always the olefinic carbon atom while the oxygen atom is either a carbonyl, (C=O) or hydroxyl, (O–H) oxygen. Both conformations

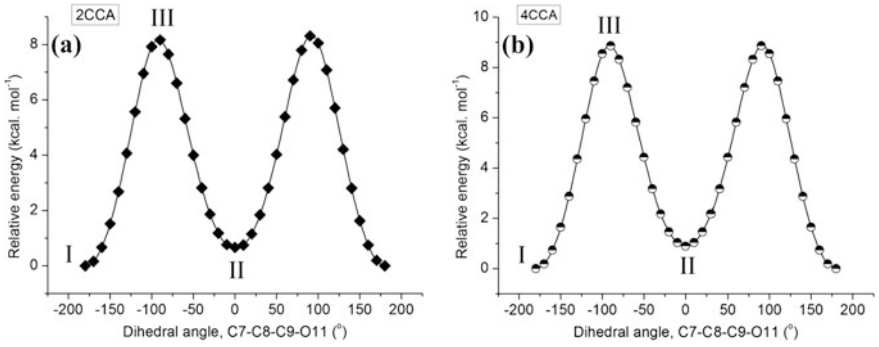

Fig. 1 Potential energy profile of **a** *trans*–2–chlorocinnamic acid (2CCA) and **b** *trans*–4–chlorocinnamic acid (4CCA)

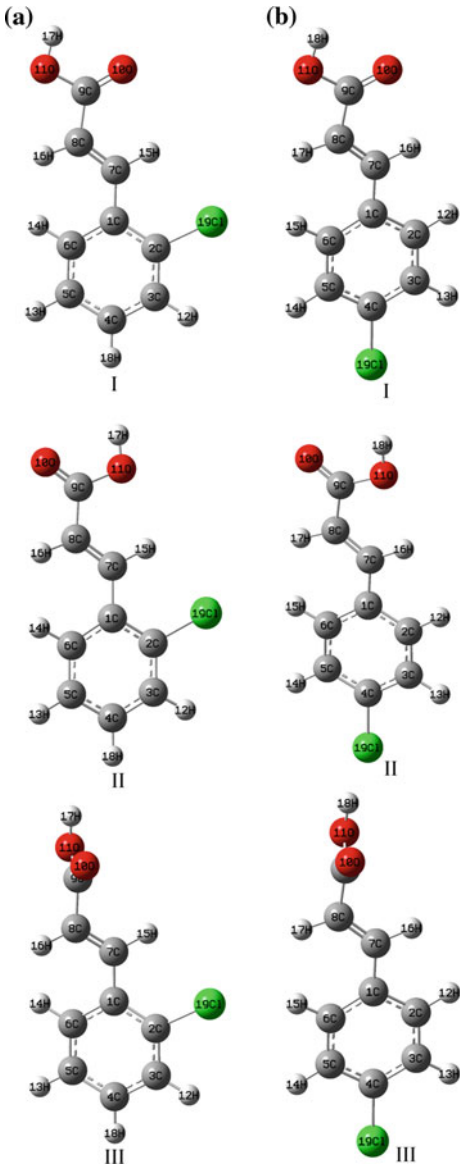

Fig. 2 The possible conformers of **a** *trans*–2–chlorocinnamic acid (2CCA) and **b** *trans*–4–chlorocinnamic acid (4CCA)

are equally abundant in the acids; however, synperiplanar conformation is exclusive in the esters (–CH=CH–COOR) [23, 37].

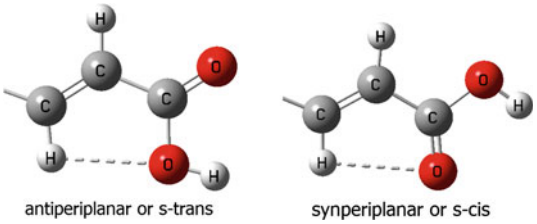

In cinnamic acid derivatives, the determination of the conformational preferences depends on the electrostatic attractive force between the carbonyl oxygen and the =C–H hydrogen to the rotational barriers. Two minima which correspond to thestructures I and II are found in the potential energy profile indicates the variation in energy with rotation of the carboxylic acid group with respect to the olefinic double bond (Fig. 1). The *s–cis* conformer (I) with a (C7–C8–C9–O11) dihedral angle equal to 180° is found to be more favoured and more stable relative to the *s–trans* (II) with the dihedral angle (C7–C8–C9–O11)=0°. This is due to delocalisation, hydrogen bonding and steric repulsion effects between the chloro and acrylic acid groups. Figure 2a, b illustrates the possible different conformers of 2CCA and 4CCA compounds.

The dihedral angle (C7–C8–C9–O10) can be used to predict the orientation of the COOH group relative to the C=C bond present in the side chain. The dihedral angle may be equal to 0° or 180°. In this molecule the dihedral angle (C7–C8–C9–O10=0°) confirmed the *s–cis* configuration of the carboxylic carbonyl (C=O) group and the side chain double bond (C7=C8). Similarly the dihedral angle (C7–C8–C9–O10=180°) shows the *s–trans* orientation of the carboxylic carbonyl group and the linear chain double bond (C7=C8). All these facts confirm the planar geometry of the compounds exhibited by the stabilisation due to π–electron delocalisation, which is more effective for a linear zig–zag like unsaturated chain, coplanar with the aromatic ring.

The potential energy surface analysis indicates that there are three possible conformers for both 2CCA and 4CCA molecules. The *s–cis* orientation (a) of the carbonyl group (C=O) and the C=C bond appears as the only stable structure in 2CCA and is more stable by 0.6648 kcal mol^{-1} than the corresponding *s–trans* conformation (b). In the stable *s–cis* (a) and *s–trans* (b), the –CH=CH–COOH group and the phenyl ring are planar to each other. In the conformer (c), the –COOH group is perpendicular with respect to the plane of the phenyl ring and is non–planar. The barrier heights between the more stable *s–cis* conformer (a) and the least stable excited state conformer (c) is 8.3143 kcal mol^{-1}. In *o*–methoxycinnamic acid [22, 23] and *o*–ethoxycinnamic acid the carbonyl group (C=O) and the alkene double bond (C=C) is also present in the *s–cis* configuration [38] and is more stable. All possible different conformers of 2CCA and 4CCA are depicted in Fig. 2a, b.

In 4CCA, the *s–cis* conformer (I) is more stable than the *s–trans* conformer (II) by 0.8939 kcal mol^{-1}. Both the conformers are planar and normally exist in the cinnamic acid molecules. The non–planar conformer III of 4CCA is less stable than the *s–cis* conformer by 8.8673 kcal mol^{-1}. Comparing the energy profile of 2CCA and 4CCA compounds, the 4CCA is more stable than 2CCA. Similarly, by comparing the potential energy profile of 2CCA and 4CCA compounds (Fig. 1), the barrier height for the interconversion of the conformers the *s–cis* I and s–trans II 4CCA require more energy than in 2CCA. The most stable *s–cis* geometry of 2CCA and 4CCA along with the numbering of atoms are presented in Fig. 3a, b.

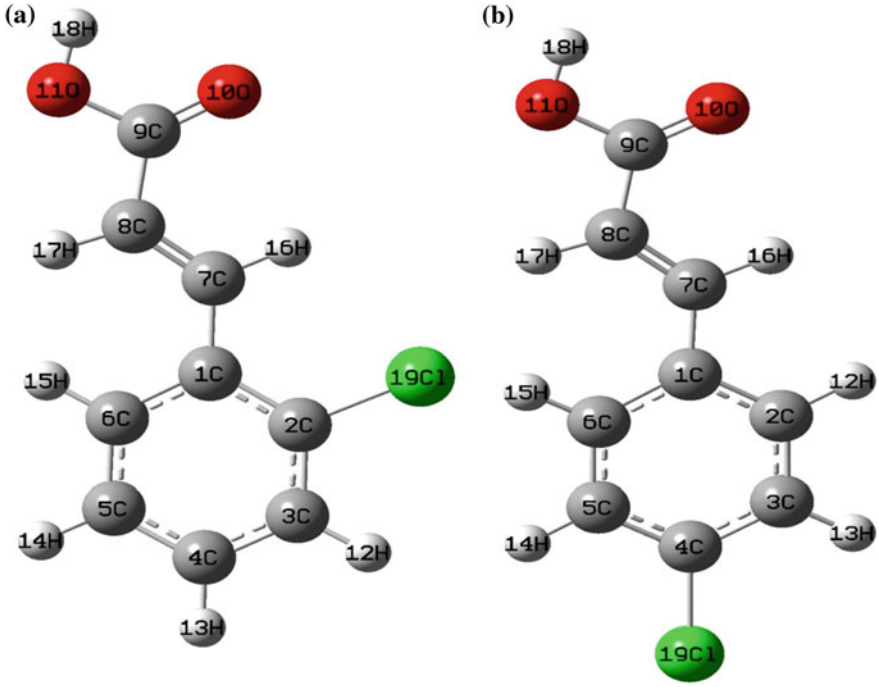

Fig. 3 The structure and atom numbering scheme of the more stable *s–cis* conformer of **a** *trans*–2–chlorocinnamic acid and **b** *trans*–4–chlorocinnamic acid

4.2 Structural Properties

The optimised structural parameters namely bond length, bond angle and the dihedral angle for the stable *s–cis* geometry of 2CCA and 4CCA molecules determined by B3LYP methods with 6–311++G** and cc–pVTZ basis sets are given in Table 1. The data of B3LYP/cc–pVTZ method have been considered for discussion and correlation unless otherwise stated.

There is no significant differences are observed in the C–C bond lengths of aromatic ring of 2CCA and 4CCA. The bond length of propionic acid substituent C1–C7 and C8–C9 are longer than the C–C bond distances of the aromatic ring. Easy delocalisation of electrons towards chlorine is possible by the larger attraction on valance electron cloud of the ring by chlorine and thereby decreases in force constant and increase in C1–C7 bond length. Similarly, the C8–C9 bond distance increases due to the electron withdrawing nature of the carbonyl group by the partial ionic nature.

Analysing the bond angle of aromatic ring of 2CCa and 4CCA molecules, the geometry of the benzene ring is relatively perturbed due to the presence of chloro and propionic acid group substituents. The electron attracting chloro group leads to

Table 1 Structural parameters of the more stable *s–cis–* conformer of *trans–*2–chlorocinnamic acid (2CCA) and *trans–*4–chlorocinnamic acid (4CCA) determined by B3LYP method with 6–311 ++G** and cc–pVTZ basis sets

Structural parameters	2CCA		4CCA		Experimental[a]
	B3LYP/6–311++G**	B3LYP/cc–pVTZ	B3LYP/6–311++G**	B3LYP/cc–pVTZ	
Internuclear distance (Å)					
C1–C2	1.41	1.41	1.40	1.40	1.40
C1–C6	1.41	1.41	1.40	1.40	1.40
C1–C7	1.46	1.46	1.46	1.46	1.46
C2–C3	1.39	1.38	1.39	1.39	
C2–Cl19	1.76	1.75			
C4–Cl19			1.75	1.75	
C2–H12			1.09	1.09	1.08
C3–C4	1.39	1.39	1.39	1.39	1.39
C3–H12	1.09	1.09			1.08
C3–H13			1.09	1.09	1.08
C4–C5	1.40	1.39	1.40	1.40	1.40
C4–H13	1.09	1.09			1.08
C5–C6	1.39	1.39	1.39	1.39	1.39
C5–H14	1.08	1.08	1.08	1.08	1.08
C6–H15	1.08	1.08	1.08	1.08	1.08
C7–C8	1.34	1.34	1.34	1.34	1.35
C7–H16	1.09	1.08	1.09	1.09	1.08
C8–C9	1.48	1.47	1.47	1.47	1.47
C8–H17	1.08	1.08	1.08	1.08	1.08
C9=O10	1.21	1.21	1.21	1.21	1.25
C9–O11	1.36	1.36	1.36	1.36	1.31
O11–H18	0.97	0.97	0.97	0.97	1.01
Bond angle (°)					
C2–C1–C6	116.7	116.7	117.9	117.9	118.6
C2–C1–C7	121.6	121.5	118.7	118.7	119.0
C6–C1–C7	121.6	121.8	123.3	123.4	122.4
C1–C2–C3	121.9	121.8	121.5	121.6	120.4
C1–C2–Cl19	120.9	121.0			
C3–C2–Cl19	117.2	117.2			
C1–C2–H12			119.3	119.2	[b]118.7
C3–C2–H12			119.2	119.2	[b]118.7
C2–C3–C4	119.7	119.8	119.0	119.0	120.4

(continued)

Table 1 (continued)

Structural parameters	2CCA		4CCA		Experimental[a]
	B3LYP/6–311++G**	B3LYP/cc–pVTZ	B3LYP/6–311++G**	B3LYP/cc–pVTZ	
C2–C3–H12	119.4	119.4			119.3
C2–C3–H13			120.8	120.8	120.4
C4–C3–H12	120.8	120.8			120.2
C4–C3–H13			120.2	120.2	120.2
C3–C4–C5	119.9	119.9	121.0	121.0	119.7
C3–C4–H13	119.6	119.6			119.3
C5–C4–H13	120.5	120.5			120.6
C3–C4–Cl19			119.6	119.6	[b]119.7
C5–C4–Cl19			119.4	119.4	[b]119.0
C4–C5–C6	119.8	119.8	119.3	119.4	120.0
C4–C5–H14	120.3	120.3	120.0	119.9	120.9
C6–C5–H14	119.9	119.9	120.7	120.7	119.1
C1–C6–C5	121.9	122.0	121.2	121.2	120.8
C1–C6–H15	118.7	118.7	120.2	120.1	120.8
C5–C6–H15	119.3	119.2	118.7	118.7	118.4
C1–C7–C8	126.3	126.6	127.7	127.8	122.8
C1–C7–H16	116.9	116.7	115.9	116.0	114.2
C8–C7–H16	116.8	116.6	116.5	116.3	119.7
C7–C8–C9	120.3	120.3	120.2	120.3	122.8
C7–C8–H17	123.3	123.3	123.3	123.2	120.2
C9–C8–H17	116.4	116.4	116.5	116.5	117.7
C8–C9–O10	126.7	126.6	126.7	126.6	120.2
C8–C9–O11	111.1	111.1	111.2	111.2	116.5
	122.2	122.3	122.2	122.2	123.3

(continued)

Table 1 (continued)

Structural parameters	2CCA		4CCA		Experimental[a]
	B3LYP/6–311++G**	B3LYP/cc–pVTZ	B3LYP/6–311++G**	B3LYP/cc–pVTZ	
O10–C9–O11					
C9–O11–H18	106.9	106.5	107.0	106.5	110.1

[a]values are taken from [39] and [b]values are taken from [40]

significant perturbations in the ring, in a reverse manner. The bond angles C1–C2–C3 (121.8°) in 2CCA and C3–C4–C5 (121°) in 4CCA are greater than 120° due to the attachment of electron donating chloro groups. The bond angle C2–C1–C6 (116.7°/117.9°) indicates the withdrawing nature of propionic acid group.

The reliability and accuracy of the DFT methods used in this investigations can be ascertained by comparing the theoretically determined bond lengths and bond angles of 2CCA and 4CCA with the corresponding experimental data of *trans*–cinnamic acid [39] and methyl–(2Z)–2–bromomethyl–3–(2,4–dichlorophenyl) prop–2–enoate [40]. They are well agreed with each other.

The total thermal energy, vibrational energy contribution, the rotational constants and the dipole moment values are evaluated and presented in Table 2. The energy of the compounds 2CCA and 4CCA determined by B3LYP/cc–pVTZ method are −958.0450 and −958.0451 Hatrees, respectively. The dipole moment of 2CCA and 4CCA molecules determined by B3LYP/cc–pVTZ method are 3.5 D and 1.13 D, respectively. This shows that 2CCA is more polar than 4CCA molecule. The determined hardness and softness of the molecules suggests that there is no much difference between 2CCA and 4CCA.

5 Analysis of Molecular Electrostatic Potential

The molecular shape, size, dipole moments of the molecule and electrostatic potential (electron + nuclei) distributions are displayed by the molecular electrostatic potential surface (MEP). The relative polarity [22] of the molecules can be visualised by MEP surface. The procedure, applications and the colour scheme of molecular electrostatic potential are illustrated in the previous paper [22, 23]. The charge distributions illustrates how the molecules interact with one another. The total electron density and MEP surfaces of the molecules are constructed by B3LYP/cc–pVTZ method. The total electron density mapped with electrostatic potential surface is depicted in Fig. 4a, b. The MEP mapped surface of the compounds and electrostatic potential contour map for positive and negative potentials are shown in Figs. 5a, b and 6a, b. The range of MEP of 2CCA is between $+1.155e \times 10^{-2}$ and $-1.155e \times 10^{-2}$ while for 4CCA it is $+1.285e \times 10^{-2}$ to $-1.285e \times 10^{-2}$. The total electron density of 2CCA spreads in the range

Table 2 The calculated thermodynamic parameters of the more stable *s–cis–* conformer of *trans–*2–chlorocinnamic acid (2CCA) and *trans–*4–chlorocinnamic acid (4CCA) determined with B3LYP methods by using 6–311++G** and cc–pVTZ basis sets

Thermodynamic parameters (298 K)	*trans–*2–chlorocinnamic acid		*trans–*4–chlorocinnamic acid	
	B3LYP/6–311++G**	B3LYP/cc–pVTZ	B3LYP/6–311++G**	B3LYP/cc–pVTZ
SCF energy (a.u)	−957.9905	−958.0450	−957.9939	−958.0451
Total energy (thermal), E_{total} (kcal.mol^{-1})	93.81	94.02	93.80	94.04
Heat capacity at const. volume, C_v (cal.mol^{-1}.K^{-1})	39.33	39.16	39.34	39.13
Entropy, S (cal.mol^{-1}.K^{-1})	98.92	99.17	105.19	104.89
Vibrational energy, E_{vib} (kcal.mol^{-1})	92.03	92.24	92.02	92.26
Zero–point vibrational Energy, E_0 (kcal.mol^{-1})	87.12	87.35	87.11	87.38
Rotational constants (GHz)				
A	1.38	1.39	3.58	3.60
B	0.44	0.45	0.27	0.27
C	0.34	0.34	0.25	0.25
Dipole moment (Debye)				
μ_x	−2.05	−1.89	0.56	0.45
μ_y	−2.96	−2.94	−0.99	−1.04
μ_z	−0.25	−0.21	0.00	0.00
μ_{total}	3.61	3.50	1.14	1.13
LUMO+1 (eV)		−0.9592		−1.0455
LUMO (eV)		−2.3475		−2.3451
HOMO (eV)		−6.9009		−6.7817
HOMO—1 (eV)		−7.3583		−7.7950
LUMO—HOMO (eV)		4.5533		4.4366
Ionisation potential, I (eV)		8.68		8.54
Electron affinity, A (eV)		0.61		0.63
Electronegativity (χ)		4.65		4.58
Chemical potential (μ)		−4.64		−4.58
Electrophilicity (ω)		2.67		2.65
Hardness (η)		4.04		3.96
Softness (S)		0.12		0.13
Electrofugality (ΔE_e)		9.34		9.21
Nucleofugality (ΔE_n)		0.05		0.05

$+5.251e \times 10^{-2}$ to $-5.251e \times 10^{-2}$ while for 4CCA it is $+5.433e \times 10^{-2}$ to $-5.433e \times 10^{-2}$. The MEP and total electron density shows that the 2CCA is less polar, less reactive and more stable than 4CCA molecule. The electron density

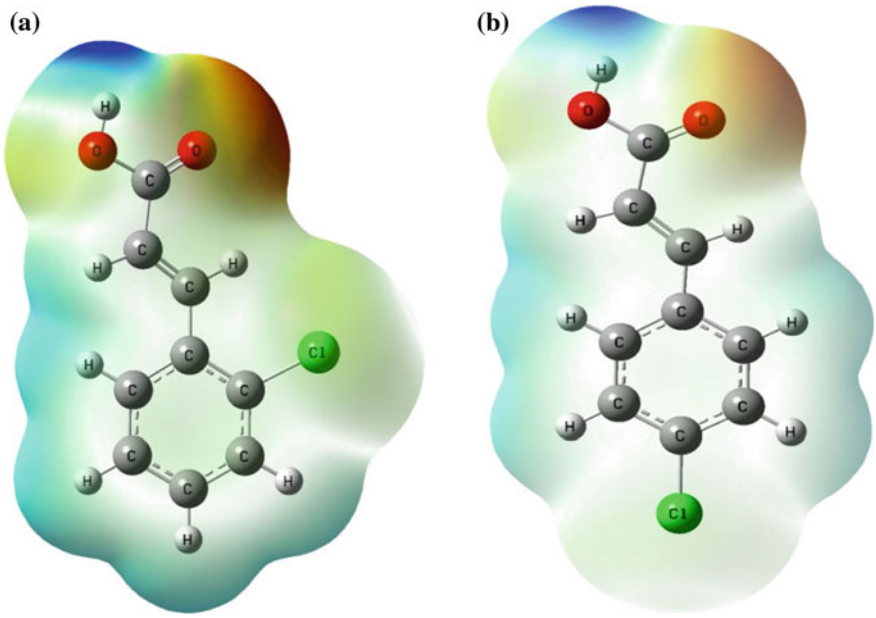

Fig. 4 The total electron density mapped with electrostatic potential surface of *s–cis* conformer of **a** *trans*–2–chlorocinnamic acid, **b** *trans*–4–chlorocinnamic acid

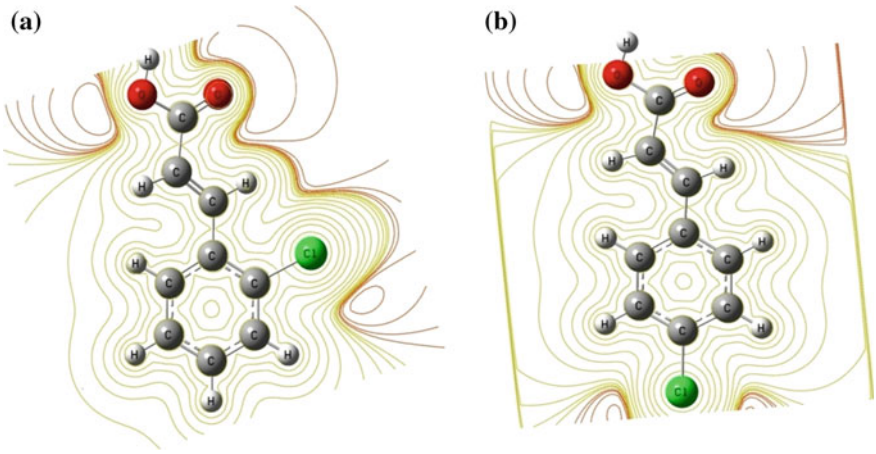

Fig. 5 The contour map of the electrostatic potential of *s–cis* conformer of **a** *trans*–2–chlorocinnamic acid, **b** *trans*–4–chlorocinnamic acid

isosurface and the electrostatic potential contour maps reveals that the carbonyl oxygen of both 2CCA and 4CCA molecules possess more negative charges due to the partial ionic character of the C=O group of –COOH. More positive charge lies

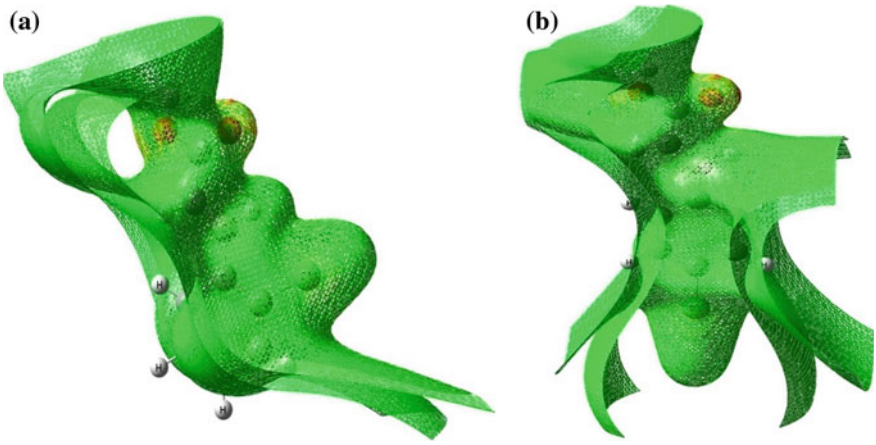

Fig. 6 The electrostatic potential surface of the *s–cis* conformer of **a** *trans*–2–chlorocinnamic acid, **b** *trans*–4–chlorocinnamic acid

on the hydroxyl hydrogen atom of both the molecules due to the delocalisation of the lone pair of electrons present in the hydroxyl oxygen towards the carbonyl group.

6 Analysis of Electronic Properties

The energies of LUMO+1, LUMO, HOMO and HOMO–1 molecular orbitals of 2CCA and 4CCA are calculated by using B3LYP/cc–pVTZ method and presented in Table 2. The frontier molecular orbitals and their respective positive and negative regions are shown in Figs. 7 and 8, respectively for 2CCA and 4CCA.

The energies of molecular orbitals provide insight into the nature of reactivity and some physical properties of molecules. Conjugation, aromaticity and lone pairs are well illustrated by molecular orbitals [22, 23].

The positive and negative regions are represented in red and green colour, respectively. The HOMO of 2CCA is mainly overlapped in the carbonyl group while the LUMO spread on the π–bond of the ring molecules. The electronic transition from HOMO to LUMO is attributed to n → π* transition. The Fig. 7 indicates that HOMO–1 to LUMO transition is mainly to π → π* type. But in the case of 4CCA, the reverse trend of 2CCA is observed from the Fig. 8. That is, the transition of the type π → π* belongs to HOMO → LUMO while the n → π* transition is attributed to HOMO–1 → LUMO orbital. The frontier orbital energy gap of 2CCA and 4CCA are 4.5533 and 4.4366 eV, respectively shows that 4CCA is highly reactive than 2CCA molecule. The energies of HOMO, LUMO, HOMO–1, LUMO + 1 for 2CCA are −6.9009, −2.3475, −7.3583 and −0.9592 eV,

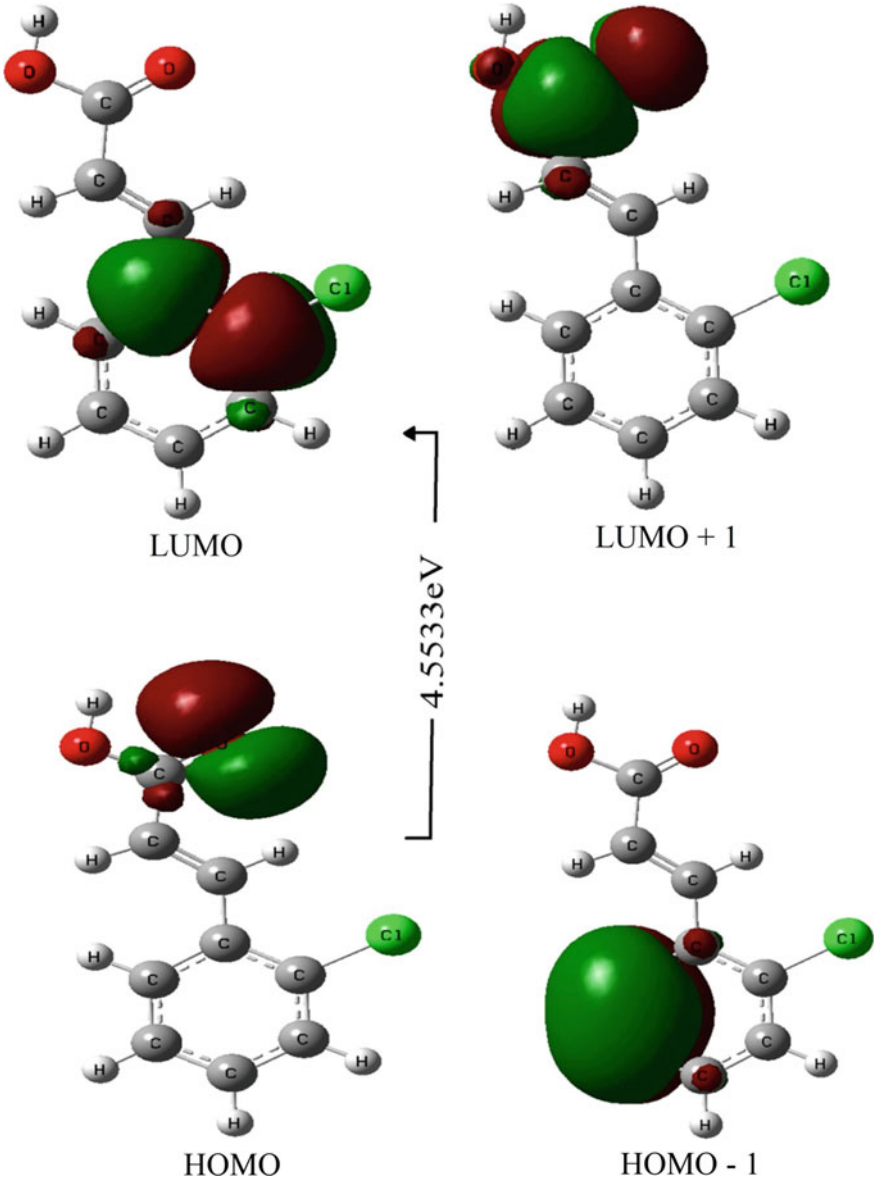

Fig. 7 Frontier molecular orbitals of *s–cis* conformer of *trans*–2–chlorocinnamic acid

respectively. The corresponding energies of 4CCA are −6.7817, −2.3451, −7.7950 and −1.0455 eV.

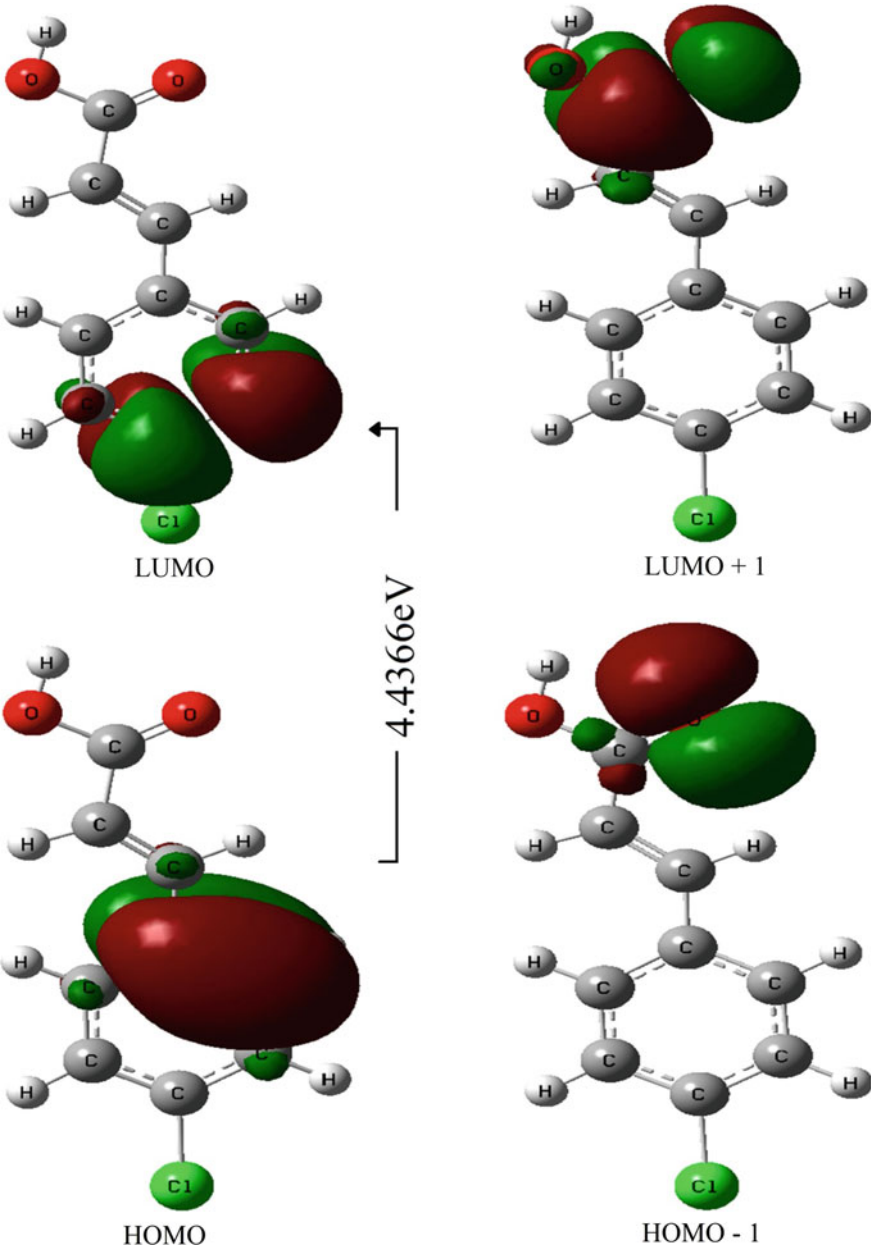

Fig. 8 Frontier molecular orbitals of *s–cis* conformer of *trans*–4–chlorocinnamic acid

7 Natural Bond Orbital Analysis

The type of bond orbital, the atom label, their occupancies, the natural atomic hybrids of which the NBO is composed, giving the percentage of the NBO on each hybrid and a hybrid label showing the hybrid orbital (sp^x) composition (the amount of *s*–character, *p*–character, etc.) can be determined by natural bond orbital (NBO) analysis [22, 23]. The charges of atoms of the neutral and ionic molecules of 2CCA and 4CCA calculated by NBO analysis using the B3LYP/cc–pVTZ method are presented in Tables 3 and 4. The variation in the atomic charges of ring carbon atoms are found significantly between 2CCA and 4CCA arised upon the electronic effects exerted by the chlorine atom. The atomic charges of C9 and O10 confirm the partial ionic nature of the carbonyl groups of 2CCA and 4CCA molecules.

Second order perturbation theory analysis of 2CCA and 4CCA by NBO method using B3LYP/cc–pVTZ method are summarised in Tables 5 and 6, respectively. The bonding orbital C1–C6 of 2CCA with 1.9673 electrons has 51.26 % C1 character in a $sp^{1.94}$ hybrid and has 48.74 % C6 character in a $sp^{1.81}$ hybrid orbital while for 4CCA the bonding orbital C1–C6 with 1.9754 electrons has 50.68 % C1 character in a $sp^{1.94}$ hybrid and has 49.32 % C6 character in a $sp^{1.77}$ hybrid orbital . The bonding orbital C9=O10 of 2CCA with 1.99677 electrons has 35.71 % C9 character in a $sp^{1.86}$ hybrid and has 64.29 % O10 character in a $sp^{1.52}$ hybrid orbital while in 4CCA the bonding orbital C9–O11 with 1.9968 electrons has 35.69 % C9 character in a $sp^{1.87}$ hybrid and has 64.31 % O11 character in a $sp^{1.53}$ hybrid orbital . The C9–O11 with 1.9951 electrons has 32.46 % C9 character in a $sp^{2.65}$hybrid and has 67.54 % O11 character in a $sp^{2.16}$ hybrid for 2CCA. In 4CCA bonding orbital for C9–O11 with 1.9951 electrons has 32.47 % C9 character in a $sp^{2.65}$ hybrid and has 67.53 % O11 character in a $sp^{2.16}$ hybrid. This confirms the delocalization of lone pair of electrons from the hydroxyl oxygen to carbonyl group.

Table 3 The charges and Fukui functions of *trans*–2–chlorocinnamic acid determined by B3LYP/cc–pVTZ method

Atom	Neutral	Anion	Cation	f_{k+}	f_{k-}	f_{k^o}	$\Delta f_{(k)}$
C1	–0.1124	–0.1303	0.0115	–0.0179	–0.1239	–0.0709	0.1060
C2	0.0253	–0.0153	0.0840	–0.0406	–0.0588	–0.0497	0.0182
C3	–0.2256	–0.2434	–0.2291	–0.0178	0.0035	–0.0072	–0.0213
C4	–0.1692	–0.3066	–0.0365	–0.1374	–0.1327	–0.1351	–0.0046
C5	–0.2000	–0.2091	–0.1359	–0.0091	–0.0642	–0.0366	0.0550
C6	–0.1548	–0.2301	–0.1498	–0.0752	–0.0051	–0.0402	–0.0702
C7	–0.1069	–0.2375	–0.0988	–0.1307	–0.0081	–0.0694	–0.1226
C8	–0.3037	–0.4347	–0.0962	–0.1310	–0.2074	–0.1692	0.0764
C9	0.7558	0.7123	0.7223	–0.0435	0.0335	–0.0050	–0.0770
O10	–0.5934	–0.6921	–0.5034	–0.0987	–0.0900	–0.0944	–0.0087
O11	–0.6739	–0.7138	–0.6414	–0.0399	–0.0326	–0.0362	–0.0073
Cl19	–0.0043	–0.0702	0.1489	–0.0659	–0.1532	–0.1095	0.0873

Table 4 The charge distributions and Fukui functions of *trans*–4–chlorocinnamic acid determined by B3LYP/cc–pVTZ method

Atom	Neutral	Anion	Cation	f_{k+}	f_{k-}	f_{k^o}	$\Delta f_{(k)}$
C1	−0.0846	−0.0998	0.0245	−0.0152	−0.1090	−0.0621	0.0938
C2	−0.1503	−0.1953	−0.1078	−0.0450	−0.0426	−0.0438	−0.0025
C3	−0.2262	−0.2602	−0.1920	−0.0340	−0.0342	−0.0341	0.0002
C4	0.0047	−0.0987	0.0992	−0.1034	−0.0944	−0.0989	−0.0090
C5	−0.2204	−0.2285	−0.1947	−0.0081	−0.0257	−0.0169	0.0176
C6	−0.1532	−0.2344	−0.1151	−0.0812	−0.0381	−0.0596	−0.0431
C7	−0.1121	−0.2366	−0.1089	−0.1245	−0.0032	−0.0639	−0.1213
C8	−0.3200	−0.4262	−0.1025	−0.1061	−0.2175	−0.1618	0.1114
C9	0.7524	0.7068	0.7180	−0.0456	0.0345	−0.0056	−0.0801
O10	−0.5815	−0.6922	−0.4825	−0.1107	−0.0991	−0.1049	−0.0116
O11	−0.6878	−0.7188	−0.6679	−0.0311	−0.0199	−0.0255	−0.0112
Cl19	−0.0010	−0.0918	0.1829	−0.0908	−0.1839	−0.1373	0.0932

Table 5 Second order perturbation theory analysis of trans–2–chlorocinnamic acid by NBO method using B3LYP/cc–pVTZ method

Donor (i) → Acceptor (j)	$E^{(2)a}$ (kJ.mol^{-1})	E(j) − E(i)[b] (a.u.)	F(i, j)[c] (a.u.)
π(C1–C2) → π*(C3–C4)	19.28	0.29	0.068
π(C1–C2) → π*(C5–C6)	17.85	0.30	0.066
π(C1–C2) → π*(C7–C8)	13.64	0.31	0.062
π(C3–C4) → π*(C1–C2)	21.47	0.27	0.070
π(C3–C4) → π*(C5–C6)	18.55	0.28	0.066
π(C5–C6) → π*(C1–C2)	19.79	0.27	0.067
π(C5–C6) → π*(C3–C4)	20.93	0.28	0.069
π(C7–C8) → π*(C1–C2)	12.19	0.29	0.057
π(C7–C8) → π*(C9–O10)	21.21	0.29	0.072
n(O10) → σ*(C8–C9)	20.45	0.67	0.107
n(O10) → σ*(C9–O11)	33.12	0.61	0.129
n(O11) → π*(C9–O10)	44.27	0.34	0.112
π(C1–C2) → π*(C3–C4)	252.31	0.01	0.080
π(C1–C2) → π*(C5–C6)	203.28	0.01	0.081
π(C1–C2) → π*(C7–C8)	55.24	0.03	0.068
π(C9–O10) → π*(C7–C8)	48.73	0.02	0.073

[a]Stabilisation (delocalization) energy
[b]Energy difference between *i*(donor) and *j*(acceptor) NBO orbitals
[c]Fock matrix element *i* and *j* NBO orbitals

Table 6 Second order perturbation theory analysis of *trans*–4–chlorocinnamic acid by NBO method using B3LYP/cc–pVTZ method

Donor (i) → Acceptor (j)	$E^{(2)a}$ (kJ.mol^{-1})	E(j) – E(i)[b] (a.u.)	F(i, j)[c] (a.u.)
π(C1–C2) → π*(C5–C6)	19.89	0.28	0.068
π(C1–C2) → π*(C7–C8)	17.17	0.29	0.068
π(C3–C4) → π*(C1–C2)	19.31	0.30	0.068
π(C3–C4) → π*(C5–C6)	18.46	0.30	0.067
π(C5–C6) → π*(C1–C2)	18.68	0.28	0.066
π(C5–C6) → π*(C3–C4)	21.20	0.27	0.069
π(C7–C8) → π*(C1–C2)	11.56	0.30	0.056
π(C7–C8) → π*(C9–O10)	21.56	0.29	0.073
n(O10) → σ*(C8–C9)	20.31	0.68	0.107
n(O10) → σ*(C9–O11)	32.97	0.61	0.129
n(O11) → π*(C9–O10)	44.33	0.34	0.112
n(Cl19) → σ* (C3–C4)	13.13	0.33	0.063
π(C1–C2) → π*(C7–C8)	91.65	0.01	0.066
π(C3–C4) → π*(C1–C2)	258.75	0.01	0.084
π(C3–C4) → π*(C5–C6)	203.58	0.01	0.079
π(C9–O10) → π*(C7–C8)	51.90	0.02	0.073

[a]Stabilisation (delocalization) energy
[b]Energy difference between *i*(donor) and *j*(acceptor) NBO orbitals
[c]Fock matrix element *i* and *j* NBO orbitals

7.1 Donor–Acceptor Interactions Analysis

The stabilisation energy of different kinds of interactions between 'filled' (donor) Lewis–type NBOs and 'empty' (acceptor) non–Lewis NBOs are estimated by 2nd order perturbation theory [22, 23]. An interaction with a bonding pair as the acceptor may strengthen the bond. In 2CCA and 4CCA molecules, the lone pair donor orbital, $n_O \rightarrow \pi^*_{CO}$ interaction between the oxygen (O11) lone pair and the C9–O10 antibonding orbital seems to give a strong stabilization by 44.28 and 44.28 kcal mol^{-1}, respectively. The bond pair donor orbital, $\pi_{CC} \rightarrow \pi^*_{CC}$ interaction from C3–C4 bond pair to C1–C2 and C5–C6 antibonding orbitals have the stabilisation energies 252.31 and 203.28 kcal mol^{-1}, respectively. In the case of 4CCA, $\pi_{CC} \rightarrow \pi^*_{CC}$ interaction from C1–C2 bond pair to C3–C4 and C5–C6 antibonding orbitals gives the strongest stabilisation of 258.75 and 203.58 kcal mol^{-1}.

8 Analysis of Structure–Activity Descriptors

The global reactivity descriptors namely chemical potential (μ), ionisation potential (I), electron affinity (A), global hardness (η), global softness (S), electronegativity (χ) and electrophilicity (ω) are predicted by the conceptual density functional theory and are summarized in Table 2.

The local reactivity and site selectivity are possible to study with the global parameters, however, the Fukui functions and local softness are extensively used to analyse the local reactive sites. All these global and local reactivity descriptors and the working equations for their computation have been described earlier [41–44]. The Fukui functions of the individual atoms of the neutral, cationic and anionic species of 2CCA and 4CCA compounds calculated by B3LYP/cc–pVTZ method are presented in Tables 5 and 6. The molecules under investigation mainly gives electrophilic and nucleophilic substitution reactions. It is clearly understood that the atoms C9 are favorable for nucleophilic attack. The ring atoms are favorable for electrophilic and nucleophilic attack.

The local softness, relative electrophilicity (s_k^+ / s_k^-) and relative nucleophilicity (s_k^- / s_k^+) indices, the dual local softness Δs_k and the multiphilicity descriptors ($\Delta\omega_k$) have also been determined to predict the reactive sites of the molecule and are summarised in Tables 7 and 8. The local philicity quantities describing for nucleophilic, electrophilic and free radical attack reveals the electron rich/deficient nature of the individual atoms. From the dual local softness (Δs_k) and the multiphilicity descriptors ($\Delta\omega_k$) one can understand that the atoms C1, C2, C3, C5 and C8 are favorable for nucleophilic attack. The other atoms are favorable for electrophilic attack. The local reactivity descriptors of the individual atoms of the molecule $s_k^a = f_k^a S$ $\omega_k^a = \omega f_k^a$ and f_k^a where, a = +, − and 0 are presented in Tables 7 and 8.

9 Vibrational Analysis

The geometry of the 2CCA and 4CCA molecules possesses C_S point group symmetry. All fundamental vibrations are distributed into the irreducible representations as $\Gamma_{vib} = 35A' + 16A''$. All vibrations are active in both IR and Raman spectra. The FTIR and FT–Raman spectra of 2CCA and 4CCA are given in Figs. 9 and 10, respectively. The FTIR and FT–Raman wavenumbers, the relative intensities and the assignments 2CCA and 4CCA are summarised in Tables 9 and 10, respectively along with the theoretically determined infrared and Raman frequencies.

Table 7 The Fukui functions (local reactivity descriptors) of *trans*–2–chlorocinnamic acid determined by B3LYP/cc–pVTZ method

Atom	s_k^+	s_k^-	s_k^0	Δs_k	ω_k^+	ω_k^-	ω_k^0	$\Delta\omega_k$	Electro philicity	Nucleo philicity
C1	−0.0022	−0.0155	−0.0089	0.0133	−0.0489	−0.3384	−0.1936	0.2895	0.1446	6.9179
C2	−0.0051	−0.0074	−0.0062	0.0023	−0.1109	−0.1605	−0.1357	0.0496	0.6909	1.4474
C3	−0.0022	0.0004	−0.0009	−0.0027	−0.0487	0.0096	−0.0195	−0.0583	−5.0769	−0.1970
C4	−0.0172	−0.0166	−0.0169	−0.0006	−0.3752	−0.3625	−0.3688	−0.0127	1.0350	0.9662
C5	−0.0011	−0.0080	−0.0046	0.0069	−0.0249	−0.1752	−0.1001	0.1503	0.1422	7.0340
C6	−0.0094	−0.0006	−0.0050	−0.0088	−0.2055	−0.0138	−0.1097	−0.1917	14.8696	0.0673
C7	−0.0164	−0.0010	−0.0087	−0.0154	−0.3568	−0.0220	−0.1894	−0.3348	16.1908	0.0618
C8	−0.0164	−0.0260	−0.0212	0.0096	−0.3579	−0.5665	−0.4622	0.2086	0.6317	1.5830
C9	−0.0055	0.0042	−0.0006	−0.0096	−0.1189	0.0914	−0.0138	−0.2103	−1.3013	−0.7685
O10	−0.0124	−0.0113	−0.0118	−0.0011	−0.2696	−0.2458	−0.2577	−0.0238	1.0969	0.9117
O11	−0.0050	−0.0041	−0.0045	−0.0009	−0.1089	−0.0890	−0.0990	−0.0200	1.2244	0.8167
Cl19	−0.0083	−0.0192	−0.0137	0.0109	−0.1798	−0.4183	−0.2991	0.2384	0.4300	2.3257

Table 8 The Fukui functions (local reactivity descriptors) of *trans*–4–chlorocinnamic acid determined by B3LYP/cc–pVTZ method

Atom	s_k^+	s_k^-	s_k^0	Δs_k	ω_k^+	ω_k^-	ω_k^0	$\Delta\omega_k$	Electro philicity	Nucleo Philicity
C1	−0.0019	−0.0139	−0.0079	0.0120	−0.0178	−0.1275	−0.0727	0.1097	0.1397	7.1589
C2	−0.0057	−0.0054	−0.0056	−0.0003	−0.0527	−0.0498	−0.0512	−0.0029	1.0580	0.9451
C3	−0.0043	−0.0044	−0.0043	0.0000	−0.0398	−0.0400	−0.0399	0.0002	0.9953	1.0047
C4	−0.0132	−0.0120	−0.0126	−0.0012	−0.1210	−0.1104	−0.1157	−0.0106	1.0956	0.9127
C5	−0.0010	−0.0033	−0.0022	0.0022	−0.0095	−0.0301	−0.0198	0.0206	0.3165	3.1597
C6	−0.0103	−0.0048	−0.0076	−0.0055	−0.0950	−0.0445	−0.0697	−0.0505	2.1335	0.4687
C7	−0.0159	−0.0004	−0.0081	−0.0155	−0.1456	−0.0037	−0.0747	−0.1419	38.9094	0.0257
C8	−0.0135	−0.0277	−0.0206	0.0142	−0.1242	−0.2544	−0.1893	0.1303	0.4880	2.0493
C9	−0.0058	0.0044	−0.0007	−0.0102	−0.0534	0.0403	−0.0065	−0.0937	−1.3234	−0.7556
O10	−0.0141	−0.0126	−0.0134	−0.0015	−0.1295	−0.1159	−0.1227	−0.0136	1.1172	0.8951
O11	−0.0040	−0.0025	−0.0032	−0.0014	−0.0363	−0.0233	−0.0298	−0.0131	1.5616	0.6404
Cl19	−0.0116	−0.0234	−0.0175	0.0119	−0.1062	−0.2151	−0.1606	0.1090	0.4935	2.0264

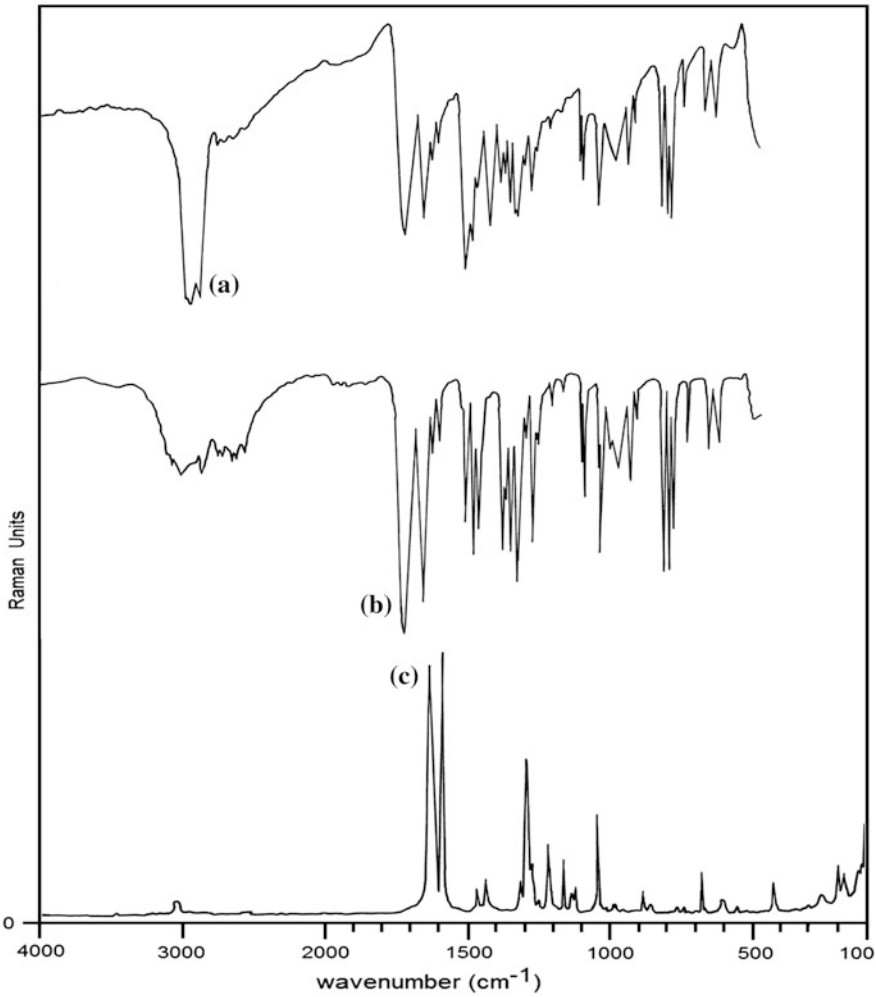

Fig. 9 FTIR **a** Nujol, **b** KBr and **c** FT–Raman spectra of *trans*–2–chlorocinnamic acid

9.1 Carbon–Carbon Vibrations

The carbon–carbon stretching modes of the phenyl group are expected in the range from 1640 to 1200 cm^{-1}. The actual positions of these modes are determined not so much by the nature of the substituents but by the form of substitution around the ring [45, 46]. The C–C stretching of 2CCA molecule is found in the IR spectrum at 1591, 1559, 1471, 1442 1288 and 1279 cm^{-1} while in Raman spectrum these are

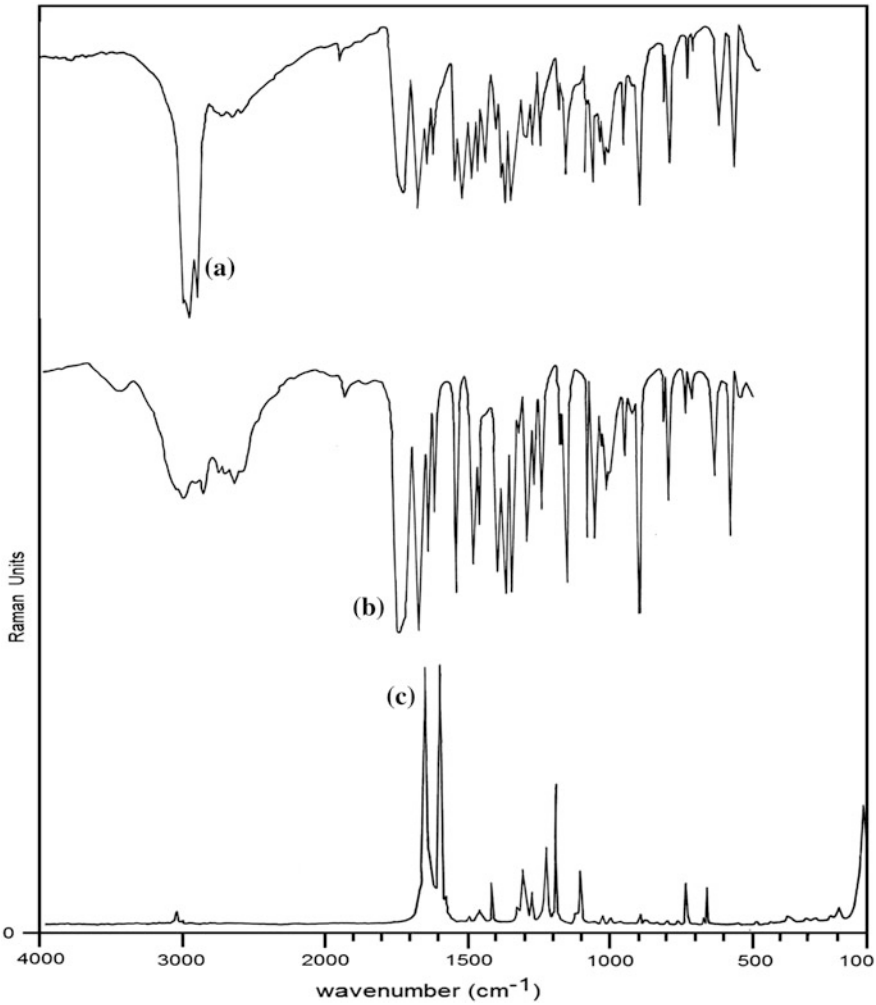

Fig. 10 FTIR **a** Nujol, **b** KBr and **c** FT–Raman spectra of *trans*–4–chlorocinnamic acid

observed at 1591, 1468, 1289 and 1274 cm^{-1}. Similarly the strong and very strong lines observed in the infrared spectrum of 4CCA at 1593, 1571, 1492, 1406, 1338 and 1285 cm^{-1} and in Raman the medium to strong lines observed at 1593, 1572, 1491, 1407 and 1295 cm^{-1} are ascribed to the C–C stretching modes. The propionic acid chain of 2CCA and 4CCA shows the C=C stretching vibrations at 1623 and 1627 in IR while in Raman at 1636 and 1640 cm^{-1}. This well agreed with the C=C stretching vibration conjucated with C=O group expected at around

1600 cm^{-1} [47]. The wavenumbers observed at 1228 and 1115 cm^{-1} in IR are assigned to C–C stretching mode of the propionic acid group of 2CCA. The wavenumbers seen at 1232 and 1119 cm^{-1} in the IR spectrum of 4CCA are attributed to the C–C stretching mode of the propionic acid group. Ring breathing mode appears near 1000 cm^{-1} in substituted benzenes [46]. In 2CCA ring breathing mode and the CCC trigonal bending vibrations exhibit the characteristic frequencies at 856 and 1039 cm^{-1} in infrared while in Raman at 858 and 1040 cm^{-1}, respectively. In 4CCA the corresponding ring breathing and trigonal bending modes are 1013 and 875 cm^{-1} in the IR spectrum. All the other CCC fundamental modes belong to in–plane and out of plane bendings are presented in Tables 9 and 10.

9.2 C–H Vibrations

The aromatic C–H stretching vibrations are normally found between 3100 and 3000 cm^{-1} [45, 46]. The C–H stretching of 2CCA and 4CCA are observed in this region. The C–H stretching vibrations are overlapped with the stretching of =C–H stretching vibrations. The =C–H stretching present in the acrylic acid part of 2CCA is found at 3023 cm^{-1}. The in–plane bending frequencies of olefenic hydrogen (=C–H) are normally observed in the higher wavenumber region than the C–H in–plane bending vibrations of phenyl group. Thus, the wavenumbers observed in the infrared spectrum of 2CCA at 1339 and 1307 cm^{-1} are assigned to the =C–H inplane bending vibration. In 4CCA, the corresponding frequencies are red shifted to 1306 and 1270 cm^{-1} in FTIR spectrum. The ring C–H in–plane bending of 2CCA are attributed to the wavenumbers 1051 and 1013 in IR and Raman spectra, respectively. The wavenumbers observed at 1178, 1095 and 984 in infrared spectrum of 4CCA are assigned to the C–H in–plane bending modes. The C–H out of plane bending modes are observed in the region 1000–600 cm^{-1}.

9.3 Carbon–Chlorine Vibrations

Strong characteristic absorption of C–X stretching vibration is influenced by neighbouring atoms or groups. The smaller the halide atom, the greater the influence of the neighbor [47]. The C–Cl stretching absorption is observed in the broad region between 850 and 550 cm^{-1}. The C–Cl stretching of 2CCA and 4CCA are observed as medium bands at 675 and 717 cm^{-1}. The in–plane bending and out of plane bending modes of C–Cl bond are presented in Tables 9 and 10.

Table 9 The observed FTIR, FT–Raman and calculated frequencies determined by B3LYP method with, 6–311++G** and cc–pVTZ basis sets along with their relative intensities and probable assignments of *trans*–2–chlorocinnamic acid[a]

Species	Experimental wavenumber (cm^{-1})		B3LYP/6–311++G**					B3LYP/cc–pVTZ				Depolarization ratio	Assignment
	FTIR	FTR	Unscaled (cm^{-1})	Scaled (cm^{-1})	IR intensity	Raman intensity	Depolarization ratio	Unscaled (cm^{-1})	Scaled (cm^{-1})	IR intensity	Raman intensity		
A′	3410 vw		3751	3405	101.07	184.75	0.28	3768	3401	111.98	173.68	0.26	νO–H
A′	3061 m		3207	3057	5.03	227.15	0.15	3205	3053	4.56	229.31	0.13	νC–H
A′			3201	3037	9.92	86.67	0.29	3198	3030	8.91	89.45	0.27	ν=C–H
A′			3195	3031	1.94	57.75	0.40	3193	3025	1.76	51.49	0.46	νC–H
A′		3036 w	3187	3032	6.24	66.69	0.69	3185	3028	6.33	72.98	0.67	νC–H
A′	3023 w		3183	3019	2.26	52.95	0.22	3180	3015	1.34	45.32	0.18	ν=C–H
A′			3176	3013	0.57	50.88	0.75	3174	3007	0.51	48.31	0.75	νC–H
	2811 w												1442 + 1339
	2606 m												2 × 1307
	2595 m												2 × 1288
	2531 m												2 × 1279
A′	1689 vs		1792	1686	279.36	56.52	0.28	1786	1683	336.47	84.87	0.30	νC=O
A′	1623 vs	1636 vs	1683	1633	205.18	954.54	0.30	1678	1630	233.30	1064.05	0.29	νC=C
A′	1591 m	1591 vs	1634	1588	23.16	462.68	0.41	1631	1585	23.82	502.61	0.42	νC–C
A′	1559 w		1602	1556	3.83	3.07	0.31	1599	1553	5.75	3.74	0.51	νC–C
A′	1471 s	1468 w	1506	1468	25.59	48.83	0.34	1500	1465	24.86	46.50	0.37	νC–C
A′	1442 s	1440 w	1476	1439	31.21	25.18	0.40	1468	1436	31.51	26.83	0.37	νC–O(H)
A′			1384	1354	144.41	13.56	0.17	1375	1343	150.22	18.99	0.17	νC–C

(continued)

Table 9 (continued)

Species	Experimental wavenumber (cm^{-1})		B3LYP/6–311++G**					B3LYP/cc–pVTZ				Depolarization ratio	Assignment
	FTIR	FTR	Unscaled (cm^{-1})	Scaled (cm^{-1})	IR intensity	Raman intensity	Depolarization ratio	Unscaled (cm^{-1})	Scaled (cm^{-1})	IR intensity	Raman intensity		
A′	1339 s		1351	1337	14.71	45.13	0.37	1348	1334	10.54	45.19	0.35	β=C–H
A′	1307 s	1315 w	1313	1313	13.76	92.78	0.34	1310	1310	17.28	61.74	0.37	β=C–H
A′	1288 s	1289 s	1310	1287	3.17	38.10	0.28	1305	1284	5.42	73.44	0.28	νC–C
A′	1279 s	1274 m	1275	1277	18.62	60.42	0.35	1271	1274	19.12	59.02	0.33	νC–C
A′	1228 s		1230	1226	10.77	51.75	0.25	1227	1223	11.06	53.15	0.24	νC–C
A′			1190	1164	3.88	27.68	0.44	1187	1158	3.50	27.51	0.42	βC–H
A′	1155 vw	1160 m	1146	1153	32.91	53.97	0.18	1144	1155	25.51	52.53	0.18	βO–H
A′	1115 vw	1121 w	1137	1119	492.31	59.34	0.29	1135	1116	541.04	71.42	0.30	νC–C
A′	1051 m		1073	1049	5.04	11.77	0.10	1070	1046	4.63	15.79	0.06	βC–H
A′	1039 m	1040 s	1057	1038	50.19	69.99	0.17	1052	1035	55.66	75.70	0.14	TB
A′		1013 vw	1037	1011	24.88	18.30	0.34	1027	1008	30.26	26.93	0.32	βC–H
A″	985 s	986 vw	1006	984	0.58	0.69	0.35	998	981	0.89	0.79	0.53	γ=C–H
A′	975 m		977	973	3.02	2.42	0.45	970	970	7.41	5.63	0.72	βC=C
A″	920 m		964	918	15.96	8.38	0.73	960	915	6.79	4.66	0.75	γ=C–H
A′			907	896	14.10	8.93	0.74	903	880	13.74	8.66	0.74	βC–H
A″	875 m	886 w	886	884	0.81	1.00	0.29	875	881	0.38	1.49	0.33	γC–H
A′	856 s	858 vw	857	854	1.75	6.72	0.73	854	853	2.51	6.99	0.71	RB
A′	758 s	768 vw	783	766	59.87	0.52	0.46	777	763	68.46	1.48	0.54	βC=O
A″	736 s	740 vw	763	738	8.63	2.13	0.54	754	735	8.77	1.63	0.42	γC–H
A″			720	711	22.22	1.70	0.67	716	698	27.47	1.09	0.40	γC–H

(continued)

Table 9 (continued)

Species	Experimental wavenumber (cm^{-1})		B3LYP/6–311++G**					B3LYP/cc–pVTZ				Depolarization ratio	Assignment
	FTIR	FTR	Unscaled (cm^{-1})	Scaled (cm^{-1})	IR intensity	Raman intensity	Depolarization ratio	Unscaled (cm^{-1})	Scaled (cm^{-1})	IR intensity	Raman intensity		
A′	675 m	683 m	713	681	15.33	0.33	0.30	708	679	12.73	0.36	0.69	νC–Cl
A″	600 m	610 w	656	608	11.32	15.54	0.29	654	606	11.01	17.26	0.24	γC=O
A″			600	592	83.66	3.93	0.75	591	575	93.51	2.14	0.68	γO–H
A″	561 m	558 vw	587	559	57.99	1.61	0.54	585	557	57.87	1.62	0.51	γC–H
A′			544	538	7.93	0.37	0.66	544	529	9.25	0.25	0.47	βC–O
A″			523	517	4.42	0.23	0.75	519	505	6.12	0.38	0.74	γC–C–C
A′	436 w	430 m	459	435	2.55	1.38	0.44	457	432	3.14	1.65	0.50	βC–Cl
A′		416 w	413	415	7.38	8.63	0.26	413	412	7.91	9.58	0.24	βCC
A′			397	384	1.57	0.75	0.45	398	386	1.51	0.68	0.34	βCCC
A′		307 w	296	306	0.59	2.29	0.61	295	303	0.73	2.73	0.50	βCC
A″		260 w	237	259	0.36	2.44	0.20	237	256	0.10	1.95	0.18	γC–O
A″		205 m	232	204	1.03	2.11	0.75	231	201	1.21	2.04	0.68	γC–Cl
A″		163 w	168	162	0.00	2.65	0.70	165	159	0.01	1.81	0.72	γC–C–C
A″		134 m	131	133	0.98	3.27	0.46	133	130	1.09	4.17	0.51	γC–C–C
A″		101 w	85	100	0.06	0.67	0.75	84	97	0.06	0.60	0.75	γC–C
A″			79	77	0.07	3.19	0.74	78	72	0.08	2.81	0.72	γC–C
A″			20	18	0.94	1.44	0.57	27	23	0.97	1.68	0.62	γC–C

[a] *ν*—stretching; *β*—in–plane bending; *δ*—deformation; *ρ*—rocking; *γ*—out of plane bending; *ω*—wagging and *τ*—twisting

Table 10 The observed FTIR, FT–Raman and calculated frequencies determined by B3LYP method with 6–311++G** and cc–pVTZ basis sets along with their relative intensities and probable assignments of *trans*–4–chlorocinnamic acid[a]

Species	Experimental wavenumber (cm^{-1})		B3LYP/6–311++G**					B3LYP/cc–pVTZ					
	FTIR	FTR	Unscaled (cm^{-1})	Scaled (cm^{-1})	IR intensity	Raman intensity	Depolarization ratio	Unscaled (cm^{-1})	Scaled (cm^{-1})	IR intensity	Raman Intensity	Depolariza–tion ratio	Assignment
A′	3421 w		3751	3421	106.75	190.96	0.28	3768	3422	118.31	177.06	0.26	νO–H
A′			3207	3048	1.45	214.65	0.19	3205	3045	1.53	216.17	0.16	νC–H
A′		3035 vw	3206	3036	3.89	38.56	0.71	3203	3035	3.18	42.54	0.62	νC–H
A′			3198	3039	3.81	25.06	0.49	3196	3036	3.73	22.92	0.47	ν=C–H
A′			3185	3027	3.51	19.60	0.75	3183	3024	3.55	20.96	0.75	νC–H
A′			3177	3019	4.59	62.61	0.49	3175	3016	4.38	62.19	0.49	νC–H
A′			3152	2995	0.41	37.50	0.25	3150	2993	0.43	36.64	0.24	ν=C–H
	2991 m												2 × 1492
	2976 m												1593 + 1406
	2671 m												2 × 1338
	2630 m												2 × 1306
	2590 m												2 × 1285
	2525 m												2 × 1270
A′	1701vs		1789	1703	298.95	69.89	0.30	1781	1700	359.14	103.61	0.32	νC=O
A′	1627vs	1640 vs	1685	1646	268.86	1346.90	0.31	1681	1643	302.32	1506.21	0.30	νC=C
A′	1593 s	1593 vs	1632	1595	90.60	1164.62	0.38	1629	1592	105.27	1243.95	0.39	νC–C
A′	1571 s	1572 w	1602	1573	13.58	36.98	0.36	1599	1571	14.10	39.73	0.36	νC–C

(continued)

Table 10 (continued)

Species	Experimental wavenumber (cm^{-1})		B3LYP/6–311++G**					B3LYP/cc–pVTZ					
	FTIR	FTR	Unscaled (cm^{-1})	Scaled (cm^{-1})	IR intensity	Raman intensity	Depolarization ratio	Unscaled (cm^{-1})	Scaled (cm^{-1})	IR intensity	Raman Intensity	Depolariza–tion ratio	Assignment
A′	1492 vs	1491 vw	1529	1494	67.72	10.71	0.34	1522	1491	74.09	13.11	0.28	νC–C
A′	1406 s	1407 w	1442	1409	34.22	27.34	0.40	1436	1406	33.76	29.37	0.40	νC–C
A′	1338 s		1385	1340	146.77	22.19	0.20	1376	1337	157.76	24.51	0.18	νC–O
A′	1318 s	1326 w	1358	1328	9.37	46.80	0.24	1354	1325	8.97	51.46	0.22	νC–C
A′	1306 vs	1305 w	1329	1308	2.75	5.97	0.73	1323	1305	1.98	6.32	0.72	β=C–H
A′	1285 vs	1295 m	1318	1297	0.81	2.71	0.39	1315	1294	2.30	5.93	0.32	νC–C
A′	1270 w	1263 w	1279	1273	9.12	154.63	0.32	1275	1269	8.35	150.99	0.31	β=C–H
A′	1232 s	1224 m	1232	1235	16.64	100.39	0.30	1229	1231	17.26	104.70	0.28	νC–C
A′	1178 m	1177 s	1206	1181	6.21	139.59	0.26	1203	1177	6.68	153.51	0.26	βC–H
A′			1141	1121	304.99	93.51	0.29	1139	1115	348.38	115.41	0.31	βO–H
A′	1119 w	1121w	1131	1124	168.21	22.42	0.36	1129	1120	163.09	23.05	0.39	νC–C
A′	1095 m		1103	1098	175.15	152.18	0.20	1101	1094	193.04	162.38	0.18	βC–H
A′	1013 s	1024 vw	1037	1027	25.81	1.67	0.75	1028	1022	29.81	11.65	0.16	TB
A′	984 s	997 vw	1033	987	25.18	12.57	0.18	1026	982	31.34	1.83	0.75	βC–H
A″			989	971	0.00	0.12	0.75	980	995	0.00	0.12	0.75	γ=C–H
A′	968 w		980	945	1.81	0.38	0.75	965	940	22.02	15.83	0.70	βC=C
A″	942 m		965	895	26.46	16.22	0.66	964	890	1.67	0.42	0.75	γ=C–H

(continued)

Table 10 (continued)

Species	Experimental wavenumber (cm^{-1})		B3LYP/6–311++G**					B3LYP/cc–pVTZ					
	FTIR	FTR	Unscaled (cm^{-1})	Scaled (cm^{-1})	IR intensity	Raman intensity	Depolarization ratio	Unscaled (cm^{-1})	Scaled (cm^{-1})	IR intensity	Raman Intensity	Depolariza–tion ratio	Assignment
A′		892 vw	907	878	5.42	8.31	0.75	900	873	6.89	9.73	0.75	βC–H
A′	875 m		856	863	14.08	6.26	0.34	853	858	17.19	7.56	0.29	RB
A″	860 w		852	825	63.34	0.20	0.75	840	820	68.43	0.08	0.75	γC–H
A″	822 vs		840	826	0.04	1.05	0.75	831	812	0.59	0.07	0.75	γC–H
A′	747 w	733 w	764	750	5.26	1.15	0.75	757	745	4.39	1.90	0.75	βCCC
A″			719	720	12.58	2.13	0.75	713	697	13.00	0.83	0.75	γC–H
A′	717 m	710 w	707	708	22.18	19.21	0.16	706	715	22.72	22.34	0.14	νC–Cl
A″	642 w	637 w	650	645	0.47	7.87	0.71	647	640	0.54	8.50	0.71	γC=O
A′			623	614	31.09	2.03	0.52	622	608	29.27	2.14	0.48	βC=O
A″	549 m	553 vw	600	556	98.76	3.71	0.75	585	551	113.41	1.49	0.75	γO–H
A″			524	517	6.05	0.44	0.60	523	511	6.57	0.32	0.53	γC–H
A″	493 s	485 vw	508	496	5.04	0.39	0.75	504	491	3.84	0.15	0.75	γC–C–C
A′		437 vw	446	440	34.61	0.32	0.63	445	435	36.48	0.34	0.71	βCC
A″			420	415	0.01	0.04	0.75	418	408	0.01	0.00	0.75	γC–C–C
A″			353	349	0.27	1.24	0.75	350	341	0.50	1.11	0.75	γC–C–C
A′			343	339	2.55	0.74	0.72	344	335	2.66	0.81	0.72	βCC
A″		281 vw	260	258	1.08	1.56	0.15	260	279	1.10	1.75	0.11	γC–O
A′		200 vw	210	204	0.42	2.61	0.29	209	198	0.39	2.95	0.26	βCO
A′			182	182	0.03	0.59	0.75	180	174	0.08	0.25	0.75	βC–Cl
A″		116 m	137	120	1.01	0.91	0.75	134	114	1.21	0.78	0.75	γC–C–C

(continued)

Table 10 (continued)

Species	Experimental wavenumber (cm^{-1})		B3LYP/6–311++G**					B3LYP/cc–pVTZ					
	FTIR	FTR	Unscaled (cm^{-1})	Scaled (cm^{-1})	IR intensity	Raman intensity	Depolarization ratio	Unscaled (cm^{-1})	Scaled (cm^{-1})	IR intensity	Raman Intensity	Depolariza–tion ratio	Assignment
A″			85	87	0.50	0.36	0.64	85	81	0.52	0.34	0.64	γC–Cl
A″			58	61	1.02	0.13	0.75	57	54	0.96	0.09	0.75	γC–C
A″			35	38	0.39	0.39	0.75	34	31	0.36	0.18	0.75	γ C–C

v—stretching; *β*—in–plane bending; *δ*—deformation; *ρ*—rocking; *γ*—out of plane bending; *ω*—wagging and *τ*—twisting

9.4 Carboxylic Acid Group Vibrations

The O–H stretching is observed in the region 3600–3200 cm^{-1} as a broad band [48]. The weak intensity bands seen at 3410 and 3421 cm^{-1} is due to O–H stretching vibration of 2CCA and 4CCA. The C=O stretching vibration is normally found in the region 1800–1600 cm^{-1}. The wavenumbers observed at 1689 and 1701, the very strong modes in FTIR, are assigned to the C=O stretching vibrations of 2CCA and 4CCA molecules, respectively. Another strong band appears around 1700 cm^{-1} (1700–1680 cm^{-1} for aromatic acids) due to C–O stretching. The C–O stretching mode is the strongest band in the infrared spectrum and appears with diminished intensity in the Raman spectrum. The very strong IR band observed at 1442 cm^{-1} and 138 cm^{-1} in FTIR are assigned to the C–O stretching of 2CCA and 4CCA mplecules, respectively. All other in–plane and out of plane bending vibrations of the –COOH group are presented in Tables 9 and 10.

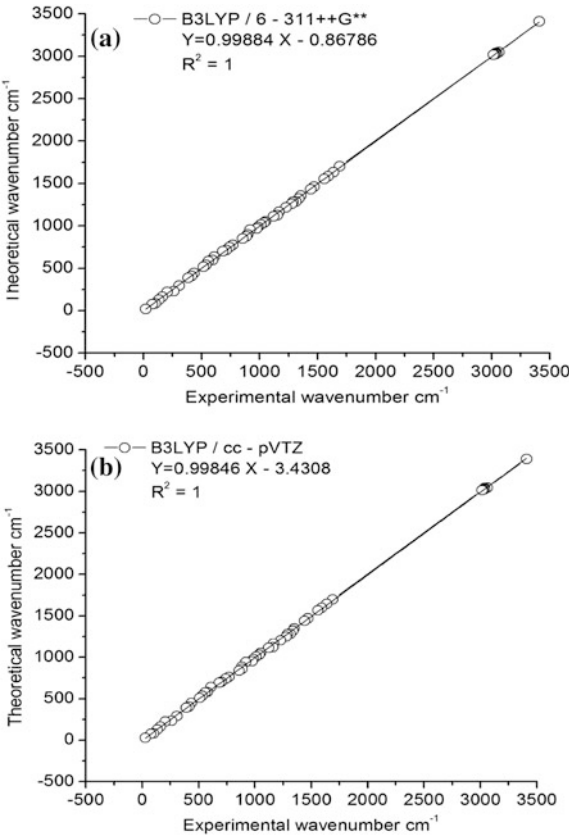

Fig. 11 Correlation of the experimental and theoretical wavenumbers of *trans*–2–chlorocinnamic acid by **a** B3LYP/6-311++G** and **b** B3LYP/cc-pVTZ methods

10 Scale Factors

The inclusion of anhormonicty in the computed frequencies can be eliminated by scaling the theoretical wavenumbers. The linear scaling equation method has been used [22, 23, 49–52] that brings the experimental and theoretical vibrational frequencies closer together. The scaling equation $y = 0.9988x - 0.8679$ and $y = 0.9985x - 3.4308$ are used in the case of 2CCA with 6–311++G** and cc–pVTZ basis sets, respectively. In the case of 4CCA, the scaling equations $y = 1.0009x - 2.4978$ and $y = 0.9990x + 3.7016$ are used to found the scaled wavenumbers with cc–pVTZ and 6–311 ++G** basis sets, respectively. The RMS deviation between the experimental and observed wavenumbers are 2.38 and 5.35 for 2CCA while for 4CCA these are 2.78 and 1.59 using cc–pVTZ and 6–311 ++G** basis sets, respectively. The correlation of the experimentally observed and theoretically determined wavenumbers of 2CCA and 4CCA are shown in Figs. 11a, b and 12a, b, respectively.

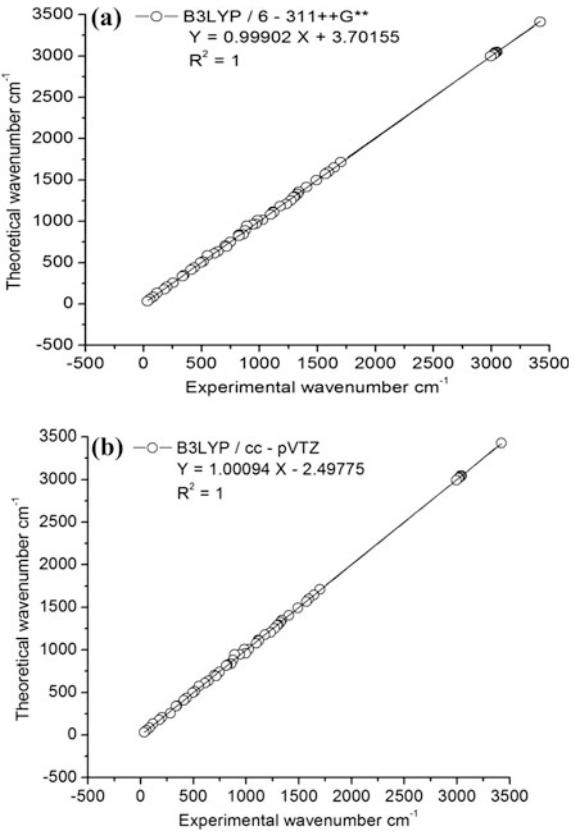

Fig. 12 Correlation between the experimental and theoretical wavenumbers of *trans*–4–chlorocinnamic acid by **a** B3LYP/6-311++G** and **b** B3LYP/cc-pVTZ methods

11 Conclusion

The bond distances, bond angles, dihedral angles, the kinetic and thermodynamic stability of the molecule, global and local reactivity parameters, the energy gap between the frontier molecular orbitals, the probable electronic transitions and bonding concepts of 2CCA and 4CCA compounds are elaborated in the present investigation.

(i) The most stable geometry of *trans*–2–chloro–cinnamic acid and *trans*–4–chloro–cinnamic acid under investigation are identified by conformational analysis and the exact geometry are determined by the optimisation with B3LYP method using cc–pVTZ and 6–311++G** basis sets.

(ii) The *s–cis* orientation of the carbonyl group (C=O) and the C=C bond appears as the only stable structure in 2CCA and is more stable by 0.6648 kcal mol–1 than the corresponding *s–trans* conformation. In 4CCA, the *s–cis* conformer is more stable than the *s–trans* conformer by 0.8939 kcal mol^{-1}.

(iii) Complete vibrational assignments of the observed modes in FTIR and FT–Raman spectra of the *s–cis* conformers of 2CCA and 4CCA have been done and analysed.

(iv) The relative stabilities, HOMO–LUMO energy gap and implications of the electronic properties are examined and discussed. The frontier orbital energy gap of 2CCA and 4CCA are 4.5533 and 4.4366 eV, respectively shows that 4CCA is highly reactive than 2CCA molecule.

(v) Significant variation in the atomic charges of ring carbon atoms are found between 2CCA and 4CCA arised upon the electronic effects exerted by the chlorine atom. The atomic charges of C9 and O10 confirm the partial ionic nature of the carbonyl groups of 2CCA and 4CCA molecules.

(vi) The bond pair donor orbital, $\pi CC \rightarrow \pi^*CC$ interaction from C3–C4 bond pair to C1–C2 and C5–C6 antibonding orbitals have the stabilisation energies 252.31 and 203.28 kcal mol^{-1}, respectively. In the case of 4CCA, $\pi CC \rightarrow \pi^*CC$ interaction from C1–C2 bond pair to C3–C4 and C5–C6 antibonding orbitals gives the strongest stabilisation of 258.75 and 203.58 kcal mol^{-1}

vii The chemical reactivity and site selectivity of the molecule has been determined with the help of global and local reactivity descriptors. It is clearly understood that the atoms C9 are favorable for nucleophilic attack. The ring atoms are favorable for electrophilic and nucleophilic attack.

References

1. Tonari, K., Mitsiu, K., Yonemoto, K.: J. Olea. Sci. **51**, 271 (2002)
2. Tawata, S., Taira, S., Kobamoto, N., Zhu, J., Ishihara, M., Toyama, S.: Biosci. Biotechnol. Biochem. **60**, 909 (1996)

3. Epifano, F., Curini, M., Genovese, S., Blaskovich, M., Hamilton, A., Sebti, S.M.: Bioorg. Med. Chem. Lett. **17**, 2639 (2007)
4. Kroon, P.A., Williamzon, G.: J. Sci. Food Agric. **79**, 355 (1999)
5. Mizoguchi, K., Hasegawa, E.: Polym. Adv. Technol. **7**, 471 (1996)
6. Lee, E.J., Kim, S.R., Kim, J., Kim, Y.C.: Planta Med. **68**, 407 (2002)
7. Natella, F., Nardini, M., Felice, M., Scaccini, C.: J. Agric. Food Chem. **47**, 1453 (1999)
8. Liu, I.M., Hsu, F.L., Chen, C.F., Cheng, J.T.: Br. J. Pharmacol. **129**, 631 (2000)
9. Sheena Mary, Y. Raju, K., Yohannan Panicker, C., Al–Saadi, A.A., Thiemann, T., Van Alsenoy, C.: Spectrochim **128A**, 638 (2014)
10. Sheena Mary, Y., Raju, K., Yohannan Panicker, C., Al–Saadi, A., Thiemann, T.: Spectrochim **131A**, 471 (2014)
11. Sert, Y., Dogan, H., Navarrete, A., Somanathan, R., Aguirre, G., Cirak, C.: Spectrochim. Acta **128A**, 119 (2014)
12. Mizoguchi, K., Hasegawa, E.: Polym. Adv. Technol. **7**, 471 (1996)
13. Reichmanis, E., Nalamasu, O., Houlihan, F.M., Novembre, A.E.: Polym. Int. **48**, 1053 (1999)
14. Sakai, Y., Ueda, M., Fukuda, T., Matsuda, M.J.: Polym. Sci., Part A. Polym. Chem. **37**, 1321 (1999)
15. Balaji, R., Grande, D., Nanjundan, S.: Polymer **45**, 1089 (2004)
16. Decker, C. : In: Meijer, H.E.H. (ed.) Materials Science and Technology, vol. 18, pp. 615–657. VCH, Weinheim (1997)
17. Fernandes, M.A., Levendis, D.C.: Acta Cryst. **B60**, 315 (2004)
18. Bryan, R.F., Freyberg, D.P.: J. Chem. Soc. Perkin Trans. **2**, 1835 (1975)
19. Xia, Z., Correa, R.G., Das, J.K., Farhana, L., Castro, D.J., Yu, J., Oshima, R.G., Fontana, J. A., Reed, J.C., Dawson, M.I.: J. Med. Chem. **55**, 233 (2012)
20. Xia, Z., Farhana, L., Correa, R.G., Das, J.K., Castro, D.J., Yu, J., Oshima, R.G., Reed, J.C., Fontana, J.A., Dawson, M.I.: J. Med. Chem. **54**, 3793 (2011)
21. Sun, F.M., Wang, J.S., Traxler, R.W.: Chemosphere **40**, 1417 (2000)
22. Arjunan, V., Anitha, R., Marchewka, M.K., Mohan, S., Yang, H.: J. Mol. Struct. **1080**, 122 (2015)
23. Arjunan, V., Anitha, R., Thenmozhi, S., Marchewka, M.K., Mohan, S.: J. Mol. Struct. **1113**, 42 (2016)
24. Hohenberg, P., Kohn, W.: Phys. Rev. B **136**, 864 (1964)
25. Becke, A.D.: J. Chem. Phys. **98**, 5648 (1993)
26. Becke, A.D.: Phys. Rev. A **38**, 3098 (1988)
27. Lee, C., Yang, W., Parr, R.G.: Phys. Rev. B **37**, 785 (1988)
28. Frisch, M.J., Trucks, G.W., Schlegel, H.B., Scuseria, G.E., Robb, M.A., Cheeseman, J.R., Scalmani, G., Barone, V., Mennucci, B., Petersson, G.A., Nakatsuji, H., Caricato, M., Li, X., Hratchian, H.P., Izmaylov, A.F., Bloino, J., Zheng, G., Sonnenberg, J.L., Hada, M., Ehara, M., Toyota, K., Fukuda, R., Hasegawa, J., Ishida, M., Nakajima, T., Honda, Y., Kitao, O., Nakai, H., Vreven, T., Montgomery Jr., J.A., Peralta, J.E., Ogliaro, F., Bearpark, M., Heyd, J. J., Brothers, E., Kudin, K.N., Staroverov, V.N., Kobayashi, R., Normand, J., Raghavachari, K., Rendell, A., Burant, J.C., Iyengar, S.S., Tomasi, J., Cossi, M., Rega, N., Millam, J.M., Klene, M., Knox, J.E., Cross, J.B., Bakken, V., Adamo, C., Jaramillo, J., Gomperts, R., Stratmann, R.E., Yazyev, O., Austin, A.J., Cammi, R., Pomelli, C., Ochterski, J.W., Martin, R.L., Morokuma, K., Zakrzewski, V.G., Voth, G.A., Salvador, P., Dannenberg, J.J., Dapprich, S., Daniels, A.D., Farkas, O., Foresman, J.B., Ortiz, J.V., Cioslowski, J., Fox, D.J.: Gaussian 09, Revision A.02. Gaussian, Inc., Wallingford (2009)
29. Schlegel, H.B.: J. Comput. Chem. **3**, 214 (1982)
30. Keresztury, G., Holly, S., Besenyei, G., Varga, J., Wang, A., Durig, J.R.: Spectrochim. Acta **49A**, 2007 (1993)
31. Murray, J.S., Sen, K.: Molecular Electrostatic Potentials, Concepts and Applications. Elsevier, Amsterdam (1996)
32. Chidangil, S., Shukla, M.K., Mishra, P.C.: J. Mol. Model. **4**, 250 (1998)

33. Dennington, R.I., Keith, T., Millam, J.: GaussView, Version 5.0.8. Semichem, Inc., Shawnee Mission, KS (2008)
34. Parr, R.G., Yang, W.: J. Am. Chem. Soc. **106**, 4049 (1984)
35. Yang, W., Parr, R.G.: Proc. Natl. Acad. Sci. U.S.A. **82**, 6723 (1985)
36. Anderson, J.E., Doecke, C.W., Pearson, H.: J. Chem. Soc. Perkin **II**, 336 (1976)
37. Palinko, I.: Acta Cryst. **B55**, 216 (1999)
38. Fernandes, M.A., Levendis, D.C.: Acta Cryst. **B60**, 315 (2004)
39. Howard, J.A., Mahon, M.F., Raithby, P.R., Sparkes, H.A.: Acta Cryst. **B65**, 230 (2009)
40. Hsieh, T.-J., Su, C.-C., Chen, C.-Y., Liou, C.-H., Lu, L.-H.: J. Mol. Struct. **741**, 193 (2005)
41. Parr, R.G., Yang, W.: Density Functional Theory of Atoms and Molecules. Oxford University Press, Oxford (1989)
42. Pearson, R.G.: Chemical Hardness e Applications from Molecules to Solids. VCH Wiley, Weinheim (1997)
43. Geerlings, P., De Proft, F., Langenaeker, W.: Chem. Rev. **103**, 1793 (2003)
44. Chattaraj, P.K. (ed.), Special Issue of J. Chem. Sci. On Chemical Reactivity, vol. 117 (2005)
45. Bellamy, L.J.: The Infrared Spectra of Complex Molecules, 3rd edn. Wiley, New York (1975)
46. Varsanyi, G.: Assignments for Vibrational Spectra of Seven Hundred Benzene Derivatives, vol. I. Adam Hilger, London (1974)
47. Scorates,G., Infrared Characteristic Group: Frequencies. Wiley, New York (1981)
48. Silverstein, R.M., Webster, F.X.: Spectroscopic Identification of Organic Compound, 6th edn. John Wiley & Sons, New York (1998)
49. Hameka, H.F., Jensen, J.O.: J. Mol. Struct. (Theochem) **362**, 325 (1996)
50. Jensen, J.O., Banerjee, A., Merrow, C.N., Zeroka, D., Lochner, J.M.: J. Mol. Struct. (Theochem) **531**, 323 (2000)
51. Scott, A.P., Radom, L.: J. Phys. Chem. **100**, 16502 (1996)
52. Alcolea Palafox, M., Gill, M., Nunez, N.J., Rastogi, V.K., Mittal, L.: Int. J. Quant. Chem. **103**, 394 (2005)

Analysis of Vibrational, Electronic and Reactivity Properties of Adenine Using Spectroscopic and Computational Tools

D. Bakkiyaraj, S. Periandy, S. Xavier and Joazaizulfazli Jamalis

Abstract The pharmaceutical important adenine was investigated theoretically and the data are compared with the experimental results. The geometrical and vibrational analyses were carried out on the confirmed stable structure of the compound. The chemical shift and electronic spectra of the title compound were carried out and compared with experimental data. The charge analysis, NBO, HOMO-LUMO, thermodynamic analysis and NLO properties were studied.

1 Introduction

Adenine [1] is a purine derivative (nucleobase) and it is an important component in all biological systems. It is present in the deoxyribonucleic acid (DNA), where it pairs with nucleobase cytosine. Adenine is also known as 6-aminopurine which possesses the structure of the pyrimidyl pyrine. In biochemistry Adenine plays variety of roles as an organic purine especially in cellular respiration with its derivatives of adenine like adenosine triphosphate (ATP), nicotinamide adenine dinucleotide (NAD) and flavin adenine dinucleotide (FAD). It functions as a chemical component of RNA and DNA in the proton synthesis [2]. ATP is being employed in cellular metabolism to transfer energy between the reactions. Adenine

D. Bakkiyaraj (✉)
Research & Development Centre, Bharathiar University,
Coimbatore 641046, India
e-mail: bakkiyaraj2009@gmail.com

S. Periandy
Department of Physics, Kanchi Mamunivar Centre
for Post Graduate Studies, Puducherry, India

S. Xavier
Department of Physics, St. Joseph College of Arts and Science,
Cuddalore, Tamil Nadu, India

J. Jamalis
Department of Chemistry, Universiti Teknologi Malaysia, Skudai, Malaysia

J. Ebenezar (ed.), *Recent Trends in Materials Science and Applications*,
Springer Proceedings in Physics 189, DOI 10.1007/978-3-319-44890-9_53

was sometimes called as vitamin B_4 [3], but it can never be considered a true vitamin or part of vitamin B complex. As important cofactors of NAD and FAD, the two B vitamins, niacin and riboflavin is being connected with the derivatives.

Many works have been carried out on adenine [1–8] based on its pharmaceutical uses. Nowak et al. [6] have recorded the argon (Ar) matrix spectrum of adenine and analyzed it using harmonic calculations. Lappi et al. [8] have the analyzed of adenine matrix isolation spectra, by B3-LYP/6-31G* and GGA/DNP computational methods. However, the NBO, HOMO-LUMO, UV and NMR studies have not yet been described so far on Adenine. This study will fulfill the void by investigating structural, vibrational, NBO, UV–Vis, NMR analysis in the field of research. It also adds the investigation of thermal properties, Mullikan population analysis, APT charge analysis and NLO studies were carried out in the present research.

2 Characterization of the Sample

The compound adenine was purchased from Sigma Aldrich chemicals, USA, which was in 99 % of spectrographic grade. The Bruker IFS 66 V spectrometer was used in the range of 4000–400 cm^{-1}, to record the FT-IR spectrum, with the spectral resolution of ± 2 cm^{-1}. The same instrument with an FRA 106 Raman module equipped with a Nd: YAG laser source operating at 1064 nm line width with 200 mW power, the FT-Raman spectrum was recorded in the range of 4000–100 cm^{-1} with a scanning speed of 30 cm^{-1} min^{-1} and spectral width 2 cm^{-1}. The 300 and 75 MHz NMR spectrometer were used to measure the chemical shift of ^{1}H and ^{13}C in DMSO solvent phase. The UV-1700 series instrument was used to record the UV spectrum in ethanol solvent phase in the wavelength range of 200 and 400 nm with the scanning interval of 0.2 and slit width 1.0 nm.

3 Theoretical Analysis

All the calculations were made on the Gaussian 09 software programs [9, 10] using the Pentium IV/3.02 GHz personal computer. The optimization and frequency calculations were carried out using B3LYP and B3PW91 methods in combination with 6-311++G (d, p) basis set. From the optimized structure the values of geometrical parameters were tabulated. The same method and basis set have been employed in computing NBO and HOMO-LUMO analysis. The electronic spectra of the compound is computed using TD-SCF functional along with B3LYP method and 6-311++G (d, p). The NMR chemical shifts were calculated using the same functional group supported by IEF-PCM and Gauge Independent Atomic Orbital (GIAO) method. The dipole moment, polarizability and the hyperpolarizability of the title molecule were computed using the same method. The vibrational assignments were made according to the results of the total energy distribution

(TED) using Vibrational Energy Distribution analysis (VEDA) 4 program [11, 12], and also in comparison with the literatures and Gauss view programs. To rationalize the computed values with the experimental values scaling was made using the following scaling factors: 0.915 for the range of wave numbers above 1700 cm^{-1} and by the factor 0.965 below 1700 cm^{-1}, for B3LYP and B3PW91method.

4 Results and Discussion

4.1 Structural Analysis

The lowest energy structure of the title molecule adenine along with symbol and labels is presented in Fig. 1. Geometrical parameters of the molecule are calculated by both B3LYP and B3PW91 functional with same basis set 6-311++G (d, p) are presented in Table 1 and values are compared with the crystallographic data [13, 14]. The graphical representations of geometry are given in Fig. 2a, b respectively.

In pyrimidine ring, there are two CC bonds and one of which should be a double bond according to the valence. But their bond lengths in B3LYP are 1.400 and 1.406 Å and in B3PW91, which are 1.399 and 1.404 Å and it is closer to the experimental value 1.386 and 1. 408 Å. This shows that both CC bond lengths are equal which means there is no distinction between single bond and double bond between them. The above said value that implies there is conjugation of electrons within the pyrimidine ring, like in benzene ring. In comparing the previous works values [15, 16], the benzene ring, the computed CC bond length value by B3LYP method is also around 1.4 Å, which means the electron conjugation is almost the same in both benzene and pyrimidine ring. The bond length of four CN bonds in the ring in B3LYP is 1.332, 1.347, 1.325, and 1.341 Å, and the experimental values are 1.362, 1.356, 1.307 and 1.365 Å. Here there is not much difference between

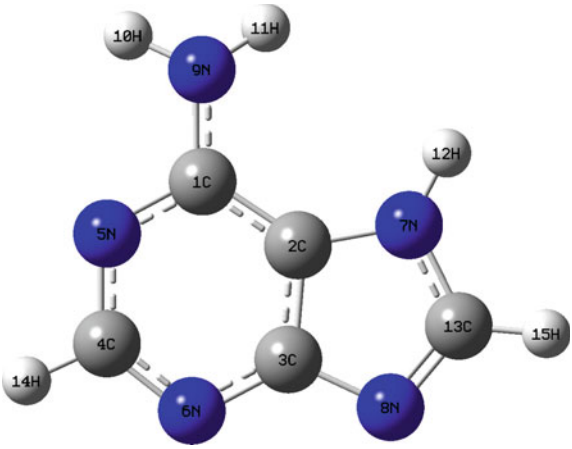

Fig. 1 Optimized structure of adenine

Table 1 The optimized geometrical parameters of adenine

Geometrical parameter	B3LYP/6-311++G (d, p)	B3PW91/6-311++G(d, p)	XRD[a]
Bond length (A°)			
C_1–C_2	1.400	1.399	1.408
C_2–C_3	1.406	1.404	1.386
C_1–N_9	1.378	1.373	1.316
C_3–N_6	1.341	1.338	1.365
C_3–N_8	1.382	1.377	1.384
C_1–N_5	1.332	1.330	1.362
C_4–N_5	1.347	1.343	1.356
C_4–N_6	1.325	1.322	1.307
C_2–N_7	1.385	1.379	1.351
C_{13}–N_7	1.375	1.369	1.362
C_{13}–N_8	1.306	1.304	1.314
C_4–H_{14}	1.085	1.087	0.930
C_{13}–H_{15}	1.080	1.081	0.930
N_7–H_{12}	1.007	1.006	0.860
N_9–H_{10}	1.010	1.010	0.881
N_9–H_{11}	1.008	1.007	0.890
Bond angle (°)			
C_1–C_2–C_3	118.63	118.57	117.95
C_2–C_1–N_5	117.93	117.90	120.27
C_2–C_1–N_9	123.81	123.94	125.78
C_1–C_2–N_7	136.09	136.18	131.67
C_3–C_2–N_7	105.27	105.23	106.25
C_2–C_3–N_6	123.04	123.13	126.89
C_2–C_3–N_8	110.14	110.19	110.38
C_1–N_5–C_4	118.63	118.59	123.73
C_3–N_6–C_4	113.43	113.26	112.15
C_2–N_7–C_{13}	105.85	105.89	103.24
C_3–N_8–C_{13}	104.86	104.71	103.24
N_6–C_3–N_8	126.81	126.66	126.85
N_5–C_4–N_6	128.29	128.50	125.32
N_5–C_1–N_9	118.19	118.09	120.27
N_7–C_{13}–N_8	113.85	113.96	114.06
C_2–N_7–H_{12}	127.97	128.00	126.97
C_1–N_9–H_{10}	113.69	113.57	116.34
C_1–N_9–H_{11}	118.02	118.09	123.79
N_5–C_4–H_{14}	115.10	115.00	117.37
N_6–C_4–H_{14}	116.59	116.48	117.37
H_{12}–N_7–C_{13}	125.80	125.79	126.98
H_{10}–N_9–H_{11}	114.32	114.42	123.79

(continued)

Table 1 (continued)

Geometrical parameter	B3LYP/6-311++G (d, p)	B3PW91/6-311++G(d, p)	XRD[a]
N_7–C_{13}–H_{15}	121.10	121.09	122.93
N_8–C_{13}–H_{15}	125.04	124.94	123.01
Dihedral angle (°)			
N_5–C_1–C_2–C_3	1.47	1.48	0.610
N_5–C_1–C_2–N_7	−179.21	−179.21	−178.96
N_9–C_1–C_2–C_3	178.72	178.72	179.83
N_9–C_1–C_2–N_7	−1.96	−1.96	0.60
C_2–C_1–N_5–C_4	−0.63	−0.63	1.26
N_9–C_1–N_5–C_4	−178.04	−178.04	179.15
C_2–C_1–N_9–H_{10}	170.50	170.50	179.39
C_2–C_1–N_9–H_{11}	32.50	32.50	1.16
N_5–C_1–N_9–H_{10}	−12.24	−12.24	−1.09
N_5–C_1–N_9–H_{11}	−150.25	−150.25	−179.31
C_1–C_2–C_3–N_6	−1.12	−1.12	0.56
C_1–C_2–C_3–N_8	179.58	179.58	179.87
N_7–C_2–C_3–N_6	179.37	179.37	179.87
N_7–C_2–C_3–N_8	0.08	0.08	−0.48
C_1–C_2–N_7–H_{12}	6.81	6.81	−179.68
C_1–C_2–N_7–C_{13}	−179.83	−179.8	−179.99
C_3–C_2–N_7–H_{12}	−173.81	−173.81	−179.68
C_3–C_2–N_7–C_{13}	−0.46	−0.46	−179.99
C_2–C_3–N_6–C_4	−0.12	−0.12	−1.05
N_8–C_3–N_6–C_4	179.04	179.04	179.78
C_2–C_3–N_8–C_{13}	0.35	0.35	0.32
N_6–C_3–N_8–C_{13}	−178.90	−178.90	179.64
N_6–C_4–N_5–C_1	−0.75	−0.75	0.80
H_{14}–C_4–N_5–C_1	179.79	179.79	179.14
N_5–C_4–N_6–C_3	1.11	1.11	0.37
H_{14}–C_4–N_6–C_3	−179.43	−179.43	179.68
C_2–N_7–C_{13}–N_8	0.75	0.75	−0.22
C_2–N_7–C_{13}–H_{15}	−179.41	−179.41	179.82
H_{12}–N_7–C_{13}–N_8	174.29	174.29	179.93
H_{12}–N_7–C_{13}–H_{15}	−5.87	−5.87	−0.11
C_3–N_8–C_{13}–N_7	−0.69	−0.69	−0.07
C_3–N_8–C_{13}–H_{15}	179.48	179.48	179.89

[a]Values taken from [13, 14]

computed and experimental data. All these values are almost equal which again confirms the electron conjugation within the pyrimidine ring, strictly two of which should be double bonded and the remaining should be single bonded but no distinction is observed as in the case of CC bonds. There is one C-N single bond lie

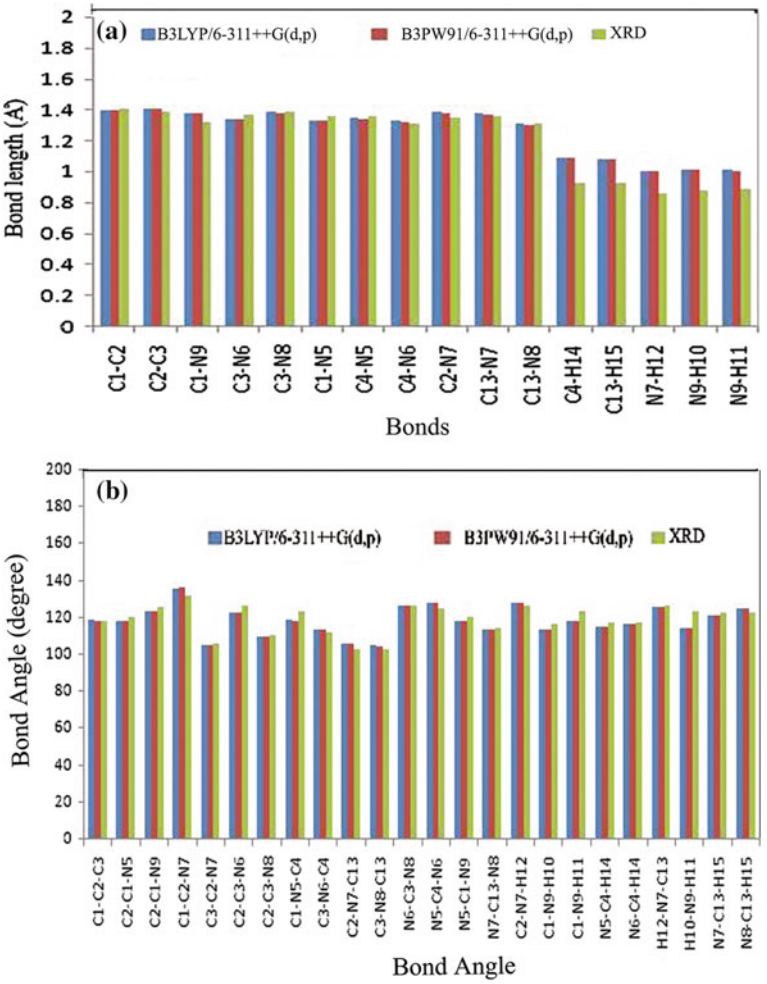

Fig. 2 **a** Geometrical parameter (*Bond length*) of adenine, **b** Geometrical parameter (*Bond angle*) of adenine

outside the ring whose length in B3LYP is 1.378 Å and in B3PW91 is 1.373 Å and in experimental 1.316 Å, which shows a clear cut distinction with inside values. Similarly, within pyrine ring, there are four CN bonds, but there is a clear cut characteristic between single and double bonds, the double bond length is found to be in B3LYP 1.306 Å, and 1.314 Å is its experimental value, the single bond lengths are found to be 1.375, 1.382 and 1.385 Å and they closer to the experimental values 1.351, 1.362 and 1.384 Å. This shows there is no such electron conjugation within pyrine ring, unlike in pyrimidine ring. All these CC and CN bond length values in both methods coincide with the experimental values.

There are three N–H and two C–H bonds in the molecule, the bond lengths of C–H bonds are found to be 1.080 and 1.085 Å and the bond lengths of N–H bonds are found to be 1.007, 1.008 and 1.010 Å in B3LYP method, almost the same values are observed in other method as well as experimentally. The lesser bond length of N–H compared to C–H confirms that the electron pulling capacity of C is lesser than that of N. In this molecule there is bond N_5–H_{10} in computation due to Vander wall's force, this weak bond was formed between nitrogen-hydrogen. By steric effect the negatively charged atom get attracted towards the positively charged atoms, similar trend is observed here that hydrogen with positive charge has weak bond with the nitrogen atom which is negatively charged, with the bond length 2.43789 Å [17–19].

The angle between the bonds in the pyrimidine ring should be 120° if it is regular hexagonal in shape like in benzene ring, but here the angles are C_2–C_1–N_5 (117.93°), C_1–C_2–C_3 (118.63°), C_1–N_5–C_4 (118.63°), C_3–N_6–C_4 (113.43°), N_5–C_4–N_6 (128.29°) and N_6–C_3–C_2 (123.04°) and the corresponding experimental values are 120.27°, 117.95°, 123.73°, 112.25°, 125.32° and 126.89° respectively. This shows that there is no regular shape to pyrimidine ring, which naturally due to the different hybridization of N and C atoms within the ring. The shape would also be distorted slightly due to the two substitutions. The angles in the pyrine ring are C_3–C_2–N_7 (105.27°), C_2–N_7–C_{13} (105.85°), C_{13}–N_8–C_3 (104.86°), N_7–C_{13}–N_8 (113.85°) and N_8–C_3–C_2 (110.14°) and experimental values are 106.25°, 103.24°, 103.24°, 114.06° and 110.38°. These values show that three angles are closer to 105° and the remaining two angles to 110°, which means there is a kind of regularity in the shape and the variation is only due to the single and double CN bonds.

4.2 Atomic Charge Analysis

To know the structure and charge mobility of the molecule, the atomic charge analysis plays very important role. It is a basis data which leads to know better knowledge of the dipole moment, molecular polarizability, electronic structure and molecular reactivity of the system. It also paves ways to measure the chemical shift of the hydrogen and carbon in the NMR analysis. Two types of the charges (Mulliken and APT) of the same molecule have been calculated for analysis using B3LYP functional with 6-311++G (d, p) basis set, and the values are presented in Table 2, the corresponding graph is shown in Fig. 3.

It is usual that all the carbon atoms in the benzene rings show negative charges [20]. Here in this pyrimidine ring, there are four carbon atoms, where at C_1 the amino group is attached and C_2 and C_3 are common to both pyrine and pyrimidine rings. C_1 and C_3 are highly negative in MPA where as highly positive in APT, the prediction by APT is reasonable as C_1 and C_3 are connected to two N atoms in two sides and with one C atom at the third side and hence their charges would be pulled more towards these nitrogen atoms. Similarly, C_2 is slightly negative in APT and highly positive in MPA, C_2 is connected with two carbon atoms in two sides and with

Table 2 Atomic charge analysis of adenine at B3LYP/6-311++G (d, p)

Atom	B3LYP/6-311++G (d, p)	
	Mulliken charge	APT charge
C_1	−0.38438	0.93887
C_2	0.50437	−0.14911
C_3	−0.57331	0.51116
C_4	0.02475	0.48866
N_5	−0.19371	−0.65166
N_6	−0.12594	−0.53822
N_7	−0.29061	−0.22503
N_8	−0.15061	−0.51799
N_9	−0.30190	−0.31489
H_{10}	0.29710	0
H_{11}	0.22472	0
H_{12}	0.30475	0
C_{13}	0.23498	0.45817
H_{14}	0.22264	0
H_{15}	0.20715	0

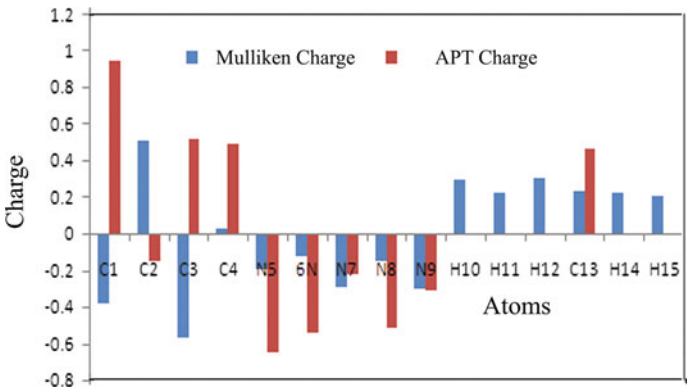

Fig. 3 Atomic charge analysis of adenine

nitrogen atom in third side. Hence, it cannot be completely positive as predicted by MPA. C_4 which is connected to two N atoms on either side is almost neutral in MPA whereas highly positive in APT. Here the prediction by MPA may be correct as it is also connected to H atom on the third side which can donate its electron to this carbon atom. In pyrine ring, the charge of C_{13} atom is predicted as positive in both the methods; APT charge is relatively larger in magnitude than that of MPA.

It is usual that all the hydrogen atoms are found to have almost equal positive charges [20], with small variation based on the carbon or nitrogen atoms with which they are attached, in MPA all are positive, but in APT all hydrogen atoms are found

to be zero. In this case, the prediction by MPA is certainly correct as zero charge on hydrogen atom is not possible, as certainly they lose their electrons to either C or N atoms to which they are attached. All the Nitrogen atoms in the compound are negative in both the methods, with marked difference in magnitude of charges between the two methods except on N9 where both are almost equal.

4.3 NMR Spectral Analysis

The carbon −13 NMR and proton NMR chemical shift of the adenine were done by gauge independent atomic orbital (GIAO) method with B3LYP/6-311+G (2d, p) combination [21], the calculation were performed with DMSO solvent phase. The theoretical and experimental ^{13}C and ^{1}H NMR chemical shifts are given in Table 3. The Figs. 4 and 5 shows the observed and simulated UV spectra.

Generally the aromatic carbon atoms have chemical shift values in gas phase in the range 120–130 ppm [22] in comparison with TMS. This observation is made in this molecule approximately for carbon atom C_2 with the experimental shift 119 ppm and theoretical shift at 113 ppm. The slight decrease in value is due to the slight decrease in negative charge as predicted by APT. For other carbon atoms C_1, C_3 and C_4, the shift are 153, 156 and 153 ppm experimentally and 153, 168 and 159 ppm theoretically. All these high values are due to the positive charges (predicted by APT) on these atoms which are purely due to the presence of two N atoms surrounding these atoms. The only carbon atom in the pyrine group C_{13} has the chemical shift 140 ppm experimentally and 144 ppm theoretically. All these chemical shift values are in tune with the charges predicted by APT method.

In the case of Hydrogen atoms, the chemical shift is usually between 7 and 8 ppm for hydrogen atoms which are attached to benzene ring [23]. The same range is observed experimentally in this molecule also for all hydrogen atoms except H_{14}, even though three of them attached to nitrogen atoms instead of carbon atoms. This

Table 3 Experimental and calculated ^{1}H and ^{13}C NMR chemical shifts (ppm) of adenine

Atom	Experimental (ppm)	Gas	DMSO
		B3LYP/6-311+G (2d, p) (ppm)	B3LYP/6-311+G (2d, p) (ppm)
C_1	153.36	153.10	156.21
C_2	119.07	113.63	116.10
C_3	156.36	168.22	166.97
C_4	153.36	159.88	158.84
C_{13}	140.30	144.07	148.02
H_{10}	7.09	4.34	4.619
H_{11}	7.09	3.43	4.40
H_{12}	8.14	7.95	8.95
H_{14}	12.6	8.86	8.67
H_{15}	8.14	8.01	8.30

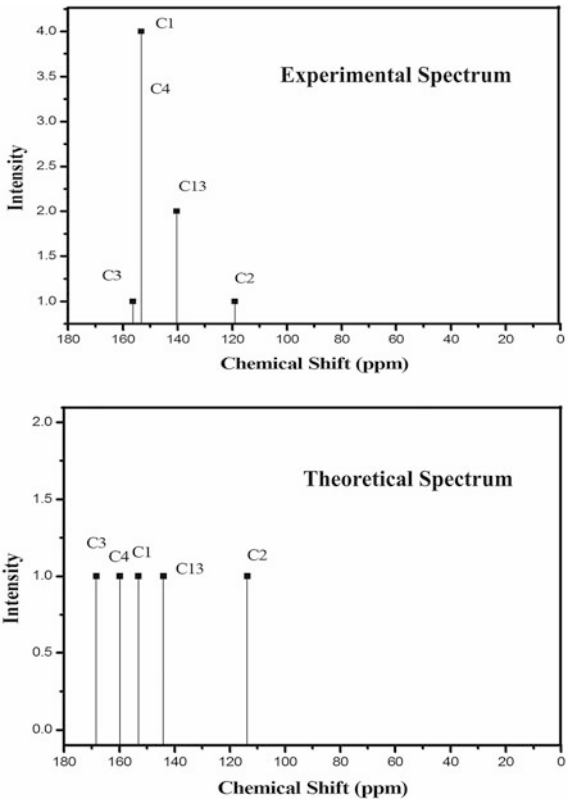

Fig. 4 Experimental and theoretical spectra of ^{13}C NMR of adenine

observation is in agreement with positive charges predicted for these atoms by MPA method, which shows almost same magnitude of charges for both carbons attached and nitrogen attached hydrogen atoms. However, theoretically for H_{10} and H_{11} in the NH_2 group, the chemical shift predicted are 3 and 4 ppm which is closer to methyl group values but no such peak is observed in the experimental spectrum.

4.4 NBO Analysis

The intra and inter molecular interactions of the molecule were investigated by the NBO analysis supported by using second-order perturbation theory [24, 25]. The donor (i) and acceptor orbital (j), the stabilization energy $E^{(2)}$ related with electron is computed by the relation

$$E^{(2)} = \Delta E_{ij} = q_i \frac{F(i,j)^2}{\varepsilon_j - \varepsilon_i}$$

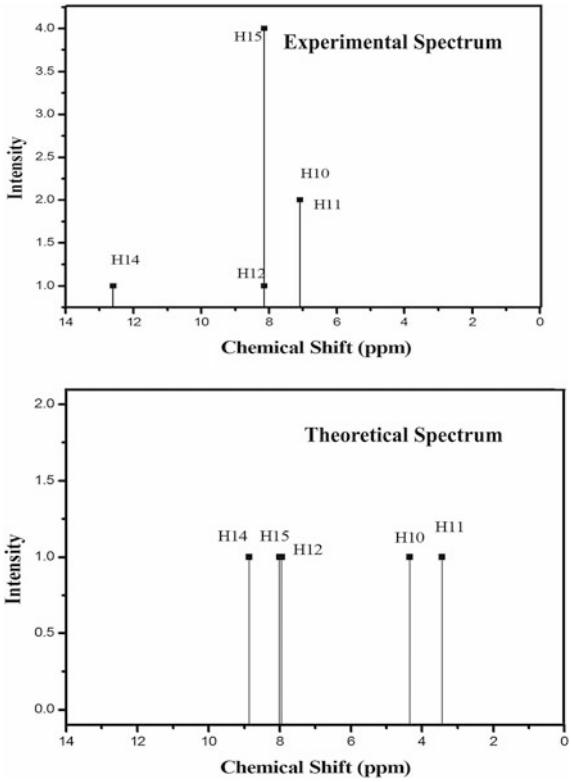

Fig. 5 Experimental and theoretical spectra of ^{1}H NMR of adenine

Where q_i is the donor orbital occupancy, ε_i, ε_j are diagonal elements (orbital energies) and F (i, j) is the off-diagonal NBO Fock matrix element. In this study, all the above NBO parameters computed using B3LYP/6-311G++G (d, p) level of theory is presented in Table 4. The larger the $E^{(2)}$ value, more is the intensive of the interaction between donors and acceptors.

The observation reveals that there are seven transition with higher stabilization energy among the various transitions occur between donor and acceptor: They are $N_7 \rightarrow N_8$–C_{13} (n–π* 44.33 kcal mol^{-1}), $N_9 \rightarrow C_1$–N_5 (n–π* 34.39 kcal mol^{-1}), C_2–$C_3 \rightarrow C_1$–N_5 (π–π* 32.12 kcal mol^{-1}), C_1–$C_5 \rightarrow C_4$–N_6 (π–π* 31.67 kcal mol^{-1}), $N_7 \rightarrow C_2$–C_3 (n–π* 28.42 kcal mol^{-1}), C_4–$N_6 \rightarrow C_2$–C_3 (π–π* 27.30 kcal mol^{-1}) and N_8–$C_{13} \rightarrow C_2$–C_3 (π–π* 21.43 kcal mol^{-1}). Five of them are from pyrimidine group and two from the pyridine group. Three of them are n–π* transitions while the remaining four are π–π* transitions. All these transitions are not identified in the UV spectrum. The first transition with higher stabilization energy is found in the UV spectrum. Other transitions reveal the heavy flow of the energy among the donor and acceptor regions.

Table 4 Second order Perturbation theory of Fock matrix in NBO basis of adenine using B3LYP with 6-311++g (d, p)

Donor	Type of bond	Occupancy	Acceptor	Type of bond	Occupancy	Energy E(2) kcal/mol	Energy difference E (j)–E (i) a.u.	Polarized energy F (i, j) a.u.
C_1–C_2	σ	1.97465	C_2–C_3	σ*	0.04767	3.94	1.27	0.063
	σ		C_2–N_7	σ*	0.02716	3.03	1.15	0.053
C_1–N_5	σ	1.98039	C_1–C_2	σ*	0.03997	2.88	1.37	0.056
	σ		C_2–N_7	σ*	0.02716	4.32	1.25	0.066
	π	1.73543	C_2–C_3	π*	0.44879	9.35	0.32	0.051
	π		C_4–N_6	π*	0.32521	31.67	0.32	0.092
C_1–N_5	σ	1.99161	C_4–N_5	σ*	0.03021	2.11	1.36	0.048
C_2–C_3	σ	1.96997	C_1–C_2	σ*	0.03997	4.32	1.23	0.065
	σ		C_1–N_9	σ*	0.03358	4.57	1.13	0.064
	σ		C_3–N_6	σ*	0.02539	2.11	1.23	0.046
	σ		N_7–H_{12}	σ*	0.01760	4.61	1.07	0.063
	π	1.62075	C_1–N_5	π*	0.45341	32.12	0.27	0.084
	π		C_4–N_6	π*	0.32521	11.44	0.28	0.052
	π		N_8–C_{13}	π*	0.31227	12.49	0.27	0.052
C_2–N_7	σ	1.98456	C_1–C_2	σ*	0.03997	2.54	1.36	0.053
	σ		C_3–N_6	σ*	0.02539	2.97	1.36	0.057
	σ		C_{13}–H_{15}	σ *	0.02165	2.35	1.22	0.048
C_3–N_6	σ	1.98422	C_4–H_{14}	σ *	0.02974	2.33	1.25	0.048
C_3–N_8	σ	1.97781	C_1–C_2	σ*	0.03997	2.22	1.31	0.048
	σ		C_{13}–H_{15}	σ*	0.02165	4.96	1.17	0.068
C_4–N_5	σ	1.98603	C_1–N_9	σ*	0.03358	4.36	1.25	0.066
C_4–N_6	σ	1.98484	C_3–N_8	σ*	0.03058	6.16	1.3	0.08
	π	1.77288	C_1–N_5	σ*	0.45341	8.85	0.29	0.048
	π		C_2–C_3	π*	0.44879	27.30	0.31	0.087

(continued)

Table 4 (continued)

Donor	Type of bond	Occupancy	Acceptor	Type of bond	Occupancy	Energy E(2) kcal/mol	Energy difference E (j)–E (i) a.u.	Polarized energy F (i, j) a.u.
C_4–H_{14}	σ	1.98132	C_1–N_5	σ*	0.02092	4.69	1.05	0.063
	σ		C_3–N_6	σ*	0.02539	4.49	1.05	0.061
N_7–C_{13}	σ	1.98915	C_1–C_2	σ*	0.03997	4.85	1.37	0.073
N_8–C_{13}	σ	1.98382	C_3–N_6	σ*	0.02539	6.13	1.38	0.082
	σ		N_7–H_{12}	σ*	0.01760	2.10	1.23	0.045
	π	1.86070	C_2–C_3	π*	0.44879	21.43	0.33	0.082
N_9–H_{10}	σ	1.98859	C_1–C_2	σ*	0.03997	4.12	1.2	0.063
N_9–H_{11}	σ	1.98453	C_1–N_5	σ*	0.02092	3.70	1.21	0.06
C_{13}–H_{15}	σ	1.98542	C_2–N_7	σ*	0.02716	2.58	0.99	0.045
	σ		C_3–N_8	σ*	0.03058	2.85	1.04	0.049
N_5	n	1.90402	C_1–C_2	σ *	0.03997	9.49	0.88	0.083
	n		C_1–N_9	σ *	0.03358	4.16	0.77	0.051
	n		C_4–N_6	σ *	0.02513	10.18	0.9	0.087
	n		C_4–H_{14}	σ *	0.02974	3.41	0.77	0.047
N_6	n	1.90651	C_2–C_3	σ *	0.04767	9.60	0.87	0.082
	n		C_3–N_8	σ *	0.03058	2.38	0.81	0.04
	n		C_4–N_5	σ *	0.03021	11.36	0.86	0.09
	n		C_4–H_{14}	σ *	0.02974	3.68	0.77	0.048
N_7	n	1.62473	C_2–C_3	π*	0.44879	28.42	0.31	0.085
	n		N_8–C_{13}	π*	0.31227	44.33	0.29	0.103
N_8	n	1.91807	C_2–C_3	σ *	0.04767	5.69	0.9	0.064
	n		N_7–C_{13}	σ *	0.03701	8.49	0.79	0.074
	n		C_{13}–H_{15}	σ *	0.02165	2.13	0.76	0.036
N_9	n	1.81593	C_1–N_5	π*	0.45341	34.39	0.31	0.099

4.5 Electronic Transitions

The absorption wavelength, excitation energies and oscillator strength presented in Table 5, are computed by using at B3LYP/6-311++G (d, p) level supported by TD-SCF approach in both gas and solvent phase. The Fig. 6 shows recorded and simulated UV spectra.

As noted from Table 5, the energy of the probable electronic transitions at liquid phase are 4.872, 5.016, 5.334, 5.532 and 5.561 eV respectively, similarly the absorption wavelengths are 254, 247, 232, 224 and 222 nm respectively, and

Table 5 Experimental and theoretical electronic absorption wavelength of adenine using TD-SCF/B3LYP/6-311++G (d, p)

Experimental			Theoretical			Major contribution	Assignment
λ (nm)	E (eV)	f	TD-SCF				
			λ (nm)	E (eV)	F		
			265	4.677	0.0052	H-1 → L (91 %)	n–π*
			256	4.833	0.0193	H → L (17 %)	n–π*
			251	4.931	0.1052	H → L (65 %)	π–π*
			233	5.320	0.0005	H-1 → L + 2 (85 %)	π–π*
			227	5.457	0.0098	H-2 → L (38 %)	n–π*
Ethanol							
255		0.439	254	4.872	0.1844	H → L (85 %)	n–π*
			247	5.016	0.0177	H-1 → L (91 %)	n–π*
			232	5.334	0.0299	H-2 → L (25 %)	π–π*
			224	5.532	0.0007	H-1 → L + 1 (91 %)	π–π*
			222	5.561	0.0097	H → L + 2 (95 %)	n–π*

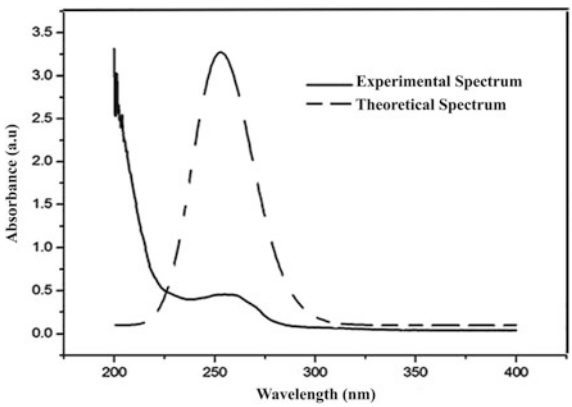

Fig. 6 Experimental and theoretical UV spectra of adenine

corresponding computed oscillator strengths are 0.1844, 0.0177, 0.0299, 0.0007 and 0.0097 respectively. The oscillator strength reveals that the higher the oscillator strength stronger is the intensity of the spectrum, in the observed UV spectrum there is only a peak which is found to be with higher intensity having the wavelengths 254 nm. The same wavelengths may be correlated with the transition observed in NBO analysis having higher stabilization energy for this peak is $N_7 \rightarrow N_8$–C_{13} (n–π* 44.33 kcal mol^{-1}).

Similarly the energy values observed in gas phase are 4.677, 4.833, 4.931, 5.320 and 5.457 eV, wavelengths-265, 256, 251, 233 and 227 nm and corresponding oscillator strengths are 0.0052, 0.0193, 0.1052, 0.0005 and 0.0098. In the UV spectrum the intensity line corresponding to the third value 251 nm is observed. The transition is again correlated to the transition computed in NBO analysis. In comparison with the liquid and gas phase the values of wavelengths vary for each peak. The first peak is observed with higher wavelengths in the liquid phase whereas in gas phase third peak is found with higher wavelengths. Thus there is a variation in the intensity of the peaks in liquid and gas phase.

4.6 HOMO-LUMO Analysis

The investigation on HOMO and LUMO analysis was made using B3LYP functional supported by the basis set 6-311++G (d, p). The pictorial representation of the HOMO-LUMO was shown in Fig. 7. The reactivity descriptors of the molecule were presented in Table 6. There is a sharp difference between the energy gap of optimized and transition state 7.2128 and 5.3775 eV respectively, this implies that since the energy gap in the transition state is less compared to optimised state the energy flow in the transition state much higher than the other one. The electronegativity of the molecule in transition state and the optimized state are same. And the chemical hardness is 3.6064 and 2.6887 eV respectively in both optimized and transition state. The decrease in chemical hardness in transition state confirms the high rate of energy flow in the state. On the contrary the electrophilicity indices 2.1355 and 2.9890 eV are high in the transition state and less in the optimised state. The dipole moment 6.9586 and 9.5707 Debye both in the two states respectively, are found higher in the transition state which again reaffirms the high flow of the energy in the transition state.

4.7 Density of States

The density of states were computed and created by introducing them into the molecular orbital information drawing the Gaussian curves of unit height and FWHM of 0.3 eV using Gauss Sum 2.2 program [26]. The density of state (DOS) shows the bonding, anti-bonding and non bonding nature of the interactions

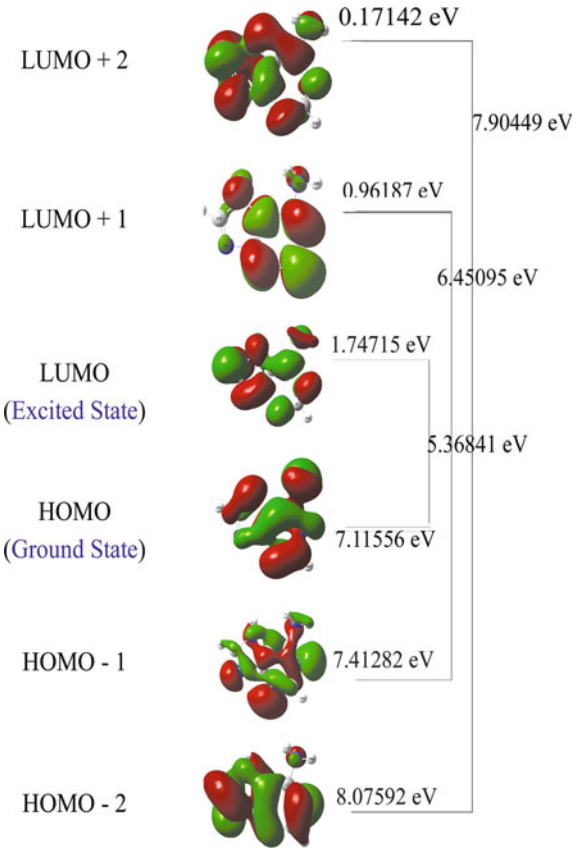

Fig. 7 The frontier molecular orbital of adenine

Table 6 HOMO, LUMO, Kubo gap, global electro negativity, global hardness and softness, global electrophilicity index of adenine

Parameters	Adenine		
	Optimized state	Transition state by TD-SCF	
	B3LYP/6-311++G (d, p)	Gas	DMSO
E_{HOMO} (eV)	7.5311	6.7154	6.6980
E_{LUMO} (eV)	0.3183	1.2560	1.3205
$\Delta E_{HOMO\text{-}LUMO\ gap}$ (eV)	7.2128	5.4594	5.3775
Electro negativity (χ) (eV)	3.9247	3.9857	4.0092
Global hardness (η) (eV)	3.6064	2.7297	2.6887
Global softness (σ) (eV)	0.2772	0.3663	0.3719
Electrophilicity index (ω) (eV)	2.1355	2.9098	2.9890
Dipole moment (μ) (Debye)	6.9586	7.0193	9.5707

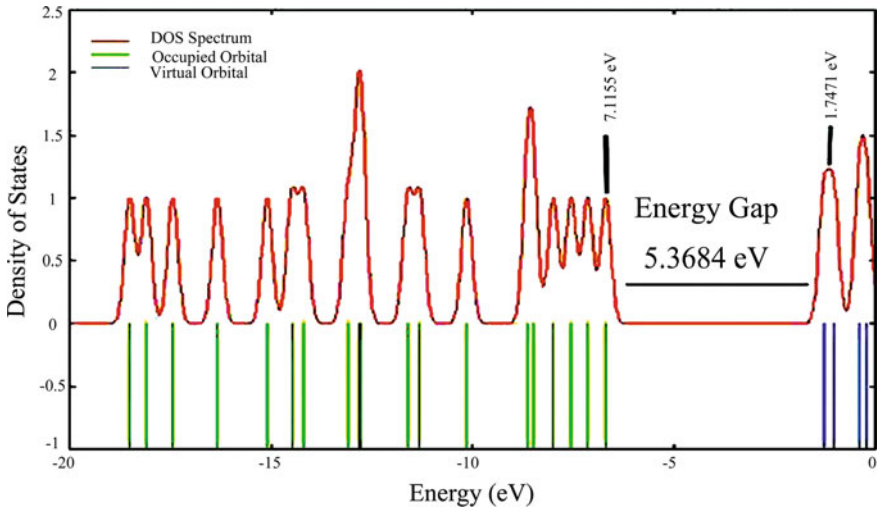

Fig. 8 Density of state of adenine

between two orbital, atoms or groups. Positive value of DOS shows a bonding interaction, negative value shows anti-bonding interactions and zero value corresponds to the non-bonding interactions [27]. The HOMO-LUMO energy gap and delocalization of the electron density are mapped. The HOMO is considered to the electron rich site and LUMO the energy electron poor site. Taking into account of higher dipole moment (6.95 Debye) and as a consequence higher transitions occur and the electron flow from HOMO to LUMO is considered to be high in this molecule. The DOS clearly exhibits the possible energy flow occupied to the virtual states in Fig. 8.

4.8 Electrostatic Potential Map Analysis

The molecular electrostatic potential surface of the molecule is investigated with the help of B3LYP/6-311++G (d, p) and the three dimensional picture of the molecule is shown in Fig. 9. The picture depicts the charge flow from donor to acceptor and different parts of the molecule, this helps to identify the charge centres of the molecule and nature of the chemical bond in the molecule [28, 29]. The colour red indicates the lowest electrostatic potential energy and the colour blue indicates highest electrostatic potential energy. Intermediate colour indicates intermediate electrostatic potential. Areas with low potential are characterised by an abundance of electrons and high potentials are characterised by the relative absence of

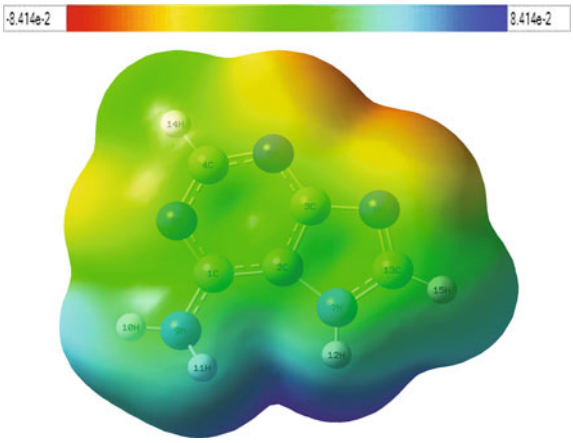

Fig. 9 MEP map of adenine

electrons. The colour code of this map in the title compound is lies between −8.415 and 8.415 a.u. The Fig. 9 shows the region around the nitrogen atoms N_6 and N_8 linked with carbon atoms are most negative potential region (red) and H_{11} and H_{12} hydrogen atoms are linked with nitrogen indicates most positive potential region (blue).

4.9 Vibrational Frequency Investigations

The title molecule having the C_1 point group symmetry, whose two atoms lie out of plane of the symmetry, consists of 15 atoms. As the title molecule is non-linear, it has 39 modes of the vibrations which are distributed as:

$$\tau_{vib} = 28A_g + 11A_u$$

A_g represents modes which lie in the same plane of molecule and A_u which lie out of this plane. To ratify the theoretical values with the experimental frequencies, the theoretical values are suitably scaled by scaling factor 0.915 for the range of wave numbers above 1700 cm^{-1} and by the factor 0.965 below 1700 cm^{-1}, for B3LYP and B3PW91 method for the same basic set 6-311++G (d, p). Most of the modes of the vibrations are observed complementarily both in FT-IR and FT-Raman spectra. The wave numbers both calculated and experimental are presented in Table 7. The assignments are carried out using the total energy distribution (TED) values and also in comparison with literatures and with Gauss view software [10]. The experimental FT-IR and FT-Raman spectra for the title molecule are presented in Figs. 10 and 11 respectively.

Table 7 The observed FTIR, FT–Raman and calculated frequencies using B3LYP/B3PW91 method with 6-311++G (d, p) basis set of the molecule adenine

Sl. No.	Symmetry species	Observed frequency (cm^{-1})		Scaled frequency (cm^{-1})		Vibrational assignment	% TED
		FT-IR	FT-Raman	B3LYP	B3PW91		
1	A_g	3354 w		3363	3387	ν N–H	ν N-H(99)
2	A_g	3296 m		3343	3364	ν N–H	ν N-H(99)
3	A_g	3269 m		3262	3282	ν N–H	ν N-H(99)
4	A_g	3118 s		3012	3013	ν C–H	ν C-H(99)
5	A_g	2977 m		3057	2903	ν C–H	ν C-H(100)
6	A_g	1672 vs		1605	1622	ν C=C	ν CC(42) + β HNH(12)
7	A_g		1624 vw	1585	1588	β N–H	ν CC(14) + β HNH(57)
8	A_g	1602 vs		1532	1549	β N–H	ν CN(51) + ν CC(22)
9	A_g		1571 vw	1475	1488	β N–H	ν CN(51) + β HCN(17)
10	A_g		1494 vw	1450	1463	ν C=N	ν CN(37) + β HCN(32)
11	A_g	1419 s	1417 vw	1368	1382	ν C=N	ν CN(27) + β HNC(40)
12	A_g		1398 vw	1340	1355	ν C=N	ν CN(21) + ν CC (25) + β HCN(13)
13	A_g	1367 m		1329	1344	β C–H	ν CN(25) + β HCN(12)
14	A_g		1350 vw	1306	1314	β C–H	ν CN(16) + β HCN(43)
15	A_g	1334 s		1261	1287	ν C–C	ν CN(59)
16	A_g		1327 m	1240	1247	ν C–N	ν CN(45) + β HCN(26)
17	A_g		1307 m	1191	1199	ν C–N	ν CC(10) + β HNC(29) + β CCN (12)
18	A_g	1251 m		1085	1097	ν C–N	ν CN(43) + β CNC(10)
19	A_g		1231 m	1053	1062	ν C–N	ν CN(44) + β HNC(29) + β HCN (12)
20	A_g	1089 w		996	1000	ν C–N	ν CN(26) + β HNC(32)
21	A_g		957 m	941	944	ν C–N	δ HCNC(77) + δ CNCN(16)
22	A_g	939 s		914	915	β C–N	β NCN(66)

(continued)

Table 7 (continued)

Sl. No.	Symmetry species	Observed frequency (cm^{-1})		Scaled frequency (cm^{-1})		Vibrational assignment	% TED
		FT-IR	FT-Raman	B3LYP	B3PW91		
23	A_u		895 vw	863	865	δ N–H	β NCN(40) + β CNC (20)
24	A_u	869 w	852 vw	840	841	δ N–H	δ HCNC(83) + δ CNCN(11)
25	A_u	796 m		769	769	δ N–H	δ CNCN(11) + δ CCN(10) + δ NCNC(51)
26	A_u	723 s	720 vs	700	704	δ C–H	ν NC(37) +β CNC (26)
27	A_u		702 vw	676	677	δ C–H	δ CNCN(18) + δ NCNC(51)
28	A_u	640 m	640 vw	611	613	δ C–N	δ HNCN(13) + δ NCCN (17) + δ HNCN(10)
29	A_g	621 m	612 m	593	593	β C=C–C	β CNC(23) + β NCN(27)
30	A_g		580 vw	562	561	β C–C=N	δ HCNC(14) + δ CNCN(18) + δ NCCN(25) +δ HNCN(72)
31	A_g		560 vw	535	532	β C=N–C	δ HNCC(49) + δ HNCN(10)
32	A_g	542 m	535 s	516	516	β C–N–C	β NCN(45) + δ HNCC(10)
33	A_g		525 vw	506	505	β N–C=N	β CCN(37) +β CNC(20) +β NCN(15)
34	A_g		384 vw	382	397	β C=N–C	δ HNCN(75) + δ CNCN(14)
35	A_u		329 s	345	346	δ N–C=N	δ HNCN(72) + δ HNCC(10)
36	A_u		297 vw	287	287	δ C=N–C	δ CNCN(24) + δ NCCN(33)+ δ NCNC(22)
37	A_u		253 vw	277	278	δ N–C–C	β NCN(67)
38	A_u		199 vw	194	194	δ N–C–C	δ CNCN(80)
39	A_u		123 s	149	147	δ C–C–N	δ CNCN(79)

vs Very strong; *s* strong; *m* medium; *w* weak; *vw* very weak

ν- stretching; β- in-plane vibrations; δ- out-of-plane vibrations

A_g—modes which lie in the same plane of molecule

A_u—modes which lie out of the plane

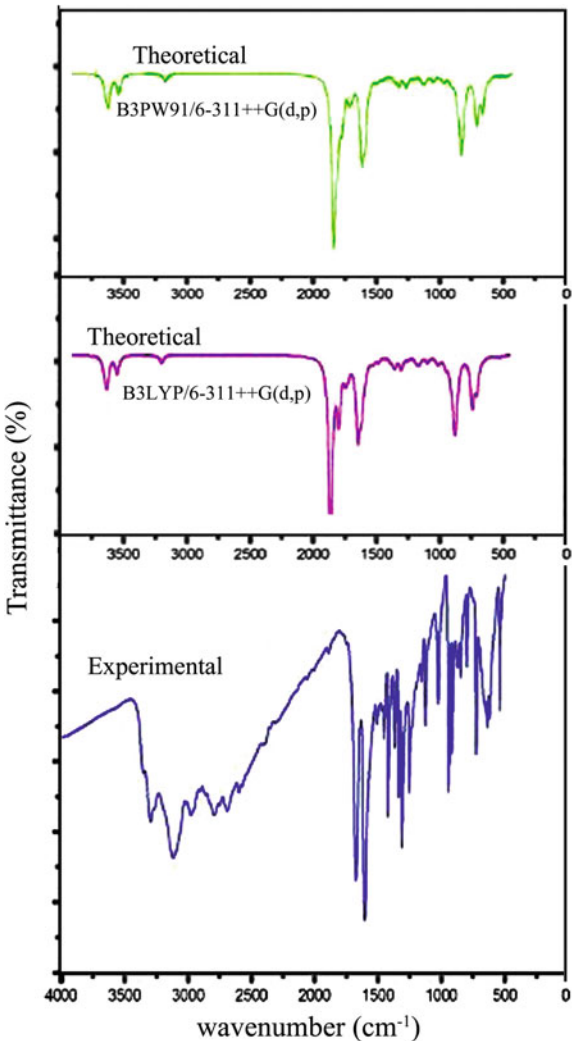

Fig. 10 Theoretical and experimental FT-IR spectra of adenine

4.9.1 C–H Vibrations

The CH bands are one of the significant intensities which help to elucidate the structure of the molecule. They are found predominant in the benzene substituted molecule. These bands were notably affected by electronic property, mesomeric or inductive substituent. The literature reveals that [30–32] in infrared spectrum, single nucleus and multi nuclear benzene compounds observed with three or four peaks in the region 3000–3100 cm^{-1} [33], these peaks are due to the stretching vibrations.

In the target molecule bands at 3118 and 2977 cm^{-1} are assigned to C–H stretching vibrations of adenine in the FT-IR spectrum. The first band 3118 cm^{-1}

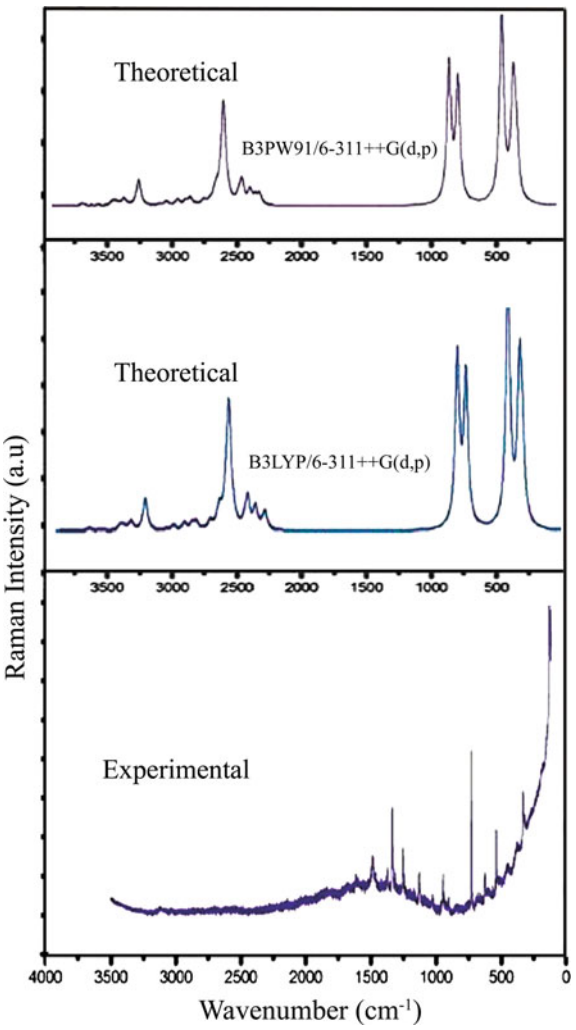

Fig. 11 Theoretical and experimental FT-Raman spectra of adenine

represents the C–H stretching in the pyrimidine ring while the second band 2977 cm^{-1} represent in the pyrine ring, which clearly shows the electron conjugation in these two rings are completely different that of the benzene ring. The TED shows the total intensity of C–H modes of vibrations is found 99 %. The first band is above the limit which indicates the high electron density inside the pyrimidine ring and the second band is below the limit, which is aliphatic C–H range which shows there is no conjugation at all. The respective in-plane bending and out-of plane bending vibrations are observed at 1367 and 1350 cm^{-1} and 720 and 702 cm^{-1}, for the corresponding range 1550–1200 cm^{-1} [34, 35] and 1000–675 cm^{-1} [36]. Among in-plane bending the first one observed in FT-IR with medium intensity and the second is observed in FT-Raman with very weak

intensity. In out-of plane bending vibrations, the first band observed in both FT-IR and FT-Raman with strong intensity and the second one is in FT-Raman with very weak intensity. Though they are well within the literature range, their differences indicate the effect of conjugation inside these rings.

4.9.2 C=C, C–C Vibrations

The ring C=C and C–C stretching vibrations are otherwise called as breathing vibrations observed at 1400–1625 cm^{-1} [36–38] in benzene rings, whose bond lengths values show no difference between single and double bond, this is because, according to Socrates [39], the presence of conjugate substituent such as CC causes a heavy doublet formation around the region 1625–1575 cm^{-1} [40]. In the present molecule, there is one C=C bond and one C–C bond inside the pyrimidine ring following the convention though there is no distinction theoretically, which are assigned to 1672 and 1334 cm^{-1} respectively. Both the bands are observed in FT-IR with very strong to strong intensity. The first band corresponding to C=C bond shows higher value than the expected range for benzene rings, which again shows its different type of conjugation from that of benzene ring. The second band for C–C appear lesser than the usual range for benzene ring, which is naturally due to the interference of C–N and β N–H bands which also fall in this range.

4.9.3 N–H Vibrations

The N–H group substituted in the aromatic ring usually shows its stretching absorption in the region 3500–3200 cm^{-1} [41, 42]. In this case, there are two N–H bonds of NH_2 group attached to pyrimidine ring and one in pyrine ring. Their stretching frequencies are observed at 3354, 3296 and 3269 cm^{-1} and its TED values 99 %. The first band is large compared with the other two; this is due to the asymmetric stretching and the second one due to the symmetric stretching of the NH_2 group. The third band of NH from pyrine ring is almost equal to the value of CH and found much below the NH range. All the bands are observed in FT-IR spectrum. The corresponding in-plane and out-of plane bending vibrations are observed at 1624, 1602 and 1571 cm^{-1} and 895, 869 and 796 cm^{-1} respectively. Among the three values of in-plane bending vibrations, the second one was observed in FT-IR with strong intensity and the remaining bands are observed in FT-Raman with weak intensity. In the out-of-plane bending the first one observed in FT-Raman with very weak intensity and the remaining are observed in FT-IR spectrum. The suggested literature ranges for these values are 1650–1580 and 910–665 cm^{-1} respectively. All these values are exactly well within the literature range, but the differences among the three values in each mode indicate the group in which they are embedded.

4.9.4 C–N Vibrations

The CN group vibrations are mixed with the other modes of vibrations in the molecule, a clear assignment to the group usually carries difficulty. Silverstein et al. [43] have assigned the C–N stretching in the range 1386–1266 cm^{-1} [44] and C=N in the range 1531–1447 cm^{-1}. In the present molecule, the C=N bands are observed at 1494, 1419 and 1398 cm^{-1}. The first and third bands are observed in FT-Raman with weak intensity and the second one observed in both FT-IR and FT-Raman spectrum. The C–N bands are observed at 1327, 1307, 1231 and 957 cm^{-1} in FT-Raman with medium intensity and 1251 and 1089 cm^{-1} are observed in FT-IR spectrum with medium and weak intensity respectively. All these values once again confirm that these are very delicate bands whose values are easily changed due to the interference of other bands. In this molecule, the C–H and N–H in-plane bending modes have considerably influence these CN modes, all their values are observed considerably below their expected range.

4.10 NLO Properties

The properties like dipole moment, polarizability and hyperpolarizability are computed in the relation NLO property investigation with B3LYP functional using 6-311++G (d, p) basis set. The polarizability (α_{ij}) and hyperpolarizability tensors (β_{ijk}) are obtained from Gaussian frequency output file. The output values are written in terms of electrostatic unit (esu) by using the relation, for α; 1a. u. = 0.1482×10^{-24} esu and for β; 1a.u. = 8.6393×10^{-33} esu. The computed values of the above properties μ_0, α_{total} and $\Delta\alpha$ are tabulated in Table 8.

Table 8 The Dipole moment (μ) (Debye), Polarizability (α) and hyperpolarizability (β) of Adenine

Parameter	a.u	$\times 10^{-24}$ e.s.u	Parameter	a.u.	$\times 10^{-33}$ e.s.u
α_{xx}	−56.26	−8.33	β_{xxx}	4.73	40.90
α_{xy}	−6.89	−1.02	β_{xyy}	−13.74	-118.77
α_{yy}	−52.21	−7.73	β_{xzz}	0.14	1.29
α_{xz}	−2.08	−0.30	β_{yyy}	-48.31	-417.42
α_{yz}	−2.21	−0.32	β_{yxx}	-32.04	-276.81
α_{zz}	−59.55	−8.82	β_{yzz}	-0.73	-6.39
α_{tot}	−56.00	–8.38	β_{zzz}	0.54	4.67
$\Delta\alpha$	168.35	24.95	β_{yyz}	5.24	45.29
μ_x (Debye)	−0.13		β_{xxz}	2.73	23.60
μ_y (Debye)	−6.92		β_{tot}	82.02	708.63
μ_z (Debye)	0.67				
μ_{tot} (Debye)	6.9586				

The total dipole moment μ_0 is found to be 6.9586 Debye. The $\mu_{y,}$ is 6.9248 Debye, which is found higher among the dipole tensor and the lowest value is along x direction μ_x is 0.1309 Debye. The average polarizability and anisotropy of the polarizability are 8.3807 and 24.9508 $\times$ 10^{-24} esu, respectively. Similarly the hyperpolarizability is the key factor to determine the NLO character of the molecule in comparison with the reference molecule Urea (dipole moment and hyperpolarizability of urea are 1.3732 D and 372.89 $\times$ 10^{-33} esu respectively [45]) is 708.6348 $\times$ 10^{-33} esu. In the comparison with the reference molecule the target molecule has more values of the NLO character.

4.11 Temperature Dependence of Thermodynamic Properties

From the vibrational frequency calculation run at B3LYP/6-311G++ (d, p) level the standard statistical thermodynamic functions: standard heat capacities (C) standard entropies (S), and standard enthalpy (H) were obtained and listed in Table 9. These values show that there is increase for each temperature rise from 100 to 500 k due to the fact that the molecular vibrational intensities increase with temperature [22]. The linear fit correlation graph between the above properties and temperatures were fitted by quadratic formulas and the corresponding fitting factors (R^2) for respective properties are 0.9979, 0.9988 and 0.9986. The fitting equations for the each correlation graphs shown in Fig. 12 are as follows:

$$C = 4.36033 + 0.04898T + 9.451933.615 \times 10^{-5}T^2 (R^2 = 0.9979)\,(SD = 0.14228)$$

$$S = 47.5944 + 0.14144T - 9.10509 \times 10^{-5}T^2 (R^2 = 0.9988)\,(SD = 0.4429)$$

$$H = 84.325 + 0.00149T + 4.22395 \times 10^{-5}T^2 (R^2 = 0.9986)\,(SD = 0.02324)$$

Thermodynamical parameters reveals that the as the temperature is raised the internal energy of the system changes, due to the change in the population of the atoms in the energy levels [34]. This phenomenon was analysed and represented in graph.

Table 9 Thermodynamic properties at different temperatures at the B3LYP/6-311++G (d, p) of adenine

T (K)	C (cal mol^{-1} K^{-1})	S (cal mol^{-1} K^{-1})	H (Kcal mol^{-1})
100	9.52	62.15	69.63
200	18.51	72.74	71.01
300	28.51	82.96	73.36
400	37.37	92.99	76.67
500	44.53	102.57	80.78

T Temperature; *C* Heat capacity; *S* Entropy; *H* Enthalpy

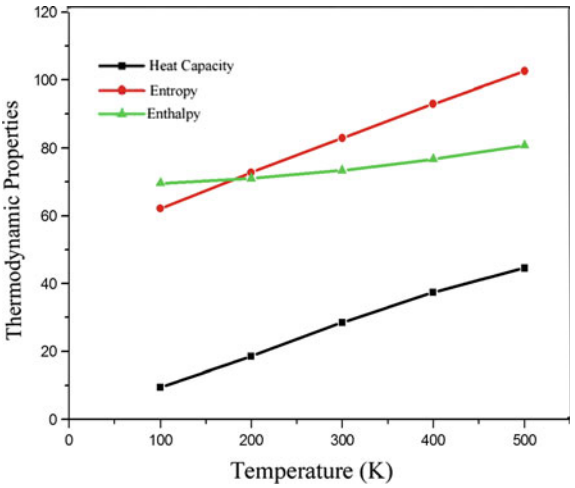

Fig. 12 Thermodynamic parametric variations with temperature

5 Conclusion

Structural analysis reveals that by the addition of pyrine part, no change in bond length and bond angle of adenine. NBO analysis reveals that the most probable transition in adenine is $N_7 \rightarrow N_8$–C_{13} (n–π*; 44.33 kcal mol^{-1}) with higher stabilization energy. From the MEP map of the adenine, the region around the nitrogen atoms N_6 and N_8 linked with carbon atoms are most negative potential region (red) and H_{11} and H_{12} hydrogen atoms are linked with nitrogen indicates most positive potential region (blue).

HOMO LUMO analysis reveals that the energy separation between the HOMOs and LUMOs gives significant information about the title compound. UV spectral analyses reveals that the most probable electronic transition is $N_7 \rightarrow N_8$–C_{13} (n–π*; 44.33 kcal mol^{-1}) transition having higher stabilization energy.

The density of state (DOS) clearly exhibits the possible energy flow occupied to the virtual states. According to vibrational analysis, all the vibrations are lie in the expected range. However the vibrations are mixed with other modes in the finger print region. The rationalized the computational wave number with the experimental the scaling factor was used.

The NLO study bring out that the value of hyperpolarizability reveals that adenine has more value of NLO character. Thermodynamical parameters reveals that the as the temperature is raised the internal energy of the system changes, due to the change in the population of the atoms in the energy levels. This phenomenon was analysed and represented in graph.

References

1. Hirakawa, A.Y., Okada, H., Sasagawa, S., Tsuboi, M.: Infrared and Raman spectra of adenine and its ^{15}N and ^{13}C substitution products. Spectrochim. Acta A. **41**, 209–216 (1985)
2. Stepanian, S.G., Sheina, G.G., Radchenko, E.D., Blagoi, Y.P.: Theoretical and experimental studies of adenine, purine and pyrimidine isolated molecule structure. J. Mol. Struct. **131**, 333–346 (1985)
3. Majoube, M.: Vibrational spectra of adenine and d-substituted analogues. J. Mol. Struct. **143**, 427–430 (1986)
4. Kuczera, J.W., Karplus, M.: Ab initio study of the vibrational spectra of N_9–H and N_7–H adenine and 9-methyladenine. J. Am. Chem. Soc. **112**, 5324–5340 (1990)
5. Colarusso, P., Zhang, K., Guo, B., Bernath, P.F.: The infrared spectra of uracil, thymine and adenine in gas phase. Chem. Phys. Lett. **269**, 39–48 (1997)
6. Nowak, M.J., Lapinski, L., Kwiatkowski, J.S., Leszczynski, J.: Molecular structure and infrared spectra of adenine. Experimental matrix isolation and density functional theory study of adenine ^{15}N isotopomers. J. Phys. Chem. **100**, 3527–3534 (1996)
7. Ten, G.N., Nechaev, V.V., Zotov, N.B., Baranov, V.I.: Interpretation of the vibrational spectra of polycrystalline adenine. Opt. Spectrosc. **107**, 58–66 (2009)
8. Lappi, S.E., Collier, W., Franzen, S.: Density functional analysis of anharmonic contributions to adenine matrix isolation spectra. J. Phys. Chem. A **106**, 11446–11455 (2002)
9. Frisch, M.J., Trucks, G.W., Schlegel, H.B., Scuseria, G.E., Robb, M.A., Cheeseman, J.R., Montgomery Jr, J.A., Vreven, T., Kudin, K.N., Burant, J.C., Millam, J.M., Iyengar, S.S., Tomasi, J., Barone, V., Mennucci, B., Cossi, M., Scalmani, G., Rega, N., Petersson, G.A., Nakatsuji, H., Hada, M., Ehara, M., Toyota, K., Fukuda, R., Hasegawa, J., Ishida, M., Nakajima, T., Honda, Y., Kitao, O., Nakai, H., Klene, M., Li, X., Knox, J.E., Hratchian, H.P., Cross, J.B., Adamo, C., Jaramillo, J., Gomperts, R., Stratmann, R.E., Yazyev, O., Austin, A. J., Cammi, R., Pomelli, C., Ochterski, J.W., Ayala, P.Y., Morokuma, K., Voth, A., Salvador, P., Dannenberg, J.J., Zakrzewski, V.G., Dapprich, S., Daniels, A.D., Strain, M.C., Farkas, O., Malick, D.K., Rabuck, A.D., Raghavachari, K., Foresman, J.B., Ortiz, J.V., Cui, Q., Baboul, A.G., Clifford, S., Cioslowski, J., Stefanov, B.B., Liu, G., Liashenko, A., Piskorz, P., Komaromi, I., Martin, R.L., Fox, D.J., Keith, T., Al-Laham, M.A., Peng, C.Y., Nanayakkara, A., Challacombe, M., Gill, P.M.W., Johnson, B., Chen, W., Wong, M.W., Gonzalez, C., Pople, J.A.: Gaussian Inc. Wallingford CT (2004)
10. Frisch, A., Neilson, A.B., Holder, A.J.: Gaussview User Manual. Gaussian Inc, Pittsburgh, PA (2000)
11. Jamroz, M.H.: Vibrational Energy Distribution Analysis VEDA 4. Warsaw (2004)
12. Jamroz, M.H.: Vibrational energy distribution analysis (VEDA): scopes and limitations. Spectrochim. Acta A. **114**, 220–230 (2013)
13. Zelenak, V., Vargova, V., Cisarova, I.: Adeninium perchloride adenine dehydrate. Acta. Cryst. E **60**, 742–744 (2004)
14. Kistenmacher, T.J., Shigematsu, T.: The crystal structure of adenine dihydrochloride. Acta Cryst. B **30**, 1528–1533 (1974)
15. Arjunan, V., Santhanam, R., Sakiladevi, S., Marchewka, M.K., Mohan, S.: Synthesis and characterization of an anticoagulant 4-hydroxy-1-thiocoumarin by FTIR, FT-Raman, NMR, DFT, NBO and HOMO-LUMO analysis. J. Mol. Struct. **1037**, 305–316 (2013)
16. Ghalla, H., Issaoui, N., Govindarajan, M., Flakus, H.T., Jamroz, H.M., Oujia, B.: Spectroscopic and molecular structure investigation of 2-furanacrylic acid monomer and dimer using HF and DFT methods. J. Mol. Struct. **1059**, 132–143 (2014)
17. Sebastian, S., Sylvestre, S., Jayabharathi, J., Ayyapan, S., Amalanathan, M., Oudayakumar, K., Herman, I.A.: Study on conformational stability, molecular structure, vibrational spectra, NBO, TD-TFT, HOMO and LUMO analysis of 3,5-dinitrosalicylic acid by DFT techniques. Spectrochim. Acta A. **136**, 1107–1118 (2014)

18. Kavitha, E., Sundaraganesan, N., Sebastian, S., Kurt, M.: Molecular structure, anharmonic vibrational frequencies and NBO analysis of naphthalene acetic acid by density functional theory calculations. Spectrochim. Acta A. **77**, 612–619 (2010)
19. Chandra, S., Saleem, H., Sundaraganesan, N., Sebastian, S.: The spectroscopic FT-IR gas phase, FT-IR, FT-Raman, polarizabilities analysis of Naphthoic acid by density functional methods. Spectrochim. Acta A. **74**, 704–713 (2009)
20. Bakkiyaraj, D., Periandy, S., Xavier, S.: Molecular structural investigation of adenosine using spectroscopic and quantum computational calculations. J. Mol. Struct. **1119**, 490–504 (2016)
21. Melinda, A.J.D.: Solid state NMR Spectroscopy; Principles and Applications. Cambridge Press (2003)
22. Karunakaran, V., Balachandran, V.: Experimental and theoretical investigation of the molecular structure, conformational stability, hyperpolarizability, electrostatic potential, thermodynamic properties and NMR spectra of pharmaceutical important molecule: 4′-Methylpropiophenone. Spectrochim. Acta A. **128**, 1–14 (2014)
23. Sivaranjani, T., Xavier, S., Periandy, S.: NMR, FT-IR, FT-Raman, UV spectroscopic, HOMO-LUMO and NBO analysis of cumene by quantum computational methods. J. Mol. Struct. **1083**, 39–47 (2015)
24. Schwenke, D.W., Truhlar, D.G.: Systematic study of basis set superposition errors in the calculated interaction energy of two HF molecules. J. Chem. Phys. **82**, 2418–2427 (1985)
25. Chidan Kumar, C.S., Yohannan Panicker, C., Fun, H.K., Sheena Mary, Y., Harikumar, B., Chandraju, S., Quah, C.K., Ooi, C.W.: FT-IR, molecular structure, first order hyperpolarizability, HOMO and LUMO analysis, MEP and NBO analysis of 2-(4-chlorophenyl)-2-oxoethyl 3-nitrobenzoate. Spectrochim. Acta A. **126**, 208–219 (2014)
26. O'Boyle, N.M., Tenderholt, A.L., Langner, K.M.: A library for package independent computational chemistry algorithms. J. Comp. Chem. **29**, 839–845 (2008)
27. Chem, M., Waghmare, U.V., Friend, C.M., Kaxiras, E.: A density functional study of clean and hydrogen covered α-MoO3(010): Electronic structure and surface relaxation. J. Chem. Phys. **109**, 6854–6860 (1998)
28. James, C., Amalraj, A., Raghunathan, R., Joe, H., Jayakumar, V.S.: Structural conformation and vibrational spectroscopic studies of 2,6-bis(p-N, N-dimethyl benzylidene)cyclohexanone using density functional theory. J. Ram. Spectr. **37**, 1381–1392 (2006)
29. Polat, T., Bulut, F., Arıcan, I., Kandemirli, F., Yildirim, G.: Vibrational assignments, spectroscopic investigation (FT-IR and FT-Raman), NBO, MEP, HOMO-LUMO analysis and intermolecular hydrogen bonding interactions of 7-bromoisatin and 1-methylisatin-a comparative study. J. Mol. Struct. **1101**, 189–211 (2015)
30. Socrates, G.: Infrared and Raman Characteristic Group Frequencies, 3rd edn. Wiley, New York (2001)
31. Krishnakumar, V., Balachandran, V.: Structures and vibrational frequencies of 2-hydroxy-3-methyl-5-nitrobenzaldehyde and 2-methoxyl-1-naphthaldehyde based on density functional theory calculations. Spectrochim. Acta A. **63**, 464–476 (2006)
32. Nagabalasubramanian, P.B., Karabacak, M., Periandy, S.: Molecular structure, polarizability, hyperpolarizability analysis and spectroscopic characterization of 1-(chloromethyl)-2-methylnaphthalene with experimental (FT-IR and FT-Raman) techniques and quantum chemical calculations. Spectrochim. Acta A. **85**, 43–52 (2012)
33. Balachandran, V., Santhi, G., Karpagam, V., Revathi, B., Karabacak, M.: Spectroscopic investigation, natural bonding orbital analysis, HOMO-LUMO and thermodynamic functions of 2-tert-butyl-5-methylanisole using DFT (B3LYP) calculations. Spectrochim. Acta A. **136**, 451–463 (2015)
34. Rico, M., Orza, J.M., Morcilla, J.: Fundamental vibrations of thiophene and its deuterated derivatives. Spectrochim. Acta A. **21**, 689–719 (1965)
35. Karthick, T., Balachandran, V., Perumal, S.: Spectroscopic investigations, molecular interactions, and molecular docking studies on the potential inhibitor "thiophene-2-carboxylicacid". Spectrochim. Acta A. **141**, 104–112 (2015)

36. Krishnakumar, V., John Xavier, R.: FT-IR and FT-Raman spectra, HOMO-LUMO and NBO analysis of 2-Bromo-4-Nitrotoluene: an Ab Initio and DFT approach. Indian J. Pure Appl. Phys. **41**, 95–98 (2003)
37. Suresh, D.M., Amalanathan, M., Sebastian, S., Sajan, D., Hubert Joe, I., BenaJothy, V., Nemec, I.: Vibrational spectral investigation and natural bonding orbital analysis of pharmaceutical compound 7-Amino-2, 4-dimethylquinoliniumformate—DFT approach. Spectrochim. Acta A. **115**, 595–602 (2013)
38. Green, J.H.S., Harrison, D.J., Stockley, C.P.: Vibrational spectra of pentachlorophenol and pentachlorothiophenol. J. Mol. Struct. **33**, 307–314 (1976)
39. Silverstein, M., Webster, F.X.: Spectrometric Identification of Organic Compounds, 6th edn. John willey, Asia (2003)
40. Sathyanarayana, D.N.: Vibrational Spectroscopy Theory and Application. New Age International Publishers, New Delhi (2004)
41. Palafox, M.A., Nunez, J.L., Gil, M.: Accurate scaling of the vibrational spectra of aniline and several derivatives. J. Mol. Struct. (Theochem.) **593**, 101–131 (2002)
42. Tocon, I.L., Woolley, M.S., Otero, J.C., Marcos, J.I.: Vibrational spectrum of 3-methyl and 4-methylpyridine. J. Mol. Struct. **470**, 241–246 (1998)
43. Silverstein, M., Basseler, G.C., Morill, C.: Spectroscopic Identification of Organic Compound, 7th Edn., John Wiley & Sons, New York (2005)
44. Anand, S., Sundararajan, R.S., Ramachandraraja, C., Ramalingam, S., Durga, R.: Molecular vibrational investigation [FT-IR, FT-Raman,UV-Visible and NMR] on Bis(thiourea) Nickel chloride using HF and DFT calculations. Spectrochim. Acta A. **138**, 203–215 (2015)
45. Bakkiyaraj, D., Periandy, S., Xavier, S.: Spectroscopic (FT-IR, FT-Raman, FT-NMR and UV-Vis) investigation on benzyl dioxime using quantum computational methods. J. Mol. Struct. **1108**, 33–45 (2016)

Geometrical Structure, Vibrational Spectra, NLO, NBO, Electronic Transitions and Thermo Dynamical Analysis of 5-Fluoro-2-Methylbenzonitrile by DFT Computational Method

Arockiasamy Ajaypraveenkumar, R. Ganapathi Raman and S. Sebastian

Abstract Equilibrium geometric structure of 5-fluoro-2-methylbenzonitrile (5F2MBN) has been carried out through quantum mechanical calculations aided by Density Functional Theory (DFT) theory. Geometrical parameters (bond length, bond angle and dihedral angle) are predicted by using the DFT levels employing B3LYP method with 6-311++G (d, p), cc-pvdz and Aug- cc-pvdz as basis sets. The FT-IR and FT-Raman spectra of the 5F2MBN were recorded and analyzed by the same level of theory. Frequency doubling and Second Harmonic Generation (SHG) applications are exist in the title molecule, so that the Non Liner Optical (NLO) properties are calculated by the same method with different basis sets. Stability of the molecule occurring from hyper conjugative interactions, charge delocalization has been investigated by Natural Bond Orbital (NBO) analysis. The FMOs (Frontier Molecular Orbitals) reports energies and properties of many electron states. These FMOs is very important for predicting the optical and electric properties of the molecule. The various thermodynamic properties like entropy, enthalpy, Gibbs free energy, and elevated heat energy have been calculated. At last Molecular Electrostatic Potential (MEP) derived charges were also identified by the same theoretical calculations.

A. Ajaypraveenkumar · R. Ganapathi Raman (✉)
Department of Physics, Noorul Islam Centre for Higher Education, Kumaracoil, Kanyakumari Dist 629180, Tamilnadu, India
e-mail: ganapathiraman83@gmail.com

A. Ajaypraveenkumar · R. Ganapathi Raman
Nano Computational Laboratory, Department of Nano Technology, Noorul Islam Centre for Higher Education, Kumaracoil, Kanyakumari Dist 629180, Tamilnadu, India

S. Sebastian
PG and Research Department of Physics, St. Joseph's College of Arts and Science (Autonomous), Cuddalore 607001, Tamilnadu, India

J. Ebenezar (ed.), *Recent Trends in Materials Science and Applications*,
Springer Proceedings in Physics 189, DOI 10.1007/978-3-319-44890-9_54

1 Introduction

Benzonitrile is a vast and versatile component in the chemicals, which is called cyanobenzone or phenyl cyanide. The special benzonitrile derivatives like organic acids (benzoic acid, mandelic acid), amines (benzyl amine, pyridine), neutrals (benzonitrile, toluene) and benzonitrile herbicides. Benzonitrile is an applicable as solvent and precursor to number of derivatives. One of the benzonitrile derivatives is used in Pharmaceutical and Agrochemical Intermediates, Epoxy curing agent. Moreover Benzonitrile is mainly used for the agriculture fields, which households to control the growth of weeds and their residues persist in the environment [1]. In the Dye industries, benzonitrile components are being used for producing the aniline blue phthalocyanine dyes and are used for persevering for food [2]. These phthalocyanine dyes had the enormous applications in the medical field like photo redox reactions and photodynamic cancer therapy [3].

Dye-Sensitized Solar Cells (DSSCs) are recently the most efficient and low-cost third-generation solar technology, which is the trendiest tremendous interest as a green and renewable energy conversion device [4]. In the DSSC, the dye sensitizers are act as a superior and crucial part in the future researches [5]. The properties of the dye sensitizers like physical, electronic, thermal are required for the DSSC synthesis. So the theoretical and computational investigations of these dyes sensitizers have become an essential phenomena, to identify the innovative dye sensitizers with the enhancing properties.

The detail interpretation of crystal structure, vibrational frequency compared to experimental and theoretical of 2-Fluro-5-Methylnezonitrile has been studied by [2]. The vibrational spectrum of 2-Fluro-6-Methylnezonitrile has been studied by [6]. The bond-antibond stabilization energies are also investigated by applying the Natural Bond Orbital (NBO) analysis. Molecular energy stability calculations, vibrational analysis, electronic transitions and energy eigenvalues are evaluated for 2-Bromo-4-Methylnezonitrile compound done by [3].

Prakasam et al. reported Ultraviolet-Visible (UV-Vis) spectrum of 4-methoxybenzonitrile. In the paper, Electronic absorption spectra and sensitized mechanism are determined using gaseous state and solvent as Acetonitrile. The author had drawn the isodensity plots of frontier molecular spectra. The role of nitro group in 4-methoxybenzonitrile in geometries, electronic structures, and spectral properties analyzed [7]. Mohan et al. [8] reported vibrational frequency and Raman spectrum of 2-chloro-6-methylbenzonitrile and calculated the electronic transitions and thermal properties of the title compound.

Nitrile group dyes are very commonly used dyes that have a good mechanical and thermal stability. So it produces the fruitful outputs of the solar technology. Nitrile has a peak temperature up to 350 °C at the end of the life period. So that, the derivatives of nitrile are used for spacecraft, marine engineering, and electronic and integrated circuit packaging [7]. The research aims at behind the theoretical investigations on 5-Fluoro-2-methylbenzonitrile compound of the optimized

structure, which does not exist still now in my knowledge. Computational calculations are predicted by using the dynamic basic sets.

2 Computational Details

Density Functional theoretical computations of 5F2MBN are predicted by GAUSSIAN 09W program [9, 10] with the original version at the Becke-Lee-Yang-Parr hybrid method in correlation with three parameter functional by way of applying B3LYP level with 6-311++G (d, p), cc-pvdz, and Aug cc-pvdz basis sets on Intel Core i3 1.9 GHz processor personal computer to derive the complete geometry optimization [2]. Gaussian software is a super positioning tool for developing fields of computational physics like substituent effects, reaction mechanisms, potential energy surfaces, and excitation energies of the compound [11]. Computing energies at specific molecular structures and the related molecular properties are predicted by single point energy calculation. Geometry optimizations calculating equilibrium structure of molecules, optimizing transition structures and energy minimizations at dynamic basic sets. Frequency calculations are computing the second derivatives of the energy, this is using for calculating the FT-IR, Raman frequencies and intensities plots are done by the Gauss sum program. Make the use of GAUSSVIEW program by regularity considerations along with obtainable linked molecules vibrational frequency assignments are made with an elevated degree of precision.

UV–Vis spectra and electronic properties such as HOMO (higher occupied molecular orbital) and LUMO (lowest unoccupied molecular orbital) orbital energy distribution, HOMO and LUMO energy gap, Mulliken atomic charge distribution and thermo dynamical parameters are determined by time-dependent DFT (TD-DFT) [12] and the energy absorption spectra and energy gap plot drawn from Gauss view 5.0 program [13]. Electrostatic Potential map had been drawn by MOLKEL. Bond interactions and electron high density delocalization are analyzed using NBO in Gaussian 09 DFT with same basic sets. The polarizability and hyperpolarizability is calculated to understand the frequency doubling the SHG behavior of 5F2MBN.

3 Results and Discussion

3.1 Molecular Geometry Optimizations

The geometry optimized molecular structure of 5F2MBN has 16 atoms with 42 normal modes of vibrations that are obtained chemcraft program is shown in Fig. 1 [14]. It belongs to the C_1 point group symmetry. The computed minimizations energy of title compound by the DFT/B3LYP method with three basic sets is

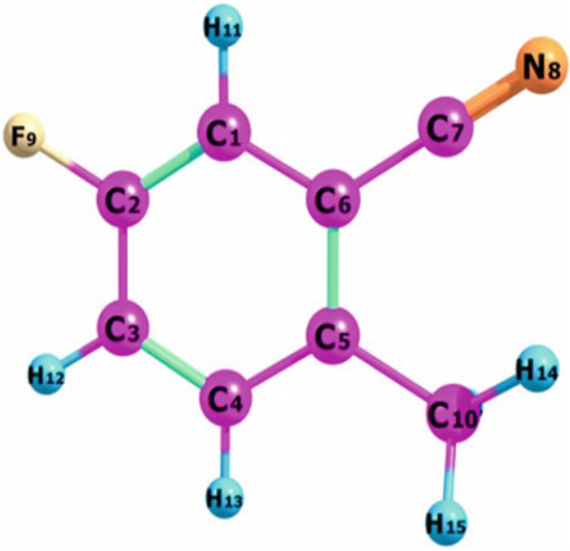

Fig. 1 Optimized geometrical structure of dye 5F2MBN

Table 1 Universal minimizations energy of 5-fluro-2-methlybenzonitrile

Basic sets	Energy (a.u)
6-311++G (d, p)	−463.1727458
cc-pvdz	−463.1727459
Aug-cc-pvdz	−463.0990167

tabulated in Table 1. The least minimizations energy is evaluated by the DFT/B3LYP method with Aug-cc-pvdz basic set. Table 2. Shows the various atomic distances, angles and dihedral angles are found to be almost at dynamic basic sets. The current investigation values on 5F2MBN merged with its experimental value which is taken through microwave (benzonitrile) in the solid phase obtained by [2, 15]. While comparing the microwave data and the gas phase data, that microwave data should be weaker than the gas phase, the DFT determined the ideal bond length of the 5F2MBN in the gas phase.

The bond length between the benzene ring carbon atoms C_1–C_2, C_2–F_9, C_3–C_4 and C_5–C_6 are giving a misleading in B3LYP with the three basic sets values are (1.36, 1.36 and 1.4 Å) smaller than the bonds between the C_1–C_6, C_2–C_3, C_4–C_5, C_5–C_{10}, and C_6–C_7 atoms bond length (1.54, 1.54 and 1.4 Å). The microwave data is 1.4 Å. It shows the B3LYP/Aug cc-pvdz level bond lengths are merged and gives fruitful results with the microwave data while compared to the other two basic sets. In the benzene ring all the carbon atoms had equal atomic lengths and angles approximately, which results and denotes the various physical and chemical property changes [16, 17] and the C_1–C_{11}, C_3–H_{12}, C_4–H_{13}, C_{10}–H_{14}, C_{10}–H_{15} and C_{10}–H_{16} bond lengths are predicted value is 1.07 Å.

The hexagonal structure of the bond angles between all atoms that has almost the same and microwave data also merged. Calculate the parameter values of different

Table 2 Atomic geometrical optimized parameters of 5-fluro-2-methlybenzonitrile

Parameters	B3LYP			Microwave data (benzonitrile)
Bond length (Å)	6-311++G (d, p)	Aug-cc-pvdz	cc-pvdz	
C_1–C_2	1.36	1.36	1.40	1.40
C_1–C_6	1.54	1.54	1.40	1.40
C_1–H_{11}	1.07	1.07	1.07	
C_2–C_3	1.54	1.54	1.40	1.39
C_2–F_9	1.35	1.35	1.35	1.35 [17, 40]
C_3–C_4	1.36	1.36	1.40	1.39
C_3–H_{12}	1.07	1.07	1.07	
C_4–C_5	1.54	1.54	1.40	1.39
C_4–H_{13}	1.07	1.07	1.07	
C_5–C_6	1.36	1.36	1.40	1.39
C_5–C_{10}	1.54	1.54	1.54	
C_6–C_7	1.54	1.54	1.40	
C_7–N_8	1.15	1.15	1.15	1.15
C_{10}–H_{14}	1.07	1.07	1.07	
C_{10}–H_{15}	1.07	1.07	1.07	
C_{10}–H_{16}	1.07	1.07	1.07	
C_2–C_1–C_6	120	120	119.9941	
C_2–C_1–H_{11}	120	120	119.9997	
C_6–C_1–H_{11}	120	120	120.0062	
C_1–C_2–C_3	120	120	119.9991	122.8 [17, 40]
C_1–C_2–F_9	120	120	120.0073	118.7 [17, 40]
C_3–C_2–F_9	120	120	119.9936	118.5 [17, 40]
C_2–C_3–C_4	120	120	120.0009	119.9
C_2–C_3–H_{12}	120	120	119.9959	
C_4–C_3–H_{12}	120	120	120.0032	
C_3–C_4–C_5	120	120	119.9994	120.2
C_3–C_4–H_{13}	120	120	120.0041	
C_5–C_4–H_{13}	120	120	119.9965	
C_4–C_5–C_6	120	120	119.9995	120.1
C_4–C_5–C_{10}	120	120	120.0055	
C_6–C_5–C_{10}	120	120	119.995	
C_1–C_6–C_5	120	120	120.007	120.2
C_1–C_6–C_7	120	120	120.0165	
C_5–C_6–C_7	120	120	119.9766	
C_5–C_{10}–H_{14}	109.4712	109.4712	109.466	
C_5–C_{10}–H_{15}	109.4712	109.4712	109.4745	
C_5–C_{10}–H_{16}	109.4712	109.4712	109.477	
H_{14}–C_{10}–H_{15}	109.4712	109.4712	109.4727	

(continued)

Table 2 (continued)

Parameters	B3LYP			Microwave data (benzonitrile)
Bond length (Å)	6-311++G (d, p)	Aug-cc-pvdz	cc-pvdz	
H_{14}–C_{10}–H_{16}	109.4713	109.4713	109.4707	
H_{15}–C_{10}–H_{16}	109.4712	109.4712	109.4664	
C_6–C_1–C_2–C_3	0	0	−0.0025	
C_6–C_1–C_2–F_9	180	180	−179.9983	
H_{11}–C_1–C_2–C_3	180	180	179.9963	
H_{11}–C_1–C_2–F_9	0	0	0.0005	
C_2–C_1–C_6–C_5	0	0	−0.0079	
C_2–C_1–C_6–C_7	180	180	179.9913	
H_{11}–C_1–C_6–C_5	180	180	179.9932	
H_{11}–C_1–C_6–C_7	0	0	−0.0076	
C_1–C_2–C_3–C_4	0	0	0.0038	
C_1–C_2–C_3–H_{12}	180	180	−179.9935	
F_9–C_2–C_3–C_4	180	180	179.9996	
F_9–C_2–C_3–H_{12}	0	0	0.0023	
C_2–C_3–C_4–C_5	0	0	0.0055	
C_2–C_3–C_4–H_{13}	180	180	−179.9931	
H_{12}–C_3–C_4–C_5	180	180	−179.9973	
H_{12}–C_3–C_4–H_{13}	0	0	0.0041	
C_3–C_4–C_5–C_6	0	0	−0.0159	
C_3–C_4–C_5–C_{10}	180	180	179.9868	
H_{13}–C_4–C_5–C_6	180	180	179.9826	
H_{13}–C_4–C_5–C_{10}	0	0	−0.0146	
C_4–C_5–C_6–C_1	0	0	0.0172	
C_4–C_5–C_6–C_7	180	180	−179.9821	
C_{10}–C_5–C_6–C_1	180	180	−179.9856	
C_{10}–C_5–C_6–C_7	0	0	0.0152	
C_4–C_5–C_{10}–H_{14}	−150	−150	−90.018	
C_4–C_5–C_{10}–H_{15}	−30.0001	−30.0001	29.9826	
C_4–C_5–C_{10}–H_{16}	89.9999	89.9999	149.9823	
C_6–C_5–C_{10}–H_{14}	30	30	89.9847	
C_6–C_5–C_{10}–H_{15}	149.9999	149.9999	−150.0146	
C_6–C_5–C_{10}–H_{16}	−90.0001	−90.0001	−30.015	

Taken from [2, 15, 17, 20]

basic sets of the fluro and nitrile (C_2–F_9 and C_7–N_8) atomic distances are coincided with microwave data. It gives the fruitful agreement with DFT calculations. The calculated geometric optimized parameters can be applicable for determine the other parameters of 5F2MBN.

3.2 FT-IR and FT-Raman Intensities

The compound 5-Fluoro-2-methylbenzonitrile (5F2MBN) is obtained from sigma-Aldrich Chemical Company, the USA with a steady purity of greater than 99 % and it was used as such without further purification. The FT-Raman spectrum of 5F2MBN has been recorded using 1064 nm line of Nd:YAG laser as excitation wavelength in the region 50–3500 cm^{-1} on a EZRaman, Enwaveoptronics, USA IFS 66 V spectrometer. The Fourier transform infrared (FTIR) spectrum was recorded using 8400 S Bruker, Alpha T, Germany infrared spectrophotometer using KBr pellet technique in the region 4000–400 cm^{-1}. The spectra were recorded at room temperature with scanning speed of 30 cm^{-1} min^{-1}. The comparison of both experimental and theoretical FT-IR and FT-Raman spectra of 5F2MBN compound are shown in Figs. 2 and 3. The spectral measurements are carried out at the Department of Nanotechnology, Noorul Islam Centre for Higher Education (NICHE), kumaracoil, Thackalay, Kanyakumari District.

The predicted Fourier Transform Infrared Spectroscopy and Raman Spectroscopy are computerized using the B3LYP with basic sets of 6-311++G

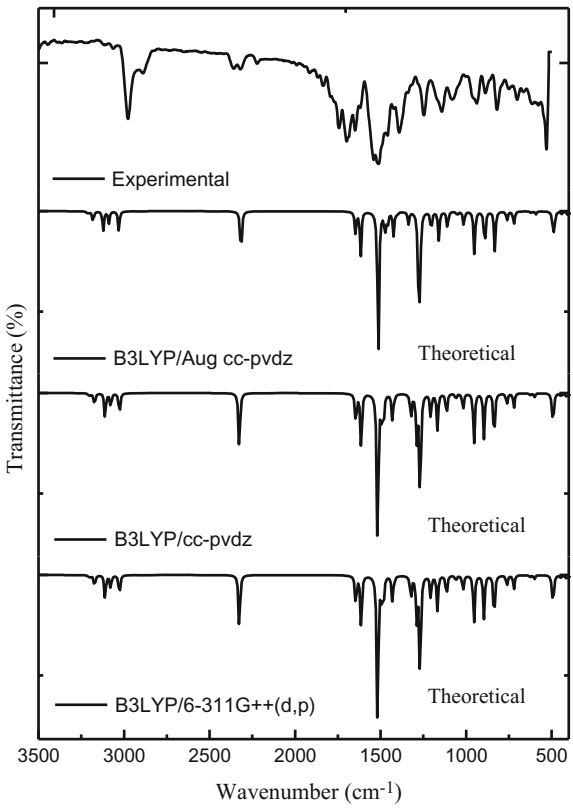

Fig. 2 Comparison of the FT-IR spectra

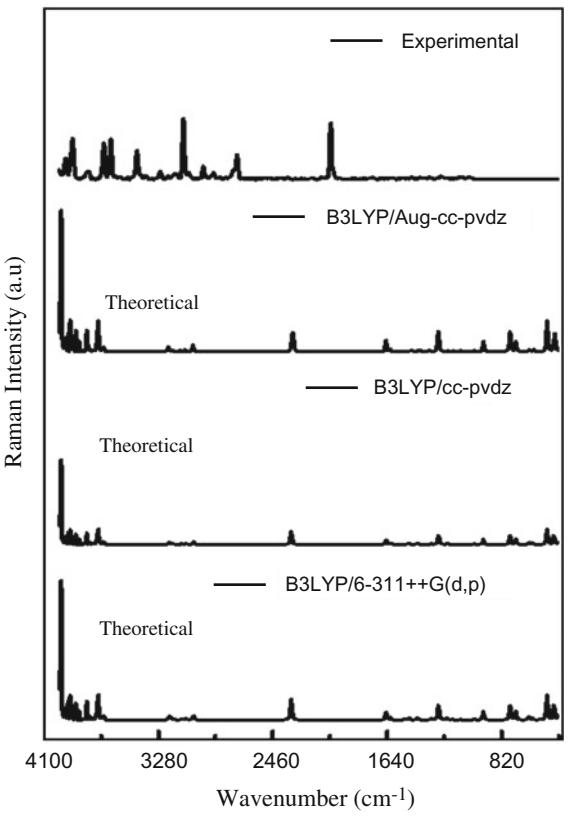

Fig. 3 Comparison of the FT-Raman spectra

(d, p)/ cc-pvdz. The output spectra are monitored threw Gauss sum program, which gives the Raman intensities spectra directly. This program equating the intensity theory of Raman scattering derived relationship and produces the modified Raman intensities data.

The assignments give the same results while compared with the three basic sets. The Raman intensity data also merged with the dynamic basic sets which confirmed the formation of methylbenzonitrile. The calculated vibrational frequencies are tabulated as shown in Table 3.

3.3 Vibrational Assignments

5-Fluro-2-methylbenzonitrile molecules contain 16 atoms and possessions to the point group Cs. The three Cartesian displacements of the 16 atoms offer 48 internal modes. The entire the elementary vibrations are vigorous in cooperation IR and Raman. Designed for N atomic molecules 2N-3 of every vibration is in-plane and

Table 3 Calculation of observed (FT-IR, FT-Raman) and calculated vibrational frequencies of the title compound

Normal modes		Experimental (cm^{-1})		Scaled wavenumbers (cm^{-1})				Vibrational assignments
Mode	Label	FT-IR	FT-Raman	B3LYP/6-311++G (d, p)	B3LYP/cc-pvdz	IR intensity (Km/mol)	Raman activity	
1	A			79	80	0.13	0.4102	τ CH_3
2	A		128	130	130	0.21	0.7025	τ C≡N
3	A		144	143	143	0.23	3.9458	β C≡N
4	A		154	154	154	0.25	0.2942	γ C–CH_3 + γ C≡N
5	A		304	304	304	0.48	0.426	β C–CH_3 + β C–F
6	A		338	337	337	0.54	2.0035	ω C–F
7	A		404	403	403	0.64	1.4563	γ C–CH_3
8	A		414	415	415	0.66	0.5394	16a γ C–C–C
9	A		446	446	446	0.71	5.7741	β C–C–C
10	A		492	492	492	0.78	0.474	16b γ C–C–C
11	A	499	498	498	498	0.79	9.3586	16b β C–C–C
12	A	602	602	602	602	0.96	1.2148	16a β C–C–C
13	A	628	628	627	627	1.00	1.9935	6a δ
14	A	720	720	720	720	1.15	0.3561	γ C–C–C + t C≡N
15	A	723	722	723	723	1.15	7.6416	γ C–C–C + t C≡N
16	A	764	764	764	764	1.22	16.5348	β C–C–C + t C–F
17	A	838	838	838	837	1.33	0.0978	17b γ C–H
18	A	897	898	898	898	1.43	0.0739	γ C–H + τ C≡N
19	A	955	956	955	955	1.52	14.6849	10a γ C–H
20	A	965	966	965	965	1.54	0.072	Ring breathing
21	A	1021	1020	1020	1020	1.63	2.5262	Trigonal bending
22	A	1062	1062	1062	1062	1.69	0.134	ρ CH_3

(continued)

Table 3 (continued)

Normal modes		Experimental (cm^{-1})		Scaled wavenumbers (cm^{-1})				Vibrational assignments
Mode	Label	FT-IR	FT-Raman	B3LYP/6-311++G (d, p)	B3LYP/cc-pvdz	IR intensity (Km/mol)	Raman activity	
23	A	1117	1118	1117	1117	1.78	2.1453	β CH + υ C–F
24	A	1171	1170	1170	1170	1.86	1.8219	β CH
25	A	1209	1210	1209	1209	1.93	6.4833	β CH + υ C–F
26	A	1272	1272	1272	1272	2.03	60.2073	β CH
27	A	1291	1292	1292	1291	2.06	2.5717	υ C–F
28	A	1325	1326	1325	1325	2.11	6.1959	γ C–CH_3
29	A	1423	1424	1423	1423	2.27	11.9581	CH_3 asym.deform
30	A	1435	1434	1434	1434	2.29	2.551	CH_3 asym.deform
31	A	1484	1484	1484	1484	2.36	8.6356	14 υ C–C
32	A	1496	1496	1495	1496	2.38	4.7715	β CH_3
33	A	1521	1522	1521	1521	2.42	4.2765	19a υ C–C
34	A	1616	1616	1617	1617	2.58	16.1349	8b υ C–C (semi-circle stretch)
35	A	1649	1648	1648	1648	2.63	60.4469	8a υ C–C
36	A	2230	2230	2230	2230	3.71	390.9454	γ C≡N
37	A	3034	3034	3033	3033	4.83	195.3965	υsym CH_3
38	A	3083	3084	3084	3083	4.91	63.8787	20a** arom. υ C–H
39	A	3117	3118	3116	3116	4.97	55.0693	υ C–H
40	A	3178	3178	3179	3179	5.07	73.9126	υ C–H
41	A	3202	3202	3203	3203	5.10	162.9662	υ C–H
42	A	3212	3212	3212	3212	5.12	85.3282	υ C–H

υ-stretching; υsym-symmetric stretching; υasy- asymmetric stretching; β-in plane bending; γ-out-of-plane bending; ω-wagging; t-twisting; δ-scissoring; τ-torsion; *-wilson's notion; IR int-IR intensities

N-3 is out of plane. As a result for 5F2MBN 29 of all 42 vibrations are in-plane and 13 out of plane.

The harmonic vibrational frequencies premeditated for 5F2MBN at B3LYP level by 6-311++G (d, p) and cc-pvdz basis sets have been specified in table. The pragmatic FT-IR and FT-Raman frequencies for an assortment of modes of vibrations are obtainable in table. Contrast of the frequencies designed by B3LYP functional tends to misjudge the essential modes. It is observed that scaling factor has to be used for obtaining the substantial healthier conformity among experimental data.

C–H Vibrations

The C–H stretching modes more often does not emerge with strong Raman intensity and are extremely polarized. May be due to this high polarization, Raman band has been pragmatic in experimental spectra. The C–H stretching vibrations of benzene derivatives usually become visible above 3000 cm^{-1} [6, 18, 19]. In the FT-IR spectrum of 5F2MBN the bands of 3033 and 3083 cm^{-1} are assigned to C-H stretching vibrations of aromatic ring. In the FT-Raman spectra the band observed at 3084 and 3034 cm^{-1} are attributed to C–H stretching vibrations. The computed vibrations in the 3098–3065 cm^{-1} [2, 20] are in agreement with experimental assignment 3045–3080 cm^{-1} [2, 21]. The three in plane C–H bending vibrations appear in the range 1000–1300 cm^{-1} for the substituted benzenes and the three out of plane bending vibrations occur in the frequency range 750–1000 cm^{-1} [2, 22]. Generally, the C–H plane out-of-plane deformation of the higher wave numbers has weaker intensity than those absorbing at lower wave numbers. In the present study, the C–H out-of—plane vibrations are identified at in the FT-IR and FT-Raman spectrum. The C–H bending vibrations are expected to interact a little around 1600–1300 cm^{-1} with ring vibrations [23].

The C–H in plane bending vibrations assignment in the region 1106–1234 cm^{-1} smooth while establish to be infected by C–F stretching vibrations are in the range originate former [2, 24, 25] at the same time as the experimental observations are at 1117–1272 cm^{-1} in FT-IR and 1118–1272 cm^{-1} in FT-Raman spectra correspondingly.

Hypothetically computed vibrational frequency by B3LYP/6-311++G (d, p) technique 1291, 1272, 1209, 1171, 1117, 1062, 1021 cm^{-1} (modes 27–21) are assigned to C–H in plane bending vibrations. The measured frequencies 965, 955, 897, 838, 764, 723, 720 cm^{-1} (modes 20–14) by B3LYP (6-311++G (d, p) for C–H out of plane bending vibrations filled in the FT-IR value at 965–720 cm^{-1}.

C–F Vibrations

The vibration belonging to the bond stuck between the ring and halogen atoms is appeal to argue here, because integration of the vibrations is probable owing to the lowering of the molecular equilibrium and the being there of heavy atom on the fringe of the molecule [6, 26]. Sundaraganesan et al. [2] assigned vibrations of C–X group (X=F, C and N) in the frequency range 1275–412 cm^{-1}. In FT-IR spectrum of 5F2BMN the strong bands at 1272 cm^{-1} in FT-Raman spectrum are assigned to C–F stretching vibrations. The theoretically computed values are found at

1272 cm^{-1} by B3LYP/6-311++G (d, p)/cc-pvdz methods show good agreement with recorded spectral data. The C–F in-plane bending modes contain strapping to average intensity usually in the region 550–250 cm^{-1} [6, 27]. In the present study, the strong bands at 498 cm^{-1} was assigned to the C–F in-plane bending of FMBN. The bands observed at 143 cm^{-1} was assigned to the C–F out-of-plane bending mode of FMBN.

C–N vibrations Nitrogen compounds featuring triple or calculated doubled bounds such as cyanides or nitriles and cyanates, all offer a single spectrum classically with a single normally intense absorption in the range 2280–2200 cm^{-1} (for cyano compounds) and 2285–1990 cm^{-1} (for cyantes, isocyantes and thiocyanates) [28–30]. The geometry of the cyano group (C=N) is exaggerated considerably by a novel substituent of the phenyl ring. Hence the vibrational wave numbers on the cyano group relics almost unaffected from the benzonitrile molecule. Electron withdrawing groups such as –Cl, –F, –Br, $–NO_2$, –OH, and CF_3 decrease the IR band intensity and increase the wave numbers value to the higher limit of the characteristics spectral regions, whereas electron donating groups, such as amino group, increase the intensity and decrease the wave numbers. For the aromatic compound which bears a C=N group attached to the ring, a band of very good intensity has been observed in the region 2240–2221 cm^{-1} [31] and it is being attributed to C=N stretching vibrations. A strong IR band at 2230 cm^{-1} in 5F2MBN indicate the C=N stretching vibration. The theoretically computed and assigned by the Gauss view package at 2230 cm^{-1} by B3LYP/6-311++G (d, p)/cc-pvdz at (mode no. 36) is assigned to C=N stretching vibrations.

Contribution of the bending in-plane mode and out-of-bend modes of C=N group, by contrast appear with the IR intensity and with null Raman activity and strongly coupled with C–C–C bending modes. Contribution of the bending in-plane mode are resolute in the bands at roughly 600, 550 and 30 cm^{-1} while the out-of-plane mode is identified in the IR band at 420 cm^{-1}, in contradiction with that reported in MFBN [6, 32] at 606 cm^{-1}. Hence in the present study, the C=N in-plane and out-of-plane bending modes are recorded at 628 cm^{-1} in FT–IR. These bands are in good agreement with the calculated values are found at 627 cm^{-1}.

Methyl Group Vibrations

The title molecule 5F2MBN under deliberation possesses only one CH_3 group in second position of the ring [2]. For the assignments of CH_3 group frequencies, one can expect nine fundamentals can be associated to each CH_3 group, namely the symmetrical stretching in CH_3 (CH_3 sym. stretch) and asymmetrical stretching (CH_3 asym. stretch), in-plane stretching modes (i.e., in-plane hydrogen stretching mode); the symmetrical (CH_3 sym. deform) and asymmetrical (CH_3 asy. deform) deformation modes; the in-plane rocking (CH_3 ipr), out-of-plane rocking (CH_3 opr) and twisting (tCH_3) modes. Methyl groups are generally referred as electron donating substitution in the aromatic ring system [6].

At about 1440 ± 1455 cm^{-1} the asymmetric deformations, at about 1370 ± 1380 cm^{-1} the symmetric deformation and in the 1040 ± 970 cm^{-1} range the methyl group rocking modes. These frequencies are in agreement with those

found in the characteristic group frequency tables [33] and for methylpyrazine [23]. It is seen that the transport of the scale factors reproduces the predictable experimental behavior of the methyl group. Some bands corresponding to the methyl group fundamentals are not experimentally observed. For example, of the two possible bands corresponding to the das (CH_3) modes, only the bands at about 1435 and 1434 cm^{-1}, respectively, are observed, in 5F2MBN. However, the $\delta(CH_3)$ mode is observed in the IR and Raman for both derivatives at a frequency of approximately 1325 cm^{-1} [34].

The rocking vibrations of (CH_3) have been identified at 1021 cm^{-1} i.e. ρr. The theoretically calculated value by BELYP method using 6-311++G (d, p) basis set is at 1020 cm^{-1}. The asymmetric and symmetric in-plane bending modes of CH_3 group are at 1325 and 1291 cm^{-1} (mode no. 28 and 27) [2]. Likewise, a medium strong FT-Raman band observed at 1171 cm^{-1} with mixed contribution to the υCC, with no FT-IR band observed in 5F2MBN molecule has been assigned to out-of-plane deformation. In the research paper have found that the vibrational bands corresponding to methyl vibrations virtually stay put the equal in magnitude and intensity. Methyl rocking frequencies are mass sensitive and variable in position due to the interaction through skeletal stretching modes [35]. Normally, these bands are observed weakly in the range 1120–1050 and 900–800 cm^{-1} [36, 37]. For the FMBN, only a very strong FT-IR band at 1117 cm^{-1} combined with computed ones have been assigned, since the medium FT-IR band at 897 cm^{-1} with significant contribution to the β. Rigd and Rtrigd, which have been assigned to in-plane rocking and out-of-plane rocking modes, respectively. As CH_3 twisting mode is expected below 400 cm^{-1}, the computed bands at 79 and 80 cm^{-1} by B3LYP/6-311G++ (d, p) and cc-pvdz methods without support by PEDs, are assigned to this mode, for no spectral measurements were possible in the region due to instrumental limits [6].

3.4 Frontier Molecular Orbital

Highest Occupied Molecular Orbital (HOMO) and Lowest Unoccupied Molecular Orbital (LUMO) interactions are held between acid-base. In general, when the orbital reacts with one another is produced another two orbital which has the filled-empty interaction for the stabilization. Those interactions are most welcomed orbital in molecules for reactivity and kinetic stability. The HOMO is the orbital that could act as fulfilled electron pair, most available for bonding, most weakly held electrons and characteristic for nucleophilic component [38]. The LUMO is the orbital that could act as the empty and characteristic for electrophilic component. These orbital are placed in a final boundary level of electron of the molecule, so it is called the frontier orbital (FMO's). HOMO energy, LUMO energy and chemical potential analyzed by different basic sets and listed in Table 4. The bond between

Table 4 Calculated some of the frontier orbital energies for the title compound

Basic set	6-311++G (d, p)	cc-pvdz	Aug-cc-pvdz
SCF energy (a.u)	−463.132	−463.168	−463.058
Dipole moment (Debye)	3.985	3.984	3.974
LUMO (eV)	−2.05	−2	−2.05
HOMO (eV)	−7.42	−7.35	−7.42
ENERGY GAP (eV)	−5.37	−5.35	−5.37
Electro negativity (χ)	−4.735	−4.675	−4.735
Chemical Potential (μ)	4.735	4.675	4.735
Global Hardness (η)	2.685	2.675	2.685
Global softness (s)	0.372439479	0.3738318	0.372439479
Electrophilicity Index (ω)	6.3567375	6.2528125	6.3567375
EHOMO-1 (eV)	−7.91	−7.83	−7.91
ELUMO + 1 (eV)	−1.09	−1.14	−1.09
EHOMO-1—ELUMO + 1 (eV)	−6.82	−6.69	−6.82

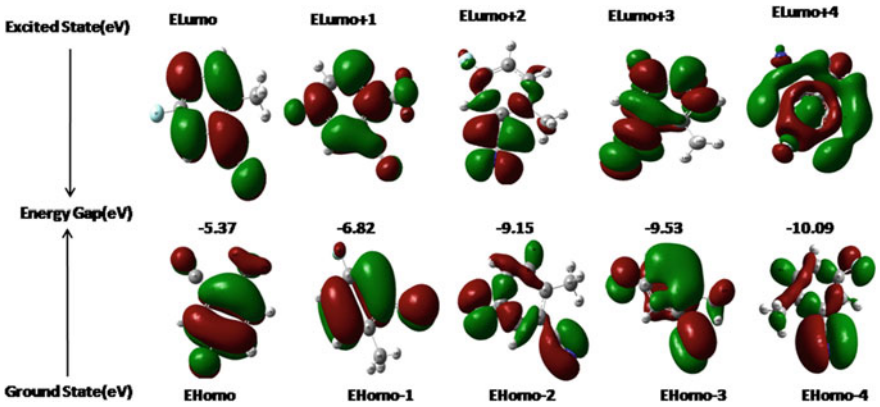

Fig. 4 Energy gap plot of 5-fluoro-2-methylbenzonitrile

atomic orbital compositions is described by the HOMO and LUMO diagram shown in Fig. 4. Both orbital have the higher standard value [39].

In General a molecule could be excited by an external source (i.e. photons) and an electron can jump from an occupied state to an unoccupied state and an excited molecule. Sometimes this molecule reacts differently than the ground state molecule. For example in Ir 3+ complexes, often used as catalyst, you can have an "unspinning" process. By Irradiation with light, an electron pair (spin +1/2 1/ 2) in

the highest occupied d orbital is excited and the electron jump in the unoccupied d orbital. By doing this you create 2 singlet with +1/2 spin. This now can relax also by transferring (or taking) one of these electrons to a Legend (or the molecule attached to the catalytic Center). The process is not completely well understood, as these active Transition states, are very hot, so they have a short life, but with DFT could be simulated quite well. As what happen will depend a lot on the specific electronic structure of the molecule, and on the allowed or not allowed transitions. It suggests looking at some photochemistry literature, as there the transitions are often well described.

This small HOMO-LUMO energy gap for the title compound is 5.6 eV indicate that molecular charge transfer occurs in the compound. Energy gap is little and it is trouble-free to observe that they can be sensitive to the influence of the polar environment. When go to the Homo, Lumo +1, +2, +3, and +4 energy gap increased respectively. Determination of the energy gap, the dipole moment and first order hyperpolarizability shows that the title molecule is an attractive object for future studies of non-linear optical properties [40].

The 3D images of the orbital computed for the 5F2MBN molecules are illustrated in Fig. 4. The energy gap projected the equalized charge transfer interactions taking place within the molecule and it is also can be supported with NLO results [41].

3.5 NLO Properties

In the fields such as communication, signal processing and optical interconnections, NLO enhance the functions for frequency shifting, optical modulation, optical switching and optical logic for the developing technologies [40]. The first hyperpolarizability (β), dipole moment (μ) and polarizability (α) of 5F2MBN is calculated using DFT with the 6-311++G (d, p) basic set for the NLO applications like frequency doubling and SHG. Based on the finite-field approach, the non-linear optical parameters such as dipole moment, polarizability, and first order hyperpolarizability of 5F2MBN molecules are calculated using the 6-311++G (d, p) basis set for more reliability. The numerical values of above mentioned parameters are listed in Table 5. In the presence of an external electric field (E), the energy of the system is a function of the electric field. First hyperpolarizability is a third-rank tensor that can be described by a 3 3 3 matrix.

In this research paper, 5F2MBN compound has been computed and tabulated the polarizability. The hyperpolarizability tensors [40] are predicted only on the software with basic set and results obtained from the equations already programmed by software. However, values should be modulated from the atomic units to electronic units (esu) [17]. It is well known that the higher values of dipole moment, molecular polarizability, and hyperpolarizability are important for more active NLO

Table 5 Functions of the optical using B3LYP method 6-311 ++G (d, p) basic level of the 5F2MBN

Parameters	B3LYP
	6-311++G (d, p)
μ x	0.8197256
μ y	−0.01
μ z	1.3473167
μ=	1.577 Debye
α xx	101.757788
α xy	−0.3604599
α yy	53.7128032
α xz	−4.5871788
α yz	0.28
α zz	128.7684006
α0	198.393×10^{-33} esu
α=	1713.98×10^{-33} esu
β xxx	80.156319
β xxy	−2.4476356
β xyy	26.3796534
β yyy	−8.36091
β xxz	−35.3219987
β xyz	6.6626508
β yyz	28.5648953
β xzz	21.4224614
β yzz	3.8015823
β zzz	−81.8304551
β0	1345.907×10^{-33} esu

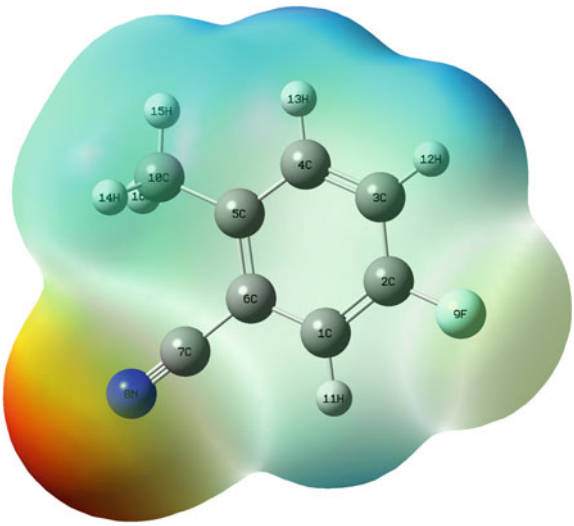

Fig. 5 Electrostatic potential surface of 5-fluoro-2-methylbenzonitrile

properties. The calculated dipole moment is equal to 1.577Debye in 5F2MBN. The calculated polarizability aij are dominated by the diagonal components while have non-zero and zero values. The α value of the compound equated as 1713.98 × 10^{-33}esu for title molecules. The values β of the title compounds with 6-311++G (d, p) basic set is 1345.907 × 10^{-33} esu.

The calculated values of polarizability (α) and first hyperpolarizability (β) comes out to be as 198.607 and 154.879 a.u. Threshold values for NLO effects is that of Urea used for comparison purposes whose polarizability and first hyperpolarizability values are compared with our title compound values. It has been shown the enhancing NLO property [42]. Since from the computed results, the values are 6 times that of standard values. So it is proposed that the compound under investigation is a strong potential material for NLO applications like frequency doubling and SHG.

4 Other Molecular Properties

4.1 Thermodynamic Parameters

Several calculated thermodynamic parameters are given in Table 5. Scale factors have been recommended [43] for an accurate predication in determining the zero-point vibration energies (ZPVE), and the entropy(S) vibration(T) and they can be used with the values of this table [44]. On the other hand, the accurate prediction of Entropy, Enthalpy, Gibbs free energy, elevated heat energy and minimum energy had been calculated. The margin values of 5F2MBN at room temperature at different methods, which gives the changes in the total entropy. The total energies and the change in the total entropy and Self consistent field energy of 5F2MBN at room temperature at different basic sets are also tabulated in Table 6.

4.2 Electrostatic Potential

Molecular Electrostatic Potential (ESP) surface plotted the optimized electronic structure of 4F3MBN, intended for predicting reactive sites of the molecules by using the B3LYP/6-311++G (d, P) basis set using the computer software Molekel. To comprehend the qualified polarity of the molecules threw the visual technique. Learn association among the molecular structures as well as the physiochemical properties [45]. The Electrostatic potential is adopted for analyzing the process on the recognition of each molecule. This is applicable in a drug-receptor and enzyme substitute interactions [46–48]. In the MEP, generated a charge distribution gap

Table 6 Thermodynamic parameters of 5-fluro-2-methylbenzonitrile

Thermodynamic parameters of DMAP	B3LYP		
	6-311++G (d, p)	cc-pvdz	Aug-cc-pvdz
Self-consistent field energy (a.u)	−463.133	−463.168	−463.058
Zero point vibrational energy (kcal/mol)	73.966	73.964	73.883
Rotational constant (GHz)	2.283	2.284	2.275
	1.044	1.044	1.036
	0.720	0.720	0.715
Rotational temperature (K)	0.110	0.110	0.109
	0.050	0.050	0.050
	0.035	0.035	0.034
Thermal energy (kcal/mol)			
Total	79.422	79.419	79.327
Translational	0.889	0.889	0.889
Rotational	0.889	0.889	0.889
Vibrational	77.645	77.642	77.550
Specific heat capacity at constant volume (cal/mol K)			
Total	32.274	32.275	32.381
Translational	2.981	2.981	2.981
Rotational	2.981	2.981	2.981
Vibrational	26.313	26.313	26.419
Dipole moment (Debye)	3.579	3.550	3.678
Lumo (eV)	−1.790	−1.500	−1.790
Homo (eV)	−7.400	−7.180	−7.400
Energy gap (eV)	−5.610	−5.680	−5.610
Entropy(S) (cal/mol K)			
Total	91.776	91.751	91.333
Translational	40.614	40.614	40.614
Rotational	29.617	29.617	29.635
Vibrational	21.545	21.520	21.085
Gibbs free energy	0.084	0.084	0.084
Enthalpy	0.128	0.128	0.127

around the molecule, which is exceedingly useful in accepting the reactive sites for nucleophilic and electrophilic attack in studies of biological identification and hydrogen bonding interactions [49, 50]. The region with red color is regarded as most electronegative (electrophilic) region and the region with blue color is most positive (nucleophilic) region, where as the bluish green color surrounded by the ring system of APN is related to less positive region. The electrophilic and nucleophilic have red and blue color respectively. Red color is regarded as most

electronegative region and blue color is most positive region. For the zero regions represent the color of green [40]. The dissimilar colors are represented as dissimilar values of the electrostatic potential at the surface are shown inthe (Fig. 5).

4.3 Mulliken Population Analysis

The Mulliken analysis is the oldest and finest population analysis method. The electron population of each atom of the molecules is identifying, because of calculating the mulliken charges as explained by the density functional methods. The charge distribution of the 5F2MBN gives the Carbon and Hydrogen charges had both signs. It has positive charge as well as negative with different basic sets. Fluruo and Nitrile atoms have negative charges in all basic sets, which are donor atoms. Mulliken atomic charge calculation has an important role in the application of quantum chemical calculation to molecular system because of atomic charge effect, dipole moment, molecular polarizability, electronic structure and a lot of properties of molecular systems. The Gaussian output shown in the Table 7. The title molecule has different charge distribution with respect to the dynamic basic sets and quantum calculations. The predicted atomic charges are explained through graphical representation (Fig. 6). In order to change the every basic set, the charge distribution should be change [51]. The charge changes with basis set due to

Table 7 Calculated net charges by Mulliken Population Method

Atoms	B3LYP		
	6-311++G (d, p)	cc-pvdz	Aug-cc-pvdz
C_1	−0.194	0.224	0.829
C_2	−0.260	−0.307	−0.166
C_3	0.213	0.250	0.533
C_4	−0.442	−0.313	1.417
C_5	−0.130	0.028	−0.444
C_6	1.858	1.852	1.632
C_7	−1.383	−1.484	−0.969
N_8	−0.159	−0.178	−0.069
F_9	−0.152	−0.170	−0.570
C_{10}	−0.413	−0.498	1.060
H_{11}	0.201	0.200	−0.855
H_{12}	0.210	0.204	−0.758
H_{13}	0.175	0.168	−0.968
H_{14}	0.155	0.179	−0.211
H_{15}	0.140	0.139	−0.327
H_{15}	0.181	0.154	−0.134

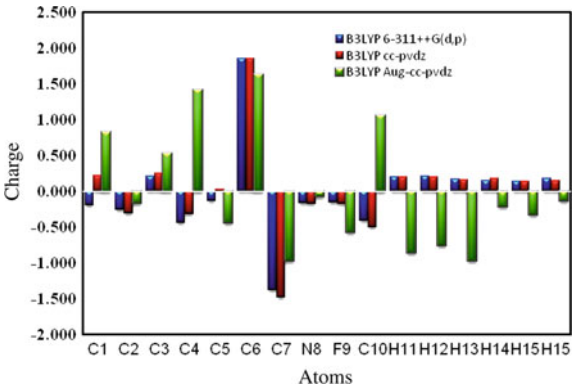

Fig. 6 Mulliken charge comparison graph by B3LYP with the three basic sets

polarization For example, the charge of H(15) and H(16) atoms are 0.140, 0.181e, 0.212e at B3LYP/6-311++G (d, p), 0.139e, 0.154e at B3LYP/cc-pvdz and −0.327e, −0.134e at B3LYP/cc-pvdz in 5F2MBN.

4.4 Natural Bond Orbitals

The high electron density in orbital bonding is predicted Natural Bond Orbital (NBO) analysis. In the natural localized orbital sets, NBOs is the one of the sequence. Natural localized orbital calculate the electron density in atom and bonding of the atoms. The molecular systems investigating charge transfer or conjugative interaction in a convenient basis. To evaluate the interactions of the orbital in the NBO analysis the second order Fock matrix should be carried out. The micro disturbance theory also is reported for resulting the electron donor orbital, acceptor orbital and the interacting stabilization energy [52]. The perfect Lewis structure into an empty non-Lewis orbital predicting the solution of interaction is a loss of occupancy from the concentration of electron NBO. For each donor and acceptor, the stabilization energy E (2) associated with the delocalization i–j is estimated as:

$$E(2) = -n_\sigma \frac{\langle \sigma | F | \sigma \rangle^2}{\varepsilon_\sigma^* - \varepsilon_\sigma} = -n_\sigma \frac{F_{ij}^2}{\Delta E}. \quad (1)$$

The larger is the E (2) value, the more intensive is the interaction between electron donors and electron acceptors, i.e., the more donating tendency from electron donors to electron acceptors and the greater the extent of conjugation of the whole system. Delocalization of electron density between occupied Lewis type (bond or lone pair) NBO orbital and formally unoccupied (antibonding and

Rydgberg) non-Lewis NBO orbital correspond to a stabilizing donor–acceptor interaction. The NBO analysis has been performed on the compound using NBO 3.1 program as implemented in the Gaussian 09 W package at the DFTB3LYP/6-311++G (d, p) level of theory in order to elucidate the intermolecular interaction, hybridization and delocalization of electron density within the molecule, which are presented in Table 8. The ICT (Intra molecular charge transfer) causing stabilization of the system, because of the intermolecular hyper conjugative interactions are formed by the orbital overlap between σ(C–C)–σ*(C–C), π(C–C)–π*(C–C). ICT is one of the strongest causes for the NLO activity [34]. These interactions are

Table 8 Second order perturbation theory analysis of fockmatrix in NBO basis for 5F2MBN

Donor (i)	Type	Ed/e	Acceptor (j)	Type	Ed/e	E (2)	E (i)–E (j)	f (i,j)
C_1–C_2	Σ	1.97828	C_2–C_3	σ*	0.02733	5.26	1.34	0.075
C_1–C_2	π	1.66045	C_3–C_4	π*	0.0142	22.44	0.3	0.073
C_1–C_6	σ	1.95921	C_5–C_6	σ*	0.03305	5	1.28	0.071
C1–C6	σ	1.95921	C_7–N_8	σ*	0.01175	4.39	1.65	0.077
C_1–H_{11}	σ	1.97592	C_2–C_3	σ*	0.02733	3.95	1.13	0.06
C_2–C_3	σ	1.97969	C_1-C_2	σ*	0.02622	5.26	1.34	0.075
C_2–F_9	σ	1.99504	C_1–C_6	σ*	0.0251	1.31	1.56	0.041
C_3–C_4	σ	1.97155	C_2–F_9	σ*	0.03366	4.49	0.97	0.059
C_3–C_4	π	1.66057	C_1–C_2	π*	0.3454	22.63	0.28	0.071
C_3–H12	σ	1.97683	C_1–C_2	σ*	0.02622	3.96	1.13	0.06
C_4–C_5	σ	1.97571	C_5–C_6	σ*	0.03305	3.35	1.28	0.059
C_4–H_{13}	σ	1.97999	C_5–C_6	σ*	0.03305	4.37	1.11	0.062
C_5–C_6	σ	1.9635	C_7–N_8	σ*	0.01175	4.95	1.66	0.081
C_5–C_6	π	1.63837	C_1–C_2	π*	0.3454	21.28	0.28	0.07
C_5–C_{10}	σ	1.9807	C_1–C_6	σ*	0.0251	3.32	1.16	0.055
C_6–C_7	σ	1.97705	C_7–N_8	σ*	0.01175	9.59	1.69	0.114
C_7–N_8	σ	1.99336	C_6–C_7	σ*	0.03151	8.28	1.61	0.104
C_7–N_8	δ	1.95761	C_5–C_6	π*	0.39706	8.33	0.36	0.054
C_{10}–H_{14}	σ	1.9853	C_4–C_5	σ*	0.02035	3.32	1.08	0.054
C_{10}–H_{15}	Σ	1.98661	C_5–C_6	σ*	0.03305	3.47	1.08	0.055
C_{10}–H_{16}	Σ	1.9763	C_5–C_6	π*	0.39706	4.2	0.54	0.047
LP								
N_8	Σ	1.97161	C_6–C_7	σ*	0.03151	11.35	1.05	0.098
F_9	Σ	1.98986	C_2–C_3	σ*	0.0273	1.2	1.63	0.04
F_9	Π	1.97209	C_1–C_2	π*	0.3454	5.91	1.01	0.069
F_9	Δ	1.92898	C_1–C_2	π*	0.3454	18.1	0.44	0.085

[a]E(2) means energy of hyper conjugative interaction (stabilization energy)
[b]Energy difference between donor and acceptor i and j NBO Orbitals
[c]$F_{(i;\ j)}$ is the Fock matrix element between i and j NBO Orbitals

observed as increase in electron density (ED) in C–C antibonding orbital that weakens the respective bonds. The stabilization energy (18.1 kJ/mol) of lone pair F_9 (δ) with that of anti-bonding C_1–C_2 is the most valuable interactions in the whole molecule. The resulting stabilization (22.63 kJ/mol) energy transfer occurs from C_3 to C_4 with antibonding C_1–C_2, which one is the very largest delocalization. The resulting stabilization energy of (1.2 kJ/mol) loan pair F_9 (σ) with that anti bonding C_2–C_3 is the smallest delocalization, as listed in Table 6. In the substitution, least energy transfer is exist only on carbon-fluorine interactions, C_7–F_9 (σ) to C_1–C_6 (σ*) (1.31 kJ/mol).

4.5 UV–Visible

The UV–Visible spectrum of 5F2MBN is drawn in Fig. 7. In the electronic transition spectra cut off wavelength is the most important parameters. In our title compound has high delocalization of π-electrons which absorbed 300 nm and these band is due to the electronic transition of π–π* [53]. The benzonitrile dyes have the electron injection, Especially when electrons are being injected from the excited dye to semiconductor surface.

Computational calculations with basic level to observe the electronic transitions of 5F2MBN and electronic absorption spectra were graphed. The UV–Vis region is the stronger region while compare with the absorption in the visible region, which results have a red-shift. This result indicates the excited state of 5F2MBN molecule has the good absorption value, so in the research paper use on DSSC applications and the other NLO applications, which enhancing well.

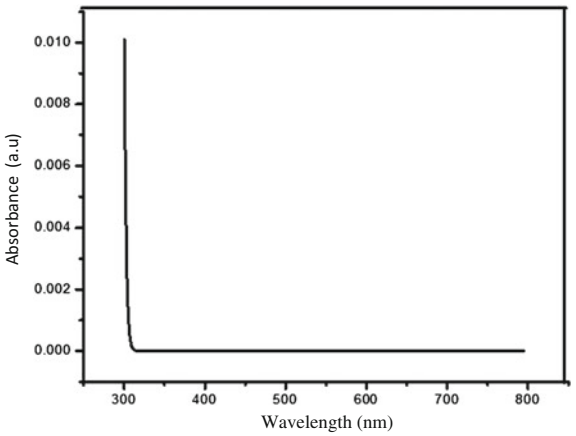

Fig. 7 Theoretical electronic absorption spectra of 5F2MBN

5 Conclusion

B3LYP level with the B3LYP similar basis sets are utilized to conduct a detailed study of the structures, geometrical parameters, molecular electrostatic potential map and thermodynamic parameters of 5F2MBN. The significant changes in bond lengths of the 5F2MBN are explained with the help of NBO analysis. In the NBO analysis, elucidate the intermolecular interaction, hybridization and delocalization of electron density within the molecule. The ICT (Intra molecular charge transfer) causing stabilization of the system, because of the intermolecular hyper conjugative interactions are formed by the orbital overlap between σ(C–C)–σ*(C–C), π(C–C)–π*(C–C). The lowering of the HOMO-LUMO energy gap value has substantial influence on the ICT and bioactivity of the molecules. ICT is one of the strongest causes for the NLO activity. Mulliken atomic charge calculation shows the atomic charge effect, dipole moment, molecular polarizability, electronic structure and a lot of properties of molecular systems. Threshold values for good NLO effects of polarizability and first hyperpolarizability values are approximately 6 times greater than urea. The accomplished compound is a prolific component of prospect studies in the NLO. An electron density isosurface mapped with electrostatic potential surface depicts the size, shape, charge density and site of chemical reactivity of the molecules. The MEP map contour shows that the negative potential sites are on electronegative atoms as well as the positive potential sites are around the hydrogen atoms. The thermo chemical parameters are predicted for find the property changes of the title compound. Natural bond orbital (NBO) analysis divulges the delocalization or hyper-conjugation interaction, intermolecular charge transfer and stabilization energy of molecule. From the NBO outcome, able to settle on the idyllic Lewis type structure. The anticipated the consequences of this study will facilitate researchers to examine and create new-fangled resources.

References

1. Lovecka, P., Thimova, M., Grznarova, P., Lipov, J., Knejzlik, Z., Stiborova, H., Tjokorda, G., de Tirta, N., Demnerova, K., Ruml, T.: Corp. Bio Med. Res. (2015). (Article ID 381264)
2. Sundaraganasan, N., Elango, G., Sebastian, S., Subramani, P.: Molecular structure, vibrational spectroscopic studies and analysis of 2-fluoro-5-methylbenzonitrile. Ind. J. Pure App. Phy. **47**, 481 (2009)
3. Shahid, M., Munawar Ali, M., Nadeem, S., Nasir, W., Salim, M.: 2-Bromo-4-methylbenzonitrile. Acta. Crys. Sec. **E65,** o3166 (2009)
4. Yoon, S., Tak, S., Kim, J., Jun, Y., Kang, K., Park, J.: Application of transparent dye-sensitized solar cells to building integrated photovoltaic systems. Build. Envir. **46**, 1899 (2011)
5. Robertson, N.: Angew. Chem. Int. Ed. **45**, 2338 (2006)
6. Murugan, M., Balachandran, V., Karnan, M.: Vibrational spectra and electrostatic potential surface of 2-fluoro-6- methoxybenzonitrile based on quantum chemical calculations. J. Chem. Pharm. Res. **4**(7), 3400 (2012)

7. Prakasam, A., Sakthi, D., Anbarasan, P.M., Lett, I.: DFT studies on the electronic structures of 4-methoxybenzonitrile dye for Dye-Sensitized Solar Cell International Letters of Chemistry. Chem. Phy. Ast. **12**, 8 (2013)
8. Mohan, S., Murugan, R., Srinivas, S.: Proc. Natl. Acad. Sci. India (Phys. Sci.) **62**, 121 (1992)
9. Govidasamy, P., Gunasekaran, S., Srinivasan, S.: Molecular geometry, conformational, vibrational spectroscopic, molecular orbital and Mulliken charge analysis of 2-acetoxybenzoic acid. Spectrochim. Acta Part A Mol. Biomol. Spectrosc. **130**, 329 (2014)
10. Frisch, M.J., Trucks, G.W., Schlegel, H.B., Scuseria, G.E., Robb, M.A., Cheeseman, J.R., Montgomery, J.A., Jr., Vreven, T., Kudin, K.N., Burant, J.C., Millam, J.M., Iyengar, S.S., Tomasi, J., Barone, V., Mennucci, B., Cossi, M., Scalmani, G., Rega, N., Petersson, G.A., Nakatsuji, H., Hada, M., Ehara, M., Toyota, K., Fukuda, R., Hasegawa, J., Ishida, M., Nakajima, T., Honda, Y., Kitao, O., Nakai, H., Klene, M., Li, X., Knox, J.E., Hratchian, H.P., Cross, J.B., Adamo, C., Jaramillo, J., Gomperts, R., Stratmann, R.E., Yazyev, O., Austin, A. J., Cammi, R., Pomelli, C., Ochterski, J.W., Ayala, P.Y., Morokuma, V., Voth, G.A., Salvador, P., Dannenberg, J.J., Zakrzewski, V.G., Dapprich, S., Daniels, A.D., Strain, M.C., Farkas, O., Malick, D.K., Rabuck, A.D., Raghavachari, K., Foresman, J.B., Ortiz, J.V., Cui, Q., Baboul, A.G., Clifford, S., Cioslowski, J., Stefanov, B.B., Liu, G., Liashenko, A., Piskorz, P., Komaromi, I., Martin, R.L., Fox, D.J., Keith, T., AlLaham, M.A., Peng, C.Y., Nanayakkara, A., Challacombe, M., Gill, P.M.W., Johnson, B., Chen, W., Wong, M.W., Gonzalez, C., Pople J.A.: Gaussian 09, Revision A 02 (Inc., Wallingford CT) (2009)
11. Saravanan, R.R., Seshadri, S., Gunasekaran, S., Mendoza-Merono, R., Garcia-Granda, S.: X-ray crystallographic, FT-IR, FT-Raman, DFT, MEP and molecular docking studies on 1-(1-(3-methoxyphenyl)ethylidene) thiosemicarbazide. Spectrochim. Acta Part A Mol. Biomol. Spectrosc. **139**, 321 (2015)
12. Premkumar, S., Jawahar, A., Mathavan, T., Kumara Dhas, M., Sathe, V.G., Benial, A.M.F.: DFT calculation and vibrational spectroscopic studies of 2-(tertbutoxycarbonyl (Boc) - amino)-5-bromopyridine. Spectrochim. Acta Part A Mol. Biomol. Spectrosc. **129**, 74 (2014)
13. Gunasekaran, S., Rajalakshmi, K., Kumaresan, S.: Vibrational analysis, electronic structure and nonlinear optical properties of Levofloxacin by density functional theory. Spectrochim. Acta Part A Mol. Biomol. Spectrosc. **112**, 351 (2013)
14. Swarnalatha, N., Gunasekaran, S., Nagarajan, M., Srinivasan, S., Sankari, G., Ramkumaar, G. R.: Vibrational, UV-spectra, NBO, first order hyperpolarizability and HOMO-LUMO analysis of carvedilol. Spectrochim. Acta Part A Mol. Biomol. Spectrosc. **136**, 567 (2015)
15. Casado, J., Nygaard, L., Sorenson, G.O.: Microwave spectra of isotopic benzonitriles refined molecular structure of benzonitrile. J. Mol. Struct. **8**, 211 (1971)
16. Socrates, G.: Infra. Char. group freq. John wiley, Newyork (1987)
17. Balachandran, V., Parimala, K.: Molecular structures, FT-IR and FT-Raman spectra, NBO analysis, NLO properties, reactive sites and quantum chemical calculations of keto-enol tautomerism(2-amino-4-pyrimidinol and 2-amino-pyridine-4(1H)-one). Spectrochim. Acta Part A Mol. Biomol. Spectrosc. **102**, 30 (2013)
18. Anbarasan, P.M., Subramanian, M.K., Manimegala, S., Suguna, K., Ilangovan, V., Sundaraganesan, N.: 4-Chlorotoluene: Spectral studies and quantum chemical calculations. J. Chem. Pharm. Res. **3**(3), 123 (2011)
19. Colthup, N.B., Daly, L.H., Wiberley, S.E.: Introduction to Infrared and Raman Spectroscopy. Academic Press Inc., London, (1964)
20. Rastogi, K., Palafor, M.A., Tanwar, R.P., Mital, L.: 3, 5-Difluorobenzonitrile: ab initio calculations, FTIR and Raman spectra. Spectrochim. Acta **58A**, 1989 (2002)
21. Silverstein, M., Besseler, G.C., Moril, C.: Spectrometic Identification of Organic Compounds. Wiley, New York (1981)
22. Govindarajana, M., Ganasan, K., Periandy, S., Karabacak, M., Mohan, S.: Vibrational spectroscopic analysis of 2-chlorotoluene and 2-bromotoluene: A combined experimental and theoretical study, Spectrochimica Acta Part A **77**, 1005 (2010)
23. Arenas, P.J.F., Tocon, I.L., Otero, J.C., Marcos, J.I.: A priori scaled quantum mechanical vibrational spectra of trans-and cis-stilbene. J. Phys. Chem. **99**, 11392 (1995)

24. Beck, D.: Structural studies on some dithiophosphonato complexes of Ni(II), Cd(II), Hg(II) and theoretical studies on a dithiophosphonato Ni(II) complex using density functional theory. J. Chem Phys. **98**, 5648 (1993)
25. Lee, C., Yang, W., Parr, R.G.: Development of the Colle-Salvetti correlation-energy formula into a functional of the electron density. Phys. Rev. **37B**, 785 (1998)
26. Udhayakala, P., Rajendiran, T.V., Seshadri, S., Gunasekaran, S.: Quantum chemical vibrational study, molecular property and HOMO-LUMO energies of 3-bromoacetophenone for Pharmaceutical application. J. Chem. Pharm. Res. **3**(3), 610 (2011)
27. Singh, P., Singh, N.P., Yadav, R.A.: Quantum Mechanical Studies of Conformers, Molecular Structures and Vibrational Characteristics of Hetero-cyclic Organics: Nicotinic acid and 2-Fluoronicotinic acid. J. Chem. Pharm. Res. **3**(1), 737 (2011)
28. Kumar, V., Panikar, Y., Palafox, M.A., Vats, J.K., Kostova, I., Lang, K., Rastogi, V.K.: Ab-initio calculations, FT-IR and FT-Raman spectra of 2-chloro-6-methyl benzonitrile. Indian J. Pure Appl. Phys. **48**, 85 (2010)
29. Roges, N.P.: A Guide to the Complete Interpretation of Infrared Spectra of Organic Structures. Wiley, New York (1994)
30. Coates, J: Encyclopedia of analitical chemistry. In: Meyers, R.A. (ed.) Interpretation of Infrared Spectrum, A practical Approach. John Eiley, Chichester (2000)
31. George, W.O., Mcintyre, P.S.: Infrared Spectrtosc. John Wiley & Sons (1987)
32. Green, J.H.S., Harrison, D.J.: Vibrational spectra of benzene derivatives-XVII. Benzonitrile and substituted benzonitriles. Spectrochim. Acta **32**, 1279 (1976)
33. Varsanyi, G.: Vibrational Spectra of Benzene Derivatives. Academic Press, New York (1969)
34. Tocon, I.L., Woolley, M.S., Otero, J.C., Marcos, J.I.: Vibrational spectrum of 3-methyl and 4-methylpyridine. J. Mol. Struct. **470**, 241 (1998)
35. Bellamy, L.J.: The Infrared Spectra of Compound Molecules. Chapman and Hall, London (1975)
36. Colthup, N.B., Daly, L.H., Wiberley, S.E.: Introduction to Infrared and Raman Spectroscopy. Academic Press Inc., London (1964)
37. Huralikoppi, A.M.: Investigation on the spectra of some substituted aromatic molecules. Ph. D. thesis, Department of Physics, Karnataka University Dharrwad (1995)
38. Zheng, M., Wang, J., Zhang, J., Luo, S.: 3-Fluoro-4-(4-hydroxyphenoxy)- benzonitrile. Acta Cryst. **66**, 1856 (2010)
39. Alen, S., Sajan, D., JobSabu, K., Sundius, T., Chitanya, K., Blockhuys, F., BenaJothy, V.: Vibrational spectral analysis, electronic absorption and non-linear optical behavior of (E)-1-(2,4,6-trimethoxyphenyl)pent-1-en-3-one. Vib. Spec. **79**, 1 (2015)
40. Demircioğlu, Z., Albayrak, C., Buyukgungor, O.: Experimental (X-ray, FT-IR and UV–vis spectra) and theoretical methods (DFT study) of (E)-3-methoxy-2-[(p-tolylimino)methyl] phenol. Spectrochim. Acta Part A Mol. Biomol. Spectrosc. **128**, 748 (2014)
41. Sambathkumar, K., Jeyavijayan, S., Arivazhagan, M.: Electronic structure investigations of 4-aminophthal hydrazide by UV–visible, NMR spectral studies and HOMO–LUMO analysis by ab initio and DFT calculations. Spectrochim. Acta Part A Mol. Biomol. Spectrosc. **147**, 124 (2015)
42. Diwaker, C.S., Kumar, C., Kumar, A., Chandraju, S., Fun, H.-K., Quah, C.K.: Spectroscopic characterization and computational studies of 2-(4-bromophenyl)-2-oxoethyl 3-methylbenzoate by density functional theory. J. Mol. Struct. **1092**, 192 (2015)
43. Hubert Joe, I., Kostova, I., Ravikumar, C., Amalanathan, M., Pinzaru, S.C.: Theoretical and vibrational spectral investigation of sodium salt of acenocoumarol. J. Raman Spectrosc. **40**, 1033 (2009)
44. Senthilkumar, J., Arivazhagan, M., Thangaraju, P.: Vibrational Spectra, NLO analysis, and HOMO-LUMO studies of 2-chloro-6-fluotobenzoic acid and 3,4-dichlorobenzoic acid by density functional method. Spectrochim. Acta Part A Mol. Biomol. Spectrosc. **147**, 235 (2015)

45. Chen, Y., Yang, J., Li, Z., Li, R., Ruan, W., Zhuang, Z., Zhao, B.: Experimental and density functional theory study of Raman and SERS spectra of 5-amino-2-mercaptobenzimidazole. Spectrochim. Acta Part A Mol. Biomol. Spectrosc. **153**, 344 (2016)
46. Saglam, E.G., Ebinç, A., Zeyrek, C.T., Ünver, H., Hökelek, T.: Structural studies on some dithiophosphonato complexes of Ni(II), Cd(II), Hg(II) and theoretical studies on a dithiophosphonato Ni(II) complex using density functional theory. J. Mol. Struct. **1099**, 490 (2015)
47. Scrocco, E., Tomasi, J.: The electrostatic molecular potential as a tool for the interpretation of molecular properties. Topics in Current Chemistry. Springer, Berlin (1973)
48. Fleming, I.: Frontier Orbitals and Organic Chemical Reactions. Wiley, London (1976)
49. Sharmi Kumar, J., Renuga Devi, T.S., Ramkumaar, G.R., Bright, A.: Ab initio and density functional theory calculations of molecular structure and vibrational spectra of 4-(2-Hydroxyethyl) piperazine-1-ethanesulfonic acid. Spectrochim. Acta Part A Mol. Biomol. Spectrosc. **152**, 509 (2016)
50. Murray, J.S., Sen, K.: Molecular Electrostatic Potentials Concepts and Applications. Elsevier, Amsterdam (1996)
51. Renjith, R., Sheena Mary, Y., Tresa Varghese, H., Yohannan Panicker, C., Thiemann, T., Van Alsenoy, C.: Vibrational spectra, molecular structure, NBO, HOMO–LUMO and first order hyperpoalarizability analysis of 1,4-bis(4-formylphenyl) anthraquinone by density functional. Spectrochim. Acta Part A Mol. Biomol. Spectrosc. **131**, 225 (2014)
52. Veeraiah, A.: FT-IR, FT-Raman, UV/Vis spectra and fluorescence imaging studies on 2-(bromoacetyl)benzo(b)furan by ab initio DFT calculations. Spectrochim. Acta Part A Mol. Biomol. Spectrosc. **147**, 212 (2015)
53. Sambathkumar, K.: Vibrational spectra, NBO, HOMO–LUMO and conformational stability studies of 4-hydroxythiobenzamide. Spectrochim. Acta Part A Mol. Biomol. Spectrosc. **147**, 51 (2015)

Molecular Structure, Vibrational Spectra, HOMO, LUMO and NMR Studies of Methylphenylcyclopropenone Based on Density Functional Theories

P. Senthil Raj, S. Periandy, S. Xavier and Mohamad I. Attia

Abstract The Fourier-Transform infrared and FT-Raman spectra of Methylphenylcyclopropenone (MPCP) were recorded in the region 4000–100 cm^{-1}. Quantum mechanical calculation of energies, geometrical structure and vibrational wavenumbers of MPCP were carried out using density functional B3LYP method with 6-31G++(d,p) and 6-311G++(d,p) basis set. The computed wave numbers were scaled so as to agree with the observed values and the scaling factors are reported. A study on the electronic properties, such as HOMO and LUMO energies, were performed by time-dependent SCF method. Mulliken charges of the compound were also calculated and interpreted. The thermodynamic properties (heat capacity, entropy, and enthalpy) at different temperatures were calculated in DMSO, chloroform and gas phases and the results are interpreted. NBO analysis is carried out to analyze the charge delocalization of the molecule. The ^{1}H and ^{13}C nuclear magnetic resonance (NMR) chemical shifts of the molecule were studied using the gauge independent atomic orbital (GIAO) method.

1 Introduction

Cyclopropane ring systems [1] are ubiquitous in nature and are contained in a large number of natural products, insecticides, and pharmaceutical drug candidates. Designing small molecules that bind to therapeutically important biological targets

P. Senthil Raj (✉)
PRIST University, Vallam, Thanjavur, India
e-mail: senstarphy@gmail.com

S. Periandy
Department of Physics, Kanchi Mamunivar Centre for Post Graduate Studies, Lawspet, Puducherry, India

S. Xavier
Bharathiyar University, Coimbatore, Tamil Nadu, India

M.I. Attia
Pharmaceutical Chemistry Department, College of Pharmacy, King Saud University, Riyadh, Kingdom of Saudi Arabia

J. Ebenezar (ed.), *Recent Trends in Materials Science and Applications*,
Springer Proceedings in Physics 189, DOI 10.1007/978-3-319-44890-9_55

with high affinity and selectivity is a major goal in contemporary bioorganic and medicinal chemistry. The reactivity of cyclopropanes allows them as versatile intermediates in the synthesis of complex molecules, and is frequently employed as versatile building blocks in organic syntheses. Generally, electron donating or accepting substituent are involved in their reactions to make polar processes more favorable, such activated cyclopropanes represent an important class of synthons acting as electrophiles. Thus, ring cleavage or ring enlargement is the most common phenomenon observed in cyclopropanes.

The study of multi-substituted cyclopropanes has been a subject of great interest due to their roles as the basic structural elements in a wide range of biologically active compounds. It also plays an important role as an intermediate in the synthesis of organic compound. Their diverse applications in synthetic, agricultural, and medicinal chemistry as well as in material science, makes it a compound of great interest. Cyclopropane equivalents have also been found to exhibit diverse biological applications such as antibacterial, antifungal, antiviral, anti-HIV, anticancer, antitumor, antimycobacterial, antiestrogenic, agonist, COX-II inhibitor properties. Many works [2–6] have been already published on the synthesis and application of multi-substituted cyclopropanes. Kimura et al. [2] have studied the X-ray structural analysis of 2-cyclo propyle-1-(2,4,6-tri-trt-butyl phenyl)-phosphaetthene and confirmed the cylo prophyl group has largely interact with the phosphaetthene compared with carbon analogues. Duncan [4] has re-analyzed the parallel IR bands of the cyclopropane and proposed many combinational and fundamental bands. He also analysed the intensities of many perpendicular bands. The earlier literature [1–6] indicates that neither quantum mechanical calculations nor experimental study was done on methyl phenyl cyclopropenone (MPCP). Hence the compound MPCP was chosen to make thorough and complete vibrational studies, the frontier molecular studies with emphasis on HOMO–LUMO and UV-Visible spectral analysis was done.

2 Experimental Details

The FT-IR and FT-Raman spectra of the title compound namely MPCP were purchased from the spectral library of Sigma Aldrich chemicals, U.S.A. The FT-IR spectrum of the compound, according to the manual, was recorded in Bruker IFS 66V spectrometer in the range of 4000–100 cm^{-1}. The spectral resolution is ± 2 cm^{-1} and the FT-Raman spectrum of compound was also recorded in the same instrument with FRA 106 Raman module equipped with Nd: YAG laser source operating at 1.064 μm line widths with 200 mW power. The Raman spectrum was also recorded in the same range 4000–100 cm^{-1}, with the scanning speed of 30 cm^{-1} min^{-1} and spectral width 2 cm^{-1}. The frequencies of all sharp bands are accurate to ± 1 cm^{-1}.

3 Quantum Mechanical Calculations

All quantum mechanical calculations of MPCP were performed with Gaussian—09W program package [7] on Pentium IV processor personal. The optimized geometrical parameters of the title molecule were determined by Hartree–Fock (HF) and density functional theory (DFT) [8] with the three-parameter hybrid functional (B3) [9] for the exchange part and the Lee–Yang–Parr (LYP) [10] correlation functional, using Pople basis set, namely 6-31++G(d,p) and 6-311++G (d,p). The vibrational frequencies of MPCP were calculated with HF and DFT/B3LYP methods in 6-31++G(d,p) and 6-311++G(d,p) basis sets. In order to improve the agreement between the calculated frequencies and the experimental frequencies, it is necessary to scale down the calculated harmonic frequencies [11, 12]. Hence, the vibrational frequencies calculated at HF level were scaled by 0.9230 and B3LYP values by 0.9822. The ^{13}C and ^{1}H NMR chemical shift of the title molecule were calculated by both HF and DFT (B3LYP) methods with 6-311++G (d,p) basis set in combination with GIAO method. The charge distribution of the molecule were computed by HF and DFT method with 6-311++G(d,p) basis set.

The electronic absorption spectra for MPCP was simulated with DFT at 6-311++G(d,p) level in gas phase and solvent (DMSO and chloroform) phase. Furthermore, the change in thermodynamic functions (specific heat, entropy and enthalpy) was investigated for different temperature from the vibrational frequencies of the molecule.

4 Results and Discussion

4.1 Molecular Geometry

The optimized structure of the title compound is shown in Fig. 1. The comparative structural parameters computed by different methods; bond length and bond angles are presented in Table 1. The comparison between the bond length and bond angle for different atoms in different methods are shown in Figs. 2 and 3 respectively.

Carthigayan et al. [13] have studied the molecular geometry of 3-methyl-1-phenylpyrazole and observed that the bond length of the C–C atoms in the phenyl ring were of the order 1.388 Å. In the title molecule, the bond length of the C(10)–C(12) (1.383 Å), C(11)–C(14) (1.386 Å), C(12)–C(16) (1.389 Å) and C(14)–C(16) (1.387 Å) carbon atoms in the phenyl ring showed good agreement with the literature studies. However the bond length of C(9)–C(10) (1.394 Å) and C(9)–C(11) (1.392 Å) carbon atoms is marginally greater than the remaining carbon atoms in the phenyl ring, this may be attributed to the attachment of the cyclopropenone to the C(9) carbon atom in the phenyl ring. Lin et al. [14] have studied structural characteristics of diphenylcyclopropenone and found that the bond length of the CC bonds in the cyclopropenone ring were 1.40, 1.41 and 1.36 Å for C(1)–C(2), C(1)–

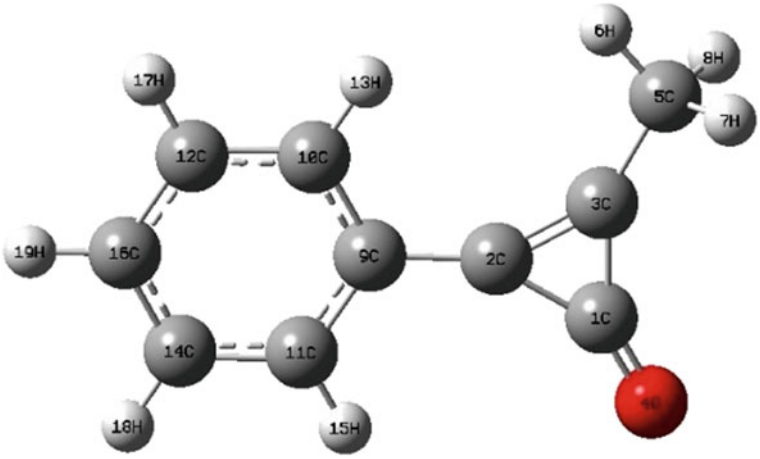

Fig. 1 Optimized structure of methyl phenyl cyclopropenone

Table 1 Optimized geometrical parameters for methyl phenyl cyclopropenone computed at HF and B3LYP methods using 6-31++G(d,p) and 6-311++G(d,p) basis sets

Geometrical parameters	HF		B3LYP	
	6-31++G(d,p)	6-311++G(d,p)	6-31++G(d,p)	6-311++G(d,p)
Bond length (Å)				
C1–C2	1.408	1.409	1.434	1.432
C1–C3	1.404	1.405	1.426	1.424
C1–O4	1.201	1.194	1.220	1.212
C2–C3	1.340	1.339	1.363	1.360
C2–C9	1.458	1.458	1.451	1.449
C3–C5	1.486	1.486	1.484	1.482
C5–H6	1.083	1.083	1.094	1.092
C5–H7	1.085	1.085	1.096	1.094
C5–H8	1.085	1.085	1.096	1.094
C9–C10	1.394	1.392	1.408	1.405
C9–C11	1.392	1.391	1.407	1.404
C10–C12	1.384	1.382	1.393	1.390
C10–H13	1.075	1.075	1.086	1.084
C11–C14	1.386	1.385	1.395	1.391
C11–H15	1.075	1.075	1.086	1.084
C12–C16	1.390	1.388	1.400	1.396
C12–H17	1.075	1.075	1.086	1.084
C14–C16	1.387	1.385	1.398	1.395
C14–H18	1.075	1.075	1.086	1.084
C16–H19	1.076	1.075	1.086	1.084

(continued)

Table 1 (continued)

Geometrical parameters	HF		B3LYP	
	6-31++G(d,p)	6-311++G(d,p)	6-31++G(d,p)	6-311++G(d,p)
Bond angle (°)				
A(C2–C1–O4)	151.2	151.2	151.2	151.2
A(C3–C1–O4)	152.0	152.0	151.9	151.9
A(C1–C2–C9)	150.3	150.5	151.1	151.3
A(C3–C2–C9)	148.2	148.1	147.7	147.4
A(C1–C3–C5)	150.5	150.6	151.0	151.1
A(C2–C3–C5)	147.8	147.7	147.1	147.0
A(C3–C5–H6)	111.7	111.8	112.4	112.4
A(C3–C5–H7)	109.6	109.6	109.9	109.8
A(C3–C5–H8)	109.6	109.6	109.9	109.8
A(H6–C5–H7)	109.1	109.1	108.9	108.9
A(H6–C5–H8)	109.1	109.1	108.9	108.9
A(H7–C5–H8)	107.6	107.6	106.8	106.8
A(C2–C9–C10)	121.2	121.2	121.4	121.4
A(C2–C9–C11)	119.1	119.2	119.2	119.3
A(C10–C9–C11)	119.7	119.7	119.4	119.3
A(C9–C10–C12)	120.1	120.2	120.2	120.3
A(C9–C10–H13)	119.9	119.9	119.6	119.6
A(C12–C10–H13)	120.0	120.0	120.2	120.1
A(C9–C11–C14)	120.1	120.1	120.2	120.2
A(C9–C11–H15)	119.4	119.4	119.1	119.1
A(C14–C11–H15)	120.5	120.5	120.7	120.7
A(C10–C12–C16)	119.9	119.9	120.0	120.0
A(C10–C12–H17)	120.0	120.0	119.9	119.9
A(C16–C12–H17)	120.1	120.1	120.0	120.0
A(C11–C14–C16)	120.0	120.0	120.1	120.1
A(C11–C14–H18)	119.9	119.9	119.8	119.9
A(C16–C14–H18)	120.1	120.2	120.1	120.1
A(C12–C16–C14)	120.2	120.2	120.1	120.1
A(C12–C16–C19)	119.9	119.9	119.9	119.9
A(C14–C16–C19)	119.9	119.9	120.0	120.0

C(3) and C(2)–C(3) respectively. The bond length of the carbon atoms C(1)–C(2) (1.408 Å), C(1)–C(3) (1.404 Å) and C(2)–C(3) (1.339 Å) in the cyclopropenone ring are found to be in good agreement with the findings of Lin et al. The shortening of the bond length (1.33 Å) of C(2)–C(3) is due to the presence of double bond between C(2) and C(3). The bond length for 2C–9C (1.45 Å) clearly indicates that this bond is single bond CC. The bond lengths 3C–1C and 2C–1C (1.40 Å) indicates that there is some conjugation of electrons in the cyclo propene also. As usual

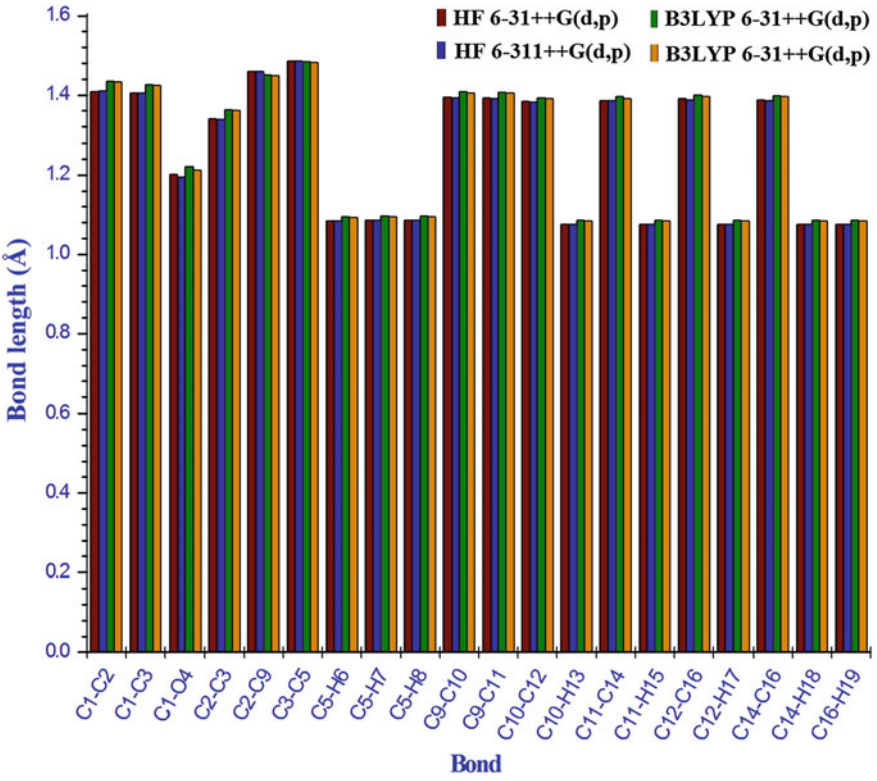

Fig. 2 Bond length of methyl phenyl cyclopropenone

all the bonds in the benzene ring lies in between the double bond and single bond due to the strong conjugational effect.

The bond length of the C–H atoms in phenyl ring is of the order 1.07 Å [13]. In agreement with the literature, the bond length of the C–H atoms in the phenyl ring of the title compound was found to be of the order 1.075 Å. The C–H bond lengths in methyl group are found to be 1.08 Å, these are in tune with the literature values which shows all the C–H bonds in the molecules are remain undisturbed.

From the bond angle values (Table 1), it can be observed that all the angles within the phenyl ring are found to be closer to 119°, which is the angle observed in pure benzene compound, except at 11C and 10C where the substitution propene group is attached. This shows a slight distortion is made the cyclic nature of the phenyl ring. In the case propene cycle, one angle is 56° and the other two angles are 61.69° and 61.41°, this is obviously due to the presence of one double bond and two single bonds within the cycle. These angles are found to be 50° and 64° in the case of 3,3-dimethyl 1-(X(CH3)) cyclo propene, this shows the geometry of cyclopropene is subjected to the geometry of the attached compound.

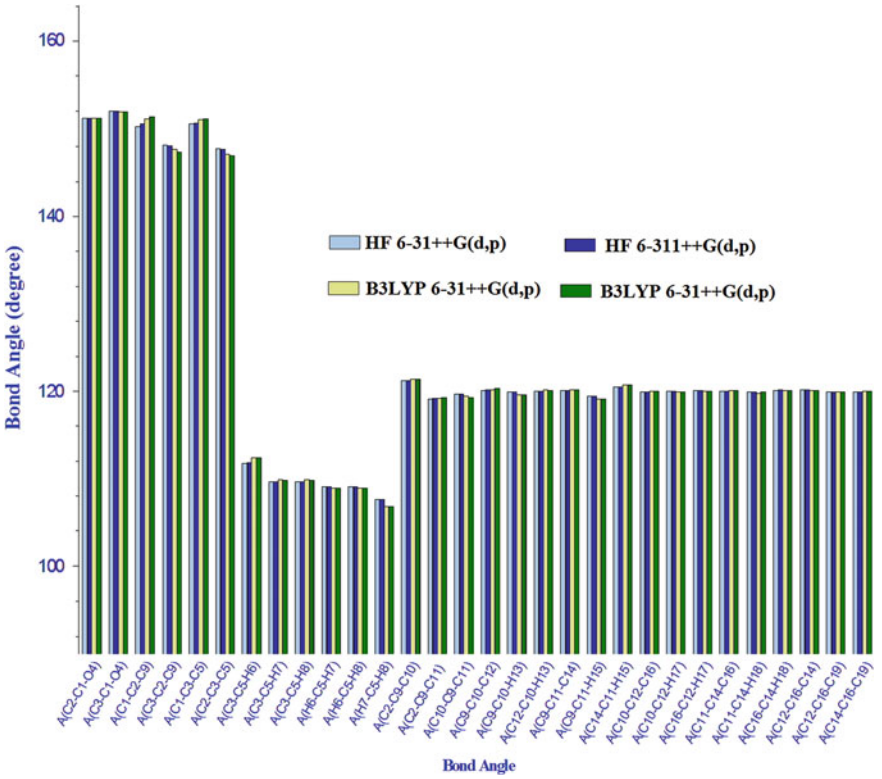

Fig. 3 Bond angle of methyl phenyl cyclopropenone

4.2 Vibrational Analysis

The title compound has 19 atoms and hence it undergoes 51 normal modes of vibrations. In agreement with the C1 symmetry the title compound was distributed as 35a′ (in-plane) and 16a″ (out-of-plane) modes of vibration.

$$\Gamma_{\text{Vib}} = 35a' + 16a''$$

All the modes are found to be active in both IR and Raman spectra. Vibrational frequencies of IR and Raman spectra along with the computed values by HF and B3LYP methods, with 6-31++G(d,p) and 6-311++G(d,p) basis set, are tabulated in Table 2 with the probable assignments. The comparison of scaled and unscaled values with the experimental values is presented in Table 3. The experimental and simulated infrared and Raman spectra are shown in Figs. 4 and 5 respectively. Theoretical values of IR and Raman intensities for both the methods are given in Tables 4 and 5.

Table 2 Observed and calculated [scaled] vibrational frequencies (cm^{-1}) at HF and DFT (B3LYP) with 6-31++G(d,p) and 6-311++G(d,p) basis sets of methyl phenyl cyclopropenone

S. No	Experimental		HF		B3LYP		Species	Vibrational assignments
	FT-IR	FT-Raman	6-31++G(d,p)	6-311++G(d,p)	6-31++G(d,p)	6-311++G(d,p)		
1	3090s		3086	3091	3091	3094	a′	υ (C–H)
2	3080s		3080	3085	3085	3088	a′	υ (C–H)
3	3050w		3072	3077	3078	3081	a′	υ (C–H)
4		3045vw	3065	3069	3070	3073	a′	υ (C–H)
5	3015vw		3056	3059	3063	3065	a′	υ (C–H)
6	2995w	2995w	2995	3001	3006	3008	a′	υ (C–H)
7	2980w		2980	2985	2985	2985	a′	υ (C–H)
8	2920m		2918	2928	2925	2932	a′	υ (C–H)
9	1860vs	1860s	1892	1904	1856	1864	a′	υ (C=O)
10	1660vs		1691	1697	1635	1640	a′	υ (C=C)
11		1630vs	1636	1641	1584	1585	a′	υ (C=C)
12	1590w	1590w	1614	1619	1560	1562	a′	υ (C=C)
13	1560vw	1560w	1511	1516	1469	1473	a′	υ (C=C)
14	1495vw	1495m	1463	1469	1426	1431	a′	υ (C–C)
15	1460w		1459	1468	1422	1428	a′	υ (C–C)
16	1450m	1450vs	1458	1465	1421	1427	a′	υ (C–C)
17	1390w	1390m	1404	1408	1351	1355	a′	υ (C–C)
18		1380m	1345	1348	1310	1311	a′	υ (C–C)
19	1340vw	1340m	1324	1326	1293	1290	a′	υ (C–C)
20	1325m	1325m	1223	1222	1269	1269	a′	υ (C–C)
21	1190m	1190vw	1178	1183	1157	1163	a′	β (C–H)
22	1170w	1170vw	1161	1166	1142	1147	a′	β (C–H)
23	1150w	1150vw	1117	1115	1130	1134	a′	β (C–H)
24		1075vw	1076	1077	1066	1071	a′	β (C–H)
25	1050vw		1042	1045	1013	1017	a′	β (C–H)
26		1040vw	1038	1045	997	1002	a′	β (C–H)
27	1025vw		1034	1033	989	994	a′	β (C–H)
28		1015vw	1017	1021	975	980	a′	β (C–H)
29	1010vw		1015	1018	973	974	a′	β (C=O)
30		995vw	991	994	953	957	a′	β (C–C)
31	975vw		968	972	935	940	a′	β (C–C)
32		955vw	964	967	908	914	a″	δ (C–H)
33		845vw	872	875	827	829	a″	δ (C–H)
34	785w		785	792	753	761	a″	δ (C–H)
35		775vs	769	771	748	749	a″	δ (C–H)
36		715vw	698	704	680	685	a″	δ (C–H)

(continued)

Table 2 (continued)

S. No	Experimental		HF		B3LYP		Species	Vibrational assignments
	FT-IR	FT-Raman	6-31+ +G(d,p)	6-311+ +G(d,p)	6-31+ +G(d,p)	6-311+ +G(d,p)		
37	700vs		695	702	676	682	a″	δ (C–H)
38	690vw	690vs	686	690	661	669	a″	δ (C–H)
39		665m	657	678	628	641	a″	δ (C–H)
40	610m		613	618	603	609	a″	δ (C=O)
41	550w	550s	563	572	545	550	a″	δ (C–C)
42		435vw	425	431	411	413	a″	δ (C–C)
43	415m		412	415	397	398	a″	Γ(C–C=C)
44		405w	400	403	395	397	a″	Γ(C=C–C)
45	315w	315s	315	318	305	307	a″	Γ(C–C=C)
46	215w	215s	236	240	219	220	a″	Γ(C=C–C)
47		180m	200	201	190	191	a″	Γ(C–C=C)
48	110vw		100	102	95	96	a″	Γ(C=C–C)
49	95vw		89	90	84	86	a″	Γ(C–C–C)
50		75s	72	67	64	60	a″	Γ(C–C–C)
51		45m	42	41	43	41	a″	Γ(C–C–C)

vs very strong, *s* strong, *m* medium, *w* weak, *vw* very weak. *υ* stretching, *β* in plane bending, *δ* out of plane bending, *Γ* torsion

Table 3 Observed and calculated unscaled frequencies of MPCP by HF/DFT (B3LYP) with 6-31 ++G(d,p) and 6-311++G(d,p) basis sets

S. No	Observed frequencies	HF		B3LYP	
		6-31++G(d,p)	6-311++G(d,p)	6-31++G(d,p)	6-311++G(d,p)
1	3190	3380	3357	3213	3196
2	3150	3374	3351	3207	3190
3	3105	3365	3342	3200	3183
4	3090	3357	3334	3192	3175
5	3060	3347	3323	3184	3166
6	3045	3281	3260	3125	3107
7	3015	3264	3243	3103	3084
8	2995	3196	3180	3040	3029
9	1675	1891	1884	1783	1725
10	1630	1852	1844	1699	1694
11	1600	1792	1783	1646	1638
12	1590	1768	1759	1622	1614
13	1560	1656	1647	1527	1521
14	1495	1603	1596	1483	1478

(continued)

Table 3 (continued)

S. No	Observed frequencies	HF		B3LYP	
		6-31++G(d,p)	6-311++G(d,p)	6-31++G(d,p)	6-311++G(d,p)
15	1460	1598	1594	1479	1475
16	1450	1597	1592	1478	1474
17	1390	1538	1529	1404	1400
18	1380	1473	1464	1362	1355
19	1340	1450	1440	1344	1333
20	1325	1340	1328	1320	1311
21	1190	1291	1285	1203	1201
22	1170	1272	1267	1187	1185
23	1150	1223	1211	1174	1172
24	1075	1179	1170	1108	1106
25	1050	1142	1135	1053	1051
26	1040	1137	1135	1036	1035
27	1025	1133	1122	1028	1027
28	1015	1114	1109	1013	1013
29	1010	1112	1106	1012	1007
30	995	1085	1080	990	989
31	975	1060	1055	972	971
32	955	1056	1050	944	944
33	845	955	950	859	857
34	785	860	860	783	786
35	775	842	837	777	774
36	715	765	765	707	707
37	700	762	763	703	704
38	690	752	750	687	691
39	665	720	736	653	662
40	610	672	671	627	629
41	550	617	621	566	568
42	435	466	468	427	426
43	415	451	451	413	411
44	405	438	438	410	411
45	315	345	345	317	318
46	215	259	261	228	228
47	180	219	218	197	198
48	110	109	111	98	98
49	95	97	97	87	88
50	75	73	69	65	61
51	45	43	42	44	42

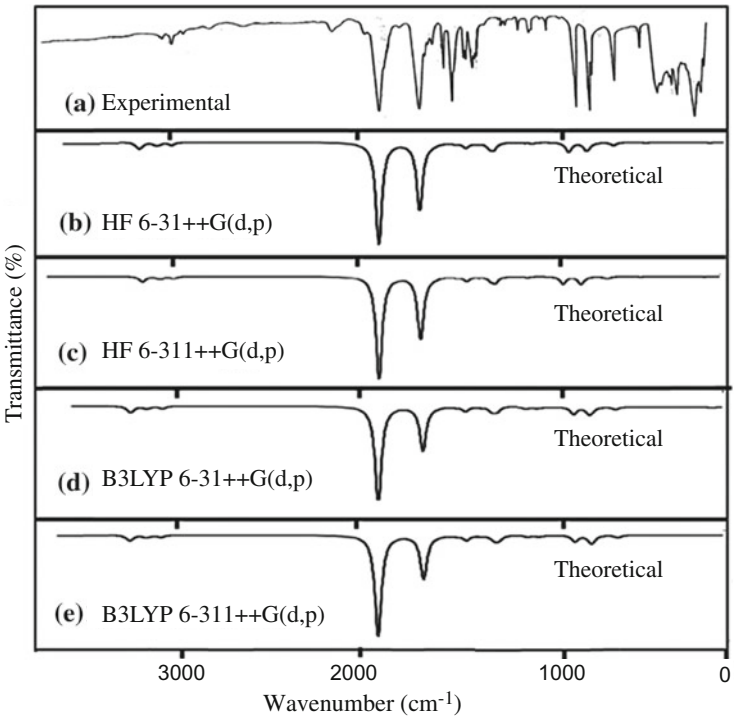

Fig. 4 **a** Experimental, and **b–e** theoretical FT-IR spectra of methyl phenyl cyclopropenone

4.2.1 C–H Vibrations

The aromatic C–H stretching vibration in the phenyl compound is to be found in the region 3100–3000 cm^{-1} [15–17]. In agreement with the literature the bands observed in this molecule at 3090, 3080, 3050, 3045, and 3015 cm^{-1} were attributed to C–H stretching of phenyl group. In this region the band are not appreciably affected by the substituents. Generally, the C–H stretching vibrations occur in the region of 2975–2850 cm^{-1} [18, 19] for aliphatic hydrocarbons, but this value increases for strained ring systems [20–23]. Baker and Lord [3] did a complete Vibrational and structural study of cyclopropane and observed C–H stretching vibration of aliphatic cyclopropane at 3009, 3028 and 3075 cm^{-1}. The asymmetric and symmetric vibrations of the methyl group in acetates are expected in the regions 2940–3040 and 2910–2930 cm^{-1} [24]. Here in the present study the vibrations observed at 2995, 2980 and 2920 cm^{-1} were assigned to the C–H stretching of the methyl group. All the values observed were almost in good agreement with the literature. This confirms that the methyl group is very little affected by its attachment with the cyclopropenone ring.

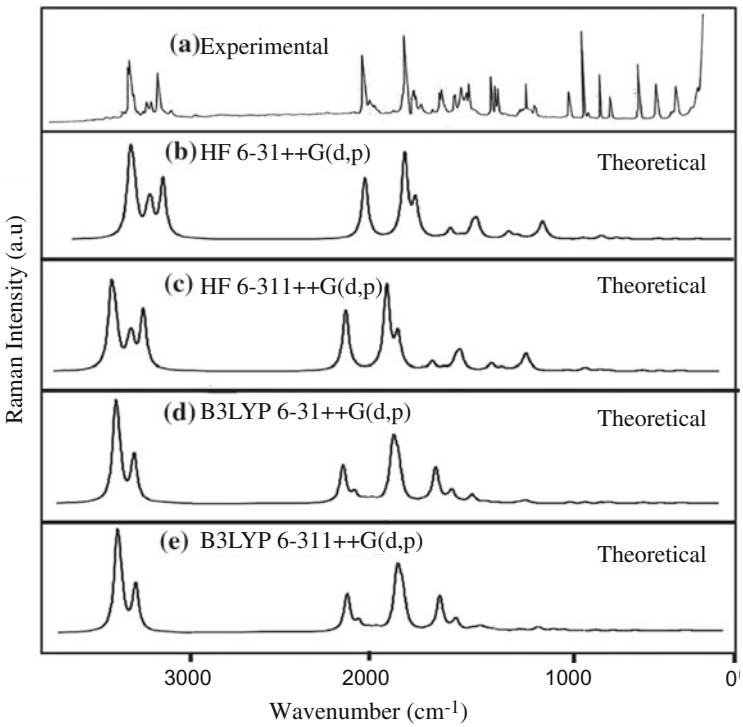

Fig. 5 **a** Experimental, and **b–e** theoretical FT-Raman spectra of methyl phenyl cyclopropenone

Table 4 Comparative values of IR intensities between HF/DFT (B3LYP) at 6-31++G(d,p) and 6-311++G(d,p) basis sets of methyl phenyl cyclopropenone

S. No.	HF		B3LYP	
	6-31++G(d,p)	6-311++G(d,p)	6-31++G(d,p)	6-311++G(d,p)
1	10.370	9.293	3.281	7.732
2	19.136	18.261	10.533	14.007
3	15.662	15.346	5.977	12.393
4	2.305	2.422	10.872	2.059
5	0.462	0.356	8.399	0.617
6	15.473	15.386	1.574	12.098
7	8.660	63.818	0.475	4.517
8	18.871	17.408	9.725	13.582
9	682.892	727.515	6.407	635.881
10	447.280	443.852	1.170	273.439
11	6.420	6.409	720.068	1.545

(continued)

Table 4 (continued)

S. No.	HF		B3LYP	
	6-31++G(d,p)	6-311++G(d,p)	6-31++G(d,p)	6-311++G(d,p)
12	5.330	5.404	3.975	2.146
13	7.275	7.503	13.319	4.978
14	19.914	14.893	12.297	13.174
15	8.020	8.335	11.583	8.646
16	5.507	10.517	24.514	8.303
17	8.060	6.541	13.870	4.688
18	31.069	26.075	9.294	3.122
19	40.198	43.777	18.189	29.205
20	2.309	1.940	1.000	25.734
21	2.219	2.061	0.200	1.888
22	1.860	2.371	29.188	0.292
23	7.493	8.221	4.326	2.378
24	0.890	0.354	6.200	4.820
25	2.068	2.129	5.254	0.374
26	0.033	0.030	0.728	0.393
27	0.014	0.018	1.137	9.391
28	6.937	6.872	0.031	0.761
29	0.207	0.155	0.129	0.091
30	0.148	0.227	21.074	0.149
31	3.683	3.924	3.398	7.739
32	3.764	3.485	2.824	2.861
33	0.176	0.163	0.147	0.198
34	63.965	57.134	11.591	39.185
35	0.200	0.092	3.157	0.741
36	43.184	43.326	2.244	1.014
37	5.019	7.919	12.794	42.280
38	11.608	8.489	39.031	14.140
39	1.628	2.420	0.277	0.082
40	0.132	0.120	4.531	0.167
41	18.937	17.952	40.001	14.693
42	1.014	1.043	4.629	0.579
43	0.014	0.006	0.002	1.960
44	3.783	3.543	3.945	0.002
45	1.129	0.974	0.238	0.357
46	1.304	1.194	0.133	0.464
47	1.266	1.071	1.262	0.463
48	0.331	0.296	0.011	0.186
49	3.338	3.174	1.617	2.311
50	1.668	1.208	2.887	1.478
51	1.988	2.379	0.427	1.782

Table 5 Comparative values of Raman activities between HF/DFT (B3LYP) at 6-31++G(d,p) and 6-311++G(d,p) basis sets of methyl phenyl cyclopropenone

S. No.	HF		B3LYP	
	6-31++G(d,p)	6-311++G(d,p)	6-31++G(d,p)	6-311++G(d,p)
1	266.543	264.426	90.572	289.759
2	27.596	24.656	310.605	55.512
3	59.304	55.436	89.263	68.753
4	97.417	94.689	35.050	109.092
5	29.609	29.299	71.368	29.752
6	68.735	63.818	105.129	82.686
7	108.918	101.886	25.242	126.091
8	241.651	246.333	290.258	355.250
9	251.225	253.469	6.218	185.401
10	348.470	353.455	233.733	626.590
11	145.010	140.672	58.484	239.093
12	3.442	3.169	17.740	4.338
13	4.044	3.957	9.541	11.320
14	4.508	11.588	8.615	12.335
15	8.737	7.317	4.993	7.843
16	28.195	17.275	200.873	40.000
17	10.918	9.206	186.339	17.649
18	49.151	39.475	29.829	10.226
19	68.526	2.913	175.414	73.637
20	1.107	1.708	6.452	127.613
21	4.878	1.153	6.373	12.020
22	27.360	26.685	219.984	7.524
23	13.422	11.690	3.154	19.922
24	2.954	4.091	6.179	0.291
25	2.362	2.762	9.121	8.978
26	1.296	1.203	71.449	1.176
27	0.805	0.710	4.290	5.254
28	6.892	4.952	0.365	69.538
29	0.005	0.007	0.003	0.306
30	68.135	68.924	54.792	0.011
31	9.162	8.606	0.647	9.703
32	0.034	0.036	11.527	0.037
33	0.643	0.496	0.404	0.044
34	5.014	4.275	3.297	1.899
35	1.825	1.502	1.324	4.842
36	0.500	0.313	0.014	12.729
37	8.364	5.636	5.088	0.028
38	7.530	10.340	1.208	1.832

(continued)

Table 5 (continued)

S. No.	HF		B3LYP	
	6-31++G(d,p)	6-311++G(d,p)	6-31++G(d,p)	6-311++G(d,p)
39	0.050	0.004	7.123	0.013
40	6.786	7.011	13.753	6.229
41	4.801	4.439	2.452	2.389
42	1.001	0.909	0.481	0.525
43	0.031	0.015	0.014	4.656
44	4.536	4.514	8.753	0.024
45	3.985	3.966	7.808	5.946
46	1.422	1.415	0.637	1.414
47	4.026	4.145	7.635	7.602
48	0.824	0.820	1.114	0.892
49	0.498	0.520	2.154	0.948
50	0.014	0.011	1.072	0.058
51	1.091	1.017	0.190	1.095

Parr [25] observed the bands due to C–H in plane bending were in the region of 1300–1000 cm^{-1}. In agreement with the literature, the vibrations observed from 1190 to 1015 cm^{-1} in the title molecule were assigned to in plane bending of C–H. The C–H out of plane vibrations appears with the range of 900–475 cm^{-1} [16]. The vibrations identified in the region 955–665 cm^{-1} were thus assigned to C–H out of plane bending. After scaling, the theoretically observed vibrations in both HF and DFT methods were found to be in good agreement with the experimental and literature value. This confirms that the bands due to the bending of C–H are having least substitutional effect.

4.2.2 C–C Vibrations

The bands between 1600–1400 cm^{-1} are generally due to the CC stretching modes [16, 17, 26]. In the title molecule, two very strong CC stretching vibrations were observed at 1630 and 1450 cm^{-1} in FT-Raman and a medium band was observed at 1660 cm^{-1} in FT-IR. The remaining bands were of variable intensities observed at 1675, 1590, 1560, 1495, 1460, 1450, 1390, 1380 and 1325 cm^{-1}. The highest value 1675 cm^{-1} is naturally due the double bond CC in the propene cycle, the other three values 1660, 1590 and 1560 cm^{-1} are due to the double bond in the phenyl ring. All the remaining values 1495, 1460, 1450, 1390, 1380, 1340 and 1325 cm^{-1} are due to the CC single bonds; first three values are due to the benzene CC single bonds and the next two values due to the propane cycle CC single bonds and the remaining two values are due to the linear chain CC single bonds. The observation of all these values, for both double bond and single bond CC stretchings, in comparison with the literature values show that some of the band values are higher

than the expected values and some of them are lower than the expected values, there is stretching of values on both ends of the expected region, which is naturally due to Fermi resonance effect between these values.

After scaling, these experimental values were found to be in good agreement with the vibrations observed in HF and DFT methods. The two bands observed at 1010 and 995 cm^{-1} were assigned to C–C in plane bending in the cyclopropenone group and the bands appearing at 550 and 435 cm^{-1} were assigned to out of plane bending vibrations. These assignments were little more than the assignments proposed by Thilagavathi et al. [27]. This was due to the substitution of heavier cyclopropenone to the phenyl compared to the amino group substitution done by Thilagavathi et al.

4.2.3 C=O Vibrations

The C=O stretching normally lies in the range 1750–1860 cm^{-1}, and is very intense in the infrared spectrum [16] and particularly in carboxylic acids they appear at 1725 with ±65 cm^{-1} [28]. In this case a very strong band is observed at 1660 cm^{-1} in IR, as there is no other band which can be assigned to this mode in the cited region, this band is due to C=O stretching only. The drastic decrease in the value only indicates the influence of cyclic propane group with which this group C=O is attached. It also confirms that this group is not a part of carboxylic group. The band observed at 1010 cm^{-1} was assigned to in-plane bending of C=O vibration and the band observed at 610 cm^{-1} was assigned to out-of-plane bending of C=O. In the case of literature [16], these values were observed at 720 and 398 cm^{-1} respectively. Here, the observed values for the present molecules are found to be greater than the literature values, which is contradictory to stretching value. The scaled theoretical values calculated in HF and DFT/B3LYP methods were found to be in good agreement with the experimental values.

4.3 Mulliken Atomic Charges

The charge distribution has an important influence on the Vibrational spectra of the molecule. As the charge distribution could affect the dipole moment, molecular polarisability, electronic structure and other similar properties, the calculation of Mulliken atomic charges becomes more important. Mulliken atomic charges were calculated in HF and DFT/B3LYP methods with 6-311++G(d,p) basis set in both the case. The values thus calculated are tabulated in Table 6. The illustration of the atomic charge distribution is also given in Fig. 6. Here, it could be noted that the C atoms near to the O atoms were highly electropositive because of the electron withdrawing property of the O atom. The effect of O atom was also felt in the neighboring substituent phenyl. Due to this effect, the C(9) carbon atom of the phenyl ring which was very close to O atom was found to be positive and hence

Table 6 Mulliken atomic charges of Methyl phenyl cyclopropenone

Atoms	Methylphenylcyclopropenone	
	HF/6-311G++(d,p)	B3LYP/6-311G++(d,p)
C(1)	0.7324	0.5771
C(2)	1.1731	1.0406
C(3)	1.2540	0.9734
O(4)	−0.4712	−0.3426
C(5)	−0.6331	−0.5453
H(6)	0.1659	0.1634
H(7)	0.1705	0.1723
H(8)	0.1705	0.1723
C(9)	0.8746	0.8342
C(10)	−0.5679	−0.6973
C(11)	−1.5068	−1.3229
C(12)	−0.1231	−0.0564
H(13)	0.0952	0.0540
C(14)	−0.0257	0.0139
H(15)	0.1830	0.1538
C(16)	−0.6794	−0.5804
H(17)	0.2257	0.1894
H(18)	0.2272	0.1890
H(19)	0.1997	0.1655

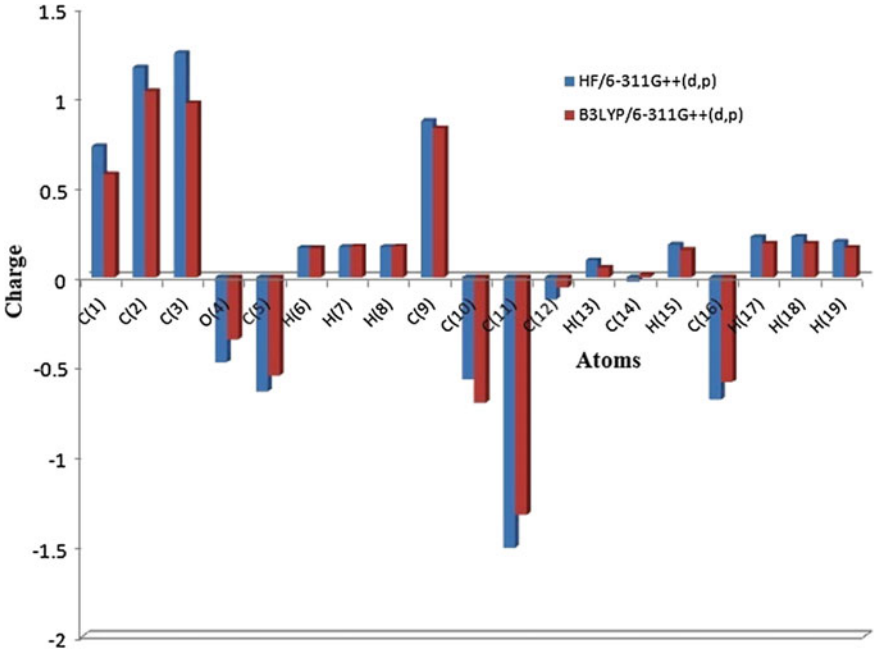

Fig. 6 Mulliken atomic charges of methyl phenyl cyclopropenone

making the nearby C(11), C(16) and C(12) carbon atom highly electronegative. The charge distribution was found to be high in HF method when compared to B3LYP method. The charge distribution of MPCP showed positive value for all hydrogen atoms. Compared to the methyl group hydrogen atoms, the hydrogen atom attached to the phenyl group were marginally more electropositive.

4.4 NMR Analysis

The optimized structure of MPCP was used to calculate the NMR chemical shift at HF and B3LYP levels in combination with GIAO methods, with 6-311++G(d,p) basis set. The ^{1}H and ^{13}C chemical shifts computed in ppm relative to TMS are shown in Table 6 and Fig. 7a, b.

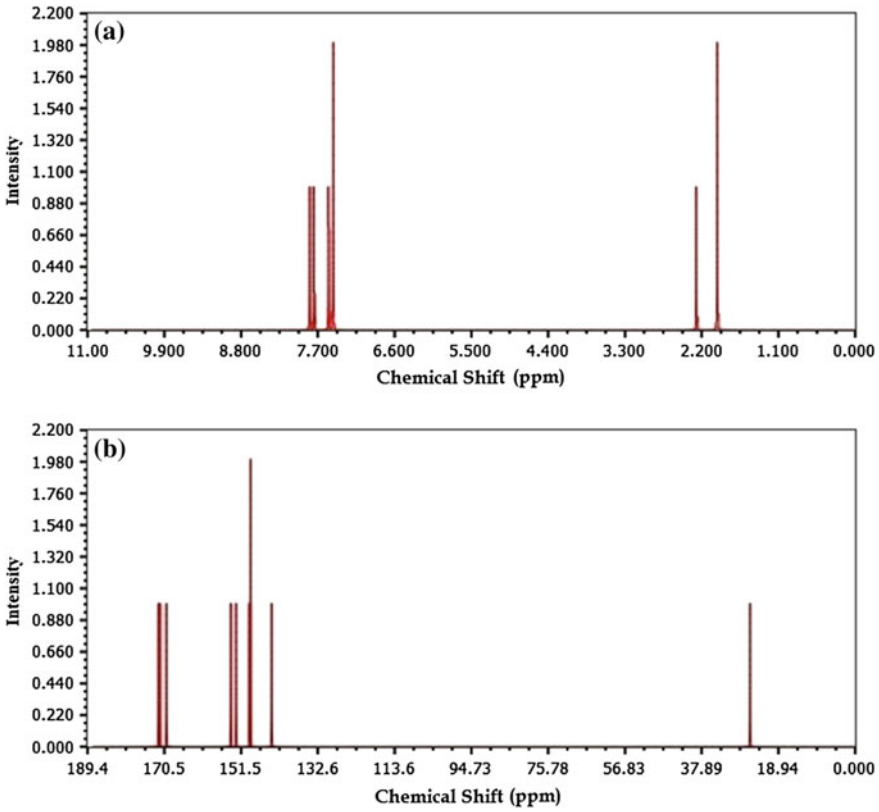

Fig. 7 **a** ^{1}H NMR chemical shift of MPCP by DFT/B3LYP 6-311++G(d,p) method, **b** ^{13}C NMR chemical shift of MPCP by DFT/B3LYP 6-311++G(d,p) method

In the case of cyclic propenone, the oxygen has the most electronegative property [29], The ^{13}C peaks calculated using HF/6-311++G(d,p) revealed that the C(1) atom, which is bonded to the oxygen atom, had high chemical shifts (160.68 ppm) and the C(2) atom, which is attached to the phenyl ring, had the next high chemical shift (153.86) and the C(3) atom attached to the methyl group showed the least shift (151.09 ppm). An identical pattern was obtained for B3LYP method also. The peaks were observed at 172.24, 171.66 and 170.07 ppm respectively. This is also evident from the high Mullikan charge value of C(1), C(2) and C(3) atoms (Table 7).

In the case of phenyl ring, all the carbon atoms have almost the same shift between the range 130–150 ppm. The C(11) atom has the maximum chemical shift 146.64 ppm, the next value is 142.37 ppm for C10, which agrees with the high negative charge of these two atoms as discussed in the Mulliken analysis and the C(9) has the minimum chemical shift 133.18 ppm which is found to be positive in charge. The carbon atom in the methyl group has the lowest chemical shift of all the carbon atoms in the molecule, 14.67 ppm, which shows how drastically the electron distribution varies between phenyl ring, propene cycle and methyl group.

The studied molecule has hydrogen atom attached to the phenyl and the methyl group. However, the chemical shift calculated for the ^{1}H atoms in the methyl group were quite low when compared to the chemical shift calculated in the phenyl group. The chemical shift of the ^{1}H atoms in the methyl group range from 2.44 to 2.85 ppm in HF/6-311++G(d,p) and 1.98 to 2.28 ppm in DFT/B3LYP 6-311++G (d,p) method. Whereas, the chemical shift of the ^{1}H atoms attached to the phenyl

Table 7 Experimental and calculated ^{1}H and ^{13}C NMR chemical shifts (ppm) of methyl phenyl cyclopropenone

Atom position	HF	B3LYP
C(1)	160.68	172.24
C(2)	153.86	171.66
C(3)	151.09	170.07
C(5)	14.67	26.05
H(6)	2.85	2.28
H(7)	2.44	1.98
H(8)	2.44	1.98
C(9)	133.18	144.07
C(10)	142.37	149.56
C(11)	146.64	154.39
C(12)	138.67	149.47
H(13)	8.56	7.76
C(14)	139.00	149.47
H(15)	8.62	7.82
C(16)	145.23	152.97
H(17)	8.08	7.48
H(18)	8.08	7.48
H(19)	8.22	7.55

ring range from 8.08 to 8.62 ppm in HF method and 7.48 to 7.82 ppm in DFT/B3LYP, which is naturally due to the presence of the six carbon atoms present in the phenyl ring, which is not there in the case of methyl group.

4.5 Frontier Molecular Orbitals (FMOs)

Frontier Molecular orbitals are common name given to highest occupied molecular orbitals (HOMO) and lowest unoccupied molecular orbitals (LUMO). The importance FMOs in the quantum mechanical calculations was discussed by Fleming in his work [30]. The energy gap between HOMO and LUMO can be used in the determination for kinetic stability, chemical reactivity, optical polarisability and chemical hardness—softness [29–31].

In order to understand the energy behavior of the title compound, the theoretical studies of the title compound was carried out in DMSO, chloroform and gas phase. The energies of four important molecular orbitals of MPCP: the highest occupied and second highest MO's (HOMO and HOMO − 1), the lowest and the second lowest unoccupied MO's (LUMO and LUMO + 1) were calculated using B3LYP/6-311++G(d,p) and are presented in Table 8. The 3D plots of the HOMO − 1, HOMO, LUMO and LUMO + 1 orbitals computed at the B3LYP/6-311G++(d,p) level for the title molecule (in gas phase) are illustrated in Fig. 8.

It is clear from the figure that LUMO is localized in most part of the molecule, while HOMO is mostly localized around the cyclopropenone ring. The calculated values of HOMO were −6.6151, −6.5031 and −6.2178 eV in DMSO, chloroform and gas phase respectively. Similarly, the values of LUMO were −1.7496, −1.7632 and −1.8258 eV in DMSO, chloroform and gas phase respectively. In the title molecule, the energy gap was found to be 4.8626, 4.7402 and 4.3891 eV in DMSO, chloroform and gas phase, respectively, which shows that the title molecule is less stable. The electronegativity (χ), Chemical hardness (η), electrophilicity index (ω)

Table 8 Calculated energies values of Methyl phenyl cyclopropenone in solvent (DMSO and chloroform) and gas phase

TD-DFT/B3LYP/6-311++G(d,p)	DMSO	Chloroform	Gas
E_{total} (Hartree)	−461.170	−461.166	−461.157
E_{HOMO} (eV)	−6.6151	−6.5031	−6.2178
E_{LUMO} (eV)	−1.7496	−1.7632	−1.8258
$\Delta E_{HOMO–LUMO\ gap}$ (eV)	4.8626	4.7402	4.3891
E_{HOMO} − 1 (eV)	−7.1130	−7.096	−7.0722
E_{LUMO} + 1(eV)	−0.7755	−0.8000	−0.9088
Chemical hardness η (eV)	−0.0893	−0.0871	−0.0806
Electronegativity χ (eV)	0.1537	0.1519	0.1478
Chemical potential μ (eV)	−0.1537	−0.1519	−0.1478
Electrophilicity index ω (eV)	−0.1322	−0.1324	−0.1355

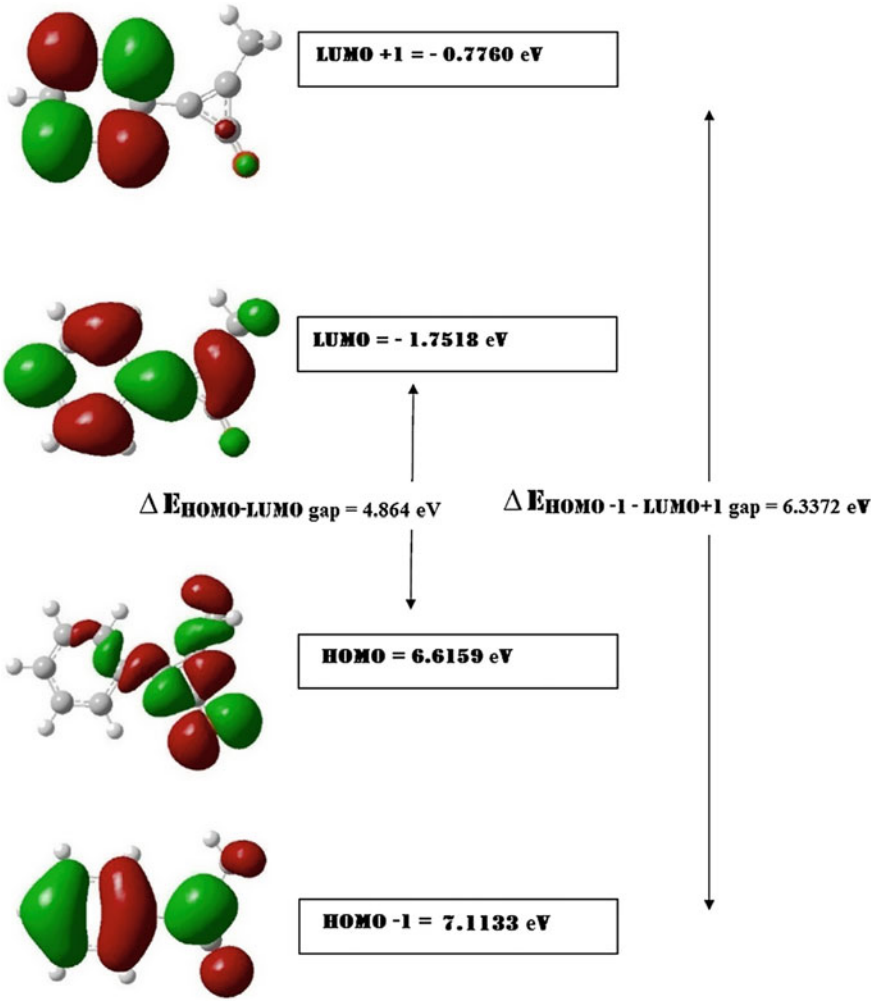

Fig. 8 Frontier molecular orbitals (HOMO–LUMO) of methyl phenyl cyclopropenone

and chemical potential (μ) of the title molecule is found to be 0.1537, −0.0893, −0.1322 and −0.1537 in DMSO. These values were found to decrease in chloroform and gas phase.

4.6 Molecular Electrostatic Potential (MEP) Maps

Molecular electrostatic potential was calculated at the B3LYP/6-311++G(d,p) for optimized geometry. The different values of the electrostatic potential at the surface

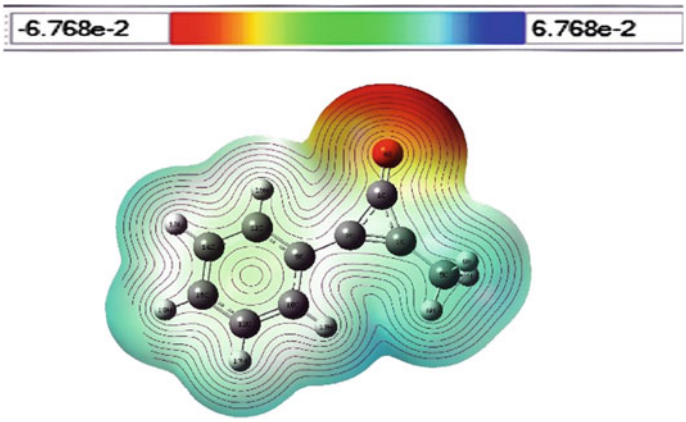

Fig. 9 Molecular electrostatic potential (MEP) and contour map of methyl phenyl cyclopropenone calculated by B3Lyp/6-311++G(d,p) method

are represented by different colors. Potential increases in the order red < orange < yellow < green < blue. The color code of these maps is in the range between −0.06768 a.u. (deepest red) and 0.06768 a.u. (deepest blue) in compound. The positive (blue) regions of MEP were related to electrophilic reactivity and the negative (green) regions to nucleophilic reactivity, shown in Fig. 9. As it can be seen from the MEP map of the title molecule, the negative regions were mainly localized around the oxygen atom; whereas, the maximum positive region was localized near the carbon atom of cyclopropenone around C(2) and C(9). This indicated that C(2) and C(9) was possible site for nucleophilic attack [32].

4.7 NBO Analysis

NBO analysis is an important tool for studying hybridization and occupancy effects [33]. Here for the title molecule the NBO analysis was performed using B3LYP/6-311++(d,p) method. This analysis provides a useful method to study the inter and intra molecular attraction among the bond pairs. The electron donor orbital, acceptor orbital and interaction stabilization energy are tabulated in Table 9. For each donor and acceptor, the strength of various types of interactions or stabilisation energy E_2 associated with electron delocalisation between donor and acceptor is estimated by the second-order energy lowering equation [34–36].

Carthigayan et al. [13] have analysed the NBO properties of 3-methyl-1-phenylpyrazole and observed the most probable electronic transition in the phenyl ring was between the C–C bonds and they are of $\pi \rightarrow \pi^*$ type in the range 20.85 kcal/mol. In MPCP, the following electronic transitions were observed: C10–C12 to C9–C11 (38.03 kcal/mol $\pi \rightarrow \pi^*$), C10–C12 to C14–C16 (43.25 kcal/mol

Table 9 Second order perturbation theory of Fock matrix in NBO basis of Methylphenylcyclopropenone

Donor	Type of bond	Occupancy	Acceptor	Type of bond	Occupancy	Energy $E^{(2)}$ kcal/mol	Energy difference E(j) − E(i) a.u.	Polarized energy F(i,j) a.u.
C1–C2	σ	1.94794	C1–C3	σ*	0.07378	4.15	1.46	0.07
			C1–O4	σ*	0.02744	3.84	1.71	0.073
			C2–C3	σ*	0.02681	7.41	1.59	0.097
			C2–C9	σ*	0.04805	4.62	1.52	0.075
			C3–C5	π*	0.03601	33.52	1.45	0.197
			C9–C10	π*	0.02285	3.06	1.58	0.063
C1–C3	σ	1.95229	C1–C2	σ*	0.07289	3.59	1.54	0.067
			C1–O4	σ*	0.02744	4.26	1.72	0.077
			C2–C3	σ*	0.02681	6.37	1.6	0.091
			C2–C9	σ*	0.04805	32.88	1.53	0.201
			C3–C5	σ*	0.03601	2.94	1.46	0.059
C1–O4	σ	1.99758	C1–C2	σ*	0.07289	2.77	2.08	0.069
			C1–C3	σ*	0.07378	3.1	2.02	0.072
C2–C3	σ	1.94787	C1–C2	σ*	0.07289	6.01	1.63	0.089
			C1–C3	σ*	0.07378	5.97	1.56	0.087
			C1–O4	σ*	0.02744	32.24	1.8	0.216
			C2–C9	σ*	0.04805	7.65	1.62	0.099
			C3–C5	σ*	0.03601	4.8	1.54	0.077
			C9–C11	σ*	0.0214	2.34	1.68	0.056
C2–C3	π	1.65713	C1–O4	π*	0.3077	152.27	0.52	0.254
			C9–C11	π*	0.3652	16.37	0.49	0.08
C2–C9	σ	1.98123	C1–C2	π*	0.07289	2.43	1.67	0.058
			C2–C3	π*	0.02681	6.45	1.73	0.094
			C9–C10	σ*	0.02285	3.82	1.72	0.072
			C9–C11	σ*	0.0214	3.93	1.73	0.074
			C2–C3	σ*	0.02681	4.39	1.71	0.078
C9–C10	σ	1.97337	C1–C2	σ*	0.07289	3.14	1.68	0.066
			C2–C9	σ*	0.04805	4.28	1.67	0.076
			C9–C11	σ*	0.0214	5.91	1.73	0.09
			C10–C12	σ*	0.0126	3.57	1.77	0.071
C9–C11	σ	1.97311	C2–C3	π*	0.02681	3.53	1.73	0.07
			C2–C9	π*	0.04805	3.92	1.66	0.072
			C9–C10	σ*	0.02285	5.84	1.73	0.09
			C11–C14	σ*	0.01237	3.37	1.77	0.069
			C2–C3	π*	0.09081	23.65	0.53	0.107
			C10–C12	π*	0.30476	41.73	0.48	0.128
			C14–C16	π*	0.31658	36.72	0.48	0.12

(continued)

Table 9 (continued)

Donor	Type of bond	Occupancy	Acceptor	Type of bond	Occupancy	Energy $E^{(2)}$ kcal/mol	Energy difference E(j) − E(i) a.u.	Polarized energy F(i,j) a.u.
C10–C12	σ	1.98061	C2–C9	σ*	0.04805	4.22	1.68	0.076
			C9–C10	σ*	0.02285	3.87	1.75	0.073
			C12–C16	σ*	0.0141	3.58	1.77	0.071
C10–C12	π	1.66499	C9–C11	π*	0.3652	38.03	0.48	0.122
			C14–C16	π*	0.31658	43.25	0.49	0.13
C11–C14	σ	1.98081	C2–C9	σ*	0.04805	3.97	1.68	0.073
			C9–C11	σ*	0.0214	3.68	1.75	0.072
			C14–C16	σ*	0.01408	3.57	1.77	0.071
C12–C16	σ	1.98127	C10–C12	σ*	0.0126	3.61	1.78	0.072
			C14–C16	σ*	0.01408	3.36	1.77	0.069
C14–C16	σ	1.98150	C11–C14	σ*	0.01237	3.55	1.78	0.071
			C12–C16	σ*	0.0141	3.37	1.77	0.069
C14–C16	π	1.64672	C9–C11	π*	0.3652	47.94	0.48	0.135
			C10–C12	π*	0.30476	37.48	0.48	0.121
O4	σ	1.97880	C1–C2	π*	0.07289	4.92	1.68	0.082
			C1–C3	σ*	0.07378	5.25	1.61	0.083
O4	π	1.87405	C1–C2	σ*	0.07289	31.21	1.14	0.171
			C1–C3	σ*	0.07378	30.22	1.07	0.163

π → π*), C14–C16 to C9–C11 (47.94 kcal/mol π → π*) and C14–C16 to C10–C12 (38.03 kcal/mol π → π*). In MPCP, it was noted that the E2 values of the carbon atoms in the phenyl ring are more when compared with 3-methyl-1-phenylpyrazole, this may be due to the attachment of the cyclopropenone to the phenyl ring. The highest E2 value was noted in C2–C3 to C1–O4 (152.27 kcal/mol π → π*) this reveals that C1–O4 prefers to be an acceptor rather than a donor. These values indicate that the most probable three electronic transitions in the molecule are C2–C3 to C1–O4, C14–C16 to C9–C11 and C10–C12 to C14–C16.

4.8 UV-Vis Spectral Analysis

Table 10 shows the electrical absorption spectra of MPCP calculated using DFT/B3LYP method with 6-311++G(d,p) basis set in DMSO, chloroform and gas phase. The UV-Vis absorption shows three different possible transitions with the

Table 10 Theoretical electronic absorption spectra of methyl phenyl cyclopropenone [absorption wavelength λ (nm), excitation energies E (eV) and oscillator strengths (f)] using DFT/B3LYP/6-311++G(d,p) method in DMSO, chloroform and gas phase

DMSO			Chloroform			Gas			Assignment
λ (nm)	E (eV)	(*f*)	λ (nm)	E (eV)	(*f*)	λ (nm)	E (eV)	(*f*)	
321.74	3.8535	0.0002	331.73	3.7375	0.0002	363.48	3.4110	0.0002	π–π*
252.39	4.9124	0.0332	252.64	4.9075	0.1449	268.88	4.6111	0.0000	π–π*
249.64	4.9664	0.5998	251.12	4.9372	0.4832	252.76	4.9052	0.2178	π–π*

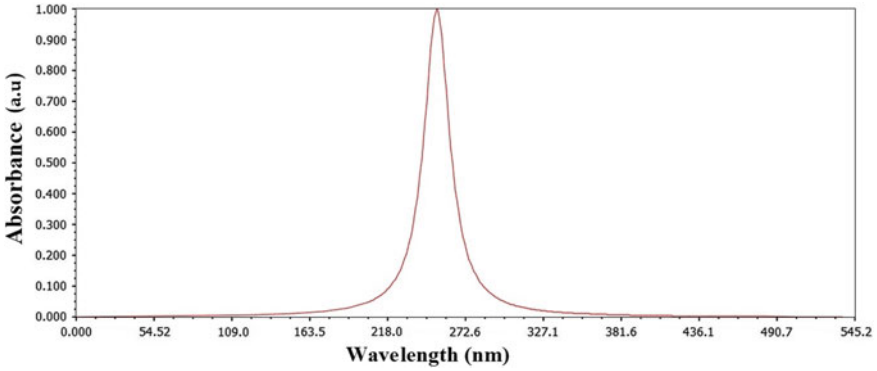

Fig. 10 UV-Vis absorption spectrum of methyl phenyl cyclopropenone

maximum absorption wavelength of 363.48, 268.88 and 252.76 nm in gas phase. The oscillator strength for respective transitions were found to be 0.0002, 0.0000 and 0.2178. This shows that, only the third transitions state will present in the UV-Vis spectrum, as shown in the Fig. 10. According to NBO analysis the transitions which gives out peak in the UV-Vis spectrum at 252 nm was found to be C10–C12 to C14–C16 (43.25 kcal/mol $\pi \rightarrow \pi^*$).

4.9 Thermodynamic Studies

Different thermodynamic parameters like Zero point Vibrational energies, specific heat, entropy, enthalpy, etc., were calculate theoretically by HF and B3LYP methods with 6-311++G(d,p) and 6-31++G(d,p) basis set and are listed in Table 11. Zero point Vibrational energies (ZPVEs) were found to be higher in HF method when compared with B3LYP. An identical pattern was observed while recording rotational constants, dipole moment and enthalpy values. The ZPVE has a

maximum value of 415915.8 J mol^{-1} at HF6-31++G(d,p) and a minimum value of 382412.0 at B3LYP6-31++G(d,p). On the other-hand, specific heat values were found to be higher in B3LYP (35.67 cal mol^{-1} K^{-1}) when compared to HF (33.01 cal mol^{-1} K^{-1}). The dipole moment, which gives the molecular charge distribution, was studied to depict the charge moment across the molecule. As a result, it was observed that the title molecule has a maximum dipole moment of 5.8556 Debye at HF/6-31++G(d,p) and a minimum value of 5.3778 at B3LYP6-311++G(d,p).

The variation of thermodynamic parameters: heat capacity (C), entropy (S) and enthalpy (H), with the increase in temperature (100–500 K) was recorded and tabulated in Table 12. Figure 11a–c shows the increase in the value of specific heat capacity (C), entropy (S) and enthalpy (H) with the increase in temperature, this agrees with the fact that molecular Vibrational intensities increase with temperature [25].

Table 11 Calculated thermo dynamical parameters of methyl phenyl cyclopropenone molecule in ground state at 298.15 K

Basic set		HF	HF	B3LYP	B3LYP
		6-31++G(d,p)	6-311++G(d,p)	6-31++G(d,p)	6-311++G(d,p)
SCF energy (a.u)		−458.169	−458.250	−461.039	−461.160
Zero point Vib. energy (J mol^{-1})		415915.8	413982.1	382412.0	387030.0
Rotational Constants (GHz)	A	2.34383	2.34912	2.29619	2.30799
	B	0.68924	0.69052	0.68049	0.68337
	C	0.53435	0.53540	0.5266	0.5289
Specific heat (C_v) (cal mol^{-1} K^{-1})		33.018	33.063	35.662	35.674
Entropy (S) (cal mol^{-1} K^{-1})		97.681	97.386	99.723	99.911
Dipole moment (Debye)		5.8556	5.7898	5.4450	5.3778
Enthalpy (K Cal/Mol)		105.203	104.729	98.970	98.661

Table 12 Thermodynamic properties at different temperatures at the B3LYP/6-311++G(d,p) level of methyl phenyl cyclopropenone

T (K)	C (cal mol^{-1} K^{-1})	S (cal mol^{-1} K^{-1})	H (kcal mol^{-1})
100	16.196	71.935	93.637
200	25.123	87.154	95.685
300	35.878	100.148	98.727
400	46.448	112.515	102.853
500	55.524	124.330	107.966

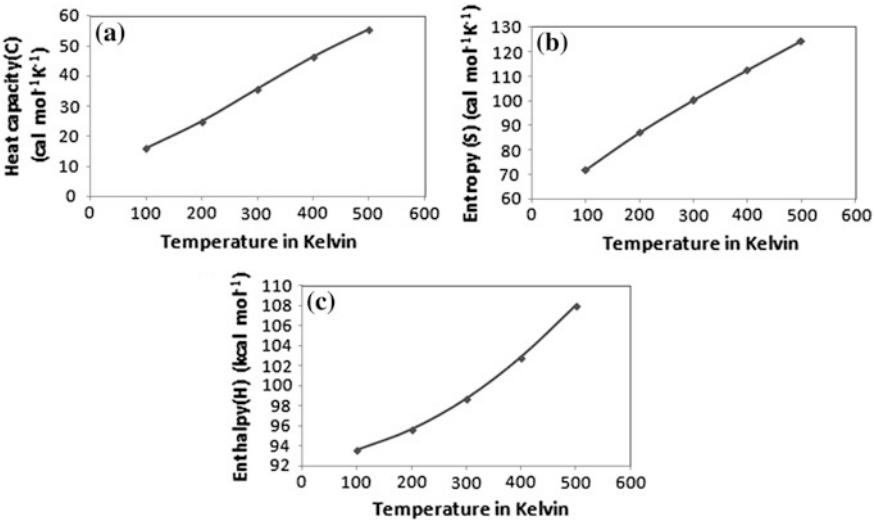

Fig. 11 Correlation graph between **a** temperature and heat capacity, **b** temperature and entropy and **c** temperature and enthalpy

5 Conclusion

In the present work, a complete vibrational analysis was made by HF and B3LYP methods with 6-31++G(d,p) and 6-311++G(d,p) basis set. The molecular geometry indicates that there is some conjugation of electrons in the cyclo propene group and it implies a slight distortion in the cyclic nature of phenyl ring. The vibrational frequencies of the fundamental modes of the compound has been precisely assigned and analyzed. The theoretical results were compared with the experimental vibrations and found to be in good agreement. The charge distribution of the compound was studied with the calculated Mulliken atomic charges. The atoms surrounding the O atom was found to be more electropositive. The theoretical ^{1}H and ^{13}C chemical shift values (with respect to TMS) were reported. The chemical reactivity descriptors such as chemical hardness (η), electronegativity (χ), chemical potential (μ) and electrophilicity indexes (ω) were calculated from the energy levels of HOMO and LUMO, which were calculated in solvent (DMSO and chloroform) and gas phase. The nucleophilic region and electrophilic region were identified using molecular electrostatic potential, calculated at B3LYP/6-311++G(d,p). It was evident from the MEP map that the negative regions were mainly localized around the oxygen atom. The NBO analysis showed that the the most probable three electronic transitions in the molecule were C2–C3 to C1–O4, C14–C16 to C9–C11 and C10–C12 to C14–C16. The NBO analysis indicated that the transition from C10–C12 to C14–C16 (43.25 kcal/mol $\pi \rightarrow \pi^*$) was responsible for the peak in the UV-Vis spectrum at 252 nm. The different thermodynamic parameters like specific heat

capacity (C), entropy (S) and enthalpy (H) were studied and they were found to increase with the increase in temperature.

References

1. Ajay Kumar K.: Int. J. Pharmacy Pharm. Sci. **5** (2013)
2. Kimura, S., Ito, S., Yushifuji, M., Veszpremi, T.: J. Org. Chem. **68**, 6820–6823 (2003)
3. Baker, A.W., Lord, R.C.: J. Chem. Phys. **23**, 1636–1643 (1955)
4. Duncan, J.L.: J. Mol. Spectrosc. **25**, 451–466 (1968)
5. Yamamoto, S., Nakata, M., Fukuyama, T., Kuchitsu, K.: J. Phys. Chem. **89**, 3298–3302 (1985)
6. Everaet, G.P., Herrebout, W.A., Van der Veken, B.J., Lundell, J., Rasanen, M.: Chem. Eur. J. **2**, 321–327 (1998)
7. Frisch, M.J., et al.: Gaussion 09 Program. Gaussian Inc, Wallingford (2004)
8. Hohenberg, P., Kohn, W.: Phys. Rev. B **136**, 864–871 (1964)
9. Becke, A.D.: J. Chem. Phys. **98**, 5648–5652 (1993)
10. Lee, C., Yang, W., Parr, R.G.: Phys. Rev. B **37**, 785–789 (1988)
11. Hakan, A., Öztekin, A.: Int. J. Mol. Sci. **8**, 760–776 (2007)
12. Karabacak, M., Kurt, M.: Spectrochim. Acta A **71**, 876–883 (2008)
13. Carthigayan, K., et al.: Spectrochim. Acta Part A Mol. Biomol. Spectrosc. **142**, 350–363 (2015)
14. Lin, C.L., et al.: J. Organomet. Chem. **535**, 149–154 (1997)
15. Silverstein, R.M., Bassler, G.C., Morrill, T.C.: Spectrometric Identification of Organic Compounds. John Wiley, Chichester (1991)
16. Socrates, G.: Infrared Raman Characteristic Group Frequencies—Tables and Charts, 3rd edn. Wiley, New York (2001)
17. Krishnakumar, V., John Xavier, R.: Indian J. Pure Appl. Phys. **41**, 597 (2003)
18. Parr, R.G., Szentpaly, L.V., Liu, S.: J. Am. Chem. Soc. **121**, 1922 (1999)
19. Perez, P., Toro-Labbe, A., Aizman, A., Contreras, R.: J. Org. Chem. **67**, 4747 (2002)
20. Haslam, J., et al.: Identification and Analysis of Plastics. IIiffe, London (1972)
21. Heath, R., Saykally, R.J.: The Structures and Vibrational Dynamics of Small Carbon Clusters. In: Reynolds, P.I. (eds.), pp. 7–21. North-Holland, Amsterdam (1993)
22. Heinniker, C.J.: Infrared Analysis of Industrial Polymers. Academic Press, New York (1967)
23. Hester, R.E., Clark, R.J.H. (eds.): Advances in Infrared and Raman Spectroscopy. Heyden, London (1981)
24. Madhavan, V.S., et al.: Spectrochim. Acta Part A **89**, 308–316 (2012)
25. Parr, R.G., Pearson, R.G.: J. Am. Chem. Soc. **105**, 7512 (1983)
26. Furic, K., Mohacek, V., Bonifacic, M., Stefanic, I.: J. Mol. Struct. 267–270 (1992)
27. Thilagavathi, G., Arivazhagan, M.: Spectrochim. Acta Part A **79**, 389–395 (2011)
28. Asha, R., Raju, K., Varghese, H.T., Granadeiro, C.M., Helena, I.S., Nogueiradand, C., Panicker, Y.: J. Braz. Chem. Soc. 549–559 (2009)
29. Ramalingam, S., Periandy, S., Karabacak, M., Karthikeyan, N.: Mol. Biomol. Spectrosc. **104**, 337–351 (2013)
30. Fleming, I.: Front. Orbitals Org. Chem. React. Wiley, New York (1976)
31. Asiri, A.M., Karabacak, M., Kurt, M., Alamry, K.A.: Spectrochim. Acta A **82**, 444–455 (2011)
32. Pauling, L.: The Nature of the Chemical Bond. Coruell University Press, Ithaca (1960)
33. Srivastava, A., Mishra, R., Joshi, B.D., Gupta, V., Tandon, P.: Mol. Simul. **40**(14), 1099–1112 (2014)

34. Snehalatha, M., Ravikumar, C., Hubert, I.J., Sekar, N., Jayakumar, V.S.: Spectroscopic analysis and DFT calculations of a food additive Carmoisine. Spectrochim. Acta A **72**, 654–662 (2009)
35. Reed, A.E., Curtiss, L.A., Weinhold, F.: Intermolecular interactions from a natural bond orbital, donor–acceptor viewpoint. Chem. Rev. **88**, 899–926 (1988)
36. Liu, C.G., Su, Z.M., Guan, X.H., Muhammad, S.: Redox and photoisomerization switching the second-order nonlinear optical properties of a tetrathiafulvalene derivative across six states: a DFT study. J. Phys. Chem. C **115**, 23946–23954 (2011)

Some Novel Mannich Bases-Synthesis, Crystal Structure, Docking Studies, Anti-microbial Activity, and Cytotoxicity

M. Seeni Mubarak, R. Kathirvel, M. Sathyanarayanan and S. Mohamed Rabeek

Abstract A simple and elegant method for the synthesis of substituted piperidin-4-one derivatives using 1,3-diphenyl acetone, variously substituted aldehydes and ammonium formate in ethanol medium under the reflux-free condition is described. This reaction seems to be probably achieved via an intermolecular Mannich base route. Nitrogen containing piperidin-4-ones are obtained even when the normally used ammonium acetate is replaced by more convenient ammonium formate. Thus, the Mannich bases, 2,3,5,6-Tetraphenyl-piperidin-4-one (a), 2,6-bis(4-methoxy-phenyl)3,5-diphenyl-piperidin-4-one (b) and 2,6-bis (4-nitro-phenyl)-3,5-diphenyl-piperidin-4-one (c) have been prepared. The synthesized compounds are characterized through spectral studies such as FT-IR, ^{1}H NMR, and ^{13}C NMR. The structure of 2,3,5,6-Tetraphenyl-piperidin-4-one is conformed by single crystal XRD analysis. Further these synthesized compounds subjected to biological studies.

1 Introduction

Mannich reaction is an important both in biology and chemistry due to its simple style of synthesis, adaptability and diverse range of applications. Heterocyclic compounds with piperidone skeletons are attractive targets for organic synthesis, where in the piperidone moiety possess aromatic substitution in 2nd and 6th positions [1]. From the survey of the literature, it appears that the piperidone moieties present in many alkaloid compounds gain importance owing to their pharmacological activities and stereochemical significance. In this work, the reactions involve treatment of 1,3-diphenyl acetone with substituted benzaldehydes in the presence of ammonium formate. In the view of above remarkable considerations

M. Seeni Mubarak · R. Kathirvel (✉) · M. Sathyanarayanan · S. Mohamed Rabeek
PG and Research Department of Chemistry, Jamal Mohamed College (Autonomous), Tiruchirappalli 620020, Tamil Nadu, India
e-mail: Kathirchem66@gmail.com

J. Ebenezar (ed.), *Recent Trends in Materials Science and Applications*,
Springer Proceedings in Physics 189, DOI 10.1007/978-3-319-44890-9_56

an attempt has been made to synthesize of piperidone derivatives. The synthesized compounds have been characterized using spectral studies.

1.1 Docking Studies

The compounds are thought to act by inhibiting 1skf, 1ai9, 3qwq proteins (1skf-Antibacterial, 1ai9-Antifungal, 3qwq-Anticancer proteins). These are supported by docking studies of the synthesized piperidin-4-one, using enzyme GLIDE module of Schrodinger 3.7. The molecular Dynamics simulations were performed using Gromacs 4.5.5 [2]. Selected the best three protein candidates from the docking study. We used MD for performing protein-ligand as described. The topology file for the selected small molecules was generated using the automated topology builder (ATB) [3] in the frame work of GROMS 53A6 force-field. The protein-ligand then solved with protein data bank BCR-ABL (1skf, 1ai9 and 3qwq) explicit water molecules and placed in the center of a cubic box size $24 \times 24 \times 24$ Å. Minimum 1.0 Å distance simulation box so that protein can fully immerse with water and rotate freely. The removed hydrogen atoms, protein structure energy was minimized until the average root mean square was reached 0.30 Å. An active site or binding site residues include 1skf (ASN-71, R-216(**3b**), ALA-220, SER-73, GLU-34, LYS-38), 1ai9 (GLU-32, ARG-34) 3QWQ-(ASN-328, SER-326) chem draw assistance has been taken to sketch the synthesized three molecules. The sketched was then prepared by Ligand Preparation (LigPrep), were organized to 3D structure and different tautomers were also the results of LigPrep [4]. Ligand was an ionized at a pH range about 7.0 ± 2.0 to preserve the qualities for molecular docking Glide was employed for the rapid docking of three molecules into the active site of the target receptor. The Glide algorithm operated with a systematic search of positions, orientations, and conformations of the ligand in the receptor binding site using type approach and followed a unique scoring method. Glide energy and inhibitory constant internal energy were analyzed using XP visualize.

Then, particle mesh Ewald (PME) method [5] was used for the electrostatic energy calculation. It permitted the use of the Ewald Summation at a simple truncation method of 10 Å or less than, and the linear constrain solver (LINCS 38) algorithm was used for covalent bond constraints. The steepest descent approach (1000 ps) was used for each protein-ligand for energy minimization. Further, NVT was performed for 100 ps to equilibrate the system with protein and ligand for constant volume, pressure (1 atm) and temperature (300 K). The final MD run was set to 10,000 ps for each protein-ligand, were saved for further, analysis using xmgrace and UCFC chimera software [6]. We focused to dock the most potent compound in a manner.

1.2 Anti-microbial Activity

Piperidin-4-ones as another kind of important heterocyclic system, was frequently encountered in a variety of biologically active molecules. For example, Anti bacterial, Antifungal activity, anticancer, anti-inflammatory and anesthetic etc. The anti-microbial activity of the given sample was carried out by Disc Diffusion Technique [7]. The test microorganisms of *Staphylococcus aureus, Bacillus subtilis* and *E. coli, Klebsiella aerogenes and Fungus Aspergillus niger, Candida albicans* were obtained from National Chemical Laboratory (NCL) Pune and maintained by periodical sub culturing on Nutrient agar and Sabouraud dextrose agar medium for bacteria and fungi respectively. The effect produced by the sample was compared with the effect produced by the positive control (Reference standard Ciprofloxacin 5 μg/disc for bacteria; Nystatin 100 μg/disc for fungi).

1.3 Evaluation of Cytotoxicity: Methodology

1.3.1 Cell Lines and Culture Medium

The human cervical cancer cell line (HeLa) was obtained from National Centre for Cell Science (NCCS), Pune and grown in Eagles Minimum Essential Medium containing 10 % fetal bovine serum (FBS). The cells were maintained at 37 °C, 5 % CO_2, 95 % air and 100 % relative humidity. Maintenance cultures were passaged weekly, and the culture medium was changed twice a week [8].

1.3.2 Cell Treatment Procedure

The monolayer cells were detached with trypsin-ethylenediaminetetraacetic acid (EDTA) to make single cell suspensions and viable cells were counted using a hemocytometer and diluted with medium containing 5 % FBS to give final density of 1×10^5 cells/ml. One hundred microlitres per well of cell suspension were seeded into 96-well plates at plating density of 10,000 cells/well and incubated to allow for cell attachment at 37 °C, 5 % CO_2, 95 % air and 100 % relative humidity. After 24 h the cells were treated with serial concentrations of the test samples. They were initially dissolved in neat dimethylsulfoxide (DMSO) and an aliquot of the sample solution was diluted to twice the desired final maximum test concentration with serum free medium. Additional four serial dilutions were made to provide a total of five sample concentrations. Aliquots of 100 μl of these different sample dilutions were added to the appropriate wells already containing 100 μl of medium, resulting in the required final sample concentrations. Following sample addition, the plates were incubated for an additional 48 h at 37 °C, 5 % CO_2, 95 % air and 100 % relative humidity. The medium containing without samples were served as control and triplicate was maintained for all concentrations.

1.3.3 MTT Assay

3-[4,5-dimethylthiazol-2-yl]2,5-diphenyltetrazolium bromide (MTT) is a yellow water soluble tetrazolium salt. A mitochondrial enzyme in living cells, succinate-dehydrogenase, cleaves the tetrazolium ring, converting the MTT to an insoluble purple formazan. Therefore, the amount of formazan produced was directly proportional to the number of viable cells. After 48 h of incubation, 15 µl of MTT (5 mg/ml) in phosphate buffered saline (PBS) was added to each well and incubated at 37 °C for 4 h. The medium with MTT was then flicked off and the formed formazan crystals were solubilized in 100 µl of DMSO and then measured the absorbance at 570 nm using micro plate reader [9]. The percentage cell viability was then calculated with respect to control as follows

$$\% \text{ Cell viability} = [\text{A}]\text{Test}/[\text{A}]\text{control} \times 100$$

2 Materials and Methods

All the reagents were obtained from commercial suppliers and used without any further purification unless otherwise noted. Melting points were determined on an EZ-Melt automated melting point apparatus without corrections. TLC was performed on silica coated glass. The 2,3,5,6-Tetraphenyl piperidin-4-one compound (a) was synthesized according to the procedure for the Scheme 1 cited in the literature [10]. 1,3-Diphenyl acetone (0.1 mol; 2.1 g), benzaldehyde (0.2 mol; 6 ml) and ammonium formate (0.1 mol; 4 g) in ethanol medium [11–14] were heated in a water bath for 3 h, and treated with ether followed by few drops of Con. HCl. The piperidine hydrochloride obtained was suspended in acetone and few drops of ammonia were added to get the product (a) [15–17]. The same procedure was adopted with appropriately substituted benzaldehydes to get the compounds b and c. IR spectra were recorded in SHIMADZU FT-IR 8400s spectrometer instrument using KBr pellets. ^{1}H NMR and ^{13}C NMR spectra were recorded in dpx200-MHz instrument BRUKER DRX-300 MHz and using $CDCl_3$ and DMSO-d_6 as the solvent chemical shifts were reported relative to TMS as the internal standard. The chemical shift values were expressed in ppm.

The molecular interaction and inhibitory activity of piperidone derivatives were studied by in silico docking studies. From the literature, active and interacting protein target had been selected. These were supported by docking studies of the synthesized piperidin-4-one, using enzyme GLIDE module of Schrodinger 3.7. Binding poses of the compounds (a, b and c) lead molecules. The proposed binding mode of the lead molecules had been shown in the stick formal. Residues involved in hydrogen bonding had labeled with hydrogen bond in dotted yellow lines and bond lengths had been shown in Angstrom. The ligand molecules were drawn using chemdraw and prepared by LigPrep, were 2D structure got organized into a 3D structure and different tautomers were also the result of LigPrep.

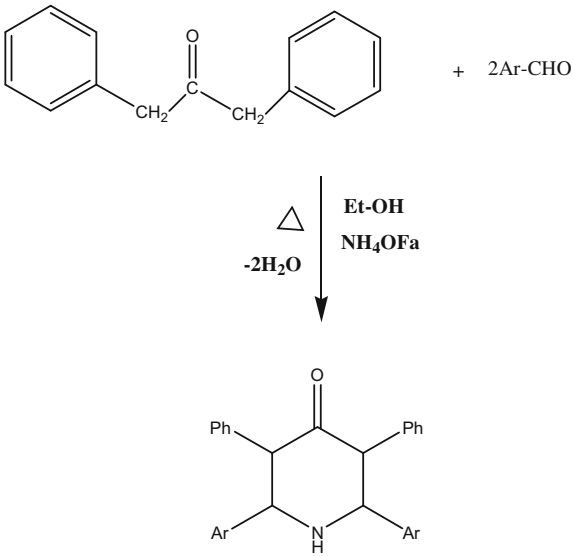

a. Ar = C_6H_5
b. Ar = *p-OMe*-C_6H_5
c. Ar = *m-*NO_2-C_6H_5

Scheme 1 2,6-piperidin-4-one derivatives

3 Results and Discussion

FT-IR spectra of the compounds (a, b and c) showed N–H stretching frequencies around 3300–3100 cm^{-1} aromatic C–H stretching and aliphatic C–H stretching around 2922–3068 cm^{-1} respectively. The presence of carbonyl group was confirmed by the stretching absorption in the range of 1713–1716 cm^{-1} [18]. The peak assignment for ^{1}H and ^{13}C NMR data of the compounds were made based on the computer programme ChemDraw 12.0. The various chemical shift data confirmed the structures of the compound as given in Scheme 1. The compounds were characterised by FT-IR, ^{1}H NMR, ^{13}C NMR and single crystal X-ray diffraction analysis. They were also subjected to molecular auto docking studies and biological studies.

3.1 Single Crystal X-ray Diffractometry

The large 62 mm square 4-kappa goniometer fastest APEX II CCD detector and KRYOFLEX low temperature cooling device [19, 20]. High-resolution single crystal X-ray diffraction data were collected at 293(2) K on a Bruker KAPPA APEX II CCD diffract meter, equipped with a graphite monochromator and a fine—

focus sealed tube [λ(Mo − K_α) = 0.71073 Å]. The single crystal was mounted in a Lindmann capillary and 2400 Frames were recorded with scanning angle ω of 0.3°, each for 5 s exposure with 0.5 mm Collimated X-ray. The distance between, crystal and detector was kept 62 mm. The structure was solved by direct methods using SHELXS-97 and the refinement was carried out against F^2 using SHELXL-97. The molecular-packing diagram was generated by Hg of CCDC [21, 22].

3.1.1 Description of the Crystal Structure

The structure of the compound is shown in ortep diagram (Fig. 1). The unit cell parameters are listed in Table 1. The crystal system is Orthorhombic, Pca21 space group with all atoms located at general positions (Fig. 2) and such a molecule in the unit cell (Z = 4, 1.228 Mg/m^3 and R indices [I > 2r(I)] – R1 = 0.0551, wR2 = 0.1372, R indices (all data) – R1 = 0.0673, wR2 = 0.1447). The fractional atomic coordinates and isotropic or equivalent isotropic displacement parameters are given in Table 2. The analysis of bond lengths and bond angles are given in Table 3. The anisotropic displacement parameters are given in Table 4. From XRD study, the molecular formula of the compound 2,3,5,6-Tetraphenyl-piperidin-4-one for to be $C_{29}H_{25}NO$. The crystal structure obtained indicates the presence of one oxygen

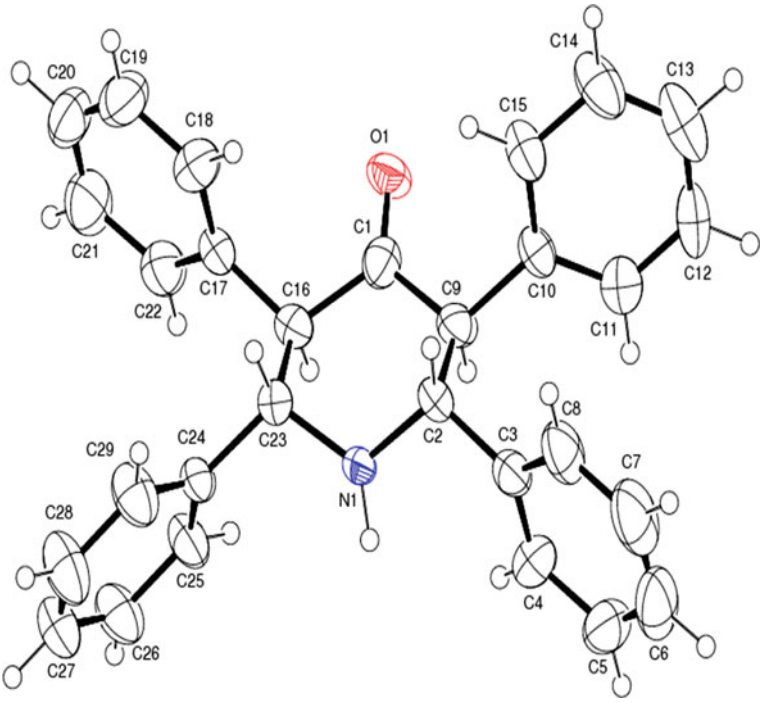

Fig. 1 Thermal ellipsoidal plots with 50 % probability for H atoms

Table 1 Crystal data and structure refinement for 2,3,5,6-Tetraphenyl-piperidin-4-one

Crystal data	
Empirical formula	$C_{29}H_{25}NO$
Formula weight	403.5
Temperature	293(2) K
Wavelength	0.71073 A
Crystal system, space group	Orthorhombic, Pca21
Unit cell dimensions	a = 33.296(7) A, alpha = 90°
	b = 5.8860(10) A, beta = 90°
	c = 11.133(2) A, gamma = 90°
Volume	2181.8(7) A^3
Z, Calculated density	4, 1.228 Mg/m^3
Data collection	
Absorption coefficient	0.074 mm^{-1}
F(000)	856
Crystal size	0.30 × 0.20 × 0.20 mm
Theta range for data collection	1.22°–22.97°
Limiting indices	$-36 \leq h \leq 33, -6 \leq k \leq 6, -12 \leq l \leq 12$
Reflections collected/unique	16798/2938 [R(int) = 0.0359]
Completeness to theta	= 22.97, 98.0 %
Absorption correction	Semi-empirical from equivalents
Max. and min. transmission	0.9894 and 0.9713
Refinement	
Refinement method	Full-matrix least-squares on F^2
Data/restraints/parameters	2938/15/316
Goodness-of-fit on F^2	1.115
Final R indices [$I > 2\sigma(I)$]	R1 = 0.0551, wR2 = 0.1372
R indices (all data)	R1 = 0.0673, wR2 = 0.1447
Absolute structure parameter	−1(4)
Extinction coefficient	0.0071(13)
Largest diff. peak and hole	0.156 and −0.175 $e.A^{-3}$

atom attached to C_1 carbon as keto group. oxygen bond length, angle C_9–O–C_{16} (1.489(12)–1.511(11) 115.4(8)–128.7) are identified by XRD (Tables 2 and 3).

3.2 Molecular Docking Studies

The compound structures (a, b and c) were 1skf-antibacterial extracted from protein data bank, showed the highest binding energy with XP score of −5.5 kcal/M (Fig. 3a, b, c and Table 5). To get an insight into their interacting pattern, we used UCFC chimera molecular visualization tool and Glide for generating bonds

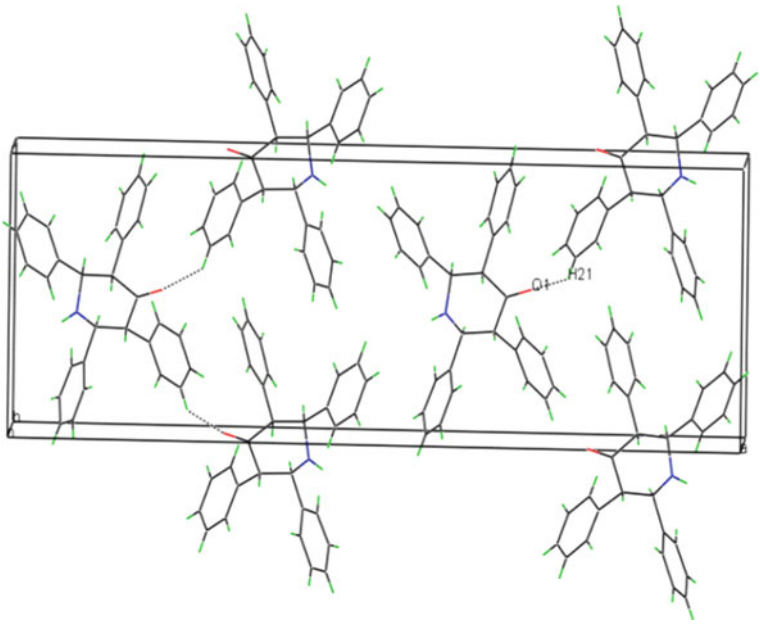

Fig. 2 Packing of crystal structure 2,3,5,6-Tetraphenyl-piperidin-4-one

Table 2 Atomic coordinates ($\times 10^4$) and equivalent isotropic displacement parameters ($A^2 \times 10^3$) for 2,3,5,6-Tetraphenyl-piperidin-4-one (a). U(eq) is defined as one third of the trace of the orthogonalized Uij tensor

Atoms	x	y	z	U(eq)
N(1′)	1645(4)	3240(30)	5064(10)	56(5)
C(1)	1733(4)	2470(20)	4904(12)	50(5)
O(1)	2071(2)	2478(10)	5178(5)	53(2)
C(1′)	821(4)	3580(40)	4453(15)	59(6)
O(1′)	482(3)	3600(20)	4182(7)	121(4)
N(1)	905(3)	2790(20)	4309(9)	42(3)
C(2)	974(1)	2631(7)	5637(3)	49(1)
C(3)	657(1)	1199(7)	6222(3)	51(1)
C(4)	523(1)	−758(8)	5680(4)	63(1)
C(5)	248(1)	−2159(9)	6228(6)	83(2)
C(6)	104(2)	−1562(17)	7334(7)	114(3)
C(7)	231(2)	365(16)	7868(5)	107(2)
C(8)	505(1)	1755(9)	7328(4)	70(1)
C(9)	1391(1)	1510(8)	5678(3)	52(1)
C(10)	1530(1)	1040(7)	6956(3)	47(1)

(continued)

Table 2 (continued)

Atoms	x	y	z	U(eq)
C(11)	1449(1)	−1000(8)	7508(4)	65(1)
C(12)	1559(2)	−1348(8)	8676(4)	71(1)
C(13)	1747(2)	271(11)	9312(5)	85(2)
C(14)	1836(2)	2323(9)	8787(4)	78(2)
C(15)	1725(1)	2729(8)	7594(3)	60(1)
C(16)	1575(1)	3489(7)	3731(3)	49(1)
C(17)	1883(1)	5031(7)	3181(3)	47(1)
C(18)	2000(1)	6986(7)	3755(4)	60(1)
C(19)	2271(1)	8464(8)	3222(6)	76(1)
C(20)	2424(2)	8007(10)	2117(5)	82(2)
C(21)	2309(2)	6098(11)	1536(5)	83(2)
C(22)	2045(1)	4555(9)	2071(4)	65(1)
C(23)	1152(1)	4545(7)	3704(3)	47(1)
C(24)	995(1)	4968(7)	2449(3)	45(1)
C(25)	1014(1)	3381(7)	1568(3)	57(1)
C(26)	860(2)	3754(8)	439(4)	67(1)
C(27)	677(1)	5760(8)	193(4)	68(1)
C(28)	650(2)	7401(9)	1055(4)	82(2)
C(29)	813(1)	6981(8)	2164(4)	68(1)

Table 3 Bond lengths [A] and angles [deg] for 2,3,5,6-Tetraphenyl-piperidin-4-one

Atoms	Bond lengths
N(1′)–C(9)	1.489(12)
N(1’)–C(16)	1.511(11)
N(1′)–H(1′)	0.92(2)
C(1)–O(1)	1.167(12)
C(1)–C(16)	1.530(13)
C(1)–C(9)	1.536(13)
C(1)–H(1′)	1.00(7)
O(1)–H(1′)	0.91(11)
C(1′)–O(1′)	1.169(12)
C(1′)–C(23)	1.492(14)
C(1′)–C(2)	1.519(14)
C(1′)–H(1)	1.21(5)
O(1′)–H(1)	1.29(8)
N(1)–C(23)	1.484(10)
N(1)–C(2)	1.499(10)
N(1)–H(1)	0.93(2)
C(2)–C(3)	1.500(5)
C(2)–C(9)	1.538(5)
C(2)–H(2)	0.9800

(continued)

Table 3 (continued)

Atoms	Bond lengths
C(3)–C(8)	1.371(6)
C(3)–C(4)	1.375(6)
C(4)–C(5)	1.375(6)
C(4)–H(4)	0.93
C(5)–C(6)	1.367(9)
C(5)–H(5)	0.9300
C(6)–C(7)	1.348(9)
C(6)–H(6)	0.9300
C(7)–C(8)	1.365(8)
C(7)–H(7)	0.9300
C(8)–H(8)	0.9300
C(9)–C(10)	1.521(5)
C(9)–H(9)	0.9800
C(10)–C(11)	1.375(6)
C(10)–C(15)	1.384(6)
C(11)–C(12)	1.366(6)
C(11)–H(11)	0.9300
C(12)–C(13)	1.341(7)
C(12)–H(12)	0.9300
C(13)–C(14)	1.374(8)
C(13)–H(13)	0.9300
C(14)–C(15)	1.400(6)
C(14)–H(14)	0.9300
C(15)–H(15)	0.9300
C(16)–C(23)	1.539(5)
C(16)–H(16)	0.9800
C(17)–C(18)	1.372(6)
C(18)–C(19)	1.387(6)
C(18)–H(18)	0.9300
C(19)–C(20)	1.359(7)
C(19)–H(19)	0.9300
C(20)–C(21)	1.352(7)
C(20)–H(20)	0.9300
C(21)–C(22)	1.398(6)
C(22)–H(22)	0.9300
C(23)–C(24)	1.512(5)
C(23)–H(23)	0.9800
C(24)–C(25)	1.356(5)
C(25)–C(26)	1.375(6)
C(25)–H(25)	0.9300
C(26)–C(27)	1.356(6)
C(26)–H(26)	0.9300
C(27)–C(28)	1.365(7)

(continued)

Table 3 (continued)

Atoms	Bond lengths
C(27)–H(27)	0.9300
C(28)–C(29)	1.372(6)
C(28)–H(28)	0.9300
C(29)–H(29)	0.9300
C(9)–N(1′)–C(16)	115.4(8)
C(9)–N(1′)–H(1′)	128(7)
C(16)–N(1′)–H(1′)	110(7)
O(1)–C(1)–C(16)	123.7(10)
O(1)–C(1)–C(9)	124.7(10)
C(16)–C(1)–C(9)	111.6(8)
O(1)–C(1)–H(1′)	49(6)
C(16)–C(1)–H(1′)	104(6)
C(9)–C(1)–H(1′)	118(6)
C(1)–O(1)–H(1′)	56(3)
O(1′)–C(1′)–C(23)	124.4(12)
O(1′)–C(1′)–C(2)	123.3(12)
C(23)–C(1′)–C(2)	112.2(9)
O(1′)–C(1′)–H(1)	66(3)
C(23)–C(1′)–H(1)	109(4)
C(2)–C(1′)–H(1)	99(4)
C(1′)–O(1′)–H(1)	58.5(17)
C(23)–N(1)–C(2)	113.9(7)
C(23)–N(1)–H(1)	130(4)
C(2)–N(1)–H(1)	116(4)
N(1)–C(2)–C(3)	110.8(5)
N(1)–C(2)–C(1′)	21.6(9)
C(3)–C(2)–C(1′)	110.4(6)
N(1)–C(2)–C(9)	101.2(5)
C(3)–C(2)–C(9)	112.4(3)
C(1′)–C(2)–C(9)	119.1(7)
N(1)–C(2)–H(2)	123.4
C(3)–C(2)–H(2)	104.4
C(1′)–C(2)–H(2)	104.4
C(9)–C(2)–H(2)	104.4
C(8)–C(3)–C(4)	118.3(4)
C(8)–C(3)–C(2)	121.1(4)
C(4)–C(3)–C(2)	120.5(4)
C(5)–C(4)–C(3)	121.5(5)
C(5)–C(4)–H(4)	119.2
C(3)–C(4)–H(4)	119.2
C(6)–C(5)–C(4)	118.7(6)
C(6)–C(5)–H(5)	120.7
C(4)–C(5)–H(5)	120.7

(continued)

Table 3 (continued)

Atoms	Bond lengths
C(7)–C(6)–C(5)	120.2(6)
C(7)–C(6)–H(6)	119.9
C(5)–C(6)–H(6)	119.9
C(6)–C(7)–C(8)	121.3(6)
C(6)–C(7)–H(7)	119.4
C(8)–C(7)–H(7)	119.4
C(7)–C(8)–C(3)	120.0(6)
C(7)–C(8)–H(8)	120.0
C(3)–C(8)–H(8)	120.0
N(1′)–C(9)–C(10)	112.4(5)
N(1′)–C(9)–C(1)	21.5(8)
C(10)–C(9)–C(1)	111.6(6)
N(1′)–C(9)–C(2)	101.9(7)
C(10)–C(9)–C(2)	112.3(3)
C(1)–C(9)–C(2)	119.6(6)
N(1′)–C(9)–H(9)	110.0
C(10)–C(9)–H(9)	110.0
C(1)–C(9)–H(9)	91.3
C(2)–C(9)–H(9)	110.0
C(11)–C(10)–C(9)	121.2(4)
C(15)–C(10)–C(9)	119.4(4)
C(12)–C(11)–C(10)	120.3(5)
C(12)–C(11)–H(11)	119.9
C(10)–C(11)–H(11)	119.9
C(13)–C(12)–C(11)	121.3(5)
C(13)–C(12)–H(12)	119.3
C(11)–C(12)–H(12)	119.3
C(12)–C(13)–C(14)	120.1(4)
C(14)–C(13)–H(13)	119.9
C(13)–C(14)–C(15)	119.7(5)
C(13)–C(14)–H(14)	120.2
C(15)–C(14)–H(14)	120.2
C(10)–C(15)–C(14)	119.3(4)
C(10)–C(15)–H(15)	120.4
C(14)–C(15)–H(15)	120.4
C(17)–C(16)–N(1′)	110.7(5)
C(17)–C(16)–C(1)	110.4(6)
N(1′)–C(16)–C(1)	21.4(8)
C(17)–C(16)–C(23)	111.9(3)
N(1′)–C(16)–C(23)	101.6(7)
C(1)–C(16)–C(23)	119.3(6)
C(17)–C(16)–H(16)	110.8
N(1′)–C(16)–H(16)	110.8

(continued)

Table 3 (continued)

Atoms	Bond lengths
C(1)–C(16)–H(16)	91.9
C(23)–C(16)–H(16)	110.8
C(18)–C(17)–C(22)	118.5(4)
C(18)–C(17)–C(16)	120.8(4)
C(22)–C(17)–C(16)	120.7(4)
C(17)–C(18)–C(19)	120.8(5)
C(17)–C(18)–H(18)	119.6
C(19)–C(18)–H(18)	119.6
C(20)–C(19)–C(18)	120.5(5)
C(20)–C(19)–H(19)	119.8
C(18)–C(19)–H(19)	119.8
C(21)–C(20)–C(19)	119.4(5)
C(21)–C(20)–H(20)	120.3
C(20)–C(21)–C(22)	121.0(5)
C(17)–C(22)–C(21)	119.8(5)
C(17)–C(22)–H(22)	120.1
C(21)–C(22)–H(22)	120.1
N(1)–C(23)–C(1′)	22.0(10)
N(1)–C(23)–C(24)	110.1(5)
C(1′)–C(23)–C(24)	109.0(6)
N(1)–C(23)–C(16)	102.5(5)
C(1′)–C(23)–C(16)	120.7(7)
C(24)–C(23)–C(16)	113.6(3)
N(1)–C(23)–H(23)	123.1
C(1′)–C(23)–H(23)	103.9
C(24)–C(23)–H(23)	103.9
C(16)–C(23)–H(23)	103.9
C(25)–C(24)–C(29)	116.7(3)
C(25)–C(24)–C(23)	122.6(4)
C(29)–C(24)–C(23)	120.7(4)
C(24)–C(25)–C(26)	122.3(4)
C(24)–C(25)–H(25)	118.8
C(26)–C(25)–H(25)	118.8
C(27)–C(26)–C(25)	119.4(4)
C(27)–C(26)–H(26)	120.3
C(25)–C(26)–H(26)	120.3
C(28)–C(27)–H(27)	119.9
C(27)–C(28)–C(29)	118.6(4)
C(29)–C(28)–H(28)	120.7
C(24)–C(29)–C(28)	122.7(4)
C(28)–C(29)–H(29)	118.6

Table 4 Symmetry transformations used to generate equivalent atoms: Anisotropic displacement parameters ($A^2 \times 10^3$) for 2,3,5,6-Tetraphenyl-piperidin-4-one. The anisotropic displacement factor exponent takes the form: $-2\pi^2$ [h^2 a^{*2} U11 + ⋯ + 2 h k a* b* U12]

Atoms	U11	U22	U33	U23	U13	U12
N(1′)	43(6)	91(12)	34(6)	12(6)	−18(5)	−15(7)
C(1)	61(11)	45(7)	43(6)	−2(5)	5(5)	−6(6)
O(1)	36(3)	78(4)	47(3)	1(3)	−7(2)	2(3)
C(1′)	29(8)	98(16)	49(7)	0(8)	−8(6)	0(8)
O(1′)	79(7)	215(12)	70(5)	48(6)	−21(5)	−45(7)
N(1)	32(5)	60(7)	34(4)	10(4)	−7(4)	−13(5)
C(2)	55(3)	55(2)	36(2)	7(2)	−12(2)	−9(2)
C(3)	44(2)	67(3)	43(2)	9(2)	−6(2)	−2(2)
C(4)	54(3)	68(3)	66(3)	6(2)	3(2)	−15(2)
C(5)	61(3)	79(3)	108(4)	26(3)	−16(3)	−18(3)
C(6)	56(4)	171(8)	114(6)	83(6)	4(4)	−12(4)
C(7)	74(4)	186(7)	60(4)	43(5)	15(3)	5(5)
C(8)	68(3)	101(4)	42(3)	11(3)	6(2)	9(3)
C(9)	44(2)	77(3)	35(2)	1(2)	−2(2)	−12(2)
C(10)	55(2)	54(3)	31(2)	−2(2)	−2(2)	7(2)
C(11)	70(3)	69(3)	57(3)	8(2)	−1(2)	−6(2)
C(12)	95(3)	62(3)	57(3)	28(3)	12(3)	20(3)
C(13)	104(4)	107(5)	44(3)	9(3)	−3(3)	45(4)
C(14)	119(4)	66(3)	48(3)	−17(3)	−24(3)	20(3)
C(15)	84(3)	55(3)	42(2)	1(2)	−8(2)	13(2)
C(16)	47(2)	58(2)	41(2)	2(2)	−7(2)	−8(2)
C(17)	49(2)	53(2)	38(2)	6(2)	−7(2)	0(2)
C(18)	52(2)	55(3)	72(3)	−1(2)	3(2)	−3(2)
C(19)	66(3)	58(3)	103(4)	9(3)	−8(3)	−13(3)
C(20)	57(3)	88(4)	101(5)	38(3)	−1(3)	−15(3)
C(21)	67(3)	117(4)	66(3)	18(4)	13(3)	−4(3)
C(22)	61(3)	78(3)	57(3)	3(2)	−1(2)	−5(2)
C(23)	49(2)	53(2)	40(2)	8(2)	−4(2)	−11(2)
C(24)	46(2)	60(3)	29(2)	4(2)	−2(2)	−8(2)
C(25)	76(3)	48(2)	47(3)	1(2)	−18(2)	8(2)
C(26)	90(3)	71(3)	41(2)	−15(2)	−10(2)	10(3)
C(27)	82(3)	77(3)	45(3)	7(3)	−10(2)	7(3)
C(28)	118(4)	67(3)	62(3)	6(3)	−15(3)	27(3)
C(29)	95(3)	61(3)	47(3)	−10(2)	−8(2)	15(3)

(H_bonds) interactions with the ATP binding site residues of BCR-ABL. Here, we observed single H_bond with ALA-220, SER-73 and GLU-34, LYS-38, R-216 and ASN-73 residued with a bond length of 2.8 and 3.3 Å while two H_bond formations were observed with GLY-34, SER-73 and A-220 with the bond length of 3.3–2.8 Å compound c (Table 6) [23, 24].

Other proteins 1ai9-Antifungal, 3qwq-Anticancer following (Figs. 4a–c and 5a–c) showed high binding affinity with XP scores of −6.54 kcal/M (compound b;

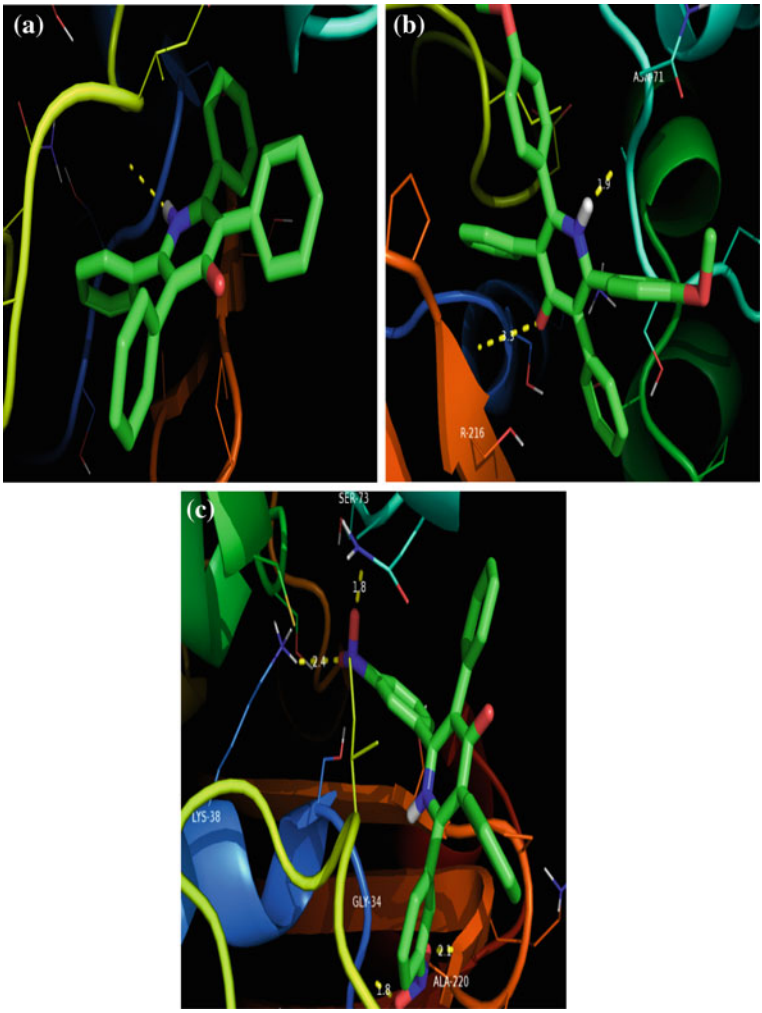

Fig. 3 **a**–**c** Shows the binding poses of the different compounds **a** 2,3,5,6-Tetraphenyl-piperidin-4-one, **b** 2,6-bis(4-methoxy-phenyl)3,5-diphenyl-piperidin-4-one and **c** 2,6-bis(4-nitro-phenyl)-3,5-diphenyl-piperidin-4-one in Protein-1skf (antibacterial) lead molecules

Table 7, 8) and −6.44 kcal/M compound c (Table 9), respectively. Here, it was noticeable that key residues of ARG-34, GLU-32 (compound c; Fig. 5c) and ASN-331 to SER 324 involved in the more five H_bonds interactions, the bond length 3.2–3.1 Å (Table 10). Although (3qwq-anticancer) exhibits XP docking scored above the cutoff value, we considered it as a potent inhibitor for BCR-ABL because it showed the highest number of H_bond with the hot spot residues of BCR-ABL.

Table 5 Docking score results, protein: 1skf (antibacterial)

Parameter	Compound (a)	Compound (b)	Compound (c)
Binding energy	−5.5	−2.59	−5.3
Inhibitory constant	90 micM	12 Mm	117 micM
Internal energy	−5.2	−4.1	−5.53
VdW	−5.26	−3.97	−5.26
Electorsatic	0.12	−0.15	0.26
HB	–	1	1

Table 6 Hydrogen bond:1skf (antibacterial)

S. No	Inhibitor	Hydrogen donor	Hydrogen acceptor	Bond length distance
1	Compound (a)	–	–	–
2	Compound (b)	Lig-NH	R216-O	2.8
		Lig-OH	N71-O	3.3
3	Compound (c)	R34-NH	Lig-N1O2	3.3
		S73-NH	Lig-N1O1	2.8
		A220-NH	Lig-N2O2	3.0

The more hydrogen bonded (donor) present in the compound (c) Fig. 5c with ASN-331, ASN-328, ASP-323, SER-324, SER-326. Therefore, we considered 3qwq-anticancer compound (c) for our further analysis to the bioactive of these selected lead compounds and anticancer [25].

3.3 Antimicrobial Activity

The antimicrobial activity of the piperidone derivatives was determined using the Disc diffusion technique method, using different concentrations (50, 100, 500 and 1000 µg). The sterile Muller Hinton agar and Sabouraud dextrose agar were used for bacteria and fungi respectively. Two Gram-positive, two Gram-negative and two fungal strains were used to study the antimicrobial activity. All these strains were obtained from National Collection of Industrial Microorganisms (NCIM), Pune. The watt-man 2 filter paper of 6 mm diameter was loaded with 100 µl of the diluted sample placed at equal intervals over the uniformly inoculated plate along with a standard disc Ciprofloxacin 5 mcg/disc for bacteria and Nystatin 100 units/disc for fungi were also placed along with the sample to maintain quality control. Followed by incubation at 37 ºC for 24 h and 25 ºC for two days for bacteria and fungi were observed for a zone of inhibition. The zone of inhibition was measured by using a standard scale. The diameter of the zone of inhibition

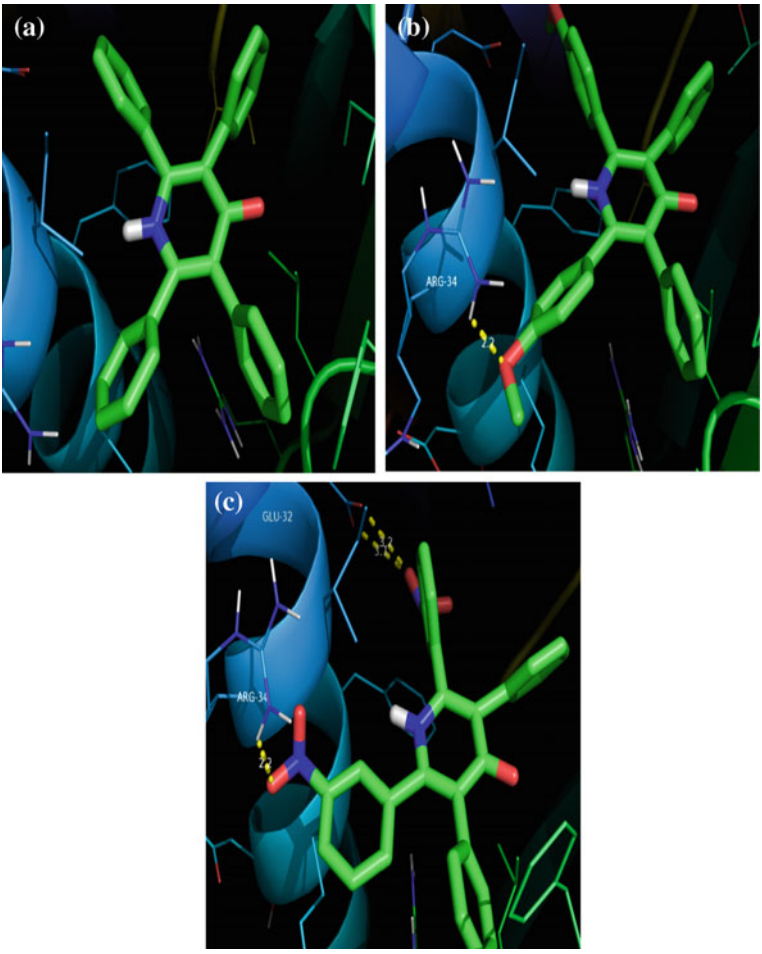

Fig. 4 **a**–**c** Shows the binding poses of the different compounds **a** 2,3,5,6-Tetraphenyl-piperidin-4-one, **b** 2,6-bis(4-methoxy-phenyl)3,5-diphenyl-piperidin-4-one and **c** 2,6-bis (4-nitro-phenyl)-3,5-diphenyl-piperidin-4-one in Protein-1ai9 (antifungal) lead molecules

directly proportional to the amount of active constituent present in the sample. The compounds (a, b and c) were found (Tables 11, 12 and 13) to be effective against Gram positive (*Staphylococcus aureus* and *Bacillus subtilis*). Among these two Gram positive the effect was found to be remarkable at low concentration (100 µl) towards *Bacillus subtilis.* The compound b was found to be more effective against Gram negative *E. coli* and *Klebsiella aerogenes.* In general, compounds (a, b and c) showed better response towards fungal strains *Aspergillus niger* and *Candida albicans.* The effect of compounds against *Candida albicans* was tremendous for compound b at all the concentrations.

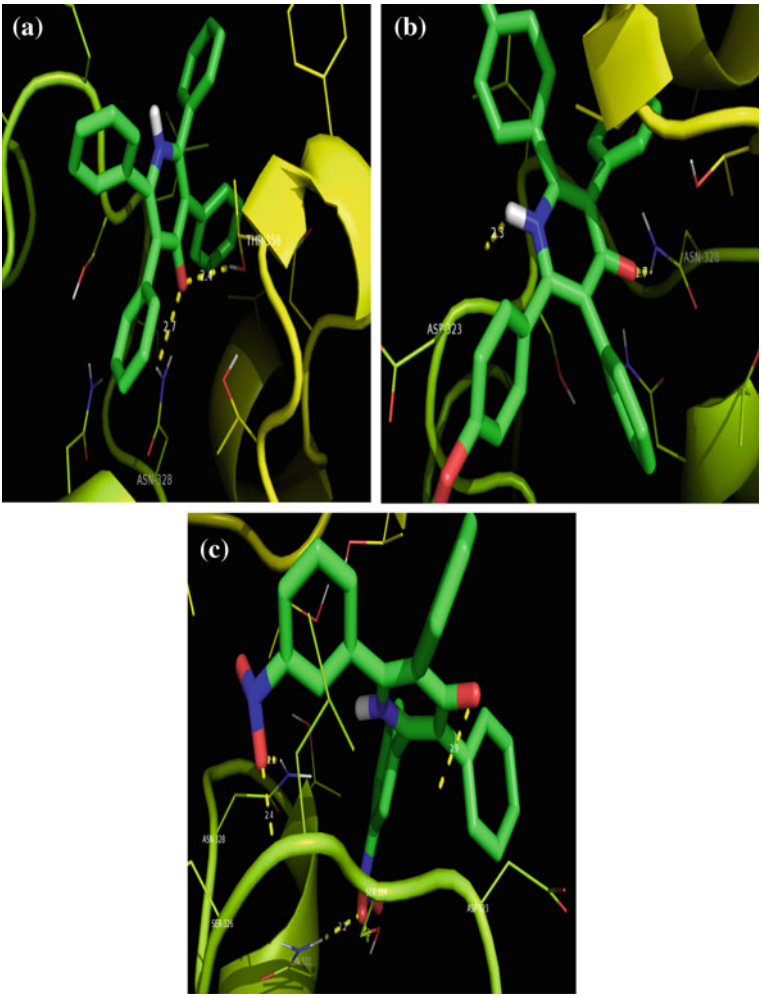

Fig. 5 **a**–**c** Shows the binding poses of the different compounds **a** 2,3,5,6-Tetraphenyl-piperidin-4-one, **b** 2,6-bis(4-methoxy-phenyl)3,5-diphenyl-piperidin-4-one and **c** 2,6-bis (4-nitro-phenyl)-3,5-diphenyl-piperidin-4-one in Protein-3qwq (anticancer) lead molecules

3.4 Cytotoxicity

The human cervical cancer cell line (HeLa) was taken for five different concentrations such as 0.25, 2.5, 25, 50, 100 μM tested with each compounds of a, b and c in high non-polar solvent with DMSO as control in the MTT assay. The percentage (%) of cell viability was calculated with respect to control as shown in Table 14. When drug concentration was increased, the amount of cell viability was decreased.

Table 7 Protein 1ai9 (antifungal)

Parameter	Compound (a)	Compound (b)	Compound (c)
Binding energy	−6.16	−6.54	−6.2
Inhibitory Constant	30 micM	16 micM	28 micM
Internal energy	−5.79	−6.65	−7.52
VdW	−5.8	−6.72	−7.59
Electorsatic	0.01	0.07	0.07
HB	–	1	1

Table 8 Hydrogen bond:1ai9 (antifungal)

S. No	Inhibitor	Hydrogen donor	Hydrogen acceptor	Bond length distance
1	Compound (a)	–	–	–
2	Compound (b)	R34-NH	Lig-O1	3.1
3	Compound (c)	R34-NH	Lig-N1O2	3.1
		E32-NH	Lig-N2O2	3.1

Table 9 Protein 3qwq (anticancer)

Parameter	Compound (a)	Compound (b)	Compound (c)
Binding energy	−4.35	−3.62	−6.44
Inhibitory constant	648 micM	2.23 mM	19 micM
Internal energy	−4.05	−4.17	−6.46
VdW	−4.02	−3.97	−6.41
Electorsatic	−0.04	−0.27	0.08
HB	–	1	3

On the other hand, the cell viability was found to increase in the presence of control DMSO (Fig. 6). The future molecular modifications should be aimed at producing N-substituted Mannich bases.

3.5 Spectral Characterization

*2,3,5,6-Tetraphenyl-piperidin-4-one (**a**) Yield: 86–92 %; mp: 214–216 °C.* FT-IR (KBr): 3402 (υ_{N-H}), 3026($\upsilon_{aromatic\text{-}CH}$), 2922 ($\upsilon_{aliphatic\text{-}CH}$), 1716 ($\upsilon_{C=O}$), 1587, 1452 ($\upsilon_{C=C}$) cm^{-1}, ^{1}H NMR (300 MHz, DMSO-d_6, δ in ppm); 7.35–7.04 (m, 16H, aromatic-H); 4.58–4.53 (d, 4H, benzylic-H) (C_2 and C_6 protons); 4.33–4.30 (d, 4H, benzylic-H) (C_3 and C_5 protons); 3.01 (hump, 1H, NH). ^{13}CNMR (100 MHz,

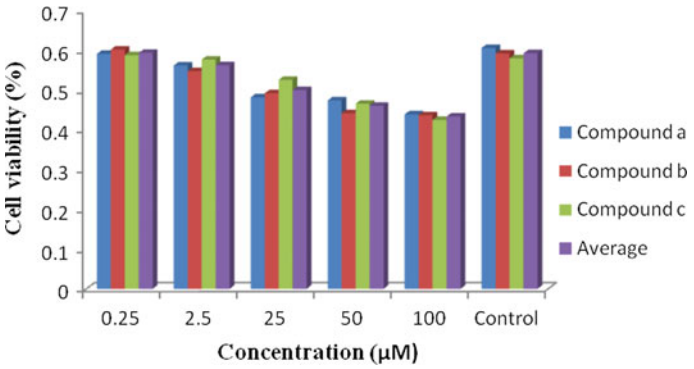

Fig. 6 Bar diagram of concentration versus cell viability for three compounds

Table 10 Hydrogen bond:3qqwq (anticancer)

S. No	Inhibitor	Hydrogen donor	Hydrogen acceptor	Bond length distance
1	Compound (a)	T358-OH	Lig-O	3.2
		N328-NH	Lig-N	2.7
2	Compound (b)	Lig-NH	D323-O	3.2
		N328-NH	Lig-O	2.8
3	Compound (c)	N331-NH	Lig-N2O1	3.1
		N328-NH	Lig-N1O2	3.0
		D323-NH	Lig-O	2.9
		S324-OH	Lig-N2O2	3.0
		S326-NH	Lig-N1O1	3.2

Table 11 2,3,5,6-Tetraphenyl-piperidin-4-one

S. No	Name of the microorganisms	Zone of inhibition in mm					
		50 mcg	100 mcg	500 mcg	1000 mcg	Solvent control	Standard
1	*Staphylococcus aureus* (NCIM2079)	12	13	16	22	–	35
2	*Bacillus subtilis* (NCIM2063)	16	20	22	22	–	40
3	*Klebsiella aerogenes* (NCIM2098)	10	12	15	18	–	30
4	*E. coli* (NCIM2065)	10	12	12	14	–	38
5	*Aspergillus niger* (NCIM2105)	12	15	15	20	–	35
6	*Candida albicans* (NCIM3102)	12	14	14	15	–	32

Standard-Ciprofloxacin 5 μg/disc for bacteria: Nystatin 100 units/disc for fungi. Solvent-DMSO

Table 12 2,6-bis(4-methoxy-phenyl)3,5-diphenyl-piperidin-4-one

S. No	Name of the microorganisms	Zone of inhibition in mm					
		50 mcg	100 mcg	500 mcg	1000 mcg	Solvent control	Standard
1	*Staphylococcus aureus* (NCIM2079)	12	14	18	20	–	35
2	*Bacillus subtilis* (NCIM2063)	20	22	22	24	–	40
3	*Klebsiella aerogenes* (NCIM2098)	10	16	20	22	–	30
4	*E. coli* (NCIM2065)	16	20	20	21	–	38
5	*Aspergillus niger* (NCIM2105)	12	15	16	16	–	35
6	*Candida albicans* (NCIM3102)	18	20	24	26	–	32

Standard-Ciprofloxacin 5 μg/disc for bacteria: Nystatin 100 units/disc for fungi. Solvent-DMSO

Table 13 2,6-bis(4-nitro-phenyl)-3,5-diphenyl-piperidin-4-one

S. No	Name of the microorganisms	Zone of inhibition in mm					
		50 mcg	100 mcg	500 mcg	1000 mcg	Solvent control	Standard
1	*Staphylococcus aureus* (NCIM2079)	15	15	18	19	–	35
2	*Bacillus subtilis* (NCIM2063)	18	20	20	21	–	40
3	*Klebsiella aerogenes* (NCIM2098)	14	14	17	20	–	30
4	*E. coli* (NCIM2065)	15	15	16	18	–	38
5	*Aspergillus niger* (NCIM2105)	14	16	16	16	–	35
6	*Candida albicans* (NCIM3102)	13	15	15	18	–	32

Standard-Ciprofloxacin 5 μg/disc for bacteria: Nystatin 100 units/disc for fungi. Solvent-DMSO

Table 14 Cell viability for different concentrations of three compounds

Concentration	0.25 μM	2.5 μM	25 μM	50 μM	100 μM	Control
Compound (a)	0.591	0.562	0.482	0.474	0.439	0.606
Compound (b)	0.602	0.548	0.492	0.442	0.437	0.592
Compound (c)	0.588	0.577	0.526	0.466	0.425	0.58
Average	0.593667	0.562333	0.5	0.460667	0.433667	0.592667

DMSO-d_6, δ in ppm): 205.5 (>C=O), 141.2, 135.1, 128.1, 127.8, 127.6, 127.5, 126.7, 68.1, 65.3.

*2,6-Bis(4-methoxy-phenyl)-3,5-diphenyl-piperidin-4-one (**b**) Yield: 65–68 %; mp: 238–240 °C.* FT-IR (KBr): 3411 (υ_{N-H}), 3025 ($\upsilon_{aromatic-CH}$), 2957 ($\upsilon_{aliphatic-CH}$), 1713 ($\upsilon_{C=O}$), 1503, 1450 ($\upsilon_{C=C}$) cm^{-1}, ^{1}H NMR (300 MHz, DMSO-d_6, δ in ppm); 7.26–6.70 (m, 14H, aromatic-H); 4.50–4.46 (d, 4H, benzylic-H) (C_2 and C_6 protons); 4.28–4.25 (d, 4H, benzylic-H) (C_3 and C_5 protons); 3.63 (s, 6H, methoxy protons, 2.77) (hump, 1H, NH). ^{13}CNMR (100 MHz, DMSO-d_6, δ in ppm): 206.4 (>C=O), 158.0, 136.6, 133.6, 133.9, 130.0, 128.8, 127.4, 126.14, 66.0, 63.6, 54.8.

*2,6-Bis(3-nitro-phenyl)-3,5-diphenyl-piperidin-4-one (**c**) Yield: 68–70 %; mp: 220–222 °C.* FT-IR (KBr): 3402 (υ_{N-H}), 3068 ($\upsilon_{aromatic-CH}$), 3034 ($\upsilon_{aliphatic-CH}$), 1714 ($\upsilon_{C=O}$), 1524, 1455 ($\upsilon_{C=C}$) cm^{-1}, ^{1}H NMR (300 MHz, DMSO-d_6, δ in ppm); 8.30–7.08 (m, 14H, aromatic-H), 4.80–4.75 (d, 4H, benzylic-H) (C_2 and C_6 protons); 4.42–4.39 (d, 4H, benzylic-H) (C_3 and C_5 protons); 3.86–3.83 (hump, 1H, NH). ^{13}CNMR (100 MHz, DMSO-d_6, δ in ppm): 204.2(>C=O), 147.4, 143.9, 135.6, 134.8, 130.0, 129.3, 127.7, 126.5, 122.3, 122.1, 65.7, 63.1.

3.6 Crystal Growth

In order to grow the crystal, the compound was dissolved in benzene medium, and allowed to stand for 6 days. The colourless needle-like crystals were obtained compound (a), The brown colour needle-like crystals were obtained at same medium solvent used compound (b) for 5 days and a mixture of solvent used for benzene-DMSO needle like brown colour compound (c) for 7 days.

4 Conclusion

A simple and elegant method for the synthesis of the compounds (a, b and c) are described in this work. Nitrogen containing piperidine-4-ones are obtained, when more convenient ammonium formate is employed instead of the deliquescent ammonium acetate. All these compounds are characterized by FT-IR, ^{1}H NMR, ^{13}C NMR and single crystal X-ray diffraction analysis (Bond angles, bond lengths and cell parameters). Further, the biological activity of the compounds are tested. The microorganisms of *Staphylococcus aureus, Bacillus subtilis, E. coli, Klebsiella aerogenes, Fungus Aspergillus niger* and *Candida albicans* are used for the test. Autodock studies of different proteins (1skf, 1ai9, 3qwq) are carried-out using various evaluation of antibacterial, antifungal and cancer cell activities. The highly negative value is ascribed taking for more binding energy. The human cervical cancer cell line (HeLa) is tested with five concentration of the each compound using

MTT assay method and high non polar solvent control DMSO. When increased the amount of drug concentration, the amount of cell death was decreased. Further investigation on the application of stereochemical study and few more microbial evaluations for these compounds are currently underway in our laboratory.

Acknowledgements The authors are grateful to Principal and Management Committee members, Jamal Mohamed College, Trichy for providing necessary facilities, and IIT Chennai for X-ray crystallographic studies. The authors are also thanks to Prof. M.I. Fazal Mohamed for fruitful discussions during the course of the work.

References

1. Baliah, V., Jeyaraman, R., Chandrasekaran, L.: Synthesis of 2,6-disubstituted piperidines, oxane and thianes. J. Am. Chem. Soc. Rev. **83**, 379–423 (1983)
2. Pronk, S., et al.: GROMACS 4.5: a high-throughput and highly parallel open source molecular simulation toolkit. Bioinformatics **29**, 845–854 (2013)
3. Oostenbrink, A.C., Villa, A., Mark, A.E., van Gunsteren, W.F.: A biomolecular force field based on the enthalpy of hydrogen and salvation: the GROMOS force-field parameter 53A5 and 53a6. J. Comput. Chem. **25**, 1656–1676 (2004)
4. Halgren, T.A., Murphy, R.B., Friesner, R.A., Beard, H.S., Frye, L.L., Pollard, W.T., Banks, J. L.: Glide: a new approach for rapid, accurate docking and scoring. 2. Enrichment factors in database screening. J. Med. Chem. **47**, 1750–1759 (2004)
5. Wang, H., Dommert, F., Holm, C.: Optimizing working parameters of the smooth particle mesh Ewald algorithm in terms of accuracy and efficiency. J. Chem. Phys. **133**, 034117 (2010)
6. Pettersen, E.F., et al.: UCSF Chimera-a visualization system for exploratory research and analysis. J. Comput. Chem. **25**, 1605–1612 (2004)
7. Indian Pharmacopeia **11**, The controller of publication, New Delhi; A-105 (1996). Website: ipc.nic.in
8. Mosmann, T.: Rapid colorimetric assay for cellular growth and survival: application to proliferation and cytotoxicity assays. J. Immunol. Methods **65**, 55–63 (1983)
9. Monks, A., Scudiero, D., Skehan, P., Shoemaker, R., Paull, K., Vistica, D., Hose, C., Langley, J., Cronise, P., Vaigro-Wolff, A., Gray-Goodrich, M., Campbell, H., Mayo, J.: Boyd, feasibility of high flux anticancer drug screen using a diverse panel of cultured human tumour cell lines. J. Natl. Cancer Inst. **83**, 757–766 (1991)
10. Noller, C., Baliah, V.: J. Am. Chem. Soc. **70**, 3853 (1948)
11. Baliah, V., Ekambaram, A., Govindarajan, T.S.: Curr. Sci. **23**, 264 (1954)
12. Finer, I.L.: Org. Chem. ELBS **2** (1975)
13. Baliah, V., Chandrasekaran, J.: Indian J. Chem. **15B**, 55S (1977)
14. Baliah, V., Gopalakrishnan, V., Jeyaraman, R.: Indian J. Chem. Soc. Sec. B **6B**, 1065 (1978)
15. Baliah, V., Gopalakrishnan, V., Jeyaraman, R.: Indian J. Chem. Soc. Sec. B **16B**, 1065 (1978)
16. Fazal Mohamed, M.I., Krishnapillay, M.: Indian Chem. Soc. **70**, 258 (1993)
17. Fazal Mohamed, M.I., Krishnapillay, M.: Indian J. Chem. **36B**, 50 (1997)
18. Silverstein, R.M., Francis, X.W., David, J.K.: Spectrometric Identification of Organic Compounds, 7th edn. John Wiley & Sons, Inc. New Jersey, USA (2005)
19. Lovejoi, D.B., Richardson, D.R.: Blood **100**(2), 666 (2002)
20. Hong, M., Yill, H., Wang, D., Gao, Z.: Acta Cryst. **E61**, m801 (2005)
21. Steiner, T.: J. Mol. Struct. **39**, 447 (1998)

22. EI-Sayed, R.: Synthesis, antibacterial and surface activity of 1,2,4-triazole derivatives Indian. J. Chem. **45**(B), 738–746 (2006)
23. Wang, R., Wang, Y., Lu, S.: J. Med. Chem. **46**, 2287–2303 (2003)
24. Taher, A.T., Helwa, A.A.: Chem. Pharm. Bull. **60**(4), 521–530 (2012)
25. Abdelhafez, O.M., Amin, K.M., Ali, H.I., Abdalla, M.M.: J. RSC Adv. **4**, 11569–11579 (2014)

Mathematical and Experimental Analysis of Ultrasound Velocity and Refractive Index in Binary Mixtures of Pharmaceutically Important Polymer—PEG 600

R. Padmanaban, K. Venkatramanan, S. Girivel, K. Kasthuri, A. Usharani, A. Gayathri and Roy Vellaichamy

Abstract The estimation of ultrasonic velocity, refractive index and acoustical parameters are being increasingly used as tools for investigation of the properties of pure components and the nature of intermolecular interactions between the liquid mixture constituents. Polyethylene glycol (PEG) is a chemical that has a variety of applications in the world of medicine. It is used as a base to manufacture certain medicines, assist in drug delivery and is also used as an agent for some medical procedures. The present study proposes to estimate the viscosity of Polyethylene Glycol (Molar mass: 600) (PEG 600) at different concentrations (2, 4, 6, 8, 10, 12, 14, 16, 18 and 20 % w/v), in the temperature range from 303 to 318 K in steps of 5 K. The activation energy is determined and the impact of the solvent is studied from the experimental data. Density, ultrasonic velocity and refractive index have been estimated for aqueous solutions of PEG 600 at 303 K. The experimental ultrasound velocities are compared with theoretically calculated values obtained by using various mathematical methods like Vandeal Vangeal Relation, Nomotto's Relation, Rao's specific sound velocity and Impedance Relation. Similarly the experimental refractive index values are compared with theoretical values obtained from various mathematical methods like Lorentz-Lorentz relation, Newton relation, Heller relation, Arago-Biot relation, Gladstone-Dale equation and Eyring-John equation. The average percentage error (APE) is determined to identify the most suited method that agrees with the experimental values and discussions are made in the light of molecular interactions that occur in the binary liquid systems.

R. Padmanaban · K. Venkatramanan (✉) · S. Girivel · K. Kasthuri · A. Usharani
Department of Physics, SCSVMV University, Kanchipuram 631561, India
e-mail: kv.scsvmv@gmail.com

A. Gayathri
Department of Mathematics, SCSVMV University, Kanchipuram 631561, India

R. Vellaichamy
Department of Physics and Materials Science, City University of Hong Kong, Kowloon, Hong Kong

J. Ebenezar (ed.), *Recent Trends in Materials Science and Applications*,
Springer Proceedings in Physics 189, DOI 10.1007/978-3-319-44890-9_57

Comparative study of estimated theoretical ultrasound velocities and refractive indices with experimental values helps to understand the nature of the interaction occurring among the component molecules in the mixtures. This kind of study is useful to identify and predict a comprehensive theoretical model for a specific liquid mixture. Also, various molecular interaction parameters like viscous relaxation time, inter-atomic free length, free volume, internal pressure, etc. are calculated and discussed in terms of polymer-solvent interactions.

1 Introduction

Ultrasonic study has become an interesting research tool in the field of polymers to determine the structure and molecular interactions in liquid systems. Polyethylene glycol is widely applicable in textiles, rubber, leather and pharmaceutical and industries. Liquids, liquid mixtures and solutions have found wide applications in chemical, textile, leather and nuclear industries, which is well explained by few researchers [1, 2]. Venkatramanan et al. [3] have studied the ultrasonic velocity, viscosity and density of polyethylene glycols in water mixture. In the recent years ultrasonic measurements are very useful in chemical and food processing, material testing under water ranging and cleaning. The measurements of ultrasonic velocity and viscosity have been adequately used to study the nature of molecular systems and thermodynamical behavior in liquid mixtures. Various literature studies on binary and ternary mixtures [4–9] help to understand that measurement of ultrasound velocity and isentropic compressibility are highly useful in knowing molecular interactions of mixtures. Acoustical properties of polymer solutions have shown that ultrasonic velocity and its derived parameters provide much information on molecular interactions, which are of utmost importance for processes involving polymer production and their uses [10]. Many researchers [11–13] have calculated the ultrasonic parameters of polyethylene glycol. But for polyethylene glycol of molecular weight 600, available literature are very few. Therefore in the present investigation, PEG of molecular weight 200 is taken. In the present study, density, viscosity, ultrasonic velocity and refractive index studies have been estimated for aqueous solutions of PEG 600 at different concentrations (2, 4, 6, 8, 10, 12, 14, 16, 18 and 20 % w/v) at a temperature of 303 K. The theoretical values of ultrasonic velocity determined by using various mathematical methods like Nomotto's relation, Vandeal Vangeal relation, Impedance relation, and Rao's specific sound velocity are compared with experimental velocities. In the case of non ideal mixtures, refractive index and density measurements of binary liquid mixtures are very important for the estimation of composition of binary mixtures and these are important where direct experimental measurements are performed over the entire composition range [14]. The experimental refractive index values are compared with theoretical values obtained from various mathematical methods like Lorentz-Lorentz relation, Newton relation, Heller relation, Arago-Biot relation, Gladstone-Dale equation and Eyring-John equation. The average percentage error

(APE) is determined to identify the most suited method that agrees with the experimental values and discussions are made in the light of molecular interactions that occur in the binary liquid systems. Such theoretical study is useful in defining a comprehensive theoretical model for a specific liquid mixture. Also, various molecular interaction parameters like adiabatic compressibility, free volume, internal pressure, viscous relaxation time, surface tension, etc. are calculated and discussions are made to understand interactions that are taking place between polymer and solvent.

2 Materials and Methods

Polyethylene glycol (PEG) 600 (Spectra grade) is obtained from SOUTHERN INDIA SCIENTIFIC COMPANY, Trichy, India. The polymer solutions are prepared by dissolving the polymer in double distilled water in order to get required concentrations (2, 4, 6, 8, 10, 12, 14, 16, 18 and 20 % w/v). A magnetic stirrer (REMI make) operating at a rate of 700 rpm is used for proper mixing of solutions. The relative viscosity of polymer solutions at different temperatures for above concentrations is determined using Brookfield viscometer (accuracy ±0.01 cP). The viscometer is connected to an electronically controlled thermostat having a thermal stability of ±0.05 K for taking measurements at different temperatures. The density values are measured using pycnometric method. K-Roy make electronic balance, having an accuracy of ±0.001 g is used to measure the mass of the liquid. The ultrasonic velocity measurements are performed using Ultrasonic velocity meter at 2 MHz (VCT-70A model) (accuracy ±0.1 m/s). The refractive index measurements are performed using Mittal make Abbe refractometer (accuracy ±0.001). The temperature of viscometer, ultrasonic interferometer and refractometer are maintained at 303 K by circulating water from a thermostat with a thermal stability of ±0.05 K.

3 Results and Discussion

3.1 Activation Energy Studies

Viscosity measurements are carried out for aqueous solutions of PEG 600 in the concentration range from 2 to 20 % at different temperatures from 303 to 318 K in steps of 5 K. Table 1 and Fig. 1 shows the variation of relative viscosity against concentration for the above systems. In all the cases, with increase in concentration, the relative viscosity increases and it decreases with the raise in temperature. It may be due to the development of more frictional forces that are developed between the layers of the solution.

Table 1 Variation of relative viscosity and density of aqueous solutions of PEG 600 with concentration

Concentration (w/v) (%)	Relative viscosity ($\times 10^{-3}$ Ns m^{-2})				Density at 303 K (kg m^{-3})
	303 K	308 K	313 K	318 K	
2	0.92	0.90	0.88	0.86	999.59
4	1.02	1.01	1.00	0.99	1001.70
6	1.26	1.14	1.04	1.01	1004.11
8	1.34	1.23	1.12	1.02	1007.22
10	1.41	1.29	1.17	1.06	1009.93
12	1.50	1.36	1.24	1.13	1014.05
14	1.62	1.46	1.37	1.26	1015.46
16	1.79	1.54	1.47	1.35	1017.77
18	1.96	1.72	1.55	1.42	1020.18
20	2.09	1.87	1.70	1.60	1023.19

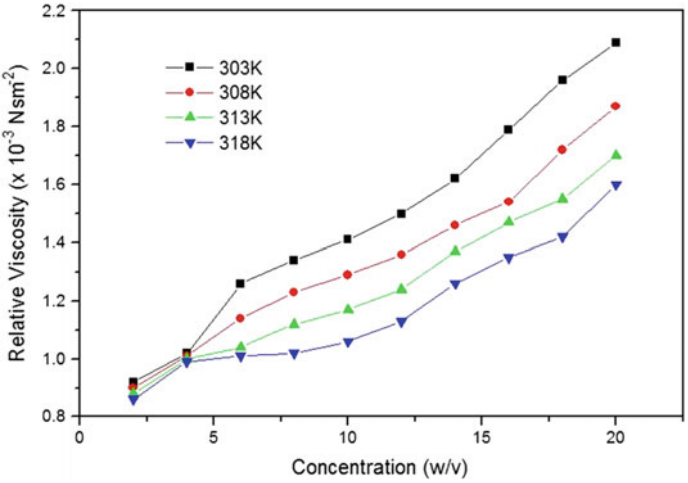

Fig. 1 Variation of relative viscosity against concentration of aqueous solution of PEG 600

The Arrhenius expression which is valid for pure solvents and also for dilute polymer solutions is given by

$$\eta = A\mathrm{e}^{Q/RT} \tag{1}$$

where A is the pre-exponential term with an activation entropy significance and Q is the apparent activation energy of flow. The logarithm of this equation leads to a straight-line type given by

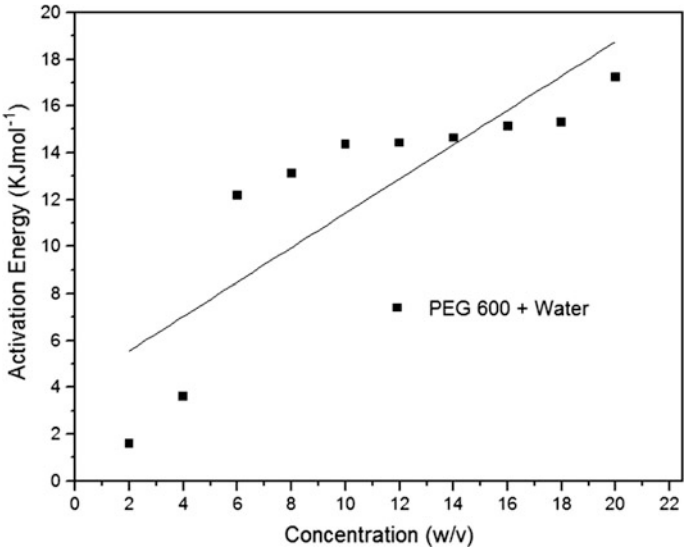

Fig. 2 Variation of activation energy against concentration of PEG 600

$$\ln \eta = \ln A + \left(\frac{Q}{R}\right)\left(\frac{1}{T}\right) \tag{2}$$

The plot of the logarithm of relative viscosity against the inverse of temperature for PEG 600 gives the values of activation energy. The variation of activation energy (Q) with concentration (C) of aqueous solutions of PEG is shown in Fig. 2. This shows that the activation energy increases with increase in concentration. This reveals that as concentration increases, more amount of energy is required to move the molecules into the structure. Similar results are observed by few researchers [3, 15].

3.2 Ultrasonic Studies

Propagation of sound waves in a medium may be treated as a series of compressions and rarefactions travelling along the direction of propagation such that the molecular planes of the medium are displaced from their mean position. Propagation of ultrasound in a medium is concentration dependent. Ultrasonic velocity values of aqueous solutions of PEG 600 are measured at 303 K. The experimental values along with the values calculated mathematically using Nomoto's model, Ideal mixture relation, impedance relation model and Rao's specific sound velocity method are determined for the above systems.

3.3 Mathematical Estimation for Ultrasonic Velocity

Nomoto's empirical formula [16] is based on the assumption of the linear dependence of the molecular sound velocity on concentration and the additivity of the molar volume in the liquid mixture. The ultrasonic velocity U is given by

$$U = [(X_1R_1 + X_2R_2)/(X_1V_1 + X_2V_2)]^3 \tag{3}$$

In the above equation,

$$R_1 = (M_1/\rho_1)(U_1)^{1/3},\ R_2 = (M_2/\rho_2)(U_2)^{1/3},\ V_1 = (M_1/\rho_1),\ V_2 = (M_2/\rho_2)$$

In above equations, X_1 and X_2 are the mole fraction of component liquids. M_1, M_2, U_1, U_2, V_1 and V_2 are the molecular weights, ultrasonic velocity and molar volumes of components of binary liquids mixtures.

Van Deal and Van Geel [17] developed a relation to estimate the value of ultrasound velocity U_{IMR} in an ideal mixture using the sound velocities in the pure components According to Jacobson's theory of free length, the ultrasonic velocity is given by

$$U_{IMR} = \left[1/(X_1M_1 + X_2M_2)^{1/2}\right]\left\{1/\left[(X_1/M_1U_1^2) + (X_2/M_2U_2^2)\right]^{1/2}\right\}. \tag{4}$$

The product of ultrasonic velocity (U) and density (ρ) of the mixture gives the value of acoustic impedance (Z) of the mixture. The sound velocity [18] in the mixture can be calculated by knowing the values of acoustic impedance and the density of the pure components.

$$U_{IDR} = (X_1Z_1 + X_2Z_2)/(X_1\rho_1 + X_2\rho_2) \tag{5}$$

where $Z_1 = U_1\rho_1 \quad Z_2 = U_2\rho_2$.

Rao's specific velocity [19]

$$U_R = (\Sigma X_i r_i \rho_i)^3 \tag{6}$$

where X_i = mole fraction, ρ_i = density and r_i = Rao's specific sound velocity of the mixture.

Ultrasonic velocity and density for the pure components of PEG 600 with water values are measured at 303 K. The experimental values along with the values calculated numerically using Nomoto's relation, ideal mixture relation, impedance relation and Rao's specific sound velocity relation for the system PEG 600 + water is given in Table 2.

It can be seen from Table 2 that the mathematical values of ultrasonic velocity calculated by using various theories show deviation from experimental values. The

Table 2 Experimental and mathematical ultrasonic velocity of aqueous solutions of PEG 600

Concentration (w/v) (%)	Ultrasonic velocity (m/s)				
	Experimental values	Nomotto's relation	Vandeal Vangeal	Impedance relation	Rao's specific sound velocity
2	1505.905	1496.180	1478.239	1493.814	1493.806
4	1515.144	1497.455	1463.231	1493.866	1493.852
6	1523.869	1498.682	1448.710	1493.919	1493.898
8	1529.531	1499.865	1434.651	1493.971	1493.944
10	1540.983	1501.005	1421.031	1494.023	1493.990
12	1550.009	1502.104	1407.827	1494.075	1494.036
14	1557.831	1503.166	1395.018	1494.127	1494.081
16	1564.409	1504.191	1382.587	1494.179	1494.127
18	1572.377	1505.182	1370.515	1494.231	1494.172
20	1579.752	1506.140	1358.786	1494.282	1494.218

limitations and approximation incorporated in these theories are responsible for the deviations of mathematical values from experimental values. According to Nomoto's model, the interaction between the molecules of two liquids takes place when two liquids re mixed. This interaction is due to the presence of different types of forces like hydrogen bonding, dipole-dipole, dispersive forces, charge transfer and dipole-induced dipole interactions. The deviation of experimental values from mathematically estimated values calculated using Van Dael and Van Geel equation might be due to the high value of adiabatic compressibility of the component liquids present in the mixture. The deviation of experimental values and values calculated from impedance relation and Rao's relation imply non-additivity of acoustic impedance and Rao's velocity in the liquid mixture. This observed deviation in the velocity reveals the existence of molecular interactions that are taking place between the unlike molecules in the liquid mixture.

The variation of percentage of deviation for different compositions of PEG 600 in water at 303 K is shown in Table 3.

In this system, we understand that the percentage of deviation is more in Van Deal and Van Geel method and less in Nomotto's relation method. From this, it shall be concluded that Nomotto's mathematical model is the most suitable method for determining the ultrasound velocity for the systems that are taken for the present research work.

3.4 Density Studies

From Table 1, it is noted that as the concentration of PEG 600 increases, the density also increases. This may be due to the fact that as the polymer concentration

Table 3 Percentage deviation of ultrasonic velocity of aqueous solutions of PEG 600

Concentration (w/v) (%)	Percentage of deviation			
	Nomotto's relation	Vandeal Vangeal	Impedance relation	Rao's specific sound velocity
2	0.645816	1.837144	0.802877	0.803388
4	1.167506	3.426252	1.404303	1.405232
6	1.652829	4.932077	1.965389	1.966728
8	1.939579	6.203160	2.324880	2.326629
10	2.594349	7.784108	3.047383	3.049528
12	3.090612	9.172973	3.608599	3.611139
14	3.50906	10.45120	4.089254	4.092183
16	3.849243	11.62236	4.489221	4.492539
18	4.273464	12.83797	4.969927	4.973624
20	4.659701	13.98738	5.410296	5.414371

increases, the number of polymer chains attached to the solution may also found to increase. This also contributes to the increase in the density of the system taken for study.

3.5 Refractive Index Studies

In order to know the structural characterization of liquid mixtures, it is essential to know the values of refractive index of these mixtures for different temperatures. In addition to available thermodynamic data, refractive index values are also helpful for calculating various engineering applications. Knowledge of refractive index is highly essential to determine the purity of various substances and also to calculate their molecular electronic polarizability. To determine the boiling point using Meissner's method or to estimate various rheological properties such as viscosity and other thermodynamic properties, study of an optical property (refractive index) will be highly useful.

The experimental refractive index along with the values calculated mathematically using Lorentz-Lorentz model, Newton's method, Heller relation, Arago-Biot model, Gladstone-Dale equation and Eyring and John equation for the above systems are reported in Table 3.

Lorentz-Lorentz (L-L): It is given by:

$$(n_{12}^2 - 1)/(n_{12}^2 + 2) = (\phi_1(n_1^2 - 1)/(n_1^2 + 2) + \phi_2(n_2^2 - 1)/(n_2^2 + 2)) \quad (7)$$

where n_{12} is refractive index of the mixture, n_1 and n_2 are refractive indices of pure components of 1 and 2 respectively. Here φ_1 and φ_2 are volume fractions of components 1 and 2 respectively and the relation is given by

$$\phi_i = X_i V_i / \Sigma X_i V_i$$

where X_i and V_i are the mole fraction and molar volume of *i*th constituent of binary mixture.

Newton model (Nw):

$$(n_{12}^2 - 1) = (n_1^2 - 1)\phi_1 + (n_2^2 - 1)\phi_2 \tag{8}$$

Heller model (H):

$$(n_{12} - n_1)/n_1 = 3/2\phi_2\left((n_2/n_1)^2 - 1\right)/\left((n_2/n_1)^2 + 2\right) \tag{9}$$

Arago-Biot relation (A-B):

$$n_{12} = n_1\phi_1 + n_2\phi_2 \tag{10}$$

Gladstone-Dale (G-D) equation:

$$(n_{12} - 1) = (n_1 - 1)\phi_1 + (n_2 - 1)\phi_2 \tag{11}$$

Eyring and John Equation (E-J):

$$n_{12} = n_1\phi_1^2 + 2(n_1 n_2)^{1/2}\phi_1\phi_2 + n_2\phi_2^2 \tag{12}$$

Table 4 reveals that the values of the refractive index determined using Arago-Biot and Gladstone-Dale mixing rules are similar for the above system. But, little variation is observed in the mathematical values calculated by Eyring and John than Lorentz-Lorentz and Newton equation. Large deviation is observed in Heller model. The estimated experimental values of refractive index are compared with the results obtained from the above-mentioned numerical models. The percentage of deviation of refractive index values of numerical model from experimental values is determined and they are given in Table 5. It is evident from Table 5 that in all these systems, there exist a good similarity between experimental and numerical values of the refractive index calculated by six different mixing rules. Comparison of deviations in the above system shows that excellent agreement between theoretical and experimental values is observed for concentrations 2, 4, 12 and 14 % followed by Arago-Biot and Gladstone-Dale mixing rules. These results show that the above mentioned mathematical mixing rules perform well within the limits of experimental error. The deviation between the theoretical and observed values of refractive index for the above systems can be minimized by taking excess volume values into consideration [19, 20], because analysis of excess volume is also an indirect measure of molecular interaction of liquid systems.

Table 4 Experimental and mathematical refractive index values of aqueous solutions of PEG 600

Concentration (w/v) (%)	Refractive index						
	Experimental values	L-L	Nw	H	A-B	G-D	E-J
2	1.3415	1.3414	1.3416	1.3399	1.3415	1.3415	1.3415
4	1.3440	1.3438	1.3442	1.3424	1.3440	1.3440	1.3439
6	1.3460	1.3461	1.3467	1.3448	1.3464	1.3464	1.3462
8	1.3480	1.3483	1.3491	1.3471	1.3486	1.3486	1.3484
10	1.3500	1.3504	1.3514	1.3493	1.3508	1.3508	1.3506
12	1.3530	1.3524	1.3536	1.3515	1.3530	1.3530	1.3527
14	1.3550	1.3544	1.3557	1.3535	1.3550	1.3550	1.3547
16	1.3575	1.3563	1.3577	1.3555	1.3570	1.3570	1.3566
18	1.3600	1.3581	1.3597	1.3575	1.3589	1.3589	1.3585
20	1.3620	1.3599	1.3616	1.3593	1.3607	1.3607	1.3603

Table 5 Percentage of deviation of refractive index of aqueous solutions of PEG 600

Concentration (w/v) (%)	Refractive index					
	L-L	Nw	H	A-B	G-D	E-J
2	0.003899	−0.013420	0.118150	−0.004892	−0.0048923	−0.00053
4	0.013964	−0.019290	0.118041	−0.002405	−0.0024052	0.005963
6	−0.006760	−0.054700	0.087851	−0.030141	−0.0301412	−0.01808
8	−0.021400	−0.082850	0.064372	−0.051257	−0.0512575	−0.03579
10	−0.030280	−0.104210	0.047213	−0.066140	−0.0661405	−0.04753
12	0.040200	−0.045170	0.109895	−0.001183	−0.0011833	0.02031
14	0.041765	−0.054200	0.104207	−0.004756	−0.0047566	0.01941
16	0.084994	−0.020720	0.140615	0.033731	0.0337316	0.06035
18	0.132668	0.017970	0.181893	0.077019	0.0770190	0.10590
20	0.147897	0.024870	0.191138	0.088167	0.0881671	0.11915

3.6 Molecular Interaction Parameters

Compressibility of a liquid system gives an idea with which a medium can be compressed. Table 6 shows that the adiabatic compressibility decreases with increase in concentration. This is as per the general trend observed for polymer solutions. In high concentrated solution, more cohesion is expected and this leads to a decrease in adiabatic compressibility. The decrease in adiabatic compressibility results in the increase of ultrasonic velocity. The increase in adiabatic compressibility for a decrease of concentration of the solution may be due to the dispersion of solvent molecules around ions which are supporting weak ion-solvent interactions. This trend indicates the formation of strong hydrogen bonding between solute and solvent. Adiabatic compressibility is more in the case of bulky and less polar

Table 6 Various molecular interaction parameters

Concentration (w/v) (%)	Adiabatic compressibility ($\times 10^{-10}$ m^2 N^{-1})	Inter molecular free length ($\times 10^{-11}$ m)	Classical absorption co-efficient ($\times 10^{-14}$ m^{-1} s^{-2})	Relaxation time ($\times 10^{-13}$ s)	Gibbs free energy ($\times 10^{-24}$ kJ mol^{-1})
2	4.4114	4.3582	0.7085	5.4114	5.1394
4	4.3486	4.3271	0.7697	5.9141	5.5110
6	4.2886	4.2971	0.9323	7.2049	6.3369
8	4.2438	4.2746	0.9775	7.5823	6.5504
10	4.1697	4.2371	1.0031	7.8391	6.6898
12	4.1045	4.2039	1.0443	8.2092	6.8828
14	4.0578	4.1799	1.1094	8.7650	7.1568
16	4.0146	4.1576	1.2077	9.5817	7.5295
18	3.9646	4.1316	1.2993	10.3610	7.8566
20	3.9162	4.1063	1.3622	10.9130	8.0738

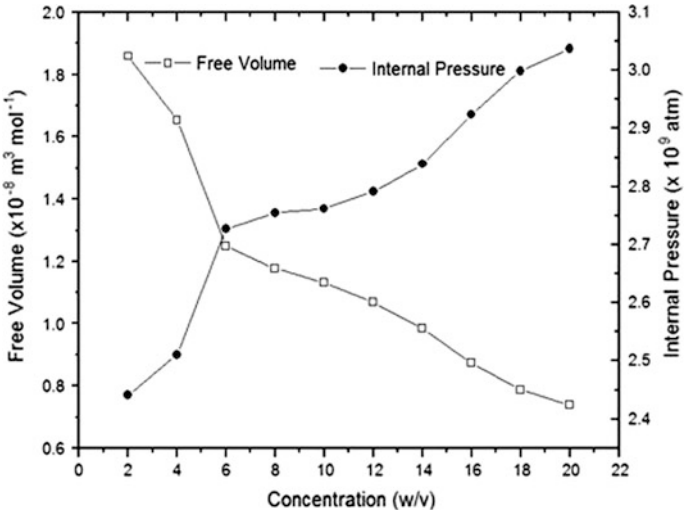

Fig. 3 Variation of free volume and internal pressure against concentration of aqueous solution of PEG 600

substituent. Intermolecular free length also behaves in the same fashion like adiabatic compressibility. Compressibility and free length are the deciding factors of the ultrasonic velocity in liquid systems. Free volume may be defined as the average volume in which the central molecule can move inside the hypothetical cell freely without getting affected by the repulsion of surrounding molecules. Viscous relaxation time increases with increase in concentration and this shows that viscous forces play a dominant role in the relaxation process. This indicates that the solution is highly ordered due to outstanding hydration and such solution generally absorbs more ultrasonic energy [3]. Similar trend is observed for classical absorption co-efficient values. Gibb's energy increases with increasing concentration of PEG 600. The increase in Gibb's free energy in the liquid mixture reveals that more time will be taken for the rearrangement of molecules in the liquid mixture which increases the energy of the system This increase in energy leads to dissociation of molecules. Free volume follows the reverse trend of viscosity. Therefore, viscosity rather than velocity determines the free volume of the present system. Since the viscosity of the polymer is varied due to molecular interaction or polymer salvation, same parameters are influencing the free volume also. Free volume decreases when the internal pressure increases (Fig. 3).

The decrease in free volume shows that the strength of interaction decreases gradually with the increase in solute concentration. It represents that there is a weak interaction between the solute and solvent molecules. The internal pressure may give information regarding the nature and strength of forces existing between the molecules. From Fig. 3, it is evident that the internal pressure increases with

increase in the concentration of PEG600. The reason for the increase in internal pressure may be due to the presence of attractive forces between the solvent - polymer molecules.

4 Conclusion

Relative viscosity of polyethylene glycol (PEG 600) in water is determined for various concentrations at different temperatures from 303 to 318 K in steps of 5 K. Density, ultrasonic velocity and refractive index values are determined at 303 K.

(1) It is found that the activation energy of PEG 600 is increased with increase in concentration for all the systems.
(2) Density and Ultrasonic velocity vary linearly with increase in concentration.
(3) Nomato's relation, Van Deal and Van Geel ideal mixing relation, Impedance relation and Rao's specific velocity relation are used for mathematical computation of ultrasonic velocities in the binary liquid mixtures of PEG 600 + water at 303 K. From these numerically calculated values of ultrasonic velocities, it is concluded that Nomotto's relation is found to be best suited to experimental values by having minimum percentage error over a whole concentration range. Mathematical evaluation of ultrasonic velocity in binary liquid mixtures and their comparison with experimental values reflects the existence of molecular interaction.
(4) It is observed that refractive index for the above system is found to increase with increase in concentration. All six mixing rules could be successfully applied. All six theoretical mixing rules are performed well within the limits of experimental error. The deviation between theoretical and observed values of refractive index for the above system taken for study can be reduced if the concept of excess molar volume is taken into consideration.
(5) Variation of molecular interaction parameters with concentration suggested the presence of strong polymer-solvent interaction at higher concentration and the effect of concentration is analyzed.

Acknowledgements The authors acknowledge the financial support rendered by SCSVMV University, Enathur, Kanchipuram, in carrying out this research work.

References

1. Acree, W.E.: Thermodynamics Properties of Nonelectrolytic Solutions, 1st edn. Academic Press, New York, Orlando (1984)
2. Prausnitz, J.M., Linchenthalr, B., Azevedi, E.G.: Molecular Thermodynamics of Fluid-Phase Equilibria, 2nd edn. Prentice Hall Inc, Prentice (1986)

3. Venkatramanan, K., Padmanaban, R., Arumugam, V.: Acoustic, thermal and molecular interactions of Polyethylene Glycol (2000, 3000, 6000). Phys. Procedia **70**, 1052–1056 (2015)
4. Sheba, S.G.S., Priakumari, R.O.: Ultrasonic investigation of molecular interaction in binary liquid mixture of Polyethylene Glycol with ethanol. Int. J. Chem. Mol. Nucl. Mater. Metall. Eng. **8**, 156–160 (2014)
5. Ganapathi Rao, G., Mehar, M.V.K., Prasad, K.V., Samatha, K.: Ultrasonic studies and excess properties of binary mixtures of Ethylmethylketone and Chlorobenzene at 308.15 K. Int. J. Innovative Res. Sci. Eng. Technol. **4**, 5512–5520 (2015)
6. Rajavelu, S.: Ultrasonic study of molecular interaction in binary liquid mixtures at 303 K, 308 K and 313 K. Int. J. Sci. Res. **3**, 845–848 (2014)
7. Sherif, A., Afsar, N., Narayanan, S.: Ultrasonic studies of molecular interactions of certain Zinc electrolytes in Poly (Ethylene Glycol). J. Chem. Pharm. Res. **7**, 657–662 (2015)
8. Dash, A.K., Paikaray, R.: Ultrasonic studies on molecular interaction in ternary liquid mixture of Dimethyl Acetamide at different frequencies. Int. J. Adv. Sci. Technol. **66**, 89–104 (2014)
9. Sumathi, T., Maheswari, J.U.: Ultrasonic and theoretical studies of some ternary liquid mixtures at various temperatures. Indian J. Pure Appl. Phys. **47**, 782–786 (2009)
10. Saxena, R.: Molecular interactions of aqueous solution of Polyethylene Glycol. Int. J. Sci. Res. **3**, 1465–1469 (2014)
11. Palani, R., Balakrishnan, S., Roomy, A.M.S.: Acoustical and thermodynamical properties of PEG in non-electrolytes at 303, 313 and 323 K. Arch. Phys. Res. **1**, 111–118 (2010)
12. Gayathri, A., Venugopal, T., Venkatramanan, K.: A comparative analysis of ultrasound velocity in binary liquid systems of PPG by mathematical and experimental methods. Phys. Procedia **70**, 241–244 (2015)
13. Venkatramanan, K., Arumugam, V.: Viscosity studies on polypropylene glycol and its blend. Int. J. Thermophys. **27**, 66–78 (2006)
14. Sharma, S., Patel, P.B., Patel, R.S., Vora, J.J.: Density and comparative refractive index study on mixing properties of binary liquid mixtures of Eucalyptol with Hydrocarbons at 303.15, 308.15 and 313.15 K. E-J. Chem. **4**, 343–349 (2007)
15. Guadalupe Olayo, M., Cruz, G.J., Lopez, S., Morales, J., Olayo, R.: Conductivity and activation energy in polymers synthesized by Plasmas of Thiophene. J. Mex. Chem. Soc. **54**, 18–23 (2010)
16. Narendra, K., Sudhamsa, B., Sarath Babu, M.: Theoretical evaluation of speeds of sound in liquid mixtures containing Diethyl carbonate and Aniline at various temperatures. Res. J. Chem. Sci. **4**, 42–45 (2014)
17. Santhi, N., Sabarathinam, P.L., Madhumitha, J., Alamelumangai, G., Emayavaramban, M.: Theoretical evaluation of ultrasonic velocity in binary liquid mixtures of Alcohols [S] + Benzene. Int. Lett. Chem. Phys. Astron. **2**, 18–35 (2013)
18. Ramteke, J.N., Khasare, S.B.: Comparison of theoretical ultrasonic velocities in binary liquid mixture containing α-Picoline in Ethanol. Adv. Appl. Sci. Res. **3**, 3415–3420 (2010)
19. Sridevi, G., Fakruddin, S.K.: Experimental and theoretical studies of ultrasonic velocity in binary liquid mixtures of methyl benzoate at different temperatures. J. Chem. Pharm. Res. **4**, 3792–3796 (2010)
20. Baluja, S., Pandaya, N., Kachhadia, N., Solanki, A.: Theoretical evaluation of refractive index in binary liquid mixtures. E-J. Chem. **2**, 157–160 (2005)

Thermal and Rheological Studies of Aqueous Solutions of PEG 400 and PEG 1500 Having Pharmaceutical Applications

R. Padmanaban, K. Venkatramanan, S. Girivel, K. Kasthuri, A. Usharani and Roy Vellaichamy

Abstract Polyethylene glycol is formed by the interaction of ethylene oxide with water, ethylene glycol or ethylene glycol oligomers. Acidic or basic catalysts are used as catalysts in this reaction. Ethylene glycol and its oligomers are preferable as a starting material instead of water because it allows the creation of polymers with a low polydispersity. Polyethylene glycol has many desirable applications like an anti-dusting agent in agricultural formations, dye carrier in paints and ink and mold release agent, etc. Molecular interaction studies of PEG in various solvents are reported by many researchers. It is proposed to determine the activation energy and the molecular interaction properties of Polyethylene Glycol (PEG 400 and PEG 1500) in water for various concentrations ranging from 1 to 5 % at different temperatures from 303 to 318 K in steps of 5 K from the knowledge of relative viscosity which can be determined using a suitable viscometer.

1 Introduction

The material taken for the present analysis is Polyethylene glycol which has a lot of applications in pharmaceutical preparations, cosmetics, medical devices and in the metal casting process [1]. Thermodynamic properties of polymer solutions have shown that ultrasonic velocity and its derived parameters provide much information on molecular interactions, which are of utmost importance for processes involving polymer production and their uses. Many reports [1–3] are there in the literature on

R. Padmanaban (✉) · K. Venkatramanan · S. Girivel · K. Kasthuri · A. Usharani
Department of Physics, SCSVMV University, Kanchipuram 631561, India
e-mail: padhu.mphil@gmail.com

R. Vellaichamy
Department of Physics and Materials Science, City University of Hong Kong, Kowloon, Hong Kong

J. Ebenezar (ed.), *Recent Trends in Materials Science and Applications*,
Springer Proceedings in Physics 189, DOI 10.1007/978-3-319-44890-9_58

ultrasonic studies of solutions of PEG in binary aqueous + non-aqueous solvent systems. Activation energy is a term used to describe the minimum energy that must be available for initiating a chemical process. For analyzing the properties and interactions taking place in polymer-polymer systems, knowledge of rheological properties is essential and viscometry is one of the efficient techniques for studying the properties. A positive and attractive interaction enhances the viscosity of the systems taken for this analysis. The effect of temperature in determining the viscosity of polymers was reported by many researchers over a period of time [4–6]. In the present proposal, it is planned to apply Arrhenius equation to dilute polymer solutions. It has been reported by many researchers [7–9] that the concentration, molecular weight, chain stiffness and coil expansion of polymers play a vital role for the activation energy of flow. The pre-exponential term also depends on these parameters. It is also observed that the variation between the activation energy of the solution and the solvent is very much greater than that of the flexible chains. Guadalupe Olayo et al. [10] have studied the electrical conductivity, activation energy, and morphology of polythiophene synthesized by radio frequency resistive plasmas. In the present proposal, aims to determine the activation energy and the molecular interaction properties of Polyethylene Glycol (PEG 400 and PEG 1500) in water for various concentrations ranging from 1 to 5 % at different temperatures from 303 to 318 K in steps of 5 K from the knowledge of relative viscosity. Various molecular interaction parameters such as free volume, intermolecular free length, internal pressure and adiabatic compressibility are calculated and the results are interpreted.

2 Materials and Methods

The polymers used for the present study (PEG 400 and PEG 1500, SPECTRA Grade) are supplied by SOUTHERN INDIA SCIENTIFIC, Trichy. The polymers PEG 400 and PEG 1500 are dissolved in double distilled water and the polymer solutions are prepared for various concentrations (1, 2, 3, 4 and 5 %). A REMI make magnetic stirrer operating at a rate of 1000 rpm is used for preparing the polymer solutions. Ubbelohde Viscometer is used to determine the relative viscosity of the prepared polymer solutions at different concentrations at 303, 308, 313 and 318 K. A RACER make digital stopwatch is used to measure the timings (± 0.01 s). The viscometer was kept in an electronically controlled thermostat having a thermal stability of ± 0.05 K for taking measurements at different temperatures. Pycnometric method is employed to determine the density of the solutions. A K-ROY electronic balance having an accuracy of ± 0.001 g is used to measure the mass of the liquid. A digital ultrasonic velocity meter (VCT-70A model, VI MICROSYSTEMS) is used to measure the ultrasonic velocity.

The measurements were taken at a frequency of 2 MHz (accuracy ±0.1 m/s). The ultrasound velocity measurements are taken at 303 K by circulating water from a thermostat having a thermal stability of ±0.05 K.

3 Results and Discussion

3.1 Determination of Activation Energy

Viscosity measurements are taken for Polyethylene glycol (PEG 400 and PEG 1500) in aqueous solution in the concentration range from 1 to 5 % at different temperatures from 303 to 318 K in steps of 5 K. Table 1 shows the variation of relative viscosity against concentration for PEG 400 and PEG 1500 in water at temperatures from 303 to 318 K. The results show that the relative viscosity increases as concentration increases and the relative viscosity decreases with rising temperature. The reason for this behavior may be due to the development of large frictional force between the layers of the solution.

The Arrhenius expression which is valid for pure solvents and also for dilute polymer solutions is give by Moore et al. [11] as mentioned below

$$\eta = A e^{Q/RT} \tag{1}$$

where A is the pre-exponential term with an activation entropy significance and Q is the apparent activation energy of flow. The logarithm of this equation leads to a straight-line type. Activation energy is obtained by plotting a graph between logarithm of relative viscosity and inverse of temperature for PEG (400, 1500).

Table 1 Relative viscosity and activation energy values of aqueous PEG

Compound	Concentration (w/v) (%)	Relative viscosity ($\times 10^{-3}$ Nsm^{-2})				Activation energy (KJ mol^{-1})
		303 K	308 K	313 K	318 K	
PEG 400	1	1.0583	1.0512	1.0210	1.0132	2.4854
	2	1.0731	1.0623	1.0321	1.0210	2.7790
	3	1.0812	1.0731	1.0432	1.0306	2.6746
	4	1.0934	1.0802	1.0614	1.0556	1.9284
	5	1.1121	1.1050	1.0733	1.0690	2.2998
PEG 1500	1	1.0731	1.0593	1.0330	1.0296	2.3165
	2	1.0851	1.0731	1.0451	1.0399	2.3871
	3	1.0923	1.0851	1.0552	1.0431	2.5767
	4	1.1256	1.1091	1.0762	1.0656	3.0106
	5	1.1531	1.1321	1.0913	1.0876	3.2920

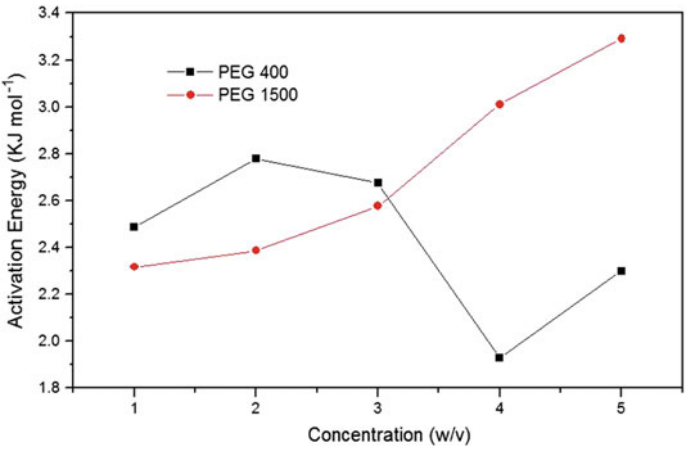

Fig. 1 Variation of activation energy against concentration of aqueous solutions of PEG

The variation of activation energy (Q) against concentration (C) of aqueous solution of PEG 400 in water is shown in Fig. 1. In this system, it is observed that the activation energy suddenly decreases for 2 % concentration. It is understood that as polymer concentration increases the activation energy for the viscous flow of polymer solution also increases and this is not observed in critical mixtures [12]. The reason for sudden decrease is that the activation energy for the viscous flow of polymer solutions in poor solvent decreases with polymer concentration at high dilution and this is ascribed to the temperature dependence of the limiting viscosity number [13]. Figure 1 depicts the change in activation energy of aqueous solution of PEG 1500 against concentration (C). It is observed that as concentration increases the activation energy also increases, which reveals that more amount of energy is required to move the molecules into the structure [10].

3.2 Density and Ultrasonic Velocity Studies

Figure 2 shows that the density of the polymer solutions taken for the study increases with concentration. The reason for this increase is because of the addition of more number of polymer chains with increase in the concentration of polymer solutions. The molecular weight of the polymers is comparatively higher than that of the solvents. This characteristic feature may also contribute to the increase in the density of the solution.

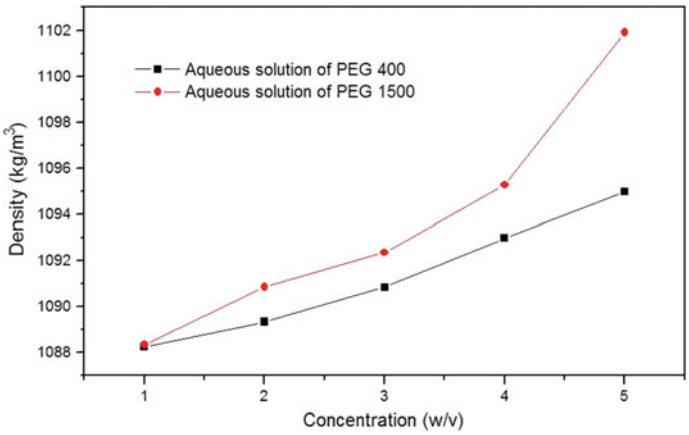

Fig. 2 Variation of density against concentration of aqueous solutions of PEG

The variation of ultrasonic velocity (Fig. 3) against concentration indicates the presence of strong solute-solvent interaction. As density increases, number of particles in the given region also increases, which leads to quick transfer of sound velocity and hence ultrasonic velocity increases with concentration.

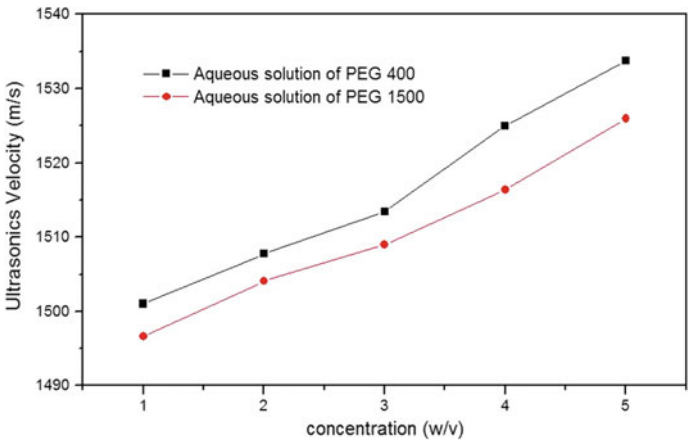

Fig. 3 Variation of ultrasonic velocity against concentration of aqueous solutions of PEG

3.3 Molecular Interaction Analysis

It is observed that as concentration increases the adiabatic compressibility decreases. This indicates that the molecules may be closely packed and less ionic repulsion exists between the molecules. This also reveals that the bond strength is enhanced at higher concentration. The inverse behavior of adiabatic compressibility with ultrasonic velocity is clearly observed. This reveals the existence of the significant interaction between solute and solvent molecules. This indicates the formation of complexes among the molecules. Table 2 shows that there is a decrease in the intermolecular free length with increase in concentration. Due to dominant repulsive force a weak molecular interaction is exhibited by the molecules at lower concentration. Significant interaction exists at higher concentration. In view of greater forces of interaction between solute and solvent molecules forming hydrogen bonding, there will be a decrease in free length in the mixture. Free volume is defined as the average volume in which the central molecule can move inside the hypothetical cell freely without getting affected by the repulsion of surrounding molecules. A reverse trend of viscosity with free volume is observed in the present case. So it is understood that ultrasound velocity may be responsible for the free volume of the polymer solutions taken for analysis than the viscosity of the systems. Since the viscosity of the polymer is varied due to molecular interaction or polymer salvation, same parameters may influence the free volume also. It is observed that the free volume decreases with increase in internal pressure. The molecular interaction of the liquid is understood from the knowledge of the internal pressure of the liquid. As the concentration of polyethylene glycol increases the internal pressure of the system also increases. This increase in the internal pressure of the polymer may be due the presence of strong attractive force between the polymer and solvent molecules.

Table 2 Various molecular interaction parameters of aqueous PEG

Compound	Concentration (w/v) (%)	Adiabatic compressibility ($\times 10^{-10}$ m^2 N^{-1})	Free length ($\times 10^{-11}$ m)	Free volume ($\times 10^{-8}$ m^3 mol^{-1})	Internal pressure ($\times 10^9$ atm)
PEG 400	1	4.0784	4.1905	1.4778	2.8072
	2	4.0381	4.1697	1.4777	2.7916
	3	4.0024	4.1512	1.4900	2.7692
	4	3.9339	4.1156	1.5027	2.7480
	5	3.8824	4.0885	1.4978	2.7376
PEG 1500	1	4.1020	4.2026	1.4416	2.8300
	2	4.0522	4.1770	1.4493	2.8110
	3	4.0204	4.1606	1.4631	2.7868
	4	3.9706	4.1347	1.4292	2.7958
	5	3.8971	4.0963	1.4114	2.8011

4 Conclusion

Different concentrations of aqueous solutions of polyethylene glycol (PEG 400 and PEG 1500) are prepared. The relative viscosity is determined for various temperatures (303, 308, 313, and 318 K) for these samples. From these values, activation energy is calculated. From Fig. 1, it is noted that there is a decrease in the activation energy of the system taken for the study. From this, it is concluded that the activation energy for the viscous flow of polymer solution in a poor solvent decreases with polymer concentration at high dilution and this is due to the temperature dependence of the limiting viscosity number. But for PEG 1500, the activation energy varies linearly. This reveals that as concentration increases more amount of energy is required to move the molecules into the structure. From these systems, it may be concluded that water is a poor solvent for PEG 400 and acts as a good solvent for PEG 1500. Density and ultrasonic studies are done at 303 K. It is found that the activation energy increases with increase in concentration for all the systems. Density and ultrasonic velocity are found to increase with an increase in concentration. The presence of strong interaction between polymer and solvent at higher concentrations is observed by analyzing the variation of molecular interaction parameters with increase in concentration. This helps to analyse the effect of concentration on the system taken for study.

Acknowledgements The authors acknowledge the financial support of SCSVMV University, Enathur, Kanchipuram for carrying out this research work.

References

1. Syal, V.K., Chauhan, A., Chauhan, S.: Ultrasonic velocity, viscosity and density studies of poly (ethylene glycols) (PEG-8000, PEG-20,000) in acetonitrile (AN) and water (H_2O) mixtures at 25 °C. J. Pure Appl. Ultrason. **27**, 61–69 (2005)
2. Venkatramanan, K.: A study on the molecular interaction of PEG 1000 and its blend in toluene using ultrasonic technique. Int. Rev. Chem. Eng. **3**, 308–311 (2011)
3. Venkatramanan, K., Padmanaban, R., Arumugam, V.: Acoustic, thermal and molecular interactions of polyethylene glycol (2000, 3000, 6000). Phys. Proc. **70**, 1052–1056 (2015)
4. Han, F., Zhang, J., Chen, G., Wei, X.: Density, viscosity, and excess properties for aqueous Poly(ethylene glycol) solutions from (298.15 to 323.15) K. J. Chem. Eng. Data **53**, 2598–2601 (2008)
5. Abbas, K., Iram, B., Seemab, P., Khalid, M., Mohammad, S.: Surface tension, density and viscosity studies on the associative behaviour of oxyethylene-oxybutylene diblock copolymers in water at different temperatures. Int. J. Org. Chem. **2**, 82–89 (2012)
6. Regupathi, I., Govindarajan, R., Pandian Amaresh, S., Murugesan, T.: Densities and viscosities of polyethylene glycol 6000+ triammonium citrate + water systems. J. Chem. Eng. Data **54**, 3291–3295 (2009)
7. Venkatramanan, K., Arumugam, V.: Viscosity studies on PPG and its blend in toluene. Int. J. Thermophys. **27**, 66–78 (2006)
8. Padmanaban, R., Venkatramanan, K.: On the analysis of activation energy of PS 35000 in various solvents, vol. 1675. In: AIP Conference Proceedings, 020019-1-4 (2015)

9. Al-Furhood, J.A., Alsewailem, F.D., Almutabaqani, L.A.: Activation energy for the pyrolysis of polymer wastes. Eur. Chem. Bull. **3**, 93–97 (2014)
10. Guadalupe Olayo, M., Cruz, G.J., Lopez, S., Morales, J., Olayo, R.: Conductivity and activation energy in polymers synthesized by plasmas of thiophene. J. Mex. Chem. Soc. **54**, 18–23 (2010)
11. Moore, W.R., Brown, A.M.: Viscosity-temperature relationships for dilute solutions of cellulose derivatives: I. Temperature dependence of solution viscosities of ethyl cellulose. J. Colloid Sci. **14**, 1–12 (1959)
12. Debye, P., Chu, B., Woermann, D.: Viscosity of critical mixtures. J. Poly Sci. Part A Poly. Chem. **1**, 249–254 (1963)
13. Okada, R., Tanzawa, H.: Apparent activation energy for the viscous flow of polymer solutions. J. Poly. Sci. Part A General Papers **3**, 4294–4296 (1965)

About the Author

Dr. Jeyasingh Ebenezar is with Jamal Mohamed College (Autonomous), Tiruchirappalli, Tamil Nadu, India, identified as a A-grade college with potential for excellence by the UGC, Government of India, as an Assistant Professor of Physics since August 2006. He completed his pre-doctoral program (M.Phil) and doctoral program (Ph.D), from Department of Physics, Anna University, Chennai, in Biophotonics, and post-doctoral research at the Department of Physics, Laser Group, King Saud University, Riyadh, Saudi Arabia. Prior to joining Jamal Mohamed College (Autonomous), he was working as a Senior Scientist and research group leader in Centre for Laser Spectroscopy, Manipal University, Manipal.

He has to his credit 10 research papers in peer-reviewed journals and 15 research articles presented in national and international conference proceedings. He has collaboration with the Distinguished Prof. Robert R. Alfano, Institute of Ultrafast Spectroscopy Laser (IUSL), the City College of the City University of New York, New York, USA and visiting fellow at the same laboratory. He has a rich experience spanning about two decades in research in Biophotonics, covering the design, prototyping, and clinical testing of optical imaging system (OIS) to detect, diagnose, treat and monitor the molecular spectral signatures of cancers of oral, breast, cervix and skin cancers. He is a pioneer in Stokes Shift Spectroscopy. Presently, he is working on the synthesis/development of biocompatible core shell nanoparticles to be used in biomedical field for imaging, drug release, targeted drug delivery, cell labelling and tissue engineering applications especially for combined diagnosis and therapy of cancers or other diseases.

J. Ebenezar (ed.), *Recent Trends in Materials Science and Applications*,
Springer Proceedings in Physics 189, DOI 10.1007/978-3-319-44890-9

Index

J. Ebenezar (ed.), *Recent Trends in Materials Science and Applications*,
Springer Proceedings in Physics 189, DOI 10.1007/978-3-319-44890-9